

به نام خدا



مرکز دانلود رایگان  
مهندسی متالورژی و مواد

[www.Iran-mavad.com](http://www.Iran-mavad.com)



# Ceramics and Composites Processing Methods

---

# CERAMICS AND COMPOSITES PROCESSING METHODS

---

EDITED BY  
Narottam P. Bansal  
Aldo R. Boccaccini



 **WILEY**

A JOHN WILEY & SONS, INC., PUBLICATION

Copyright © 2012 by The American Ceramic Society. All rights reserved.

Published by John Wiley & Sons, Inc., Hoboken, New Jersey.

Published simultaneously in Canada.

No part of this publication may be reproduced, stored in a retrieval system, or transmitted in any form or by any means, electronic, mechanical, photocopying, recording, scanning, or otherwise, except as permitted under Section 107 or 108 of the 1976 United States Copyright Act, without either the prior written permission of the Publisher, or authorization through payment of the appropriate per-copy fee to the Copyright Clearance Center, Inc., 222 Rosewood Drive, Danvers, MA 01923, (978) 750-8400, fax (978) 750-4470, or on the web at [www.copyright.com](http://www.copyright.com). Requests to the Publisher for permission should be addressed to the Permissions Department, John Wiley & Sons, Inc., 111 River Street, Hoboken, NJ 07030, (201) 748-6011, fax (201) 748-6008, or online at <http://www.wiley.com/go/permissions>.

**Limit of Liability/Disclaimer of Warranty:** While the publisher and author have used their best efforts in preparing this book, they make no representations or warranties with respect to the accuracy or completeness of the contents of this book and specifically disclaim any implied warranties of merchantability or fitness for a particular purpose. No warranty may be created or extended by sales representatives or written sales materials. The advice and strategies contained herein may not be suitable for your situation. You should consult with a professional where appropriate. Neither the publisher nor author shall be liable for any loss of profit or any other commercial damages, including but not limited to special, incidental, consequential, or other damages.

For general information on our other products and services or for technical support, please contact our Customer Care Department within the United States at (800) 762-2974, outside the United States at (317) 572-3993 or fax (317) 572-4002.

Wiley also publishes its books in a variety of electronic formats. Some content that appears in print may not be available in electronic formats. For more information about Wiley products, visit our web site at [www.wiley.com](http://www.wiley.com).

***Library of Congress Cataloging-in-Publication Data:***

Ceramics and composites processing methods / edited by Narottam P. Bansal, Aldo R. Boccaccini.  
p. cm.

Includes bibliographical references and index.

ISBN 978-0-470-55344-2

1. Ceramic materials. 2. Composite materials. I. Bansal, Narottam P. II. Boccaccini, A. R. (Aldo R.)

TA455.C43C469 2012

666--dc23

2011041443

Printed in the United States of America.

10 9 8 7 6 5 4 3 2 1



---

# CONTENTS

---

Preface	vii
Contributors	ix
<b>PART I DENSIFICATION</b>	<b>1</b>
<b>1 SINTERING: FUNDAMENTALS AND PRACTICE</b>	<b>3</b>
<i>Rajendra K. Bordia and Héctor Camacho-Montes</i>	
<b>2 THE ROLE OF THE ELECTRIC CURRENT AND FIELD DURING PULSED ELECTRIC CURRENT SINTERING</b>	<b>43</b>
<i>K. Vanmeensel, A. Laptev, S. G. Huang, J. Vleugels, and O. Van der Biest</i>	
<b>3 VISCOUS-PHASE SILICATE PROCESSING</b>	<b>75</b>
<i>Ralf Müller and Stefan Reinsch</i>	
<b>PART II CHEMICAL METHODS</b>	<b>145</b>
<b>4 COLLOIDAL METHODS</b>	<b>147</b>
<i>Rodrigo Moreno</i>	
<b>5 PROCESSING AND APPLICATIONS OF SOL-GEL GLASS</b>	<b>183</b>
<i>Esther H. Lan and Bruce Dunn</i>	
<b>6 GELCASTING OF CERAMIC BODIES</b>	<b>199</b>
<i>Katherine T. Faber and Noah O. Shanti</i>	
<b>7 POLYMER PROCESSING OF CERAMICS</b>	<b>235</b>
<i>Emanuel Ionescu and Ralf Riedel</i>	

<b>8</b>	<b>CHEMICAL VAPOR DEPOSITION OF STRUCTURAL CERAMICS AND COMPOSITES</b>	<b>271</b>
	<i>Takashi Goto</i>	
<b>9</b>	<b>CVI PROCESSING OF CERAMIC MATRIX COMPOSITES</b>	<b>313</b>
	<i>Andrea Lazzeri</i>	
<b>10</b>	<b>REACTIVE MELT-INFILTRATION PROCESSING OF FIBER-REINFORCED CERAMIC MATRIX COMPOSITES</b>	<b>351</b>
	<i>Natalie Wali and J.-M. Yang</i>	
<b>11</b>	<b>COMBUSTION SYNTHESIS: AN UPDATE</b>	<b>391</b>
	<i>S. B. Bhaduri</i>	
<b>PART III</b>	<b>PHYSICAL METHODS</b>	<b>415</b>
<b>12</b>	<b>DIRECTIONAL SOLIDIFICATION</b>	<b>417</b>
	<i>Víctor M. Orera and José I. Peña</i>	
<b>13</b>	<b>SOLID FREE-FORM FABRICATION OF 3-D CERAMIC STRUCTURES</b>	<b>459</b>
	<i>James E. Smay and Jennifer A. Lewis</i>	
<b>14</b>	<b>MICROWAVE PROCESSING OF CERAMIC AND CERAMIC MATRIX COMPOSITES</b>	<b>485</b>
	<i>Cristina Leonelli and Paolo Veronesi</i>	
<b>15</b>	<b>ELECTROPHORETIC DEPOSITION</b>	<b>517</b>
	<i>Maria Cannio, Saša Novak, Laxmidhar Besra, and Aldo R. Boccaccini</i>	
<b>16</b>	<b>PROCESSING OF CERAMICS BY PLASMA SPRAYING</b>	<b>551</b>
	<i>Robert Vaßen</i>	
	<b>Index</b>	<b>567</b>

---

# PREFACE

---

There is increasing interest in the application of advanced ceramic materials in areas as diverse as transport, energy, environment, communications, health, and aerospace. The increasing scope for the utilization of ceramic materials in a wide range of applications makes the in-depth understanding of processing technologies more necessary than ever before, which can lead to ceramic products and components having the desired properties and performance in-service. This book was conceived to offer in a single volume a broad selection of key processing techniques for ceramics and their composites incorporating different chapters written by internationally recognized experts in their respective fields. This book includes traditional fabrication routes as well as advanced approaches, which are being developed to tackle the increasing demand for more reliable ceramic materials.

This book is divided into three sections: “Densification,” “Chemical Methods,” and “Physical Methods.” The fundamentals and practice of sintering, pulsed electric current sintering and viscous phase silicate processing are covered in the first section on Densification. The Chemical Methods section consists of eight chapters covering colloidal methods, sol–gel, gel casting, polymer processing, chemical vapor deposition, chemical vapor infiltration, reactive melt infiltration, and combustion synthesis. The chapters on directional solidification, solid free-form fabrication, microwave processing, electrophoretic deposition, and plasma spraying are included under Physical Methods. Each chapter is focused on a particular processing method/approach based on the expertise of the respective authors who are specialists and internationally renowned researchers from various countries. The readers of this book will thus be able to find at one place state-of-the-art and comprehensive information on various approaches, techniques, and methods for processing and fabrication of advanced ceramics and ceramic composites.

This book is directed toward scientists, engineers, technologists, and researchers working in the industry, national research laboratories, and academia with interest in traditional and advanced ceramics as well as ceramic composites. Senior undergraduates as well as graduate students pursuing a degree in ceramics or materials science and engineering will also find this book useful. All the chapters are stand-alone pieces. Some duplication, especially in the introductory sections, and nonuniformity of symbols and nomenclature may be present.

This book is the result of truly an international effort with contributions by authors from 10 different countries. The editors are grateful to all the authors for their valuable contributions as well as their cooperation, which led to the timely publication of this volume. Thanks are due to Ms. Anita Lekhwani, Senior Acquisitions Editor for Chemistry, Biotechnology, and Materials Science, John Wiley & Sons, Inc., for her help, cooperation, and understanding through the entire publication process of this book.

Narottam P. Bansal  
*Cleveland, Ohio*

Aldo R. Boccaccini  
*Erlangen, Germany*

---

# CONTRIBUTORS

---

- Narottam P. Bansal**, NASA Glenn Research Center, Structures and Materials Division, Cleveland, OH
- Laxmidhar Besra**, Institute of Minerals and Materials Technology (IMMT), Bhubaneswar, Orissa, India
- S. B. Bhaduri**, Departments of MIME and Surgery, University of Toledo, Toledo, OH
- Aldo R. Boccaccini**, Institute of Biomaterials, University of Erlangen-Nuremberg, Erlangen, Germany
- Rajendra K. Bordia**, Department of Materials Science and Engineering, University of Washington, Seattle, WA
- Héctor Camacho-Montes**, Basic Science Department, Institute for Engineering and Technology (UACJ), Cd. Juárez, Chih., Mexico
- Maria Cannio**, Department of Materials and Environmental Engineering, University of Modena and Reggio Emilia, Modena, Italy
- Bruce Dunn**, Department of Materials Science and Engineering, University of California at Los Angeles, Los Angeles, CA
- Katherine T. Faber**, Department of Materials Science and Engineering, Robert R. McCormick School of Engineering and Applied Science, Northwestern University, Evanston, IL
- Takashi Goto**, Institute for Materials Research, Tohoku University, Japan
- S. G. Huang**, K.U.Leuven, Department of Metallurgy and Materials Engineering (MTM), Heverlee, Belgium
- Emanuel Ionescu**, Technische Universität Darmstadt, Institut für Materialwissenschaft, Darmstadt, Germany
- Esther H. Lan**, Department of Materials Science and Engineering, University of California at Los Angeles, Los Angeles, CA
- A. Laptev**, K.U.Leuven, Department of Metallurgy and Materials Engineering (MTM), Heverlee, Belgium and Donbass State Engineering Academy, Department of Mechanical Engineering, Kramatorsk, Ukraine
- Andrea Lazzeri**, Department of Chemical Engineering, Industrial Chemistry and Materials Science, University of Pisa, Pisa, Italy

- Cristina Leonelli**, Department of Materials and Environmental Engineering, University of Modena and Reggio Emilia, Modena, Italy
- Jennifer A. Lewis**, Department of Materials Science and Engineering, University of Illinois, Urbana, IL
- Rodrigo Moreno**, Instituto de Cerámica y Vidrio, CSIC, Madrid, Spain
- Ralf Müller**, BAM Federal Institute for Materials Research and Testing, Berlin, FRG
- Saša Novak**, Department for Nanostructured Materials, Jožef Stefan Institute, Ljubljana, Slovenia
- Víctor M. Orera**, Instituto de Ciencia de Materiales de Aragón, CSIC-Universidad de Zaragoza, Facultad de Ciencias, Zaragoza, Spain
- José I. Peña**, Instituto de Ciencia de Materiales de Aragón, CSIC-Universidad de Zaragoza, Facultad de Ciencias, Zaragoza, Spain
- Stefan Reinsch**, BAM Federal Institute for Materials Research and Testing, Berlin, FRG
- Ralf Riedel**, Technische Universität Darmstadt, Institut für Materialwissenschaft, Darmstadt, Germany
- Noah O. Shanti**, Department of Materials Science and Engineering, Robert R. McCormick School of Engineering and Applied Science, Northwestern University, Evanston, IL
- James E. Smay**, School of Chemical Engineering, Oklahoma State University, Stillwater, OK
- O. Van der Biest**, K.U. Leuven, Department of Metallurgy and Materials Engineering (MTM), Heverlee, Belgium
- K. Vanmeensel**, K.U. Leuven, Department of Metallurgy and Materials Engineering (MTM), Heverlee, Belgium
- Robert Vaßen**, IEF-1, Forschungszentrum Jülich GmbH, 52425 Jülich, Germany
- Paolo Veronesi**, Department of Materials and Environmental Engineering, University of Modena and Reggio Emilia, Modena, Italy
- J. Vleugels**, K.U. Leuven, Department of Metallurgy and Materials Engineering (MTM), Heverlee, Belgium
- Natalie Wali**, Honeywell Aerospace, Phoenix, AZ
- J.-M. Yang**, Department of Materials Science and Engineering, University of California, Los Angeles, CA

---

# PART I

---

## DENSIFICATION

---

# SINTERING: FUNDAMENTALS AND PRACTICE

RAJENDRA K. BORDIA AND HÉCTOR CAMACHO-MONTES

## 1.1 INTRODUCTORY OVERVIEW

Although sintering has been practiced for thousands of years [1], significant advances in scientifically understanding the phenomenon have been made only in the last six decades. In a broad sense, sintering is the extension of the contact area between powder particles by the transport of material to or around pores under appropriate conditions of temperature, pressure, and environment [2]. The goal of the sintering practice, in general, is to produce a coherent body (from rather fragile green bodies) with controlled microstructure, in some cases with controlled porosity [3, 4]. The emphasis of sintering theory, modeling, and analysis is to predict the path of the microstructural development and its dependence on controllable parameters (e.g., temperature, time, environment, and particle size).

Numerous attempts have been made to model the sintering phenomenon, and many experimental studies have been conducted to evaluate the theories and also the important effects of process parameters. Some of the important aspects of the sintering theory and practice are reviewed in this chapter. Readers are referred to many excellent reviews, monographs, and textbooks for a more in-depth study [5–16]. Section 1.2 deals



with the physical description of the process, viz., the stages of sintering and the thermodynamic driving force for sintering. The next three sections deal with the classical models for sintering (Section 1.3 for viscous sintering, Section 1.4 for solid-state sintering, and Section 1.5 for liquid-phase sintering [LPS]). Section 1.6 focuses on constrained sintering and Section 1.7 summarizes the advanced kinetic and microstructural evolution models. Section 1.8 focuses on the effect of external stresses on sintering. Section 1.9 focuses on the newly discovered significant effect of external fields on sintering. Finally, in Section 1.10, some of the important aspects of sintering practice are presented.

## 1.2 PHYSICAL DESCRIPTION

### 1.2.1 The Stages of Sintering

It is widely accepted to divide the overall sintering process in three sequential stages. In general, these stages are not discrete, and usually, there is a considerable overlap between two consecutive ones. These stages are defined according to the morphology of the grains and the porosity.

The first stage or the *initial stage* of sintering corresponds to the situation when necks are forming and growing between particles, and they remain distinct as shown schematically in Figure 1.1a,b. At the end of this stage, the contact area increases by up to 20% with only a small densification (interparticle penetration). Consequently, the compact densification is only a few percent. A marked decrease in the specific surface area of the compact occurs due to surface smoothing. The grain boundaries between the particles remain in the contact plane due to the tensile stresses resulting from the surface tension.

The second stage, or the *intermediate stage* of sintering, is characterized by a more or less continuous network of pore channels along the grain edges (Fig. 1.1c). During this stage, the pore channel shrinks and grains grow. Most of the densification, and also the growth in the contact area, occurs during this stage.

The pore channels continue to shrink until they pinch off and form isolated spheriodized pores (Fig. 1.1d). This marks the beginning of the third or the *final stage* of densification. In this stage, the pore volume fraction asymptotically approaches zero. In some cases, these closed pores may trap gases, making their elimination difficult.

### 1.2.2 The Thermodynamic Driving Force

There is broad agreement in the literature regarding the driving force for sintering. The starting particulate configuration is far from the equilibrium state, and the driving force comes from the excess free energy. Hence, the reduction of the free energy is taken as the sintering driving force.

This excess free energy exists in the powder compact due to the large surface area and defects. In the classical sintering literature, emphasis has been on the excess free energy due to surfaces. As sintering proceeds, porosity decreases, leading to a reduction

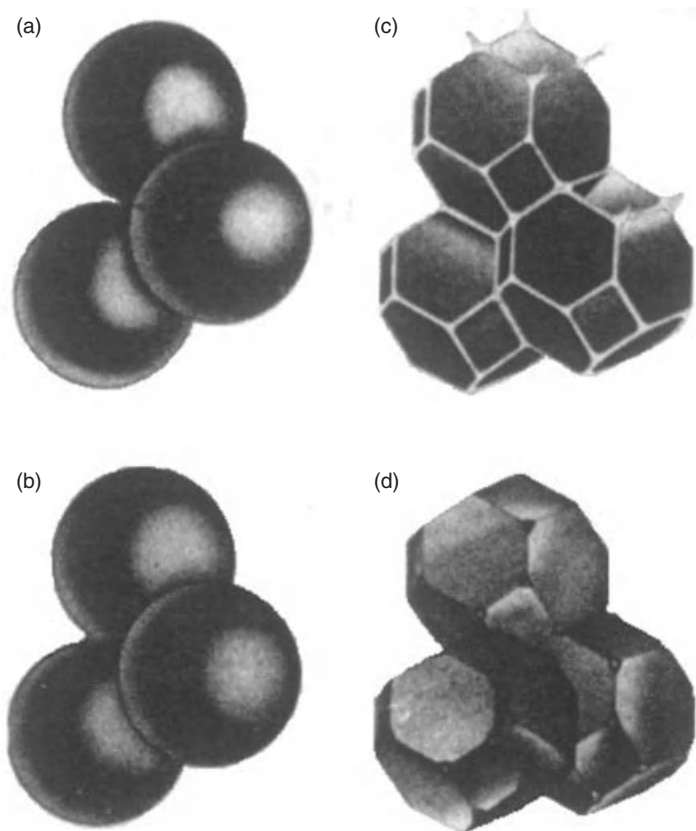


**Figure 1.1.** Illustrations of the stage of sintering: (a) initial stage—spheres in tangential contact; (b) near the end of the initial stage, the neck between particles starts to grow; (c) intermediate stages with continuous pore channels at grain edges and large contact area between grains; (d) final stage, tetrahedral pores at four grain intersections. Reprinted with permission from Coble [17], copyright 1961, American Institute of Physics.

of the solid–vapor interfacial area. The solid–vapor interfaces are replaced by solid–solid interfaces. When grain growth occurs, the solid–solid interfacial area also decreases. Thermodynamically, the change in free energy can be written as

$$\delta G_{\text{system}} = \delta \int \gamma_{\text{sv}} dA_{\text{sv}} + \delta \int \gamma_{\text{ss}} dA_{\text{ss}}, \quad (1.1)$$

where  $\delta G_{\text{system}}$  is the change in the free energy of the sintering system,  $\gamma_{\text{sv}}$  is the energy per unit area of the solid–vapor interface, and  $\gamma_{\text{ss}}$  is the energy/area of the solid–solid interface. In this equation, during sintering, the first term is negative since the area of the solid–vapor interface ( $A_{\text{sv}}$ ) decreases. Considering that grain growth implies a

decrease of the solid–solid interface, the second term may be either positive or negative since grain boundary area ( $A_{ss}$ ) may increase or decrease depending on how fast grain growth is going on. If grain growth does not occur, the second term is always positive as grain contacts grow during sintering. As long as  $\delta G_{\text{system}}$  is negative, a driving force for sintering exists.

Some powder preparation techniques like mechanical milling increase the defect concentration. In many cases, high defect concentration leads to faster sintering because of higher diffusion. Hence, the process of defect reduction may enhance the sintering driving force.

There are two distinct pathways of total energy reduction. If the surface energy ( $\gamma_{sv}$ ) is more than the solid–solid surface energy ( $\gamma_{ss}$ ) (true for all crystalline solids), then, in the early stages of sintering, the total energy can be lowered by the transport of atoms from the contact area to the pore, leading to a reduction in the solid–vapor interface ( $A_{sv}$ ) and an increase in the grain boundary area ( $A_{ss}$ ). This would lead to a reduction in the total pore volume, leading to an increase in density. This process is called *densification*. Another process is the transport of material from one part of the pore to another (e.g., in the case where the pore surface has different radii of curvature). In this case, the pore surface area decreases, but its volume does not change. In addition, there is no change in the solid–solid surface area. This process is called *coarsening*. Another example of coarsening is the coalescence of small pores in to a large pore. In this case also, the solid–vapor area decreases without any change in the pore volume.

In practice, densification and coarsening are concurrent and competing processes since they both reduce the driving force for sintering (excess surface energy). Note that coarsening is a relevant consideration only for the sintering of crystalline materials. Amorphous materials do not have grain boundaries and hence the solid–solid surface energy ( $\gamma_{ss}$ ) is identically equal to zero. If the goal is to produce a high-density final product of crystalline materials, the coarsening processes must be suppressed. Some of the successful sintering practices do this quite effectively as discussed in Section 1.10.

### 1.3 VISCOUS SINTERING

For amorphous materials, sintering proceeds due to transport of matter over the entire volume, and in general, sintering proceeds at a fast rate. In addition, there is no interface between the particles (no grain boundaries). Thus, the overall energy always decreases due to the reduction of the solid–vapor interfacial area. Amorphous materials have lower viscosity (than their crystalline counterpart), and the entire solid part is involved in matter transport as schematically shown in Figure 1.2. Therefore, from a processing point of view, viscous sintering offers significant advantages. However, from a performance standpoint, viscous materials may not be desirable.

For viscous sintering, the three stages have been analyzed by Frenkel (initial stage), Scherer (intermediate stage), and Mackenzie–Shuttleworth (MS) (final stage). The kinetics of viscous sintering can be calculated following the energy balance approach

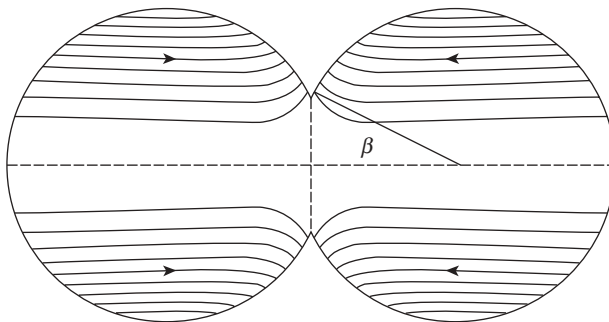


**Figure 1.2.** Viscous flow during amorphous sintering. Reprinted with permission from Martínez-Herrera and Derby [18], copyright 1995, John Wiley & Sons.

suggested by Frenkel [19]. In this under quasi equilibrium, the energy gained by the reduction in the surface area is dissipated in viscous flow leading to

$$\dot{E}_s + \dot{E}_f = 0, \quad (1.2)$$

where  $\dot{E}_s$  and  $\dot{E}_f$  are the energy rates for surface area reduction and viscous flow. This balance has also been considered by Scherer [20] and Mackenzie and Shuttleworth [21].

Frenkel analyzed the kinetics of the initial stage of viscous sintering and developed the following relationship for the sintering of spheres by viscous flow [19]:

$$\beta^2 = \frac{3\gamma t}{2\pi\eta R}, \quad (1.3)$$

where  $\beta$  is the angle shown in Figure 1.2.

Scherer [20] used a cell model to geometrically describe the intermediate sintering state, and Mackenzie and Shuttleworth [21] used a closed porosity model for the final stage. These two models have the capacity to describe experimental results very well. The advantage of the Scherer model is that it can describe the sintering over a very broad density range. For example, it has been successfully used to determine the densification rate of sol-gel-derived low initial density systems. The Scherer cell model works well up to a relative density of 0.95. The MS model describes the late stages including the final stages of sintering. Both models have been proposed and used to successfully calculate the sintering kinetics over a broad density range. It has been shown that in the relative density interval of 0.3–0.95, the two models predict the same densification kinetics, which has been confirmed experimentally for several systems.

The MS analysis of a spherical shell is a description of the final stage when the pores become isolated. The free sintering rate for the MS model is given by [21]

$$\dot{\epsilon}_f = -\frac{1}{2} \left( \frac{4\pi}{3} \right)^{1/3} \left( \frac{\gamma n^{1/3}}{\eta} \right) \left( \frac{1}{\rho} - 1 \right)^{2/3}, \quad (1.4)$$

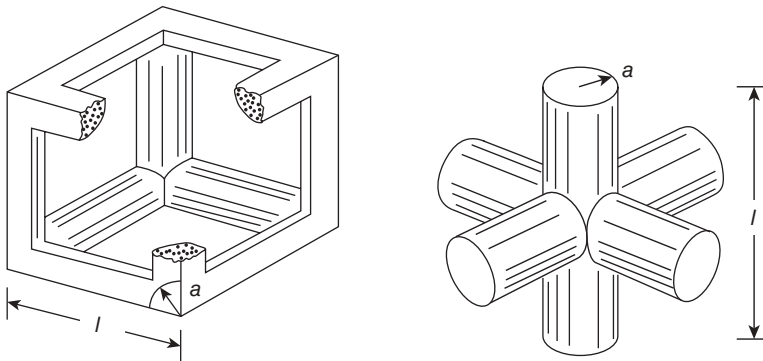


**Figure 1.3.** Cylindrical array geometric unit cell for the Scherer cell model. Reprinted with permission from Scherer [20], copyright 1991, John Wiley & Sons.

where  $n$  is the number of pores per unit volume,  $\rho$  is the normalized density (normalized by the theoretical density),  $\eta$  is the viscosity of the material, and  $\gamma$  is the surface energy.

For the intermediate stage of sintering, Scherer proposed the cell model shown in Figure 1.3. It was originally developed for gels and other low-density materials. In this model, an array of cylinders meet at right angles.

For this model, Scherer derived a densification rate given by [20]

$$\dot{\epsilon}_f = - \left( \frac{\gamma n^{1/3}}{\eta} \right) \frac{\pi - 4\sqrt{2}x}{x^{1/3} (3\pi - 8\sqrt{2}x)^{2/3}}. \quad (1.5)$$

The relative density  $\rho$  and  $x$  are related through the equation

$$\rho = 3\pi x^2 - 8\sqrt{2}x^3. \quad (1.6)$$

Using the geometric model shown in Figure 1.3, Scherer derived the number density of pores in terms of the geometric parameters and green density [20]:

$$n^{1/3} = \frac{1}{l_0 \rho_0^{1/3}}, \quad (1.7)$$

where

$$l_0 = \frac{\sqrt{\pi} d_0}{2(1 - 2x_0)^2} \quad (1.8)$$

and  $x_0$  is the root of Equation 1.6 considering that  $\rho = \rho_0$ , where  $\rho_0$  is the initial relative density and  $d_0$  is the initial particle diameter. In the density range of 0.3–0.95, both the

MS (Eq. 1.4) and the Scherer models (Eq. 1.5) give the same dependence of the densification rate on the density.

In addition, the Scherer cell model provides a method to calculate the viscous Poisson's ratio and the uniaxial viscosity as a function of the relative density (discussed in detail in Section 1.6). These equations work well over the entire densification cycle:

$$\nu_p = \frac{1}{2} \left[ \frac{\rho}{3-2\rho} \right]^{1/2} \quad (1.9)$$

and

$$E_p = 3\eta \frac{\rho}{3-2\rho}. \quad (1.10)$$

The use of these parameters for sintering problems will be discussed in Section 1.6.

## 1.4 SOLID-STATE SINTERING

Solid-state sintering is the relevant mechanism for crystalline materials. Even though it has common features with viscous sintering for amorphous powder compacts, the physical picture has remarkable differences. The first difference is that not the entire solid body is involved in sintering. The transport of matter is highly localized and occurs in the vicinity of the pores. This leads to several mechanisms depending on the source, sink, and the matter transport path. For initial-stage sintering, the solid-state sintering mechanisms are shown in Figure 1.4 and are described in Table 1.1.

For solid-state sintering, the matter sources and sinks are surfaces, grain boundaries, and line defects; this is a characteristic and defining feature of the sintering of crystalline. For amorphous materials, the entire solid is involved in matter transport. In contrast, in solid-state sintering, defects (including surfaces and boundaries) are the focal points for matter transport.

For the solid-state sintering, we can hypothetically consider two reference volumes as shown in Figure 1.4. Volume V1 is in the equilibrium part of the particles and volume V2 includes defects (such as grain boundaries or surfaces). The free energy for volume V2 is higher than that of volume V1. This free energy difference is the driving force for material transport leading to solid-state sintering.

### 1.4.1 Initial-Stage Solid-State Sintering Models

Following Frenkel [19] and Kuczynski's [23] pioneering work, numerous models for initial-stage solid-state sintering have been developed. These models predict the rate of neck growth and densification for simple geometries like a pair of wires or spheres. Equations have been proposed to calculate the neck size as a function of time for different transport mechanisms, for example, Equation 1.11. Ashby developed an elegant, graphical approach to capture the regions of dominance of different mechanisms in

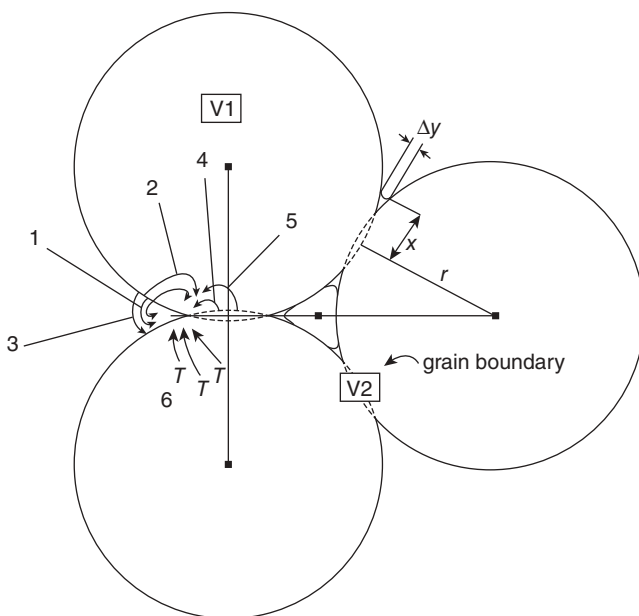


**Figure 1.4.** Six paths for matter transport. All lead to neck growth. Only mechanisms 4, 5, and 6 lead to densification (see Table 1.1 for sources and sinks for each path). Reprinted with permission from Kingery et al. [22], copyright 1975, John Wiley & Sons.

**TABLE 1.1.** The Transport Paths, Sources, and Sinks of Matter and Whether Densification Occurs or Not for Various Initial-Stage Sintering Mechanisms

Mechanism No.	Transport Path	Source of Atoms	Sink of Atoms	Densification
1	Surface diffusion	Surface	Neck	No
2	Lattice diffusion	Surface	Neck	No
3	Vapor transport	Surface	Neck	No
4	Boundary diffusion	Boundary	Neck	Yes
5	Lattice diffusion	Boundary	Neck	Yes
6	Lattice diffusion	Dislocations	Neck	Yes

For a schematic illustration of the mechanism, see Figure 1.4 [22].

“sintering maps” [24]. Although all transport mechanisms contribute to neck growth, the rates for each mechanism are different and Ashby’s sintering maps [24, 25] provide a convenient graphical visualization of the dominant mechanisms for a given set of temperature, neck size, and particle size. In these sintering maps, at the boundaries between two fields, the neck growth rates from the two neighboring mechanisms are the same. Far away from the boundaries, a particular mechanism dominates. Figure 1.5 shows an example of a sintering map for copper spheres with radii of  $57\ \mu\text{m}$ .

One of the most important applications of this approach analysis has been in identifying the dominant mechanism for sintering under a given set conditions. The experi-

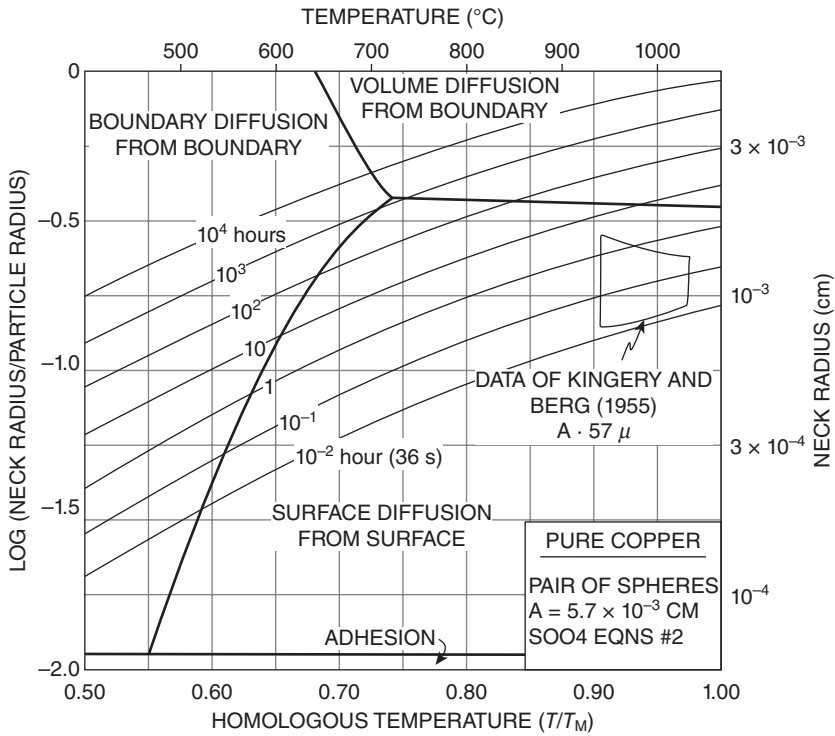


Figure 1.5. Sintering map for copper powder. Reprinted with permission from Ashby [24], copyright 1974, Elsevier.

ments are conducted on model systems like two spheres, or two wires, or a sphere and a plate. The neck size is measured as a function of time. Several authors, including Kuczynski, have supported the relation

$$(x^n / a^m) \propto t, \quad (1.11)$$

where  $x$  and  $a$  are half the neck radius and the particle radius, respectively, and  $t$  is the sintering time (typically, time at a specific isothermal sintering temperature).

The values of the exponents  $n$  and  $m$  for different mechanisms and calculated by different investigators are given in Table 1.2. Also included in the table are the values of the scaling exponent,  $z$ , as proposed by Herring [26]. According to this, if two partially sintered systems are geometrically similar, except that the linear dimension of one system is  $\lambda$  times the other, then the time required to produce geometrically similar changes in the two systems, at the same temperature, is very simply related as

$$\Delta t_2 = \lambda^z \Delta t_1. \quad (1.12)$$

$z$  depends on the mechanism of sintering (Table 1.2).



TABLE 1.2. Values of Exponents  $n$ ,  $m$ , and  $z$  in Equations 1.11 and 1.12 Calculated by Different Authors for Initial-Stage Sintering Mechanisms

Mechanism	Author	$n$	$m$	$z$
1	Kuczynski [23]	7	3	4
	Burton et al. [27]	5	2	
	Pines et al. [28]	6	2	
	Rockland [29]	7	3	
2	Kuczynski [23]	5	2	3
	Cabrera [27]	5	2	
	Pines et al. [28]	4	1	
	Rockland [30]	5	2	
3	Kuczynski [23]	3	2	2
	Kingery and Berg [31]	3	1	
	Pines et al. [28]	7	3	
	Hobbs and Mason [32]	5	2	
4	Rockland [30]	6	2	—
	Coble [33]	6	2	
	Johnson [34]	6	2	
	Rockland [30]	4	1	
Viscous	Frenkel [19]	2	1	1

The mechanism numbers correspond to those in Table 1.1.

Many experimental studies have been conducted to test these models (Eqs. 1.11 and 1.12). However, the approach has come under considerable criticism regarding, for instance, the simplifying assumptions for the neck geometry and the inability, experimentally, to ensure that a single mechanism dominates. This has resulted in an inability to critically evaluate the predictions of the models. In spite of this criticism, this approach has led to important technological implications including strategies to suppress the coarsening mechanism and the significant importance of fine particle size. For example, Herring's scaling law suggests that decreasing the particle size by an order of magnitude would lead to a reduction in the sintering time of  $10-10^4$ . As will be highlighted in Section 1.10, this realization has led to significant attention on making and processing ultrafine and nanoscale powders.

## 1.4.2 Intermediate-Stage Solid-State Sintering Models

A representative model for the solid-state sintering intermediate stage has been proposed by Coble [17]. Microstructure with porosity is modeled as cylinders around the edges of tetrakaidecahedron-shaped grains (Fig. 1.6). The densification rate is calculated for the case of matter transport by volume and grain boundary diffusions. For volume diffusion, the densification rate is given by

$$\frac{1}{V} \frac{dV}{dt} = -457 \frac{D_v \gamma \Omega}{kT d^3}, \quad (1.13)$$

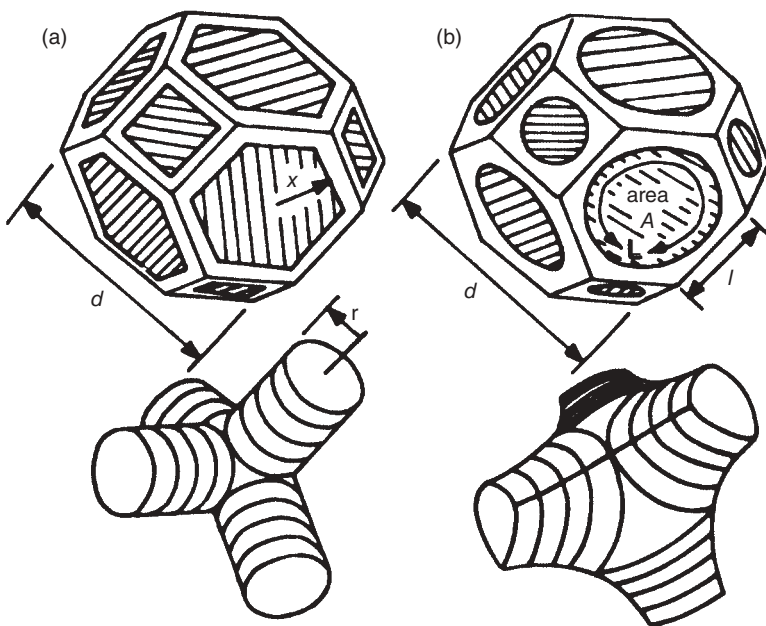


**Figure 1.6.** Representative unit cell for intermediate-stage solid-state sintering. (a) Original model of Coble [17] and (b) modification by Beere [38].

and for grain boundary diffusion, the densification rate is given by

$$\frac{1}{V} \frac{dV}{dt} = -40 \frac{\delta_b D_b \gamma \Omega}{k T d^4} \frac{l}{r}, \quad (1.14)$$

where  $1/V dV/dt$  is the volumetric densification rate.  $D_v$  and  $D_b$  are the diffusion coefficients for volume and grain boundary diffusion, respectively.  $\Omega$  is the atomic volume,  $\gamma$  is the surface energy,  $\delta_b$  is the width for grain boundary diffusion,  $k$  is the Boltzmann constant, and  $T$  is the absolute sintering temperature. The parameters  $r$ ,  $l$ , and  $d$  characterize the microstructure, and they are shown in Figure 1.6.

Johnson [35] and Eadie et al. [36, 37] have used similar geometry but allowed for parallel transport paths. Johnson [35] has developed the shrinkage rate for combined volume and grain boundary diffusions in terms of geometric parameters and has obtained the following densification rate:

$$\frac{1}{V} \frac{dV}{dt} = -8 \frac{\bar{H} \gamma \Omega}{\bar{x} k T} \{D S_v + \delta_b D_b L_v\}, \quad (1.15)$$

where  $\bar{H}$  and  $\bar{x}$  are the average value of the pore curvature and of the grain boundary radius, respectively.  $S_v$  is the pore surface area per unit volume and  $L_v$  is the length of the grain boundary/pore intersection per unit volume.

Apart from this, the only other significant development to intermediate-stage sintering has been the work of Beere [38]. In this work, the pore is assumed to have a thermodynamically correct shape requiring the correct dihedral angle (Fig. 1.6b). The pore shape is calculated by minimizing the surface area for a fixed volume. The calculated densification then depends on the dihedral angle ( $\theta$ ). The calculated densification rate shows that fast densification is possible for materials with large dihedral angles. Small values of the dihedral angle have been given as one of the reasons for difficulty in sintering covalent solids. The pore shapes assumed by Beere have been experimentally confirmed by Lee et al. [39]. The rate expressions given by these various intermediate-stage models have been reviewed by Beere [40]. It has been shown that densification rates predicted by various models can differ by as much as two orders of magnitude, and Coble's relation gives the lowest rates.

An important criticism of these models has been the fact that none of them take care of concurrent grain growth. In addition, the geometric model of uniform pores and grain throughout the sintering body is far from correct [41]. Coble [17] introduced an empirical grain growth equation. This equation assumes the volume of individual grains to be proportional to sintering time. With this assumption, the well-known semilogarithmic sintering law was derived:

$$P - P_0 = K \ln \left( \frac{t}{t_0} \right), \quad (1.16)$$

where  $K$  contains all material parameters for sintering and grain growth.  $P_0$  and  $t_0$  are the porosity and the time at the onset of intermediate-stage sintering. In spite of the criticism regarding idealized geometry, Coble's equation has been extensively used to analyze experimental results. It has been shown to semiquantitatively predict experimental results for a wide variety of materials.

### 1.4.3 Final-Stage Solid-State Sintering Models

This stage of sintering is geometrically the simplest. The pore is isolated and assumed to be at four grain junctions. Coble [17] has calculated the rate of densification for this geometry. Additional models are those derived from creep cavitation literature [42–44]. The porosity is modeled as equilibrium-shaped cavities on the grain boundaries, and the densification rate is calculated by deriving the rate of shrinkage of these cavities under the compressive surface tension force. The practical difficulties that arise in this stage of densification are

- i. abnormal grain growth, which leaves pores inside the grains, and
- ii. slowly diffusing entrapped gases in the closed pores. This essentially leads to termination of shrinkage when the gas pressure within the pores equals the surface pressure. In addition, the trapped gas can change the equilibrium dihedral angle and can further affect shrinkage.

One of the most serious shortcomings of the intermediate- and final-stage sintering models has been that the calculated diffusion coefficients and the activation energy

from sintering are higher than those obtained from tracer diffusion experiments. Various explanations have been provided for this discrepancy, but none of them have been satisfactory.

#### 1.4.4 Pore–Boundary Interaction

During the intermediate and final stages of sintering of crystalline materials, there is a strong interaction between grain boundaries and pores. Alexander and Balluffi, in their classical experiments on copper wires, showed that only the pores that were on the grain boundaries shrank [45]. As a result, normal grain growth has been investigated in detail in porous materials. It was shown that pores on the boundary lead to a reduction in grain growth rate [46, 47]. A very significant advance in the understanding of grain growth in porous materials was made initially by Kingery and Francois [48] and later extended by Brook [49]. As curved boundaries move during grain growth, the pores can either remain attached to the boundary or be left behind. In the case in which they remain attached, the velocity of the boundary could be limited by pore mobility (boundary mobility higher than pore mobility) or by the intrinsic mobility of the boundary (pore mobility higher than boundary mobility). By using standard expressions for pore and boundary mobility, regimes of grain size and pore size were identified in which separation occurs. It was shown that in the intermediate pore size, separation occurs. Very small pores remain attached to the boundary whose velocity is controlled by intrinsic boundary mobility. Large pores also remain attached to the boundary, but in this case, the pores control the boundary mobility.

This analysis was further refined by Hsueh et al. [50, 51]. They properly calculated the pore and boundary mobility in porous materials and showed the important effect of dihedral angle. The pore velocity was shown to be a function of dihedral angle, and it was shown that the pore size should be below a critical size (which depends on the grain size and dihedral angle) to avoid pore breakaway.

Another important effect of dihedral angle and pore–boundary interaction was highlighted by Kellett and Lange [52]. It was shown that thermodynamically, some pores grow and others shrink. The condition of pore stability is governed by the dihedral angle and the number of nearest neighbors. It was shown that materials with low dihedral angles are difficult to sinter to high density, and this is one of the reasons for the difficulty in sintering covalent materials that have low dihedral angles.

### 1.5 LPS

The differences between viscous and solid-state sintering have been pointed out in the previous sections. Practically, it would be desirable to develop a fast sintering approach for solid-state materials. In some ways, this is possible through the technique known as LPS. In addition, for covalent materials, due to their low dihedral angles, solid-state sintering is almost impossible. In these cases also, LPS is the preferred sintering approach. In LPS, the system has a small volume fraction of viscous liquid phase at the sintering soak temperature. This fraction is generally less than 5 vol %. It is

customary to use a practical nomenclature for these compounds. The particle solid forming the major component is written first, and the liquid producing component is written in parentheses, for example,  $\text{Si}_3\text{N}_4(\text{MgO})$  and  $\text{ZnO}(\text{Bi}_2\text{O}_3)$ , where  $\text{MgO}$  and  $\text{Bi}_2\text{O}_3$  are the additives that lead to the formation of the liquid phases for  $\text{Si}_3\text{N}_4$  and  $\text{ZnO}$ , respectively.

What LPS has in common with other sintering techniques is that the process is divided in three stages and that the driving force is connected with the decreases of free energy and surface area. However, the mechanisms and the structural evolution are quite different from other techniques. First, it is necessary to emphasize that a necessary condition for LPS is that the liquid must wet the solid phase. Figure 1.7 illustrates the wetting behavior between a liquid and a solid, schematically showing cases of nonwetting and wetting liquids.

Good or complete wetting is a precondition for LPS. Ideally, the liquid phase should perfectly wet the grain surfaces as shown in Figure 1.8 [54]. Then, the matter

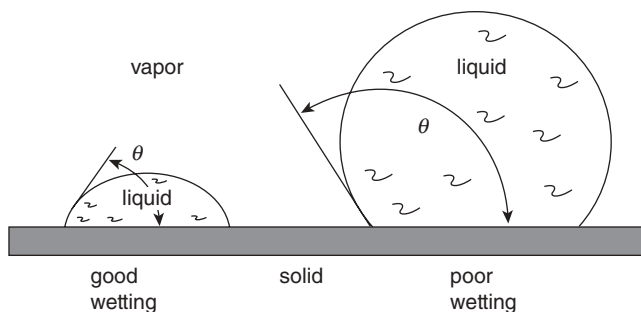


**Figure 1.7.** Wetting behavior between a liquid and a solid showing good wetting and poor wetting. The wetting angle  $\theta$  is governed by the thermodynamic equilibrium between the different surface energies. Reprinted with permission from German et al. [53], copyright 2008, Springer.

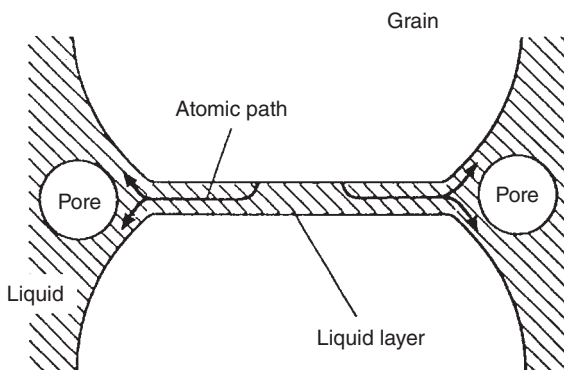


**Figure 1.8.** Schematic of an idealized liquid-phase sintering microstructure. Reprinted with permission (via Copyright Clearance Center) from Rahaman [54], copyright 1995, CRC Press.

transport occurs through the liquid, leading to an enhancement of the densification rate due to the higher diffusion or lower viscosity of the liquid phase. Ideally, pores should be trapped in the liquid phase (as opposed to being at the liquid–solid surface). The pressure difference across the surface of a spherical pore of radius  $r$  in the liquid phase may be described by the equation

$$\Delta p = -\frac{2\gamma_{lv}}{r}, \quad (1.17)$$

where  $\gamma_{lv}$  is the liquid–vapor surface energy.

This pressure difference is the driving force for LPS. Kinetically, LPS is also divided in three stages. They are (1) rearrangement, (2) solution–precipitation, and (3) Ostwald ripening. These stages are schematically illustrated in Figure 1.9.

Rearrangement takes place as the liquid phase is formed. For a successful LPS, the composition of the powder compact must be such that good wetting between the liquid and the solid particle is achieved. In addition, it is also important to have low liquid solubility in the solid and higher solid solubility in the liquid. At this point, the tendency for the system to decrease the surface energy results in capillary forces

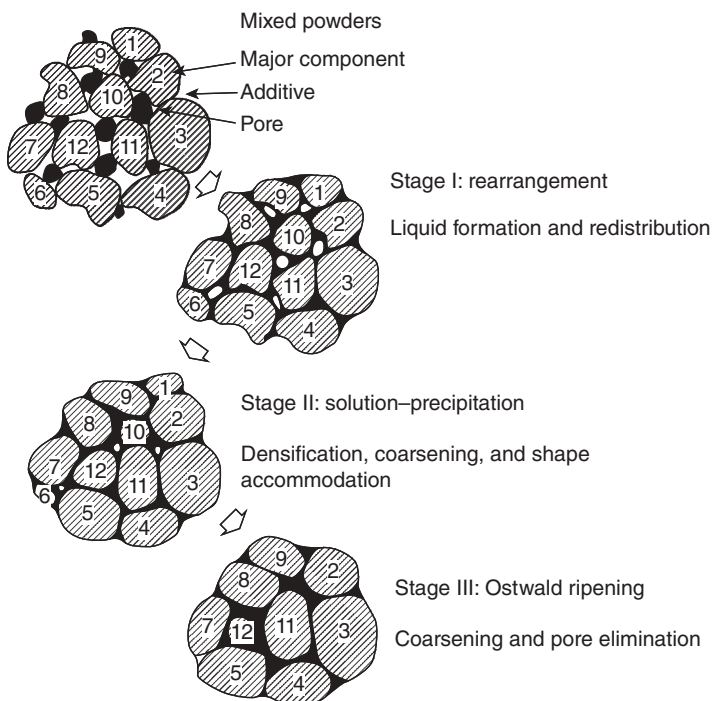


**Figure 1.9.** Stages of liquid-phase sintering. Reprinted with permission (via Copyright Clearance Center) from Rahaman [54], copyright 1995, CRC Press.

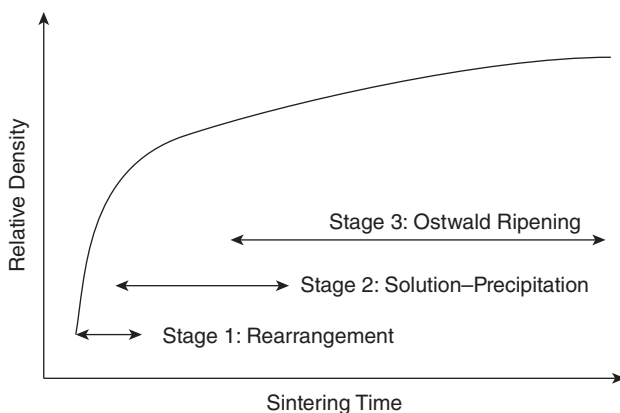


**Figure 1.10.** Schematic diagram illustrating the three stages of liquid-phase sintering curves. Reprinted with permission (via Copyright Clearance Center) from Rahaman [54], copyright 1995, CRC Press.

that play a key role in the particle rearrangement. Shrinkage and densification may occur as can be observed in Figure 1.10. In general, the first stage only lasts a few minutes.

As densification by rearrangement slows, the solution precipitation process becomes dominant. Solution of the solid phase takes place at the interfaces with higher chemical potential; matter is transported through the liquid phase and precipitated at a liquid–solid interface with lower chemical potential. Then, as shown in Figure 1.8, a bridge is formed between contact particles and the capillary force may attract a particle. During this stage, densification is accompanied by considerable coarsening (grain growth) and by grain shape changes.

When the Ostwald ripening process becomes dominant, that is, grain coarsening due to the solution–precipitation process, the third stage of the LPS has started. This is the longest-lasting stage where densification is slow (Fig. 1.10). During this stage, grain shape accommodation allows a more efficient packing of the structure as shown in Figure 1.11. The degree of change in the grain morphology and accommodation depends on the fraction of the liquid phase. For a higher liquid volume fraction, more shape change and accommodation takes place.

Polycrystalline particles go through an extra process of particle rearrangement also known as secondary rearrangement [55]. Figure 1.12 illustrates this process, in which tension at the interfaces between crystallites and the liquid phase can induce the separation of crystallites such that they become individual particles.

The significant advantage of LPS is the densification enhancement and the ability to sinter materials that just cannot be sintered in the solid state (e.g., silicon nitride). As a result, this process is commonly used in sintering practice. However, the liquid phase remains as glass (amorphous phase), and this represents a problem for those applications where good mechanical properties, especially at high temperatures, are

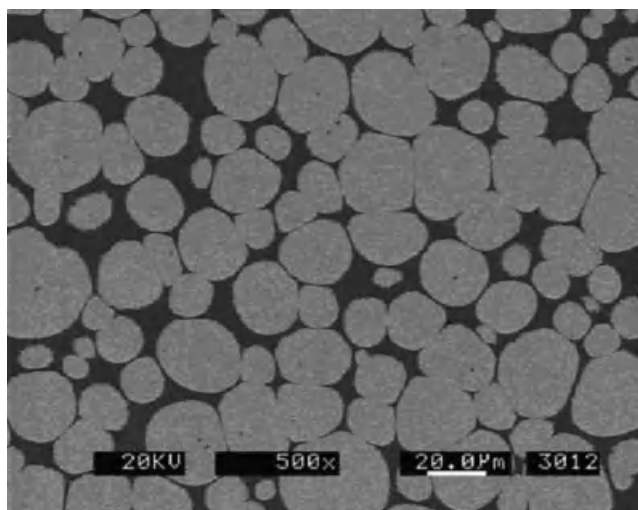


**Figure 1.11.** Micrographs of an 88 wt % W heavy alloy with 15.4 wt % Ni and 6.6 wt % Fe. The alloy was held for 30 min at 1500°C. Reprinted with permission from German et al. [53], copyright 2008, Springer.



**Figure 1.12.** Schematic of secondary rearrangement for polycrystalline particles during liquid-phase sintering.

needed. Also, the glass phase may be a disadvantage for electric and magnetic materials. Innovative strategies have been developed to minimize the glass phase including postsintering annealing steps to crystallize it.

## 1.6 DENSIFICATION AND DEFORMATION IN CONSTRAINED SINTERING

In many practical situations, sintering bodies are subjected to physical constraint. Specific examples include the sintering of coatings or films on dense substrates and the sintering of composites. Continuum mechanics has been used to characterize



densification and deformation during constrained sintering [56–58]. The most common approach has been to use the viscoelastic analogy. In this approach, the constitutive laws for linear viscous incompressible fluid can be written as

$$s_{ij} = 2\eta \dot{\epsilon}_{ij} \quad (1.18)$$

and

$$\dot{\epsilon} = 3\dot{\epsilon}_f. \quad (1.19)$$

Viscoelastic analogy allows us to replace the strains and the elastic coefficients in the elastic equations by corresponding strain rates and effective viscous coefficients for a porous sintering powder compact. Therefore, Equations 1.18 and 1.19 may be written as

$$s_{ij} = 2G_p \dot{\epsilon}_{ij} \quad (1.20)$$

and

$$\sigma = K_p(\dot{\epsilon} - 3\dot{\epsilon}_f). \quad (1.21)$$

In these relations,  $G_p$  and  $K_p$  are the shear and the bulk viscosities;  $s_{ij}$  and  $\dot{\epsilon}_{ij}$  are the deviatoric stress and strain rates;  $\sigma$  and  $\dot{\epsilon}$  are the hydrostatic stress and the volumetric strain rates; respectively; and  $\dot{\epsilon}_f$  is the free linear strain rate (densification rate one would get in the absence of internal or external stresses) of the sintering body. Equations 1.20 and 1.21 reduce to Equations 1.18 and 1.19 for the case of fully dense (relative density equal to 1) incompressible viscous materials for which  $G_p = 2\eta$  and  $K_p \rightarrow \infty$ . For a porous body,  $G_p$  and  $K_p$  depend on the microstructure of the sintering body and evolve as the material sinters (so does the free sintering strain rate). These parameters are called shear and bulk viscosities.

These equations are valid for linear isotropic viscous materials. It has been shown that there are many amorphous and crystalline powder compacts whose densification and deformation behavior are governed by these relations. Both viscous sintering materials (e.g., glass or filled glasses) and even polycrystalline ceramics at low stresses follow these constitutive laws. This is especially true for polycrystalline bodies if the boundaries act as a perfect source and sink for defects.

Equation 1.21 shows that the volumetric strain rate  $\dot{\epsilon}$  is a lineal superposition of the free sintering rate and the volumetric strain rate induced by the stress, where  $\sigma$  is the hydrostatic stress induced due to the constraint or due to external stresses.

In analogy with linear elasticity, there are two other viscous parameters for a sintering body. These are the uniaxial viscosity,  $E_p$ , and the viscous Poisson's ratio,  $\nu_p$ . Analogous to linear elasticity, there are two relations between the four constitutive parameters:

$$G_p = E_p / [2(1 + \nu_p)] \quad (1.22)$$

and

$$K_p = E_p / [3(1 - 2\nu_p)]. \quad (1.23)$$

Using the uniaxial viscosity and the viscous Poisson's ratio, Equations 1.20 and 1.21 can be rewritten as [56]

$$\dot{\epsilon}_x = \dot{\epsilon}_f + E_p^{-1}[\sigma_x - \nu_p(\sigma_y + \sigma_z)], \quad (1.24)$$

$$\dot{\epsilon}_x = \dot{\epsilon}_f + E_p^{-1}[\sigma_x - \nu_p(\sigma_y + \sigma_z)], \quad (1.25)$$

and

$$\dot{\epsilon}_x = \dot{\epsilon}_f + E_p^{-1}[\sigma_x - \nu_p(\sigma_y + \sigma_z)]. \quad (1.26)$$

These equations have been widely used to study densification and deformation during constrained sintering for isotropic powder compacts.

Using these relations, the volumetric densification rate is

$$\dot{\epsilon}_\rho = \frac{\dot{\rho}}{\rho} = -(\dot{\epsilon}_x + \dot{\epsilon}_y + \dot{\epsilon}_z). \quad (1.27)$$

As a side note, it is important to point out that the densification rates given by Equations 1.13–1.15 and 1.27 assume that the mass remains constant during sintering.

The viscous responses to uniaxial stress ( $E_p$ ), to shear stress ( $G_p$ ), and to hydrostatic stress ( $K_p$ ) are functions of the powder compact's microstructure and density. A number of models have been proposed in the literature. Sintering microstructures are rather complex and include parameters including the relative density, average grain size, average pore size, grain size distribution, and pore size distribution. At the minimum, the models must be dependent on the density and should meet the limiting condition of incompressibility for the fully dense state. This corresponds to the viscous Poisson's ratio equal to 0.5 (equivalent to the bulk modulus,  $K_p \rightarrow \infty$ ). One example of the microstructure-based model was presented in Section 1.3 for viscous materials. The free densification rate,  $\dot{\epsilon}_f$ , the uniaxial viscosity,  $E_p$ , and the viscous Poisson's ratio,  $\nu_p$ , is given by Equation 1.4 or 1.5, 1.9, and 1.10, respectively.

A significant advantage of this continuum approach is that complex sintering problems like the codensification of multimaterial systems can be analyzed. In addition, the approach can be readily implemented in numerical simulations. An example is shown in Figure 1.13 for the cofiring of a metal ceramic multimaterial system. The regions A1, A2, and A3 correspond to metal powders, and the rest of the material is a ceramic. Practically, this case is an idealized representation of surface and buried conductor lines in a dielectric in an electronic package. Figure 1.13 shows the evolution profiles for shape deformation, von Mises stresses, relative density map, and displacement field during sintering. Several important effects of constraint are highlighted in this analysis, including the "unexpected deformation" (difference from the initial shape) due to a nonuniform displacement field. The nonuniform densification is a result of the nonuniform stress distribution. In this analysis, the metal powder located in areas 1, 2, and 3

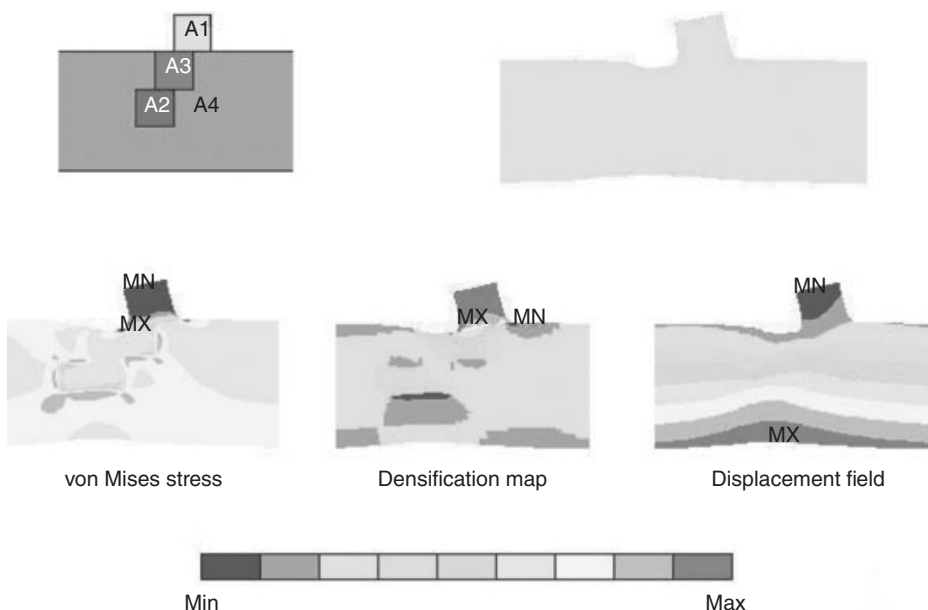


**Figure 1.13.** An example of the use of continuum models to numerically simulate the processing of a complex multimaterial system. Regions A1, A2, and A3 correspond to a metal powder and A4 to a ceramic powder compact.

and the ceramic powder located in area 4 are assumed to have different uniaxial viscosities and free sintering rates. Hence, these parts of the sample shrink at different rates; consequently, stress gradients appear near the interfaces between the two constituents.

In the literature, many examples of constrained sintering may be found where Equations 1.24–1.26 are used to study systems such as sintering in the presence of rigid inclusions and constrained sintering of thin films among others. Both theoretical and experimental studies have been conducted. Illustrative examples are in References 59 and 60 for sintering of composites and in References 61–63 for sintering of constrained films. It has been shown that the presence of rigid inclusions retards the densification of the matrix and under some conditions can lead to the formation of cracklike processing defects. Similarly, the densification rate of constrained films is less than that of free films, and if the films are thicker than a critical thickness, cracks perpendicular to the substrate can be formed during sintering.

## 1.7 MICROSTRUCTURE-BASED MODELS

### 1.7.1 Relationship between Mass Transport and Viscosity

Solid-state sintering is controlled by matter transport. Matter transport is driven by the chemical potential gradient. Although globally sintering is controlled by a decrease in

overall free energy (Section 1.2), the local mass transport is the mechanism of achieving this. Thus, there has to be a relation between the change in free energy and the chemical potential gradients. The gradient of chemical potential is related to material flow through the Einstein–Nernst equation:

$$J_i = \frac{\Omega v_i}{kT} D_i \cdot \nabla \mu, \quad (1.28)$$

where  $J_i$  is the mass flux,  $\nabla$  is the bidimensional gradient at the coordinate interface;  $v_i$  is the atomic frequency,  $D_i$  is the diffusion coefficient,  $k$  is the Boltzmann constant,  $\Omega$  is the atomic volume, and  $T$  is the absolute temperature.

The chemical potential at the surface ( $\mu = \mu_s$ ) is given in terms of the surface geometry (curvature) and surface energy through the well-known Herring equation:

$$\mu_s = \mu_0 + \left[ \left( \frac{1}{R_u} + \frac{1}{R_v} \right) \gamma + \left( \frac{1}{R_u} \right) \gamma n_u n_u + \left( \frac{1}{R_v} \right) \gamma n_v n_v \right] \Omega, \quad (1.29)$$

where  $\mu_0$  corresponds to the chemical potential at a plane flat surface,  $u$  and  $v$  are the local principal directions,  $R_u$  and  $R_v$  are the radii of curvature in the directions  $u$  and  $v$ , and  $n_u$  and  $n_v$  denote the second derivate of the surface energy  $\gamma$  with respect to the angle of the two principle directions  $u$  and  $v$ . For the case of a plane grain boundary, Herring stated that

$$\mu_s = \mu_0 - \Omega \sigma_n, \quad (1.30)$$

where  $\sigma_n$  is the normal component of stress at the grain boundary. In Equations 1.29 and 1.30, the surface energy and the atomic volume are material properties, then the surface curvature and boundary stress may be seen as solid-state sintering driving forces.

The combination of Equations 1.28 and 1.29 for the case of surface diffusion leads to the following relation:

$$j_i = -\frac{2\gamma_s \Omega \delta D_s}{kT} \nabla \kappa, \quad (1.31)$$

where it is assumed that  $v_i = \delta/\Omega$ ,  $\delta$  is the diffusion width, and  $\nabla \kappa$  is the gradient of surface curvature (the term in the square brackets in Eq. 1.29). Combining Equations 1.28 and 1.30 for boundary diffusion leads to

$$j_i = \frac{\Omega \delta D_b}{kT} \nabla \sigma_n. \quad (1.32)$$

Equations 1.31 and 1.32 illustrate that the surface curvature gradient and stress gradient are the driving force for pore surface and grain boundary diffusion during solid-state sintering.

The energy balance can be stated as it was done for the amorphous sintering by Frenkel [19]. The rate of energy dissipation can be written as

$$\dot{W} = \frac{1}{2} \sum_l \left( \dot{u}_n^{(l)} F_n^{(l)} + \dot{u}_{t,i}^{(l)} F_{t,i}^{(l)} \right) = V \sigma_{ij} \dot{\epsilon}_{ij}, \quad (1.33)$$

where  $\frac{1}{2}$  is to consider that each grain boundary interface belongs to two grains; the index  $l$  is for each grain boundary.  $V$  is the volume of the representative volume.  $\dot{u}_n^{(l)}$  and  $\dot{u}_{t,i}^{(l)}$  are the normal and the tangential components of the displacement rate of the  $(l)$ -grain contact;  $F_n^{(l)}$  and  $F_{t,i}^{(l)}$  are the normal and the tangential components of the force at the  $(l)$ -grain contact.

In addition, using the continuum approach, the stress and strain rates for a sintering body are related by

$$\sigma_{ij} = C_{ijkl} \dot{\epsilon}_{kl} + \delta_{ij} \sigma_s, \quad (1.34)$$

where  $C_{ijkl}$  is the viscous coefficient;  $\sigma_s$  is known in the literature as the sintering stress or the sintering potential. It is defined as the external hydrostatic stress required to completely suppress sintering. Further mathematical details may be found in the literature [64–66]. The continuum relations, Equations 1.24–1.26, are related to Equation 1.34. Specifically, for an isotropic body, the sintering potential,  $\sigma_s = -3K_p \dot{\epsilon}_f$  and  $C_{ijkl}$  are general viscous coefficients, which, for an isotropic material, are given by two of the four constitutive parameters:  $E_p$ ,  $\nu_p$ ,  $G_p$ , and  $K_p$ .

For statistically homogeneous orientation of the contacts, the material is isotropic. Then, their viscous properties may be characterized only by two constants, let say, the shear and bulk viscosities. In terms of the diffusion and material parameters, these are given by [65]

$$G_p = C_{1212} = \rho_0^{2/3} \rho^{1/3} Z \frac{3c^2}{20R} \left\{ \frac{kTc^4}{12\Omega\delta D_b} + \eta_s \right\} \quad (1.35)$$

and

$$K_p = \frac{1}{3} (C_{1111} + C_{1122} + C_{1133}) = \frac{\rho_0^{2/3} \rho^{1/3} Z k T c^4}{48\Omega\delta D_b R}, \quad (1.36)$$

where  $\rho_0$ ,  $Z$ ,  $c$ ,  $R$ , and  $\eta_s$  are the initial relative density, the average number of contacts per particle, the grain size, the particle size, and the sliding viscosity between particles, respectively.

Equations 1.35 and 1.36 are for connected porosity (intermediate-stage sintering); for closed porosity (final-stage sintering), the bulk viscosity is given by [65]

$$K_p = \frac{kTR^3}{18\Omega\delta D_b \rho} \left( -2 \ln \omega - \frac{33}{64} + \omega - \frac{\omega^2}{16} \right). \quad (1.37)$$

$\omega$  is the area fraction of the particle contact covered by pore [65]. In order to calculate  $G_p$ , the ratio of  $G_p/K_p$  is used, which is reported to be between 0.269 and 1.5 [65]. Most models predict a gradual decrease of  $G_p/K_p$  toward zero as  $\rho = 1$ . This is to be expected since the bulk viscosity for a fully dense body must be infinite.

Equations 1.35–1.37 give the viscosities of a body undergoing solid-state sintering in terms of important microstructural parameters like the relative density, the number of contacts, initial density, and particle size. As can be expected, many of these parameters evolve during sintering, and therefore the constitutive parameters evolve.

Thus, it can be seen that even for isotropic sintering, the precise and correct physical description is complicated. Any simplifying assumptions must be considered carefully since their applicability may be limited. In part due to the complexity associated with the analytical description of sintering, recently, there has been a significant interest in developing a multiscale computer simulation of the process. The essential elements of this are presented next.

## 1.7.2 Advanced Structural Evolution Models

In the last 15 years, sintering modeling has experienced considerable advances in three main directions: (1) simulations of multiparticle systems; (2) more realistic structures as representative volumes of sintering for the analysis of complex geometries, including anisotropy; and (3) simulations at multiple-length scales. This topic is quite broad and is still developing. Here we present just a few examples of this rapidly evolving field.

**1.7.2.1 Discrete Element Simulations (DESS).** DES is a tool that has been recently introduced to study the microstructural evolution during the sintering of powder compacts [67, 68]. Figure 1.14 illustrates the changes in microstructure over a broad density range of a multiparticle assembly. DES provides a practical way to consider particle rearrangement because the force equilibrium is calculated for each individual particle or discrete element. Comparisons with experimental data have shown good agreement regarding the evolution of average grain size and average contact area between particles. In addition, good agreement has been shown for shrinkage and densification (between experimental results and DES simulations). Finally, DES has been also useful in describing the evolution of anisotropic microstructures and the development of defects during sintering [69, 70].

**1.7.2.2 Representative Volume Elements.** The representative volume first proposed by Svoboda et al. [64] and Riedel et al. [65] has been developed further to take into consideration a more realistic structural evolution [71]. Figure 1.15 shows an example with different contacts sizes. In addition, special care is focused on precise surface curvature and its evolution.

**1.7.2.3 Multiscale Models.** A significant advance in the simulation and understanding of the sintering phenomenon has been accomplished with the recent development of multiscale models for sintering. This is due to the realization that sintering is fundamentally characterized by phenomena at different length scales [72].

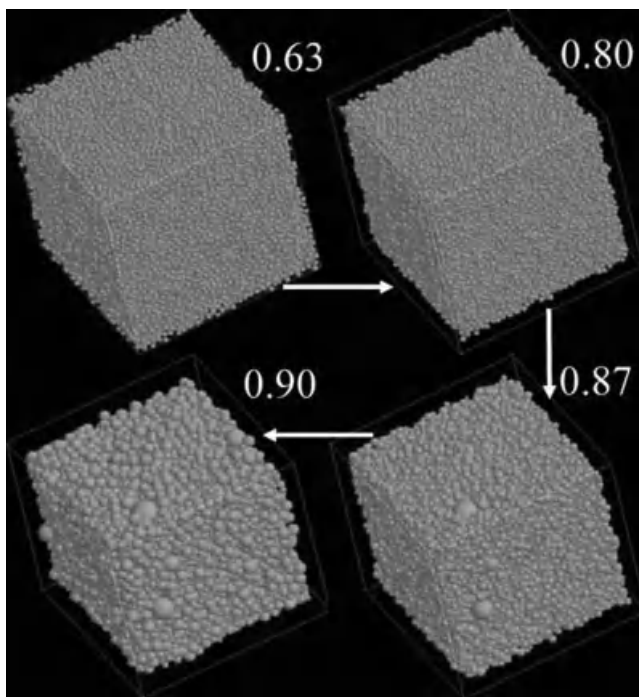


**Figure 1.14.** Discrete element simulations of a multiparticle system highlighting the evolution of the microstructure over a broad density range. Reprinted with permission from Martin et al. [67], copyright 2006, Elsevier.

Figure 1.16 shows the three main scales to study sintering. The macroscale is characterized by the continuum description parameters such as densification, shrinkage, strain rate, and viscosity (Section 1.6). These macroscopic parameters are a consequence of the mesostructural evolution. In the sintering literature, the mesoscale is known as the microstructural scale. Since these two scales must be connected, one must be able to obtain the parameters for the continuum scale from the mesoscale. In the literature, few studies have explicitly demonstrated this multiscale connection. For example, the Monte Carlo approach has been used to study the mesostructure evolution and coupled to the continuum description [73]. In principle, several models to estimate viscosity and free sintering rate, such as the Scherer cell model and the Riedel model, deal with the multiscale nature of sintering because their representative volume may be considered as the mesoscale models. Similarly, DES (described in Section 1.7.2.1) is an example of mesoscale simulation. Using this to obtain the parameters for the continuum scale is an example of multiscale simulations. The smallest length scale is the microscale, where simulations at the atomic scale (e.g., molecular dynamics) are used to calculate parameters like the diffusion coefficient. Olevsky has also developed an anisotropic multiscale model. He reports unexpected deformations resulting from the anisotropic nature of the porosity [74].

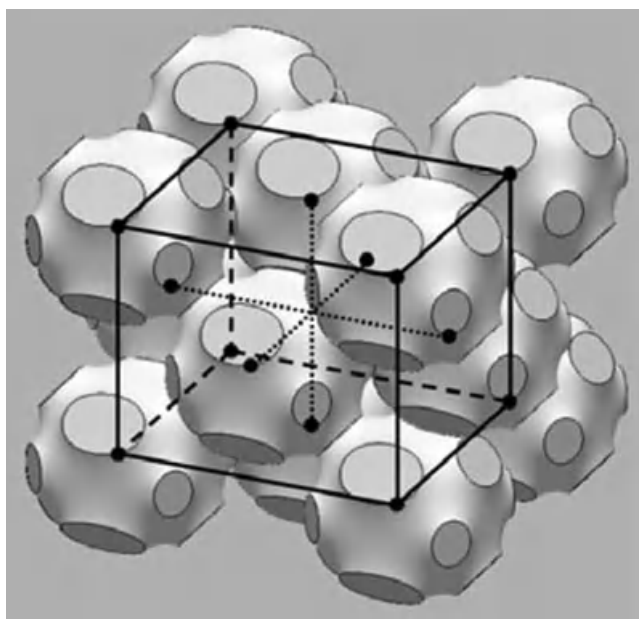


**Figure 1.15.** A representative volume element for sintering studies. The particle contacts are realistically represented in three dimensions with the possibility of anisotropic contacts. Reprinted with permission from Wakai and Shinoda [71], copyright 2009, Elsevier.

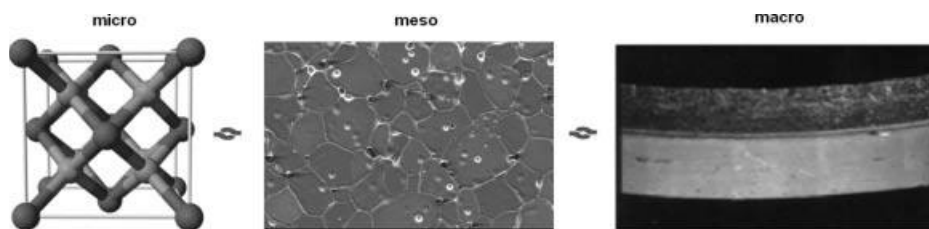


**Figure 1.16.** Schematic representation of the three relevant scales for sintering.

## 1.8 STRESS-ASSISTED SINTERING

For several crystalline materials, a high level of densification cannot be achieved by pressureless sintering. This is particularly true for covalent solids like nitrides and carbides. In these cases, external compressive stresses are used to assist the densification process. In other cases, external stresses are applied to obtain sintering in a short time and to maintain a fine-grained microstructure.

Several techniques have been developed to assist sintering with applied compressive stresses:

1. *Hot Pressing.* The powder compact is confined inside a die and the stress is applied through a piston (Fig. 1.17a).



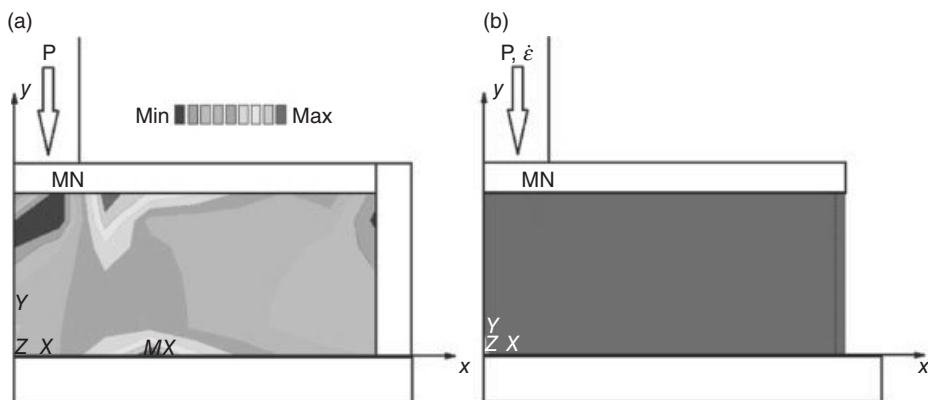


**Figure 1.17.** Hot pressing (a) and hot forging (b) experimental setups. The color scale represents the stress distribution. No friction is considered between die walls and platens and the powder compact. Reprinted with permission from Camacho-Montes et al. [75], copyright 2008, John Wiley & Sons.

2. *Hot Forging.* The powder compact is placed between two platens and the stress is applied in one direction. The faces of the sample that are perpendicular to the direction of the stress are free of any constraint (Fig. 1.17b).
3. *Hot Isostatic Pressing.* A powder compact is placed inside an isolated membrane and the body is subjected to hydrostatic compressive stresses (using high-pressure gas). Specialized pieces of equipment are available for these techniques. As discussed in Section 1.10, hot pressing and hot isostatic pressing are used for many important commercial ceramics.

Figure 1.17 shows the stress distribution during stress-assisted sintering assuming no friction between mold walls, the platens, and the powder compact [75]. The reason compressive stresses assist sintering is because external compressive stress acts as an additional driving force for matter transport (in addition to the surface curvature-driven local stress). Equation 1.32 shows that matter flux can increase because of stress gradients. Equations 1.24–1.26 also show that strain rate can increase because of the applied stress, which leads to an increased densification rate (Eq. 1.27). Thus, the application of external compressive stress reduces the required time for densification. This has the added advantage of reducing grain growth, leading to a more homogeneous fine-grained microstructure. In many cases, this is the primary reason for stress-assisted sintering. Hot forging has the possibility of a uniform stress distribution (Fig. 1.17b), which may be an advantage when a homogeneous structure is desired. As has been noted earlier, for most ceramics, the dependence of the densification rate on applied stress is linear (Eqs. 1.24–27) especially at low applied stresses.

The effect of applied stress on the structure evolution is an important issue to address during stress-assisted sintering. According to Equation 1.32, if the applied stresses are anisotropic, the enhancement in the flux of matter will also be anisotropic.

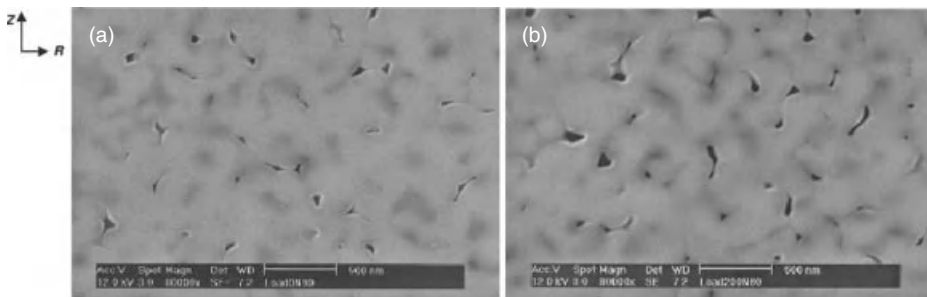


**Figure 1.18.** Microstructural images of alumina samples with a final density of 80% attained by (a) free sintering and (b) sinter forging, respectively, at 1250°C. Reprinted with permission from Zuo et al. [76], copyright 2003, John Wiley & Sons.

This leads to the appearance of a preferred orientation in the microstructure as can be observed in Figure 1.18 [76]. In Figure 1.18a, it can be observed that the orientation of the porosity is random during free sintering. However, during sinter forging, an anisotropic pore orientation develops with the pores oriented preferentially parallel to the applied compressive stress (Fig. 1.18b). Since in many of the stress-assisted sintering situations the microstructure becomes anisotropic, the continuum mechanics approach discussed in Section 1.6 has been modified [77].

## 1.9 FIELD-ASSISTED SINTERING (FAST)

In recent years, there has been significant fundamental and applied research conducted on the effect of electric fields on sintering [78–81]. The primary focus has been on the use of microwaves or a technique referred to as “spark plasma sintering” (SPS). Several advantages of the external field have been highlighted including the ability to densify in a short time, to maintain an ultrafine grain size (even nanostructured in some cases), and to densify materials without conventional sintering additives [82, 83].

Fundamentally, the effect of the field on sintering is essentially focused on the effect of the field on the mass transport. Chemical potential may be written as

$$\mu = \mu_0 + Z^* e \phi. \quad (1.38)$$

where  $Z^*$  is the valence of the diffusing ion and  $e$  is the electric charge of an electron. Hence, from Equation 1.28 and considering that the electric field  $E$  is the gradient of the electric potential  $\phi$ , it can be stated that

$$j_{EM} = -\frac{ND}{kT} eZ^* E, \quad (1.39)$$

where  $j_{EM}$  is the flux contribution from electromigration, which is supposed to play a key role in field-assisted sintering. The activation energy for diffusion may also be affected by an applied field:

$$D = D_0 \exp\left(-\frac{U - \alpha}{kT}\right), \quad (1.40)$$

where  $\alpha$  is the decrease in the activation energy due to the electric field. A more complex physical picture may occur in some systems when specific diffusions mechanisms may be activated because of the application of an electric field or a pulsed current.

### 1.9.1 SPS

Since 1933, the use of applied currents during sintering to aid in the sintering of powders or the sinter joining of metals has been reported [84]. In the 1950s, this technique was called “spark sintering.” Starting in the 1960s, it has been shown that the rapidly changing electric field could also assist in the sintering of nonconducting materials (ceramics). The term “spark plasma sintering” (SPS) started in the 1960s and 1970s in Japan when it was postulated that this was due to the formation of plasma (gas of ionized particles) inside the powder compact. Since then, this field has expanded rapidly with commercial systems available for sintering materials under rapidly varying electric fields (and a modest pressure). There is very little evidence of a spark or plasma under these conditions, but the term SPS is commonly used. A more appropriate term, in our opinion, is FAST.

An important point to note is that during SPS or FAST, the temperature and current are not independent parameters, and the thermal effect of the current, that is, Joule heating, must be considered as part of the heat source. As a result, the electrical properties of the system (including the sample) are important.

FAST has been shown to offer several advantages over conventional methods including pressureless sintering and stress-assisted sintering. These advantages include lower sintering temperature, shorter holding time, and higher heating rate. Consequently, better control over the microstructure becomes a real possibility. Grain growth may be reduced drastically, and it is possible to sinter nanometric powders to near theoretical values and to maintain fine grain size. In fact, FAST is a powerful method to reach full density with negligible grain growth. Such a finer microstructural control leads to better control for the final properties and, in many cases, materials with significantly better properties. A schematic of the FAST setup is shown in Figure 1.19.

In most FAST studies, an external compressive stress is also applied. Hence, the most important parameters to control during FAST are (1) temperature, (2) electrical parameters (voltage, frequency, and power), and (3) applied pressure. Figure 1.20 illustrates the microstructure difference between samples sintered under a field and compressive stress and those sintered under only a compressive stress. The exact reasons for this difference are still under debate, but one clear advantage of FAST is the extremely rapid heating rate.

Due to its practical advantages and open scientific questions, this is an area of intense current research.

Several significant and important fundamental investigations are being conducted to understand the role of the different factors in FAST. An example is shown in

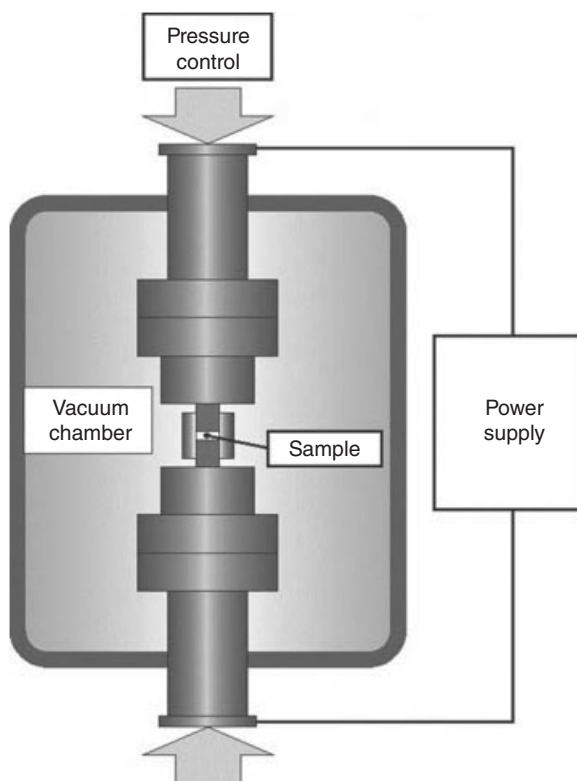


**Figure 1.19.** Experimental setup for field-assisted sintering (also called spark plasma sintering). Reprinted with permission from Munir et al. [82], copyright 2006, Springer.

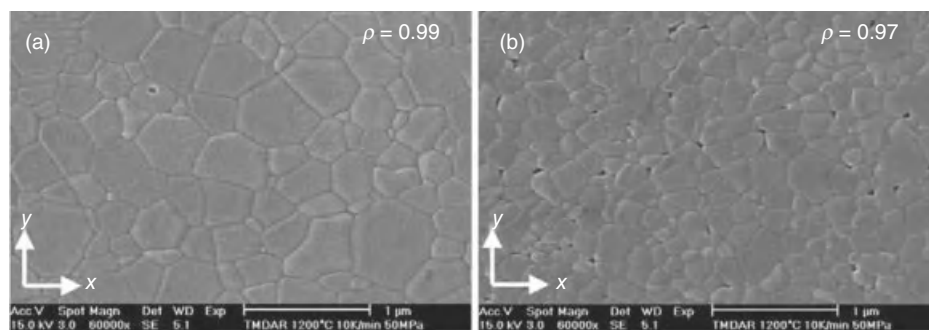


**Figure 1.20.** Difference between FAST and hot-pressed (HP) sintered alumina: (a) FAST and (b) HP sintered alumina at 1200°C, with a stress of 50 MPa, a heating rate of 10 K/min and a dwell time of 1 h. Reprinted with permission from Langer et al. [83], copyright 2009, Elsevier.

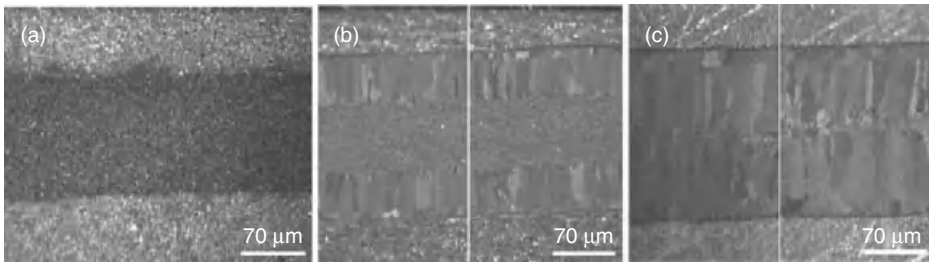


**Figure 1.21.** Effect of the electric current on the microstructure of an intermetallic product layer at two Al/Au interfaces, annealed at 450°C for 4 h (outer layers are Al and inside layer is Au): (a) no current, (b) current density =  $0.51 \times 10^3$  A/cm<sup>2</sup>, and (c) current density =  $1.02 \times 10^3$  A/cm<sup>2</sup>. Reprinted with permission from Munir et al. [82], copyright 2006, Springer.

Figure 1.21, where the focus is on the effect of the electric current on the microstructure. This result suggests that the applied current regime may offer a powerful technique for microstructural control. As a general rule, FAST is used to reach high densification, but, regarding microstructural control, the optimum electric field conditions may be determined by the material composition.

### 1.9.2 Microwave-Assisted Sintering

The use of microwaves in ceramic processing is a relatively recent development. Microwave heating is a volumetric phenomena involving conversion of electromagnetic waves (energy) into thermal energy across the entire volume. It works only with non-conducting ceramics and only with those that couple to the microwaves. In recent years, it has been successfully used to sinter a broad range of ceramics and specific advantages have been demonstrated [85–91].

Although additional research is necessary to fully understand the sintering mechanism involved in microwave-assisted sintering, the important features have been identified. First, microwave heating may be characterized by the transformation of electromagnetic energy into thermal energy. Electromagnetic dissipation may be described as

$$P = 2\pi f \epsilon_0 \epsilon'_r \tan \delta |E|^2, \quad (1.41)$$

where  $f$ ,  $\epsilon_0$ , and  $\epsilon'_r$  are the electric field lineal frequency, the vacuum dielectric conductivity, and the sintering material relative dielectric constant.  $\tan \delta$  is the loss tangent and is given by

$$\tan \delta = \frac{\epsilon''}{\epsilon'} = \frac{\epsilon''_r}{\epsilon'_r}, \quad (1.42)$$

where  $\epsilon''$  and  $\epsilon'$  are known as the imaginary and real parts of the complex dielectric constant. The subscript  $r$  is referred relative to the vacuum dielectric constant. The

imaginary part describes the ability of the material to dissipate the electric field energy into heat. However, the loss tangent is easier to directly measure it.

Hence, the loss factor characterizes the ability of the material to transform the microwave energy into heat. The heating due to the absorbed microwaves inside of the powder compact leads to an increase in its temperature given by

$$\frac{\Delta T}{\Delta t} = \frac{2\pi f \epsilon_0 \epsilon_r'' |E|^2}{\rho C_p}. \quad (1.43)$$

$\rho$  and  $C_p$  are the apparent density and the heat capacity per unit mass. The depth of penetration is also an important parameter to be considered for the experimental setup since it determines the uniformity of heating, that is, the uniformity of the energy supply for any sintering-related phenomena such as densification and grain growth. High frequency and large values of the dielectric property will result in only near surface heating, which may lead to nonuniform microstructure and stress gradients between the bulk and the surface due to the different densification rate. Low frequencies and small values of dielectric properties will result in a more volumetric heating with higher possibilities of uniform microstructure and densification. It can be expressed as

$$d = \frac{3\lambda_0}{8.686\pi f \tan \delta \sqrt{\epsilon_r' / \epsilon_0}}, \quad (1.44)$$

where  $\lambda_0$  is the microwave incident wave length.

The microwave part of the electromagnetic spectrum corresponds to frequencies between 300 MHz and 300 GHz. In general, the higher the frequency, the higher is the power dissipation (Eq. 1.41). Because of this and for practical reasons (equipment design), most sintering applications of microwaves are in the range of 915 MHz–2.45 GHz. Based on their microwave interaction, most materials can be classified into one of three categories—opaque, transparent, and absorbers. For microwaves to effectively heat the material, it must be a good absorber of microwaves. For ceramics, the degree of microwave absorption (Eq. 1.44), and consequently the heating rate (Eq. 1.43), strongly depends on  $\epsilon$  polarization and loss factor  $\tan \delta$ .

The most significant advantage of microwave heating is that it is a volumetric effect. The microwave heating is from the core of the sample to the surface (Fig. 1.22b).

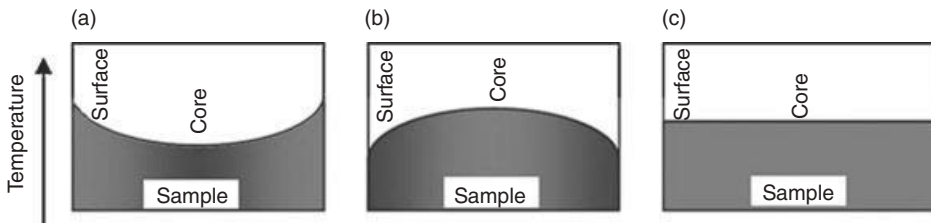


**Figure 1.22.** Temperature profile within the sample in (a) conventional heating, (b) microwave heating, and (c) microwave hybrid heating. Reprinted with permission from Oghbaei and Mirzaee [92], copyright 2010, Elsevier.

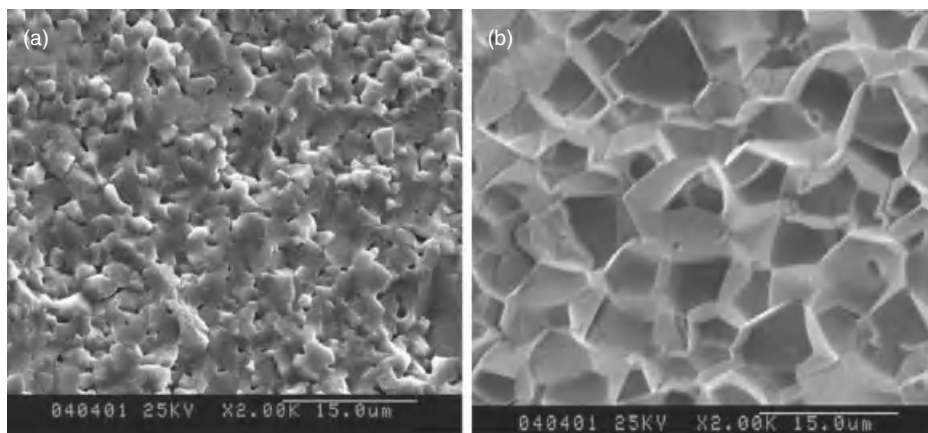


**Figure 1.23.** Scanning electron microscopy (SEM) micrographs of Ni-Zn-Cu ferrite samples sintered at 980°C by the (a) conventional sintering technique and the (b) microwave sintering technique. Reprinted with permission from Oghbaei and Mirzaee [92], copyright 2010, Elsevier.

In conventional heating, on the other hand, the surface is heated by convection and then the interior by conduction through the sample (Fig. 1.22a). Since most ceramics are poor conductors of heat, the temperature gradients, especially in conventional heating, can be significant. Thus, both microwave and conventional heating can lead to temperature nonuniformities and possible inhomogeneous densification. One solution is to combine the two heating methods. This method is known as microwave hybrid heating, and the possible temperature distribution with this approach is schematically shown in Figure 1.22c.

In fact, the reaction between microwaves and materials also leads to a change in the microstructural evolution as may be described by Equations 1.39 and 1.40. A much faster heating rate (Eq. 1.43) may induce a more homogeneous microstructure with less grain growth. One of the main advantages of microwave hybrid heating is the uniformity of the microstructure. Figure 1.23 shows the difference between the microstructure of Ni-Zn-Cu ferrites sintered under conventional and microwave heating.

The processing advantages of microwave heating over conventional ones may be summarized as rapid heating rates and considerable reduction in sintering time and temperature. Generally, a higher density and a more uniform grain size distribution can be achieved through microwave sintering. In addition, microwave sintering is an attractive approach to sinter samples of large sizes.

## 1.10 SINTERING PRACTICE

The developments in sintering theory summarized above have, at least, led to a qualitative description of the effect of critical parameters on densification and final microstructure.



It has been recognized that the control of the green compact is particularly important in sintering practice [93]. To achieve a dense fine-grained sintered body, it is desirable to have small particles with a narrow size distribution. The powder should be nonagglomerated, equiaxed, and of high purity or controlled dopant level [94]. These requirements have led to the development of chemical techniques to produce ceramic powders of high purity and controlled size. In addition, emphasis has been placed on green state processing, in particular, ways to avoid agglomeration by pH and counterion control in aqueous systems [95], or stabilization of the colloids by surfactants [96].

Using sintering science as a guide, Yan identified the desired conditions during sintering to obtain good microstructural control during densification [9]. In addition to the desired characteristics of the green compact highlighted above, the other important factors are dopant level, sintering atmosphere, and firing schedule. Although each of these has to be optimized for a specific system, some general guidelines are clear. Basically, the nondensifying (i.e., the coarsening) mechanisms should be suppressed and the densifying mechanisms should be promoted. Therefore, dopants, sintering atmosphere, and heating schedules that favor grain boundary and/or volume diffusion over surface diffusion and vapor transport are desirable. In addition, conditions that minimize exaggerated grain growth (so that pores are not trapped in the grain in the final stages) are favored. Several strategies have been devised to ensure this, including the use of appropriate dopants [9] or by making use of the second phase (in some cases transient) to pin grain boundaries [97].

A classic and technologically important example of the role of dopants is the use of MgO as a dopant in  $\text{Al}_2\text{O}_3$  [98]. It is now well-known that MgO-doped  $\text{Al}_2\text{O}_3$  does not undergo abnormal grain growth and hence can be sintered to high density. Since then, the mechanism of this effect has been a topic of significant research and controversy [99, 100]. There is agreement that MgO reduces the grain growth rate. However, the mechanism for this continues to be debated.

An example of the effect of sintering atmosphere is that  $\text{Al}_2\text{O}_3$  doped with MgO can be sintered to full density (translucent) in a hydrogen or oxygen environment but not in air, nitrogen, argon, or helium [101]. This is because hydrogen and oxygen have good solubility and high diffusivity in  $\text{Al}_2\text{O}_3$ . Another important feature that has been recognized is the interaction between dopants and the atmosphere. Usually, these reactions have the tendency to remove the dopants and thereby reduce their effectiveness. Therefore, in general, these reactions should be avoided.

Finally, the heating schedule has been shown to have a significant effect on densification and final microstructure. This is because in general, the rate-controlling transport mechanism for densification, grain growth, and coarsening has different activation energies and hence dominates in different temperature regimes. In general, the coarsening mechanisms dominate at lower temperatures (due to lower activation energies). Three significant developments are noteworthy. In rate-controlled sintering, the heating rate is controlled to maintain a constant densification rate. It has been shown that this type of heating profile minimizes grain growth [102]. In fast firing, the temperature is raised rapidly and held at a high temperature for a short time. This minimizes the time spent in temperature regions in which the coarsening mechanisms dominate [103]. Finally, FAST (discussed in Section 1.9) may be an example of the effectiveness of controlling the heating rate.



### 1.10.1 Processing Defects

A major concern in sintering is the effect of the green structure and processing parameters on the defects in the sintered microstructure. These processing flaws have been postulated to be the main cause of the poor reliability of structural ceramics [104]. A very thorough and comprehensive study that clearly highlights the effect of processing on strength-limiting defects was conducted by Lange and coworkers. The material chosen for this study was  $0.7 \text{ Al}_2\text{O}_3\text{--}0.3 \text{ ZrO}_2$ . First, these materials were dry pressed and sintered. The average flexural strength was found to be 560 MPa. From fractography, the strength-limiting flaws were found to be soft agglomerates, which sintered away from the matrix, leaving behind large circumferential cracks [105]. These soft agglomerates were removed by using colloidal processing followed by slip casting and sintering. These materials had an average flexure strength of 895 MPa. The strength-limiting flaws in these materials were small hard agglomerates [106, 107]. Finally, in the next step, these agglomerates were removed by sedimentation prior to slip casting. These materials had an average flexure strength of 1045 MPa, in which the strength-limiting flaws were irregularly shaped cracks postulated to be the burnout of organic inclusions (e.g., lint).

It has been shown that differential densification rates in inhomogeneous powder compacts lead to internal stresses during sintering [108]. For an inclusion with a sintering rate less than the matrix, the circumferential stress at the interface between the inclusion and the matrix is tensile. This could lead to radial cracks. On the other hand, for an inclusion that sinters faster than the matrix, the radial stresses are tensile, which can lead to circumferential cracks. In Reference 109, it has been shown that there is a critical inclusion (or inhomogeneity size) such that for inclusions less than this, cracks are not formed. The critical size depends on the difference in the sintering rate and the constitutive parameters (particularly the viscous Poisson's ratio).

## 1.11 SUMMARY

Sintering is an important approach to manufacture ceramics and hard metals of controlled density. It is used for a broad range of applications, from pottery to high-tech electronic and structural ceramics. In the last 70 years, our understanding of sintering science and technology has advanced considerably.

This chapter provides an overview of these advances. The basics, including the thermodynamics and kinetics of sintering, have been presented. The various models for sintering of powder compacts in different geometric stages have been discussed for different types of sintering (viscous, solid state, and liquid phase). Some of the important areas of current research including the sintering of multicomponent materials (constrained sintering), microstructure-based models, multiscale models, sintering under external stresses, and FAST are summarized. The important lessons from the science and their application in sintering practice have also been highlighted.

Although considerable progress has been made, several areas of active research remain. In addition to the emerging areas like constrained sintering and FAST, the

precise, quantitative description of sintering remains an active area of research and development. The microstructure-based models and multiscale modeling are promising approaches.

## ACKNOWLEDGMENT

RKB acknowledges partial support during the writing of this chapter from the Air Force Office of Scientific Research (FA95550-09-1-0633) and from the National Science Foundation (DMR-1008600). RKB and HCM gratefully acknowledge the support of Consejo Nacional de Ciencia y Tecnología (Mexico) for the sabbatical stay of HCM in the research group of RKB.

## REFERENCES

1. S. L. Sass, *The Substance of Civilization: Materials and Human History from the Stone Age to the Age of Silicon*. Arcade Publishing, New York, 1998.
2. R. F. Walker (1955) Mechanism of materials transport during sintering, *J. Am. Ceram. Soc.*, **38** 187–197.
3. H. H. Hausner, *Handbook of Powder Metallurgy*, Chemical Publishing, New York, 1973.
4. F. J. Klug, W. D. Pasco, and M. P. Borom (1982) Microstructure development of aluminum oxide: Graphite mixture during carbothermic reduction, *J. Am. Ceram. Soc.*, **65** 619–624.
5. F. Thümmel and W. Thomma (1967) The sintering process, *Metall. Rev.*, **12** 69–108.
6. W. J. Huppmann, in *Sintering and Catalysis*, ed. G. C. Kuczynski, p. 359, Plenum Press, New York, 1975.
7. H. E. Exner and G. Petzow, in *Sintering Process*, ed. G. C. Kuczynski, p. 107, Plenum Press, New York, 1980.
8. R. L. Coble and R. M. Cannon, in *Processing of Crystalline Solids*, eds. H. Palmour, III, R. F. Davis, and T. M. Hare, p. 151, Plenum Press, New York, 1978.
9. M. F. Yan (1981) Microstructural control in the processing of electronic ceramics, *Mat. Sci. Eng.*, **48** 53–72.
10. H. E. Exner and E. Arzt, in *Physical Metallurgy*, 3rd edition, Chapter 30, eds. R. W. Cahn and P. Hassen, pp. 1885–1912, Elsevier Science Publishers, Amsterdam, 1983.
11. C. A. Handwerker, J. E. Blendell, and W. A. Kaysser (eds.), in *Sintering of Advanced Ceramics: Ceramics Transactions*, Vol. 7, The American Ceramic Society, Westerville, OH, 1989.
12. R. M. German, *Sintering Theory and Practice*, John Wiley & Sons, New York, 1996.
13. R. M. German, G. L. Messing, and R. G. Cornwall (eds.), *Sintering Technology*, Marcel Dekker, New York, 1996.
14. S.-J. L. Kang, *Sintering Densification, Grain Growth and Microstructure*. Elsevier Butterworth-Heinemann, Burlington, VT, USA, 2005.
15. R. Bordia and E. Olevsky (2009) Guest Editors for Advances in sintering science and technology, special issue of the *J. Am. Ceram. Soc.*, **92**[7] 1383.
16. R. K. Bordia and E. Olevsky (eds.), *Advances in Sintering Science and Technology: Ceramic Transactions*, Vol. 209, The American Ceramic Society, Westerville, OH, 2010.

17. R. L. Coble (1961) Sintering crystalline solids. intermediate and final state diffusions models, *J. Appl. Phys.*, **32** 787–792.
18. J. I. Martínez-Herrera and J. J. Derby (1995) Viscous sintering of spherical particles via finite element analysis, *J. Am. Ceram. Soc.*, **78**[3] 645–649.
19. J. Frenkel (1945) Viscous flow of crystalline bodies under the action of surface tension, *J. Phys. USSR*, **9** 385–391.
20. G. W. Scherer (1991) Cell models for viscous sintering, *J. Am. Ceram. Soc.*, **74**[7] 1523–1531.
21. J. K. Mackenzie and R. Shuttleworth (1949) A phenomenological theory of sintering, *Proc. Phys. Soc. B*, **62**[12] 833–852.
22. W. D. Kingery, H. K. Bowen, and D. R. Uhlmann, *Introduction to Ceramics*, A Wiley-Interscience Publication, John Wiley & Sons, New York, 1975.
23. G. C. Kuczynski (1949) Self-diffusion in sintering of metallic particles, *Trans. AIME*, **185** 169–178.
24. M. F. Ashby (1974) A first report on sintering diagrams, *Acta Metall.*, **22** 275–289.
25. F. B. Swinkles and M. F. Ashby (1981) A second report on sintering diagrams, *Acta Metall.*, **29** 259–281.
26. C. Herring (1950) Effect of change of scale on sintering phenomena, *J. Appl. Phys.*, **21** 301–303.
27. W. K. Burton, N. Cabrera, and F. C. Frank (1951) The growth of crystals and the equilibrium structure of their surfaces, *Philos. Trans. R. Soc.*, **243A** 299–358.
28. Y. E. Geguzin, L. O. Markno, and B. Y. Pines (1952) Self-diffusion and viscous flow (sintering and creep) in compressed metal powders, *Dokl. Akad. Nauk SSSR*, **87**[4] 577–580.
29. J. G. R. Rockland (1966) On the rate equation for sintering by surface diffusion, *Acta Metall.*, **14** 1273–1279.
30. J. G. R. Rockland (1967) The determination of the mechanism of sintering, *Acta Metall.*, **15** 277–286.
31. W. D. Kingery and M. Berg (1955) Study of the initial stages of sintering solids by viscous flow, evaporation-condensation, and self-diffusion, *J. Appl. Phys.*, **26** 1205–1212.
32. P. V. Hobbs and B. J. Mason (1964) The sintering and adhesion of ice, *Phil. Mag.*, **9** 181–197.
33. R. L. Coble (1958) Initial sintering of alumina and hematite, *J. Am. Ceram. Soc.*, **41** 55–62.
34. D. L. Johnson (1969) New method of obtaining volume, grain-boundary, and surface diffusion coefficients from sintering data, *J. Appl. Phys.*, **40** 192–200.
35. D. L. Johnson (1970) A general model for the intermediate stage of sintering, *J. Am. Ceram. Soc.*, **53** 574–577.
36. R. L. Eadie and G. C. Weatherly (1975) Solutions for the shrinkage rate in the intermediate stage of sintering, *Scr. Metall.*, **9** 285–294.
37. R. L. Eadie, G. C. Weatherly, and K. T. Aust (1978) A study of sintering of spherical silver powder—I. The intermediate stage, *Acta Metall.*, **26** 759–767.
38. W. K. Beere (1975) A unifying theory of the stability of penetrating liquid phases and sintering pores, *Acta Metall.*, **23** 131–138.
39. W. K. Lee, R. L. Eadie, G. C. Weatherly, and K. T. Aust (1976) Method for three-dimensional studies of sintering compacts, *Prakt. Metall./Pract. Metall.*, **13**[5] 241–247.

40. W. Beere, in *Vacancies'76*, eds. R. E. Smallman and J. E. Harris, p. 149, The Metals Society, London, 1977.
41. G. C. Kuczynski (1977) Science of sintering, *Sci. Sinter.*, **9**[3] 243–264.
42. R. Raj and M. F. Ashby (1975) Intergranular fracture at elevated temperature, *Acta Metall.*, **23** 653–666.
43. D. Hull and D. E. Rimmer (1959) The growth of grain-boundary voids under stress, *Phil. Mag.*, **4**[42] 673–687.
44. R. Raj, H. M. Shih, and H. H. Johnson (1977) Correction to: Intergranular fracture at elevated temperature, *Scr. Metall.*, **11** 839–842.
45. B. H. Alexander and R. W. Balluffi (1957) The mechanism of sintering of copper, *Acta Metall.*, **5** 666–677.
46. J. E. Burke, in *Ceramic Microstructures*, eds. R. M. Fulrath and J. A. Pask, p. 681, Wiley, New York, 1968.
47. K. W. Lay, in *Sintering and Related Phenomenon*, eds. G. C. Kuczynski, p. 65, Plenum Press, New York, 1973.
48. W. D. Kingery and B. Francois, in *Sintering and Related Phenomenon*, eds. G. C. Kuczynski, N. A. Hooten, and C. F. Gibbon, p. 471, Gordon Breach, New York, 1967.
49. R. J. Brook (1969) Pore-grain boundary interactions and grain growth, *J. Am. Ceram. Soc.*, **52** 56–57.
50. C. H. Hsueh, A. G. Evans, and R. L. Coble (1982) Microstructure development during final/intermediate stage sintering—I. Pore/grain boundary separation, *Acta Metall.*, **30** 1269–1279.
51. M. Sakarcı, C. H. Hsueh, and A. G. Evans (1983) Experimental assessment of pore breakaway during sintering, *J. Am. Ceram. Soc.*, **66** 456–461.
52. B. J. Kellett and F. F. Lange (1989) Thermodynamics of densification. I. Sintering of simple particle arrays, equilibrium configurations, pore stability, and shrinkage, *J. Am. Ceram. Soc.*, **71**[5] 725–734.
53. R. M. German, P. Suri, and S. J. Park (2009) Review: Liquid phase sintering, *J. Mater. Sci.*, **44** 1–39.
54. M. N. Rahaman, *Ceramic Processing and Sintering*, 2nd edition, CRC Press, New York, 2003.
55. R. M. German, *Liquid Phase Sintering*, 1st edition, Plenum Press, New York, 1985.
56. R. K. Bordia and G. W. Scherer (1988) On constrained sintering—I. Constitutive model for a sintering body, *Acta Metall.*, **36**[9] 2393–2417.
57. R. K. Bordia and G. W. Scherer (1988) On constrained sintering—II. Comparison of constitutive models, *Acta Metall.*, **36**[9] 2393–2417.
58. E. A. Olevsky (1998) Theory of sintering from discrete to continuum, *Mater. Sci. Eng.*, **R23**[2] 41–100.
59. R. K. Bordia and G. W. Scherer (1988) Constrained sintering: III. Rigid inclusions, *Acta Metall.*, **36** 2411–2416.
60. S. M. Salamone, L. C. Stearns, R. K. Bordia, and M. P. Harmer (2003) Effect of rigid inclusions on the densification and constitutive parameters of liquid phase sintered  $\text{YBa}_2\text{Cu}_3\text{O}_{6+x}$  powder compacts, *J. Am. Ceram. Soc.*, **86**[6] 883–892.
61. R. K. Bordia and R. Raj (1985) Sintering behavior of ceramic films constrained by a rigid substrate, *J. Am. Ceram. Soc.*, **68**[6] 287–292.

62. R. K. Bordia and A. Jagota (1993) Crack growth and damage in constrained sintering films, *J. Am. Ceram. Soc.*, **76**[10] 2475–2485.
63. O. Guillon, E. Aubach, R. K. Bordia, and J. Rödel (2007) Constrained sintering of alumina thin films: Comparison between experiments and modeling, *J. Am. Ceram. Soc.*, **90**[6] 1733–1737.
64. J. Svoboda, H. Riedel, and H. Zipse (1994) Equilibrium pore surfaces, sintering stresses and constitutive equations for the intermediate and late stage of sintering—I. Computation of equilibrium surfaces, *Acta Metall. Mater.*, **42**[2] 435–443.
65. H. Riedel, H. Zipse, and J. Svoboda (1994) Equilibrium pore surfaces, sintering stresses and constitutive equations for the intermediate and late stage of sintering—II. Diffusional densification and creep, *Acta Metall. Mater.*, **42**[2] 445–452.
66. T. Kraft and H. Riedel (2004) Numerical simulation of solid state sintering; model and application, *J. Eur. Ceram. Soc.*, **24** 345–361.
67. C. L. Martin, L. C. R. Schneider, L. Olmos, and D. Bouvard (2006) Discrete element modeling of metallic powder sintering, *Scr. Mater.*, **55** 425–428.
68. A. Wonisch, O. Guillon, T. Kraft, M. Moseler, H. Riedel, and J. Rodel (2007) Stress-induced anisotropy of sintering alumina: Discrete element modelling and experiments, *Acta Mater.*, **55** 5187–5199.
69. C. L. Martin and R. K. Bordia (2009) The effect of substrate on the sintering of constrained films, *Acta Mater.*, **57**[2] 549–558.
70. C. L. Martin, H. Camacho-Montes, L. Olmos, D. Bouvard, and R. K. Bordia (2009) Evolution of defects during sintering: Discrete element simulations, *J. Am. Ceram. Soc.*, **92**[7] 1435–1441.
71. F. Wakai and Y. Shinoda (2009) Anisotropic sintering stress for sintering of particles arranged in orthotropic symmetry, *Acta Mater.*, **57** 3955–3964.
72. D. J. Green, O. Guillon, and J. Rödel (2008) Constrained sintering: A delicate balance of scales, *J. Eur. Ceram. Soc.*, **28** 1451–1466.
73. E. A. Olevsky, V. Tikare, and T. Garino (2006) Multi-scale study of sintering: A review, *J. Am. Ceram. Soc.*, **89**[6] 1914–1922.
74. A. Kuzmov, E. Olevsky, and A. Maximenko (2008) Multi-scale modeling of viscous sintering, *Modell. Simul. Mater. Sci. Eng.*, **16** 035002 10 pp.
75. H. Camacho-Montes, P. E. García-Casillas, R. Rodríguez-Ramos, M. E. Fuentes-Montero, and L. E. Fuentes-Cobas (2008) Simulation of stress-assisted densification behavior of a powder compact: Effect of constitutive laws, *J. Am. Ceram. Soc.*, **91** 836–845.
76. R. Zuo, E. Aulbach, R. K. Bordia, and J. Rodel (2003) Critical evaluation of hot forging experiments: Case study in alumina, *J. Am. Ceram. Soc.*, **86**[7] 1099–1105.
77. R. K. Bordia, R. Zuo, O. Guillon, S. M. Salamone, and J. Rödel (2006) Anisotropic constitutive laws for sintering bodies, *Acta Mater.*, **54** 111–118.
78. G. Bernard-Granger and C. Guizard (2007) Spark plasma sintering of a commercially available granulated zirconia powder: I. Sintering path and hypotheses about the mechanism(s) controlling densification, *Acta Mater.*, **55** 3493–3504.
79. Z. Shen, M. Johnsson, Z. Zhao, and M. Nygren (2002) Spark plasma sintering of alumina, *J. Am. Ceram. Soc.*, **85**[8] 1921–1927.
80. J. Räthel, M. Herrmann, and W. Beckert (2009) Temperature distribution for electrically conductive and non-conductive materials during field assisted sintering (FAST), *J. Eur. Ceram. Soc.*, **29** 1419–1425.

81. Y. Zhou, K. Hirao, Y. Yamauchi, and S. Kanzaki (2004) Densification and grain growth in pulse electric current sintering of alumina, *J. Eur. Ceram. Soc.*, **24** 3465–3470.
82. Z. A. Munir, U. Anselmi-Tamburini, and M. Ohyanagi (2006) The effect of electric field and pressure on the synthesis and consolidation of materials: A review of the spark plasma sintered method, *J. Mater. Sci.*, **41** 763–777.
83. J. Langer, M. J. Hoffmann, and O. Guillon (2009) Direct comparison between hot pressing and electric field-assisted sintering of submicron alumina, *Acta Mater.*, **57** 5454–5465.
84. G. F. Taylor (1933) U.S. Patent No. 1,896,854.
85. S. Nath, B. Basu, and A. Sinha (2006) A comparative study of conventional sintering with microwave sintering of hydroxyapatite synthesized by chemical route, *Trends Biomater. Artif. Organs*, **19**[2] 93–98.
86. A. Chatterjee, T. Basak, and K. G. Ayappa (1998) Analysis of microwave sintering of ceramics, *Materials, Interfaces, and Electrochemical Phenomena. AIChE J.*, **44**[10] 2302–2311.
87. K. E. Haque (1999) Microwave energy for mineral treatment processes—A brief review, *Int. J. Miner. Process.*, **57** 1–24.
88. D. E. Clark (1996) Microwave processing of materials, *Annu. Rev. Mater. Sci.*, **26** 299–331.
89. E. T. Thostenson and T.-W. Chou (1999) Microwave processing: Fundamentals and applications, *Composites A*, **30** 1055–1071.
90. J. D. Katz (1992) Microwave sintering of ceramics, *Annu. Rev. Mater. Sci.*, **22** 153–170.
91. D. E. Clark, D. C. Folz, and J. K. West (2000) Processing materials with microwave energy, *Mater. Sci. Eng.*, **A287** 153–158.
92. M. Oghbaei and O. Mirzaee (2010) Microwave versus conventional sintering: A review of fundamentals, advantages and applications, *J. Alloys Comp.*, **494** 175–189.
93. G. Y. Onoda, Jr. and L. L. Hench (eds.), *Ceramic Processing before Firing*. John Wiley, New York, 1978.
94. P. Reynen, in *Sintering Processes* ed. G. C. Kuczynski, pp. 46–54, Plenum Press, New York, 1980.
95. P. J. Anderson and P. Murray (1959) Zeta potentials in rheological properties of oxide slips, *J. Am. Ceram. Soc.*, **42** 70–74.
96. G. D. Parfitt and J. Peacock, in *Surface and Colloid Science*, ed. E. Matijevic, p. 163, Wiley-Interscience, New York, 1978.
97. W. H. Rhodes (1981) Controlled transient solid second-phase sintering of yttria, *J. Am. Ceram. Soc.*, **64** 13–19.
98. W. C. Johnson and R. L. Coble (1978) A test of the second-phase and impurity segregation models for MgO-enhanced densification of sintered alumina, *J. Am. Ceram. Soc.*, **61**[3–4] 110–114.
99. S. J. Bennison and M. P. Harmer (1988) History of the role of MgO in the sintering of alpha-Al<sub>2</sub>O<sub>3</sub>, *Cer. Trans.*, **7** 13–49.
100. I.-J. Bae and S. Baik (1997) Abnormal grain growth of alumina, *J. Am. Ceram. Soc.*, **80**[5] 1149–1156.
101. R. L. Coble (1962) Sintering alumina: Effect of atmospheres, *J. Am. Ceram. Soc.*, **45** 123–127.

102. H. Palmour, III, M. L. Huckabee, and T. M. Hare Rate controlled sintering: Principles and practice. Sintering—New Developments, Fourth International Round Table Conference on Sintering, Elsevier, Amsterdam 46–56, 1979.
103. M. P. Harmer, *Rapid sintering of pure and doped alpha alumina*, PhD thesis, University of Leeds, Leeds, UK, 1980.
104. F. F. Lange (1984) Structural ceramics: A question of fabrication reliability, *J. Mat. Energy Syst.*, **6**[2] 107–113.
105. F. F. Lange (1983) Processing-related fracture origins: I, observations in sintered and isostatically hot-pressed  $\text{Al}_2\text{O}_3/\text{ZrO}_2$  composites, *J. Am. Ceram. Soc.*, **66** 396–398.
106. I. A. Aksay, F. F. Lange, and B. A. Davis (1983) Uniformity of  $\text{Al}_2\text{O}_3\text{-ZrO}_2$  composites by colloidal filtration, *Comm. J. Am. Ceram. Soc.*, **66** C190–C192.
107. F. F. Lange, B. A. Davis, and I. A. Aksay (1983) Processing-related fracture origins: III, differential sintering of  $\text{ZrO}_2$  agglomerates in  $\text{Al}_2\text{O}_3/\text{ZrO}_2$  composite, *J. Am. Ceram. Soc.*, **66** 407–408.
108. R. K. Bordia and G. W. Scherer, *Ceramic Transactions*, Vol. 1, eds. G. L. Messing, E. R. Fuller, Jr., and H. Hausner, pp. 872–886, American Ceramic Society, Westerville, OH, 1988.
109. R. Raj and R. K. Bordia (1984) Sintering behavior of bi-modal powder compacts, *Acta Metall.*, **32**[7] 1003–1019.

# THE ROLE OF THE ELECTRIC CURRENT AND FIELD DURING PULSED ELECTRIC CURRENT SINTERING

K. VANMEENSEL, A. LAPTEV, S. G. HUANG, J. VLEUGELS,  
AND O. VAN DER BIEST

## 2.1 INTRODUCTION

Pulsed electric current sintering (PECS), also known as spark plasma sintering (SPS), field-assisted sintering technique (FAST), plasma-assisted sintering (PAS), electric current-assisted sintering (ECAS), or plasma pressure compaction ( $P^2C$ ), is a *rapid, commercial sintering process* developed over the past few decades [1]. As early as 1913, the first patent was issued for a powder compaction method and equipment that heated and sintered powders by passing electric current through them [2–4]. In 1967, Inoue patented in Japan a machine for rapidly sintering powders by a spark discharge between the particles [5].

Current PECS technology uses a *high-amperage, low-voltage pulsed DC* and uni-axial loading to consolidate powders [1, 6]. A schematic of the PECS process is shown in Figure 2.1. PECS is usually performed in a vacuum or in a chamber with controllable atmosphere. The powder is loaded in a die and contained between two electrically conductive punches. A minimum pressure needs to be applied on the die and punches in order to guarantee a good electrical contact between the electrodes and the tool as well as to guide the current. The powder is heated directly by Joule heating using a



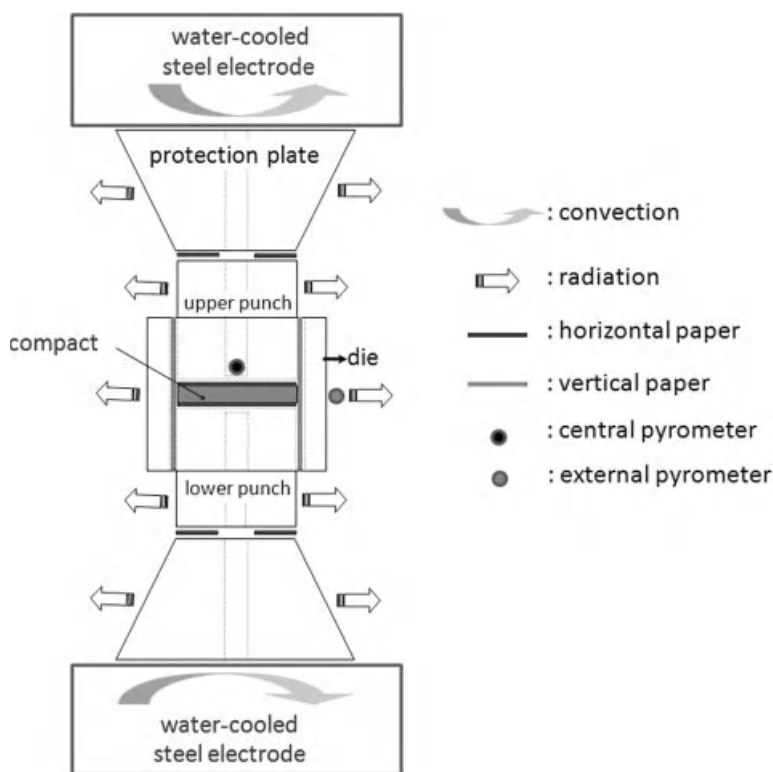


**Figure 2.1.** Schematic of the PECS setup. Usually, graphite tool parts are used, separated from each other by graphite papers. The diameter of the water-cooled steel electrodes inside a FAST HP D 25/1 device (FCT Systeme, Rauenstein, Germany) is 80 mm. Graphite dies (20, 30, and 40 mm) are conventionally used. The die wall thickness varies between 8.5 and 18 mm. Joule heat is generated by passing a low-voltage (0–10 V), high-amperage (0–10 kA) pulsed DC through a specifically designed symmetrical tool setup. The temperature is measured by a central pyrometer (CP) focusing at the bottom of a borehole inside the upper punch, 5 mm away from the top of the sintering powder compact. An external pyrometer (EP) can be focused on the outer die wall surface. Four flexible thermocouples can be positioned at different locations inside the PECS tool setup.

pulsed DC in the presence of an electric field, while a uniaxial pressure is simultaneously applied. The temperature is measured using thermocouples or an optical pyrometer. The importance of a correct temperature measurement will be discussed in detail in the following paragraph. A temperature profile is programmed by the user and the current is adjusted by the PECS controller accordingly.

Although the PECS technique has proven its successful application in novel material synthesis and powder consolidation [7–9], limited scientific background is available on the impact of the electric current or the electric field on the *mass transport processes*

or grain growth during powder compact sintering in a PECS unit. Therefore, this chapter aims to provide a general overview of mass transport mechanisms that are present during a pressure-assisted sintering process and to highlight the influence of an electric current on each of them.

Due to the *complex interplay between thermal, electric, and mechanical fields* during PECS consolidation of a powder compact, the peculiarities of the PECS process and how they influence a powder compact's sintering behavior will be discussed from both macroscopic (i.e., experimentally measurable temperature, pressure, and current density gradients inside the PECS tool setup and sample) and microscopic (i.e., temperature, pressure, and current density distributions at the particle scale) points of view. The microscopic effects will be labeled either thermal or athermal, following a categorization that was suggested by Olevsky and Froyen [10].

Before discussing the role of the current on the specific events occurring during powder compaction, the different grain growth and mass transport mechanisms will be summarized.

## 2.2 GRAIN GROWTH DURING SINTERING

At all stages during a typical sintering process, *grain growth*, resulting in microstructural coarsening, competes with *densification*. The thermodynamic driving force for both competing processes is identical, that is, a decrease in the internal energy of the sintering powder compact. The mechanisms that are responsible for grain growth and densification, however, are different. At low temperatures and high porosities, surface diffusion and evaporation–condensation (Fig. 2.2) are mainly responsible for grain growth, while at higher temperatures and lower porosities, grain growth occurs by grain boundary migration. At high relative densities of the powder compact, all pores are isolated and cannot effectively pin the grain boundaries anymore, resulting in quick grain growth [11].

Grain growth refers to the increase in the size of grains (crystallites) in a material at high temperature. It occurs when the reduction in the internal energy of a polycrystalline material is achieved by reducing the total grain boundary area.

*Ideal grain growth* is a special case of normal grain growth ( $n = 2$  in Eq. 2.1) where grain boundary motion is driven only by the reduction of the total amount of grain boundary surface. Additional contributions to the driving force by, for example, elastic strains or temperature gradients are neglected. If it holds that the rate of growth is proportional to the driving force and that the driving force is proportional to the total amount of grain boundary energy, then it can be shown that the time  $t$  required to reach a given grain size is approximated by the equation:

$$d^n - d_0^n = kt, \quad (2.1)$$

where  $d_0$  is the initial grain size,  $d$  is the final grain size,  $n$  depends on the grain growth mechanism, and  $k$  is a temperature-dependent constant given by an Arrhenius-type equation:

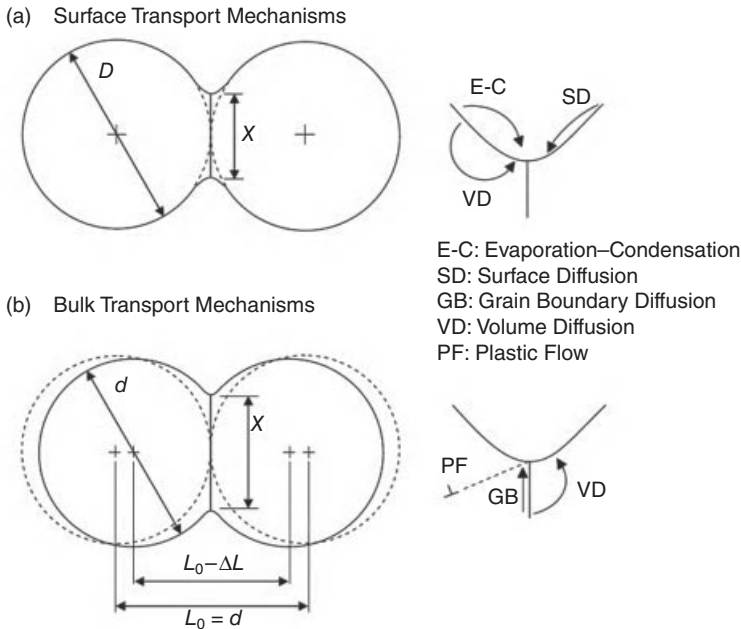


**Figure 2.2.** Idealized two-sphere sintering model showing the different surface and bulk transport processes. Adapted from German [12, 13].

$$k = k_0 \exp\left(-\frac{Q}{RT}\right), \quad (2.2)$$

where  $k_0$  is a constant,  $T$  is the absolute temperature, and  $Q$  is the activation energy for boundary mobility. Theoretically, the activation energy for boundary mobility should equal that for self-diffusion, but this is often found not to be the case. In general, these equations are found to hold for ultra-high-purity materials but rapidly fail when even tiny concentrations of solute are introduced.

When *discontinuous grain growth* occurs, that is, the consumption of smaller grains by large grains, in a process called Ostwald ripening, the exponent  $n$  in Equation 2.1 equals 3.

## 2.3 MASS TRANSPORT DURING SINTERING PROCESSES

### 2.3.1 Pressureless Sintering

*Sintering* is the consolidation of powders into solid parts [12–14]. The theoretical models first developed by Kuczynski, Coble, Kingery, Berg, Johnson, and others provide the background for sintering theory today [15–21].

*Pressureless sintering* can be defined as the bonding of particles by the diffusion of atoms accompanied by a reduction of surface area. Diffusion is a thermally activated process, requiring a minimum energy to begin. The activation energy is related to the diffusivity by the Arrhenius-type relation

$$D = D_0 \exp((-Q)RT), \quad (2.3)$$

where  $D$  is the diffusivity,  $D_0$  the diffusivity pre-exponential coefficient,  $Q$  the activation energy for self-diffusion,  $R$  the gas constant, and  $T$  the temperature in kelvin [22].

As atoms diffuse, some will move into positions that reduce the total surface energy and thus reduce the surface area. The driving force for atoms to move to positions that reduce the surface energy is associated with the stress at the particle surface. The *Young–Laplace equation* gives the stress across a curved surface,  $\sigma$ , by

$$\sigma = \gamma \left( \frac{1}{R_1} + \frac{1}{R_2} \right), \quad (2.4)$$

where  $\gamma$  is the surface energy, and  $R_1$  and  $R_2$  are the principal radii of surface curvature. Small radii of curvature lead to high surface stresses [23]. Thus, when two particles are touching, there is a driving force to reduce the stress and surface area by increasing the radii of curvature at the contact point. As a result, the atoms diffuse to the contact region; a neck, or the initial bond, forms between the particles. This process is called neck formation.

After *initial neck formation*, atoms continue to diffuse to the neck region, increasing the radius of curvature and, in turn, slowing down the sintering process due to a reduction in surface stress and energy. After the initial neck growth, during the *intermediate sintering stage*, the total pore volume is decreased and the initial pore structure changes from being irregular and angular to an interconnected nearly cylindrical structure along the grain boundaries.

As pore volume continues to decrease, the structure becomes unstable (the breakdown is where the ratio of the pore length to the radius becomes larger than  $2\pi$ ) and in the *final stage of sintering*, the pore structure collapses into isolated spherical pores. The isolated pores do not inhibit grain growth as much as the interconnected structure does, which leads to increasing grain size during late-stage sintering and, correspondingly, to a reduction in the grain boundary diffusion rate [24]. Grain growth and isolated pores at late-stage sintering can slow the rate of densification, especially if the pores contain trapped gas.

Generally, *diffusion processes* during sintering fall into two main categories: surface and bulk transport, illustrated in Figure 2.2. Surface transport (Fig. 2.2A) involves the rearrangement of particles to form a neck without any shrinkage or densification.

Due to *surface diffusion*, atoms fill sites at the interface between particles that reduce the curvature and thereby reduce the surface stress. Surface diffusion is the dominating mechanism at low temperatures in most polycrystalline materials. Metals with high vapor pressure also undergo evaporation–condensation surface transport [25].

*Bulk transport processes* involve the movement of mass from the interior of the particle to the neck region and cause shrinkage (Fig. 2.2B). Bulk transport includes volume diffusion, grain boundary diffusion, and eventual viscous flow. Viscous flow, where materials with decreased viscosity at elevated temperatures flow under surface stress, is typically more important during liquid-phase sintering or when liquid is present at grain boundaries. Grain boundary diffusion is the main diffusion mechanism in most polycrystalline metals as it is more energetically favorable than diffusion through the lattice.

Two types of equations have been suggested to describe the initial sintering stage, either relating the neck,  $X$ , to the particle,  $d$ , diameter ratio,  $X/d$ , or the relative change in distance between two particle centers,  $\Delta L/L_0$ , to the particle diameter,  $d$ , and the time,  $t$ , at a certain temperature,  $T$ :

$$\left(\frac{X}{d}\right)^n = \frac{Bt}{d^m} \quad (2.5)$$

and

$$\left(\frac{\Delta L}{L_0}\right)^n = \frac{B_1 t}{2^n d^m}, \quad (2.6)$$

where  $B_1 = B \exp\left(\frac{-Q}{RT}\right)$  indicates an exponential temperature dependency. The values of  $B$ ,  $m$ , and  $n$  depend on the sintering mechanism and are given in Table 2.1 [26], with  $\gamma$  as the surface energy,  $\eta$  the viscosity,  $b$  the Burgers vector,  $k$  the Boltzmann constant,  $T$  the absolute temperature,  $\rho$  the theoretical density,  $\delta$  the grain boundary width,  $D_v$  the volume diffusivity,  $D_s$  the surface diffusivity,  $D_b$  the grain boundary diffusivity,  $P$  the vapor pressure,  $M$  the molecular weight, and  $\Omega$  the atomic volume.

Equations 2.5 and 2.6 indicate that *smaller particles* sinter more rapidly and that surface as well as grain boundary diffusion are more significant for smaller particles. Furthermore, an exponential dependence on temperature is observed, while neck growth is proportional to time, indicating that time is expected to have a smaller impact on sintering than temperature.

TABLE 2.1. Initial-Stage Sintering Mechanisms for Equations 2.5 and 2.6

Mechanism	n	m	B
Viscous flow	2	1	$3\gamma/\eta$
Plastic flow	2	1	$9\pi\gamma b D_v/kT$
Evaporation–condensation	3	2	$(3P\gamma/\rho^2)(\pi/2)^{1/2}(M/kT)^{3/2}$
Volume diffusion	5	3	$80D_v\gamma\Omega/kT$
Grain boundary diffusion	6	4	$20\delta D_b\gamma\Omega/kT$
Surface diffusion	7	4	$56D_s\gamma\Omega^2/3kT$

*Intermediate-stage sintering* is the most important for densification and for determining the final properties of the sintered material but is the most complex and least understood. During intermediate-stage sintering, pore rounding, densification, and grain growth occur simultaneously. There are no good fundamental models for intermediate-stage sintering, but empirical models have been developed [27]. Curvature gradients at the pores have been largely eliminated at this stage, and the driving force becomes the elimination of the remaining surface energy.

As stated previously, the pore structure collapses from an interconnected network into a set of isolated pores during final-stage sintering. Grain growth becomes more active as the isolated pores have less of a pinning effect. Normally, pore closure starts at 15% porosity, and all pores are closed at 5% porosity. Final-stage sintering is a slow process where grain growth and densification are in competition. The rate of densification by *volume diffusion during the final-stage sintering* is given by

$$\frac{d\rho_s}{dt} = \frac{12D_v\Omega}{kTG^2} \left( \frac{4\gamma}{d_p} - P_g \right), \quad (2.7)$$

with  $d_p$  as the pore radius and  $P_g$  as the gas pressure in the pore. Similar to the intermediate sintering stage equation, densification is inversely proportional to the cube of the grain size  $G$ . The application of stress during sintering may be required in order to attain desirable densification and to eliminate porosity [28].

### 2.3.2 Pressure-Assisted Sintering

An *applied pressure* will supplement the inherent sintering stress and increase the densification process, especially at high temperatures due to the decreased yield stress and the acceleration of dislocation-based creep. Temperature plays a similar role in pressure-assisted sintering as in traditional sintering by increasing mass motion as well as decreasing the yield strength of the material, inducing an increased response to an applied stress [29].

At all stages of densification, the densification rate is strongly dependent on *stress and grain size*. The exact dependence is determined by the *controlling mechanism*. Three primary deformation mechanisms exist during pressure-assisted sintering: plastic deformation, linear or nonlinear creep, and diffusion. *Viscous flow*, which can be referred to as a linear creep, occurs in materials where a glass or liquid is the deformable phase. *Plastic flow* is the deformation within the compact at von Mises stresses equal to the yield stress of the material. The yield stress decreases with increasing temperature. At particle contacts, the effective stress quickly equals the yield stress, and deformation occurs by plastic flow in the neck zones. As particle contacts grow, the effective pressure decreases, but deformation will continue by creep or diffusional flow. Another important densification mechanism during the initial sintering stage is particle rearrangement resulting from shear stress and plastic flow. Grain boundary and volume diffusion become dominant as densification continues. Diffusion-controlled processes have a relatively small dependence on stress compared to their dependence on temperature [30]. Diffusional flow and stress combine to form a diffusion-controlled

*creep* densification process. Depending on the temperature, pressure, and grain size, diffusional creep occurs by different mechanisms. *Nabarro–Herring creep* (volume diffusion-controlled creep) occurs by vacancy diffusion in response to the stress gradient between grain boundaries in tension and those in compression. The shrinkage rate for volume diffusion-controlled creep is given by

$$\frac{d\left(\frac{\Delta L}{L_0}\right)}{dt} = \frac{13.3D_v\Omega P_E}{kTG^2}, \quad (2.8)$$

with  $\Delta L/L_0$  as the linear shrinkage and  $P_E$  as the effective pressure. Coble creep is accommodated by diffusion along the grain boundaries. The shrinkage rate depends on atom removal from the grain boundary and deposition at the neck. The *Coble creep* shrinkage rate is estimated by

$$\frac{d\left(\frac{\Delta L}{L_0}\right)}{dt} = \frac{47.5\delta D_B\Omega P_E}{kTG^2}. \quad (2.9)$$

Smaller particles increase the total grain boundary surface and thus promote densification. The third creep model, the dislocation-based power law creep, occurs at both high temperature and pressure and depends on the rate of dislocation climb. The empirical equation for shrinkage rate for the *power law creep* is given by

$$\frac{d\left(\frac{\Delta L}{L_0}\right)}{dt} = \frac{Cb\mu D_v}{kT} \left(\frac{P_E}{\mu}\right)^q, \quad (2.10)$$

where  $C$  is a material constant,  $b$  is the Burgers vector,  $q$  is the pressure exponent, and  $\mu$  is the shear modulus [31].

Among the different pressure-assisted sintering techniques, *hot pressing in a die* is most similar to PECS. Both during hot pressing and PECS, the applied load is uniaxial, but radial stresses are generated due to the forces exerted from the die wall. The radial stress depends on the axial stress and the nature of the processed material. The radial and axial pressure differential causes a shear effect that improves bonding, the collapse of large flaws, and can disrupt the surface contamination of powders [12, 13, 32, 33]. Graphite dies are typically used during hot pressing. The initial densification during hot pressing occurs by particle rearrangement and plastic flow at the particle contacts.

As the particle contacts grow, thus decreasing the Mises stress to the point where it falls below the yield stress, densification occurs by creep, grain boundary, and volume diffusion. A generalized equation for densification during hot pressing is given by

$$\frac{1}{\rho} \frac{d\rho_s}{dt} = \frac{HD\phi^q}{G^g kT} P_A^q, \quad (2.11)$$

TABLE 2.2. Values of the Exponents  $q$  and  $g$  in Equation 2.11 for Hot Pressing (HP)

Mechanism	$g$	$q$
Volume diffusion	2	1
Grain boundary diffusion	3	1
Dislocation controlled creep	0	$\geq 3$
Viscous flow	0	1

where  $H$  is a collection of material constants and parameters related to the deformation mechanism,  $D$  is the diffusivity coefficient,  $\phi$  is the stress intensification factor,  $G$  is the grain size,  $k$  is the Boltzmann constant,  $T$  is temperature,  $P_A$  is the applied pressure, while the pressure exponent  $q$  and the grain size exponent  $g$  are determined by the densification mechanism. Determining the exponents can give insight into the mechanism of hot pressing. Their values are given in Table 2.2.

Within the following paragraphs, the influence of a high-amperage, low-voltage pulsed DC, typically present during the PECS process, on the different mass transport mechanisms will be discussed in detail. The main difference between traditional hot pressing and PECS is the way the powder compact is heated. While during hot pressing heat is usually transferred by radiation from an external heating element toward the tool setup and eventually the powder compact, the tool and possibly the powder compact itself act as the actual heating element during PECS. This direct way of heating results in effects that are typical for PECS both on macroscopic (i.e., on the scale of the tool and the sample) and microscopic (i.e., inside a sintering powder compact) scales. The next paragraphs will try to summarize and critically review the different parameters and phenomena, playing on both the *macroscopic* and *microscopic* scales, and differentiating PECS from more traditional hot pressing.

## 2.4 MACROSCOPIC PECS EFFECTS

### 2.4.1 Macroscopic Temperature Distributions

**2.4.1.1 Temperature Measurement.** The accuracy of the temperature measurements during PECS processing depends on several factors. Generally, the *die wall temperature*, which is used to control the electric current in most PECS devices, is much lower than the actual *sample temperature* [34–40]. The difference between the sample temperature and die wall temperature increases with increasing temperature [35, 37, 38]. During heating of electrically conductive samples, the die wall temperature lags behind the sample temperature, but for nonconductive samples, the opposite is true [41]. The most accurate method of measuring the actual temperature of relatively thin samples is to record the temperature at the bottom of a borehole inside the upper punch, where the temperature measurement point is close to the sample [35, 37, 38, 41, 42], as illustrated by the finite element simulations in Figure 2.3. Therefore, throughout all



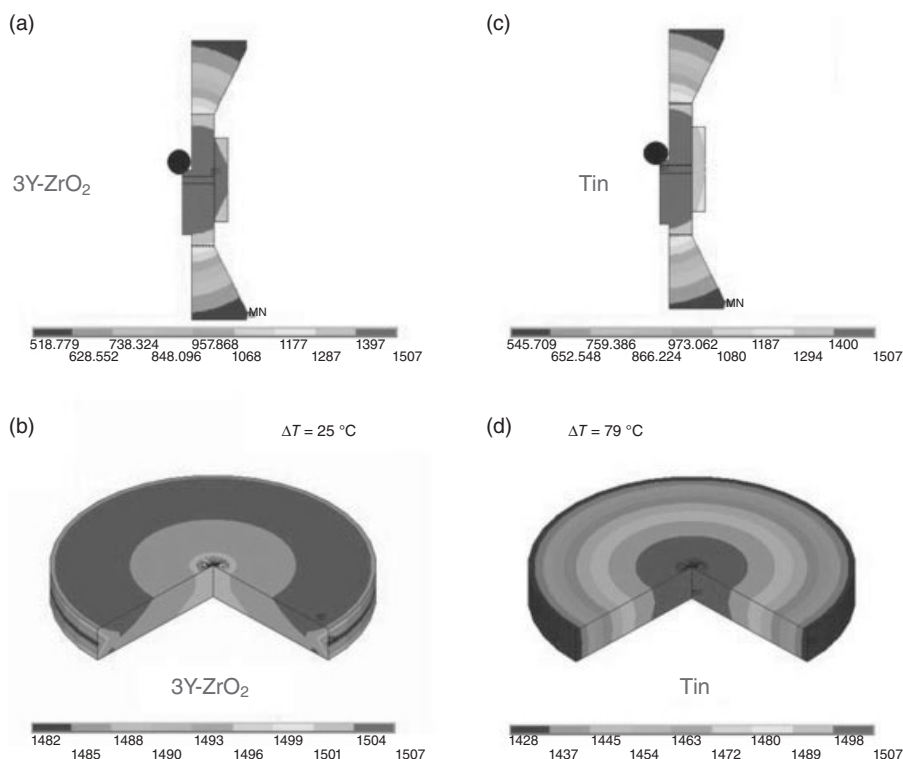


**Figure 2.3.** Influence of the electrical properties of a compact on the temperature distribution during PECS at 1500°C both inside the tool (A–C) and a 40-mm-diameter sample (B–D). In case an electrically insulating 3Y-ZrO<sub>2</sub> sample is placed inside the PECS tool (A,B), the die wall temperature is similar to the sample temperature, and the radial temperature gradient in the sample is limited. However, when an electrically conductive TiN sample is placed inside the PECS tool, the die wall temperature is lower as compared with the sample temperature, and a large radial temperature gradient exists inside the sample. The black dot indicates the focus point of the central pyrometer.

experimental descriptions within this chapter, a 10-V to 10-kA PECS device (type HP D 25/1, FCT Systeme, Rauenstein, Germany [43]), equipped with a *central pyrometer setup*, hereby guaranteeing an accurate and reproducible temperature measurement, was used as indicated schematically in Figure 2.3. Independent on the electrical properties (electrically insulating 3Y-ZrO<sub>2</sub> in Figure 2.3A,B or electrically conductive TiN in Figure 2.3C,D) of a fully dense, 40-mm diameter, 5-mm-thick compact, placed inside a typical graphite PECS tool setup, the temperature difference between the center of the compact and the pyrometer focus point was less than 7°C during a final dwell period at 1500°C. However, a radial temperature gradient existed in both cases inside the dense compact. It was much more pronounced in the case of the electrically conductive TiN

sample. During the dwell stage, the temperature difference between an electrically conductive sample and the die wall is less for samples with higher thermal conductivity [37, 41]. Furthermore, the temperature difference increases with increasing die wall thickness and sample diameter [37, 42].

**2.4.1.2 Influence of Die Design on Current Density and Temperature Distribution.** Due to the direct way of heating, high heating rates, up to  $1000^{\circ}\text{C}/\text{min}$ , can be obtained during PECS. Since *nondensifying diffusion mechanisms* such as surface diffusion and evaporation–condensation have low activation energy, they are predominant in the low-temperature region. Therefore, their contribution can be minimized through the application of high heating rates, especially at low temperatures.

However, the application of high heating rates might also result in the generation of *temperature gradients*, both within the PECS tool setup and, more importantly, within the densifying powder compact. Eventually, this can lead to an inhomogeneous sintering behavior inside the shrinking powder compact, resulting in residual stress generation, inhomogeneous mechanical and other properties, and possibly in sample fractures. Therefore, special attention needs to be paid to the die design in order to guarantee an as homogeneous as possible sintering behavior inside the powder compact.

**TOOL MATERIAL.** Traditionally, graphite dies are used during PECS. However, for low-temperature PECS applications, metal tools, such as steel [44] or refractory metals [45], WC-Co cemented carbide [46] or even electrically insulating die materials [47] have been used. Considering that the electrical resistivity of commercial graphite grades ( $8\text{--}40\ \mu\Omega\text{-m}$ ) [48] is significantly higher than that of steel ( $0.1\text{--}1\ \mu\Omega\text{-m}$ ) [49] or WC-Co cemented carbide ( $0.2\ \mu\Omega\text{-m}$ ) [50], one has to bear in mind that a sufficient ohmic tool resistance is needed in order to have Joule heating occurring in the tool and not in the current conducting electrodes. Figure 2.4 shows the ohmic tool resistance of different molybdenum alloy (TZM)-based PECS dummies that were used to experimentally measure the contact resistances in the different dummy setups.

As shown, the D dummy, consisting of two cylindrical TZM (Plansee, Austria) punches, two conical TZM protection plates, two steel plates separating the protection plates from the steel electrodes, and two horizontal graphite papers, separating the punches from the protection plates, exhibits an ohmic resistance of  $1.4\ \text{m}\Omega$  at room temperature and a constant pressure of 60 MPa. The dummy resistance decreased as a function of temperature due to the reduced contact resistances at different locations in the TZM dummy setup. When the ohmic resistances of the A and B dummies are considered, it can be observed that the values are much lower than the D dummy resistance and are constant as a function of temperature. In these cases, no heating above  $800^{\circ}\text{C}$  was possible since the tool resistance was so low that overheating of the transformer took place. The presence of steel plates and horizontal graphite papers was essential to allow heating of a TZM dummy setup up to  $1200^{\circ}\text{C}$ . A graphite dummy with the same geometry, however, had an ohmic resistance varying between 5 and  $3\ \text{m}\Omega$  and could be heated up to  $2200^{\circ}\text{C}$  without any problem. The main advantage of using TZM instead of graphite tools is the possibility of using elevated pressures, above the fracture stress

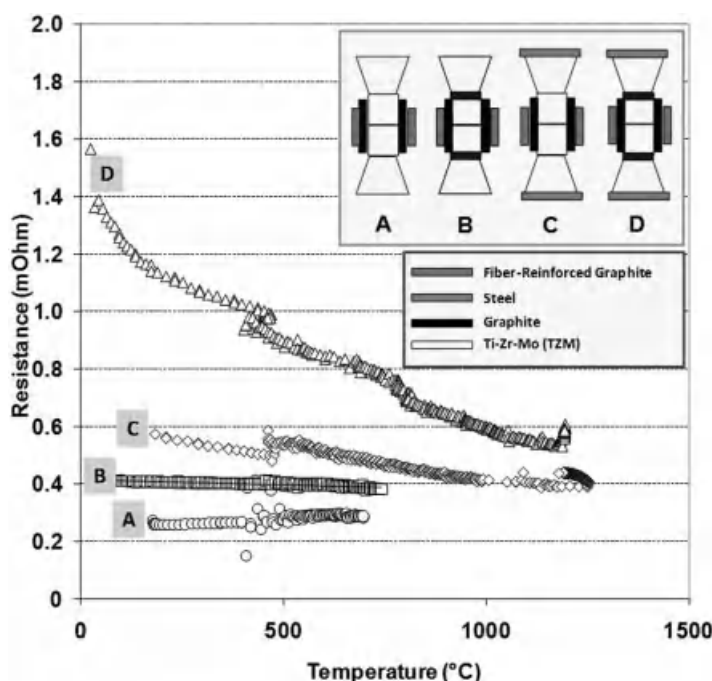


**Figure 2.4.** Overview of electrical resistance values of different PECS dummy setups, combining 30-mm-diameter TZM punches and conical protection plates with a graphite die and a fiber-reinforced graphite ring. The number of graphite papers and the presence of steel plates were varied in order to homogenize the temperature distribution in the center of the tool setup, that is, where the powder compact will be located. Voltage probes were located close to the interface between the electrodes and the protection plates.

of high-strength graphite grades, provided that the TZM recrystallization temperature ( $\sim 1300^{\circ}\text{C}$ ) is not exceeded.

**TOOL GEOMETRY.** Besides the tool material, the tool geometry directly influences the ohmic resistance of the tool and, thus, the amount of Joule heat generated inside the tool. When the electrical properties of the compact are kept constant, the ohmic resistance of a graphite tool decreases with an increasing *punch diameter* since the current is allowed to flow through a larger cross-sectional area. When the diameter of a graphite die is increased from 20 to 40 mm, the current density inside a sintering electrically conductive powder compact increases with the increasing punch, and thus sample, diameter.

The higher the *electrical conductivity of a sintering powder compact*, the higher the current density through it in the same basic setup. When discussing the microscopic PECS effects, it will be shown that the current density, flowing through an electrically conductive powder compact, directly influences its densification behavior. Besides the intrinsic electrical conductivity of an electrically conductive sample material, the ratio

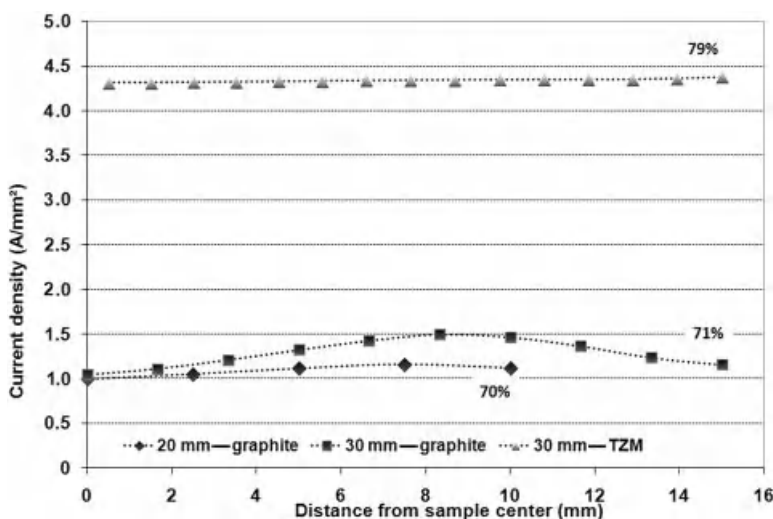


**Figure 2.5.** Current densities during PECS at 1200°C inside sintering TiN powder compacts, densified under identical conditions (1200°C, 60-MPa constant pressure, 100°C/min heating rate) in three different tools: (a) 20-mm diameter—graphite, (b) 30-mm diameter—graphite, (c) 30-mm diameter—TZM. The relative densities obtained are listed along with the current density curves.

of the die wall thickness over the sample radius influences the current density through the sintering powder compact. Insulating the die electrically from an electrically conductive sintering powder compact guarantees the highest possible current density flowing through the compact, as will be discussed in the following paragraph. As a main conclusion, one should highlight that sintering two identical electrically conductive powder compacts in dies with different geometries and/or made of different tool materials will result in two different end products. The densification behavior is directly related to the current density flowing through the compact, as indicated in Figure 2.5, where the calculated current density values inside sintering TiN compacts, densified in different tools, are related to their obtained relative density values.

**THERMAL AND ELECTRICAL INSULATION.** As shown in Figure 2.3, a *radial temperature gradient* develops inside a powder compact processed by PECS. The temperature inside electrically conductive samples is lower at the sample edge, close to the die wall, as compared with the temperature of the sample center. The observed temperature difference increases when (1) the thermal conductivity of an electrically conductive sample decreases, (2) the ratio of the die wall thickness over the sample radius increases, and (3) the sample radius increases. An efficient way to reduce the radial temperature gradient in electrically conductive samples is to minimize the radiation heat losses from the die wall at elevated temperatures by surrounding the die with thermally insulating material (e.g., by porous carbon felt), resulting in a more homogeneous temperature distribution in the sample. Furthermore, in the case of electrically conductive samples,

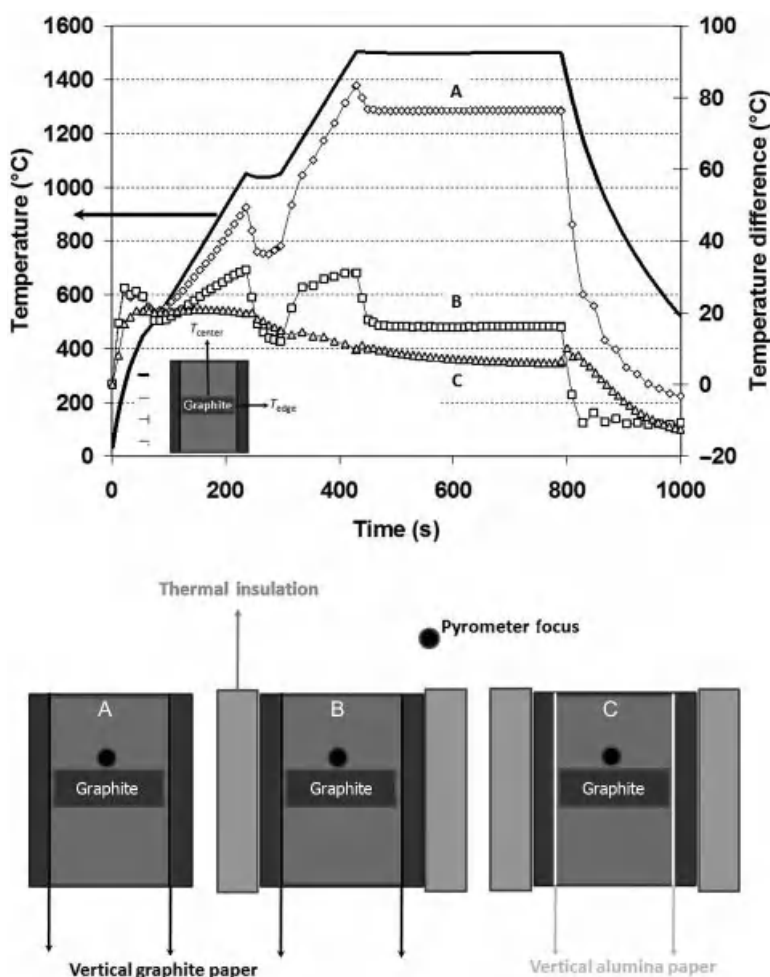
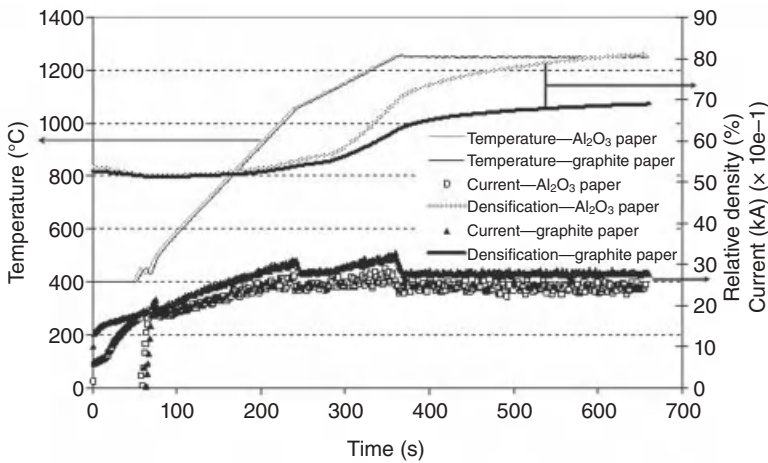


Figure 2.6. Simulated temperature difference ( $T_{\text{center}} - T_{\text{edge}}$ ) between the center and the edge of a 40-mm-diameter graphite sample positioned inside different PECS tool setups: (A) vertical graphite papers—no thermal insulation, (B) vertical graphite papers—thermal insulation, (C) vertical alumina papers—thermal insulation.

it is beneficial to electrically insulate the die from the sintering powder compact, as indicated by the calculated temperature distributions in Figure 2.6, showing the effect of thermal and electrical insulations on the temperature distribution and power consumption when a 400-mm-diameter, 5-mm-thick graphite sample is heated up inside a PECS tool setup.

Furthermore, the electrical insulation does not only homogenize the temperature distribution in the graphite compact but also reduces the power consumption during a predefined PECS cycle.



**Figure 2.7.** Evolution of the relative density and the current flow through the tool during two predefined sintering cycles with identical temperature profiles in case a vertical graphite or alumina paper was used to separate a sintering TiN compact from the die.

Figure 2.7, describing the densification behavior of a TiN compact in PECS tool setups B and C, shown in Figure 2.6, indicates that the current density, flowing through an electrically conductive powder compact, directly influences its densification behavior. Although the macroscopically measured temperature profiles, registered by an optical pyrometer located just above the powder compact (Fig. 2.1), are identical throughout both experiments, the higher current densities in the powder compact, located in the electrically insulated die, induce *local microscopic overheating*, as will be discussed in the following paragraphs, resulting in an enhanced densification behavior, as illustrated by the relative density evolution of the two TiN powder compacts in Figure 2.7.

Composite powder compacts, consisting of an electrically insulating powder matrix phase and a secondary electrically conductive powder phase, might experience a drastic change in electrical conductivity during densification once a *percolating network of conducting particles* is formed. Correspondingly, the current density distribution and concomitant temperature distribution inside the sample and PECS tool setup change drastically during densification. The shape and dispersion of the electrically conductive secondary phase particles determine at which critical volume fraction percolation takes place. In the particular case of sintering ZrO<sub>2</sub>-TiCN nanocomposite compacts, percolation already takes places when 20 vol % of the densifying compact consists of conductive particles [51]. Establishing percolation, the new electric current distribution also influences the densification behavior, as illustrated in Figure 2.8 by a comparison of the shrinkage curves of two identical ZrO<sub>2</sub>-TiCN (60/40) (volume percent) nanocomposite powder compacts, densified under identical sintering conditions in a PECS unit and in traditional hot press (HP). After percolation during PECS, the initial neck formation and growth as well as the shrinkage during the intermediate sintering stage are

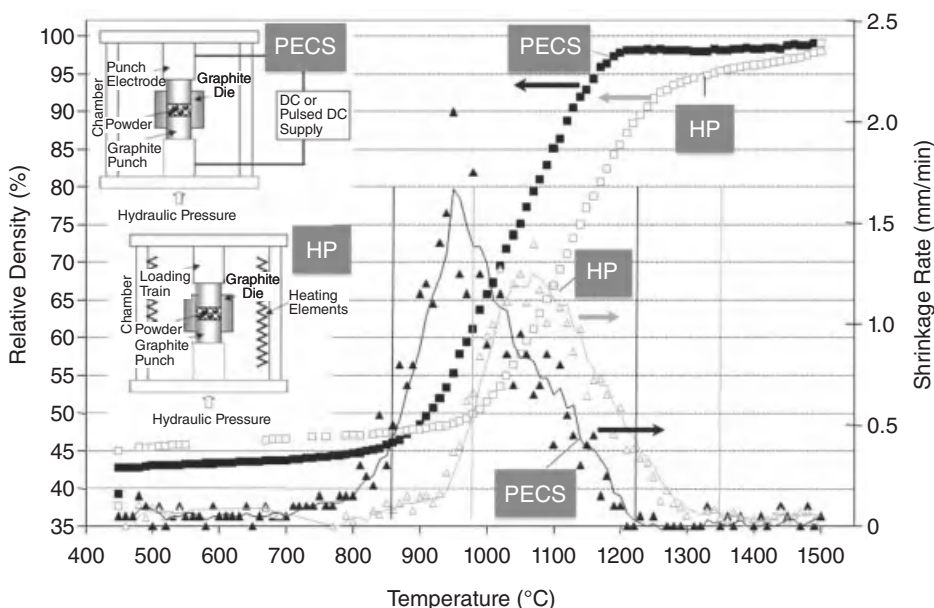


**Figure 2.8.** Comparison of the densification behavior of identical  $\text{ZrO}_2\text{-TiCN}$  (60/40) (volume percent) nanocomposite powder compacts, densified under identical conditions ( $1450^\circ\text{C}$ – $60\text{ MPa}$ – $50^\circ\text{C/min}$ ) by hot pressing (HP) or pulsed electric current sintering (PECS).

enhanced due to the current flow through the powder compact. It is believed that the current passage through narrow interparticle necks generates a locally overheated neck zone, hereby enhancing mass transport by diffusion during the initial stage of sintering, as dictated by Equation 2.1.

As densification proceeds, pore closure by pressure application during the initial and intermediate stage of sintering mainly occurs by plastic deformation and creep. As will be discussed in the following paragraph, the effective pressure experienced by a powder compact during sintering is much higher than the applied pressure on the punches, especially at low relative densities. The local overheating of the neck zones can further decrease the flow stress in the neck zones so that plastic deformation and dislocation creep are enhanced. These statements can be confirmed by the shift of the onset temperature of densification toward lower temperatures and the higher shrinkage rates observed when a current is flowing through the powder compact, as illustrated in Figure 2.8.

## 2.4.2 Pressure Influence

When pressure is applied during a sintering process, one has to distinguish between applied pressure and *effective pressure*. Depending on the microstructure, the effective pressure can be much higher than the applied pressure during pressure-assisted sintering. The applied load is not distributed evenly across the entire area of the sample but



rather across the particle contact surfaces. Therefore, smaller contact points experience larger stresses, and as the contact points grow, the stress diminishes. Stress amplification at particle contacts enhances sintering by even low, externally applied pressures.

Since the applied pressure is generally constant, the effective pressure, or pressure at the contacts, decreases with densification and correspondingly affects the densification rate. Various models for the relationship between applied and effective stress have been proposed, all of which are functions of the fractional density. The models also assume the stress is uniform for all contacts, neither of which is true in reality [52].

Since densification by *plastic deformation* (when the effective stress is equal to the yield stress) and creep (when the effective stress is lower than the yield stress) are enhanced by the application of higher pressures, PECS tools that can withstand higher pressures, as compared with traditional graphite tools (maximum of 120–150 MPa), are to be developed. The key prerequisites are that the tool material should exhibit a sufficient electrical conductivity and maintain its strength at elevated temperatures. Additional challenges that have to be solved are (1) the ohmic resistance of the tool should be higher than that of the current conducting electrodes in order to mainly generate Joule heat in the tool and (2) the temperature measurement by an optical pyrometer should be carefully adjusted since it will be focused on materials with an emissivity different from graphite. Besides steel dies, which have been commonly used for low-temperature applications [44], refractory alloys [45] and WC-Co [46] tools have been used in the intermediate temperature region (1000–1300°C).

A *high-pressure tool*, consisting of a graphite outer die and a SiC and binderless WC inner die, has been described for PECS experiments up to 1400°C and pressures of nearly 1 GPa. Both the refractory alloy tool and the SiC/WC-based tool enabled full densification of various nanoparticle compacts without substantial grain growth at a significantly lower temperature as compared to specimens processed in traditional graphite tools [53].

Besides the intensification of pressure-assisted densification mechanisms, the pressure strongly influences the thermal and electrical *contact resistances* between the different parts of a PECS tool. An exact determination of these resistances, both as function of temperature and pressure, however, is crucial to fully understand the current density and temperature distributions inside a PECS tool setup, especially when low resistivity tool materials are used. This was confirmed by the experimentally measured resistance values of different TZM dummy setups, shown in Figure 2.4.

## 2.5 MICROSCOPIC PECS EFFECTS

Since there is a continuous interaction between thermal, electric, and mechanical fields during PECS, the influence and contribution of local Joule heating will be discussed as an *extrinsic* or thermal current effect.

Furthermore, the *intrinsic* or athermal current effects of an electric current as well as an electric field on the densification behavior, grain growth, and deformation behavior of electrical conductive, ionic conductive, and electrical insulating materials will be discussed in detail.



## 2.5.1 Thermal or Extrinsic Current Effects

**2.5.1.1 Highly Nonuniform Local Temperature Distribution.** Several investigations show indirect evidence of the existence of highly nonuniform local temperature distributions due to the existence of *preferential current paths* and locally overheated zones, both in densifying powder compacts [54] and in stacked metal layers for joining applications [55].

When electrically conductive powder compacts are used, an electrical resistance develops during the initial stage of sintering due to the *constriction* offered by the conducting spots. The developed electrical resistance, called constriction resistance, depends on the resistivity of the base material, the curvature of the conducting particles, the number and the near-neighbor distance of the conducting spots, and the aspect ratio of the contacting area. The increase in resistance is a direct result of the concentration of equipotential lines through the contact [56]. As the necks grow and the overall density of the material increases, the constriction resistance decreases and a more uniform temperature distribution is obtained in the neck zones.

Indirect evidence of the existence of preferential current paths was also obtained after PECS densification of the  $\text{ZrO}_2\text{-TiC}_{0.5}\text{N}_{0.5}$  (60/40) (volume percent) *nanocomposites* presented in Figure 2.8. After densification, the unit cell parameters of an HP and PECS densified composite material were calculated by Rietveld refinement of their collected neutron diffraction patterns. It was proven that the inward diffusion of the  $\text{Ti}^{4+}$  cation into the  $3\text{Y-ZrO}_2$  lattice was enhanced by the electric current, resulting in a smaller  $3\text{Y-ZrO}_2$  unit cell since  $\text{Ti}^{4+}$  partially replaced  $\text{Zr}^{4+}$  in the tetragonal unit cell. This directly influenced the high-temperature deformation behavior of the processed composite materials. Very high strain rates, in the order of  $10^{-1}/\text{s}$ , were observed when the PECS densified material was deformed at  $1400^\circ\text{C}$ , applying an initial pressure of 44 MPa, allowing superplastic shaping of the PECS processed materials, as shown in Figure 2.9.

Combined discrete and finite element simulations of current flows and concomitant temperature distributions in 2-D stacked powder particles confirmed the existence of preferred current paths resulting in *local heating zones*. Furthermore, the temperature distribution after applying a pulsed current was more homogeneous compared to a constant DC with the same heating power, hereby suggesting that the pause time between the different pulses homogenizes the temperature distribution inside the heated powder compact [57].

The existence of locally overheated zones during PECS has been experimentally and theoretically demonstrated when coarse copper particles were densified by means of PECS [58]. *In situ* transmission electron microscopy (TEM) experiments, observing the sintering behavior of Ni nanopowder particles, showed the formation of sintering necks due to local overheating in the neck zones when a current was sent through the powder compact, although *no macroscopic temperature increase* of the powder compact was measured [59].

**2.5.1.2 High Local Temperature Gradients Resulting in Thermal Diffusion.** *Thermal diffusion* promotes components' (atoms and vacancies) separation under

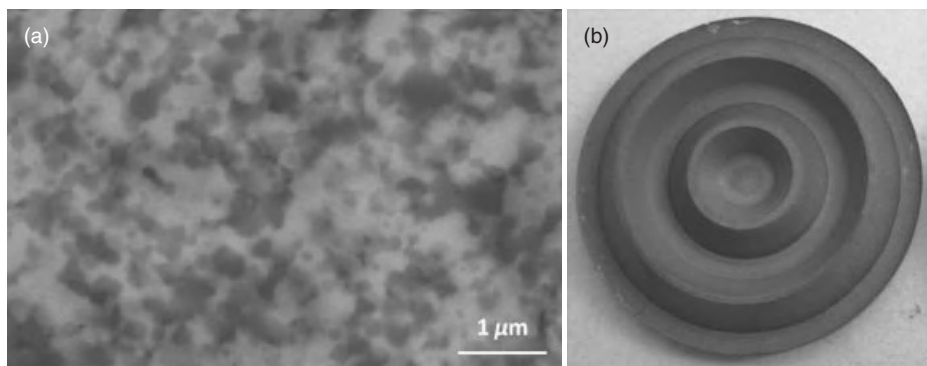


**Figure 2.9.** Superplastically shaped 3Y-ZrO<sub>2</sub>-TiCN (60/40) (volume percent) component (a). The intrinsic nanostructure of the starting powder is maintained after PECS densification and subsequent deformation (b). The light gray phase represents 3Y-ZrO<sub>2</sub>, while the dispersed TiC<sub>0.5</sub>N<sub>0.5</sub> particles are dark. The material is electrically conductive and can be further machined by electrical discharge machining (EDM).

the influence of a large temperature gradient. At the early stages of sintering, this should lead to the growth of interparticle necks, which corresponds to the enhancement of sintering. At the final stages of sintering, however, the pores may serve as vacancy sinks under thermal diffusion conditions, which impedes sintering.

Olevsky and Froyen [10] developed a constitutive model, combining the contribution of surface curvature and external pressure-driven grain boundary diffusion, power law creep, and thermal diffusion to describe the shrinkage rate during PECS. The main conclusion of their work was that thermal diffusion, requiring the existence of large temperature gradients on a relatively small scale, only has a significant contribution to PECS densification when (1) electrically conductive powders are to be densified, (2) high operating temperatures are applied, and (3) small particle sizes are used.

## 2.5.2 Athermal or Intrinsic Current Effects

Before discussing the effect of an electric current and electric field on the densification behavior of powder compacts, its influence on grain growth and impact on *deformation* behavior in fully dense materials will be highlighted. The underlying mechanisms, governing grain growth and deformation, also influence the PECS sintering behavior of a powder compact. Therefore, it is relevant to first separately discuss the influence of an electric field or current on grain growth and deformation before addressing the actual sintering behavior of a powder compact.

**2.5.2.1 Influence on Grain Growth.** The influence of an electric field on grain growth has been described in the case of electrodeposited copper layers [60] and in the case of Y-ZrO<sub>2</sub> [61]. In the case of Cu, a high electric field of 5 kV/cm, a condition that is not comparable with usual PECS conditions, was applied during annealing

studies on the deposited Cu layers. It was stated that the field retarded grain growth by altering the pre-exponential parameter  $k_0$  in Arrhenius-type Equation 2.1. In case of 3Y-ZrO<sub>2</sub>, a much smaller DC field of 4 V/cm has proven to have a significant effect on the grain growth kinetics. Within the discussion on the exact influence of an electric field on grain growth in 3Y-ZrO<sub>2</sub>, the concept of a space charge was introduced. The space charge zone is depleted with oxygen vacancies that are responsible for oxygen ion conduction in 3Y-TZP polycrystals. Therefore, the grain boundary resistance in 3Y-ZrO<sub>2</sub> is higher as compared to the bulk resistance, resulting in a higher temperature of the space charge layer as compared to the crystal matrix, when Joule heating is active.

It was stated that grain growth is the product of driving force, that is, grain boundary energy, and grain boundary mobility, which is determined by the interface kinetics. The higher temperature of the space charge zone due to Joule heating will enhance the grain boundary diffusivity, but it was claimed that the electric field at the same time decreases the interfacial free energy, hereby lowering the driving force for grain growth.

The value of the grain growth exponent characterizes the rate-controlling process [62]. Grain growth in porous compacts is primarily controlled by the pore mobility rather than by the mobility of the grain boundary, as in fully dense materials. In the former case, the grain size exponent  $n = 2$  represents grain growth controlled by grain boundary diffusion;  $n = 3$  represents grain growth controlled by either volume diffusion or diffusion through liquid; and  $n = 4$  represents surface diffusion. However, if the densification rate is very high at the beginning, further grain growth takes place in a relatively dense material, and therefore the given value of the grain size exponent may represent a different atomistic mechanism for the grain growth.

**2.5.2.2 Influence on Deformation Behavior (Electroplasticity).** The *electroplastic effect*, first defined in 1963 by Trotskii and Likhman, is a term used to describe the reduced yield stress of metals subjected to strong electric current pulses at room temperature [63]. Nowadays, it is well-known that the resistance to deformation of various electrically conductive materials sufficiently decreases when the current density exceeds a critical value, typically of  $10^3$ – $10^4$  A/cm<sup>2</sup>. Conrad reported up to five orders of magnitude increase in the strain rate when the current density approaches  $10^6$  A/cm<sup>2</sup> [64]. These values of current density can be easily reached in the standard PECS process, especially at the early stages of densification when the contact area between neighboring particles is small in size. The electroplastic effect has been observed both at room and at elevated temperatures. An increase in the resulting elongation and a decrease in creep exponent were reported during the superplastic deformation of a 7475 aluminum alloy within the 400–550°C temperature range [65]. Furthermore, a decrease in the material strength was observed proportional to the magnitude of the current density. Besides this, a significant increase in ductility and reduced grain growth were found.

The early explanations for the electroplastic effect in metals were addressing the interaction between drift electrons and atoms or dislocations. This phenomenon is known in the literature as an *electron wind*. Later research showed, however, that the additional stresses produced by an electron wind were relatively small (around 0.1 MPa for Cu) [66]. Therefore, other mechanisms had to be taken into consideration, for

instance, an increase in the frequency of the oscillating atoms [65, 66]. The authors believe that the directional motion of electrons broadens the Gauss energy distribution of the oscillating atoms. As a result, a larger fraction of atoms is able to overcome the energetic barriers for dislocation slip and for diffusional migration in the presence of an electric current, as schematically shown in Figure 2.10. Up to date, these and other

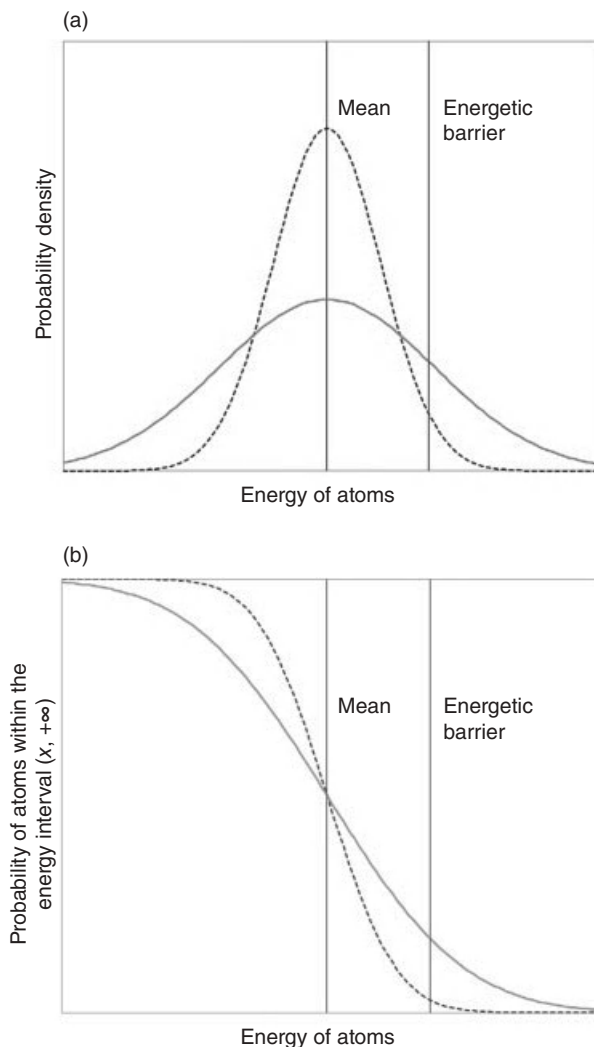


**Figure 2.10.** Influence of an electric current on the width of the Gauss normal distribution of the atom's energy (a) and on the probability to overcome an energetic barrier (b). Dotted lines representing distributions in the absence of current and solid lines correspond to the distribution when current is flowing through the material.

possible mechanisms are under discussion. But it is known that the nonthermal part of Equation 2.12 is most sensitive to an applied electric current.

Recently, Conrad and Yang reviewed the effects of electric currents and fields on the deformation of 3Y-ZrO<sub>2</sub>, MgO, and Al<sub>2</sub>O<sub>3</sub> [67]. The applied electric fields ranged from 0 to 400 V/cm. In general, the reduction in flow stress  $\Delta\sigma_E$  at a given strain consisted of three components, namely,

$$\Delta\sigma_E = \Delta\sigma_T + \delta\sigma_E^* + \Delta\sigma_E^{str}, \quad (2.12)$$

where  $\Delta\sigma_T$  was a minor component due to Joule heating and could be considered as an extrinsic current effect,  $\delta\sigma_E^*$ , a rapid, reversible component, and  $\Delta\sigma_E^{str}$ , an irreversible, cumulative component. While all three components contributed to the reduction in flow stress for Y-TZP, only  $\Delta\sigma_T$  and  $\delta\sigma_E^*$  occurred for MgO and Al<sub>2</sub>O<sub>3</sub>. Significant effects of the electric field on the deformation behavior of 3Y-ZrO<sub>2</sub> were already observed at field strengths as low as 5 V/cm, while higher fields, in the range of 100 V/cm, were needed in case of MgO and Al<sub>2</sub>O<sub>3</sub>. Therefore, differences in PECS densification behavior, as compared to traditional hot pressing, are only expected in 3Y-ZrO<sub>2</sub> and not in MgO or Al<sub>2</sub>O<sub>3</sub> [68].

It was concluded that the mechanism responsible for  $\delta\sigma_E^*$  is a *reduction* by the field in the electrochemical potential for the formation of vacancies corresponding to the diffusion of the rate-controlling ions in the space charge region at the grain boundaries. Furthermore, it was proposed that  $\Delta\sigma_E^{str}$  resulted from the retardation of dynamic grain growth by the electric field. Finally, it was suggested that the field had an influence on one or more of the parameters that governed *grain boundary mobility* within the space charge zone, such as an increase in the concentration of the segregated solute, a decrease in grain boundary energy, or an increase in the activation energy for the migration of the solute atoms.

**2.5.2.3 Influence on Densification Behavior.** ELECTRICAL CONDUCTORS. Different phenomena have been mentioned to describe the enhanced densification behavior of electrically conductive powder compacts during PECS. Besides the existence of overheated zones due to local Joule heating, an extrinsic current effect that was described in the previous paragraph, the occurrence of dielectric breakdown, arcing phenomena, plasma generation, and electromigration have been mentioned.

One could see two metallic particles, each covered with an oxide shell, as a capacitor with the oxide shell forming the dielectric. When the dielectric is stressed beyond its dielectric strength, *electrical breakdown* occurs. This results in the sudden transition of part of the dielectric material from an insulating state to a highly conductive state. This transition is characterized by the formation of an electric spark and, possibly, an *electric arc* through the material. Physical and chemical changes along the path of the discharge will cause permanent degradation and significant reduction in the material's dielectric strength [69].

Since the dielectric breakdown constants of most oxides are larger than 10<sup>8</sup> V/m, oxide films with a thickness of 100 nm can be perturbed by an applied voltage of 10 V. Chaim claimed that, provided that electrical conductivity persists above and below an

oxide nanoparticle, for example, by the presence of a conductive surface film, dielectric breakdown could even occur during the PECS of oxide nanoparticles [70].

When the dielectric material between two conducting metal particles is a gas, which is the case in powder packings during the initial stages of sintering, breakdown of the gas might occur, eventually resulting in *plasma formation*. The existence of plasma was investigated using *in situ* atomic emission spectroscopy, direct visual observations, and ultrafast *in situ* voltage measurements. Using a variety of powders and PECS conditions, all of the experimental methods employed indicated, however, that there is no plasma, sparking, or arcing during the PECS process, neither during the initial nor the final stages of sintering [71].

Yanagisawa et al. [72] developed a special device, equipped with an optical microscope, that was capable of generating 500-ms pulses with a current density of 17–170 A/mm<sup>2</sup> while applying a pressure of 7–16 MPa. Coarse, spherical copper particles ( $d_{50}$ : 250  $\mu\text{m}$ ) were loaded into an electrically insulating Al<sub>2</sub>O<sub>3</sub> die using copper punches so that the applied current pulse was forced to flow through the powder compact. *Sparks* were observed just after applying the current pulse and were more likely to occur at lower mechanical pressures and larger current densities. At the positions where sparks were observed, the powder particles were joined by melting. Even when sparks were not observed, however, necks were frequently created at the interparticle contacts, confirming the existence of local overheated zones, as described in a previous paragraph.

*Electromigration* is the transport of material caused by the gradual movement of the ions in a conductor due to the momentum transfer between conducting electrons and diffusing metal atoms. Two forces affect ionized atoms in a conductor: the direct electrostatic force  $F_e$  and the force generated from the exchange of momentum with other charge carriers  $F_p$ . In metallic conductors,  $F_p$  is caused by a so-called electron wind or ion wind [73]. The resulting force  $F_{res}$  on an activated ion in the electric field is

$$F_{res} = F_e - F_p \quad (2.13)$$

Electromigration occurs when some of the momentum of a moving electron is transferred to a nearby activated ion. This causes the ion to move from its original position. In a homogeneous crystalline structure, because of the uniform lattice structure of the metal ions, there is hardly any momentum transfer between the conduction electrons and the metal ions. However, this symmetry does not exist at the grain boundaries and material interfaces, and so here momentum is transferred much more vigorously. Since the metal ions in these regions are bonded more weakly than in a regular crystal lattice, once the electron wind has reached a certain strength, atoms become separated from the grain boundaries and are transported in the direction of the current. This direction is also influenced by the grain boundary itself because atoms tend to move along grain boundaries. Normally, the amount of momentum imparted by the relatively low-mass electrons is not enough to permanently displace the atoms. However, in high-power situations, if many electrons bombard the atoms with enough force to become significant, this will accelerate the process. High current density increases the number of

electrons scattering against the atoms of the conductor and, hence, the speed at which those atoms are displaced. Due to the high required current densities, in the order of  $10^6$ – $10^7$  A/cm<sup>2</sup>, electromigration will only be active during the initial sintering stage when the total current has to pass through the narrow neck zones [10]. Munir et al. argued that electromigration was not active during intermetallic MoSi<sub>2</sub> formation at the interface between Mo and Si metal sheets since there was no directional influence on the final product formation [74].

Recently, Prette and coworkers described the drastically enhanced sintering rate of a Co<sub>2</sub>MnO<sub>4</sub> spinel compound, an electrically conductive material that is commonly used as an interconnect in solid oxide fuel cell (SOFC) applications [75]. While initiation of neck growth and full densification were achieved at about 800 and 1300°C, respectively, during conventional sintering, the application of a modest DC field of 12.5 V/cm lowered the sintering temperature to 325°C and reduced the sintering time to just a few seconds. At lower electric fields, comparable to those used during PECS processing, the sintering rates increased gradually with the applied field. The enhanced densification rates were ascribed to the higher electrical resistance of the grain boundaries and particle–particle contacts, concentrating the power dissipation at the interfaces, that is, an extrinsic current effect, thereby producing a giant increase in the rate of diffusional transport. The process was described as *flash sintering*. Contrary to the flash sintering behavior of 3Y-ZrO<sub>2</sub>, the grain growth was not retarded by the application of an electric field during the densification process [76].

**IONIC CONDUCTORS.** Recently, many investigations have focused on the influence of electric fields on the densification behavior of ionic conductors [77–79]. AC, DC, and pulsed DC fields were applied during the densification of the ionic conductor 3Y-ZrO<sub>2</sub>, while a DC field was applied during sintering of a Co<sub>2</sub>MnO<sub>4</sub> spinel compound, an electrical conductor used as an interconnect for SOFC applications.

In the case of 3Y-ZrO<sub>2</sub>, it was clearly shown that a DC field in the 0- to 10-V/cm range, comparable to typical PECS conditions, did not influence the surface diffusion kinetics that govern *neck growth* during the early sintering stages [79].

However, during the *intermediate stages of sintering*, a pulsed DC field had greater impact, as compared with an AC field and a constant DC field, which could be related to the root mean square values of the electric field during the three signals, containing a similar amount of power [77]. A retardation of grain growth was observed under the influence of an electric field, as mentioned in a previous paragraph during isothermal grain growth experiments [78]. The smaller grain size increased the driving force for sintering, resulting in fully dense materials with a refined microstructure, as shown in Figure 2.11.

Recently, Cologna and coworkers described the “flash” sintering behavior of nanograined zirconia. Y-TZP could be sintered in a few seconds at ~850°C to full density, starting from a green density of 0.5, by the application of a 120-V/cm DC electric field. It should be highlighted that the applied field is significantly higher as compared with those typically applied during PECS. The flash effect was explained by local Joule heating at the grain boundaries, that is, an extrinsic current effect. On one hand, Joule heat promoted grain boundary diffusion, a kinetic effect, while at the same



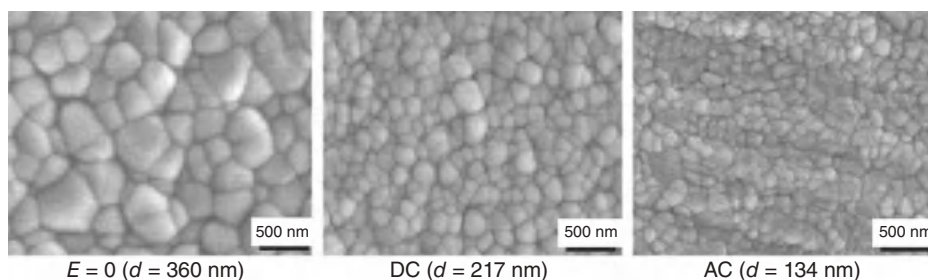


**Figure 2.11.** Scanning electron micrographs showing the effect of a small DC (b) and AC (c) field ( $E = 19 \text{ V/cm} - 60 \text{ Hz}$  in the case of the AC field) on the grain size of fully dense 3Y-TZP, as compared to the same material sintered without the electric field (a). Reprinted from Yang and Conrad [77].

time it restricted grain growth, a thermodynamic effect. The smaller grain size and the higher temperature at the grain boundaries acted synergistically to enhance the rate of sintering [76].

**ELECTRICAL INSULATORS.** The influence of an electric field or current on the densification behavior of electrical insulators, using a direct comparison with traditional hot pressing, has only merely been addressed [80]. In case of alumina, different studies investigated the different stages of sintering, both during hot pressing and PECS. Stanciu et al. concluded that the rate of neck growth increased during the initial stages of the PECS densification of both a nanostructured and submicrometer-sized  $\alpha\text{-Al}_2\text{O}_3$  powder due to enhanced surface diffusion [81]. Langer and coworkers observed that PECS sintered samples reached higher densities compared with hot pressing. The main densification mechanism during intermediate-stage sintering, however, was grain boundary diffusion in both cases. Increasing the heating rate up to  $150^\circ\text{C/min}$  did not modify the densification mechanism. It was claimed that PECS specimens started to densify at lower temperatures due to rapid transient overheating during the initial stage of sintering. The effect was more pronounced when a nanopowder was used. The sintering trajectories showed that the grain size was only dependent on density and was insensitive to the sintering method [82].

## 2.6 CONCLUSIONS AND FUTURE PROSPECTS

The influence of an electric field, applied during PECS, on the densification behavior of powder compacts has been discussed.

Macroscopic temperature gradients, both inside the PECS tool setup and the sintering powder compact, are generated due to current density inhomogeneities and heat losses due to convection and radiation. The influence of technological aspects, characteristic of the PECS technology, such as die design and pressure application, on the generated current density and concomitant temperature distribution has been discussed



in detail. The importance of an accurate temperature measurement and the impact of thermal and electrical insulation on both temperature homogenization and power consumption were highlighted.

Microscopic PECS effects include both the thermal (extrinsic) and athermal (intrinsic) impacts of an electric current on mass transport phenomena occurring at the particle scale. Among the extrinsic effects, local Joule heating inside the neck zones has been described in detail. Furthermore, the possibility of thermal diffusion to take place has been discussed critically. The intrinsic effects of an electric current as well as an electric field on the grain growth and the deformation behavior of polycrystalline materials have been described before addressing their impact on the densification behavior of powder compacts. In each case, the specific effects, occurring in either electrical conductors, ionic conductors, or insulators, have been summarized.

It has been extensively shown that several parameters, simultaneously active during a typical PECS process, effectively influence the densification behavior of sintering powder compacts. Under typical PECS conditions, that is, very high applied currents and relatively low voltages, the most pronounced effects have been observed for electrical conductors.

Recent research, however, indicates that the application and influence of high electric fields has a much more significant influence on material densification behavior, rather than the high electric currents, applied during PECS. Therefore, future research, and possibly its industrial application, should be oriented toward the application of higher electric fields, rather than higher electric currents, during powder compact densification.

## ACKNOWLEDGMENTS

K. Vanmeensel thanks the Research Fund Flanders (FWO) for his postdoctoral fellowship. A. Laptev acknowledges the Research Council of K.U.Leuven for his research fellowship (No. F+/08/009). This work was performed within the framework of the K.U.Leuven project GOA/08/007.

## REFERENCES

1. Z. A. Munir, U. Anselmi-Tamburini, et al. (2006) The effect of electric field and pressure on the synthesis and consolidation of materials: A review of the spark plasma sintering method, *Journal of Materials Science*, **41**[3] 763–777.
2. G. Weintraub and H. Rush (1913) U.S. Patent No. 1,071, 488.
3. G. F. Taylor (1933) Apparatus for making hard metal compactions. US Patent No. 1896854.
4. G. F. Taylor (1933) Welding process. US Patent No. 1896853.
5. K. Inoue (1967) Method of electrically sintering discrete bodies. US Patent No. 3340052.
6. F. V. Lenel (1955) Resistance sintering under pressure, *Transactions of the American Institute of Mining and Metallurgical Engineers*, **203**[1] 158–167.

7. T. Hungria, J. Galy, et al. (2009) Spark plasma sintering as a useful technique to the nano-structuration of piezo-ferroelectric materials, *Advanced Engineering Materials*, **11**[8] 615–631.
8. G. D. Zhan, J. D. Kuntz, et al. (2003) Single-wall carbon nanotubes as attractive toughening agents in alumina-based nanocomposites, *Nature Materials*, **2**[1] 38–42.
9. S. Grasso, Y. Sakka, and G. Maizza (2009) Electric current activated/assisted sintering (ECAS): A review of patents 1906–2008, *Science and Technology of Advanced Materials*, **10** 1–23.
10. E. Olevsky and L. Froyen (2006) Constitutive modeling of spark-plasma sintering of conductive materials, *Scripta Materialia*, **55**[12] 1175–1178.
11. R. M. German and S. J. Park, *Mathematical Relations in Particulate Materials Processing: Ceramics, Powder Metals, Cermets, Carbides, Hard Materials and Minerals*. John Wiley & Sons, Hoboken, NJ, 2008.
12. R. M. German, *Sintering Theory and Practice*. 1st ed., John Wiley & Sons, New York, 1996.
13. R. M. German, *Powder Metallurgy & Particulate Materials Processing*, 1st edition, Metal Powder Industries Federation, Princeton, NJ, 2005.
14. J. E. Burke (1984) A history of the development of the science of sintering, in the 86th Meeting of the American Ceramics Society. Pittsburg, PA.
15. R. L. Coble (1961) Sintering crystalline solids. 1. Intermediate and final state diffusion models, *Journal of Applied Physics*, **32**[5] 787–791.
16. R. L. Coble (1961) Sintering crystalline solids .2. Experimental test of diffusion models in powder compacts, *Journal of Applied Physics*, **32**[5] 793–799.
17. C. Herring (1950) Effect of change of scale on sintering phenomena, *Journal of Applied Physics*, **21** 301–303.
18. D. L. Johnson (1969) New method of obtaining volume, grain boundary, and surface diffusion coefficients from sintering data, *Journal of Applied Physics*, **40**[1] 192–200.
19. W. D. Kingery and M. Berg (1955) Study of the initial stages of sintering solids by viscous flow, evaporation–condensation, and self-diffusion, *Journal of Applied Physics*, **26**[10] 1205–1212.
20. G. C. Kuczynski (1948) Self-diffusion in sintering of metallic particles, *Transactions of the American Institute of Mining and Metallurgical Engineers*, **185** 169–178.
21. G. C. Kuczynski (1950) Measurement of self-diffusion of silver without radioactive tracers, *Journal of Applied Physics*, **21** 632–635.
22. R. L. Coble (1970) Diffusion models for hot pressing with surface energy and pressure effects as driving forces, *Journal of Applied Physics*, **41**[12] 4798–4807.
23. C. Argento, A. Jagota, et al. (1997) Surface formulation for molecular interactions of macroscopic bodies, *Journal of the Mechanics and Physics of Solids*, **45**[7] 1161–1183.
24. A. L. Maximenko and E. A. Olevsky (2004) Effective diffusion coefficients in solid-state sintering, *Acta Materialia*, **52**[10] 2953–2963.
25. Z. M. He, J. Ma, et al. (2005) Constitutive modeling of the densification and the grain growth of hydroxyapatite ceramics, *Biomaterials*, **26**[14] 1613–1621.
26. D. L. Johnson and I. B. Cutler (1963) Diffusion sintering .1. Initial stage sintering models and their application to shrinkage of powder compacts, *Journal of the American Ceramic Society*, **46**[11] 541–545.

27. D. L. Johnson (1970) A general model for intermediate stage of sintering, *Journal of the American Ceramic Society*, **53**[10] 574–.
28. A. L. Yurkov, T. A. Sarkisyan, et al. (1997) Final stages of sintering of ceramic materials: Effect of residual porosity and microstructure on mechanical characteristics of surface, *Ceramics International*, **23**[5] 389–399.
29. M. J. Kirchhof, H. J. Schmid, et al. (2009) Three-dimensional simulation of viscous-flow agglomerate sintering, *Physical Review E*, **80**[2] 026319, 1–9.
30. D. B. Knorr, R. M. Cannon, et al. (1989) An analysis of diffusion and diffusional creep in stoichiometric and hyperstoichiometric uranium-dioxide, *Acta Metallurgica*, **37**[8] 2103–2123.
31. M. F. Ashby (1969) On interface-reaction control of Nabarro–Herring creep and sintering, *Scripta Metallurgica*, **3**[11] 837–842.
32. K. R. Anderson, J. R. Groza, et al. (1999) Surface oxide debonding in field assisted powder sintering, *Materials Science and Engineering A-Structural Materials Properties Microstructure and Processing*, **270**[2] 278–282.
33. M. Omori (2000) Sintering, consolidation, reaction and crystal growth by the spark plasma system (SPS), *Materials Science and Engineering A-Structural Materials Properties Microstructure and Processing*, **287**[2] 183–188.
34. K. Vanmeensel, A. Laptev, et al. (2007) Field assisted sintering of electro-conductive  $ZrO_2$ -based composites, *Journal of the European Ceramic Society*, **27**[2–3] 979–985.
35. U. Anselmi-Tamburini, S. Gennari, et al. (2005) Fundamental investigations on the spark plasma sintering/synthesis process—II. Modeling of current and temperature distributions, *Materials Science and Engineering A-Structural Materials Properties Microstructure and Processing*, **394**[1–2] 139–148.
36. K. Vanmeensel, A. Laptev, et al. (2005) Modelling of the temperature distribution during field assisted sintering, *Acta Materialia*, **53**[16] 4379–4388.
37. K. Vanmeensel, A. Laptev, et al. (2007) The influence of percolation during pulsed electric current sintering of  $ZrO_2$ -TiN powder compacts with varying TiN content, *Acta Materialia*, **55**[5] 1801–1811.
38. A. Zavaliangos, J. Zhang, et al. (2004) Temperature evolution during field activated sintering, *Materials Science and Engineering A-Structural Materials Properties Microstructure and Processing*, **379**[1–2] 218–228.
39. R. S. Dohedoe, G. D. West, et al. (2005) Spark plasma sintering of ceramics: Understanding temperature distribution enables more realistic comparison with conventional processing, *Advances in Applied Ceramics*, **104**[3] 110–116.
40. H.-T. Kim, M. Kawahara, et al. (2000) Specimen temperature and sinterability of Ni powder by spark plasma sintering, *Journal of the Japan Society of Powder and Powder Metallurgy*, **47**[8] 887–891.
41. D. Tiwari, B. Basu, et al. (2009) Simulation of thermal and electric field evolution during spark plasma sintering, *Ceramics International*, **35**[2] 699–708.
42. J. Rathel, M. Herrmann, et al. (2009) Temperature distribution for electrically conductive and non-conductive materials during field assisted sintering (FAST), *Journal of the European Ceramic Society*, **29**[8] 1419–1425.
43. H. U. Kessel and J. Hennicke (2010) Short-time sintering for cost-efficient production and material development, *CFI-Ceramic Forum International*, **87**[10] E23–E26.

44. K. Y. Sastry, L. Froyen, et al. (2006) Field assisted sintering consolidation of Al-Si-Fe-X alloy powder/flakes produced through air atomization/melt spinning, *Materials Science Forum*, **519–521** 1409–1414.
45. K. Vanmeensel, E. Jothinathan, S. H. Huang, O. Van Der Biest, and J. Vleugels (2009) High pressure pulsed electric current sintering, Proceedings of the 11th International Conference and Exhibition of the European Ceramic Society, June 21–25, Krakow, Poland.
46. R. Aalund (2009) Unveiling spark plasma sintering high-throughput processing, *Ceramic Transactions*, **220** 3–10.
47. A. M. Locci, A. Cincotti, et al. (2010) A methodology to investigate the intrinsic effect of the pulsed electric current during the spark plasma sintering of electrically conductive powders, *Science and Technology of Advanced Materials*, **11**[4] 045005, 1–13.
48. G. E. Childs, L. J. Ericks, et al. (1973) Thermal-conductivity of solids at room-temperature and below—Review and compilation of literature, *Nbs Monograph*, **M131** 1–608.
49. A. N. Bhagat, S. Ranganathan, et al. (2003) Electrical resistivity studies in low carbon and HSLA-100 steels, *Materials Science and Technology*, **19**[3] 343–346.
50. A. Laptev, S. S. Ponomarev, et al. (2001) Solid-phase consolidation of fine-grained WC-16% Co hardmetal, *Journal of Advanced Materials*, **33**[3] 42–51.
51. K. Vanmeensel, S. G. Huang, et al. (2008) Pulsed electric current sintering of electrically conductive ceramics, *Journal of Materials Science*, **43**[19] 6435–6440.
52. J. E. Garay (2010) Current-activated, pressure-assisted densification of materials, *Annual Review of Materials Research*, **40** 445–468.
53. U. Anselmi-Tamburini, J. E. Garay, et al. (2006) Fast low-temperature consolidation of bulk nanometric ceramic materials, *Scripta Materialia*, **54**[5] 823–828.
54. T. Grosdidier, G. Ji, et al. (2007) Processing dense hetero-nanostructured metallic materials by spark plasma sintering, *Scripta Materialia*, **57** 525–528.
55. J. F. Fan, L. D. Chen, et al. (2004) Joining of Mo to CoSb<sub>3</sub> by spark plasma sintering by inserting a Ti interlayer, *Materials Letters*, **58**[30] 3876–3878.
56. J. R. Groza and A. Zavaliangos (2000) Sintering activation by external electrical field, *Materials Science and Engineering A-Structural Materials Properties Microstructure and Processing*, **287**[2] 171–177.
57. Z. Jing, A. Zavaliangos, et al. (2002) Numerical simulation of thermal-electrical phenomena in field activation sintering., Modelling the Performance of Engineering Structural Materials III. Proceedings of a Symposium, 299–309396.
58. X. Y. Song, X. M. Liu, et al. (2006) Neck formation and self-adjusting mechanism of neck growth of conducting powders in spark plasma sintering, *Journal of the American Ceramic Society*, **89**[2] 494–500.
59. T. B. Holland, A. M. Thron, et al. (2010) Field assisted sintering of nickel nanoparticles during *in situ* transmission electron microscopy, *Applied Physics Letters*, **96**[24] 243106, 1–3.
60. K. Jung and H. Conrad (2007) Retardation of grain growth in electrodeposited Cu by an electric field, *Journal of Materials Science*, **42**[11] 3994–4003.
61. S. Ghosh, A. H. Chokshi, et al. (2009) A huge effect of weak dc electrical fields on grain growth in zirconia, *Journal of the American Ceramic Society*, **92**[8] 1856–1859.
62. Z. Shen and M. Nygren (2005) Microstructural prototyping of ceramics by kinetic engineering: Applications of spark plasma sintering, *Chemical Record*, **5** 173–184.

63. O. A. Trotskii, V. I. Likhthman, et al. (1963) Joint action of mercury and radioactive emissions on mechanical properties of single zing crystals, *Doklady Akademii nauk SSSR*, **148** 332.
64. H. Conrad (2000) Electroplasticity in metals and ceramics, *Materials Science and Engineering A-Structural Materials Properties Microstructure and Processing*, **287**[2] 276–287.
65. Y. Li, H. Chen, et al. (1996) Effect of electric current pulse on superplasticity of aluminium alloy 7475, *Transactions of the Nonferrous Metals Society of China/Transactions of the Nonferrous Metals Society of China*, **6**[1] 77–79, 84.
66. S. D. Antolovich and H. Conrad (2004) The effects of electric currents and fields on deformation in metals, ceramics, and ionic materials: An interpretive survey, *Materials and Manufacturing Processes*, **19**[4] 587–610.
67. H. Conrad and D. Yang (2010) Influence of an applied dc electric field on the plastic deformation kinetics of oxide ceramics, *Philosophical Magazine*, **90**[9] 1141–1157.
68. Z. J. Shen, M. Johnsson, Z. Zhao, and M. Nygren (2002) Spark plasma sintering of alumina, *Journal of the American Ceramic Society*, **85** 1921–1927.
69. R. A. Serway and J. W. Jewett, *Physics for Scientists and Engineers*, 6th edition, Thomson, Brooks/Cole, 2004.
70. R. Chaim (2007) Densification mechanisms in spark plasma sintering of nanocrystalline ceramics, *Materials Science and Engineering A-Structural Materials Properties Microstructure and Processing*, **443** 25–32.
71. D. M. Hulbert, A. Anders, J. Andersson, E. J. Lavernia, and A. K. Mukherjee (2009) A discussion on the absence of plasma in spark plasma sintering, *Scripta Materialia*, **60** 835–841.
72. O. Yanagisawa, H. Kuramoto, K. Matsugi, and M. Komatsu (2003) Observation of particle behavior in copper powder compact during pulsed electric discharge, *Materials Science and Engineering A-Structural Materials Properties Microstructure and Processing*, **350** 184–189.
73. P. Dandu, X. J. Fan, Y. Liu, and C. Diao (2010) Finite element modeling on electromigration of solder joints in wafer level packages, *Microelectronics Reliability*, **50**[4] 547–555.
74. U. Anselmi-Tamburini, J. E. Garay, and Z. A. Munir (2005) Fundamental investigations on the spark plasma sintering/synthesis process III. Current effect on reactivity, *Materials Science and Engineering A-Structural Materials Properties Microstructure and Processing*, **407** 24.
75. A. Prette, M. Cologna, et al. (2010) Flash-sintering of  $\text{Co}_2\text{MnO}_4$  spinel for SOFC applications, *Journal of Power Sources*, **19**[4] 2061–2065.
76. M. Cologna, B. Rashkova, et al. (2010) Flash sintering of nanograin zirconia in <5 s at 850°C, *Journal of the American Ceramic Society*, **93**[11] 3556–3559.
77. D. Yang and H. Conrad (2010) Enhanced sintering rate of zirconia (3Y-TZP) by application of a small AC electric field, *Scripta Materialia*, **63**[3] 328–331.
78. D. Yang, R. Raj, et al. (2010) Enhanced sintering rate of zirconia (3Y-TZP) through the effect of a weak dc electric field on grain growth, *Journal of the American Ceramic Society*, **93**[10] 2935–2937.
79. M. Cologna and R. Raj (2010) Surface diffusion-controlled neck growth kinetics in early stage sintering of zirconia, with and without applied DC electrical field, *Journal of the American Ceramic Society*, **94**[2] 391–395.

80. O. Guillon and J. Langer (2010) Master sintering curve applied to the field-assisted sintering technique, *Journal of Materials Science*, **45**[19] 5191–5195.
81. L. Stanciu, D. Quach, et al. (2007) Initial stages of sintering of alumina by thermo-optical measurements, *Journal of the American Ceramic Society*, **90**[9] 2716–2722.
82. J. Langer, M. J. Hoffmann, et al. (2009) Direct comparison between hot pressing and electric field-assisted sintering of submicron alumina, *Acta Materialia*, **57**[18] 5454–5465.

# VISCOUS-PHASE SILICATE PROCESSING

RALF MÜLLER AND STEFAN REINSCH

The presence of viscous silicate phases is often utilized in the manufacturing of ceramics and composites. Thus, for sintered glasses (SG), sintered glass-ceramics (SGC), and glass matrix composites (GMC), ceramic processing of premelted glass powders is utilized to attain technological benefits and product properties and densification proceeds via viscous sintering. Due to the related moderate process temperature, glass powder properties like particle size and shape, surface roughness, milling impurities, particle alignment, or nonregular and nonhomogeneous packing may largely control sintering and crystallization. In this context, knowledge and experience in ceramic processing has to overlap with a thorough kinetic understanding of viscous sintering and crystallization. It is the aim of this chapter to focus attention on this intersection.

## 3.1 INTRODUCTION

### 3.1.1 Processing Concepts

The presence of viscous silicate phases is often utilized in manufacturing a large variety of ceramic and composite materials including glass-ceramics (GC), SGs and SGC, GMCs, glass-bonded ceramics (GBC), and even ceramics.

---

*Ceramics and Composites Processing Methods*, First Edition. Edited by Narottam P. Bansal and Aldo R. Boccaccini.

© 2012 The American Ceramic Society. Published 2012 by John Wiley & Sons, Inc.

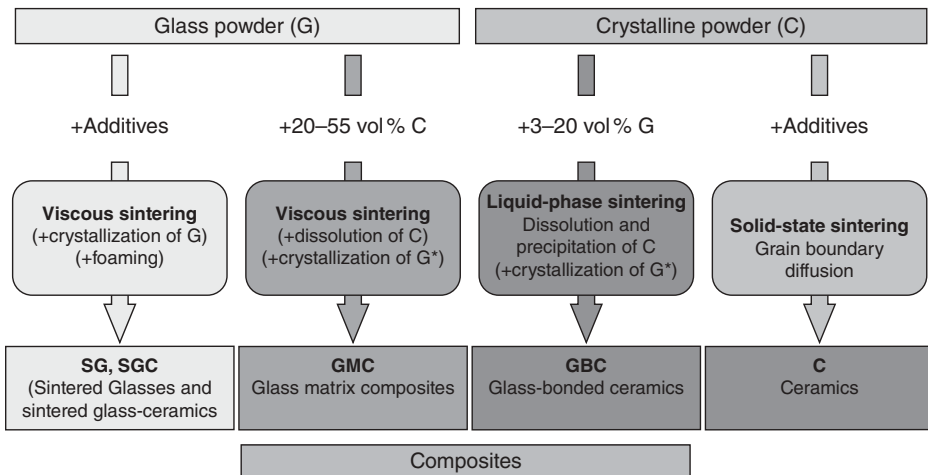


Figure 3.1. Powder processing routes classified according to the starting mixture of crystalline (C) and glass powders (G). G\*, residual glass. Initial crystal and glass volume fractions of GMC and GBC are typical for low-temperature cofired ceramics [2].

**3.1.1.1 Glass Forming and Crystallization.** GCs are made by well-established glass forming technologies like blowing, casting, pressing, and rolling followed by nucleation and crystallization annealing steps. Nucleation agents are used to achieve high crystal nucleation density. This glass-ceramic processing route results in several outstanding properties including a high uniformity of the microstructure, the absence of porosity, and minor volume changes during the controlled crystallization step [1]. In this technology, the viscosity of the glass-forming silicate melt is of utmost importance for shaping and control of crystallization and microstructure.

**3.1.1.2 Sintering of Glass and Crystal Powders.** The presence of viscous silicate phases is also crucial for several sintering processing routes starting from mixtures of glass and crystal powders (Fig. 3.1). This powder technology allows low fabrication temperatures, complex shapes, or coating applications.

SGs and SGCs are made from differently grained glass powders formed by ceramic shaping technologies like cold pressing, extrusion, slip, and tape casting. Densification proceeds via *viscous sintering* driven by the surface energy of the melt and limited by its viscosity. The latter controls all important densification phenomena including neck formation, redistribution of glass particles, and pore shrinkage. Sintering, however, must be complete prior to crystallization if dense SGC products are required. Due to the strong nucleation tendency of the glass surface, a quasi-homogeneous crystal distribution throughout the bulk of SGC can be achieved even in cases when the use of nucleation agents fails. SG and SGC processing routes are also used for glass-ceramic coatings. Porous glasses can be made from SG using foaming aids. On the other hand,



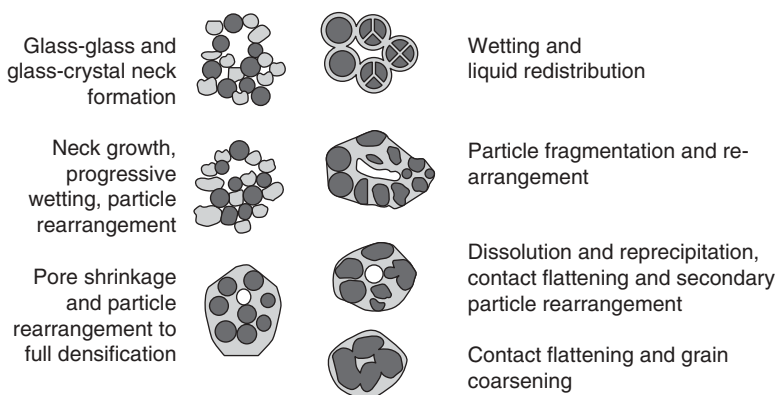


**Figure 3.2.** Schematic illustrations of viscous sintering of GMC (left) and liquid-phase sintering of GBC (right). Light gray: glass melt; dark gray: crystal phase; white: pores. This schematic representation does not account for partial dissolution and crystallization, which may or may not occur.

SG as, for example, silica and sol–gel-derived glasses can be manufactured at much lower temperatures as their melted counterparts [3].

In the case of GMC, large glass volume fractions enable easy formation of a thoroughly connected glass matrix, wherein rigid, mostly crystalline inclusions like fibers, platelets, or other particles are dispersed. Since sintering is driven by the pore and crystal interfacial energies of a viscous melt and proceeds via matter transport by viscous flow, this sintering mechanism is also referred to as “viscous sintering” even if bad wetting of rigid particles occurs [4]. Figure 3.2 (left) illustrates related key phenomena of viscous sintering of GMCs neglecting partial dissolution phenomena. Nevertheless, partial dissolution, crystallization, and phase boundary reactions may occur as even desirable in some cases, decisively influencing sintering kinetics, microstructure evolution, and final material properties. GMCs stand out by their ease of densification, low cost, and high performance [1, 5]. Other advantages result from the large variety of possible combinations of glass powder and filler particles with respect to their chemistry, volume fraction, and particle size, which allow continuous tuning of product properties.

In the case of GBC, small volume fractions of low melting glasses are added to ceramic powders in order to reach the superior properties of ceramics at lower densification temperatures. According to Kingery [6] and German [7], this sintering mechanism is referred to as *liquid-phase sintering*. This mechanism combines liquid and crystal redistribution as well as dissolution and reprecipitation phenomena within a low viscous liquid. Once formed by heating, this liquid wets crystal particles and penetrates the pore and grain structure by a combination of reaction and capillarity [7]. During the first stage of liquid-phase sintering, densification proceeds by capillarity, particle

fragmentation, and rearrangement by viscous flow (Fig. 3.2, right). During the subsequent dissolution and reprecipitation stage, contact flattening, grain shape accommodation, coarsening, and secondary particle rearrangement occur. During the final stage, the solid skeletal network densifies by intergranular neck growth, coarsening, and pore filling by liquid redistribution phenomena.

Other powder processing routes start from crystal powders (C) entirely. Nonetheless, liquid phases can develop from the mixture of raw materials during firing. Thus, a major part of commercial ceramics is densified with the aid of a small amount of reactive liquid phase [8].

**3.1.1.3 Sintering and Melting.** In other cases, large amounts of viscous silicate phases can occur as, for example, during firing of clay, feldspar, and quartz raw materials in manufacturing porcelains [9]. Within this context, another classification was forwarded by Rabinovich [3] with respect to the preparation of glass by sintering. He classified solidification as sintering with melting or pure sintering if consolidation takes place fully above or below the liquidus temperature, respectively. Above that temperature, liquid phases do not crystallize even at a low viscosity. Low viscous liquid phases are utilized for numerous processing routes notwithstanding the initial crystal volume fraction of the starting powders like the foaming step of sintered cellular glasses, the melting stage of fritted glazes and enamels, and even for the capillary-driven densification stage of GBC.

## 3.1.2 Ceramic Processing of Glass Powders

In this chapter, we will focus on SG, SGC, and GMC where ceramic processing of premelted glass powders is utilized to attain desired technological benefits and product properties and where densification proceeds via viscous sintering. Compared to low viscous liquid-phase sintering, viscous sintering is more strongly affected by glass powder processing because most of related particle and powder properties as, for example, particle size and shape, surface roughness, milling impurities, and particle alignment do not essentially degrade before sintering starts. For this reason, knowledge and experience in *ceramic processing* have to overlap with a thorough *kinetic understanding of viscous sintering and crystallization*.

The aim of this chapter is to focus attention to this intersection. While Sections 3.2–3.5 outline basic phenomena of glass surface nucleation, overall crystallization, viscous sintering, and viscous sinter retardation, we finally present a few selective application fields for which these phenomena are highly essential. Due to the large scale of phenomena covered by this chapter, many explanations could not be given in full detail. Instead, they are first and foremost intended to refer to the excellent corresponding literature background.

Beyond that scope, we would like to refer to the numerous textbooks and review articles, which comprehensively discuss related basic aspects like the structure and properties of silicate glasses and melts [10], the glass surface [11] fundamentals of the vitreous state and glass crystallization [12, 13], concepts of GC technology [14, 15], fundamentals of sintering [7, 8, 16], and ceramic processing [17]. A comprehensive

review of sintering phenomena in the presence of a liquid phase as utilized for GBC is given by German [18], while a respective sintering model is given in References 19 and 20.

## 3.2 SURFACE NUCLEATION

### 3.2.1 Surface Nucleation Kinetics

Crystallization of silicate glasses starts most readily from their surface [21]. This surface is highly susceptible to mechanical damaging or local chemical impurities, in particular, during glass powder processing. Once formed, for example, by milling, surface heterogeneities can strongly promote nucleation and can influence surface nucleation kinetics in a complex manner. These effects can be illustrated in terms of the classical nucleation theory (CNT) [22, 23], although more advanced attempts have recently been made, for example, with respect to the composition of crystal nuclei [24] or discussing floppy regions of the glass structure instead of molecular building units [25]. In terms of CNT, the homogeneous steady-state nucleation rate,  $I$  ( $\text{m}^{-3}\text{s}^{-1}$ ), is

$$I(T) \approx \frac{kT}{3\pi\lambda_M^3\eta(T)} \cdot n_0 \cdot \exp\left(-\frac{W(T)}{kT}\right), \quad (3.1)$$

where  $W$  is the work of forming a critical nucleus,  $T$  is the temperature, and  $\eta$  is the viscosity of the melt.  $\lambda_M$  denotes the jump distance and the size of molecular building units of the melt.  $n_0$  is their number per unit volume. At a nucleation site, or within a neighbored activated volume  $v^*$ ,  $W$  is lowered to  $W^* = \phi W$  ( $\phi < 1$ ). As shown in Figure 3.3 [26], this decrease substantially increases  $I$  to the *heterogeneous nucleation rate*  $I^* = I(W^*)$  and shifts its maximum to higher temperatures, where crystal growth can occur simultaneously.

By this way, nucleation sites are often quickly *used up* by fast nucleation and crystal growth before nucleation occurs elsewhere. The current number of such “active” nucleation sites will therefore dominate nucleation kinetics. Such a situation is sketched in Figures 3.4 and 3.5 for surface nucleation. The measured surface nucleation rate,  $dN/dt$  ( $\text{m}^{-2}\text{s}^{-1}$ ), is thus proportional to the number density of active surface nucleation sites *not used up* according to Equation 3.2 [31], where  $H$  is the initial number density of surface nucleation sites ( $\text{m}^{-2}$ ),  $N$  is the number density of surface crystals, and  $I_H = I^* \cdot v^*$  ( $\text{s}^{-1}$ ) their “using-up rate.” After using up all sites, nucleation is saturated at  $H$ :

$$dN/dt = [H - N(t)]I_H. \quad (3.2)$$

For large  $I_H$ , that is, highly active sites, this saturation occurs before any crystal can grow to a detectable size (Fig. 3.5, curve 1, left gray area). This *site saturation* phenomenon is typical for many silicate glasses if nucleation is not promoted by nucleating additives or prolonged nucleation pretreatments [21, 32]. With further growth, a nearly uniform crystal size is reached since differences in crystal size due to different

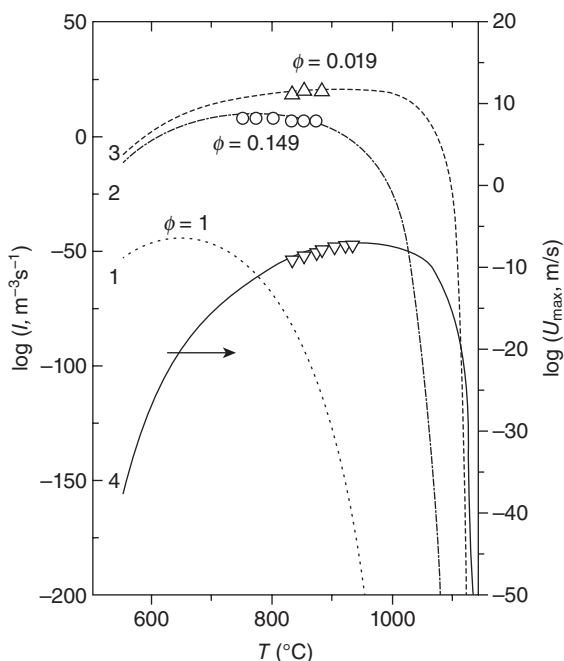


**Figure 3.3.** Rates of homogeneous nucleation (1), heterogeneous bulk nucleation (2), surface nucleation (3), and crystal growth (4) for  $\mu$ -cordierite crystals versus temperature in  $48\text{SiO}_2$ - $32\text{Al}_2\text{O}_3$ - $13\text{MgO}$ - $8\text{TiO}_2$  (rounded, weight percent) glasses [26]. Curves 1–3: calculated according to Equation 3.1 with  $W^* = W \cdot \phi$ ,  $\phi \leq 1$ . Experimental points for 3 were calculated from crystal size data by Köster's method [27, 28] (see References 29 and 30 for a similar figure).

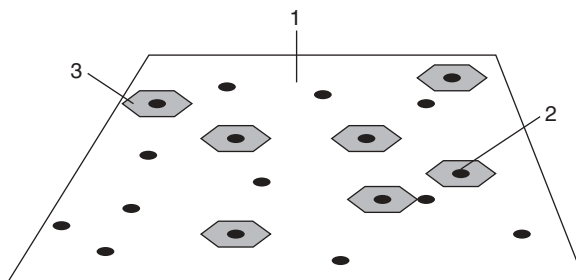


**Figure 3.4.** "Using-up" surface nucleation sites (schematic). 1, glass surface; 2, randomly distributed surface nucleation sites; 3, surface crystals [37].

nucleation times are small compared to the average crystal size [28]. Such situation is, for example, shown in Figures 3.6 and 3.7, 3.9 and 3.10, and 3.27 and 3.29.

For small  $I_H$  (Fig. 3.5, curve 2), that is, less active sites,  $N(t)$  steadily increases with time. Nonetheless, surface nucleation data analysis is difficult since  $I^*$  and  $v^*$  remains unknown and  $H$  can be obtained only for appropriate ratios between  $H$ ,  $I_H$ , and the crystal growth rate.

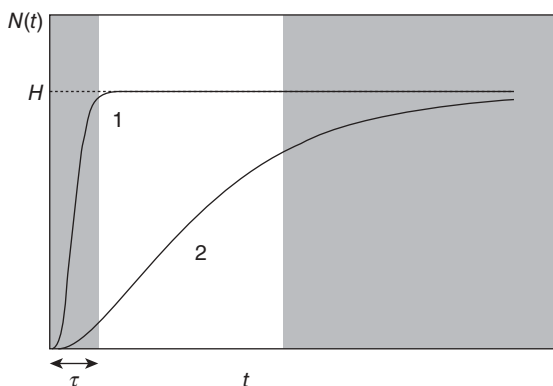


**Figure 3.5.** Scheme of heterogeneous surface nucleation kinetics. Curves 1 and 2: large and low using-up rates of nucleation sites, respectively. Shaded regions: experimental limits due to the minimum size of detectable crystals (left) and crystal impingement (right).  $\tau$  is the nonsteady time lag of nucleation;  $H$  is the initial number density of active surface nucleation sites [37].

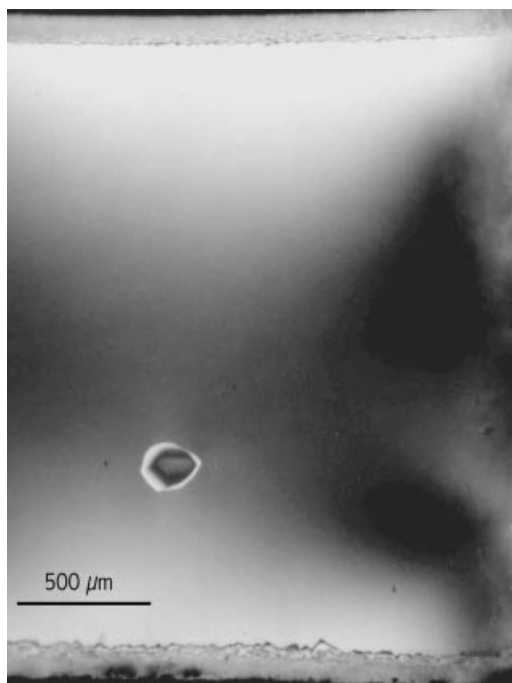


**Figure 3.6.** Low surface nucleation density ( $N \approx 6 \cdot 10^{-8}/\mu\text{m}^2$ ) at a cordierite glass surface fractured and annealed in vacuum (980°C, 30 min). Top view, optical micrograph, crossed nicols. A compact crystalline surface layer additionally grew from the SiC-ground sample surface (top and bottom) [30].

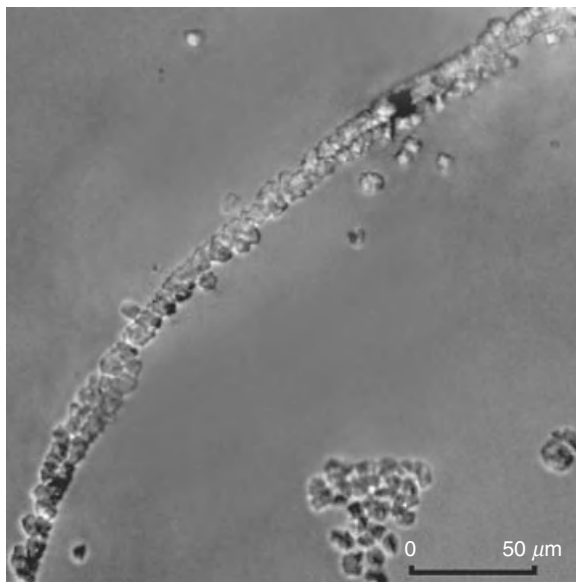


**Figure 3.7.** Diopside crystals growing from a diamond-made scratch on a fractured diopside glass surface prior to crystallization annealing. Top view, transmitting light micrograph. Annealing: 830°C, 210 min [50].

Moreover, nucleation kinetics can be complicated by a time-dependent number density [33, 34] and time-dependent size of surface nucleation sites [34, 35] as well as by the presence of nucleation sites, which are specific for different crystal phases [36]. Thus, comparisons of surface nucleation data among different systems and conclusions on the nature of active nucleation sites are difficult and are not fully understood up to now.

### 3.2.2 Surface Nucleation Sites

Against that background, the nature of surface nucleation sites and their effect on the surface nucleation kinetics have been studied within a cooperative effort of the TC7 of ICG, chaired by W. Pannhorst [38]. The surface crystallization of  $\mu$ -cordierite in cordierite glasses of the isochemical composition  $2\text{MgO}-2\text{Al}_2\text{O}_3-5\text{SiO}_2$  was studied as a model case. The main results, as some of them are briefly mentioned below, are reviewed in Reference 37. More recent reviews on internal and surface nucleation in silicate glasses are presented, for example, by Deubener [39], Zanotto and Fokin [40], Fokin et al. [41], and Schmelzer et al. [24]. In the following section,  $N$  is sometimes expressed by the mean next neighbor distance of surface nuclei,  $2\ell$ , which might help

for better visualization. Assuming that, at the average, each site is surrounded by an area of  $(2\ell)^2$ , free of other sites,  $\ell$  is given by Equation 3.3:

$$N \approx \frac{1}{(2\ell)^2}. \quad (3.3)$$

**3.2.2.1 Mechanical Damage.** Mechanical damage was found to have a most striking effect on  $N$ . Thus, maximum nucleation densities are evident for glass powders ( $N \approx 10^{-1}$ – $10^{-3}/\mu\text{m}^2$ ;  $2\ell \approx 3$ – $30 \mu\text{m}$ ) [42] and ground surfaces ( $N \approx 10^{-2}/\mu\text{m}^2$ ;  $2\ell \approx 10 \mu\text{m}$ ) [43–45]. Medium values are evident for mechanically polished and “as-received” surfaces (float glass surface, microscopic slide;  $N \approx 10^{-2}$ – $10^{-5}/\mu\text{m}^2$ ;  $2\ell \approx 10$ – $300 \mu\text{m}$ ) [43–49]. Low nucleation density occurs for freshly fractured and fire-polished glass surfaces ( $N \approx 10^{-3}$ – $10^{-8}/\mu\text{m}^2$ ;  $2\ell \approx 30 \mu\text{m}$ – $10 \text{ mm}$ ) [43, 47, 49]. This strong effect of mechanical damaging is also illustrated by Figure 3.6, where one crystal grew from a smooth fractured cordierite glass surface, whereas high surface nucleation density is indicated by the compact crystalline surface layer, which has been grown from the outer SiC-ground surfaces (top and bottom). The nucleation activity of a scratch is illustrated in Figure 3.7.

More detailed studies [30, 50–52] revealed that sharp glass surface tips and corners provide most active surface nucleation sites as schematically shown in Figure 3.8 (left). The respective nucleation activity was found to increase with the absolute relative crystal glass density difference,  $\delta$ :

$$\delta = \left| \frac{\rho_C - \rho_G}{\rho_G} \right|, \quad (3.4)$$

where  $\rho_G$  and  $\rho_C$  denote the glass and crystal density, respectively [37]. Thus, densely packed double chains of diopside crystals ( $\delta \approx 15\%$ ) grew from the adjacent crack edges in isochemical diopside glass (Fig. 3.7). On the other hand, a much less crystal

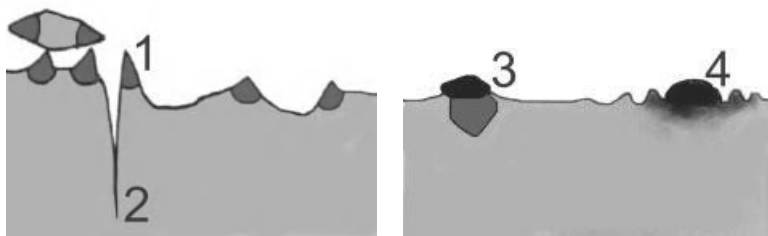


**Figure 3.8.** Schematic representation of active nucleation sites. 1, sharp convex surface tips or edges; 2, sharp concave surface tips or edges; 3, chemically and thermally stable solid foreign particle; 4, unstable particle [37].

number density of  $\mu$ -cordierite crystals occurred along scratches and edges on cordierite glass surfaces ( $\delta \approx 2\%$ ) as also for cristobalite crystals growing from float glass surfaces [37]. In contrast to these points of sharp *convex* curvature, almost no nucleation activity, however, was found at the inner tips of large cracks (sharp *concave* curvature, Fig. 3.8, left).

**ELASTIC ENERGY.** According to Feltz [53] and Schmelzer et al. [51, 54], these findings can be explained assuming that volume nucleation is substantially suppressed by the elastic energy required for the growth of crystals within a matrix of different density. Far from the glass surface ( $z = \infty$ ), the elastic energy per monomer,  $\epsilon_0^\infty$ , depends on  $\delta^2$ , Young's modulus  $E$ , Poisson's ratio  $\nu$ , and the volume of the crystal monomer  $v_C$ , according to [54]

$$\epsilon_0^\infty = \left( \frac{E}{9(1-\nu)} \right) \cdot \delta^2 v_C. \quad (3.5)$$

$\epsilon_0$  directly affects  $W$  in Equation 3.1, which strongly affects the nucleation rate [54].  $\epsilon_0$ , however, decreases near the glass surface and even disappears at sharp surface tips, thus explaining their high nucleation activity. On the other hand,  $\epsilon_0$  at the inner crack tips is  $\approx \epsilon_0^\infty$  since the local elastic response is similar to that of the bulk.

**LOCAL VISCOUS FLOW.** The activity of surface tips, discussed above, might also been explained by local viscous flow [55], which can be expected at these points during heating. The effects of pressure and shear stress on melt crystallization were reported by Seidel and Friedrich [56] and Durschang et al. [57] and were thoroughly discussed in terms of the effects of pressure upon undercooling, interfacial energy, and viscosity in Reference 57. Möller et al. [58] discussed the effects of flow gradients on the monomer impingement to the spatially extended nucleus and the respective increase of nucleation rate.

**3.2.2.2 Solid Foreign Particles.** For smooth, for example, polished or fractured, glass surfaces,  $N$  is strongly affected by *solid foreign particles*. Thus, as early as 1739, Réaumur [59] triggered surface nucleation of glassware by contamination with foreign solid particles. Confirming similar observations by Swift [60] and Zanotto [47], airborne solid particles were frequently found at the center of surface crystals growing from smooth glass surfaces (Fig. 3.9). The random occurrence of nucleating dust particles also explains the typically large scatter of  $N$  when commercial laboratory furnaces are used, whereas this scatter is strongly reduced in fused silica tube furnaces or in vacuum [47, 61, 62].

The nucleation activity of solid foreign substrates,  $\phi$ , for heterogeneous bulk nucleation was explained in terms of the cohesion forces in the solid foreign substrate  $\Psi_{ss}$  and its lattice misfit to the crystal nucleus by Dobrev and Gutzow [63–65].  $\Psi_{ss}$  hereby reflects the heat of sublimation or melting of the solid foreign substrate and can be correlated to its melting temperature. For zero misfit,  $\phi$  decreases linearly with



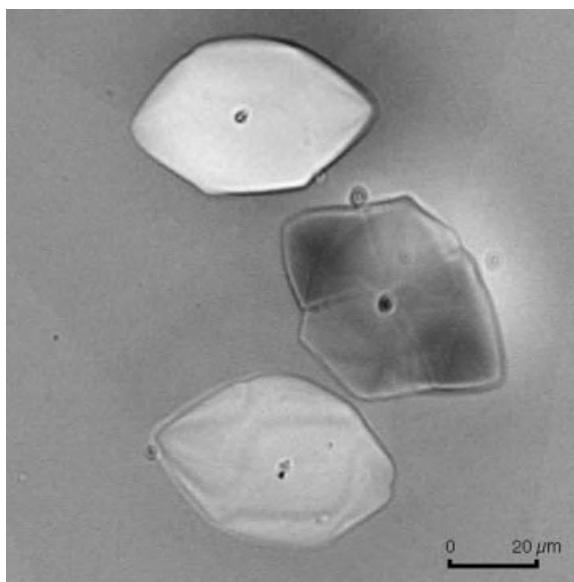


**Figure 3.9.**  $\mu$ -Cordierite crystals grown from dust particles spread over a fractured cordierite glass surface. Top view, transmitting light micrograph. Annealing: 960°C, 15 min [30].

$(\Psi_{ss}/\Psi_{cc})^{1/2}$ , where  $\Psi_{cc}$  denotes the cohesive forces in the crystal. The surface nucleating efficiency of solid foreign particles at the glass surface, however, can be also affected by the ambient atmosphere. Thus, as a first precondition of their nucleating efficiency, foreign particles have to be chemically and thermally stable [37], as schematically shown in Figure 3.8 (right).

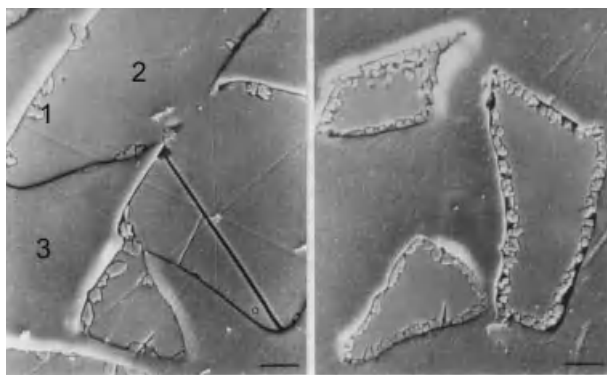
Oxide particles, dusted onto cordierite glass surfaces prior to the nucleation treatment, were mostly found providing active nucleation sites for  $\mu$ -cordierite surface crystals [50, 62]. Among them,  $ZrO_2$  stood out as most efficient, and its activity was affected by its crystal morphology. Dusted  $\mu$ -cordierite,  $\alpha$ -cordierite, quartz, and fire-clay powders also provided active nucleation sites [50, 55]. The nucleation activity of  $Al_2O_3$ ,  $Fe_2O_3$ ,  $CeO_2$ , and  $MgO$  decreased from a moderate to a slight increase.  $TiO_2$  and  $WO_3$  could even reduce  $N$  probably by easier *dissolution* into the silicate melt.

*Nonoxide* dust particles studied in References 50, 55, and 62, however, did not increase  $N$  except in vacuum ( $p < 10^{-4}$  mbar), where better oxidation stability was guaranteed. Thus, SiC and  $Si_3N_4$  had no influence, whereas WC, W,  $TiB_2$ , and  $B_4C$  even decreased  $N$  in air. The lack of nucleation enhancement of SiC and  $Si_3N_4$  in air is probably due to the formation of an amorphous  $SiO_2$  surface layer. Obviously, chemical reactions with the glass and ambient atmosphere can decrease the nucleating efficiency of solid foreign particles. A slight increase of  $N$  by dusting with SiC, WC, and  $B_4C$  in vacuum supports that explanation. In the case of larger concentrations of chemically unstable particles (W, WC,  $B_4C$ ) or less stable oxides such as  $WO_3$  and  $B_2O_3$ , a rippled glass surface and the occurrence of additional crystalline phases were observed, indicating chemical interaction or dissolution.

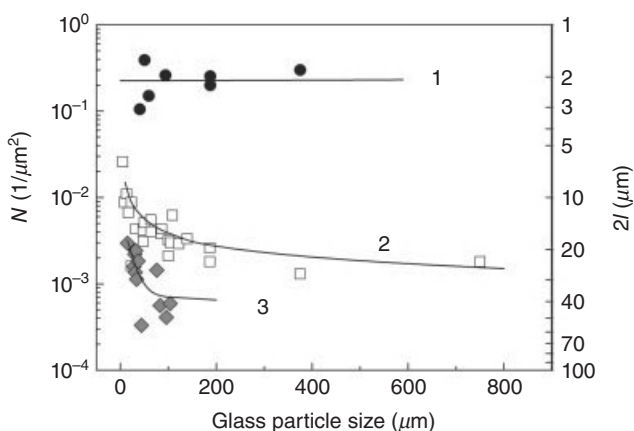
### 3.2.3 Crystal Nucleation from Glass Powder Surfaces

Figure 3.10 illustrates that crystal surface nucleation density can strongly depend on powder milling. Thus, the surface nucleation density of  $\mu$ -cordierite,  $N$ , was found to increase with an increasing *milling time* of cordierite glass powders [42]. This finding can be explained as discussed above since prolonged milling will cause progressive mechanical damage and increased amounts of milling impurities.

Second,  $N$  was found substantially increasing with decreasing *particle size* even when small and large particles were taken from the same powder probe, that is, exposed to the same milling time (see Fig. 3.11). This effect confirms the strong nucleating effect



**Figure 3.10.** Electron micrograph of differently prepared cordierite glass powders cut, embedded, polished, and etched (1% hydrofluoric acid [HF]). Left: steel mortar, right: 45-min vibratory ball milling with agate, bars = 10  $\mu\text{m}$ . (1)  $\mu$ -Cordierite crystals, (2) cordierite glass, (3) resin [42].



**Figure 3.11.** Influence of glass particle size on the surface nucleation density  $N$ , of  $\mu$ -cordierite for different milling. Curve 1: 5-min vibratory ball milling, agate; curve 2: 10-s vibratory disk milling, tungsten carbide; curve 3: 1-min planetary ball milling, steel [42].

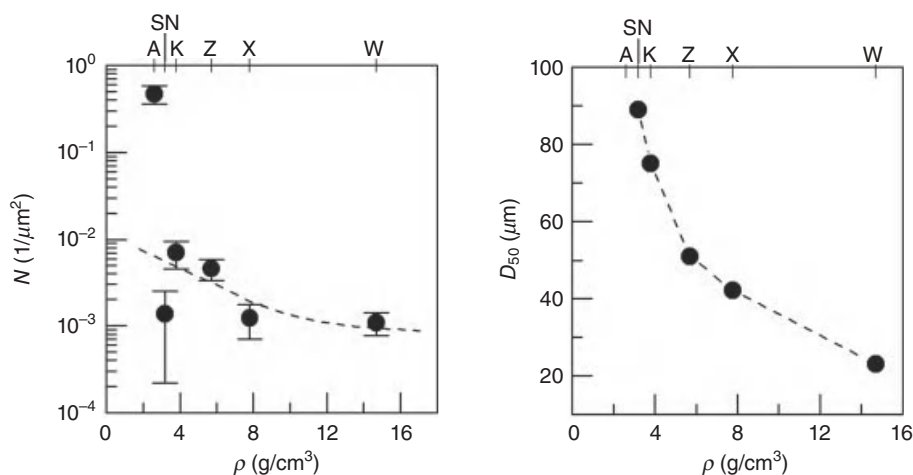


**Figure 3.12.** Left: surface nucleation density of  $\mu$ -cordierite for cordierite glass particles selected from 1-min planetary ball-milled glass powders (5-min milling for agate) versus density of milling material. Right: milling efficiency of 1-min planetary ball milling with these milling materials: A, agate; SN,  $\text{Si}_3\text{N}_4$ ; K,  $\alpha\text{-Al}_2\text{O}_3$ ; Z,  $\text{ZrO}_2$ ; X, steel; W, WC (upper abscissa).  $D_{50}$  after 1-min agate milling is out of range [42].

of sharp corners and edges, which more frequently appear for small glass particles per unit area. Further, it is known that milling efficiency decreases with particle size. Thus, particle size distribution (PSD) narrows and shifts to smaller particle size during milling. That suggests that the average surface of large particles is more juvenile than that of fine particles. In this sense, the generally high values of  $N$  provided by agate milling (Fig. 3.11, curve 1) may result from required prolonged milling, which may cause strong surface damage even for the remaining large particles.

$N$  was also affected by *milling materials*. Figure 3.12 (left) shows their influence on  $N$  measured for cordierite glass particles of 30–100  $\mu\text{m}$  in size by optical microscopy. All particles were picked out from 1-min planetary ball-milled glass powders. The nucleating activity tends to decrease with the increasing density of milling materials.

As illustrated in Figure 3.12 (right), this effect is at least partially related to the milling efficiency. This efficiency increases with the increasing density of the milling material. If the milling efficiency is high, a low milling time is required to obtain a certain finely ground glass powder, which therefore has a more juvenile and smooth fractured surface. Thus, the effect of the milling material can be largely attributed to the influence of milling time and progressive mechanical damage as discussed above. However, this effect is superimposed by the nucleating effect of oxide and nonoxide milling impurities as indicated by the substantially reduced nucleating activity of silicon nitride.

### 3.3 OVERALL CRYSTALLIZATION OF GLASS POWDERS

#### 3.3.1 Formal Kinetic Approach

Overall crystallization kinetics of glasses is often described in terms of the formal theory of transformation kinetics developed by Kolmogorov [66], Johnson and Mehl [67], Avrami [68–70], and Erofeyev [71] (“KJMAE”). Comprehensive reviews of the KJMAE theory were published by Young [72] and Christian [73]. For (1) constant temperature, (2) spatially random nucleation, and (3) growth rates not depending on time explicitly, the crystallized volume fraction,  $x(t)$ , is

$$x(t) = 1 - \exp(-kt^n), \quad (3.6)$$

where  $t$  is the reaction time,  $n$  is the Avrami parameter or *reaction dimensionality*, and  $k$  is the effective reaction rate. For a constant number of nucleation sites,  $n$  is the *growth dimensionality*.  $kt^n$  is referred to as the *extended volume* [74]. For  $t \rightarrow 0$  and the three-dimensional growth of spherical crystals from a constant number of crystal nuclei,  $kt^n = H \cdot (4/3)\pi U^3 t^3$  is the crystal volume fraction, where  $U$  is the crystal growth rate and  $H$  is the number density of the nucleation sites [75]. For large  $t$ , however,  $kt^n$  summarizes the fictive volume of all individual crystals as they would grow neglecting any crystal impingement.  $kt^n$  therefore steadily increases to values far above the crystal volume fraction. Differentiation of Equation 3.6 reveals that  $x'$ , the overall transformation rate of crystallization, is proportional to  $1 - x$ , the current volume fraction of the nontransformed parent phase, according to

$$x'(t) = \{1 - x(t)\} \cdot nkt^{n-1}. \quad (3.7)$$

In a rewritten form, Equation 3.6 is often used to conclude on  $n$  according to

$$\ln[\ln(1 - x)^{-1}] = \ln k + n \ln t. \quad (3.8)$$

Based on this concept, manifold techniques have been developed and widely used for easy determination of  $n$  and activation energies of crystallization even from nonisothermal differential thermal analysis (DTA) or differential scanning calorimetry (DSC) measurements as critically reviewed by Henderson [76] and Weinberg [77]. Matusita and Sakka [78] also included surface crystallization of glass powders by generalizing Equation 3.8 with a new formal parameter.

The application of this generalized formal kinetic concept to glass powder crystallization is difficult, however, since the KJMAE theory applies only to systems of infinite dimensions for which the assumption of spatially random nucleation is valid. Many authors like, for example, Fokin et al. [79], Zanutto et al. [80], Yinnon and Uhlmann [81], Henderson [76], Weinberg [82, 83], and Donald [84] have thus critically revisited the application of the KJMAE theory for glass powder crystallization regarding various aspects and have shown that prior knowledge of crystallization mechanism is often required to apply nonisothermal formal kinetic analysis in a meaningful manner.

### 3.3.2 Topokinetic Approach

**3.3.2.1 Change of Growth Dimensionality.** On the other hand, topokinetic approaches state clear assumptions about the reaction geometry, which can be easily proved for most glass crystallization phenomena. Topokinetic approaches were introduced by Mampel [85, 86] and Todes [87] for spatially random nucleation at the surface of spheres. However, no analytic solution was given for this case. Weinberg [82, 83] analyzed the kinetics of site saturated surface nucleated crystallization in spherical particles of finite size even for competing bulk nucleation of constant nucleation rate and could show that plots of Equation 3.8 are not linear in any case. A similar approach was made by Gutzow et al. [74] for spherical glass particles and spherical surface crystals assuming preexisting, randomly distributed surface nuclei. He could demonstrate that the Avrami parameter  $n$  in Equation 3.6, which is now the growth dimensionality, depends on particle size (Fig. 3.13).

The typical change of growth dimensionality,  $n$ , for surface crystallization of glass powders from a constant number of nuclei is illustrated in Figure 3.14 [88]. This cross-sectional micrograph shows cordierite glass powder particles of different sizes exposed to the same crystallization treatment.

For the fine glass particle in Figure 3.14, the entire volume obviously crystallized by the three-dimensional growth of separate crystals ( $n = 3$ ), as for any volume

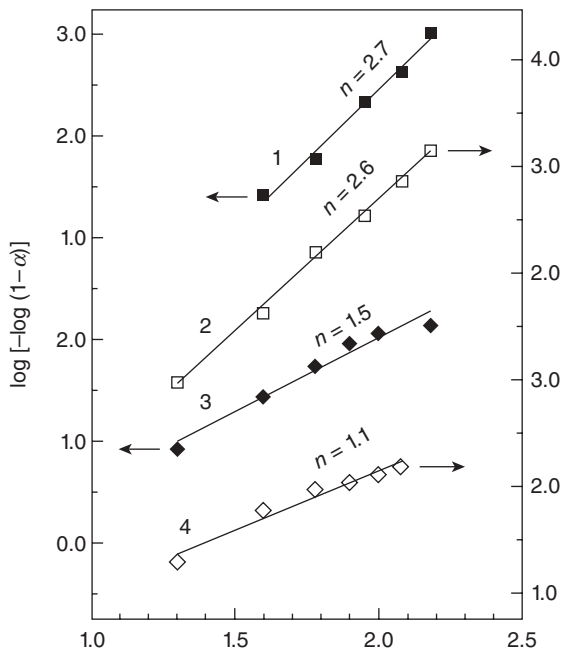


**Figure 3.13.** Overall kinetic data for the crystallization of  $\text{NaPO}_3$  glass powders of different particle sizes presented in Avrami coordinates and obtained Avrami parameter,  $n$ . Particle radius 1: <0.04 mm, 2: 0.05–0.08 mm, 3: 0.2–0.25 mm, 4: 0.375–0.25 mm [74].

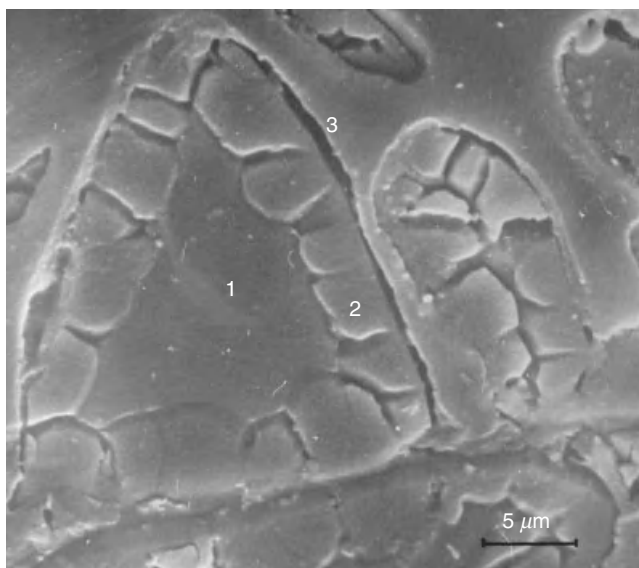


**Figure 3.14.**  $\mu$ -Cordierite crystals (2) grown from the surface of cordierite glass powder particles (1) annealed at 920°C for 5 min, quenched in air, and embedded in synthetic resin (3). Scanning electron microscopy (SEM) cross section [88].

nucleated crystallization. Such crystallization can even appear from the former glass surface after full sintering as sometimes called quasi-homogeneous bulk crystallization from “ghost surfaces” [14].

For the coarse particle in Figure 3.14, however, only a certain volume fraction crystallized this way and further crystallization will proceed via the one-dimensional growth of a compact crystalline surface layer ( $n = 1$ ). The glass particle size, at which the dimensionality of crystal growth is changing, depends on surface nucleation density.

**3.3.2.2 DTA Curves for Surface Crystallization of Glass Powders.** The DTA signal is proportional to the overall crystallization rate,  $x'$  ( $s^{-1}$ ). This rate is  $U \cdot A$ , where  $A$  ( $m^{-1}$ ) is the area of glass–crystal interface per unit volume and  $U$  (m/s) the crystal growth rate perpendicular to this interface. Thus, DTA peaks indicate the temperatures of maximum of  $U \cdot A$  and easily allow conclusions on the geometry and kinetics of overall crystallization.

In this context, it is often helpful to consider powders of different particle sizes. The effects of particle size ( $2R_0$ ) and mean next neighbor distance of surface nucleation sites ( $2\ell$ ) on the peak temperature and shape of DTA curves were demonstrated in Reference 89 in terms of the model illustrated in Figure 3.15. Beside the simplified cubic geometry, which may even does not deviate more from real particle shapes than spheres would do, interface-controlled crystal growth, site saturation, and regularly arranged surface nucleation sites were adopted. This way,  $x'$  could be derived from simple geometric considerations. This model most simply demonstrates the effect of

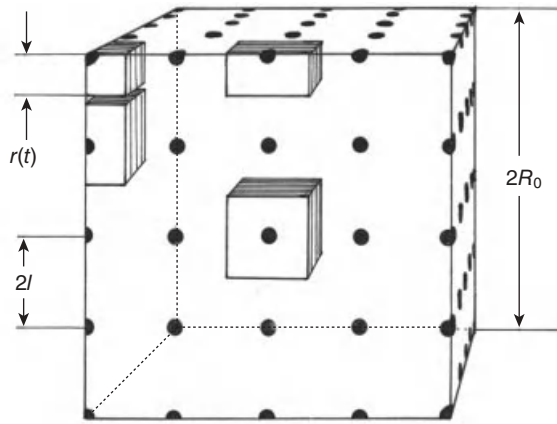


**Figure 3.15.** Topokinetic model for the calculation of DTA curves.  $2l$ , constant mean distance of surface nucleation sites;  $2R_0$ , glass particle diameter;  $r$ , crystal size [89].

$R_0$  and  $2l$  on DTA curves as illustrated in Figure 3.16 and can help to explain the effect of glass powder milling on the overall crystallization.

For  $R_0 \gg l$  (very large number of surface nuclei per particle), broad DTA peaks occur shifting to lower temperature with decreasing particle size. These DTA peaks occur at  $r(t) = R_0/3$  arising from two competing effects: the increase of crystal growth rate  $U$  with increasing temperature  $T$  and the decrease of the glass–crystal interfacial area  $A$  when the surface layer grows toward the bulk [89]. This case is, for example, shown in Figure 3.16 ( $R_0 > 90 \mu\text{m}$ ) for glass powders with  $2l \approx 10 \mu\text{m}$ .

For  $R_0 \geq l$  (moderate number of surface nuclei per particle),  $x'$  substantially decreases at  $r(t) = l$  by surface crystal impingement and the related reduction of the glass–crystal interface. This effect is significant when the surface layer formed hereby covers a large volume fraction, as given in Figure 3.14. Due to the faster three-dimensional growth before impingement, DTA curves are narrow. The decrease of  $x'$  at  $r = l$  can cause DTA shoulders (Fig. 3.16,  $R_0 > l = 19 \mu\text{m}$ ) or peaks (Fig. 3.16,  $R_0 = 5 \mu\text{m}$ ).

For  $R_0 < l$  (less than one surface nucleus per particle), crystallization stops at  $r(t) = R_0$ . This effect decreases the DTA peak temperature and height with decreasing  $R_0$  (Fig. 3.16,  $R_0 < 5 \mu\text{m}$ ).

This behavior allows estimating  $2l$  from a series of DTA curves of differently sized glass powders or directly from the impingement temperature,  $T_i$  ( $\approx 980^\circ\text{C}$  in Fig. 3.16), and the related crystal size,  $r_i$ . The latter might be estimated from crystal growth rate data. For constant heating and if the crystal growth rate  $U$  entirely depends on temperature according to the Arrhenius law,  $r(t)$  can be approximated as [89]:

$$r(t) \approx t \cdot \left( \frac{R\alpha t}{E_a} \right) \cdot u_0 \exp\left( \frac{-E_a}{R\alpha t} \right), \quad (3.9)$$

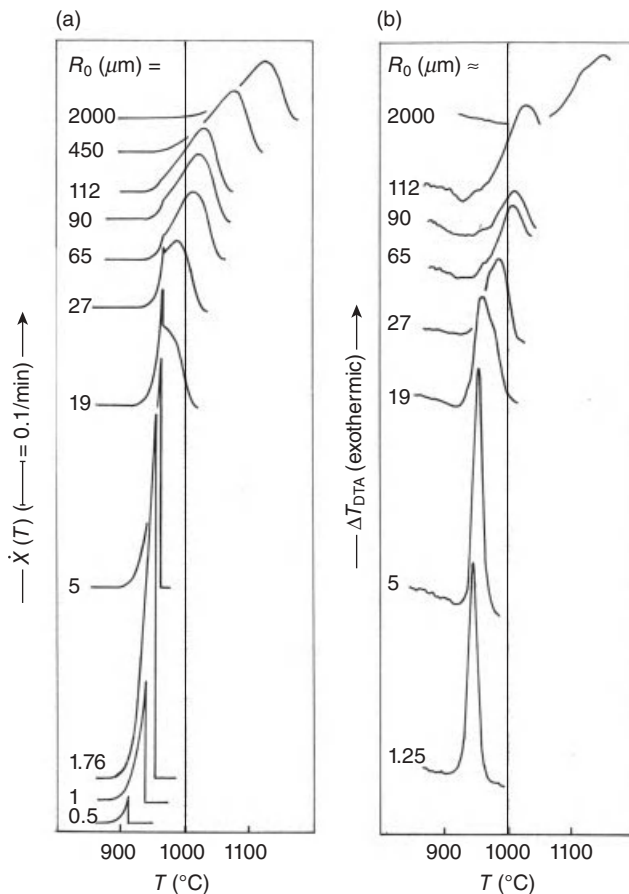


**Figure 3.16.** Experimental DTA curves (arb. units) attributed to the primary growth of  $\mu$ -cordierite from the surface of cordierite glass powders during heating at 10 K/min (right).  $2\ell \approx 10 \mu\text{m}$  was obtained by optical microscopy. The secondary crystallization  $\mu$ -cordierite to  $\alpha$ -cordierite is hidden for better clarity. DTA curves calculated according to Müller [89] with  $\ell = 5 \mu\text{m}$ ,  $u_0 = 10^{18} \mu\text{m/min}$  and  $E_a = 420 \text{ kJ/mol}$  [89] (left).

where  $t$ ,  $\alpha$ ,  $R$ ,  $u_0$ , and  $E_a$  denote the time, heating rate, gas constant, exponential prefactor, and activation energy of the crystal growth.

### 3.4 VISCOUS SINTERING

This section intends to illustrate the effects of glass powder processing and related basic parameters like particle size, particle shape, particle size distribution, or particle arrangement on viscous sintering. In order to illustrate these influences most simply, a few sintering models are briefly referred to below within the respective context. No



systematic introduction to the theory of viscous sintering, however, is intended here. Comprehensive reviews of the sintering theory and praxis are given, for example, by German [18] and Chiang [8], and an introduction to the advanced continuum theory of sintering was published by Olevsky [16].

### 3.4.1 Particle Size

Particle size is an important factor of viscous sintering affected by powder processing. The effect of the particle radius  $R_0$  on the *excess powder surface energy* as the driving force of sintering is illustrated by Chiang [8]. From typical values of surface energy  $\gamma \approx 0.3\text{--}1.0 \text{ J/m}^2$  and glass density  $\rho_G \approx 3\text{--}7 \text{ g/cm}^3$ , he estimated a powder surface energy per gram of spherical particles ( $E_s \approx 3\gamma/R_0\rho_G$ ) of  $\approx 4 \text{ J/g}$  for  $R_0 = 0.1 \text{ }\mu\text{m}$  and  $\approx 0.04 \text{ J/g}$  for  $R_0 = 10 \text{ }\mu\text{m}$ .

The effect of particle size on *viscous sintering kinetics* can be most easily illustrated in terms of Frenkel's model [90] for the coalescence of two glass spheres. Frenkel obtained the linear sintering rate,  $s'$ , by equating the energy gained by the decrease in surface area and that dissipated in viscous flow. In its corrected form [91, 92], his model is most frequently used as [8]

$$s' = \frac{3\gamma}{8\eta R_0} \cdot k_f, \quad (3.10)$$

where  $\eta$  is the Newtonian shear viscosity and  $k_f$  is an adjustable parameter, often regarded as the particle shape factor. While Equation 3.10 applies for the initial stage of sintering, the late sintering of isolated pores was treated by Mackenzie and Shuttleworth [93], yielding

$$\rho' = \frac{3\gamma}{\eta} \cdot \left( \frac{O^{1/3}}{2R_0} \right) \cdot (1-\rho)^{2/3} \cdot \rho^{1/3}, \quad (3.11)$$

where  $\rho' = dp/dt$  is the relative densification rate and  $\rho$  is the relative compact density. Illustrating the effect of the initial particle size, the number of pores per unit volume,  $n$ , used in Reference 93, is expressed here by the number of pores per particle,  $O$ , with  $n \approx 3O/4\pi R_0^3$  [94].

As a simple approximation, Equations 3.10 and 3.11 can be extended even to medium sintering stages below and above  $\rho = 0.8$  ( $t = t_{0.8}$ ), respectively, and can be combined for numerical integration of linear shrinkage,  $s(t)$  [88, 95–97]. For this purpose, however,  $s$  and  $\rho$  have to be converted into each other. For isotropic sintering, one can utilize  $\rho_0/\rho = V/V_0 = (1-s)^3$ , which gives  $s = 1 - (\rho_0/\rho)^{1/3}$  and  $s'/\rho' = \rho_0^{1/3}/3\rho^{4/3}$ , where  $\rho_0$  is the relative green density. For  $t > t_{0.8}$ , this yields

$$s(t) = \int_0^{t_{0.8}} s'(\xi) d\xi + \int_{t_{0.8}}^t \rho'(\xi) \left( \rho_0^{1/3}/3\rho(\xi)^{4/3} \right) d\xi. \quad (3.12)$$

In order to ensure continuous slope of the linear shrinkage curve at  $\rho = 0.8$ , one has to set  $O^{1/3} \approx 2k_f$ . The effect of particle size on nonisothermal sintering during heating at 5 K/min is illustrated by dashed curves in Figure 3.20. The left, middle, and right dashed curves were calculated with Equations 3.10–3.12 for  $R_0 = 0.3$ , 3.0, and 10.0  $\mu\text{m}$ , respectively, showing a shift of  $\approx 60$  K within that range.

### 3.4.2 Submicron Particles

Any such extrapolation to submicron particle size, however, should be made with care. Due to their large specific surface area, powders of submicron particles are strongly affected by interparticle adhesion forces. This effect causes lower packing density by particle alignment to chains or aggregates as, for example, reported by Clasen [98] for submicron silica glass powder compacts.

The possible related effect on sintering is illustrated in Figure 3.17 [99] for a sol-gel-derived cordierite glass powder with insufficient ceramic processing as an example. In this case, small aggregates during early sintering were indicated by BET, whereas optical microscopy revealed large aggregates caused by milling of calcinated sol-gel powders. Figure 3.17 shows that the initial and final sintering can be described by Equations 3.10–3.12 for small ( $R_0 = 90$  nm, curve 1) and large particle size ( $R_0 = 15$   $\mu\text{m}$ , curve 2), while a pronounced shoulder occurs between.

Strong interparticle adhesion of submicron particles may even result in *skeletal microstructures* during sintering as illustrated in Figure 3.18 (left). The respective sintering kinetics was developed by Scherer [100]. In terms of his cubic cylinder model,

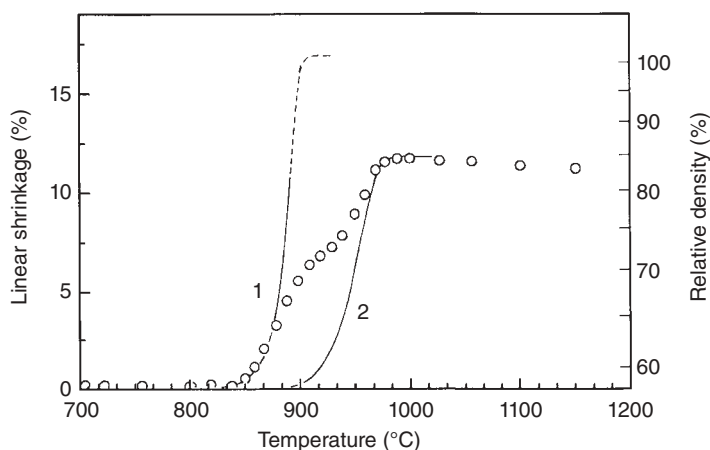


**Figure 3.17.** Linear shrinkage of sol-gel-derived cordierite glass powders during heating at 10 K/min (spheres). Curves: fitted according to Equations 3.10–3.12 with  $\log(\eta/\text{Pa s}) = -1.96 + (4265^\circ\text{C}/(T - 777^\circ\text{C}))$ ,  $\gamma = 0.36$  N/m,  $R_0 = 90$  nm,  $k_f = 1$  (curve 1), and  $R_0 = 15$   $\mu\text{m}$ ,  $k_f = 3$  (curve 2). The retarding effect of crystallization at  $\rho \approx 85\%$  was calculated according to Equations 3.9, 3.23, and 3.24 with  $2\ell = 5$   $\mu\text{m}$ ,  $u_0 = 10^{18}$   $\mu\text{m}/\text{min}$  and  $E_a = 420$  kJ/mol [99].

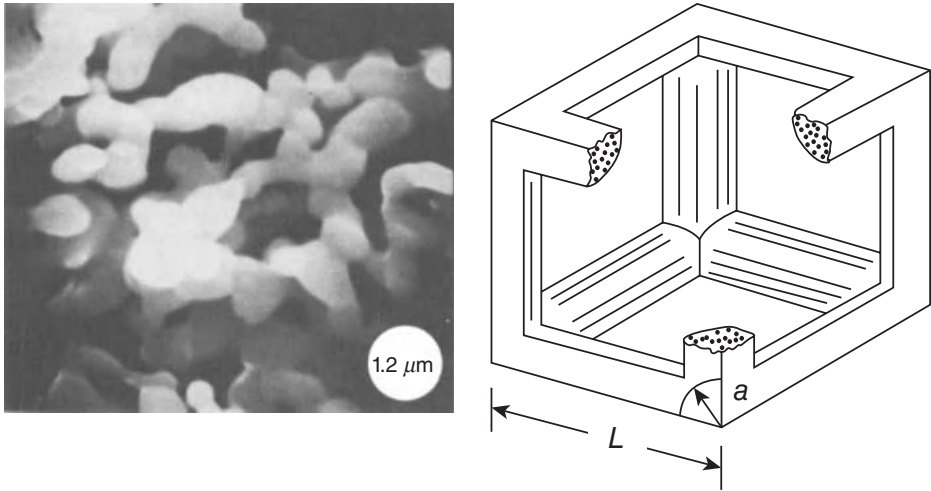


**Figure 3.18.** Structure of  $\text{Al}_2\text{O}_3$  preform made by flame hydrolysis of  $\text{AlCl}_3$  and the unit cell of the cylinder model for sintering low-density microstructures developed by Scherer [100].  $L$ , edge length;  $a$ , cylinder radius.

where  $a$  is the diameter and  $L$  is the length of the cylinders (Fig. 3.18, right) he derived for the free compaction strain rate,  $\epsilon'_f = -\rho'/3\rho$  [101]

$$\epsilon'_f = -\left(\frac{\gamma}{\eta}\right)\left(\frac{1}{V_s}\right)^{1/3} \frac{6\pi - 24\sqrt{2}(a/L)}{6(a/L)^{1/3} [3\pi - 8\sqrt{2}(a/L)]^{2/3}}, \quad (3.13)$$

where  $V_s$  is the constant volume of the solid phase in the unit cell.  $a/L$  is correlated to the relative density by  $\rho = V_s / L^3 = 3\pi(a/L)^2 - 8\sqrt{2}(a/L)^3$ .  $a$  is related to the initial particle size,  $R_0$ , while  $(a/L)$  depends on the degree of particle alignment. This equation holds to  $\rho = 0.942$  when  $a/L = 1/2$ . For larger  $\rho$ , the cells contain closed pores and sintering should be treated in terms of the model of Mackenzie and Shuttleworth [93]. Comparing calculations showed that the cylinder model is consistent with the predictions of the models of Frenkel and Mackenzie–Shuttleworth in the early and late stages of sintering, respectively [94, 102–104].

### 3.4.3 Particle Shape

Crushed or milled glass powder particles differ from spherical shape (Fig. 3.19). Thus, the adjustable parameter  $k_f$  in Equation 3.10 is often treated as a particle shape factor. In fact, Cutler and Henrichsen [105] observed up to a fivefold accelerated sintering rate for jagged particles compared to spherical particles. In other studies,  $k_f$  was found between 1.8 and 3.5 [88], 1.3 [96], and between 1.8 [106] and 3.0 [107].  $k_f = 1.2$  was fitted in Figure 3.20.

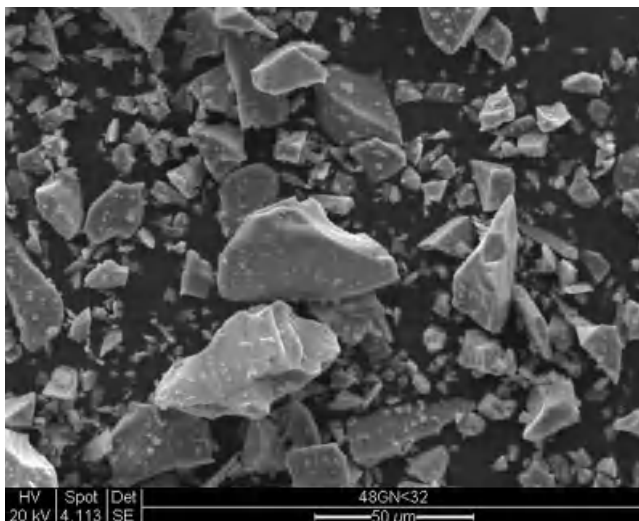


**Figure 3.19.** Mixed alkaline earth silicate glass powders after 30-min wet milling in an agate ball mill, meshed <32  $\mu\text{m}$  [108].

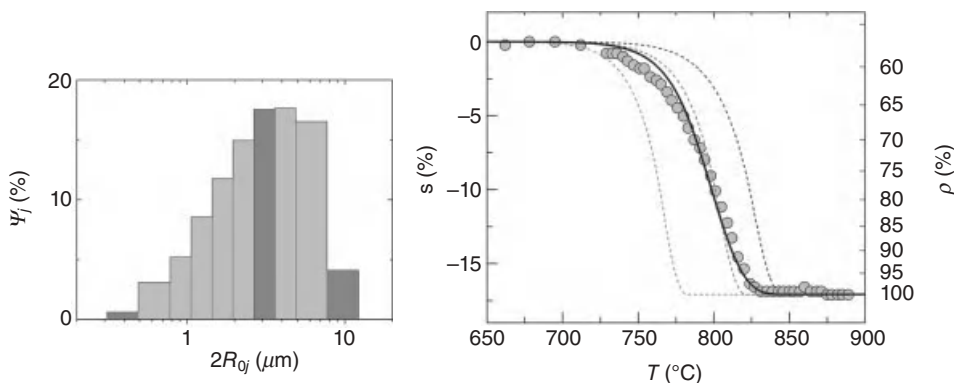


**Figure 3.20.** Particle size distribution (left) and linear shrinkage of  $12\text{BaO}-9\text{Al}_2\text{O}_3-15.4\text{B}_2\text{O}_3-63.6\text{SiO}_2$  glass powders versus temperature,  $T$ , during heating at 5 K/min (right). Spheres: experimental data. Left, middle, and right dashed curves were calculated according to Equations 3.10–3.12 with  $\log(\eta/\text{Pa s}) = -4.27 + (7484^\circ\text{C}/T - 202^\circ\text{C})$ ,  $\gamma = 240 \text{ mN/m}$ , and  $k_f = 1.2$  for the smallest, most frequent, and largest size fraction, respectively. The solid curve is a weighed superposition of shrinkage curves analogously calculated for the 10 classes of particle size shown left according to Equation 3.15 [111].

Overcoming this uncertainty, a stereology-based model for the isotropic viscous sintering of glass powders was derived by Exner and Giess [109]. Instead of particle size and shape, the specific compact solid/pore interface was introduced, which can be rigorously measured. After some rearrangements and in terms of the notation used here, his final kinetic equation yields

$$s' = \frac{2\pi\gamma}{3\eta} \frac{1}{\lambda_0} \left\{ 1 - \left( \frac{s}{s_{\max}} \right) \right\}, \quad (3.14)$$

where  $\lambda_0 = 4V_s/S_0$  represents the powder properties with  $V_s$  and  $S_0$  as the total solid volume in the sample and the pore/solid interface area, respectively.  $s_{\max} = 1 - \rho_0^{1/3}$  is the maximum isotropic shrinkage expected for the relative green density  $\rho_0$ . It should be noted that Equation 3.14 does not contain any adjustable parameters. The effect of particle size on  $s'$  can be seen approximating  $\lambda_0$  by  $4/3 R_0$ , which is valid for ideal spheres.

### 3.4.4 Particle Size Distribution (PSD)

**3.4.4.1 Narrow PSD.** For a narrow PSD, its average particle size can be sufficiently used for sinter kinetic modeling [110, 111]. Figure 3.20 illustrates this facilitation for a PSD typically applied for low-temperature cofired ceramics (LTCC).

The experimental shrinkage (spheres) is roughly approximated by the shrinkage curve calculated for the mean particle size according to Equations 3.10–3.12 (middle dashed curve). Nonetheless, systematic deviation is seen. As the most simple approximation, the effect of a narrow PSD can be described assuming that sintering is superimposed by the contribution of each particle size weighed by its relative frequency,  $\Psi(R_{0j})$ , according to [95]

$$s \approx \sum_j \Psi_j(R_{0j}) \cdot s_j, \quad (3.15)$$

where  $s_j$  is the shrinkage of powder fraction  $j$ . This assumption neglects any interaction between particles of different sizes as illustrated, for example, in Figure 3.22. The thus obtained result is shown by the solid curve in Figure 3.20, where  $s_j$  was calculated according to Equations 3.10–3.12. Despite some underestimation of the initial sintering rate, a sufficient fit is attained by this way. This concept, later called “cluster model,” was applied and further advanced by Prado, Zanotto, and colleagues in a series of studies on sintering and crystallization of glass powders [96, 97, 106, 107, 112–115].

**3.4.4.2 Broad PSD.** This approximation fails, however, for a broad (polymodal) PSD with  $\Psi_j > 10\%$  between 2 and 80  $\mu\text{m}$  as shown by Prado et al. [95]. In this case, a nonregular particle arrangement was evident (Fig. 3.21). For sufficient fitting experimental shrinkage data, a *neck-forming ability* factor describing the number of necks, which can be formed by small particles surrounding a larger one, had to be introduced as an additional weighing factor. This way, the contribution of small particles to the overall sintering rate was weighed higher. For green compacts of mono-dispersed spheres, the number of necks per particle was later found to vary between three and eight (six is expected for cubic packing) [107, 114]. In more recent studies on glass powder sintering of smaller PSD [96, 111], however, this correction was not required.

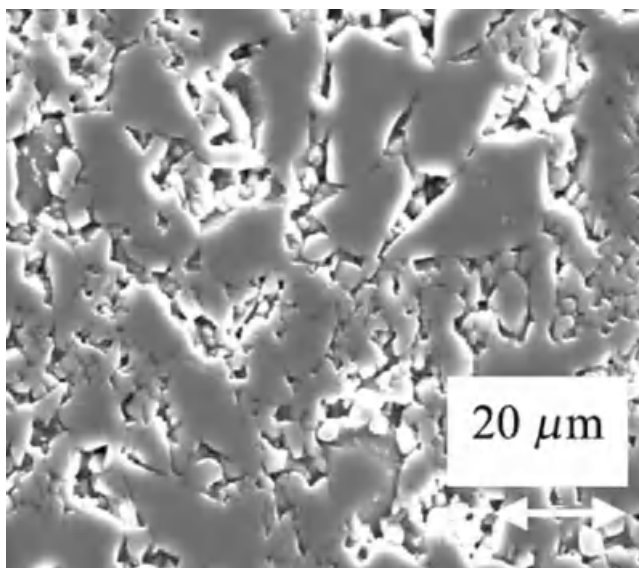


**Figure 3.21.** Scanning electron microscopy (SEM) micrograph of a compact of polydispersed alumo-borosilicate glass powders after a linear shrinkage of 8% [95].

### 3.4.5 Anisotropic Sintering and Particle Arrangement

Ceramic fabrication routes often cause nonhomogeneous or nonisotropic microstructure and properties. Thus, ceramic *shaping* like uniaxial pressing, extrusion, tape casting, or injection molding often leads to the preferred orientation of the pore/solid interface or inhomogeneous green density distribution [116]. After shaping, even the relaxation of stress and orientation in the *organic* vehicle by its flow, flocculation, and the non-uniform loss of organic vehicles from junctions can contribute to this effect [117]. Sintering can also be constrained by *rigid inclusions*, external *loads*, or sample–substrate *adhesion*. Such constraints are often not fully avoidable or may be even utilized as in LTCC zero-shrinkage techniques [118].

When spatially extended to the sample size itself, these effects can result in non-isotropic free shrinkage and shape deformation, delamination, or crack formation. Even when small against the sample size, microstructure heterogeneities can cause local stress, which matures into defects or crack formation during sintering [119] or merely retard densification. In this sense, even particle aggregates, exceptionally large particles, and bimodal-sized powders have to be considered here.

**3.4.5.1 Continuum Theory of Sintering.** Any such constrained sintering phenomena cannot be described by a straightforward generalization of the aforementioned local sintering kinetic concepts [16]. Instead, they should be treated in terms of the continuum theory of sintering. This concept was developed by Skorohod [120], Scherer [121, 122], Bordia [123–125], Rahaman [104], and Olevski [16] and considers

heterogeneities, stress, and flow fields *large compared to* the sintering *particles*. The sintering porous matrix is thus regarded as a continuum. Its properties were defined by the elastic–viscous analogy [126] between the elastic strain,  $\Delta x/x_0$ , and the viscous strain rate,  $d/dt (\Delta x/x(t))$ , both proportional to the stress,  $\sigma_x$ . For isotropic compacts, the linear strain rate,  $\varepsilon'_i$ , ( $i = x, y, z$ ) is [127, 101]

$$\begin{aligned}\varepsilon'_x &= \varepsilon'_f + \frac{1}{E_m} [\sigma_x - \nu_m (\sigma_y + \sigma_z)], \\ \varepsilon'_y &= \varepsilon'_f + \frac{1}{E_m} [\sigma_y - \nu_m (\sigma_x + \sigma_z)],\end{aligned}\tag{3.16}$$

and

$$\varepsilon'_z = \varepsilon'_f + \frac{1}{E_m} [\sigma_z - \nu_m (\sigma_x + \sigma_y)],$$

where  $\varepsilon'_f = -\rho'/3\rho$  is the free sintering compaction strain rate,  $E_m$  is the uniaxial viscosity, that is, the viscous response of a porous material to a uniaxial stress, and  $\nu_m$  its viscous Poisson's ratio. Equation 3.16 assumes that sintering and stress-induced strain rates are linearly additive. By means of sinter-forging experiments, where, for example, the diameter strain is balanced out by an axial stress-induced radial flow, Equation 3.16 allows to conclude on the hydrostatic sintering stress,  $\Sigma = \sigma_i$ :

$$\varepsilon'_f = \frac{\Sigma}{E_m/(1-2\nu_m)},\tag{3.17}$$

where  $\Sigma$  is the hydrostatic sintering stress and  $K_m = E_m/(3[1-2\nu_m])$  is the apparent bulk viscosity, that is, the viscous response of the matrix to hydrostatic stress. Alternatively, the apparent shear viscosity of the matrix,  $G_m = E_m/(2[1+\nu_m])$  can be used in calculations. While local sintering kinetic concepts predict shrinkage from initial powder properties like  $\gamma$ ,  $\eta$ ,  $R_0$  and  $\rho_0$ , prediction of  $\varepsilon'_i$  from  $\sigma_i$  requires explicit knowledge of  $\Sigma$ ,  $E_m$ , and  $\nu_m$ .

All quantities, however, change with  $\rho$  during sintering.  $\Sigma(\rho)$  was estimated for cubic packaging of uniform particles by Ducamp and Raj[128]:

$$\Sigma = \frac{2\gamma}{R_0} \left( \frac{\rho}{1-\rho} \right)^{\frac{1}{3}}.\tag{3.18}$$

For the most cases of practical relevance, however,  $\Sigma(\rho)$  has to be measured. This can be realized by sinter-forging techniques [104, 128–135].  $\Sigma(\rho) \approx 100\text{--}500$  kPa was measured for commercial mixed alkaline earth alumo-borosilicate glass powder compacts ( $2R_0 \approx 3 \mu\text{m}$ ) [128],  $\Sigma(\rho) \approx 20\text{--}100$  kPa for borosilicate glass powder compacts ( $2R_0 \approx 8 \mu\text{m}$ ) [131], and  $\Sigma(\rho) \approx 100\text{--}500$  kPa for an anorthite glass/alumina LTCC GMC (Ceramtape GC) [133].

The change of  $E_m$  and  $v_m$  with  $\rho$  was estimated by Scherer [121] according to

$$E_m \approx 3\eta \left( \frac{\rho}{3-2\rho} \right) \quad (3.19)$$

and

$$v_m \approx \frac{1}{2} \left( \frac{\rho}{3-2\rho} \right)^{\frac{1}{2}}, \quad (3.20)$$

with  $v_m = 1/2$  at  $\rho = 1$ .  $E_m(\rho)$  and  $v_m(\rho)$  have been measured with different methods like continuous [132, 136–139] and discontinuous sinter forging [140, 141], cyclic loading dilatometry [142, 143], and constrained sintering [144–146].

**3.4.5.2 Bimodal PSD and Aggregates.** Particles with bimodal size distribution are often obtained in case of powder mixtures. As one of the most basic related effects, the *packing densities* of these powders depend on the size and volume fractions  $v_s$  and  $v_L$  of small and large particles, respectively. While  $\rho_0 \approx 60\%$  is typical for loosely packed monosized non-submicron particles, a maximum packing density can be expected at some ratio of  $v_s/v_L$ . Such effects have been comprehensively reviewed by German [18]. Experimental data are given, for example, by Smith and Messing for bimodal distributed alumina powders [147].

Related effects on sintering are more complex. Thus, aggregation and crack formation caused by faster sintering of small particles can occur as schematically illustrated in Figure 3.22.

Vice versa, large particles, forming a slow sintering, “rigid” skeleton, can constrain sintering of interstitial small particles and cause residual porosity. Large pores formed between particle aggregates during sintering can strongly retard final densification and may cause sintering shoulders as seen in Figures 3.17 and 3.23.

The effect of broad PSD on sintering has been studied extensively. Solomin and Tomilov [148] could correct the effect of a broad pore size distribution in terms of Equations 3.10–12 and 3.15. Evans [119] showed that stresses due to inhomogeneous sintering are of the order of the effective sintering stress within the zones susceptible to rapid, unconstrained sintering. Raj and Bordia [149] found that the maximum tensile stress generated by incompatible sintering is sensitive to the ratio of creep and densification rate.

In terms of the continuous sintering theory and his cell model (see Subsection 3.4.2) Scherer studied the effects of a broad distribution of pore sizes [150] and bimodal pore size distributions [94]. The effect of pore size distribution was found to be small except for a very large size distribution. The related deviation in shrinkage behavior is restricted to the last few percents of shrinkage since the largest pores close slowly. In contrast, substantial effects were shown for bimodal powders [94]. As an example, Figure 3.23 illustrates the effect of varying the volume ratio of small and large particles of a bimodal size distribution on densification.



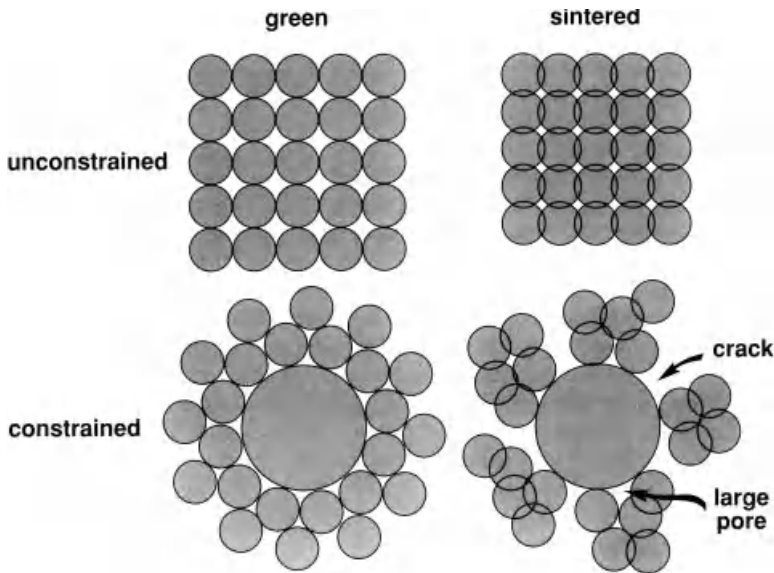


**Figure 3.22.** Local stress and formation of aggregates during sintering of bimodal powders (schematic) [18].

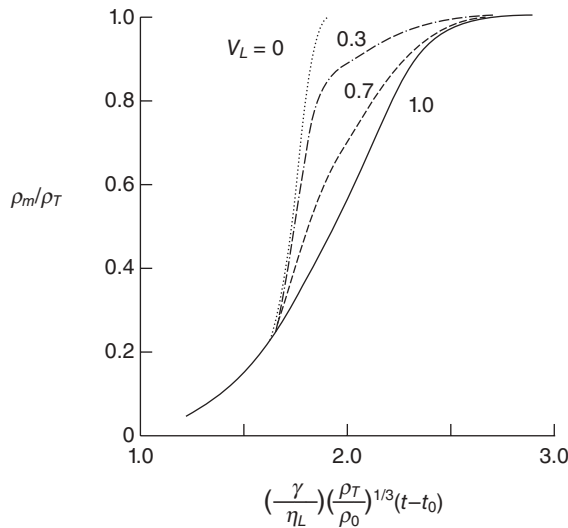


**Figure 3.23.** Relative density of a sintering matrix,  $\rho_m/\rho_T$ , versus reduced time for a mixture of unit cells of Scherer's cylinder model (pore diameters of 0.05 and 20  $\mu\text{m}$ ). The curve parameter  $V_L$  is the initial volume fraction of the large cells,  $L$  the length of large unit cells.  $\rho_0$ ,  $\rho_m$ , and  $\rho_T$  are the initial, the matrix, and the theoretical density, respectively [94].

**3.4.5.3 Nonisotropic Particle Arrangement.** Free sintering anisotropy has been frequently reported for glass powder sintering, for example, by Rahaman [104, 131], Exner and Giess [151], Giess et al. [152], and Boccaccini et al. [116, 153–157] and should occur in most cases of practical relevance although perhaps sometimes ignored in the common practice of dilatometry [116].

To study such phenomena, heating microscopy [158] and other methods of optical dilatometry [159, 160] have been used. These methods can quantify shrinkage anisotropy of cylinder-shaped compacts according to Exner and Giess [151]:

$$\frac{\Delta V}{V_0} = \left(1 - \frac{\Delta H}{H_0}\right) \left(1 - \frac{\Delta D}{D_0}\right)^2, \quad (3.21)$$

where  $H$  and  $D$  denote height and diameter, respectively. The shrinkage anisotropy factor is defined as the axial-to-radial relative shrinkage ratio [151]:

$$k_A = \frac{\Delta H/H_0}{\Delta D/D_0}. \quad (3.22)$$

Applying this technique, it was revealed that even usual horizontal dilatometric stresses (<5 kPa) should not be neglected [116].

Pronounced anisotropy for early sintering of uniaxially pressed cordierite glass powders was reported in Reference 151. As shown in Figure 3.24,  $k_A$  increased from  $\approx 0.4$  to 0.7 during sintering. This behavior could be attributed to a similar pore orientation factor, measured by the ratio of mean linear intercept in the axial and radial direction and the progressive rounding of initially elongated pores. A minor effect of particle size and shape, however, was found here. Thus, a highly oriented pore/solid interface should have been caused even by the uniaxial pressing of spherical particles. The dominating effect of shaping on shrinkage anisotropy was also demonstrated by Boccaccini and Conradt [156], who found isotropic shrinkage ( $k_A \approx 1$ ) for platelet containing glass powders after isostatic compaction.

Nonetheless, elongated particles are more susceptible to orientation during shaping, at least when embedded in organic aids and forced to flow. Thus, strong shrinkage anisotropy up to 14% was found for tape-casted alumina by Raj et al. [161]. A marked effect of particle size on the degree of orientation after LTCC tape casting and firing was also reported by Besendörfer and Roosen [162] (see Fig. 3.25). Thus, shrinkage in casting direction was always found smaller than in traverse direction, and the use of powders with  $D_{50} \approx 3 \mu\text{m}$  instead of  $1.8 \mu\text{m}$  increased the respective shrinkage difference from 1% to 1.85% (3.6–7.6% for laminates). Shrinkage anisotropy was also increased by increasing the amount of organic binders and decreasing that of solvents.

Several previous, sometimes apparently controversial, findings might be explained by the complex interplay between particle shape and size as well as the glass particle, rigid filler, and organic vehicle volume fractions as indicated above. Thus, in contrast to Exner and Giess [151], even  $k_A > 1$  (more pronounced axial strain) was reported by Rahaman et al. [104] virtually not depending on  $\rho$  for uniaxially pressed spherical

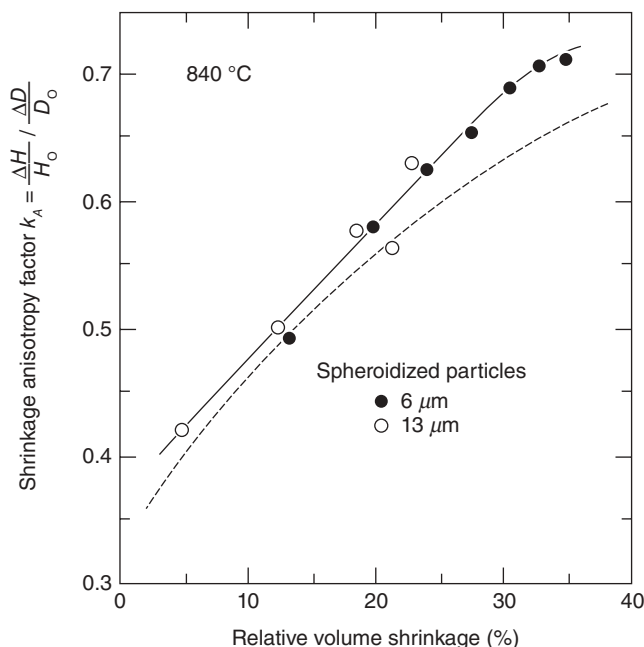


**Figure 3.24.** Shrinkage anisotropy factor,  $k_A = (\Delta H/H_0)/(\Delta D/D_0)$ , for two fractions of spheroidized glass powder (compacted uniaxially at 75 MPa). The dashed curve is for jagged powder.  $k_A = 1$  denotes isotropic shrinkage [151].

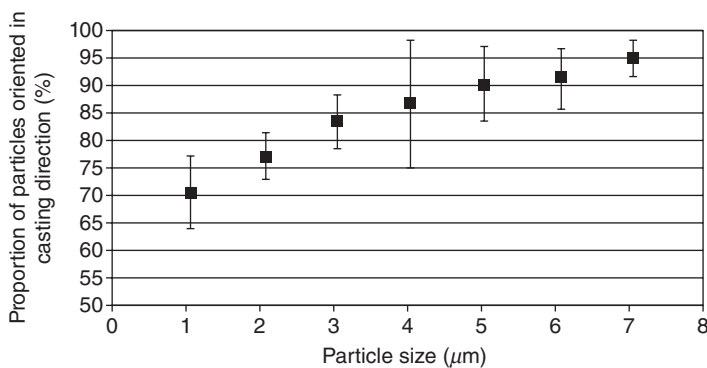


**Figure 3.25.** Degree of particle orientation dependent on the particle size of low-temperature cofired ceramic tapes from a powder with  $D_{50} \approx 1.8 \mu\text{m}$  [162].

borosilicate glass powders. A constant  $k_A \approx 0.7$  was also found by Boccaccini for uniaxially pressed nonspherical borosilicate [157] and alumo-silicate glass powders [153]. More complex effects of  $\rho$  and the alumina volume fraction on  $k_A$  was reported by Eberstein et al. [163] for uniaxially pressed barium-alumo-borosilicate/alumina GMC.

### 3.5 VISCOUS SINTER RETARDATION

Free viscous sintering of glass powders can be retarded by concurrent crystallization or the presence of rigid inclusions. Several phenomena, like (a) a reduction of the noncrystallized fraction of the powder surface, the increased effective viscosity of (b) partially crystallized and (c) inclusion bearing melts, or (d) the presence of large rigid inclusions, may govern or partially influence the retardation of viscous sintering (see Fig. 3.26). In case of finely grained powders, sinter crystallization phenomena can even occur for glasses of low crystallization tendency.

#### 3.5.1 Sintering with Concurrent Surface Crystallization

Pronounced impeding of viscous sintering can be expected for strong surface crystallization tendency as, for example, reported by Watanabe and Giess [164] and Rudolph et al. [165] for cordierite glass powders. In this case, illustrated in Figures 3.26a and 3.27, sintering stops when surface crystals impinge each other forming a compact surface layer.

Sinterability of such glass powders therefore strongly depends on the surface nucleation density,  $N$ , which is sensitive to glass powder milling as shown in Subsection 3.2.3. Thus, glass powder milling can strongly affect the attainable shrinkage as illustrated in Figure 3.28.

Although such a strong impeding effect of surface crystallization might be exceptional for most cases of practical relevance, it easily illustrates the potential effects of glass powder processing on sinterability. The related kinetics of sintering retardation could be approximated assuming that the sintering rate  $s'$  is proportional to the non-crystallized fraction of the glass powder surface,  $[1 - x_s]$  [88, 166]:

$$s' = s'_0 [1 - x_s], \quad (3.23)$$

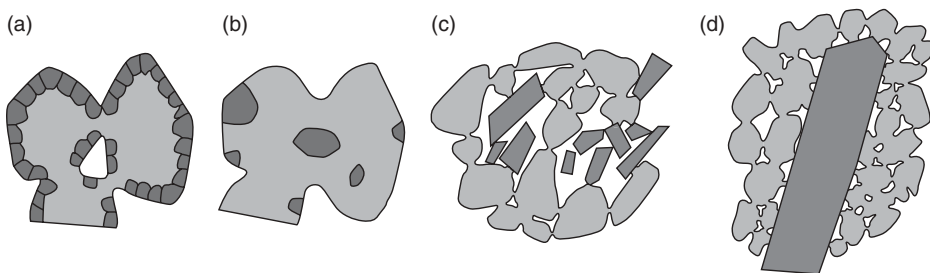


**Figure 3.26.** Viscous sinter retardation phenomena (schematic). (a) Reduced area fraction of a glassy powder surface caused by surface crystallization. (b) Increased effective viscosity of crystal-bearing melts. (c) Increase of effective viscosity by small rigid inclusions. (d) Large rigid inclusions.

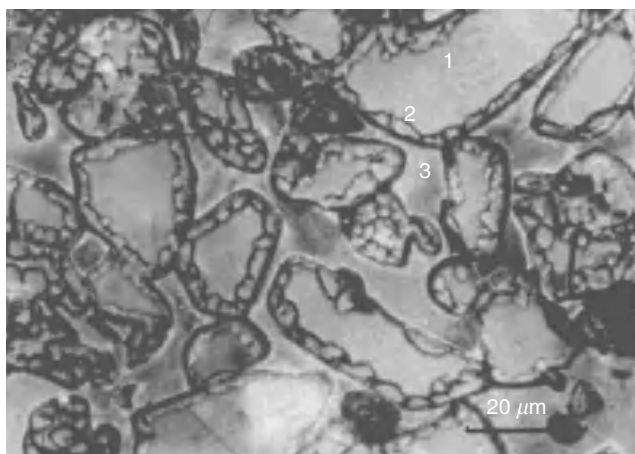


**Figure 3.27.** Sintering of a cordierite glass powder ( $40\text{--}63\text{ }\mu\text{m}$ ) compact stopped by surface crystallization. The sample was heated at  $10\text{ K/min}$  to  $980^\circ\text{C}$  and quenched in air. Incident light micrograph, polished cross section. 1, glass; 2, surface crystals; 3, resin. Vibratory ball milling, agate [166].

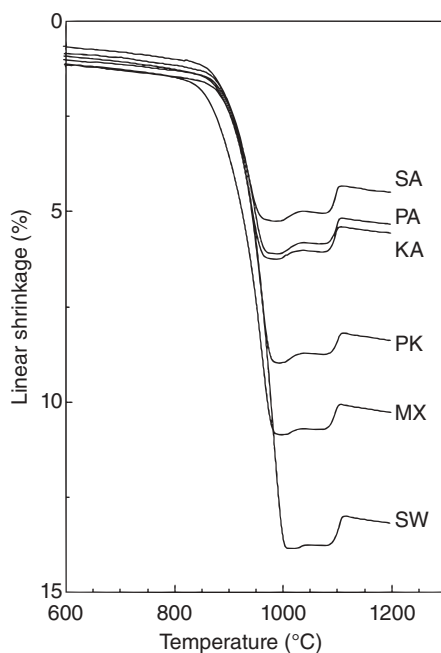


**Figure 3.28.** Effect of milling on sintering of cordierite glass powder compacts ( $63\text{--}125\text{ }\mu\text{m}$ ) during heating at  $10\text{ K/min}$ . See Table 3.1 for curve parameters [167].

TABLE 3.1. Milling and Surface Nucleation Density,  $N$ , of Cordierite Glass Powders Shown in Figure 3.28

Curve	$N$ ( $1/\mu\text{m}^2$ )	$2\ell$ ( $\mu\text{m}$ )	Milling	Milling Material
SA	0.1	3	Vibratory disk	Agate ( $\text{SiO}_2$ )
PA	0.09	3	Planetary ball	Agate ( $\text{SiO}_2$ )
KA	0.1	3	Vibration ball	Agate ( $\text{SiO}_2$ )
PK	0.0018	23	Planetary ball	Corundum
MX	0.006	13	Mortar	Steel
SW	0.0025	20	Vibratory disk	Tungsten carbide

$N$  was measured by optical microscopy for glass particles of  $D \approx 20 \mu\text{m}$ .

$2\ell$ , next neighbor distance of surface nuclei [167].

where  $x_s(t)$  is the crystallized surface fraction and  $s'_0$  is the nonretarded sintering rate.  $[1 - x_s]$  can be deduced from simple statistic considerations for instantaneous crystal growth from a constant number density of nucleation sites and nonregular distributed surface nuclei according to [166]

$$[1 - x_s] = \exp\left(-\frac{r(t)^2}{\ell^2}\right), \quad (3.24)$$

where  $r(t)$  is the size of uniform crystals according to Equation 3.9 and  $2\ell$  is their mean next neighbor distance according to Equation 3.3. Note that  $[1 - x_s]$  entirely depends on crystal growth and surface nucleation density and that the time of crystal impingement at  $r(t) \approx \ell$  does not depend on particle size. Therefore, finer glass powders, which shrink more rapidly, can attain better or even full densification prior to crystal impingement. In this sense, improved densification can also result from reduced surface nucleation densities.

$[1 - x_s]$  in Equation 3.23 was later substituted by  $[1 - x_s]^2$  [114], thus only excluding sintering of crystal-crystal contacts. More recent studies on sintering diopside glass spheres by Reis et al. [168] show that, if surface crystals grow slowly during sintering,  $x_s$  can be locally increased at the sintering necks. This effect, shown in Figure 3.29, was found to retard sintering more pronouncedly as expected by Equation 3.23 [168], in which a uniform surface nucleation density is assumed.

Combining Equations 3.10–3.12, 3.15, and 3.23 and more generalized equations for  $[1 - x_s]$  instead of Equation 3.24, Prado, Zanotto, and colleagues developed a cluster model for the sintering of glass powders with concurrent crystallization [106, 107, 113–115]. Attention was focused on mono- and polydispersed crystallizing glass powders [112, 113], the effect of particle shape and size [106, 115], and isothermal and nonisothermal sintering [106, 112]. The experimental studies hereby comprised cordierite, soda lime, and alumo-borosilicate glasses. This model was also applied to crystallizing borosilicate glasses by Pascual and Duran [96].



**Figure 3.29.** SEM micrograph of diopside surface crystals grown during sintering at 810°C for 120 min from diopside glass microspheres spherodized in gas flame [168].

Based on this cluster model and considering certain ratios between the characteristic times and half width of the sintering and crystallization curves, Prado et al. [97] derived a sinterability factor  $S$  according to

$$S = \frac{\gamma}{\sqrt{NU\eta R_0}}. \quad (3.25)$$

Due to the model calculations,  $S > 10$  should allow full densification, whereas experimental observation suggests that  $S > 50$  is required. Figure 3.30 shows that  $S$  increases with temperature; that is, high temperatures prefer sintering against crystallization. Since  $\gamma$  has a weak dependence on temperature and  $N$  can often be regarded as constant (see Section 3.2), this effect reflects the difference in temperature dependence between viscosity,  $\eta$ , and the crystal growth rate,  $U$ . This difference is thus correlated to the atomic mechanism and the thermodynamic driving force of crystallization, which vanishes at the melting point [169, 170].

In fact, many authors reported that better densification of crystallizing glass powders was reached for high heating rates [115, 171–176] (see Fig. 3.31).

### 3.5.2 Simultaneous Sintering and Crystallization

The situation depicted in Figure 3.26b indicates low surface nucleation density ( $2\ell \gg R_0$ ) and slow crystal growth during sintering. This way, detectable sintering and

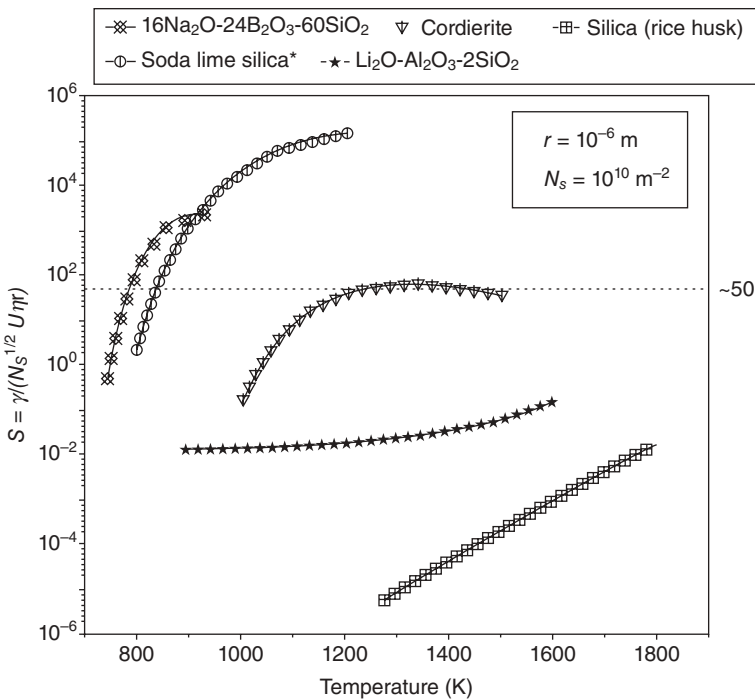


**Figure 3.30.** Calculated sinterability parameters  $S$  versus temperature using experimental crystal growth rate data and viscosity of different glasses. Surface nucleation density and average particle radius are denoted by  $N_s$  and  $r$  instead of  $N$  and  $R_0$  as used elsewhere in this chapter [97].

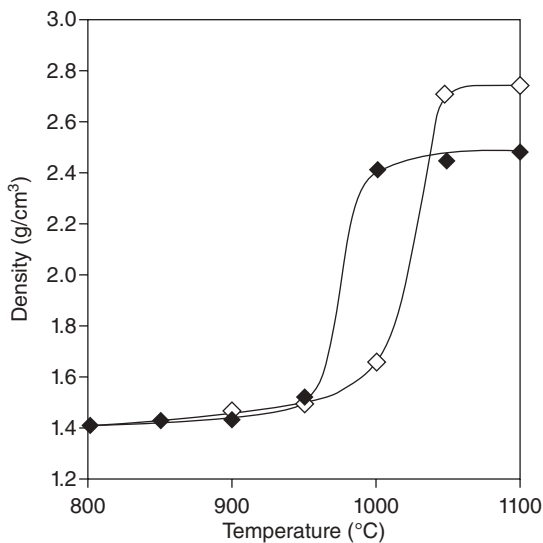


**Figure 3.31.** Relative density versus sintering temperature for barium magnesium aluminosilicate glass powder compacts sintered at two different heating rates: (◆) 1 K/min and (◇) 15 K/min [175].



crystallization can occur simultaneously. This situation can be expected for fine powders if their surface crystallization tendency was reduced by careful milling (see Section 3.2.3) or chemical etching [171, 177]. Slow crystal growth can be anticipated for multicomponent glasses as observed for many stable commercial glasses as, for example, mixed alkaline earth–alumo-silicate glasses [171]. Thus, case (b) might have more practical relevance than case (a) in Figure 3.26.

(i) Contrasting case (a), case (b) results in similar *surface and volume fractions* of the crystal phase  $x_s$  and  $x$ , respectively. In this case,  $s'$  can be linked to overall crystallization data and

$$s' = s'_0 [1 - x] \quad (3.26)$$

can be adopted. This concept was followed by Gutzow et al. [74], who derived for the initial stage of isothermal sintering equations of the form

$$s' = s'_0 \left[ \exp \left( -\frac{t}{\tau} \right) \right], \quad (3.27)$$

where the initial sintering rate  $s'_0$  corresponds to Frenkel's model and  $\tau(R_0, \ell)$  was introduced as a characteristic impingement time for the isotropic growth of surface crystals toward the interior of glass spheres.

(ii) As a second particularity, the situation of case (b) suggests that modeling of sintering kinetics has additionally to consider the *effective shear viscosity* of the crystal-bearing melt as proposed by Dutton et al. [178] (for sintering of GMC), Gutzow et al. [74], and Karamanov and Pelino [179]. Thus, Karamanov and Pelino [179] calculated  $s'_0$  for the initial stage of isothermal sintering according to Equation 3.10, replacing  $\eta$  by the effective shear viscosity of the crystal-bearing melt,  $\eta_c = \eta \cdot (1 + bx^n)$ :

$$s' = \frac{3\gamma}{8R_0\eta(1+bx^n)} [1 - x_s], \quad (3.28)$$

where  $b$  and  $n$  are adjustable parameters. Instead of Equation 3.26 as suggested in Reference 74, however, Equation 3.23 was used describing the impeding effect of crystallization. Because of its utmost importance for the sintering of GMCs, many authors have studied the effective shear viscosity,  $\eta_c$ , of crystal-bearing silicate melts. Thus, Sältzer and Schulz [180] and Boccaccini et al. [181, 182] derived

$$\frac{\eta_c}{\eta} = (1 - \Phi)^m \quad (3.29)$$

from basic considerations, where  $\Phi$  is the volume fraction of the rigid, that is, nondeformable, inclusions ( $\Phi \equiv x$  in Eq. 3.28). The parameter  $m$  was modeled for spheroid inclusions as

$$m = \frac{3F - 2}{3F(1 - 2F)}, \quad (3.30)$$

where  $F$  is a shape factor ranging between 0 and 0.5 for particle shapes ranging between platelets and fibers, respectively [181], which yields  $m < 0$ . Equation 3.30 holds for  $\Phi$  well below the percolation limit, that is, for melts containing isolated and well-distributed inclusions. This percolation threshold is intuitively seen from rheological models including a maximum volume fraction of rigid inclusions,  $\Phi_{\max}$ , at which  $\eta_c$  goes to infinity. Among them, the Einstein–Roscoe equation [183],

$$\frac{\eta_c}{\eta} = \left( 1 - \frac{\Phi}{\Phi_{\max}} \right)^m, \quad (3.31)$$

taking  $m < 0$  as an adjustable parameter, is widely used. The non-Newtonian flow behavior of crystal-bearing melts has been thoroughly studied by Brückner and Deubener [184, 185]. Comprehensive reviews of rheological models are given by Honek et al. [186] and Tadros [187] (see also, e.g., References 188 and 189).

### 3.5.3 Sintering with Small Rigid Inclusions

Many applications like enamels, seals or solders, ceramic inks, or LTCC utilize dispersed rigid inclusions for achieving the desired color, thermal expansion, high-temperature viscosity or dielectric properties. For the sake of good homogeneity and sinterability, glass particles and rigid inclusions of similar small particle sizes are often intended. This situation is depicted in Figure 3.26c.

**3.5.3.1 Steric Effects.** Steric effects of small rigid inclusions on the kinetics of sintering have been recently studied for barium-alumo-borosilicate glass/alumina composites (BABS/A), where glass and alumina particles are similar in size and dissolution and crystallization during sintering could be neglected [111, 163, 190].

As shown in Figure 3.32, such small rigid particles have a minor effect on sintering for small crystal volume fractions,  $\Phi$ , as also reported by Boccaccini [191] and Dutton and Rahaman [136] for  $\Phi < 0.15$ . With an increasing  $\Phi$ , however, (1) the sintering rate markedly decreases, which increases the final densification temperature, and (2) the maximum shrinkage is reduced. This latter reduction was found to increase proportional to  $\Phi^3$  and could be attributed to remaining pores formed in the center of three alumina particle agglomerates, which were not fully penetrated by the melt [111]. For ideal mixing, the probability of such triparticle clusters is  $\approx \Phi^3$ .

Following a similar approach in Reference 192, this sintering behavior could be described assuming that sintering is linearly superimposed of the weighed shrinkage

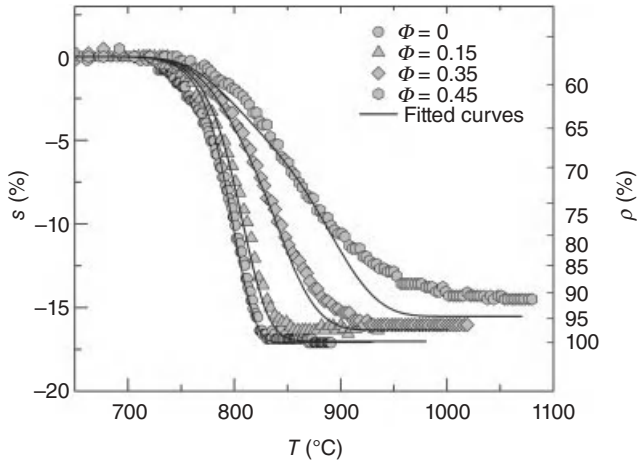


**Figure 3.32.** Linear shrinkage,  $s$ , of BABS/A composite compacts during heating at 5 K/min versus temperature. Points: experimental data for different alumina volume fractions,  $\Phi$ . Curves: fitted according to Equations 3.10–3.12, 3.15, 3.31, and 3.32–3.34 with  $\gamma = 240$  mN/m,  $\log(\eta/\text{Pa}\cdot\text{s}) = 4.27 + 7484^\circ\text{C}/(T - 202^\circ\text{C})$ ,  $k_f = 1.2$ ,  $\Phi_m = 0.6$ ,  $m = -4.5$ ,  $\lambda_{15} = 1.3$ ,  $\lambda_{35} = 2$ , and  $\lambda_{45} = 2.5$  [111].

contributions of triparticle clusters composed of glass (g) or alumina (c) particles (ggg, gcg, ccg, and ccc) neglecting any stress phenomena due to different sintering [111]:

$$s = \sum_{i,j} \Psi_j \cdot P_i \cdot s_{ij}. \quad (3.32)$$

Here,  $\Psi_j(R_{0j})$  is the relative frequency of particle size and  $P_i(\Phi)$  is the occurrence probability of the different triparticle clusters ( $i = 1-4$  refers to ggg–ccc).  $s_{ij}$  is the sintering contribution of the different triparticle clusters formed by particles of the radius  $R_{0j}$ .  $s_{ij}$  was calculated according to Equations 3.10–3.12 with additional assumptions. Thus, the shrinkage rate,  $s'_{ij}$ , was weighed by the glass fraction of cluster  $i$ . As a rule of mixture, this correction term slows the sintering of mixed glass–crystal clusters and makes sure that alumina clusters (ccc) do not shrink. Furthermore, the glass viscosity,  $\eta$ , was replaced by the composite *effective shear viscosity*,  $\eta_c$ . The latter property was obtained from densified compacts. The thus obtained experimental results,  $\eta_c^\infty(\Phi)$ , could be well fitted according to Equation 3.31. Sufficient fitting of experimental shrinkage data was only achieved, however, assuming that  $\eta_c$  steadily increases with progressive wetting during sintering from  $\eta$  to  $\eta_c^\infty$  according to

$$\frac{\eta_c(\rho)}{\eta} = 1 + f(\rho) \cdot \left[ \frac{\eta_c^\infty}{\eta} - 1 \right], \quad (3.33)$$

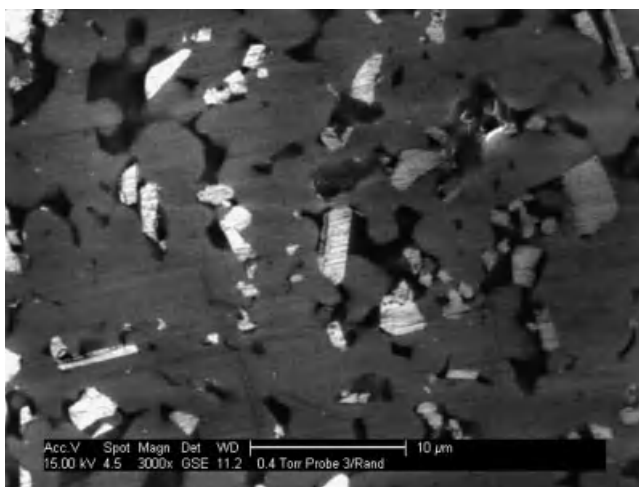


**Figure 3.33.** Partially wetted small rigid inclusions (alumina particles, bright) in a barium-alumo-borosilicate/15 vol % alumina GMC. Cross-sectional micrograph of a powder compact partially sintered during heating at 5 K/min to 825°C [111].

where  $f(\rho)$  is the wetted surface fraction of alumina particles. Since  $f(\rho)$  increases from 0 ( $\rho = \rho_0$ ) to 1 ( $\rho = 1$ ), Equation 3.33 makes sure that  $\eta_c(\rho)$  shifts from  $\eta$  to  $\eta_c^\infty$ .  $f(\rho)$  was measured from cross-sectional micrographs as seen in Figure 3.33 and could be approximated with Equation 3.34 [111], where  $\lambda$  is an adjustable parameter:

$$f(\rho) = \left( \frac{\rho - \rho_0}{1 - \rho_0} \right)^\lambda. \quad (3.34)$$

As illustrated in Figure 3.32, this sintering model is applicable up to  $\Phi \approx 35$  vol %. Note that calculations are entirely based on easy accessible parameters like particle size, surface tension, glass viscosity, and wetted surface area fraction and that only one adjustable parameter,  $k_f$  in Equation 3.10, is used for all curves.

It should be emphasized that the *wetting* behavior and the *shape* of rigid inclusions are of crucial importance. Thus, the wetting behavior, represented by  $\lambda$  above, strongly affects  $\eta_c$  via Equations 3.33 and 3.34, thus dominating sinter retardation. On the other hand, the wetting behavior and shape of rigid inclusions decide which shape of rigid inclusion cluster cavities cannot be penetrated by the melt within the timescale of viscous sintering. The latter effect directly affects attainable shrinkage. For other shape and wetting behaviors of rigid inclusions, other dependencies of reduced shrinkage on  $\Phi$  (e.g., proportional to  $\Phi^{n=2}$  or  $\Phi^{n=4}$ ) might occur. The parameter  $n$  should therefore be measured for each system and cluster modeling should be adapted.

Confirming observations were made by Pascual et al. [193] for  $\text{ZrO}_2$  fiber-reinforced sodium-borosilicate glass powder compacts. Here, bad wetting of the fibers were observed and porosity was mainly associated with the fibers. In this sense, only glass–

glass contacts were taken into account to contribute to sintering in the sinter kinetic modeling of this system [192]. Due to the rule of mixture, this restriction would cause a reduction of the linear shrinkage of  $\approx \Phi^1$ . A similar finding was reported by Boccaccini and Conradt [156] for platelet containing soda lime glass powders, where shrinkage was reduced by  $\approx 10\%$  for  $\Phi \approx 10\%$ .

The latter authors [156], however, attributed this effect to the percolation threshold of rigid inclusions. This threshold was found to be sensitive not only to  $\Phi$  but also to the shape of inclusion and even to their agglomeration and may explain the often reported existence of a critical value beyond which further densification is impeded [156].

**3.5.3.2 Dissolution Phenomena.** With decreasing particle size and increasing volume fraction of rigid inclusions, chemical interactions like dissolution phenomena can progressively affect the glass matrix and strongly influence sintering and crystallization as schematically illustrated in Figure 3.34.

(i) As a first effect, partial dissolution of, for example, alumina particles (C0) will enrich the glass composition with  $\text{Al}_2\text{O}_3$  ( $G0 \rightarrow G1$ ). This effect can increase *glass viscosity* as known for peralkaline alumo-silicate glasses [10] and can thereby retard sintering. On the other hand, this effect can be utilized to avoid phase separation, undesired crystallization, or bloating. In order to affect a sufficient volume fraction of the composite, however, the thickness of the Al diffusion layer should cover a large

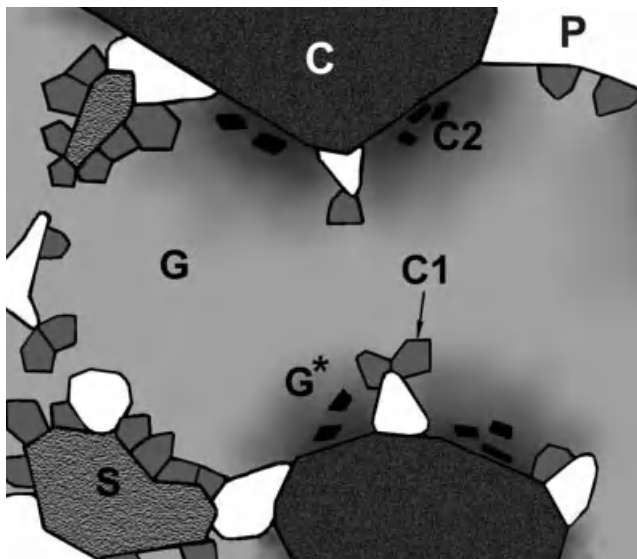


**Figure 3.34.** Effects of dissolution phenomena on sintering and crystallization of GMC containing small rigid inclusions (schematic). C, rigid inclusion; C1, primary crystals; C2, secondary crystals; S, crystal nucleation seeds (if necessary); G, parent glass; G\*, residual glass; P, pore [2].

part of the mean distance between neighbored alumina particles. Thus, Fang and Jean [194] found significant sinter retardation in  $K_2O$ - $CaO$ - $SrO$ - $BaO$ - $B_2O_3$ - $SiO_2$  glass/alumina GMC for LTCC, only for very small alumina particles ( $0.05 \mu m$ ,  $\Phi = 20 \text{ vol } \%$ ). Minor effects of dissolution phenomena on sintering were also observed for a calcium-alumo-borosilicate glass/alumina (CABS/A) LTCC composite ( $D_{50} \approx 2 \mu m$ ,  $\Phi = 25 \text{ vol } \%$ ) [195].

(ii) On the other hand, even minor dissolution from rigid inclusion can prevent their *crystal nucleating effect* with respect to the primary crystal phase (C1) as it is known for chemically inert nucleation substrates [42, 63–65]. Thus, no seeding effect of alumina on the primary wollastonite crystallization in the above-mentioned CABS/A composites could be observed [195].

(iii) At higher temperatures, better glass/alumina wetting [196] and increased Al diffusivity [197–199] is evident. The more pronounced compositional shift of the glass matrix caused by progressive alumina dissolution may even fully prevent nondesired glass crystallization as shown by Imanaka et al. [197]. Pronounced alumina dissolution at elevated temperatures can also promote new desired secondary crystal precipitations (C2). Such effect, illustrated in Figure 3.35, was, for example, found for the aforementioned CABS/A composites, where up to 60 wt % anorthite ( $CAS_2$ ) could precipitate at the expense of alumina and wollastonite (CS) after full densification [195].

### 3.5.4 Sintering with Large Rigid Inclusions

The term large rigid inclusion might be used, for example, for platelets and fibers much larger than the sintering glass particles. Since large inclusions are fixed within the porous matrix by numerous wetting contacts even at early stages of sintering, large-scale stress fields and constrained sintering phenomena might occur, which have to be treated in terms of the continuum theory of sintering (Eqs. 3.16–3.20).

(i) The effect of inclusion-induced *stress* on sintering of GMC was analyzed by Scherer [127] within that concept. In terms of his composite sphere (cs) model, where large spherical inclusions are embedded within a matrix shell of small sintering particles, Scherer derived for the linear sintering strain rate of the composite,  $\epsilon'_c$ :

$$\epsilon'_c = \left[ 1 + v_i (\text{as Index}) \left( \frac{4G_m}{3K_m} \right) \right]^{-1} \cdot (1 - v_i) \cdot \epsilon'_{fm}, \quad (3.35)$$

where  $\epsilon'_{fm}$  is the linear sintering strain rate of the free matrix. Two terms contribute to shrinkage retardation.  $(1 - v_i)$  represents the rule of mixtures, where  $v_i$  is the current volume fraction of inclusions in the porous matrix according to

$$v_i = \rho \left[ \rho + \frac{1 - \Phi}{\Phi} \right]^{-1}. \quad (3.36)$$

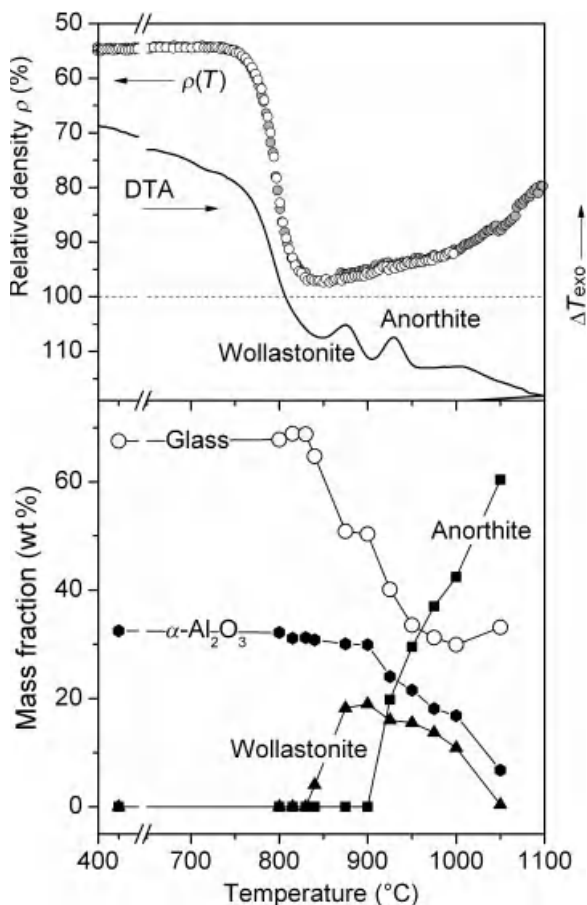


**Figure 3.35.** Sintering, crystallization, and phase evolution (X-ray diffraction (XRD) Rietveld data) during heating at 5 K/min versus temperature for a calcium-alumo-borosilicate glass/alumina composite with  $\Phi = 25$  vol % [195].

The effect of hydrostatic pressure on sintering is represented by the term in brackets, which depends on the ratio of shear viscosity,  $G_m$ , to bulk viscosity,  $K_m$ . This ratio simply results from the viscous Poisson's ratio,  $\nu_m$ , (see Subsection 3.4.5.1) as

$$\left( \frac{4G_m}{3K_m} \right) = \frac{2(1-2\nu_m)}{(1+\nu_m)}. \quad (3.37)$$

In Scherer's self-consistent model (s-c),  $G_m$  is replaced by  $G_c$  in Equation 3.35, the shear viscosity of the composite.  $G_c/G_m$  can be approximated according to Hashin and Shtrikman [200] with

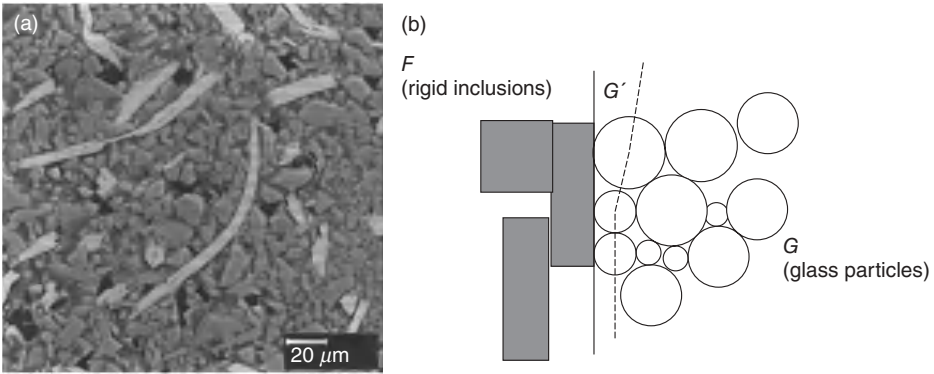


**Figure 3.36.** (a) Scanning electron micrograph of a sodium-borosilicate glass/YSZ fiber GMC with large rigid inclusion. (b) Three different volumes considered for kinetic modeling of sintering.  $G$  contains only glass–glass contacts;  $G'$  includes rigid inclusion–glass contacts;  $F$  contains fiber–fiber contacts [192].

$$\left( \frac{G_c}{G_m} \right) = \left[ 1 + \frac{15}{2} \left( \frac{v_i}{1-v_i} \right) \left( \frac{1-v_m}{4-5v_m} \right) \right]. \quad (3.38)$$

Both models, however, predict small shrinkage retardation factors  $\epsilon'_c/\epsilon'_{fm} > 0.7$  even for  $\Phi = 40$  vol %. Scherer concluded that the strong decrease in densification rates often caused by large rigid inclusions cannot be attributed to hydrostatic stresses [127].

(ii) Dutton and Rahaman [136] could show, however, that this strong retardation can be explained when measured *effective viscosity* data are used instead of  $G_C$  in calculation. This concept was adopted by Pascual et al. [192] for the kinetic modeling of the sintering of devitrifying glass/yttria-stabilized zirconia (YSZ) fiber GMC (Fig. 3.36, a). Their extended cluster model is based on Equations 3.10–3.12, 3.15, 3.23, and 3.35–3.37. Equation 3.24 was generalized to include an increasing number density of surface crystals during sintering. Sinter retardation was modeled by the use of the effective shear viscosity,  $\eta_c = \eta \cdot \exp(-2.5\Phi/[1 - a\Phi])$  in Equation 3.11. Further, a retardation stress factor  $H = (1 + \Phi 4G_C/3K_m)^{-1}$  was introduced into Equation 3.10 with  $G_C/K_m = \eta_c/\eta$ . Good fitting of the experiment was achieved for  $a = 2$  and by considering  $\eta$  as an adjustable parameter for each sintering temperature.

(iii) Further, the already mentioned *bad wettability* of these fibers ([193]; see Subsection 3.5.3.1) was accounted here in cluster modeling assuming that shrinkage occurs only within the glass volume fraction  $G$  (see Fig. 3.36, b). This way, the large sinter retardation of 8–18% for different glass PSDs caused by the small fiber volume fractions of 9% could be explained by bad wetting. Bad wetting could also



explain the reduction of attainable shrinkage in case of small rigid inclusions since it controls the penetration of inclusion particle aggregates by the melt and thus residual porosity.

### 3.6 APPLICATIONS AND PROCESSES

The following section is intended to illustrate a variety of applications and technologies where the basic phenomena discussed above are of potential importance. Therefore, only few, highly selective examples from different application fields are mentioned.

#### 3.6.1 GMC for Structural Applications

In order to overcome disadvantageous mechanical properties of glass and glass-ceramic materials, numerous attempts have been made to reinforce glass or glass-ceramic matrices with a second constituent of higher modulus, higher strength, and/or higher ductility [201–206]. This concept comprises dispersion-reinforced [204, 205, 207] and continuous fiber-reinforced composites [208, 209].

(i) *Dispersion-reinforced GMCs* are prepared by the sintering of glass powders with large (chopped fibers, whiskers, platelets) or small (particle) rigid inclusions. Particle reinforcement provides only a moderate increase in strength and fracture toughness, and the failure of these systems remains catastrophic [203]. Better strength was attained by transformation toughening using, for example, tetragonal  $\text{ZrO}_2$ , but these materials still remain brittle. Reinforcement with discontinuous fibers even yields a decrease in strength but improves fracture toughness. The use of ductile reinforcements like metal particles [210, 211] or short metal fibers [212, 213] results in an increase in strength and fracture toughness ( $K_{Ic} \approx 5\text{--}7 \text{ MPa m}^{1/2}$ ) [203].

Application areas of dispersion-reinforced glass and glass-ceramic matrix composites comprise domestic, industrial, and military fields, including, for example, electrical, high-temperature, environmental resistance and dimensional stability applications. Comprehensive reviews are given, for example, by Boccaccini [204, 205] and Roether and Boccaccini [207].

(ii) The high fracture toughness of *continuous fiber-reinforced GMC* is caused by deflecting matrix cracks parallel to the fiber and the subsequently required “pullout” of fibers from their cracked matrix [206]. This is only possible if the fiber–matrix interface has lower strength [214]. For SiC- and C-fibers, for example, this effect is provided by a carbon-rich interface. At the same time, this interface layer allows load transfer from matrix to fiber so that strengthening takes place. This way, high bending strength up to 1.5 GPa and fracture toughness up to  $35 \text{ MPa m}^{1/2}$  (work of fracture up to  $40 \text{ kJ/m}^2$ ) [201, 203] were attained for up to 45 vol % SiC- or C-fiber GMC. But also other ceramic [206, 209] and metallic fibers (700 MPa bending strength and  $50 \text{ kJ/m}^2$  work of fracture) [203, 209, 215] have been used. Composites with

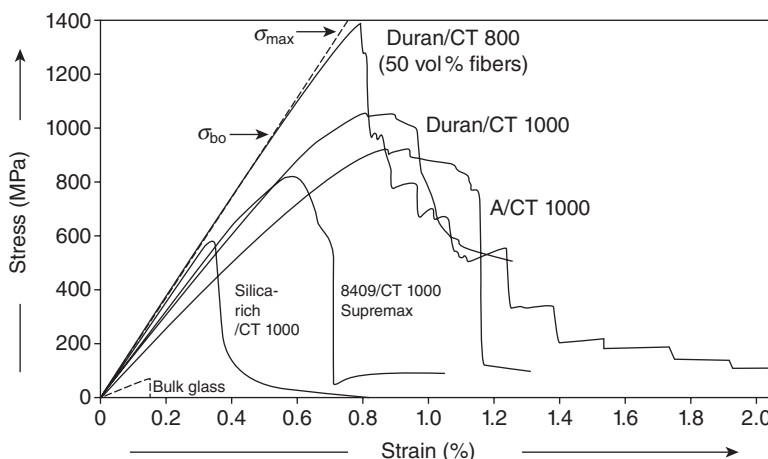


**Figure 3.37.** Stress–strain diagrams of various C-fiber T1000 and T800 (40 and 50 vol %) reinforced glasses from SCHOTT Glaswerke, Mainz.  $\sigma_{max}$  bending strength;  $\sigma_{bo}$  bendover stress [201].

glass-ceramic matrixes reach lower values but can be used at higher temperatures [201, 206, 216, 217].

Figure 3.37 illustrates the stress–strain behavior of different C-fiber composites in comparison with bulk glass. In oxidative atmospheres and higher temperatures, however, the carbon-rich interface layer is slowly decomposed, causing again a brittle fracture behavior [206, 209].

Nonetheless, under appropriate circumstances, fiber-reinforced GMC possess high oxidation and corrosion resistance, high-temperature capability, high strength-to-weight ratio, higher toughness and spalling resistance than monolithic ceramics, and good performance in thermal shock loading and aggressive tribological interactions [206, 209]. These properties make them promising structural materials for aerospace applications, impact resistant applications, brake and gear systems in automotive applications, high-temperature components, as well as for bearings and seals in pump manufacturing. A first well-known commercial application is Fortadur™ [218] (Fig. 3.38), which is, for example, used for hot glass handling. For many other potential applications, however, sufficient cost-effective manufacturing technologies have not yet been developed.

(iii) *Processing of reinforced GMC* involves the viscous sintering of glass powders with small and large rigid inclusions. This process route may suffer from several sinter retardation phenomena explained in Subsections 3.5.3 and 3.5.4. This retardation and the presence of chemically stable crystal inclusions (see Subsection 3.2.2.2) can substantially increase the impeding effect of surface crystallization (see Subsections 3.5.1 and 3.5.2) since sintering is slowed and shifted to a higher temperature. Due to this and



**Figure 3.38.** Fiber-reinforced glass matrix composite parts with different shapes all fabricated by hot pressing (Fortadur™ produced by SCHOTT Medica) [218].

other effects like bad wetting and sintering stress phenomena, these composites are mostly densified by hot pressing. Some examples of differently shaped components made by hot pressing are shown in Figure 3.38.

While powder technology and hot pressing of dispersion-reinforced composites can follow standard processing techniques [204, 205, 207], processing of continuous fiber-reinforced composites comprises two-steps: preparation of the prepreg and its sintering with or without pressure. One frequently applied procedure of prepreg preparation is the slurry technique [5, 219, 220]. The disadvantage of this method is the use of organic binder, which has to be burned out before hot pressing. An advancement of this method is the so-called sol–gel–slurry method, which uses alkoxide sols as a binder (see Fig. 3.39) [201, 221, 222]. Another method is to infiltrate prebuilt fiber bodies with a glass powder/binder (organic or sol) suspension [5, 201]

### 3.6.2 SG and SGC for Seals and Solders for Solid Oxide Fuel Cells (SOFCs)

Viscous sintering and crystallization is also utilized, for example, for manufacturing glass seals and solders for SOFCs [223, 224]. Despite many other requirements, these sealing materials have to match the coefficient of thermal expansion (CTE) of joining materials (metal and electrolyte) for avoiding stresses during joining and operation. The target range of CTE and  $T_g$  is  $10.5\text{--}12.5 \cdot 10^{-6}/\text{K}$  and  $600\text{--}750^\circ\text{C}$ , respectively [225]. Further, seals for SOFC have to resist temperatures between  $700$  and  $900^\circ\text{C}$  during joining and operation [226]. At operating temperatures, sealants have to be chemically stable under wet oxidizing and reducing atmospheres ( $\text{O}_2$ ,  $\text{H}_2$ ) and must be compatible with other cell components [223, 226]. As a matter of course, the sealing has to be electrically insulating (both ionic and electronic) [227]. Alkali metal-containing glasses are generally avoided because they may react with other fuel cell components [228] and can enhance the volatility of chromium [229], which, in turn, can poison the

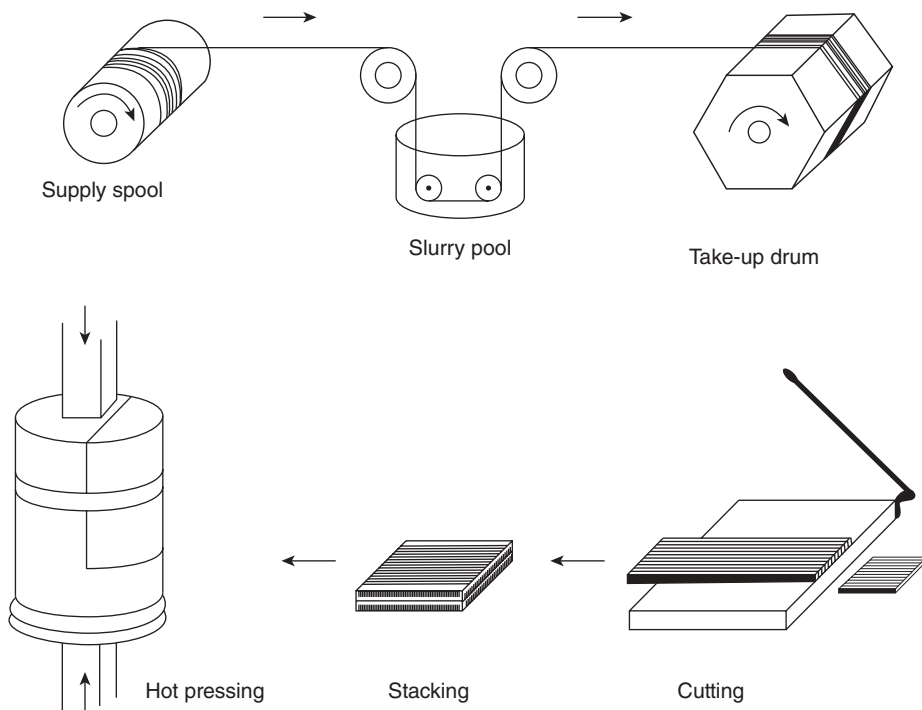


**Figure 3.39.** Schematic presentation of the fabrication process of fiber-reinforced glasses or glass-ceramics by the sol-gel-slurry method [222].

cathode [223]. But also other constituents of the sealant may react especially with the interconnect steel [230]. Therefore, each steel composition needs a specially adapted glass-ceramic material for successful long-term operation [231].

Although most of these desired properties are predominantly determined by chemical long-term interfacial phenomena, and although any microstructure, initially affected by powder processing, will steadily change toward a thermodynamic equilibrium, glass powder processing can be utilized to attain important technological goals. Thus, glass powders must wet, sinter, and flow sufficiently to provide adequate sealing while maintaining, however, sufficient mechanical stiffness [223]. This balance and stack stability during operation can be achieved by crystallization of the sealant, that is, by using SGC technologies [232–239]. As another advantage, dispersed crystals may help to attain the desired CTE. Both effects, of course, can be achieved by GMC as well [240–242].

Within that context, many effects of powder processing on sintering and crystallization mentioned in the foregoing Sections 3.2–3.5 have to be taken into account. So, of course, the glass should sinter to full density prior to crystallization [223]. On the other

hand, if stiffness during sealing needs to be increased, crystallization can be seeded with nucleating oxide particles mixed to the precursor powder before sintering [243]. The latter concept is advantageous because these particles cannot cause nucleation before being wetted during sintering. By this way, crystallization can be enhanced without impeding the joining process.

### 3.6.3 SGC and GMC for Architectural Applications

SGC and GMC are even used for architectural components on a large scale. Since 1974, for example, Nippon Electric Glass Co Ltd. supplies SGC for building applications. Under the brand name Neopariés™, this material is widely used for interior and exterior wall facing [14, 244, 245] (Fig. 3.40). More recently, diopside ( $\text{CaO}\cdot\text{MgO}\cdot 2\text{SiO}_2$ ) sintered marble-like SGCs were developed by Karamanov et al. [246].

In both cases, the natural stonelike appearance is achieved by sintering large glass particles of several millimeters in size, which crystallize from their initial surface after densification as illustrated by Figure 3.41. By this way, the initial grains stay visible to the naked eye. For a dense product of such stonelike appearance, it is necessary, however, to allow both complete sintering and pronounced surface crystallization from the former (“ghost”) particle surfaces. Within this context, it was necessary to carefully consider the related kinetics of viscous sintering and surface crystallization in the course of materials development [74, 179] (see Subsection 3.5.2).



**Figure 3.40.** Examples for applications of Neopariés™. Left: internal walls, subway station of Düsseldorf (Düsseldorf, Germany); right: external walls, Compal Electronics Inc. Head Office (Taipei, Taiwan) [247].

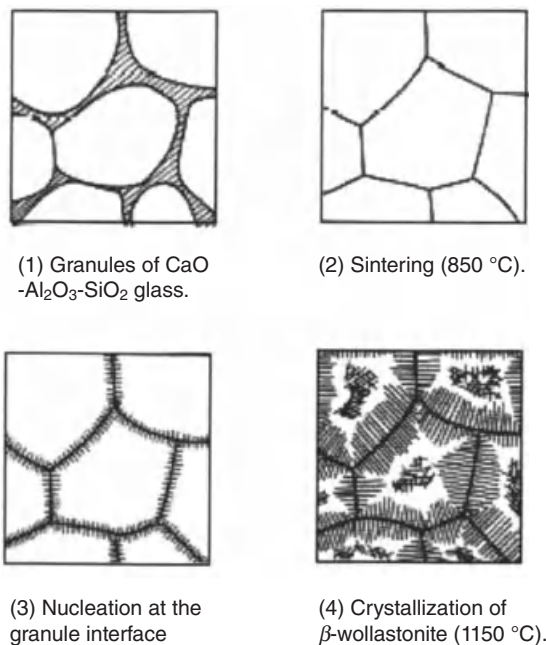


**Figure 3.41.** Schematic drawing of the sintering process of a surface crystallization glass-ceramic (Neopariés) [245].

### 3.6.4 SGC and GMC from Wastes

Numerous investigations were carried out concerning the use of silicate-based wastes for the manufacturing of SGC and GMC. Although previous studies were mainly focused on GC, like “Silceram” [248] and “Slagsital” [249], more recent papers deal with the simpler and less expensive [250, 251] SGC or GMC technology. Thus, various waste-based SGCs have been developed by several research groups in Italy (e.g., Bernardo et al. [250, 252, 253], Barbieri et al. [254, 255], Karamanov et al. [256]), in the United Kingdom (e.g., Kim et al. on the basis of Silceram glass [257]), and in Germany (e.g., Boccaccini et al. [258]). Analogous studies by Boccaccini et al. [259], Ferraris et al. [260], Bernardo et al. [261, 262], and Rozenstrauha et al. [263] were focused on waste-based reinforced GMC as already described in Subsection 3.6.1. Also, glass-ceramic tiles with an appearance similar to natural stone (e.g., marble or granite) are fabricated by sinter-crystallization of glass frits from industrial wastes [251, 264–269]. An example is shown in Figure 3.42.

Processing of SGC from wastes often involves the vitrification of silicate wastes, mixtures of wastes, or mixtures of wastes and other raw materials (e.g., sand). Here, wastes such as slag from steel production, coal combustion ash, fly ash and filter dusts from waste incinerators, different types of sludge, mud from metal hydrometallurgy, or glass cullets are used [270]. Waste vitrification was reviewed, for example, in References 271–273.

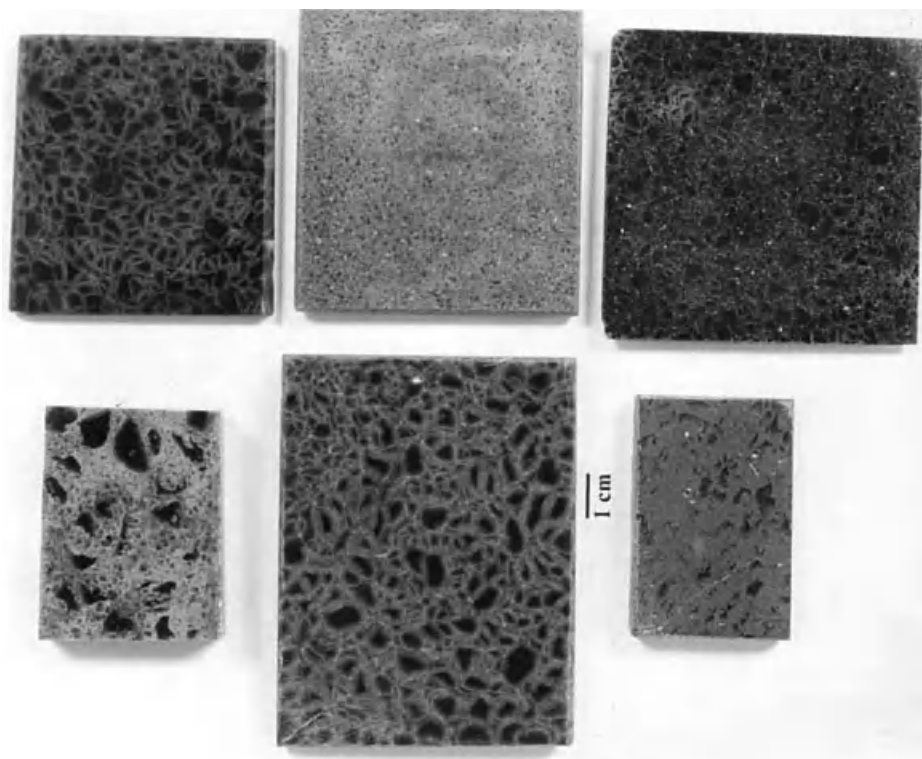


**Figure 3.42.** Some examples of sintered glass-ceramics based on municipal solid waste ash [251].

Because of a high crystallization tendency of many waste-derived glasses, the complex interaction between viscous sintering and crystallization illustrated in Subsections 3.5.1 and 3.5.2 is of increased importance for the SGC fabrication route [257].

For the manufacture of waste-based SGC, several pilot plants have been successfully operated [270, 274], but nevertheless, GCs from waste are not yet widely commercially available [270]. This might be due to the high energy consumption of waste vitrification, which can be even expected to increase in the future, compared to the waste landfill costs [271, 272, 275]. Another difficulty within this context is the varying composition of the incoming waste [271]. A recent literature review about GC, SGC, and GMC made from wastes is published by Rawlings et al. [270], and a valuable review about vitrification of waste and related applications is published by Colombo et al. [272].

### 3.6.5 SGC, GMC, and GBC for LTCC

Low temperature cofiring ceramics (LTCC) technology is a promising packaging technology for electronic components and microsystems [276–278]. During *cofiring*, ceramic substrates, metal strip lines, and integrated functional elements like resistors



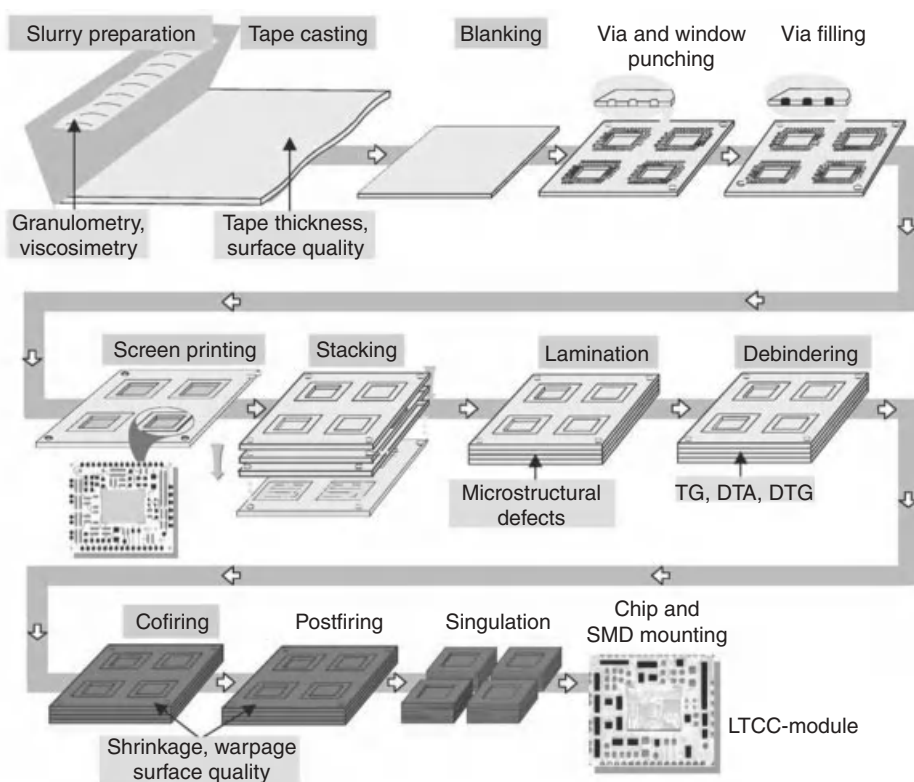


**Figure 3.43.** Scheme of LTCC multilayer technology [280]. TG, thermal gravimetry; DTG, differential thermal gravimetry; SMD, surface mount device.

or capacitors are sintered simultaneously. *Low temperature* indicates that densification is attained well below the melting point of good metal conductors. LTCC materials thus combine superior chemical, thermal, and mechanical properties of ceramic substrates, their low dielectric loss, and thermal expansion and take advantage of the low electric resistance of Cu, Ag, Ag–Pd, or Au metallization. For these reasons, LTCC has the merit of excellent connection reliability for high-density packaging and is regarded as promising future technology for high-density packaging components for high-frequency communication components (e.g., Bluetooth, GPS, WLAN), in automotive electronics, sensor, and medical applications [278]. A scheme of LTCC multilayer laminate technology is shown in Figure 3.43.

The LTCC multilayer technology offers numerous advantages based both on materials and technologies, such as [2]

- easy control of material properties and functionality by combining different glass and crystal powders in different volume fractions;
- tunable final material properties by controlled, for example, seeded, glass crystallization or by precipitation of new crystal phases promoted by the partial dissolution of crystal filler particles;



- good thin film compatibility due to the achievable reduction of residual porosity and surface roughness provided by large amounts of glass phase;
- possible access to new synthesis routes for powders and composites;
- system in package by possible integration of advanced functional tapes or pastes into LTCC modules by cofiring; and the
- availability of (lateral) “zero-shrinkage” techniques [118, 279].

Commercial LTCCs are made from GMC (i.e., Heraeus CT700, Ceramtape GC, DuPont DP951, Sumitomo metal electrodevice), or GBC (e.g., Heraeus CT765), or SGC (e.g., FerroA6M) [278, 281]. Figure 3.44 illustrates typical glass volume fraction and densification temperature ranges for those LTCC materials.

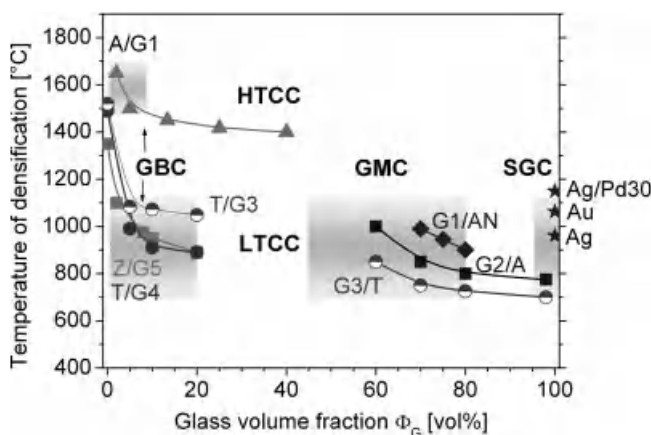


**Figure 3.44.** Typical ranges of the initial volume fraction of glass phase,  $\Phi_g$ , and final densification temperatures for LTCC based on GBC, GMC, and SGC (shadowed areas). Experimental points refer to the LTCC examples shown in Table 3.2. Some high-temperature cofired ceramics (HTCC) are shown for the sake of comparison. Stars indicate the melting points of metal conductors [2].

**TABLE 3.2.** Examples for LTCC Based on GBC and GMC Taken from Schiller et al. [2] Shown in Figure 3.44

Glass	Dispersed Crystals	Processing	Code	Reference
CaO-Al <sub>2</sub> O <sub>3</sub> -B <sub>2</sub> O <sub>3</sub> -SiO <sub>2</sub>	Al <sub>2</sub> O <sub>3</sub>	GBC (HTCC)	A/G1	[282]
La <sub>2</sub> O <sub>3</sub> -B <sub>2</sub> O <sub>3</sub> -TiO <sub>2</sub>	BaLa <sub>2</sub> Ti <sub>4</sub> O <sub>12</sub>	GBC	T/G3	[283]
Bi <sub>2</sub> O <sub>3</sub> -B <sub>2</sub> O <sub>3</sub> -SiO <sub>2</sub> -ZnO	BaLa <sub>2</sub> Ti <sub>4</sub> O <sub>12</sub>	GBC	T/G4	[284]
Bi <sub>2</sub> O <sub>3</sub> -ZnO-B <sub>2</sub> O <sub>3</sub>	ZrO <sub>2</sub>	GBC	Z/G5	[285]
CaO-Al <sub>2</sub> O <sub>3</sub> -B <sub>2</sub> O <sub>3</sub> -SiO <sub>2</sub>	AlN	GMC	G1/AN	[286]
Ka <sub>2</sub> O-B <sub>2</sub> O <sub>3</sub> -SiO <sub>2</sub>	Al <sub>2</sub> O <sub>3</sub>	GMC	G2/A	[287]
La <sub>2</sub> O <sub>3</sub> -B <sub>2</sub> O <sub>3</sub> -TiO <sub>2</sub>	BaLa <sub>2</sub> Ti <sub>4</sub> O <sub>12</sub>	GMC	G3/T	[283, 288]

Processing of LTCC GMC can be affected by virtually all crystallization and sinter retardation phenomena mentioned in Sections 3.2–3.5. Thus, due to the desired postfiring stability of LTCC components, crystallizing glasses have to be used, which requires careful tuning of crystallization (e.g., by nucleation seeding) and its impeding effect on sintering. Further, for example, in achieving certain electrical or thermomechanical properties, small rigid inclusions like alumina particles are often required, which can strongly affect sintering. Due to the small glass and inclusion particle size, for example, required for low-temperature viscous sintering prior to crystallization, dissolution phenomena can occur as illustrated in Figure 3.34. Moreover, since tape casting may cause oriented microstructure and due to different applied pressure-sintering or zero-shrinkage techniques, anisotropic sintering phenomena and the continuum theory of sintering have to be taken into account. Due to these complex phenomena, only careful exploiting of the aforementioned temperature- and microstructure-dependent kinetic balances between sintering, crystallization, and dissolution makes it possible to delay undesired concurrent crystallization during sintering, to minimize the amount of residual glass phase in the dense composite, and to tune final properties of functional LTCC GMC materials.

### 3.6.6 SGC for Dental Applications

Leucite, leucite-apatite, and apatite dental SGC for dental applications were developed by Höland, Frank, Schweiger, and Rheinberger [289–292]. A comprehensive review was given by Höland and Beall [14]. Due to the large variety of different dental applications, these impressive materials offer specially tuned complex property combinations comprising optical appearance, thermal expansion, mechanical strength, toughness, abrasion resistance, and chemical durability.

*Leucite SGCs* are successfully used for inlays, onlays, anterior and posterior crowns, and veneers on a large commercial scale. Despite other advantages, the high CTE of leucite crystals can cause dispersion strengthening of the glass matrix. Due to the lack of appropriate nucleation agents, this material is produced by controlled simultaneous sintering and surface crystallization of glass powders. Precursor ingots obtained in this way are supplied under the brand name IPS Empress® by Ivoclar Vivadent AG [289]. For the fabrication of dental restorations, these ingots are heated again and their viscous crystal-bearing melt is pressed into hollow molds within specially designed laboratory furnaces. Molds are prepared by the dentist via lost-wax techniques beforehand. It hardly needs mentioning that this production process is affected by many of the basic phenomena mentioned in the foregoing sections.

A different glass-ceramic system, which was developed to produce *leucite-apatite SGC*, possibly combined with stains, can be subsequently glazed or layered onto the restoration surface (special metal frameworks). These layers provide excellent optical properties including opalescence and translucence, closely matching the appearance of the natural teeth. This latter advantage mainly arises from coprecipitated apatite needles, mimicking needlelike apatite crystals in natural teeth. Since leucite and apatite crystallization is surface and volume nucleated, respectively, carefully controlled glass powder processing and firing are required to achieve the required microstructures.



**Figure 3.45.** Lithium disilicate metal-free three-unit bridge veneered with a fluoroapatite containing SGC [293].

Figure 3.45 shows a metal-free three-unit bridge consisting of a lithium disilicate framework veneered with a leucite-free *fluoroapatite* SGC (IPS Empress 2) [290–292].

## ACKNOWLEDGMENTS

The authors gratefully acknowledge the long-standing inspiring cooperations among the members of TC7 of the International Commission on Glass: W. Pannhorst, E. D. Zanotto, W. Höland, V. Fokin, G. Völksch, I. Szabo, I. Donald, P. James, M. Weinberg, M. Davis, L. Pickney, T. Komatsu, and A. Sakamoto, in particular, during the cooperative effort of the TC7 on surface-induced crystallization of glass. Our sincere thanks also go to J. Schmelzer and I. Gutzow for their continuous interest and crucial inspirations with respect to our studies on surface nucleation and overall crystallization kinetics. With respect to our studies on sintering and crystallization of LTCC, we like to express our deep gratitude to J. Deubener, M. Eberstein, and W. A. Schiller for pleasant and stimulating cooperation.

## ABBREVIATIONS

Symbols Repeatedly Used in This Chapter (in the text, rates are denoted by a prime)

Symbol	Unit	Meaning
$t$	s	Time
$T$	K	Temperature
$\alpha$	K/min	Heating rate
$W$	J	Work of formation of a crystal nucleus
$\phi$	–	Nucleation activity

(Continued)

Symbol	Unit	Meaning
$N$	$\text{m}^{-2}$	Surface crystal nucleation density
$I$	$\text{m}^{-3}\text{s}^{-1}$	Steady-state homogeneous volume nucleation rate
$I_s$	$\text{m}^{-2}\text{s}^{-1}$	Surface crystal nucleation rate
$H$	$\text{m}^{-2}$	Number density of active surface nucleation sites
$I_H$	$\text{s}^{-1}$	Using-up rate of active surface nucleation sites
$2\ell$	$\text{m}$	Next neighbor distance of surface crystal nuclei
$r$	$\text{m}$	Crystal radius
$U$	$\text{m/s}$	Crystal growth rate
$\delta$	—	Relative crystal glass density difference
$D$	$\text{m}$	Particle diameter
$R_0$	$\text{m}$	Particle radius
$E_a$	$\text{kJ/mol}$	Activation energy of crystal growth
$R$		Gas constant
$u_0$	$\text{m/s}$	Pre-exponential factor of crystal growth rate
$x$	—	Crystal volume fraction
$x_s$	—	Crystallized surface fraction
$n$	—	Avrami parameter of growth dimensionality
$\eta$	$\text{Pa}\cdot\text{s}$	Newtonian shear viscosity
$\gamma$	$\text{N/m}$	Interfacial surface energy glass–vacuum
$s$	—	Linear shrinkage ( $\Delta$ length/initial length)
$H, D$		Height and diameter of cylindrical samples
$S$	—	Linear shrinkage of composite compacts
$k_f$	—	Adjustable particle shape factor
$\rho$	—	Relative density
$\varepsilon$	—	Linear strain ( $\Delta$ length/length)
$\Sigma$	$\text{Pa}$	Hydrostatic sintering stress
$E_{mc}$	$\text{Pa}\cdot\text{s}$	Uniaxial viscosity of a porous glass matrix composite
$K_{mc}$	$\text{Pa}\cdot\text{s}$	Viscous bulk modulus of a porous glass matrix composite
$\nu_{mc}$	—	Viscous Poisson's ratio of a porous glass matrix composite
$K_A$	—	Anisotropy factor of sintering
$\Phi$	—	Crystal volume fraction

## REFERENCES

1. P. F. James (1995) Glass-ceramics—New compositions and uses, *Journal of Non-Crystalline Solids*, **181**[1-2] 1–15.
2. W. A. Schiller, R. Müller, M. Eberstein, S. Reinsch, and T. Rabe (2008) Sintering of LTCC, *cfi/Berichte der DKG*, **85**[13] 12–17.
3. E. M. Rabinovich (1985) Preparation of glass by sintering, *Journal of Materials Science*, **20**[12] 4259–4297.
4. S. Kemethmüller, M. Hagymasi, A. Stiegelschmitt, and A. Roosen (2007) Viscous flow as the driving force for the densification of low-temperature co-fired ceramics, *Journal of the American Ceramic Society*, **90**[1] 64–70.

5. K. M. Prewo, Fibre reinforced glasses and glass-ceramics, in *Glasses and Glass-ceramics*, ed. M. H. Lewis, pp. 336–368, Chapman and Hall, London, 1989.
6. W. D. Kingery (1959) Densification during sintering in the presence of a liquid phase .1. Theory, *Journal of Applied Physics*, **30**[3] 301–306.
7. R. M. German, *Liquid Phase Sintering*. Plenum Press, New York, 1985.
8. Y.-M. Chiang, D. P. Birnie III, and W. D. Kingery, *Physical Ceramics*. John Wiley & Sons, New York, 1997.
9. A. F. Gualtieri (2007) Thermal behavior of the raw materials forming porcelain stoneware mixtures by combined optical and in situ X-ray dilatometry, *Journal of the American Ceramic Society*, **90**[4] 1222–1231.
10. B. O. Mysen and P. Richet, *Silicate Glasses and Melts, Properties and Structure*, Elsevier, Amsterdam, Boston, London, New York, Oxford, Paris, San Diego, San Francisco, Singapore, Sydney, Tokyo, 2005.
11. H. H. Dunken, *Physikalische Chemie der Glasoberfläche*, 1st edition, VEB Deutscher Verlag für Grundstoffindustrie, Leipzig, 1981.
12. I. Gutzow and J. Schmelzer, *The Vitreous State*. Springer-Verlag, Berlin, Heidelberg, New York, 1995.
13. A. K. Varshneya, *Fundamentals of Inorganic Glasses*. Academic Press, San Diego, CA, 1994.
14. W. Höland and G. H. Beall, *Glass-Ceramic Technology*. The American Ceramic Society, Westerville, OH, 2002.
15. E. D. Zanotto (2010) A bright future for glass-ceramics, *American Ceramic Society Bulletin*, **89**[8] 19–27.
16. E. A. Olevsky (1998) Theory of sintering: From discrete to continuum, *Materials Science & Engineering R-Reports*, **23**[2] 41–100.
17. R. J. Brook, volume editor, *Processing of Ceramics Part I, Materials Science and Technology, A Comprehensive Treatment*. Vol. 17A, eds. R. W. Cahn, P. Haasen, and E. J. Kramer, VCH, Weinheim, New York, Basel, Cambridge, Tokyo, 1996.
18. R. M. German, *Sintering Theory and Practice*. John Wiley & Sons, New York, Chichester, Brisbane, Toronto, Singapore, 1996.
19. J. Svoboda, H. Riedel, and R. Gaebel (1996) A model for liquid phase sintering, *Acta Materialia*, **44**[8] 3215–3226.
20. H. Riedel, H. Zipse, and J. Svoboda (1994) Equilibrium pore surfaces, sintering stresses and constitutive-equations for the intermediate and late stages of sintering .2. Diffusional densification and creep, *Acta Metallurgica et Materialia*, **42**[2] 445–452.
21. E. D. Zanotto (1987) Isothermal and adiabatic nucleation in glass, *Journal of Non-Crystalline Solids*, **89**[3] 361–370.
22. I. Gutzow (1980) Kinetics of crystallization processes in glass forming melts, *Journal of Crystal Growth*, **48**[4] 589–599.
23. P. F. James (1985) Kinetics of crystal nucleation in silicate-glasses, *Journal of Non-Crystalline Solids*, **73**[1-3] 517–540.
24. J. W. P. Schmelzer, V. M. Fokin, A. S. Abyzov, E. D. Zanotto, and I. S. Gutzow (2010) How do crystals form and grow in glass-forming liquids: Ostwald's rule of stages and beyond, *International Journal of Applied Glass Science*, **1**[1] 16–26.
25. I. Avramov, R. Keding, and C. Russel (2000) Crystallization kinetics and rigidity percolation in glass-forming melts, *Journal of Non-Crystalline Solids*, **272**[2-3] 147–153.

26. V. M. Fokin and E. D. Zanotto (1999) Surface and volume nucleation and growth in TiO<sub>2</sub>-cordierite glasses, *Journal of Non-Crystalline Solids*, **246**[1-2] 115–127.
27. U. Köster (1988) Surface crystallization of metallic glasses, *Materials Science and Engineering*, **97** 233–239.
28. R. Müller, S. Reinsch, and W. Pannhorst (1996) Nucleation at cordierite glass surfaces: Kinetic aspects, *Glastechnische Berichte-Glass Science and Technology*, **69**[1] 12–20.
29. R. Müller, R. Naumann, and S. Reinsch (1996) Surface nucleation of  $\mu$ -cordierite in cordierite glass: Thermodynamic aspects, *Thermochimica Acta*, **280** 191–204.
30. R. Müller (1997) Surface nucleation in cordierite glass, *Journal of Non-Crystalline Solids*, **219** 110–118.
31. S. Toshev and I. Gutzow (1972) Nichtstationäre Keimbildung: Theorie und Experiment, *Kristall und Technik*, **7**[1-3] 43–73.
32. E. D. Zanotto and M. C. Weinberg (1989) Trends in homogeneous crystal nucleation in oxide glasses, *Physics and Chemistry of Glasses*, **30**[5] 186–192.
33. N. S. Yuritsyn, V. M. Fokin, A. M. Kalinina, and V. N. Filipovich (1994) Surface crystal nucleation in cordierite glass: Kinetics and a theoretical model, *Glass Physics and Chemistry*, **20** 125–132.
34. M. C. Weinberg (1991) Heterogeneous nucleation on developing substrate particles, *Physics and Chemistry of Glasses*, **32**[4] 168–173.
35. M. C. Weinberg, E. D. Zanotto, and S. Manrich (1992) Classical nucleation theory with a size dependent interfacial-tension—Li<sub>2</sub>O-2SiO<sub>2</sub> crystal nucleation, *Physics and Chemistry of Glasses*, **33**[3] 99–102.
36. J. Deubener, R. Bruckner, and H. Hessenkemper (1992) Nucleation and crystallization kinetics on float glass surfaces, *Glastechnische Berichte-Glass Science and Technology*, **65**[9] 256–266.
37. R. Müller, E. D. Zanotto, and V. M. Fokin (2000) Surface crystallization of silicate glasses: Nucleation sites and kinetics, *Journal of Non-Crystalline Solids*, **274**[1-3] 208–231.
38. W. Pannhorst (2000) Surface nucleation. Brochure of the TC7 of the International Commission on Glass ICG.
39. J. Deubener (2005) Structural aspects of volume nucleation in silicate glasses, *Journal of Non-Crystalline Solids*, **351**[18] 1500–1511.
40. E. D. Zanotto and V. M. Fokin (2003) Recent studies of internal and surface nucleation in silicate glasses, *Philosophical Transactions of the Royal Society of London Series A-Mathematical Physical and Engineering Sciences*, **361**[1804] 591–612.
41. V. M. Fokin, E. D. Zanotto, N. S. Yuritsyn, and J. W. P. Schmelzer (2006) Homogeneous crystal nucleation in silicate glasses: A 40 year perspective, *Journal of Non-Crystalline Solids*, **352**[26-27] 2681–2714.
42. R. Müller, S. Reinsch, R. Sojref, M. Gemeinert, and F. G. Wihsman (1995) Nucleation at cordierite glass powder surfaces, in Proceedings of the XVII International Congress on Glass, ed. G. Fangtian, Beijing, pp. 564–569.
43. S. Reinsch, R. Müller, and W. Pannhorst (1994) Active nucleation sites at cordierite glass surfaces, *Glastechnische Berichte-Glass Science and Technology*, **67C** 432–435.
44. P. W. McMillan (1982) The crystallization of glasses, *Journal of Non-Crystalline Solids*, **52**[1-3] 67–76.
45. R. Müller and D. Thamm (1990) Surface induced nucleation of cordierite glass, in Proceedings of the 4th International Otto Schott Colloquium, pp. 86–87, Jena.

46. E. Wittman and E. D. Zanotto (2000) Surface nucleation and growth in anorthite glass, *Journal of Non-Crystalline Solids*, **271**[1-2] 94–99.
47. E. D. Zanotto (1991) Surface crystallization kinetics in soda lime silica glasses, *Journal of Non-Crystalline Solids*, **129**[1-3] 183–190.
48. E. D. Zanotto (1991) Surface nucleation in a diopside glass, *Journal of Non-Crystalline Solids*, **130**[2] 217–219.
49. N. S. Yuritsyn, V. M. Fokin, A. M. Kalinina, and V. N. Filipovich (1994) Crystal nucleation and growth in the surface crystallization of cordierite glass, *Glass Physics and Chemistry*, **20** 116–124.
50. S. Reinsch and R. Müller, Nucleation at silicate glass surfaces, in *Analysis of the Composition and Structure of Glass and Glass Ceramics*, eds. H. Bach and D. Krause, pp. 379–398, Springer-Verlag, Berlin, Heidelberg, New York, 1999.
51. J. Schmelzer, J. Möller, I. Gutzow, R. Pascova, R. Müller, and W. Pannhorst (1995) Surface-energy and structure effects on surface crystallization, *Journal of Non-Crystalline Solids*, **183**[3] 215–233.
52. J. Chladek, R. Müller, L. Weh, and S. Reinsch (2004) Viscous flow and surface crystallization caused by Vickers indentation, *Glass Science and Technology*, **77**[1] 1–6.
53. A. Feltz, *Amorphe und glasartige anorganische Festkörper*. Akademie Verlag, Berlin, 1983.
54. J. Schmelzer, R. Pascova, J. Möller, and I. Gutzow (1993) Surface-induced devitrification of glasses—The influence of elastic strains, *Journal of Non-Crystalline Solids*, **162**[1-2] 26–39.
55. S. Reinsch, Oberflächenkeimbildung von Silikatgläsern der Stöchiometrie des Cordierits und des Diopsids, Dr. Ing. Thesis, Fakultät III—Prozesswissenschaften, TU Berlin, 2001.
56. T. Seidel and C. Friedrich (1992) Influence of shear rate and temperature on the crystallization of spontaneous crystallizing glass-ceramic, *Journal of Materials Science*, **27**[1] 263–269.
57. B. Durschang, G. Carl, C. Rüssel, and I. Gutzow (1996) Influence of pressure and shear flow on the crystallization behaviour of a glass melt based on the  $\text{Li}_2\text{Si}_2\text{O}_5$ -composition, *Berichte der Bunsen-Gesellschaft-Physical Chemistry Chemical Physics*, **100**[9] 1456–1458.
58. J. Möller, I. Gutzow, and K. I. Jacob (1999) Kinetic enhancement of nucleation by flow, *Phase Transitions*, **70**[3] 161–182.
59. R. A. de Réaumur (1739) Art de faire une nouvelle espèce de porcelaine par des moyens extrêmement simples et faciles ou de transformer le verre en porcelaine, *Mémoires de l'Académie Royale de Sciences*, 370–388.
60. H. R. Swift (1947) Some experiments on crystal growth and solution in glasses, *Journal of the American Ceramic Society*, **30**[6] 165–169.
61. E. D. Zanotto (1993) Experimental studies of surface nucleation and crystallization of glasses, *Ceramic Transactions, Nucleation and Crystallization in Liquids and Glasses*, **30** 65–74.
62. R. Müller, S. Reinsch, G. Volksch, and K. Heide (1996) Nucleation sites at cordierite glass surfaces, *Berichte der Bunsen-Gesellschaft-Physical Chemistry Chemical Physics*, **100**[9] 1438–1442.
63. A. Dobрева and I. Gutzow (1993) Activity of substrates in the catalyzed nucleation of glass-forming melts .1. Theory, *Journal of Non-Crystalline Solids*, **162**[1-2] 1–12.



64. A. Dobрева and I. Gutzow (1993) Activity of substrates in the catalyzed nucleation of glass-forming melts .2. Experimental-evidence, *Journal of Non-Crystalline Solids*, **162**[1-2] 13–25.
65. I. Gutzow (1980) Induced crystallization of glass-forming systems—A case of transient heterogeneous nucleation .2., *Contemporary Physics*, **21**[3] 243–263.
66. A. N. Kolmogorov (1937) On the statistical theory of metal crystallization (in Russian), *Izvestiya Akademii Nauk SSSR, Seriya Matematicheskaya*, **3** 355.
67. W. A. Johnson and R. F. Mehl (1939) Reaction kinetics in processes of nucleation and growth, *Transactions of the American Institute of Mining and Metallurgical Engineers*, **135** 416–442.
68. M. Avrami (1939) Kinetics of phase change I—General theory, *Journal of Chemical Physics*, **7**[12] 1103–1112.
69. M. Avrami (1940) Kinetics of phase change II—Transformation-time relations for random distribution of nuclei, *Journal of Chemical Physics*, **8**[2] 212–224.
70. M. Avrami (1941) Granulation, phase change, and microstructure—Kinetics of phase change. III, *Journal of Chemical Physics*, **9**[2] 177–184.
71. B. V. Erofeev (1946) A generalized equation of chemical kinetics and its application in reactions involving solids, *Comptes Rendus (Doklady) de l'Académie des Sciences de l'URSS*, **LII**[6] 511–514.
72. D. A. Young, *Decomposition of Solids*, Vol. 1, Pergamon Press, Oxford, London, Edinburgh, New York, Toronto, Paris Braunschweig, 1966.
73. J. W. Christian, *Theory of Transformations in Metals and Alloys*, 2nd edition, Pergamon, Oxford, 1975.
74. I. Gutzow, R. Pascova, A. Karamanov, and J. Schmelzer (1998) The kinetics of surface induced sinter crystallization and the formation of glass-ceramic materials, *Journal of Materials Science*, **33**[21] 5265–5273.
75. E. D. Zanotto and P. F. James (1988) Experimental test of the general-theory of transformation kinetics—Homogeneous nucleation in a BaO.2SiO<sub>2</sub> glass, *Journal of Non-Crystalline Solids*, **104**[1] 70–72.
76. D. W. Henderson (1979) Thermal-analysis of nonisothermal crystallization kinetics in glass forming liquids, *Journal of Non-Crystalline Solids*, **30**[3] 301–315.
77. M. C. Weinberg (1991) On the analysis of nonisothermal thermoanalytical crystallization experiments, *Journal of Non-Crystalline Solids*, **127**[2] 151–158.
78. K. Matusita and S. Sakka (1981) Kinetic study on non-isothermal crystallization of glass by thermal analysis, *Bulletin of the Institute for Chemical Research, Kyoto University*, **59**[3] 159171.
79. V. M. Fokin, A. A. Cabral, R. M. C. V. Reis, M. L. F. Nascimento, and E. D. Zanotto (2010) Critical assessment of DTA-DSC methods for the study of nucleation kinetics in glasses, *Journal of Non-Crystalline Solids*, **356**[6–8] 358–367.
80. E. D. Zanotto and A. Galhardi (1988) Experimental test of the general-theory of transformation kinetics—Homogeneous nucleation in a Na<sub>2</sub>O.2CaO.3SiO<sub>2</sub> glass, *Journal of Non-Crystalline Solids*, **104**[1] 73–80.
81. H. Yinnon and D. R. Uhlmann (1983) Applications of thermoanalytical techniques to the study of crystallization kinetics in glass-forming liquids .1. Theory, *Journal of Non-Crystalline Solids*, **54**[3] 253–275.



82. M. C. Weinberg (1991) Surface nucleated transformation kinetics in 2-dimensional and 3-dimensional finite systems, *Journal of Non-Crystalline Solids*, **134**[1-2] 116–122.
83. M. C. Weinberg (1992) Transformation kinetics of particles with surface and bulk nucleation, *Journal of Non-Crystalline Solids*, **142**[1–2] 126–132.
84. I. W. Donald (2004) Crystallization kinetics of a lithium zinc silicate glass studied by DTA and DSC, *Journal of Non-Crystalline Solids*, **345–46** 120–126.
85. K. L. Mampel (1940) Time-conversion formula for heterogenic reactions in phase-boundaries of soloid bodies. 1. The development of mathematical methods and the derivation of planar conversion formula, *Zeitschrift für Physikalische Chemie-Abteilung a-Chemische Thermodynamik Kinetik Elektrochemie Eigenschaftslehre*, **187**[1] 43–57.
86. K. L. Mampel (1940) Time-conversion formulae for heterogenous reactions in phase limits of solid bodies. 2. The time-conversion formulae for a powder from globular particles, *Zeitschrift für Physikalische Chemie-Abteilung a-Chemische Thermodynamik Kinetik Elektrochemie Eigenschaftslehre*, **187**[4] 235–249.
87. O. M. Todes (1940) Kinetic of topochemical reactions (in Russian), *Journal of Physical Chemistry*, **14** 1224–1228.
88. R. Müller (1994) On the kinetics of sintering and crystallization of glass powders, *Glastechnische Berichte-Glass Science and Technology*, **67C** 93–98.
89. R. Müller (1989) The influence of grain-size on the overall kinetics of surface-induced glass crystallization, *Journal of Thermal Analysis*, **35**[3] 823–835.
90. J. Frenkel (1945) Viscous flow of crystalline bodies under the action of surface tension, *Journal of Physics (Moscow)*, **9** 385–391.
91. J. D. Eshelby in the discussion that accompanies the following paper: A. J. Shaler (1949) Seminar on the kinetics of sintering, *Transactions of the American Institute of Mining and Metallurgical Engineers*, **185**[11] 796–813.
92. V. V. Skorochod (1995) Development of the ideas of YA. I. Frenkel in the contemporary rheological theory of sintering, *Powder Metallurgy and Metal Ceramics*, **34**[9] 521–527.
93. J. K. Mackenzie and R. Shuttleworth (1949) A phenomenological theory of sintering, *Proceedings of the Physical Society London*, **62** 833–852.
94. G. W. Scherer (1984) Viscous sintering of a bimodal pore-size distribution, *Journal of the American Ceramic Society*, **67**[11] 709–715.
95. M. O. Prado, E. D. Zanotto, and R. Müller (2001) Model for sintering polydispersed glass particles, *Journal of Non-Crystalline Solids*, **279**[2-3] 169–178.
96. M. J. Pascual and A. Duran (2003) Sintering with concurrent crystallisation of a borosilicate glass, *Physics and Chemistry of Glasses*, **44**[6] 409–415.
97. M. O. Prado, M. L. F. Nascimento, and E. D. Zanotto (2008) On the sinterability of crystallizing glass powders, *Journal of Non-Crystalline Solids*, **354**[40-41] 4589–4597.
98. R. Clasen (1989) Sintering behavior of sub-micron silica particles, *Glastechnische Berichte-Glass Science and Technology*, **62**[7] 234–243.
99. R. Müller, D. Sporn, and H. Bertagnolli, *Untersuchungen zur Kinetik der Sinterung und Kristallisation amorpher (Sol-Gel- und Glaspulver)* final research report to the Deutsche Forschungsgemeinschaft, Bonn, 1994.
100. G. W. Scherer (1977) Sintering of low-density glasses .1. Theory, *Journal of the American Ceramic Society*, **60**[5-6] 236–239.
101. G. W. Scherer (1991) Cell models for viscous sintering, *Journal of the American Ceramic Society*, **74**[7] 1523–1531.

102. G. W. Scherer, Viscous sintering of inorganic gels, in *Surface and Colloid Science*, Vol. 14, eds. E. Matijevic and R. J. Good, pp. 265–300, Springer, London, 1987.
103. M. D. Sacks and T. Y. Tseng (1984) Preparation of SiO<sub>2</sub> glass from model powder compacts .2. Sintering, *Journal of the American Ceramic Society*, **67**[8] 532–537.
104. M. N. Rahaman, L. C. Dejonghe, G. W. Scherer, and R. J. Brook (1987) Creep and densification during sintering of glass powder compacts, *Journal of the American Ceramic Society*, **70**[10] 766–774.
105. I. B. Cutler and R. E. Henrichsen (1968) Effect of particle shape on the kinetics of sintering of glass, *Journal of the American Ceramic Society*, **51**[10] 604–605.
106. M. O. Prado, C. Fredericci, and E. D. Zanotto (2002) Glass sintering with concurrent crystallisation. Part 2. Nonisothermal sintering of jagged polydispersed particles, *Physics and Chemistry of Glasses*, **43**[5] 215–223.
107. M. O. Prado and E. D. Zanotto (2002) Glass sintering with concurrent crystallization, *Comptes Rendus Chimie*, **5**[11] 773–786.
108. S. Gross, personal communication, 2010.
109. H. E. Exner and E. A. Giess (1990) A stereology based equation for isotropic shrinkage during sintering by viscous flow, in *Proceedings of the Seventh World Round Table Conference on Sintering*, ed. D. P. Uskokvic, pp. 73–82, Herceg-Nov, Yugoslavia.
110. A. R. Boccaccini and R. Kramer (1995) Experimental-verification of a stereology-based equation for the shrinkage of glass powder compacts during sintering, *Glass Technology*, **36**[3] 95–97.
111. R. Müller, M. Eberstein, S. Reinsch, W. A. Schiller, J. Deubener, and A. Thiel (2007) Effect of rigid inclusions on sintering of low temperature co-fired ceramics, *Physics and Chemistry of Glasses-European Journal of Glass Science and Technology Part B*, **48**[4] 259–266.
112. M. O. Prado, C. Fredericci, and E. D. Zanotto (2003) Isothermal sintering with concurrent crystallization of polydispersed soda lime-silica glass beads, *Journal of Non-Crystalline Solids*, **331**[1–3] 145–156.
113. E. D. Zanotto and M. O. Prado (2001) Isothermal sintering with concurrent crystallisation of monodispersed and polydispersed glass particles. Part 1, *Physics and Chemistry of Glasses*, **42**[3] 191–198.
114. M. O. Prado, E. D. Zanotto, and C. Fredericci (2003) Sintering polydispersed spherical glass particles, *Journal of Materials Research*, **18**[6] 1347–1354.
115. M. O. Prado, C. Fredericci, and E. D. Zanotto (2003) Non-isothermal sintering with concurrent crystallization of polydispersed soda lime-silica glass beads, *Journal of Non-Crystalline Solids*, **331**[1–3] 157–167.
116. A. R. Boccaccini (1998) Shrinkage anisotropy of glass powder compacts sintered in dilatometers, *Journal of Materials Research*, **13**[6] 1693–1697.
117. J. R. G. Evans (1997) Particle contact before firing, *Journal of the European Ceramic Society*, **17**[2–3] 161–169.
118. T. Rabe, W. A. Schiller, T. Hochheimer, C. Modes, and A. Kipka (2005) Zero shrinkage of LTCC by self-constrained sintering, *International Journal of Applied Ceramic Technology*, **2**[5] 374–382.
119. A. G. Evans (1982) Considerations of inhomogeneity effects in sintering, *Journal of the American Ceramic Society*, **65**[10] 497–501.

120. V. V. Skorokhod (1995) Development of the ideas of Ya.I. Frenkel' in the contemporary rheological theory of sintering, *Powder Metallurgy and Metal Ceramics*, **34**[9–10] 521–527.
121. G. W. Scherer (1979) Sintering inhomogeneous glasses—Application to optical-waveguides, *Journal of Non-Crystalline Solids*, **34**[2] 239–256.
122. G. W. Scherer and S. M. Rekhson (1982) Viscoelastic-elastic composites .1. General-theory, *Journal of the American Ceramic Society*, **65**[7] 352–360.
123. R. K. Bordia and G. W. Scherer (1988) On constrained sintering .1. Constitutive model for a sintering body, *Acta Metallurgica*, **36**[9] 2393–2397.
124. R. K. Bordia and G. W. Scherer (1988) On constrained sintering .2. Comparison of constitutive models, *Acta Metallurgica*, **36**[9] 2399–2409.
125. R. K. Bordia and G. W. Scherer (1988) On constrained sintering .3. Rigid inclusions, *Acta Metallurgica*, **36**[9] 2411–2416.
126. J. N. Goodier (1936) LIII. Slow viscous flow and elastic deformation, *Philosophical Magazine Series 7*, **22**[148] 678–681.
127. G. W. Scherer (1987) Sintering with rigid inclusions, *Journal of the American Ceramic Society*, **70**[10] 719–725.
128. V. C. Ducamp and R. Raj (1989) Shear and densification of glass powder compacts, *Journal of the American Ceramic Society*, **72**[5] 798–804.
129. K. R. Venkatachari and R. Raj (1986) Shear deformation and densification of powder compacts, *Journal of the American Ceramic Society*, **69**[6] 499–506.
130. G. W. Scherer (1986) Viscous sintering under a uniaxial load, *Journal of the American Ceramic Society*, **69**[9] C206–C207.
131. M. N. Rahaman and L. C. Dejonghe (1990) Sintering of spherical glass powder under a uniaxial-stress, *Journal of the American Ceramic Society*, **73**[3] 707–712.
132. E. Aulbach, R. Zuo, and J. Rödel (2004) Laser-assisted high-resolution loading dilatometer and applications, *Experimental Mechanics*, **44**[1] 71–75.
133. J. B. Ollagnier, O. Guillon, and J. Rödel (2007) Effect of anisotropic microstructure on the viscous properties of an LTCC material, *Journal of the American Ceramic Society*, **90**[12] 3846–3851.
134. D. J. Green, O. Guillon, and J. Rödel (2008) Constrained sintering: A delicate balance of scales, *Journal of the European Ceramic Society*, **28**[7] 1451–1466.
135. O. Guillon, J. Rödel, and R. K. Bordia (2007) Effect of green-state processing on the sintering stress and viscosity of alumina compacts, *Journal of the American Ceramic Society*, **90**[5] 1637–1640.
136. R. E. Dutton and M. N. Rahaman (1992) Sintering, creep, and electrical-conductivity of model glass-matrix composites, *Journal of the American Ceramic Society*, **75**[8] 2146–2154.
137. R. Z. Zuo, E. Aulbach, R. K. Bordia, and J. Rödel (2003) Critical evaluation of hot forging experiments: Case study in alumina, *Journal of the American Ceramic Society*, **86**[7] 1099–1105.
138. R. Z. Zuo, E. Aulbach, and H. Rödel (2004) Shrinkage-free sintering of low-temperature cofired ceramics by loading dilatometry, *Journal of the American Ceramic Society*, **87**[3] 526–528.

139. R. J. Xie, R. Z. Zuo, E. Aulbach, U. Mackens, N. Hirotsaki, and H. Rödel (2005) Uniaxial viscosity of low-temperature cofired ceramic (LTCC) powder compacts determined by loading dilatometry, *Journal of the European Ceramic Society*, **25**[4] 417–424.
140. J. B. Ollagnier, O. Guillon, and J. Rödel (2006) Viscosity of LTCC determined by discontinuous sinter-forging, *International Journal of Applied Ceramic Technology*, **3**[6] 437–441.
141. R. Z. Zuo, E. Aulbach, and J. Rödel (2003) Viscous Poisson's coefficient determined by discontinuous hot forging, *Journal of Materials Research*, **18**[9] 2170–2176.
142. A. Mohanram, G. L. Messing, and D. J. Gren (2004) Measurement of viscosity of densifying glass-based systems by isothermal cyclic loading dilatometry, *Journal of the American Ceramic Society*, **87**[2] 192–196.
143. C. D. Lei and J. H. Jean (2005) Effect of crystallization on the stress required for constrained sintering of  $\text{CaO-B}_2\text{O}_3\text{-SiO}_2$  glass-ceramics, *Journal of the American Ceramic Society*, **88**[3] 599–603.
144. A. Mohanram, S. H. Lee, G. L. Messing, and D. J. Green (2005) A novel use of constrained sintering to determine the viscous Poisson's ratio of densifying materials, *Acta Materialia*, **53**[8] 2413–2418.
145. J. B. Ollagnier, D. J. Green, O. Guillon, and J. Rödel (2009) Constrained sintering of a glass ceramic composite: II. Symmetric laminate, *Journal of the American Ceramic Society*, **92**[12] 2900–2906.
146. J. B. Ollagnier, O. Guillon, and J. Rödel (2010) Constrained sintering of a glass ceramic composite: I. Asymmetric laminate, *Journal of the American Ceramic Society*, **93**[1] 74–81.
147. J. P. Smith and G. L. Messing (1984) Sintering of bimodally distributed alumina powders, *Journal of the American Ceramic Society*, **67**[4] 238–242.
148. N. V. Solomin and G. M. Tomilov (1970) Sintering kinetics of vitreous silica, *Izvestiya Akademii Nauk SSSR, Neorganicheskie Materialy*, **6**[10] 1853–1856.
149. R. Raj and R. K. Bordia (1984) Sintering behavior of bi-modal powder compacts, *Acta Metallurgica*, **32**[7] 1003–1019.
150. G. W. Scherer (1977) Sintering of low-density glasses .3. Effect of a distribution of pore sizes, *Journal of the American Ceramic Society*, **60**[5-6] 243–246.
151. H. E. Exner and E. A. Giess (1988) Anisotropic shrinkage of cordierite-type glass powder cylindrical compacts, *Journal of Materials Research*, **3**[1] 122–125.
152. E. A. Giess, J. P. Fletcher, and L. W. Herron (1984) Isothermal sintering of cordierite-type glass powders, *Journal of the American Ceramic Society*, **67**[8] 549–552.
153. A. R. Boccaccini (1993) Anisotropic densification of glass powder compacts, *Journal of the European Ceramic Society*, **32**[1] 27–30.
154. A. R. Boccaccini and G. Ondracek (1992) Viscous sintering of nonspherical borosilicate-glass powder, *Glastechnische Berichte-Glass Science and Technology*, **65**[3] 73–78.
155. A. R. Boccaccini and E. A. Olevsky (1999) Processing of platelet-reinforced glass matrix composites: Effect of inclusions on sintering anisotropy, *Journal of Materials Processing Technology*, **96**[1–3] 92–101.
156. A. R. Boccaccini and R. Conradt (2001) Isotropic shrinkage of platelet containing glass powder compacts during isothermal sintering, *International Journal of Inorganic Materials*, **3**[2] 101–106.

157. A. R. Boccaccini (1993) Anisotropic densification during sintering of glass powder compacts, *Journal of Materials Science Letters*, **12**[12] 943–945.
158. A. R. Boccaccini and B. Hamann (1999) In situ high-temperature optical microscopy, *Journal of Materials Science*, **34**[22] 5419–5436.
159. M. Wagner, A. Roosen, A. Stiegelschmitt, D. Schwanke, and F. Bechtholt (2002) In situ shrinkage measurements of LTCC multilayers by means of an optical dilatometer, *Key Engineering Materials*, **206–213** 1281–1284.
160. F. Raether, R. Springer, and S. Beyer (2001) Optical dilatometry for the control of microstructure development during sintering, *Materials Research Innovations*, **4**[4] 245–250.
161. P. M. Raj, A. Odulena, and W. R. Cannon (2002) Anisotropic shrinkage during sintering of particle-oriented systems—Numerical simulation and experimental studies, *Acta Materialia*, **50**[10] 2559–2570.
162. G. Besendörfer and A. Roosen (2008) Particle shape and size effects on anisotropic shrinkage in tape-cast ceramic layers, *Journal of the American Ceramic Society*, **91**[8] 2514–2520.
163. M. Eberstein, S. Reinsch, R. Müller, J. Deubener, and W. A. Schiller (2009) Sintering of glass matrix composites with small rigid inclusions, *Journal of the European Ceramic Society*, **29**[12] 2469–2479.
164. K. Watanabe and E. A. Giess (1985) Coalescence and crystallization in powdered high-cordierite ( $2\text{MgO} \cdot 2\text{Al}_2\text{O}_3 \cdot 5\text{SiO}_2$ ) glass, *Journal of the American Ceramic Society*, **68**[4] C102–C103.
165. T. Rudolph, K. L. Weisskopf, W. Pannhorst, and G. Petzow (1991) Microstructural development of a  $\text{P}_2\text{O}_5$ -modified cordierite glass ceramic during sintering .2. Densification experiments, *Glastechnische Berichte-Glass Science and Technology*, **64**[12] 305–309.
166. R. Müller, D. Thamm, and M. Kirsch (1990) Sintering and crystallization of cordierite glass powders, *Fortschrittsberichte der DKG/CFI, Werkstoffe, Verfahren, Anwendung*, **7**[1] 217–224.
167. H. Müller, R. Müller, and H. Fischer (1994) Studies on the kinetics of sintering and crystallization of amorphous (sol-gel- and glass) powders. Internal Report, BAM.
168. R. M. C. V. Reis, E. B. Ferreira, and E. D. Zanotto (2010) Further tests of sinter-crystallization of spherical diopside glass particles, Poster at the 22nd International Congress on Glass, Salvador, Bahia, Brazil 2010, <http://www.icg2010.com.br/index.php>.
169. I. Gutzow, D. Kashchiev, and I. Avramov (1985) Nucleation and crystallization in glass-forming melts—Old problems and new questions, *Journal of Non-Crystalline Solids*, **73**[1–3] 477–499.
170. S. Reinsch, M. L. F. Nascimento, R. Müller, and E. D. Zanotto (2008) Crystal growth kinetics in cordierite and diopside glasses in wide temperature ranges, *Journal of Non-Crystalline Solids*, **354**[52–54] 5386–5394.
171. T. J. Clark and J. S. Reed (1986) Kinetic processes involved in the sintering and crystallization of glass powders, *Journal of the American Ceramic Society*, **69**[11] 837–846.
172. P. C. Panda and R. Raj (1989) Sintering and crystallization of glass at constant heating rates, *Journal of the American Ceramic Society*, **72**[8] 1564–1566.
173. P. C. Panda, W. M. Mobley, and R. Raj (1989) Effect of the heating rate on the relative rates of sintering and crystallization in glass, *Journal of the American Ceramic Society*, **72**[12] 2361–2364.

174. J. Zimmer, F. Raether, and G. Müller (1997) In situ investigations of sintering and crystallization of lithium aluminosilicate glass-ceramics, *Glastechnische Berichte-Glass Science and Technology*, **70**[6] 186–188.
175. A. R. Boccaccini, W. Stumpfe, D. M. R. Taplin, and C. B. Ponton (1996) Densification and crystallization of glass powder compacts during constant heating rate sintering, *Materials Science and Engineering A-Structural Materials Properties Microstructure and Processing*, **219**[1-2] 26–31.
176. K. Lambrinou, O. van der Biest, A. R. Boccaccini, and D. M. R. Taplin (1996) Densification and crystallisation behaviour of barium magnesium aluminosilicate glass powder compacts, *Journal of the European Ceramic Society*, **16**[11] 1237–1244.
177. S. Reinsch, R. Müller, and G. Völksch (1998) Possibilities of reducing surface nucleation of cordierite glass, in *Proceedings of the XVIIIth International Congress on Glass*, eds. M. K. Choudhary, N. T. Huff, and C. H. Drummond, III, San Francisco.
178. R. E. Dutton, S. Shamasundar, and S. L. Semiatin (1995) Modeling the hot consolidation of ceramic and metal powders, *Metallurgical and Materials Transactions a-Physical Metallurgy and Materials Science*, **26**[8] 2041–2051.
179. A. Karamanov and M. Pelino (2006) Sinter-crystallisation in the diopside-albite system part I. Formation of induced crystallisation porosity, *Journal of the European Ceramic Society*, **26**[13] 2511–2517.
180. W.-D. Sältzer and B. Schulz, An attempt to treat the viscosity as a transport property of two phase materials, in *Continuum Models of Discrete Systems 4: Proceedings of the Fourth International Conference on Continuum Models of Discrete Systems*, Stockholm, Sweden, June 29-July 3, ed. O. Brulin and R. K. T. Hsieh, pp. 423–430, North-Holland, Amsterdam, 1981.
181. A. R. Boccaccini (1998) On the viscosity of glass composites containing rigid inclusions, *Materials Letters*, **34**[3–6] 285–289.
182. A. R. Boccaccini, K. D. Kim, and G. Ondracek (1995) On the viscosity of glass melts and porous sintered glasses, *Materialwissenschaft und Werkstofftechnik*, **26**[5] 263–268.
183. R. Roscoe (1952) The viscosity of suspensions of rigid spheres, *British Journal of Applied Physics*, **3**[Aug] 267–269.
184. R. Brückner and J. Deubener (1997) Description and interpretation of the two phase flow behaviour of melts with suspended crystals, *Journal of Non-Crystalline Solids*, **209**[3] 283–291.
185. J. Deubener and R. Brückner (1997) Influence of nucleation and crystallisation on the rheological properties of lithium disilicate melt, *Journal of Non-Crystalline Solids*, **209**[1-2] 96–111.
186. T. Honek, B. Hausnerova, and P. Saha (2005) Relative viscosity models and their application to capillary flow data of highly filled hard-metal carbide powder compounds, *Polymer Composites*, **26**[1] 29–36.
187. T. F. Tadros (1980) Physical stability of suspension concentrates, *Advances in Colloid and Interface Science*, **12**[2-3] 141–261.
188. M. Thies, Herstellung und rheologische Eigenschaften von porösen Kalk-Natron-Silicatschmelzen, Dr. rer. nat. Thesis, Fakultät III Prozesswissenschaften, TU Berlin, 2002.
189. A. Thiel, Fließverhalten von Glasmatrixkompositen für LTCC-Anwendungen, Dr.-Ing. Thesis, Fakultät für Natur- und Materialwissenschaften, TU Clausthal, 2009.
190. M. Eberstein, R. Müller, S. Reinsch, T. Rabe, W. A. Schiller, A. Thiel, and J. Deubener (2007) Kinetic modelling of LTCC shrinkage: Effect of alumina content, *Journal of Microelectronics and Electronic Packaging*, **4**[4] 173–180.



191. A. R. Boccaccini (1994) Sintering of glass matrix composites containing  $\text{Al}_2\text{O}_3$  platelet inclusions, *Journal of Materials Science*, **29**[16] 4273–4278.
192. M. J. Pascual, A. Duran, M. O. Prado, and E. D. Zanotto (2005) Model for sintering devitrifying glass particles with embedded rigid fibers, *Journal of the American Ceramic Society*, **88**[6] 1427–1434.
193. M. J. Pascual, A. Duran, and L. Pascual (2002) Sintering behaviour of composite materials borosilicate glass- $\text{ZrO}_2$  fibre composite materials, *Journal of the European Ceramic Society*, **22** 1513–1524.
194. Y. C. Fang and J. H. Jean (2007) Effects of alumina on densification of a low-temperature cofired crystallizable glass plus alumina system, *Japanese Journal of Applied Physics Part I-Regular Papers Brief Communications & Review Papers*, **46**[6A] 3475–3480.
195. R. Müller, R. Meszaros, B. Peplinski, S. Reinsch, M. Eberstein, W. A. Schiller, and J. Deubener (2009) Dissolution of alumina, sintering, and crystallization in glass ceramic composites for LTCC, *Journal of the American Ceramic Society*, **92**[8] 1703–1708.
196. D. A. Weirauch, J. E. Lazaroff, and P. D. Ownby (1995) Wetting in an electronic packaging ceramic system .2. Wetting of alumina by a silicate glass melt under controlled  $\text{P}(\text{O}_2)$  conditions, *Journal of the American Ceramic Society*, **78**[11] 2923–2928.
197. Y. Imanaka, S. Aoki, N. Kamehara, and K. Niwa (1995) Cristobalite phase-formation in glass/ceramic composites, *Journal of the American Ceramic Society*, **78**[5] 1265–1271.
198. J. Liu, F. Verhaeghe, M. Guo, B. Blanpain, and P. Wollants (2007) In situ observation of the dissolution of spherical alumina particles in  $\text{CaO-Al}_2\text{O}_3\text{-SiO}_2$  melts, *Journal of the American Ceramic Society*, **90**[12] 3818–3824.
199. B. J. Monaghan and L. Chen (2004) Dissolution behavior of alumina micro-particles in  $\text{CaO-SiO}_2\text{-Al}_2\text{O}_3$  liquid oxide, *Journal of Non-Crystalline Solids*, **347**[1–3] 254–261.
200. Z. Hashin and S. Shtrikman (1963) A variational approach to the theory of the elastic behaviour of multiphase materials, *Journal of the Mechanics and Physics of Solids*, **11**[2] 127–140.
201. R. Brückner (1992) Glass composites, *Boletin de la Sociedad Española de Cerámica y Vidrio*, **31C**[1, Invited lectures] 97–118.
202. I. W. Donald and P. W. McMillan (1976) Review ceramic-matrix composites, *Journal of Materials Science*, **11**[5] 949–972.
203. I. W. Donald (1995) Preparation, properties and applications of glass and glass-ceramic matrix composites, *Key Engineering Materials*, **108–110** 123–144.
204. A. R. Boccaccini (1999) Glass matrix composite materials with dispersion reinforcement. A review. Part 1: Historical development and fabrication techniques, *Verre*, **5**[2] 3–14.
205. A. R. Boccaccini (1999) Glass matrix composite materials with dispersion reinforcement. A review. Part 2: Properties and applications, *Verre*, **5**[3] 3–11.
206. A. R. Boccaccini (2001) Glass and glass-ceramic matrix composite materials, *Journal of the Ceramic Society of Japan*, **109**[7] S99–S109.
207. J. A. Roether and A. R. Boccaccini, Dispersion-reinforced glass and glass-ceramic matrix composites, in *Handbook of Ceramic Composites*, ed. N. Bansal, pp. 485–509, Kluwer Academic Publishers, Boston/Dordrecht/London, 2005.
208. A. R. Boccaccini (2003) Glass and glass-ceramic matrix composites, *Glass Science and Technology*, **76C1** 8–13.

209. A. R. Boccaccini, Continuous fibre reinforced glass and glass-ceramic matrix composites, in *Handbook of Ceramic Composites*, ed. N. Bansal, pp. 461–484, Kluwer Academic Publishers, Boston/Dordrecht/London, 2005.
210. Y. Waku, M. Suzuki, Y. Oda, and Y. Kohtoku (1997) Improving the fracture toughness of  $\text{MgO-Al}_2\text{O}_3\text{-SiO}_2$  glass/molybdenum composites by the microdispersion of flaky molybdenum particles, *Journal of Materials Science*, **32**[17] 4549–4557.
211. E. Claxton, B. A. Taylor, and R. D. Rawlings (2002) Processing and properties of a bioactive glass-ceramic reinforced with ductile silver particles, *Journal of Materials Science*, **37**[17] 3725–3732.
212. R. H. Dungan, J. A. Gilbert, and J. C. Smith (1973) Preparation and mechanical properties of composites of fused  $\text{SiO}_2$  and W fibers, *Journal of the American Ceramic Society*, **56**[6] 345–345.
213. A. R. Boccaccini, G. Ondracek, and C. Syhre (1994) Borosilicate glass matrix composites reinforced with short metal fibers, *Glastechnische Berichte-Glass Science and Technology*, **67**[1] 16–20.
214. J. J. Brennan and K. M. Prewo (1982) Silicon-carbide fiber reinforced glass-ceramic matrix composites exhibiting high-strength and toughness, *Journal of Materials Science*, **17**[8] 2371–2383.
215. I. W. Donald, B. L. Metcalfe, and D. J. Bradley (1990) Metal filament and ceramic fibre reinforced glass-ceramic matrix composites, *Institute of Physics Conference Series No.*, **111** 207–216.
216. S. Reinsch, C. Reich, and R. Brückner (1995) Optimized preparation parameters of unidirectionally c-fiber-reinforced glass-ceramics of the systems mas and bmas, *Journal of Materials Science*, **30**[22] 5632–5638.
217. C. Reich and R. Brückner (1997) Effect of preparation parameters on the properties of unidirectional SiC-fibre-reinforced MAS and BMAS glass-ceramics, *Composites Science and Technology*, **57**[5] 533–541.
218. A. G. Schott (2010) Fiber-reinforced glass, collaborations on composites, [http://www.schott.com/magazine/english/info102/si102\\_106\\_cooperation.html](http://www.schott.com/magazine/english/info102/si102_106_cooperation.html). In *Online Magazine—Info102*.
219. S. R. Levitt (1973) High-strength graphite fiber lithium aluminosilicate composites, *Journal of Materials Science*, **8**[6] 793–806.
220. R. A. J. Sambell, D. C. Phillips, and D. H. Bowen (1974) The technology of carbon-fibre-reinforced glasses and ceramics, in Proceedings of the International Conference “Carbon Fibres: Their Place in Modern Technology, pp. 105–113, London.
221. H. Hegeler and R. Brückner (1989) Fiber reinforced glasses, *Journal of Materials Science*, **24**[4] 1191–1194.
222. W. Pannhorst, M. Spallek, R. Brückner, H. Hegeler, C. Reich, G. Grathwohl, B. Meier, and D. Spelmann (1990) Fiber-reinforced glasses and glass ceramics fabricated by a novel process, *Ceramic Engineering and Science Proceedings*, **11**[7-8] 947–963.
223. J. W. Fergus (2005) Sealants for solid oxide fuel cells, *Journal of Power Sources*, **147**[1-2] 46–57.
224. R. N. Singh (2007) Sealing technology for solid oxide fuel cells (SOFC), *International Journal of Applied Ceramic Technology*, **4**[2] 134–144.
225. P. Geasee, T. Schwickert, U. Diekmann, and R. Conradt (2001) Glass from the system  $\text{RO-R}_2\text{O}_3\text{-SiO}_2$  as sealants of high chromium steel components in the planar SOFC, in



- Proceedings of the 7th International Symposium on Ceramic Materials and Components for Engines, eds. J. G. Heinrich and F. Aldinger, pp. 57–62.
226. T. Schwickert, R. Sievering, P. Geasee, and R. Conradt (2002) Glass-ceramic materials as sealants for SOFC applications, *Materialwissenschaft Und Werkstofftechnik*, **33**[6] 363–366.
  227. P. Holtappels and U. Stimming, Solid oxide fuel cells (SOFC), in *Handbook of Fuel Cells—Fundamentals, Technology and Applications*, Vol 1, Part 4, eds. W. Vielstich, A. Lamm, and H. A. Gasteiger, pp. 335–354, John Wiley & Sons, Chichester, 2003.
  228. K. L. Ley, M. Krumpelt, R. Kumar, J. H. Meiser, and J. Bloom (1996) Glass-ceramic sealants for solid oxide fuel cells .1. Physical properties, *Journal of Materials Research*, **11**[6] 1489–1493.
  229. S. P. Jiang, L. Christiansen, B. Hugan, and K. Foger (2001) Effect of glass sealant materials on microstructure and performance of Sr-doped LaMnO<sub>3</sub> cathodes, *Journal of Materials Science Letters*, **20**[8] 695–697.
  230. I. W. Donald, B. L. Metcalfe, and L. A. Gerrard (2008) Interfacial reactions in glass-ceramic-to-metal seals, *Journal of the American Ceramic Society*, **91**[3] 715–720.
  231. N. H. Menzler, D. Sebold, M. Zahid, S. M. Gross, and T. Koppitz (2005) Interaction of metallic SOFC interconnect materials with glass-ceramic sealant in various atmospheres, *Journal of Power Sources*, **152**[1] 156–167.
  232. N. P. Bansal and E. A. Gamble (2005) Crystallization kinetics of a solid oxide fuel cell seal glass by differential thermal analysis, *Journal of Power Sources*, **147**[1-2] 107–115.
  233. S. Ghosh, A. D. Sharma, P. Kundu, and R. N. Basu (2008) Glass-ceramic sealants for planar IT-SOFC: A bilayered approach for joining electrolyte and metallic interconnect, *Journal of the Electrochemical Society*, **155**[5] B473–B478.
  234. S. M. Gross, T. Koppitz, J. Rimmel, and U. Reisgen (2005) Glass-ceramic materials of the system BaO-CaO-SiO<sub>2</sub> as sealants for SOFC applications, in *Proceedings of the Ceramic Engineering and Science Proceedings*, eds. N. Bansal, D. Zhu, and W. M. Kriven, pp. 239–245.
  235. K. D. Meinhardt, D. S. Kim, Y. S. Chou, and K. S. Weil (2008) Synthesis and properties of a barium aluminosilicate solid oxide fuel cell glass-ceramic sealant, *Journal of Power Sources*, **182**[1] 188–196.
  236. M. J. Pascual, A. Guillet, and A. Duran (2007) Optimization of glass-ceramic sealant compositions in the system MgO-BaO-SiO<sub>2</sub> for solid oxide fuel cells (SOFC), *Journal of Power Sources*, **169**[1] 40–46.
  237. J. Piao, K. Sun, and X. Chen (2008) Compatibility between glass sealants and electrode materials of solid oxide fuel cells, *Rare Metals*, **27**[4] 378–383.
  238. A. Rost, J. Schilm, M. Kusnezoff, and A. Michaelis (2010) Degradation of sealing glasses under electrical load, in *Proceedings of the 9th European Solid Oxide Fuel Cell Forum*, ed. P. Connor, pp. 13-12–13-23 Luzern.
  239. F. Smeacetto, M. Salvo, F. D. D. Bytner, P. Leone, and M. Ferraris (2010) New glass and glass-ceramic sealants for planar solid oxide fuel cells, *Journal of the European Ceramic Society*, **30**[4] 933–940.
  240. S. M. Gross, T. Koppitz, I. Rimmel, U. Reisgen, V. Verlotski, and R. Conradt (2005) Glass-ceramic composite as a new sealing material for SOFCs, in *Proceedings of the 9th International Symposium on Solid Oxide Fuel Cells*, pp. 1924–1931, Quebec.

241. S. M. Gross, D. Federmann, J. Remmel, and M. Pap (2010) Reinforced composite sealants for SOFC applications, in Proceedings of the 9th European Solid Oxide Fuel Cell Forum, ed. P. Connor, pp. 13-24-13-31, Luzern.
242. S. M. Gross, T. Koppitz, J. Remmel, J. B. Bouche, and U. Reisgen (2006) Joining properties of a composite glass-ceramic sealant, *Fuel Cells Bulletin*, **2006**[9] 12-15.
243. K. Eichler, G. Solow, P. Otschik, and W. Schaffrath (1999) BAS ( $\text{BaO} \cdot \text{Al}_2\text{O}_3 \cdot \text{SiO}_2$ )-glasses for high temperature applications, *Journal of the European Ceramic Society*, **19**[6-7] 1101-1104.
244. S. Nakamura (1976) Crystallized glass article having a surface pattern, Patent US000003955989A.
245. A. Sakamoto and S. Yamamoto (2010) Glas-ceramics: Engineering principles and applications, *International Journal of Applied Glass Science*, **1**[3] 237-247.
246. A. Karamanov, I. Gutzow, I. Penkov, J. Andreev, and B. Bogdanov (1994) Diopside marble-like sintered glass-ceramics, *Glastechnische Berichte-Glass Science and Technology*, **67**[7] 202-206.
247. L. Nippon Electric Glass Co. Neopariés gallery, <http://www.neg.co.jp/arch/>.
248. M. W. Davies, B. Kerrison, W. E. Gross, M. J. Robson, and D. F. Wichall (1970) Slagceram—A glass ceramic from blast-furnace slag, *Journal of the Iron and Steel Institute*, **208** 348-34&.
249. P. D. Sarkisov (1989) The modern state of technology and application of glass-ceramics, in Proceedings of the XVth International Congress on Glass, pp. 411-441, Leningrad.
250. E. Bernardo, M. Varrasso, F. Cadamuro, and S. Hreglich (2006) Vittrification of wastes and preparation of chemically stable sintered glass-ceramic products, *Journal of Non-Crystalline Solids*, **352**[38-39] 4017-4023.
251. A. Karamanov (2009) Granite like materials from hazardous wastes obtained by sintercrystallisation of glass frits, *Advances in Applied Ceramics*, **108**[1] 14-21.
252. E. Bernardo, R. Castellan, S. Hreglich, and I. Lancellotti (2006) Sintered sanidine glass-ceramics from industrial wastes, *Journal of the European Ceramic Society*, **26**[15] 3335-3341.
253. E. Bernardo, R. Castellan, and S. Hreglich (2007) Sintered glass-ceramics from mixtures of wastes, *Ceramics International*, **33**[1] 27-33.
254. L. Barbieri, A. Corradi, and I. Lancellotti (2000) Bulk and sintered glass-ceramics by recycling municipal incinerator bottom ash, *Journal of the European Ceramic Society*, **20**[10] 1637-1643.
255. L. Barbieri, A. Corradi, I. Lancellotti, G. C. Pellacani, and A. R. Boccaccini (2003) Sintering and crystallisation behaviour of glass frits made from silicate wastes, *Glass Technology*, **44**[5] 184-190.
256. A. Karamanov, M. Aloisi, and M. Pelino (2005) Sintering behaviour of a glass obtained from MSWI ash, *Journal of the European Ceramic Society*, **25**[9] 1531-1540.
257. H. S. Kim, R. D. Rawlings, and P. S. Rogers (1989) Sintering and crystallization phenomena in silceram glass, *Journal of Materials Science*, **24**[3] 1025-1037.
258. A. R. Boccaccini, M. Bucker, and J. Bossert (1996) Glass and glass-ceramics from coal fly-ash and waste glass, *Tile & Brick International*, **12**[6] 515-518.
259. A. R. Boccaccini, M. Bucker, J. Bossert, and K. Marszalek (1997) Glass matrix composites from coal flyash and waste glass, *Waste Management*, **17**[1] 39-45.

260. M. Ferraris, M. Salvo, F. Smeacetto, L. Augier, L. Barbieri, A. Corradi, and I. Lancellotti (2001) Glass matrix composites from solid waste materials, *Journal of the European Ceramic Society*, **21**[4] 453–460.
261. E. Bernardo, F. Andreola, L. Barbieri, and I. Lancellotti (2005) Sintered glass-ceramics and glass-ceramic matrix composites from CRT panel glass, *Journal of the American Ceramic Society*, **88**[7] 1886–1891.
262. E. Bernardo, G. Scarinci, and S. Hreglich (2005) Development and mechanical characterization of  $\text{Al}_2\text{O}_3$  platelet-reinforced glass matrix composites obtained from glasses coming from dismantled cathode ray tubes, *Journal of the European Ceramic Society*, **25**[9] 1541–1550.
263. I. Rozenstrauha, R. Cimmins, L. Berzina, D. Bajare, J. Bossert, and A. R. Boccaccini (2002) Sintered glass-ceramic matrix composites made from Latvian silicate wastes, *Glass Science and Technology*, **75**[3] 132–139.
264. E. B. Ferreira, E. D. Zanotto, and L. A. M. Scudeller (2002) Glass and glass-ceramic from basic oxygen furnace (BOF) slag, *Glass Science and Technology*, **75**[2] 75–86.
265. V. Gorobinskay, I. Kravtchenko, J. Bossert, and J. Stäblein (1998) Sintered crystallization of waste containing harmful components, in Proceedings of the XVIIIth International Congress on Glass, eds. M. K. Choudhary, N. T. Huff, and C. H. Drummond, III, San Francisco.
266. A. Karamanov, M. Aloisi, and M. Pelino (2007) Vitrification of copper flotation waste, *Journal of Hazardous Materials*, **140**[1-2] 333–339.
267. A. Karamanov, I. Gutzow, I. Chomakov, J. Christov, and L. Kostov (1994) Synthesis of wall-covering glass-ceramics from waste raw-materials, *Glastechnische Berichte-Glass Science and Technology*, **67**[8] 227–230.
268. A. Karamanov, M. Pelino, and A. Hreglich (2003) Sintered glass-ceramics from municipal solid waste-incinerator fly ashes—Part 1: The influence of the heating rate on the sinter-crystallisation, *Journal of the European Ceramic Society*, **23**[6] 827–832.
269. A. Karamanov, G. Taglieri, and M. Pelino (1999) Iron-rich sintered glass-ceramics from industrial wastes, *Journal of the American Ceramic Society*, **82**[11] 3012–3016.
270. R. D. Rawlings, J. P. Wu, and A. R. Boccaccini (2006) Glass-ceramics: Their production from wastes—a review, *Journal of Materials Science*, **41**[3] 733–761.
271. P. A. Bingham and R. J. Hand (2006) Vitrification of toxic wastes: A brief review, *Advances in Applied Ceramics*, **105**[1] 21–31.
272. P. Colombo, G. Brusatin, E. Bernardo, and G. Scarinci (2003) Inertization and reuse of waste materials by vitrification and fabrication of glass-based products, *Current Opinion in Solid State & Materials Science*, **7**[3] 225–239.
273. R. Gutmann (1996) Thermal technologies to convert solid waste residuals into technical glass products, *Glastechnische Berichte-Glass Science and Technology*, **69**[9] 285–299.
274. M. Pelino (2000) Recycling of zinc-hydrometallurgy wastes in glass and glass ceramic materials, *Waste Management*, **20**[7] 561–568.
275. E. Bernardo (2008) Fast sinter-crystallization of a glass from waste materials, *Journal of Non-Crystalline Solids*, **354**[29] 3486–3490.
276. R. R. Tummala (1991) Ceramic and glass-ceramic packaging in the 1990s, *Journal of the American Ceramic Society*, **74**[5] 895–908.
277. D. L. Wilcox and M. Oliver (2002) LTCC, an interconnect technology morphing into a strategic microsystem integration technology, in Proceedings of the Advanced Technology Workshop on Ceramic Applications for Microwave and Photonic Packaging, Providence, RI.

278. Y. Imanaka, *Multilayered Low Temperature Cofired Ceramics (LTCC) Technology*. Springer, New York, 2005.
279. C. Modes, A. Kipka, and F. Gora (2008) Zero-shrinkage LTCCs, *CFI-Ceramic Forum International*, **85**[4] E29–E31.
280. T. Rabe, Hochintegrierte LTCC multilayer, in *Technische Keramische Werkstoffe*, Vol. 118, Ergänzungslieferung, ed. J. Kriegsmann, pp. 1–48, Deutsche Keramische Gesellschaft (DKG), HvB-Verlag GbR, Ellerau, 2010.
281. M. Gemeinert, Über LTCC-Werkstoffe aus dem Stoffsystem  $\text{CaO-La}_2\text{O}_3\text{-Al}_2\text{O}_3\text{-B}_2\text{O}_3$ , Dr.-Ing Thesis, Faculty of Mechanical, Process and Energy Engineering, Technische Universität Bergakademie Freiberg, 2009.
282. G. Riedel and W. Schiller (1990) Korundkeramik mit niedriger Sintertemperatur, *Keramische Zeitschrift*, **42**[3] 168–173.
283. M. Eberstein and W. A. Schiller (2003) Development of high-permittivity glasses for microwave LTCC tapes, *Glass Science and Technology*, **76**[1] 8–16.
284. O. Dernovsek, A. Naeini, G. Preu, W. Wersing, M. Eberstein, and W. A. Schiller (2001) LTCC glass-ceramic composites for microwave application, *Journal of the European Ceramic Society*, **21**[10–11] 1693–1697.
285. W. A. Schiller (2008) Keramische Multilayer für Mikrosysteme in den Bereichen: Sensorik, Automobilelektronik, Energietechnik und Biomedizin, in *Proceedings of the Vision Keramik 2008+*, Fraunhofer IKTS, Dresden, Germany.
286. W. A. Schiller (1995) Neue glaskeramische Kompositwerkstoffe mit hoher Wärmeleitfähigkeit für Multilayer-Substrate. In BMBF-Report 03M2726B3.
287. W. A. Schiller (1998) Entwicklung neuartiger Folien zur Herstellung innovativer Multilayer-Keramik-Substrate mit einer Funktionsebene in Dünnschichttechnik. In BMBF-Report 03N1010C0.
288. O. Dernovsek, G. Preu, W. Wersing, C. Modes, M. Eberstein, W. A. Schiller, W. Güther, and B. Schulz (2000) Glaskeramikmasse und Verwendung der Glaskeramikmasse, Patent DE 100 43 194 A1.
289. W. Höland, M. Frank, M. Schweiger, and V. Rheinberger (1994) Development of translucent glass-ceramics for dental application, *Glastechnische Berichte-Glass Science and Technology*, **67C** 117–122.
290. M. Frank, M. Schweiger, V. Rheinberger, and W. Höland (1998) High-strength translucent sintered glass-ceramics for dental application, *Glastechnische Berichte-Glass Science and Technology*, **71C** 345–348.
291. M. Schweiger, W. Höland, M. Frank, H. Drescher, and V. Rheinberger (1999) IPS Empress®2: A new pressable high strength glass-ceramic for esthetical ceramic restoration, *Quintessence of Dental Technology*, **22** 143–152.
292. W. Höland, M. Schweiger, M. Frank, and V. Rheinberger (2000) A comparison of the microstructure and properties of the IPS Empress®2 and the IFS Empress® glass-ceramics, *Journal of Biomedical Materials Research*, **53**[4] 297–303.
293. W. Höland, V. Rheinberger, E. Apel, and C. Ritzberger (2004) Lithiumdisilicate metal-free three-unit bridge. TC Presentation, ICG, Kyoto.

---

# PART II

---

## CHEMICAL METHODS

---

# COLLOIDAL METHODS

RODRIGO MORENO

## 4.1 INTRODUCTION

New engineered materials with enhanced properties are necessary to meet the increasing demands of emerging technologies. This makes it necessary to improve the properties of the materials involved in every device as the technical exigencies are always growing. When searching a new material, the first issue to be considered is the profile of properties it must satisfy. A second aspect is the capability to produce a component with the desired geometry, size, and microstructure; that is, the choice of materials and processing routes is intimately related. However, the shaping itself can change or even determine the properties of the final material [1].

It is possible to classify the different engineering materials into three families: ceramics (with a unified vision that would include glasses and glass-ceramics), polymers (including plastics and elastomers), and metals [2]. *Metals* are usually stiff and tough, but also soft and easily deformed, although they can be made strong by alloying and by mechanical and heat treatment [3]. The ductility of metals allows them to be formed by deformation processes. *Ceramics* are nonmetallic, inorganic solids that harden after a thermal treatment that provides high resistance to corrosion and chemicals, high refractoriness, hardness, and so on [4]. However, a major limitation of

---

*Ceramics and Composites Processing Methods*, First Edition. Edited by Narottam P. Bansal and Aldo R. Boccaccini.

© 2012 The American Ceramic Society. Published 2012 by John Wiley & Sons, Inc.

ceramic materials is their inherent brittleness. This gives low tolerance to stress concentrations, and thus makes processing more difficult than for metals. Since ceramics are usually formed from powders, some typical shaping processes of metals like deformation methods cannot be used for ceramics. An important drawback of powder processing is the strong tendency of powders to agglomeration, which is one of the most important parameters to be controlled in processing science and technology. *Polymers* are organic solids built up from the association of unit chains of carbon atoms, the so-called monomers. Polymers are light and floppy, and the properties strongly depend on temperature. They are easy to shape into complicated parts by melting and pouring or injection into a mold cavity.

Regarding the raw materials, metals and ceramics have several factors in common, as mining and powder processing on one hand and the need for a thermal treatment to get the final microstructure on the other hand. As a consequence, ceramics and metal-ceramic composites have many similarities and can be processed using the same techniques. This is not possible for polymer derivatives and composites since any thermal treatment would destroy the polymer structure.

A great effort has been devoted in the last two decades to improve the performance of ceramics for thermal, wear, corrosion, and structural applications. During this period, typical values of strength and toughness have multiplied by three times. Strength is a measurement of the resistance to formation of a crack or structural damage in the material when a load is applied. Toughness indicates the resistance of the material to the propagation of a crack or extension of damage to the point of failure [4, 5]. The Weibull modulus is a measurement of the uniformity in strength.

The major weakness of ceramics continues to be brittleness since the partial covalency of the bonds is very rigid and does not allow plasticity. The toughness ( $K_{IC}$ ) of a material is directly proportional to the fracture stress and is inversely proportional to the square root of the flaw size ( $c$ ):

$$\sigma_f \propto \frac{K_{IC}}{\sqrt{c}}. \quad (4.1)$$

This simple equation relates the defect size and the toughness; that is, it constitutes the basis for the establishment of the proper relationships between processing and properties. Better strength can be obtained in two ways: on one hand, by increasing the toughness of the material, which is possible by selecting new tougher materials or by the enhancement of the properties through a suitable microstructural design; on the other hand, the strength increases when the critical flaw size decreases, that is, by controlling the different steps involved in the processing cycle.

Ashby et al. [1] have done a taxonomic classification of the types of materials and the types of processes for their manufacture. Materials can be divided into classes, subclasses, and members, each of which is characterized by a set of *attributes*: its properties. Similarly, a taxonomic classification of processes can be also established, as reported by Ashby et al. [1] These authors classify also the manufacturing processes into three families, namely, *shaping*, *joining*, and *surface treatment*, each one dividing into classes, such as casting, deformation, molding, special procedures, and prototyping, which are the six

families of shaping. Molding can be classified into the following subclasses: injection, extrusion, rotation, transfer, compression, blowing, and so on. The choice of the process depends on the material properties, on one hand, and on the shape, dimensions, tolerance, roughness, thickness, lot size, and production costs, on the other hand [6]. However, this classification may not be the best for ceramics since some of these processes cannot be used, as in the case of deformation methods, for example. The manufacture of ceramics is less controlled as it starts in most cases from powders, so that powder processing techniques are mainly used. In ceramic processing, the starting powders are transformed into a complex-shaped part through several processing steps, each one being a possible source of defects. The defects introduced at any stage will persist in the subsequent stages. If the starting powders have defects, they could not be removed during their consolidation, so that the purity and control of the starting powders is a first key parameter to obtain defect-free materials. This explains the great development of the synthesis routes and their implications in ceramics [6–8]. But this also requires a careful control of every parameter at any step to avoid the creation of new defects [9, 10].

## 4.2 INTRODUCTION TO CERAMIC PROCESSING

The overall fabrication of a ceramic product consists of a series of discrete steps whose number depends on the complexity of the method itself. These steps are known as processing steps. During processing, one or more starting powders have to be transformed into a solid product with the desired shape and microstructure [11–14].

Ceramics are mainly produced by powder processing techniques according to the following processing steps: (1) powder synthesis and/or preparation for further consolidation; (2) consolidation of powders into a self-supported shaped body, the so-called *green body*; (3) drying and burnout of organics; (4) sintering at high temperature to reach the final microstructure and properties; and (5) final machining and shaping, which is the most expensive step due to the hardness of ceramics. Maximum control at any stage is necessary since defects introduced in one step are very difficult to remove and will persist in the next steps.

Figure 4.1 summarizes the main steps of a ceramic processing cycle. In the first step, the raw materials are selected. These raw materials can be natural or synthetic. These powders normally require a transformation through different processes in order to make them suitable for further consolidation. These transformation operations are referred to as *beneficiation processes*, which include milling and mixing, washing, separation, filtration, and granulation [13, 14]. It must be considered that even in the case of dry pressing, suspensions are frequently used because the starting powders are normally spray-dried to produce controlled agglomerates able to deform plastically during pressing, thus contributing to improve compaction and to obtain higher green densities.

Once the powders have been properly modified, they must be consolidated into bodies by some shaping procedure [11–14]. Forming methods can be classified according to three categories, depending on the relative content of the liquid characteristic of the process: (1) dry pressing methods, where the liquid content is typically lower than



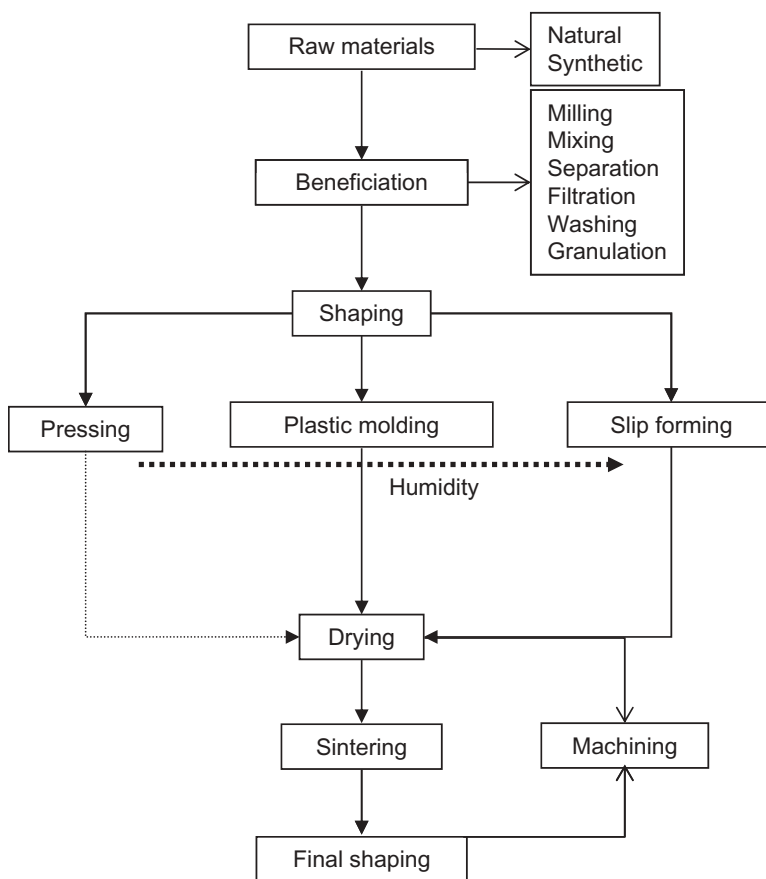


**Figure 4.1.** Flowchart of the different steps of a ceramic processing cycle.

7%; (2) plastic forming, with typical liquid contents of 15–20% for extrusion or up to 30–40% in the case of injection molding; and (3) colloidal shaping methods that make use of suspensions, where the content of liquid is generally higher than 50%.

The most widely used forming techniques are those based in the simple compaction of powders into a die by the application of pressure through a piston (axial pressing) or by applying the pressure uniformly in all directions, this being the principle of so-called isostatic pressing.

When the moisture content increases over 15–20 vol %, a viscous paste that can deform plastically is formed. The origin of this kind of processes is associated with the intrinsic plasticity of clays and is referred to as plastic molding. The first technique that one can imagine within this group is the pottery wheel, and later, jiggering, which is industrially used for the production of bowls, plates, and cups. Another plastic-forming technique with great industrial significance is extrusion, where a viscous paste is introduced in the extruder and a piston or screw moves the extrusion column to a nozzle.

Extrusion is very commonly used in the manufacture of building components, such as bricks and roof tiles, and in the production of filters and catalysts. Considering the plasticity of the viscous pastes used, the injection molding process can be considered as a plastic-forming technique. In this case, the ceramic powder is dispersed in a polymer melt; in the most general case, a thermoplastic polymer and the mixture is prepared on heating. The hot mixture is injected into a mold cavity, which is refrigerated so that the injected paste consolidates in a few seconds. However, once the body is formed, it contains a large amount of organics (up to 40 vol % or more), which have to be slowly removed. For so doing, the sintering schedule should include a previous stage for the debinding, and there is a relatively large number of pieces that must be rejected. This technique is so complicated, expensive, and both energy- and time-consuming so that it can be used only with many restrictions.

If the moisture content increases over 50 vol %, then suspensions are formed in which particles are dispersed in a liquid (normally water). The control of the interparticle forces allows one to produce stable suspensions in which particles repel each other, and this repulsion is maintained even during consolidation. This means that very homogeneous and dense green bodies can be obtained at a very low cost and practically no investment. The reference technique for suspensions forming is slip casting, which is the source of a number of forming methods, such as those based on filtration like pressure casting or centrifugal casting, and other methods based in consolidation mechanisms different from filtration, such as evaporation, flocculation, polymerization, and gelation, among others. This will be studied in detail later.

### 4.3 ADDITIVES FOR CERAMIC PROCESSING

As stated before, ceramic manufacturing consists of different steps from the raw materials to the final shaped body, and these transformation steps are commonly performed with the help of processing aids that allow the control of the characteristics of the powders at the different stages as desired. These processing aids are known as additives and can be classified at the first level as organic and inorganic additives [15, 16].

The additives are basically the same for any processing technique, although some specific tasks must be considered for each technique depending on size, thickness, consistency, and so on. In the first approach, processing aids can be divided into two categories, depending on whether they promote repulsion or attraction among particles, that is, dispersion aids or binding additives. Dispersing substances include obviously the liquid media and solvents, deflocculants, and other substances like the so-called wetting agents, homogenizers, and others. All these additives are used in wet processing, and all of them can be considered as dispersants. Similarly, extrusion and dry pressing make use of lubricants, which are fatty acids, stearates, and so on, the same used in suspensions as nonionic surfactants. Many times, the same additives receive different names in different sectors. The second group of additives serves the opposite purpose, to approach particles that come into contact. This is the case of binders and plasticizers, flocculants and coagulants, gelling additives, and so on. Table 4.1 summarizes the different types of additives used in ceramic processing.

TABLE 4.1. Types of Additives Used in Ceramic Processing

Type of Additive	Inorganic	Organic
Deflocculants	Potential determining ions (pH) Electrolytes Salts ( $\text{NaCO}_3$ , $\text{Na}_2\text{SiO}_4$ , tripolyphosphates, hexametaphosphates, sulfonates)	Surfactants (nonionic, anionic, cationic, zwitterionic) Steric stabilizers (polymers) Electrosteric stabilizers (polyelectrolytes: cationic, poly(ethylenimine) (PEI); anionic, PAA)
Binders	Colloidal silica  Clays Silicates Cements	Cellulose derivatives (methyl cellulose [MC], carboxymethyl cellulose [CMC], hydroxyethyl cellulose [HEC]) Poly(vinyl alcohol) Poly(vinyl butyral) Alginates, starches, dextrans, gums
Plasticizers	Clays, bentonites	Glycols, phthalates
Lubricants	Colloidal talc, colloidal graphite	Fatty acids, oils, stearates
Coagulants	$\text{CaCl}_2$ , $\text{AlCl}_3$ , $\text{CaCO}_3$	Alginates, urea
Gel formers		Alginates, methylcellulose, starches Agar, agarose, carrageenan, gelatin

Liquids are used in ceramic processing to provide fluidity during formation for any suspension processing technique and to dissolve the additives to improve their dispersion and mixture with the powder. Water is always preferred because of environmental, health, and cost considerations. However, water has some drawbacks, such as its strong ability to form hydrogen bonds with hydroxyl groups at the particle surface and the low evaporation rate, which has limited its use in the production of thick films and tapes, as the drying gradient leads to cracking.

Organic solvents are preferred in the following cases: (1) when fast evaporation is needed, as in the tape-casting process; (2) to allow good dispersion and careful drying, as requested for milling operations, where water would lead to reagglomeration by hydrogen bonding; and (3) when powder can be affected by water, as in the case of metal powders or nonoxidic ceramics, or when the powders are hygroscopic (e.g., in  $\text{CaO}$ ,  $\text{MgO}$ ,  $\text{CaSO}_4$ ) or can dissolve under certain pH conditions (like  $\text{BaTiO}_3$  or  $\text{BaZrO}_3$ , or metals). However, the flammability, waste disposal, and toxicity have encouraged materials engineers toward increasing the use of water systems.

Deflocculants are used to provide repulsion among particles. This can be achieved by three general mechanisms: (1) electrostatic charging in the presence of electrolytes that promote electrostatic repulsion; (2) adsorption of polymers that provide steric hindrance and impedes particles to touch each other; and (3) adsorption of charged polymers (polyelectrolytes) where a steric hindrance avoids the contact at near-to-contact distance, whereas the charges promote an electrostatic repulsion at larger separation distances [17]

Binders are long-chain polymers that provide strength to the green bodies forming organic interparticle bridges, resulting in strong adhesion after solvent evaporation. There is a big variety of substances that can act as binders, either naturally occurring or synthetic. Most of them are soluble in organic solvents, being more difficult to select water-soluble binders [16, 18].

Plasticizers are organic molecules with low molecular weight, whose main role is to soften the rigid large molecules of the binder. A characteristic parameter of binders is the glass transition temperature ( $T_g$ ), which is usually between 40 and 50°C. The function of plasticizers is to attach to the binder molecules in order to reduce the  $T_g$  of the binders providing flexibility. The most frequently used plasticizers, in addition to water (pottery wheel with clay-based materials where water provides plasticity), are glycols and phthalates with low molecular weights [18].

## 4.4 INTRODUCTION TO COLLOIDAL SCIENCE

### 4.4.1 Colloidal Dispersions

A colloidal dispersion is defined as a multiphase system in which one phase (or more) is dispersed in a continuous phase or medium. At least one dimension lies within the nanometer ( $10^{-9}$  m) to micrometer ( $10^{-6}$  m) range, so that colloidal dispersions are mainly systems containing large molecules and/or small particles. The main factor determining the properties of a colloidal system are the particle size and shape, the surface properties, the interparticle interactions, and the interactions between particles and the dispersing medium. The interface between the dispersed phase and the dispersing medium plays an essential role in the surface properties, including adsorption, surface charge, electrical double layer, and so on. There are many reference textbooks on colloid and surface science where the reader can find complementary information [19–22].

The colloidal dispersions may be classified considering the state in which either the dispersed phase or the dispersing medium are present (solid, liquid, or gas). In early ceramic processing steps (i.e., before firing), the most common dispersion type is the suspension of powders in liquids. A colloidal dispersion may be *liophilic*, when the particles have affinity by the dispersing medium and tend to be wetted or solvated by the last, or *liophobic*, when particles repeal the liquid. If the dispersing medium is water, the terms *hydrophilic* and *hydrophobic* are used.

Suspensions are complex systems in which several interaction forces operate, such as the gravity, the Brownian motion, the attractive interaction by van der Waals forces, and the repulsive interactions necessary to overcome attraction and to avoid agglomeration [23–25].

### 4.4.2 The Attractive Potential

The attractive term of the interaction pair potential is generally the result of London–van der Waals dispersion forces. The van der Waals force is the result of the interaction

between a permanent dipole with another permanent dipole (Keesom interaction) or with a polarizable atom that produces an induced dipole (Debye interaction), or, when no permanent dipoles are present, instantaneous dipoles are formed arising from fluctuations in the distribution of electronic charge (London dispersion interaction). The latter is always present and plays a key role in the stability of the colloidal suspension.

The attractive interaction between two similar spherical particles of radius  $a$  at distance  $D$  (the distance between the centers being  $R = 2a + D$ ), as proposed by Hamaker, is

$$V_A = -\frac{A}{6} \left( \frac{2a^2}{R^2 - 4a^2} + \frac{2a^2}{R^2} + \ln \frac{R^2 - 4a^2}{R^2} \right), \quad (4.2)$$

where  $A$  is the *Hamaker constant*, which depends on the properties of both the particle and the dispersing medium. In the original Hamaker's treatment, known as the microscopic approach, the Hamaker constant is given by

$$A = \pi^2 \rho_1 \rho_2 B, \quad (4.3)$$

$\rho_i$  being the number of atoms (molecules) per cubic centimeter of each bulk phase and  $B$  the London constant, where  $B \sim 1/\alpha_0^2$ ,  $\alpha_0$  being the polarizability. This model considers Coulomb's theory, valid for small separation distances. For longer distances (molecular range), there is a retardation effect associated with a characteristic time ( $\lambda_0$ ) needed for the propagation, which makes the power law change to the inverse seventh power [26].

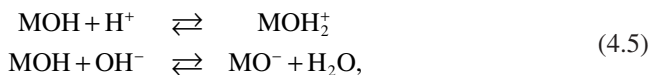
The Hamaker constants for most solvents are in the range  $4-8 \cdot 10^{-20}$  J; for polymers,  $6-10 \cdot 10^{-20}$  J; and for metals and ionic solids,  $10-30 \cdot 10^{-20}$  J. For two particles in a medium,  $A = A_{pp} + A_{mm} - 2A_{pm}$ , where  $A_{pp}$  and  $A_{mm}$  are the constants for the particles and for the medium and  $A_{pm}$  is associated with the particle-medium interaction and is generally assumed to be  $A_{pm} = (A_{pp}A_{mm})^{1/2}$ ; hence,  $A = (A_p^{1/2} - A_m^{1/2})^2$ , where  $A$  is always positive. For distances much higher than the particle radius, the attractive van der Waals interaction simply behaves as

$$V_A = -\frac{Aa}{12D}, \quad (4.4)$$

and it is extremely strong near the contact distance.

#### 4.4.3 The Repulsive Electrostatic Potential

Hydrous oxide surfaces are amphoteric and can be modeled by the following acid-base reactions:



where protons and hydroxyl ions can specifically adsorb. For this reason,  $H^+$  and  $OH^-$  are referred to as potential determining ions. The surface charge ( $\sigma_0$ ) can be expressed by the difference in adsorption density between  $H^+$  and  $OH^-$  adsorbed on the surface ( $\Gamma_H^+$  and  $\Gamma_{OH^-}$ , respectively), which is proportional to the adsorption density of cationic and anionic species:

$$\sigma_0 = F(\Gamma_{H^+} - \Gamma_{OH^-}) = f(\Gamma_{MOH_2^+} - \Gamma_{MO^-}), \quad (4.6)$$

$F$  being the Faraday constant (96,485 C).

The surface charge is negative at high pH values and the protons are attracted. When the concentration of the potential determining ion is altered, the relative adsorption of ions on the surface varies. There is a definite concentration for which the activities of positive and negative species are equal and the surface potential will be zero. This concentration is referred to as the *zero point of charge* (ZPC) [27, 28]. The ZPC defines the maximum destabilization, as there is no net surface charge. Hence, suspensions are stable only if the pH is kept far enough from the ZPC, as illustrated in Figure 4.2. In general, the ZPC decreases as the charge of the cation increases, being above 11–12 for MgO and CaO, about 9 for  $Al_2O_3$  and  $Y_2O_3$ , and decreasing to 5–6 for  $ZrO_2$  and  $TiO_2$ , and slightly lower for  $SiO_2$  (2–3). Moreover, the ZPC depends on the degree of hydration and on the presence of impurities and dopants. When a particulate system is dispersed in a polar liquid (aqueous or nonaqueous), a double layer is developed around each particle. The separation of charge occurring at an interface between two phases is called an *electrical double layer* because it consists ideally of two regions of opposite charge.

Gouy and Chapman proposed a diffuse double-layer model, consisting in a monolayer of *counterions* (e.g., inert electrolyte ions having the opposite charge of the

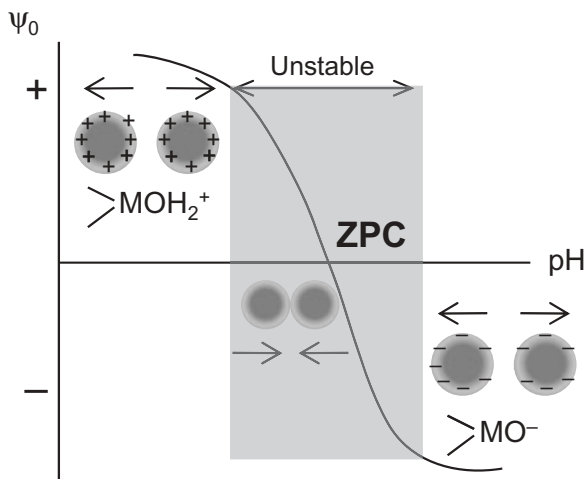


Figure 4.2. Variation of surface potential with pH.

surface charge) strongly adsorbed onto the surface (with an electrostatic potential,  $\psi_0$ ) and a diffuse double layer in which counterion concentration decreases as the distance from the surface increases. When different types of ions coexist in solution (i.e., there is added electrolyte), then the surface charge is given by the Grahame equation:

$$\sigma^2 = 2\epsilon\epsilon_0 kT \left[ \sum_i \rho_{\infty i} \exp\left(\frac{-ze\psi_0}{kT}\right) - \sum_i \rho_{\infty i} \right], \quad (4.7)$$

where  $\psi_0$  is the contact value of  $\psi_x$  (that at the surface) and  $\rho_{\infty i}$  is the ionic concentration of ions  $i$  in the bulk, at  $x = \infty$ , where  $\psi_\infty = 0$ . For low potentials, below 25 mV, the Grahame equation simplifies to

$$\sigma = \epsilon\epsilon_0 \kappa \psi_0, \quad (4.8)$$

where

$$\kappa = \left( \frac{\sum_i \rho_{\infty i} e^2 z_i^2}{\epsilon\epsilon_0 kT} \right)^{1/2}, \quad (4.9)$$

that defines a condenser whose two plates are separated by a distance  $1/\kappa$ , which is known as the Debye length and gives the thickness of the double layer. Its magnitude depends only on the medium properties and not on the properties of the surface, such as the charge and the potential.

Stern proposed that the electrolyte ions could not be considered as point charges because the finite size of the ions, hydrated or not, limits their maximum concentration and their distance of closest approach to the surface, as shown in Figure 4.3. If the surface is positive, the unhydrated anions are in contact with the surface, and the plane formed by the centers of the anions is called the inner Helmholtz plane (IHP). The cations remain hydrated and the plane crossing their centers is the outer Helmholtz plane (OHP).

When a particle is moving through the liquid, the Stern layer and part of the diffuse layer move with the particle. The potential at this plane of shear is referred to as the *zeta potential* ( $\zeta$ ), and it indicates the gradient of electrical potential when the surface potential is constant. The isoelectric point is defined as the pH value at which the zeta potential is zero. When there is no specific adsorption, the isoelectric point and the ZPC are the same. When specific adsorption occurs, the measurements of the zeta potential show that the isoelectric point shifts toward acidic pH values if the adsorbed species are anionic and toward basic pH values when the adsorbed species are cationic.

The total interaction potential between two particles is given by

$$V_R = \left( \frac{64\pi kT a \rho_\infty \gamma^2}{\kappa^2} \right) \exp(-\kappa D). \quad (4.10)$$

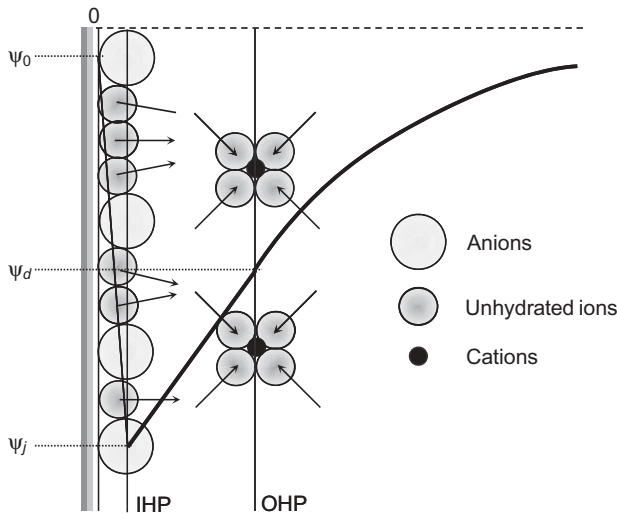


Figure 4.3. Stern model of the double layer.

#### 4.4.4 The Derjaguin–Landau and Verwey–Overbeek (DLVO) Theory

Derjaguin–Landau and Verwey–Overbeek proposed that the total interparticle potential in a polar liquid or electrolyte is obtained by the addition of the electrostatic repulsion  $V_R$  due to the overlap of the double layers and the van der Waals attraction  $V_A$  arising from electromagnetic fluctuations. Substituting the respective forms of both potentials,  $V_R$  and  $V_A$ , the interparticle potential is given by

$$V_T = V_R + V_A = \left( \frac{64\pi kTa\rho_\infty\gamma^2}{\kappa^2} \right) \exp(-\kappa D) - \frac{Aa}{12D}. \quad (4.11)$$

Figure 4.4 shows the resulting interaction potentials as a function of the distance, in which the following three characteristics can be observed:

1. A potential barrier preventing contact between particles
2. A primary minimum in which agglomerated particles are bound, and coagulation occurs
3. A secondary minimum, not always present, that can provide some stabilization by means of a liquid film between the particles. At this minimum, the suspension becomes flocculated. As the concentration of electrolyte increases, the total interaction curve shifts to lower values; that is, the double-layer thickness decreases. Above a certain critical electrolyte concentration (known as critical coagulation concentration [ccc]) the energy barrier falls below the  $V = 0$  axis, and particles coagulate rapidly.



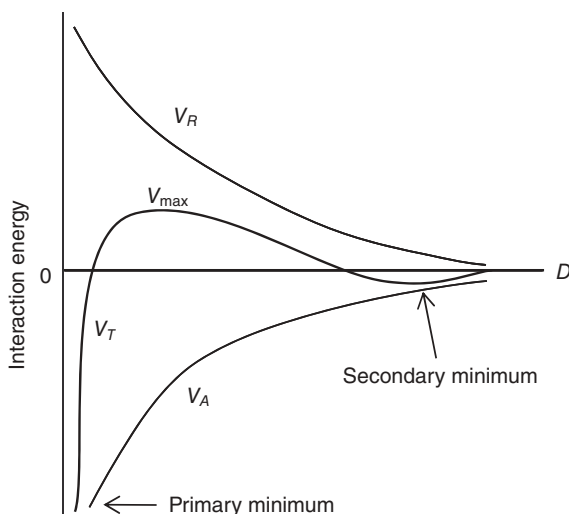


**Figure 4.4.** Potential energy of interaction as a function of distance according to the DLVO theory.

The efficiency of an electrolyte to precipitate or sequester depends on the tendency of its ions to hydrate. Then, we can establish a lyotropic series with decreasing precipitating power, according to the so-called Hofmeister series:  $\text{Mg}^{2+} > \text{Ca}^{2+} > \text{Sr}^{2+} > \text{Ba}^{2+} > \text{Li}^+ > \text{Na}^+ > \text{K}^+ > \text{NH}_4^+ > \text{Rb}^+ > \text{Cs}^+$ , and for anions,  $\text{citrate} > \text{SO}_4^{2-} > \text{Cl}^- > \text{NO}_3^- > \text{I}^- > \text{CNS}^-$ . The ccc varies as  $\rho_\infty \propto 1/z^6$ . This is referred to as the *Schultz-Hardy rule*. The flocculation values for counterions with charges 1, 2, and 3 decrease in the ratio 100.0:1.6:0.13, respectively. This is the reason why dispersants should contain monovalent cations because a small concentration of a divalent one is enough to produce flocculation.

So far, the interaction between similar particles has been described. When more than one type of particle is present, the situation becomes more complex. Interactions between dissimilar particles (in nature or in size) are referred to as heterocoagulation. From the DLVO theory, for spherical particles with  $\kappa a > 10$  and  $\psi_0 > 50$  mV, the potential energy of repulsion for two particles with radii  $a_1$  and  $a_2$  and potentials  $\psi_1$  and  $\psi_2$ , is given by the equation proposed by Hogg, Healy, and Fuerstenau:

$$V_R = \frac{2\pi\epsilon\epsilon_0 a_1 a_2}{(a_1 + a_2)} \left[ 2\psi_1 \psi_2 \ln \left( \frac{1 + \exp(-\kappa D)}{1 - \exp(-\kappa D)} \right) + (\psi_1^2 + \psi_2^2) \ln [1 - \exp(-\kappa D)] \right], \quad (4.12)$$

which becomes Equation 4.10 when  $a_1 = a_2$  and  $\psi_1 = \psi_2$ . Combining this with the appropriate form of the Hamaker equation, the total interparticle potential may be calculated.

When mixtures are to be prepared, the surface properties of each material should be evaluated independently. If particles have different isoelectric points, there is a region of pH values where particles with opposite charges are present, thus promoting

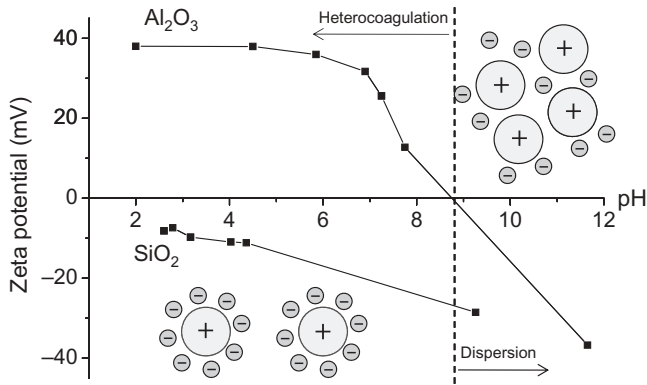


**Figure 4.5.** Zeta potentials of alumina and silica suspensions with different sizes and interactions by dispersion or heterocoagulation depending on pH conditions [31].

attractive electrostatic forces. Under these conditions, an agglomerated material will be obtained. However, heterocoagulation can be useful when particles are very different in nature or in size and shape. Let us consider the dispersion of a nanosized phase in a matrix of submicronic particles. This is a suitable procedure to obtain core-shell structures and to coat bigger particles with smaller ones [29–31]. Figure 4.5 illustrates the interaction between two phases with different size ranges, that is, a submicronic alumina and a nanosized silica, which are heterocoagulated to produce mullite by reaction sintering at high temperature [31]. The negatively charged silica nanoparticles are attracted to the surface of the positively charged alumina, which has a positive surface charge. There is a strong attraction that allows the formation of a shell layer of silica on the alumina one.

#### 4.4.5 Polymeric Stabilization

In some cases, stabilization with pH and/or electrolytes is not enough to provide the required stabilization because an excessive concentration of acid or base can lead to dissolution, aggressive conditions for handling, mold attack, or can simply provide very high ionic strength. Hence, the addition of suitable polymeric dispersants is commonly used to create stable colloidal suspensions [32, 33]. Polymeric stabilization may be achieved by two different mechanisms:

1. steric stabilization, where the macromolecules are attached to the particle surface, and
2. depletion stabilization, in which the macromolecules are free in suspension.

A schematic representation of both steric and depletion mechanisms is shown in Figure 4.6. Moreover, steric stabilization can be divided into two groups, dealing with either uncharged or charged systems. The last mechanism is known as *electrosteric* and results

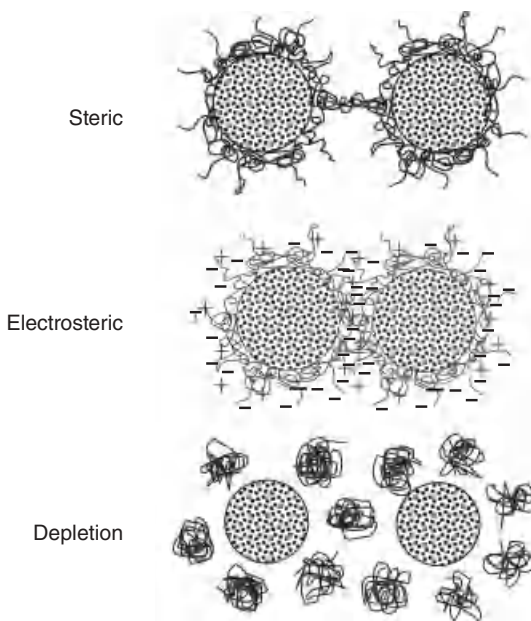


**Figure 4.6.** The different types of polymeric stabilization.

from the combination of electrostatic and steric contributions to the total interaction pair potential. In electrosteric stabilization, the electrostatic component may be due to a net charge on the particle surfaces and/or charges associated with the attached polymer. These charged polymers are referred to as polyelectrolytes and are widely used in most ceramic processes.

The best steric stabilizers are amphipathic block or graft copolymers. One of the comonomers generates a homopolymer that is not soluble in the dispersion medium and the other polymerizes to give a polymer that is soluble in the dispersion medium. The insoluble polymer attaches itself to the particle and is referred to as the anchor polymer. The role of the soluble part is to provide steric stabilization. For this reason, such chains are known as the *stabilizing moieties*.

The main requirements for steric stabilization of colloidal suspensions are (1) strong anchoring to the particle surface, (2) sufficient extension of the adsorbed long chain, (3) full coverage of the adsorbed polymer layer, and (4) *good solvent* condition of stabilizing moieties.

The conformation of polymers on the particle surface can take the form of trains, loops, and tails depending on the interaction strength between the polymer monomers and the surface, the solvency of the polymer chain, and also the polymer charge density in the case of polyelectrolytes. Increasing the molecular weight usually results in an increase of adsorption, thicker layers, and a larger relative fraction of loops at the expense of tails. Improved solvency reduces the overall adsorption but frequently increases the size of loops and tails and their extension into solution. Finally, increasing

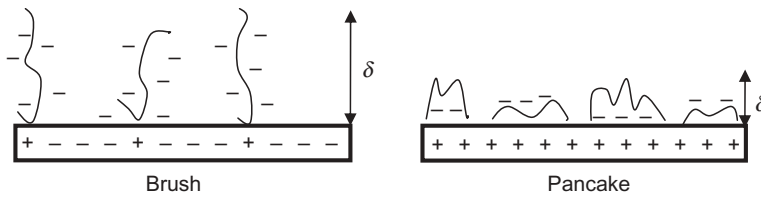


**Figure 4.7.** Schematic illustration of the conformation of an anionic polyelectrolyte on a ceramic surface as a function of pH ( $\delta$  is the thickness of the adsorbed polymer layer).

the strength of the monomer surface interaction leads to an increase of adsorption and an increase of the loop and tail extensions into solution. For suspensions dispersed in water with polycarboxylic acids (polyacrylic acid [PAA] or polymethylmethacrylate [PMMA])), the polyelectrolyte can take a brush conformation, at a pH slightly higher than the isoelectric point, where there are few positive charges at the surface and the strong repulsion of the charged polymer causes it to extend toward the medium. Oppositely, at a pH well below the isoelectric point, the oxide ceramic is positively charged and strongly interacts with the negatively charged polyelectrolyte, which remains near the surface according to a pancake configuration [34, 35]. Figure 4.7 shows a schematic illustration of the conformation of an anionic polyelectrolyte on a ceramic surface as a function of pH.

Steric stabilization has been explained with Napper's model [32, 33], which distinguishes three domains of close approach determined by the relative spans of the attached polymer layers ( $L$ ) and the separation distance between particles ( $D$ ). An interpenetrational domain is defined for which an interpenetration between the adsorbed polymer layers occurs, at separation distances of  $L \leq D \leq 2L$ . As particles continue to approach to less than the layer thickness  $D < L$  (interpenetrational plus compressional domain), the moieties on a surface are compressed by the opposite surface. The free energy in this domain has two components, a solvent–segment mixing term and an elastic term, that arise from the compression of the moieties, which reduces the configurational entropy. Consequently, the elastic term is repulsive.

The mixing free energy in the interpenetrational domain can be calculated as

$$\Delta G_{\text{mix}} = 4\Pi a\omega^2 N_A \left( \frac{\bar{v}_2^2}{\bar{V}_1} \right) kT \left( \frac{1}{2} - \chi_1 \right) \left( 1 - \frac{D_0}{2L_s} \right)^2, \quad (4.13)$$

where  $\Pi$  is the osmotic pressure,  $\omega$  is the weight of the adsorbed polymer layer,  $\bar{v}_2^2$  is the partial specific volume,  $\bar{V}_1$  is the molar volume of the dispersing medium,  $\chi_1$  is the Flory interaction parameter, and  $D_0$  is the minimum distance between particle surfaces. For a polyelectrolyte having  $i$  charges per monomer unit, and considering an aqueous solvent containing  $c_s$  mole of 1:1 electrolyte per unit volume, the interaction energy may be expressed by

$$\Delta G_M = 2\Pi akT\omega^2 N_A \left( \frac{\bar{v}_2^2}{\bar{V}_1} \right) \left( \frac{1}{2} - \chi_1 + \frac{i^2}{4\bar{V}_s c_s} \right) S_M, \quad (4.14)$$

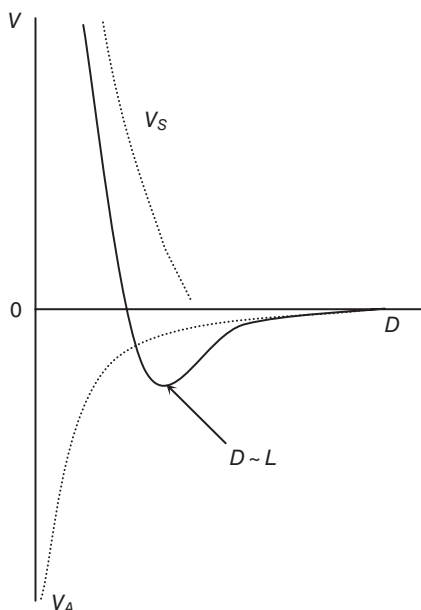


**Figure 4.8.** Potential energy curve for sterically dispersed suspensions.

$\bar{V}_s$  being the molar volume of a monomer unit. At the temperature  $-\theta$ , that is, for a specific concentration of salt and a certain temperature,  $\Delta G_M = 0$ .

The typical shape of the potential energy curve for a suspension stabilized by steric hindrance is that shown in Figure 4.8, where there is no primary minimum, so that there is no coagulation. This implies that steric stabilization provides thermodynamic stability, whereas electrostatically stabilized suspensions are only metastable, as they can coagulate when particles approach to near contact distances.

## 4.5 RHEOLOGY OF CERAMIC SUSPENSIONS

### 4.5.1 Flow Behavior

Rheology has been properly defined as the study of the flow and deformation of matter, with special emphasis being usually placed on the former [36–38]. Most ceramic operations include the manipulation of concentrated suspensions and pastes that can be submitted to a number of processing steps including milling and mixing, spray drying, transfer by tubes, and so on, or specific consolidation into bulk bodies through wet shaping methods or deposition on substrates to form coatings.

When a stress ( $\sigma$ ) is applied to a solid, it deforms elastically according to Hooke's law:

$$\sigma = G \frac{dL}{dy} = G \cdot \tan \gamma \approx G \cdot \gamma, \quad (4.15)$$

where  $G$  is the elastic modulus (Young's modulus) and  $\gamma$  is the strain. When the strain falls to zero, the sample recovers its original shape, which is commonly illustrated by a spring. The elastic modulus has units of  $F/A$  ( $N/m^2 = \text{Pascal [Pa]}$ ) and the deformation is dimensionless. In general, a modulus is given by the ratio stress/deformation, whereas the ratio deformation/stress is referred to as capacitance. The equations relating stress and deformation are called constitutive equations.

If the shear is large, then the structure of the sample can break, and hence it does not only deform but starts to flow. In the simplest case, the response follows Newton's law:

$$\sigma = \eta \dot{\gamma}, \quad (4.16)$$

where  $\dot{\gamma}$  is the velocity gradient (also known as the *shear rate*) and  $\eta$  is a coefficient of viscosity (or simply the *viscosity*). The unit of shear rate is  $s^{-1}$  and that of viscosity is  $Pa \cdot s$ . By definition, Newtonian behavior is when the viscosity is independent of shear rate and does not depend on the shear history. Most simple liquids like water, acetone, or oils are Newtonian. Liquids showing any variation from this behavior are referred to as non-Newtonian.

The flow behavior can be represented by plotting either the shear stress versus the shear rate, which is known as flow curve, or the viscosity versus the shear rate, which is referred to as the viscosity curve. Figure 4.9 shows the different types of rheological behavior, including Newtonian, shear thinning, where the shear stress and the viscosity decrease with increasing shear rate, and shear thickening, when the shear stress and the viscosity increase with increasing shear rate. These types of behavior have been traditionally called pseudoplasticity and dilatancy. The simplest non-Newtonian behavior

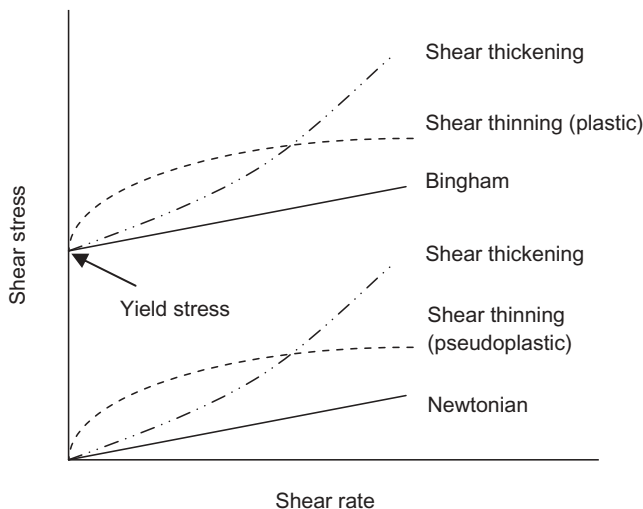


Figure 4.9. Types of rheological behavior.

TABLE 4.2. Common Rheological Models and Their Equations

Model	Equation
Newton	$\sigma = \eta \dot{\gamma}$
Bingham	$\sigma = \sigma_0 + \eta_p \dot{\gamma}$
Ostwald–de Waele	$\sigma = K (\dot{\gamma})^n$
Herschel–Bulkley	$\sigma = \sigma_0 + K_1 (\dot{\gamma})^n$
Casson	$\sigma^{1/2} = (\sigma_0)^{1/2} + K_1 (\dot{\gamma})^{1/2}$
Modified Casson	$\sigma^{1/2} = (\sigma_0)^{1/2} + K_1 (\dot{\gamma})^{n_1}$
Ellis	$\dot{\gamma} = K_1 \sigma + K_2 (\sigma)^{n_1}$
Modified Herschel–Bulkley	$\sigma^m = (\sigma_0)^{n_1} + K_1 (\dot{\gamma})^{n_2}$
Power series	$\sigma = K_1 \sigma + K_2 \sigma^3 + K_3 \sigma^5 \dots$
Cross	$\frac{\eta_0 - \eta}{\eta - \eta_\infty} = (K \dot{\gamma})^m$
Carreau	$\frac{\eta - \eta_\infty}{\eta_0 - \eta_\infty} = \frac{1}{(1 + (K_1 \dot{\gamma})^2)^{m/2}}$

$K_1, K_2, K_3, n_1$  y  $n_2$  are arbitrary constants and power indexes, respectively, obtained experimentally.

corresponds to the Bingham plastic flow, which means the linear flow curve is independent of the shear rate above  $\sigma_0$ :

$$\sigma = \sigma_0 + \eta_p \dot{\gamma}, \quad (4.17)$$

where  $\eta_p$  is referred to as the plastic viscosity. This model assumes the existence of a critical stress that must be reached in order to start the flow. This critical stress is referred to as the yield stress or the yield point. In most cases, the flow curve above  $\sigma_0$  is shear dependent. Some rheological models have been proposed to describe this behavior, such as the Herschel–Bulkley model or the Casson model.

To predict the shape of the general flow curve, it is necessary to well differentiate both the low and the high shear rate regions so that four parameter models are needed. One such equation is given by the Cross model (Table 4.2), where  $\eta_0$  and  $\eta_\infty$  refer to asymptotic values of viscosity at very low and very high shear rates,  $k$  is a constant with dimensions of time, and  $m$  is a dimensionless constant. From a technological point of view, it is of fundamental importance to know the shear rate at which the sample will be submitted. Table 4.3 shows the typical values of shear rate for some ceramic processes [38]

Another parameter affecting the rheological behavior is time. When viscosity decreases on shearing and the structure gradually recovers when the stress is removed defines the so-called thixotropy. Contrarily, the increasing viscosity under a constant

TABLE 4.3. Shear Rate Values of Some Common Ceramic Processes

Process	Typical Shear Rate ( $\text{s}^{-1}$ )
Spraying, printing, brushing	$10^3$ – $10^4$
Injection molding	$10^2$ – $10^4$
Extrusion	$10^2$ – $10^3$
Mixing, agitation, pumping	$10^1$ – $10^3$
Tape casting, dipping	$10^1$ – $10^2$
Low-pressure injection molding	$10^1$ – $10^2$
Slip casting (filtration step)	$<10^1$

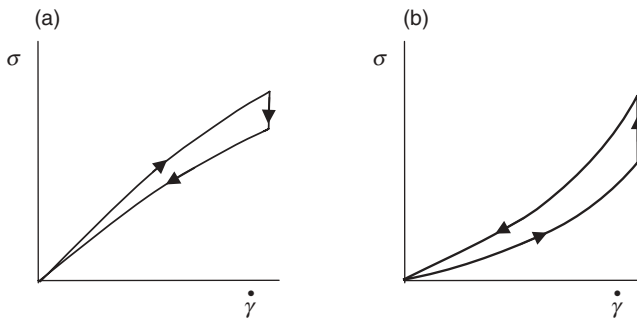


Figure 4.10. Time-dependent rheological behavior: (a) thixotropy and (b) rheopexy.

shear is called anti-thixotropy or rheopexy. Thixotropy is normally associated with a time-dependent shear thinning, and rheopexy to a shear thickening behavior. Both types of behavior are plotted in Figure 4.10.

Many ceramic processes need concentrated suspensions in order to reduce the amount of water to be removed during drying and sintering. Thus, the effect of particle concentration on viscosity and the prediction of the maximum solid content that can be prepared while maintaining flowability are of great interest [39–41]. The first model to describe the effect of volume fraction of particles on the viscosity was the Einstein' model:

$$\eta = \eta_s(1 + 2.5\phi), \quad (4.18)$$

where  $\eta$  is the viscosity of the suspension,  $\eta_s$  is the viscosity of the suspending liquid, and  $\phi$  is the volume fraction of particles. The relation between them defines the relative viscosity  $\eta_r$ . Hard-sphere suspensions are frequently described by the semiempirical Krieger–Dougherty model, which introduces the term “intrinsic viscosity” ( $[\eta]$ ):

$$\eta_r = \left(1 - \frac{\phi}{\phi_m}\right)^{-[\eta]\phi_m}. \quad (4.19)$$



This equation has been successfully used to predict the maximum solid loading at which a suspension maintaining flowability can be prepared.

### 4.5.2 Viscoelasticity

All materials have a characteristic time factor for deformation,  $\lambda$ , which is infinite for ideal elastic solids and almost zero for ideal liquids. Because deformation processes depend on time  $t$ , we can define a “Deborah number”,  $\lambda/t$ , that is high for a solid-like behavior and low for a liquid-like behavior [38–40]. When the Deborah number is around unity, the response is viscoelastic. Concentrated suspensions can behave as a solid or as a liquid depending on the characteristic time behavior  $\lambda$  and the process related time. If the experiment is performed for a time long enough, the material will behave as a liquid (viscous response), whereas if the experiment is fast, it will have a solid-like behavior (elastic response). According to this, we can define viscoelasticity as any behavior between extreme elastic and viscous responses. Viscoelasticity can be measured by two types of dynamic testing techniques: transient methods and oscillation. Transient methods include tests of start-up flow, cessation of steady shear flow, step strain, creep, and recoil. Oscillation implies the application of a sinusoidal stress or strain.

The creep–recovery test is performed in two steps below the yield stress. In the first step (creep), the sample is subjected to an instantaneous stress that deforms constantly for a given time and the resulting deformation is measured  $\chi(t)$ . In the second step, the recovery of the sample is measured after the release of the stress. Data from creep and stress relaxation tests can be described in terms of mechanical models which result from the combination of a spring and a dashpot in parallel or in series, respectively. In an elastic solid, the sample deforms during the application of a stress and completely recovers when the stress disappears (spring). In a liquid, the sample deforms when a stress is applied, but the sample remains deformed after the stress cessation (dashpot). Intermediate behaviors respond to viscoelasticity. Figure 4.11 shows a creep–recovery test for a Burger model, which is made up of two springs and two dashpots. This model is representative of the behavior of most real materials.

Another approach to measure viscoelasticity is by means of forced oscillation methods (also known as dynamic measurements), which measure the response of the sample to a small amplitude oscillatory shear. The sample structure is slightly perturbed with respect to that at rest, but not destroyed.

The elastic response (spring) to a sinusoidal strain ( $\gamma$ ) is given by

$$\gamma = \gamma_0 \sin(\omega t), \quad (4.20)$$

where  $\gamma_0$  is the maximum deformation,  $\omega$  is the angular velocity ( $\omega = 2\pi f$ ,  $f$  being the frequency), and  $t$  is time. From this equation, a stress function can be written in the form

$$\sigma = \sigma_0 \sin(\omega t + \delta) = G \sigma_0 \sin(\omega t + \delta). \quad (4.21)$$

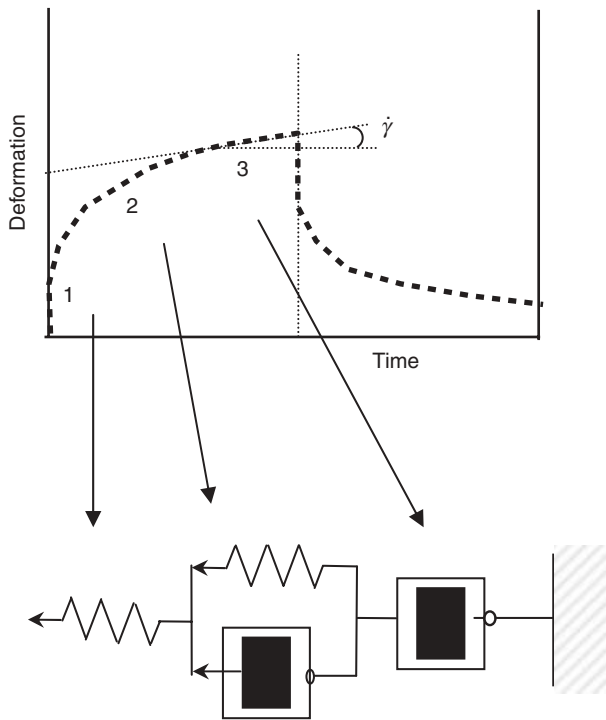


**Figure 4.11.** Creep-recovery test of a viscoelastic material.

For an elastic material, both strain and stress are in phase, but for a pure liquid with a purely viscous response (dashpot), the stress function is given by

$$\sigma = \eta \dot{\gamma} = \eta \omega \gamma_0 \cos(\omega t), \quad (4.22)$$

where strain and stress are out of phase with a shift angle of  $90^\circ$ . A viscoelastic fluid is then characterized by a phase angle  $0 < \delta < 90^\circ$ . Figure 4.12 shows the mechanical and elastic representation of the models of elastic solid, Newtonian liquid, and viscoelastic fluids.

In oscillatory shear, the so-called complex shear modulus  $G^*$  is defined as

$$G^* = G' + iG'' \quad (4.23)$$

so that

$$\sigma = G' \gamma_0 \sin \omega t + G'' \gamma_0 \cos \omega t, \quad (4.24)$$

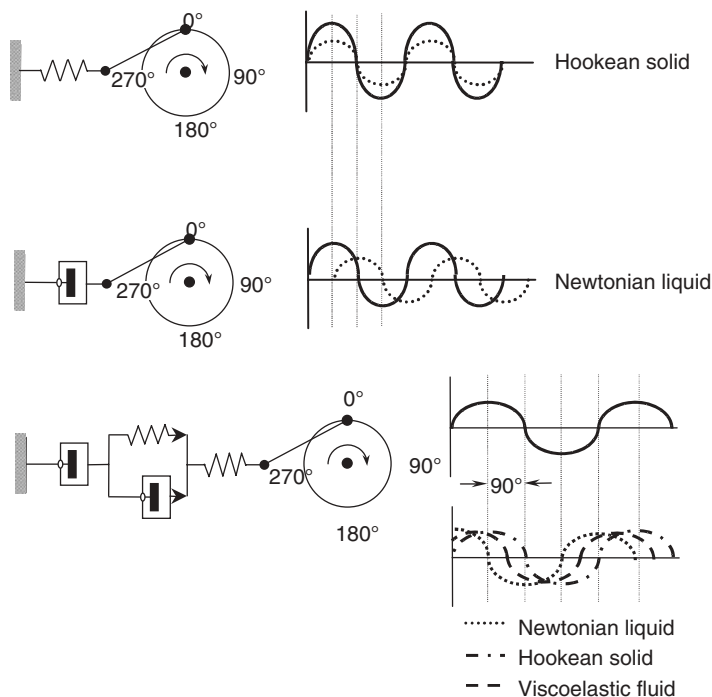


Figure 4.12. Mechanical and elastic representation of the models of elastic solid, Newtonian liquid, and viscoelastic fluids.

where

$$G' = G^* \cos \delta = \frac{\sigma_0}{\gamma_0} \cdot \cos \delta \quad (4.25)$$

and

$$G'' = G^* \sin \delta = \frac{\sigma_0}{\gamma_0} \cdot \sin \delta. \quad (4.26)$$

$G'$  is referred to as elastic or storage modulus indicating that the stress energy is stored during the test, but it recovers immediately afterward.  $G''$  is the viscous or loss modulus and is used to determine the energy for flow to start and is irreversibly lost as heat of shear. In an ideal solid,  $G^* = G'$ , whereas in an ideal liquid,  $G^* = G''$ . In practice, a suspension is considered to be solid-like when  $G' > G''$  and behaves as a liquid when  $G'' > G'$ .

## 4.6 SHAPING

### 4.6.1 Suspension Forming Techniques

Colloidal processing has demonstrated to be very efficient for producing near-net-shaping bodies with tailored microstructures by controlling the colloidal interactions among particles during all processing steps. Shaping refers to the consolidation of powders to obtain a green compact after liquid removal. Then, it is possible to classify the general types of suspension forming techniques as a function of the consolidation mechanisms, as summarized in Table 4.4 [42].

The most popular methods are slip casting and related techniques, in which solid–liquid separation occurs through a filtration process [12–14]. The main requirement is to have a well-dispersed suspension to maintain microstructural uniformity. A second group of forming techniques arises from the flocculation–coagulation mechanism, where a stable suspension is suddenly flocculated or coagulated, so that the structure is blocked giving rise to a physical gel, and the liquid is lost by drying outside the molds. In a third group of techniques, consolidation occurs by the formation of a chemical gel, by either thermogelation or *in situ* polymerization. The common issue of all these techniques is that all of them are mainly used for the manufacture of bulk, 3-D pieces. The last group of techniques in Table 4.4 deals with the manufacture of substrates and coatings, that is, 2-D structures, in which the suspension is deposited on a substrate and then evaporates to form a film or tape. This group includes techniques of spraying, tape casting, or electrophoretic deposition (EPD), in which deposition is performed with the assistance of an electric field. Nevertheless, they can be used in a sequential process to obtain multilayers and laminates.

### 4.6.2 Filtration Techniques

Slip casting consists of the preparation of a well-dispersed suspension or slip with moderate to high solid content (30–40 vol. %) that is poured into the cavity of a

TABLE 4.4. Classification of Conventional Suspension Forming Techniques

Filtration	Flocculation– Coagulation	Gelation	Deposition– Evaporation
Slip casting	Short-range forces	Gelcasting	Screen printing
Pressure	Temperature induced	Injection molding	Tape casting
Vacuum	Coagulation casting	Thermogelation	Electrophoresis
Centrifugal	Direct solidification	Protein casting	Chemical vapor
Microwaves		Starch consolidation	deposition
Filter pressing		Freeze casting	(CVD), physical
			vapor deposition
			(PVD), and so on
			Dipping
			Spin coating
			Spraying

permeable mold. The mold serves to absorb the water of the suspension by capillarity while the particles attach to the mold forming a cake that continues to lose water until it becomes dry and slightly shrinks. This allows removing easily the cast cake from the mold for drying outside before the piece is sintered at high temperature to produce the final product. This method has been used to produce any ceramic composition [43, 44]. The mechanism of slip casting involves the flow of a liquid in a permeable mold, and as it absorbs water, a cake is formed adhered to the mold walls [45–47] so that the process is treated in terms of liquid flow through the porous consolidated layer. The wall thickness ( $L$ ) formation follows a parabolic growth with casting time ( $t$ ):

$$L_c^2 = \frac{2k \frac{dp}{dx} t}{\eta_L (\phi_c / \phi_s - 1)}, \quad (4.27)$$

$\phi_c$  and  $\phi_s$  being the volume fraction of solids in the cast and in the suspension;  $\eta_L$  is the liquid viscosity;  $k$  is the permeability; and  $dp/dx$  is the gradient pressure across the compact. According to this parabolic law, there is a maximum thickness, which is possible to reach by slip casting, usually of a few millimeters.

An accurate control of the layer thickness can be obtained by determining the casting kinetics with the sintered layer thicknesses [48], thus allowing to produce any microstructure as illustrated in Figure 4.13, which plots the decreasing thickness obtained for the same casting times. To obtain laminates with layers of the same thickness, as that shown in the picture for an  $\text{Al}_2\text{O}_3/\text{Al}_2\text{O}_3\text{-ZrO}_2$  multilayer, subsequent layers need increased casting times.

The limitations of slip casting are the slow production rate, the need for continuous mold replacement, the large space necessary to accumulate the casting line, new molds, drying molds, as-cast pieces for drying, and so on, and, the most important, technical limitation dealing with the restricted thickness that can be obtained by filtration. The casting kinetics can be increased with the aid of an external force, such as centrifuga-

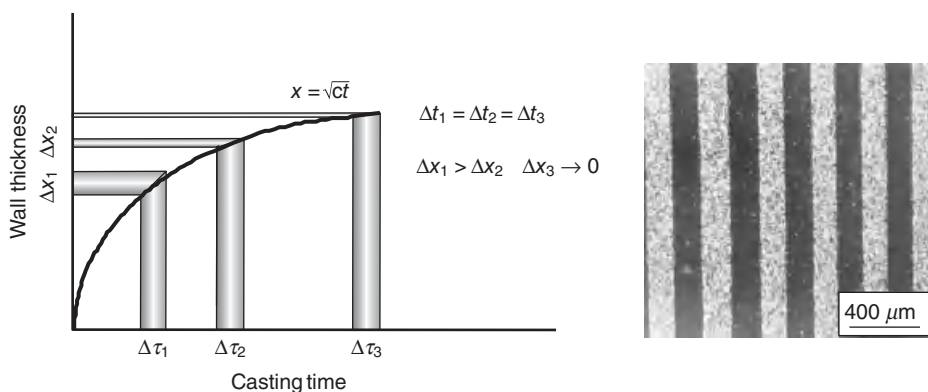


**Figure 4.13.** Design of multilayers and FGMs by sequential slip casting from the casting kinetics.

tion, the use of microwaves, the application of vacuum, and the most popular, the application of an external pressure [49–51]. This last is the so-called pressure casting process, which has been demonstrated to be a powerful route for the manufacture of large series of pieces with complex geometry. In particular, pressure casting has been successfully applied in the production of sanitaryware and whiteware [52, 53]. Some of these traditional ceramics products can be produced with low pressure and plaster molds can be used. However, in the most general case, pressures are higher and plaster does not have sufficient mechanical strength, thus making the use of metallic or resin molds necessary. However, problems have been observed with pressure-cast bodies of advanced ceramics, such as the clogging effect produced by small particles in the porosity channels of the molds, the very high pressure necessary to consolidate submicronic particles (which requires high-pressure machines and pressure-resistant molds), and the possible heterogeneities and lack of control at the earlier stages of casting since the first layers of the cake are formed by simple filtration before pressure is applied [54].

#### 4.6.3 Consolidation by Coagulation and Gelation Methods

Much effort has been devoted recently to develop near-net-shaping methods in water because of the obvious health, safety, and environmental benefits. A variety of shaping techniques have been recently described for manufacturing complex-shaped parts aiming for the removal or minimization of the machining step. All these processes have received the generic name of near-net-shaping techniques.

In opposition to slip casting, in these techniques, the liquid is not removed during consolidation, but the starting suspension is blocked inside the mold and then removed for drying outside. There are several mechanisms inside this broad group:

1. flocculation and coagulation,
2. chemical gelation by polymerization or thermogelation of monomers, and
3. freeze casting of suspensions by freezing at low temperature and water sublimation.

Flocculation and coagulation lead to the formation of a network structure of the particles when electrostatic repulsion is minimized by shifting the pH toward the isoelectric point or by increasing the ionic strength (direct coagulation casting, claylike forming) or by polymeric bridging when particles are dispersed with polymers and/or the solvency conditions change [55–57]. The last is referred to as the temperature-induced forming process.

Gelation can be induced chemically by the polymerization of monomers through a catalyst (i.e., gel-casting process) [58, 59] or thermally, where an aqueous suspension containing a gelling binder gels on either heating (methylcellulose derivatives, starches) [60, 61] or cooling (agaroids) [62, 63]. Chemical gelation is faster and leads to higher mechanical resistance of the green bodies, whereas thermogelation of polysaccharides is performed with biopolymers in a concentration lower than 1 wt % so that it has no handling risks and does not need debinding cycles. However, these processes

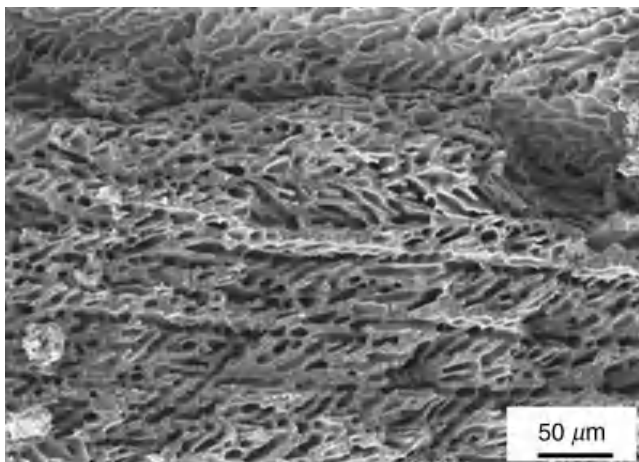


**Figure 4.14.** SEM microstructure of a freeze-cast alumina body with aligned porosity.

are still under development, and scarce information on their application in the preparation of composites is available [64]. A final consolidation mechanism is freeze casting, in which the suspension is suddenly frozen and water is sublimated [65, 66].

In general, these methods are useful for manufacturing dense 3-D bulk bodies, except for gelation with starches, which has been successfully used to produce macroporosity, or freeze casting, which allows the alignment of pores into channels corresponding to the direction of ice sublimation. Figure 4.14 shows a scanning electron microscopy (SEM) picture of a typical porous structure with channels formed by freeze casting in a nonporous mold, which is refrigerated with liquid nitrogen at the bottom, and cold propagates to the upper surface [67].

#### 4.6.4 Deposition/Evaporation Methods

This consolidation mechanism is based in the deposition of a suspension by any procedure (pouring on a nonporous surface, spraying, immersion, electrophoresis, etc.) and the further loss of solvent by evaporation. There are two main groups of techniques depending on the final material to be obtained: substrates and coatings.

**4.6.4.1 Substrates** Tape casting, also referred to as the doctor-blade method, consists of the preparation of a concentrated suspension that is spread over a surface covered by a flexible sheet that is rolled full-length to prevent direct contact and sticking. The most frequently employed carrier films are Mylar, tempered glass, and so on. The blade is adjusted to provide the desired thickness of the tape. After casting, the solvent evaporates, thus allowing the rolling and storage of the tape [68, 69]. The cast tape must have the consistency and flexibility necessary to avoid cracking during handling. This is possible with the addition of binders and plasticizers to typical concentrations of 10–20 vol %. For this reason, most tape-casting formulations are prepared in

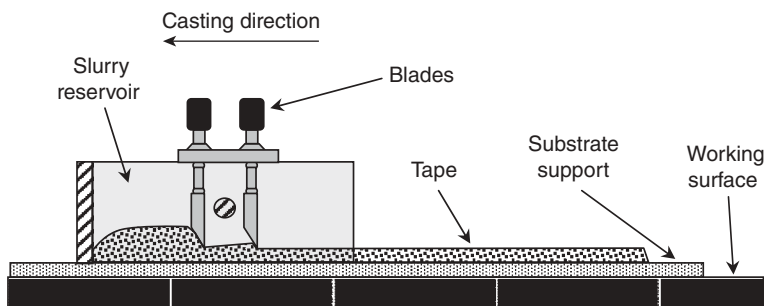


Figure 4.15. Schematic view of a tape-casting device.

organic solvents, although water-based systems have received increased interest in recent years [70, 71].

There is a big variety of formulations and components that have been produced by tape casting. Typical thicknesses of the tapes are between 50 and 400  $\mu\text{m}$ , although lower thicknesses can be also prepared. Typical formulations are prepared in organic solvents, with phosphate esters, glyceryl trioleate, and menhaden fish oil as the most popular deflocculants [41]. Once a well-dispersed, stable slurry is prepared, the binding system (i.e., binders and plasticizers) is then added. Since competitive adsorption among the different additives may occur, the deflocculated suspension is first prepared usually by ball milling, and the binding system is added in a second milling step [72].

In the industry, tape-casting machines are long enough to allow continuous casting and drying before the tape is rolled at the other extreme. Such machines are a few meters long and have driers to facilitate controlled drying. They usually have a stationary blade system and the carrier surface moves. At the laboratory level, tapes are short and it is customary to have a stationary carrier surface with a moving reservoir with the blades. Figure 4.15 shows a schematic view of a tape-casting device. The casting parameters to be controlled are the casting speed and the blade height. Typical casting speed ranges between 15 and 50 cm/min, depending on the thickness to be obtained, the type of machine, the desired thickness, and the solvent volatility. For a thin sheet, a solvent with high volatility must be used; for a thick sheet, a solvent with low volatility is preferred. The binder solution must be matched to the solvent. Drying occurs by evaporation from the top surface, but the bottom surface adheres to the carrier film and hence evaporation takes place in the thickness. The final thickness of the dry tape can reduce up to one-half of the blade height.

The main market of tape casting is related to electroceramics, for the production of circuits, multilayer capacitors, solid oxide fuel cells, and so on, but tape casting is very useful for the production of structural materials. Since the green tapes can be easily laminated, machined, and shaped, tape casting is a powerful route for the production of coatings, laminates, and functionally graded materials (FGMs) [73, 74].

**4.6.4.2 Coatings** Tape casting is suitable for the manufacture of thick self-sustained substrates. The manufacture of coatings onto substrates can be realized by different methods, such as spraying, dipping, and electrophoretic deposition (EPD).



In contrast with the other coating techniques, EPD uses an external electric field during coating. For this reason, it is not necessary to use concentrated suspensions. The process consists in the preparation of a stable suspension to which an electric field is applied, which promotes migration of charged particles by electrophoresis to the electrode of opposite charge [75–78]. There is no agreement yet about the deposition mechanism, although it seems that it is related to double-layer distortion during electrophoresis and thinning at the electrode vicinity so that coagulation occurs. The typical device for EPD includes a power source and a deposit or a glass that contains the electrodes, the so-called working electrode, where deposition occurs, and the counter-electrode. Electrode materials are usually conductive (i.e., metals), but semiconductors (like graphite) and even nonconductive materials can be used.

The success of EPD depends on the properties of the suspension, on one side, and the imposed geometrical and electrical conditions, on the other side. As in any other colloidal processing method, the suspension must have high stability. In most cases, the solid loading is low, and hence the measurement of the rheological properties is meaningless and the suspension parameters to be controlled are the zeta potential and the conductivity. With regard to electrical parameters, deposition could be performed under constant voltage or under constant intensity. To assure a constant electric field during EPD, the geometry of the electrophoretic cell must be constant, and the process should be developed maintaining a constant current density.

The electrophoretic rate,  $v_e$ , decreases with the intensity of the electric field, that is, when the charge at the particle surface increases. EPD must be performed considering a compromise between high particle mobility ( $v$ ) and low particle charge per unit weight, and hence the concentration of the deflocculant should be the minimum necessary to avoid destabilization since an excess could result in increased charge per unit weight:

$$v_e = u_e E, \quad (4.28)$$

$u_e$  being the electrophoretic mobility and  $E$  the electric field. The kinetics follows a simple equation proposed by Hamaker (Eq. 4.29), which relates the deposited mass per unit area ( $m$ ) with the slurry properties (concentration  $C$  and electrophoretic mobility  $u_e$ ) and the physical and electrical fixed conditions (electric field  $E$  and deposition time  $t$ ):

$$m = C u_e E t. \quad (4.29)$$

In opposition to the linearity provided by the previous equation, most experimental data demonstrate that deviations of linearity occur, either because of the consumption of powder during subsequent deposition steps or when EPD tests are performed at constant voltage, since a resistive deposit is being formed [75]. These situations are illustrated in Figure 4.16.

The interest on EPD for technical ceramics grew in the 1990s using nonaqueous suspensions; however, the advantages of using water are evident and have received increased attention. However, aqueous EPD also has important limitations, such as electrochemical reactions in the electrodes (water electrolysis, electroosmosis, and

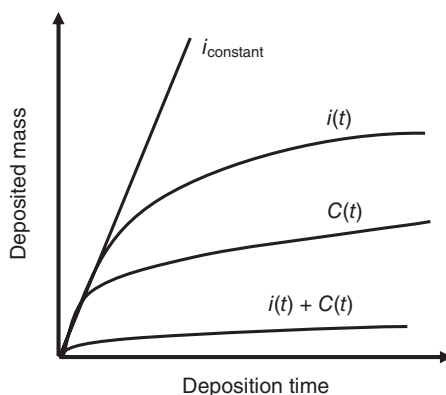


**Figure 4.16.** EPD kinetics according to the linear Hamaker's law and considering the loss of particles and/or the decreasing electric field when working at a constant voltage.

reactions with the electrode) when a current is passing through, which seriously decreases the efficiency of the process and the uniformity of the deposit. These problems have been technologically solved by designing adequate molds to avoid a galvanostatic reaction, as graphite porous substrates (where the pore size is fixed in order to promote the oxygen bubbling produced due to water electrolysis), or by studying the passivation ranges of selected metal substrates.

EPD has some obvious advantages over other forming techniques because the substrates can be dense or porous, easily formed, or have complex geometries; they are not limited by component size, and the coating times are short, in addition to the low cost and simplicity of the equipments. Although it is better for coatings, EPD has been also used to produce 3-D bulk bodies, infiltrated materials, porous materials, and so on. It is particularly advantageous to produce laminates combining materials with different thermal expansion coefficients or FGMs with thin layers, or even to combine this with other techniques to produce complex-shaped parts.

Another coating process is immersion or dipping [79], which consists of the immersion of a substrate into a sol or a suspension, followed by start-up, deposition, drainage, and evaporation, as illustrated in Figure 4.17. Dipping is mainly used in sol-gel technology because conventional ceramic suspensions do not wet the substrates, an exception made of suspensions containing binders and gelling additives. Multistep dipping has been widely used to thicken sol-gel coatings without change of composition. Figure 4.18 shows a SEM picture of a material of Ni-yttria-stabilized zirconia (YSZ) produced by sequential dipping as well as the multistep dipping procedure followed for the manufacture [80]. It has a graded composition from a Ni substrate to coatings with powder of Ni, and Ni with 50, 35, and 15 vol % YSZ. The layer adhesion was reached by adding a binder to the slurry (5 wt % on a dry solid basis). The fourth layer is poorly defined and very thin because it is in the limit of the adhesion capabilities. Thicker and denser films could be produced by EPD.

A great advantage of colloidal processing is the wide number of possibilities to combine forming methods and consolidation mechanisms to produce a variety of

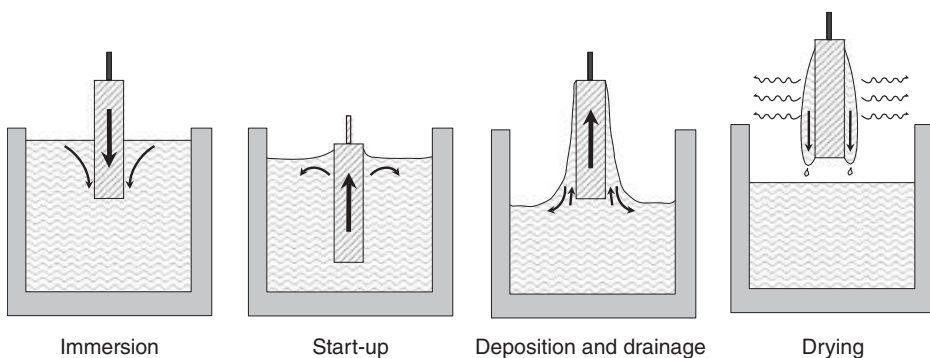


**Figure 4.17.** Steps of the dipping process.

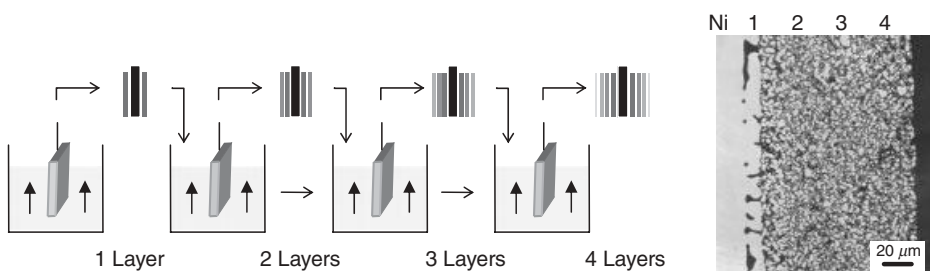


**Figure 4.18.** SEM picture of a continuous graded material of Ni-YSZ produced by sequential dipping as well as the multistep dipping procedure followed for the manufacture [80].

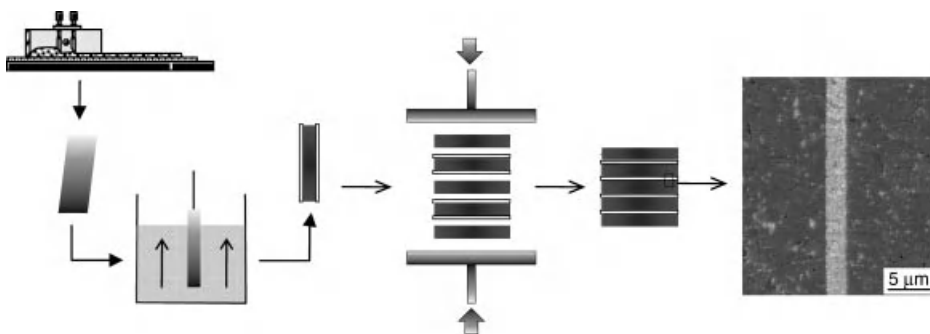


**Figure 4.19.** Green tape coated by dipping and lamination of coated and uncoated tapes to produce a laminate with internal thin layers.

composites. This makes it possible to produce a thick film by tape casting and to coat it in the green state to obtain a coated material or a multilayer. In the case of tape casting, the binder present in the tape gives the consistency for lamination, but it can be used also a substrate to be used for dipping or for EPD. In Figure 4.19, the lamination process for alumina-zirconia tapes uncoated and coated with zirconia is shown.

After sintering, laminated materials with very thin layers are obtained by a simple route able to produce defect-free, uniform layers integrated in complex structures [81].

Other techniques based on slurry processing are available, the main requirement being always the preparation of well-dispersed slurries. One powerful method for producing porous coatings is the wet powder spraying and the atmospheric plasma spraying. A spraying gun is used to project the powder or the slurry with a controlled motion of either the gun or the piece. The key parameters are the nozzle size of the gun, the distance between nozzle tip and the substrate surface, the viscosity and the feed rate of the suspension, the operating pressure, and the operating speed between the gun and the structural part [82]. However, to obtain homogeneous coatings by plasma spraying, it is necessary to have a free-flowing granulate material passing to the gun easily, and this is better achieved with an accurate rheological control of concentrated suspensions before spray drying.

## 4.7 CONCLUDING REMARKS

The colloidal approach has been demonstrated to be a powerful way to produce ceramics and ceramic-metal composites with better microstructural uniformity and higher reliability. The precise manipulation of the interaction potentials between the particles in suspension and the addition of proper deflocculants allows one to maintain particles repelling each other during all processing stages. In order to optimize the powder properties and the process requirements, the role of processing aids is of great importance. The forming step is probably the most important of the whole processing cycle since it is at this stage when particles rearrange into a consolidated body with the desired shape and microarchitecture. Conventional suspension forming methods include slip and pressure casting, gel forming, freeze casting, tape casting, EPD, and dipping, among others. These techniques are relatively simple, and the most important parameter is the stability of the suspension. Moreover, the simplicity of the instrumentation and the reliability are very attractive for manufacturing ceramics and composites with tailored microstructures. There are two main concerns: First, the colloidal approach can be applied to other particulate systems, such as metals, as it has been demonstrated elsewhere; second, the combination of different forming techniques allows one to produce very complex parts with precisely controlled designs of phases, layers, and microstructures. For example, a bulk body produced by slip or gelcasting can be coated by dipping using binders or by EPD, depending on the size, shape, and coating thickness to be obtained. Similarly, substrates produced by tape casting can be laminated or can be coated to produce a tailored distribution of layers in a laminate. Most of these processes are usually performed in aqueous media, and there is a strong effort to redesign those using organics into water-based processes.

## REFERENCES

1. M. Ashby, H. Shercliff, and D. Cebon, *Materials. Engineering, Science, Processing and Design*. Elsevier, Oxford, UK, 2007.

2. A. Mari *Los Materiales Cerámicos*. Alsina, Buenos Aires (Argentina), 1998.
3. W. D. Callister, *Materials Science and Engineering, An Introduction*, 7th edition, John Wiley, New York, 2007.
4. D. W. Richerson, Advanced ceramic materials, in *Handbook of Advanced Materials*, ed. J. K. Wessel, pp. 65–88, John Wiley & Sons, Hoboken, NJ, 2004.
5. R. W. Hertzberg, *Deformation and Fracture of Engineering Materials*, 3rd edition, Wiley, New York, 1989.
6. W. Jaschinski and A. Nagel (1993) Possibilities and limits in the shaping of ceramic powders, *Interceram*, **42**[3] 135–139.
7. J. Brinker, D. E. Clark, and D. R. Ulrich (eds.), *Better Ceramics Through Chemistry*. Mat. Res. Soc. Proc., Vol. 32, North-Holland, New York, 1984.
8. L. L. Hench and D. R. Ulrich (eds.), *Ultrastructure Processing of Ceramics, Glasses and Composites*. John Wiley & Sons, New York, 1984.
9. J. A. Pask (1979) Ceramic processing. A ceramic science, *Am. Ceram. Soc. Bull.*, **58** 1163.
10. P. F. Messer (1983) Ceramic processing: A systematic approach, *Trans. Br. Ceram. Soc.*, **82**[6] 190–192.
11. G. Y. Onoda and L. L. Hench (eds.), *Ceramic Processing before Firing*. John Wiley & Sons, New York (EEUU), 1978.
12. F. F. Y. Wang (ed.), *Treatise on Materials Science and Technology*, Vol. 9, Ceramic Fabrication Processes. Academic Press, New York (EEUU), 1978.
13. J. S. Reed, *Introduction to the Principles of Ceramic Processing*, 2nd edition, John Wiley & Sons, New York, 1995.
14. M. N. Rahaman, *Ceramic Processing and Sintering*, 2nd edition, Marcel Dekker, New York.
15. G. Y. Onoda, The rheology of organic binder solutions, in *Ceramic Processing before Firing*, eds. G. Y. Onoda and L. L. Hench, pp. 235–251, Wiley, New York, 1978.
16. D. J. Shanefield, *Organic Additives and Ceramic Processing*, 2nd edition, Kluwer Academic Publishers, Boston, MA, 2000.
17. R. Moreno (1992) The role of slip additives in tape-casting technology: Part 1. Solvents and dispersants, *Am. Ceram. Soc. Bull.*, **71**[10] 1521–1531.
18. R. Moreno (1992) The role of slip additives in tape-casting technology: Part 2. Binders and plasticizers, *Am. Ceram. Soc. Bull.*, **71**[11] 1647–1657. 64R. M. Pashley and M. E.
19. R. J. Hunter, *Foundations of Colloid Science*, Vol. 1. Clarendon Press, Oxford, UK, 1987.
20. J. N. Israelachvili, *Intermolecular and Surface Forces*. Academic Press, London, UK, 1985.
21. D. J. Shaw, *Introduction to Colloid and Surface Chemistry*, 4th edition, Butterworth-Heinemann, Oxford, Boston, 1992.
22. D. H. Everett, *Basic Principles of Colloid Science*. The Royal Society of Chemistry, London, UK, 1988.
23. F. F. Lange (1989) Powder processing science and technology for increased reliability, *J. Am. Ceram. Soc.*, **72**[1] 3–15.
24. W. M. Sigmund, N. S. Bell, and L. Bergström (2000) Novel powder-processing methods for advanced ceramics, *J. Am. Ceram. Soc.*, **83**[7] 1557–1574.
25. J. A. Lewis (2000) Colloidal processing of ceramics, *J. Am. Ceram. Soc.*, **83**[10] 2341–2359.
26. L. Bergstrom (1997) Hamaker constants of inorganic materials, *Adv. Colloid Interface Sci.*, **70** 125–169.

27. G. A. Parks and P. L. De Bruyn (1962) The zero point of charge of oxides, *J. Phys. Chem.*, **66** 967–972.
28. R. J. Hunter, *Zeta Potential in Colloid Science*. Academic Press, New York, 1981.
29. M. D. Sacks, N. Bozkurt, and G. W. Scheiffele (1991) Fabrication of mullite–matrix composites by transient viscous sintering of composite powders, *J. Am. Ceram. Soc.*, **74**[10] 2428–2437.
30. P. Garcia-Perez, C. Pagnoux, F. Rossignol, and J. F. Baumard (2006) Heterocoagulation between SiO<sub>2</sub> nanoparticles and Al<sub>2</sub>O<sub>3</sub> submicron particles; influence of the background electrolyte, *Colloid Surf. A: Physicochem. Eng. Asp.*, **281** 58–66.
31. O. Burgos-Montes, M. I. Nieto, and R. Moreno (2007) Mullite compacts obtained by colloidal filtration of alumina powders dispersed in colloidal silica suspensions, *Ceramics Int.*, **33**[3] 327–332.
32. D. H. Napper (1977) Steric stabilization, *J. Colloid Interface Sci.*, **58**[2] 390–407.
33. D. H. Napper, *Polymeric Stabilization of Colloidal Dispersions*. Academic Press, London, UK, 1983.
34. J. Cesarano III, I. A. Aksay, and A. J. Bleier (1988) Stability of aqueous  $\alpha$ -Al<sub>2</sub>O<sub>3</sub> suspensions with poly(methacrylic acid) polyelectrolyte, *J. Am. Ceram. Soc.*, **71**[4] 250–255.
35. J. Cesarano III and I. A. Aksay (1988) Processing of highly concentrated  $\alpha$ -Al<sub>2</sub>O<sub>3</sub> suspensions stabilized with polyelectrolytes, *J. Am. Ceram. Soc.*, **71**[12] 1062–1067.
36. H. A. Barnes, J. F. Hutton, and K. Walters, *An Introduction to Rheology*. Elsevier, Amsterdam, 1989.
37. A. Y. Malkin, *Rheology Fundamentals*. ChemTech Publishing, Ontario, Canada, 1994.
38. G. Schramm, *A Practical Approach to Rheology and Rheometry*. Haake GmbH, Karlsruhe, Germany, 1994.
39. L. Bergström, Rheology of concentrated suspensions, in *Surface and Colloid Chemistry in Advanced Ceramics Processing*, eds. R. J. Pugh and L. Bergström, pp. 193–244, Marcel Dekker, New York, 1994.
40. R. Moreno, *Reología de Suspensiones Cerámicas*. CSIC, Madrid, Spain, 2005.
41. R. G. Larson, *The Structure and Rheology of Complex Fluids*. Oxford University Press, New York, 1999.
42. R. Moreno (2000) Tendencias en el Conformado a partir de Suspensiones, *Bol. Soc. Esp. Ceram. Vidr.*, **39**[5] 601–608.
43. E. F. Adams, Slip cast ceramics, in *High Temperature Oxides, Part IV*, ed. A. M. Alper, pp. 145–184, Academic Press, New York, 1971.
44. J. Holly, D. Hampton, S. B. Savage, and R. A. L. Drew (1992) Experimental analysis of fine-particle migration during ceramic filtration processes, *J. Am. Ceram. Soc.*, **75**[10] 2726–2732.
45. I. A. Aksay, F. F. Lange, and B. I. Davis (1983) Uniformity of Al<sub>2</sub>O<sub>3</sub>-ZrO<sub>2</sub> composites by colloidal filtration, *J. Am. Ceram. Soc.*, **66**[10] C190–C192.
46. D. S. Adcock and I. C. McDowall (1957) The mechanism of filter pressing and slip casting, *J. Am. Ceram. Soc.*, **40**[10] 355–362.
47. F. M. Tiller and C. D. Tsai (1986) Theory of filtration of ceramics: I. Slip casting, *J. Am. Ceram. Soc.*, **69**[12] 882–887.
48. J. Requena, R. Moreno, and J. S. Moya (1989) Alumina and alumina/zirconia multilayer composites obtained by slip casting, *J. Am. Ceram. Soc.*, **72**[8] 1511–1513.

49. W. Huisman, T. Graule, and L. J. Gauckler (1994) Centrifugal slip casting of zirconia (Y-TZP), *J. Eur. Ceram. Soc.*, **13**[1] 33–39.
50. J. G. P. Binner (1992) The effect of raising temperature using microwaves on the slip casting of alumina based ceramics, *Br. Ceram. Trans. J.*, **91**[1] 48–51.
51. B. Leach, H. Wheeler, and B. Lynne (1996) Analysis of pressure casting rates, *Am. Ceram. Soc. Bull.*, **75**[8] 49–51.
52. E. G. Blanchard (1988) Pressure casting improves productivity, *Am. Ceram. Soc. Bull.*, **67**[10] 1680–1683.
53. Pressure casting-an established production process, *Interceram*, **39**[6] 45–47. (1990).
54. R. Moreno, A. Salomoni, I. Stamenkovic, and S. M. Castanho (1999) Colloidal filtration of silicon nitride aqueous slips. Part II: Slip casting and pressure casting performance, *J. Eur. Ceram. Soc.*, **19**[1] 49–59.
55. T. J. Graule, F. H. Baader, and L. J. Gauckler (1994) Shaping of ceramic green compacts direct from suspensions by enzyme catalyzed reactions, *Cfi/Ver. DKG*, **71** 317–323.
56. B. V. Velamakanni, J. C. Chang, F. F. Lange, and D. S. Pearson (1990) New method for efficient colloidal particle packing via modulation of repulsive lubricating hydration forces, *Langmuir*, **6**[7] 1323–1325.
57. L. Bergström and S. Sjöström (1999) Temperature induced gelation of concentrated ceramic suspensions: Rheological properties, *J. Eur. Ceram. Soc.*, **19** 2117–2123.
58. O. O. Omatete, M. A. Janney, and R. A. Sthrelow (1991) Gelcasting-a new ceramic forming process, *Am. Ceram. Soc. Bull.*, **70**[10] 1641–1649.
59. O. O. Omatete, M. A. Janney, and S. D. Nunn (1997) Gelcasting: From laboratory development toward industrial production, *J. Eur. Ceram. Soc.*, **17**[2–3] 407–413.
60. O. Lyckfeldt and J. M. F. Ferreira (1998) Processing of porous ceramics of starch consolidation, *J. Eur. Ceram. Soc.*, **18** 131–140.
61. J. E. Schuetz (1986) Methylcellulose polymers as binders for extrusion of ceramics, *Am. Ceram. Soc. Bull.*, **65**[12] 1556–1559.
62. A. J. Fanelli, R. D. Silvers, W. S. Frei, J. V. Burlew, and G. B. Marsh (1989) New aqueous injection molding process for ceramic powders, *J. Am. Ceram. Soc.*, **72**[10] 1833–1836.
63. A. J. Millán, M. I. Nieto, and R. Moreno (2002) Near-net shaping of aqueous alumina slurries using carrageenan, *J. Eur. Ceram. Soc.*, **22**[3] 297–303.
64. A. J. Sánchez-Herencia, A. J. Millán, M. I. Nieto, and R. Moreno (2000) Gel-forming of nickel powders from aqueous slurries, *Adv. Mater.*, **12**[16] 1192–1195.
65. T. Fukasawa, M. Ando, T. Ohji, and S. Kanzaki (2001) Synthesis of porous ceramics with complex pore structure by freeze-drying processing, *J. Am. Ceram. Soc.*, **84** 230–232.
66. K. Araki and J. W. Halloran (2005) Porous ceramic bodies with interconnected pore channels by a novel freeze casting technique, *J. Am. Ceram. Soc.*, **88**[5] 1108–1114.
67. C. Tallon, R. Moreno, and M. I. Nieto (2009) Shaping of porous alumina bodies by freeze-casting, *Adv. Appl. Ceram.*, **108**[5] 307–313.
68. R. E. Mistler and E. R. Twiname, *Tape Casting. Theory and Practice*. The American Ceramic Society, Westerville, OH, 2000.
69. R. E. Mistler, D. J. Shanefield, and R. B. Runk, Tape casting ceramics, in *Ceramic Processing before Firing*, eds. G. Y. Onoda and L. L. Hench, pp. 4114–4188, Wiley, New York, 1978.



70. T. Chartier and A. Bruneau (1993) Aqueous tape casting of alumina substrates, *J. Eur. Ceram. Soc.*, **12** 243–247.
71. D. Hotza and P. Greil (1995) Aqueous tape casting of ceramic powders, *Mater. Sci. Eng. A.*, **202**[1–2] 206–217.
72. D. J. Shanefield, Competing adsorptions in tape casting, in *Advanced in Ceramics*, Vol. 19. Multilayer Ceramic Devices, eds. J. B. Blum and W. R. Cannon, pp. 155–160, Am. Ceram. Soc., Westerville, OH, EEUU, 1986.
73. T. Chartier and T. Rouxel (1997) Tape-cast alumina-zirconia laminates: Processing and mechanical properties, *J. Eur. Ceram. Soc.*, **17**[2–3] 299–308.
74. P. Z. Cai, D. J. Green, and G. L. Messing (1997) Constrained densification of alumina/zirconia hybrid laminates, 1. Experimental observations of processing defects, *J. Am. Ceram. Soc.*, **80**[8] 1929–1939.
75. P. Sarkar and P. S. Nicholson (1996) Electrophoretic deposition (EPD): Mechanisms, kinetics, and application to ceramics, *J. Am. Ceram. Soc.*, **79**[8] 1897–2002.
76. R. Moreno and B. Ferrari (2000) Advanced ceramics via EPD of aqueous Slurries, *Am. Ceram. Soc. Bull.*, **79** 44–48.
77. L. Besra and M. Liu (2007) A review on fundamentals and applications of electrophoretic deposition (EPD), *Prog. Mater. Sci.*, **52** 1–61.
78. I. Corni, M. P. Ryan, and A. R. Boccaccini (2008) Electrophoretic deposition: From traditional ceramics to nanotechnology, *J. Eur. Ceram. Soc.*, **28** 1353–1367.
79. C. J. Brinker and G. W. Cherrer, *Sol-Gel Science: The Physics and Chemistry of Sol-Gel Processing*. Academic Press, San Diego, 1990.
80. I. Santacruz, B. Ferrari, M. I. Nieto, and R. Moreno (2004) Graded ceramic coatings produced by thermogelation of polysaccharides, *Mater.Lett.*, **58**[21] 2579–2582.
81. I. Nicolaidis, J. Gurauskis, C. Baudín, R. Moreno, and A. J. Sánchez-Herencia (2008) Forming of ceramic laminates comprising thin layers of a few particles, *J. Am. Ceram. Soc.*, **91**[7] 2124–2129.
82. H. P. Buchkremer and N. H. Menzler, Ceramic processing, in *Material Processing Handbook*, eds. J. R. Groza, J. F. Shackelford, E. J. Lavernia, and M. T. Powers, pp. 24-1 to 24-29, CRC Press, Boca Raton, FL, 2007.



# PROCESSING AND APPLICATIONS OF SOL–GEL GLASS

ESTHER H. LAN AND BRUCE DUNN

## 5.1 INTRODUCTION AND BACKGROUND

The sol–gel process is a simple benchtop synthesis method that can be used to prepare transparent, amorphous solids at ambient temperature. This synthesis approach has become widely popular over the past 20 years. While the initial interest was in the synthesis of inorganic systems, the method has proven to be widely adaptable to hybrid organic–inorganic materials. One can prepare both inorganic and hybrid organic–inorganic glasses by simply making an appropriate choice of liquid metal alkoxide precursors. The sol–gel approach is a high-purity process that leads to excellent homogeneity, and one can produce a variety of forms including monoliths, thin films, fibers, and powders. The room temperature and mild synthesis conditions enable the incorporation of relatively delicate dopants, such as organic dyes or biological molecules, within the sol–gel matrix. It would not be possible to incorporate such dopants using conventional glass melting techniques due to the high temperatures required.

The synthesis of inorganic or hybrid organic–inorganic glasses begins with the reaction of starting liquid metal alkoxides which undergo hydrolysis and condensation polymerization [1, 2]. Although silica-based glasses are the most widely studied system, a wide range of other metal alkoxides ( $\text{TiO}_2$ ,  $\text{Al}_2\text{O}_3$ ,  $\text{V}_2\text{O}_5$ , etc.) can also be prepared

---

*Ceramics and Composites Processing Methods*, First Edition. Edited by Narottam P. Bansal and Aldo R. Boccaccini.

© 2012 The American Ceramic Society. Published 2012 by John Wiley & Sons, Inc.

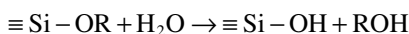
by the sol-gel method. In addition, one can prepare multicomponent compositions. In general, the sol-gel process proceeds by the following steps: sol formation, gelation, drying, and densification [3]. A colloidal sol first forms from hydrolysis and condensation of metal alkoxide precursors. As hydrolysis and condensation proceed, the liquid sol becomes a gel as the solid phase forms a network that extends throughout the container. After the sol-to-gel transition, there is a sharp increase in viscosity as the structure becomes rigid, with essentially no change in volume. At this point, the pores of the glass matrix are filled with interstitial fluid comprising the solvent as well as products of the hydrolysis and condensation reactions. Because of the presence of fluid in the pores, the material is considered a “wet” gel at this stage. This sol-to-gel transition is irreversible, and as the gel ages, its structure and properties continue to change. If the interstitial pore liquid is allowed to evaporate under ambient conditions, the gel begins to dry, forming a “xerogel” [3]. As the pore liquid evaporates, the pores collapse due to large capillary forces, and drying is accompanied by considerable volume shrinkage. After drying, the gel can be further densified to form a fully dense glass by heating to achieve sintering. If, on the other hand, pore liquid is extracted by supercritical drying and not dried by evaporation, one can form an “aerogel.” An aerogel is formed without pore collapse and volume shrinkage so that one can obtain a lightweight, highly porous solid [4].

In this chapter, we will detail the fundamental aspects of the sol-gel synthesis method, review some specific applications involving the integration of sol-gel materials with biomolecules, and discuss the general aspects and future directions for this technology. We will focus on two specific applications: The first is optical biosensing using transparent sol-gel materials doped with antibodies, and the second is electrically conductive sol-gel electrodes for biofuel cells based on combining sol-gel materials with carbon nanotubes (CNTs).

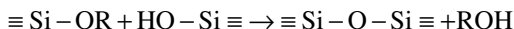
## 5.2 METHOD/TECHNIQUE/APPROACH

The sol-gel process begins with the hydrolysis and condensation of metal alkoxide precursors. Since the precursors are liquids, one of the advantages of this process is the versatility of casting the materials into a variety of shapes and forms. In the case of fabricating amorphous silica, the most common sol-gel system, a suitable starting alkoxide would be tetraethylorthosilicate ( $\text{Si}(\text{OC}_2\text{H}_5)_4$ , TEOS) or tetramethylorthosilicate ( $\text{Si}(\text{OCH}_3)_4$ , TMOS). The alkoxide is mixed with water in the presence of a catalyst (acid or base). Since the alkoxide and water are immiscible, a mutual solvent such as ethanol or methanol can be included to form a homogeneous solution. In the hydrolysis reaction, silanol ( $\text{Si}-\text{OH}$ ) groups are formed. These species are intermediates as they react further to form siloxane bonds ( $\text{Si}-\text{O}-\text{Si}$ ) accompanied by the formation of a by-product alcohol ( $\text{ROH}$ ) or  $\text{H}_2\text{O}$ . The reactions are listed below [5], where R is an alkyl group,  $\text{R} = \text{C}_x\text{H}_{2x+1}$ :

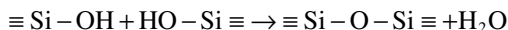
Hydrolysis and formation of silanol groups:



Alcohol condensation and the formation of siloxane groups:



Water condensation and the formation of siloxane groups:



The hydrolysis and condensation reactions proceed concurrently, and the hydrolysis of the alkoxide need not be complete before condensation starts. Parameters that affect the hydrolysis and condensation reactions include temperature, solution pH, the particular alkoxide precursor, the solvent, the relative concentrations of each constituent, and the type of catalyst used (acid or base) [1, 2].

The conditions under which hydrolysis and condensation occur have a profound effect on the resulting gel microstructure. Generally, acid-catalyzed solutions with low water content (conditions that produce linear polymers) offer the best type of solution for producing fibers. Silicate gels prepared at low pH (<3) and low water content (<4 mol water per mol alkoxide) produce primarily linear polymers with low crosslink density. Silicate gels prepared under more basic conditions (pH 5–7) or higher water contents typically produce more highly branched clusters, and gelation occurs by linking clusters together [5].

As hydrolysis and condensation reactions continue, viscosity increases until the liquid sol becomes a rigid gel, an irreversible transition. The time to gelation depends on the solution chemistry. The rigid wet gel has two phases, amorphous solid particles (nanometer size) with an interstitial liquid phase. After initial gelation, gels are usually subjected to an aging process from hours to days. To prevent solvent loss and volume shrinkage, gels are aged in sealed containers. During the aging process, condensation reactions continue, increasing the degree of cross-linking in the network. The mechanical strength and rigidity of aged gels increase with aging time.

The drying process involves the removal of the liquid phase, whereby aged gels become xerogels. The drying stage is a critical part of the sol–gel process because capillary stresses that arise during evaporation of pore liquid can cause catastrophic cracking. Stresses may be minimized by a low rate of solvent evaporation and/or the use of a drying control additive (e.g., a low vapor pressure solvent such as formamide). Usually, evaporation is allowed to occur at low temperature and ambient conditions. During drying, pore collapse occurs as liquid evaporates from the pores, decreasing the pore size and causing significant volume shrinkage. At this stage, the material is termed a xerogel. To form a fully densified sol–gel glass, the materials must be heated to relatively high temperatures. At moderate temperatures (above 150°C but below the  $T_g$ ), some densification occurs, but there can still be residual porosity. At higher temperatures ( $\sim T_g$ ), viscous sintering removes porosity, forming fully dense sol–gel glasses [5].

In contrast to forming dense materials, the sol–gel process can also be used to produce materials with as much as 99% porosity. In this case, one can utilize supercritical drying to produce an aerogel [6–9]. Aerogels possess a three-dimensional (3-D) network of nanometer-sized solid particles surrounded by a continuous macroporous

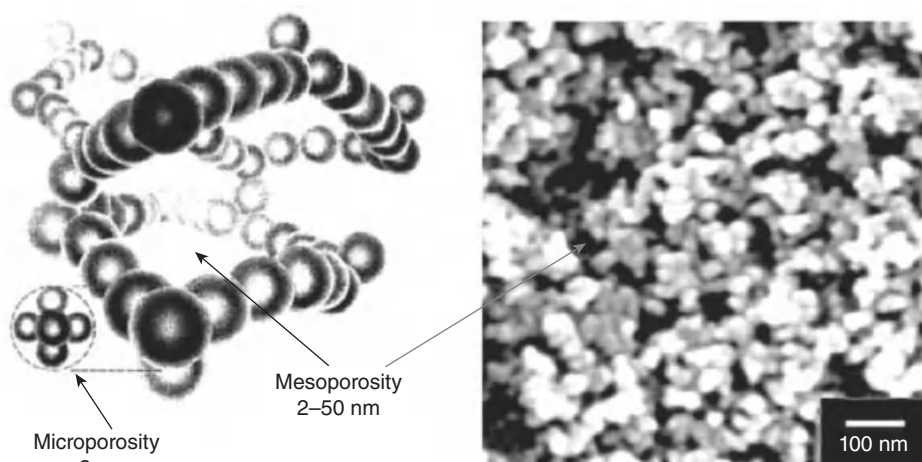


**Figure 5.1.** Structure of an aerogel with microporosity and mesoporosity [10].

(>50 nm) and mesoporous (2–50 nm) volume (Fig. 5.1) [10]. It should be noted that in an aerogel, the interstitial volume is filled with air, whereas in a wet or aged gel, the interstitial volume is filled with liquid.

The key factor in the formation of an aerogel is to remove the liquid phase from the pores of the wet or aged gel with no or minimal capillary stresses. To prepare gels for supercritical drying, the initial pore solvent (alcohol and  $H_2O$ ) must be replaced with liquid  $CO_2$ . Since water and alcohol are immiscible with liquid  $CO_2$ , the procedure requires an intermediate step to exchange the pore solvent with acetone. At this stage, the gels can be placed in an autoclave where liquid  $CO_2$  now fills the pores, fully replacing the acetone in a second solvent exchange step. The temperature and pressure inside the autoclave are raised until the  $CO_2$  is in its supercritical phase ( $\sim 42^\circ C$  and 10 MPa). Above the critical point,  $CO_2$  is no longer liquid but is in a supercritical gaseous phase, at which time it can be vented from the autoclave and the sample returns to ambient temperature and pressure. The supercritical drying process is illustrated in Figure 5.2 [11]. Using this process, a liquid–vapor interface never develops and no capillary forces are exerted on the solid network. The resulting aerogels that are formed are highly porous with high surface area and low density. These materials are solids in which nanometer-scale solid domains are networked with a high volume of continuous pores.

A variation of the supercritical drying approach leads to the synthesis of aerogel-like materials called “ambigels.” In this case, the pore liquid is replaced with a nonpolar solvent such as cyclohexane or pentane after solvent exchanging with acetone. The cyclohexane or pentane is then evaporated from the pores via ambient drying (Fig. 5.2). The nonpolar solvent minimizes pore collapse, and the resulting ambigels are somewhat denser and less porous than supercritically dried aerogels, with a lower surface area (Table 5.1) [4]. These materials also tend to have a narrower pore size distribution as

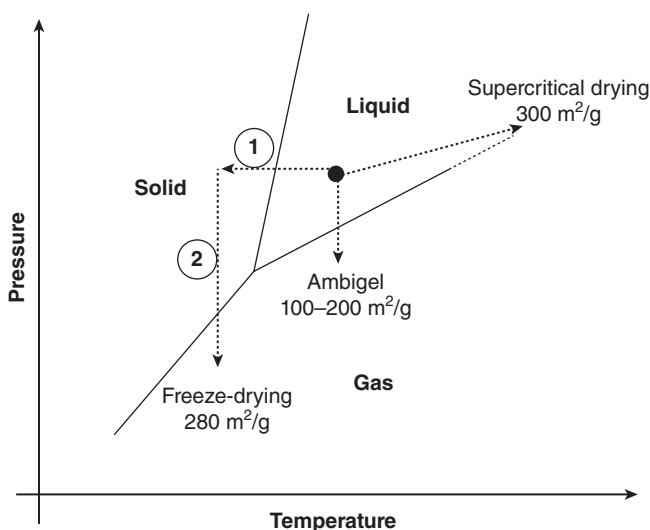


**Figure 5.2.** Illustration of the supercritical drying and ambigel processes. In supercritical drying, pore liquid is exchanged with liquid  $\text{CO}_2$ , and temperature and pressure inside the autoclave are raised until the  $\text{CO}_2$  is in its supercritical phase, at which time the gas is vented from the autoclave. In the ambigel process, pore liquid is exchanged with a nonpolar solvent and is evaporated from the pores via ambient drying [11].

**TABLE 5.1.** Surface Areas and Total Pore Volumes for Vanadium Oxide Supercritically Dried Aerogel, Ambigel, and Xerogel

Drying Solvent	Surface Area ( $\text{m}^2/\text{g}$ )	Total Pore Volume ( $\text{cm}^3/\text{g}$ )
Cyclohexane (ambigel)	155	0.87
Heptane (ambigel)	200	0.60
Hexane (ambigel)	165	0.40
Pentane (ambigel)	180	0.48
Supercritical $\text{CO}_2$ (aerogel)	280	0.50
Acetone (xerogel)	<10	<0.01

shown in Figure 5.3 [4]. Although ambigels have a lower surface area than aerogels, ambient pressure synthesis represents a considerably easier process than the supercritical drying method for producing materials with porosity levels as high as 80%. The evolution of a wet gel to different microstructures is illustrated in Figure 5.4 [10].

### 5.3 APPLICATIONS

One application of sol–gel materials that has emerged is that of optically transparent bioactive glasses for biosensors [12–17]. A wide range of biomolecules, including

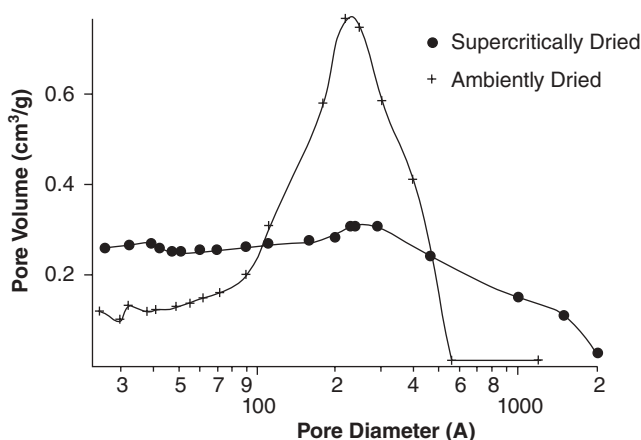


**Figure 5.3.** Pore size distribution for  $V_2O_5$  aerogel (supercritically dried) and ambigel (dried in pentane). Most of the pore volume in the ambigel occurs between 10 and 30 nm, whereas the aerogel has a broad pore size distribution [4]. A comparison of the surface area and total pore volume for the aerogel and ambigel is shown in Table 5.1.

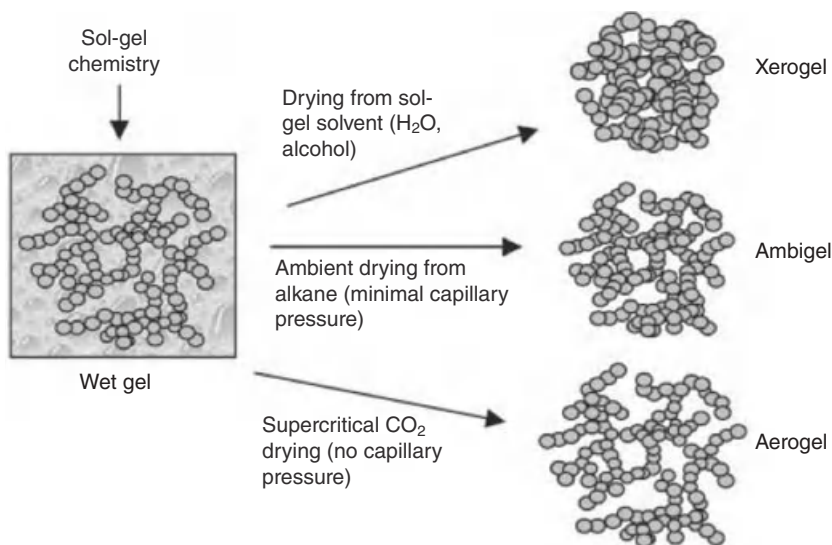


**Figure 5.4.** An illustration of the microstructures of xerogels, ambigels, and aerogels [10].

enzymes, and globular and membrane-bound proteins, have been immobilized in the pores of sol-gel glasses, resulting in a material that is not only bioactive but also rugged and mechanically, thermally, and chemically stable. Sol-gel matrices can also be highly transparent, making them suitable for optical sensing. Sol-gel synthesis is carried out at room temperature and can be tailored so as to not denature biomolecules. Therefore, the biomolecules immobilized in the sol-gel glass retain their characteristic reactivities

and spectroscopic properties [14, 18, 19]. There is evidence that the amorphous solid network forms around the biomolecules, thus confining these molecules within the pores of the inorganic network. One key feature of sol-gel-based materials is the microstructure of the matrix. The resulting pore structure is such that while relatively large biomolecules are trapped within the network, small ions and molecules are able to diffuse into and out of the interconnected pores.

We developed biohybrid materials in which sol-gel immobilized antibodies were used for optical sensing of cortisol, a stress-related hormone. The successful immobilization of antibodies in sol-gel matrices for sensing, catalysis, and other purposes has been well demonstrated [20–22]. The biohybrid material approach provides an important benchmark for sol-gel sensing and immunoassays because of (1) the use of thin films (antibody-doped) in the assay, (2) the ability to detect cortisol at concentrations in the physiological range (2–28  $\mu\text{g/dL}$ ), (3) the ability to measure cortisol in human serum, and (4) completion of the assay in 30 min or less [23, 24]. Our assays were conducted using solutions containing 100  $\mu\text{L}$  cortisol standard (in serum), 1.2 mL phosphate-buffered saline (PBS), and 1.5  $\mu\text{L}$  of 20  $\mu\text{M}$  Oregon Green (OG)-cortisol. The latter refers to cortisol that is conjugated to the fluorophore OG. In this work, we demonstrated that sol-gel silica thin films with anticortisol antibodies were able to bind cortisol in a competitive immunoassay format. In the assay, fluorescently labeled cortisol (OG-cortisol) and unlabeled cortisol in human serum compete for binding to the antibody in the sol-gel film. A calibration curve using a range of unlabeled cortisol concentrations (cortisol standard solutions in serum) shows the expected behavior with the fluorescence signal decreasing with the logarithmic increase in unlabeled cortisol concentration (Fig. 5.5) [24].

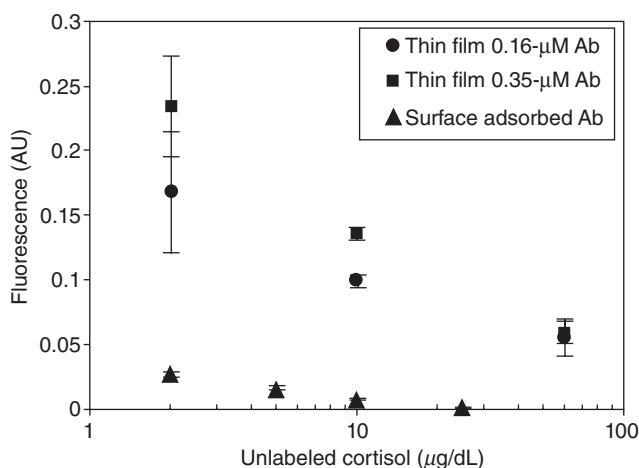


**Figure 5.5.** Calibration curve from competitive immunoassays conducted with sol-gel silica thin films containing anticortisol and with surface-adsorbed anticortisol. Both show the expected behavior of a negative linear relationship between fluorescence signal and the logarithm of unlabeled cortisol concentration. A much higher signal was obtained with the sol-gel antibody-doped film as compared to the surface-adsorbed antibody [24].

Our studies demonstrated that one distinct advantage of sol-gel encapsulation arises from immobilizing a significantly higher number of biomolecules per unit area as compared with surface adsorption, which typically has monolayer coverage. In comparing competitive immunoassay results for anticortisol immobilized by the two routes, the fluorescence signals measured using  $\sim 1 \mu\text{m}$  sol-gel films were as much as 10 times higher than those measured using surface-adsorbed antibody (Fig. 5.5) [24]. This result was obtained simply because a significantly higher number of antibody molecules can be immobilized in the pores of a 3-D silica matrix as compared to what can be adsorbed on a surface.

In a subsequent research, we modified our immunoassay format to make accurate cortisol measurements in actual human serum test samples as opposed to using calibration standards [23]. Luminescence from other biomolecules in the human serum (background fluorescence) interfered with the fluorescence from the OG-cortisol. To circumvent the background fluorescence, we pretreated the human serum by using a standard addition protocol, similar to the Gran plot addition method. In this pretreatment, a  $600 \mu\text{L}$  human serum sample of unknown cortisol concentration was divided into three equal volumes ( $200 \mu\text{L}$  each), and then  $6.9 \mu\text{L}$  of  $60 \mu\text{g/dL}$  unlabeled cortisol was added to the first tube;  $6.9 \mu\text{L}$  of  $600 \mu\text{g/dL}$  unlabeled cortisol was added to the second tube; and  $6.9 \mu\text{L}$  of  $1800 \mu\text{g/dL}$  unlabeled cortisol was added to the third tube. These three “spiked” serum samples were then used in a competitive immunoassay format similar to previous experiments. Using the fluorescence intensity data points taken from the three spiked samples, we calculated the concentration of the unlabeled cortisol in the human serum using the equation:  $f = m \times \ln(c) + b$ , where  $f$  is the fluorescence intensity,  $c$  is the final cortisol concentration in the human serum, and  $m$  and  $b$  are the slope and y-intercept of the line. Since we have three equations with three different final cortisol concentrations, we can determine the unknown variables  $c$ ,  $m$ , and  $b$ . One benefit of this standard addition method is that a separate calibration curve was not required.

Once we developed the standard addition protocol with human serum, we compared the cortisol concentrations obtained from our sol-gel immunoassay with those obtained by a National Aeronautics and Space Administration (NASA) group using a chemiluminescent assay (Fig. 5.6) [23]. The cortisol concentrations determined from our sol-gel immunoassay were correlated to within 15% of the values obtained by the traditional method, thus validating the accuracy of the sol-gel immunoassay. It should be noted that for several samples, the discrepancy was less than 5%. The cortisol concentrations of the serum samples ranged from 4.3 to  $17.9 \mu\text{g/dL}$ , well within the physiologically relevant range in an adult, 2–28  $\mu\text{g/dL}$ . In addition, using the standard addition protocol, the sol-gel immunoassay had good reproducibility as the average standard deviation was  $\sim 9.4\%$ . The total time to perform the measurement with the sol-gel immunoassay was approximately 30 min. Thus, our results showed promise for developing a miniaturized sol-gel bioassay system that enables quick and accurate on-orbit monitoring of biomarkers of interest to NASA.

In another application of bioactive sol-gel materials, we incorporated enzymes and CNTs into sol-gel-derived  $\text{SiO}_2$  for bioelectrodes [25, 26]. Biofuel cells are an attractive source of alternative energy because they are nonpolluting and use benign organic fuels and renewable catalysts. One of the most common biofuel cells is the enzymatic biofuel



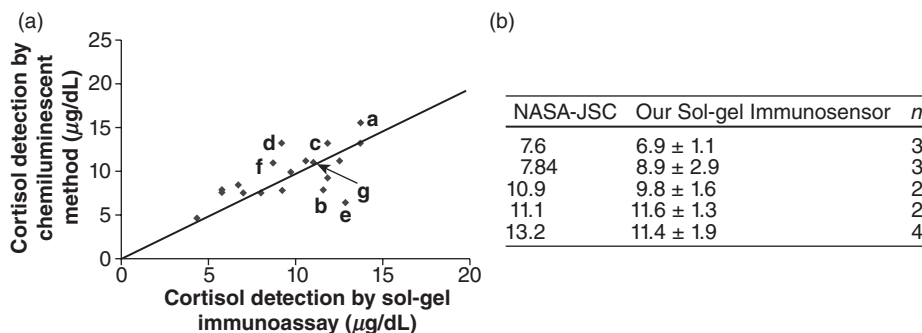


**Figure 5.6.** The figure (left) shows a comparison of cortisol concentration values ( $\mu\text{g/dL}$ ) reported by NASA-JSC (chemiluminescent method) versus values obtained by the sol-gel immunoassay (standard addition method). The slope of the curve is unity. The table (right) lists the standard deviations from the mean for specific samples. The number of times ( $n$ ) an individual serum sample was analyzed is also shown [23].

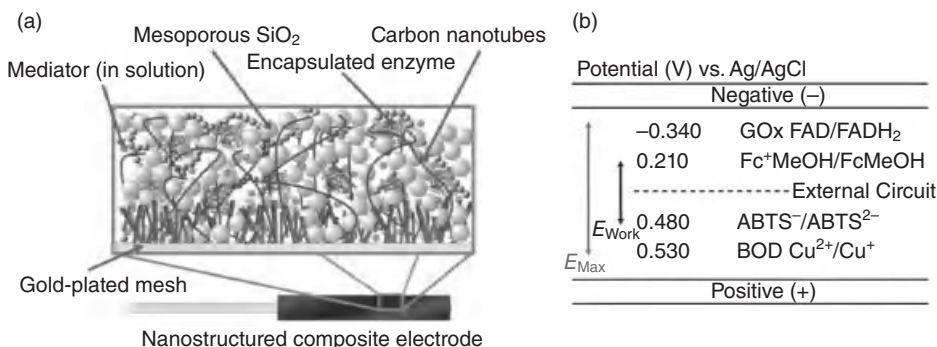


**Figure 5.7.** (a) Schematic of a nanostructured silica sol-gel/CNT composite electrode. The enzyme was encapsulated in sol-gel silica while the mediator can move through the solvent-filled pores. The current collector was a gold-plated mesh. (b) Redox potentials of biofuel cell components, showing the maximum potential and the working (operating) potential [26].

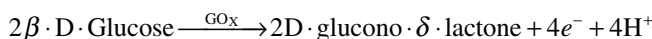
cell, where enzymes catalyze electrochemical oxidation/reduction to produce electrical energy [27–29]. We developed nanostructured electrodes for biofuel cells by using the sol-gel process to encapsulate enzymes adsorbed to a carbon electrode. Because most sol-gel-derived oxides are not electrically conductive, CNTs were included as an electrically conductive “filler” in the electrode. CNTs are especially attractive as a conductive component because of their excellent electrical conduction, low percolation thresholds, and high surface area.

We fabricated enzymatic glucose–oxygen biofuel cells using nanostructured composite electrodes containing sol-gel silica and CNTs (Fig. 5.7) [26]. Whereas the CNTs provide pathways for electron transport, the sol-gel silica matrix provided long-term retention of biological activity because of the enhanced stability of biomolecules upon

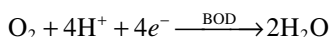
encapsulation [16, 30]. The ability to control porosity is critical for this application since the sol-gel silica needs to be sufficiently porous so that glucose and oxygen have access to the enzymes even though the enzyme remains immobilized.

The enzymatic glucose-oxygen biofuel cell is based on electrochemical oxidation of the fuel, glucose, and the electrochemical reduction of dioxygen to water. The active components for the anode were glucose oxidase (GOx) as the enzyme and ferrocene methanol as a redox mediator, while those of the cathode were bilirubin oxidase (BOD) as the enzyme and 2,2'-azino-bis(3-ethylbenzothiazoline-6-sulfonic acid) diammonium salt (ABTS) as a redox mediator. With these enzymes, glucose and oxygen were the fuel and oxidant, respectively. The redox reactions associated with these electrodes are as follows:

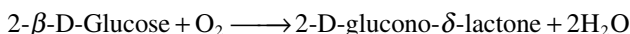
Anode reaction:



Cathode reaction:



Net reaction:



In the fabrication of the electrodes, silica sol was added to a thick slurry of multiwalled carbon nanotubes (MWCNTs) with polyethylene glycol (PEG). The enzyme in the PBS buffer was then added to the mixture. The reason for incorporating PEG was that it enabled us to achieve a more uniform dispersion of the MWCNTs (MWCNTs aggregate in silica sol and buffer in the absence of PEG). PEG also serves to maintain enzyme stability. As gelation progressed, the consistency of the mixture became that of a thick paste, which was then applied to a gold-plated mesh current collector. The resulting nanostructured composite electrodes contained 7.0 wt % MWCNTs. We subsequently constructed a glucose-oxygen biofuel cell comprising the anode and cathode nanocomposite electrodes separated by a Nafion membrane. A power curve for the biofuel cell was generated by measuring voltage as a function of varying loads (between 500 k $\Omega$  and 500  $\Omega$ ). As observed in Figure 5.8, we were able to achieve a power density  $\sim 120 \mu\text{W}/\text{cm}^2$  at a 500- $\Omega$  load (0.24 V) [26]. This power level is in the range reported for other glucose-oxygen biofuel cells. For example, Kim et al. achieved  $50 \mu\text{W}/\text{cm}^2$  at 0.5 V in their glucose-oxygen biofuel cells [31] and Mano and Heller achieved  $244 \mu\text{W}/\text{cm}^2$  at 0.36 V [32]. Both of the cited biofuel cells used GOx and BOD, similar to our biofuel cell.

In addition to biofuel cell operation, we carried out separate biocatalysis studies to characterize the effect of sol-gel encapsulation on electrode performance. For enzymes adsorbed on carbon current collectors, the GOx slowly desorbs over time so that by the 80th cycle, the anode has lost all catalytic activity. In contrast, for GOx encapsulated in sol-gel silica, a strong oxidation current was retained even after 100 cycles. Moreover, enzymatic activity was maintained for over 3 weeks using the sol-gel

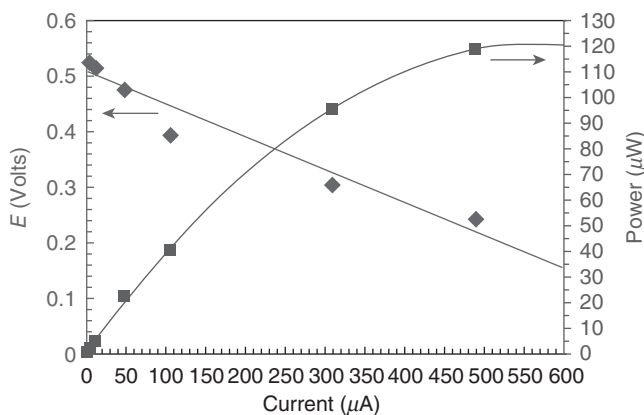


**Figure 5.8.** Potential–current relation for glucose–oxygen biofuel cell based on nanostructured silica sol–gel/CNT composite electrodes. Load resistance was varied between 500  $\text{k}\Omega$  and 500  $\Omega$ . The power curve (right-hand axis) peaks at approximately 120  $\mu\text{W}$  [26].

encapsulated enzyme. These results underscore the benefit of using sol–gel encapsulation for biofuel cell electrodes [26].

In our work on enzymatic glucose–oxygen biofuel cells, we added a mediator to serve as a shuttle between the electrode and the active site of the enzyme. While this approach is useful for generating reasonable levels of current, it does decrease the working voltage of the device. In addition, the presence of the mediator requires the biofuel cell to have a membrane to effectively separate the anode and cathode compartments in order to avoid short circuits. A more attractive, albeit difficult, approach is to achieve direct electron transfer (DET) between the electrode and the enzyme. Aside from obtaining a higher voltage, DET enables one to use membraneless fuel cell designs, which are simpler to fabricate and have lower ohmic loss.

We recently demonstrated that DET can occur between the BOD enzyme and the electrode in the absence of a mediator. The conditions for DET are related to proximity, enzyme orientation, and electrode material. The proximity of the enzyme redox active site needs to be within the electron tunneling distance and, ideally, the distances should be such that the enzyme’s biocatalytic reaction becomes the limiting process. DET is especially attractive in biofuel cell cathodes because four-electron reduction of  $\text{O}_2$  can occur at an operating potential close to the redox potential of the enzyme. Our results showed that DET can occur in a nanostructured sol–gel CNT composite electrode with the BOD enzyme encapsulated in sol–gel  $\text{SiO}_2$  along with PEG and CNTs [25].

Cyclic voltammetry was used to characterize the DET reactions. In the experiments, we observed that a large biocatalytic reduction wave begins near 450 mV for a BOD- $\text{SiO}_2$ /PEG-CNT nanocomposite electrode when tested in saturated oxygen (Fig. 5.9) [25]. This reduction was not observed when tested in argon or in saturated oxygen without the presence of BOD in the electrode. The initiation of reduction at 450 mV corresponds well with the redox potential of the BOD enzyme, 460 mV. These studies

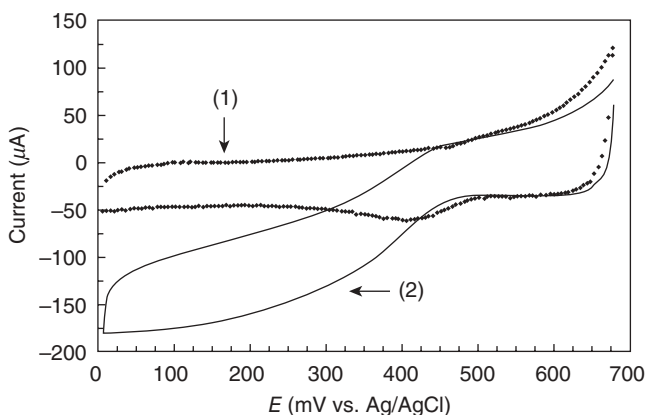


**Figure 5.9.** Cyclic voltammetry (25°C) of nanocomposite electrode containing BOD, exposed to both argon and saturated oxygen. The sweep rate was 1 mV/s and the sweep commenced at 670 mV versus Ag/AgCl. The potential wave for oxygen reduction occurs in saturated oxygen (bold line curve 2). The control shows the response under argon (dotted curve 1) [25].

establish that our nanostructured sol-gel cathode can be extended to DET processes. We are currently investigating nanostructured anodes that can support DET.

## 5.4 GENERAL DISCUSSION

The sol-gel process offers advantages for the fabrication of a broad spectrum of inorganic oxides. The oxide materials go well beyond silica and include aluminum oxide, titanium oxide, vanadium oxide, iron oxide, as well as mixed oxides that possess specific properties such as nonlinear optical absorption, ferroelectricity, electrochromism, or superconductivity. Using the sol-gel process, one can control composition, microstructure, and purity and form various shapes at low temperatures. Films and coatings were the first commercial applications of sol-gel materials. Development of sol-gel-based materials for optical applications has also been quite successful. One of the limitations of the sol-gel process, however, is the ability to fabricate relatively large, high-quality (i.e., crack-free) monoliths. In the case of forming a dense sol-gel-derived glass, there is significant shrinkage accompanying drying and the accompanying stresses may lead to cracking. The final volume depends on synthesis conditions and can be 10–15% of the original volume. In the case of forming an aerogel, the size of the component is limited by the size of the supercritical dryer.

One of the important factors to consider when using sol-gel-derived matrices with biomolecules is the interaction between these two components arising from surface charges. At near neutral pH (pH of PBS buffer), silica (pI ~2) is negatively charged. In our studies with cortisol, nonspecific binding of cortisol to the silica sol-gel matrix was minimal. Biomolecules such as proteins typically have surfaces that are highly charged,

depending on the amino acid residues at the surface. Our studies have shown that a cationic surfactant such as cetyl trimethylammonium bromide (CTAB) can increase nonspecific binding dramatically [24]. In control experiments with cortisol, a combination of both CTAB and OG-cortisol resulted in high levels of nonspecific binding. OG-cortisol alone, serum alone, serum with OG-cortisol, and serum with CTAB all gave low, nonspecific binding signals. CTAB is a single-chained cationic surfactant that forms flexible micelle structures that can adapt to restrictive environments such as the pores in a silica matrix. The positively charged CTAB head group was readily adsorbed to the negatively charged silica matrix, while the hydrophobic tail aggregated into various pre-micellar structures. We hypothesize that the aromatic rings in OG-cortisol attached to the hydrophobic tail of CTAB, tethering the OG to the silica matrix and producing a significant increase in nonspecific binding.

Studies have established that biomolecules encapsulated in sol-gel-derived silica are more thermally stable than biomolecules in liquid buffer [16, 30]. Silica, however, is not electrically conductive, and for electrochemical applications, one must include a conductive phase (e.g., CNTs) as an electron pathway. We have shown that enzymes and MWCNTs can be incorporated into sol-gel silica, resulting in bioactive electrodes (cathodes and anodes). Our results suggest that exposure to elevated temperatures may promote leaching of the enzyme from the electrode or may cause interactions that lead to enzyme deactivation. In studies *without* CNT or PEG, the sol-gel encapsulated BOD showed no decrease in relative activity until over 50°C, whereas BOD in liquid buffer experienced a 40% loss in activity at 40°C. Therefore, sol-gel immobilization clearly enhanced the thermal stability of the enzyme. In the presence of CNTs, however, there was a ~50% decrease in the relative activity of BOD at 50°C [25]. The incorporation of CNTs led to the loss of some thermal stability.

## 5.5 CONCLUDING REMARKS AND FUTURE DIRECTIONS

Research in the area of immobilization of biomolecules in sol-gel matrices has shown that these bioactive materials can be effective in a wide variety of applications, from optical biosensing to biofuel cell electrodes. With the facile fabrication of sol-gel materials, there is the possibility of integrating these materials into integrated circuits, microelectromechanical systems, and miniaturized biofuel cells. One of the future directions of this field is to incorporate sol-gel bioactive elements into actual devices. Sol-gel encapsulation can enhance the chemical and thermal stability of biomolecules, but there is limited research on the long-term storage stability of these materials (on the order of years and longer). Nearly all of the sol-gel biomolecular studies are based on immobilizing large biomolecules while small analytes diffuse through the porous network. Materials development is needed to create materials that can immobilize selected large biomolecules and yet allow diffusion of other large biomolecules. Finally, the encapsulation of more delicate biomolecules such as membrane-bound proteins (e.g., ion channels) into sol-gel matrices and integration into micromachines and devices would be an exciting new direction in this field.

## ACKNOWLEDGMENTS

We appreciate the contributions of Prof. Jeffrey Zink, Dr. James Lim, Dr. Jonathan Fang, Dr. Jing C. Zhou, Nicolas Cirigliano, and Peter Malati to the work described in this review. We also appreciate the collaboration of Dr. Scott Smith at NASA-Johnson Space Center in the cortisol immunoassay research. The support for this research from NASA (grant NAG9-1252 and NASA University Research, Engineering and Technology Institute NCC 2-1364) is also gratefully acknowledged.

## REFERENCES

1. C. J. Brinker and G. W. Scherer, *Sol-Gel Science: The Physics and Chemistry of Sol-Gel Processing*, Academic Press, San Diego, CA, 1990.
2. L. L. Hench and J. K. West (1990) The sol-gel process, *Chemical Reviews*, **90**[1] 33–72.
3. B. Dunn and J. I. Zink (2007) Molecules in glass: Probes, ordered assemblies, and functional materials, *Accounts of Chemical Research*, **40**[9] 747–755.
4. W. Dong, D. R. Rolison, and B. Dunn (2000) Electrochemical properties of high surface area vanadium oxide aerogels, *Electrochemical and Solid State Letters*, **3**[10] 457–459.
5. B. Dunn, Sol-gel process, in *AccessScience McGraw-Hill Encyclopedia of Science and Technology*, McGraw-Hill, New York, 2008.
6. N. Husing and U. Schubert (1998) Aerogels airy materials: Chemistry, structure, and properties, *Angewandte Chemie-International Edition*, **37**[1–2] 23–45.
7. S. S. Kistler (1931) Coherent expanded aerogels and jellies, *Nature*, **127** 741–741.
8. G. A. Nicolaon and S. J. Teichner (1968) Preparation of silica aerogels from methyl ortho-silicate in alcoholic medium and their properties, *Bulletin de la Societe chimique de France*, **5** 1906–1912.
9. G. M. Pajonk (1991) Aerogel catalysts, *Applied Catalysis*, **72**[2] 217–266.
10. D. R. Rolison and B. Dunn (2001) Electrically conductive oxide aerogels: New materials in electrochemistry, *Journal of Materials Chemistry*, **11**[4] 963–980.
11. G. Sudant, E. Baudrin, B. Dunn, and J. M. Tarascon (2004) Synthesis and electrochemical properties of vanadium oxide aerogels prepared by a freeze-drying process, *Journal of the Electrochemical Society*, **151**[5] A666–A671.
12. D. Avnir, T. Coradin, O. Lev, and J. Livage (2006) Recent bio-applications of sol-gel materials, *Journal of Materials Chemistry*, **16**[11] 1013–1030.
13. J. W. Aylott, D. J. Richardson, and D. A. Russell (1997) Optical biosensing of gaseous nitric oxide using spin-coated sol-gel thin films, *Chemistry of Materials*, **9**[11] 2261–2263.
14. L. M. Ellerby, C. R. Nishida, F. Nishida, S. A. Yamanaka, B. Dunn, J. S. Valentine, and J. I. Zink (1992) Encapsulation of proteins in transparent porous silicate-glasses prepared by the sol-gel method, *Science*, **255**[5048] 1113–1115.
15. S. Ferretti, S. K. Lee, B. D. MacCraith, A. G. Oliva, D. J. Richardson, D. A. Russell, K. E. Sapsford, and M. Vidal (2000) Optical biosensing of nitrite ions using cytochrome *cd<sub>1</sub>* nitrite reductase encapsulated in a sol-gel matrix, *Analyst*, **125**[11] 1993–1999.

16. E. H. Lan, B. C. Dave, J. M. Fukuto, B. Dunn, J. I. Zink, and J. S. Valentine (1999) Synthesis of sol-gel encapsulated heme proteins with chemical sensing properties, *Journal of Materials Chemistry*, **9**[1] 45–53.
17. R. Wang, U. Narang, P. N. Prasad, and F. V. Bright (1993) Affinity of antiluorescein antibodies encapsulated within a transparent sol-gel glass, *Analytical Chemistry*, **65**[19] 2671–2675.
18. B. C. Dave, B. Dunn, J. S. Valentine, and J. I. Zink (1994) Sol-gel encapsulation methods for biosensors, *Analytical Chemistry*, **66**[22] A1120–A1127.
19. J. I. Zink, J. S. Valentine, and B. Dunn (1994) Biomolecular materials based on sol-gel encapsulated proteins, *New Journal of Chemistry*, **18**[10] 1109–1115.
20. A. Bronshtein, N. Aharonson, D. Avnir, A. Turniansky, and M. Altstein (1997) Sol-gel matrixes doped with atrazine antibodies: Atrazine binding properties, *Chemistry of Materials*, **9**[11] 2632–2639.
21. C. Roux, J. Livage, K. Farhati, and L. Monjour (1997) Antibody-antigen reactions in porous sol-gel matrices, *Journal of Sol-Gel Science and Technology*, **8**[1–3] 663–666.
22. D. Shabat, F. Grynspan, S. Saphier, A. Turniansky, D. Avnir, and E. Keinan (1997) An efficient sol-gel reactor for antibody-catalyzed transformations, *Chemistry of Materials*, **9**[11] 2258–2260.
23. J. Fang, J. C. Zhou, E. H. Lan, B. Dunn, and J. I. Zink (2009) Bio-hybrid materials for immunoassay-based sensing of cortisol, *Journal of Sol-Gel Science and Technology*, **50**[2] 176–183.
24. J. C. Zhou, M. H. Chuang, E. H. Lan, B. Dunn, P. L. Gillman, and S. M. Smith (2004) Immunoassays for cortisol using antibody-doped sol-gel silica, *Journal of Materials Chemistry*, **14**[14] 2311–2316.
25. J. Lim, N. Cirigliano, J. Wang, and B. Dunn (2007) Direct electron transfer in nanostructured sol-gel electrodes containing bilirubin oxidase, *Physical Chemistry Chemical Physics*, **9**[15] 1809–1814.
26. J. Lim, P. Malati, F. Bonet, and B. Dunn (2007) Nanostructured sol-gel electrodes for biofuel cells, *Journal of the Electrochemical Society*, **154**[2] A140–A145.
27. M. Gelo-Pujic, H. H. Kim, N. G. Butlin, and G. T. R. Palmore (1999) Electrochemical studies of a truncated laccase produced in *Pichia pastoris*, *Applied and Environmental Microbiology*, **65**[12] 5515–5521.
28. Y. Xiao, F. Patolsky, E. Katz, J. F. Hainfeld, and I. Willner (2003) “Plugging into enzymes”: Nanowiring of redox enzymes by a gold nanoparticle, *Science*, **299**[5614] 1877–1881.
29. A. T. Yahiro, S. M. Lee, and D. O. Kimble (1964) Bioelectrochemistry .I. Enzyme utilizing bio-fuel cell studies, *Biochimica et Biophysica Acta*, **88**[2] 375–383.
30. D. T. Nguyen, M. Smit, B. Dunn, and J. I. Zink (2002) Stabilization of creatine kinase encapsulated in silicate sol-gel materials and unusual temperature effects on its activity, *Chemistry of Materials*, **14**[10] 4300–4306.
31. H. H. Kim, N. Mano, X. C. Zhang, and A. Heller (2003) A miniature membrane-less biofuel cell operating under physiological conditions at 0.5 V, *Journal of the Electrochemical Society*, **150**[2] A209–A213.
32. N. Mano and A. Heller (2003) A miniature membraneless biofuel cell operating at 0.36 V under physiological conditions, *Journal of the Electrochemical Society*, **150**[8] A1136–A1138.

# GELCASTING OF CERAMIC BODIES

KATHERINE T. FABER AND NOAH O. SHANTI

## 6.1 INTRODUCTION AND BACKGROUND

Net-shape and near-net-shape forming techniques have long been appealing in the production of ceramic materials. The high hardness and low toughness of ceramics make post-densification machining both costly and time-consuming, providing strong incentive for the development and optimization of net-shape techniques. The oldest of these forming techniques is slip casting. However, extrusion of cylindrical shapes, tape casting of laminates, and gelcasting, freeze casting, and injection molding of complex shapes have received considerable attention. Selective laser sintering, where shapes are determined via a computer-controlled localized heating profile, and robocasting, where material from a syringe or fine extruder is deposited in robotically controlled patterns, have garnered more recent interest. Each of these techniques relies on the suspension of a ceramic powder in a liquid vehicle or binder system for the forming stage of the operation. The shaped component is solidified through drying, cooling, or gelling. Once residual liquid is evaporated and binders are burned out, traditional densification methods, such as sintering, are employed.

Treated here is gelcasting, one of the more promising forming methods for complex-shaped ceramic and powdered metal components. This method was patented by Janney

---

*Ceramics and Composites Processing Methods*, First Edition. Edited by Narottam P. Bansal and Aldo R. Boccaccini.

© 2012 The American Ceramic Society. Published 2012 by John Wiley & Sons, Inc.



and Omatete in the early 1990s [1–3] and was explored in detail by them and their coworkers at Oak Ridge National Laboratory [4–8]. In their originally conceived method, a low-viscosity slurry is produced by mixing a ceramic powder into an aqueous-based monomer solution, while Venkataswamy et al. used monomers that required organic solvents [9]. The slurries have characteristically high solids loadings, often greater than 50 vol %, but have sufficiently low viscosity to flow easily. Through the addition of a chemical initiator and, in some cases, a catalyst, polymerization commences, at which point the slurry should be cast. The chemically cross-linked network that is formed through polymerization renders the ceramic powder particles immobile. The filled gel conforming to the shape of the mold is rigid enough to be removed for further processing. The high water content makes a controlled drying process critical to prevent warping and cracking. Low binder concentrations (generally <5 wt %) can be removed quickly and the body sintered. Sintering to full density is promoted by the high solids loading that can be achieved in gel-casting slurries [4].

Gelcasting should not be confused with sol–gel processing. In gelcasting, ceramic (or precursor) powders are suspended in a monomer or polymer solution to form slurries for casting. The monomer/polymer solution gels without reacting with the suspended powder, in essence locking the particles in place; the same gel would form in the absence of any ceramic. In sol–gel processing, ceramic precursors are integral to the gel formation process (through hydrolysis, polycondensation, etc.) Metal alkoxides, hydroxides, and the like form the backbone of the gel network and are converted to ceramic in later processing steps [10].

In this chapter, we first describe the categories of gel-casting systems and the chemistry of gelation in each type. Following this is a description of the processing steps from gel preparation to densification. An account of the variety of structural classes that are afforded by gelcasting is then presented. In addition to the processing of conventional bulk ceramics, gelcasting of textured ceramics, porous bodies, and laminates is described. Finally, gel-casting challenges and opportunities are highlighted.

## 6.2 GEL-CASTING SYSTEMS

All gel-casting systems rely upon the formation of a polymer network enveloped in a liquid. The polymers are tangled or cross-linked in such a way that the liquid is trapped, while at the same time, the liquid precludes the polymer network from collapse. Three general systems are reviewed here. The first is based on the polymerization of monomers, which, as noted above, was the original gel-casting system. Second, the cross-linking of polymer solutions is discussed. The physical aggregation of polymers or polysaccharides provides a third method of gelation.

### 6.2.1 Polymerization of Monomers

Polymerizable liquids for tape casting were reported as early as 1984 by Tormey et al. [11] However, the earliest report of gelcasting was by Young et al. through the polym-

erization of a pair of reactive organic molecules: monofunctional acrylamide (AM) and difunctional *N,N'*-methylenebisacrylamide (MBAM) [1, 4]. Both are soluble in water. Free radical polymerization in this system, as described by Tanaka [12], occurs through the addition of an initiator, typically ammonium persulfate (APS). The polymerization and cross-linking reaction process is shown pictorially in Figure 6.1. The reaction can be accelerated through the addition of a catalyst or by heat (up to 85°C in the AM system). Catalysts such as *N,N,N',N'*-tetramethylethylenediamine (TEMED) are effective [4].

Because the monofunctional AM originally used is a neurotoxin, efforts were made by Janney et al. to identify gel-casting systems of low toxicity that included both monomers and free radical initiators [8]. In addition to low toxicity, their criteria included solubility in water and low cost. The most successful systems resulting from their studies were monofunctional monomers of methacrylamide (MAM), methoxy poly(ethylene glycol) monomethacrylate (MPEGMA), and *n*-vinyl pyrrolidone (NVP). Hydroxymethylacrylamide (HMAM) is also favored. The difunctional monomers identified were MBAM, described above, and poly(ethylene glycol) dimethacrylate (PEG[1000] DMA). In addition to the APS/TEMED described earlier, initiators of azobis [2-(2-imidazolin-2-yl) propane] HCl (AZIP) and azobis (2-amidinopropane) HCl (AZAP) fit Janney et al.'s criteria. These were found to be successful in casting Al<sub>2</sub>O<sub>3</sub>, Si<sub>3</sub>N<sub>4</sub>, tool steels, Ni-based and Al alloys [8]. Other lower toxicity systems are 2-hydroxyethylmethacrylate (HEMA) [13] and acrylic acid [14]. These methods that rely on the polymerization of monomers will be referred to as traditional gelcasting for the remainder of the chapter.

## 6.2.2 Cross-Linking of Polymer Solutions

Gelcasting can also be accomplished via cross-linking of existing polymers. A prime example of this reaction is polyvinyl alcohol (PVA), which can be cross-linked by the addition of a cage-structured organotitanate [15–17]. Morissette and Lewis describe this cross-linking reaction as a two-step reaction involving fully hydrolyzed PVA shown in Figure 6.2. Initiation of the reaction is controlled by temperature ( $T > 100^{\circ}\text{C}$ ) or pH (6–10).

Morissette and Lewis also characterized the phase behavior of the PVA-Ti system to identify regions where gelation would occur [15]. A critical concentration of Ti was defined where PVA chains would interlink, causing a marked increase in viscosity, defining the solution–gel transition. The addition of solids reduces the amount of Ti needed for gelation, as can be seen in Figure 6.3, where the critical Ti concentration is shown as a function of solids loading of Al<sub>2</sub>O<sub>3</sub>. It has been speculated that this reduction is due to the enhanced reactivity of the Ti with Al<sub>2</sub>O<sub>3</sub> present or a contribution by the Al<sub>2</sub>O<sub>3</sub> to the structure of the gel.

## 6.2.3 Physical Cross-Linking of Polysaccharides and Polymers: Thermoreversible Systems

More recent advances provide reversibility in the early stages of the gel-casting process, which in turn allows for an infinite processing window and recyclability of flawed

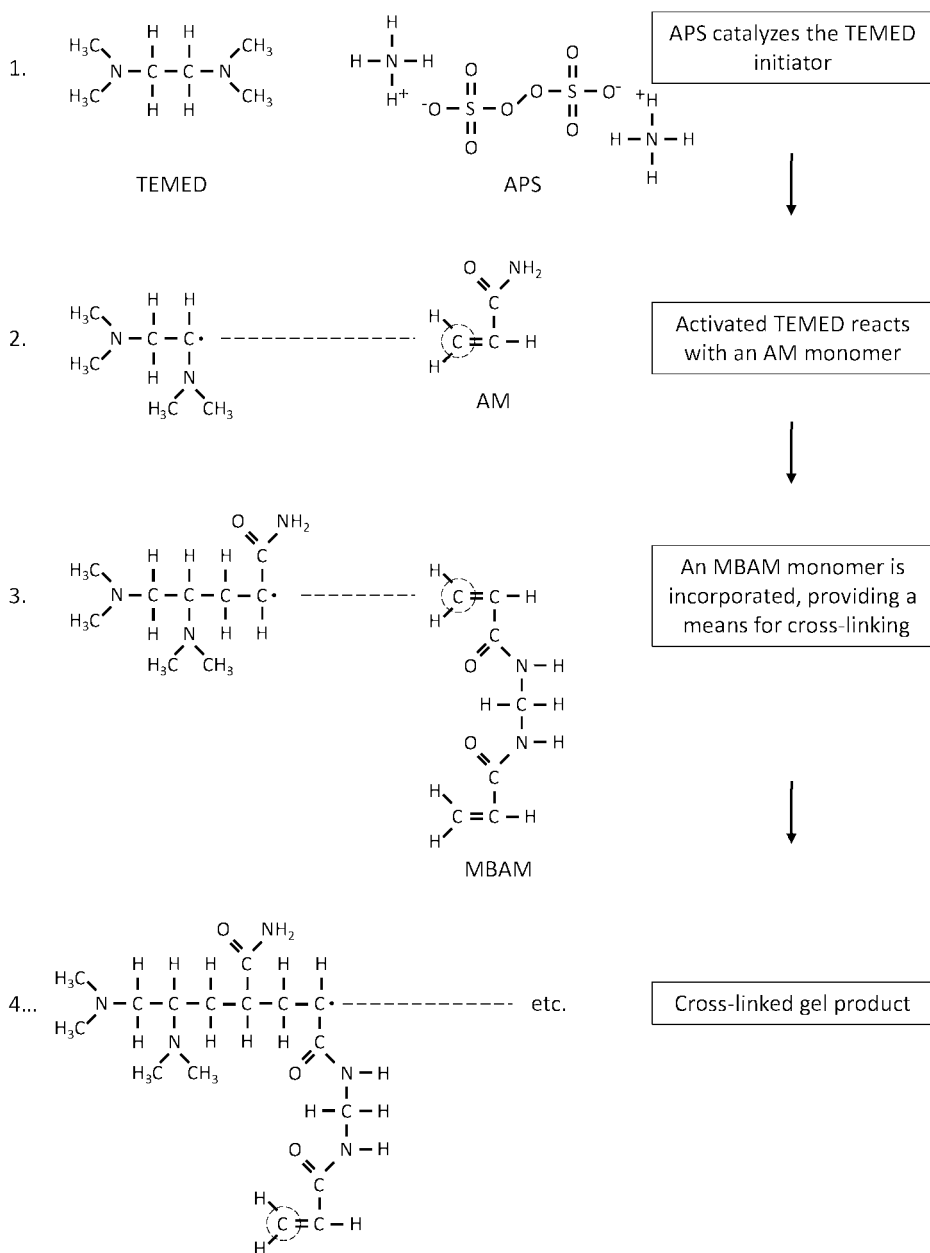


Figure 6.1. Schematic of polymerization in the acrylamide system. Reprinted from Tanaka [12].

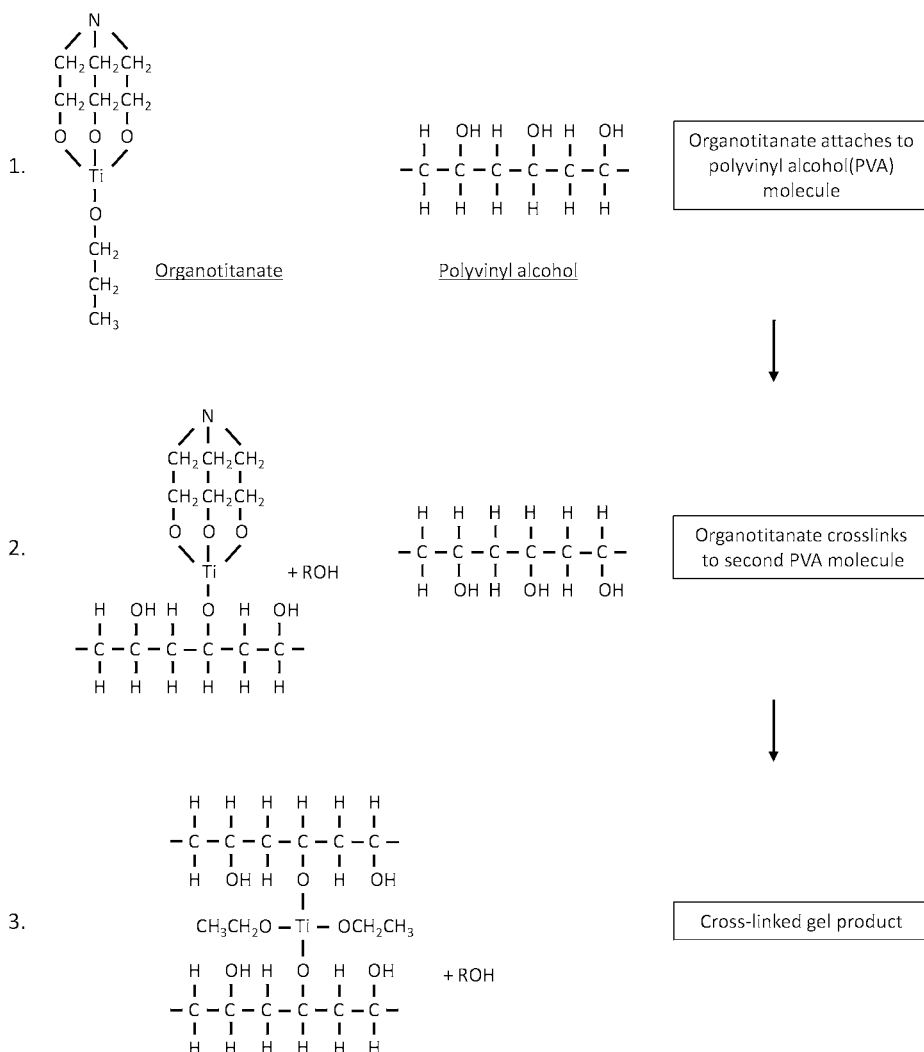
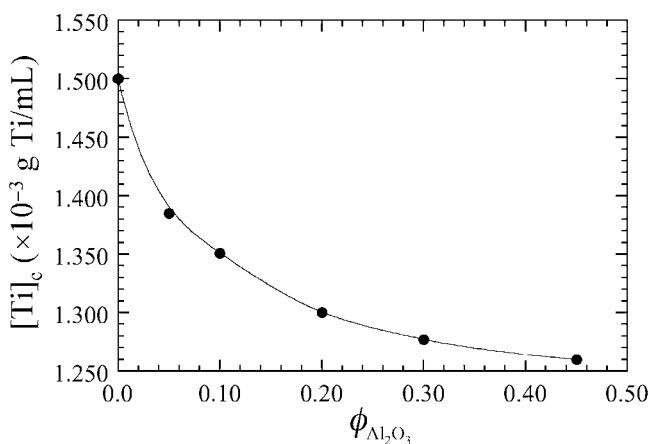


Figure 6.2. Schematic of cross-linking of an organotitanate coupling agent and PVA.

castings. Gel systems in this group include gelatin, starch, polysaccharides, and triblock copolymers [18–21]. The first three fall into a class of ecologically friendly casting systems—nontoxic and soluble in water. Examples of these polysaccharides include agar [21–22], agarose [22–23], and carrageenan [22, 24–25], which are shown schematically in Figure 6.4, as well as alginate [26].

Gelation of the hydrated polysaccharides occurs upon cooling by the formation of ordered double helices. A polysaccharide chain can belong to two or more such helical structures, leading to a cross-linked network. These structures revert to disordered,



**Figure 6.3.** Concentration of Ti needed to promote gelation as a function of  $\text{Al}_2\text{O}_3$  solids loading (in volume percent) in 5 vol % polyvinyl alcohol (PVA) suspensions. Reprinted from Reference 15 with permission from John Wiley & Sons.

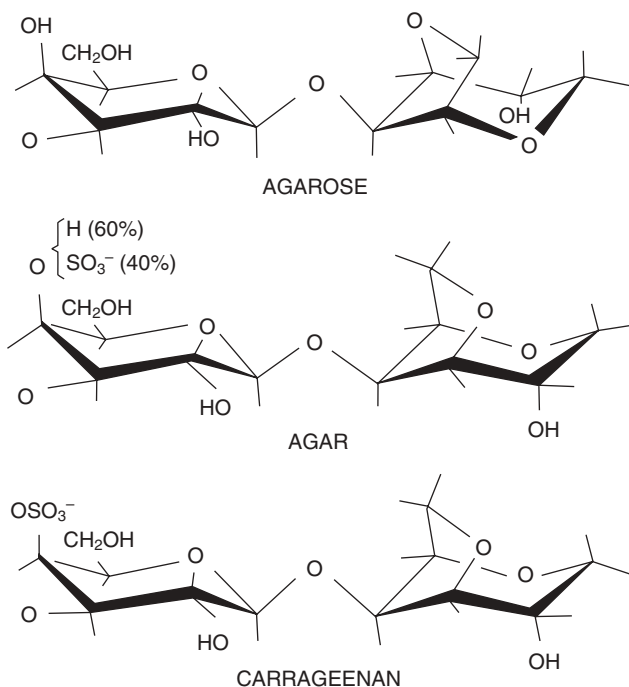


**Figure 6.4.** Repeating unit for three common polysaccharides used for gelcasting. Reprinted from Reference 22 with permission from Elsevier.

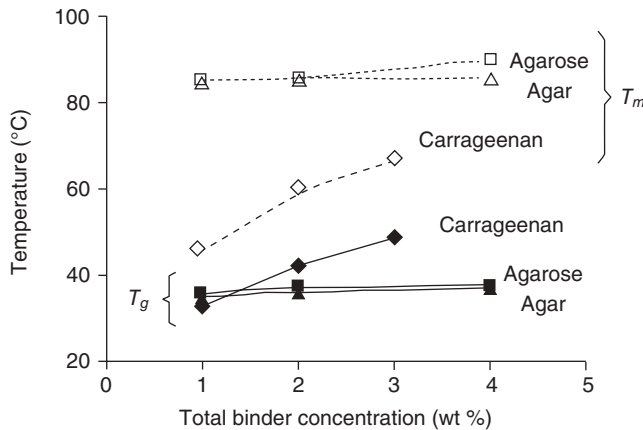


**Figure 6.5.** Gelation hysteresis of three polysaccharides as a function of concentration. Reprinted from Reference 22 with permission from Elsevier.

coiled chains upon reheating. Because chain complexation is required for gelation, polysaccharides are slow to gel and exhibit a large hysteresis between their gelling and “melting” temperatures, as demonstrated in Figure 6.5 for agar, agarose, and carrageenan. For example, the melting temperature of carrageenan gels is  $\sim 20\text{--}25^\circ\text{C}$  above the gelling temperature (and higher for agar and agarose) [22, 25], reflecting the excess thermal energy required to break the hydrogen bonds between interacting molecules.

Unlike the chemical cross-linking that occurs in traditional gelcasting, triblock copolymers are effective in gel-casting processes due to physical cross-linking. Successful candidates require an ABA-type triblock copolymer and a solvent that selectively dissolves the midblock of the triblock—the “B” chemical block. The insoluble end blocks aggregate but are linked through the well-solvated midblocks to form the gel, even in the presence of ceramic particles. Ideal triblock-based thermoreversible gel casting (TRG) systems have a rapid liquid-to-gel transition at a temperature close to ambient and utilize an easily evaporated solvent. Acrylic systems with poly(methyl methacrylate) (PMMA) end blocks and either a poly(*n*-butyl acrylate) (PnBA) or a poly(*tert*-butyl acrylate) (PtBA) midblock in solvents of ethanol, isopropanol, pentanol, or 2-ethylhexanol (2EH) are used successfully [18, 27–28]. Isopropanol and pentanol are the preferred solvents since their moderate volatilities ensure negligible solvent loss during mixing and casting while still allowing for reasonable drying times. Further discussion on solvent choice can be found in Section 6.5.

The use of these acrylics for ceramic processing is afforded by the strong temperature dependence of the interaction between end blocks and solvent, described by the schematic in Figure 6.6. Above a critical temperature, known as the critical micelle temperature (CMT), both the end blocks and midblocks are well solvated and the material behaves as a free-flowing liquid. As the liquid is cooled below the CMT, end blocks aggregate into spherical micelles, while the midblocks remain well solvated, serving

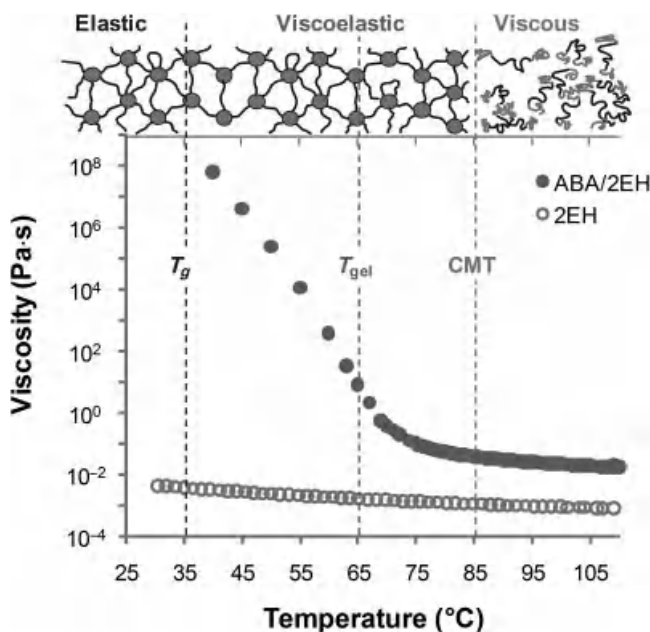


**Figure 6.6.** Viscosity of 2-ethylhexanol (2EH) and thermoreversible gel with 17.5 wt % PMMA<sub>25</sub>PnBA<sub>116</sub>PMMA<sub>25</sub> in 2EH as a function of temperature. Approximate values of the critical micelle temperature (CMT),  $T_{gel}$ , and  $T_g$  are indicated along with a schematic of gel/solution behavior. Reprinted from Reference 30 with permission from John Wiley & Sons.

as cross-links to the micelles [27]. On further cooling, the aggregates undergo a glass transition, effectively locking the end blocks in position and giving rise to an elastic gel. Between the CMT and glass transition temperature ( $T_g$ ), the gel behaves as a viscoelastic solid.

Because aggregation is highly temperature dependent, a rapid increase in viscosity with decreasing temperature in this region ensues, for example, eight orders of magnitude in approximately 30°C in PMMA<sub>25</sub>PnBA<sub>116</sub>PMMA<sub>25</sub> in 2EH (Fig. 6.6). Consequently, the mechanical response of the gel network undergoes a sharp transition from liquid-like behavior to solid-like behavior over a narrow temperature range, as demonstrated in the storage and loss moduli ( $G'$  and  $G''$ , respectively) measurements as functions of temperature [29]. It is convenient to define the gel point,  $T_{gel}$ , as the temperature at which  $G'$  and  $G''$  cross (for a given oscillatory frequency). Below the gel point,  $G' \gg G''$ , indicating a highly elastic behavior, while viscous-dominated behavior takes place above the gel point, where  $G'' \gg G'$ .  $T_{gel}$  is highly dependent on the length of the end blocks; changing endblock length from 9 to 25 kg/mol in the PMMA–PnBA–PMMA system causes  $T_{gel}$  to increase by approximately 20°C [30].

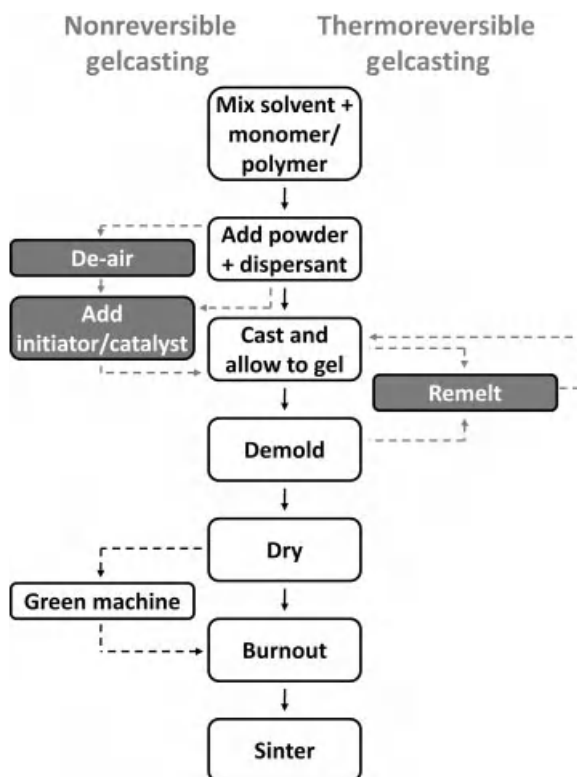


Figure 6.7. Processing flowchart for gelcasting. Shaded boxes (left) refer to traditional or nonreversible gelcasting, while the shaded box (right) applies to thermoreversible systems.

### 6.3 THE GEL-CASTING PROCESS: CASTING THROUGH SINTERING

The general scheme for gelcasting is shown in the flowchart in Figure 6.7. The main steps in the process are common to the three generic systems described in Section 6.2. However, traditional gel-casting systems require the addition of an initiator and sometimes a catalyst, noted on the left-hand side of the diagram. Gelation of thermoreversible systems depends only on temperature, and bodies can therefore be recycled until an optimum casting is produced. The recasting window is noted on the right-hand side of the flowchart. Each of the main steps in the process is described herein.

#### 6.3.1 The Casting Suspension

Casting using any of the systems described in the preceding section requires first that powders be well dispersed in the suspension. Often this requires ball milling to break up large agglomerates in the premix along with the use of dispersants. Appropriate



dispersants are often identified by trial and error, as demonstrated by Young et al. for  $\text{Al}_2\text{O}_3$  [4]. These must be adjusted both for the ceramic powder and the premix solution, exemplified by Janney et al. for  $\text{Al}_2\text{O}_3$  and  $\text{Si}_3\text{N}_4$  [8]. Although dispersion methods are well defined for an assortment of micron-sized ceramic powders and permit solids loadings of 55 vol %, the dispersion of nanosized particles remains a challenge. In some of the first gel-casting studies on nanopowders, Wasche and Steinborn found that solids loadings of TiN were limited to 22 vol % [31]. Tallon et al. mixed nanosized  $\text{Al}_2\text{O}_3$  with micron-sized  $\text{Al}_2\text{O}_3$  (in volume ratios of 1:9) and found that 50 vol % loadings could be achieved. However, sintered densities are compromised by a few percent compared to those produced from solely micron-sized powders [32]. Recent success was realized by placing  $\text{BaTiO}_3$  nanoparticles in an optimized suspension prior to the addition of the gelling agent, resulting in a homogeneous green body [33].

Selected gel-casting systems require no dispersants. All-acrylic block copolymers, as described in Section 6.2.3, act as built-in dispersants for micron-sized particles [34–35]. For submicron particles; however, the van der Waals forces resulting from the increased powder surface area are sufficiently strong that a dispersant must be added to keep powders in suspension [18].

The second requirement for casting suspensions is that the suspension must be able to flow freely into the mold. Viscosities naturally increase with the addition of powders. Hence, there is a trade-off between high solids loading and castability. In general, the viscosity of the suspension,  $\eta$ , can be described by a modified Krieger–Dougherty equation [36]:

$$\eta_r = \frac{\eta}{\eta_o} = \left(1 - \frac{\phi}{\phi_m}\right)^{-n},$$

where  $\eta_r$  is the relative viscosity,  $\eta_o$  is the viscosity of the premix or solvent with no solids added,  $\phi$  is the solids loading, and  $n$  and  $\phi_m$  are fitting parameters. Figure 6.8 displays the relative viscosity of 5 vol %  $\text{PMMA}_{23}\text{PtBA}_{92}\text{APMMA}_{23}/95$  vol % 2EH slurries as a function of  $\text{Al}_2\text{O}_3$  loading at 60°C. Solids loadings of 50 vol % are feasible while still maintaining easy flow [18].

In certain gel-casting systems, the viscosity can be independently controlled to some extent. For acrylic-based TRG systems, this is accomplished by decreasing the triblock copolymer molecular weight and concentration [37]. While reducing the copolymer molecular weight will lower the viscosity at high temperature, the endblock molecular weight must be large enough to ensure that the gel behaves elastically at room temperature. If the end blocks are too short, the gel will flow during the drying process, and dimensional tolerance and detail replication will not be maintained. In casting with polysaccharides and polymer solutions, base solution viscosity is a function of molecular weight and concentration [38]. Like with acrylic triblock systems, reducing concentration too much will lead to weak gels and green bodies. In gelcasting with monomer solutions, base viscosity is not as easily manipulated since monomer additions will not affect the viscosity of water greatly. More important is to cast the slurry before the polymerization reaction proceeds too far and viscosity starts to rapidly increase.

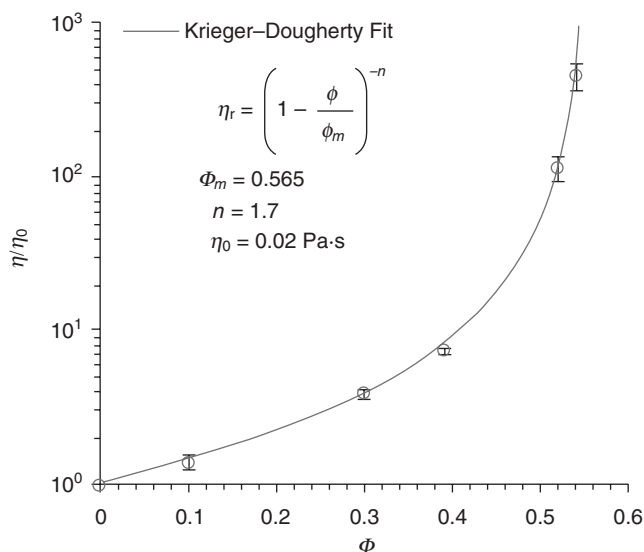


**Figure 6.8.** Viscosity as a function of  $\text{Al}_2\text{O}_3$  volume fraction in 5 vol %  $\text{PMMA}_{23}\text{PtBA}_{92}\text{PMMA}_{23}/2$ -ethylhexanol base gel at  $60^\circ\text{C}$  fit with a Krieger–Dougherty expression. Reprinted from Reference 30 with permission from John Wiley & Sons.

### 6.3.2 Gelation and the Casting Atmosphere

In traditional gel-casting systems, the window for casting is determined by the time interval between the addition of the initiator (or initiator and catalyst) and the commencement of gelation. Because the polymerization reaction is exothermic, this idle, or lag, time can be established by monitoring the temperature of the premix, as shown in Figure 6.9. The idle time can be controlled both by temperature and concentration of both initiator and catalyst. In the AM/MBAM system, idle times are found to range from 5 to 120 min [4].

The Arrhenius plot of Figure 6.10 demonstrates how idle time varies with both temperature and catalyst concentration. Activation energies for free radical generation are reduced by 50% with the addition of a catalyst. Ceramic powders and dispersants are also known to reduce idle time [4, 39]. Although casting is effective at ambient temperatures, many investigators transfer castings to ovens to accelerate the gelation.

The presence of oxygen in monomer solutions in traditional gel-casting systems can prematurely terminate free radical polymerization by reacting to form a peroxide group at the end of a growing chain [40–42]. Ha, for example, found that  $\text{Al}_2\text{O}_3$  cast in air or vacuum showed exfoliated surface layers, while castings in  $\text{N}_2$  were robust [40]. If sufficient oxygen is present, the gel can be weakened substantially, and in severe cases, gelation will not occur at all. This can be especially problematic when casting laminated components since poorly polymerized gel at interfaces will result in poor interlaminar strength. For this reason, a slurry is often de-aired prior to casting, or slurry

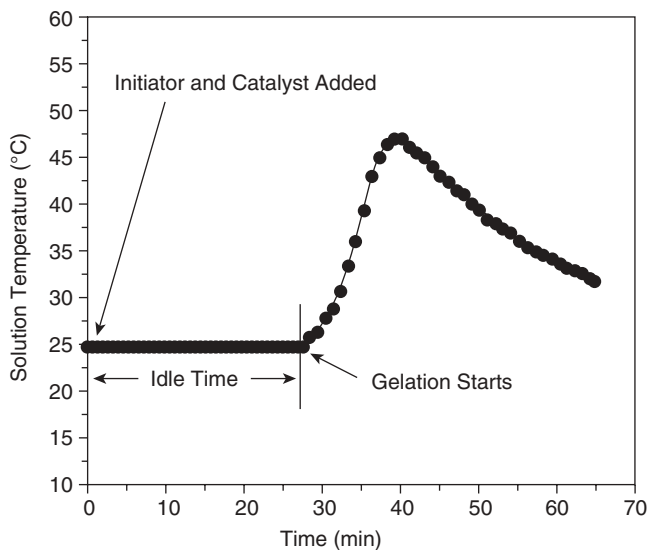


**Figure 6.9.** Change in temperature of acrylamide premix solution during gelation. Reprinted from Reference 4 with permission from John Wiley & Sons.

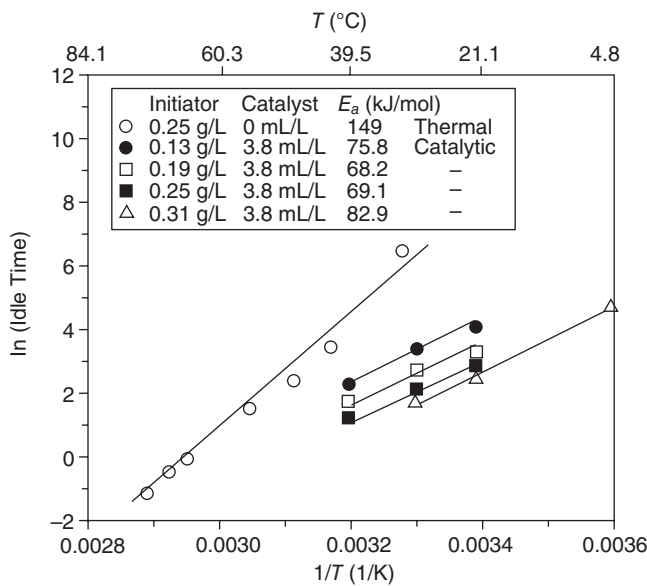


**Figure 6.10.** Idle time versus inverse temperature for catalytic and thermally driven gelation of acrylamide premix solutions. Reprinted from Reference 4 with permission from John Wiley & Sons.

production and casting are performed under an inert atmosphere. The latter, especially, causes increased production costs. De-airing has the added advantage of removing large pores from the casting. An alternate solution was proposed by Ma et al. for the AM system [41]. They added up to 15 wt % poly(vinylpyrrolidone) (PVP) to a premix solution of monomers and water. Although the PVP increased the viscosity of the casting suspension, it allowed polymerization of the surface AMs and prevented surface spallation. Thermoreversible gelcasting, with either acrylic-based triblocks or polysaccharides, can proceed in air since it does not rely on polymerization.

Oxygen ingress should also be considered in mold design for traditional gel-casting systems. Although most metal and ceramic molds are essentially impermeable to oxygen, the same is not true for polymers. Shanti et al. presented a listing of polymers with low oxygen permeability, which can be used as molds, mold liners, and top sealing layers [30].

### 6.3.3 Drying

Cracking and warping occur during drying as a result of high capillary stresses that form at liquid–vapor interfaces within pore channels between ceramic powder particles. Scherer provides a general background of drying in ceramic processing, and Omatete et al. [43] present specifics of drying gelcast bodies. Drying initially occurs at a steady rate since liquid is close to the surface of the body. Thus, this first of three generally recognized drying periods is known as the constant rate period (CRP). As solvent evaporates, the body shrinks due to capillary pressure,

$$P = -\frac{2\gamma_{LV}}{r},$$

reaching a maximum pressure of

$$P_{\max} = (\gamma_{SV} - \gamma_{SL}) \frac{S_P}{V_P} = \gamma_{LV} \cos \theta \frac{S_P}{V_P},$$

where  $r$  is the radius of curvature of the liquid meniscus;  $S_P/V_P$  is the surface area-to-volume ratio (or hydraulic radius) of the filled pore channel;  $\gamma_{LV}$ ,  $\gamma_{SL}$ , and  $\gamma_{SV}$  are the liquid–vapor, solid–liquid, and solid–vapor surface energies, respectively; and  $\theta$  is the solid–liquid contact angle (note that surfactants will reduce  $\theta$  and therefore  $P$ ) [44]. The capillary pressure acts as a compressive stress on the body, causing it to shrink. At the critical point, where  $P = P_{\max}$ , the liquid front begins to recede into the body and the drying rate begins to slow—the CRP gives way to the falling rate period (sometimes further distinguished as the first and second falling rate periods). Different areas of a cast body will reach this transition point at different times—especially for large or complex-shaped parts, or when one side of the body is exposed to air while another side is effectively sealed (e.g., resting on an impervious surface). The result is significant pressure gradients that lead to warping. Furthermore, dried regions of a partially dried casting are unable to accommodate the evolving stresses through relaxation or

flow, causing cracking and void opening. Ensuring uniform liquid distribution by drying slowly—at least initially—is necessary to prevent these types of damage.

Two strategies can be employed to reduce drying stresses and, hence, the propensity for warping and cracking. The first relies upon slowing the rate at which drying occurs in the early stages of drying. This is realized by controlling the solvent partial pressure in the drying atmosphere. For aqueous systems, this is tantamount to humidity control and has been successfully used by a number of investigators [40, 43, 45–47]. For example, Ghosal et al. [45] were able to reduce drying flaws while actually reducing the total drying time of a gelcast  $\text{Si}_3\text{N}_4$  rotor by 65% using a temperature–humidity profile optimized through modeling. In the acrylate triblock copolymer/alcohol systems, controlled drying can be accomplished inside in a sealed container alongside a reservoir of solvent.

The second approach to preclude warping and cracking requires that the gelcast body be made more resistant to drying stresses, which entails an increase in strength and permeability of the green body. More difficult to control than drying atmospheres, green body strength is a function of the binder composition and amount, as discussed below. Permeability relies on solids loading and binder concentration. Because binder and solids loading will also influence the full casting, drying, and sintering process, few have taken only this route to prevent warpage. Advanced methods that show promise in reducing drying-induced flaws by eliminating capillary stresses are introduced in Section 6.5.2.

Although gelcasting is meant to be a net-shape forming technique, strength for handling or green machining is still required. The polymeric binders in any of the systems described provide some level of mechanical robustness. Green body strengths for various systems are reported in Table 6.1. A disadvantage of thermoreversible systems, whether polysaccharides or acrylate triblock copolymers, is their lower green strengths than traditional gel-casting systems. However, even with modest green body strengths (<12 MPa), machining by lathing, drilling, or milling is possible as detailed by Prabhakaran and Pavithran (Fig. 6.11) [14].

TABLE 6.1. Green Strength of Gelcast Ceramics

System <sup>a</sup>	Strength (MPa)	Test Configuration	Reference
55% $\text{Al}_2\text{O}_3$ , 3.4% AM/MBAM	30.8	Three-point bend	Ha [40]
55% $\text{Al}_2\text{O}_3$ , 6% acrylic acid	11.5	Diametral compression	Prabhakaran and Pavithran [14]
~57% $\text{Al}_2\text{O}_3$ 1% agarose	6.7	Three-point bend	Santacruz et al. [48]
50% $\text{Al}_2\text{O}_3$ , 3% agar	$4.0 \pm 0.5$	Three-point bend	Millan et al. [49]
45.3% $\text{Al}_2\text{O}_3$ , 1.5% PMMA <sub>23</sub> PnBa <sub>31</sub> PMMA <sub>23</sub>	$2.8 \pm 0.5$	Ball on ring	Seitz et al. [37]
33.4% $\text{Al}_2\text{O}_3$ , 4.9% PMMA <sub>23</sub> PnBa <sub>31</sub> PMMA <sub>23</sub>	$6.1 \pm 0.8$	Ball on ring	Seitz et al. [37]

<sup>a</sup> Percentages listed in volume percent ceramic in slurry and weight percent binder of ceramic + binder.



**Figure 6.11.** Photograph of machined Al<sub>2</sub>O<sub>3</sub> green body with a 6 wt % binder showing recessed steps by lathing, a center cavity by drilling, and a groove by milling. Reprinted from Reference 14 with permission from Elsevier.

Green machining also benefits from green body toughness. Seitz et al. demonstrated that by changing the midblock in the acrylic triblock copolymers from glassy to rubbery, one could adjust the mechanical behavior of the green body from strong and stiff to ductile [37]. PtBA has a glass transition of 43°C, while  $T_g$  of PnBA is -84°C [50]. The load-displacement response of green disks loaded in biaxial tension demonstrates the linear elastic behavior of the PtBA-containing material and a significant nonlinear extension for the rubbery (PnBA) material. It is then possible to choose a triblock that imparts the necessary combination of strength and toughness for green machining.

### 6.3.4 Binder Burnout and Sintering

Once drying is complete, gelcast bodies require a binder burnout process followed by densification, normally by sintering. Since the concentration of organic binder is relatively small (<5 wt %) compared to bodies formed by injection molding or tape casting, for example, the binder burnout process proceeds rapidly and with relative ease. A network of channels from solvent evaporation provides pathways for binder removal. For laboratory-sized samples, binder burnout for the AM/MBAM system is approximately 5 h at 550°C, while the acrylic-based thermoreversible system requires only an hour at 250°C [51].

Some investigators isopress samples after binder burnout to promote densification. Others, particularly in the thermoreversible systems, presinter to give the body added strength for handling. However, the gelcast body can feasibly be taken to the sintering temperature in the same cycle. Some ceramic systems are designed for

reaction sintering. For example, Hovis and Faber gelcast  $\text{BaCO}_3$  and  $\text{Fe}_2\text{O}_3$ , which reacted to form  $\text{BaFe}_{12}\text{O}_{19}$  during sintering [52]. Others produced solids for postsintering reactions, for example, reaction-bonded  $\text{SiC}$  [53] and porous  $\text{Ti}$  by the decomposition of gelcast and sintered  $\text{TiH}_2$  [54].

Densification to full density relies upon the green density, particle size, atmosphere, and temperature, as related to well-developed sintering theories. A full discussion of sintering can be found in this volume in Chapter 1. The high solids loading and uniform particle distribution achievable in gelcasting ensure that sintering to full density without warping occurs easily for most materials.

## 6.4 APPLICATIONS IN PROCESSING/FABRICATION OF GELCAST CERAMICS

### 6.4.1 Bulk Ceramics

Although  $\text{Al}_2\text{O}_3$  has been the prototypic material for demonstration of nearly all of the gel-casting systems described in Section 6.2, a plethora of materials have been successfully gelcast. Table 6.2 provides a listing of these, grouped by application. As is evident, functions range from structural materials for aerospace and power generation to electronic materials for varistors, thermistors, thermoelectrics, and fuel cells. Foams and porous solids have been gelcast for biomedical applications, filters, porous membranes, and insulation. Oxides, carbides, nitrides, and phosphates have all been successfully cast.

Replication of fine details, as in the leading edges of the rotor shown in Figure 6.12, makes the technique particularly attractive for complex, bulk components. A second example is the  $\text{SiAlON}$  radome displayed in Figure 6.13 [55]. This casting required 4 kg of ceramic powder ( $\text{Si}_3\text{N}_4$ ,  $\text{AlN}$ ,  $\text{Al}_2\text{O}_3$ ,  $\text{Y}_2\text{O}_3$ , and  $\text{SiO}_2$ ) and a mold weighing more than 150 kg. Because of the size and thin walls of the radome, drying was a particular challenge, as the tip of the radome dried more slowly than the bulk of the walls. Ultimately, drying was accomplished using liquid desiccant solvent extraction discussed more thoroughly in Section 6.5.2.

### 6.4.2 Textured Materials

The idle time associated with the period between the addition of the initiator and the onset of gelation in chemically cross-linked systems, described in Section 6.3.2, offers an opportunity to control orientation of the suspended ceramic powders. Likewise, thermoreversible systems allow for orientation in the liquid state; the system is then cooled quickly to preserve the desired structure. Zimmerman et al. in  $\text{FeTi}_2\text{O}_5$  demonstrated the first example of texturing during gelcasting where texture was imposed by casting the suspension in a magnetic field [104–106].  $\text{FeTi}_2\text{O}_5$  is paramagnetic and grains align along their  $b$ -axes in a magnetic field. Texture is assessed through pole figures obtained from an orientation distribution function determined from X-ray mea-

TABLE 6.2. Applications of Gelcast Materials

Application	Material
Aerospace: turbines/stators/nozzles	$\text{Si}_3\text{N}_4$ [56], $\text{ZrC}$ [57]
Armor	$\text{AlN}$ [58]
Biomedical: dental/orthopedics/drug delivery/medical devices	Calcium phosphate [59], tricalcium phosphate [59–61], hydroxyapatite [59, 62], ZTA [63], bioglass [64], porcelain [65]
Capacitors	$\text{BaTiO}_3$ [33]
Catalyst supports	$\text{Al}_2\text{O}_3$ [66]
Electronic substrates	Cordierite [67], $\text{AlN}$ [58]
Filters: cross-flow/diesel particulate	Cordierite [67–68], $\text{SiC}$ [69], $\text{Al}_2\text{O}_3$ [70]
Foams	$\text{Al}_2\text{O}_3$ [70–72], calcium phosphate [59], hydroxyapatite [73–74], cordierite [67–68, 75], $\text{Si}_3\text{N}_4/\text{Si}_2\text{N}_2\text{O}$ [76], $\text{SiC}$ [77]
Fuel cells	Lanthanum strontium manganate [78], $\text{LaCoO}_3$ [79–83], $\text{NiO/YSZ}$ [84], $\text{La}_{10}\text{Si}_6\text{O}_{27}$ [85], $\text{CaZrO}_3$ [86]
Heat exchangers	$\text{SiC}$ [87]
Insulation	$\text{Al}_2\text{O}_3$ [70]
Interpenetrating composites/preforms	$\text{Al}_2\text{O}_3$ ; [70] $\text{SiC-B}_4\text{C}$ [88]
Investment casting cores	$\text{Al}_2\text{O}_3$ [89]
Magnetic components	$\text{Bi}_4\text{Ti}_3\text{O}_{12}$ [90], $\text{BaFe}_{12}\text{O}_{19}$ [91]
Membranes	$\text{Al}_2\text{O}_3$ [92]
Nuclear fuel	$\text{UO}_2$ [93]
Piezoelectrics	$\text{BaTiO}_3$ [94], lead zirconate titanate (PZT) [95–96]
Radomes	Spinel [97], $\text{Si}_3\text{N}_4$ [98], $\text{SiAlON}$ [55]
Refractories	Alumina [97], spinel [97], $\text{SiAlON}$ [99], $\text{AlN}$ [58], cordierite [67]
Thermistors	$\text{BaTiO}_3$ [100]
Thermoelectrics	$\text{ZnAl}_2\text{O}$ [101]
Transparent components	$\text{Al}_2\text{O}_3$ [102], hydroxyapatite [62]
Varistors	$\text{ZnO}$ [103]

surements in samples where the magnetic field was in the plane of the specimen and where the magnetic field was normal to the plane of the specimen.

Pole figures are represented in gray scale or in color, where the gray or color scale represents texture strength in multiples of a random distribution (MRD). A uniform distribution of grain orientations would result in a pole figure of a single shade corresponding to  $\text{MRD} = 1$  [107]. This is demonstrated in Figure 6.14a, where  $\text{FeTi}_2\text{O}_5$  was cast with no magnetic field. In contrast, using a magnetic field of 8.4 T, strong fiber-type texture, where the  $\{0k0\}$  poles align parallel to the magnetic field, results in peak MRDs of 48 (Fig. 6.14b).

Microstructural texture can also be imposed via gelcasting using nonequiaxed particles. Wei et al. used  $\text{Al}_2\text{O}_3$  platelets to produce highly textured  $\text{Al}_2\text{O}_3$  layers in laminates with fine-grained, texture-free alumina, alumina toughened zirconia, and reaction-bonded mullite [108–109]. Alumina platelets, 10–15  $\mu\text{m}$  in diameter, in



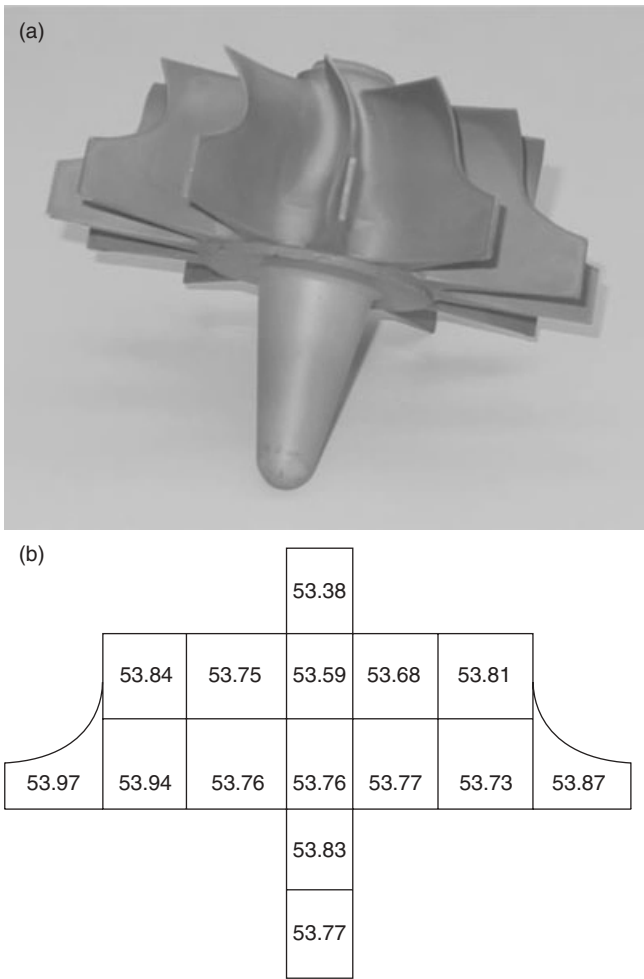


**Figure 6.12.** (a) Gelcast  $\text{Si}_3\text{N}_4$  radial-vane turbine rotor (~18 cm in diameter). (b) Schematic showing uniform green density in segments of dried, gelcast rotor; average green density was 53.77%  $\rho_{\text{th}}$ . Reprinted from Reference 8 with permission from John Wiley & Sons.

fractions up to 17% by volume, were added to submicron  $\alpha\text{-Al}_2\text{O}_3$  powders. A Na-alginate aqueous-based gel was used for tape casting sheets for lamination. Texture strengths as high as 16 MRDs were observed.

A second method of achieving microstructural texture is one in which gelcasting is coupled with freeze casting, a technique in which the suspension liquid is frozen in the mold and serves as a template for pores in the system. To achieve microstructural texture, both the freezing direction and the temperature gradient are prescribed. Chen et al. demonstrated this coupling of techniques using  $\text{Al}_2\text{O}_3$  in *tert*-butyl alcohol with AM and MBAM [110]. A processing schematic of freeze gelcasting is shown in Figure

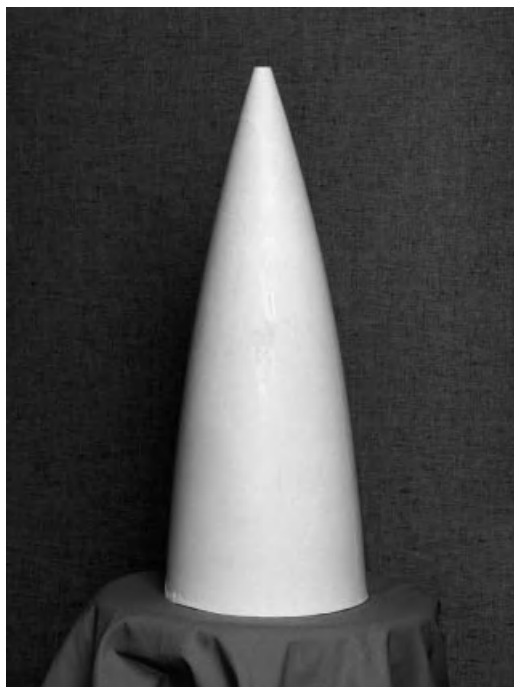


**Figure 6.13.** SiAlON green body of a radome, ~53 cm tall and ~20 cm in diameter. Reprinted from Reference 99 with permission from John Wiley & Sons.

6.15. The resultant microstructures show axial texture of the pore channels along the freezing direction (Fig. 6.16). By imposing a temperature gradient, with one end near the melting temperature of the *tert*-butyl alcohol, more complex texture patterns, such as axial pore gradients, are possible.

### 6.4.3 Porous Materials

Porous ceramics have received increased attention of late for applications as heat exchangers, filters, catalyst supports, and biological scaffolds for cell growth, among others. There are three primary methods by which porous ceramics can be produced, as reviewed by Studart et al. [111] These include replication, direct foaming, and sacrificial templating. In the replication technique, a scaffold with the desired pore microstructure is used as a “positive” template, which is converted into the desired ceramic material. The foaming method, on the other hand, is the simplest technique with the least amount of tailorability. In this technique, a gas is incorporated into a ceramic slurry to produce a foam typically by bubbling air or an inert gas through the slurry. The third technique incorporates a fugitive filler, or porogen, as a “negative” sacrificial template. In this method, an organic phase is added to a ceramic slurry; after casting, molding, or other shaping process, the filler is burned out, resulting in porosity.

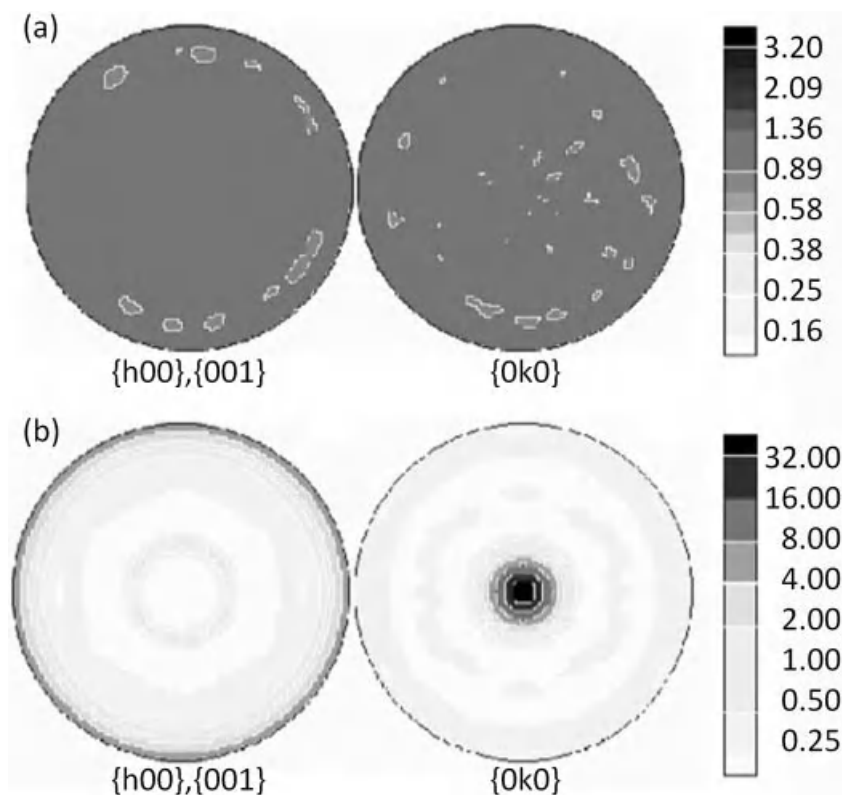


**Figure 6.14.** Axial pole figures calculated from orientation distribution functions for (a) a control  $\text{FeTi}_2\text{O}_5$  sample processed without an applied magnetic field and (b)  $\text{FeTi}_2\text{O}_5$  processed in an 8.4-T applied magnetic field, where the magnetic field was normal to the plane of the specimen. Adapted from Reference 106.

Advantages of using fugitive fillers are the ease in which they are incorporated into traditional ceramic processing techniques and the simplicity in which new structures can be produced simply by altering the fillers used.

Both foaming and sacrificial templates have been used in conjunction with gelcasting. Sepulveda and Binner have pioneered the foaming of gelable systems [112]. The process involves aqueous suspensions of ceramic powders mixed with an acrylate monomer along with polyacrylate dispersants. Foaming agents are added to this mixture in a sealed vessel under nitrogen. Polymerization is induced via an initiator and catalyst, typically APS and TEMED [113], described in Section 6.2.1. By virtue of the induction time prior to polymerization, timing can be adjusted such that polymerization initiates concomitantly with casting.

Foam volume is a function of stirring time and the effectiveness of the foaming agent, shown for alumina in Figure 6.17 [112]. The initial increase in volume occurs as the foaming agent is drawn into the suspension. At steady state, the foam volume

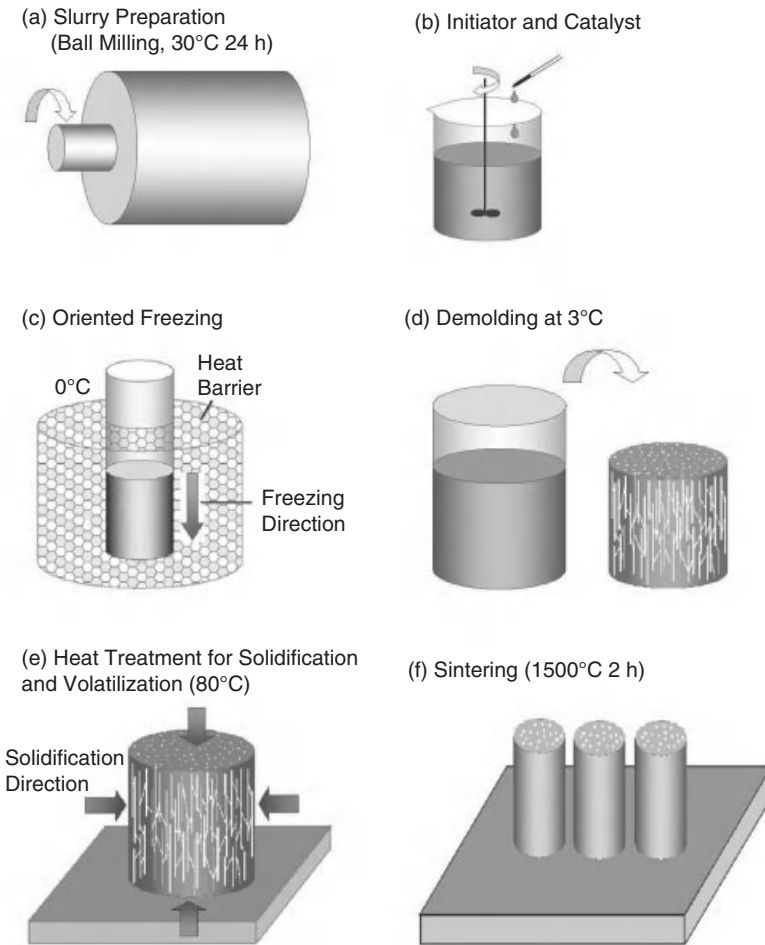


**Figure 6.15.** Processing schematic for ceramics with textured porosity via the freeze-gelcasting technique. Reprinted from Reference 111 with permission from John Wiley & Sons.

coincides with the minimum film thickness to maintain a stable foam. The size of the cells can be enlarged by reducing the pressure in the system (via a vacuum pump) just prior to gelation. Figure 6.18 represents the densities of alumina, which can be achieved by foaming, both in the green and sintered states [112]. These values represent sintered densities of 7–47% of theoretical. Neither replication nor sacrificial templates result in densities as low as foaming processes.

A useful example of foamed gelcast materials is hydroxyapatite for bone implants shown in Figure 6.19 [113]. Noteworthy is the pore size distribution, which includes pores greater than the 100  $\mu\text{m}$  needed for cell growth. By adjusting the pore fraction, one can tailor the elastic modulus to compare well to bone—a requirement to prevent stress-shielding effects for implants [114]. The permeability of these solids at relative densities below 20% may also afford applications in water filtration.

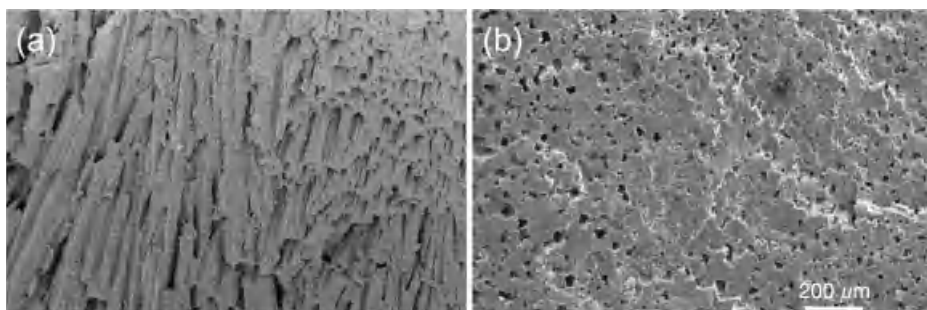


**Figure 6.16.** Scanning electron micrographs of  $\text{Al}_2\text{O}_3$  with long-range unidirectional pore channels fabricated by freeze-gelcasting, observed (a) parallel to the freezing direction and (b) perpendicular to the freezing direction. Reprinted from Reference 111 with permission from John Wiley & Sons.

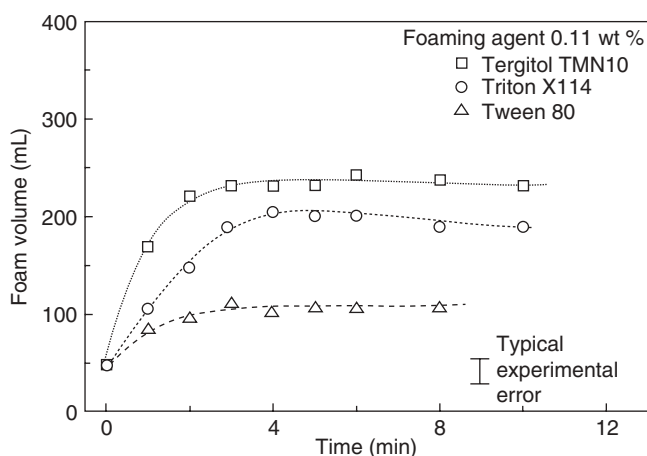


**Figure 6.17.** Foam volume generated with suspensions containing 74.1 wt %  $\text{Al}_2\text{O}_3$  with three different commercial foaming agents (courtesy of P. Sepulveda).

The earliest reports of porous gelcast ceramics prepared by the sacrificial template method are from Wang et al. [115]. Here, a fugitive filler of carbon powder is used to create the pore network in the fabrication of  $\alpha\text{-Al}_2\text{O}_3$ . The pore characteristics, related to the size and shape of the carbon with respect to the alumina grain size, resulted in angular crack-like pores. All candidate fillers are required to be organic and to burn away cleanly during the binder burnout process. Furthermore, they must be stable in the solvent used, neither dissolving nor swelling. Fillers that meet these criteria include starches, such as corn, potato, tapioca, or wheat starch, all of which have been successfully used in gelcasting [116–118]. Simple organic polymers, such as polyethylene and polypropylene, have also been exploited [119–120].

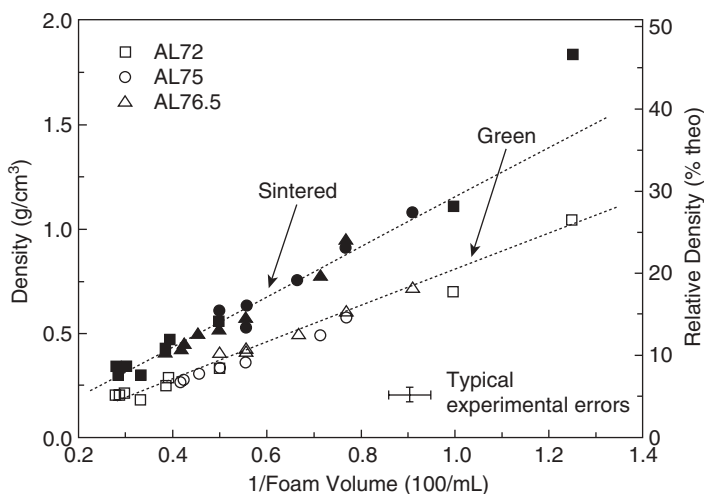


**Figure 6.18.** Foamed  $\text{Al}_2\text{O}_3$  green density and sintered density after 3 h at  $1550^\circ\text{C}$ . AL72 (square), AL75 (circle), and AL76.5 refer to foaming levels; gel time was approximately 1 min (courtesy of P. Sepulveda).

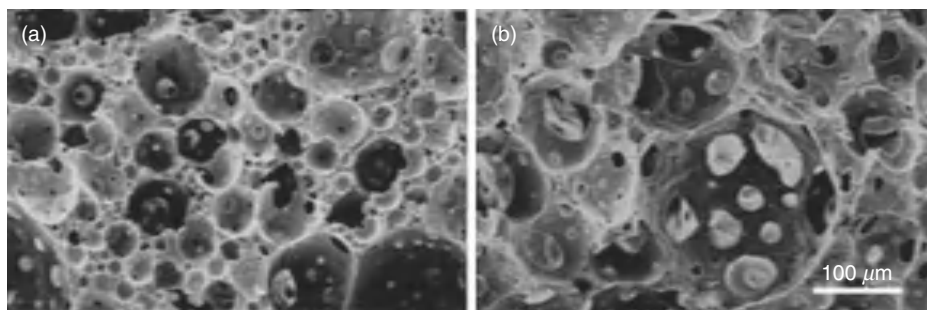


**Figure 6.19.** Scanning electron micrographs of foamed hydroxyapatite at relative densities of (a) 0.241 and (b) 0.108. Reprinted from Reference 114 with permission from John Wiley & Sons.

With low concentrations of fillers, the porogens are generally isolated and their shape is reproduced with great fidelity in the sintered body. Pores shrink in proportion to the overall component shrinkage that occurs with sintering. Consequently, the volume fraction of porosity is very close to the volume fraction of the filler, as shown in Figure 6.20. A fundamental change in porosity arises once the volume fraction of filler reaches the percolation threshold, the statistically derived concentration that defines long-range connectivity in a random network [121]. Once the percolation threshold is reached, pores created during the burnout of fillers will coalesce during sintering. Although the general pore shape remains, it is now a secondary feature in a much larger pore network.

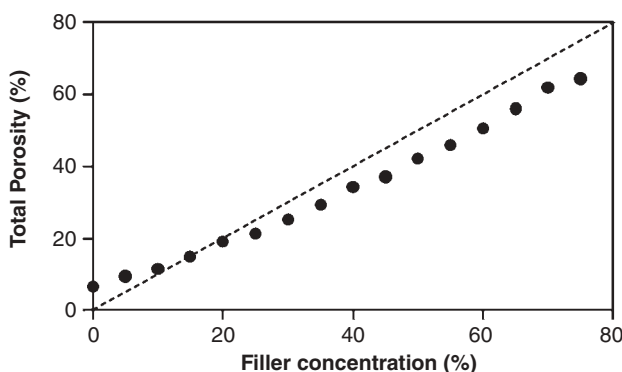


**Figure 6.20.** Porosity in thermoreversibly gelcast  $\text{Al}_2\text{O}_3$  samples versus fugitive filler concentration. Total solids loading ( $\text{Al}_2\text{O}_3$  + corn starch filler) in slurries was approximately 50 vol %. The base gel was 5% polymer using  $\text{PMMA}_{25}\text{PtBA}_{116}\text{PMMA}_{25}$  and  $\text{PMMA}_{23}\text{PtBA}_{31}\text{PMMA}_{23}$  in pentanol or isopropyl alcohol. All samples were sintered at  $1600^\circ\text{C}$  in air.

Likewise, because the pores merge during sintering, the volume fraction of porosity is less than the initial filler concentration, evident at volume fractions greater than 20% in Figure 6.20.

#### 6.4.4 Laminates

Gel network formation provides advantages for laminate production, as investigated by Baskin [122], Hovis [52, 91], and Montgomery [18, 117, 123] and summarized by Shanti et al. [30]. Schematics of the molding techniques used to produce laminates by gelcasting are shown in Figure 6.21. In the simplest method (not shown), two laminae are cast and gelled separately and stacked. In thermally reversible systems, one surface of each is locally heated prior to stacking, which allows them to fuse [123]. In the second method, a mold consisting of a polymer gasket on a glass slide is filled with the first slurry and covered with another slide, similar to the method in Figure 6.21a [117]. After gelation is complete, the top slide is removed, a second gasket added, and a second slurry cast. Residual heat from the second slurry is sufficient to fuse the two layers, providing strong interfacial bonding.

For laminates in which a small gradation in composition or structure is desired, slurries are cast in the order of increasing density. First, the lower density suspension is cast into the empty mold. Using a narrow funnel, the higher density suspension is cast beneath the first (Fig. 6.21b). The two then gel together. This method also precludes air entrapment between layers. The above lamination methods have been used to produce laminates of dense/porous  $\text{Al}_2\text{O}_3$  [18, 116–117, 123].

Another laminate strategy consists of a rectangular boxlike mold with removable dividers (Fig. 6.21c). Every other chamber is filled with slurry and the layers are allowed to gel. Once gelation is complete, the mold partitions are removed, exposing

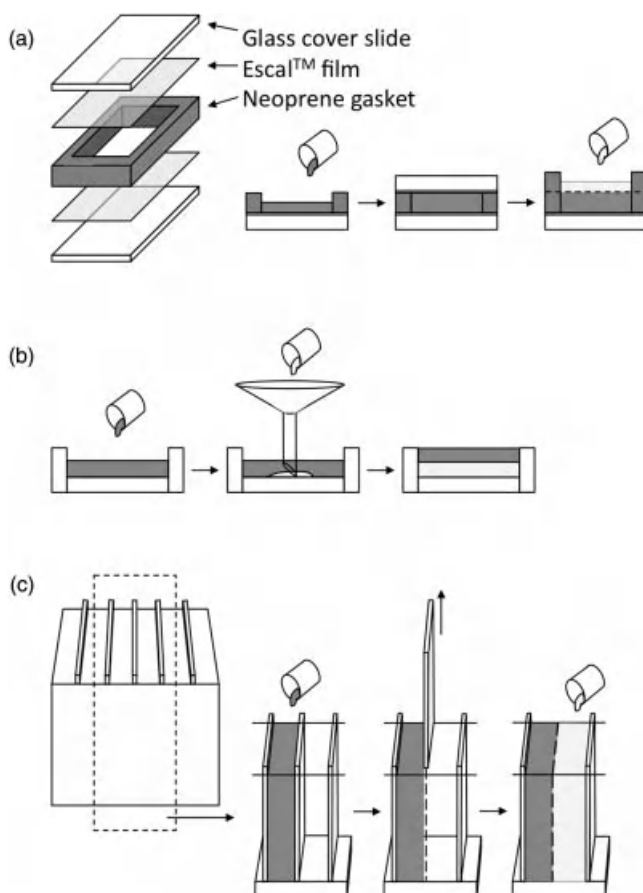


**Figure 6.21.** Mold designs for laminate gelcastings: (a) stackable arrangement of gaskets and oxygen barrier film, (b) funnel to cast lower, denser layer, and (c) a mold with removable dividers. Adapted from Reference 123.

faces of the previously gelcast layers. The alternate chambers are filled with the second slurry and are allowed to gel and bond to the adjacent layers.

Texturing by magnetic field can be coupled with lamination techniques as shown by Hovis et al. [30, 52, 91, 124], who used ferrimagnetic  $\text{BaFe}_{12}\text{O}_{19}$  to produce textured laminates. Because  $\text{BaFe}_{12}\text{O}_{19}$  is highly anisotropic with easy magnetization along its *c*-axis, permanent magnets combined with templated grain growth are sufficient to induce a substantial crystallographic texture [91]. Using the stacking technique illustrated in Figure 6.21a, multilayers of alternate crystallographic orientation could be produced. Figure 6.22a demonstrates the cross lamellar microstructure, here as a fracture surface, with alternating  $\text{BaFe}_{12}\text{O}_{19}$  layers of (111)- and  $(\bar{1}\bar{1}\bar{1})$ -type texture. Proof



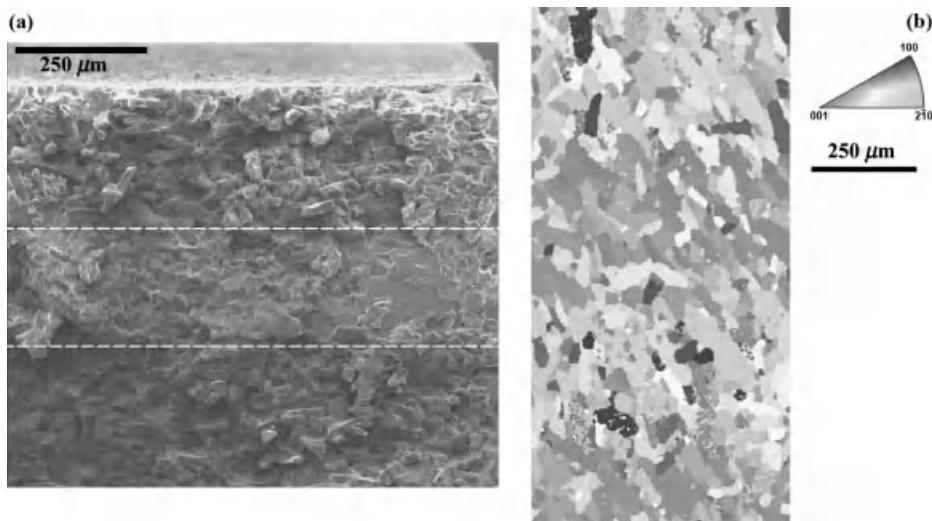


**Figure 6.22.** (a) Fracture surface of textured  $\text{BaFe}_{12}\text{O}_{19}$  laminate showing microstructural texture. (b) Electron backscatter diffraction inverse pole figure demonstrating crystallographic texture. Laminates are approximately 95–95% dense. Reprinted from Reference 30 with permission from John Wiley & Sons.

of the alternating texture is provided from electron backscatter diffraction (EBSD) mapping, shown in Figure 6.22b. Grains of similar color are oriented along the same axis. Four layers, each approximately  $150\ \mu\text{m}$  thick, are clearly differentiated by their crystal orientation.

In a more recent development, triblock copolymer thermoreversible gels have been found to be suitable for tape casting. By tuning relative lengths of midblock and end blocks in the copolymers, it is possible to significantly alter the rheological properties of the solution. Seitz et al. found that short end blocks, such as those found in  $\text{PMMA}_{25}\text{Pt-BA}_{116}\text{PMMA}_{25}$  or  $\text{PMMA}_9\text{PtBA}_{53}\text{PMMA}_9$  (both from Kuraray, Inc.) in 2EH, provided low viscosity in the liquid state and short relaxation times [29]. A modified tape-casting system was developed to use TRG slurries [28]. Instead of a room-temperature slip reservoir and a heated drying bed as in a traditional tape-casting system, the customized unit was fitted with a heated reservoir and a chilled bed. The latter is necessary to rapidly cool the suspension to induce gelation before significant relaxation of the cast layer occurred. By rewinding the tape after each casting, a second and third layer could be produced. The thermoreversible nature of the suspensions allows the layers to bond strongly. The anode support, anode active layer, and electrolyte layer of a solid oxide fuel cell (SOFC) were produced by direct lamination, as shown in Figure 6.23. The discrete highly porous Ni–yttria-stabilized zirconia (YSZ) anode support, microporous Ni–YSZ anode, and nearly dense YSZ electrolyte layers are clearly well bonded as required for high performance. This example also demonstrates that both thick and thin

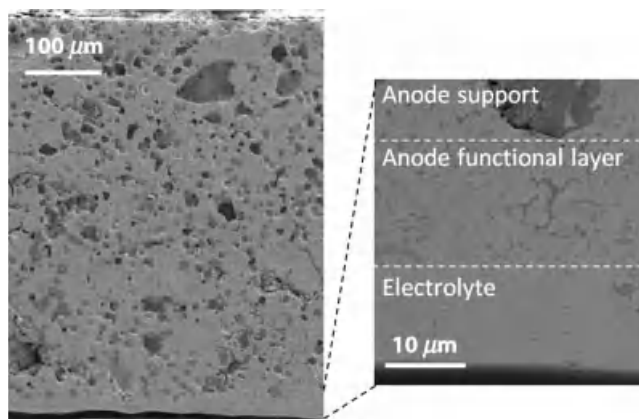


**Figure 6.23.** Scanning electron microscopy (SEM) micrograph of a polished cross section of SOFC anode support, anode active layer, and electrolyte produced by tape casting with thermoreversible gel slurries. Anode support is Ni-YSZ with ~50% porosity induced with corn-starch fugitive filler and the reduction of NiO to Ni; the anode is Ni-YSZ with porosity induced by the reduction of NiO to Ni; and the electrolyte is dense YSZ.

laminae can be produced using this combined gel-casting and tape-casting techniques, unlike in traditional tape casting or any other ceramic casting technique.

## 6.5 CHALLENGES AND OPPORTUNITIES IN GELCASTING

### 6.5.1 Toxicity/Environmental Concerns

Each of the gel-casting systems described in Section 6.2 suffers from some shortcoming. The AM monomers, though soluble in water, are toxic. The polysaccharides are also water soluble but are slow to gel (compared to the acrylic triblock systems) and are characterized by a large hysteresis between gelation and melting. Thermoreversible gels based on solvated triblock copolymers suffer from the use of alcohols as solvents. To diminish the environmental impact of the use of alcohols in the acrylic-based systems, drying can be conducted under vacuum with an in-line solvent trap. Shanti was able to recover all alcohol using this treatment [28]. To date, there are no triblock copolymers that are fully water soluble at a higher temperature with only the midblocks soluble at a lower temperature. However, zwitterionic compounds may provide some options [125]. These polymers phase separate on cooling in water and may lend themselves to the design of more environmentally friendly gel-casting systems.

### 6.5.2 Alternate Drying Methods

Warping and cracking can be greatly reduced by eliminating capillary stresses during the initial drying process. Instead, osmotic pressure arising from concentration

gradients can be used to remove solvent by techniques such as liquid desiccant solvent extraction, supercritical drying, and freeze drying. While the magnitude of the osmotic stresses is not necessarily lower than the capillary pressure in traditional drying, it is spread over the length scale of the concentration gradient rather than applied fully at an interface [28].

In liquid desiccant solvent extraction, the gelcast body is immersed in a concentrated polymer solution. As the concentration of the polymer in the desiccant is greater than that of the gel, solvent diffuses from the gel to the surrounding bath. Since the gel is cross-linked, it maintains its shape though in a liquid environment. An example of this technique is the drying of hollow, cone-shaped SiAlON radomes cast using an aqueous MAM-NVP-MBAM gel and dried using an aqueous PEG solution [55]. In this case, the interior of the radome was filled with the liquid desiccant for 1.5 h and then dried in air. This improved both the drying uniformity and drying speed.

Supercritical drying and freeze drying are two additional methods to dry components while avoiding the liquid–vapor interface. In supercritical drying, pressure and temperature are increased above the critical point of the solvent. In freeze drying, pressure and temperature are reduced so that the solvent freezes and then sublimates. Commercially available apparatus are available for both techniques.

While supercritical drying is not commonly used in gelcasting, it is quite common in the production of aerogels by the sol–gel process, and therefore much is known about the process relating to drying gels. In the simplest form, the component is brought to the solvent critical point with excess solvent so that a supercritical fluid atmosphere is formed. The pressure is then slowly released, allowing the gel to dry. As the critical point for water is 374°C and 22 MPa and that of ethanol is 243°C and 6.4 MPa, a displacement fluid such as CO<sub>2</sub> (critical point at 31°C and 7.4 MPa) is often used [126]. In order to substitute CO<sub>2</sub> for water or alcohol, the component is placed in a chamber with pressurized, liquid CO<sub>2</sub>. After flushing the water/alcohol from the liquid environment, the temperature is raised to produce supercritical CO<sub>2</sub> and the gel is dried by slowly decreasing the pressure.

### 6.5.3 Texturing with Electric Fields

Texturing in gelcast systems is effective using magnetic fields for paramagnetic and ferrimagnetic materials with anisotropic magnetic properties. The same should be true for paraelectric or ferroelectric materials in an electric field. Some examples of ceramics that may be likely candidates for study are the titanates, such as BaTiO<sub>3</sub>, PbTiO<sub>3</sub>, and so on. Because these perovskite structures are hosts for a wealth of substitutional ions, the list of candidate materials is extensive.

## 6.6 FINAL REMARKS

This chapter identified all of the attributes of an optimal gel-casting system: no toxicity, aqueous solubility, high solids loading, controllable gelation rates, reversibility, drying without warpage, high green strength, and sinterability to full density. None of the

systems described meet each of these constraints. This is, in part, due to a lack of a firm understanding of all of the factors that control dispersion and gelation. For example, some ceramic powders inhibit gelation, while some metals accelerate the process [127]. Interactions with mold materials also play a role. Although “work-arounds” exist for the bulk of these challenges, they highlight the need for more fundamental research studies both in the design of new gel systems and in the surface chemistry studies for process understanding and control.

## ACKNOWLEDGMENTS

The authors are grateful to Mark Janney, Maria Isabel Nieto Jiménez, Jennifer Lewis, Stephen Nunn, Kuttan Prabhakaran, Pilar Sepulveda, and Chang-An Wang for providing figures for the chapter. Thanks also to Mark Janney for sharing unpublished work, including thoughts on unexplored gel-casting studies. Financial support was provided by the National Science Foundation under Grant #DMR-0520513.

## REFERENCES

1. M. Janney (1990) Method for forming ceramic powders into complex shapes, U.S. Patent 4,894,194.
2. M. Janney and O. Omatete (1991) Method for molding ceramic powders using a water-based gelcasting, U.S. Patent 5,028,362.
3. M. Janney and O. Omatete (1992) Method for molding ceramic powders using a water-based gelcasting process, U.S. Patent 5,145,908.
4. A. C. Young, O. O. Omatete, M. A. Janney, and P. A. Menchhofer (1991) Gelcasting of alumina, *Journal of the American Ceramic Society*, **74**[3] 612–618.
5. M. A. Janney (1995) Gelcasting superalloy powders, *P/M in Aerospace, Defense and Demanding Applications*, 139–146.
6. O. O. Omatete, M. A. Janney, and S. D. Nunn (1997) Gelcasting: From laboratory development toward industrial production, *Journal of the European Ceramic Society*, **17**[2–3] 407–413.
7. M. A. Janney, W. J. Ren, G. H. Kirby, S. D. Nunn, and S. Viswanathan (1998) Gelcast tooling: Net shape casting and green machining, *Materials and Manufacturing Processes*, **13**[3] 389–403.
8. M. A. Janney, O. O. Omatete, C. A. Walls, S. D. Nunn, R. J. Ogle, and G. Westmoreland (1998) Development of low-toxicity gelcasting systems, *Journal of the American Ceramic Society*, **81**[3] 581–591.
9. K. Venkataswamy, R. Waack, B. Novich, and J. Halloran (1990) Forming whisker reinforced sintered ceramics with polymerizable binder precursors, U.S. Patent 4,978,643.
10. L. C. Klein (1985) Sol-gel processing of silicates, *Annual Review of Materials Science*, **15** 227–248.
11. E. Tormey, R. Prober, H. Bowen, and P. Calvert, Tape casting—future developments., in *Advances in Ceramics*, Vol. 9, eds. J. Mangels and G. Messing, pp. 140–149, American Ceramic Society, Columbus, OH, 1984.

12. T. Tanaka (1981) Gels, *Scientific American*, **244**[1] 124–138.
13. K. Cai, Y. Huang, and J. L. Yang (2005) Alumina gelcasting by using HEMA system, *Journal of the European Ceramic Society*, **25**[7] 1089–1093.
14. K. Prabhakaran and C. Pavithran (2000) Gelcasting of alumina from acidic aqueous medium using acrylic acid, *Journal of the European Ceramic Society*, **20**[8] 1115–1119.
15. S. L. Morissette and J. A. Lewis (1999) Chemorheology of aqueous-based alumina-poly(vinyl alcohol) gelcasting suspensions, *Journal of the American Ceramic Society*, **82**[3] 521–528.
16. S. L. Morissette, J. A. Lewis, J. Cesarano, D. B. Dimos, and T. Y. Baer (2000) Solid freeform fabrication of aqueous alumina-poly(vinyl alcohol) gelcasting suspensions, *Journal of the American Ceramic Society*, **83**[10] 2409–2416.
17. M. A. Huha and J. A. Lewis (2000) Polymer effects on the chemorheological and drying behavior of alumina-poly(vinyl alcohol) gelcasting suspensions, *Journal of the American Ceramic Society*, **83**[8] 1957–1963.
18. J. K. Montgomery, P. L. Drzal, K. R. Shull, and K. T. Faber (2002) Thermoreversible gelcasting: A novel ceramic processing technique, *Journal of the American Ceramic Society*, **85**[5] 1164–1168.
19. Y. L. Chen, Z. P. Xie, J. L. Yang, and Y. Huang (1999) Alumina casting based on gelation of gelatine, *Journal of the European Ceramic Society*, **19**[2] 271–275.
20. O. Lyckfeldt and J. M. F. Ferreira (1998) Processing of porous ceramics by “starch consolidation,” *Journal of the European Ceramic Society*, **18**[2] 131–140.
21. S. M. Olhero, G. Tari, M. A. Coimbra, and J. M. F. Ferreira (2000) Synergy of polysaccharide mixtures in gelcasting of alumina, *Journal of the European Ceramic Society*, **20**[4] 423–429.
22. A. J. Millan, R. Moreno, and M. I. Nieto (2002) Thermogelling polysaccharides for aqueous gelcasting—Part 1: A comparative study of gelling additives, *Journal of the European Ceramic Society*, **22**[13] 2209–2215.
23. E. Adolphsson (2006) Gelcasting of zirconia using agarose, *Journal of the American Ceramic Society*, **89**[6] 1897–1902.
24. I. Santacruz, M. I. Nieto, and R. Moreno (2002) Rheological characterization of synergistic mixtures of carrageenan and locust bean gum for aqueous gelcasting of alumina, *Journal of the American Ceramic Society*, **85**[10] 2432–2436.
25. E. Gregorova, W. Pabst, and J. Stetina (2006) Viscoelastic behavior of ceramic suspensions with carrageenan, *Journal of the European Ceramic Society*, **26**[7] 1185–1194.
26. Y. Jia, Y. Kanno, and Z. P. Xie (2002) New gel-casting process for alumina ceramics based on gelation of alginate, *Journal of the European Ceramic Society*, **22**[12] 1911–1916.
27. P. L. Drzal and K. R. Shull (2003) Origins of mechanical strength and elasticity in thermally reversible, acrylic triblock copolymer gels, *Macromolecules*, **36**[6] 2000–2008.
28. N. O. Shanti, Microstructurally tailored ceramics for energy applications by thermoreversible gelcasting, PhD Thesis, Northwestern University, Evanston, IL, 2010.
29. M. E. Seitz, W. R. Burghardt, K. T. Faber, and K. R. Shull (2007) Self-assembly and stress relaxation in acrylic triblock copolymer gels, *Macromolecules*, **40**[4] 1218–1226.
30. N. O. Shanti, D. B. Hovis, M. E. Seitz, J. K. Montgomery, D. M. Baskin, and K. T. Faber (2009) Ceramic laminates by gelcasting, *International Journal of Applied Ceramic Technology*, **6**[5] 593–606.

31. R. Wasche and G. Steinborn (1997) Influence of the dispersants in gelcasting of nanosized tin, *Journal of the European Ceramic Society*, **17**[2–3] 421–426.
32. C. Tallon, D. Jach, R. Moreno, M. I. Nieto, G. Rokicki, and M. Szafran (2009) Gelcasting of alumina suspensions containing nanoparticles with glycerol monoacrylate, *Journal of the European Ceramic Society*, **29**[5] 875–880.
33. I. Santacruz, M. I. Nieto, J. Binner, and R. Moreno (2009) Wet forming of concentrated nano-BaTiO<sub>3</sub> suspensions, *Journal of the European Ceramic Society*, **29**[5] 881–886.
34. H. S. Allami, N. C. Billingham, and P. D. Calvert (1992) Controlled structure methacrylic copolymers as dispersants for ceramics processing, *Chemistry of Materials*, **4**[6] 1200–1207.
35. J. Orth, W. H. Meyer, C. Bellmann, and G. Wegner (1997) Stabilization of aqueous alpha-Al<sub>2</sub>O<sub>3</sub> suspensions with block copolymers, *Acta Polymerica*, **48**[11] 490–501.
36. L. Bergstrom (1996) Rheological properties of Al<sub>2</sub>O<sub>3</sub>-SiC whisker composite suspensions, *Journal of Materials Science*, **31**[19] 5257–5270.
37. M. E. Seitz, K. R. Shull, and K. T. Faber (2009) Acrylic triblock Copolymer design for thermoreversible gelcasting of ceramics: Rheological and green body properties, *Journal of the American Ceramic Society*, **92**[7] 1519–1525.
38. A. J. Millan, M. I. Nieto, C. Baudin, and R. Moreno (2002) Thermogelling polysaccharides for aqueous gelcasting—Part II: Influence of gelling additives on rheological properties and gelcasting of alumina, *Journal of the European Ceramic Society*, **22**[13] 2217–2222.
39. A. A. Babaluo, M. Kokabi, and A. Barati (2004) Chemorheology of alumina-aqueous acrylamide gelcasting systems, *Journal of the European Ceramic Society*, **24**[4] 635–644.
40. J. S. Ha (2000) Effect of atmosphere type on gelcasting behavior of Al<sub>2</sub>O<sub>3</sub> and evaluation of green strength, *Ceramics International*, **26**[3] 251–254.
41. J. T. Ma, Z. P. Xie, H. Z. Miao, L. J. Zhou, Y. Huang, and Y. B. Cheng (2003) Elimination of surface spallation of alumina green bodies prepared by acrylamide-based gelcasting via poly(vinylpyrrolidone), *Journal of the American Ceramic Society*, **86**[2] 266–272.
42. L. Y. Shen, M. J. Liu, X. Z. Liu, L. Deng, and B. Li (2007) Investigation of the influencing factors on surface exfoliation on Al<sub>2</sub>O<sub>3</sub>-ZrO<sub>2</sub> green bodies prepared by gelcasting, *Materials Science and Engineering a-Structural Materials Properties Microstructure and Processing*, **464**[1–2] 63–67.
43. O. Omatete, R. Strehlow, and C. Walls, Drying of gelcast ceramics, in *Forming Science and Technology for Ceramics*, Vol. 26, ed. M. J. Cima, pp. 101–107, American Ceramic Society, Westerville, OH, 1992.
44. G. W. Scherer (1990) Theory of drying, *Journal of the American Ceramic Society*, **73**[1] 3–14.
45. S. Ghosal, A. Emami-Naeini, Y. P. Harn, B. S. Draskovich, and J. P. Pollinger (1999) A physical model for the drying of gelcast ceramics, *Journal of the American Ceramic Society*, **82**[3] 513–520.
46. C. G. Ha, Y. G. Jung, J. W. Kim, C. Y. Jo, and U. Paik (2002) Effect of particle size on gelcasting process and green properties in alumina, *Materials Science and Engineering a-Structural Materials Properties Microstructure and Processing*, **337**[1–2] 212–221.
47. Christian and P. J. A. Kenis (2007) Fabrication of ceramic microscale structures, *Journal of the American Ceramic Society*, **90**[9] 2779–2783.
48. I. Santacruz, C. Baudin, R. Moreno, and M. I. Nieto (2004) Improved green strength of ceramics through aqueous gelcasting, *Advanced Engineering Materials*, **6**[8] 672–676.



49. A. J. Millan, M. I. Nieto, R. Moreno, and C. Baudin (2002) Thermogelling polysaccharides for aqueous gelcasting—Part III: Mechanical and microstructural characterization of green alumina bodies, *Journal of the European Ceramic Society*, **22**[13] 2223–2230.
50. J. Brandrup, E. Immergut, and E. Grulke, *Polymer Handbook*. Wiley, New York, 1999.
51. J. K. Montgomery, Processing and mechanical characterization of alumina laminates, PhD Thesis, Northwestern University, Evanston, IL, 2002.
52. D. B. Hovis and K. T. Faber (2001) Textured microstructures in barium hexaferrite by magnetic field assisted gelcasting and templated grain growth, *Scripta Materialia*, **44**[11] 2525–2529.
53. L. F. Nie, Y. J. Zhang, H. Y. Gong, and T. Zhang (2009) Fabrication and properties of reaction-bonded SiC prepared by gelcasting, *Journal of Ceramic Processing Research*, **10**[1] 11–15.
54. K. A. Erk, D. C. Dunand, and K. R. Shull (2008) Titanium with controllable pore fractions by thermo reversible gelcasting of TiH<sub>2</sub>, *Acta Materialia*, **56**[18] 5147–5157.
55. M. A. Janney, C. A. Walls, D. M. Kupp, and K. W. Kirby (2004) Gelcasting SiAlON radomes, *American Ceramic Society Bulletin*, **83**[7] 1.
56. M. H. Bocanegra-Bernal and B. Matovic (2009) Dense and near-net-shape fabrication of Si<sub>3</sub>N<sub>4</sub> ceramics, *Materials Science and Engineering A-Structural Materials Properties Microstructure and Processing*, **500**[1–2] 130–149.
57. M. B. Dickerson, P. J. Wurm, J. R. Schorr, W. P. Hoffman, P. G. Wapner, and K. H. Sandhage (2004) Near net-shape, ultra-high melting, recession-resistant ZrC/W-based rocket nozzle liners via the displacive compensation of porosity (DCP) method, *Journal of Materials Science*, **39**[19] 6005–6015.
58. I. Ganesh, S. M. Olhero, and J. M. F. Ferreira (2009) Phosphoric acid treated AlN powder for aqueous processing of net-shape dense AlN and beta-SiAlON parts, *Advances in Applied Ceramics*, **108**[2] 111–117.
59. M. Potoczek, A. Zima, Z. Paszkiewicz, and A. Slosarczyk (2009) Manufacturing of highly porous calcium phosphate bioceramics via gel-casting using agarose, *Ceramics International*, **35**[6] 2249–2254.
60. B. Q. Chen, Z. Q. Zhang, J. X. Zhang, Q. L. Lin, and D. L. Jiang (2008) Fabrication and mechanical properties of beta-TCP pieces by gel-casting method, *Materials Science & Engineering C-Biomimetic and Supramolecular Systems*, **28**[7] 1052–1056.
61. B. Q. Chen, D. L. Jiang, J. X. Zhang, M. J. Dong, and Q. L. Lin (2008) Gel-casting of beta-TCP using epoxy resin as a gelling agent, *Journal of the European Ceramic Society*, **28**[15] 2889–2894.
62. A. John, H. K. Varma, S. Vijayan, A. Bernhardt, A. Lode, A. Vogel, B. Burmeister, T. Hanke, H. Domaschke, and M. Gelinsky (2009) In vitro investigations of bone remodeling on a transparent hydroxyapatite ceramic, *Biomedical Materials*, **4**[1] Article No. 015007.
63. S. M. Olhero, I. Ganesh, P. M. C. Torres, F. J. Alves, and J. M. F. Ferreira (2009) Aqueous colloidal processing of ZTA composites, *Journal of the American Ceramic Society*, **92**[1] 9–16.
64. S. Padilla, S. Sanchez-Salcedo, and M. Vallet-Regi (2007) Bioactive glass as precursor of designed-architecture scaffolds for tissue engineering, *Journal of Biomedical Materials Research Part A*, **81A**[1] 224–232.
65. J. W. Kim, S. H. Park, Y. G. Jung, and H. S. Lee (2006) Evaluation and control of crack propagation in dense porcelain/porous alumina layered structures for dental material applications, *Science of Engineering Ceramics III*, **317–318** 457–460.

66. J. J. Liu, H. Watanabe, M. Fuji, and M. Takahashi (2009) Electrocatalytic evolution of hydrogen on porous alumina/gelcast-derived nano-carbon network composite electrode, *Electrochemistry Communications*, **11**[1] 107–110.
67. I. Santacruz, R. Moreno, and J. B. Rodrigues (2008) Preparation of cordierite materials with tailored porosity by gelcasting with polysaccharides, *International Journal of Applied Ceramic Technology*, **5**[1] 74–83.
68. M. Fuji, Y. Shiroki, R. L. Menchavez, H. Takegami, M. Takahashi, H. Suzuki, S. Izuhara, and T. Yokoyama (2007) Fabrication of cordierite filter by in-situ solidification for high temperature dust collection, *Powder Technology*, **172**[1] 57–62.
69. J. Homa, S. Zellhofer, and J. Stampfl (2009) Solid free form fabrication of silicon carbide cross flow filters, *Journal of Ceramic Processing Research*, **10**[1] 25–32.
70. J. Luyten, S. Mullens, J. Coymans, A. M. D. Wilde, I. Thijs, and R. Kemps (2009) Different methods to synthesize ceramic foams, *Journal of the European Ceramic Society*, **29**[5] 829–832.
71. X. J. Mao, S. Z. Shimai, and S. W. Wang (2008) Gelcasting of alumina foams consolidated by epoxy resin, *Journal of the European Ceramic Society*, **28**[1] 217–222.
72. Z. F. Zhou, S. M. Wang, and M. M. Wu (2008) Preparation of reticulated ceramics by gelcasting, *Journal of Inorganic Materials*, **23**[1] 203–208.
73. M. Potoczek (2008) Hydroxyapatite foams produced by gelcasting using agarose, *Materials Letters*, **62**[6–7] 1055–1057.
74. I. Ganesh, N. Thiagarajan, G. Sundararajan, S. M. Olhero, and J. M. F. Ferreira (2008) A non-aqueous processing route for phosphate-protection of AlN powder against hydrolysis, *Journal of the European Ceramic Society*, **28**[11] 2281–2288.
75. J. K. Park, J. H. Park, J. W. Park, H. S. Kim, and Y. I. Jeong (2007) Preparation and characterization of porous cordierite pellets and use as a diesel particulate filter, *Separation and Purification Technology*, **55**[3] 321–326.
76. Y. F. Shao, D. C. Jia, Y. Zhou, and B. Y. Liu (2008) Novel method for fabrication of silicon nitride/silicon oxynitride composite ceramic foams using fly ash cenosphere as a pore-forming agent, *Journal of the American Ceramic Society*, **91**[11] 3781–3785.
77. R. Mouazer, I. Thijs, S. Mullens, and J. Luyten (2004) SiC foams produced by gel casting: Synthesis and characterization, *Advanced Engineering Materials*, **6**[5] 340–343.
78. B. A. Haleem, R. Bhuvana, and A. Udayakumar (2009) Gelcasting of strontium doped lanthanum manganite for solid oxide fuel cell applications, *Transactions of the Indian Ceramic Society*, **68**[3] 139–144.
79. C. S. Cheng, L. Zhang, Y. J. Zhang, and S. P. Jiang (2008) Synthesis of LaCoO<sub>3</sub> nano-powders by aqueous gel-casting for intermediate temperature solid oxide fuel cells, *Solid State Ionics*, **179**[7–8] 282–289.
80. S. P. Jiang, L. Z. Ab, and Y. Zhang (2007) Lanthanum strontium manganese chromite cathode and anode synthesized by gel-casting for solid oxide fuel cells, *Journal of Materials Chemistry*, **17**[25] 2627–2635.
81. M. R. Pillai, D. Gostovic, I. Kim, and S. A. Barnett (2007) Short-period segmented-in-series solid oxide fuel cells on flattened tube supports, *Journal of Power Sources*, **163**[2] 960–965.
82. L. Zhang, S. P. Jiang, W. Wang, and Y. J. Zhang (2007) NiO/YSZ, anode-supported, thin-electrolyte, solid oxide fuel cells fabricated by gel casting, *Journal of Power Sources*, **170**[1] 55–60.



83. X. G. Liu, G. J. Li, J. F. Tong, and D. M. Chen (2004) Low cost fabrication and characterization of thin-substrate YSZ solid electrolyte, *Ceramics International*, **30**[8] 2057–2059.
84. L. S. Zhang, J. F. Gao, M. F. Liu, and C. R. Xia (2009) Effect of impregnation of Sm-doped CeO<sub>2</sub> in NiO/YSZ anode substrate prepared by gelcasting for tubular solid oxide fuel cell, *Journal of Alloys and Compounds*, **482**[1–2] 168–172.
85. S. P. Jiang, L. Zhang, H. Q. He, R. K. Yap, and Y. Xiang (2009) Synthesis and characterization of lanthanum silicate apatite by gel-casting route as electrolytes for solid oxide fuel cells, *Journal of Power Sources*, **189**[2] 972–981.
86. M. Dudek (2009) Usefulness of gel-casting method in the fabrication of nonstoichiometric CaZrO<sub>3</sub>-based electrolytes for high temperature application, *Materials Research Bulletin*, **44**[9] 1879–1888.
87. H. C. Liu, H. Tsuru, A. G. Cooper, and F. B. Prinz (2005) Rapid prototyping methods of silicon carbide micro heat exchangers, *Proceedings of the Institution of Mechanical Engineers Part B-Journal of Engineering Manufacture*, **219**[7] 525–538.
88. L. F. Nie, Y. J. Zhang, H. Y. Gong, L. Zhao, and J. Wang (2009) Preparation and characteristics of gelcast RBSC-B<sub>4</sub>C composite, *Advances in Applied Ceramics*, **108**[5] 314–318.
89. H. H. Wu, D. C. Li, Y. P. Tang, B. Sun, and D. Y. Xu (2009) Gelcasting of alumina based ceramic cores containing yttria for single crystal and directional solidification blades, *Advances in Applied Ceramics*, **108**[7] 406–411.
90. W. W. Chen, Y. Kinemuchi, K. Watari, T. Tamura, and K. Miwa (2006) Grain-oriented Bi<sub>4</sub>Ti<sub>3</sub>O<sub>12</sub> ferroelectric ceramics prepared by magnetic alignment, *Journal of the American Ceramic Society*, **89**[2] 490–493.
91. D. B. Hovis, K. T. Faber, and E. A. Kenik (2008) Texture and microstructural development in gelcast barium hexaferrite, *Journal of Materials Science*, **43**[6] 1836–1843.
92. K. Prabhakaran, P. K. Ojha, N. M. Gokhale, and S. C. Sharrna (2009) Effect of polymer concentration on porosity and pore size characteristics of alumina membrane substrates prepared by gelcasting, *Ceramics International*, **35**[5] 2083–2085.
93. W. L. Guo, T. X. Liang, X. Y. Zhao, S. C. Hao, and C. L. Li (2009) Preparing UO<sub>2</sub> kernels by gelcasting, *Nuclear Science and Techniques*, **20**[2] 124–128.
94. H. Li, D. X. Zhou, S. P. Gong, and K. Han (2008) Aqueous gelcasting for 0.94Na<sub>0.5</sub>Bi<sub>0.5</sub>TiO<sub>3</sub>-0.06BaTiO<sub>3</sub> lead-free piezoceramic, *Journal of Inorganic Materials*, **23**[3] 631–635.
95. D. Guo, K. Cai, L. T. Li, and Z. L. Gui (2009) Investigation of the additive induced doping effects in gelcast soft lead zirconate titanate ceramics, *Journal of Applied Physics*, **106**[5] 054104.
96. D. Guo, K. Cai, L. T. Li, and Z. L. Gui (2003) Application of Gelcasting to the fabrication of piezoelectric ceramic parts, *Journal of the European Ceramic Society*, **23**[7] 1131–1137.
97. I. Ganesh, S. M. Olhero, P. M. C. Torres, and J. M. F. Ferreiraw (2009) Gelcasting of magnesium aluminate spinel powder, *Journal of the American Ceramic Society*, **92**[2] 350–357.
98. S. Q. Li, Y. C. Pei, C. Q. Yu, and J. L. Li (2009) Mechanical and dielectric properties of porous Si<sub>2</sub>N<sub>2</sub>O-Si<sub>3</sub>N<sub>4</sub> in situ composites, *Ceramics International*, **35**[5] 1851–1854.
99. I. Ganesh (2009) Near-net shape beta-Si<sub>4</sub>Al<sub>2</sub>O<sub>2</sub>N<sub>6</sub> parts by hydrolysis induced aqueous gelcasting process, *International Journal of Applied Ceramic Technology*, **6**[1] 89–101.

100. D. X. Zhou, Z. P. Zheng, S. P. Gong, G. H. Huang, and Y. X. Hu (2006) The influence of shaping process on microstructure and properties of BaTiO<sub>3</sub>-based chip thermistors, *Ceramics International*, **32**[7] 839–842.
101. H. Kaga, Y. Kinemuchi, S. Tanaka, A. Makiya, Z. Kato, K. Uematsu, and K. Watari (2006) Fabrication of c-axis oriented Zn<sub>0.98</sub>Al<sub>0.02</sub>O by a high-magnetic-field via gelcasting and its thermoelectric properties, *Journal of the Ceramic Society of Japan*, **114**[1335] 1085–1088.
102. X. J. Mao, S. Z. Shimai, M. J. Dong, and S. W. Wang (2008) Gelcasting and pressureless sintering of translucent alumina ceramics, *Journal of the American Ceramic Society*, **91**[5] 1700–1702.
103. N. S. Bell, J. A. Voigt, B. A. Tuttle, and D. B. Dimos (2004) Colloidal processing of chemically prepared zinc oxide varistors. Part II: Near-net-shape forming and fired electrical properties, *Journal of Materials Research*, **19**[5] 1341–1347.
104. M. H. Zimmerman, K. T. Faber, E. R. Fuller, K. L. Kruger, and K. J. Bowman (1996) Texture assessment of magnetically processed iron titanate, *Journal of the American Ceramic Society*, **79**[5] 1389–1393.
105. M. H. Zimmerman, K. T. Faber, and E. R. Fuller (1997) Forming textured microstructures via the gelcasting technique, *Journal of the American Ceramic Society*, **80**[10] 2725–2729.
106. S. W. Paulik, M. H. Zimmerman, K. T. Faber, and E. R. Fuller (1996) Residual stress in ceramics with large thermal expansion anisotropy, *Journal of Materials Research*, **11**[11] 2795–2803.
107. J. S. Kallend, U. F. Kocks, A. D. Rollett, and H. R. Wenk (1991) Operational texture analysis, *Materials Science and Engineering A-Structural Materials Properties Microstructure and Processing*, **132** 1–11.
108. M. Wei, D. Zhi, and D. G. Brandon (2006) Oxide ceramic laminates with highly textured alpha-alumina interlayers: I. Texture control and laminate formation, *Journal of Materials Science*, **41**[22] 7425–7436.
109. M. Wei, D. Zhi, and D. G. Brandon (2005) Microstructure and texture evolution in gel-cast alpha-alumina/alumina platelet ceramic composites, *Scripta Materialia*, **53**[12] 1327–1332.
110. R. F. Chen, C. A. Wang, Y. Huang, L. G. Ma, and W. Y. Lin (2007) Ceramics with special porous structures fabricated by freeze-gelcasting: Using tert-butyl alcohol as a template, *Journal of the American Ceramic Society*, **90**[11] 3478–3484.
111. A. R. Studart, U. T. Gonzenbach, E. Tervoort, and L. J. Gauckler (2006) Processing routes to macroporous ceramics: A review, *Journal of the American Ceramic Society*, **89**[6] 1771–1789.
112. P. Sepulveda and J. G. P. Binner (1999) Processing of cellular ceramics by foaming and in situ polymerisation of organic monomers, *Journal of the European Ceramic Society*, **19**[12] 2059–2066.
113. P. Sepulveda, F. S. Ortega, M. D. M. Innocentini, and V. C. Pandolfelli (2000) Properties of highly porous hydroxyapatite obtained by the gelcasting of foams, *Journal of the American Ceramic Society*, **83**[12] 3021–3024.
114. S. J. Simske, R. A. Ayers, and T. A. Bateman (1997) Porous materials for bone engineering, *Porous Materials for Tissue Engineering*, **250** 151–182.

115. H. T. Wang, X. Q. Liu, and G. Y. Meng (1997) Porous  $\alpha$ - $\text{Al}_2\text{O}_3$  ceramics prepared by gelcasting, *Materials Research Bulletin*, **32**[12] 1705–1712.
116. J. K. Montgomery, A. S. Botha, P. L. Drzal, K. R. Shull, and K. T. Faber (2003) A thermoreversible gelcasting technique for ceramic laminates, *Scripta Materialia*, **48**[6] 785–789.
117. J. K. Montgomery and K. T. Faber (2005) Processing and surface flaw tolerance of alumina bilayers, *Journal of the American Ceramic Society*, **88**[2] 287–292.
118. A. Cosijns, C. Vervaet, J. Luyten, S. Mullens, F. Siepmann, L. Van Hoorebeke, B. Masschaele, V. Cnudde, and J. P. Remon (2007) Porous hydroxyapatite tablets as carriers for low-dosed drugs, *European Journal of Pharmaceutics and Biopharmaceutics*, **67**[2] 498–506.
119. M. Lombardi, L. Montanaro, L. Gremillard, and J. Chevalier (2009) A modified gelcasting procedure to prepare alumina porous components: Process optimization and preliminary mechanical tests, *Advances in Bioceramics and Porous Ceramics*, **29**[7] 287–297.
120. J. M. Tulliani, V. Naglieri, M. Lombardi, and L. Montanaro (2009) Porous alumina and zirconia bodies obtained by a novel gel casting process, *Advances in Bioceramics and Porous Ceramics*, **29**[7] 327–338.
121. D. Stauffer, *Introduction to Percolation Theory*. Taylor & Francis, London, 1985.
122. D. M. Baskin, M. H. Zimmerman, K. T. Faber, and E. R. Fuller (1997) Forming single-phase laminates via the gelcasting technique, *Journal of the American Ceramic Society*, **80**[11] 2929–2932.
123. J. K. Montgomery and K. T. Faber (2000) Processing of stepped-density alumina via gelcasting and reaction bonding techniques, *Scripta Materialia*, **42**[3] 283–287.
124. D. B. Hovis, Designed microstructures in textured barium hexaferrite, PhD Thesis, Northwestern University, Evanston, IL, 2004.
125. P. Mary, D. Bendejacq, M.-P. Labeau, and P. Dupuis (2007) Reconciling low- and high-salt solution behavior of sulfobetaine polyelectrolytes, *Journal of Physical Chemistry B*, **111** 7767–7777.
126. P. H. Tewari, A. J. Hunt, and K. D. Lofftus (1985) Ambient-temperature supercritical drying of transparent silica aerogels, *Materials Letters*, **3**[9–10] 363–367.
127. M. Janney, personal communication, 2010.

# POLYMER PROCESSING OF CERAMICS

EMANUEL IONESCU AND RALF RIEDEL

## 7.1 INTRODUCTION

Polymer-derived ceramics (PDCs) are materials that have been intensively studied in the last four decades [1]. PDCs describe a new class of ceramics that can be prepared without any additives by thermal handling of appropriate precursors in an inert or reactive atmosphere. They present exceptional properties such as oxidation and corrosion stability as well as crystallization and creep resistance up to very high temperatures. Several review papers and books have been published on this topic, including special issues in the *Journal of the American Ceramic Society* (entitled “Ultrahigh-Temperature Polymer Derived Ceramics”) [2], *Journal of the European Ceramic Society* (“Polymer Derived Ceramics”) [3] and *Soft Materials* (“Preceramic Polymers”) [4], which focused on the synthesis and properties of PDCs [5–11].

Besides their exceptional properties, PDCs exhibit the advantage that they can be processed similarly to thermoplastic materials to obtain complex three-dimensional (3-D) shapes. Furthermore, the polymer-derived route allows for obtaining high-purity

ceramics with very good homogeneity at rather low temperatures (ranging from 1000 to 1400°C). Moreover, the polymer route has been shown to be the only possible route to obtain ternary and multinary ceramics in the systems  $\text{Si(M)OC}$  and  $\text{Si(M)CN}$ , with M being B, Al, Ti, Fe, Co, Ni, Zr, Hf, and so on.

In this chapter, we will address the processing of PDCs starting from silicon-containing polymers, and we will discuss within this context different techniques to produce PDC powders, monoliths, fibers, coatings and membranes, porous parts, or microcomponents.

## 7.2 SILICON-CONTAINING PRECERAMIC POLYMERS: SYNTHESIS, CROSS-LINKING, AND CERAMIZATION

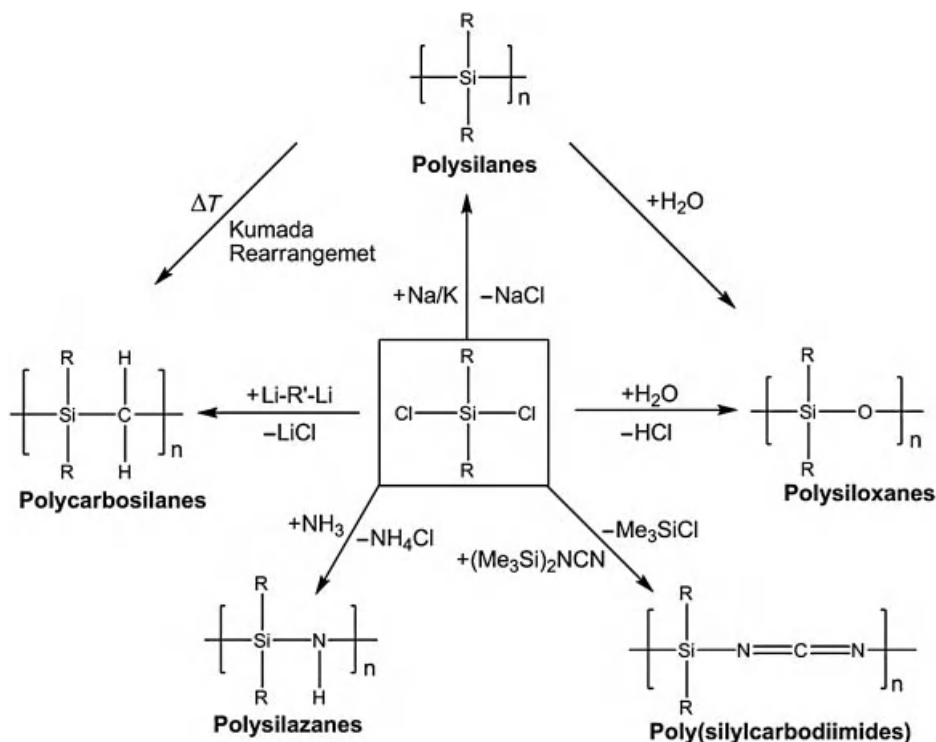
The overall process for the formation of PDCs consists of three major steps: (1) synthesis of preceramic polymers from suitable monomers; (2) polymer cross-linking at moderated temperatures to furnish an infusible organic/inorganic network (preceramic networks, duroplastics); (3) ceramization process (pyrolysis) of the cross-linked materials, which are converted into inorganic amorphous materials by heat treatment at temperatures from 1000 to 1300°C.

Common preceramic polymers for the preparation of PDCs are polysilanes, polycarbosilanes, polysiloxanes, as well as polysilazanes and poly(silylcarbodiimides) [12–14]. Since the Yajima process to synthesize silicon carbide fibers using polycarbosilanes, significant development in the PDC synthesis and processing has been achieved. Thus, by using silicon-based polymers, technologically important ceramic components such as complex-shaped monoliths, fibers, coatings, or infiltrated porous media and powders can be prepared.

The molecular structure and the type of preceramic polymer influence not only the composition but also the amount of phases as well as the phase distribution and the microstructure of the final ceramic. In this way, the chemical and physical properties of PDCs can be varied and adjusted to a great extent by the design of the molecular precursor. Thus, synthesis of preceramic polymers is one of the key issues in the PDC field.

The synthesis of silicon-based polymers mainly involves reactions of organochlorosilanes with Li/Na/K to give polysilanes and polycarbosilanes, with water to give polysiloxanes, with ammonia or amines for the preparation of polysilazanes and with bis(trimethylsilyl)carbodiimide to synthesize poly(silylcarbodiimides) (see Scheme 7.1).

Preceramic precursors for silicon oxycarbide ( $\text{SiOC}$ )-based materials can be synthesized also by sol–gel techniques starting from various substituted alkoxysilanes [15–18]. In the 1990s, Riedel et al. developed a nonoxidic sol–gel process for the synthesis of silicon carbonitride ( $\text{SiCN}$ )- and silicon borocarbonitride ( $\text{SiBCN}$ )-based materials based on reactions of bis(trimethylsilyl)carbodiimide with chlorosilanes [19, 20] or B-trichloroborazine [21, 22]. Due to the similar electronegativity of the carbodiimide group and oxygen, polysilylcarbodiimide gels can be regarded analogous to classical oxide gels, for example, to tetraethylorthosilicate (TEOS)- ( $\text{Si}(\text{OC}_2\text{H}_5)_4$ ) or tetramethy-



**Scheme 7.1.** Synthetic routes from dichlorosilanes to silicon-containing preceramic polymers.

lorthosilicate (TMOS)-based ( $\text{Si}(\text{OCH}_3)_4$ ) systems, with respect to their structural, spectroscopic, and rheological properties [23].

There are several requirements for preceramic polymers to be effective for the thermal decomposition process. The polymers should possess a sufficiently high molecular weight in order to avoid volatilization of low molecular components, appropriate rheological properties and solubility for the shaping process, and latent reactivity (i.e., the presence of functional groups) for subsequent curing and cross-linking steps.

The cross-linking process is a crucial step for the processing of PDCs. The polymeric precursors are converted during the cross-linking into organic/inorganic materials at low temperatures ( $100\text{--}400^\circ\text{C}$ ). This transformation prevents the loss of low-molecular-weight components of the polymer precursors, as well as fragmentation processes during the pyrolysis process, and thus increases the ceramic yield. Furthermore, the cross-linking process leads to infusible materials (duroplastics) that retain their shape during pyrolysis, as the ceramization process occurs without melting.

Cross-linking of polycarbosilanes can be achieved by oxygen [24] or e-beam curing [25]. They can be obtained starting from polysilanes, which rearrange by heat treatment to polycarbosilanes via Kumada mechanism [26]. This occurs via radical reactions, which in the first step involve cleavage of Si–Si bonds to form silyl radicals

and Si-H-containing fragments. These react subsequently to give Si-CH<sub>2</sub>-Si linkages [27–29]. Cross-linking of polycarbosilanes in the presence of oxygen has been found to occur also via radical mechanisms: Oxidation of Si-H and Si-CH<sub>3</sub> bonds occurs with the formation of Si-OH, Si-O-Si, and C=O groups, as supported by means of infrared spectroscopy (IR) [30, 31], X-ray photospectroscopy (XPS) [32], and solid-state <sup>29</sup>Si magic angle spinning nuclear magnetic resonance spectroscopy (MAS NMR) investigations [33]. Oxidative cross-linking of polycarbosilanes leads to SiC materials (such as fibers) showing an oxygen content of 10–12%. Cross-linking of polycarbosilanes in absence of oxygen involves reactions of Si-H bonds with Si-CH<sub>3</sub> groups leading to Si-CH<sub>2</sub>-Si linkages as supported by IR [34] and solid-state <sup>29</sup>Si MAS NMR [35] studies. Interestingly, no Si-Si bond formation occurs. Silicon carbide materials synthesized out of e-beam cross-linked polycarbosilanes show very low oxygen contents (0.2–0.3%) compared with the oxidative cross-linked materials.

Polysiloxanes can be cross-linked via condensation, transition metal catalyzed addition, as well as by free radical initiation mechanisms [11]. Polysiloxanes containing methyl or vinyl groups can be cross-linked thermally using peroxides [36]. Furthermore, cross-linking reactions can occur between silicon hydride units and Si-vinyl groups either thermally or via metal salt catalysis [37, 38]. For polysiloxanes which are composed of hydroxyl and alkoxy groups, condensation of Si-OH units with *in situ* release of water as well as *in situ* hydrolysis of alkoxy groups leads to Si-O-Si bond formation [39].

Polysilazanes can be cross-linked either thermally or by using chemical reagents, such as catalysts and peroxides. There are four major reactions that can occur during the thermal cross-linking process of appropriately substituted polysilazanes: hydrosilylation, vinyl polymerization, transamination, and dehydrocoupling (Si-H/Si-H or Si-H/N-H) [13]. Hydrosilylation occurs in polysilazanes that exhibit Si-H and vinyl groups [40, 41]. This reaction is fast even at low temperatures (it starts at 100–120°C) and leads to the formation of Si-C linkages, which are not affected by thermal depolymerization reactions. The presence of catalysts can remarkably increase the hydrosilylation rate. Dehydrocoupling reactions start at higher temperatures (ca. 300°C) and lead to the formation of Si-N and Si-Si bonds. Transamination processes occur at temperatures from ca. 200 to 400°C and are associated with mass loss (i.e., evolution of amines, ammonia, or oligomeric silazanes) and lead to a decrease of the nitrogen content in the ceramic materials upon pyrolysis. The vinyl polymerization (addition) process occurs at higher temperatures (>300°C) and involves no mass loss [11, 13].

The ceramization process of the cross-linked precursors consists of the thermolysis and evolution of their organic groups at elevated temperatures, that is, 600–1000°C. In this temperature range, the conversion of the preceramic materials into amorphous covalent ceramics (ACC) occurs [11]. The complex mechanisms involved in the pyrolysis of preceramic polymers are not well understood yet. This is mainly due to the amorphous structure of the highly cross-linked polymeric materials and the resulting amorphous ceramics. The reactions that occur during pyrolysis can be investigated, for instance, by means of solid-state NMR, FTIR, and Raman spectroscopy, as well as via thermogravimetric analysis coupled with *in situ* mass spectrometry and FTIR spectroscopy [11].

Polycarbosilanes can be pyrolyzed at temperatures ranging from 800 to 1000°C and lead to silicon carbide-based materials. At temperatures between 550 and 800°C



they transform into inorganic materials with the evolution of hydrogen and methane, as supported by differential thermal analysis (DTA) and thermogravimetry analysis (TGA) coupled with mass spectrometry (MS) investigations [42]. Solid-state  $^{29}\text{Si}$  NMR studies of the materials pyrolyzed in this temperature range showed the presence of a single peak corresponding to  $\text{SiC}_4$  units. Thus, the ceramics obtained upon pyrolysis at  $T > 800^\circ\text{C}$  can be described as hydrogenated silicon carbide with excess carbon, and they start to crystallize at temperatures exceeding  $1000^\circ\text{C}$  into silicon carbide with evolution of hydrogen [43, 44].

Cross-linked polysiloxanes are converted upon pyrolysis into SiOC glasses [15, 45, 46]. Ceramization occurs via the evolution of hydrocarbons (mainly  $\text{CH}_4$ ) and hydrogen. Additionally, various redistribution reactions between Si–O, Si–C, and Si–H bonds can occur [47]. Usually, these rearrangement reactions lead to the evolution of low-molecular-weight silanes and thus decrease the ceramic yield. At temperatures between 600 and  $1000^\circ\text{C}$ , extensive C–H, Si–C, and Si–O bond cleavage occurs and furnishes ceramic materials consisting of amorphous SiOC and residual free carbon.

Several investigations have elucidated the complex processes during pyrolysis of polysilazanes and poly(carbo)silazanes. At temperatures above  $550^\circ\text{C}$ , polyhydridosilazanes show reactions between Si–H and Si– $\text{CH}_3$  groups to form Si– $\text{CH}_2$ –Si linkages with methane evolution. Additionally, parallel reactions involving N–H groups proceed to lead to  $\text{SiN}_4$  units and methane evolution by the successive replacement of methyl groups [48, 49]. The ceramization behavior of vinyl-substituted polysilazanes has been shown to be completely different. Thus, TG/MS/FTIR investigations revealed that at lower temperatures, cross-linking reactions such as hydrosilylation and vinyl polymerization are observed. At temperatures up to  $600^\circ\text{C}$ , ammonia is evolved due to transamination reactions. At higher temperatures (i.e.,  $600$ – $800^\circ\text{C}$ ) FTIR and Raman spectroscopy studies show a remarkable decrease of Si–H, Si– $\text{CH}_3$ , and N–H bonds accompanied by evolution of hydrogen (Si–H/N–H dehydrocoupling reactions) and/or methane (Si– $\text{CH}_3$ /N–H reactions) [50].

Polysilylcarbodiimide derivatives may be used to synthesize novel ternary solid-phase Si–C–N materials [51]. For instance, silicon dicarbodiimide,  $[\text{Si}(\text{NCN})_2]_n$ , was prepared by reacting tetrachlorosilane with bis(trimethylsilyl)carbodiimide [52]. Subsequent annealing at temperatures from 400 to  $800^\circ\text{C}$  leads to the formation of crystalline  $\beta$ -silicon dicarbodiimide ( $\beta\text{-SiC}_2\text{N}_4 \equiv \beta\text{-Si}(\text{NCN})_2$ ). Further heat treatment of  $\text{SiC}_2\text{N}_4$  at  $900$ – $1000^\circ\text{C}$  leads to the formation of silicon(carbodiimide)nitride  $\text{Si}_2\text{CN}_4$  (i.e.,  $\text{Si}_2(\text{NCN})\text{N}_2$ ) with the simultaneous loss of nitrogen and  $\text{C}_2\text{N}_2$ . At temperatures exceeding  $1000^\circ\text{C}$ ,  $\text{Si}_2\text{CN}_4$  starts to convert into amorphous SiCN, which consists of two phases, that is, an amorphous carbon phase embedded in an amorphous silicon nitride phase. The decomposition mechanism was supposed to proceed via rearrangement of carbodiimide to isomeric cyanamide structures [51].

### 7.3 PDC MONOLITHS: FILLER-CONTROLLED PYROLYSIS

Precursor-derived ceramics obtained upon pyrolysis of preceramic polymers suffer from high volumetric shrinkage (up to 50 vol % depending on the precursor)



and residual porosity. Many studies in the last two decades were directed to reduce shrinkage and porosity by optimizing precursor compositions and finding suitable processing conditions, for example, with respect to cross-linking and ceramization.

During pyrolysis, ceramization is characterized by the thermolysis and evolution of the organic constituents and densification. Preceramic polymers usually have densities of ca. 1 g/cm<sup>3</sup>, while the corresponding ceramic materials exhibit densities in the range of 2–3 g/cm<sup>3</sup>. Thus, the conversion into ceramic is obviously accompanied by the generation of residual stresses that lead to defects and cracking of ceramic parts [53]. Fillers can be used to minimize the overall shrinkage upon ceramization. There are two types of fillers for this purpose. One is a passive filler (Fig. 7.1), which serves as a space holder and is not involved in reactions during pyrolysis (its size and composition remain constant); the other is an active filler (Fig. 7.2), which reacts during pyrolysis either with the polymer matrix, the decomposition volatiles, or with the pyrolysis atmosphere, thus changing/tailoring the shrinkage behavior and the composition of the final ceramic composites [54, 55].

Inert fillers are metal oxides, carbides, or nitrides (e.g., Al<sub>2</sub>O<sub>3</sub>, SiO<sub>2</sub>, Y<sub>2</sub>O<sub>3</sub>, SiC, B<sub>4</sub>C, Si<sub>3</sub>N<sub>4</sub>, and BN). The volumetric shrinkage of a system consisting of a preceramic polymer and an inert filler ( $\omega_V(IF)$ ) can be described as

$$\omega_V(IF) = \left(1 - \frac{V_F}{V_F^*}\right) \omega_V(P), \quad (7.1)$$

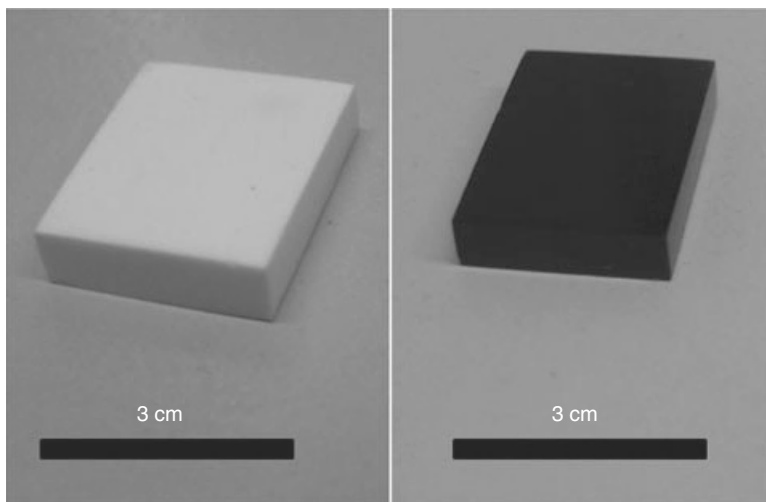


**Figure 7.1.** Dense and crack-free green body (left) and ceramic part (right) processed via cross-linking and pyrolysis of an alumina-filled polysilsesquioxane (reprinted from R. Riedel, L. Toma, C. Fasel, and G. Miehe (2009) Polymer-derived mullite-SiC-based nanocomposites, *J. Eur. Ceram. Soc.*, **29** 3079–3090, with permission of Elsevier).

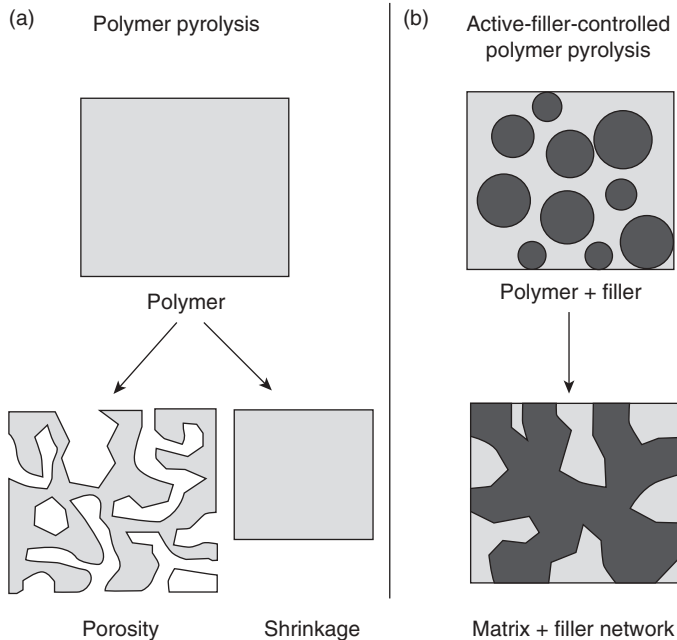


**Figure 7.2.** Polymer-to-ceramic transformation of a preceramic polymer (A) and of a polymer filled with an active filler (B) (reprinted from P. Greil (1995) Active-filler-controlled pyrolysis of preceramic polymers, *J. Am. Ceram. Soc.*, 78 835–848, with the permission of Wiley-Blackwell).

where  $V_F$  is the volume fraction of the inert filler,  $V_F^*$  is the critical volume fraction of the inert filler, and  $\omega_v(P)$  represents the volumetric shrinkage of the preceramic polymer. The critical volume fraction of the inert filler is the volume fraction at which the filler particles start to form a rigid network; that is, further shrinkage of the system is not possible. Hence, at volume fractions  $\geq V_F^*$ , the total system shrinkage is zero.

Active fillers are mainly used to produce near-net-shape parts since they compensate the shrinkage of the precursors during pyrolysis. Usually, reactive powders are used, such as pure metals, intermetallics, metal hydrides, or metal carbonyl complexes. The active filler usually reacts with the decomposition products or with the reactive pyrolysis atmosphere forming new phases that expand in volume. Therefore, the volumetric shrinkage of a system consisting of a preceramic polymer and an active filler,  $\omega_v(AF)$ , can be described as [54, 55]

$$\omega_v(AF) = \left[ \left( 1 - \frac{V_F}{V_F^*} \right) \omega_v(P) \right] + V_F \omega_v(F), \quad (7.2)$$

where  $\omega_v(F)$  is the shrinkage/expansion value resulting from the filler transformation reaction, and other symbols have the same meaning—as applicable to the active filler—as defined for Equation 7.1.

Thus, the critical volume fraction of an active filler,  $V_{AF}^*$ , to achieve net zero shrinkage in the bulk composite part is defined as [54, 55]

$$V_{AF}^* = \frac{\omega_V(P)}{\left(\frac{\omega_V(P)}{V_F^*}\right) - \omega_V(AF)} \quad (7.3)$$

The near-net-shape processing of PDC parts using active fillers has been denoted by Greil as active-filler-controlled pyrolysis (AFCP) [54].

Composite systems with near zero shrinkage can be designed with both passive and active fillers. However, in the case of active fillers, lower filler volume fractions are necessary to achieve zero shrinkage.

The use of filler particles not only reduces shrinkage during pyrolysis but may also allow for tailoring properties of the composite. In this way, special properties such as mechanical strength, thermal and electrical conductivity, magnetism, or surface features can be incorporated.

## 7.4 PDC FIBERS

Although the first reports of nonoxide PDCs were in the early 1960s [56], the first practical application was for manufacturing small-diameter  $\text{Si}_3\text{N}_4/\text{SiC}$ -fibers for high-temperature use in the 1970s [57]. The first synthesis of SiC material from polycarbosilane precursors was reported at the same time by Fritz and Raabe [58] and Yajima et al [59]. The Yajima process for the synthesis of SiC-fibers by thermolysis of polycarbosilanes was reported at the end of the 1970s [60]. High-temperature-resistant ceramic fibers are commonly known as Si-based systems such as SiC, SiOC, SiCN(O), or SiBCN. Their processing is performed using preceramic polymers or even low-molecular-weight compounds, which exhibit rheological properties suitable for fiber spinning by dry or melt spinning processes. The obtained green fibers are subsequently hardened (chemically or by means of radiation) and pyrolyzed to give ceramic fibers with high yields.

Polymer-derived SiC-fibers can be obtained by melt spinning of polycarbosilanes followed by cross-linking and pyrolysis. Cross-linking of polycarbosilane-based green fibers can be achieved by oxygen or by e-beam curing [61]. Cross-linking of polycarbosilanes in the presence of oxygen occurs via radical mechanisms: oxidation of Si-H and Si-CH<sub>3</sub> bonds occurs with the formation of Si-OH, Si-O-Si, and C=O groups, according to IR [62,63], XPS [64], and solid-state <sup>29</sup>Si MAS NMR investigations [65]. This leads to SiC ceramic fibers with an oxygen content of 10–20 wt %. Fibers of high oxygen content easily decompose at temperatures beyond 1200°C releasing SiO and CO.

Cross-linking of polycarbosilane-based green fibers in the absence of oxygen involves reactions of Si-H bonds with Si-CH<sub>3</sub> groups leading to Si-CH<sub>2</sub>-Si linkages as supported by IR [66] and solid-state <sup>29</sup>Si MAS NMR [67] studies. Interestingly, no Si-Si bond formation occurs. Preceramic polycarbosilane fibers cross-linked via e-beam radiation show low oxygen content (0.2–0.3%) compared with those cross-linked under an oxidative atmosphere. The use of oxygen-free precursors as well as curing under

inert conditions leads to SiC-fibers with highly improved mechanical and thermal properties [68].

SiCN ceramic fibers were first produced by Bayer AG using polyorganosilazanes synthesized via the reaction of trichlorosilanes or dichlorosilanes with ammonia or methylamine, which were thermally cross-linked [69, 70]. Seyferth et al. used mixtures of dichloromethylsilane and dichloromethylvinylsilane, which were reacted with ammonia and subsequently cured via UV radiation [71]. SiCN ceramic fibers with very low oxygen content can be obtained by melt spinning of ABSE polycarbosilazane precursor followed by e-beam curing and pyrolysis in an inert atmosphere [72–74].

SiBCN fibers were prepared for the first time by Takamizawa et al. via melt spinning of mixtures consisting of polyorganosilanes and organoborazines followed by curing (either under oxidative conditions or by means of e-beam radiation) and pyrolysis in nitrogen atmosphere. [75]. The first spinnable SiBCN precursor was developed by Sneddon et al. with the synthesis of polyborosilazanes using borane and borazine as pendant units in hydridopolysilazane [76, 77]. The SiBCN fibers prepared via this method remain amorphous upon annealing at 1600°C, thus showing a considerable improvement over ceramics obtained via pyrolysis of nonmodified hydridopolysilazane. A different synthetic approach for SiBCN fiber precursors involves the preparation of N-methyl polyborosilazanes. Their degree of cross-linking and thus viscosity can be tuned by using different substituted amines. The green fibers obtained by melt spinning were cured in  $\text{HSiCl}_3$  and were subsequently pyrolyzed in an inert atmosphere up to 1500°C. [78–80]. The resulting SiBCN fibers exhibited 3.0-GPa tensile strength and no significant decomposition in He atmosphere up to 1750°C. Another preparation method for SiBCN preceramic polymers involves the reaction of a molecular precursor, that is, tris(dichloromethylsilyl)ethylborane [81], with methylamine, which leads to a polymer suitable for melt spinning. [82, 83]. Curing of the obtained green fibers was performed thermally (at 200°C) in an ammonia atmosphere, followed by pyrolysis at 1000–1400°C in nitrogen. The SiBCN fibers prepared via this method revealed 1.3- to 1.5-GPa tensile strength; they phase separated and crystallized upon annealing at 1600°C into SiC,  $\text{Si}_3\text{N}_4$ , and BN/carbon.

The examples presented here emphasize the unique opportunity of using preceramic polymers for the production of silicon-containing ceramic fibers in binary (SiC) or multicomponent (SiCN, SiBCN) amorphous systems. The silicon-based polymers can be easily tuned with respect to rheological properties and thus can be melt spun to green fiber with a diameter ranging from a few micrometers to 100  $\mu\text{m}$  and a length of up to several hundred meters. Furthermore, fiber curing can be achieved thermally or by radiation (e-beam, UV) in either oxidative or inert conditions. The main challenges are in finding the appropriate compositions of the precursors that can deliver fibers that can withstand temperatures exceeding 1400–1500°C in oxidizing and corrosive environments.

## 7.5 PDC COATINGS AND MEMBRANES

Preceramic polymers exhibit a crucial advantage to produce ceramic coatings due to the easy preparation and handling of preceramic solutions and slurries as well as their

simple application on surfaces. Thus, PDC-based coatings can be prepared using different application techniques (e.g., spin coating, spraying, or dip coating) followed by cross-linking and pyrolysis processes. The choice of the coating method mainly depends (1) on the slurry properties (such as composition, rheology, etc.), (2) on the substrate (size, shape complexity, roughness), and (3) on the coating thickness. [84], Thin layers can be deposited on planar, smooth surfaces (e.g., metals, Si wafer) by means of spin coating; the thickness can be adjusted by varying the spin rate [85, 86]. By using dip-coating techniques, thicker layers can be prepared; furthermore, complex-shaped substrates can be coated via this technique [87, 88]. Other methods, like spray coating or screen printing, can be used in order to coat substrates with layers having thicknesses up to 50  $\mu\text{m}$  [89]. However, one should note that there is a critical coating thickness ( $h_{\text{CCT}}$ ) above which delamination and cracking of the coating occur during the pyrolysis process [90, 91]. With respect to delamination processes,  $h_{\text{CCT}}$  depends on the adhesive strength between the coating and the substrate ( $\vartheta_a$ ) on the coating shear modulus ( $G$ ) and on the shrinkage ratio  $\alpha$ :

$$h_{\text{CCT}} = \frac{\vartheta_a}{G\alpha(1 + \alpha^6 - 2\alpha^3)} \quad (7.4)$$

For the preparation of thick coatings (i.e., up to several hundred micrometers), two methods can be envisaged: (1) multiple layer deposition (with or without intermediate layer treatment) or (2) deposition of polymer/filler particle systems to reduce shrinkage and cracking during ceramization (Fig. 7.3).

In general, the ceramization process is performed in an inert (nitrogen, argon) or reactive (ammonia, air) atmosphere to furnish the PDC coatings. In the case of low-melting-point substrates, advanced pyrolysis techniques can be used, such as laser pyrolysis or ion beam-induced cross-linking and ceramization. For instance, laser pyrolysis has been used to obtain ceramic coatings on plastic or aluminum substrates. [92]. Furthermore, using focused laser beam, well-defined ceramic patterns on different substrates can be prepared [93].

PDC coatings were shown to protect substrates like metals or carbon-based surfaces from thermal loading and oxidative degradation. HfB<sub>2</sub>-filled SiC-based PDC coatings have been shown to exhibit improved thermal oxidation resistance if compared with that of nonfilled SiC coatings, thus constituting interesting composite materials for aerospace applications (e.g., protection toward harsh reentry conditions) [94]. Furthermore, SiC-filled PDC coatings also showed good resistance against aggressive chemicals such as chlorine or chlorine-containing hot gases [95]. Coatings consisting of SiOC filled with TiSi<sub>2</sub> particles were shown to protect stainless steel surfaces from thermal oxidation up to temperatures of 800°C [88]. Also, other substrate materials such as silicon wafers [96, 97], titanium, graphite, quartz [98], glass rods [99], alumina [100], or ceramic porous parts were coated with PDC-based materials, which had a beneficial influence on the high-temperature behavior of the substrates used. In a recent synthetic approach, silver-filled SiCN-based PDC coatings have been shown to exhibit antibacterial functionality [101].

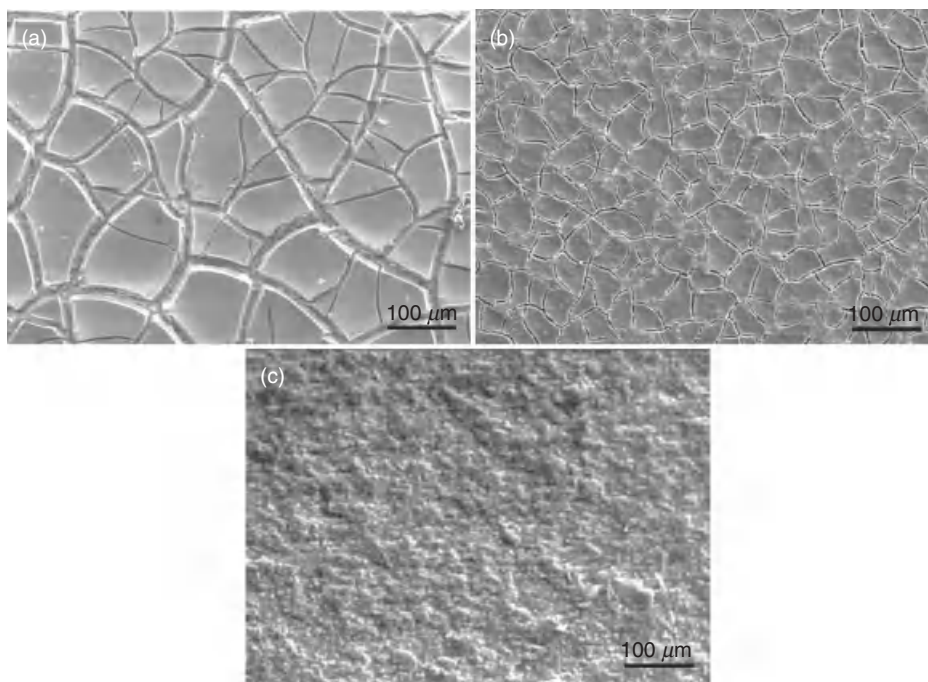


**Figure 7.3.** Scanning electron microscopy (SEM) micrographs of SiCN-based coatings with a thickness of 20–30  $\mu\text{m}$ , prepared via pyrolysis at 1100°C in an inert atmosphere: (a) without use of fillers, (b) with 4.2 vol % alumina, (c) with 15 vol % alumina. One can observe that the addition of fillers suppresses crack formation upon pyrolysis (reprinted from C. Konetschny, Hartstoffhaltigen Si-C-N-Keramiken aus polysilazanen, Ph.D. Thesis, Darmstadt, Shaker Verlag, Aachen, Germany, 1999). (Illustration courtesy of R. Riedel, TU Darmstadt, Germany.)

Microporous ceramic membranes are excellent candidates for gas separation applications. It is known that for steam reforming of natural gas (in order to produce hydrogen), high-temperature reactors, which operate at ca. 800°C, are used. However, the high temperatures needed for this process lead to high costs related to the synthesis of  $\text{H}_2$ ; this is a consequential drawback of using this process as an alternative technology to the conventional hydrocarbon fuels. Recently, at significantly lower temperatures (ca. 500°C), high-pressure membrane reactors have shown their potential for achieving conversion efficiency similar to that obtained in conventional reactors [102–105]. Furthermore, the membrane reactors have the advantage that synthesis and purification of hydrogen gas can be performed within one step, thus leading to a remarkable development of highly efficient hydrogen production. Two types of membranes are used for high-temperature membrane reactors: (1) dense palladium-based membranes and (2) microporous ceramic membranes. Palladium-based membranes exhibit an excellent hydrogen permittivity. However, they are very expensive, susceptible to poisoning by sulfur, and sensitive toward cracking or pinhole formation due to hydrogen

embrittlement. Microporous precursor-derived ceramic membranes have been shown also to exhibit relatively high gas permeances and a good stability at high temperatures, which make them superior to polymer-based membranes concerning, for instance, dehydrogenation of hydrocarbons or steam reforming reaction for hydrogen synthesis [106]. Furthermore, the precursor route allows for *in situ* controlling the micro-/mesoporous structure development [107].

Microporous amorphous silica-based membranes can be prepared as thin films on permeable alumina porous supports having a graded and layered porous structure, with pore sizes ranging from several hundred nanometers to a few nanometers [108, 109]. The gas transport properties of amorphous silica-based membranes deposited on mesoporous anodic alumina capillary were investigated. The gas permeances for small molecules (such as He or H<sub>2</sub>) were found to be much higher than those for larger gas molecules. This behavior emphasizes the potential of these membranes to be used in gas separation properties [110]. Oyama et al. synthesized amorphous silica-based membranes by means of chemical vapor deposition (CVD) techniques. Whereas He and H<sub>2</sub> permeate through the membrane, the permeation of molecules with a kinetic diameter larger than 0.3 nm (such as CO, CO<sub>2</sub>, or CH<sub>4</sub>) is suppressed. This emphasizes the great potential of these membranes in applications related to the hydrogen purification. An amorphous silica-based membrane was also synthesized by the pyrolysis of a polysilazane in air deposited on a silicon nitride porous support and exhibited a hydrogen permeance of  $1.3 \times 10^{-8}$  mol/m<sup>2</sup>/s/Pa at 300°C and a H<sub>2</sub>/N<sub>2</sub> selectivity of 141 (which is comparable to the permselectivity of other amorphous silica- or SiOC-based membranes) [111].

Amorphous ceramic membranes were also prepared in nonoxide systems, such as Si-C, Si-N, as well as Si-C-N and Si-B-C-N. The possibility of a molecular sieve amorphous SiC ceramic membrane was first indicated for a polysilastyrene-derived composite membrane on a porous Vycor glass [112]. Amorphous silicon carbide ceramic membranes were prepared by thermal [113], e-beam [114], or chemical [115] curing of polycarbosilanes followed by pyrolysis in an inert atmosphere. Hydrogen permselective SiOC-based membranes were prepared via curing of polycarbosilanes in air and subsequent pyrolysis in argon [116–118].

Amorphous silicon nitride-based ceramic membranes were prepared by the pyrolysis of a polysilazane in an ammonia atmosphere at 650°C. The as-synthesized membrane showed a hydrogen permeance of  $1.3 \times 10^{-8}$  mol/m<sup>2</sup>/s/Pa at 200°C and a H<sub>2</sub>/N<sub>2</sub> selectivity of 165, whereas after hydrothermal treatment at 300°C, the permeances were higher than  $1.0 \times 10^{-7}$  mol/m/s/Pa at 300°C with H<sub>2</sub>/N<sub>2</sub> selectivity beyond 100 [107].

Recently, novel polymer precursors have been synthesized for the preparation of high-temperature stable amorphous ceramic membranes in the systems Si-C-N and Si-B-C-N. The SiCN-based ceramic membrane was prepared via pyrolysis of a novel polysilylcarbodiimide precursor, which was synthesized via a nonoxidic sol-gel process based on reactions of bis(trimethylsilyl)carbodiimide with chlorosilanes. Nitrogen sorption isotherm analysis of a 500-nm SiCN layer deposited on a porous support surface indicated the existence of pores with sizes in the range 2–5 nm [119]. Amorphous SiBCN-based ceramic membranes with a thickness of ca. 1.75 μm were prepared by dip coating of a polyborosilazane on a macroporous alumina support, followed by



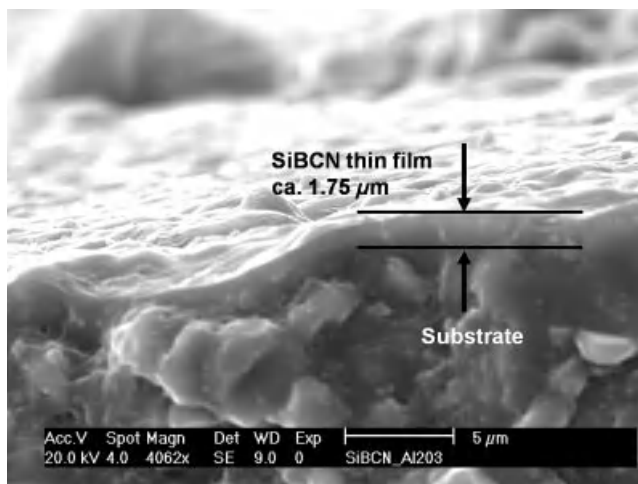


**Figure 7.4.** Polymer-derived ceramic SiBCN membrane deposited on a porous alumina substrate (reprinted from R. Hauser, S. Nahar-Borchard, R. Riedel, Y. H. Ikuhara, and Y. Iwamoto (2006) Polymer-derived SiBCN ceramics and their potential application for high temperature membranes, *J. Cer. Soc. Jpn.*, **114** 524–528, with the permission of the Ceramic Society of Japan).

pyrolysis in an inert atmosphere [120]. The pore analysis revealed a trimodal distribution of the pore sizes with maxima at 0.6, 2.7, and 6 nm (Fig. 7.4).

Recently, a multilayered  $\alpha$ -SiBCN/ $\gamma$ -Al<sub>2</sub>O<sub>3</sub>/ $\alpha$ -Al<sub>2</sub>O<sub>3</sub> membrane with gradient porosity was prepared and investigated with respect to H<sub>2</sub> and CO permeances. A permeance of  $1.05 \times 10^{-8}$  mol/m<sup>2</sup>/s/Pa and a H<sub>2</sub>/CO permselectivity of 10.5 were determined, showing the potential of this membrane in gas separation applications such as hydrogen purification (Fig. 7.5) [121]. Thus, materials based on SiCN or SiBCN are highly promising amorphous nonoxidic ceramics that can withstand ultrahigh temperatures and are, therefore, of great interest for hot gas separation or filtration applications.

## 7.6 PDC FOAMS

Highly porous ceramics, that is, having a porosity higher than 55–60 vol %, are used in various advanced engineering applications such as filtration, catalyst supports, gas sorption, reinforcement for metal matrix composites (MMCs), components in solid oxide fuel cells (SOFCs), lightweight sandwich structures, heat exchangers, and so on [122, 123]. Porous PDCs (Fig. 7.6) are prepared usually as foams using different foaming techniques, which will be briefly discussed here, namely, (1) direct foaming techniques, (2) infiltration of porous preforms, or (3) sacrificial fillers [124, 125].

Direct foaming techniques allow the manufacture of closed- or open-cell foams as well as of macro- or microcellular ceramics. Usually, gas bubbles are generated in



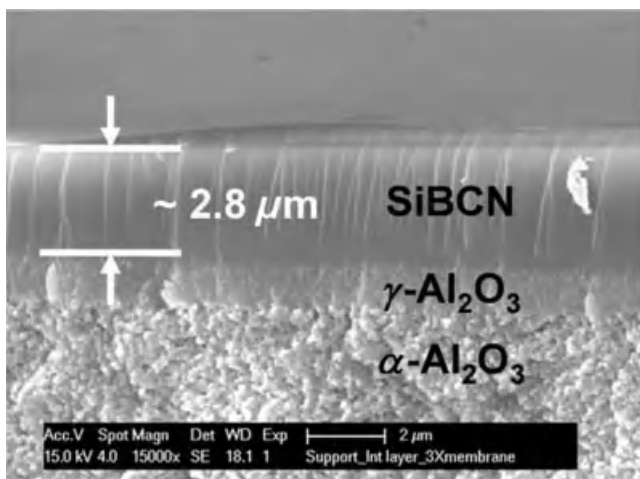


**Figure 7.5.** Scanning electron microscopy (SEM) micrograph of the cross section of an a-SiBCN/ $\gamma$ -Al<sub>2</sub>O<sub>3</sub>/ $\alpha$ -Al<sub>2</sub>O<sub>3</sub> membrane (reprinted from R. M. Prasad, Y. Iwamoto, R. Riedel, and A. Gurlo (2010) Multilayer amorphous-SiBCN/ $\gamma$ -Al<sub>2</sub>O<sub>3</sub>/ $\alpha$ -Al<sub>2</sub>O<sub>3</sub> membranes for hydrogen purification, *Adv. Eng. Mater.*, **12** 522–528, with the permission of Wiley-VCH, Weinheim).

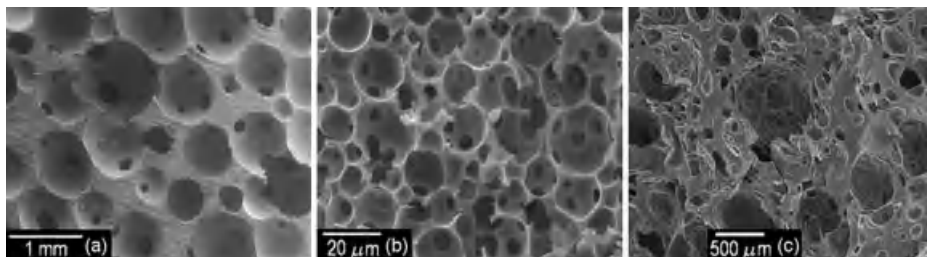


**Figure 7.6.** Porous SiOC foams obtained via pyrolysis of polysiloxane resin: (a) macrocellular open-cell foam, (b) microcellular open-cell foam, and (c) highly porous sample (reprinted from C. Vakifahmetoglu, I. Menapace, A. Hirsch, L. Bassetto, R. Hauser, R. Riedel, and P. Colombo (2009) Highly porous macro and micro-cellular ceramics from a polysilazane precursor, *Ceramics Int.*, **35**[8] 3281–3290, with the permission of Elsevier).

preceramic polymers, that is, by using blowing agents; this step is followed by curing in order to retain the obtained porosity. The blowing agents that are used can be described as extrinsic (i.e., low boiling point solvents or additives, which decompose upon heating to form gaseous species) [126–130], or intrinsic, which generate porosity due to chemical reactions [131–133] or phase separation [134, 135]. For instance, the use of polyurethane precursors as extrinsic blowing agents was shown by Colombo et al. to allow for producing large complex-shaped parts with tailored porosity. However, the high-temperature performance of the porous parts was limited by the presence of the excess carbon generated via decomposition of the polyurethane precursors upon

pyrolysis [136–139]. A recently developed strategy to generate in one step large macroporous ceramic components is the mixing of precursors that show different molecular structures and ceramic yields (i.e., a high ceramic yield component and a low yield precursor) and exhibit upon pyrolysis different shrinkage and release of gaseous species. Thus, the difference in mass loss and shrinkage for the different precursors generates porosity in the ceramic part. The pore size (few micrometers to hundreds of micrometers), shape, and interconnectivity depend, for instance, on the degree of cross-linking of the precursors used as well as on the relative miscibility and weight ratio of the precursors. Intrinsic blowing agents are species that are released *in situ* upon cross-linking. As the viscosity increases during cross-linking, the foam structure is preserved upon pyrolysis. This was shown, for instance, with a polysiloxane precursor that generates during the cross-linking step ethanol and water (acting as blowing agents) [140]. Tailoring the viscosity and the degree of cross-linking of the precursor used allows furthermore for controlling the cell size [141].

Infiltration of porous preforms followed by their elimination (e.g., burnout, decomposition, dissolution) leads to porous ceramic with pore sizes ranging from the nanometer to the millimeter scale. For instance, polyurethane foams were infiltrated with preceramic polymers and were subsequently pyrolyzed, leading to ceramic foams with either hollow [142] or dense [143, 144] struts. Furthermore, nanocasting was used to produce mesoporous silicon carbide ceramics via infiltration of nanoporous silica templates (e.g., SBA-15) with a polycarbosilane followed by pyrolysis in an inert atmosphere at 1000°C and dissolution of the silica template with hydrofluoric acid [145, 146]. Also, other mesoporous templates were used for the fabrication of various mesoporous PDC materials such as carbon template (for SiCN) [147] and wood [148–150] or templates with paper-based structures [151] (for SiOC/SiC).

A very convenient way to produce ceramic foams involves the use of the so-called sacrificial fillers. These are solid particles that are added to a preceramic polymer and are subsequently eliminated by decomposition upon thermal loading (pyrolysis) or leaching. Depending on the volume fraction of the sacrificial filler, the obtained ceramics exhibit open, closed, or mixed cells.

Furthermore, the sacrificial filler has a strong influence on the shape and size of the pores. The processing of ceramic foams using sacrificial fillers involves several steps: (1) mixing of the polymer with the fillers; (2) shaping and cross-linking; (3) removal of the fillers, either by burnout or by dissolution; and (4) pyrolysis process. As sacrificial fillers either dense [152–159] or hollow [160–162] submicron or microspheres comprising, for example, poly(methylmethacrylate) (PMMA), polystyrene (PS), and so on, can be used.

## 7.7 MICROFABRICATION OF PDC-BASED COMPONENTS FOR MICROELECTROMECHANICAL SYSTEMS (MEMS) APPLICATIONS

The preparation of miniaturized ceramic components using the ceramic powder route is limited. Many components for MEMS can be produced with the same set of materials and processes as used for microelectronics. This includes materials like

silicon and polysilicon as well as standard microfabrication processes like bulk or surface micromachining, which include techniques such as etching, lithography, oxidation, deposition, and so on, to mention the most important. Other materials like metals and polymers combined with the LIGA process (lithography, electroforming and molding) can also be used to obtain other types of MEMS.

However, neither silicon metals nor polymers are suitable for harsh environments. They decompose at temperatures higher than  $1000^{\circ}\text{C}$  and they easily react with oxygen. MEMS that present potential applications for systems to be used under harsh environments are ceramic MEMS, which can withstand temperatures higher than  $1000^{\circ}\text{C}$ , as well as thermal shocks. They present outstanding mechanical properties (reduced thermal expansion coefficient, high-temperature strength, and high hardness) and good tribological properties; they are resistant to corrosion; and they are chemically inert. Furthermore, functional ceramics, such as dielectric, piezoelectric, pyroelectric, ferroelectric, or conducting materials are of great technological interest due to their ability to interact with the surrounding environment in order to sense, act upon, or generate power [163]. For this reason, ceramic MEMS are a promising technology, for instance, in the production of sensor devices in gas engines or for space applications, microscale turbine engines, microscale combustion chambers for MEMS power generation, microchemical reactors, and so on.

Ceramic MEMS have been obtained from ceramic powders, ceramic deposition techniques coupled with surface micromachining techniques or preceramic sol-gel or polymer precursors.

The patterning of ceramic powders after sintering is a time-consuming and costly procedure and is completely impossible for several microstructured parts. Thus, near-net-shape forming methods (pressing, molding, and casting) by which shaping of ceramic powders is carried out in the green, that is, unsintered, state, have been developed.

Pressing of ceramic powders is limited to rather simply shaped parts. When structures with a high aspect ratio are required, the friction of the particles during pressing causes density gradients, which increases the shrinkage and cracking during sintering [164]. Here, emphasis should be placed on the importance of the aspect ratio in microcomponents, which determines the ratio of the structure height to the lateral dimensions. Molding [165–167] (injection molding [168], embossing [169], soft lithography [170], etc.) and casting (slip casting, tape casting, etc.) [171, 172] of powder ceramics have also been studied. In these cases, the powder ceramic is mixed with binders, plasticizers, resins, or dispersants in order to improve the flowability of the powder. However, some problems are observed, like significant shrinkage during pyrolysis or low reproduction accuracy and surface roughness because of the presence of particles during shaping. Furthermore, in cases where an organic binder is used, a debinding process is required to achieve dimensionally stable microstructures, and features smaller than  $20\text{ }\mu\text{m}$  are difficult to produce.

Ceramic MEMS (based on  $\text{SiO}_2$ ,  $\text{SiC}$ , and  $\text{Si}_3\text{N}_4$  microcomponents) have been produced using the CVD technique of silanes followed by surface micromachining, which is a combination of standard photolithography and selective chemical etching [173]. However, it is a time-consuming technique and is expensive due to the special

equipment that is required. Moreover, 3-D structures with high aspect ratios are difficult to obtain.

The pyrolysis of preceramic MEMS, patterned through different micromachining techniques, has gained the attention of the scientific community since it represents a more facile route with versatile materials to synthesize 3-D ceramic MEMS at low costs. Preceramic materials include polymer precursors as well as sol-gel precursors. The latter are not included in this chapter. Some studies combining sol-gel precursor solutions with micromolding technologies (mainly soft lithography) in order to obtain oxide ceramic MEMS or more complex ceramic MEMS such as lead zirconate titanate ( $\text{PbZr}_x\text{Ti}_{1-x}\text{O}_3$ , PZT),  $\text{Sr}_2\text{Nb}_2\text{O}_7$ , or others have been reported [174, 175]. The addition of organic components or ceramic nanoparticles reduces the high shrinkage that occurs during drying and pyrolysis [176].

Ceramic MEMS derived from polymer precursors represent a new technology based on the fabrication developed for polymer-derived bulk ceramics [177]. In this context, silicon-based inorganic polymers like polysilazanes, polysilanes, polysiloxanes, and polycarbosilanes can be applied to obtain SiCN,  $\text{Si}_3\text{N}_4$ , SiC, or SiOC components for MEMS applications, depending on the synthetic conditions. These preceramic polymers can be easily shaped using various forming processes and then cross-linked by exposure to heat or radiation to form an infusible solid. The consolidated preceramic polymer MEMS are finally pyrolyzed at high temperatures to transform into dense ceramic microparts.

Various micromachining processes have been reported in the literature for the manufacturing of PDC microcomponents. Some of them are used to obtain the master or the mold that will be used to shape the precursors. The same processes and others are used to directly shape the precursors. In particular, these processes include the following techniques: (1) lithography; (2) LIGA; (3) stereolithography; (4) micromolding techniques, which include hot-embossing and soft-lithography methods.

Lithography microstructuring methods use a photoresist, that is, the photosensitive liquid precursor to be patterned, which is deposited on a planar substrate by spin, dip, or spray coating. Subsequently, selected parts of it are exposed to UV light, X-rays, or electrons (photolithography, X-ray lithography, and electron-beam lithography, respectively) by using a mask with a patterned emulsion of a metal film on one side. The irradiation process initiates a series of photochemical reactions in the photoresist, which alter the physical and chemical properties of the exposed areas. In this sense, the solubility of the photoresist toward a certain developer is modified, either increasing the solubility of the exposed areas yielding a positive image after development or decreasing the solubility to yield a negative-tone photoresist [178, 179]. Preceramic polymers used for direct lithography microfabrication of MEMS components mostly act as negative type photoresists due to the presence of vinyl groups, which can be easily activated. Lithographic microfabrication usually leads to free-standing microstructured patterns on the substrate. In order to obtain PDC microcomponents, the preceramic resists have to be pyrolyzed after irradiation and curing (Fig. 7.7). As in bulk bodies, the shrinkage upon pyrolysis has a significant influence on the quality of the components. In the case of substrate-bonded structures, this can lead to delaminating and partial damage due to thermal expansion mismatch. However, ceramic structures with a diameter  $<50\text{ }\mu\text{m}$  and

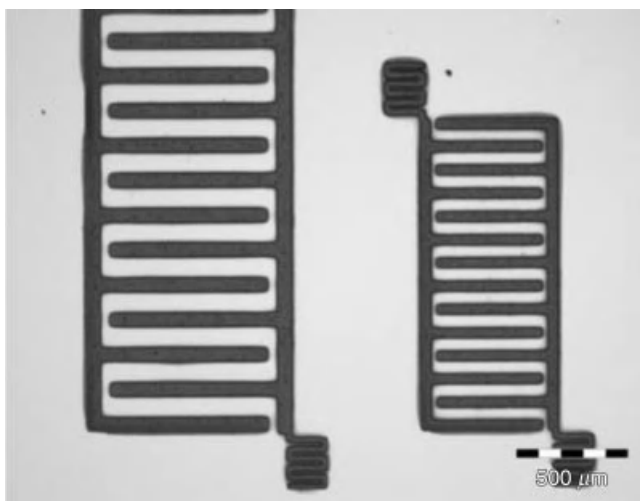


**Figure 7.7.** Polymer-derived ceramic SiOC-based microstructured patterns on silicon wafer produced via UV irradiation of a polysiloxane followed by cross-linking and pyrolysis (reprinted from S. Martinez Crespiera, E. Ionescu, M. Schlosser, K. Flittner, G. Mistura, H. Schlaak, and R. Riedel (2011) Fabrication of silicon oxycarbide-based microcomponents via photolithographic and soft lithography approaches, *Sensors Actuators A Phys.*, **169** 242–249, with the permission of Elsevier).

a thickness of ca. 20  $\mu\text{m}$  have been obtained upon pyrolysis without cracking and delaminating [180]. Different techniques using ceramic powder fillers added to preceramic polymers have been reported in the literature to control the shrinkage and to suppress cracking and delaminating. However, microfabrication has to be adapted since the filler particles induce scattering during the irradiation step and therefore can induce unwanted absorption in the direct lithographic process [181].

In other preparative approaches, the lithographically produced microstructures are separated from the substrate prior to pyrolysis and sintering. A sharp blade can be used for the removal of the structures from a weakly adhering Teflon or silicon substrate. Furthermore, in order to produce free-standing micro-sized parts, the microstructures were produced on sacrificial substrates (such as NaCl), which were dissolved in water after the lithographic step [182].

Using nanostereolithography or two-photon stereolithography, complex-shaped microparts such as woodpile, microtube, or microcruciform structures have been realized using a polysilazane as a preceramic photoresist [183, 184].

LIGA is an acronym for the German name denoting the three process steps “lithographie, galvanoförmung und abförmung” and is a combination of deep X-ray lithography, electroforming, and injection molding or embossing. This technology allows the formation of structures in the micrometer range with submicrometer precision and a height on the order of several hundred micrometers; therefore, high aspect ratios can be produced. In the first step, very precise miniaturized structures can be produced using X-ray synchrotron radiation. The void area in the developed miniaturized structures is filled with a metal by electroforming. After removal of the remaining resist

from the metal structures, the complementary metallic forms can be filled with a polymer using molding or reaction-molding processes [185]. Metal microparts developed using this process have been used, for instance, as molds in hot-embossing processes.

*Micromolding* is a group of patterning techniques that have been explored during the last decade to enable micro- and nanoprocessing of plastics without the use of lithographic techniques that require higher costs. In this process, a surface relief of a well-engineered master tool (also named mold or stamp) is transferred into a soft material. This initial fluid is allowed to acquire its final geometry by solidifying in this master. This technology allows the reproduction of fine details of the mold. Micromolding can be divided into two categories: (1) molding using hard molds (hot embossing, nanoimprint lithography [NIL], and thermal injection molding) and (2) molding using soft molds, which refers to soft-lithography techniques.

Hard masters are typically fabricated from silicon or silicon dioxide and reactive ion etching (RIE) technologies, from the SU-8 system or from PMMA and the lithography process or from metals (nickel) and the LIGA process [186, 187]. It should be mentioned that in this context, microcasting and micromolding are used as synonyms.

The basis of hot embossing is the shaping of precursor polymers by conformal contact with a microstructured mold using heat and pressure. The viscosity of the material is significantly reduced by increasing the temperature of the prepolymer above  $T_g$ , and pressure application causes the precursor liquid to flow into the cavities of the mold. By further heating, the polymer cross-links and subsequently the mold can be separated from the polymer leaving a stable reproduction of the relief. Using this technique, ceramic microgears have been obtained from a polysilsesquioxane (Fig. 7.8); thus, the polymer was uniaxially warm pressed ( $P = 20$  MPa at  $T = 150^\circ\text{C}$ ) against a steel mold, produced by the LIGA process, and subsequently pyrolyzed at  $1100^\circ\text{C}$  in an argon atmosphere [39].

Liew et al. have produced SiCN microgears by microcasting of a polysilazane on SU-8 molds (obtained by means of photolithography), followed by thermosetting at

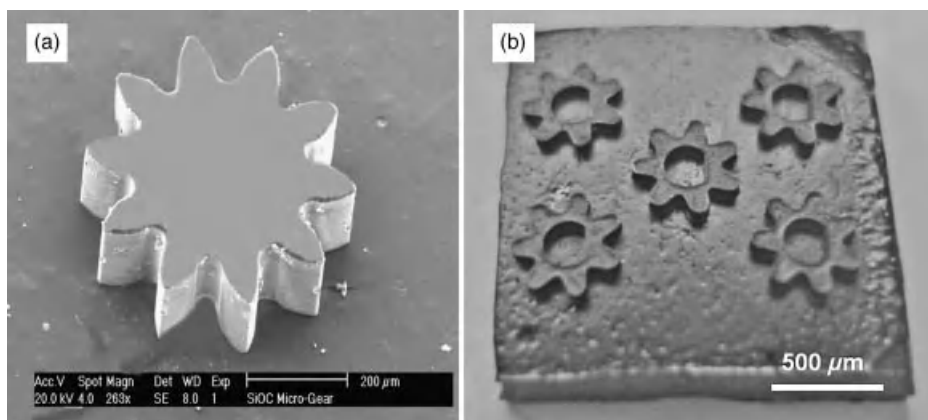


**Figure 7.8.** SiOC-based microcomponents produced via hot embossing (a) and soft-lithography techniques (b) of preceramic precursors followed by pyrolysis in an inert atmosphere.



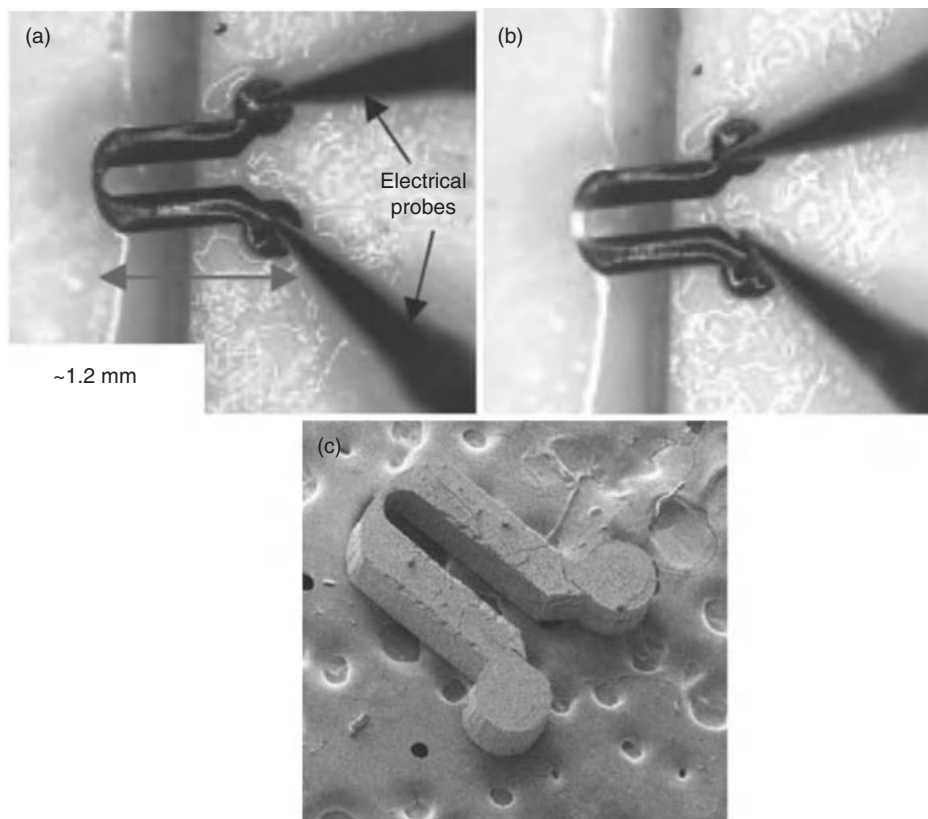


**Figure 7.9.** Silicon carbonitride-based micro glow plug (MPG) in “off” (a) and “on” (b) states as well as SEM micrograph of a single MPG device (c) (reprinted from L. A. Liew, V. M. Bright, and R. Raj (2003) A novel micro glow plug fabricated from polymer-derived ceramics: in situ measurement of high-temperature properties and application to ultrahigh-temperature ignition, *Sens. Actuators A Phys.*, **104**[3] 246–262, with permission of Elsevier).

250°C, cross-linking at 400°C and pyrolysis at 1000°C (Fig. 7.9) [188, 189]. The release of SU-8 mold occurs during pyrolysis. In order to minimize the residues on the walls of the microstructure, extended bake and extended UV exposure of the SU-8 are performed following the mold fabrication but prior to casting.

*Soft lithography* is the collective name for a set of nonphotolithographic techniques: microcontact printing ( $\mu$ CP), replica molding (REM), microtransfer molding ( $\mu$ TM), micromolding in capillaries (MIMIC), and solvent-assisted micromolding (SAMIM). In all of these methods, an elastomeric block, whose surface has been patterned with specific relief structures, is used as a stamp or mold to form patterns with a wide range of materials (Fig. 7.10).

The first step is the creation of a hard master. Usually, microlithographic techniques such as photolithography with SU-8, micromachining or electron-beam writing tech-

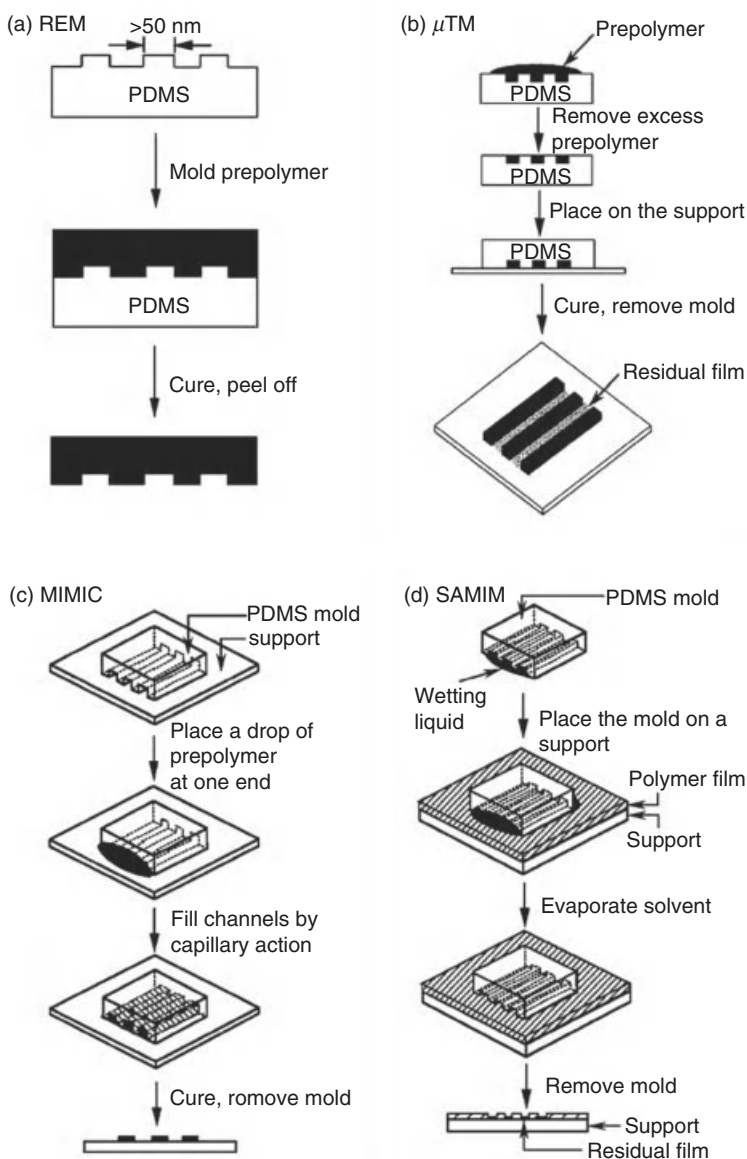


**Figure 7.10.** Schematic illustration of soft-lithography procedures for (A) replica molding (REM), (B) microtransfer molding ( $\mu$ TM), (C) micromolding in capillaries (MIMIC), and (D) solvent-assisted micromolding (SAMIM) (reprinted from Y. Xia and G. M. Whitesides (1998) Soft lithography, *Angew. Chem.*, **110** 568–594, with the permission of Annual Reviews).



niques are applied. In the next step, a negative of the pattern of the master is produced by cast molding of an elastomeric material. The most widely implemented and successful elastomeric material for microfabrication is poly(dimethylsiloxane) (PDMS), obtained from the commercially available Sylgrad 184 (Dow Corning), which is a two-part kit consisting of a prepolymer and a curing agent. The PDMS elastomer is the mold that can be used in a subsequent molding process. Its elastomeric character allows it to be released easily from the master or the molded polymer. Moreover, its low interfacial free energy and chemical inertness reduce irreversible adhesion. Its surface properties can be modified by plasma treatment or by reaction with organosilanes [190–192].

Liquid preceramic polymers are suitable for nanoimprinting and soft-lithography techniques. Since these techniques can be easily performed also in an inert atmosphere, a high number of polymers can be used in comparison with direct lithographic techniques.

Ceramic SiBCN-based honeycomb-shaped microcomponents were prepared via vacuum-assisted MIMIC and  $\mu$ TM techniques [193].

A method similar to MIMIC was reported to produce so-called three-cylinder structures for application as photonic crystals (Fig. 7.11). In the first step PMMA positive resist was patterned using deep X-ray lithography. Subsequently, the produced structures were filled with a liquid preceramic precursor. By repeated exposure of the tilted stack of mask and resist, the 3-D master structure was fabricated. After developing, the microchannels were filled with a polysilazane and were subsequently cross-

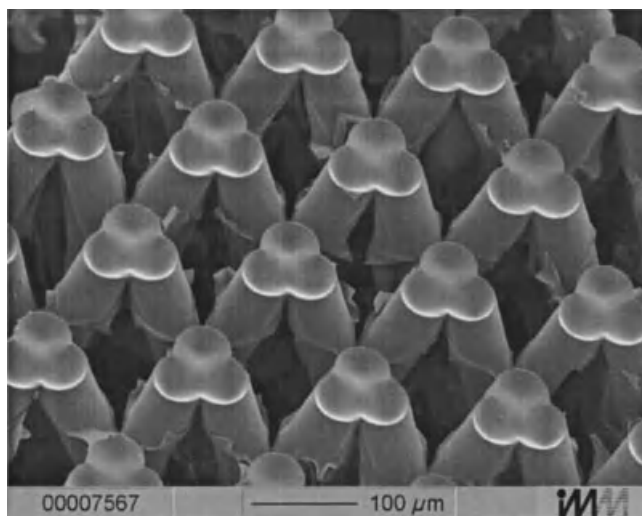


**Figure 7.11.** SiCN photonic crystals produced via deep X-ray lithography (reprinted from G. Feiertag, W. Ehrfeld, H. Freimuth, H. Kolle, H. Lehr, M. Schmidt, M. M. Sigalas, C. M. Soukoulis, G. Kiriakidis, T. Pedersen, J. Kuhl, and W. Koenig (1997) Fabrication of photonic crystals by deep X-ray lithography, *Appl. Phys. Lett.*, **71**[11] 1441–1443, with the permission of the American Institute of Physics).

linked and pyrolyzed at 1100°C. The lattice constant of the obtained photonic crystal was 85  $\mu\text{m}$  and the rod diameter was 22  $\mu\text{m}$  [194].

PDC microcomponents have a great potential for use in harsh environments as it was shown for microstructured SiCN parts. Thus, SiCN-based microigniters and micro-grippers were prepared and tested [193, 195], emphasizing the enormous potential of PDCs in MEMS/nano electromechanical systems (NEMS) applications.

## 7.8 NONCONVENTIONAL PROCESSING TECHNIQUES

Usually, PDCs are prepared upon pyrolysis of preceramic polymers in conventional furnaces. However, there are several nonconventional pyrolysis techniques that have also been used to obtain PDCs. They involve ceramization of the samples upon exposure to laser, microwave, or radiation pyrolysis conditions. The main advantages of these techniques include selective heating, relatively short pyrolysis time, and uniform heating. Furthermore, in the case of pyrolysis via ion irradiation, near ambient temperature conditions are sufficient for the ceramization. Laser and microwave pyrolysis have been used, for instance, to produce PDC powders. Via ion irradiation PDC coatings have been realized [196]. However, bulk ceramic parts with complex shapes can also be prepared, for example, by laser pyrolysis (layer-by-layer technique) or by solid free-forming methods (inkjet printing, laser curing followed by pyrolysis, etc.).

*Laser pyrolysis* has been used to prepare ceramic powders from silicon-containing polymers, such as polysilanes [197] and polysilazanes [198–201]. Furthermore, this technique was applied to prepare complex 3-D-shaped parts using a layer-by-layer approach. Thus, laser pyrolysis combines shaping and pyrolysis into one step. That way, silicon carbide ceramic parts were prepared by laser pyrolysis of polycarbosilane [202]. Despite the rather large dimensions (5–10 mm<sup>2</sup>) achieved in short times (ca. 10 s), the obtained ceramic parts exhibited only 30% relative density, which was attributed to high porosity (due to poor packing of the powder and absorbed water and outgases during pyrolysis).

*Microwave pyrolysis* was also used to fabricate PDC powders. It was shown that microwave processing leads to ceramic samples with different microstructures and crystallinity if compared to those produced by conventional techniques. Thus, Shan and Cozzens observed that polycarbosilane-derived SiC samples conventionally pyrolyzed at 1400°C were still X-ray amorphous, whereas SiC-based samples processed via microwave exhibited  $\beta$ -SiC as a crystalline phase [203]. A systematic study on the influence of the microwave conditions on the structure and crystallinity of PDCs was performed using polycarbosilanes, polysiloxanes, and polysilazanes. Also within this study, differences were observed with respect to microstructure and crystalline phase composition between the samples processed by conventional pyrolysis and the samples processed via microwave-assisted techniques [204]. Thus, transmission electron microscopy (TEM) and X-ray diffraction (XRD) investigation showed that whereas conventionally pyrolyzed high carbon content polysiloxanes developed more  $\beta$ -SiC upon annealing at high temperatures than those processed via microwaves, the opposite trend

was observed in the case of a polysilazane. Generally, it can be stated that microwave processing leads to results that are similar to those of conventional processing, but at lower temperatures or shorter processing times.

*Ion irradiation* was used to produce PDC coatings on inorganic substrates. Thus, preceramic polymers were spin coated on silicon substrate and irradiated with C or Au ions at 500 and 1000 keV, respectively, and with doses in the range from  $10^{14}$  to  $5 \times 10^{15}/\text{cm}^2$  [205]. It was concluded that the ion irradiation furnishes results similar to those obtained via conventional pyrolysis at ca.  $1000^\circ\text{C}$ . However, ion irradiation promotes the release of hydrogen from polymers and stabilizes the carbon within the materials, whereas conventional pyrolysis leads to the release of hydrogen in addition to the partial removal of carbon in the form of hydrocarbons, CO, or  $\text{CO}_2$  [206]. Due to the diamond-like segregation of the carbon in the ceramic films obtained upon irradiation with carbon ions, SiOC films obtained that way were found to exhibit hardness values twice higher than those of pure silica [207].

## 7.9 CONCLUSION

PDCs are unique materials that can be synthesized via ceramization of preceramic polymers and exhibit very interesting (and intriguing) properties, such as outstanding oxidation, corrosion, crystallization, and creep resistance. This chapter highlighted the different processing techniques that can be used to produce ceramic powders, monoliths, fibers, as well as coatings, membranes, porous parts, and microcomponents. The main advantage of the PDCs with respect to processing is that they can be processed through techniques similar to those used for polymer processing. Thus, shaping techniques such as pressing, melt spinning, spin or spray coating, or lithography methods can be used in order to obtain green bodies with complex geometries, which are subsequently transformed into ceramic parts via the pyrolysis process. In this chapter also, some nonconventional processing techniques are presented, such as laser pyrolysis or ion irradiation.

Despite the extensive research performed in the past few decades, there are still open questions related, for instance, to the microstructure–property relations of PDCs. Thus, further studies are needed. This will require synergistic and interdisciplinary approaches to materials design, processing optimization, as well as device engineering.

## ACKNOWLEDGMENTS

The authors thank Mrs. Böhling for proofreading the manuscript. Authors are also grateful for the support provided by the Priority Program SPP1181 NANOMAT funded by the German Research Foundation (DFG, Bonn, Germany). The Fonds der Chemische Industrie (Frankfurt, Germany) is acknowledged for continuous financial support.

## REFERENCES

1. P. Colombo, G. Mera, R. Riedel, and G. D. Soraru (2010) Polymer-derived ceramics: 40 years of research and innovation in advanced ceramics, *J. Am. Ceram. Soc.*, **93**[7] 1805–1837.
2. R. Raj, R. Riedel, and G. D. Soraru (eds.) (2001) Special issue on ultrahigh-temperature polymer derived ceramics, *J. Am. Ceram. Soc.*, **84**[10] 2158–2456.
3. F. Babonneau, P. Miele, R. Riedel, and G. D. Soraru (eds.) (2005) Special issue on polymer derived ceramics, *J. Eur. Ceram. Soc.*, **25** 89–291.
4. R. Riedel and E. Ionescu (eds.) (2006) Special triple issue on preceramic polymers, *Soft Mater.*, **4**[1–3] 105–299.
5. R. Riedel (1995) From molecules to materials—A novel route for the synthesis of advanced ceramics, *Naturwissenschaften*, **82** 12–20.
6. J. Bill and F. Aldinger (1995) Precursor-derived covalent ceramics, *Adv. Mater.*, **7** 775–787.
7. P. Greil (2000) Polymer derived engineering ceramics, *Adv. Eng. Mater.*, **2** 339.
8. R. Riedel, G. Mera, R. Hauser and A. Klonczynski (2006) Silicon-based polymer-derived ceramics: Synthesis, properties and applications—A review, *J. Ceram. Soc. Jpn.*, **114** 425–444.
9. J. Bill, F. Wakai, and F. Aldinger (eds.), *Precursor-Derived Ceramics*. Wiley-VCH, Weinheim, 1999.
10. Colombo P. Colombo, R. Riedel, G. D. Soraru, and H.-J. Kleebe (eds.), *Polymer Derived Ceramics. From Nano-Structure to Applications*. DeSTech Publications, Lancaster, PA, 2009.
11. E. Ionescu, Polymer derived ceramics, in *Ceramics Science and Technologies*, Vol. 3, eds. R. Riedel and I.-W. Chen, Wiley-VCH, Weinheim, 2012, 457–500.
12. M. Birot, J. P. Pillot, and J. Dunogues (1995) Silicon-based polymer-derived ceramics: Synthesis, properties and applications—A review, *Chem. Rev.*, **95** 1443–1477.
13. E. Kroke, Y. Li, C. Konetschny, E. Lecomte, C. Fasel, and R. Riedel (2000) Silazane derived ceramics and related materials, *Mater. Sci. Eng. R*, **26** 97–199.
14. R. Riedel, E. Kroke, A. Greiner, A. O. Gabriel, L. Ruwisch, and J. Nicolich (1998) Inorganic solid-state chemistry with main group element carbodiimides, *Chem. Mater.*, **10**[10] 2964–2979.
15. F. Babonneau, K. Thorne, and J. D. Mackenzie (1989) Dimethyldiethoxysilane/tetraethoxysilane copolymers: Precursors for the silicon-carbon-oxygen system, *Chem. Mater.*, **1** 554.
16. G. D. Soraru (1994) Silicon oxycarbide glasses from gels, *J. Sol-Gel Sci. Technol.*, **2** 843–848.
17. C. G. Pantano, A. K. Singh, and H. X. Zhang (1999) Silicon oxycarbide glasses, *J. Sol-Gel Sci. Technol.*, **14** 7–25.
18. S. Walter, G. D. Soraru, H. Brequel, and S. Enzo (2002) Microstructural and mechanical characterization of sol gel-derived Si–O–C glasses, *J. Eur. Ceram. Soc.*, **22** 2389–2400.
19. A. O. Gabriel and R. Riedel (1997) Preparation of non-oxidic silicon ceramics by an anhydrous sol-gel process, *Angew. Chem. Int. Ed.*, **36** 384–386.

20. A. O. Gabriel, R. Riedel, S. Storck, and W. F. Maier (1997) Synthesis and thermally induced ceramization of a non-oxidic poly(methylsilsesquicarbodi-imide) gel, *Appl. Organomet. Chem.*, **11** 833–841.
21. E. Kroke, K. W. Völger, A. Klonczynski, and R. Riedel (2001) A sol-gel route to  $B_4C$ , *Angew. Chem. Int. Ed.*, **40** 1698–1700.
22. K. W. Völger, E. Kroke, C. Gervais, T. Saito, F. Babonneau, R. Riedel, Y. Iwamoto, and T. Hirayama (2003) B/C/N materials and  $B_4C$  synthesized by a non-oxide sol–gel process, *Chem. Mater.*, **15** 755–764.
23. Balan C. and Riedel R. (2006) Rheological investigations of a polymeric precursor for ceramic materials: experiments and theoretical modeling, *J. Optoelec. Adv. Mater.* **8** 561.
24. S. Yajima, Y. Hasegawa, J. Hayashi, and M. Imura (1978) Synthesis of continuous silicon carbide fibre with high tensile strength and high young's modulus, *J. Mater. Sci.*, **13** 2569–2576.
25. R. M. Laine and F. Babonneau (1993) Preceramic polymers routes to silicon carbide, *Chem. Mater.*, **5** 260–279.
26. K. Okamura (1987) Ceramic fibres from polymer precursors, *Composites*, **18** 107–120.
27. H. Sakurai, R. Koh, A. Hosomi, and M. Kumada (1966) The pyrolysis of organodisilanes, *Bull. Chem. Soc. Jpn.*, **39** 2050–2051.
28. K. Shina and M. Kumada (1958) Thermal rearrangement of hexamethyldisilane to trimethyl(dimethylsilylmethyl)-silane, *J. Org. Chem.*, **23** 139–140.
29. H. Sakurai, A. Hosomi, and M. Kumada (1968) Thermolysis of hexamethyldisilane, *Chem. Commun.*, 930.
30. Y. Hasegawa, M. Imura, and S. Yajima (1980) Synthesis of continuous silicon carbide fibre, *J. Mater. Sci.*, **15** 720–728.
31. H. Ichikawa, F. Machino, S. Mitsuno, T. Ishikawa, K. Okamura, and Y. Hasegawa (1986) Synthesis of continuous silicon carbide fibre. Part 5. Factors affecting stability of polycarbosilane to oxidation, *J. Mater. Sci.*, **21** 4352–4358.
32. Y. Hasegawa (1988) Synthesis of continuous silicon carbide fibre. Part 6. Pyrolysis process of cured polycarbosilane fibre and structure of SiC fibre, *J. Mater. Sci.*, **24** 1177–1190.
33. T. Taki, S. Maeda, K. Okamura, M. Sato, and T. Matsuzawa (1987) Oxidation curing mechanism of polycarbosilane fibres by solid-state  $^{29}Si$  high-resolution NMR, *J. Mater. Sci. Lett.*, **6** 826–828.
34. Y. Hasegawa and K. Okamura (1983) Synthesis of continuous silicon carbide fibre, *J. Mater. Sci.*, **18** 3633–3648.
35. G. D. Soraru, F. Babonneau, and J. Mackenzie (1990)  $^{29}Si$  MAS-NMR investigation of the conversion process of a polytitanocarbosilane into SiC-TiC ceramics, *J. Mater. Sci.*, **5** 3664–3670.
36. M. L. Dunham, D. L. Bailey, and R. Mixer R. (1957) New curing system for silicon rubber, *Ind. Eng. Chem.*, **49** 1373–1376.
37. E. M. Valles and Ch. M. Macosco (1979) Properties of networks formed by end linking of poly(dimethylsiloxane), *Macromolecules*, **12** 673–679.
38. M. Heidingsfeldova and M. Capka M. (1985) Rhodium complexes as catalysts for hydrosilylation crosslinking of silicone rubber, *J. Appl. Polym. Sci.*, **30** 1837–1846.

39. R. Harshe, C. Balan, and R. Riedel (2004) Amorphous Si(Al)OC ceramic from polysiloxanes: Bulk ceramic processing, crystallization behavior and applications, *J. Eur. Ceram. Soc.*, **24**[12] 3471–3482.
40. N. S. Choong Kwet Yive, R. J. P. Corriu, D. Leclercq, P. H. Mutin, and A. Vioux (1992) Silicon carbonitride from polymeric precursors: Thermal cross-linking and pyrolysis of oligosilazane model compounds, *Chem. Mater.*, **4** 141–146.
41. A. Lavendrine, D. Bahloul, P. Goursat, N. S. Choong Kwet Yive, R. J. P. Corriu, D. Leclercq, P. H. Mutin, and A. Vioux (1991) Pyrolysis of polyvinylsilazane precursors to silicon carbonitride, *J. Eur. Ceram. Soc.*, **8** 221–227.
42. G. D. Soraru, F. Babonneau, and J. D. Mackenzie (1990)  $^{29}\text{Si}$  MAS-NMR investigation of the conversion process of a polytitanocarbosilane into SiC-TiC ceramics, *J. Mater. Sci.*, **25** 3664–3670.
43. G. D. Soraru, F. Babonneau, and J. D. Mackenzie (1988) Structural concepts on new amorphous covalent solids, *J. Non-Cryst. Solids*, **106** 256–261.
44. M. Monthieux, A. Oberlin, and E. Bouillon (1990) Relationship between microtexture and electrical properties during heat treatment of SiC fibre precursor, *Composites Sci. Technol.*, **37** 21–35.
45. R. J. P. Corriu, D. Leclercq, P. H. Mutin, and A. Vioux (1997) Preparation and structure of silicon oxycarbide glasses derived from polysiloxane precursors, *J. Sol-Gel. Sci. Technol.*, **8** 327–330.
46. C. G. Pantano, A. K. Singh, and H. Zhang (1999) Silicon oxycarbide glasses, *J. Sol-Gel Sci. Technol.*, **14** 7–25.
47. V. Belot, R. J. P. Corriu, D. Leclercq, P. H. Mutin, and A. Vioux (1992) Thermal redistribution reactions in crosslinked polysiloxanes, *J. Poly. Sci. A: Polym. Chem.*, **30** 613–623.
48. J. Seitz, J. Bill, N. Egger, and F. Aldinger (1996) Structural investigations of Si/C/N-ceramics from polysilazane precursors by nuclear magnetic resonance, *J. Eur. Ceram. Soc.*, **16** 885–891.
49. J. Bill, J. Seitz, G. Thurn, J. Dürr, J. Canel, B. Z. Janos, A. Jalowiecki, A. Sauter, S. Schempp, H. P. Lamparter, J. Mayer, and F. Aldinger (1998) Structure analysis and properties of Si-C-N ceramics derived from polysilazanes, *Phys. Stat. Solidi A*, **166** 269–296.
50. Y. Li, E. Kroke, R. Riedel, C. Fasel, C. Gervais, and F. Babonneau (2001) Thermal cross-linking and pyrolytic conversion of poly(ureamethylvinyl)silazanes to silicon-based ceramics, *Appl. Organomet. Chem.*, **15** 820–832.
51. R. Riedel, E. Kroke, A. Greiner, A. O. Gabriel, L. Ruwisch, and J. Nicolich (1998) Inorganic solid-state chemistry with main group element carbodiimides, *Chem. Mater.*, **10** 2964–2979.
52. R. Riedel, A. Greiner, G. Miehe, W. Dressler, H. Fuess, J. Bill, and F. Aldinger (1997) The first crystalline solids in the ternary Si-C-N system, *Angew. Chem. Int. Ed.*, **36** 603–606.
53. P. Greil and M. Seibold (1992) Modelling of dimensional changes during polymer-ceramic conversion for bulk component fabrication, *J. Mater. Sci.*, **27** 1053–1060.
54. P. Greil (1995) Active-filler-controlled pyrolysis of preceramic polymers, *J. Am. Ceram. Soc.*, **78** 835–848.
55. P. Greil (1998) Near net shape manufacturing of polymer derived ceramics, *J. Eur. Ceram. Soc.*, **18** 1905–1914.

56. (a) F. W. Ainger and J. M. Herbert, The preparation of phosphorus-nitrogen compounds as non-porous solids, in *Special Ceramics*, ed. P. Popper, p. 168, Academic Press, New York, 1965; (b) P. G. Chantrell and P. Popper, Inorganic polymers and ceramics, in *Special Ceramics*, ed. P. Popper, p. 76, Academic Press, New York, 1965.
57. (a) W. Verbeek (1973) *Ger. Pat.* No. 2218960 (Bayer AG), U.S. Patent No. 3853567; (b) W. Verbeek and G. Winter (1974) *Ger. Patent* No. 2236078 (Bayer AG); (c) G. Winter, W. Verbeek, and M. Mansmann (1974) *Ger. Patent* No. 2243527.
58. G. Fritz and B. Raabe (1956) Bildung siliciumorganischer Verbindungen. V. Die Thermische Zersetzung von  $\text{Si}(\text{CH}_3)_4$  und  $\text{Si}(\text{C}_2\text{H}_5)_4$ , *Z. Anorg. Allg. Chem.*, **286** 149–167.
59. S. Yajima, J. Hayashi, and M. Imori (1975) Continuous silicon carbide fiber of high tensile strength, *Chem. Lett.*, **9** 931–934.
60. S. Yajima, Y. Hasegawa, K. Okamura, and I. Matsuzawa (1978) Development of high tensile strength silicon carbide fibre using an organosilicon polymer precursor, *Nature (London)*, **273** 525–527.
61. R. M. Laine and F. Babonneau (1993) Preceramic polymer routes to silicon carbide, *Chem. Mater.*, **5** 260–279.
62. Y. Hasegawa, M. Imura, and S. Yajima (1980) Synthesis of continuous silicon carbide fibre. Part 2. Conversion of polycarbosilane fibre into silicon carbide fibres, *J. Mater. Sci.*, **15** 720–728.
63. H. Ichikawa, F. Machino, S. Mitsuno, T. Ishikawa, K. Okamura, and Y. Hasegawa (1986) Synthesis of continuous silicon carbide fibre. Part 5. Factors affecting stability of polycarbosilane to oxidation, *J. Mater. Sci.*, **21** 4352–4358.
64. Y. Hasegawa (1989) Synthesis of continuous silicon carbide fibre. Part 6. Pyrolysis process of cured polycarbosilane fibre and structure of SiC fibre, *J. Mater. Sci.*, **24** 1177–1190.
65. T. Taki, S. Maeda, K. Okamura, M. Sato, and T. Matsuzawa (1987) Oxidation curing mechanism of polycarbosilane fibres by solid-state  $^{29}\text{Si}$  high-resolution NMR, *J. Mater. Sci. Lett.*, **6** 826–828.
66. Y. Hasegawa and K. Okamura (1983) Synthesis of continuous silicon carbide fibre. Part 3. Pyrolysis process of polycarbosilane and structure of the products, *J. Mater. Sci.*, **18** 3633–3648.
67. G. D. Soraru, F. Babonneau, and J. D. Mackenzie (1990)  $^{29}\text{Si}$  MAS-NMR investigation of the conversion process of a polytitanocarbosilane into SiC-TiC ceramics, *J. Mater. Sci.*, **25** 3664–3670.
68. T. Seguchi, N. Kasai, K. Okamura, H. Ichikawa, M. Taeda, and M. Nishii M. (1993) U.S. Patent 5283044.
69. W. Verbeek (1973) Patent DE 2218960.
70. G. Winter, W. Verbeek, and M. Mansmann (1974) Patent DE 2243527.
71. D. Seyferth, G. H. Wiseman, C. A. Poutasse, J. M. Schwark, and Y.-F. Yu (1987) Organosilicon polymers as precursors for silicon-containing ceramics: Recent developments, *Polym. Prepr.*, **28** 389–392.
72. G. Motz, J. Hacker, G. Ziegler, B. Claus, and D. Schawaller (2002) Low-cost ceramic SiCN fibers by an optimized polycarbosilazane and continuous processing, *Adv. Inorg. Str. Fiber Comp.*, 47–54.
73. G. Motz (2006) Synthesis of SiCN-precursors for fibers and matrices, *Adv. Sci. Technol.*, **50** 24–30.



74. S. Kokott and G. Motz (2007) Cross-linking via electron beam treatment of a tailored polysilazane (ABSE) for processing of ceramic SiCN-fibers, *Soft Mater.*, **4** 165–174.
75. M. Takamizawa, T. Kobayashi, A. Hayashida, and Y. Takeda (1986) U.S. Patent 4604367.
76. T. Wideman, E. Cortez, E. E. Remsen, G. A. Zank, P. J. Carroll, and L. G. Sneddon (1997) Reactions of monofunctional boranes with hydridopolysilazanes: Synthesis, characterization, and ceramic conversion reactions of new processible precursors to SiNCB ceramic materials, *Chem. Mater.*, **9** 2218–2230.
77. T. Wideman, P. J. Fazen, K. Su, E. E. Remsen, G. A. Zank, and L. G. Sneddon (1998) Second-generation polymeric precursors for BN and SiNCB ceramic materials, *Appl. Organomet. Chem.*, **12** 681–693.
78. H.-P. Baldus, O. Wagner and M. Jansen (1992) Synthesis of advanced ceramics in the systems silicon-boron-nitrogen and silicon-boron-nitrogen-carbon employing novel precursor compounds, *Mat. Res. Soc. Symp. Proc.*, **271** 821–826.
79. H.-P. Baldus, G. Passing, D. Sporn, and A. Thierauf (1995) Si–B–(N,C) a new ceramic material for high performance applications, *Ceram. Trans.* 75–84.
80. H.-P. Baldus, M. Jansen, and D. Sporn (1999) Ceramic fibers for matrix composites in high-temperature engine applications, *Science* **285**, 699–703.
81. R. Riedel, A. Kienzle, W. Dressler, L. Ruwisch, J. Bill, and F. Aldinger (1996) A silicoboron carbonitride ceramic stable to 2000°C, *Nature*, **382** 796–798.
82. S. Bernard, M. Weinmann, D. Cornu, P. Miele, and F. Aldinger (2005) Preparation of high-temperature stable Si–B–C–N fibers from tailored single source polyborosilazanes, *J. Eur. Ceram. Soc.*, **25** 251–256.
83. S. Bernard, M. Weinmann, P. Gerstel, P. Miele, and F. Aldinger (2005) Boron- modified polysilazane as a novel single-source precursor for SiBCN ceramic fibers: Synthesis, melt-spinning, curing and ceramic conversion, *J. Mater. Chem.*, **5** 289–299.
84. F. A. Scheffler and J. D. Torrey, Coatings, in *Polymer Derived Ceramics. From Nano-Structure to Applications*, eds. P. Colombo, R. Riedel, G. D. Soraru, and H.-J. Kleebe, p. 358, DEStech Publications, Lancaster, PA, 2009.
85. G. Marletta, A. Toth, I. Bertoti, T. Minh Duc, F. Sommer, and K. Ferencz (1998) Optical properties of ceramic-like layers obtained by low energy ion beam irradiation of polysiloxane films, *Nucl. Instrum. Meth., B*, **141**[1–4] 684–692.
86. Q. D. Nghiem, J.-K. Jeon, L.-Y. Hong, and D.-P. Kim (2003) Polymer derived Si–C–B–N ceramics via hydroboration from borazine derivatives and trivinylcyclotrisilazane, *J. Organomet. Chem.*, **688**[1–2] 27–35.
87. J. D. Torrey and R. K. Bordia (2008) Processing of polymer-derived ceramic composite coatings on steel, *J. Am. Ceram. Soc.*, **91**[1] 41–45.
88. J. D. Torrey and R. K. Bordia (2008) Mechanical properties of polymer-derived ceramic composite coatings on steel, *J. Eur. Ceram. Soc.*, **29**[1], 253–257.
89. O. Goerke, E. Feike, T. Heine, A. Trampert, and H. Schubert (2004) Ceramic coatings processed by spraying of siloxane precursors, *J. Eur. Ceram. Soc.*, **24**[7] 2141–2147.
90. H. Lei, L. F. Francis, W. W. Grberich, and L. E. Craven (2001) *Mat. Res. Soc. Symp. Proc.*, **653** Z.10.5.1.
91. H. Kozuka, S. Takenaka, H. Tokita, T. Hirano, Y. Higashi, and T. Hamatani (2003) Stress and cracks in gel-derived ceramic coatings and thick film formation *J. Sol-Gel Sci. Technol.*, **26** 681–686.



92. H.-J. Krauß and Motz (2002) Laser pyrolysis of polysilazane—A new technique for the generation of ceramic-like coatings and structures, *Key Eng. Mater.*, **206–213** 467–470.
93. G. Motz and G. Ziegler (2002) Simple processibility of precursor-derived SiCH coatings by optimized precursors, *Key Eng. Mater.*, **206–213** 475–478.
94. M. Pavese, P. Fino, C. Badini, A. Ortona, and G. Marino (2008) HfB<sub>2</sub>/SiC as protective coating for 2D Cf/SiC composites: Effect of high temperature oxidation on mechanical properties, *Surf. Coat. Technol.*, **202**[10] 2059–2067.
95. P. Cromme, M. Scheffler and P. Greil (2002) Ceramic tapes from preceramic polymers, *Adv. Eng. Mater.*, **4**[11] 873–877.
96. J.-G. Kho, K.-T. Moon, G. Nouet, P. Ruterana, and D.-P. Kim (2001) Boron-rich boron nitride (BN) films prepared by a single spin\_coating process of a polymeric precursor, *Thin Solid Films*, **389**[1–2] 78–83.
97. S. Jou, C.-T. Sun, and X. Chen (2005) Silicon Carbide films from polycarbosilane and their usage as buffer layers for diamond deposition, *Diamond Relat. Mater.* **14** 1688–1694.
98. H. Termoss, B. Toury, A. Brioude, J. Dazord, J. Le Brusq, and P. Miele (2007) High purity boron nitride thin films prepared by the PDC route, *Surf. Coat. Technol.*, **201**[18] 7822–7828.
99. Y. D. Blum, R. M. Platz and E. J. Crawford (1990) Glass strenghtening by polymer-derived ceramic coatings, *J. Am. Ceram. Soc.*, **73**[1] 170–172.
100. M. R. Mucalo, N. B. Milestone, I. C. Vickridge, and M. V. Swain (1994) Preparation of ceramic coatings from pre-ceramic precursors. Part 1. SiC and Si<sub>3</sub>N<sub>4</sub>/Si<sub>2</sub>N<sub>2</sub>O coatings on alumina substrates, *J. Mater. Sci.*, **29**[17] 4487–4499.
101. V. Bakumov, K. Gueinzus, C. Hermann, M. Schwarz, and E. Kroke (2007) Polysilazane-derived antibacterial silver-ceramic nanocomposites, *J. Eur. Ceram. Soc.*, **27**[10] 3287–3292.
102. K. Jarosch and H. I. de Lasa (1999) Novel riser simulator for methane reforming using high temperature membranes, *Chem. Eng. Sci.*, **54** 1455–1460.
103. E. Kikuchi, Y. Nemoto, M. Kajikawa, S. Uemiya, and T. Kojima (2000) Steam reforming of methane in membrane reactors: Comparison of electroless-plating and CVD membranes and catalyst packing modes, *Catal. Today*, **56** 75–81.
104. A. K. Prabhu and S. T. Oyama (2000) Highly hydrogen selective ceramic membranes: Application to the transformation of greenhouse gases, *J. Membr. Sci.*, **176** 233–248.
105. S. Kurungot, T. Yamaguchi, and S. Nakao (2003) Rh/ $\gamma$ -Al<sub>2</sub>O<sub>3</sub> catalytic layer integrated with sol-gel synthesized microporous silica membrane for compact membrane reactor applications, *Cat. Lett.*, **86** 273–278.
106. Y. Iwamoto (2007) Precursors-derived ceramic membranes for high-temperature separation of hydrogen, *J. Cer. Soc. Jpn.*, **115**[12] 947–954.
107. Y. Iwamoto, Membranes, in *Polymer Derived Ceramics. From Nano-Structure to Applications*, eds. P. Colombo, R. Riedel, G. D. Soraru, and H.-J. Kleebe, p. 396, DEStech Publications, Lancaster, PA, 2009.
108. Y. Yoshino, T. Suzuki, B. N. Nair, H. Taguchi, and N. Itoh (2005) Development of tubular substrates, silica based membranes and membrane modules for hydrogen separation at high temperature, *J. Membr. Sci.*, **267** 8–17.
109. R. Kojima, K. Sato, T. Nagaono, and Y. Iwamoto (2006) Gas permeation properties of amorphous SiC membranes synthesized from polycarbosilane without oxygen-curing process, *J. Cer. Soc. Jpn.*, **114** 533–538.

110. T. Nagano, N. Uno, T. Saito, S. Yamazaki, and Y. Iwamoto (2007) Gas permeance behavior at elevated temperature in mesoporous anodic oxidized alumina synthesized by pulse-sequential voltage method, *Chem. Eng. Commun.*, **194** 158–169.
111. Y. Iwamoto, K. Sato, T. Kato, T. Inada, and Y. Kubo (2005) Hydrogen permselective amorphous silica membrane derived from polysilazane, *J. Eur. Ceram. Soc.*, **25** 257–264.
112. A. B. Shelekhin, E. J. Grosgogeat, and T. S. Hwang (1991) Gas separation properties of a new polymer/inorganic composite membrane, *J. Membr. Sci.*, **66** 129–141.
113. T. Nagano, K. Sato, T. Saito, and Y. Iwamoto (2006) Gas permeation properties of amorphous SiC membrane synthesized from polycarbosilane without oxygen-curing process, *J. Cer. Soc. Jpn.*, **114** 533–538.
114. R. A. Wach, M. Sugimoto, and M. Yoshikawa (2007) Formation of silicon carbide membrane by radiation curing of polycarbosilane and polyvinylsilane and its gas separation up to 250°C, *J. Am. Ceram. Soc.*, **90** 275–278.
115. H. Suda, H. Yamauchi, Y. Uchimaru, I. Fujiwara, and K. Haraya (2006) Structural evolution of polycarbosilane precursor into silicon carbide-based microporous membranes, *J. Cer. Soc. Jpn.*, **114** 539–544.
116. K. Kusakabe, Z. Y. Li, H. Maeda, and S. Morooka (1995) Preparation of supported membrane by pyrolysis of polycarbosilane for gas separation at high temperature, *J. Membr. Sci.*, **103** 175–180.
117. Z. Y. Li, K. Kusakabe, and S. Morooka (1996) Preparation of thermostable amorphous Si-C-O membrane and its application to gas separation at elevated temperature, *J. Membr. Sci.*, **118** 159–168.
118. D. Lee, L. Zhang, S. T. Oyama, S. Niu, and R. F. Saraf (2004) Synthesis, characterization and gas permeation properties of a hydrogen permeable silica membrane supported on porous alumina, *J. Membr. Sci.*, **231**, 117–126.
119. K. W. Völger, R. Hauser, E. Kroke, R. Riedel, Y. H. Ikuhara, and Y. Iwamoto (2006) Synthesis and characterization of novel non-oxide sol-gel derived mesoporous amorphous Si-C-N membranes, *J. Cer. Soc. Jpn.*, **114** 576–560.
120. R. Hauser, S. Nahar-Borchard, R. Riedel, Y. H. Ikuhara, and Y. Iwamoto (2006) Polymer-derived SiBCN ceramics and their potential application for high temperature membranes, *J. Cer. Soc. Jpn.*, **114** 524–528.
121. R. M. Prasad, Y. Iwamoto, R. Riedel, and A. Gurlo (2010) Multilayer amorphous-SiBCN/ $\gamma$ -Al<sub>2</sub>O<sub>3</sub>/α-Al<sub>2</sub>O<sub>3</sub> membranes for hydrogen purification, *Adv. Eng. Mater.*, **12** 522–528.
122. P. Colombo and M. Scheffler, Highly porous components, in *Polymer Derived Ceramics. From Nano-Structure to Applications*, eds. P. Colombo, R. Riedel, G. D. Soraru, and H.-J. Kleebe, p. 379, DEStech Publications, Lancaster, PA, 2009.
123. P. Colombo (2008) In praise of pores, *Science*, **322** 381–383.
124. P. Colombo (2006) Conventional and novel processing methods for cellular ceramics, *Phil. Trans. R. Soc. A*, **364** 109–124.
125. P. Colombo and J. R. Hellmann (2002) Ceramic foams from preceramic polymers, *Mat. Res. Innovat.*, **6** 260–272.
126. G. M. Renlund, W. P. Minnear, and A. A. Bracco (1991) U.S. Patent 4981829.
127. G. M. Renlund, L. N. Lewis, J. Stein, and A. A. Bracco (1993) U.S. Patent 5180694.
128. D. E. Daws, N. T. Castelluci, H. W. Carpenter, and M. W. Colby (1997) U.S. Patent 5643512.

129. P. Colombo, M. Griffoni, and M. Modesti (1998) Ceramic foams from a preceramic polymer and polyurethanes: Preparation and morphological characterization, *J. Sol-Gel Sci. Technol.*, **13** 195–199.
130. P. Colombo and E. Bernardo (2003) Macro- and micro-cellular porous ceramics from preceramic polymers, *Comp. Sci. Technol.*, **63** 2353–2359.
131. T. Gambaryan-Roisman, M. Scheffler, P. Buhler, and P. Greil (2000) Processing of ceramic foam by pyrolysis of filler containing phenylmethyl polysiloxane, *Ceram. Trans.*, **108** 121–130.
132. J. Zeschky, F. Goetz-Neunhoeffler, J. Neubauer, S. H. Jason Lo, B. Kummer, M. Scheffler, and P. Greil (2003) Preceramic polymer derived cellular ceramics, *Comp. Sci. Technol.*, **63** 2361–2370.
133. J. Zeschky, T. Hoefner, C. Arnold, R. Weißmann, D. Bahloul-Hourlier, M. Scheffler, and P. Greil (2005) Polysilsesquioxane derived ceramic foams with gradient porosity, *Acta Mater.*, **53** 927–937.
134. L. L. Whinnery, M. C. Nichols, D. R. Wheeler, and D. A. Loy (2005) Preparation of three-dimensional ordered macroporous SiCN ceramic using sacrificing template method, *Micropor. Mesopor. Mater.*, **80** 357–362.
135. X. Bao, M. R. Nangrejo, and M. J. Edirisinghe (1999) Synthesis of silicon carbide foams from polymeric precursors and their blends, *J. Mater. Sci.*, **34** 2495–2505.
136. P. Colombo, J. R. Hellmann, and D. L. Shelleman (2001) Mechanical properties of silicon oxycarbide ceramic foam, *J. Am. Ceram. Soc.*, **84**[10], 2245–2251.
137. T. Takahashi, H. Münster, P. Colombo, and M. Modesti (2001) Thermal evolution of foamed blend of silicone resin nad polyurethane from preceramic to ceramic foam, *J. Mater. Sci.*, **36** 1627–1639.
138. T. Takahashi, H. Münster, P. Colombo, and M. Modesti (2001) Oxidation resistant ceramic foam from a silicone preceramic polymer/polyurethane blend, *J. Eur. Ceram. Soc.*, **21** 2821–2828.
139. P. Colombo and J. R. Hellman (2002) Ceramic foams from preceramic polymers, *Mat. Res. Innovat.*, **6** 260–272.
140. T. Gambaryan-Roisman, M. Scheffler, P. Buhler, and P. Greil (2000) Processing of ceramic foam by pyrolysis of filler containing phenylmethyl polysiloxane, *Ceram. Trans.*, **108** 121–130.
141. J. Zeschky, T. Hoefner, C. Arnold, R. Weißmann, D. Bahloul-Hourlier, M. Scheffler, and P. Greil (2005) Polysilsesquioxane derived ceramic foams with gradient porosity, *Acta Mater.*, **53** 927–937.
142. U. F. Vogt, L. Györfy, A. Herzog, T. Graule, and G. Plesch (2007) Macroporous silicon carbide foams for porous burner applications and catalyst supports, *J. Phys. Chem. Solids*, **68** 1234–1238.
143. M. R. Nangrejo, X. Bao, and M. J. Edirisinghe (2000) Preparation of silicon carbide-silicon nitride composite foams from pre-ceramic polymers, *J. Eur. Ceram. Soc.*, **20** 1777–1785.
144. M. R. Nangrejo, X. Bao, and M. J. Edirisinghe (2000) The structure of ceramic foams using polymeric precursors, *J. Mater. Sci. Lett.*, **19** 787–789.
145. J. Yan, A. Wang, and D.-P. Kim (2006) Preparation of ordered mesoporous SiC from preceramic polymer templated by nanoporous silica, *J. Phys. Chem. B*, **110** 5429–5433.
146. P. Krawiec, D. Geiger, and S. Kaskel (2006) Ordered mesoporous silicon carbide (OM-SiC) via polymer precursor nanocasting, *Chem. Commun.*, **23** 2469–2470.

147. J. Yan, A. Wang, and D.-P. Kim (2007) Preparation of ordered mesoporous SiCN ceramics with large surface area and high thermal stability, *Micropor. Mesopor. Mater.*, **100** 128–133.
148. P. Greil (2001) Biomorphous ceramics from lignocellulosis, *J. Eur. Ceram. Soc.*, **21** 105–118.
149. C. Zollfrank, R. Kladny, G. Motz, H. Sieber, and P. Greil (2001) Manufacturing of anisotropic ceramics from preceramic polymers and wood, *Ceram. Trans.*, **114** 43–48.
150. C. Zollfrank, R. Kladny, G. Motz, H. Sieber, and P. Greil (2004) Biomorphous SiOC/C-ceramic composites from chemically modified wood templates, *J. Eur. Ceram. Soc.*, **24** 479–487.
151. C. R. Rambo and H. Sieber (2006) Manufacturing of cellular SiAlON/SiC composite ceramics from cardboard, *J. Mater. Sci.*, **41** 3315–3322.
152. P. Colombo, E. Bernardo, and L. Biasetto (2004) Novel microcellular ceramics from a silicone resin, *J. Am. Ceram. Soc.*, **87**[1] 152–154.
153. C. M. Mitchell, D.-P. Kim, and P. J. A. Kenis (2006) Ceramic microreactors for on-site hydrogen production, *J. Catal.*, **241** 235–242.
154. Y.-W. Kim, C. Wang, and C. B. Park (2007) Processing of porous silicon oxycarbide ceramics from extruded blend of polysiloxane and polymer microbead, *J. Cer. Soc. Jpn.*, **115** 419–424.
155. M. Shibuya, T. Takahashi, and K. Koyama (2007) Microcellular ceramics by using silicone preceramic polymer and PMMA polymer sacrificial microbead, *Comp. Sci. Tech.*, **67** 119–124.
156. H. Wang, X. D. Li, J. S. Yu, and D.-P. Kim (2004) Fabrication and characterization of ordered macroporous PMS-derived SiC from a sacrificial template method, *J. Mater. Chem.*, **14** 1383–1386.
157. H. Wang, S.-Y. Zheng, X. D. Li, and D.-P. Kim (2005) Preparation of three-dimensional ordered macroporous SiCN ceramic using sacrificing template method, *Micropor. Mesopor. Mater.*, **80** 357–362.
158. I.-K. Sung, C. M. Mitchell, D.-P. Kim, and P. J. A. Kenis (2005) Tailored macroporous SiCN and SiC structures for high-temperature fuel reforming, *Adv. Funct. Mater.*, **15** 1336–1342.
159. C. Vakifahmetoglu, I. Menapace, A. Hirsch, L. Biasetto, R. Hauser, R. Riedel, and P. Colombo (2009) Highly porous macro- and micro-cellular ceramics from a polysilazane precursor, *Ceramics Int.*, **35**[8] 3281–3290.
160. S. H. Kim, Y.-W. Kim, and C. B. Park (2004) Effect of inert filler addition on pore size and porosity of closed-cell silicon oxycarbide foams, *J. Mater. Sci.*, **39** 3513–3515.
161. Y.-W. Kim, S. H. Kim, H.-D. Kim, and C. B. Park (2004) Processing of closed-cell silicon oxycarbide foams from a preceramic polymer, *J. Mater. Sci.*, **39** 5647–5652.
162. Y.-W. Kim, Y.-J. Jin, Y.-S. Chun, I.-H. Song, and H.-D. Kim (2005) A simple pressing route to closed-cell microcellular ceramics, *Scripta Mater.*, **53**, 921–926.
163. R. A. Dorey, S. A. Rocks, F. Dauchy, D. Wang, F. Bortolan, and E. Hugo (2008) Integrating functional ceramics into microsystems, *J. Eur. Ceram. Soc.*, **28** 1397–1403.
164. W. Bauer, H. J. Ritzhaupt-Kleissl, and J. Hausselt (1998) Slip casting of ceramic micro-components, *Microsyst. Technol.*, **4** 125–127.

165. J. A. Bride, S. Baskaran, N. T. Taylor, W. Halloran, W. H. Juan, S. W. Pang, and M. O'Donnell (1993) Photolithographic micromolding of ceramics using plasma etched polyimide patterns, *Appl. Phys. Lett.*, **63**[24] 3379 (3p).
166. A. Navarro, S. A. Rocks, and R. A. Dorey (2007) Micromoulding of lead zirconate titanate (PZT) structures for MEMS, *J. Electroceram.*, **19** 321–326.
167. U. P. Schönholzer, R. Hummel, and L. J. Gauckler (2000) Microfabrication of ceramics by filling of photoresist molds, *Adv. Mater.*, **12**[17] 1261–1263.
168. T. Hanemann, J. Boehm, P. Henzi, K. Honnef, K. Litfin, E. Ritzhaupt-Kleissl, and J. Hausselt (2004) From micro to nano: Properties and potential applications of micro- and nano-filled polymer ceramic composites in microsystem technology, *IEEE Proc. Nanobiotechnol.*, **151**[4] 167–172.
169. B. Su, T. W. Button, A. Schneider, L. Singleton, and P. Prewett (2002) Embossing of 3D ceramic microstructures, *Microsyst. Technol.*, **8** 359–362.
170. C. R. Martin and I. A. Aksay (2004) Submicrometer-scale patterning of ceramic thin films, *J. Electroceram.*, **12** 53–68.
171. H. J. Ritzhaupt-Kleissl, W. Bauer, E. Günther, J. Laubersheimer, and J. Hausselt (1996) Development of ceramic microstructures, *Microsyst. Technol.*, **2** 130–134.
172. R. Knitter, E. Günther, C. Odemer, and U. Maciejewski (1996) Ceramic microstructures and potential applications, *Microsyst. Technol.*, **2** 135–138.
173. C. S. Roper, C. Carraro, R. T. Howe, and R. Maboudian (2006) Silicon carbide thin films using 1,3-disilabutane single precursor for MEMS applications—A review, *ECS Trans.*, **3**[10] 267–280.
174. C. Marzolin, S. P. Smith, M. Prentiss, and G. M. Whitesides (1998) Fabrication of glass microstructures by micro-molding of sol-gel precursors, *Adv. Mater.*, **10**[8] 571–574.
175. S. Seraji, Y. Wu, N. E. Jewell-Larson, M. J. Forbess, S. J. Limmer, T. P. Chou, and G. Cao (2000) Patterned microstructure of sol-gel derived complex oxides using soft lithography, *Adv. Mater.*, **12**[19] 1421–1424.
176. C. M. Chan, G. Z. Cao, and T. G. Stoebe (2000) Net shape ceramic microcomponents by modified sol-gel casting, *Microsyst. Technol.*, **6** 200–204.
177. M. Schulz, Microfabrication and MEMS/NEMS, in *Polymer Derived Ceramics. From Nano-Structure to Applications*, eds. P. Colombo, R. Riedel, G. D. Soraru, and H.-J. Kleebe, p. 416, DEStech Publications, Lancaster, PA, 2009.
178. A. Campo and E. Arzt (2008) Fabrication approaches for generating complex micro- and nanopatterns on polymeric surfaces, *Chem. Rev.*, **108** 911–945.
179. B. D. Gates, Q. Xu, M. Stewart, D. Ryan, C. G. Willson, and G. M. Whitesides (2005) New approaches to nanofabrication: molding, printing, and other techniques, *Chem. Rev.*, **105** 1171–1196.
180. M. Schulz, M. Boerner, J. Goettert, T. Hanemann, J. Hausselt, and G. Motz (2004) Cross linking behavior of preceramic polymers effected by UV- and synchrotron radiation, *Adv. Eng. Mater.*, **6**[8] 676–680.
181. M. Schulz, M. Boerner, J. Hausselt, and R. Heldele (2005) Polymer derived ceramic microparts from X-ray lithography—Cross-linking behavior and process optimization, *J. Eur. Ceram. Soc.*, **25** 199–204.
182. L. A. Liew, V. M. Bright, and R. Raj (2002) Fabrication of SiCN MEMS by photopolymerization of preceramic polymer, *Sensors Actuators A Phys.*, **95**[2–3] 120–134.

183. T. A. Pham, D.-P. Kim, T. W. Lim, S. H. Park, D. Y. Yang, and K. S. Lee (2006) Three-dimensional SiCN ceramic microstructures via nano-stereolithography of inorganic polymer photoresists, *Adv. Func. Mater.*, **16**[9] 1235–1241.
184. T. A. Pham, P. Kim, M. Kwak, K. Y. Suh, and D.-P. Kim (2007) Inorganic polymer photoresist for direct ceramic patterning by photolithography, *Chem. Commun.*, 4021–4023.
185. W. Ehrfeld and D. Münchmeyer (1991) Three-dimensional microfabrication using synchrotron radiation, *Nucl. Instr. Methods Phys. Res. A*, **303** 523–531.
186. U. P. Schönholzer, R. Hummel, and L. J. Gauckler (2000) Microfabrication of ceramics by filling of photoresist molds, *Adv. Mater.*, **12**[17] 1261–1263.
187. T. Hanemann, J. Boehm, P. Henzi, K. Honnef, K. Litfin, E. Ritzhaupt-Kleissl, and J. Hauselt (2004) From micro to nano: properties and potential applications of micro- and nano-filled polymer ceramic composites in microsystem technology, *IEEE Proc. Nanobiotechnol.*, **151**[4] 167–172.
188. L. Liew, W. Zhang, L. An, S. Shah, R. Lou, Y. Liu, T. Cross, M. Dunn, V. Bright, J. Daily, R. Raj, and K. Anseth (2001) Ceramic MEMS—New materials, innovative processing and future applications, *Am. Ceram. Soc. Bull.*, **80**[5] 25–30.
189. L. A. Liew, V. M. Bright, and R. Raj (2003) A novel micro glow plug fabricated from polymer-derived ceramics: In situ measurement of high-temperature properties and application to ultrahigh-temperature ignition, *Sens. Actuators A Phys.*, **104**[3] 246–262.
190. Y. Xia, J. A. Rogers, K. E. Paul, and G. M. Whitesides (1999) Unconventional methods for fabricating and patterning nanostructures, *Chem Rev.*, **99** 1823–1848.
191. X. M. Zhao, Y. Xia, and G. M. Whitesides (1997) Soft-lithographic methods for nanofabrication, *J. Mater. Chem.*, **7**[7] 1069–1074.
192. Y. Xia and G. M. Whitesides (1998) Soft lithography, *Angew. Chem. Int. Ed.*, **37** 550–575.
193. H. Yang, P. Deschatelets, S. T. Brittain, and G. M. Whitesides (2001) Fabrication of high performance ceramic microstructures from a polymeric precursor using soft lithography, *Adv. Mater.*, **13**[1] 54–58.
194. G. Feiertag, W. Ehrfeld, H. Freimuth, H. Kolle, H. Lehr, M. Schmidt, M. M. Sigalas, C. M. Soukoulis, G. Kiriakidis, T. Pedersen, J. Kuhl, and W. Koenig (1997) Fabrication of photonic crystals by deep X-ray lithography, *Appl. Phys. Lett.*, **71**[11] 1441–1443.
195. L. A. Liew, R. A. Saravanan, V. M. Bright, M. L. Dunn, J. W. Daily, and R. Raj (2003) Processing and characterization of silicon carbon-nitride ceramics: Application of electrical properties towards MEMS thermal actuators, *Sens. Actuators A Phys.*, **103**[1–2] 171–181.
196. S. R. Boddapati and S. Brahmandam, Non-conventional pyrolysis and processing, in *Polymer Derived Ceramics. From Nano-Structure to Applications*, eds. P. Colombo, R. Riedel, G. D. Soraru, and H.-J. Kleebe, p. 443, DEStech Publications, Lancaster, PA, 2009.
197. G. W. Rice and R. L. Woodin (1989) Kinetics and mechanism of laser-driven powder synthesis from organosilane precursors, *J. Mater. Res.*, **4**[6] 1538–1548.
198. G. W. Rice (1986) Synthesis of Si/C/N powders from 1,1,1,3,3,3-hexamethyldisilazane, *J. Am. Ceram. Soc.*, **69**[8] C-183/C-185.
199. K. E. Gonsalves, P. R. Strutt, T. D. Xiao, and P. G. Klemens (1992) Synthesis of Si(C,N) nanoparticles by rapid laser polycondensation/cross-linking reactions of an organosilazane precursor, *J. Mater. Sci.*, **27** 3231–3238.

200. M. Suzuki, Y. Maniette, Y. Nakata, and T. Okutani (1993) Synthesis of silicon carbide-silicon nitride composite ultrafine particles using a carbon dioxide laser, *J. Am. Ceram. Soc.*, **76**[5] 1195–1200.
201. M. Cauchetier, O. Croix, N. Herlin, and M. Luce (1994) Nanocomposite Si/C/N powder production by laser-aerosol interaction, *J. Am. Ceram. Soc.*, **77**[4] 993–998.
202. K. Jakubenas and H. L. Marcus (1995) Silicon carbide from laser pyrolysis of polycarbosilane, *J. Am. Ceram. Soc.*, **78**[8] 2263–2266.
203. T.-H. A. Shan and R. Cozzens (1994) Microwave curing of silicon carbide ceramics from a polycarbosilane precursor, *Mat. Res. Soc. Symp. Proc.*, **347** 729–734.
204. G. A. Danko, R. Silbergitt, P. Colombo, E. Pippel, and J. Woltersdorf (2000) Comparison of microwave hybrid and conventional heating of preceramic polymers to form silicon carbide and silicon oxycarbide ceramics, *J. Am. Ceram. Soc.*, **83**[7] 1617–1625.
205. J. C. Pivin, P. Colombo, and M. Tonidandel (1996) Ion irradiation of preceramic polymer thin films, *J. Am. Ceram. Soc.*, **79**[7] 1967–1970.
206. J. C. Pivin and P. Colombo (1997) Ceramic coatings by ion irradiation of polycarbosilanes and polysiloxanes. Part I: Conversion mechanism, *J. Mater. Sci.*, **32** 6163–6173.
207. J. C. Pivin and P. Colombo (1997) Ceramic coatings by ion irradiation of polycarbosilanes and polysiloxanes. Part II: Hardness and thermochemical stability, *J. Mater. Sci.*, **32** 6175–6182.
208. R. Riedel, L. Toma, C. Fasel, and G. Miehe (2009) Polymer-derived mullite-SiC-based nanocomposites, *J. Eur. Ceram. Soc.*, **29** 3079–3090.
209. C. Konetschny, Hartstoffhaltigen Si-C-N-Keramiken aus polysilazanen, Ph.D. Thesis, Darmstadt, Shaker Verlag, Aachen, Germany, 1999.
210. P. Colombo (2008) Engineering porosity in polymer-derived ceramics, *J. Eur. Ceram. Soc.*, **28** 1389–1395.
211. S. M. Crespiera, E. Ionescu, and R. Riedel, unpublished results.
212. Y. Xia and G. M. Whitesides (1998) Soft lithography, *Angew. Chem.*, **110** 568–594.



# CHEMICAL VAPOR DEPOSITION OF STRUCTURAL CERAMICS AND COMPOSITES

TAKASHI GOTO

## 8.1 INTRODUCTION

Chemical vapor deposition (CVD) is a versatile technique to prepare ceramics and composites via chemical reactions in a gas phase or at a gas–substrate interface [1]. CVD has been widely used in preparing thin films for semiconductor devices and for various coatings but is also available for the preparation of massive bulk materials (hereafter, CVD bulk material) for structural use [2]. Since the preparation of thin films, particularly for electronic devices, has been studied so intensively in the past several decades and as many reviews have been published, this chapter mainly discusses thick films and bulky forms of monolithic materials and composites by CVD.

$\text{Si}_3\text{N}_4$  and  $\text{SiC}$ , which have high strength and thermal shock and oxidation resistance [3], are promising structural materials. They have been commonly fabricated through sintering techniques such as reaction sintering, pressureless sintering, and hot pressing. Sintered materials, however, generally suffer degradation at high temperature due to voids, impurities, excess Si and/or C, and particularly as the result of glassy phase formation by sintering additives at the grain boundary. On the other hand, CVD bulk materials such as CVD  $\text{Si}_3\text{N}_4$  [4] and CVD  $\text{SiC}$  [5] are highly pure and dense with



no pores and additives, and therefore are characterized by excellent intrinsic high-temperature properties. The CVD technique has the following advantages:

1. Many kinds of composites in the form of powder, films, and plates with high purity and high density can be prepared.
2. The process temperature of CVD (deposition temperature) is generally much lower than the sintering temperature.
3. Anisotropic, preferentially oriented, materials can be prepared.
4. Materials with complicated shapes (substrates) can be uniformly coated.
5. Nonequilibrium or quasi-equilibrium materials can be prepared.
6. Many types of composites can be prepared by using multicomponent gas sources.

CVD  $\text{Si}_3\text{N}_4$  and CVD  $\text{SiC}$  thick films have been employed as various corrosion-resistant and anti-abrasive coatings for crucibles [6], cutting tools, combustion chambers, and so on. Many kinds of  $\text{Si}_3\text{N}_4$ - and  $\text{SiC}$ -based composites have been also prepared by CVD. The microstructure of the composites can be controlled by changing CVD conditions. In particular, nanocomposites in which a second phase is dispersed in nanometer size can be synthesized by CVD [7].

In this chapter, the preparation by CVD of  $\text{Si}_3\text{N}_4$ ,  $\text{SiC}$ , and related compounds and composites, mainly for structural applications, is reviewed.

CVD has many process parameters, such as deposition temperature, supersaturation of source gases, total pressure in a CVD chamber, heating type of substrate, and geometry and configuration of the CVD chamber. By changing these parameters, a wide range of microstructures and morphologies of the deposits can be prepared [8]. Figure 8.1 depicts the typical morphology of deposits as a function of the main CVD parameters of deposition temperature and supersaturation. At a rather low deposition temperature and at a high supersaturation level, powder or particles may form in association with the nucleation in the gas phase, while epitaxial films or platelike single-crystalline deposits may form at a high deposition temperature and at a low level of supersaturation due to the high mobility of absorbed species on the substrate surface. Structural materials with fine polycrystals are commonly needed; in particular, thick ceramic coating on metal substrates should have columnar grains to withstand the thermal stress at the interface. Such morphology has commonly been prepared at an intermediate deposition temperature and supersaturation level.

The deposition rate of CVD generally ranges from a few to several  $10 \mu\text{m/h}$ , and therefore CVD has been usually understood to be a thin film process. However, structural usage requires thick coatings or sometimes self-standing platelike forms, and therefore the deposition rate of CVD should be significantly increased for structural applications.

A schematic of the deposition steps of CVD is presented in Figure 8.2 [1]. The film formation in CVD would occur briefly by the following sequential steps: (1) diffusion of source gas to the substrate surface, (2) chemical reaction on the substrate surface, and (3) desorption of by-product gas from the substrate. Figure 8.3 demon-

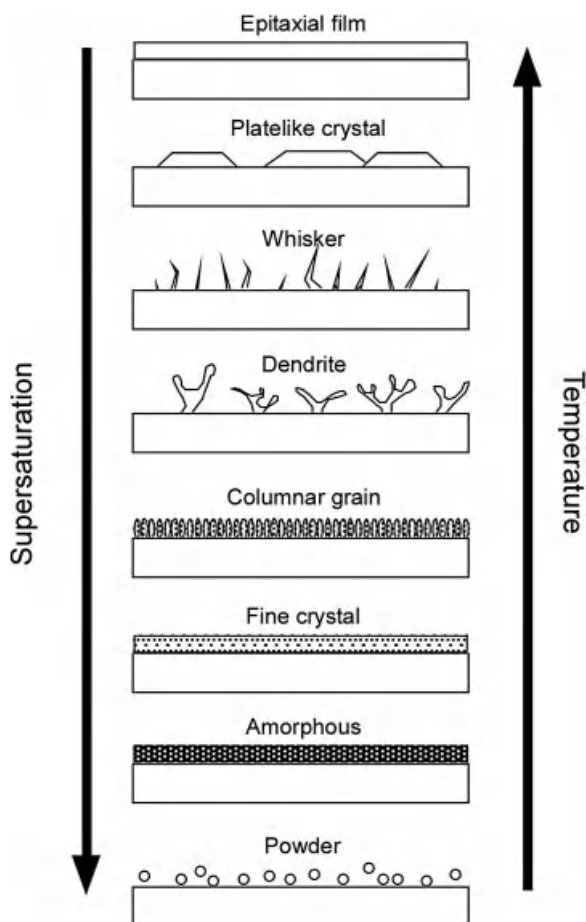


**Figure 8.1.** Morphology of deposits as functions of deposition temperature and supersaturation.

strates the general trend of temperature dependence of deposition rate in CVD [9]. In a low-temperature region, the slowest step can be a chemical reaction on the substrate surface, and the deposition rate is limited by the chemical reaction. The chemical reaction rate is accelerated exponentially with increasing temperature, and the activation energy of the deposition rate is commonly several 10–100 kJ/mol. At a higher temperature, the chemical reaction rate will be sufficiently high, and the deposition rate can be limited by the diffusion (diffusion controlling step) of source gas to the substrate or desorption of by-product gas from the substrate through a gas boundary layer. A further increase in temperature may cause a decrease in the deposition rate due to a homogeneous reaction (powder formation) in the gas phase or a decrease in the Gibbs free energy (driving force) of the chemical reaction. Since these steps are all thermally activated, conventional CVD is often termed thermal CVD. In order to increase the

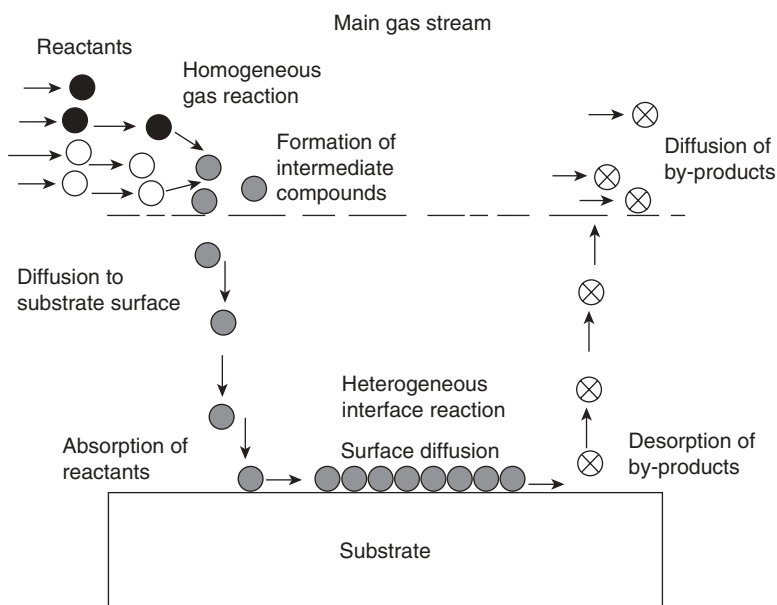


Figure 8.2. A schematic of the deposition steps of CVD.

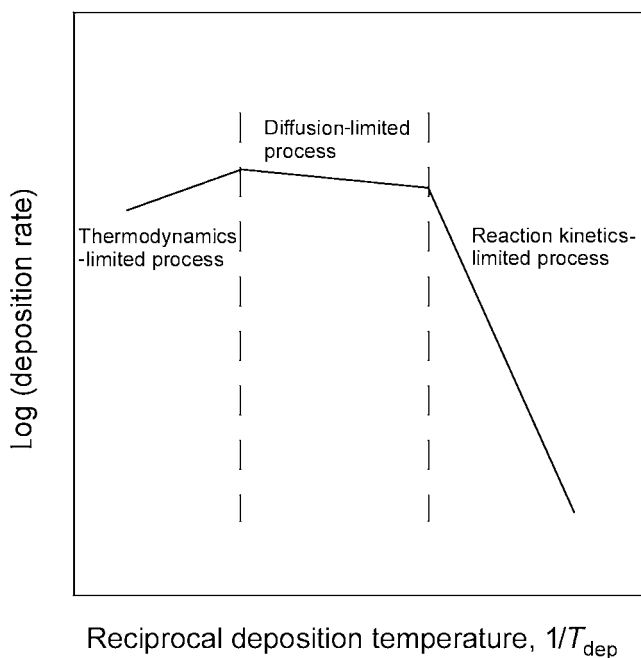


Figure 8.3. General trend of temperature dependence of deposition rate in CVD.

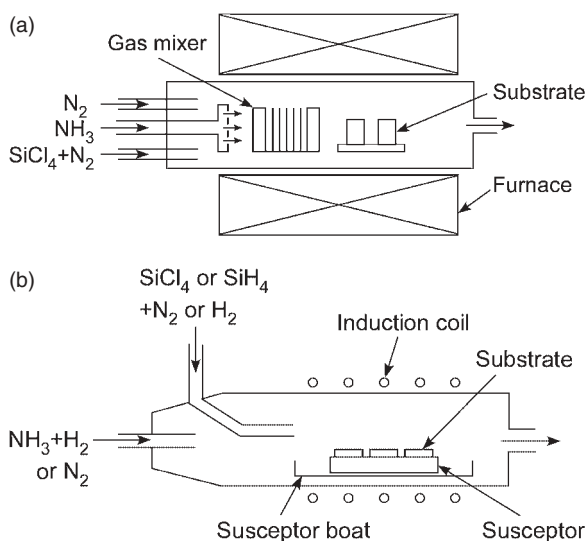


Figure 8.4. Types of CVD chambers.

deposition rate in CVD, a large amount of source gases should be transported to the substrate surface at a high temperature without premature reactions in the gas phase. However, a high concentration of source gases may accelerate powder formation in the gas phase or deposition on the wall surface of the CVD chamber. Therefore, the method of heating the substrate in the CVD chamber is one of the main parameters determining the deposition rate.

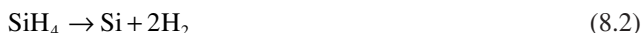
The method of heating the CVD chamber can be generally categorized into two types: a hot-wall type in which a substrate is heated by heat radiation from the hot chamber walls, and a cold-wall type in which a substrate is locally heated by direct electric current, radio frequency (RF) induction or laser (light) irradiation without intentional heating of the chamber wall. Figure 8.4 schematically illustrates the types of CVD chamber used in preparing various films [10]. Higher deposition rates can usually be achieved by the cold-wall type because of the lower deposition reaction on the wall surface and less depletion of source materials in the gas phase, while the hot-wall type is commonly employed to prepare uniform thin film coatings at relatively low deposition rates around less than a few micrometers per hour.

## 8.2 CVD OF NONOXIDE STRUCTURAL CERAMICS AND COMPOSITES

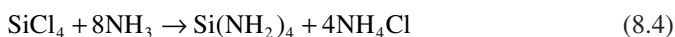
### 8.2.1 CVD $\text{Si}_3\text{N}_4$ and Related Composites

Thin and thick  $\text{Si}_3\text{N}_4$  films have been widely prepared by CVD using  $\text{SiH}_4$  or  $\text{SiCl}_4$  gas as a Si source and  $\text{NH}_3$  gas as a N source.  $\text{Si}_3\text{N}_4$  formation from the  $\text{SiH}_4\text{--NH}_3$  system

can be represented by Equation 8.1. Since  $\text{SiH}_4$  can easily decompose to free Si even below 1200 K, as indicated by Equation 8.2, excess  $\text{NH}_3$  gas is usually needed to obtain stoichiometric  $\text{Si}_3\text{N}_4$  [11]:



In the  $\text{SiCl}_4\text{--NH}_3$  system, many kinds of by-product powders such as  $\text{NH}_4\text{Cl}$ , Si imides, and Si amides may be produced according to Equations 8.4 and 8.5 [12]:



Therefore,  $\text{SiCl}_4$  and  $\text{NH}_3$  gases should be separately transported to near the substrate. The authors constructed a cold wall-type CVD chamber with a double tube nozzle to prepare thick films in which a graphite substrate was directly heated by an electric current. Figure 8.5 depicts a schematic diagram of the cold wall-type CVD chamber [13–14]. Many kinds of nonoxide thick films or plates and their composites such as SiC [15], TiC [16],  $\text{TiB}_2$  [17], and  $\text{SiB}_6$  [18] have been prepared at high deposition rates up to 2.0 mm/h. Since halide precursor gases, typically  $\text{SiCl}_4$ , are relatively more stable than other metal-organic precursor gases, high deposition rates were attained by minimizing the premature reactions by local heating of a substrate at high temperature more than 1700 K. Figure 8.6 depicts the effects of CVD conditions on the structure of CVD  $\text{Si}_3\text{N}_4$  films [13]. Amorphous and crystalline ( $\alpha$ -type)  $\text{Si}_3\text{N}_4$  films were prepared depending on the CVD conditions. Figure 8.7 demonstrates the typical surface morphology of

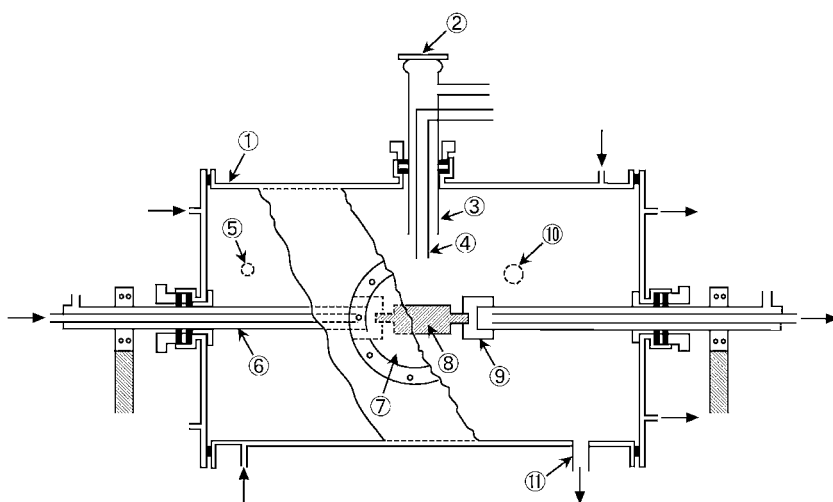


Figure 8.5. A cold wall-type CVD chamber.

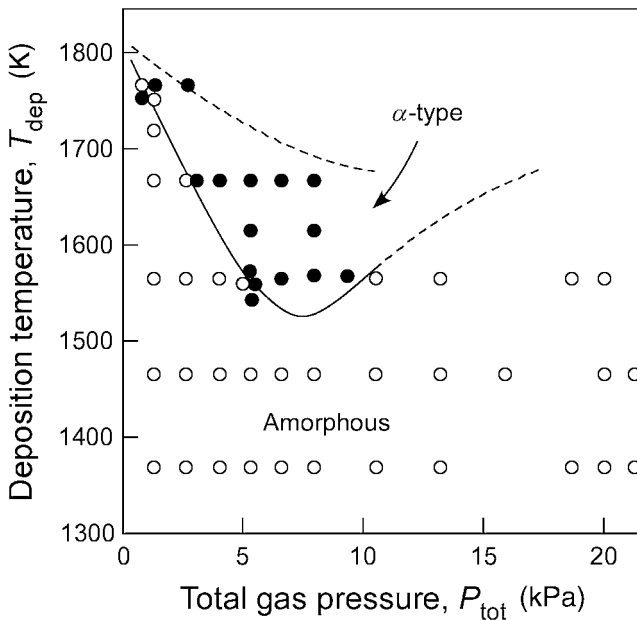
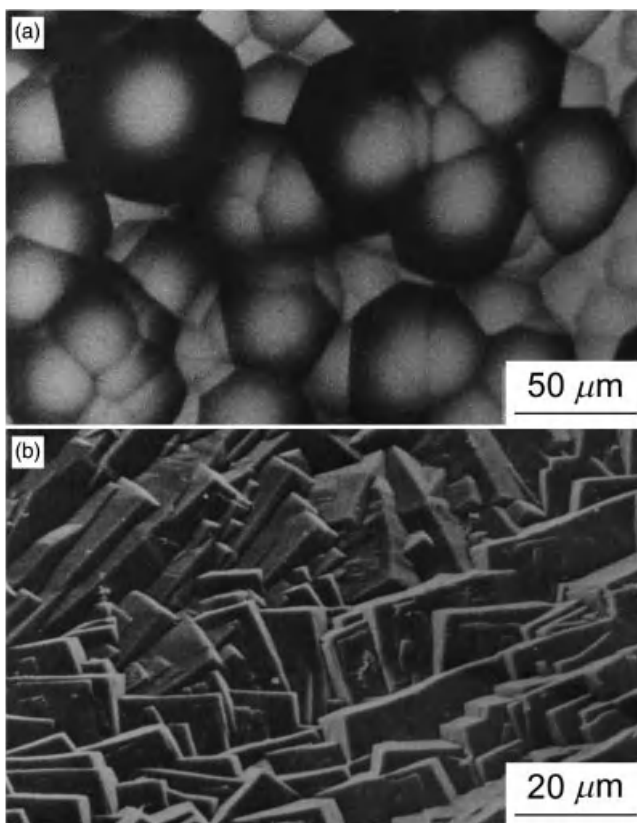


Figure 8.6. Effects of CVD conditions on the structure of CVD  $\text{Si}_3\text{N}_4$  films.

CVD  $\text{Si}_3\text{N}_4$  film. Amorphous CVD  $\text{Si}_3\text{N}_4$  film had a semispherical microstructure, which has been commonly observed in amorphous or nonoriented materials by CVD. The cross section is conelike, and such microstructure is often termed a cone structure. Figure 8.8 demonstrates the effect of total pressure in the CVD chamber on the deposition rate of amorphous and crystalline CVD  $\text{Si}_3\text{N}_4$  films. The deposition rate exhibited the maxima at 5–8 kPa, implying the significant effects of forced convection flow of source gases and powder formation at further high total pressures [19]. The highest deposition rates of amorphous and crystalline CVD  $\text{Si}_3\text{N}_4$  films were 0.4 and 1.2 mm/h, respectively. These values were several tens of times greater than those of common CVD. Amorphous CVD  $\text{Si}_3\text{N}_4$  film crystallized to  $\alpha$ - and/or  $\beta$ -type  $\text{Si}_3\text{N}_4$  by heat treatment above 1700 K. Compton scattering [20], small-angle neutron scattering [21] and positron annihilation [22] implied that the local structure of amorphous CVD  $\text{Si}_3\text{N}_4$  film was similar to that of  $\beta$ -type  $\text{Si}_3\text{N}_4$ , and about 4 vol % of voids with 0.8–1.0 nm in diameter were contained in the amorphous matrix. The crystalline CVD  $\text{Si}_3\text{N}_4$  ( $\alpha$ -type) film had a theoretical density ( $3.12 \text{ Mg/m}^3$ ) [13] calculated from hexagonal unit cell parameters of  $a = 0.7752 \text{ nm}$  and  $c = 0.5622 \text{ nm}$  [23]. The preferred orientation varied depending on total gas pressures and raw gas flow rates, and significant (110), (210), or (222) orientations were identified [19, 23].

## 8.2.2 CVD $\text{Si}_3\text{N}_4$ -Based Composites

Although CVD is primarily a nonequilibrium process, the chemical reactions in CVD should be at least thermodynamically possible, CVD can be closer to the equilibrium



**Figure 8.7.** Typical surface morphology of CVD  $\text{Si}_3\text{N}_4$  films.

state than PVD, and thus CVD is advantageous in the preparation of thermally stable composites by using multicomponent source gases. Figure 8.9 summarizes the microstructure of CVD composites [7]. Many types of composites with the  $\text{Si}_3\text{N}_4$  matrix have been prepared by CVD [7, 24].

**8.2.2.1  $\text{Si}_3\text{N}_4$ -C Composites.** Amorphous CVD  $\text{Si}_3\text{N}_4$ -C composites containing C up to 10 mass % were prepared below 1500 K by using  $\text{SiCl}_4$ ,  $\text{NH}_4$ ,  $\text{H}_2$ , and  $\text{C}_3\text{H}_8$  gases [25]. Figure 8.10 shows the effects of CVD conditions on the structures of the  $\text{Si}_3\text{N}_4$ -C composite. electron probe micro analysis (EPMA) [25], electron spectroscopy for chemical analysis (ESCA) [26], positron annihilation [22], and hydrofluoric acid (HF) treatment [27] studies have indicated that the state of C in the amorphous CVD  $\text{Si}_3\text{N}_4$ -C composite is spherical particles about 100 nm in diameter and having an amorphous (turbostratic) structure. Figure 8.11 shows the surface morphology of CVD  $\text{Si}_3\text{N}_4$ -C composites containing 6 mass % C after heat treatment in a vacuum at 1673 K [28]. The dispersoid of the C phase reacted with the matrix  $\text{Si}_3\text{N}_4$  phase forming

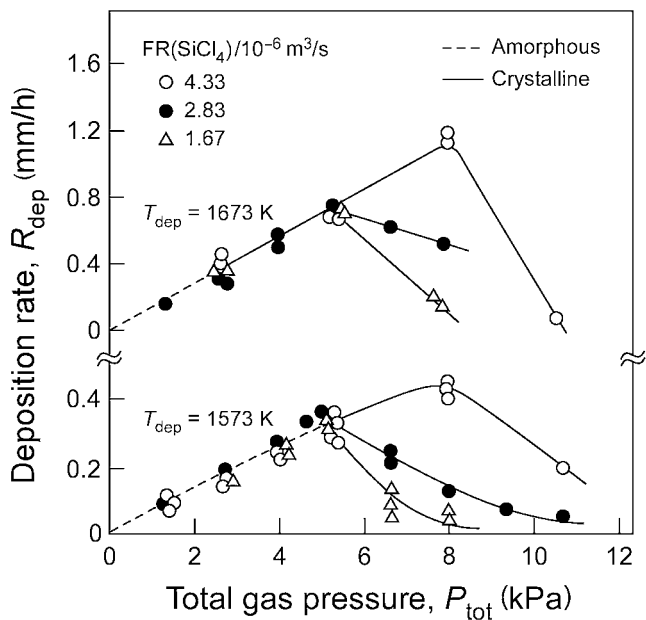
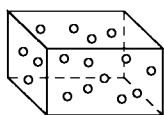
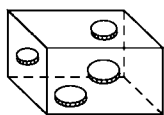


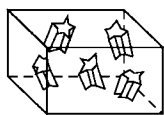
Figure 8.8. Effect of total pressure in the CVD chamber.



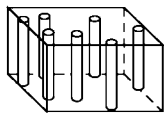
(a) Spherical partical



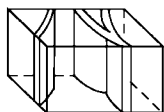
(b) Flake-like particle



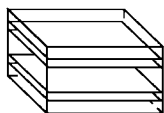
(c) Rodlike particle



(d) Fiber



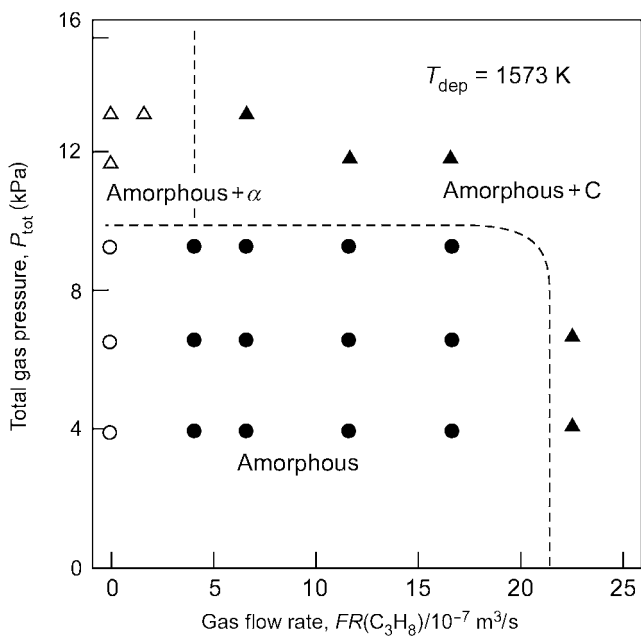
(e) Thin layer



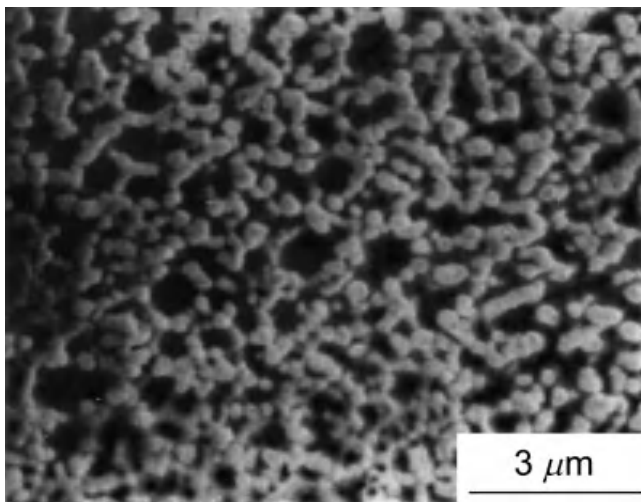
(f) Laminated

Figure 8.9. Microstructures of CVD composites.





**Figure 8.10.** Effects of CVD conditions on the structures of  $\text{Si}_3\text{N}_4\text{-C}$  composites.



**Figure 8.11.** Surface morphology of CVD  $\text{Si}_3\text{N}_4\text{-C}$  composite (6 mass % C) after a heat treatment in a vacuum at 1673 K.

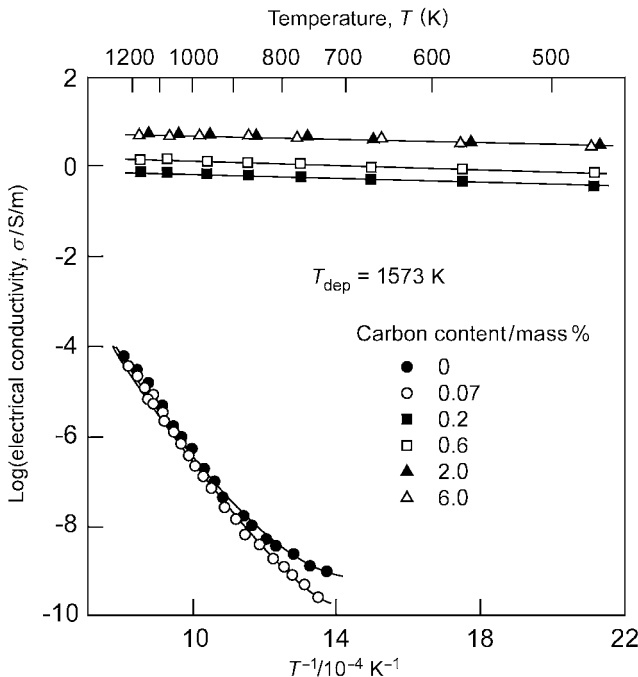


**Figure 8.12.** Temperature dependence of DC electrical conductivity of amorphous CVD  $\text{Si}_3\text{N}_4$ -C composites.

$\beta$ -SiC with a three-dimensional network structure. This implied that the C phase existed as a three-dimensionally connected network structure.

Figure 8.12 demonstrates the temperature dependence of DC electrical conductivity ( $\sigma_{\text{DC}}$ ) of amorphous CVD  $\text{Si}_3\text{N}_4$ -C composites [29]. The  $\sigma_{\text{DC}}$  changed from insulative to conductive at a C content of 0.1–0.2 mass %. The high  $\sigma_{\text{DC}}$  enabled electronic discharge machining to fabricate  $\text{Si}_3\text{N}_4$  products with complicated shapes. Figure 8.13 depicts the temperature dependence of the corrosion rate of amorphous CVD  $\text{Si}_3\text{N}_4$ -C composites in an HF solution (47% HF in  $\text{H}_2\text{O}$ ) [27]. The corrosion rates decrease with increasing C content due to a decrease in residual stress. The corrosion rate of amorphous CVD  $\text{Si}_3\text{N}_4$ -C composites can be controlled by changing the C content; that may resolve undercutting in a wet etching process during the production of amorphous CVD  $\text{Si}_3\text{N}_4$  semiconductor devices [27].

**8.2.2.2  $\text{Si}_3\text{N}_4$ -TiN Composites.** Amorphous and crystalline CVD  $\text{Si}_3\text{N}_4$ -TiN composites were prepared by using  $\text{SiCl}_4$ ,  $\text{NH}_4$ ,  $\text{H}_2$ , and  $\text{TiCl}_4$  gases. Figure 8.14 demonstrates the effects of CVD conditions on the structure of CVD  $\text{Si}_3\text{N}_4$ -TiN composites [30]. Although the stable crystal structure of  $\text{Si}_3\text{N}_4$  at a high temperature is  $\beta$ -type, only amorphous or  $\alpha$ -type (sometimes containing a small amount of  $\beta$ -type) CVD  $\text{Si}_3\text{N}_4$  films have been prepared.  $\beta$ -Type CVD  $\text{Si}_3\text{N}_4$  film in  $\beta$ -type single phase was prepared

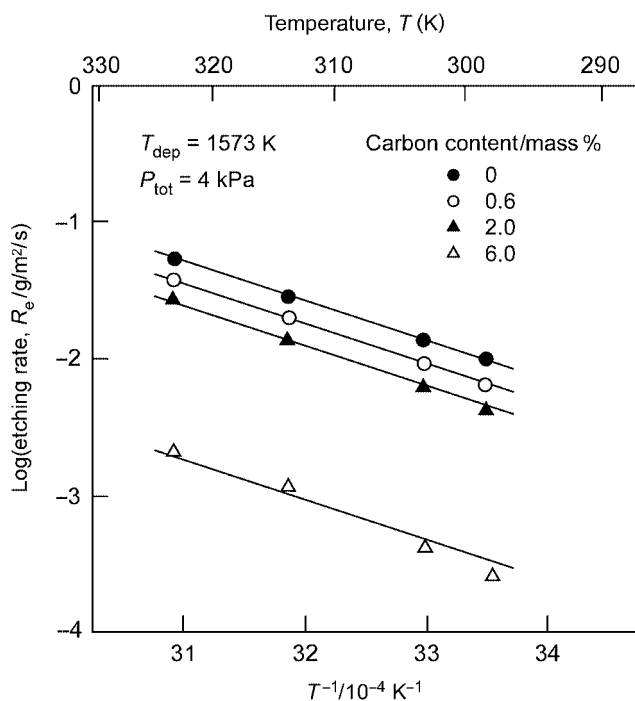


Figure 8.13. Temperature dependence of corrosion rate of amorphous CVD  $\text{Si}_3\text{N}_4$ -C composites in an HF solution (47% HF in  $\text{H}_2\text{O}$ ).

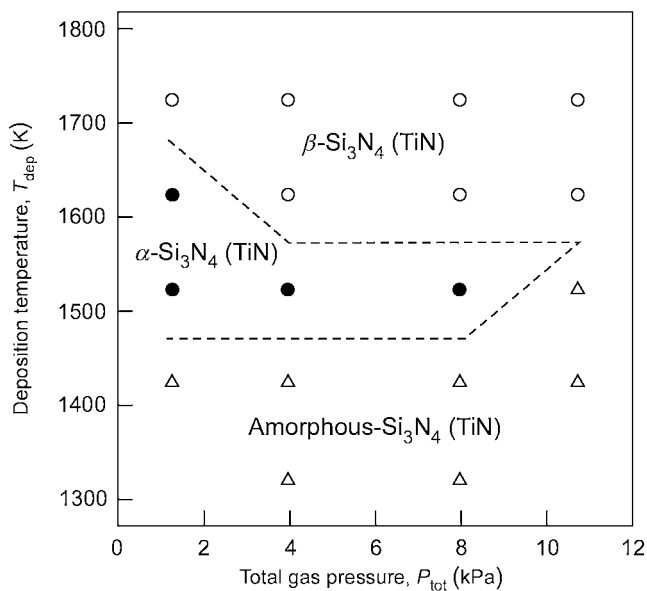
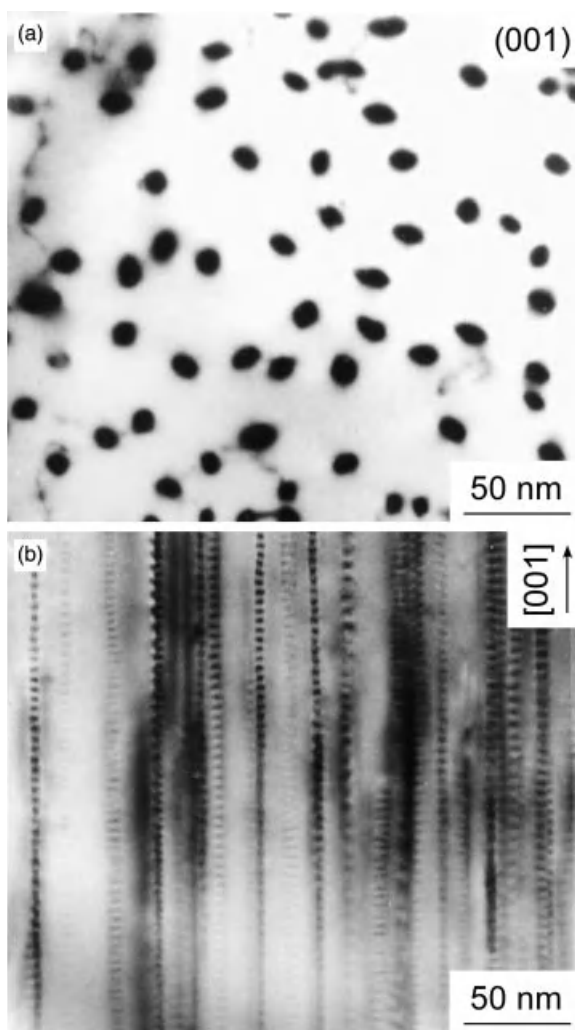
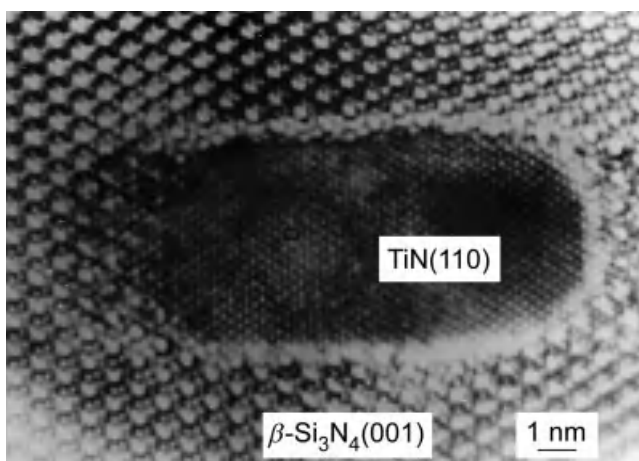


Figure 8.14. Effects of CVD conditions on the structure of CVD  $\text{Si}_3\text{N}_4$ -TiN composites.



**Figure 8.15.** Shape of TiN in a CVD  $\beta$ - $\text{Si}_3\text{N}_4$  matrix.

by adding  $\text{TiCl}_4$  vapor to the source gases [30], and Ti existed as cubic TiN in the  $\text{Si}_3\text{N}_4$  matrix. The deposition temperature of crystalline  $\text{Si}_3\text{N}_4$  ( $\alpha$ -type) was lowered in the CVD  $\text{Si}_3\text{N}_4$ -TiN composite by about 100 K more than that of pure CVD  $\text{Si}_3\text{N}_4$ . The TiN in the amorphous and  $\alpha$ -type  $\text{Si}_3\text{N}_4$  matrix was spherical particles of 3–10 nm in diameter [31]. Figure 8.15 illustrates the shape of TiN in the  $\beta$ -type CVD  $\text{Si}_3\text{N}_4$  matrix [31], while Figure 8.16 is a transmission electron microscopy (TEM) micrograph of electron beams perpendicular and parallel to the growth direction, respectively. The black region in Figure 8.15 corresponds to the TiN phase with a fiber-like microstructure of several nanometers in diameter elongated in the growth direction. The  $c$ -plane



**Figure 8.16.** Lattice image around the dispersed TiN phase.

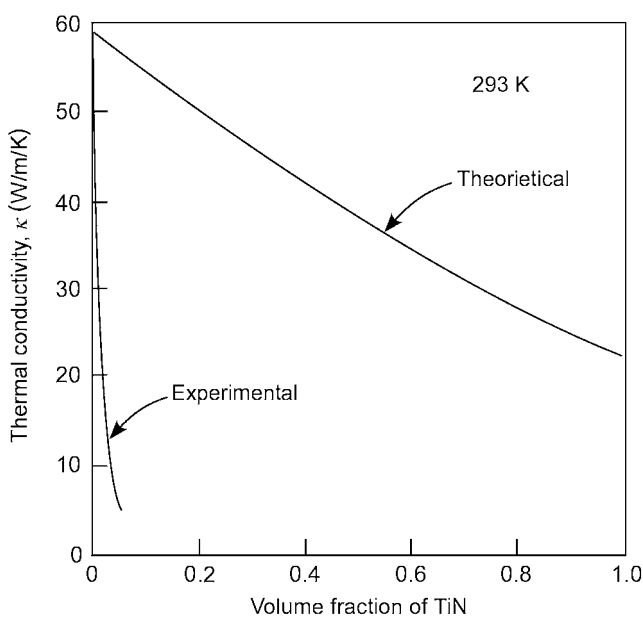


**Figure 8.17.** Effect of TiN content on the thermal conductivity of CVD  $\text{Si}_3\text{N}_4$  composites.

of the  $\beta\text{-Si}_3\text{N}_4$  matrix was oriented parallel to the substrate. Figure 8.16 is the lattice image around the dispersed TiN phase [32]. The TiN (110) plane was parallel to the  $\beta\text{-Si}_3\text{N}_4$  (001) plane, and the  $\text{Si}_3\text{N}_4$  lattice was disordered at the TiN/ $\text{Si}_3\text{N}_4$  interface.

Figure 8.17 shows the effect of TiN content on the thermal conductivity of CVD  $\text{Si}_3\text{N}_4$ -TiN composites [33]. The thermal conductivity of the  $\text{Si}_3\text{N}_4$ -TiN composite decreased significantly with increasing TiN content. The experimental values were far



**Figure 8.18.** SEM micrograph of the polished cross section of an amorphous CVD  $\text{Si}_3\text{N}_4$ -BN composite (50 mass % BN).

smaller than the calculated values by the mixture rule, suggesting significant phonon scattering by a solid solution of Ti in the matrix and the lattice distortion at the  $\text{Si}_3\text{N}_4$ -TiN interface.

**8.2.2.3  $\text{Si}_3\text{N}_4$ -BN Composites.** Amorphous CVD  $\text{Si}_3\text{N}_4$ -BN composites were prepared below 1600 K using  $\text{SiCl}_4$ ,  $\text{NH}_3$ ,  $\text{H}_2$  gases, and  $\text{B}_2\text{H}_6$  gas as a B source [34]. Infrared (IR) absorption [34], ESCA [35], and neutron small-angle scattering [36] implied that the state of B in the amorphous CVD  $\text{Si}_3\text{N}_4$ -BN composites was turbostratic BN having  $\text{sp}^2$  bonding BN and a lattice parameter ( $c_0/2$ ) 1.2 times larger than that of hexagonal BN.

Figure 8.18 shows a scanning electron microscopy (SEM) micrograph of the polished cross section of an amorphous CVD  $\text{Si}_3\text{N}_4$ -BN composite containing about 50 mass % BN, exhibiting a multilayered structure of amorphous  $\text{Si}_3\text{N}_4$  and turbostratic BN, both about 100 nm in thickness [37]. Figure 8.19 demonstrates the optical transmittance of an amorphous CVD  $\text{Si}_3\text{N}_4$ -BN composite [7] with about 80% transmittance in a visible light range. Since the surface reflection calculated from its refractive index is about 20%, the transmittance is almost 100% of the theoretical value. This transpar-

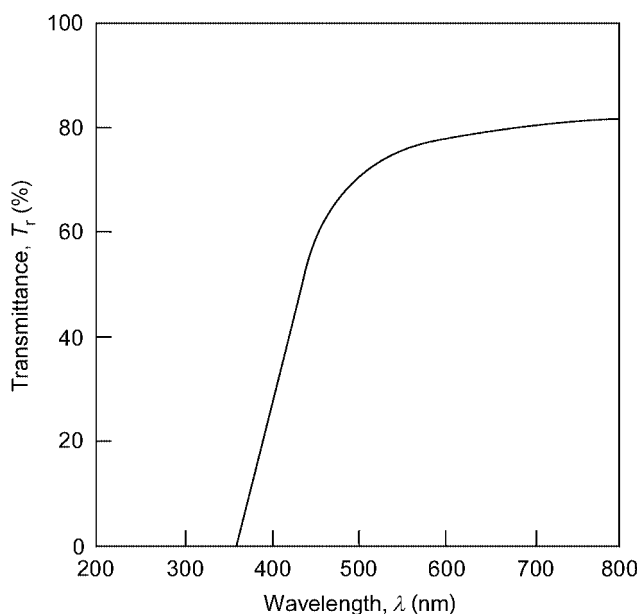


**Figure 8.19.** Optical transmittance of an amorphous CVD  $\text{Si}_3\text{N}_4$ -BN composite.

ency was still maintained after heat treatment at 1873 K in  $\text{N}_2$  or Ar atmosphere. Amorphous CVD  $\text{Si}_3\text{N}_4$  film not containing BN is opaque white due to scattering by nanoscale voids. The nanoscale voids in the amorphous CVD  $\text{Si}_3\text{N}_4$ -BN composites could have been occupied by BN clusters in the amorphous  $\text{Si}_3\text{N}_4$  matrix yielding high transparency and thermal stability [36]. The electrical conductivity of the amorphous CVD  $\text{Si}_3\text{N}_4$ -BN composites was  $10^2$ – $10^4$  times larger than that of amorphous CVD  $\text{Si}_3\text{N}_4$ . This material might be useful as a high-temperature viewing window or as an electrical insulator [38].

**8.2.2.4  $\text{Si}_3\text{N}_4$ -AlN Composites.** CVD  $\text{Si}_3\text{N}_4$ -AlN composites with crystalline AlN particles dispersed in amorphous  $\text{Si}_3\text{N}_4$  matrix were prepared by using  $\text{SiH}_4$ ,  $\text{NH}_3$ , and  $\text{AlCl}_3$  gases at 873–1473 K [39]. The diameters of the AlN particles ranged from 25 nm at 923 K to about 50 nm at 1348 K. CVD  $\text{Si}_3\text{N}_4$ -AlN composites could be useful in memory devices owing to their higher trap density and deeper trap levels [39].

## 8.2.3 CVD SiC and Related Composites

SiC ceramics have been widely applied to structural usage due to excellent mechanical properties and oxidation resistance [40]. Since many kinds of CVD precursors containing Si and C with high vapor pressures are available [41], CVD SiC films have been widely investigated for various applications, such as single-crystalline 3C-SiC epitaxial

thin film on Si wafer for power devices and for refractory usage such as SiC impregnation into porous carbon fiber composite (often called chemical vapor impregnation [CVI]) [42].

At high deposition rates, a wide variety of morphologies of CVD SiC films have been prepared, typically using  $\text{CH}_3\text{SiCl}_3$  as a precursor [43]. Although the molar ratio of Si to C in  $\text{CH}_3\text{SiCl}_3$  is a fixed value of 1, the same as the stoichiometric ratio of SiC, the composition of CVD SiC films prepared by  $\text{CH}_3\text{SiCl}_3$  depends on CVD conditions; often, Si-rich SiC films form at a deposition temperature lower than 1500 K, and C-rich SiC films form at over 1700 K. The precursors of  $\text{SiCl}_4\text{-CCl}_4$  or  $\text{SiCl}_4\text{-CH}_4$  have also been used to prepare CVD SiC films. The authors employed  $\text{SiCl}_4\text{-C}_3\text{H}_8$  gases because  $\text{SiCl}_4$  is stable at high temperature and can be transported to the high-temperature deposition zone without premature reaction, and  $\text{C}_3\text{H}_8$  is sufficiently active to form hydrocarbon radicals in the gas phase. These characteristics can be beneficial in the preparation of CVD SiC thick film or bulk materials at a high deposition rate.

Figure 8.20 demonstrates the effects of CVD conditions on the morphology of CVD SiC film by using  $\text{SiCl}_4$ ,  $\text{H}_2$ , and  $\text{C}_3\text{H}_8$  gases [15]. The morphology changed from film to granule to island depending on the CVD conditions. No deposit was obtained below 1550 K. At relatively low total pressure (4 kPa), thick, platelike SiC was prepared at relatively limited conditions of a C/Si molar ratio ( $m_{\text{C/Si}}$ ) less than 0.7, while at a high total pressure (1 MPa), platelike SiC was obtained in a wide range of conditions. Figure 8.21 depicts the typical surface morphology of a CVD SiC film. Pyramid-like faceted grains with strong (111) orientation and conelike grains with (110) orientation were obtained at relatively low and high total pressures, respectively. At a C-to-Si molar ratio ( $m_{\text{C/Si}}$ ) > 1, free C content significantly increased accompanied by a decrease of density. The density of CVD SiC film at  $m_{\text{C/Si}} > 0.7$  was far smaller than

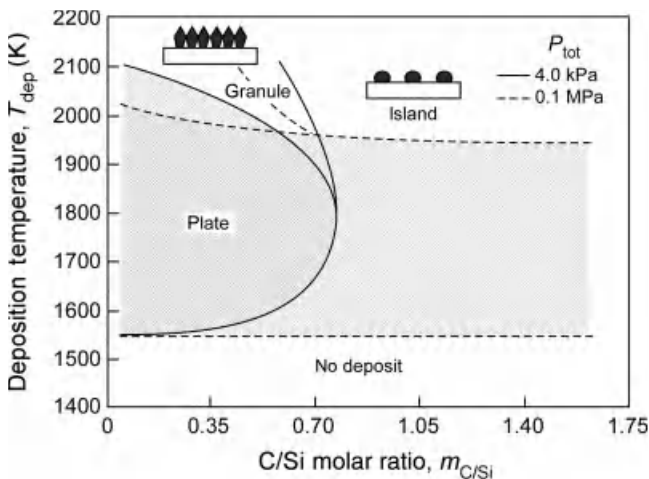
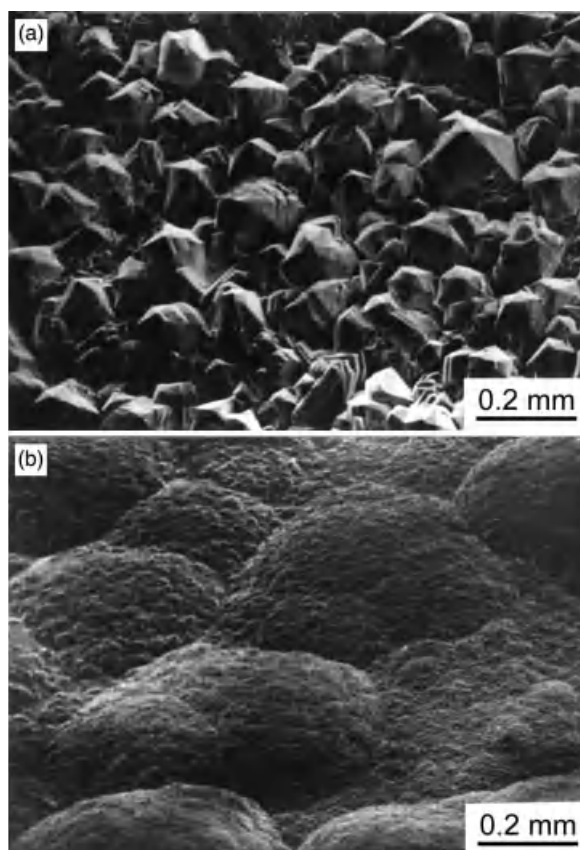


Figure 8.20. Effects of CVD conditions on the morphology of CVD SiC films.





**Figure 8.21.** Typical surface morphology of a CVD SiC film.

the calculated value from the mixture rule of pure SiC ( $3.20 \text{ Mg/m}^3$ ) and amorphous C ( $1.3 \text{ Mg/m}^3$ ), suggesting that a significant amount of voids was formed with the codeposition of free C.

By combining the cold wall-type CVD chamber, local heating of the graphite substrate and appropriate precursors ( $\text{SiCl}_4$  and  $\text{C}_3\text{H}_8$ ), the deposition rate of CVD SiC film was significantly enhanced compared with that of conventional CVD. Figure 8.22 demonstrates the effect of the deposition temperature on the deposition rate of CVD SiC film by the present authors. The deposition rates increased with increasing deposition temperature and reached  $2 \text{ mm/h}$ . At a low total pressure ( $4.0 \text{ kPa}$ ) and low  $m_{\text{C/Si}}$  ( $0.18$ ), the activation energy was  $110 \text{ kJ/mol}$ , implying a chemical reaction-limited condition, while at a high total pressure ( $0.1 \text{ MPa}$ ) and high  $m_{\text{C/Si}}$ , the diffusion-limited condition was assumed owing to a rather lower activation energy of  $40\text{--}50 \text{ kJ/mol}$ . A schematic diagram of grain growth is illustrated in Figure 8.23 [44]. Under the reaction-limited condition, nucleation may start at the kink or step, that is, the lowest energy

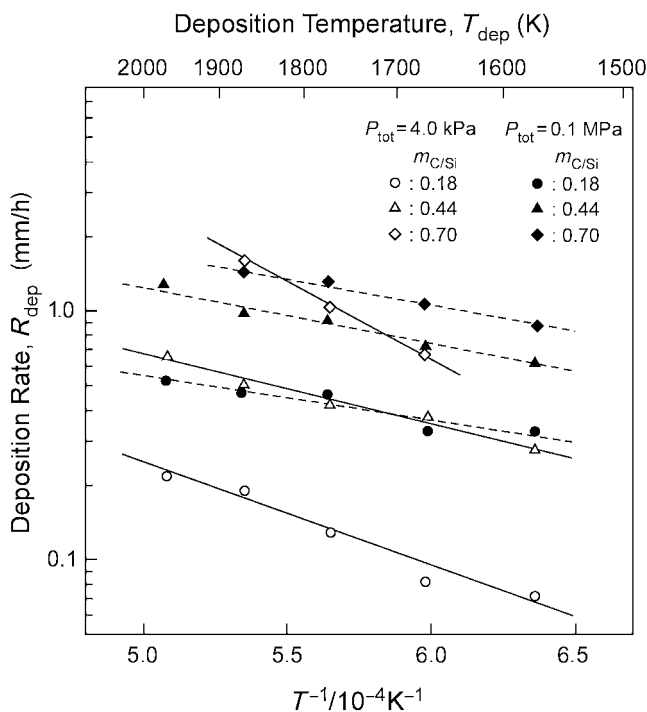
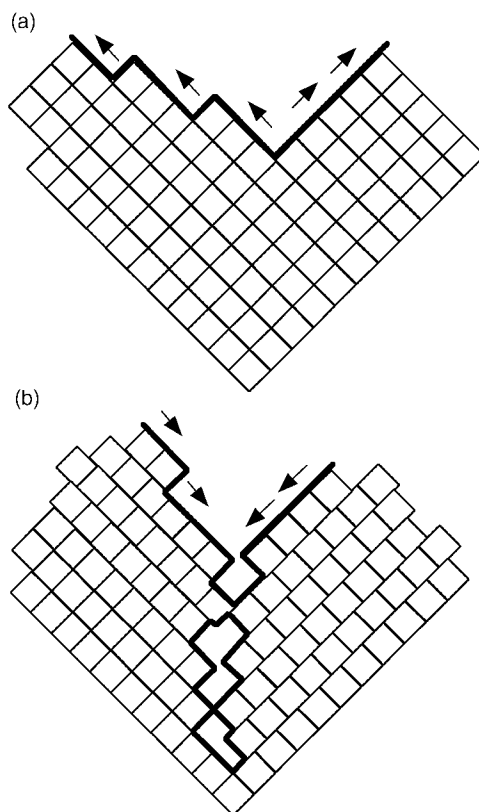


Figure 8.22. Effect of deposition temperature on the deposition rate of a CVD SiC film.

site, and the grain growth proceeds toward the top surface, and eventually, a dense and faceted microstructure will be formed as shown in Figure 8.23a. Under the diffusion-limited condition, the nucleation may start at the top surface, that is, the highest source gas concentration site, and the grain growth may advance downward leaving nanopores at the grain boundary or inside the grains with the formation of a cone structure as shown in Figure 8.23b. Highly pure and dense CVD SiC bulk materials and thick plates are now commercially available and are applied to optics, components subjected to wears, and susceptors for semiconductor devices. CVD SiC coating is promising for use in space vehicles because it can withstand even an extremely harsh reentry environment. The present authors have reported the high-temperature oxidation behavior of a CVD SiC thick film, that is, passive oxidation, active oxidation, and bubble formation [45].

SiC may decompose/sublimate above 2000 K without melting at atmospheric pressure. Therefore, SiC and its composite products have been commonly manufactured by solid-state sintering or vapor-phase deposition. The Si–C system is actually a peritectic system whose peritectic temperature (melting temperature) is around 2800 K, and SiC can only melt at high pressure [46]. However, even under atmospheric pressure, SiC can melt by mixing with other compounds. SiC-based composites with  $\text{ZrB}_2$ ,  $\text{TiB}_2$ ,  $\text{B}_4\text{C}$ ,  $\text{TiC}$ , and so on, can be melted because they belong to a quasi-binary eutectic system,



**Figure 8.23.** A schematic diagram of grain growth in CVD: (a) reaction-limited condition and (b) diffusion-limited condition.

and many kinds of SiC-based composites have been synthesized by melt solidification [47–48]. Figure 8.24 demonstrates a typical microstructure of SiC–ZrB<sub>2</sub> eutectic composites, where the gray and black parts are ZrB<sub>2</sub> and SiC phases, respectively [49]. This composite is a candidate for use as a high-temperature structural material due to its good mechanical properties and oxidation resistance [50]. Since ZrB<sub>2</sub> can accelerate passive oxidation of SiC by the formation of ZrO<sub>2</sub>, which prevents active oxidation of SiC, this composite is a promising material for use in space vehicles [51]. An SiC–TiC system is also quasi-binary eutectic, and the SiC–TiC composites have high strength and ductility. These composites have been fabricated by solid-state sintering, while melt solidification can also be applied to prepare SiC–TiC composites, as shown in Figure 8.25. The present authors have studied the Si–Ti–C system by CVD using SiCl<sub>4</sub>, CCl<sub>4</sub>, H<sub>2</sub>, and TiCl<sub>4</sub> gases as precursors [52]. CVD is applicable for the preparation of Si–Ti–C system composites by the codeposition of SiC, TiC, and other compounds. Since there are so many combinations of deposition conditions, the thermodynamic calculation

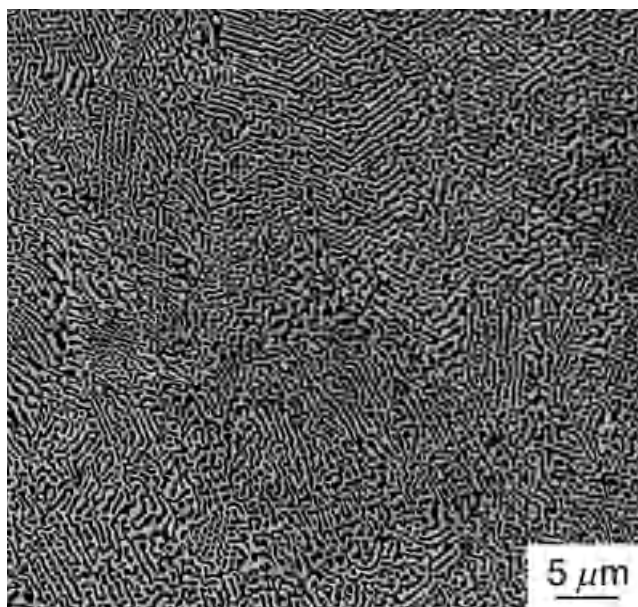


Figure 8.24. Typical microstructure of an SiC-ZrB<sub>2</sub> eutectic composite.

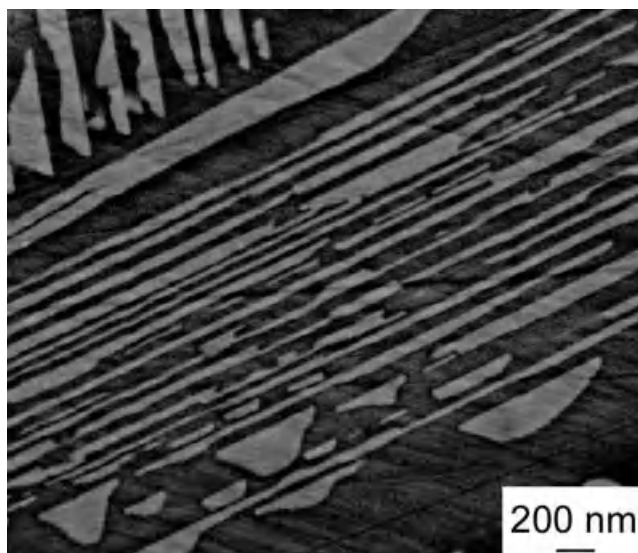
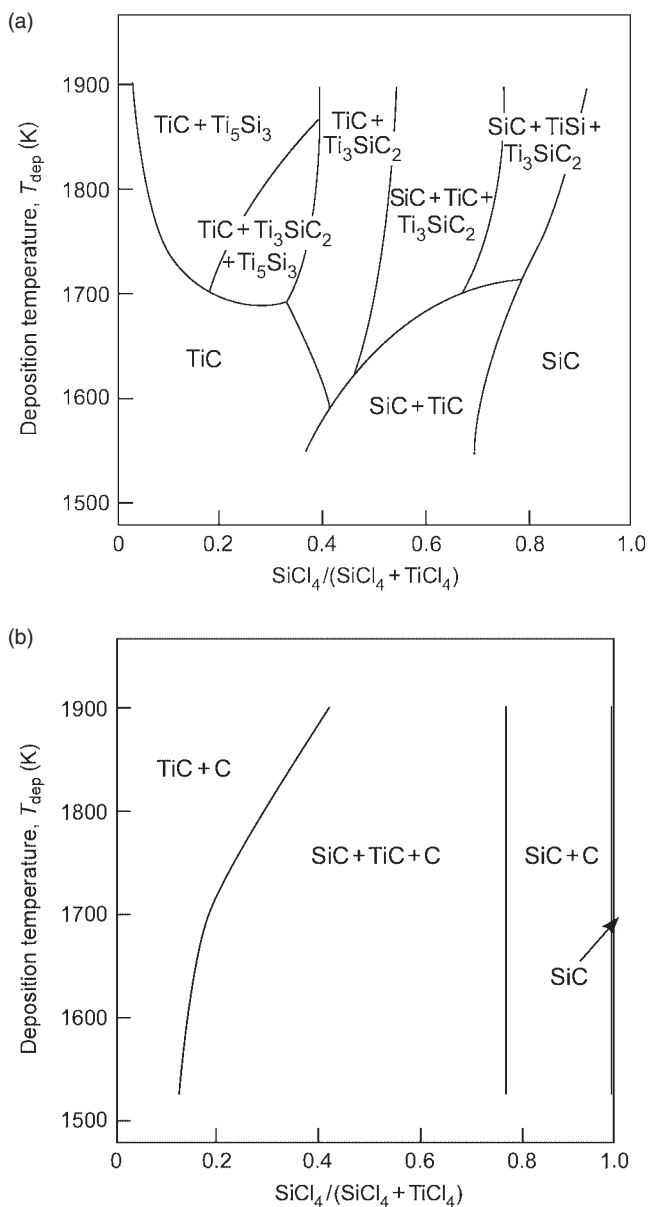
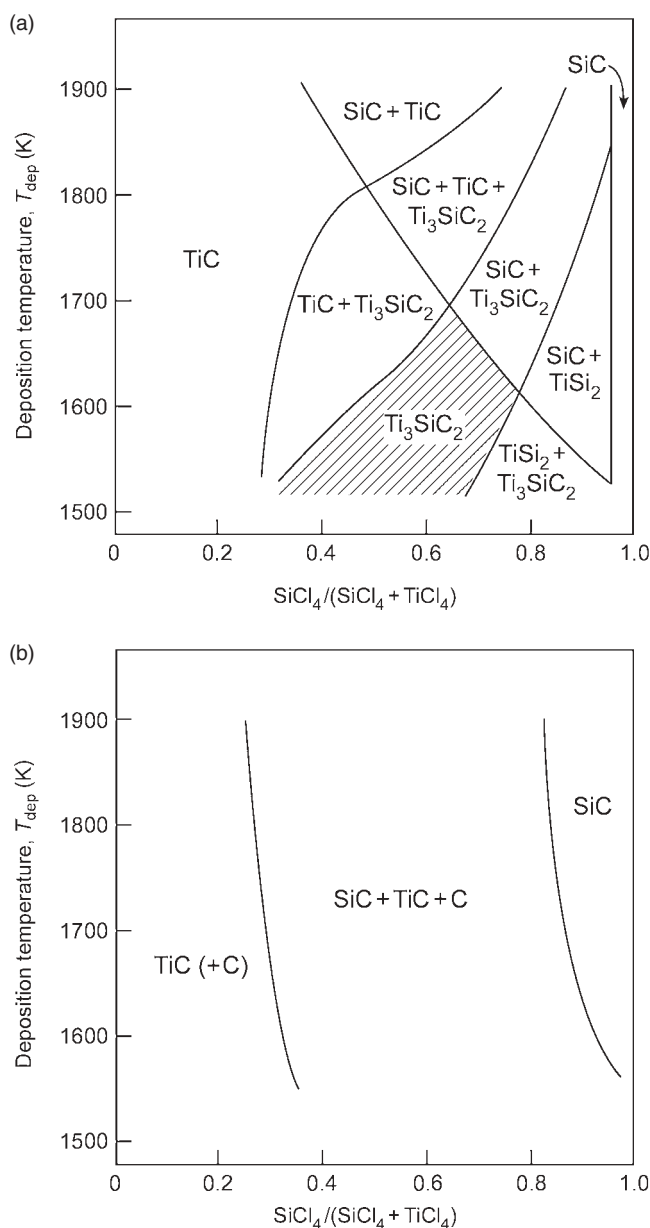


Figure 8.25. Microstructure of an SiC-TiC eutectic composite.

based on a computer code such as SOLGASMIX-PV and SAGE can be useful for the estimation of deposition conditions and the compositions of deposits [53]. In this calculation, the summation of Gibbs free energy of all solid and gas species is minimized under the mass balance condition. The present authors employed this technique to prepare SiC–TiC composites and compared calculated and experimental results. The Si–Ti–C–H–Cl system has 9 solid species (i.e., Si, Ti, C, SiC, TiC, TiSi, TiSi<sub>2</sub>, Ti<sub>5</sub>Si<sub>3</sub>, and Ti<sub>3</sub>SiC<sub>2</sub>) and 49 gas species (i.e., SiC, C, Si, and H<sub>2</sub>). By using a thermodynamic database, the equilibrium gas pressure of each gas species and amounts of solid species can be calculated. Figure 8.26 shows the calculated results of deposited phases as functions of deposition temperature and SiCl<sub>4</sub>/(SiCl<sub>4</sub> + TiCl<sub>4</sub>) molar ratio in the source gases. At a rather high C source condition (CCl<sub>4</sub>/H<sub>2</sub> = 9.7 × 10<sup>-3</sup>), SiC–TiC composites may be deposited below 1700 K, whereas Ti silicides and Ti<sub>3</sub>SiC<sub>2</sub> may be deposited at a higher temperature. Figure 8.27 exhibits the experimental results at the same CVD conditions as calculated in Figure 8.26 [52]. At the high C source condition, SiC–TiC composites were obtained as calculated in Figure 8.26. It is commonly observed in CVD that the deposition temperature of crystalline TiC is lower than that of SiC. Kinetically, it may be more feasible to deposit TiC than SiC by CVD. This could have resulted in a wider low deposition temperature region of TiC than the calculation. Figure 8.28 depicts a typical surface microstructure of a CVD SiC–TiC composite. SiC and TiC both have a cubic (fcc) structure with close lattice parameters yielding good compatibility. Figure 8.29 illustrates the polished surface of a CVD SiC–TiC composite with Vicker's indentation [54]. The white and black phases are the TiC and SiC phases, respectively. The cracks at the corners of Vicker's indentation did not extend straight beyond the dispersed SiC phase, suggesting high ductility. At a low C source condition, Ti<sub>3</sub>SiC<sub>2</sub> in a single-phase region was identified around 1600 K. Figure 8.30 depicts a polished surface of a CVD Ti<sub>3</sub>SiC<sub>2</sub> plate with Vicker's indentation. There were no cracks, but slip lines formed around the corners, implying a soft and deformable nature. The crystal structure of Ti<sub>3</sub>SiC<sub>2</sub> was first reported by using a small specimen prepared by CVD [55]. However, no study on the properties of Ti<sub>3</sub>SiC<sub>2</sub> was conducted until 1987. The present authors first synthesized a monolithic Ti<sub>3</sub>SiC<sub>2</sub> plate by CVD in the Si–Ti–C system and reported its mechanical properties [56]. Figure 8.31 depicts the unit cell structure of Ti<sub>3</sub>SiC<sub>2</sub>. The lattice parameters of the CVD Ti<sub>3</sub>SiC<sub>2</sub> plate were  $a = 0.3064$  nm and  $c = 1.7650$  nm, corresponding to the elongated grains. In common reaction sintering Ti, SiC and C powders are typically used. The TiC phase tends to form with Ti<sub>3</sub>SiC<sub>2</sub> by solid-state sintering, and the second phase significantly degrades the ductility of Ti<sub>3</sub>SiC<sub>2</sub>. On the other hand, no side reaction takes place in CVD because no deposit forms without a supply of source gases during the heating and cooling processes. Thus, CVD is advantageous in the preparation of pure materials under a definite deposition condition, and a highly pure monolithic Ti<sub>3</sub>SiC<sub>2</sub> plate was prepared by CVD. It is now understood that Ti<sub>3</sub>SiC<sub>2</sub> is one of a large group of compounds in which the Ti site can be occupied by transition metals such as V, Cr, Nb, Mo, and so on; the Si site can be occupied by Ge, Sn, Pb, and so on; and the C site can be occupied by N. These compounds are termed the  $M_{N+1}AX_N$  phase or simply the MAX phase. A comprehensive review is available [57].



**Figure 8.26.** Calculated deposited phases as functions of deposition temperature and  $\text{SiCl}_4/(\text{SiCl}_4 + \text{TiCl}_4)$  molar ratio ( $P_{\text{tot}} = 40$  kPa). (a)  $\text{CCl}_4/\text{H}_2 = 9.7 \times 10^{-3}$ , (b)  $\text{CCl}_4/\text{H}_2 = 4.6 \times 10^{-2}$ .



**Figure 8.27.** Experimental deposited phases as functions of deposition temperature and  $\text{SiCl}_4/(\text{SiCl}_4 + \text{TiCl}_4)$  ( $P_{\text{tot}} = 40$  kPa). (a)  $\text{CCl}_4/\text{H}_2 = 9.7 \times 10^{-3}$ , (b)  $\text{CCl}_4/\text{H}_2 = 4.6 \times 10^{-2}$ .

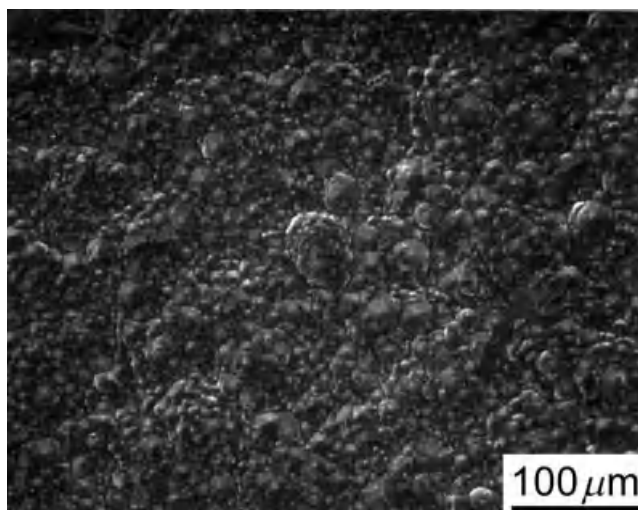


Figure 8.28. Typical surface microstructure of a CVD SiC-TiC composite.

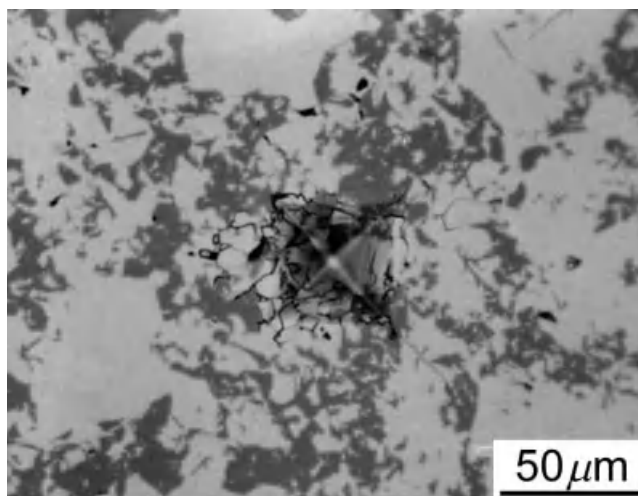


Figure 8.29. Polished surface of a CVD SiC-TiC with a Vicker's indentation.



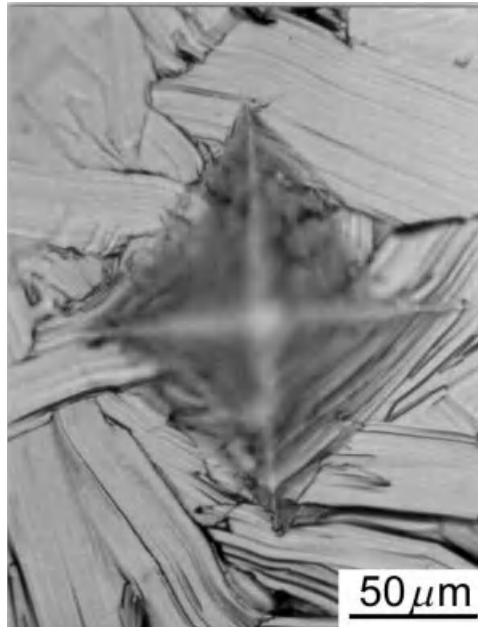


Figure 8.30. Polished surface of CVD  $\text{Ti}_3\text{SiC}_2$  film with a Vicker's indentation.

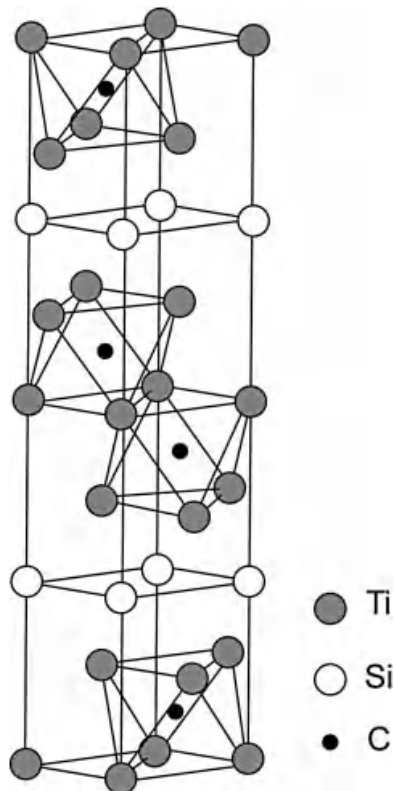


Figure 8.31. Unit cell structure of  $\text{Ti}_3\text{SiC}_2$ .

### 8.3 CVD OF OXIDE STRUCTURAL CERAMICS AND COMPOSITES

While nitrides and carbides have high potentials as structural materials, many oxides have been used for various functional materials such as dielectrics, optics, superconductors, and magnets. Since CVD can provide highly pure and dense films with good step coverage, CVD oxide thin films have been intensively studied, particularly using numerous metalorganic (MO) precursors.

MO precursors, typically alkoxides and  $\beta$ -diketonates, are in general reactive with oxygen or oxydant gas and relatively easily decompose at high temperature. Therefore, the deposition reaction on a wall of the CVD chamber or premature reactions in the gas phase are likely to take place; this would result in a decrease in deposition efficiency and deposition rate. The deposition rate of oxide film by metalorganic chemical vapor deposition (MOCVD) has been commonly less than several micrometers per hour. On the other hand, the present authors have achieved a high deposition rate of yttria-stabilized zirconia (YSZ) film of about 100  $\mu\text{m}/\text{h}$  by MOCVD using a cold wall-type CVD chamber [58] and reported the characteristics as thermal barrier coating (TBC) on an Ni-base superalloy substrate [59]. Although this deposition rate was almost the highest level among the reported values of oxide films by conventional thermal CVD, the deposition rate should be further increased in order to apply CVD YSZ film to TBC.

Auxiliary energy such as plasma and light (or laser), termed plasma CVD and photo-CVD (or laser chemical vapor deposition [LCVD]), respectively, can be effective to enhance the deposition rate and to lower the deposition temperature. YSZ thick film was prepared at about 200  $\mu\text{m}/\text{h}$  for TBC by using plasma CVD [60].

It is known that LCVD can increase the deposition rate significantly but only on a localized area of laser beam size [61]. The coating on a substrate with a complicated shape and wide area has never been achieved by LCVD. The present authors have developed a new kind of LCVD enabling high-speed wide-area coating [62].

#### 8.3.1 High-Speed Deposition by Laser CVD

The use of lasers has been widely investigated for application to material processings such as welding, surface melting, and laser ablation by taking advantage of its high energy as heat and/or light. LCVD has been employed as a thin film and low-temperature deposition process, mainly for preparing semiconductor devices [63]. Figure 8.32 shows the schematics of LCVD, which can be categorized into two types, that is, photolytic LCVD (Fig. 8.32a) and pyrolytic LCVD (Fig. 8.32b) [10]. Photolytic LCVD usually employs a high-energy laser, typically an ultraviolet laser. The laser can pass through source gases without irradiating to a substrate (no intentional heating by laser), and photochemical reactions in a gas phase will occur, yielding the deposition of film on the substrate. This process is advantageous for low-temperature deposition, particularly without affecting the impurity dopant profile of semiconductor wafer substrates. However, films cannot be prepared at high speed and in the form of thick film. On the other hand, pyrolytic LCVD commonly employs an infrared laser, where the laser serves as a heat source. A substrate is locally heated at high temperature by a high-power laser of several 100 to several 1000 W. By introducing source gases into the locally

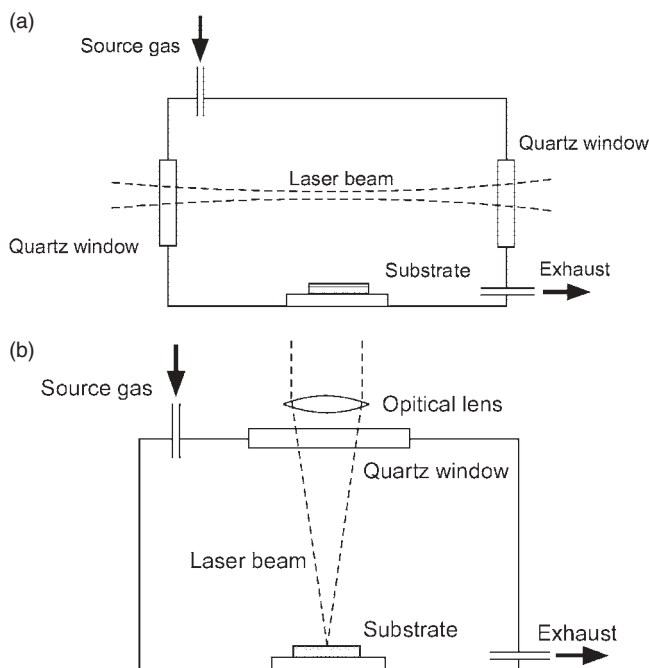


**Figure 8.32.** Schematics of an LCVD. (a) Photolytic LCVD, (b) pyrolytic LCVD.

heated area by the laser, the deposition reaction of thermal CVD by the heat of the laser may occur at a significantly high speed. Figure 8.33 is a schematic of a conventional pyrolytic LCVD used to prepare fiber- or whisker-like deposits [61]. The deposition area of the pyrolytic LCVD can be the size of a laser beam, usually less than a few millimeters. Since source gases can easily access such a small deposition area, the deposition rate increases with increasing deposition temperature without the limitation of diffusion (or mass transport), as shown in Figure 8.3. Figure 8.34 demonstrates the relationship between the deposition rate (rate of increase in length) and the laser density in pyrolytic LCVD compared to those of the LCVD by the present authors [64]. The deposition rate (rate of increase in length of deposit) can be at most  $10^7$  times as high as those of common thermal CVD (usually several micrometers per hour). However, it has been thought that attainment of a high-speed, wide-area, and thick coating should be impossible by conventional pyrolytic LCVD due to the small size of the laser beam. Engineering coatings, particularly for structural applications, obviously need a certain volume of deposits. The deposition rate in volume can be calculated by multiplying the laser beam size (deposition area) by the deposition rate in length. Figure 8.35 depicts the relationship between the volume deposition rate and the laser density in pyrolytic LCVD. The volume deposition rates of pyrolytic LCVD in the literature are far smaller than those of common thermal CVD, while those of the LCVD developed by the present authors are several orders higher than those of the common pyrolytic LCVD. In the

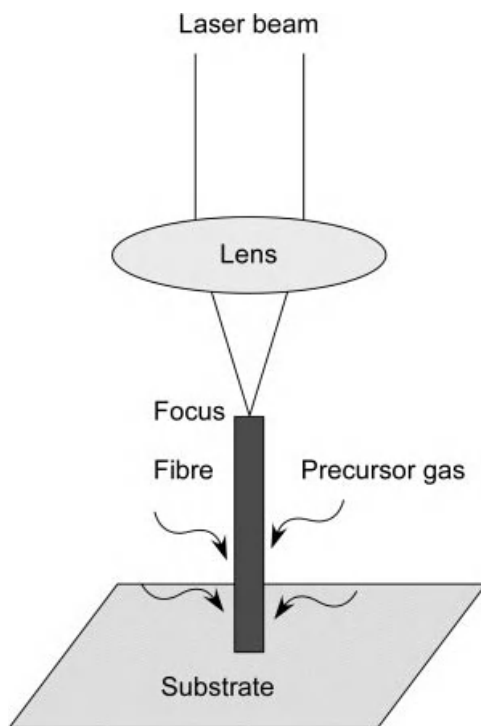


Figure 8.33. Schematic of a conventional pyrolytic LCVD.

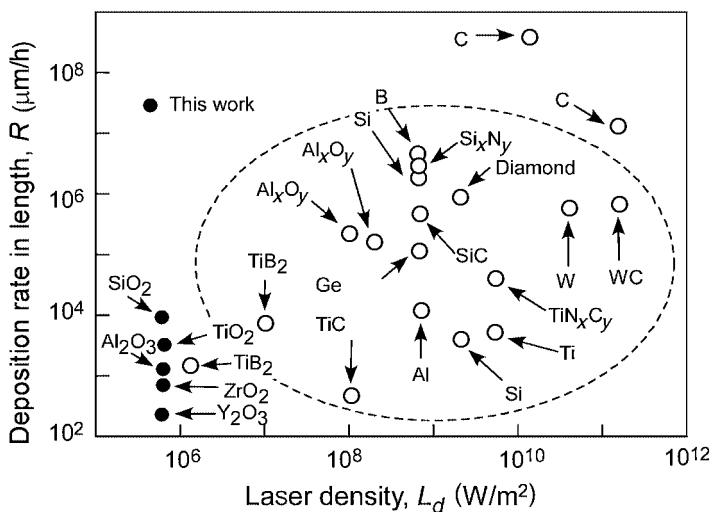
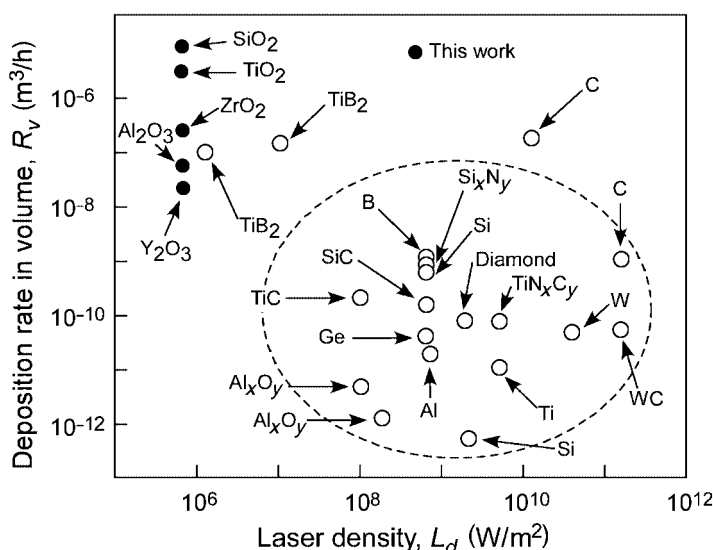


Figure 8.34. Relationship between deposition rate (rate of increase in length) and laser density in LCVD.



**Figure 8.35.** Relationship between deposition rate (rate of increase in volume) and laser density in LCVD.

case of the LCVD by the present authors, plasma forms around the deposition zone by the interaction between a high-power laser and precursor gas of high concentration. The precursor gas is ionized by laser and emits bright light. Plasma diagnosis implied that the plasma had a spectrum close to a Planck distribution with an electron temperature of about 4000 K [65]. The chemical reaction could have been significantly enhanced by plasma, and the mobility of absorbed species might have been accelerated by the laser radiation on the substrate surface. Conventional pyrolytic LCVD can be a line-of-sight process; that is, the deposition occurs only where the laser is radiated, that is, no deposition at the backside of the substrate or inside the holes. However, the LCVD by the present authors is a non-line-of-sight process in which the deposition takes place in the space of plasma. The present LCVD can be a laser-enhanced plasma CVD and is promising for many structural applications.

### 8.3.2 Structural Oxide Coating by Laser CVD

**8.3.2.1 YSZ Coating for Gas Turbine Blades.** Gas turbine blades for power generation and jet engines are commonly made of Ni-based superalloys due to their high-temperature strength, toughness, and refractoriness. The operation temperature of gas turbines used to be less 1400 K (melting point of metal substrate) until 1970s. The operation temperature of gas turbines has increased year by year up to around 1800 K nowadays owing to the development of cooling systems and TBC. The coating material for TBC should have low thermal conductivity, high thermal shock resistance, and a relatively large thermal expansion coefficient close to that of a metal

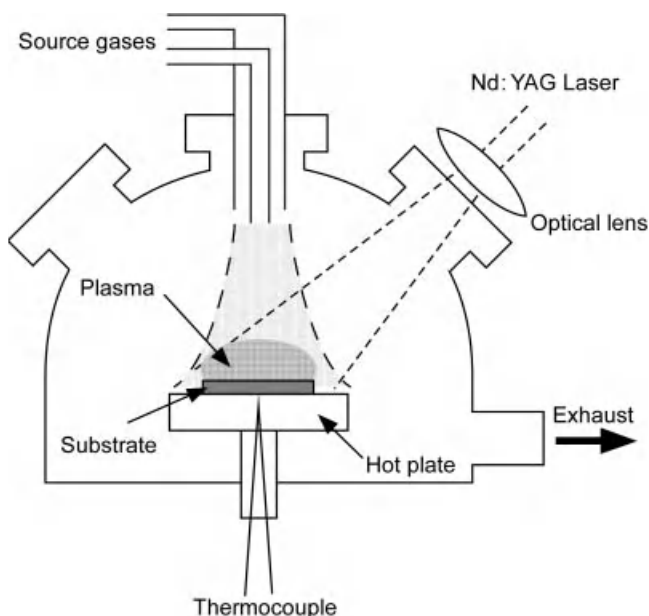


**Figure 8.36.** Schematic of an LCVD setup for preparing YSZ coating.

substrate, and thus YSZ has been widely used [66]. Although atmospheric plasma spray (APS) and electron-beam physical vapor deposition (EB-PVD) have been practically utilized for TBC, a new route for coating has been sought to extend the lifetime and to increase the operation temperature of TBC. LCVD can be a candidate process for TBC due to its high deposition rate, non-line-of-sight nature, and microstructure controllability.

Figure 8.36 is a schematic of an LCVD setup for preparing a YSZ coating by using an Nd : yttrium aluminum garnet (YAG) laser (max. 250-W continuous wave mode) and  $\text{Zr}(\text{dpm})_4$ ,  $\text{Y}(\text{dpm})_3$  (dpm: dipivaloylmethanato) precursors [67]. A laser can produce plasma by ionizing clusters or gases (i.e., plasma plume), as commonly observed in laser ablation. LCVD can also produce plasma around the substrate, and the deposition rate is significantly enhanced by the effect of plasma. Figure 8.37a,b depicts the effect of laser power on the deposition rate and on the space charge current of the plasma, respectively [65]. There is a threshold value of laser power to form plasma, that is, 70 W for preparing a YSZ coating. A significant increase in the deposition rate can be observed over the threshold laser power, which depends on the wavelength of the laser and the kinds of precursors. Plasma formation can take place only above the substrate (deposition zone), and the substrate temperature is raised by the heat radiation from the plasma. Figure 8.38 demonstrates the time dependence of the substrate temperature in LCVD [10]. Since the laser beam was slightly expanded to cover the whole substrate surface (about  $25 \times 25$  mm), the increase in temperature is insignificant, particularly for a laser-reflective substrate such as  $\text{Al}_2\text{O}_3$ . Many metals and some ceramic materials (such as AlN) are laser absorbable, and the temperature increase by laser irradiation is

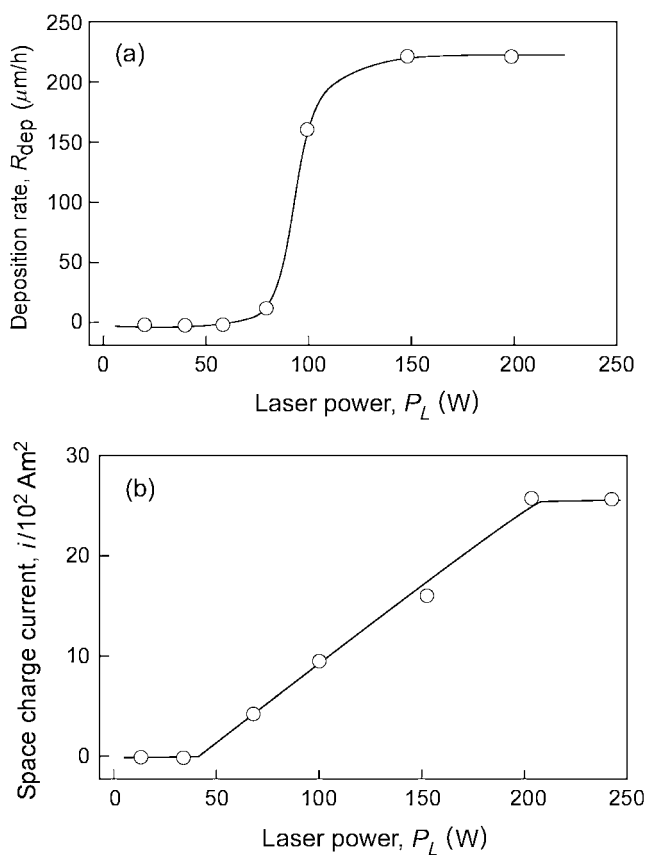


**Figure 8.37.** Effect of laser power on the deposition rate (a) and on the space charge current in the plasma (b).

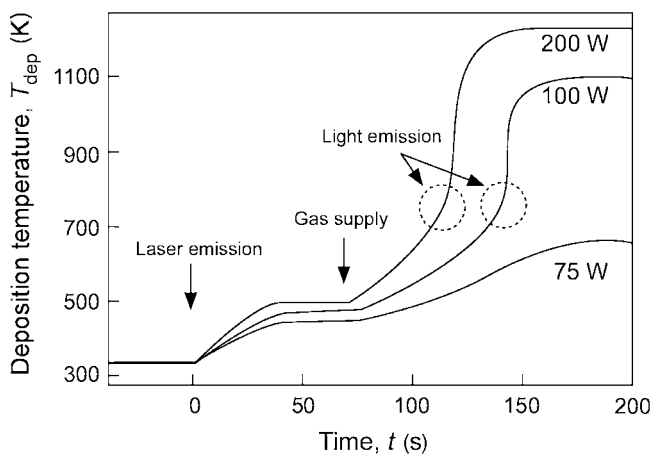


**Figure 8.38.** Time dependence of substrate temperature in LCVD.

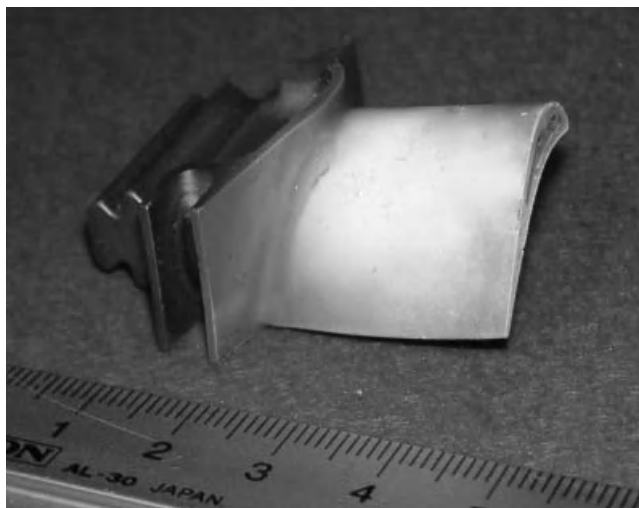
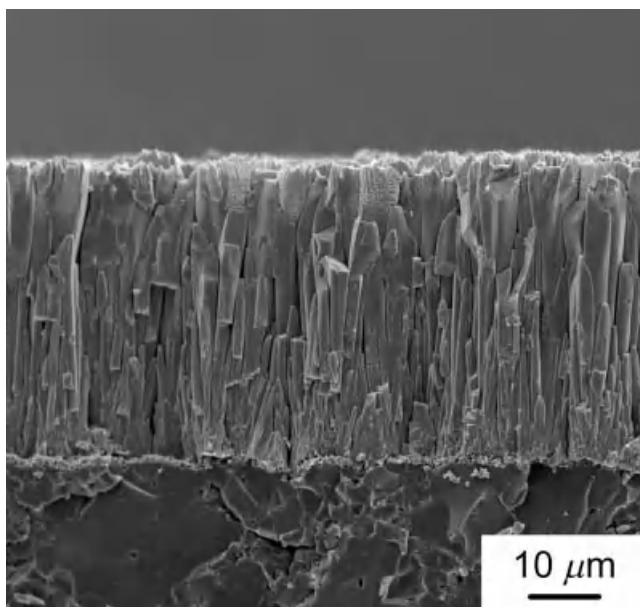


**Figure 8.39.** YSZ coating on a gas turbine blade by LCVD.

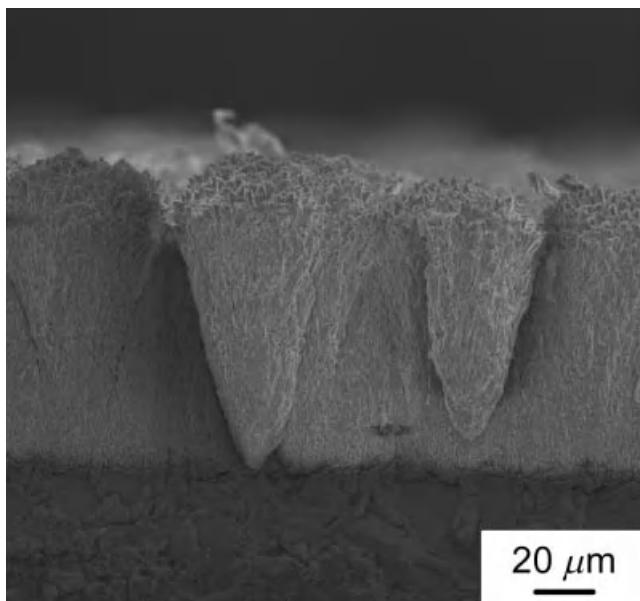
usually significant. After the source gases were introduced into the deposition zone, the deposition temperature increased up to around 1000–1200 K. The highest deposition rate of LCVD was 27.5 mm/h for  $\text{SiO}_2$  film by using a precursor of TEOS ( $\text{Si}(\text{OC}_2\text{H}_5)_4$ : tetraethoxysilane) [68].

Figure 8.39 demonstrates the YSZ coating on a gas turbine blade by LCVD [10]. By moving and rotating the gas turbine blade substrate, the whole substrate surface was uniformly coated with a thickness of about  $300\ \mu\text{m}$ . Figure 8.40 depicts the cross-sectional microstructure of YSZ coating prepared by LCVD at a deposition rate of  $230\ \mu\text{m/h}$  [69]. Vertically elongated grains, termed columnar structure, can be seen. Such microstructure is advantageous for relaxing the thermal expansion mismatch between the YSZ coating and the metal substrate. Figure 8.41 depicts the cross section of a YSZ coating prepared at a deposition rate of  $660\ \mu\text{m/h}$ , exhibiting a cone structure similar to that of CVD SiC (Fig. 8.21b). This cone structure is often observed in CVD under high-speed deposition conditions. This deposition rate ( $660\ \mu\text{m/h}$ ) is about 100 times as high as that of conventional thermal CVD. Figure 8.42 depicts voids of about 10 nm in diameter at the columnar grain boundary in a YSZ coating by LCVD. The columnar grains contain a large number of nanopores a few nanometers in diameter, as depicted in Figure 8.43. Nanopores are effective to decrease the thermal conductivity of YSZ coating, resulting in a one-fourth bulk YSZ sintered body. The microstructure of a YSZ coating by EB-PVD, in particular nanopores and porous featherlike microstructure, would be rather thermally unstable and tend to sinter (densify) at high temperature around 1500 K, resulting in oxidation of the metal substrate surface and finally delamination of YSZ coating. The nanopores prepared by LCVD were surrounded by specific crystal planes having a thermally stable microstructure yielding less increase in thermal conductivity at high temperature compared with featherlike nanopores by EB-PVD.





**Figure 8.40.** Cross-sectional microstructure of YSZ coating prepared by LCVD (deposition rate: 230  $\mu\text{m/h}$ ).



**Figure 8.41.** Cross-sectional microstructure of YSZ coating prepared by LCVD (660  $\mu\text{m/h}$ ).

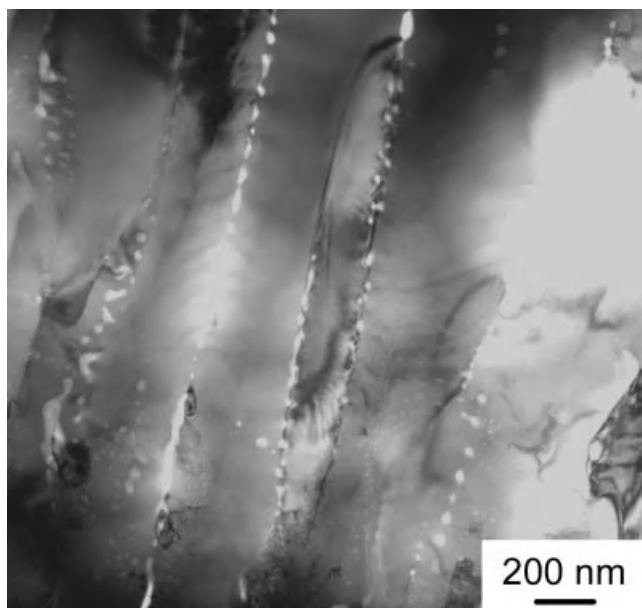


Figure 8.42. TEM micrograph of the columnar grain boundary in YSZ coating by LCVD.

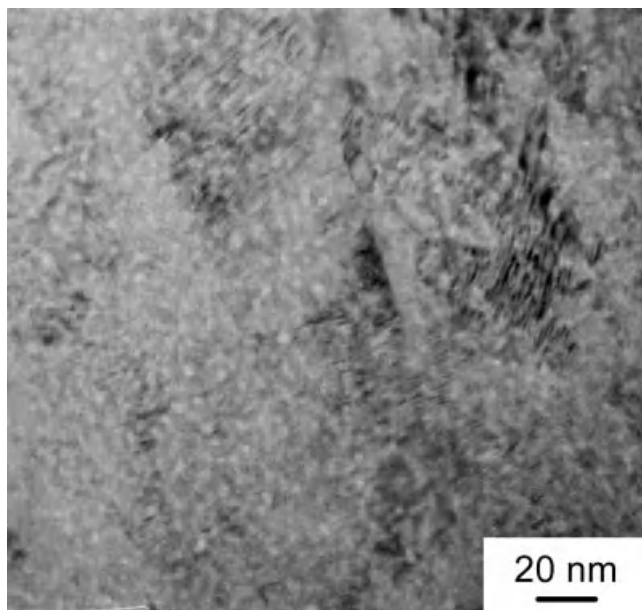
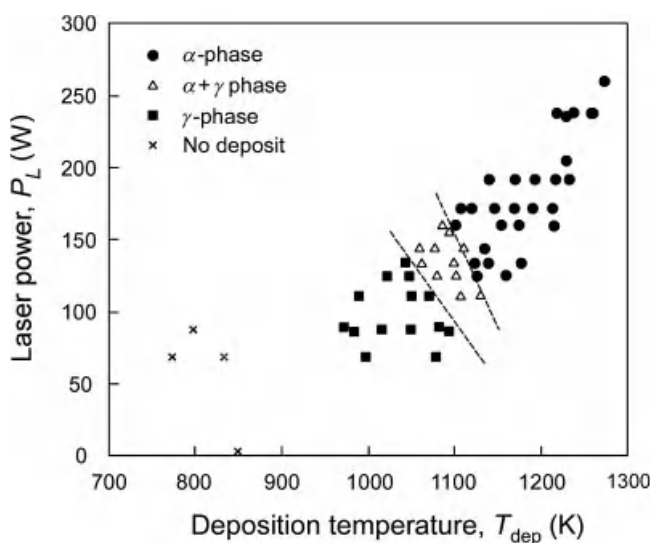


Figure 8.43. TEM micrograph of the columnar grains in YSZ coating by LCVD.

**8.3.2.2  $\alpha$ - $\text{Al}_2\text{O}_3$  Coating For Cutting Tools.** WC-based composites, typically WC-Co, have been widely employed in cutting tools due to their excellent wear resistance with high hardness and ductility [70]. Since WC is easily oxidized and may react with other materials during cutting or drilling, WC-based cutting tools are generally coated by  $\text{Al}_2\text{O}_3$  film.  $\text{Al}_2\text{O}_3$  has many crystal polytypes such as  $\alpha$ ,  $\gamma$ ,  $\sigma$ ,  $\kappa$ ,  $\theta$ , and so on. Among these polytypes of  $\text{Al}_2\text{O}_3$ ,  $\alpha$ - $\text{Al}_2\text{O}_3$  is the most stable and hardest at high temperature, and therefore the WC-based cutting tools are commonly coated by  $\alpha$ - $\text{Al}_2\text{O}_3$  film. Thermal CVD, using  $\text{AlCl}_3$  precursor (halide CVD), has been practically employed to prepare  $\text{Al}_2\text{O}_3$  coating on cutting tools. Kinetically,  $\gamma$ - $\text{Al}_2\text{O}_3$  film may be more feasible to form in thermal CVD and would transform into  $\alpha$ - $\text{Al}_2\text{O}_3$  at high temperature during usage. This would cause a volume contraction yielding cracking and delamination of the  $\text{Al}_2\text{O}_3$  coating. Since  $\alpha$ - $\text{Al}_2\text{O}_3$  would be thermodynamically stable at high temperature above 1273 K, the deposition temperature of  $\alpha$ - $\text{Al}_2\text{O}_3$  by thermal CVD has also been commonly high above 1273 K. However,  $\alpha$ - $\text{Al}_2\text{O}_3$  coating at such a high temperature would degrade mechanical properties of the WC-Co substrate, often leading to the formation of a brittle layer at the coating/substrate interface. In practical applications, the thickness of  $\alpha$ - $\text{Al}_2\text{O}_3$  coating is being increased to endure more severe cutting conditions. Therefore, the high-speed and low-temperature deposition process of  $\alpha$ - $\text{Al}_2\text{O}_3$  coating is required to develop higher-performance cutting tools.

LCVD was applied to prepare  $\alpha$ - $\text{Al}_2\text{O}_3$  coating by using Nd : YAG laser and  $\text{Al}(\text{acac})_3$  (acac: acetylacetonato) as a precursor. Figure 8.44 illustrates the effects of deposition temperature and laser power on the crystal structure of  $\text{Al}_2\text{O}_3$  coating.  $\gamma$ - $\text{Al}_2\text{O}_3$  formed at 980 K and  $\alpha/\gamma$  mixed phases were prepared at 1100 K, and  $\alpha$ - $\text{Al}_2\text{O}_3$  coating in a single phase was obtained above 1170 K. Laser power also affected the



**Figure 8.44.** Effects of deposition temperature and laser power on the crystal structure of  $\text{Al}_2\text{O}_3$  coating by LCVD.

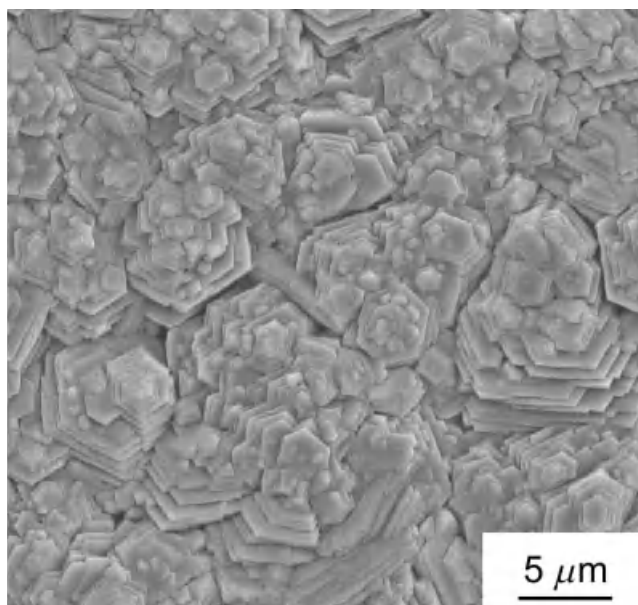


**Figure 8.45.** Typical surface microstructure of  $\alpha$ - $\text{Al}_2\text{O}_3$  coating prepared by LCVD.

crystal structure; the higher the laser power, the lower the deposition temperature for  $\gamma$  and  $\alpha$ - $\text{Al}_2\text{O}_3$  films. Halide CVD usually needs more than 1300 K to obtain  $\alpha$ - $\text{Al}_2\text{O}_3$  coating. MOCVD has been widely used to prepare  $\text{Al}_2\text{O}_3$  coating, and an amorphous-like  $\gamma$ - $\text{Al}_2\text{O}_3$  coating has been prepared below 1000 K, and  $\alpha/\gamma$  mixed  $\text{Al}_2\text{O}_3$  coating has been obtained at 1373 K [71]. The deposition temperature of  $\alpha$ - $\text{Al}_2\text{O}_3$  coating by LCVD was about 200 K lower than that of conventional MOCVD. Figure 8.45 depicts the typical surface microstructure of an  $\alpha$ - $\text{Al}_2\text{O}_3$  coating prepared by LCVD [72]. Hexagonal facets were observed on the surface, implying significant (001) orientation. Figure 8.46 demonstrates the effect of deposition temperature on the deposition rate of  $\text{Al}_2\text{O}_3$  coating, in which plasma formed in the hatched area. Almost no deposition took place below 900 K, and a significantly high deposition rate of  $\gamma$ - $\text{Al}_2\text{O}_3$  coating of about 600  $\mu\text{m}/\text{h}$  was obtained around 950 K, and the deposition rates of  $\alpha$ - $\text{Al}_2\text{O}_3$  coating decreased to about 200  $\mu\text{m}/\text{h}$  over 1050 K. The temperature dependence of the deposition rate of  $\text{Al}_2\text{O}_3$  coating by LCVD is compared to those of conventional halide and MOCVD in Figure 8.47 [72]. The highest deposition rates of  $\alpha$ - and  $\gamma$ - $\text{Al}_2\text{O}_3$  coatings in LCVD were 252 and 570  $\mu\text{m}/\text{h}$ , respectively. These values were several hundred times higher than those of conventional thermal CVD.

## 8.4 CONCLUDING REMARKS AND FUTURE DIRECTIONS

CVD has been a key technology as a thin film process, particularly for semiconductors and cutting tools. Other thin film processes such as sputtering and laser ablation, and

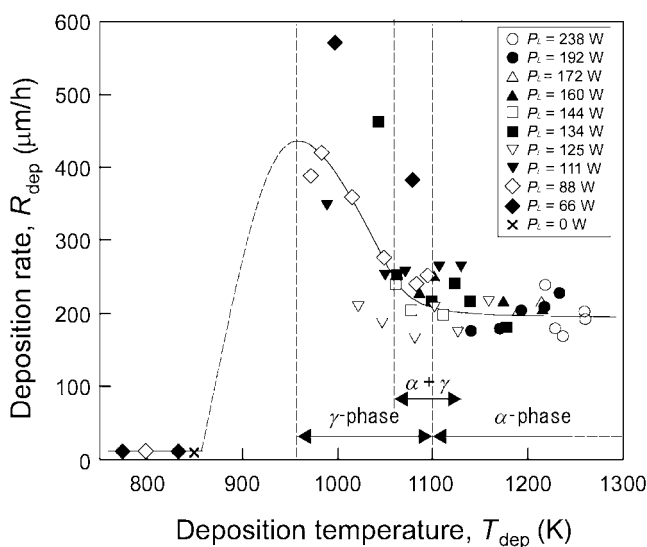


**Figure 8.46.** Effect of deposition temperature on the deposition rate of  $\text{Al}_2\text{O}_3$  coating by LCVD.

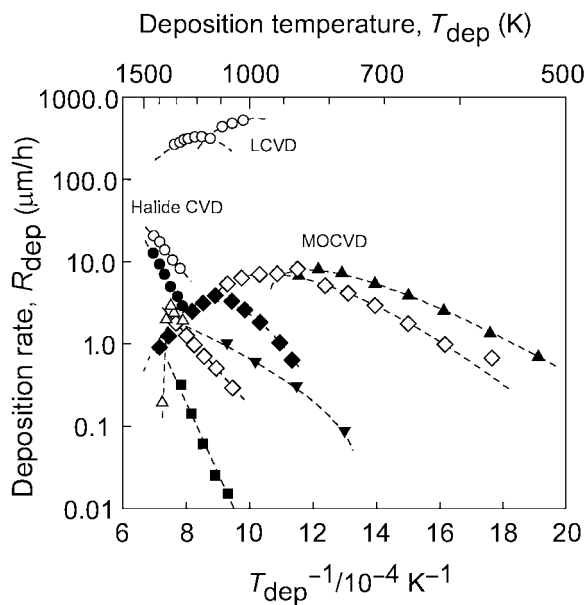


**Figure 8.47.** Effect of deposition temperature on the deposition rate of  $\text{Al}_2\text{O}_3$  coating by LCVD, halide CVD, and MOCVD.

so on, have been also intensively studied to develop micro- and nanoscale devices. Thick film coatings also have many applications, particularly for structural usage; thick coating technology, however, has not been well developed. CVD is a promising technique for high-speed, wide-area, and adherent thick coatings. The auxiliary energy of a laser has tremendous effects on the deposition rate, crystallinity, and microstructure of coatings in CVD. Although the mechanism of LCVD introduced in this chapter has not been well understood, this process is promising for thick coating for a wide range of structural applications.

## REFERENCES

1. A. K. Pattanaik and V. K. Sarin, Basic principles of CVD thermodynamics and kinetics, in *Chemical Vapor Deposition, Surface Engineering Series*, Vol. 2, ed. J.-H. Park, pp. 23–43, ASM Int., Materials Park, OH, 2001.
2. R. L. Gentilman, B. S. Bibenedetto, R. Tustison, and J. Pappis, Chemical vapor deposition of ceramics for infrared windows, in *Chemically Vapor Deposited Coatings*, ed. H. O. Pierson, pp. 47–53, Amer. Ceram. Soc., Columbus, OH, 1981.
3. A. Bennett (1986) Requirements for engineering ceramics in gas turbine engines, *Mater. Sci. Technol.*, **2** 895–899.
4. T. Hirai, K. Niihara, and T. Goto (1980) Oxidation of CVD  $\text{Si}_3\text{N}_4$  at 1550 to 1650°C, *J. Am. Soc.*, **63** 419–424.
5. T. Narushima, T. Goto, and T. Hirai (1989) High-temperature passive oxidation of CVD-SiC, *J. Am. Soc.*, **72** 1386–1390.
6. M. T. Duffy, S. Berkman, G. W. Cullen, R. V. D'Aiello, and H. I. Moss (1980) Development and evaluation of refractory CVD coating as contact materials for molten silicon, *J. Cryst. Growth*, **50** 347–365.
7. T. Hirai and T. Goto, CVD fabrication of in-situ composites of non-oxide ceramics, in *Tailoring Multiphase and Composite Ceramics*, eds. R. E. Tressler, G. L. Messing, C. G. Pantano, and R. E. Newnham, pp. 165–177, Plenum, New York, 1986.
8. J. M. Blocher, Jr. (1974) Structure-property-process relationships in chemical vapor-deposition CVD, *J. Vac. Sci. Technol.*, **11** 680–686.
9. W. A. Bryant (1977) Review the fundamentals of chemical vapour deposition, *J. Mater. Sci.*, **12** 1285–1306.
10. T. Goto (2009) Heat resisting coating by laser CVD, *J. Surf. Finish. Soc. Jpn.*, **60** 709–715.
11. H. J. Stein and H. A. R. Wegener (1977) Chemically bound hydrogen in CVD  $\text{Si}_3\text{N}_4$ : Dependence on  $\text{NH}_3/\text{SiH}_4$  ratio and on annealing, *J. Electrochem. Soc.*, **124** 908–912.
12. K. S. Mazydiyasm and C. M. Cooke (1973) Synthesis, characterization, and consolidation of  $\text{Si}_3\text{N}_4$  obtained from ammonolysis of  $\text{SiCl}_4$ , *J. Am. Ceram. Soc.*, **56** 628–633.
13. K. Niihara and T. Hirai (1976) Chemically vapour-deposited silicon nitride, part 1, *J. Mater. Sci.*, **11** 593–603.
14. T. Hirai, K. Niihara, and T. Goto (1977) Rapid chemical vapour-deposition of  $\text{Si}_3\text{N}_4$ , *J. Mater. Sci.*, **12** 631–632.
15. T. Hirai, T. Goto, and T. Kaji (1983) Preparation of silicon carbide by chemical vapor deposition, *J. Ceram. Soc. Jpn.*, **91** 502–509.

16. C.-C. Jiang, T. Goto, and T. Hirai (1990) Preparation of titanium carbide plates by chemical vapor deposition, *J. Mater. Sci.*, **25** 1086–1093.
17. M. Mukaida, T. Goto, and T. Hirai (1990) Morphology and deposition rate of  $\text{TiB}_2$  prepared by chemical vapor deposition, *J. Mater. Sci.*, **25** 1069–1075.
18. M. Mukaida, T. Goto, and T. Hirai (1992) Preparation of  $\text{SiB}_{4\pm x}$  and  $\text{SiB}_6$  plates by chemical vapor deposition of  $\text{SiCl}_4 + \text{B}_2\text{H}_6$  system, *J. Mater. Sci.*, **27** 255–262.
19. T. Hirai, K. Niihara, and T. Goto (1977) Preparation of  $\text{Si}_3\text{N}_4$  by chemical vapor deposition (effect of raw gas flow rate), *J. Jpn. Inst. Met.*, **41** 359–367.
20. F. Itoh, T. Honda, K. Niihara, T. Hirai, and K. Suzuki (1980) Chemical bond of CVD- $\text{Si}_3\text{N}_4$  by compton scattering measurement, *J. Phys. Soc. Jpn.*, **48** 561–566.
21. M. Misawa, T. Fukunaga, K. Niihara, T. Hirai, and K. Suzuki (1979) Structure, characterization of CVD amorphous  $\text{Si}_3\text{N}_4$  by pulsed neutron total scattering, *J. Non-Cryst. Solids*, **34** 316–321.
22. F. Itoh, T. Honda, T. Goto, T. Hirai, and K. Suzuki (1981) Positron annihilation study of amorphous CVD  $\text{Si}_3\text{N}_4$ -C composites, in Proc. 8th Int. Conf. Chemical Vapor Deposition, eds. J. M. Blocher, Jr., G. E. Vuillard, and G. Wahl, pp. 227–234, Electrochem. Soc., Pennington.
23. K. Niihara and T. Hirai (1977) Chemical vapour-deposited silicon nitride, part 3, *J. Mater. Sci.*, **12** 1233–1242.
24. T. Hirai and T. Goto (1989) Ceramics nanocomposites and ceramics finecomposites, *Bull. Jpn. Inst. Mat.*, **28** 960–967.
25. T. Hirai and T. Goto (1981) Preparation of amorphous  $\text{Si}_3\text{N}_4$ -C plate by chemical vapor deposition, *J. Mater. Sci.*, **16** 17–23.
26. T. Goto, F. Itoh, K. Suzuki, and T. Hirai (1983) ESCA study of amorphous CVD  $\text{Si}_3\text{N}_4$ -C composites, *J. Mater. Sci. Lett.*, **2** 805–807.
27. T. Goto and T. Hirai (1983) Etching of chemically vapour deposited amorphous  $\text{Si}_3\text{N}_4$ -C composites in HF solution, *J. Mater. Sci.*, **18** 3387–3392.
28. T. Goto and T. Hirai (1987) High temperature evaporation of amorphous  $\text{Si}_3\text{N}_4$ -C composite prepared by chemical vapour deposition, *J. Mater. Sci.*, **22** 2842–2846.
29. T. Goto and T. Hirai (1983) D. C. electrical conductivity of amorphous  $\text{Si}_3\text{N}_4$ -C composite prepared by chemical vapour deposition, *J. Mater. Sci.*, **18** 383–390.
30. T. Hirai and S. Hayashi (1982) Preparation and some properties of chemically vapour-deposited  $\text{Si}_3\text{N}_4$ -TiN composite, *J. Mater. Sci.*, **17** 1320–1328.
31. S. Hayashi, T. Hirai, K. Hiraga, and M. Hirabayashi (1982) Microstructure of  $\text{Si}_3\text{N}_4$ -TiN composite prepared by chemical vapour deposition, *J. Mater. Sci.*, **17** 3336–3340.
32. K. Hiraga, M. Hirabayashi, S. Hayashi, and T. Hirai (1983) High resolution electron microscopy of chemically vapor deposited  $\beta$ - $\text{Si}_3\text{N}_4$ -TiN composites, *J. Am. Soc.*, **66** 539–542.
33. S. Hayashi and T. Hirai (1983) Thermal conductivity of chemically vapour-deposited  $\text{Si}_3\text{N}_4$ -TiN composites, *J. Mater. Sci.*, **18** 3259–3264.
34. T. Hirai, T. Goto, and T. Sakai, Preparation of amorphous  $\text{Si}_3\text{N}_4$ -BN composites by chemical vapor deposition, in *Emergent Process Methods for High-Technology Ceramics, Materials Science Research Series*, Vol. 17, eds. R. F. Davis, H. Palmour, III, and R. L. Porter, pp. 347–358, Plenum, New York, 1984.
35. T. Goto and T. Hirai (1988) ESCA study of amorphous CVD  $\text{Si}_3\text{N}_4$ -BN composites, *J. Mater. Sci. Lett.*, **7** 548–550.



36. T. Fukunaga, T. Goto, M. Misawa, T. Hirai, and K. Suzuki (1987) Atomic-scale structure of CVD amorphous  $\text{Si}_3\text{N}_4$ -BN composite, *J. Non-Cryst. Solids*, **95/96** 1119–1126.
37. T. Hirai and T. Goto, Preparation of amorphous  $\text{Si}_3\text{N}_4$ -BN composite by chemical vapor deposition and its electrical properties, in *Amorphous Materials -Physics and Technology-*, ed. Editorial Committee of Special Project Research on Amorphous Materials, pp. 130–133, Bando print, Osaka, 1983.
38. T. Hirai and T. Goto (1984) Preparation of transparent ceramics by CVD, *Ind. Mater.*, **2** 85–92.
39. S. Zirinsky and E. A. Irene (1978) Selective studies of chemical vapor-deposited aluminum nitride -silicon nitride mixture films, *J. Electrochem. Soc.*, **125** 305–314.
40. N. S. Jacobson (1993) Corrosion of silicon-based ceramics in combustion environments, *J. Am. Ceram. Soc.*, **76** 3–28.
41. J. Schlichting (1980) Chemical vapor-deposited silicon-carbide, *Powder Metall. Int.*, **12** 196–200.
42. M. A. Pickering and W. Haigis (1993) CVD scaled up for commercial production of bulk SiC, *Am. Ceram. Soc. Bull.*, **72** 74–78.
43. J. R. Weiss and R. J. Diefendorf, Chemically vapour deposited SiC for high temperature and structural applications, in *Silicon Carbide-1973*, ed. R. C. Marshall, J. W. Faust, Jr., and C. E. Ryan, pp. 80–91, University of South Carolina Press, Columbia, SC, 1973.
44. W. R. Holman and F. J. Huegel (1974) Interrelationships between process parameters, structure, and properties of CVD tungsten and tungsten-rhenium alloys, *J. Vac. Sci. Technol.*, **11** 701–708.
45. T. Goto, Oxidation behavior of chemical vapor deposited silicon carbide, in *Developments in High-Temperature Corrosion and Protection of Materials*, eds. W. Gao and Z. Li, pp. 433–455, CRC Press, Cambridge, England, 2008.
46. E. M. Levin, C. R. Robbins, and H. F. McMurdie, *Phase Diagram for Ceramists*. Amer. Ceram. Soc., Columbus, OH, 1964.
47. I. Gunjishima, T. Akashi, and T. Goto (2002) Characterization of directionally solidified  $\text{B}_4\text{C}$ -SiC composites prepared by a floating zone method, *Mater. Trans.*, **43** 2309–2315.
48. W.-J. Li, R. Tu, and T. Goto (2005) Preparation of  $\text{TiB}_2$ -SiC eutectic composite by an arc-melted method and its characterization, *Mater. Trans.*, **46** 2504–2508.
49. R. Tu, H. Hirayama, and T. Goto (2008) Preparation of  $\text{ZrB}_2$ -SiC composites by arc melting and their properties, *J. Ceram. Soc. Jpn.*, **116** 431–435.
50. I. Akin, M. Hotta, F. C. Sahin, O. Yucel, G. Gollor, and T. Goto (2009) Microstructure and densification of  $\text{ZrB}_2$ -SiC composites prepared by spark plasma sintering, *J. Euro. Ceram. Soc.*, **29** 2379–2385.
51. R. Tu, H. Hirayama, and T. Goto (2009) Passive oxidation behavior of  $\text{ZrB}_2$ -SiC eutectic composite prepared by Arc melting, *Key Eng. Mater.*, **403** 217–220.
52. T. Goto and T. Hirai (1987) Preparation of SiC-TiC in-situ composites by chemical vapor deposition, in *Proc. 10th Int. Conf. Chemical Vapor Deposition*, ed. G. W. Cullen, pp. 1070–1079, New Jersey.
53. T. Goto and T. Hirai (1987) Thermodynamics for the chemical vapor deposition of  $\text{SiCl}_4$ - $\text{TiCl}_4$ - $\text{CCl}_4$ - $\text{H}_2$  system, *J. Chem. Soc. Jpn.*, **11** 1939–1945.
54. T. Goto and T. Hirai (1987) Microstructure of SiC-TiC in-situ composites prepared by chemical vapor deposition, *J. Powd. Metall. Jpn.*, **34** 487–490.



55. W. Jeitschko and H. Nowotny (1967) Die Kristallstruktur von  $\text{Ti}_3\text{SiC}_2$ -Ein Neuer Komplexcarbid-Typ, *Monatsh. Chem.*, **98** 329–337.
56. T. Goto and T. Hirai (1987) Chemically vapor deposited  $\text{Ti}_3\text{SiC}_2$ , *Mater. Res. Bull.*, **22** 1195–1201.
57. M. W. Barsoum (2000) The  $\text{M}_{\text{N}+1}\text{AX}_\text{N}$  phases: A new class of solids; thermodynamically stable nanolaminates, *Prog. Solid St. Chem.*, **28** 201–281.
58. R. Tu, T. Kimura, and T. Goto (2002) Rapid synthesis of yttria-partially-stabilized zirconia films by metal-organic chemical vapor deposition, *Mater. Trans.*, **43** 2354–2356.
59. R. Tu and T. Goto (2005) Thermal cycle resistance of yttria stabilized zirconia coatings prepared by MO-CVD, *Mater. Trans.*, **46** 1318–1323.
60. B. Pr  uchat and S. Drawin (2001) Properties of PECVD-deposited thermal barrier coatings, *Surf. Coat. Tech.*, **142-144** 835–842.
61. C. Duty, D. Jean, and W. J. Lackey (2001) Laser chemical vapour deposition: Materials, modelling, and process control, *Inter. Mater. Rev.*, **46** 271–287.
62. J. R. V. Garcia and T. Goto (2003) Thermal barrier coatings produced by chemical vapor deposition, *Sci. Technol. Adv. Mater.*, **4** 397–402.
63. D. B  uerle, Laser-CVD of microstructure, in *Laser Processing and Chemistry*, 3rd edition, pp. 337–373, Springer, Berlin, 2000.
64. T. Goto and T. Kimura (2006) High-speed oxide coating by laser chemical vapor deposition and their nano-structure, *Thin Solid Films*, **515** 46–52.
65. H. Miyazaki, T. Kimura, and T. Goto (2003) Acceleration of deposition rates in a chemical vapor deposition process by laser irradiation, *Jpn. J. Appl. Phys.*, **42** L316–L318.
66. D. R. Clarke and C. G. Levi (2003) Materials design for the next generation thermal barrier coatings, *Annu. Rev. Mater. Res.*, **33** 383–417.
67. T. Kimura and T. Goto (2003) Rapid synthesis of yttria-stabilized zirconia films by laser chemical vapor deposition, *Mater. Trans.*, **44** 421–424.
68. J. Endo, A. Ito, T. Kimura, and T. Goto (2010) High-speed deposition of dense, dendritic and porous  $\text{SiO}_2$  films by Nd:YAG laser chemical vapor deposition, *Mater. Sci. Eng. B*, **166** 225–229.
69. T. Goto (2005) Thermal barrier coatings deposited by laser CVD, *Surf. Coat. Tech.*, **198** 367–371.
70. S. Ruppi (2005) Deposition, microstructure and properties of texture-controlled CVD  $\alpha\text{-Al}_2\text{O}_3$  coatings, *Refract. Mat. Hard Mater.*, **23** 306–316.
71. A. Ito, R. Tu, and T. Goto (2010) Amorphous-like nanocrystalline  $\gamma\text{-Al}_2\text{O}_3$  films prepared by MOCVD, *Surf. Coat. Tech.*, **204** 2170–2174.
72. H. Kadokura, A. Ito, T. Kimura, and T. Goto (2010) Moderate temperature and high-speed synthesis of  $\alpha\text{-Al}_2\text{O}_3$  films by laser chemical vapor deposition using Nd:YAG laser, *Surf. Coat. Tech.*, **204** 2302–2306.

# CVI PROCESSING OF CERAMIC MATRIX COMPOSITES

ANDREA LAZZERI

## 9.1 INTRODUCTION AND BACKGROUND

The chemical vapor infiltration (CVI) technology is one of the most attractive industrially available methods to produce fiber-reinforced ceramic matrix composites (CMCs) [1]. CVI is a process where a porous preform is placed in a surrounding of a reactive gas mixture, which, if thermally activated, decomposes and yields a solid deposit that fills the pores inside the preform [1, 2]. The main advantages of this technique are the possibility to manufacture complex net or near-net-shape components at relatively low temperatures, avoiding potential damages of the textile structures, typically used as preform, and to control and modify the microstructure of the matrix.

This technique allows the production of strong and tough composites and is ideal to produce composites with characteristics of resistance to corrosion, erosion, and wear. These important features generally overcome the main drawbacks of the CVI process, such as the long manufacturing time of typically some days up to weeks and the run-to-run reproducibility that in some case still limits the applicability of this technology.

In particular, the CMCs that take more advantages from the CVI technology are silicon carbide (SiC) ceramic reinforced with SiC-fibers (SiC<sub>f</sub>/SiC composites [3]) and

---

*Ceramics and Composites Processing Methods*, First Edition. Edited by Narottam P. Bansal and Aldo R. Boccaccini.

© 2012 The American Ceramic Society. Published 2012 by John Wiley & Sons, Inc.

carbon (C) ceramic reinforced with C-fibers ( $C_f/C$  composites) [4].  $SiC_f/SiC$  composites produced by CVI present excellent high-temperature properties including high strength, modulus of elasticity, creep and corrosion resistance, resistance to shocks, fatigue and damage, chemical stability, and a greater fracture toughness compared to unreinforced SiC [5]. Also, the fabrication of  $C_f/C$  composites by CVI technology offers considerable advantages, like the control over the microstructure of carbon matrix (CVI-derived carbon or pyrocarbon [PyC]), which presents excellent physical and thermal properties and can be obtained under certain infiltration conditions [4]. CVI is widely used to fabricate  $C_f/C$  composites when high performance of the final material is needed, for example, for applications as aircraft disk brakes.

The good mechanical properties at room and high temperatures exhibited by CVI-processed composites largely depend on the fiber–matrix interphase. Fiber–matrix interphases in CVI composites consist of a thin coating layer (less than  $1\ \mu\text{m}$  thick) of one or more materials deposited on the fiber during the same CVI process [6, 7].

### 9.1.1 Short History of CVI

Among the different CVI techniques developed up to now, the isothermal type is the most well established. In the isothermal CVI (I-CVI) process, the temperature of the fibrous preforms is maintained constant in an isothermal zone of a hot-wall reactor (Fig. 9.1). The I-CVI process for the  $SiC_f/SiC$  composites was a natural extension of the efforts taken by several researchers in the area of  $C_f/C$  composites [8]. Even if the process conditions for the I-CVI process for  $SiC_f/SiC$  composites can vary considerably, the optimum conditions have been determined by Fitzer and Gadow [9]. The study was

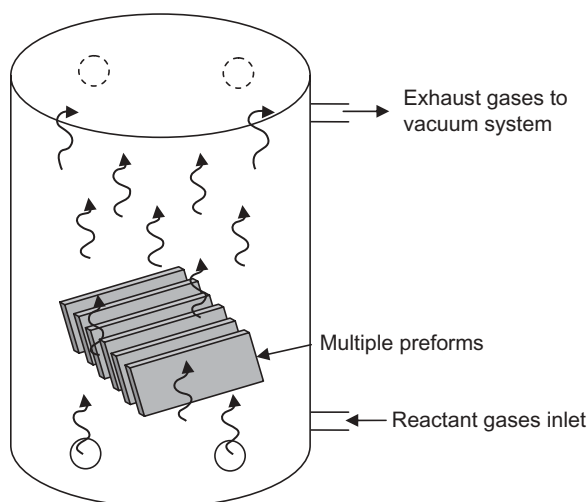


**Figure 9.1.** Schematic representation of the I-CVI process. The reactant gases, as they flow through the furnace at reduced pressure, diffuse into fibrous preforms, and effluents diffuse back to the preform surface.

carried out on a Nicalon™ preform of size  $4 \times 5 \times 50$  mm containing 40–50 vol % fibers. In particular, using an infiltration temperature of 1320 K and a total pressure of 3 kPa, a total infiltration time of 14 days was found required to achieve the maximum density. Thus, the process requires a combination of low temperatures, low reagent concentrations, and low pressures in order to avoid the sealing of the outer preform surface and to avoid the reactants to fill the inner pore volume. The optimal combination of the process parameters would make the process uneconomically slow. Therefore, in the industrial I-CVI processes, the temperatures, pressures, and reagent concentrations are required to be maintained sufficiently high in order to obtain a sufficient densification rate. By this way, the deposition will take place preferentially on the external parts of the preform than on the fibers inside the preform. Therefore, if the porosity on the substrate surface is closed by a faster deposition, a density gradient from the surface to the interior of the preforms will occur and the resulting composite will not be homogeneous. Furthermore, the wall thickness of preforms is limited to a few (~5) millimeters. Components with higher wall thickness have to be infiltrated in two or more infiltration steps, with an intermediate grinding off of the tight surface layer.

In the 1980s, despite the long time period required to obtain satisfactory results, the I-CVI process has led to the largest industrial effort in the area of CMCs by Société Européenne de Propulsion (SEP), Amercorm, Refractory Composites, and others [3], thanks to its capacity to simultaneously infiltrate a great number of complex-shaped parts of C and SiC matrix composites [10]. Major investments were made in 1987 by the American company DuPont, who obtained license rights of this technology from the French company SEP [11]. In the early 1990s, large CVI furnaces, measuring about 200 cm in diameter, for manufacturing SiC<sub>f</sub>/SiC composites were constructed by DuPont,<sup>1</sup> and the first industrial-scale CMC parts were manufactured in 1990 [11].

### 9.1.2 Theoretical Background for CVI Composites

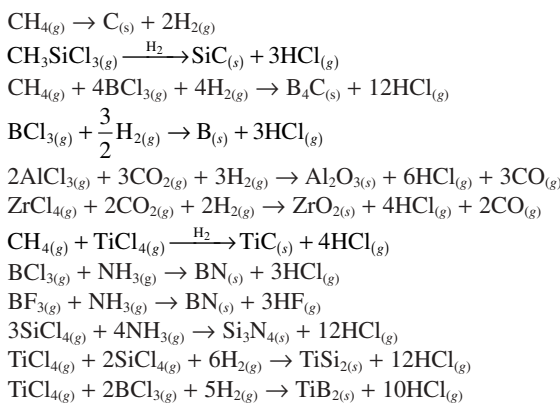
The CVI technique is based on the principle of impregnating a porous body, consisting of an array of fibers (preform), by means a mixture of precursor gases that reacts, decomposes, and precipitates the solid within the pore network of a heated substrate. The chemical reaction takes place between the gaseous species that flow by diffusion within the pores. The conditions for the application of the CVI technology to a given porous substrate are (1) interconnection of the pores and (2) thermal and chemical stability of the substrate under the CVI conditions. Porous preforms generally present a complex pore size distribution that depends on the architecture of the preform.

The principal scope of CVI is to increase the density of the porous preform by a percentage range from 100% to 900% (i.e., by a factor of 2–10), depending on the properties required by the final application.

In CVI, the different constituents of the composite, that is, the interphase, the matrix, and an external coating, are sequentially deposited from precursor gases at

<sup>1</sup> The company, based in Newark, Delaware, was later known as AlliedSignal Composites, then Honeywell Advanced Composites, and currently GE Power System Composites, following its acquisition in 2001.

TABLE 9.1. The Most Commonly Used Overall Chemical Reactions for the Formation of Ceramics by CVI [6]



moderate temperatures (900–1200°C) and under reduced pressures (or sometimes at atmospheric pressure).

The material deposited by CVI forms part or the entire matrix of the CMC, forming a significant fraction of the total mass of the final composite.

The basic chemistry of making a coating and a matrix by CVI could be considered similar as that of depositing a ceramic on a substrate by chemical vapor deposition (CVD) [6].

In CVD, a solid material is formed as a product resulting from a chemical decomposition reaction taking place between the precursor gases under suitable temperature conditions. Table 9.1 gives a few examples of the overall chemical reactions commonly used for the formation of ceramics by CVD or CVI. Usually, the chemical reactions leading to the formation of the solid phase are not so simple because (1) intermediates and by-products are frequently formed, and (2) reaction conversions are often limited [6].

For certain temperature and pressure conditions, a very complex heterogeneous chemical reaction usually can take place for the deposition of a given ceramic material. The material deposited can be either a single phase or a combination of two phases (codeposits). This depends on the initial composition of the reagent gaseous species (e.g.,  $[\text{H}_2]/[\text{CH}_3\text{SiCl}_3]$  ratio for SiC deposition). In addition, there could be the formation of some gaseous by-products (e.g., hydrocarbons, silicon subchlorides, and silanes) with a consequent decrease of the yield in solid.

Naslain et al. [6], as reported schematically in Figure 9.2, subdivided the complex mechanism according to which a solid is deposited on a substrate into at least three steps:

- (i) the diffusion of the source species through a boundary layer surrounding the substrate (preform);

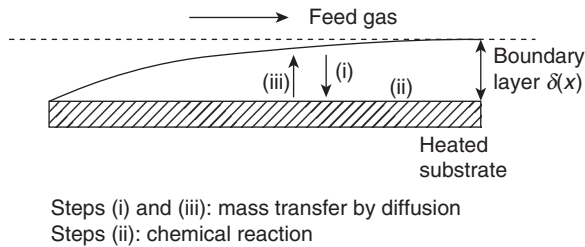


**Figure 9.2.** The different steps in the CVD process (adapted from Naslain et al. [6]).

- (ii) the adsorption of the source species (reagents) on the substrate where they react among themselves, allowing the production of the solid and the adsorbed gaseous reaction by-products; and
- (iii) the final desorption of the reaction gaseous by-products from the substrate through the boundary layer.

The deposition rates in the steps (i) and (iii) are clearly controlled by mass transfer phenomena, while step (ii) is controlled by the kinetics of surface phenomena. The slowest step determines the deposition rate. A transition between a domain where the deposition rate results controlled by surface phenomenon kinetics and a domain where it is controlled by mass transfer is often observed in the literature and is explained by the  $V = f(X)$  curves (where  $V$  is the deposition rate and  $X$  one of the CVD parameters, like temperature, pressure, and gas flow rate [6]). The effects of the boundary layer are observed in CVD processes where pressures are relatively high. Using low pressures, the hydrodynamic boundary layer is absent and the deposition rate is only determined by the surface decomposition of the reactant molecules [12].

For most inorganic source species, an activation of the chemical reaction needed to deposit the solid is generally required. This could be supplied by heating the substrate, if stable enough, to an adequate temperature, usually in the range of 900–1200°C.

The CVI process can be considered as directly derived from CVD. In this case, a porous fibrous preform is commonly used as the starting material for the subsequent infiltration. With respect to CVD, the CVI process has the aim to obtain a fully densified material. Consequently, the deposition of solid in the pore network of the preform (in-depth deposition) has to be favored over external surface coating in CVD. Therefore, the processing time needed to completely infiltrate a porous preform in conventional CVI techniques will result much longer than the deposition time in CVD.

In the isothermal process, there are no temperature or pressure gradients along the pore inside the preform. The fibrous preform is placed in a uniform temperature zone of a furnace (hot-wall reactor), up to the CVI temperature. Pressures are typically below 100 mbar and are kept constant throughout the complete deposition process. The gaseous precursors flow through the heated reactor, come into the preform where the decomposition reaction takes place, and the matrix is formed inside the preform. In many CVI processes, there is a large increase in the volume of the gaseous materials

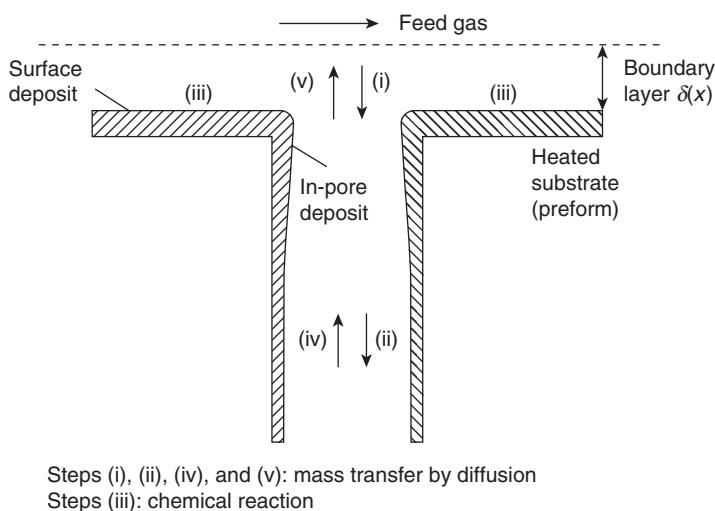


**Figure 9.3.** The different steps in the I-CVI process (adapted from Naslain et al. [6]).

due to the decomposition of the precursor. Thus, fresh precursor compounds have to diffuse into the pores against a higher flow of by-product species incoming in the opposite direction. The mass transfer mechanism by which the precursor gases flow throughout the preform, and the gaseous by-products exit the preform, is governed by chemical diffusion due to the concentration gradients existing between the entrance and the bottom of the pores inside the preform. Owing to this mechanism, the deposition of the solid matrix will take place preferentially near the outer surface of the preform.

Naslain et al. [6] divided the I-CVI process in five steps, as represented in Figure 9.3:

- (i) diffusion of the reactants through the external boundary layer;
- (ii) diffusion of the reactants along the pore length in order to reach any point of the inner surface of the pore;
- (iii) chemical reaction for the deposition of the solid inside the preform;
- (iv) diffusion of the gaseous by-products resulting from the decomposition reaction in the opposite direction, first along the pore length toward the pore entrance; and
- (v) diffusion of the gaseous by-products across the external boundary layer.

The dimensionless Thiele number  $\phi$  (Eq. 9.1), originally developed in the catalyst field [13], is a helpful parameter to approach the I-CVI process, considering the heterogeneous decomposition reaction on the surface of a hypothetical straight and cylindrical pore, at a uniform temperature:

$$\phi = \sqrt{\frac{2k_s \cdot L^2}{D \cdot R}}, \quad (9.1)$$

where  $k_s$  is the first-order reaction rate;  $D$  is the diffusivity of the multicomponent gas mixture; and  $R$  and  $L$ , respectively, are the initial radius and length of the pore.

Fitzer [14] introduced an effectiveness factor,  $\eta$  (Eq. 9.2), related to the Thiele number as follows:

$$\eta = \frac{\tanh \phi}{\phi}. \quad (9.2)$$

The effectiveness factor  $\eta$  plays an important role during the ceramic deposition inside the pore. In fact, the  $\eta$  value should be close to the unit to promote in-pore deposition, and this condition was found to be verified when  $\phi < 0.4$ . Therefore, the maximum depth for infiltration resulted to be limited by a maximum value,  $L_{\max}$ , expressed as

$$L_{\max} \leq 0.4 \left[ \frac{R \cdot D}{2 \cdot k_s} \right]^{0.5}. \quad (9.3)$$

The knowledge of chemical and physical phenomena involved in the CVI process can enable not only the obtainment of the optimal operating conditions such as pressure, temperature, reactor geometry, and flow rates but can also lead to better characteristics of the material in terms of deposition rate, uniformity, and composition of the deposit. For example, it has been shown that the mechanical properties of the CMCs are highly dependent upon nucleation and growth processes [15]. In particular, it has been demonstrated that better mechanical performance is reached in case of faceted deposits, well-developed columnar deposits, and fine-grained microstructures, which are the most common microstructures obtained by CVI [6].

Therefore, many studies have dealt with modeling of the surface kinetic mechanisms describing the thin film growth dynamics during CVI processes. Their implementation represents a big challenge for researchers because the physicochemical phenomena involved are highly complex. These include modeling of the mass transport of precursor and carrier gases, as well as gaseous by-products both in the reactor and inside the preform, and modeling of gas-phase decomposition reactions and of the surface reactions leading to ceramic deposition. In addition, the preform structure changes and evolves during the infiltration time. For this reason, CVI modeling requires a multiscale approach: from process scale down to atomic scale [16].

A summary of the studies on chemistry mechanisms of the formation of silicon carbide from chloromethylsilane precursors and carbon from hydrocarbon precursors is reported in the following paragraphs.

**9.1.2.1 Chemistry of Silicon Carbide Formation.** Models so far proposed to optimize and scale-up CVI processes have reached a high level of sophistication as far as the geometry and mass transfer conditions are concerned, but the kinetic schemes used often neglect the underlying chemistry. This leads to significant deviations from the experimental behavior.

Experiments have demonstrated that methyltrichlorosilane (MTS) is an ideal precursor for producing high-quality beta-silicon carbide ( $\beta$ -SiC) by using the CVD

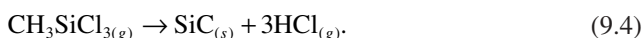


technique [17]. One possible reason is that the Si:C 1:1 ratio in MTS is the same as the Si:C ratio of the SiC deposit. Another motivation may be that the by-product HCl derived using MTS as a precursor might contribute to suppress the deposition of pure Si crystal during the growth of SiC films or crystals. Besides, the H<sub>2</sub> carrier gas may favor the reduction of the Si-Cl bonds on the growing surface of SiC, resulting thereby in an increase in deposition rate.

Two steps are involved in the deposition of SiC from MTS: the unimolecular gas-phase decomposition of MTS and the heterogeneous reaction of Si and C containing by-products on the surface to give SiC. Both of these steps can be rate limiting depending upon process conditions, for the high activation energy of the first stage and, in the second stage, for the adsorption of gaseous species that can either contribute to the deposition or limit it by blocking the free sites available. Therefore, the composition of the gas phase must be known to predict the actual rate of deposition.

Over the past few years, considerable progress has been made in the understanding of the chemical mechanism of SiC deposition from MTS, and several kinetic models have been proposed.

The formation of the SiC matrix occurs according to the overall decomposition reaction of MTS with hydrogen or argon as gas carrier:



The silicon carbide deposit can contain a second phase, either free carbon, when MTS is decomposed in an inert atmosphere, or free silicon, when hydrogen is used as the carrier gas [18]. Thermodynamic studies have indicated that the preferential deposition of SiC, with respect to C, is favored only when a high ratio  $\alpha = \frac{P_{\text{H}_2}}{P_{\text{MTS}}} = \frac{Q_{\text{H}_2}}{Q_{\text{MTS}}} (\alpha > 20)$  is used, but lower than 1000 to avoid silicon codeposition [19]. The experimental data show  $\alpha$  ranges more shifted to lower values, probably due to kinetic factors [20]. The use of pressures below 0.1 atm and temperatures above 1000 K enables theoretical yields up to over 80% in SiC [21].

Some authors [18, 22] proposed that the rate of SiC deposition is of first order with respect to MTS and follows an Arrhenius relationship:

$$S = k_0 [\text{CH}_3\text{SiCl}_3] \exp\left(-\frac{E_A}{RT}\right), \quad (9.5)$$

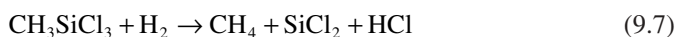
with an activation energy  $E_A = 120$  kJ/mol and a pre-exponential factor  $k_0 = 26.2$  cm/s. According to Besmann and Johnson [23], the kinetics is of zero order, at  $P = 3.3$  kPa,  $T = 1000^\circ\text{C}$ , and  $5 \leq \alpha \leq 20$ . The deposition rate does not depend upon MTS concentration and can be expressed as

$$S = k_0 \exp\left(-\frac{E_A}{RT}\right), \quad (9.6)$$

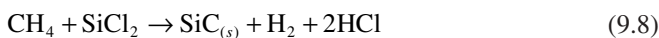
with an activation energy  $E_A = 188$  kJ/mol and a pre-exponential factor  $k_0 = 26.77$  cm/s.

This disagreement between the kinetic data is typical of phenomena controlled by diffusion. Then, the need for reliable kinetic data and the contrast among the data reported in literature have brought an intensification of kinetic studies on SiC decomposition from MTS. The reaction mechanism involves several intermediate stages. From thermodynamic data, Langlais and Prebende [24] showed that, in a certain range of experimental conditions  $1 \leq P \leq 20$  kPa,  $1100 \text{ K} \leq T \leq 1300$  K, and  $10^2 \leq \alpha \leq 10^4$ , the precursor gaseous species with larger concentration in the gas phase are  $\text{CH}_4$  and  $\text{SiCl}_2$  rather than MTS. As a consequence, they proposed the following two-stage mechanism:

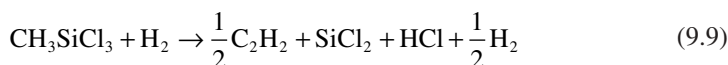
- (i) Homogeneous decomposition of MTS in the presence of hydrogen:



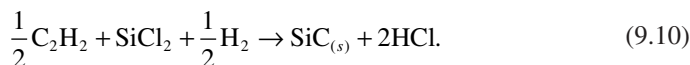
- (ii) Heterogeneous reaction for SiC deposition:



For other specific conditions (higher temperatures, lower pressures, and lower composition ratios), the same authors found that  $\text{C}_2\text{H}_2$  substitutes  $\text{CH}_4$  in the gas phase, contributing to the deposition process, as follows:



and



A study by Papasouliotis and Sotirchos [25] on the homogeneous deposition of MTS, based upon thermodynamic equilibrium, has confirmed the hypothesis of the role of acetylene and of  $\text{SiCl}_2$ , as main carbon and silicon precursors. It was found that as the total pressure, hydrogen content, and temperature increase, the formation of hydrocarbons that can react on the surface becomes kinetically favored. Moreover, the almost total absence in the gas phase of compounds containing Si-Si or Si-C links confirms that SiC deposition occurs in a two-stage process, involving two separate parallel reactions leading to the formation of Si and C.

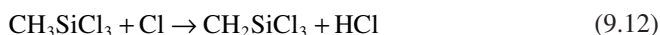
In addition, Schlichting [18] proposed the formation of cyclic carbosilanes with three to eight Si atoms, following MTS decomposition, by radical reaction in the gas phase. More recently, Allendorf and Melius [26], by means of ab initio calculations, evaluated the thermodynamic properties of the Si-C-Cl-H system and estimated the

kinetics of the reactions contributing to the depletion of MTS in the gas phase [27, 28]. According to this study, the most important reactions are the following:

- (i) The first-order unimolecular deposition of MTS via Si–C bond scission:



- (ii) The bimolecular H-atom abstraction from MTS by Cl:



- (iii) The  $\text{SiCl}_2$  insertion into a Si–Cl bond on MTS:



Atomic chlorine can be formed for the equilibrium between  $\text{SiCl}_3$  and  $\text{SiCl}_2$ :



or during the reaction of atomic hydrogen with HCl:



leading to the formation of molecular hydrogen. Also, taking into account the high activation energy of Equation 9.11 equal to 81.3 kcal/mol, it is clear from these reaction pathways that the overall decomposition reaction is of first order with respect to MTS. The rate of the recombination of the  $\text{CH}_3$  and  $\text{SiCl}_3$  radicals, that is, the reverse of Equation 9.11, was measured by Niiranen and Gutman [29] to be  $1.1 \cdot 10^{10} \text{ cm}^3/\text{mol s}$  at 303 K, while Osterheld and coworkers [27] calculated a value of  $2.4 \cdot 10^{10} \text{ cm}^3/\text{mol s}$  at the same temperature and pressure.

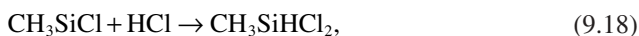
The other by-products of the reaction,  $\text{CH}_4$  and  $\text{SiCl}_4$ , are mainly produced by the bimolecular reaction between the methyl radical and hydrogen chloride:



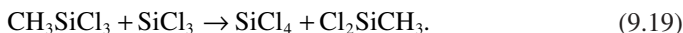
which also produces atomic chlorine and, during the decomposition reactions of  $\text{CH}_3\text{SiCl}_2\text{SiCl}_3$ , formed from  $\text{SiCl}_2$  insertion into MTS:



and



and, in minor proportion at high dilutions, by the abstraction of Cl from MTS by  $\text{SiCl}_3$ :



Atomic hydrogen can be produced by the reaction of radical  $\text{CH}_3$  with molecular hydrogen:



a reaction that is well-known from combustion studies [30]. Other reactions of  $\text{CH}_3$  and  $\text{SiCl}_3$  with MTS are probably less important at high dilutions:



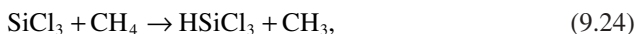
and



Trichlorosilane is produced by the reaction of  $\text{SiCl}_3$  with hydrogen or methane:



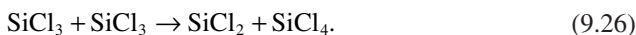
and



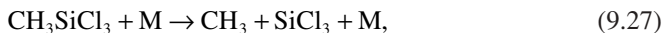
and subsequently partially decomposes to  $\text{SiCl}_2$  and  $\text{HCl}$ :



Between  $\text{SiCl}_2$ ,  $\text{SiCl}_3$ , and  $\text{SiCl}_4$ , a disproportionation equilibrium exists:

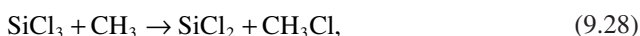


Few experimental studies have been carried out on the gas-phase decomposition of MTS. Besmann and Johnson [23] and Burgess and Lewis [31] studied the kinetics of MTS gas-phase decomposition, respectively, by means of mass and infrared spectrometry. Mass spectrometry provided evidence for the formation of three products:  $\text{CH}_4$ ,  $\text{HCl}$ , and  $\text{SiCl}_4$ , when hydrogen or helium was used as a carrier gas.  $\text{CH}_3$  and  $\text{Cl}$  radicals were also detected. Trapping experiments carried out with ethylene and acetylene showed that a significant concentration of the  $\text{SiCl}_3$  radical is present during MTS decomposition. It was also shown that the decomposition rate is faster in hydrogen than in helium, probably due to different collision interactions with the two carrier gases. They proposed for the unimolecular MTS decomposition:



where  $M$  is a collision partner, a molecule of the carrier gas or another MTS molecule, depending upon their relative abundance, and suggested a radical chain mechanism in

hydrogen, but not in helium. Similar results were obtained by Ganz et al., by the application of *in situ* coherent anti-Stokes Raman spectroscopy (CARS) [32] on the CVD of SiC in a low-pressure hot-wall reactor. In this study, the concentration of hydrocarbon compounds, such as ethane, ethylene, and acetylene, whose presence is predicted by several thermodynamic studies, was below detection limits in the hot-zone outlet of the reactor, but traces of  $C_2H_4$  were noticed by an *ex situ* mass spectrometer analysis. Evidence for the formation of chlorinated hydrocarbons was also reported in the same work, although it was not possible to conclude whether this resulted from the formation of  $CHCl_3$  or other products as  $H_2C=CCl_2$  and  $H_2C=SiCl_2$ . Ganz et al. [32] also reported the idea suggested by Allendorf and Melius [26] that the  $CH_3$  and  $SiCl_3$  radicals, apart from associating, can give rise to



although only the species  $SiCl_2$  has been detected in their study, while  $CH_3Cl$  was detected by *in situ* Fourier transform infrared (FTIR) emission spectroscopy by Hopfe et al. [33]. This work substantially supports the kinetic model proposed by Allendorf and Melius [26], although the formation of the high surface reactivity species silaethylene  $CH_2Si=Cl_2$  by 1,2-elimination of HCl has not been observed experimentally so far:



To contribute to clarify the growth kinetics of SiC by CVD, Sone et al. [34] have studied the influence of temperature and partial pressure of MTS ( $P_{MTS}$ ) on growth rates by *in situ* measurements of growth rates, obtained from the deposited weight using a modified thermogravimeter. They considered some adsorption models in order to analyze the dependence of the growth rates on  $P_{MTS}$ . A modified two-site competitive adsorption model (modified Langmuir–Hinshelwood model) resulted the best fitting for the experimental growth rates calculated. At lower temperatures, surface reactions limited the growth rates, while vapor mass transfer limited them at higher temperatures. They concluded, on the basis of adsorption coverage of  $CH_3$  on Si sites and  $SiCl_3$  on C sites, that the amount of adsorbed  $CH_3$  on Si sites is the main factor that controls the growth rates of SiC.

Recently, Ge et al. [35] have tried to clarify the mechanism of the SiC deposition by a theoretical thermodynamic study of the pyrolysis of MTS in the gas phase using second-order perturbation theory (MP2). They reported the necessity to investigate systematically and carefully the gas-phase chemistry of SiC by a theoretical point of view because the mechanisms proposed from kinetic modeling, based on the analysis of experimental data, are often incomplete or inaccurate due to the complexity of the gas-phase chemistry of SiC during the deposition. They presented and discussed the detailed reaction schemes for the production and consumption of the gas-phase species, the corresponding transition state structures, and the related thermodynamic and kinetic data compared to the experimental thermodynamic properties of various species. They reported several ways to choose significant reactions occurring in the gas phase: (1) to evaluate available experimental data in order to decide what species present high concentrations in the gas phase, (2) to review the reaction mechanism proposed in the

scientific literature and to select reasonable reactions, and finally, (3) to search for the reaction rate constants derived experimentally and/or theoretically. Ge et al. [35] observed the difficulty to propose a mechanism for the gas-phase chemistry involving MTS as precursor and  $H_2$  as carrier gas at high temperature; consequently, no reactions are initially eliminated in their study.

**9.1.2.2 Chemistry of Carbon Formation.** The most versatile deposition process used for  $C_f/C$  composites [4] is the thermal decomposition of a hydrocarbon gas starting from a porous preform typically made of polyacrylonitrile (PAN).

Two basic parameters affect the different types of allotropic forms of carbon, even if crystalline or noncrystalline: the nature and phase of the precursor and the way to deliver energy to the process.

The precursors are generally alkanes (such as methane or propane), but sometimes nonsaturated hydrocarbons (such as acetylene or propylene) or aromatic compounds (benzene and derivatives) can be used because they decompose at a lower temperature than the alkanes.

Two classes of reactions can be considered from all the numerous experimental studies carried on in order to outline an overall reaction model [4]:

- (i) homogeneous gas-phase reactions and
- (ii) heterogeneous surface reactions.

In the first type of reaction (i), radical processes are favored, giving birth to free radicals, which are recombined immediately. In this step, nonsaturated species as allenes, propyne, and butadiene are formed. After the formation of these aliphatic compounds,  $C_3$  and  $C_4$  cyclization processes occur, while at longer deposition times, aromatics and polyaromatics are produced.

Type (ii) reactions are fundamental for the rate of formation of pyrocarbons, from the nucleation and the growth processes on a given substrate. The presence of a “catalyst” is a predominant factor that influences the kinetic of this surface reaction, for example, a transition metal or a gaseous reagent such as  $H_2$ ,  $O_2$ , or  $Cl_2$ .

In his review on the infiltration processes of carbon materials, Delhaes [4] reported a simplified reaction scheme shown in Figure 9.4 for PyC deposition where aliphatic

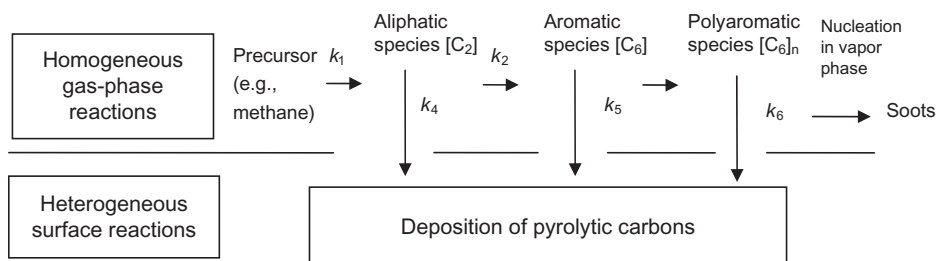


**Figure 9.4.** Reaction scheme for pyrocarbon deposition (adapted from Delhaes [4]).

formation ( $C_2$  route) involves species such as ethylene or acetylene, while the  $C_6$  aromatic route concerns aromatic compounds (e.g., benzene and polyaromatics). Due to the homogeneous nucleation in the gas phase, the formation of droplets also occurs at enough long residence times.

The kinetics of pyrocarbon deposition can be, in general, represented by an Arrhenius plot describing the typical heterogeneous reactions of gases with porous solids.

The main requirements for  $C_f/C$  composites are the quality of the matrix and the interfacial behavior. The quality of the matrix is associated with the type of the microstructure and the bulk density related to the presence and the shape of voids, residual porosity, and cracks. Also, the type of deposited PyCs has to be examined, which depends on the experimental parameters and the techniques used. Three main microstructures can be identified [4]: smooth laminar, rough laminar, and isotropic carbon. The rough laminar PyC is usually preferred due to its good high-temperature behavior (up to  $2000^\circ\text{C}$  except under oxidizing atmosphere) and mechanical performances, related to more dense grain structure, graphitability (graphitization degree), and low residual porosity. The mechanical properties are related to the mechanism of transfer of the load from the fibers to the matrix. To this aim, a good compromise between strong and weak bonding at the fiber–matrix interphase is needed [7].

The modeling of the CVI process for  $C_f/C$  composites finds its basis on the investigated CVD of pyrolytic carbon from light hydrocarbons such as methane, ethylene, acetylene, and benzene. Widely accepted results of these studies are the following: (1) Hydrocarbon species produced by gas-phase reactions present an increasing number of carbon atoms; (2) hydrocarbons with increasing size show higher deposition rates, but the inhibition of carbon deposition by hydrogen from hydrocarbons also increases due to different molecular structures; and (3) the rate-controlling step of carbon deposition should be the dissociation of carbon–hydrogen surface complexes [4].

In the past, the models developed to simulate the growth of a C matrix on fibers were based on only an overall reaction [36], with particular regard to modeling physical properties like surface area, gas permeability, and mass/heat transfer. During the past decade, many chemical reaction mechanisms have been proposed to model pyrolytic carbon deposition [37] from light species to aromatic species. More recently, Li and Deutschmann have reported an advanced transient 2-D simulation of CVI for the densification of C-fiber felts with pure  $\text{CH}_4$  or mixtures of  $\text{CH}_4$  and  $\text{H}_2$  as carrier gases [38]. This model is based on the multistep reaction and deposition model, taking into account the inhibiting effect of hydrogen on carbon deposition.

**9.1.2.3 CVI Modeling.** Important drawbacks of the I-CVI process are nonuniform preform densification and a high residual void fraction (porosity) of the composite. In order to achieve a relatively uniform infiltration, it is important that the mass transport rate results higher than the deposition rate. By this way, extremely long process times are required, up to several weeks in some cases. Therefore, the most important challenge in the I-CVI process is finding the optimal technological parameters, which minimizes the infiltration time and allows the required material quality.

To this aim, numerical modeling can become a helpful tool for the study and optimization of I-CVI. An examination of the available literature shows that there is a large

number of publications on CVI modeling [39], but most of the papers generally described 1-D models where only the phenomena occurring inside the preform have been considered, while the transport processes in the whole reactor have not been taken into account.

In fact, the description of the growth mechanism occurring during CVI through an accurate mathematical model is extremely complex [40] since the time and length scales where chemical and physical processes take place differ by several orders of magnitude (macroscale, mesoscale, microscale, and atomic scale). A macroscale model is frequently adopted if the scope of the modeling is the optimization of the film growth rate and its profile. A mesoscale model is used when the interest is toward the study of the filling between the pores. A microscale modeling can aid to investigate the film morphological evolution, while atomistic models are usually used to examine the surface and gas-phase chemistry.

In the work by Kulik et al. [41], a 2-D model of I-CVI process considering the whole reactor was developed and used for simulation of I-CVI for the production of a SiC matrix composite by analyzing flow patterns and the thermal field and distributions of species concentrations in the fibrous preform and in the gas region of the reactor. Conjugate heat and mass transport phenomena were considered for system included a 3-D-preform (the porous medium), gaseous precursors and gaseous by-products, and the solid parts of the reactor.

The model was developed for the study and optimization of I-CVI, but it could be extended also to thermal-gradient and forced-flow CVI (F-CVI).

Even if CVI modeling has reached a rather mature stage, fully integrated multiscale approaches are not yet well developed, as Vignoles [16] reported in a recent review on this subject. A multiscale model should intend to deal simultaneously with all the scales recognized in the CVI process, such as (1) a macroscopic scale (the whole reactor cavity and the preform, considered as a homogeneous medium), (2) one or more scales related in details to the pore space (their dimensions depend on the type of preforms and fabrication methods), and finally, (3) a “molecular” scale referring to the dimension of the molecules and the species reagent between each other and with the substrate. Vignoles [16] proposed a global scheme to summarize all knowledge and obtain a unique modeling tool to be used for predictions and for infiltration process parameter optimization. Three critical issues were identified: (1) reaction scheme kinetics, which involve homogeneous and heterogeneous reactions; (2) models of porous media at various densification levels, related to the description of geometry and transfer mechanism; and (3) appropriate methods for coupling.

## 9.2 DETAILED DESCRIPTION OF THE CVI METHOD

The CVI methods can be divided into several categories, depending on [2]

- the heating method: radiative or inductive;
- whether the process is isothermal (uniform temperature) or there is a thermal gradient across the perform;



- the use of plasma or other different heating methods, such as radiative or inductive;
- the type of reactor: cold wall or hot wall;
- the pressure regime: atmospheric or low pressure;
- whether the process is isobaric (pressure uniform on the preform) or a pressure gradient across the preform (forced-flow, pulsed pressure) is imposed; and
- the immersion of the preform in a precursor liquid.

As reported by Golecki [2], the various infiltration methods are at different levels of technological and industrial maturity; in some cases, data on particular methods of infiltration are unpublished or unavailable.

In Figure 9.5, the principal known CVI methods are schematically depicted. A brief description of the main processes is given below.

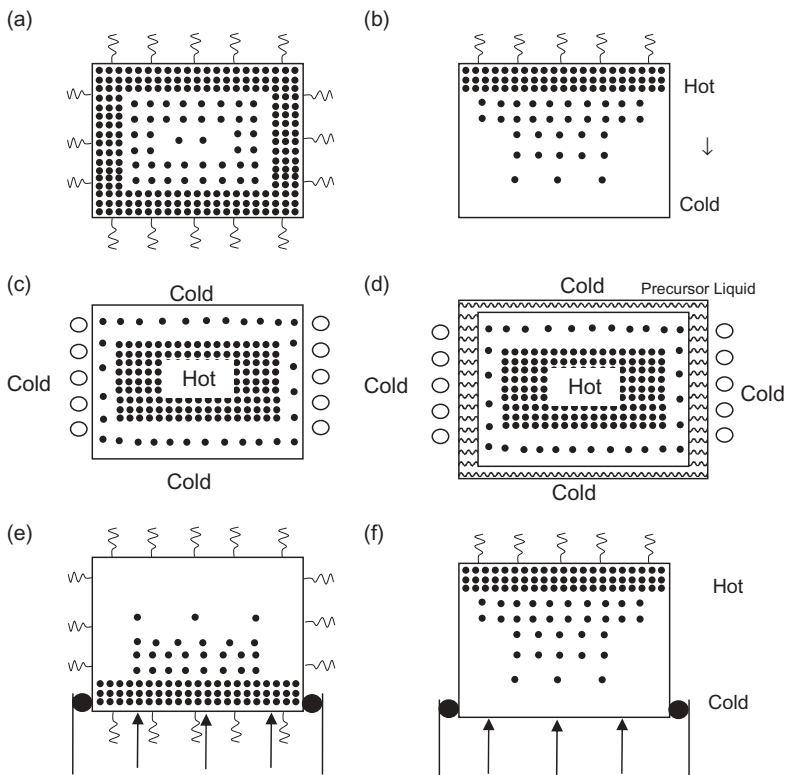


**Figure 9.5.** Principles of the main chemical vapor infiltration (CVI) methods: (a) isothermal radiantly heated (isobaric CVI), (b) thermal-gradient radiantly heated (isobaric CVI), (c) thermal-gradient inductively heated (isobaric CVI), (d) liquid immersion thermal-gradient inductively heated (isobaric CVI), (e) isothermal radiantly heated (forced-flow CVI), (f) thermal radiantly heated (forced-flow CVI) (adapted from Golecki [2]).

### 9.2.1 Isothermal/Isobaric CVI (I-CVI)

In the I-CVI (Fig. 9.5a), the fibrous preforms are set in the isothermal zone of a hot-wall deposition chamber [42]. The gaseous precursor flows outside the preforms by convection and inside the preforms by diffusion. Deposition is performed at relatively low temperatures, which decreased reaction rates, and under reduced pressures (subatmospheric or atmospheric, depending on the particular process) to promote the diffusion of the gaseous species in the pores. In these conditions, it is possible to avoid an early sealing of the pore entrance by the deposit. Therefore, the deposition yield and deposition rate are low. If necessary, due to the fact that deposition occurs preferentially near the pore entrance, the infiltration process is stopped and the preform surface machined in order to reopen the porosity or to enlarge the pore entrance.

In fact, keeping the preform porosity open until the end of the densification process is the key point of the CVI process. If the outside temperature of the preforms is higher than the interior one, the deposition will be preferential at the exterior of the preform and does not advance in the interior of the sample.

I-CVI is the oldest approach (in use since the 1960s) for the densification of refractory composites [2]. Nowadays, the I-CVI process is used for the densification of  $C_f/C$  composites [43] (e.g., for aircraft brakes) and  $SiC_f/SiC$  composites [3] (e.g., for aerospace components). The matrices more commonly produced by isothermal, isobaric CVI included [6]:  $SiC$ ,  $C$ ,  $Si_3N_4$ ,  $BN$ ,  $Al_2O_3$ ,  $B_4C$ ,  $TiC$ , and  $ZrO_2$ .

### 9.2.2 Thermal-Gradient CVI

In the thermal-gradient CVI [2], there is a thermal gradient through the thickness of the porous preform (Fig. 9.5b,c). The gaseous precursors come into the preform through the cold side, move through the preform by chemical diffusion, and decompose near the hot side depositing the solid matrix, allowing a reduction of the porosity near the hot side. In this technique, the preform can be heated more uniformly because the thermal conductivity of the infiltrated preform increased. So the highest temperature region moves toward the cold wall. Since the deposition front follows the thermal front, the infiltration progresses uniformly from the hot side to the cold side. Therefore, only large individual parts can be densified via thermal-gradient methods, such as rocket nozzles. Similar to I-CVI, due to the diffusion mechanism that governs all the reaction, the infiltration times in thermal-gradient CVI are usually long, in the order of weeks.

### 9.2.3 F-CVI

In F-CVI, the precursor reagents are made to flow through the preform and along the pore under high pressure ( $P_1 = 100\text{--}200$  kPa), while the by-products (and the unreacted species) are removed at a lower pressure,  $P_2$ . The F-CVI process exists in two different variants: isothermal F-CVI and thermal-gradient F-CVI.

In the isothermal F-CVI [44], a forced flow of reagents passes through a uniformly heated (isothermal) preform where the decomposition of the gases takes place (Fig. 9.5e). The process continues until some portion of the preform reaches a sufficiently

high density, and it become essentially impermeable to the flux of gases. At this point, the process can be considered terminated, even though other portions of the preform may present a much lower density. In particular, the regions of the preforms, where the density will be higher, are those nearer the preform surface where the reagent concentration is the maximum since the reagent gases enter there first.

In the thermal-gradient F-CVI, an inverse thermal gradient (Fig. 9.5f) can be applied along the pore. This allows the decomposition of the solid matrix near the hot side, thus reducing the porosity near the hot side. The thermal-gradient F-CVI technique was proposed by Caputo et al. [45] in the mid 1980s as an alternative process to I-CVI. Their first work was on the infiltration of SiC and Si<sub>3</sub>N<sub>4</sub> matrices in different porous preforms, in which the mass transfers were allowed by forced convection due to a pressure gradient. Therefore, the thermal conductivity of the infiltrated preform resulted to an increase, and the preform can be heated in a more uniformly way because the infiltration progresses uniformly from the hot side to the cold side. This process takes advantage of both a thermal gradient as well as forced flow of the reacting gases through the preform that enter from the cold side of the perform, allowing the matrix deposition within the preform regions where the temperature is sufficiently high.

The main advantage of the F-CVI is the significant decrease in the overall infiltration time, in comparison to the processes described before. Lackey and Starr [10] reported infiltration times of the order of 10–24 h for SiC matrix and a few hours for carbon, even for preforms more than 2.5 cm thick. Besmann et al. [46] showed the feasibility of fabrication of SiC<sub>f</sub>/SiC components approaching 30 cm in width and 2.5 cm in thickness by F-CVI.

### 9.2.4 Pulsed-Flow CVI (P-CVI)

In P-CVI [47], the furnace and the fibrous preform pore network are first evacuated by pumping, and second, the reactants are injected very quickly into the reaction chamber and inside the preforms. The solid deposition takes place during a given time, referred to as the residence time. By this way, the pore network of the preform is periodically fed with fresh reactants when the reaction products are cyclically removed. If the composition of the precursor is periodically changed, P-CVI allows the formation of multilayered ceramic deposits. For example, a multilayered PyC–SiC interphase can be deposited *in situ* on the fiber surface if a C<sub>3</sub>H<sub>8</sub> precursor is switched from an MTS/H<sub>2</sub> gas mixture [48, 49].

Due to the large furnaces needed for this process, the industrialization of the P-CVI has still not been achieved to the same degree as to that of the processes described earlier, as the practicality of for this process remains to be determined.

### 9.2.5 Microwave-Heated CVI (MW-CVI)

The use of microwave radiation is a potentially attractive alternative due to its potential for generating a controllable inverse temperature profile during the heating of a ceramic fiber preform [50, 51]. Volumetric heating of the dielectric coupled with surface heat losses results in the center of the component being hotter than the surface, potentially

by up to several hundred degrees centigrade. This allows the MW-CVI process to initiate at the center and then the reaction front to move toward the surface as the dielectric characteristics of the preform change. Premature pore closure due to crusting is completely avoided, potentially allowing densification to occur an order of magnitude faster than with I-CVI. Experimental work has yielded this inside-out densification pattern in a number of different ceramic systems, including SiC, Si<sub>3</sub>N<sub>4</sub>, Al<sub>2</sub>O<sub>3</sub>, and ZrO<sub>2</sub>.

**9.2.5.1 Recent Advances in the MW-CVI Technique.** The MW-CVI process has recently received much attention for its potential to produce a controllable temperature profile inside a preform [50–54]. Different from conventional heating, this method allows the creation of a temperature gradient from the center of the preform to its periphery [50]. The surface of the sample can be cooler than the bulk because it releases heat by conduction/convection or radiation to the surrounding atmosphere and to the cavity walls, which are much colder because they are built with low dielectric loss materials. Therefore, the deposition of the ceramic matrix proceeds from the inside to the outside, avoiding the problems connected with the sealing of the outer pores of the preform [51]. By means of the MW-CVI process, high-purity and high-density SiC matrices can be obtained and preforms of very complex geometry can be successfully infiltrated, at operating temperatures between 900 and 1200°C. Since the pressure required by the process is low (1–100 kPa), the damage of fibers and their reactions with the matrix are limited. Previous works carried out by Binner et al. [50, 55], based on SiC<sub>f</sub>/SiC components (50-mm diameter, 10 mm thick), have shown that by using microwaves to enhance the CVI process, fabrication times can be reduced from hundreds of hours to around 30 h.

Together with the advantages of microwave heating described above, some technical difficulties are associated with the possible insurgence of thermal instabilities (*thermal runaways*). In fact, in a multimode applicator, which is more suitable for heating large objects with a complex shape, the intensity of the electromagnetic field varies from point to point due to the formation of stationary waves. This means that a given specimen to be heated may receive an amount of energy which varies from point to point. This can be a major problem in materials, like ceramics, characterized by low thermal conductivity resulting in a nonhomogeneous distribution of temperature with some points much hotter than the surrounding material (hot spots). Since, for many ceramic materials, dielectric properties increase exponentially with temperature, the hot spots can reach extremely high temperatures even leading to local fusion of the material. These inhomogeneities in local temperature can even give rise to high internal stresses in the material due to the differential thermal expansion, with formation of cracks and even leading to the fracture of the sample during heating. Therefore, in order to make the most of the microwave heating in this type of application, the prediction of the temperature profile, the electromagnetic field, and the prevention of thermal instabilities is of fundamental importance.

An innovative MW-CVI pilot plant has been recently developed [53, 54] in order to produce SiC-based CMCs. A schematic representation of the MW-CVI reactor is reported in Figure 9.6. The conventional CVI process was modified and supplemented in order to reduce the CVI process time and to lower the cost of this usually expensive

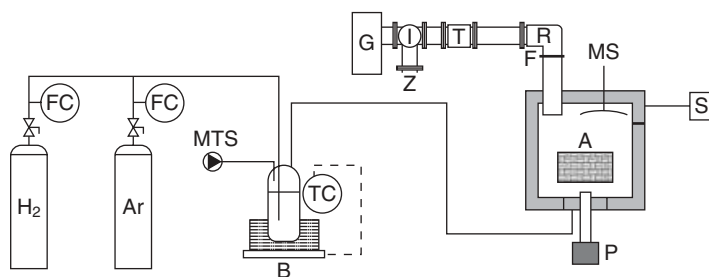


**Figure 9.6.** Schematic representation of the MW-CVI reactor (G, generator 2.45 GHz, 6 kW; I, three-port circulator; Z, water-cooled dummy load; T, autotuner; R, connected transition; F, quartz window; A, applicator; MS, mode stirrer; P, pyrometer; S, scrubber system; B, bubbler; FC, feed controller; TC, temperature controller) (adapted from Lazzeri et al. [53]).

process. In the literature, a few examples of MW-CVI processes are reported [50, 55], but only at the laboratory level. An important characteristic of this innovative research is that typical lab-scale technical solutions that are not suitable for industrial production plants have been carefully avoided in order to easily carry out a scale-up of this process and to design a pilot-scale reactor. A coupled thermal and electromagnetic model was developed by using commercial software in order to easily apply the model to every type of sample geometry. A specifically developed code was written to couple the thermal and electromagnetic analysis in order to simultaneously estimate the electromagnetic field and the temperature profile inside the reactor with a series of iterative calculation steps. Results showed a relatively constant electric field inside the sample and a rather uniform heating. The temperature and the electric field were reasonably constant in the sample, allowing a uniform heating when, in order to improve the process efficiency, a mode stirrer was used to achieve a better distribution of microwave power. The uniform deposition of MTS on SiC-fibers predicted was confirmed by the experimental evidences. An average weight increase of about 70% with respect to the initial sample was achieved in 18 h of microwave treatment. The results obtained during these MW-CVI trials suggest that the optimal heating, the deposition patterns predicted for microwave heating, and the reduced infiltration times are successfully achievable.

## 9.2.6 Rapid CVI Methods

Particularly for C/C composites, two different methods of rapid CVI densification have been developed and industrially applied for full densifications of carbon fiber preforms.

The first method is the so-called boiling film technique (Fig. 9.5d), where the porous fiber preform, which acts as susceptor, is completely immersed in the liquid state precursors (e.g., cyclohexane or toluene, which presents the higher yield in carbon). Due to inductive heating, the liquid boils and the vapor penetrates into the porous substrate. These hydrocarbons thermally decompose and the produced vapors

form a carbon deposit on the fibrous preform, which is thus densified by a process similar to conventional CVI. This technique is very efficient: A single cycle of densification for a few hours [4] is enough to completely densify  $C_f/C$ .

The second method is the rapid vapor-phase densification, where the porous preform, often carbon felt, is placed in a furnace, isothermally heated by means of an outer graphite tool, which allows a forced flow of the precursor gas between the graphite tool and the preform [56, 57].

In rapid CVI, the deposition rate is controlled by the intrinsic surface reactions (kinetic regime), since the diffusion of the gaseous species inside the porous preform is not the rate-limiting step (diffusion regime), as in conventional CVI. For both methods, a higher conversion efficiency is obtained with respect to classical processes, and also a good quality of the product (carbon matrix highly oriented and highly graphitized) is commonly obtained.

Recently, Wang et al. [58] reported the development of an improved film boiling CVI process for the fabrication of large size  $C_f/C$  composites using kerosene as precursor. The composites produced via rapid CVI presented a homogeneous density and microstructure, revealing good feasibility of the film boiling CVI technique also on large components.

## 9.2.7 Technical Equipment for a CVI Apparatus

In general, a CVI apparatus consists of three subsystems: reagent supply, the reactor where the preform is placed, and the effluent gas treatment system. The equipment for the CVI process is schematically shown in Figure 9.7.

In detail, a CVI apparatus consists of several basic components:

- A reagent delivery system for precursor supply to the reactor chamber
- A reactor chamber inside, where the deposition takes place
- A system for introducing and removing substrates, for example, mandrels
- An energy source that provides the energy or heat required to allow the precursors to react or decompose

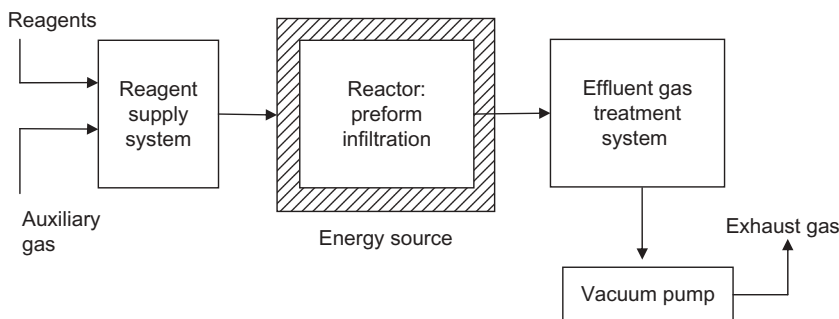


Figure 9.7. Equipment for a CVI apparatus.

- A vacuum system for the removal of volatile by-products from the reaction chamber
- An exhaust treatment system, if exhaust gases are not suitable for release into the atmosphere and require treatment or conversion to safe/harmless compounds
- A process control equipment such as gauges, controls, alarms, and safety devices to monitor process parameters like pressure and temperature

**9.2.7.1 Energy Sources.** The suitable heating sources for CVI processes include the following:

- Resistive heating (tube furnaces)
- Radiant heating (halogen lamps)
- Microwave heating (volumetric heating)
- Radio frequency heating (induction heating)
- Lasers
- UV–visible light

Standard furnaces used for CVI are rated for use up to 1600°C, with an optional upgrade to 2200°C for PyC graphite and other high-temperature deposition processes. CVI vacuum furnace vessels are manufactured with stainless steel, including the chamber, water jacket, and all flanges. Graphite hot zones are used on the CVI vacuum furnaces, including graphite resistance heating elements and low-density fibrous graphite insulation.

CVI vacuum furnaces usually present a gas supply system including mass flow controllers, automatic pressure control systems, rotameter flow indicators, and so on.

Temperature measurements can be carried out with a thermocouple, or optionally with an infrared pyrometer.

**9.2.7.2 Precursors.** Since during CVI the materials are deposited from the gaseous state, precursors for CVI processes must be volatile but at the same time stable enough to allow their delivery to the reactor chamber.

In general, precursor reagents provide only a single compound to the infiltrated preform, while by-products are volatilized during the process. However, in some cases, precursors may provide more than one compound, allowing a simplified delivery system with a reduction of the number of reactants required by the infiltration.

The most used CVI precursor materials are  $\text{CH}_4$ ,  $\text{CH}_3\text{SiCl}_3$ ,  $\text{BCl}_3$ ,  $\text{TiCl}_4$ ,  $\text{NH}_3$ ,  $\text{SiCl}_4$ ,  $\text{AlCl}_3$ , and other metal-organic compounds, complexes, and ligands.

**9.2.7.3 Materials That Can Be Produced by CVI Processes.** CVI is an extremely versatile process that can be used to process many ceramic compounds. Some of these include the following:

- Carbon: C
- Carbides:  $\text{SiC}$ ,  $\text{B}_4\text{C}$ , and  $\text{TiC}$

- Nitrides: BN and  $\text{Si}_3\text{N}_4$
- Borides:  $\text{TiB}_2$
- Oxides:  $\text{Al}_2\text{O}_3$  and  $\text{ZrO}_2$

Deposits usually grow in radial orientation around the filaments of the fibers. The silicon carbide matrix deposited by a CVI process is a homogeneous  $\beta$ -SiC with very fine crystalline structures. The carbon or BN coating of the fibers has a similar graphitic structure with the planes parallel to the filament surface.

**9.2.7.4 CVI Gaseous By-Products.** Volatile gases as a by-product of the CVI process are often neglected. Nevertheless, these gases may be toxic, corrosive, flammable, or explosive; therefore, an appropriate treatment is often needed.

In addition, a careful analysis of the gaseous by-products of a CVI process can also lead to an enhanced understanding of the CVI reaction mechanisms in order to get more information useful to refine the process.

## 9.3 APPLICATIONS IN PROCESSING/FABRICATION OF CERAMICS AND COMPOSITES

### 9.3.1 Main Properties and Applications of CVI-Processed CMCs

The main interest of fiber-reinforced ceramics is due to their nonbrittle mechanical behavior and improved reliability with respect to monolithic ceramic. This nonbrittle performance is strictly influenced by the processing, and in particular, it is observed only for well-processed materials. The CVI technique, if correctly applied, perfectly fulfills the processing requirements, resulting in CMCs with advanced mechanical and temperature properties.

Thus, it is important to take care in

- (i) avoiding fiber damage during composite processing,
- (ii) establishing a weak bonding between the fibers and the matrix by depositing a soft interphase (a thin layer of PyC or hexagonal BN), and
- (iii) protecting both the fibers and their interphases by coatings against environmental effects (e.g., oxidation).

During a tensile test, fibrous CMCs follow, under such conditions, a nonlinear stress-strain behavior. In addition, they exhibit both high crack propagation resistance and high failure energy due to different damaging mechanisms such as matrix microcracking, fiber-matrix debonding and friction, and especially, fiber pullout, which is a highly energy-absorbing mechanism.

The applications of CVI processing materials cover a wide range of CMCs such as carbon-carbon, carbon-silicon carbide, and silicon carbide-silicon carbide composites. Due to their attractive properties like great resistance to high temperature and corrosive environments, damage tolerance, and toughness, they find applications in



brakes, heat exchangers, gas turbines, structural components in aerospace industry, in nuclear reactors, and in heat engines.

**9.3.1.1 CVI SiC<sub>f</sub>/SiC Composites.** The advantageous properties of CVI SiC<sub>f</sub>/SiC composites are related to excellent mechanical strength, low density, high toughness, creep, fatigue and corrosion resistance, and high damage tolerance in case of impacts and thermal shocks, thus ensuring outstanding reliability even at very high temperatures. The properties of CVI SiC<sub>f</sub>/SiC composites are very different from those of monolithic ceramics and glasses, and from other types of composites, allowing the replacement of metals and ceramics in many technical applications, in which resistance to loads, high temperatures, and aggressive environments are strongly required.

Frequent applications of SiC-based composites are reusable thermal protections, gas turbines, and, in general, structural parts used at high temperatures and under oxidizing atmospheres.

The CVI process of SiC<sub>f</sub>/SiC composites has been studied since the 1960s, but it has become quite important since their industrialization by SNECMA (formerly SEP).

As previously reported for common CMCs, also for CVI SiC<sub>f</sub>/SiC composites, the good mechanical properties at room and high temperatures depend on the fiber–matrix interphase. PyC has been revealed to be an efficient interphase able to control fiber–matrix interactions and to influence the mechanical behavior of the composite. However, PyC presents one main drawback: its sensitivity to oxidation at temperatures higher than 450°C.

One way to protect the PyC interphase against oxidation is the development of multilayered interphases and matrices containing phases that produce sealants at high temperatures in order to avoid any contact between the oxygen and the PyC interphase. Boron-bearing species are effective to improve the oxidation resistance of PyC at relatively low temperatures (500–1000°C) because during oxidation, they can form a liquid oxide phase (B<sub>2</sub>O<sub>3</sub>), which fills cracks and slows down the oxygen diffusion [59].

Nevertheless, BN has been recently used as a very promising interphase material due to its layered crystal structure and better oxidation resistance compared with PyC. BN can be prepared by CVD from BF<sub>3</sub>(or BCl<sub>3</sub>)–NH<sub>3</sub> gas precursors [60].

**9.3.1.2 CVI C<sub>f</sub>/C Composites.** The classical isothermal and isobaric process has been largely investigated for the production of C<sub>f</sub>/C composites with good infiltration homogeneity and careful control of the matrix microstructure. However, its major drawback is the very low infiltration rate due to the low diffusion constant. It is well-known that for the CVI isothermal process, a very slow deposition speed (0.1/0.2 μm/h) is observed, while using the forced CVI method (cold-wall reactors), values of 3 μm/h can be reached. In case of using a thermal-gradient CVI (e.g., boiling technique with a very reactive hydrocarbon), higher values were reached (up to 50 μm/h) [61].

The main applications of the C<sub>f</sub>/C composites are

- (i) heat shields of space-reentry vehicles, integrated throat entrance (ITE) for small and medium size rocket nozzles [62] for military or space projects;

- (ii) military and civil aircraft brakes and brakes for terrestrial vehicles (high-speed trains, trucks, and racing cars);
- (iii) high-performance vacuum furnaces;
- (iv) biomedical applications (prosthesis devices and implants); and
- (v) solar energy applications (inner and outer protection systems of structural components such as heaters, thermal insulations, heat shields, crucibles, handling tools, and carrier systems).

Compared to traditional cast iron disks, carbon ceramic brakes offer significant weight reduction—up to 50%—and therefore lower fuel consumption. This product is more environmentally friendly, with lower CO<sub>2</sub> emissions, a longer life span, greater corrosion resistance, avoidance of fine particle dust and performance advantages, as well as a very high level of thermal stability.

C/C composites perfectly fulfill requirements like high purity levels, improved corrosion resistance against SiO attacks, ductility, cost efficiency, and low methanization rates [43].

## 9.4 GENERAL DISCUSSION

In I-CVI, the preforms are set in a hot-wall isothermal reactor fed by a flow of the gaseous precursor (the most important are reported in Table 9.2) under reduced pressure values, depending on the porosity distribution inside the preform and the nature of the precursor. As discussed in the previous section, too high temperatures and pressures could rapidly cause an early and not desired sealing of the pores.

Therefore, during the infiltration process, the parameters and conditions have to be very carefully controlled. The CVI parameters for the most important ceramic matrices for a lab-scale apparatus are reported in Table 9.2. The unreacted source species and the gaseous by-products are pumped through traps because most of these species are corrosive and toxic.

### 9.4.1 Advantages and Limitations of CVI Processes

In general, the advantages of CVI versus other CMC fabrication methods, such as hot pressing or liquid infiltration, are the following [63, 64]:

- Near-net-shape process
- Minimization of the mechanical damage of the fibers due to the much lower pressure and temperature used in CVI, with respect to those in other fabrication methods
- Higher purity of the matrix produced by CVI than that obtained, for example, by hot pressing, where sintering additives can lead to impurities.

TABLE 9.2. CVI Processing Conditions for Infiltration of Ceramic Matrices in Porous Preforms (Adapted from Golecki [2])

Matrix	Precursors	Fiber	Precursor Composition	Temperature (°C)	Pressure (kPa)	CVI Type
C	CH <sub>4</sub>	Carbon				
SiC	MTS/H <sub>2</sub>	Nicalon™, Nextel™, carbon, Al <sub>2</sub> O <sub>3</sub> , SiC	H <sub>2</sub> : MTS = 5–10	900–1100	10–100	I-CVI
			H <sub>2</sub> : MTS = 10	1100–1200	100–200	F-CVI
Si <sub>3</sub> N <sub>4</sub>	SiCl <sub>4</sub> /NH <sub>3</sub>	Nicalon, Nextel, carbon,	H <sub>2</sub> : MTS = 10	900–1000	3	I-CVI
Si <sub>3</sub> N <sub>4</sub>	SiCl <sub>4</sub> /NH <sub>3</sub> /H <sub>2</sub>					F-CVI
B <sub>4</sub> C	BCl <sub>3</sub> /CH <sub>4</sub> /H <sub>2</sub>	Carbon	BCl <sub>3</sub> : H <sub>2</sub> = 1	900–950	1–5	I-CVI
			BCl <sub>3</sub> : CH <sub>4</sub> = 4			
TiC	TiCl <sub>4</sub> /CH <sub>4</sub> /H <sub>2</sub>	Carbon	H <sub>2</sub> : CH <sub>4</sub> = 10	950	1–5	I-CVI
BN	BF <sub>3</sub> /NH <sub>3</sub>	BN, SiO <sub>2</sub> , Nextel, carbon	NH <sub>3</sub> : BF <sub>3</sub> = 1–3	1000–1100	1–5	I-CVI
Al <sub>2</sub> O <sub>3</sub>	Al <sub>2</sub> O <sub>3</sub> /H <sub>2</sub> /CO <sub>2</sub>	Nextel, carbon, Al <sub>2</sub> O <sub>3</sub> ,	H <sub>2</sub> : CO <sub>2</sub> = 1	950–1000	2–3	I-CVI
ZrO <sub>2</sub>	ZrCl <sub>4</sub> /H <sub>2</sub> /CO <sub>2</sub>	Mullite, carbon, Al <sub>2</sub> O <sub>3</sub> ,	H <sub>2</sub> : CO <sub>2</sub> = 1	900–940	1–5	I-CVI

TABLE 9.3. Advantages and Disadvantages for CMCs Produced by CVI (Adapted from Rosso [64])

Fiber	Matrix	Advantages	Disadvantages	Temperature Conditions <sup>a</sup>
Nicalon	SiC	Has been industrially developed	Slow and expensive	800–1600°C
Nextel	SiC	Best mechanical properties	Requires iterative cycles	800–1800°C
Graphite	Alumina	Ability to produce complex shapes	Slow reaction kinetics and low growth	800–1200°C
Nicalon	AlN	Properties dominated by ceramic matrix characteristics	Long processing time	800–1200°C
Nicalon	TiN, ZrN	Very pore grain boundaries	Wetting and reaction limited	800–1200°C

<sup>a</sup> Temperature limits depend on the thermal resistance of the fibers. Currently, all systems used fibers with a temperature limit at 1200°C.

However, all the CVI methods, just like other ceramic processing methods, leave a certain amount of void fraction or unfilled porosity in the composite, typically of the order of 1–10%. Residual porosity may be open (i.e., accessible from the external surface) or closed, and interconnected or not. The residual porosity can affect the performance of the final product in a measure depending on the materials, processing, and application. In Table 9.3, the advantages and disadvantages are reported for different couples of fibers and matrices.

The advantage of the I-CVI process is the wide variety of shapes and sizes of preforms that could be infiltrated. Besides, since the process is strongly dependent on diffusion mechanisms, processing times to complete an infiltration are as long as few weeks. Typical residence times for CVI impregnation of C<sub>f</sub>/C composites for aircraft brakes are 120–200 h [43]. Despite these problems, the I-CVI is the most widely used, and it also has been used extensively as an industrial process because alternative CVI methods have experienced problems in control and often show undesirable behaviors [16].

The deposited material often closes the open porosity on the outer surface before the final densification is carried out. Therefore, the composite parts have to be removed from the furnace, and an intermediate step of machining to open the closed pores is needed. Then, the composites have to be reheated before the CVI process continues up to the required final densification degree. The number of intermediate machining steps depends on the thickness of the C<sub>f</sub>/C component to be densified via CVI. For example, in cases of C<sub>f</sub>/C components with a thickness of 40 mm, the number of machining step can be up to three [43].

The use of low pressures in I-CVI allows several advantages such as

- (i) a more uniform distribution of density and microstructure within the composite due to the higher gas-phase diffusivity at lower pressure;
- (ii) a decrease in the flow rates of the inlet precursor; and
- (iii) a reduction in the unwanted gas-phase nucleation and in the formation of deleterious by-products, such as tar and soot in the case of carbon infiltration.

The main disadvantage of using low pressures results is a slower deposition rate, with consequently longer infiltration times. In order to increase the deposition rate, the infiltration process could be carried out at a higher temperature and higher pressure, but in this case, the closure of the pore surface could prematurely take place and also the undesirable by-product formation could be favored.

Another advantage of the I-CVI process is its excellent reproducibility. In the case of C/C composites, the resulting PyC matrix possesses high density, high modulus, and good graphitizing ability.

The advantages of the F-CVI process over the I-CVI technique are

- higher deposition efficiency,
- more uniform infiltration density, and
- ease of manufacturing process.

On the other hand, the disadvantages of F-CVI are the following:

- low uniformity in densification due to spatial density gradients within the perform;
- relatively low average density, potential spatial variations in the microstructure of the matrix, and nonhomogeneous physical properties of the composite;
- limitation to single-item processing;
- applicability generally only to thin-walled parts with high through-thickness permeability;
- it requires special expensive fixturing, which needs to be replaced often;
- it can cause some deformation or distortion of the preform due to the presence of fixturing;
- requirement of post-densification machining, which is time-consuming and expensive; then, the pressure is relatively high and hardly adjustable.

Therefore, both F-CVI and rapid CVI are attractive processes since infiltration times can be reduced by almost one order of magnitude with respect to I-CVI; however, they allow a much lower flexibility [48].

P-CVI, which is still an experimental process, has a similar flexibility to that of I-CVI, but it requires a more complex apparatus. Its main advantages are shorter den-

sification times and the possibility to create highly engineered multilayered ceramic composites.

Finally, the MW-CVI, which is also still an experimental process, presents the following advantages [2]:

- Thermal profile from inside to outside, under specific conditions
- Nonradiant heating of electrically insulating preforms
- High conversion efficiency in F-CVI configuration (for partially densified composites)

However, the MW-CVI presents several disadvantages including [2]

- spatially nonuniform density profiles due to the generation of hot and cold spots due to microwave heating and consequent local changes of composite properties with time and temperature, due to nonhomogeneous composition and microstructure of deposits, if care is not taken to guarantee a homogeneous microwave electromagnetic field inside the reactor; and
- limitations on the use of very low pressures due to the potential undesirable plasma generation, with an associated drop in power delivered to the preform.

#### 9.4.2 Analysis of the Costs Associated with the CVI Process

About the costs related with the production of  $\text{SiC}_f$  (Nicalon)/SiC matrix composites, Golecki compared in his review [2] (1) the isothermal, isobaric CVI process for the production of 0.3-cm-thick preforms; (2) the isothermal F-CVI for 0.3-cm-thick preforms; and (3) the F-CVI for 1.27-cm-thick preforms. Thermal-gradient F-CVI has resulted to be the least costly of the three methods, followed by isothermal F-CVI and isothermal, isobaric CVI. The relative distribution of costs (%) for the reactor (capital), reactor shutdown, materials, and machining are reported in Table 9.4.

In the isothermal, isobaric CVI technology, a few hundred preforms are infiltrated simultaneously, but the process takes numerous weeks and has to be interrupted several

TABLE 9.4. Relative Distribution of Costs (%) for the Main CVI Processes (Adapted from Golecki [2])

Process	Reactor (Capital, %)	Reactor Shutdown	Materials (%)	Machining (%)
Isothermal, isobaric CVI	54	14%	9	23
Isothermal forced-flow CVI	55	—	22	23
Thermal-gradient forced-flow CVI	44%	—	35	2

times to allow the machining of external surfaces in order to open the surface pores. The forced-flow techniques required only one cycle processing, but expensive graphite featuring and machining of the preform are needed after the densification.

The isothermal, isobaric CVI process is used successfully to densify relatively thick parts, for example, in the  $C_f/C$  ceramics.

The thermal-gradient inductively heated, isobaric CVI was also revealed significantly promising for rapidly enabling the infiltration of multiple, thick (3 cm) preforms in a single step, taking about 26–50 h [63].

The scale-up of the preform diameter, thickness, or the number of preforms per run does not present technically fundamental barriers. In fact, there are a number of advantages like the very high conversion efficiency of the precursor, the possibility to adjust pressure and precursor dilution, allowing flexibility in optimizing the densification conditions to obtain composites with the desired properties. The capital cost for a thermal-gradient inductively heated, isobaric CVI is also much lower than for a large isothermal, isobaric reactor.

Finally, a comparison between the costs of CVI processing and a polymer resin impregnation for the same type of CMC was also reported by Golecki [2]. Five impregnation pyrolysis cycles were necessary to obtain a final porosity of the preform of 18% with respect to the initial porosity of 38%. The overall time required was 320 h, divided as the following: 10 h for the impregnation, 290 h for slow heating to the pyrolysis temperature, and 20 h for slow cooling to avoid thermal stresses. Additional time was taken by the slow conversion at high temperatures of the amorphous matrix to the polycrystalline phase. Therefore, the overall processing time that resulted was quite similar to or was longer than that in isothermal, isobaric CVI, but the capital cost of the plant was considerably less than that for CVI.

### 9.4.3 Industrial Applications of CVI Processing Materials

The applications of CVI processing materials cover a wide range of CMCs such as carbon–carbon, carbon–silicon carbide, and silicon carbide–silicon carbide composites. Due to their attractive properties like large resistance to high temperatures and corrosive environments, damage tolerance, and toughness, they find applications in heat exchangers, gas turbines, structural components in aerospace industry, in nuclear reactors, and in heat engines [65].

$C_f/C$  composites find common applications in the brake field. Carbon has long been recognized as the most important constituent of friction materials for brake applications. Therefore, a  $C_f/C$  composite has been engineered to provide adequate mechanical, thermal, and friction characteristics for these disks.

The development of lightweight aircraft brakes [66] was first stimulated by the need for weight saving on aircraft, such as Concorde, due to the fact that the use of carbon brake disks offered 60% weight saving compared with steel. In particular, in 1973, Dunlop selected the CVI process as the method of manufacture of composites for Concorde brakes [67]. Dunlop applied an I-CVI process in a furnace capacity of about 10 tons of  $C/C$  brakes per process cycle and furnace, using methane as precursor gas, which can be used simultaneously for CVI infiltration and furnace heating [43].

In 1973, Dunlop provided the first C/C composite aircraft wheel brakes for initial trial on a VC10 aircraft followed a year later by standard fitment on Concorde.

The I-CVI process is time-consuming, but the quality of the composites produced is superior to that obtained by other methods, especially in the field of C/C brake disks where many companies such as Brembo SGL Carbon Ceramic Brakes (BSCCB), Meggitt Aircraft Braking Systems (trade name of the merger between Dunlop Aerospace Braking Systems and Aircraft Braking Systems Corporation), Snecma Propulsion Solide, Messier-Bugatti (a Safran Group company), Carbone Lorraine, HITCO, Honeywell Friction Materials, and others are active [43]. Brembo, a leader in the development and production of high-performance brake systems for car and motorbike applications, has developed carbon ceramic materials for Formula 1 racing and sports car applications. In 2001, the first cars were equipped with carbon ceramic brakes produced on an industrial basis, with Brembo Carbon Ceramic Brakes Systems. The CVI produced carbon ceramic brake business can also be expanded to a larger number of vehicles, thanks to the properties of the material, such as lightweight, longer lifetime, corrosion resistance, and thermal stability compared to the current cast iron brakes.

Meggitt Aircraft Braking Systems supplies aircraft C/C brakes for a range of applications from military aircraft to commercial and business jets.

HITCO has been manufacturing C/C brake materials from their initial development on high-performance military aircraft through the widespread acceptance on a commercial aircraft. More to the point, HITCO pioneered the use of carbon brakes in Formula 1 racing cars since 1980.

Carbenix<sup>®</sup> brake (a Honeywell Aerospace proprietary C/C material), consisting of 3-D needled, nonwoven PAN fabric with a CVD preform matrix, is a next generation of advanced friction materials for aircraft applications with antioxidant protection systems to enhance brake durability and reliability and to improve the service life of aircraft landing systems.

Messier-Bugatti supplies carbon brakes for civil aircraft (Airbus and Boeing models) and military aircraft.

In addition, C/C composite materials have been developed for about 40 years at Snecma Propulsion Solide [68]. These materials present very high thermal and mechanical resistance; therefore, they find application as thermostructural composite materials, in order to replace materials such as tungsten, pyrographite, and polycrystalline graphite. Depending on the type of carbon fibers used as reinforcements and the densification processes, these thermostructural composites constitute a broad class of materials [68], named as Sepcarb<sup>®</sup>, with excellent lightness, long lifetime, exceptional resistance to thermal shocks, and mechanical stability at temperatures up to 2700°C.

This range of materials originally was designed for military rocket motor nozzle applications. Today, they have been found in several other industrial applications: from brakes to thermal furnaces and semiconductor equipment. Sepcarb material is also a good candidate for very high temperature reactors (VHTRs) for the fission reactors of fourth generation due to its great mechanical performances at high operational temperatures, with particular regard to resistance to radiation and oxidation.

Because of the carbon-carbon sensibility to oxidation, the silicon carbide matrix can be used in replacement of the carbon matrix in order to perform long-life materials



in an oxidative environment or, for example, to avoid methane formation. These thermostructural C/SiC composite materials, originally designed by Snecma Propulsion Solide for fusion nuclear applications [68], are called Sepcarbinox®.

Both Sepcarb and Sepcarbinox materials take advantage of the I-CVI process, which enables the formation of a very pure and homogeneous C or SiC matrix, allowing extremely good mechanical properties and high thermal stability. Materials and parts are manufactured using mature and industrial processes. Various geometries can be infiltrated including plates, cylinders, disks, cones, tubes, beams, and complex shapes with thickness ranging from less than 1 mm to several centimeters with manufacturing capabilities that exceed  $2 \times 3$  m in size.

In addition, Snecma Propulsion Solide [68] has developed in the range of SiC/SiC composite materials Cerasep®, particularly for nuclear fusion, but with applications also in aeronautical propulsion. In fact, Cerasep presents very attractive properties: low activation, good resistance to shocks and heat cycling, strength, and maintenance of good mechanical resistance to temperatures higher than 1000°C. For example, using Cerasep as a thermostructural composite material to make the walls of combustion chambers can lead also to environmental benefits because, enabling a reduction in the flow of cooling air over the walls, it decreases the air/fuel ratio in the chamber and consequently reduces the NO<sub>x</sub> harmful emissions from the turbojet.

In conclusion, CVI processes have been demonstrated feasible for different matrices, but only a few of these (SiC and C) are produced on an industrial scale, for the production of C/C, C/SiC, and SiC/SiC composites.

To the author's knowledge, among the CVI variants, the isothermal process (I-CVI) is the most commonly applied at the industrial level for the preparation of CMCs. The low infiltration rates and the long processing times remain the major disadvantages when the I-CVI technique is industrially used, but it is basically compensated by the fact that large numbers of components can be simultaneously treated.

## 9.5 CONCLUDING REMARKS AND FUTURE DIRECTIONS

The fields of fiber-reinforced CMCs and densification of such composites by a variety of infiltration routes continue to provide exciting and active opportunities for research and development. These activities are continually driven by the superior physical properties of composites, compared to their monolithic counterparts, and by the need to reach a good compromise between the material quality and the processing conditions (reduction in time, decrease in energy consumption, and adequate plant expenses).

Several applications of CMC components produced by CVI are under field observation or development. Examples are valve components, with mechanical resistance at high temperature and pressure shocks, heat shields for racing cars, and casings for rocket engines. Future development work will be about the improvement of ceramic fiber stability at  $T > 1200^\circ\text{C}$  in corrosive environments in order to perfectly fit the material requirements for applications at high temperatures, such as heat exchangers and gas turbines. The long-term stability at high temperatures is strongly dependent on the homogeneity of the materials, which, if low, tend to change their structure via diffusion.

Significant reductions in manufacturing costs for fibers such as silicon carbide and processing costs for the deposition of the ceramic matrix will allow the rapid expansions of the markets of CMCs, in particular, for a number of applications where they can successfully be utilized from a technical point of view, but are not currently applied because of their high costs.

Of the infiltration processes used, the isothermal and forced-flow/thermal-gradient processes appear to be the most popular, and both of these processes have now been industrialized.

In particular, the isothermal, isobaric CVI, the oldest CVI process, is widely used in industrial applications. Several advantages are related to this technique: The first is the possibility to densify simultaneously a large number of complex preforms in huge furnaces, and the second is the good matrix quality, in terms of type of microstructure and low residual porosity, that can be achieved. The main drawback is the very long processing time due to the diffusion mechanism associated with low overall precursor efficiency (a few percent).

New, more effective methods to develop rapid infiltration techniques have been explored. In particular, the thermal-gradient CVI, associated with an *in situ* vaporized liquid precursor (rapid CVI) for C/C composites, and microwave-assisted processes (MW-CVI) for SiC<sub>f</sub>/SiC composites are becoming available. Even if these processes exhibit less flexibility with respect to the well-established I-CVI, they may be more appropriate for specific matrix compositions and/or specific application fields.

## REFERENCES

1. M. Leuchs, Chemical vapor infiltration processes for ceramic matrix composites: Manufacturing, properties, in *Ceramic Matrix Composites*, ed. W. Krenkel, pp. 141–164, Wiley, Weinheim, 2008.
2. I. Golecki (1997) Rapid vapor-phase densification of refractory composites, *Mater. Sci. Eng. R*, **20** 37–124.
3. J. Lamon, Chemical vapor infiltrated SiC/SiC composites (CVI SiC/SiC, in *Handbook of Ceramic Composites*, ed. N. Bansal, pp. 55–76, Kluwer Academic Publishers, Boston, 2005.
4. P. Delhaes (2002) Review—Chemical vapor deposition and infiltration processes of carbon materials, *Carbon*, **40**[5] 641–657.
5. G. Amirthan, A. Udayakumar, V. V. Bhanu Prasad, and M. Balasubramanian (2009) Properties of Si/SiC ceramic composite subjected to chemical vapour infiltration, *Ceram. Int.*, **35**[7] 2601–2607.
6. R. R. Naslain, F. Langlais, and R. Fedou (1989) The CVI-processing of ceramic matrix composites, *J. Phys.*, **50**[C5] 191–207.
7. R. R. Naslain (1999) Material design and processing of high temperature ceramic matrix composites: State of the art and future trends, *Adv. Composite Mater.*, **8**[1] 3–16.
8. J. D. Buckley (1988) Carbon-carbon, an overview, *Am. Ceram. Soc. Bull.*, **67**[2] 364–368.

9. E. Fitzer and R. Gadow (1986) Fiber reinforced silicon carbide, *Am. Ceram. Soc. Bull.*, **65**[2] 326–335.
10. W. J. Lackey and T. L. Starr, Fabrication of fiber-reinforced ceramic composites by chemical vapor infiltration: Processing, structure and properties, in *Fiber Reinforced Ceramic Composites*, ed. K. S. Mazdiyarni, pp. 397–445, Noyes Publications, Park Ridge, NJ, 1990.
11. J. R. Strife, J. J. Brennan, and K. M. Prewo (1990) Status of continuous fiber-reinforced ceramic matrix composite processing technology, *Ceram. Eng. Sci. Proc.*, **11**[7–8] 871–919.
12. H. O. Pierson, *Handbook of Chemical Vapor Deposition (CVD)*. Noyes Publications, Park Ridge, NJ, 1992.
13. E. W. Thiele (1939) Relation between catalytic activity and size of particle, *Ind. Eng. Chem.*, **31**[7] 916–920.
14. E. Fitzer (1991) Chemical vapor deposition—A review of 25 years experience, *J. Phys. IV*, **1**[C2] 509–537.
15. D. Lespiaux, F. Langlais, R. Naslain, S. Shamm, and J. Sevely (1995) Correlations between gas phase supersaturation, nucleation process and physico-chemical characteristics of silicon carbide deposited from Si-C-H-Cl system on silica substrates, *J. Mater. Sci.*, **30**[6] 1500–1510.
16. G. L. Vignoles (2006) Modeling of the CVI processes, *Adv. Sci. Tech.*, **50** 97–106.
17. G. D. Papasoulitis and S. V. Sotirchos (1999) Experimental study of the atmospheric pressure chemical vapor deposition of silicon carbide from methyltrichlorosilane, *J. Mater. Res.*, **14**[8] 3397–3409.
18. J. Schlichting (1980) Chemical vapor deposition of silicon carbide, *Powder. Metall. Int.*, **12**[3] 141–147.
19. G. S. Fischman and W. T. Petuskey (1985) Thermodynamic analysis and kinetic implications of chemical vapor deposition of SiC from SiC-C-Cl-H gas systems, *J. Am. Ceram. Soc.*, **68**[4] 185–190.
20. F. Loumagne, F. Langlais, and R. R. Naslain (1993) Kinetic laws of the chemical process in the CVD of SiC ceramics from  $\text{CH}_3\text{SiCl}_3\text{-H}_2$  precursor, *J. Phys. IV*, **3**[C3] 527–533.
21. F. Christin, R. R. Naslain, and C. Bernard, A Thermodynamic and experimental approach of silicon carbide-CVD application to the CVD-infiltration of porous carbon/carbon composites, in *Proceedings of the 7th International Conference on CVD*, T. O. Sedwick and H. Lydin, pp. 499–514, The Electrochemical Society, Princeton, NJ, 1979.
22. E. Fitzer and D. Hegen (1979) Chemical vapor deposition of silicon carbide and silicon nitride—Chemistry's contribution to modern silicon ceramics, *Angew. Chem. Int. Edit.*, **18**[4] 295–304.
23. T. M. Besmann and M. L. Johnson Kinetics of the low-pressure chemical vapor deposition of silicon carbide, in *Proceedings of the Third International Symposium on Ceramic Materials and Components for Engines*, V. J. Tennery, pp. 443–456, American Ceramic Society, Westerville, OH, 1989.
24. F. Langlais and C. Prebende, On the chemical process of CVD of SiC-based ceramics from the Si-C-H-Cl system, in *Proceedings of the Eleventh International Conference of Chemical Vapor Deposition*, eds. K. E. Spear and G. W. Cullen, pp. 686–695, The Electrochemical Society, Pennington, NJ, 1990.
25. G. D. Papasoulitis and S. V. Sotirchos (1994) On the homogeneous chemistry of the thermal decomposition of methyltrichlorosilane, *J. Electrochem. Soc.*, **141**[6] 1599–1611.

26. M. D. Allendorf and C. F. Melius (1993) Theoretical study of the thermochemistry of molecules in the Si-C-Cl-H system, *J. Phys. Chem.*, **97**[3] 720–728.
27. T. H. Osterheld, M. D. Allendorf, and C. F. Melius (1994) Unimolecular deposition of methyltrichlorosilane—RRKM calculations, *J. Phys. Chem.*, **98**[28] 6995–7003.
28. C. Raffy, E. Blanquet, M. Pons, C. Bernard, C. F. Melius, and M. D. Allendorf (1999) Contribution to the modeling of CVD silicon carbide growth, *J. Phys. IV*, **9**[P8] 205–212.
29. J. T. Niiranen and D. Gutman (1993) Silicon-carbon bond formation kinetics: Study of the reactions of methyl with silyl, trimethylsilyl, and trichlorosilyl, *J. Phys. Chem.*, **97**[37] 9392–9396.
30. J. Warnatz (1983) The mechanism of high temperature combustion of propane and butane combustion, *Combust. Sci. Technol.*, **34**[1–6] 177–200.
31. J. N. Burgess and T. J. Lewis (1974) Kinetics of the reduction of methyltrichlorosilane by hydrogen, *Chem. Ind.*, **2** 76–77.
32. M. Ganz, N. Dorval, M. Lefebvre, M. Péalat, F. Loumagne, and F. Langlais (1996) In situ optical analysis of the gas phase during the decomposition of silicon carbide from methyltrichlorosilane, *J. Electrochem. Soc.*, **143**[5] 1654–1661.
33. V. Hopfe, H. Mosebach, M. Erhard, and M. Meyer (1995) In situ FTIR emission spectroscopy in a technological environment: Chemical vapor infiltration (CVI) of SiC composites, *J. Mol. Struct.*, **347** 331–342.
34. H. Sone, T. Kaneko, and N. Miyakawa (2000) In situ measurements and growth kinetics of silicon carbide chemical vapor deposition from methyltrichlorosilane, *J. Cryst. Growth*, **219**[3] 245–252.
35. Y. Ge, M. S. Gordon, F. Battaglia, and R. Fox (2007) Theoretical study of the pyrolysis of methyltrichlorosilane in the gas phase. 1. Thermodynamics, *J. Phys. Chem. A*, **111**[8] 1462–1474.
36. B. W. Sheldon and T. M. Besmann (1991) Reaction and diffusion kinetics during the initial stages of isothermal chemical vapour infiltration, *J. Am. Ceram. Soc.*, **74**[12] 3046–3053.
37. N. Birakayala and E. A. Evans (2002) A reduced reaction model for carbon CVD/CVI processes, *Carbon*, **40**[5] 675–683.
38. A. Li and O. Deutschmann (2007) Transient modeling of chemical vapor infiltration of methane using multi-step reaction and deposition models, *Chem. Eng. Sci.*, **62**[18–20] 4976–4982.
39. V. I. Kulik, A. V. Kulik, M. S. Ramm, and Y. N. Makarov (2004) Modeling of SiC-matrix composite formation by isothermal chemical vapor infiltration, *J. Cryst. Growth*, **266**[1–3] 333–339.
40. A. Barbato and C. Cavallotti (2010) Challenges of introducing quantitative elementary reactions in multiscale models of thin film deposition, *Phys. Status Solidi B*, **247**[9] 2127–2146.
41. V. I. Kulik, A. V. Kulik, M. S. Ramm, A. S. Nilov, and M. V. Bogdanov, Two-dimensional model of conjugate heat and mass transport in the isothermal chemical vapour infiltration of 3D-preform by SiC matrix, in *Silicon Carbide and Related Materials 2004*, Vol. 483. *Materials Science Forum*, eds. R. Nipoti, A. Poggi, and A. Scorzoni, pp. 245–250, Trans Tech Publications, Zurich-Uetikon, Switzerland, 2005.
42. R. R. Naslain and F. Langlais, CVD—Processing of ceramic—Ceramic composite materials, in *Tailoring Multiphase and Composite Ceramics*, Vol. 20. *Materials Science Research*, eds.

- R. E. Tressler, G. L. Messing, C. G. Pantano, and R. E. Newnham, pp. 145–164, Plenum Press, New York, 1986.
43. R. Weiss, Carbon/carbons and their industrial applications, in *Ceramic Matrix Composites, Fiber Reinforced Ceramics and Their Applications*, ed. W. Krenkel, pp. 69–112, Wiley, Weinheim, 2006.
  44. G. Roman, M. H. J. M. de Croon, and R. Metselaar (1995) Analysis of the isothermal forced flow chemical vapor infiltration process. Part II: Experimental study, *J. Eur. Ceram. Soc.*, **15**[19] 887–898.
  45. A. J. Caputo, W. J. Lackey, and D. P. Stinton (1984) Development of a new faster process for the fabrication of ceramic fiber-reinforced ceramic composites by chemical vapor infiltration, *Ceram. Eng. Sci. Proc.*, **6** 694–705.
  46. T. M. Besmann, J. C. McLaughlin, and H. T. Lin (1995) Fabrication of ceramic composites—Forced CVI, *J. Nucl. Mater.*, **219** 31–35.
  47. S. Bertrand, J. F. Lavaud, R. E. Hadi, G. Vignoles, and R. Pailler (1998) The thermal gradient–pulsed flow CVI process: A new chemical vapor infiltration technique for the densification of fiber preforms, *J. Eur. Ceram. Soc.*, **18**[7] 857–870.
  48. R.R. Naslain, Ceramic matrix composites: Matrices and processing, in *Encyclopedia of Materials: Science and Technology*, ed. K. H. Jürgen Buschow, R. W. Cahn, M. C. Flemings, B. Ilshner, E. J. Kramer, S. Mahajan, and P. Veyssi re, pp. 1060–1066, Elsevier Science, 2001.
  49. R. R. Naslain (1998) The design of the fiber-matrix interfacial zone in ceramic matrix composites, *Compos. A Appl. Sci.*, **29**[9-10] 1145–1155.
  50. Y. Yin, J. G. P. Binner, and T. E. Cross (1997) Microwave assisted chemical vapor infiltration for ceramic matrix composites, *Ceram. Trans.*, **80** 349–356.
  51. J. G. P. Binner and B. Vaidhyanathan, When should microwaves be used to process technical ceramics? in *Advances in Ceramic Materials, Materials Science Forum*, Vol. 606, eds. P. Xiao and B. Ralph, pp. 51–59, Trans Tech Publications, Zurich-Uetikon, Switzerland, 2009.
  52. D. Jaglin, J. G. P. Binner, B. Vaidhyanathan, C. Prentice, B. Shatwell, and D. Grant (2006) Microwave heated chemical vapor infiltration: Densification mechanism of SiC<sub>f</sub>/SiC composites, *J. Am. Ceram. Soc.*, **89**[9] 2710–2717.
  53. B. Cioni, E. Origgi, and A. Lazzeri (2006) Microwave processing of SiC-matrix composites by chemical vapor infiltration (CVI), in *Proceedings of the Third National Meeting on Microwaves in the Engineering and in the Applied Science, MISA 2006*, ed. E. Caponetti, Roma, Italy.
  54. B. Cioni and A. Lazzeri (2008) Modeling and development of a microwave assisted pilot plant for the production of SiC-based matrix composites, *Int. J. Chem. React. Eng.*, **6**[A53] 1–23.
  55. L. A. Timms, W. Westby, C. Prentice, D. Jaglin, R. A. Shatwell, and J. G. P. Binner (2001) Reducing chemical vapor infiltration time for ceramic matrix composites, *J. Microsc.*, **201**[2] 316–323.
  56. A. Becker and K. J. Huttinger (1998) Chemistry and kinetics of chemical vapor deposition of pyrocarbon-I pyrocarbon deposition from ethylene, acetylene and 1,3-butadiene in the low temperature regime, *Carbon*, **36**[3] 177–199.
  57. W. Benzinger and K. J. Huttinger (1999) Chemistry and kinetics of chemical vapor infiltration of pyrocarbon-V. Infiltration of carbon fiber felt, *Carbon*, **37**[6] 941–946.
  58. J. Wang, J. Qian, G. Qiao, and Z. Jin (2006) Improvement of film boiling chemical vapor infiltration process for fabrication of large size C/C composite, *Mater. Lett.*, **60**[9–10] 1269–1272.

59. R. R. Naslain (2004) Review article—Design, preparation and properties of non-oxide CMCs for application in engines and nuclear reactors: An overview, *Compos. Sci. Technol.*, **64**[2] 155–170.
60. Y. Cheng, X. Yin, Y. Liu, S. Li, L. Cheng, and L. Zhang (2010) BN coatings prepared by low pressure chemical vapor deposition using boron trichloride–ammonia–hydrogen–argon mixture gases, *Surf. Coat. Tech.*, **204**[16–17] 2797–2802.
61. D. Rovillain, M. Trinqucoste, E. Bruneton, A. Derre, P. David, and P. Delhaes (2001) Film boiling chemical vapor infiltration an experimental study on carbon/carbon composite materials, *Carbon*, **39**[9] 1355–1365.
62. G. P. Sutton and O. Biblarz, *Rocket Propulsion Elements*. J. Wiley & Sons Inc., Hoboken, NJ, 2010.
63. I. Golecki (1997) Recent advances in rapid densification of thick, refractory composites by Inductively-heated thermal gradient, flowing gas, isobaric, chemical vapor infiltration, in Proceedings of the 14th International Conference of EuroCVD-11, eds. M. D. Allendorf and C. Bernard, pp. 568–575, Electrochemical Society Proceedings, Paris, France.
64. M. Rosso (2006) Ceramic and metal matrix composites: Routes and properties, *J. Mater. Process. Tech.*, **175**[1–3] 364–375.
65. R. R. Naslain (2005) SiC-matrix composites: Non brittle ceramics for thermo-structural application, *Int. J. Appl. Ceram. Technol.*, **2**[2] 75–84.
66. I. L. Stimson and R. Fisher (1980) Design and engineering of carbon brakes, *Philos. Trans. R. Soc. Lond A* **294**[1411] 583–590. New Fibers and Their Composites, Edited by The Royal Society, London, Great Britain.
67. G. Savage, *Carbon-Carbon Composites*. Chapman & Hall, London, 1993.
68. I. Berdoyes and J. Thebault (2005) Thermostructural composite materials: From space to advanced fission applications. Proceedings of European Congress on Advanced Materials and Processes EUROMAT 2005, pp. 1–7, Prague, Czech Republic.

# REACTIVE MELT-INFILTRATION PROCESSING OF FIBER-REINFORCED CERAMIC MATRIX COMPOSITES

NATALIE WALI AND J.-M. YANG

## 10.1 INTRODUCTION

### 10.1.1 Processes for Ceramic Matrix Composites (CMCs)

High-performance nonoxide CMCs are becoming increasingly attractive for many structural applications. These materials offer greater damage tolerance, high-temperature stability, thermal shock resistance, quasi-ductile fracture behavior, and environmental resistance than do monolithic ceramics, metals, and superalloys [1–3]. These advantageous properties are the result of the combination of a chemically stable ceramic matrix and reinforcing fibers. An ideal ceramic matrix can be made with a tailorable, controllable microstructure and near 100% density. Discontinuous reinforcements, such as short chopped fibers, platelets, and particles can be easily dispersed within the matrix. Continuous fibers in monofilament or multifilament form are difficult to manipulate without causing much damage but are appealing for their contribution to the high strength and toughness of the composite. Incorporating the reinforcements, however, presents a unique processing challenge, mostly because of the high temperatures involved in manufacturing. The complexities of CMC fabrication have helped drive the

*Ceramics and Composites Processing Methods*, First Edition. Edited by Narottam P. Bansal and Aldo R. Boccaccini.

© 2012 The American Ceramic Society. Published 2012 by John Wiley & Sons, Inc.



development and maturation of several solid-, vapor- and liquid-state processing techniques.

**10.1.1.1 Solid-State Routes.** Solid-state routes for the production of CMCs are limited to those processes that produce composites reinforced with short fibers. Hot press (HP), where applied pressure is uniaxial, and hot isostatic press (HIP), where applied pressure is hydrostatic, are typically used to consolidate powder mixtures to make monolithic ceramics. The easiest way to incorporate fibers is to create an oxide matrix with a crystalline refractory phase and a glass phase so that during heating, the glass softens and embeds the fibers. Though the resulting matrix is stable in oxidizing environments, it demonstrates poor creep resistance at higher temperatures. An option to achieve a nonoxide matrix phase is to hot press a polymeric precursor, such as polycarbosilane (PCS) for SiC [4]. The pyrolysis products from this particular process are  $\beta$ -SiC crystals, amorphous Si-O-C, silica, and free carbon. Sintering may be used to further increase densification and the microstructure typically contains an amorphous phase at the fiber-matrix interphase [4]. An issue with the HP route is the relatively high cost of the specialized tooling and the manufacturing scale limitations imposed by operation in a vacuum or inert environment. Hot pressing is typically incorporated as a final step in other composite processes to further enhance the composite density.

**10.1.1.2 Vapor-Phase Routes.** Chemical vapor infiltration (CVI) is a mature, commercialized vapor-phase process for creating a composite matrix. It is used extensively on a large manufacturing scale because many preforms can be treated all at once under low temperatures in large infiltration furnaces. Virtually any shape can be infiltrated with different precursors to form any type of ceramic with a controllable matrix microstructure and 10–15% porosity. A major advantage of CVI over other processing methods is the low deposition temperatures. A gaseous precursor infiltrates a porous preform and reacts by decomposition to form a ceramic. The preform is first coated with an interphase at low temperatures, typically at a few hundred degrees Celsius [5–7]. The coated preform is then infiltrated with the precursor, for example,  $\text{CH}_3\text{SiCl}_3$  for SiC [5, 8, 9]. Precise control over the processing temperature, gas flow, and chamber pressure is critical in CVI. Infiltration is slow and requires several cycles. The time for each cycle is long, lasting anywhere from several hours to several weeks, depending on the infiltration depth. The number of cycles needed depends upon the size and porosity of the preform. The porosity content can be incrementally reduced with multiple infiltration cycles or by combining it with slurry infiltration, but these options increase the already long processing time. Volumetric shrinkage accompanies the formation of the solid, which leads to matrix cracking. Infiltration is sometimes interrupted to machine open surface pores, but dead ends and choking off are unavoidable in the bulk of the composite. The deposition rate can also be hastened by using forced CVI methods, but this comes at the expense of cost and compositional control.

There are currently two major types of CVI methods used on a large production scale. The simplest, isothermal or isobaric CVI (I-CVI), is rather slow because mass transfer in the matrix occurs by diffusion. The resultant matrix contains residual porosity and has a noticeable density gradient. These effects are mitigated by employing



I-CVI for thin structures. Temperature gradient (TG)-CVI, also known as forced-flow CVI (F-CVI) is used to reduce the processing time by up to an order of magnitude [10]. A temperature gradient is established through the use of hot and cold faces in the tooling. Gas deposition and the subsequent decomposition reaction occur on the hot face, and the densification front moves through to the opposite side [11]. Though the processing time is reduced, TG-CVI is not suitable for complex shapes because of the specificity of the tooling required for each fiber preform type in order to establish the correct pressure and temperature gradients.

**10.1.1.3 Liquid-State Routes.** Polymer infiltration and pyrolysis (PIP) is used extensively in the fabrication of polymer matrix and C/C composites, and it is easily modified for CMC production [12–16]. The ceramic matrix is formed from a liquid organic or liquid organometallic precursor. A continuous fiber tow is first coated with an interphase by either CVI or by the particle slurry process. The coated tow is then covered with slurry or with another preceramic polymer then dried, shape formed, and cured by heating at low temperatures or by irradiation [12]. The last infiltration and thermal steps are repeated to achieve sufficient density. The composite may also be heated at higher temperatures to complete densification, to crystallize the matrix, and to remove residual stresses. The ability to tailor the precursor makes PIP flexible for the manufacture of different ceramic matrices, but matrix shrinkage and cracking are major issues. To combat these effects, several PIP cycles can be performed or an HP step can be added at the end. Additionally, an inert filler can be added to the starting liquid. Of course, these additional steps are time and labor-intensive. Another drawback to PIP is the high cost of the polymeric precursors.

Melt infiltration (MI), or liquid metal infiltration, overcomes some of these processing difficulties. In MI, a molten metal rapidly infiltrates the available space in a porous preform for a fast buildup of the matrix. There are two pathways: nonreactive and reactive. In nonreactive MI, the liquid phase rapidly fills the pores in a nonsoluble preform at high temperatures, where it crystallizes to form the matrix. An example of a nonreactive MI process is SiC–SiC particulate bonding.

Reactive melt infiltration (RMI) is also a pressureless infiltration process where the movement of the liquid metal through the preform is assisted mainly by capillary forces and surface tension. Typically, the metal or alloyed melt reacts with a previously deposited carbon source. A particular case of RMI that does not involve reaction with carbon is the directed metal oxidation (DIMOX) process [17]. An Al or Al alloy melt infiltrates a preform and reacts with a gaseous oxidant to form an Al/Al<sub>2</sub>O<sub>3</sub>-based matrix. In RMI, only one infiltration cycle is performed, taking the time to completion for a component down to only hours or days rather than weeks or months (as in the case of CVI). RMI can be used to make components with complex geometries that are up to 98% dense. General Electric (GE) developed one of the earliest versions of RMI, the SILCOMP process, in the early 1970s [18–22]. In the past few decades, RMI has been applied to other material systems, though SiC-based composites are currently the most heavily produced.

A summary of the qualitative differences between the major infiltration processing methods for CMCs is shown in Table 10.1. It is stressed that different combinations of

TABLE 10.1. A Comparison of the Common Infiltration Processes for CMCs (Data from References 8–10 and 33)

	Starting Materials	Processing Temperatures	Time to Completion	Processing Conditions	Matrix Characteristics
RMI	Liquid (metal or alloy melt)	High (>1450°C)	Short	Pressureless, one cycle	Up to 98% dense, polycrystalline ceramic phase with residual metal
PIP	Liquid (chemical + ceramic powders)	Low (800–1100°C)	Long	Can be pressureless, multiple cycles	Volume shrinkage, up to 40% porosity, amorphous microporous ceramic, low yield (up to 65%)
CVI	Gaseous (precursors)	Moderate (900–1200°C)	Long	Low pressures, multiple cycles	Up to 90% dense, polycrystalline ceramic matrix with uniform microstructure and density gradient

these types are usually employed to achieve certain properties, to reduce cost, or to protect the fibers. For example, PIP is often used in combination with liquid metal infiltration to cut down on time and cost. However, the high temperatures and reactive nature of the molten metal are detrimental to the fibers, so care must be taken in selecting the appropriate hybrid processing route.

### 10.1.2 Comparison of RMI and CVI

The single infiltration step of RMI makes it a much faster process than CVI, but the high processing temperatures are a limiting factor in the selection of raw materials. High-quality stoichiometric fibers that can survive these higher temperatures are needed for the preform. As such, the two processes are comparable in cost since the cost of the starting materials in RMI negates the savings afforded by the faster processing time.

The mechanical properties of CMCs are significantly influenced by the fiber–matrix bond strength. CMCs produced by RMI, CVI, or PIP all will exhibit similar tensile strengths and strain to failure if the same highly compliant fiber coatings have been applied. The lower processing temperatures and reactivity give CVI an advantage; however, RMI CMCs generally possess larger interlaminar shear strengths and higher proportional limit stresses because of their densities.

CVI produces composites with uniform microstructures, while in RMI, there is an unreacted metal in the matrix due to the diffusion-controlled reaction in the preform. The mechanical strength at higher temperatures becomes a concern if there is a substantial amount of residual metal in the matrix. At higher temperatures, diffusion of the metal to the surface (so-called leaching) is a concern. To reduce the amount of residual metal, a processing route combining slurry infiltration with RMI may be used to infiltrate carbon slurries prior to metal infiltration. Excess carbon, however, may increase porosity if it oxidizes and forms CO and CO<sub>2</sub>.

In terms of thermal properties, the residual porosity in CVI-produced composites contributes to a lower thermal conductivity, which is advantageous in the hot zones of aerostructures. Because RMI composites are typically denser, they have higher thermal conductivities that are suitable for uses such as in combustor liners.

A comparison of the typical microstructure of SiC–SiC composites produced by CVI and RMI is shown in Figure 10.1. Both composites contain the same fiber volume fraction (~0.35), but immediately apparent is the porosity difference.

Data on several mechanical and physical properties of CVI and RMI SiC-based composites are compiled from different studies in Table 10.2. A direct comparison of these properties is difficult to make because the tests were performed under different conditions. In addition, there is a substantial physical variation in composites from within the same batch. Again, the largest difference is seen in the porosity.

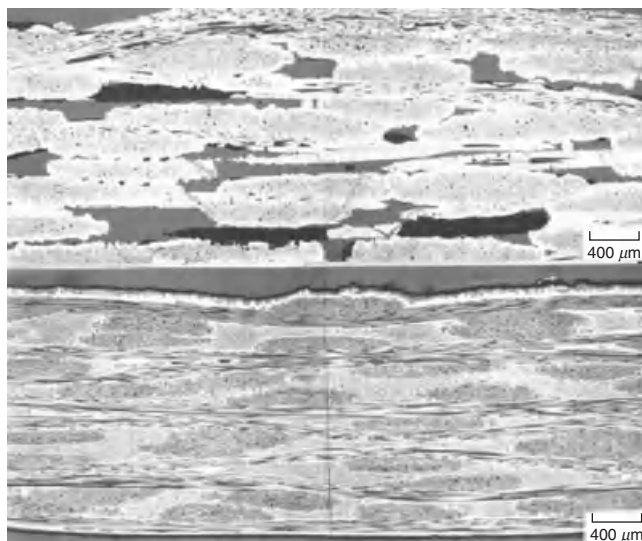


**Figure 10.1.** Example of the microstructural differences between a CVI-made SiC–SiC composite (top) and a slurry and melt-infiltrated SiC–SiC (bottom) (reprinted from J. J. Brennan (2000) Interfacial characterization of a slurry-cast melt-infiltrated SiC–SiC ceramic matrix composite, *Acta Materialia*, **48**[18–19] 4619–4628, with permission from Elsevier).

TABLE 10.2. Select Physical Properties of RMI and CVI Continuous Fiber-Reinforced Composites (Data from References 8, 21, 33, 81, and 113–115)

	CVI		RMI		
	SiC–SiC	C–SiC	SiC–SiC	C–SiC	C/C–SiC
Density (g/cm <sup>3</sup> )	2.67	2.1–2.2	2.70–2.80	2.1 ± 0.1	1.9–2.0
Porosity (%)	7.25	10–15	2	5 ± 1	2–5
Flexural strength at room temperature (MPa) (long./trans.)	170–230	163; 450–500; 160–300;	–	(165 ± 30/97 ± 25)	190
Compressive strength at room temperature (MPa) (long./trans.)	300–580	580–700; (304/276)	1190	(260 ± 41/118 ± 18)	160–300
Fracture toughness at room temperature (Mpa√m)	6.5	28.5	–	27.2	–
CTE (10 <sup>−6</sup> /K) (long./trans.)	3.2	1.09–1.93; (3/5)	(3.57/4.07)	(−1.6–2.9/2.3–5.7)	(−1–2.5/2.5–7.0)

## 10.2 RMI

RMI is applicable to any material system in which one of the starting elements for the ceramic matrix possesses a relatively low melting point and can readily wet the fibers. There are four general steps:

1. Fiber selection and pretreatment
2. Assembly of a fiber preform
3. Shaping of a fiber-reinforced green body
4. Infiltration and reaction

The different RMI processes used differ mainly in the manner in which the fibers are treated and inserted in the matrix and the way the green body is formed.

### 10.2.1 General Process

**10.2.1.1 Criteria for Fiber and Interphase Selection.** Fibers are major contributors to the mechanical properties of a composite. CMCs are inverse composites;

that is, the failure strain of the matrix is lower than that of the fibers so that under load, the matrix fails first. Continuous fibers impart toughness by pullout, debonding from the matrix, and deflecting cracks. In fact, the good damage tolerance of CMC materials is attributed to the frictional sliding at the fiber–matrix interface, which arises from weak shear coupling. Matrix cracks are either bridged by the fibers or arrested at the fiber–matrix interface. The body of literature for fibers is extensive [6, 23–30] and the reader is directed to other sources for more detailed information.

Fibers with low concentrations of free oxygen and carbon are preferred for RMI because fibers containing impurities such as O and N are unstable at higher temperatures [31]. Carbon fibers possess some attractive properties. For example, high-strength carbon fibers, like the T1000, have strengths over 6 GPa and strain levels greater than 2% [32]. These properties are larger than those of monolithic ceramics, like bulk SiC (strength of about 400 MPa and a strain level less than 0.05%) [33]. These fibers are also relatively inexpensive and are easy to handle. Unfortunately, carbon oxidizes at temperatures as low as 400–500°C. The reaction between oxygen and carbon is rate controlling and forms gaseous products, so these fibers must be coated. In addition, the anisotropic thermal expansion behavior of carbon fibers contributes to matrix cracking.

Ceramic fibers are used often in CMCs because of their contribution to damage tolerance. Nonoxide fibers, such as SiC and Si-B-N-C, are good candidates [131–133]. Of these, stoichiometric SiC-fibers (low concentrations of free Si, C, and O) demonstrate the best creep strengths and high-temperature stability [30]. The stoichiometric SiC-fibers, such as Hi-Nicalon S, Tyranno SA, and Sylramic are all crystalline, stable to 1800°C, creep resistant up to 1200–1500°C, and have thermal conductivities up to 65 W/m-K at room temperature (Table 10.3) [25–27, 31, 34]. However, they tend to be very stiff, with a Young's modulus of around 400 GPa, and have a low strain to failure (up to 0.7%) [34]. These fibers also have a tendency to undergo passive oxidation. Also, all SiC-fibers tend toward grain growth when exposed to liquid Si [25].

The fiber–matrix interface typically consists of one or more coating layers (interphase). The fiber coating provides a weak fiber–matrix interface that prevents matrix cracks from penetrating the fibers and protects the fibers from damage during composite manufacture and use. The coatings must be mechanically and chemically stable in high-temperature corrosive environments. Typical fiber coatings fall in the range of

TABLE 10.3. Physical and Thermal Properties of Several SiC-Based Ceramic Fibers (Data from References 25–27)

	Tensile Strength (GPa) (25°C)	CTE (/K) (25–1000°C)	Density (g/cm <sup>3</sup> )	Diameter (μm)	<i>k</i> (W/m-K) (25°C)
Siboramic	4.0	$3.5 \times 10^{-6}$	—	12.0–14.0	>3.0
Sylramic	2.8	$4.0 \times 10^{-6}$	>2.95	10.0	40.0–45.0
Hi-Nicalon	2.8–3.0	$4.0 \times 10^{-6}$	2.74	14.0	5.0–7.7
Tyranno (SA grade)	2.8	$4.5 \times 10^{-6}$	3.10	7.5, 10.0	65.0

0.1–0.3  $\mu\text{m}$ , though some are up to 1  $\mu\text{m}$  thick [28, 34]. Fibers and fabrics may be coated continuously, or else preforms (stacks or three-dimensional [3-D] forms) may be coated by a batch process. CVD is a routine procedure for coating continuous fibers. The fibers and fabrics may be coated continuously, or else the 3-D preforms are coated in a batch process. Though there are a number studies on different interface coatings, the toughest composites have pyrolytic carbon (PyC) or boron nitride (BN) [25]. These two interphase materials are the most commonly used; even in multilayers, one of the overcoats is typically PyC or BN.

PyC is isotropic and nongraphitizing, but when the appropriate heat treatments at 2500–3000°C are performed, the layers become laminar and graphitizable [11]. When PyC is deposited so that the graphitic layers are parallel to the fiber surface, a weak bond is formed. One detrimental property is that PyC oxidizes easily in air at low temperatures. The oxidation products are CO and CO<sub>2</sub>, which outgas and cause fiber recession and weight loss. In SiC–SiC composites, these gaps are filled by the oxidation product SiO<sub>2</sub> [35].

BN also possesses an attractive layered structure [23, 36–39]. It has either an amorphous or turbostratic structure when deposited at low temperatures, but the preferred structure is ordered hexagonal, which is obtained when BN is deposited at temperatures above 1500°C. Like PyC, BN has been demonstrated to have poor oxidation resistance in air at intermediate temperatures [40, 41]. It begins to oxidize at 850°C and is highly sensitive to moisture if it crystallizes poorly during deposition [40]. The oxidation rate of BN in dry air is lower than that of PyC because the boria (B<sub>2</sub>O<sub>3</sub>) oxidation product is a liquid rather than a gas. In the instance that SiC–fibers are used, B<sub>2</sub>O<sub>3</sub> reacts with SiO<sub>2</sub> to form a borosilicate glass [40, 41]. In the presence of moisture, boria volatilizes before the formation of a borosilicate glass occurs. The progressive oxidation of the BN and the formation of glass at the interface eventually develops a strong interfacial bond between the fiber and the matrix. This increases the interfacial shear stresses and causes embrittlement of the composite over time.

Matrix microcracks can form under high stress levels because CMCs are inverse composites, that is,  $\epsilon_m^R < \epsilon_f^R$  [42, 43]. These cracks may also form after extensive thermomechanical cycling. Oxygen can diffuse through the microcracks to oxidize the interphase layers and fibers. More work on developing oxidation-resistance interphase systems is needed.

**10.2.1.2 Preform.** The preform can be made by the layup of two-dimensional (2-D) fiber weaves, such as simple stacks or 0°/90° unidirectional fiber plies (Fig. 10.2) [44]. 3-D weaving patterns are also possible and may be preferred in applications where 2-D composites would be easily delaminated or in cases where a more complex shape is desired. The 3-D preforms may take the form of stitched fabrics, braids, or 3-D cylindrical constructions (Fig. 10.3) [45]. The machines for filament winding and weaving are varied, as these techniques are often used by the aerospace industry in the production of C/C and polymer matrix composites. The use of long, continuous fibers allows for the construction of near net shapes with complex geometries and curved surfaces that require little machining after infiltration and reaction (Fig. 10.4) [46].

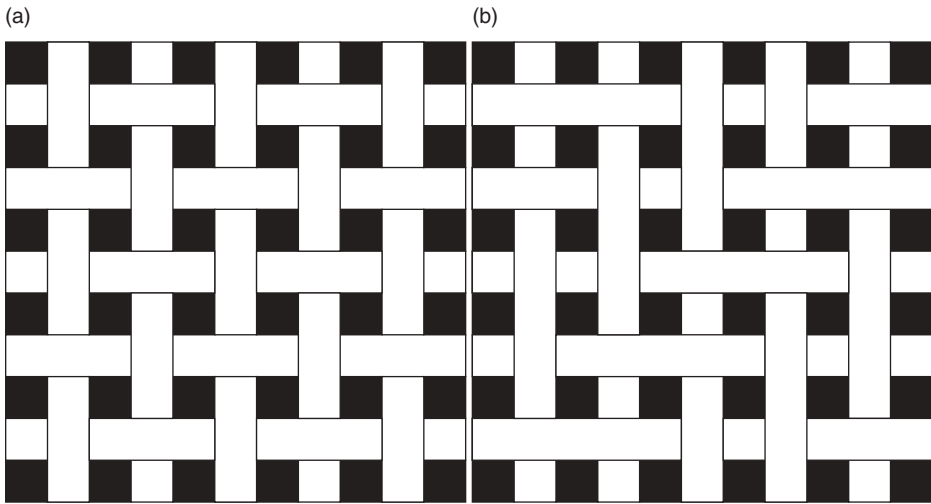


**Figure 10.2.** Example of (a) a plain weave pattern and (b) a twill weave pattern (reprinted from Ph. Vandeurzen, J. Ivens, and I. Verpoest (1996) A three-dimensional micromechanical analysis of woven-fabric composites: I. Geometric analysis, *Composites Science and Technology*, **56**[11] 1301–1315, with permission from Elsevier).

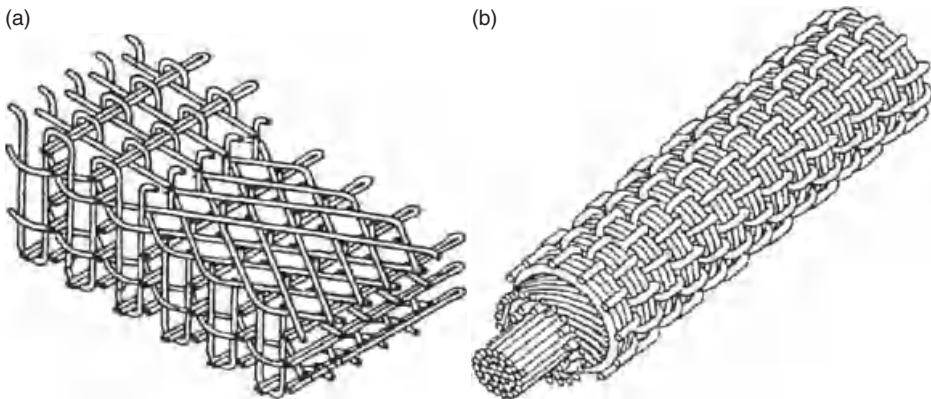


**Figure 10.3.** Examples of different three-dimensional fiber perform architectures: (a) from screw-shaft weaving and (b) from the polar weaving technique (reprinted from R. Kamiya, B. A. Cheeseman, P. Popper, and T.-W. Chou (2000) Some recent advances in the fabrication and design of three-dimensional textile performs: A review, *Composites Science and Technology*, **60** 33–47, with permission from Elsevier).

**10.2.1.3 Green Body Formation.** The green body is arranged from the coated fibers to have sufficient porosity (1) to accommodate volume expansion after reaction and (2) to provide interconnected channels for infiltration. There are two ways to produce a green body. In the first, polymer matrix-based green bodies are made, while in the second, CVI is used. Resin transfer molding (RTM), autoclave methods, or



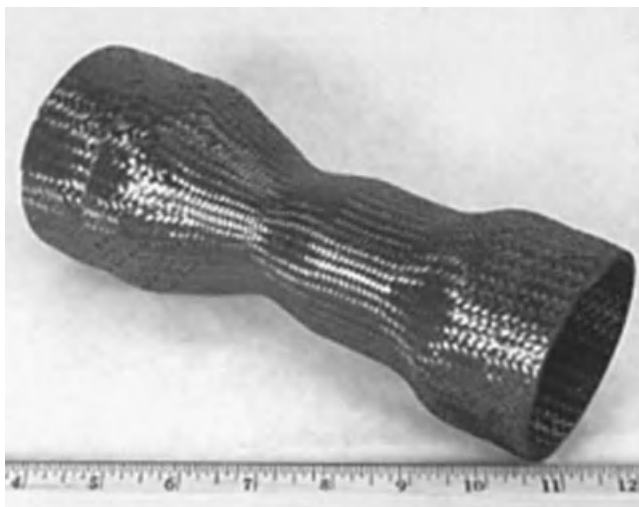


Figure 10.4. Preform in the shape of a combustion chamber for RMI (reprinted from Reference 46).

pressing can be used for the first approach. In RTM, cut fabric sheets and one-dimensional (1-D) plies are stacked together into a dry fiber preform. These preforms are infiltrated with a polymeric precursor, which is then cured to form a carbon fiber-reinforced prepreg (CFRP) green body. Pyrolysis converts the polymer matrix into amorphous carbon. With the autoclave approach, either resin impregnation of fabrics or wet drum filament winding are used to make plies. The prepregs are cut into sheets and are laminated, then compressed and autoclave cured. With CVI, a fiber preform is infiltrated with a controlled amount of gaseous precursor to form the carbon source.

**10.2.1.4 Infiltration and Reaction.** The starting melt is placed in contact with the fiber preform and enters the open pores by wicking, a form of percolation. The melt advances rapidly along the fiber tows by capillary forces, which create the only pressure gradient for fluid motion. The melt then reacts with the previously deposited carbon to form a dense ceramic matrix. Depending upon the size of the preform, the time to completion is in minutes, hours, or days.

Several artifacts are created as a result of infiltration and reaction. Unreacted metal is often left in the matrix. This is undesirable for high-temperature applications since the metal can melt and diffuse to the fibers and react, or else it may “leach” out through the surface of the composite. Metal left unreacted after RMI can be extracted by wicking, though this leaves pores. In the case of SiC-based composites, the silicon melt may be alloyed so that a refractory disilicide remains. Volume changes after reaction and a coefficient of thermal expansion (CTE) mismatch between the matrix and the interphase all contribute to matrix cracking. As such, it is important to know several physical properties of the materials used in RMI.



TABLE 10.4. Viscosities, Densities, and Surface Tension of Melt Materials

	Viscosity			Density	Surface Tension
	$T_m$ (K)	$\eta(T_m)$ ( $10^{-3}$ Pa·s)	Range (K)	$\rho(T_m)$ ( $10^3$ kg/m $^3$ )	$\gamma(T_m)$ ( $10^3$ N/m)
Si	1683	0.75	1350–1850	2.58	765
Ti	1943	4.4	1750–2050	4.17	1557
Zr	2128	4.7	1800–2300	6.21	1500
Hf	2504	5.2	2220–2670	11.82	1614
Nb	2742	4.5	2320–2915	7.73	1937
Ta	3290	8.6	3143–3393	14.75	2154
W	3695	6.9	3398–3693	16.43	2477

The properties are calculated for the temperature ranges indicated in the fourth column (data from References 116–118).

TABLE 10.5. Volume Comparisons between Solid Metal (M) to Solid Metal Carbide (MC) (Data from References 27 and 119–121)

M	Molecular Weight (g/cm $^3$ )	Molar Volume (cm $^3$ /mol)	MC	Molecular Weight (g/cm $^3$ )	Molar Volume (cm $^3$ /mol)	% Expansion, M to MC
Si	28.09	11.11	SiC	40.10	12.45	10.8
Ti	47.90	10.46	TiC	59.91	12.21	16.7
Zr	91.22	14.06	ZrC	103.23	15.62	11.1
Hf	178.49	13.41	HfC	190.50	15.04	12.2
Nb	92.91	10.84	NbC	104.92	13.45	24.1
Ta	180.95	10.64	TaC	192.96	13.31	25.1
W	183.85	9.53	WC	195.86	12.475	30.9

Possible melt materials for RMI include Si and the refractory metals: Ti, Zr, Nb, Hf, Ta, and W. The relevant properties of these metals are compiled in the following tables. The melt viscosities and surface tension play important roles in the infiltration rate. A relatively low viscosity and surface tension will lead to greater infiltration lengths in the preform, and these properties can be achieved by increasing the processing temperature. Of course, an increase in processing temperature is damaging to the fibers, so a balance must be struck between maintaining the strength integrity of the composite and enhancing infiltration length through the bulk of the preform.

The values for the metal melts are shown in Table 10.4. It is important to note that Hf, Nb, Ta, and W melt at temperatures exceeding 2000 K. For these higher melting metals, it is important to coat the fibers well for protection.

One of the contributors to matrix cracking is volume change accompanying carbide formation (Table 10.5). Of the different systems under consideration, Si to SiC exhibits the smallest volume expansion followed by Zr to ZrC. The comparisons of volume expansions between the carbides in Table 10.5 can also be supported with the values

TABLE 10.6. Coefficients of Thermal Expansion and Corresponding Temperature Range for Carbides (Data from References 112 and 122–130)

	CTE ( $\times 10^{-6}/^{\circ}\text{K}$ )	Temperature Range (K)
SiC	4.8	293
	4.5	293–1673
TiC	8.05	293–1573
	$9.5 \pm 0.3$	293–2973
ZrC	19.2–22.5	1000
	4.0	293
	10.2	2973
	6.4	293–1673
NbC	$7.6 \pm 0.2$	293–2973
	6.7	293–1273
TaC	$6.4 \pm 0.3$	298–2273
HfC	$7.3 \pm 0.2$	293–2973

of the CTE in Table 10.6. SiC exhibits the smallest CTE over a wide temperature range, while most of the other carbides fall between  $5.0$  and  $8.0 \times 10^{-6}/\text{K}$ . As a comparison, the axial thermal expansions of Tyranno fibers are between  $3.1$  and  $4.5 \times 10^{-6}/\text{K}$  from room temperature up to  $1273\text{ K}$  [27].

Considering the CTE values for fibers and carbides, it is evident that the mismatch means that matrix cracks will form. During heating, the ceramic matrix will expand relative to the volume of liquid metal; however, the expansion of carbon fibers along the axial direction is negative and along the radial direction is positive. The axial expansion of the fibers will restrain some of the matrix expansion.

## 10.3 PROCESS MODELING

### 10.3.1 Background

Material selection can be tested by careful predictive modeling verified by experimental results, but understanding the kinetics of infiltration and reaction in MI is essential to achieve meaningful results. This subsection introduces several studies that have been conducted on this topic.

Infiltration occurs by the passage of molten metal through open channels in the preform. In the simplest case, movement of the fluid front is governed by capillary forces and surface tension. When a liquid wets the channel walls, the pressure drop across the liquid/atmosphere (convex) interface forces the liquid to move up the channel. Under equilibrium conditions, this capillary force is equal to the weight of the liquid column inside the channel:

$$\Delta P = \frac{2\gamma}{r} = 2\gamma \left[ \frac{\cos(\theta)}{R} \right] = \rho gh, \quad (10.1)$$

where

- $\rho$  is the liquid density,
- $g$  is the gravitational constant, and
- $\gamma$  is the surface energy of the liquid,

and the wetting phenomenon is described by Young's law:

$$\cos(\theta) = \frac{(\gamma_{SV} - \gamma_{SL})}{\gamma_{LV}}, \quad (10.2)$$

where

- $\theta$  is the wetting angle and
- $\gamma$  are the interfacial energies of the solid–liquid (SL), solid–vapor (SV), and the liquid–vapor (LV) phases.

The wetting angle is fixed in this case. A wetting liquid on flat solid material possesses a wetting angle of  $\theta < 90^\circ$ ; that is, it spreads easily, while a nonwetting liquid possesses a wetting angle of  $\theta > 90^\circ$ ; that is, it beads up on the surface. The molten metal must wet the preform in order to advance through the capillary channels. The fact that RMI involves a reacting melt, however, makes the issue more complicated. The reaction front lags slightly behind the infiltration front and is governed by mass transfer, heat transfer, and chemical reaction. As the reactions proceed, there is an evolution of the capillary forces at the three-phase boundary [47–49].

The infiltration behavior of the melt can be assessed through modeling the viscous fluid flow. The ease with which a fluid can pass through a porous material is the permeability of the medium,  $K$ . Physically,  $K$  encompasses many of the medium's properties, such as porosity, tortuosity, pore size distribution, and, in the case of capillary-driven flow, the wetting behavior of the fluid. The more complex case of reacting flow is developed from the simpler situation of viscous fluid flow through porous media.

### 10.3.2 Infiltration

Darcy's law [134] describes the dependence of macroscopic flow velocity,  $Q$ , on the permeability of the medium,  $K$ , the pressure gradient over the fluid flow length,  $\Delta p/L$ , the cross-sectional area of the flow channel,  $A$ , and the dynamic fluid viscosity,  $\mu$  (Fig. 10.5):

$$Q = -K \frac{A \Delta p}{\mu L}. \quad (10.3)$$

The negative sign in Equation 10.1 accounts for fluid flow from areas of high pressure to low pressure. This well-known law is the basis for many relations of fluid flow in porous media.

Kozeny [50] introduced the concept of a “hydraulic radius,”  $r_h$ , to account for noncircular cross sections in the flow channels. The hydraulic radius is defined as the ratio of capillary cross-sectional area normal to the flow and the wetted perimeter. For

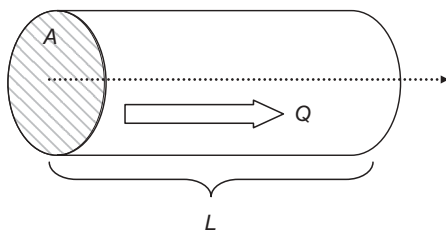


**Figure 10.5.** Darcy's law is visualized in this schematic of a pore/channel.

a capillary with a circular cross section,  $r_h$  is simply defined as  $R/2$ . With the hydraulic radius, Kozeny was also able to describe the pressure drop that occurs over the thickness of the flow medium. Carman [51] expanded upon the flow-rate pressure drop relation given by Kozeny to relate to the situation encountered by Newtonian fluids moving through beds of packed spherical particles (Eq. 10.4):

$$\frac{\Delta p}{L} = \frac{150 \bar{V}_0 \mu (1-\varepsilon)^2}{\Phi_s^2 D_p^2 \varepsilon^3}. \quad (10.4)$$

The Washburn equation [52] is considered to be rigorous for quasi-steady-state penetration into a uniform capillary tube. The pores are assumed to be parallel with uniform effective radii,  $r_{\text{eff}}$ . The time to flow distance  $x$  is described by Equation 10.5:

$$x^2 = \frac{\gamma D t \cos(\theta)}{4\eta}, \quad (10.5)$$

where  $x$  is the distance traveled,  $t$  is the time to travel,  $\theta$  is the contact angle of the melt on the capillary wall,  $\gamma$  is the surface tension of the melt,  $\eta$  is the melt viscosity, and  $D$  is the capillary diameter. In this model, however,  $r_{\text{eff}}$  cannot be assigned to a real porous medium because applying the kinetics of capillary rise produces infiltration rates that are two to three orders of magnitude larger than what is found experimentally.

Dullien [53, 54] developed 2-D and 3-D interconnected networks of nonuniform pores. In this structure, there are parallel paths with differing effective mean diameters, which are represented by repeating elements of stepped radii. This model was used to determine an equation for the rate of capillary penetration. The Dullien model was tested experimentally by measuring the rate of capillary rise of several liquids in sandstone [54]. The apparent capillary diameters were calculated from the experimental results and Washburn's equation for the different liquids used. The apparent diameters were found to be several orders of magnitude smaller than the pore diameters calculated from mercury intrusion porosimetry. Using the network model, however, yielded results that were in good agreement.

Hillig et al. [19] also developed a model to approximate the flow through random porous structures. Nonuniform capillary cross sections were modeled as cusped trian-

gular channels with tetrahedral chambers along their lengths, forming a so-called throat and chamber model. Starting with the Poiseuille capillary flow equation,

$$\frac{dV}{dt} = \frac{\pi r^4 p}{8\eta x}, \quad (10.6)$$

where  $V$  is the volume that flows through a single capillary and  $r$  is the “effective” radius, the case of capillarity-driven flow was considered when  $=2\gamma/R$ , where  $R$  is the effective maximum radius (pore chamber size). The number of capillaries per unit area can be represented as  $f/\pi r^2$ , where  $f$  is the open porosity. The flow rate is then

$$\frac{dx}{dt} = \frac{fr\gamma\left(\frac{r}{R}\right)}{8\eta} = k, \quad (10.7)$$

where  $k$  has the dimensions of a diffusion coefficient. The infiltration rates of nonreacting oxide melts that passed through a hot-pressed SiC preform were compared to what was predicted from the model. It was found that the  $k$  parameters from Equation 10.7 and from the experiment were in relatively good agreement.

### 10.3.3 Infiltration and Reaction

In these early models, it was always assumed that the liquid was nonreactive so that infiltration was mainly controlled by viscous flow. It is difficult to deal accurately with reactive flows with the assumption of thermodynamic equilibrium during flow and the use of Young’s law in the Washburn equation. Capillary flow in diffusion-controlled situations involves many transitions, such as changing capillary radii, and temperature gradients over the length of the flow. The Si–C system is an ideal model to study because of the commercial use of RMI C–SiC and SiC–SiC. Unfortunately, the kinetics of the  $\text{Si} + \text{C} \rightarrow \text{SiC}$  reaction remain a source of debate [55–61]. In particular, it is not definitely known (1) what the growth law is, (2) whether the growth process is controlled by bulk diffusion, (3) which is the dominant transport species, and (4) whether the phase state of the specie has any bearing on the growth kinetics [55]. It is generally agreed that the carbon type is a major factor in the kinetics and morphology of the SiC product [55].

Infiltration commences as soon as the silicon melt is fluid enough to enter the preform. The viscosity of the silicon is large initially but decreases with increasing temperature [62]. What is known is that the rate of silicon infiltration is dependent on the size of the preform (e.g., pore length), the pore diameter, the wetting capability of the preform surfaces, and the viscosity of silicon.

The kinetics of the SILCOMP process [55–57] were studied using a modified version of the Dullien model. The pores were approximated as a repeating unit of two different diameters. The infiltration rates in (1) reacting and (2) nonreacting systems were predicted, as well as the magnitude of the functional form of temperature rise due to the exothermic reaction. A parabolic reaction rate was determined from experiments

using liquids of varying viscosities. In the experiment, the peak temperature decreased with the progression of the melt front. This was correlated to the decrease in velocity of the front, which is a result of the slowing down of wetting and the reaction rate of the particulates into the porous preform. The carbon tapes used in the study, however, allowed the melt to preferentially wet the surface and to traverse the length. Another SILCOMP study confirmed the parabolic reaction rate from the Nernst–Noyes–Whitney equation for the mass dissolution rate of carbon [58]. The fibrous nature of the SiC was attributed to the solution reprecipitation process, wherein  $\beta$ -SiC formed in areas previously occupied by carbon.

The infiltration rates of alloyed melts are another important course of study since the infiltration properties and reaction behavior of the melt are different from those of a simple metal. For a silicon–molybdenum melt [59], the experimental results of the Si–C reaction and the Kozeny expression for permeability were used to predict the reaction kinetics. In the case of constant permeability, the infiltration kinetics would be parabolic. However, this same relation would not hold in RMI. The microstructure of the resulting composite displayed good uniformity and no choking off was observed. This work substitutes a time-varying permeability into Darcy's law to predict the behavior of silicon infiltration into a graphite preform. The reaction rate constants were taken from other data [60]. The infiltration kinetics were obtained by integrating the following equation for the volumetric flow rate:

$$q = \frac{dl}{dt} (\text{cm/s}) = -\frac{K\Delta P}{\eta l}. \quad (10.8)$$

According to the model calculations, a linear reaction rate was found to agree better for short reaction times, while a parabolic rate constant was determined for longer times. However, the assumption that permeability did not vary throughout the infiltration length led to an underestimation of infiltration depth by about 10%.

This formulation of the Si–C kinetics is markedly different in [61]. The growth of the SiC layer followed a fourth-order power law:

$$\delta = kt^{\frac{3}{4}}, \quad (10.9)$$

which relates the thickness of the reaction layer to time  $t$  and constant  $k$ , determined from the experiment. The value of  $k$  was found to be constant for various processing temperatures up to around 1500°C. This indicates that exothermic reaction produces most of the local temperature near the reaction front. Attempts to fit the kinetics to both a parabolic and linear rate law were unsuccessful.

Nelson and Colella [63] studied the infiltration dynamics of Si and the kinetics of reaction in a medium with pores approximated as uniformly distributed parallel capillaries. A major assumption was that the overall volume of the preform remained constant. In addition, the permeability was assumed to be constant. In reality, the porosity would vary in time, and the accumulation of volume expansion after reaction would cause some deformation of the preform.

The unification of a micro- and macromodel into an expression for the transverse permeability was described by Rajesh and Bhagat [64–67] for the Si–C system with hexagonally packed fibers. The permeability results were compared to those developed by Gebart for the same fiber orientation [68]. The solution to the unsteady-state problem was used to optimize several processing parameters, which include processing temperature and fiber volume fraction.

The need for better modeling of infiltration and reaction in RMI includes better computational capabilities and an improved understanding of the physical processes involved. One such study can couple the reaction and product formation along the capillary walls along with nucleation in the melt. In addition, the exothermic effects of reactions during flow are omitted in many of the current analytical models of reactive flows. Accounting for this effect is important as the surface tension and viscosity are strong functions of temperature. Local exothermic heating can alter these two parameters so that the melt penetration depth is increased. Morphological changes with the discontinuous growth of the reaction layer may also be considered. This additional roughness, plus any interfacial cracking, will slow the infiltration rate in the capillary because of the accompanying pressure drop. The reaction layer also presents a diffusion barrier to further growth, thereby slowing down the reaction process.

It is pertinent to note that no predictive modeling can accurately describe the kinetics of a system. Properties of the melt like wetting depend on the gas partial pressure, temperature, wetting surface roughness, and so on. In these instances, it may be better to rely on phenomenological expressions to analyze reacting flows through narrow channels.

## 10.4 MICROSTRUCTURE AND PROPERTIES OF MELT-INFILTRATED COMPOSITES

CMCs made by RMI have multiphase matrices composed of ceramic and metal phases. The residual metal is due to the diffusion-dominated process and the incomplete infiltration of the pore network. One major step toward increasing the ceramic yield of the matrix is to understand the relationship between processing parameters, microstructure, and properties. The next subsections detail some of the different RMI processes and the resulting composite properties.

### 10.4.1 SiC

**10.4.1.1 Reaction Bonding and the REFEL Process.** The REFEL process was one of the first commercial-scale processes that used liquid infiltration to form SiC-based composites [42, 60, 69–74]. REFEL involves reaction bonding to consolidate SiC powder with SiC produced from reaction at high temperatures. Colloidal graphite, SiC powder, and a polymeric binder are mixed and shaped by plastic forming [69, 72]. The SiC in this starting mixture acts as a seed to start further SiC nucleation in the carbon source. The mixture of powders and binder forms the green body, which is then heated to remove the binder. The porous preform is siliconized at  $\sim 1650^\circ\text{C}$ , and the resulting SiC is both  $\alpha$ -SiC (hexagonal and trigonal polytropes) and  $\beta$ -SiC (cubic

structure) phases. Some of the  $\alpha$ -SiC is the original phase, while the finer-grained  $\beta$ -SiC crystallites are precipitated from the dissolved graphite in the Si melt. The formation mechanism has been described [60, 71–74] as that of carbon dissolution in the melt and SiC precipitation from the supersaturated melt at heterogeneous nucleation sites. The low solubility of the C in Si was suggested to be the rate-controlling step in the process [74]. The heat evolved locally accelerates more carbon dissolution and increases the reaction rate. In addition, it was found that the local temperature rise also contributed to the transformation of the  $\beta \rightarrow \alpha$ -SiC phase. The microstructure is controlled by the availability of nucleation sites and the mode of carbon transport (to determine where the reaction occurs) [74].

The bulk of the strength of REFEL SiC is derived from the impingement of the formed epitaxial SiC since the  $\beta$ -SiC possesses such a small grain boundary area, though no official strength data are widely available. A study of the crystallographic texture [74] revealed no preferred orientation, but at the same time, an increase in SiC grain size in the preferred direction along the weak Si–SiC interface was observed. This anisotropy occurred through mechanical particle alignment [74]. This was tested by three-point bending. The fracture-initiating flaws were found to be the Si–SiC interface, and it was surmised that the silicon distribution in this interface is controlled by the alignment of the grains. The overall strength of the composite is compromised by the reaction of the carbon surfaces with the melt [74]. The uncontrolled infiltration pathways mean that all areas of carbon fiber surfaces are exposed to the reacting melt. In addition, the silicon matrix limits the strength as temperatures approach its melting point.

In another variation of this process, silicon carbide layers are formed from direct siliconization of the carbon source [18, 42, 72, 75–77]. Silicon carbide growth occurs from the diffusion of silicon to the SiC–C interface [69]. Porous SiC particulate preforms held together by organic binders are infiltrated with molten Si to form dense Si–SiC composites. Carbon fiber or carbon felt preforms may also be used, in which case the carbon fully converts to SiC after processing [42]. The green body contains no starting SiC and is made from woven resin precursor-coated carbon fiber fabrics. The green body is cured and pyrolyzed in a nitrogen atmosphere to fully convert the resin matrix into carbon. This step is also accompanied by matrix shrinkage, which is partially countered by the stiffness of the fibers. The silicon melt can only travel through segmentation cracks and microdelaminations in the C/C preform. The melt reacts with both fibers and matrix to form SiC (Fig. 10.6).

**10.4.1.2 SILCOMP and HiPerComp.** The SILCOMP (or the “Toughened Silcomp”) process was developed by GE in 1975 to produce Si–SiC materials in which the Si in the matrix would protect the fibers from high temperatures and oxidation [18–22, 78–80]. Molten silicon reacts with low-density monofilament carbon fibers to form  $\beta$ -SiC crystallites 1–50  $\mu\text{m}$  in size that retain the shape and direction of the fibers [20]. The resulting composite is uniaxial and highly anisotropic. The strength tested parallel to the fiber direction increases linearly with the increasing volume content of SiC, while perpendicular to the fiber direction, the composite is much weaker and shows a nonlinear relationship between the strength and the volume content of SiC [20]. This



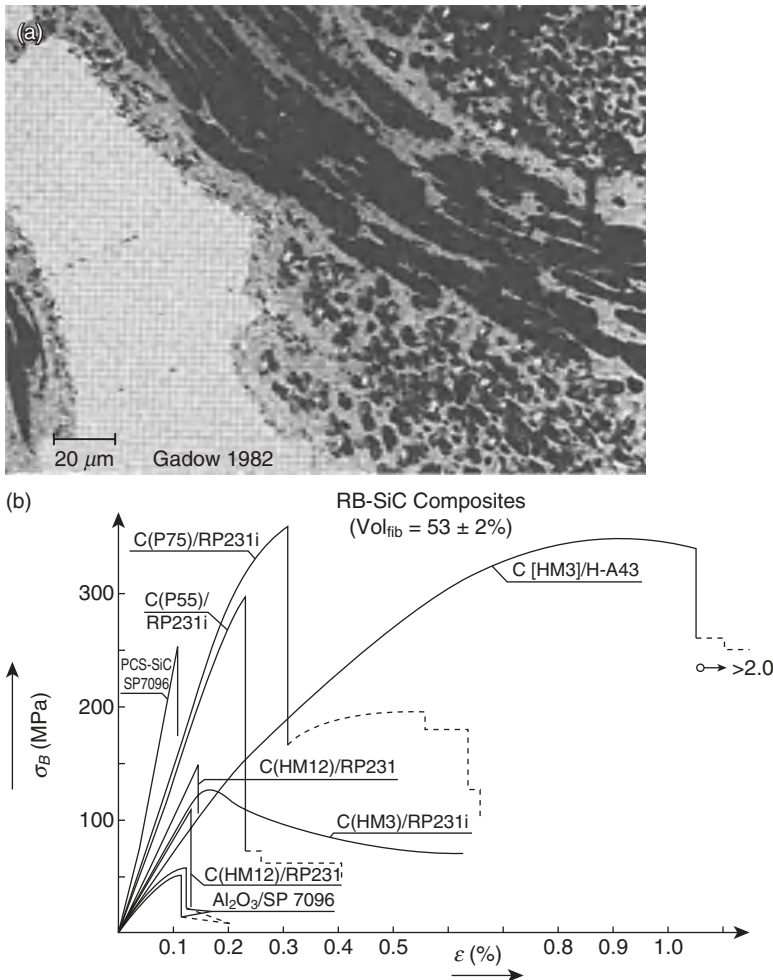


**Figure 10.6.** (a) Micrograph of a SiC composite produced by direct siliconization of C/C and (b) stress-strain curves of reaction-bonded silicon carbide composites that demonstrate improved toughness over traditional CVI-made SiC (Reprinted from E. Fitzer (1988) Composites for high temperatures, *Pure and Applied Chemistry*, **60**[3] 287–302, with permission from the Managing Editor of *Pure and Applied Chemistry*)

was attributed to the interconnectivity of the SiC in both directions. It is clear that SILCOMP produces a tailorable composite. By choosing fibers with different surface characteristics and orientations, one can control the growth density and direction of the SiC grains.

The poor mechanical properties of the SILCOMP material led to the development of another infiltration process (HiPerComp) that uses SiC-fibers [77]. HiPerComp begins with a BN-coated multifilament tow of either Hi-Nicalon or Sylramic ceramic fibers [21, 22]. Production of HiPerComp materials follows either a prepreg or a slurry-casting route.

In the prepreg approach, continuous SiC-fiber tows are coated with a BN interphase and another overcoat by CVD. The tows are then formed into unidirectional prepreg sheets by wet drum winding, after which the sheets are laid up and laminated to make the preform. The polymer matrix is converted to carbon after burning out the binder. This porous preform is then infiltrated [78–80].

The slurry-cast process differs mainly in the treatment of the fibers. The first step involves weaving them into a 2-D or 3-D cloth, which are then laid up or woven into the preform shape. The deposition of the overcoat is paused midprocess to slip cast a SiC slurry into the preform. Silicon melt infiltrates the preform in the final step. The exchange of a SiC-based fiber for the carbon fiber has proven to be effective in preventing fiber degradation, but the large diameters ( $\sim 14\ \mu\text{m}$ ) make them too stiff for complex shapes. The matrix is dense and typically contains 5–15 vol % residual Si [80].

**10.4.1.3 Liquid Silicon Infiltration (LSI) Process.** The LSI process (Fig. 10.7) produces C/C-SiC and SiC-SiC materials [42, 81]. Polymer-based green bodies are first pyrolyzed for several hours in an inert gas atmosphere to produce a porous C/C preform. Microcracks form as a result of the tension stress, creating open channels for the molten silicon to flow through. Before siliconization of the C/C preforms at  $1650^\circ\text{C}$ , a controlled amount of Si is added to form SiC. The dense inner portions of the C/C bundles are not infiltrated and remain unreacted.

The matrix is composed of  $\beta$ -SiC crystals, residual C and Si, as well as crystalline SiC particles ( $<100$  microns in size) in a SiC-SiC matrix, which is built up by slurry casting or by the prepreg method. The typical amount of residual Si ranges from 2 to 5 vol % to 17 vol % for C-SiC, C/C-SiC, and up to 18 vol % for SiC-SiC [8, 42]. Also, because of the dense carbon bundles, the volume content of carbon is higher for the LSI composites, so the SiC content is about 20–30 vol % [42]. Compared to other RMI composites, this is a low SiC content.

The mechanical properties of the resulting composites are highly dependent on the fiber content and microstructure. It was found that the MI, CVI, and PIP/liquid polymer infiltration (LPI) demonstrated similar high values of room-temperature ultimate strength and strain-to-failure capabilities [42]. However, for MI-C/C-SiC, the tensile and flexural strengths are comparatively lower at the same temperatures. It was also found that the MI-C/C-SiC materials possessed higher interlaminar shear strengths as compared with the CVI and LPI/PIP materials due to lower porosity [42]. At temperatures above  $1200^\circ\text{C}$  and in vacuum, the tensile strength of the C/C-SiC decreases due to fiber oxidation [42].

The mechanical properties of SiC-SiC are different [42]. Unlike for C/C-SiC, the overall CTE is only slightly influenced by the temperature (since the fibers and matrix are the same). The ultimate tensile strength of SiC-SiC materials decreased at high temperatures due to slow crack growth and creep cavitation in the ceramic fibers. The lifetime of these materials decreased with temperature and with increasing tensile loads up to  $\sim 950^\circ\text{C}$  because of matrix oxidation [42]. High temperatures coupled with oxygen exposure lead to recession of the fiber coating and a buildup of glassy phases. This, in turn, leads to localized fiber attack and high fiber-matrix bonding [42, 135].

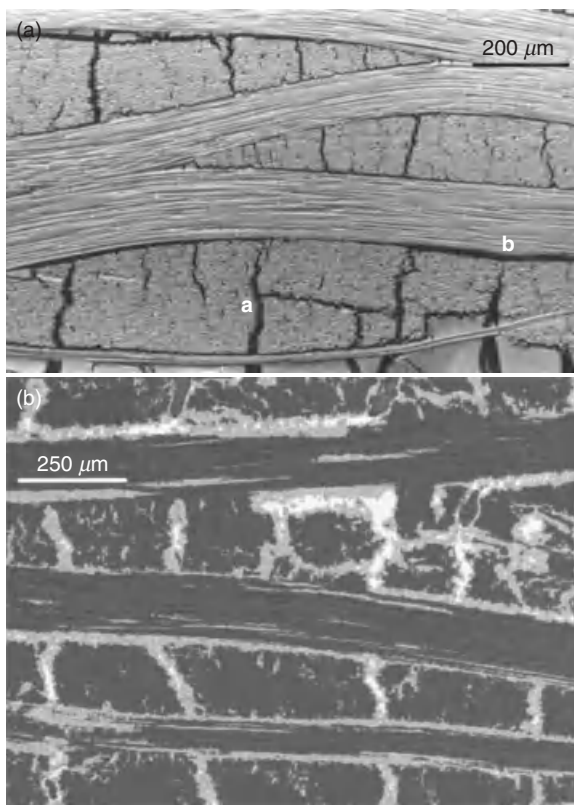


**Figure 10.7.** (a) Scanning electron microscopy (SEM) image of the microstructure of an LSI composite after carburization, where “a” and “b” designate the segmentation cracks and microdelaminations, respectively; (b) after the final processing steps. The Si phase is white, SiC is gray, and carbon is black (reprinted from J. Schulte-Fischedick, A. Zern, J. Mayer, M. Rühle, M. Frieß, W. Krenkel, and R. Kochendörfer (2002) The morphology of silicon carbide in C/C-SiC composites, *Materials Science and Engineering A*, **332**[1–2] 146–152, with permission from Elsevier).

A comparison of the room temperature properties of HiPerComp (GE) and LSI composites (DLR) are shown in Table 10.7. The elastic properties of both materials are markedly different. The larger SiC content and SiC-fibers in the HiPerComp materials are certainly the largest factor in this difference.

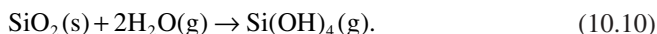
#### 10.4.2 SiC + Silicide Matrices

Silicon carbide is easily volatilized in a combustion environment, which typically contains about 10% water vapor. The presence of water vapor, along with other gases

TABLE 10.7. Comparison of Room Temperature Properties of Different Melt-Infiltrated Composites (Data from References 8, 21, 42, and 80)

	LSI C/C-SiC (yDLR)	Slurry-Cast Prepreg HiPerComp SiC-SiC (GE)	Prepreg HiPerComp SiC-SiC (GE)
Density (g/cm <sup>3</sup> )	1.9–2.0	2.70	2.80
In-plane CTE (10 <sup>-6</sup> /K)	–1–2.5	3.74	3.57
Tensile strength (MPa)	80–190	358	321
Elastic modulus (GPa)	50–70	196	285
Interlaminar shear strength (MPa)	28–33	–	135
Residual Si (vol %)		~12	5–15
Porosity (vol %)	2–5	6	<2
Typical fiber content (vol %)	55–65	35	20–25

such as hydrogen and carbon dioxide, increases the oxidation rate by more than an order of magnitude [82] and causes SiO<sub>2</sub> to volatilize:



Over extended periods of time, the rates of SiO<sub>2</sub> growth and volatilization become about the same so the layer thickness is constant. After this stage, linear weight loss and SiC recession are observed. The resistance of SiC to water vapor is also poor and the degradation is much more severe [82]. Alloyed silicon melts for reactive infiltration are attractive for minimizing the residual silicon phase [82–88]. Alloying constituents are chosen so that upon formation of the primary SiC product, the alloy solute(s) are displaced into the melt as further reaction between silicon and carbon proceeds. This continues until the melt precipitates a refractory silicide phase. Using simple alloyed melts is possible because many binary eutectic alloys exist between refractory silicides and silicon with a large single-phase field. Another advantage is that the silicides have higher melting points than silicon and exhibit ductile behavior at high temperatures. Of all the silicides, MoSi<sub>2</sub> has demonstrated the best oxidation resistance and a high melting point of ~2050°C [57] (Table 10.8).

A study by Bhatt and Hebsur [88] was conducted to determine the effects of residual silicon on the tensile strength, creep, and thermal conductivity of RMI SiC–SiC composites. At higher temperatures (~1200°C), the tensile creep and transverse thermal conductivities were not significantly affected by a residual silicon content of up to 24 vol %.

Carbon fiber and carbon felt preforms were infiltrated by alloyed melts of Si, Ti, and MoSi<sub>2</sub> [83, 84] (Fig. 10.8). The preform with the large porosity demonstrated the greatest amount of carbon fiber reaction with the alloy. The phases identified after reaction were SiC, MoSi<sub>2</sub>, and a solid solution of (Ti<sub>0.8</sub>, Mo<sub>0.2</sub>)Si<sub>2</sub>. Of the two types of

TABLE 10.8. Room Temperature Flexure Properties of SiC- and Silicide-Based Composites Tested in an Inert Environment

Preform + Matrix	Property			
	Tested at 25°C		Tested at 1600°C	
	Bending Strength <sup>a</sup> (MPa)	Bending Strain <sup>b</sup> (%)	Bending Strength <sup>a</sup> (MPa)	Bending Strain <sup>b</sup> (%)
C/C + MoSiTi (CM)	199 ± 3	0.63 ± 0.02	244	0.69
C/C + Si (CS)	206 ± 19	0.7 ± 0.04	246	1.19
Felt + MoSiTi (FM)	150 ± 7	0.34 ± 0.02	85	0.61
Felt + Si (FS)	123 ± 4	0.38 ± 0.01	56	0.52

<sup>a</sup> Three measurements at 25°C, one measurement at 1600°C.

<sup>b</sup> The strain values include the strain of apparatus and therefore can be used only for comparison.

Reprinted from M. Esfahanian, J. Guenster, J. G. Heinrich, J. Horvath, D. Koch, and G. Grathwohl (2006) High-temperature mechanical behavior of carbon-silicide-carbide composites developed by alloyed melt infiltration, *Journal of the European Ceramic Society*, **28**[6] 1267–1274, with permission from Elsevier).

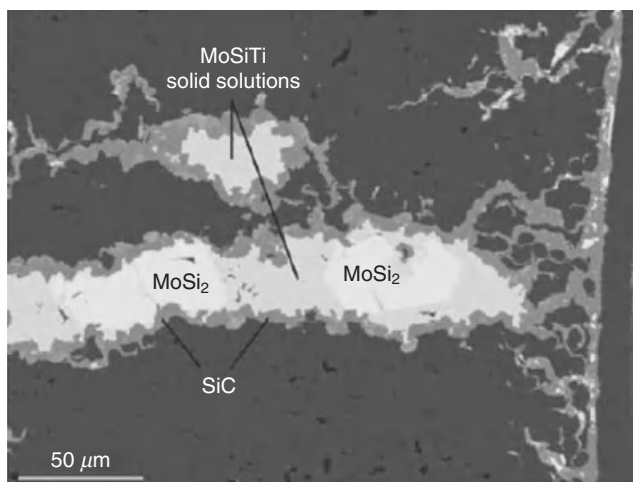


**Figure 10.8.** Microstructure of the MoSi<sub>2</sub>-containing composite after infiltration of C/C preforms (reprinted from M. Esfahanian, J. Guenster, J. G. Heinrich, J. Horvath, Dietmar Koch, and G. Grathwohl (2006) High-temperature mechanical behavior of carbon-silicide-carbide composites developed by alloyed melt infiltration, *Journal of the European Ceramic Society*, **28**[6] 1267–1274, with permission from Elsevier).

preforms used (C/C and carbon felt), the composites reinforced with C/C consistently demonstrated higher strengths in the three-point bend tests than the felts. However, when each type of preform was compared against the same type of preform infiltrated with Si, the felts infiltrated with the alloy performed better against the Si-infiltrated felts. The strengths of the alloyed C/C were comparable to those of the the C/C

TABLE 10.9. Room Temperature Flexure Strength of Melt-Infiltrated SiC- and Silicide-Containing Composites (Data from References 85 and 86)

	Si-NbSi <sub>2</sub> - $\beta$ SiC	Si-MoSi <sub>2</sub> - $\beta$ SiC
Room temperature strength (MPa)	290 $\pm$ 40	288 $\pm$ 15
$K_{IC}$ (MPa $\sqrt{m}$ )	3.7	3.3 $\pm$ 0.2

infiltrated with Si at both room temperature and at 1600°C [83, 84]. The difference between the C/C and felt composites was in the microstructure. After the felts were infiltrated by the alloy, grain growth and recrystallization produced secondary microfibers and primary crystals that helped the composite withstand higher stresses.

Microporous carbon preforms were also infiltrated with either Si-1.7 atomic%Mo or Si-3.2 atomic%Mo [85]. The microstructure was composed of MoSi<sub>2</sub> and residual Si phases distributed uniformly around a reaction-formed SiC matrix. The average room-temperature fracture toughness values were slightly higher than that of conventional reaction-bonded SiC [85]. These results can be compared to Si-Nb-SiC formed by infiltration of Si-5 at%Nb [86]. The resulting phases were  $\beta$ -SiC, NbSi<sub>2</sub>, and Si. Two types of preforms were used: small pore size preforms and medium pore size preforms. Microstructural studies confirmed the complete conversion of carbon by the melt and a uniform distribution of NbSi<sub>2</sub> and Si phases in the SiC matrix. The average room-temperature fracture toughness was higher than a Si-Mo-SiC composite made by the same method. Both composites possessed a higher room-temperature fracture toughness than that of conventionally hot pressed SiC (2.5  $\pm$  0.2 MPa $\sqrt{m}$ ), which makes sense because the porosity of the former is much lower (Table 10.9).

Chakrabarti and Das [87] prepared MoSi<sub>2</sub>/SiC by melting Si and Mo powders and by infiltrating a carbonaceous SiC preform with the melt mixture. The reaction-formed SiC and excess porosity was filled with MoSi<sub>2</sub>. Characterization of composites infiltrated by 7.14 and 29.36 wt % Mo revealed  $\alpha$ - and  $\beta$ -SiC, MoSi<sub>2</sub>, Si, and graphite. The relative proportion of MoSi<sub>2</sub> closely matched that of Mo in the starting melt. No reaction between SiC and MoSi<sub>2</sub> was observed and bonding was good. However, the densities of the final composite were relatively low (88.99–95.00%), and an intermediate zone between SiC and MoSi<sub>2</sub> was observed to contain Si and other trace metals. This was attributed to impurities in the raw material. No mechanical properties were studied, but it is certain that the strength would be lower than expected due to the presence of this intermediate zone.

Bhatt and Hebsur [88] prepared a SiC/MoSi<sub>2</sub>-SiC. The composite consisted of 60 vol % 2-D-woven BN/SiC-coated Hi-Nicalon SiC-fibers and a 40 vol % MoSi<sub>2</sub>-SiC matrix. Room temperature tensile test results showed that matrix-dominated properties, such as the elastic modulus, were not as good as those of SiC-SiC composites, which is different from what was observed in References 83 and 84. This could be due to a difference in fiber types (carbon vs. SiC) and volume fraction between both composites. Matrix cracking arose from CTE differences between MoSi<sub>2</sub> and SiC grains. The tensile strengths for Hi-Nicalon SiC/epoxy, SiC/MoSi<sub>2</sub>-SiC, and SiC-SiC composites were compared and were found to be very similar (Table 10.10) [88]. This suggests that there

TABLE 10.10. A Comparison of Room-Temperature Tensile Data for Hi-Nicalon SiC/Epoxy, SiC/MoSi<sub>2</sub>-SiC, and SiC-SiC Composites (Data from Reference 88)

Composites	Layup	<i>E</i> (GPa)	UTS (MPa)
SiC/MoSi <sub>2</sub> -SiC	PW	131 ± 7	264 ± 20
SiC/MoSi <sub>2</sub> -SiC	5HS	125 ± 24	329 ± 52
SiC/MoSi <sub>2</sub> -SiC	8HS	160 ± 3	304 ± 8
SiC-SiC	5HS	215 ± 18	215 ± 18

UTS, ultimate tensile strength.

is minimal degradation of the fibers and fiber coatings in the SiC/MoSi<sub>2</sub>-SiC composite and that fiber architecture has no major effect on the overall tensile properties.

The high-temperature strength data of these refractory disilicide/SiC composites is promising. Further study of infiltrating different alloyed melts should be conducted to create a comprehensive database of physical and mechanical properties to high temperatures. Since the residual metal is instead replaced with a refractory disilicide, it is expected that these composites will demonstrate higher strengths and oxidation resistance at high temperatures. One disadvantage to this method is less microstructural control over where the disilicide precipitates and whether or not a metal-silicon solid solution may form. The increase in ductility of the latter phase at high temperatures can reduce the overall strength as residual Si does. If a more tailorable matrix could be developed, these composites could be more favorable for high-temperature applications.

## 10.5 APPLICATIONS

The high-temperature creep resistance and microstructural stability of nonoxide CMCs are attractive properties for use in engines for reusable vehicles, aircraft engine components (such as combustors and turbines), heat exchangers, and in the stationary components of high-powered gas turbines. These composites also possess high thermal conductivities and low thermal expansion, which make them resistant to thermal stress.

### 10.5.1 Engines and Gas Turbines

Improvements in gas turbine efficiency have been driven by increasing engine temperatures. Until recently, gas turbine elements have been made of creep-resistant single-crystal or polycrystalline Ni-based superalloys. Unfortunately, these alloys melt below 1400°C. Increasing demands encountered during service go beyond the structural limits of these superalloys, which are sometimes operated at temperatures 90% of their melting points [42]. CMCs are particularly desirable as replacements because they have lower densities and do not require cooling cycles during operation. Nonetheless, CMCs are limited to stationary parts such as shrouds, combustors, and nozzles, and thus far have not lasted longer than the required minimum service time of 30,000 h [42, 89, 90].



Thus far, RMI CMC components have already been developed and tested for gas turbines [80, 89, 90]. GE first reported the potential benefits of incorporating ceramics for the 9FA gas turbine/steam turbine combined cycle power plant in 1998 [42] as a 1.1% point increase in cycle efficiency and a 3% energy output.

A GE SiC–SiC shroud and combustor liner components were manufactured to simulate a MS7001FA (160MW) gas turbine and were subjected to multiple rig and engine tests. A Ni-based alloy shroud was also tested under the same conditions. The alloy shroud exhibited warping, oxidation, and fatigue cracking after 50 thermal cycles and 2 h of testing, while the CMC shroud showed no evidence of warping and only some minor edge cracking after 200 thermal cycles and 100 total hours of exposure [89]. The incorporation of these components into turbine engines will translate into reduced cost to energy consumers and greater power output efficiency.

In a separate set of tests, SiC–SiC combustor liners were tested under the Ceramic Stationary Gas Turbine (CSGT) Program sponsored by the U.S. Department of Energy (DOE) [90]. A high rate of SiC recession was exhibited by the liners due to the volatilization of SiC and SiO<sub>2</sub>. In one such test, the wall thickness was reduced by up to 80% in some spots [90]. As mentioned before, Si-based materials form a slow-growing protective silica layer during oxidation, but the behavior is much different in a combustion environment, where the presence of water vapor, oxygen, CO<sub>2</sub>, nitrogen, and hydrogen raise the oxidation rate by more than an order of magnitude [41, 90–94]. The silica scale volatilizes rapidly and leads to high rates of degradation. Different types of environmental barrier coatings (EBCs) were developed under the High-Speed Civil Transport (HSCT) and the Enabling Propulsion Materials (EPM) programs for a rig with an inner RMI-made Hi-Nicalon SiC/Si liner and an outer Hi Nicalon/SiC. The EBC consisted of three layers (silicon, mullite, and barium strontium aluminum silicate [BSAS]), each about 125 μm thick. Before applying the EBC, the liners were sealed with a SiC coating by CVD. There were often problems with spallation and localized oxidation in cracks and pinholes in the EBC layer(s). For example, after ~14,000 h of testing, a spallation hole was observed in the inner RMI liner (Fig. 10.9) [90]. The thick SiC seal coating applied before the EBC prevented spallation in the inner liner itself. Overall, most EBCs were lost near the fuel injectors, located in the hottest areas of the liners. It was found that adding a three-layer EBC system increased the lifetime of the carbon fiber reinforced composite (CFCC) liners by almost threefold (from ~5000 to 14,000 h), but this is still nowhere near the 30,000-h lifetime goal of the program [90].

The goal of the HSCT program (phased out in 1999) was to develop an environment-friendly and economically viable aircraft capable of traveling at supersonic speeds [95–100]. The development of a gas turbine engine combustion liner for this program was carried out under the EPM program [97, 100]. The material requirements included maintaining a NO<sub>x</sub> emissions index under 5 g/kg, a high thermal conductivity, an 18,000-h service life, and an expected <100-MPa tensile stress at temperatures above 1800°C. A SiC–SiC composite with a BN/SiC interphase was developed under the EPM program [95]. This composite was tested and compared to a CVI SiC–SiC sample. The RMI SiC–SiC had a lower porosity than the CVI sample, as was expected. The roughness of the Sylramic fibers caused them to debond from the matrix. It was also determined that a BN interphase alone could not withstand the extended service life at high





**Figure 10.9.** After about 14,000 h of field testing, the inner Hi Nicalon/SiC-Si liner made by melt infiltration shows a hole in the environmental barrier coating layer (reprinted from J. Kimmel, N. Miriyala, J. Price, K. More, P. Tororelli, H. Eaton, G. Linsey, and E. Sun (2002) Evaluation of CFCC liners with EBC after field testing in a gas turbine, *Journal of the European Ceramic Society*, 22[14–15] 2769–2775, with permission from Elsevier).

temperatures in a moist environment [22]. In other U.S. development programs, such as EPM (1994–1999), Ultra Efficient Engine Technology Program (UEET, 1999–2005), and Next Generation Launch Technology (NGLT), combustion chamber liners, turbine shrouds, and turbine blades were manufactured from melt-infiltrated SiC–SiC.

Future work on developing CFCC engine parts will focus on (1) scaling up and optimizing the process for larger shroud components, (2) developing matrices with a minimal amount of Si, (3) developing lifetime calculation models, and (4) having reproducible control of EBC coating thickness. For (4), it is necessary to balance increasing the thickness of the overall EBC layers with creating an environmentally resistant top layer. There are also major issues of CTE mismatch between the coatings and the surface and cracking from thermal cycling that need to be resolved.

### 10.5.2 Brake Disks

Lightweight brakes with better wear stability are in demand in the automotive and aerospace industries. C/C composites were of interest due to their low density and easy processing; however, they were found to possess an unstable coefficient of friction (COF) and poorer wear resistance in the presence of water vapor and high temperatures. This made them unsuitable as emergency brakes in passenger cars or elevators [101, 102]. Interest then turned to C/C-SiC composites formed by stacking layers of short fiber-reinforced plates [8, 42, 101, 103–105, 136]. RMI is a good choice for making low-porosity (<5%) low-density ( $\sim 2 \text{ g/cm}^3$ ) brake disks with low CTE, a high thermal

conductivity, and good thermal shock stability [101, 103–105, 136]. Several research institutes and manufacturers have made and tested CMC brakes. LSI C/C-SiC are already produced commercially for the automotive industry, albeit for luxury vehicles. For example, C-SiC brakes were introduced into the Porsche 911 Turbo in 2000 [103]. DLR has also developed short carbon fiber-reinforced C/C-SiC composites for different braking systems [12, 101].

Table 10.11 presents a summary of the processing and properties of several C/C-SiC brake disk composites [101, 103–105, 136]. The microstructure and properties of the disks vary among different agencies and commercial manufacturers, but several characteristics are the same. The short chopped carbon fibers reduce the brittleness of SiC. Due to this, the damage tolerance of C/C-SiC brakes is of the same order of magnitude as for cast iron [101]; however, the mechanical and thermal properties are vastly different between the in-plane and transverse directions.

There are several design considerations that are unique to C/C-SiC friction systems. The COF is partly dependent on the thermal conductivity. Above a critical limit for starting velocity and pressure, the C/C-SiC tribological system cannot sustain higher braking performance and overheats locally [101]. The COF decreases, while the surface temperature increases. High transverse conductivities, however, stabilize the COF [101]. A higher transverse conductivity can be achieved by (1) using fibers with high thermal conductivities, (2) increasing the angle between the fibers and friction surface, and (3) increasing the SiC content [101]. The most cost-efficient change is to increase the ceramic content in the composite by reducing the fiber content. However, this increases the density of C/C-SiC and decreases the strength and fracture toughness; therefore, a compromise must be made between designing a system with good mechanical or good thermal properties [101].

Of particular interest is how the carbon and ceramic content affect the tribological properties of these disks. The dynamic and static COFs need to be determined in both dry and humid conditions. The higher the value of the average dynamic COF, the higher the braking efficiency, whereas the more stable the dynamic COF, the higher the efficiency of braking [105]. The data of the COF plotted against braking speed in dry conditions have been observed to follow the same behavior for different studies. A prepeak is observed in the first stages of braking. This occurs because the initial roughness of the friction surface creates a high frictional resistance that needs to be overcome. The debris from wearing down these asperities is removed during sliding, and the COF goes down as the surface becomes smoother. A friction film forms and dynamic equilibrium is reached, during which the COF stabilizes. At later braking stages, the sliding speed slows and the wear debris accumulates on the surface. The COF increases again and a tail peak is observed in the plot.

The wear resistance of C/C-SiC aircraft brake disks has been investigated at several temperatures [101, 103–105, 136], but some unique results were obtained by examining the effects of graphitization and surface coatings. Jiang et al. [104] fabricated C/C-SiC brake disks with T300 short carbon fibers. The effect of graphitization on the thermal diffusivity, COF, and wear resistance was evaluated for two disk types. The compositions of the two samples had no observable variation and the porosity values were similar. However, the sample with the larger degree of graphitization also possessed a

TABLE 10.11. Processing Conditions and Resulting Properties of C/C-SiC Composites for Advanced Friction Systems (Data from References 101 and 103–105, 136)

Carbon	C/C-SiC (Reference 101)		C/C-SiC (Reference 103)		C/C-SiC (Reference 104)		C/C-SiC (Reference 105)	
	Woven fabric (orthotropic)	Woven fabric (orthotropic)	T300 short fibers	T300 short fibers (with graphitization)	T300 short fibers (without graphitization)	T300 short	T300 felt	
Processing steps	– Stack 0°/90° – LSI	– Stack 0°/90° – LSI – Addition of Si and C to friction surfaces during siliconization	– Resin – Hot press – CFRP – LSI at 1450°C	– Resin – Hot press – CFRP – Graphitization at –2500°C – LSI at 1650°C	– Resin – Hot press – CFRP – LSI at 1600°C	– Resin – Hot press – CFRP – LSI at 1600°C	– Needled felt – CVI – CFRP – LSI at 1420–1700°C	
Open porosity (%)	3.5	<3	2	2	8	5 ± 1		
Density (g/cm <sup>3</sup> )	1.9	2.0–2.1	1.90	1.93	1.75	2.1 ± 0.1		
SiC content	30 (mass %)	50–55 (mass %)	50 (wt %)	35%	27%	27 (wt %)		
Si content	2 (mass %)	2–3 (mass %)	5 (wt %)	–	–	8 (wt %)		
Inner diameter/outer diameter of test rotor disk (mm)	110	110	55/76	55/76.7	55/76.7	55/79.8		
Braking speed in test (m/s)	15	15	5–28	28	28	28		
Braking pressure (MPa)	–	–	0.6	0.8	0.8	8.8		
Average $\mu$ at test speed	0.4	Drops from 0.35 to 0.05	0.2	0.46 (ratio of $\mu/\mu_{max}$ )	0.56 (ratio of $\mu/\mu_{max}$ )	0.34 (dry) 0.33 (moist)		
Wear rate at test speed	75 mm <sup>3</sup> /MJ	16 mm <sup>3</sup> /MJ	~22 mg/cycle (~5 $\mu$ m/cycle)	14 mg/cycle (1.1 $\mu$ m/cycle)	17 mg/cycle (1.5 $\mu$ m/cycle)	1.9 $\mu$ m/cycle		

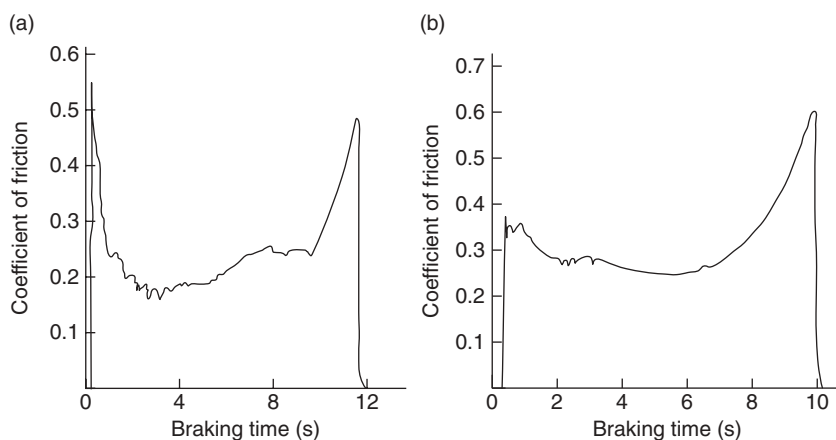


**Figure 10.10.** Curves of the coefficient of friction of ungraphitized (A) and graphitized (B) C/C-SiC brake disks versus test time. The curve of B shows that the coefficient of friction is more stable than that of A (reprinted from G. Jiang, J. Yang, Y. Xu, J. Gao, J. Zhang, L. Zhang, L. Cheng, and J. Lou (2008) Effect of graphitization on microstructure and tribological properties of C-SiC composites prepared by reactive melt infiltration, *Composites Science and Technology*, **68** 2468–2473, with permission from Elsevier).

higher SiC content, which increased the thermal diffusivity. The COF of the graphitized samples was more stable than the ungraphitized samples after numerous braking tests (Fig. 10.10). The same sample also displayed a high wear rate because the products of SiC wearing easily embedded in the softer graphite and the debris was not removed easily. Overall, graphitization resulted in friction systems with a more stable COF but also with a higher wear rate.

Hard coatings have also been explored to reduce the wear rate [101]. Though CVD seems an obvious choice for applying the coating, a more time-efficient process was developed in which additional SiC and C are added to the last siliconization step [101]. This produces a SiC coating between 0.2 and 2.0 mm that is ground to an acceptable smoothness. One issue with the coating is contraction after cooling, which results in surface microcracks, whose size increases with coating thickness. However, during braking, the friction surface heats up and the cracks narrow as the coating expands. In testing, the coatings improved the wear stability by ~85% of the uncoated C/C-SiC brakes [101]. It was also found that the COF remained fairly stable against fading for multiple braking [101].

C/C-SiC brake disks have been shown to possess advantageous properties over conventional C/C and gray cast iron, which include reduced mass, high COF, improved corrosion, and low wear rates. Various efforts have produced friction systems with tailorable microstructures. Selection of the appropriate C/C-SiC composite requires a thorough understanding of the specific mechanical and thermal properties, as well as the safety factors, required for operation.

### 10.5.3 Hypersonic and Space Vehicles

There are multiple examples of strong European efforts to incorporate melt-infiltrated CMCs in spacecraft. One of these programs was the development of a National Aeronautic and Space Administration (NASA) crew return vehicle, X-38, for the International Space Station. This vehicle prototype had hot structures composed of a C-SiC nosecone and skirts [106] made by the German Aerospace Agency (DLR) (C/C, LSI, and final CVI SiC coating). Other programs were LEA (France, MBDA, and Onera), which contained C-SiC duct structures densified by CVI and LSI [106]. The Sharp Edge Flight Experiment (SHEFEX) (Germany, DLR), contained panels made by the LSI method. The SHEFEX program moved beyond the prototype phase when a test flight achieved Mach 7 on October 27, 2005. In addition, a Russian unmanned satellite experiment, FOTON, contained C/C-SiC coatings made by DLR [106].

Other suggestions for applications that have been proposed include furnace hardware, heat exchangers, hot gas filters for pressurized fluidized bed combustion, and structures in nuclear reactors [30, 34].

## 10.6 CONCLUSIONS AND FUTURE DIRECTIONS

The demonstrated and potentially improved properties of CMC materials have been recognized through decades of research. The inclusion of melt-infiltrated composites in various industries is hindered by a lack of thorough operational experience and by the difficulty of calibrating a broad knowledge base with analytical performance models.

### 10.6.1 Cost Analysis of Component Fabrication Using RMI and CVI

Interest in improving turbine efficiency with CFCC components spurred a U.S. DOE-funded cost-analysis study at the start of the decade [107]. The goals of this study were to produce reliable and cost-effective combustion liners for gas turbines that lowered emissions while simultaneously increasing power output. A cost target of 120 engines per year was set, and it was determined whether this target could be met after considering different material processes and cost of raw materials. CVI and RMI routes to produce the liners were compared based on information provided by AlliedSignal Composites (now part of Honeywell). Despite the fact that CVI uses several infiltration cycles, the overall costs for both CVI and RMI were similar because the time savings afforded to RMI were offset by the cost of raw materials (fibers, precursors, and metal) and tooling (furnaces and fixtures). CFCC product costs can be significantly improved by reducing the cost of these raw materials. Ceramic fibers comprise an overwhelming chunk of the costs in RMI, about 40% when compared to other categories like labor and operations. For example, in 2000, Hi-Nicalon fibers were priced at \$6700 per kilogram. These findings were supported by an earlier independent report on turbine manufacture [107].

A similar analysis was performed for the LSI processing of friction systems [101]. It was surmised that the high processing temperatures would be a major contributor to the cost of manufacturing, but it was calculated that the majority of the total cost came from materials (34%) and labor (30%) [101]. A conclusion of this study was that automating some steps could afford some savings.

An excellent discussion of cost analysis as it pertains to fiber manufacture has been reported previously [25]. It should serve as the first reference for interested readers. Another source for the design and cost aspects of the RMI process was published more recently [108]. The National Material Advisory Board (NMAB) performed a survey of high-performance ceramic fibers [25]. In Reference 107, the cost of fibers made up the largest portion of the total cost of fiber-reinforced composite materials. The reason for this is the large length/unit mass, the specialized spinning machines, and the high-purity additives used to make high-quality stoichiometric fibers. According to the conclusions made by NMAB, ceramic fiber manufacturers will continue to incur significant losses. This trend will not be reversed for a long time as the ceramic composite market is still relatively immature and demand for fiber-reinforced composites is insufficient to generate hundreds of millions of U.S. dollars in a single application [25].

An argument was also made that high cost is actually not the dominant factor in the slow development of the fiber-reinforced composite market. Metal aerospace parts are very expensive, and in recent decades, CMCs have demonstrated great weight-saving and improved performance. Rather, the problem seems to be an industry-wide lack of confidence in these materials. A great technical breakthrough in processing technology is needed to bring processing costs down to a more attractive level. For now, small reductions may be achieved by automating some steps, like continuing the layup of plies and batch coating continuous fiber tows or by using a combination of fast processes as mentioned in the background.

## 10.6.2 Processing and Property Issues

Substantial improvements in the thermomechanical and chemical properties of fibers and coatings are necessary if RMI will be used for other material systems, especially for metals with higher melting points, such as W or Ta. When cyclic loading goes beyond the proportional limit of the composite, matrix cracking occurs. This damage exposes the fiber coatings to the environment and leads to rapid oxidation of the fibers and matrix. Fiber strength loss has also been observed under stress-free, high-temperature conditions [109]. This loss is caused by the diffusion of elemental metal from the matrix through boundaries in the interphase coatings. When the fibers are arranged in tows, the metal first attacks the tow surface before diffusing through to the center of the bundle. It has been observed that increasing the thickness or volume fraction of the overcoating can mitigate this effect, but more work needs to be done to predict the strength for the desired time and temperatures [109].

There have been some promising preliminary results to enhance oxidation resistance using crystalline BN and Si-doped BN [38, 110, 111] and outside debonding techniques, in which the BN interphase debonds from the matrix instead of the fiber

[112]. Further studies may focus on developing multilayer coatings that possess good oxidation resistance coupled with matrix sealing capabilities at intermediate and high temperatures. Matrix crack sealing has been briefly explored by incorporating B into the matrix.  $B_2O_3$  forms in the matrix cracks during exposure at elevated temperatures, and it acts as a crack sealant until further cracking and/or increasing temperatures cause the boron to volatilize. The inherent CTE mismatches between interphase materials and the matrix can be mitigated by exploring hybrid-matrix technology.

The fast processing times afforded by RMI are offset by the high cost of good-quality raw materials, especially of stoichiometric SiC-fibers. Higher toughness is imparted when fiber tows are coated individually rather than by batch coating an entire fabric sheet. This is, however, expensive and time-consuming. A quicker individual coating process may be done by combining deposition technologies, in which the innermost layer may be deposited from a liquid state while the PyC or BN overcoat is deposited by CVD.

The multiphase microstructure and varying porosity of materials produced by RMI means that there is significant nonuniformity in sample properties from within the same batch. Solving this reliability issue involves understanding the kinetics of the reaction involved. A diffusion-limited reaction occurs as the formed ceramic phase separates the remaining melt from the carbon source. The low-temperature mechanical properties of these materials can be good as long as failure flaws do not initiate and propagate along the metal–ceramic interface, but the high-temperature strengths and creep resistance are severely affected upon melting of the free metal phase. Several solutions have been suggested to minimize residual metal, including vaporizing it at high temperatures under vacuum, leaching, or by using alloyed melts.

For composites to mature successfully, manufacturing processes must become more productive and efficient. Though larger and more complex shapes can be made by RMI, further efforts in perfecting the production of thin sections and joining technology are needed. Better joining technology between CMCs and alloys should be developed to accommodate differences in thermal expansion. The interlaminar strengths of 2-D infiltrated composites are poorer than those with 3-D preforms. These lower strengths of the 2-D composites are detrimental for joining, for example, a thermal protection system (TPS) panel to an experimental launch vehicle. Other fiber weaving patterns may be used to mitigate this issue. Through these and other developments, MI can emerge as a low-cost process to provide damage-resistant CMC components with improved properties for many high-performance applications.

## REFERENCES

1. M. M. Opeka, I. G. Talmy, and J. A. Zaykoski (2004) Oxidation-based materials selections for 2000°C+ hypersonic aerosurfaces: Theoretical considerations and historical experience, *J. Mater. Sci.*, **39**[19] 5887–5904.
2. E. Wuchina, E. Opila, M. Opeka, W. Fahrenholtz, and I. Talmy (2007) UHTCs: Ultra-high temperature ceramic materials for extreme environment applications, *Elec. Soc. Interface*, **4** 30–36.



3. M. Gasch, D. T. Ellerby, and S. M. Johnson, Ultra high temperature ceramic composites, in *Handbook of Ceramic Composites*, ed. N. Bansal, pp. 197–224, Springer, New York, 2005.
4. X. He, Y. Guo, Y. Zhou, and D. Jia (2008) Microstructures of short-carbon-fiber-reinforced SiC composites prepared by hot-pressing, *Mater. Charact.*, **9** 1771–1775.
5. R. Naslain, F. Langlais, and R. Fedou (1989) The CVI-processing of ceramic matrix, *Compos. J. De Physique*, **50**[5] C5-191–C5-207.
6. R. Naslain (1999) Materials Design and processing of high temperature ceramic matrix composites: State of the art and future trends, *Adv. Compos. Mater.*, **8**[1] 3–16.
7. R. R. Naslain (2005) SiC-matrix composites: Nonbrittle ceramics for thermo-structural application, *Int. J. Appl. Ceram. Technol.*, **2**[2] 75–84.
8. W. Krenkel, Carbon fibre reinforced silicon carbide composites (C/SiC, C/C-SiC), in *Handbook of Ceramic Composites*, ed. N. Bansal, pp. 117–148, Springer, New York, 2005.
9. D. P. Stinton, A. J. Caputo, and R. A. Lowden (1986) Synthesis of fiber-reinforced SiC composites by chemical vapor infiltration, *Am. Ceram. Soc. Bull.*, **65**[2] 347–350.
10. K. S. Mazdiasni, *Fiber Reinforced Ceramic Composites: Materials, Processing and Technology*, ed. K. S. Mazdiasni, Noyes Publications, Park Ridge, NJ, 1990.
11. R. R. Naslain, Ceramic matrix composites: Matrices and processing, in *Concise Encyclopedia of Composite Materials*, 2nd edition, ed. A. Mortensen, pp. 140–146, Elsevier, Oxford, UK, 2001–2007.
12. K. Nakano, A. Kamiya, K. Sasaki, and H. Saka, Microstructure of carbon fiber reinforced silicon carbide and silicon nitride composites, in *High Temperature Ceramic Matrix Composites. Proc. HT-CMC-I Conf*, eds. R. Naslain, J. Lamon, and D. Doumeingts, pp. 413–420, Woodhead Publishing, Abington-Cambridge, UK, 1993.
13. K. Nakano, K. Sasaki, H. Saka, M. Fujikura, and H. Ichikawa (1995) SiC- and Si<sub>3</sub>N<sub>4</sub>-matrix composites according to the hot-pressing route, *Ceram. Trans.*, **58** 215–229.
14. I. E. Frech, Ceramic matrix composites fabrication and processing: Polymer pyrolysis, in *Handbook on Continuous Fiber-Reinforced Ceramic Matrix Composites*, eds. R. L. Lehman, S. K. El-Rahaiby, and J. B. Wachtman, Jr., CIAC, Purdue University, West Lafayette, IN, 1995.
15. K. Igashira, K. Nishio, and T. Suemitsu (1999) Development of a combustor liner composed of ceramic matrix composite (CMC), *J. Eng. Gas Turbines Power*, **121**[1] 12–17.
16. C. Grenet, L. Plunkett, J. B. Veyret, and E. Bullock (1995) Carbon fibre-reinforced silicon nitride composites by slurry infiltration, *Ceram. Trans.*, **58** 125–130.
17. V. S. R. Murthy and B. S. Rao (1995) Microstructural development in the directed melt-oxidized (DIMOX) Al-Mg-Si alloys, *J. Mater. Sci.*, **30** 3091–3097.
18. W. B. Hillig, Melt infiltration process for making ceramic matrix composites, in *Fiber Reinforced Ceramic Composites: Materials, Processing and Technology*, ed. K. S. Mazdiasni, pp. 260–277, Noyes Publications, Park Ridge, NJ, 1990.
19. W. B. Hillig, R. L. Mehan, C. R. Morelock, V. J. DeCarlo, and W. Laskow (1975) Silicon/silicon carbide composites, *Am. Ceram. Soc. Bull.*, **54**[12] 1054–1056.
20. R. L. Mehan (1978) Effect of SiC content and orientation on the properties of Si/SiC ceramic composite, *J. Mater. Sci.*, **13**[2] 358–366.
21. G. S. Corman and K. L. Luthra, Silicon melt infiltrated ceramic composites (HiPerComp™), in *Handbook of Ceramic Composites*, ed. N. Bansal, pp. 99–115, Springer, New York, 2005.
22. K. L. Luthra, R. N. Singh, and M. K. Brun (1993) Toughened Silcomp Composites: Process and preliminary properties, *Am. Ceram. Soc. Bull.*, **72**[7] 79–85.



23. R. E. Tressler (1999) Recent developments in fibers and interphases for high temperature ceramic matrix composites, *Compos. A*, **30**[4] 29–437.
24. K. T. Faber (1997) Ceramic composite interfaces: Properties and design, *Annu. Rev. Mater. Sci.*, **27**[1] 499–524.
25. P. Baldus, M. Jansen, and D. Sporn (1999) Ceramic fibers for matrix composites in high-temperature engine applications, *Science*, **285**[5428] 699–703.
26. <http://www.coicceramics.com>.
27. [http://www.upilex.jp/catalog/pdf/tyranno\\_fiber\\_e.pdf](http://www.upilex.jp/catalog/pdf/tyranno_fiber_e.pdf).
28. D. W. Johnson, A. G. Evans, R. W. Goettler, M. Harmer, J. Lipowitz, and K. L. Luthra, *Ceramic Fibers and Coatings: Advanced Materials for the Twenty-First Century. Committee on Advanced Fibers for High-Temperature Ceramic Composites*. National Academy Press, Washington, DC, 1998.
29. S. J. Grisaffe (1990) *Reinforcements-the key to high performance composite materials*, NASA TM 10320, Lewis Research Center.
30. R. Naslain (2004) Design, preparation and properties of non-oxide CMCs for application in engines and nuclear reactors: An overview, *Compos. Sci. Technol.*, **64**[2] 155–170.
31. K. L. Luthra (1986) Thermochemical analysis of the stability of continuous “SiC” fibers, *J. Am. Ceram. Soc.*, **69**[10] C-231–C-233.
32. <http://www.toraycfa.com/pdfs/T1000GDataSheet.pdf>.
33. A. L. McNaughton (2007) High temperature compression testing of monolithic silicon carbide (SiC). *Electronic Theses and Dissertations*. Paper 270.
34. R. Naslain and F. Christin (2003) SiC-matrix composite materials for advanced jet engines, *MRS Bull.*, **28**[9] 654–658.
35. K. L. Luthra (1997) Oxidation-resistant fiber coatings for non-oxide ceramic composites, *J. Am. Ceram. Soc.*, **80**[12] 3253–3257.
36. E. O. Einset, N.-B. Patibandla, and K. L. Luthra (1994) Processing conditions for boron nitride coatings in fiber bundles via chemical vapor deposition, *J. Am. Ceram. Soc.*, **77**[12] 3081–3086.
37. O. Dugne, S. Prouhet, A. Guette, R. Naslain, R. Fourmeaux, Y. Khin, J. Sevely, J. P. Rocher, and J. Cotteret (1993) Interface characterization by TEM, AES and SIMS in tough SiC (ex-PCS) fibre-SiC (CVI) matrix composites with a BN interphase, *J. Mater. Sci.*, **28**[13] 3409–3422.
38. L. U. J. T. Ogbuji (2003) Pest-resistance in SiC/BN/SiC composites, *J. Eur. Ceram. Soc.*, **23**[4] 613–617.
39. J. A. DiCarlo, H.-M. Yun, G. N. Morscher, and R. T. Bhatt, SiC/SiC composites for 1200°C and above, in *Handbook of Ceramic Composites*, ed. N. Bansal, pp. 77–98, Springer, New York, 2005.
40. N. S. Jacobson, G. N. Morscher, D. R. Bryant, and R. E. Tressler (1999) High-temperature oxidation of boron nitride: II, boron nitride layers in composites, *J. Am. Ceram. Soc.*, **82**[6] 1473–1482.
41. N. S. Jacobson, E. J. Opila, and K. N. Lee (2001) Oxidation and corrosion of ceramics and ceramic matrix composites, *Curr. Opin. Solid State Mater. Sci.*, **5** 301–309.
42. B. Heidenreich, Melt infiltration process, in *Ceramic Matrix Composites: Fiber Reinforced Ceramics and Their Applications*, ed. W. Krenkel, pp. 113–164, Wiley-VCH, Weinheim, 2008.

43. R. Naslain, A. Guette, F. Rebillat, R. Pailler, F. Langlais, and X. Bourrate (2004) Boron-bearing species in ceramic matrix composites for long-term aerospace applications, *J. Solid State. Chem.*, **177**[2] 449–456.
44. P. Vandeurzen, J. Ivens, and I. Verpoest (1996) A three-dimensional micromechanical analysis of woven-fabric composites: I. Geometric analysis, *Compos. Sci. Technol.*, **56**[11] 1303–1315.
45. R. Kamiya, B. A. Cheeseman, P. Popper, and T.-W. Chou (2000) Some recent advances in the fabrication and design of three-dimensional textile preforms: A review, *Compos. Sci. Technol.*, **60** 33–47.
46. <http://www.ultramet.com>.
47. R. Asthana (2002) Interface- and diffusion-limited capillary rise of reactive melts with a transient contact angle, *Metall. Mater. Trans. A*, **33**[7] 2119–2128.
48. N. Eustathopoulos, R. Israel, B. Drevet, and D. Camel (2010) Reactive infiltration by Si: Infiltration versus wetting, *Scr. Mater.*, **62** 966–971.
49. A. Mortensen, C. San Marchi, and V. J. Michaud, Capillarity in infiltration processing: A review of principles and their extension to reactive infiltration, in *High-Temperature Capillarity*, eds. N. Eustathopoulos and N. Sobczak, p. 249, Foundry Research Institute, Krakow, 1997.
50. J. Kozeny (1927) Sitzungberichte Akademie der Wissenschaft, *Wien. Abt. Ita*, **136** 271–306.
51. P. C. Carman (1937) Flow through granular beds, *Trans. Am. Inst. Chem. Eng.*, **15** 150–166.
52. E. W. Washburn (1921) Note on a method of determining the distribution of pore sizes in a porous material, *Proc. Natl. Acad. Sci. U. S. A.*, **7**[4] 115–116.
53. F. A. L. Dullien, *Porous Media: Fluid Transport and Pore Structure*. Academic Press, New York, 1979.
54. F. A. L. Dullien, M. S. El-Sayed, and V. K. Batral (1977) Rate of capillary rise in porous media with nonuniform pores, *J. Colloid Interf. Sci.*, **60**[3] 497–506.
55. G. S. Corman, E. O. Einset, and W. B. Hillig (1997) Observations on the kinetic processes for the formation of SiC from elemental carbon and silicon, *Technical Information Series: GE Research & Development Center*. 97CRD033.
56. E. O. Einset (1998) Analysis of reactive melt infiltration in the processing of ceramics and ceramic composites, *Chem. Eng. Sci.*, **53**[5] 1027–1039.
57. E. O. Einset (1996) Analysis of reactive melt infiltration: I. Derivation of the governing equations, *Technical Information Series: GE Research & Development Series*, 96CRD028-96CRD029.
58. R. Pampuch, E. Walasek, and J. Bialoskorski (1986) Reaction mechanism in carbon—Liquid silicon systems at elevated temperatures, *Ceram. Int.*, **12**[2] 99–106.
59. R. Messner and Y.-M. Chiang (1990) Liquid-phase reaction-bonding of silicon carbide using alloyed silicon-molybdenum melts, *J. Am. Ceram. Soc.*, **73**[5] 1193–1200.
60. E. Fitzer and R. Gadow (1986) Fiber reinforced silicon carbide, *Am. Ceram. Soc. Bull.*, **65**[2] 326–335.
61. H. Zhou and R. N. Singh (1995) Kinetics model for the growth of silicon carbide by the reaction of liquid silicon with carbon, *J. Am. Ceram. Soc.*, **78**[9] 2456–2462.
62. B. M. Turovskii and I. I. Ivanova (1974) Temperature dependence of the viscosity of fused silicon, *Inorg. Mater.*, **10**[12] 1809.

63. E. S. Nelson and P. Colella (2000) Parametric study of reactive melt infiltration, *NASA/TM-2000-209802*.
64. G. Rajesh and R. B. Bhagat (1997) Micro modeling of reactive melt infiltration for SiC/SiC ceramic-matrix composites, *J. Sci. Eng. Compos. Mater.*, **6**[3] 169–184.
65. G. Rajesh and R. B. Bhagat (1998) Modelling micro-level volume expansion during reactive melt infiltration using non-isothermal unreacted-shrinking core models, *Model. Simul. Mater. Sci. Eng.*, **6**[6] 771–786.
66. G. Rajesh and R. B. Bhagat (1999) Infiltration of liquid metals in porous compacts: Modeling of permeabilities during reactive melt infiltration transport in porous media, *Transport Porous Med.*, **36**[1] 43–68.
67. G. Rajesh, R. B. Bhagat, and K. A. Fichthorn (2000) Reactive flow in a porous medium: Formulation for spatially periodic hexagonally packed cylinders, *J. Appl. Mech.*, **67**[4] 749–757.
68. B. R. Gebart (1992) Permeability of unidirectional reinforcements for RTM, *J. Compos. Mater.*, **26**[8] 1100–1035.
69. P. Popper (1960) Reaction bonding silicon carbide, in *Special Ceramics: Proceedings of a Symposium Held at the British Ceramic Research Association*, ed. P. Popper, Heywood, London.
70. R. Naslain, et al., SiC-matrix composites for thermostructural applications: Effect of the environment, in *Proc. 10th Int. Conf. Compos. Mater. (ICCM-10)*, eds. A. Poursartip and K. Street, pp. 759–765, Woodhead Publishing, Abington-Cambridge, UK, 1995.
71. C. W. Forest, P. Kennedy, and J. V. Shennan (1972) *Special Ceramics 5*. British Ceramic Research Association. pp. 99–123.
72. J. Schulte-Fischedick, A. Zern, J. Mayer, M. Rühle, M. Freiß, W. Krenkel, and R. Kochendörfer (2002) The morphology of silicon carbide in C/C-SiC composites, *Mater. Sci. Eng. A*, **332**[1–2] 146–152.
73. G. R. Sawyer and T. F. Page (1978) Microstructural characterization of “REFEL” (reaction-bonded) silicon carbides, *J. Mater. Sci.*, **13**[4] 885–904.
74. J. N. Ness and T. F. Page (1986) Microstructural evolution in reaction-bonded silicon carbide, *J. Mater. Sci.*, **21**[4] 1377–1397.
75. W. B. Hillig (1993) Melt infiltration: A generic process for making ceramic matrix composites, *Ceram. Trans.*, **38** 3–26.
76. E. Fitzer (1987) The future of carbon-carbon composites, *Carbon*, **25**[2] 163–190.
77. E. Fitzer (1988) Composites for high temperatures, *Pure Appl. Chem.*, **60**[3] 287–302.
78. K. L. Luthra, R. N. Singh, and M. K. Brun, SiC fiber reinforced Silcomp (Si-SiC) composites, in *Proc. HT-CMC-1 Conf., High Temperature Ceramic Matrix Composites*, eds. R. Naslain, J. Lamon, and D. Doumeings, pp. 429–436, Woodhead Publishing, Abington-Cambridge, UK, 1993.
79. G. S. Corman and K. L. Luthra (1998) Toughened Silcomp (SiC-Si) composites: Material development status. Proc. 22nd Annual Conf. Composites, Cocoa Beach, FL.
80. K. L. Luthra and G. S. Corman (2001) Melt infiltrated (MI) SiC/SiC composites for gas turbine applications, GE Technical Report, Report Number 2001CRD112.
81. F. H. Gern and R. Kochendorfer (1997) Liquid silicon infiltration: Description of infiltration dynamics and silicon carbide formation, *Compos. A*, **28**[4] 335–364.
82. R. Bhatt, J. Z. Gyekenyesi, and J. B. Hurst (2000) Silicon effects on properties of melt infiltrated SiC/SiC composites, *NASA/TM-2000-210034*.

83. M. Esfahanian, J. Gunster, F. Moztarzadeh, and J. G. Heinrich (2007) Development of a high temperature  $C_f/XSi_2-SiC$  ( $X= Mo, Ti$ ) composite via reactive melt infiltration, *J. Eur. Ceram. Soc.*, **27**[2–3] 1229–1235.
84. M. Esfahanian, J. Guenster, J. Heinrich, J. Horvath, D. Koch, and G. Grathwohl (2008) High-temperature mechanical behavior of carbon-silicide-carbide composites developed by alloyed melt infiltration, *J. Eur. Ceram. Soc.*, **28**[6] 1267–1274.
85. M. Singh and D. R. Behrendt (1995) Reactive melt infiltration of silicon-molybdenum alloys into microporous carbon preforms, *Mater. Sci. Eng. A*, **194** 193–200.
86. M. Singh and D. R. Behrendt (1994) Reactive melt infiltration of silicon-niobium alloys in microporous carbons, *J. Mater. Res.*, **9**[7] 1701–1708.
87. O. Chakrabarti and P. K. Das (2000) Reactive infiltration of Si-Mo alloyed melt into carbonaceous preforms of silicon carbide, *J. Am. Ceram. Soc.*, **83**[6] 1548–1550.
88. R. Bhatt and M. Hebsur (2000) Processing and properties of  $SiC/Mo_2Si-SiC$  composites fabricated by melt infiltration, in 24th Annual Conference on Composites, Advanced Ceramics, Materials, and Structures- A: Ceramic Engineering and Science Proceedings, **21**[3], eds. T. Jessen and E. Ustundag.
89. K. L. Luthra and G. S. Corman, Melt infiltrated (MI)  $SiC/SiC$  composites for gas turbine applications, in *High Temperature Ceramic Matrix Composites*, eds. W. Krenkel, R. Naslain, and H. Schneider, pp. 744–753, Wiley-VCH, Weinheim, 2001.
90. J. Kimmel, N. Miriyala, J. Price, K. More, P. Tortorelli, H. Eaton, G. Linsey, and E. Sun (2002) Evaluation of CFCC liners with EBC after field testing in a gas turbine, *J. Eur. Ceram. Soc.*, **22** 2769–2775.
91. S. R. Levine, E. J. Opila, M. C. Halbig, J. D. Kiser, M. Singh, and J. A. Salem (2002) Evaluation of ultra-high temperature ceramics for aeropropulsion use, *J. Eur. Ceram. Soc.*, **22**[14–15] 2757–2767.
92. E. J. Opila (2004) Oxidation and volatilization of silica formers in water vapor, *J. Am. Ceram. Soc.*, **86**[8] 1238–1248.
93. Q. N. Nguyen, E. J. Opila, and R. C. Robinson (2004) Oxidation of ultrahigh temperature ceramics in water vapor, *J. Electrochem. Soc.*, **151**[10] B558–B562.
94. E. J. Opila, N. S. Jacobson, D. L. Myers, and E. H. Copland (2006) Predicting oxide stability in high-temperature water vapor, *JOM*, **58**[1] 22–28.
95. J. J. Brennan (2000) Interfacial characterization of a slurry-cast melt-infiltrated  $SiC/SiC$  ceramic-matrix composite, *Acta Mater.*, **48**[18–19] 4619–4628.
96. NASA's High-Speed Research Program: Developing Tomorrow's Supersonic Passenger Jet. <http://oea.larc.nasa.gov/PAIS/HSR-Overview2.html> (Accessed September 25, 2009).
97. J. A. DiCarlo, H. M. Yun, G. N. Morscher, and R. T. Bhatt,  $SiC/SiC$  composites for 1200°C and above, in *Handbook of Ceramic Composites*, ed. N. P. Bansal, pp. 77–98, Springer, New York, 2005.
98. J. Stephens, T. Hecht, and A. Johnson (1993) *Material requirements for the high speed civil transport*, ISABE United States, 701–710.
99. G. N. Morscher (2005) Modeling the stress strain behavior of woven ceramic matrix composites. 107<sup>th</sup> Annual American Ceramic Society Conference, April 11<sup>th</sup>.
100. S. K. Mital, R. T. Bhatt, and P. L. N. Murthy (2002) Influence of constituents on the properties of melt-infiltrated  $SiC/SiC$  composites. 43rd AIAA/ASME/ASCE/AHS/ASC Structures, Structural Dynamics, and Materials Conference, Denver, CO, April 22–25.

101. W. Krenkel, B. Heidenreich, and R. Renz (2002) C/C-SiC composites for advanced friction systems, *Adv. Eng. Mater.*, **4**[7] 427–436.
102. G. Savage, Applications of carbon/carbon composites, in *Carbon/Carbon Composites*, pp. 323–346, Chapman & Hall, London, 1992.
103. J. Zhang, Y. Xu, L. Zhang, and L. Cheng (2007) Effect of braking speed on friction and wear behavior of C/C-SiC composites, *Int. J. Appl. Ceram. Technol.*, **4**[5] 463–469.
104. G. Jiang, J. Yang, Y. Xu, J. Gao, L. Zhang, L. Cheng, and J. Lou (2008) Effect of graphitization on microstructure and tribological properties of C/SiC composites prepared by reactive melt infiltration, *Compos. Sci. Technol.*, **68**[12] 2468.
105. S. Fan, L. Zhang, Y. Xu, L. Cheng, J. Lou, J. Zhang, and L. Yu (2007) Microstructure and properties of 3D needle-punched carbon/silicon carbide brake materials, *Compos. Sci. Technol.*, **67**[11–12] 2390–2398.
106. D. E. Glass (2007) European directions for hypersonic thermal protection systems and hot structures. 31<sup>st</sup> Annual Conference on Composites Materials and Structures, Daytona Beach, FL January 22.
107. P. A. Craig and D. Godfrey (2000) Reductions in acquisition costs for state-of-the-art fabrication of CFCC turbine engine combustor liners, *J. EngGas Turbines Power*, **122**[3] 401–404.
108. W. Krenkel (2001) Cost-effective processing of CMC composites by melt infiltration (LSI-process), *Ceram. Eng. Sci. Proc.*, **22**[3] 443–454.
109. R. T. Bhatt, T. R. McCue, and J. A. DiCarlo (2003) Modeling the thermal stability of melt-infiltrated SiC/SiC composites, *Ceram. Eng. Sci. Proc.*, **24**[4B] 295–300.
110. G. N. Morscher, F. Hurwitz, and H. M. Yun (2002) High temperature Si-doped BN interphases for SiC/SiC composites, *Ceram. Eng. Sci. Proc.*, **23**[4] 884.
111. G. N. Morscher and J. D. Cawley (2002) Intermediate temperature strength degradation in SiC/SiC composites, *J. Eur. Ceram. Soc.*, **22**[14–15] 2777–2787.
112. G. N. Morscher, H. M. Yun, J. A. DiCarlo, and L. Thomas-Ogbuji (2004) Effect of a boron nitride interphase that debonds between the interphase and the matrix in SiC/SiC composites, *J. Am. Ceram. Soc.*, **87**[1] 104–112.
113. S. Tang, J. Deng, S. Wang, and W. Liu (2007) Fabrication and characterization of C/SiC composites with thickness, high density and near-stoichiometric matrix by heaterless chemical vapor infiltration, *Mater. Sci. Eng. A*, **465**[1–2] 290–294.
114. Q. Zhou, S. Dong, X. Zhang, Y. Ding, and D. Jiang (2006) Fabrication of Cf/SiC composites by vapor silicon infiltration, *J. Am. Ceram. Soc.*, **89**[7] 2338–2340.
115. S. Wu, L. Cheng, Q. Zhang, L. Zhang, and Y. Xu (2006) Thermophysical and mechanical properties of a three-dimensional Hi-Nicalon/SiC composite, *Int. J. Appl. Ceram. Technol.*, **3**[1] 75–79.
116. P.-F. Paradis, T. Ishikawa, and S. Yoda (2002) Non-contact measurements of surface tension and viscosity of niobium, zirconium, and titanium using an electrostatic levitation furnace, *Int. J. Thermophys.*, **23**[3] 825–842.
117. W.-K. Rhim and K. Ohsaka (2000) Thermophysical properties measurement of molten silicon by high-temperature electrostatic levitator: Density, volume expansion, specific heat capacity, emissivity, surface tension and viscosity, *J. Cryst. Growth*, **208**[1–4] 313–321.
118. P.-F. Paradis and W.-K. Rhim (2000) Non-contact measurements of thermophysical properties of titanium at high temperatures, *J. Chem. Thermodyn.*, **32**[1] 123–133.
119. Data taken from ICDD database for XRD.

120. G. Jiang, H. Zhuang, and W. Li (2004) Field-activated, pressure-assisted combustion synthesis of tungsten carbide-nickel composites, *Mater. Lett.*, **58**[22–23] 2855–2860.
121. V. V. Ogorodnikov and Y. I. Rogovoi (1993) Rules of change in elastic, thermal, and energy properties in a number of cubic transition metal monocarbides, *Powder Metall. Met. C+*, **32**[5] 445–449. trans. Poroshkovaya Metallurgiya 5 78–83.
122. G.-M. Song, Y. Zhou, and S. J. L. Kang (2003) Experimental description of thermomechanical properties of carbon fiber-reinforced TiC matrix composites, *Mater. Design*, **24**[8] 639–646.
123. J. H. Richardson (1965) Thermal expansion of three group IVA Carbides to 2700°C, *J. Am. Ceram. Soc.*, **48**[10] 497–499.
124. A. C. Lawson, D. P. Butt, J. W. Richardson, and J. Li (2007) Thermal expansion and atomic vibrations of zirconium carbide to 1600 K, *Philos. Mag.*, **87**[17] 2507–2519.
125. M. B. Dickerson, P. J. Wurm, J. R. Schorr, W. P. Hoffman, P. G. Wapner, and K. H. Sandhage (2004) Near net-shape, ultra-high melting, recession-resistant ZrC/W-based rocket nozzle liners via the displacive compensation of porosity (DCP) method, *J. Mater. Sci.*, **39**[19] 6005–6015.
126. P. Perrot, Carbon-uranium zirconium, in *Group IV: Physical Chemistry*, Vol. 11, ed. W. Martienssen, pp. 220–229, Springer, Berlin, Heidelberg, 2007.
127. K. Nakamura and M. Yashima (2008) Crystal structure of NaCl-type transition metal monocarbides MC (M = V, Ti, Nb, Hf, Zr), a neutron powder diffraction study, *Mater. Sci. Eng. B*, **148**[1–3] 69–72.
128. O. Dernovsek, J. C. Bressiani, A. H. A. Bressiani, W. Acchar, and P. Greil (2000) Reaction bonded niobium carbide ceramics from polymer-filler mixtures, *J. Mater. Sci.*, **35**[9] 2201–2207.
129. C. R. Houska (1964) Thermal expansion of certain group IV and group V carbides at high temperatures, *J. Am. Ceram. Soc.*, **47**[6] 310–311.
130. C. R. Houska (1964) Thermal expansion and atomic vibration amplitudes for TiC, TiN, ZrC, ZrN, and pure Tungsten, *J. Phys. Chem. Solids*, **25** 359–366.
131. S. Zhu, M. Mizuno, Y. Kagawa, and Y. Mutoh (1999) Monotonic tension, fatigue and creep behavior of SiC-fiber reinforced SiC-matrix composites: A review, *Compos. Sci. Technol.*, **59**[6] 833–851.
132. R. R. Naslain (1998) The design of the fibre-matrix interfacial zone in ceramic matrix composites, *Comp. A*, **29**[9–10] A 1145–A 1155.
133. K. M. Prewo, J. J. Brennan, and G. K. Layden (1986) Fiber reinforced glasses and glass-ceramics for high performance applications, *Am. Ceram. Soc. Bull.*, **65**[2] 305–313.
134. H. Darcy (1856) *Les fontaines publiques de la ville de Dijon Paris, Dalmont*.
135. R. C. Robinson and J. L. Smialek (1999) SiC recession caused by SiO<sub>2</sub> scale volatility under combustion conditions: I, experimental results and empirical model, *J. Am. Ceram. Soc.*, **82**[7] 1817–1825.
136. Z. S. Pak (2001) Cf/SiC/C composites for frictional applications. High Temperature Ceramic Matrix Composites: 4th International Conference on High Temperature Ceramic Matrix Composite (HT-CMC4) Proceedings, Munich, Germany.

# COMBUSTION SYNTHESIS: AN UPDATE

S. B. BHADURI

## 11.1 INTRODUCTION

Combustion synthesis (CS) technique is being used all over the world not only in synthesizing many advanced materials but also in various industrial applications. Other terminologies used to describe the process include self-propagating high-temperature synthesis (SHS), and gasless combustion. The current interest in the topic can be credited to the pioneering work of Merzhanov and his group in Russia starting in the early 1970s [1]. However, the process itself has a much longer history. As reported in Reference 2, the earliest mention of a combustion phenomenon in material synthesis can be found in 1825. While Berzelius reported that Zr metal powders burn to form the corresponding oxide, Goldschmidt explained the thermodynamics of the process in 1895 [2, 3]. In fact, Goldschmidt can be rightly called the originator of the aluminothermic process, a subgroup of CS reactions. During the next 200 years, there were some sporadic industrial discoveries utilizing the combustion phenomena [3–5]. In spite of those discoveries, there was no widespread scientific interest in the process until the vigorous research initiated by Merzhanov and his colleagues.

In this country, Walton and his colleagues started utilizing the aluminothermic processes for synthesizing cermets in 1959 [6]. This activity went on for several decades with many excellent reviews appearing in the literature. Frankhouser et al. published

---

*Ceramics and Composites Processing Methods*, First Edition. Edited by Narottam P. Bansal and Aldo R. Boccaccini.

© 2012 The American Ceramic Society. Published 2012 by John Wiley & Sons, Inc.



an extensive monograph on the subject [7]. This monograph presented a balanced review of the work done in the then-USSR and elsewhere. Soon after that, two of Munir's reviews were published [8, 9].

Reference 8 is a shorter version of the comprehensive one [9]. These two reviews together describe the important aspects of the then-Soviet work, which by then was already two decades old. Yi and Moore [10] as well as Merzhanov [11] reviewed the very similar topic. The paper by Koizumi is an important contribution in reviewing the Japanese work [12]. Other reviews also appeared in the literature including those contributed by Subrahmanyam and Vijaykumar [13] and by Moore and Feng [14, 15]. However, in spite of almost 10 reviews in the field within the last decade (i.e., almost one review per year), the contents of the reviews have not progressed much further since the publication of the seminal paper by Munir and Anselmi-Tamburini [9]. Since some of the information contained in previous reviews were actually quoted from earlier Russian references, it is believed that the data needed a second examination in view of the more recent reports. Furthermore, as active practitioners of the science and technology of this process, we feel that there have been some interesting developments in the field, which need proper attention and dissemination. To that effect, the Bhaduri group has published a review in 1998 [3]. By then, research activities in conventional CS started shrinking in this country. At the same time, such activities continued in other countries, and specifically in China, there has been a surge in activities in this field. Furthermore, another type of CS is also encountered in the literature [16]. This newer variety of CS, currently known as solution combustion synthesis (SCS), is somewhat different from conventional CS, in spite of possessing exothermicity. Indeed, there is still confusion regarding the conventional CS with this newer variety of SCS [17]. This review will not deal with such processes, which are adequately reviewed in References 16 and 17. To keep this review manageable, an introduction to the conventional CS will be presented here. The focus will be toward the synthesis of newer materials and developments of new techniques. Over the last decade, since our previous review of the subject, most of the developments took place in newer techniques, specifically, applying different fields to facilitate the combustion reactions. Hence, the major focus of this review will be on the application of external fields in enhancing combustion reactions. These external fields of application can be broadly classified as electromagnetic and gravitational fields.

This review will begin with a discussion of the thermodynamic aspects of the process. This will be followed by some specific examples of materials development, for example, silicides, borides, and carbides. The next section will review the application of electromagnetic fields in CS. The final section will review the application of gravitational fields and their effects in CS.

## 11.2 THEORETICAL CONSIDERATIONS

### 11.2.1 Thermodynamic Considerations

Once ignited, high temperatures can be achieved in very short times due to the highly exothermic nature of the reactions. The enthalpy of the synthesis reaction for the propa-



gating case,  $\Delta H_{\text{reaction}}$ , is equal to  $\Delta H_{f,298}$ , the standard enthalpy of formation of the product. For an adiabatic reaction with the reaction temperature denoted by  $T_{ad}$ , the heating of the product from 298 K to  $T_{ad}$  takes place in response to the input of  $\Delta H_{\text{reaction}}$ . Depending upon whether  $T_{ad}$  is smaller than, equal to, or larger than the product melting temperature  $T_m$ , the following three cases arise:

$$\Delta H_{f,298} = \int_{298}^{T_{ad}} C_{p(\text{product})} dT, \text{ if } T_{ad} < T_m, \quad (11.1)$$

$$\Delta H_{f,298} = \int_{298}^{T_{ad}} C_{p(\text{product})} dT + v\Delta H_m, \text{ if } T_{ad} = T_m, \quad (11.2)$$

and

$$\Delta H_{f,298} = \int_{298}^{T_{ad}} C_{p(\text{product})} dT + \Delta H_m + \int_{T_{mp}}^{T_{ad}} C_{p(\text{liquid})} dT, \text{ if } T_{ad} > T_m, \quad (11.3)$$

where  $v$  is the fraction of the liquid phase in the mixture of liquid and solid phases since both of them are expected to exist at the melting point.

For many compounds, the thermodynamic data required to calculate  $T_{ad}$  are available in the literature. However, it is pointed out that an agreement between the experimentally obtained data and theoretically calculated values is lacking. This is because the reactions are not truly adiabatic. At best, the calculations predict the upper limit of  $T_{ad}$ . Nevertheless, such calculations provide important guidelines for maintaining the exothermic state of the reactions. Based on the observations of a number of reactions [11, 16], it has been found that there is a linear correlation between  $\Delta H_{f,298}/C_{p,298}$  and  $T_{ad}$ . It has been suggested in the literature that the reaction will not be self-sustained if  $\Delta H_{f,298}/C_{p,298} < 2000^\circ\text{C}$  (or  $T_{ad}$  values are less than  $1800^\circ\text{C}$ ).

Table 11.1 shows the results of  $T_{ad}$  calculations for various silicides.  $\Delta H_{f,298}$  for the materials under consideration were obtained from Reference 18.  $C_p$  (in kilojoule per mole-kelvin) is written as  $a + bT + cT^2$ , where the coefficients  $a$ ,  $b$ , and  $c$  are taken from Reference 18 and are listed in Table 11.1. Depending on a particular case (i.e., when there is substantial melting), the calculations may require a value of  $C_{p(\text{liquid})}$ , which is taken as  $33.74.n \text{ J/mol}\cdot\text{K}$ , where  $n$  is the number of atoms in a molecule and is equal to 8, for example, in  $\text{Ti}_5\text{Si}_3$  [19]. Table 11.2 lists as-predicted values of the various silicides. These values can be compared to those reported in Reference 13, which are based on the Russian data. It is seen that the values are available only in some cases. Of those cases where comparable data exist, the agreement is quite good in many cases, while there are substantial differences in the predicted values of  $T_{ad}$  in the cases of  $\text{TiSi}$  and  $\text{CrSi}_2$ .

Tables 11.3 and 11.4 show similarly calculated  $T_{ad}$  values for various carbides as well as borides. Again, there are agreements as well as discrepancies between our data and the Russian predictions. Notable differences exist in the cases of  $\text{ZrC}$  and  $\text{HfC}$ . Also, VC is reported to have a very high  $T_{ad}$  value in excess of  $3500 \text{ K}$  in References 9, 10, and 15, which we believe is in error. According to our calculations, that value is

TABLE 11.1. Data for Thermodynamic Calculations for Various Silicides

Compound	<i>a</i>	<i>b</i>	<i>c</i>	$\Delta H_f$ (kJ/mol)	$\Delta H_m$ (kJ/mol)	M.P. (K)	$\Delta H_f/C_p$	$T_{ad}$ (K)
TiSi	47.84	11.36	-5.41	128.96	40.18	1843	2.86	2349
TiSi <sub>2</sub>	70.01	17.47	8.99	133.54	43.44	1773	2.05	1808
Ti <sub>5</sub> Si <sub>3</sub>	46.95	10.70	-4.8	138.40	178.88	2408	2.90	2528
ZrSi	44.9	8.74	2.95	153.92	58.73	2368	3.84	2909
ZrSi <sub>2</sub>	62.8	15.27	-2.78	158.50	44.75	1790	2.47	2228
Zr <sub>5</sub> Si <sub>3</sub>	188.0	30.58	-14.9	572.42	59.59	2483	3.17	2739
VSi <sub>2</sub>	71.05	11.61	-9.36	124.8	51.75	1953	2.00	1792
V <sub>5</sub> Si <sub>3</sub>	187.3	118.1	-17.2	459.26	49.08	2283	2.26	1703
NbSi <sub>2</sub>	62.82	12.57	-2.78	137.28	69.17	2203	2.14	1863
Nb <sub>5</sub> Si <sub>3</sub>	188.1	30.61	-14.9	449.28	73.51	2753	2.49	2222
TaSi <sub>2</sub>	72.84	7.67	-9.01	118.39	89.03	2473	1.82	1671
Ta <sub>5</sub> Si <sub>3</sub>	178.6	38.90	-8.86	332.80	72.10	2773	1.85	1772
CrSi	51.71	8.69	-8.36	54.50	35.12	1730	1.21	1215
CrSi <sub>2</sub>	65.23	22.38	-7.74	79.62	42.39	1730	1.26	1252
Cr <sub>5</sub> Si <sub>3</sub>	197.5	49.00	-25.5	221.73	33.02	1920	1.21	1233
MoSi <sub>2</sub>	67.44	11.90	-6.53	130.96	74.83	2303	2.06	1872
Mo <sub>5</sub> Si <sub>3</sub>	182.3	34.84	-11.9	307.84	56.65	2463	1.72	1672
W <sub>5</sub> Si <sub>2</sub>	67.43	10.98	-6.06	92.19	85.16	2433	1.44	1471
W <sub>5</sub> Si <sub>3</sub>	178.6	38.98	-8.82	133.79	63.53	2593	0.74	945
MnSi	49.00	12.69	-6.36	78.29	29.41	1548	1.71	1553
Mn <sub>5</sub> Si <sub>3</sub>	200.2	53.87	-19.5	199.68	21.71	1573	1.03	1100
ReSi	52.29	9.57	-3.74	52.42	50.16	2153	1.03	997
ReSi <sub>2</sub>	67.39	10.98	-6.07	89.86	73.22	2253	1.41	1420
Re <sub>5</sub> Si <sub>3</sub>	189.7	44.93	-13.9	156.42	46.89	2233	0.83	901

*a*, *b*, and *c* are in J/mol/K, 10<sup>-3</sup> J/mol/K, and 10<sup>5</sup> J/mol/K, respectively.

TABLE 11.2. Comparison of Theoretical and Experimental Results (Silicides)

Material	$T_{ad}$ (K) Theoretical	$T_{ad}$ (K) Experimental
TiSi	2349	2000
Ti <sub>5</sub> Si <sub>3</sub>	2528	2500
Zr <sub>5</sub> Si <sub>3</sub>	2739	2800
NbSi <sub>2</sub>	1863	1900
TaSi <sub>2</sub>	1671	1800
CrSi <sub>2</sub>	1252	1800
MoSi <sub>2</sub>	1872	1900
WSi <sub>2</sub>	1471	1500

moderately high. Similar comments can be also made in the cases of various borides. Notable differences exist in the cases of CrB<sub>2</sub> and MoB.

At this point, two comments can be made. First, since these predictions serve as important guidelines, the new values should be carefully considered before initiating any reaction. Second, it is seen that the formation of several compounds is quite slug-

TABLE 11.3. Comparison of Theoretical and Experimental Results (Carbides)

Material	$T_{ad}$ (K) Theoretical	$T_{ad}$ (K) Experimental
TiC	3290	3210
HfC	4512	3900
ZrC	3758	3400
NbC	2821	2800
VC	2228	2400
TaC	2901	2700
Mo <sub>2</sub> C	1017	1000
WC	1163	1000

TABLE 11.4. Comparison of Theoretical and Experimental Results (Borides)

Material	$T_{ad}$ (K) Theoretical	$T_{ad}$ (K) Experimental
TiB	3388	3350
TiB <sub>2</sub>	3198	3190
ZrB <sub>2</sub>	3322	3310
HfB <sub>2</sub>	3662	3520
VB <sub>2</sub>	2546	2670
NbB <sub>2</sub>	2715	2400
TaB <sub>2</sub>	2728	2700
CrB <sub>2</sub>	1475	2470
MoB	2659	1800
WB	1617	1700

gish (i.e., have  $T_{ad}$  temperatures in the range of 1000 K). There are many strategies that are followed in initiating reactions in such cases. Common methods to ignite such reactions are the “explosion mode,” the “chemical oven” and using ternary reactions with several different phases taking part in the reaction. An advancement of recent origin is the application of various types of fields such as electromagnetic and gravitational fields.

### 11.2.2 Kinetic Considerations

In order to understand the kinetics of the process, a cylindrical compact is placed vertically in a reaction chamber and ignited at the top. A self-supporting reaction wave is initiated under suitable conditions and its steady speed of combustion is measured. Of interest is the dependence of such variables of the experiment as the specimen diameter; specimen composition; size of the particles, which are pressed; and the extent of dilution with an inert component such as the reaction product itself. These are well documented in References 9, 10, 14, and 15.

Azatyán et al. [20] has derived an expression for the rate of propagation of a planar combustion front based upon an elementary model of the process. In this model, the

calculations are performed assuming a uniform radial distribution (a planar front). With the additional assumptions that a single heat source exists and the only heat loss from the body is conductive and radiative, the generalized form of Fourier's one-dimensional heat equation takes the form

$$C_p \rho \frac{fT}{ft} = k \frac{f^2 T}{fx^2} + Q \rho \phi(T, \eta) - 2 \frac{\alpha}{r} (T - T_0) - 2 \varepsilon \frac{\sigma}{r} (T^4 - T_0^4) \quad (11.4)$$

and

$$\phi(T, \eta) = 2 \frac{f\eta}{ft}, \quad (11.5)$$

where  $C_p$  is the heat capacity,  $r$  is the density,  $T$  is the temperature,  $T_0$  is the ambient temperature,  $\eta$  is the fraction reacted,  $t$  is the time,  $k$  is the thermal conductivity,  $x$  is the axial distance,  $Q$  is the heat of reaction,  $\alpha$  is the heat transfer coefficient,  $\rho$  is the sample radius,  $\varepsilon$  is the emissivity coefficient,  $\sigma$  is the Stefan–Boltzman constant, and  $\phi$  is the kinetic function.

Neglecting the transient effects from the ignition surfaces and the heat losses, the above equation can be rewritten as

$$C_p \rho \frac{\partial T}{\partial t} = k \frac{\partial^2 T}{\partial x^2} + Q \rho \phi(T, \eta). \quad (11.6)$$

The solution to the above equation can be written as

$$u^2 = \sigma_n \frac{k}{Q \rho} \frac{RT_{ad}^2}{E} K_0 \exp\left(-\frac{E}{RT_{ad}}\right), \quad (11.7)$$

where  $\sigma_n$  is a constant depending upon the order of the reaction. The apparent activation energy of the reaction can be found from a graph of  $\ln(u/T_{ad})$  versus  $1/T_{ad}$ .

The most common strategy to activate a sluggish reaction is to subject the reactants to the radiant heat of a furnace, an example of “thermal activation.” Once the reactants reach a certain temperature, they combust simultaneously through the entire sample. During the heating of samples, substantial diffusion can occur, resulting in undesirable phases. This is the reason why over the last 15 years, most of the innovations in CS research took place in field-assisted processing. The two fields that are of interest here are electromagnetic and gravitational fields. Accordingly, this review will describe the innovations in details.

### 11.3 ELECTROMAGNETIC FIELD CS

This technique can be divided into two different subtopics: direct electric field-activated combustion synthesis and microwave-activated combustion synthesis (MACS). Munir and coworkers, the pioneers of the former process, coined the term “field-activated

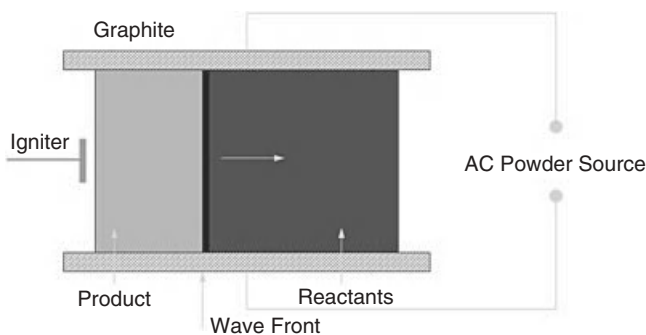


**Figure 11.1.** Schematic setup of an electric field CS.

combustion synthesis (FACS)” [21, 22]. It is inherently assumed here that electromagnetic fields are responsible in assisting and activating the reactions. As the title implies, this technique requires a direct passage of electric current. To be consistent, the latter process can be referred to as the “MACS.” In this variation, samples can be made to absorb electromagnetic energies (e.g., microwaves), simultaneously heating and activating the reactions (Fig. 11.1). No direct contacts with electrodes are necessary. A detailed comparison of these processes is presented in the following.

The FACS process applies an electric voltage (via in-contact electrodes) to a compact of reactants undergoing combustion, started with a separate triggering coil. The application of an external field creates localized joule heating (in most cases) at the tip of the propagating front. This activates a propagating front in sluggish reactions. Thus, FACS is particularly suitable for activating sluggish reactions. The applied field also influences the kinetics of propagation. A uniform propagation of the front is possible in sluggish reactions as opposed to the oscillatory motion that is usually seen in sluggish reactions. At very high field values, the reaction can be triggered by the electric field itself. The propagation can be stopped by turning off the field. This stalls the front, and reaction mechanisms can be studied by examining the phases behind and ahead of the stalled front. Finally, because of enhanced kinetics, purer phases form in FACS processed samples as compared to their conventional counterparts.

Microwaves are useful in processing advanced materials. It is well-known that certain minerals and ceramics absorb microwaves and become self-heated. Microwaves are believed to be reflected by metals and thus are not useful in heating metals (this is not always true!). Several reviews are available in the literature discussing the details of microwave heating [23–25]. In order to heat materials that couple microwaves well, a microwave absorbing susceptor is used. However, with a susceptor, a material can reach a temperature where microwaves are so efficiently coupled that they result in thermal runaway. This is exacerbated by the heat generation *in situ*. Therefore, it is important to conduct high-temperature dielectric measurements to examine such thermal runaway. Presently, we are not aware of any dielectric measurements on metallic powders. Yet, there is a compelling need to carry out such experiments (Fig. 11.2).

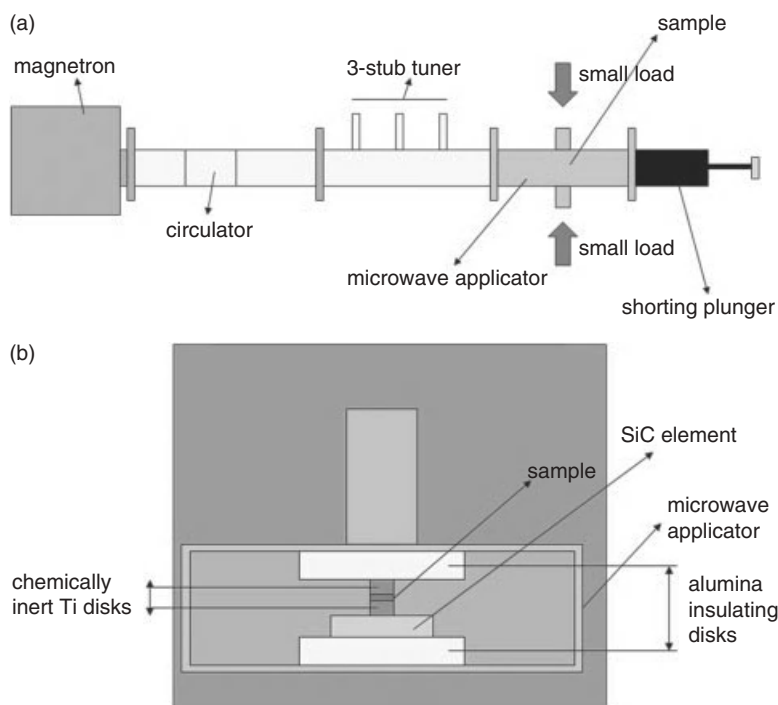


**Figure 11.2.** (a) A microwave CS setup. (b) A zoomed-in view of the furnace interior is illustrated. Microwaves generated by the magnetron propagate through the applicator and heat the sample directly and indirectly by heating the SiC element.

All of the above features of microwave heating should be kept in mind while discussing activating combustion reactions. Some of the interesting features of MACS are as follows:

- Microwaves are continuously absorbed in appropriate materials. As the temperature rises, more and more microwaves are coupled, creating and sustaining hot spots. This way, sluggish reactions can be activated with the help of microwaves. This feature of MACS is similar to that of FACS.
- An advantage of MACS is that it is able to process asymmetric shapes. FACS, in contrast, requires symmetric samples with flat ends in order to make good contacts with electrodes.
- Another advantage of MACS is its ability to process both insulators as well as conductors. Samples of optimum conductivity are preferred in FACS.
- The surface temperature of a sample in a microwave cavity is less than in the interior. Hence, the propagation direction may be different.
- MACS reactions (in most cases) need a susceptor, which plays a unique role in the process.

- Like the FACS process, MACS is a fast process and does not allow for a substantial diffusion of species to occur, thus reducing the possibility of synthesizing undesirable phases.
- Finally, the microwave power can be left on for further densification. This is also possible in the FACS process but only in a simple shape with flat ends.

There have been some efforts in modeling these activated processes. In order to put together theoretical descriptions of FACS and MACS processes, previous models need to be modified. Strategies for such modifications require starting off with a standard model of either process (e.g., microwave heating or CS) and modifying it to include the other. This was used in the formulation of FACS models [26–29].

Following this philosophy, Kidin and Filimonov [26] modified the conventional Fourier heat transfer equation to include the joule heating term in FACS. Parameters such as the direction of the applied field with respect to the direction of propagation and the magnitude of applied voltage and current on the combustion reaction were studied. The model was not validated with any experimental data.

Feng and Munir provided a more comprehensive modified Fourier heat balance equation for FACS [27]. By simultaneously performing experiments, they clearly showed that the joule heating term takes place locally at the reaction front. Furthermore, the models were two-dimensional in nature, allowing for heat loss. More refinements to the model were carried out by Carillo-Heian et al. [29], taking into consideration the effects of thermal conductivity, electrical conductivity, and density. Density is included because it affects the other two properties. While these are very useful to model FACS reactions, matter–microwave interactions must be incorporated for MACS. From this viewpoint, the effort by Skamser et al. is significant [28]. Specifically, matter–microwave interactions are included in the model. The model, however, is more applicable to a much less exothermic reaction.

### 11.3.1 Materials Considerations

Research on FACS has reached a mature level now as compared with MACS. Since electrical conduction is important in carrying out FACS, there is an abundance of papers dealing with FACS in metallic systems. The literature is full of reports on FACS of intermetallics, such as silicides and aluminides. Other systems include composites containing metals but eventually forming ceramics. Table 11.5 summarizes the diverse materials processed by electromagnetic field CS.

Work on silicides forms an important group of papers, of which  $\text{MoSi}_2$  and related materials are predominant. Heian and colleagues investigated the use of an electric field in producing  $\text{MoSi}_2/\text{SiC}$  composites [30]. Two samples of different radii underwent CS. It was noted that no ignition took place if the electric current through the die and the sample was too low. It was also noted that when the voltage was too high, the waves became unstable. The sizes of samples also played a significant role as they influenced the mode of propagation of the reaction wave. With the increase in the size of the samples, the propagation of the reaction wave was more uniform, and the direction of the wave depended on die conductivity and the voltage applied. The time for the

TABLE 11.5. Examples of Materials Processed by Electromagnetic Field CS

Authors	Materials Processed	Reference
Xue et al.	MoSi <sub>2</sub>	[31]
Gedevanishvili and Munir	MoSi <sub>2</sub> -SiC	[32]
Carrillo-Heian et al.	MoSi <sub>2</sub> and SiC	[33]
Heian et al.	MoSi <sub>2</sub> -SiC	[30]
Hu et al.	MoSi <sub>2</sub> -SiC composite	[34]
Shon, Munir	Ti <sub>5</sub> Si <sub>3</sub> - x Nb (0 ≤ x ≤ 0.35) and Ti <sub>5</sub> Si <sub>3</sub> - y ZrO <sub>2</sub> (0 ≤ y ≤ 0.3)	[35]
Munir and Gedevanishvili	NbSi	[40]
Bertolino et al.	VSi	[51]
Gedevanishvili and Munir	TiB <sub>2</sub> -TiAl <sub>3</sub> composites with molar ratios from 1.0 to 5.0	[38]
Orru et al.	Ti <sub>3</sub> Al and TiAl	[79]
Jokisaari et al.	TiAl and Ti <sub>3</sub> Al intermetallics	[42]
Naplocha and Granat	Al-Ti materials	[43]
Yun et al.	FeAl	[41]
Poli et al.	NiAl intermetallics	[44]
Naplocha and Granat	Al-Cr compounds	[45]
Morozov and Kuznetsov	Effect of magnetic field on the combustion electromotive force	[48]
Neresyan et al.	Electric and magnetic fields	[49]
Won et al.	Dense Al-Al <sub>2</sub> O <sub>3</sub> B <sub>4</sub> C FGMS	[50]
Graeve and Munir	TiC-TiNi	[51]
Park et al.	WC-10 vol % Co	[52]
Clark et al.	Various materials processed by microwaves	[53]
Vaidhyanathan et al.	Porous metal powder compact with N <sub>2</sub> gas-metal nitride products	[54]
Hu et al.	TiC-Al <sub>2</sub> O <sub>3</sub> -Al composite	[55]
Li et al.	Mg <sub>2</sub> Ni hydrogen storage alloys	[47]
Chen et al.	TiB <sub>2</sub> -Ni/TiB <sub>2</sub> -Ni <sub>3</sub> A + Ni/Ni <sub>3</sub> Al/Ni by	[56]

composites to densify took significantly less time than conventional CS procedures. There was also an enhancement in the microstructures (finer and dense) in this experiment.

Initiation of self-propagating combustion waves in dense Mo + 2Si reactants was achieved through field activation [31]. Such reactions were obtained in MoSi<sub>2</sub>B-Si composites in the FACS mode [32]. Functionally graded molybdenum disilicide-silicon carbide composites can also be formed by the same technique [33]. In this experiment, it was found that the formation of pure phases occurred when the concentration of MoSi<sub>2</sub> was high. scanning electron microscopy (SEM) results showed the formation of stoichiometric and uniformly distributed phases as well. Interestingly, when the electric field was turned off immediately after compaction, the microstructure became inhomogeneous, a sign of lesser extent of reaction completion. Munir and colleagues concluded that pressure and electric field simultaneously can make the formation of dense



MoSi<sub>2</sub>-SiC composites and layered functionally graded materials (FGMs) feasible. Hu et al. used Mo, Si, and C element powders as starting materials in a field-activated and pressure-assisted combustion synthesis (FAPACS) to synthesize high-density bulk MoSi<sub>2</sub>-SiC composites [34]. The effects of sintering temperatures on microstructures and densification were investigated. They concluded that the most suitable combination of sintering temperature and holding time for fabrication of MoSi<sub>2</sub>-SiC by FAPACS is 1600°C for 20 min.

Yet, another material of importance, Ti<sub>5</sub>Si<sub>3</sub>, with its low density and high melting point, has been subjected to FACS. Although the stoichiometric composition forms in an exothermic fashion, the addition of second phases can reduce the exothermicity, making them excellent candidates for FACS. Syntheses of Ti<sub>5</sub>Si<sub>3</sub>-Nb and Ti<sub>5</sub>Si<sub>3</sub>-ZrO<sub>2</sub> were reported and analyzed in the literature [35]. It was noted that an unstable wave propagated to the middle of the sample and then extinguished itself. Wave velocities were also noted to increase with an increase of the field, but the wave velocity with an applied voltage of 10 V was only slightly higher than in the absence of a field.

Shon and colleagues investigated the simultaneous synthesis and densification of WSi<sub>2</sub> and WSi<sub>2</sub>-20 vol % Nb composite [36]. Compared to Ti<sub>5</sub>Si<sub>3</sub>, the formation of WSi<sub>2</sub> is more sluggish. Here, an electric current of 3000 A was used with a 60-MPa compaction pressure. Results showed that final density was linearly proportional to the pressure applied, and when the samples were tested, it was concluded that the fracture toughness and microhardness increased substantially. The synthesis of silicides in the Ta-Si binary was also reported by Munir et al. [37]. In this experiment, an electric field of 6 V/cm was used to initiate a combustion wave. It was noted that Ta<sub>3</sub>Si<sub>2</sub> and Ta<sub>2</sub>Si can be activated with electric fields between 0 and 20 V/cm. A very interesting observation was that the wave velocities in Si-rich phases were considerably lower and did not show much dependence on the field. XRD, SEM, and EDS evaluations did show an intermediate phase in the nominal TaSi<sub>2</sub> composition, but there were other intermediate phases present in Ta<sub>3</sub>Si<sub>2</sub> and TaSi<sub>2</sub>. Results demonstrated that self-propagating waves could be initiated in samples with less than 78% relative density and higher values; no waves could be initiated without field activation. Similar to previous experiments, it was concluded that both the combustion wave velocity and temperature increased nearly linearly with an increase in field strength. The other important binary system, Nb-Si, was also investigated to study the activation of self-propagating combustion by Gedeonishvili and Munir [38]. Under steady-state wave propagation, the product contained the high- and low-temperature modifications of Nb<sub>5</sub>Si<sub>3</sub>, which were dependent on the applied field and on the relative density of the reactant compacts. The effect of Nb particle size and the feasibility of the synthesis of Nb/silicide composites were demonstrated. In the V-Si binary system, the field was seen to have a weak effect on the combustion macrokinetic parameters [39]. Only the VSi<sub>2</sub> and V<sub>5</sub>Si<sub>3</sub> phases were observed in the leading edge of the combustion front, with the other phases forming from solid-solid interactions in the afterburn [39].

Another important group of materials that has been experimented with was the aluminides. FACS has been used in the synthesis of TiB<sub>2</sub>-TiAl<sub>3</sub> composites [40]. Three types of boron powders were dry mixed, cold pressed, and then shaped into rhombohedral samples. It was observed that samples with molar ratios between 3.0 and 5.0

required a field to initiate synthesis. XRD and SEM evaluated that the molar ratio was proportional to the amount of  $\text{Ti}_5\text{Al}_{11}$ . Another interesting observation was that the wave velocity decreased with increasing Nb concentration. In another investigation, an electric field of 14.3 V/cm was imposed simultaneously until a propagating reaction wave started. Once this was achieved, the current passing through the die and sample was increased to about 140 A.

FACS was also used in the preparation of Fe–Al investigated by Yun and colleagues [41]. Here, Fe and Al powders were dried in an alumina ball mill and then pressed into pellets. These pellets were then ignited with the help of a 30-V DC and compaction pressures of 150, 250, and 350 MPa. It was found that the compaction pressure and electric fields correlated with the temperature and velocity of the reaction. When the samples were examined with the help of XRD and SEM processes, it was noted that unreacted Fe and Al were seen in the products, but with increased time, they reacted completely. The product consisted of  $\text{FeAl}_3$ ; the original Fe particles reacted until all the aluminum was consumed.

Alternatively, other investigators have studied the synthesis of intermetallics by applying two different CS techniques. In such a study,  $\text{TiAl}$  and  $\text{Ti}_3\text{Al}$  titanium aluminide compounds were synthesized using MACS and were compared to thermal activation CS and conventional combustion methods [42]. The results of the research revealed that  $\text{Ti}_3\text{Al}$  content in  $\text{TiAl}$  was significantly higher and more consistent for the thermal activation CS samples. Naplocha and Granat have explored possibilities with research on porous Al–Ti materials produced by MACS [43]. The synthesis process was analyzed, as well as structure formation, phase composition, homogeneity degree, and type of porosity. The cylindrical green compacts were prepared with Al and Ti powders of various stoichiometric ratios. The synthesis was performed in a specially designed microwave reactor by placing the compact in a waveguide, in an intensely focused field. Temperatures were recorded with the help of a pyrometer, and such measurements demonstrated that the synthesis propagation accelerated at the moment of  $\text{Al}_3\text{Ti}$  creation. A post-inspection of the specimens indicated that some had a regular structure with interconnected porosity. In addition, microscopic examinations revealed that rounded grains composed of  $\text{AlTi}_3$  underwent transformation into  $\text{AlTi}$  at the edge. Other researchers explored the possibilities of MACS of NiAl intermetallics with the aim of achieving the highest yields, energy efficiency, and process reproducibility [44]. The optimization procedures allowed researchers to determine and quantify the effects of main process variables on the ignition time, the NiAl production, and the specific energy consumption (Fig. 11.3).

Li et al. addressed the advantages and disadvantages of the two different preparation methods and the effect of an external physical field on the hydrogenation properties of the alloy. Other investigators applied a similar method in manufacturing porous intermetallic preforms of Al–Cr compounds intended for local reinforcement within composite materials [45]. In such experiments, green mixtures of Al and Cr were cold pressed to form cylindrical specimens and then were combusted in a microwave field. The analysis of experimental results provided evidence that the reaction temperature increased with increasing Cr content. According to the XRD patterns, the reaction proceeded between solid Cr and liquid Al to create intermetallic phases with a residue

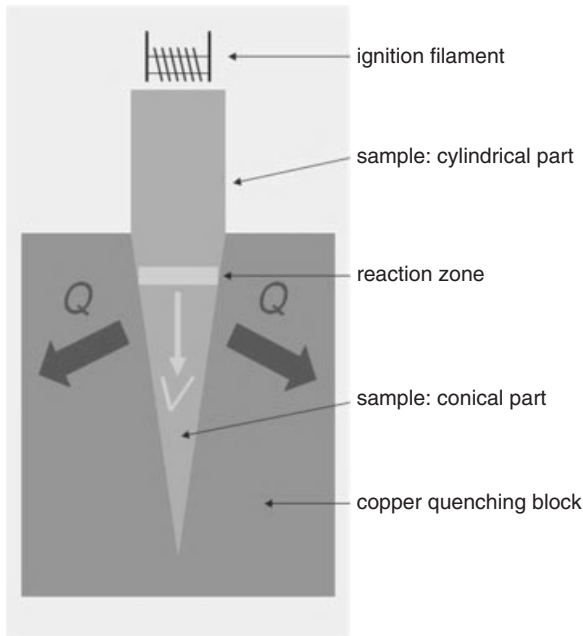


**Figure 11.3.** The cylindrical and conical sample geometries used in CS research. The propagating front wave with velocity  $V$  is quenched as the heat  $Q$  is dispersed throughout the copper quenching block.

of starting and transient phases. A SEM examination of fracture surfaces showed the porous structure of the preforms with rounded Al–Cr precipitates covered with tiny cuboid particles. Reaction zones around partially reacted Cr particles were visible from an EDS analysis of preforms. Besides experiments with only electromagnetic CS alone, others have been conducted using electromagnetic CS accompanied with pressure assistance to facilitate synthesis.

Other CS experiments have been carried out from elemental Mg and Ni powders by induction field-activated combustion synthesis (IFACS) to produce high-purity  $\text{Mg}_2\text{Ni}$ , typically used as a hydrogen storage material [46]. The effect of mechanical grinding (MG) on the hydrogen storage behavior in  $\text{Mg}_2\text{Ni}$  was also described in the study. The results indicated that the MG process developed the applicability of  $\text{Mg}_2\text{Ni}$  as a hydrogen storage material by decreasing the absorption pressures and enhancing the reaction kinetics. Similarly, in another study, Li et al. investigated the influence of various magnetic and microwave fields during the preparation process of  $\text{Mg}_2\text{Ni}$  [47]. In addition to its physicochemical properties including thermodynamic and kinetic characteristics, hydrogen absorption/desorption properties, phase composition, and morphology were analyzed.

Morozov and Kuznetsov studied the effects of magnetic fields on combustion electromotive forces [48]. Important results indicated that the combustion electromotive

force developed as a result of the chemical ionization of the initial reagents. Another important piece of information was that an electric field applied along the combustion wave front altered the parameters of combustion. Nersesyan and colleagues investigated a subject related to how magnetic fields and electric fields were generated during synthesis by the reaction [49]. After a series of experiments, they concluded that reactions consisting of  $\text{Ti} + \text{C}$ ,  $\text{Mo} + \text{B}$ , and  $\text{Nb} + \text{B}$ , which are fast-moving reactions, may generate electric and magnetic fields, and a voltage difference of up to 1 V (although not very significant) was recorded in these reactions.

Won et al. also explored the possibilities of FACS with aluminum composites, namely, functionally graded  $\text{Al}/\text{Al}_2\text{O}_3\text{-B}_4\text{C}$  by pressure-assisted synthesis [50]. Different from field-assisted synthesis, the experiment was carried out using a high-purity aluminum, carbon, and  $\text{B}_2\text{O}_3$ , which were mixed in a dry ball mill for 24 h and then dried in a vacuum oven for another 24 h at  $70^\circ\text{C}$ . After this process, the powders were charged into a graphite mold through which a DC current of 3000 A. Then they were compressed with pressures at three different levels of 5, 15, and 30 MPa, in a vacuum of  $2 \times 10^{-2}$  Torr and an 18-V/cm electric field until combustion reaction was complete. XRD and SEM were used in characterizing the samples. At 5 MPa, high porosity was found in the ceramic and composite regions, while at 15 MPa, the porosity was decreased drastically and at 30 MPa, the porosity was almost eliminated. It was concluded that a dense FGM with difference in melting points can be synthesized with the help of pressure.

Graeve and Munir investigated the effect of an electric field on the microstructural development during CS of  $\text{TiNi-TiC}$  composites [51]. After initial preparation and cold compaction, the samples were subjected to FACS. An electric field of up to 5 V/m was used in this experiment, where it was noted that the average particle size increased by a factor of 2 and wave velocities increased by a factor of 3. Also, the field had a direct effect on the velocity and temperature of the combustion wave. Some conventional results were noted in this experiment, like the increase in grain size with the increase in electric field. With the aid of SEM and XRD, Munir et al. observed that the presence of a liquid phase has a more direct effect on  $\text{TiC}$  particle growth. Park et al. researched with a few other composites, namely, WC-10 vol % Co hard material [52]. Powders were milled in alcohol and then dried in a vacuum oven at  $60^\circ\text{C}$ . Then, a uniaxial pressure of 60 mPa and a DC current of 3000 A were applied constantly until densification was achieved. After viewing the by-product with the aid of XRD and SEM, it was concluded that the fracture toughness and hardness of WC-10 were increased substantially. Other researches such as Clark and colleagues have compared and contrasted the effect on direct heating versus microwave hybrid heating on CS [53]. Their observations established that densification of some ceramic materials can be achieved at lower temperatures and in shorter times with the help of microwaves. In the experiments, 0.3 MHz–300 GHz were used, which are typical microwave frequencies. The advantages of microwave processing include rapid and uniform heating, decreased sintering temperatures, and improved mechanical and physical properties.

Apart from carbides and borides, Vaidhyanathan et al. experimented with the synthesis of nitride powders [54]. In this experiment, porous metals were synthesized under the aid of microwave and  $\text{N}_2$  gas. It was noted that the ignition and combustion tem-

peratures were a function of compaction pressure and that the products had good crystallinity, structural uniformity, and phase purity.

Subsequently, in a study by Hu et al., a dense TiC–Al<sub>2</sub>O<sub>3</sub>–Al composite was prepared with Al, C, and TiO<sub>2</sub> powders by means of FACS and infiltration of molten Al into the synthesized TiC–Al<sub>2</sub>O<sub>3</sub> ceramic [55]. They observed that FACS can result in a highly dense TiC–Al<sub>2</sub>O<sub>3</sub>–Al structure. In an experiment by Chen et al., the same FAPACS technique was used to synthesize FGM materials that were prepared under the conditions of field-assisted and hot-press [56]. The microstructure and the phase composition of the interface of the graded materials were investigated. The results showed that the metallurgical joining layer of metallurgical nature was formed between the interfaces of the TiB<sub>2</sub> and steel.

## 11.4 GRAVITY-ASSISTED CS

As opposed to the electromagnetic FACS, the role of gravity in the CS reactions is somewhat different. In fact, there could be two different effects of gravitational field on CS reacted products. Under the microgravity situation, it is possible to fabricate highly porous structures (reticulated foams) for various applications. On the other hand, high-gravity CS enables the application of very high centrifugal forces for enhanced consolidation of the reacted products. Tables 11.6 and 11.7 present the range of materials processed by CS with the help of gravity. The following sections elaborate on these topics.

### 11.4.1 Microgravity CS

Triggering CS reactions under the microgravity conditions has been reported for the last 15 years, largely in part due to the unique material properties resulting due to a low-gravity situation. In microgravity CS, reactants are cold pressed into cylindrical pellets followed by ignition of the combustion wave. The microgravity environment,

TABLE 11.6. Examples of Materials Processed by Microgravity CS

Authors	Materials Processed	Reference
Hunter and Moore	Ceramic metal composites	[57]
Yi et al.	HfB <sub>2</sub> /Al and Ni <sub>3</sub> Ti/TiB <sub>2</sub>	[58]
Varma	Aluminides	[59]
Merzhanov et al.	NiAl	[60]
Prisbrey et al.	Ti–Si	[61]
Lau et al.	NiAl–TiB <sub>2</sub> composites	[62]
Ayers et al.	Ca-phosphates	[63]
Locci et al.	Ti–B–Al	[64]
Zanotti et al.	Co–Al, Ni–Al	[65]
Vadchenko et al.	Ti–Si–Al–C	[66]

TABLE 11.7. Examples of Materials Processed by Gravitational Field CS

Authors	Materials Processed	Reference
Miyazaki and Odawara	Ti-B-C	[70]
Du et al.	$\text{Fe}_2\text{O}_3/\text{Al}_2\text{O}_3$	[71]
Lee et al. and Le et al.	$\text{Fe}_2\text{O}_3/\text{Al}_2\text{O}_3$	[72, 73]
Menske et al.	$\text{Fe}_2\text{O}_3\text{-Al}$ , $\text{Cr}_2\text{O}_3\text{-Al}$	[74]
Zhao et al.	$\text{Zr}_2\text{O}_2\text{-Al}_2\text{O}_3$	[75, 76]
Pei et al.	$\text{Al}_2\text{O}_3$	[77]
Zhao et al.	TiC-TiB <sub>2</sub>	[78]

usually between  $10^{-2}$  and  $10^{-4}$  times the earth's gravity, is simulated by either parabolic flights, free fall in underground shafts, or combustion reactors aboard vessels in low earth orbit. A large part of such research was funded by NASA, Canadian, and European Space agencies, because of the access to the facilities needed for such research.

Initial studies focused on inhomogeneous metal-ceramic systems. Presumably, the guiding principle was to use highly exothermic and frequently uncontrollable reactions that typically occur in the formation of ceramics (e.g., TiB<sub>2</sub>). These reactants, when mixed with metals or intermetallics, result in lesser exothermicity with added controls [57, 58]. Two main groups in this country performed microgravity research funded by NASA. The group led by Moore at the Colorado School of Mines initially focused on Hf-B-Al and Ti-Ni-B systems. Under normal conditions, CS in these ternary systems resulted in a lower propagation wave velocity together with a reduced combustion temperature [58]. However, under a reduced gravity condition, more pores were created. There is evidence to show that the combustion temperature is dependent on the reagents utilized in the reaction. NiAl materials synthesized by CS revealed the formation of larger grains under the reduced gravity situation [59]. Merzhanov and his group carried this type of research in Russia. The group led by Varma at Notre Dame (currently at Purdue) concentrated on the Ni-Al-B system. The main result of the formation of porous foams was the same as observed by the other groups [60]. The present authors reported the only microgravity CS reactions in silicides [61]. Ti<sub>5</sub>Si<sub>3</sub> pellets were ignited in a KC-132 aircraft during its fast descent, thereby creating a short microgravity situation. This led to the extension of pores under the microgravity condition [61].

Both high gravity and microgravity can affect the flexure strength, microstructures, and other mechanical properties. Lau and colleagues studied this behavior [62]. Their conclusions included the finding that synthesized metal matrix composites have strong bonding along their entire surface with the NiAl matrix. TiB<sub>2</sub> grains appeared due to crystallization from a liquid of complex composition (Ni-Al-Ti-B). Ayers et al. combustion synthesized materials of importance in the biomedical field. They used CaO and P<sub>2</sub>O<sub>5</sub> powders to synthesize calcium triphosphate, Ca<sub>3</sub>(PO<sub>4</sub>)<sub>2</sub>, in reduced gravity [63]. They concluded that grains displayed a spherical morphology in comparison to the longitudinal-radial shape observed at terrestrial gravity. Furthermore, they showed that a low-gravity environment has an effect on grain formation. XRD results showed that samples produced in both low gravity and 1 g formed an alpha phase of tricalcium

phosphate, the high-temperature phase presumably due to exothermic reactions. Spherical pores were produced in low gravity; longitudinal-radial pores were produced in terrestrial gravity. Simultaneously,  $\text{Ni}_3\text{Ti}$  and  $\text{NiTi}_2$  were also formed in another experiment together with the equiatomic  $\text{NiTi}$ . Blending these materials together may lead to the formation of smart implants.

Locci et al. [64] have experimented with producing  $\text{TiB}_2$  using Ti, B, and Al as the initial powders. The reaction was ignited under a terrestrial gravity situation. However, once ignited, the reaction could not spontaneously proceed in low-gravity conditions. Also, it was concluded that the combustion temperature is not significantly dependent on the gravitational level or that the ignition configuration and low g product generally present a finer and more uniform microstructure. Zanotti et al. reported CS of intermetallics in the Co-Al and Ni-Al systems under reduced gravity [65]. They found that under microgravity, temperatures are higher, and this is the effect that brings about improvement in the homogeneity of the product microstructure. Vadchenko et al. experimented with the ternary Ti-Si-Al-C system using gravity as a main ingredient [66]. Their results proved promising. Ti-Al mixtures with silicon and carbon additions were used to increase combustion temperature for the CS reaction along with gravity. With optimal conditions, desired porosity could be obtained for this experiment.

### 11.4.2 High-Gravity-Assisted CS

High-gravity-assisted CS technology was initially used for the *in situ* application of hard linings inside metal pipes. Taking the cue from the centrifugal casting technique, Odawara pioneered the process of “centrifugal thermite.” CS reactions were triggered in a thermite (aluminothermic) mixture under the influence of centrifugal forces [67–70]. The process involved triggering the exothermic reactions within pipes rotating about their central axes at high revolutions per minute. The high centrifugal forces enabled the products to be deposited on the inner surfaces of pipes with high density. Without the use of any thermal energy, the process was able to provide uniform ceramic linings with a strong bond between the metal and the lining. To improve the lining quality, various process parameters were optimized. Reference 70 extends this process to the ternary Ti-B-C system, which is known to be highly exothermic in nature. The data were obtained by changing the direction of reaction propagation and centrifugal force to evaluate the effects of centrifugal force on reaction propagation and product formation. Further improvements took place by adding different fluxes (e.g.,  $\text{SiO}_2$ ,  $\text{CrO}_3$ ,  $\text{Na}_2\text{B}_4\text{O}_7$ ), which would melt and result in denser lining by sealing pores [71–73]. Yet another additive used was  $\text{ZrO}_2$  to provide a transformation toughening mechanism to the lining. Menske et al. provided some fundamental understanding of the process mechanisms [74]. Although the process has been widely studied, important features, particularly how the reaction propagates, have not been completely revealed due to extremely high reaction rates and temperatures. Menske et al. videotaped  $\text{Fe}_2\text{O}_3$ -Al and, to a lesser degree,  $\text{Cr}_2\text{O}_3$ -Al reactions under stationary (nonrotating) and rotating conditions [74]. Video recordings clearly demonstrated that, in contradiction to the current belief, the reaction does not always propagate in a well-ordered (spiral) pattern but involves multiple, randomly distributed ignition sites.



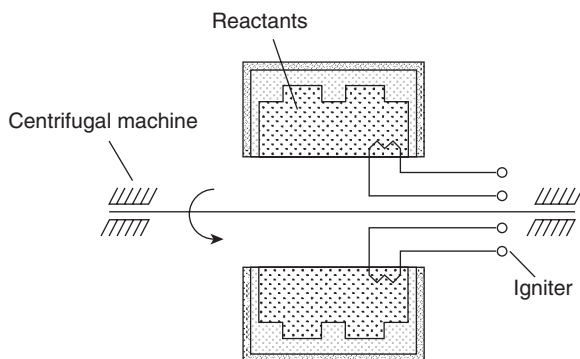


**Figure 11.4.** A sketch of the experimental setup for fabrication of  $\text{Al}_2\text{O}_3/\text{ZrO}_2$  ( $\text{Y}_2\text{O}_3$ ) composite ceramics by CS in a high-gravity field is depicted.

A high-gravity situation has been taken advantage of consolidating combustion synthesized products. Some of the recent results included the preparation of  $\text{Al}_2\text{O}_3/\text{ZrO}_2$  self-growing composites [75, 76] (Fig. 11.4). In these experiments, Zhao et al. used  $\text{CrO}_3$ ,  $\text{Fe}_2\text{O}_3$ , Al,  $\text{Al}_2\text{O}_3$ ,  $\text{ZrO}_2$ , and  $\text{Y}_2\text{O}_3$  as reactants and oxides in a centrifugal machine consisting of two graphite combustion chambers, which were under constant pressure and over 200 g's. Of particular interest is the system involving  $\text{Al}_2\text{O}_3/\text{ZrO}_2$ . Results showed that the main phases present were  $\alpha\text{-Al}_2\text{O}_3$ , t- $\text{ZrO}_2$  and m- $\text{ZrO}_2$ . In addition to this, Zhao also concluded that greater g's bring about an increase in cooling velocity and solidification resulting in the formation of a colony surrounded by a thicker interior colony. Also,  $\text{Al}_2\text{O}_3$  grew along its gravitational axis and the  $\text{ZrO}_2$  grew perpendicular to it. This orientation of the microstructure has given a significant rise in the flexure strength, fracture toughness, and other mechanical properties. The experimentation and production of  $\text{Al}_2\text{O}_3/\text{ZrO}_2$  has been further pursued by studying the influence this ceramic has when additives are mixed with it during CS [76].

The above results have been consistent in other experiments involving the same product, such as the one carried out by Pei et al. [77], where they experimented with the bulk fabrication of  $\text{Al}_2\text{O}_3$  alone. The method was similar using a centrifugal machine with the aid of gravity. Although there is not a big difference in the results, it was found that pure  $\text{Al}_2\text{O}_3$  forms at 200 g's along with metal Ni and pores. In a related note, the production of  $\text{Al}_2\text{O}_3/\text{ZrO}_2$  in a nanoscale is another effort, which has been studied by Pei et al. [77], where application of 800 g's resulted in high density, and the orientation growth of the microstructures along the axis of gravity was similar to the results reported by Zhao et al. All other properties resemble the above-stated descriptions. There have been a number of ways this ceramic has been tested and evaluated by means of CS with the aid of gravity, most of which have the same results. Finally, Zhao et al. have also been conducting research with the ternary Ti-B-C system as well [78]. In their research, they focused mostly on microstructures and properties of large bulk solidified TiC-TiB<sub>2</sub> composites. They noted unique solidification microstructures where TiB<sub>2</sub> platelets were embedded in a TiC matrix. Also, high hardness was achieved due to the absence of intermediate borides.



## 11.5 CONCLUDING REMARKS

In conclusion, this chapter begins with a presentation of the previous reviews on the subject. The emphasis here is to present some of the fundamental aspects which are rapidly moving into new developments. In this country, vigorous research in the field in the 1980s and 1990s somewhat subsided in the new millennium with a resurgence of activities in different parts of the world, most notably in China. Thus, a logical beginning is made with the thermodynamic and kinetic aspects of the process. This is followed by some specific examples of materials development, for example, silicides, carbides, and borides. Finally, field-assisted CS is described. Specifically, the effects of applications of electromagnetic and gravitational fields in CS are reviewed.

## ACKNOWLEDGMENTS

The author acknowledges several NSF grants spanning more than a decade, which helped him pursue research in this field. He is indebted to his past and present students, postdoctoral fellows, colleagues, and peer researchers, who significantly helped him in understanding the phenomenon of CS.

## REFERENCES

1. A. G. Merzhanov and I. P. Borovinskaya (1975) A new class of combustion processes, *Comb. Sci. Technol.*, **10** 195.
2. V. Hlavacek (1991) Combustion synthesis: A historical perspective, *Bull. Am. Ceram. Soc.*, **70** 240–243.
3. S. B. Bhaduri and S. Bhaduri, in *Combustion Synthesis, Non-Equilibrium Processing of Materials*, ed. C. Suryanarayana, Pergamon Press, 1999.
4. P. P. Alexander (1941) U.S. Patent No. 2 378 368.
5. S. Krapf (1964) U.S. Patent No. 3 143 413.
6. J. D. Walton and N. E. Poulos (1959) Cermets from thermite reactions, *J. Am. Ceram. Soc.*, **42** 40.
7. W. L. Frankhouser, K. W. Brendly, M. C. Kieszek, and S. T. Sullivan, *Gasless Combustion Synthesis of Refractory Compounds*. Noyes Publications, NJ, 1986.
8. Z. A. Munir (1988) Synthesis of high-temperature materials by self-propagating combustion methods, *Bull. Am. Ceram. Soc.*, **67** 342–349.
9. Z. A. Munir and U. Anselmi-Tamburini (1989) Self-propagating exothermic reactions—The synthesis of high-temperature materials by combustion, *Mater. Sci. Rep.*, **3** 279–365.
10. H. C. Yi and J. J. Moore (1990) Self-propagating high(combustion) synthesis (SHS) of powder-compacted materials, *J. Mater. Sci.*, **25** 1159–1168.
11. A. G. Merzhanov, in *Combustion & Plasma Synthesis of High Temperature Materials*, eds. Z. A. Munir and J. B. Holt, p. 1, VCH Publishers, NY, 1990.
12. M. Koizumi (1990) in *Proc. 1st US -Japan Workshop on combustion Synthesis*, eds. Y. Kaieda and J. B. Holt, p. 101, National Research Institute for Metals, Tokyo, Japan.

13. J. Subrahmanyam and M. Vijaykumar (1992) Self-propagating high temperature synthesis, *J. Mater. Sci.*, **27** 6249.
14. J. J. Moore and H. J. Feng (1995) Combustion synthesis of advanced materials: Part 1. Reaction parameters, *Prog. Mater. Sci.*, **39** 243–273.
15. J. J. Moore and H. J. Feng (1995) Combustion synthesis of advanced materials: Part 2. Reaction parameters, *Prog. Mater. Sci.*, **39** 275–316.
16. K. C. Patil, S. T. Aruna, and T. Minami (2002) Combustion synthesis- an update, *Curr. Opin. Solid State Mater. Sci.*, **6** 507–512.
17. S. T. Aruna and A. S. Mukasayan (2008) Combustion synthesis and nanomaterials, *Curr. Opin. Solid State Mater. Sci.*, **12** 44–55.
18. I. Barin, O. Knacke, and O. Kubaschewski, *Thermal Properties of Inorganic Substances*. Springer Verlag, Berlin, 1977.
19. B. Rupp, J. B. Holt, and J. Wong (1992) The calculation and analysis of the adiabatic temperature of solid combustion reactions, *J. CALPHAD*, **16** 377–386.
20. T. S. Azatyan, V. M. Maltsev, A. G. Merzhanov, and V. A. Selzenev (1979) Some principles of combustion of titanium-silicon mixtures, *Comb. Expl. Shock Waves*, **15** 35–42.
21. Z. A. Munir and K. H. Ewalds (1995) Field assisted combustion synthesis, U.S. Patent, 5,380,409.
22. Z. A. Munir (1996) The use of an electric field as a processing parameter in the combustion synthesis of ceramics and composites, *Met. Mater. Trans.*, **27A** 2080–2085.
23. W. H. Sutton (1989) Microwave processing of ceramics, *Bull. Am. Ceram. Soc.*, **68** 376–386.
24. D. M. P. Mingos (1993) Microwave synthesis of inorganic materials, *Adv. Mater.*, **5** 857–859.
25. K. J. Rao and P. D. Ramesh (1995) Use of microwaves for the synthesis and processing of materials, *Bull. Mater. Sci.*, **18** 447–465.
26. N. I. Kidin and I. A. Filimonov (1992) An SHS process in an external electric field, *Int. J. SHS*, **1** 513–518.
27. A. Feng and Z. A. Munir (1995) The effect of an electric field on self-sustaining combustion synthesis: Part II field assisted synthesis of SiC, *Met. Mater. Trans. B.*, **26** 581–587.
28. D. J. Skamser, J. J. Thomas, H. M. Jennings, and D. L. Johnson (1995) A model for microwave processing of compositionally changing ceramic systems, *J. Mater. Res.*, **10** 3160–3168.
29. E. M. Carillo-Heian, O. A. Graeve, A. Feng, J. A. Faghiih, and Z. A. Munir (1999) Microwave assisted ignition: A mathematical model, *J. Mater. Res.*, **14** 1949–1958.
30. E. M. Heian, A. Feng, and Z. A. Munir (2002) A Kinetic model for the field-activated synthesis of MoSi<sub>2</sub>/SiC composites: Simulation of SPS conditions, *Acta Mater.*, **50** 3331–3346.
31. H. Xue, Z. A. Munir, and K. Vandersall (1999) Initiation of self-propagating combustion waves in dense Mo + 2Si reactants through field-activation, *J. Am. Ceram. Soc.*, **82** 1441–1446.
32. S. Gedevarishvili and Z. A. Munir (1998) An investigation of the combustion synthesis of MoSi<sub>2</sub>-β-SiC composites through electric field activation, *Mater. Sci. Eng.*, **242** 1–6.
33. E. M. Carrillo-Heian, R. D. Carpenter, G. H. Paulino, J. C. Gibeling, and Z. A. Munir (2001) Dense layered molybdenum disilicide-silicon carbide functionally graded composites formed by field-activated synthesis, *J. Am. Ceram. Soc.*, **84** 962–968.

34. Q. Hu, P. Luo, and Y. Yan (2008) Microstructures and densification of MoSi<sub>2</sub>-SiC composite by field-activated and pressure-assisted combustion synthesis, *J. Alloys Comp.*, **468** 136–142.
35. I. J. Shon and Z. A. Munir (1997) Electric field activated combustion synthesis of Ti<sub>5</sub>Si<sub>3</sub>-Nb and Ti<sub>5</sub>Si<sub>3</sub>-ZrO<sub>2</sub> composites, *J. Mater. Sci.*, **32** 5805–5810.
36. I. J. Shon, D. H. Rho, and H. C. Kim (2000) Simultaneous synthesis and densification of WSi<sub>2</sub> and WSi<sub>2</sub>-20vol.%Nb composite by field-activated and pressure-assisted combustion, *Met. Mater. Int.*, **6** 533–538.
37. F. Maglia, C. Milanese, and Z. A. Munir (2001) Field-activated combustion synthesis of Ta-Si intermetallic compounds, *Mater. Res. Soc.*, **16** 534–544.
38. S. Gedevisanishvili and Z. A. Munir (1996) Field activated combustion synthesis in the Nb-Si system, *Mater. Sci. Eng.*, **A211** 1–9.
39. N. Bertolino, F. Maglia, C. Milanese, Z. A. Munir, and U. Anselmi-Tamburini (2001) Field activated combustion synthesis of the silicides of vanadium, *J. Alloys Comp.*, **319** 108–118.
40. S. Gedevisanishvili and Z. A. Munir (1998) The synthesis of TiB<sub>2</sub>-TiAl<sub>3</sub> composites by field-activated combustion, *Mater. Sci. Eng.*, **246** 81–85.
41. K. S. Yun, J. H. Lee, and C. W. Won (2000) Effect of current application methods on the preparation of Fe-Al intermetallic compounds by field-activated combustion synthesis, *Mater. Res. Bull.*, **35** 1709–1716.
42. J. R. Jokisaari, S. Bhaduri, and S. B. Bhaduri (2005) Microwave activated combustion synthesis of titanium aluminides, *Mater. Sci. Eng. A*, **394** 385–392.
43. K. Naplocha and K. Granat (2009) Microwave activated combustion synthesis of porous Al-Ti structures for composite reinforcing, *J. Alloys Comp.*, **486** 178–184.
44. G. Poli, R. Sola, and P. Veronesi (2006) Microwave-assisted combustion synthesis of NiAl intermetallics in a single mode applicator: Modeling and optimization, *J. Mater. Sci. Eng.*, **441** 149–156.
45. K. Naplocha and K. Granat (2009) Combustion synthesis of Al-Cr preforms activated in microwave field, *J. Alloys Comp.*, **480** 369–375.
46. Y. Kodera, N. Yamasaki, T. Yamamoto, T. Kawasaki, M. Ohyanagi, and Z. A. Munir (2007) Hydrogen storage Mg<sub>2</sub>Ni alloy produced by induction field activated combustion synthesis, *J. Alloys Comp.*, **446** 138–141.
47. Q. Li, J. Liu, and K. C. Chou (2009) Comparative study on the controlled hydriding combustion synthesis and the microwave synthesis to prepare Mg<sub>2</sub>Ni from micro-particles, *Int. J. Hydrogen Energy*, **35** 3129–3135.
48. Y. G. Morozov and M. V. Kuznetsov (1999) Effect of magnetic fields on combustion electromotive force, *Combust. Expl. Shock Waves*, **35** 18–22.
49. M. D. Nersisyan, J. R. Claycomb, and J. T. Ritchie (2001) Electric and magnetic fields generated by SHS, *J. Mater. Synth. Process.*, **9** 63–72.
50. C. W. Won, J. J. Ahn, and J. H. Lee (2002) Development of functionally graded Al/Al<sub>2</sub>O<sub>3</sub>-B4C by pressure assisted FACS process, *J. Mater. Sci. Lett.*, **21** 1407–1409.
51. O. A. Graeve and Z. A. Munir (2002) The effect of an electric field on the microstructural development during combustion synthesis of TiNi-TiC composites, *J. Alloys Comp.*, **340** 79–87.
52. C. D. Park, H. C. Kim, and I. J. Shon (2002) One step synthesis and consolidation of WC-10 vol.% Co hard material, *Met. Mater. Int.*, **8** 253–257.

53. D. E. Clark, D. C. Folz, and J. K. West (2000) Processing materials with microwave energy, *Mater. Sci. Eng.*, **287** 153–158.
54. B. Vaidhyanathan, D. K. Agrawal, and R. Roy (2000) Novel synthesis of nitride powders by microwave-assisted combustion, *Mater. Res. Soc.*, **15** 974–981.
55. Q. Hu, P. Luo, and Y. Yan (2008) Microstructures, densification and mechanical properties Of TiC–Al<sub>2</sub>O<sub>3</sub>–Al composite by field-activated combustion synthesis, *Mater. Sci. Eng.*, **486** 215–221.
56. P. Chen, Q. S. Meng, W. Liu, and Z. A. Munir (2009) Titanium diboride–nickel graded materials prepared by field-activated, pressure-assisted synthesis process, *J. Mater. Sci.*, **44** 1121–1126.
57. K. R. Hunter and J. J. Moore (1994) The effect of gravity on the combustion synthesis of ceramic and ceramic–metal composites, *J. Mater. Synth. Proc.*, **2** 355–365.
58. H. C. Yi, T. C. Woodger, J. J. Moore, and J. Y. Guigne (1998) The effect of gravity on the combustion synthesis of metal–ceramic composites, *Metal. Mater. Trans.*, **29** 889–897.
59. A. Varma (1997) Combustion synthesis in gasless systems under microgravity conditions, *J. Mater. Synth. Proc.*, **5** 391–400.
60. A. G. Merzhanov, A. S. Rogachev, E. N. Rumanov, V. N. Sanin, A. E. Sytchev, V. A. Shcherbakov, and V. I. Yukhvid (2001) Influence of microgravity on self-propagating high-temperature synthesis of refractory inorganic compounds, *Cosmic Res.*, **39** 210–223.
61. W. A. Prisbrey, S. B. Bhaduri, J. R. Jokisaari, J. R. Hagen, E. Chin, and S. B. Bhaduri (2001) Combustion synthesis of titanium silicides in different gravitational conditions, *Ceram. Eng. Sci. Proc.*, **22** 11–17.
62. C. Lau, A. Mukasyan, A. Pelekh, and A. Varma (2001) Mechanistic studies in combustion synthesis of NiAl–TiB<sub>2</sub> composites: Effects of gravity, *J. Mater. Res.*, **16** 1614–1625.
63. R. A. Ayers, D. E. Burkes, G. Gottoli, H. C. Yi, F. Zhim, L. Yahia, and J. J. Moore (2007) Combustion synthesis of porous biomaterials, *J. Biomed. Mater. Res.*, **81** 634–643.
64. A. M. Locci, R. Licheri, R. Orru, A. Cincotti, G. Cao, J. D. Wilde, F. Lemoisson, L. Froyen, I. A. Beloki, A. E. Sytschev, A. S. Rogachev, and D. J. Jarvis (2009) Low gravity combustion synthesis: Theoretical analysis of experimental evidences, *AIChE J.*, **52** 3744–3761.
65. C. Zanotti, P. Giulianu, and F. Maglia (2008) Combustion synthesis of Co–Al and Ni–Al systems under reduced gravity, *Intermetallics*, **14** 213–219.
66. S. G. Vadchenko, V. I. Ponomarev, and A. E. Sychev (2006) Self-propagating high-temperature synthesis of porous Ti–Si–Al–C based materials, *Combust. Explos. Shock Waves*, **42** 170–176.
67. O. Odawara (1985) Ceramic lined pipes produced by a centrifugal thermit process, *Trans. Jpn. Inst. Met.*, **26** 578–586.
68. O. Odawara (1990) Long ceramic-lined pipes produced by a centrifugal-thermit process, *J. Am. Ceram. Soc.*, **73** 629–633.
69. O. Odawara (1996) Ceramic linings of pipes using SHS technology, *Key Eng. Mater.*, **122** 463–478.
70. E. Miyazaki and O. Odawara (2003) Centrifugal effects on combustion synthesis of (Ti–B–C) compound system, *Mater. Res. Bull.*, **38** 1375–1386.
71. Z. Z. Du, H. G. Fu, and H. F. Fu (2005) A study of ceramic-lined compound copper pipe produced by SHS–centrifugal casting, *Mater. Lett.*, **59** 1853–1858.
72. J. Lee, M. T. Le, and H. S. Chung (2007) Physical properties of ceramic layer prepared by SHS in centrifugal field, *Mater. Trans.*, **48** 2960–2963.

73. M. T. Le, D. J. Kim, and J. R. Lee (2008) Properties of ceramic layer formed by centrifugal thermite reaction with silicon sludge replacement, *Mater. Trans.*, **49** 1868–1873.
74. O. Menske, J. V. Wood, and D. S. Riley (2006) Investigation of  $\text{Fe}_2\text{O}_3\text{-Al}$  and  $\text{Cr}_2\text{O}_3\text{-Al}$  reactions using a high speed camera, *Mater. Sci. Tech.*, **22** 199–205.
75. Z. M. Zhao, L. Zhang, Y. G. Song, and W. G. Wang (2008) Microstructures, properties and in situ toughening of rapidly solidified  $\text{Al}_2\text{O}_3\text{/YSZ}$  composite ceramics prepared by combustion synthesis, *Key Eng. Mater.*, **368** 771–774.
76. Z. Zhao, L. Zhang, Y. Song, and W. Wang (2008)  $\text{Al}_2\text{O}_3\text{/ZrO}_2$  ( $\text{Y}_2\text{O}_3$ ) self-growing composites prepared by combustion synthesis under high gravity, *Scr. Mater.*, **58** 207–210.
77. J. Pei, J. T. Li, G. H. Liu, and K. X. Chen (2009) Fabrication of bulk  $\text{Al}_2\text{O}_3$  by combustion synthesis melt-casting under ultra-high gravity, *J. Alloys Comp.*, **476** 854–858.
78. Z. Zhao, L. Zhang, Y. Song, W. Wang, and H. Liu (2009) Microstructures and properties of large bulk solidified  $\text{TiC-TiB}_2$  composites prepared by combustion synthesis under high gravity, *Scr. Mater.*, **61** 281–284.
79. R. Orru, G. Cao, and Z. A. Munir (1999) Field activated combustion synthesis of titanium aluminides, *Met. Mater. Trans. A*, **30** 1101–1108.
80. I. J. Shon, H. C. Kim, and D. H. Rho (1999) Simultaneous synthesis and densification of  $\text{Ti}_5\text{Si}_3$  and  $\text{Ti}_5\text{Si}_3\text{-20 vol\% ZrO}_2$  composites by field-activated and pressure-assisted combustion, *Mater. Sci. Eng.*, **269** 129–135.
81. D. Mingfeng, X. Kai, L. Xiaogang, C. Xintai, F. F. Tai, J. K. Hsiao, S. S. Lee, and S. T. Chen (2006) *Chin. J. Process Eng.*, **6** 249.
82. R. K. Sahu, A. K. Ray, S. K. Das, A. J. Kailath, and L. C. Pathak (2006) Microwave-assisted combustion synthesis of Ni powder using urea, *J. Mater. Res.*, **21** 1664–1673.
83. F. Keqin, B. Chenguang, Y. Yi, W. Wenjuan, and J. Fang (2007) Combustion synthesis of  $\text{TiC-Fe}$  composites under the action of an electric field, *ISIJ Int.*, **47** 648–651.

---

# PART III

---

## PHYSICAL METHODS

---

# DIRECTIONAL SOLIDIFICATION

VÍCTOR M. ORERA AND JOSÉ I. PEÑA

## 12.1 INTRODUCTION

Solidification from the melt involves a complex interplay of several effects such as heat release, thermal conduction, density changes, and mass transport. The solidification of composite materials involves preferential rejection or incorporation of the components at the liquid–solid interface. Solidification of eutectic composites produces a solid with a microstructure of separated phases, lamellae, fibers, or more complex morphologies, well aligned along the solidification direction. The technique of directional solidification has been applied to the growth of eutectic ceramics, defined as *in situ* produced fully dense ceramic composites with very fine and homogeneous microstructures. They show unusual properties very different from those expected from the simple addition of the component phases [1]. Figure 12.1 shows an idealized phase diagram of a typical binary eutectic alloy, with *A* and *B* being the two compounds whose melting temperatures are  $T_m^A$  and  $T_m^B$ , respectively. The lowest melting temperature of the alloy is defined as the eutectic temperature  $T_E$  and corresponds to the eutectic composition  $c_E$  (weight percent). If the binary liquid of composition  $c_E$  is solidified at the temperature  $T_l < T_E$ , the decrease in the free energy of the liquid is the driving force for the growth of two

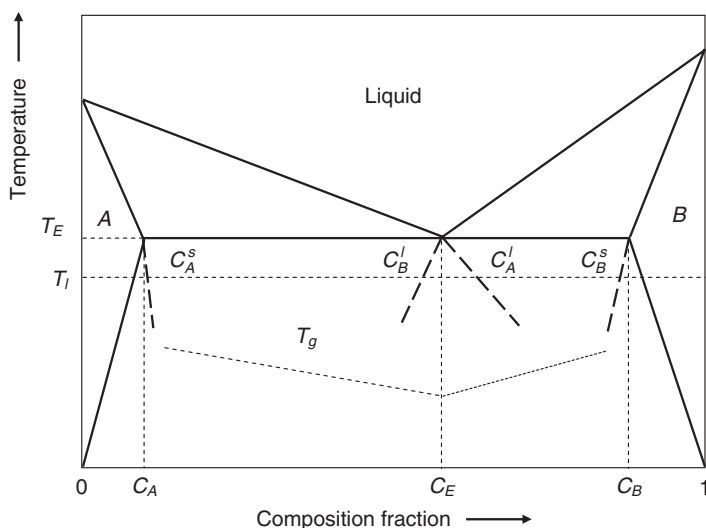


**Figure 12.1.** Typical temperature–composition phase diagram of a binary eutectic with a lamellar structure. The liquidus and solidus lines are assumed straight; thus, the liquidus slope  $m$  and the partition coefficient  $k_{A,B}$  are independent of concentration. The tie line between  $A$  and  $B$  solid solution fields at the eutectic temperature  $T_E$  gives the equilibrium concentrations of the eutectic phases. Notice that due to overcooling, the solidification temperature  $T_I < T_E$ .  $T_g$  is the glass transition temperature.

$A$  and  $B$  crystalline phases of compositions  $c_A^s$  and  $c_B^s$ , respectively. In this way, a eutectic microstructure of thin crystalline phases with the volume fraction corresponding to the compositions given above is produced. Directionally solidified eutectics show aligned structures with single-crystal domains growing perpendicular to the solidification front. The size of the phases in directionally solidified eutectic ceramic (DSEC) materials ranges from hundreds of micrometers to tens of nanometers [2]. In addition, component phases are connected by clean interfaces at the atomic scale. Moreover, unidirectional alignment along the solidification direction of eutectic structures induces anisotropic properties in otherwise isotropic composites. More interestingly, the size and morphology of the eutectic structure can often be modified to some extent by simply changing the growth rate. In this way, rapid solidification gives materials with very fine microstructures at the nanometer scale and enhanced mechanical properties [3].

Since most useful material properties generally depend on the material microstructure, directional solidification of metallic eutectics has been the object of scientific and technological attention for decades because of the superior mechanical properties of eutectics when compared to conventional ceramics intrinsic to the presence of huge amounts of clean and good-quality interfaces [4]. However, DSECs received less attention due in part to difficulties in preparation because of their high melting point and the high reactivity of the melts. Improvement in preparation techniques such as those related to laser melting technologies has revitalized the study of ceramic eutectics



seeking for the excellent mechanical response and thermal and chemical stability of these composites. In fact, the small phase size and the high quality of interfaces hinder the presence of large defects, and as a result, DSEC showed improved mechanical strength. Moreover, the extraordinary regularity of the eutectic microstructure and the neatness of the interfaces usually prevent particle coarsening at high temperatures. The high resistance of the DSEC microstructure to homogeneous coarsening provides thermal stability to these compounds [5]. Directionally solidified eutectic (DSE) oxides also present excellent resistance to oxidation owing to the intrinsic stability of these compounds and also to the absence of impurities at the interfaces [1, 6]. As a summary of properties, we can say that DSEC presents higher mechanical and thermal shock resistance and fracture strength than single crystals and glasses, and a better thermal stability and retention of mechanical resistance up to temperatures near to the melting point than conventional ceramics [7]. Recently, superplastic behavior has been reported to occur in some nanofibrillar DSECs [8].

Also of significance is the large diversity of microstructure morphologies that can be obtained in ceramic eutectics. Due in part to the large variety of microstructures, current interest for DSEC is not restricted to mechanical properties but also to functional applications. Since the pioneering work of Galasso [9] more than four decades ago, many different applications, namely, in the fields of photonics, electronics, and magnetism, have been foreseen: In particular, the possibility of creating dielectric–dielectric, dielectric–semiconducting (or metallic), and dielectric–ferroelectric eutectics with aligned microstructures could potentially generate a new category of composite functional materials.

This chapter is an overview of the basic aspects and recent progress in studies of eutectics looking at the development of new functional and structural ceramics. Its advantages, limitations, and future are discussed.

## 12.2 BACKGROUND

### 12.2.1 Basic Aspects of Eutectic Growth

Low melting entropy, single-phase materials such as metals and some organic compounds grow as nonfaceted crystals. In a classic paper, Jackson used thermodynamics to show that the type of growth of a given compound, faceted or nonfaceted, could be predicted by the thermodynamic parameter  $\alpha$  defined as  $\alpha = \xi(\Delta S_m/R)$ , where  $\Delta S_m$  is the melting entropy and  $\xi$  a geometrical factor close to but less than 1 [10]. According to this, compounds with  $\alpha \leq 2$  grow almost isotropically in the form of unfaceted crystals. Hunt and Jackson [4] transformed these ideas to the case of eutectics and proposed that if in a binary eutectic both phases have  $\alpha \leq 2$ , the eutectic grows with lamellar or rod regular structure and the primary phases will form dendrites. In these binary eutectics, it has been established that there is a composition and temperature range where the simultaneous growth of both phases (cooperative growth) is faster than that of each phase separately. However, as can be seen in Table 12.1, ceramics tend to present high melting entropy values, so they tend to grow in the form of faceted crystals,

TABLE 12.1. Nondimensional Melting Entropy Values of Some Components of DSEC

Compound	$\Delta S_m/R$
$Y_3Al_5O_{12}$	14.7
$MgAl_2O_4$	9.82
$Al_2O_3$	5.74
$ZrO_2$	3.55
$MgO$	3.01
$NiO$	2.94
$CoO$	3.15
$NaMgF_3$	6.09
$CaF_2$	2.11
$BaF_2$	1.71
$LiF$	2.9
$NaCl$	3.1
$NaF$	3.15

which, as we will see later on, is of great importance to understand the kind of microstructures developed by DSEC systems.

In nonfaceted eutectic systems under coupled eutectic growth conditions, the presence of either a rod- or lamellae-like microstructure depends on the phase volume fractions in the composite. This prediction derives from very simple energy arguments. We must take into account that the energy necessary to create the solid–solid interfaces separating the crystal phases of the eutectic system is provided by the decrease in the Gibbs energy, which, for a given undercooling  $\Delta T$ , is given by

$$-\Delta G = \frac{L\Delta T}{T_E} - E_{\text{int}}, \quad (12.1)$$

where  $L$  is the heat of fusion per unit volume of the mixture and  $E_{\text{int}}$  is the interfacial energy. The latent heat term does not depend on the microstructure, but the interfacial energy is strongly dependent on the number of interfaces being built up during solidification:

$$E_{\text{int}} = S_v \cdot \gamma_{AB}. \quad (12.2)$$

$\gamma_{AB}$  is the solid–solid interfacial energy and  $S_v$  is the density of interfaces given as the interface area per unit volume, which also depends on the geometry of the microstructure. For a lamellar microstructure, the density of interfaces is independent of the phase volume fraction and is given by  $S_v = 2/\lambda$ ,  $\lambda$  being the lamellar interspacing. For a regular hexagonal distribution of rods, the density of interfaces is given by  $S_v = 3.81 \cdot \sqrt{f}/\lambda$ , where  $f$  is the volume fraction of the minority phase. Minimization of  $\Delta G$  versus  $f$  results in a crossover in which a regular hexagonal rodlike microstructure is favored

when  $f < 0.275$ . A square array of fibers extends the transition to  $f < 0.32$ . Otherwise, the microstructure is always lamellar.

Under cooperative growth conditions and for nonfaceted components, Hunt and Jackson developed a complete analysis of the eutectic growth dynamics based on the solution of the diffusion equations (JH theory) [11]. Updated formulations of the JH theory can be found, for example, in Kurtz's and Fisher's [12] book, which describes the fundamentals of solidification including eutectic and rapid solidification growth from a very tutorial point of view, and also in the books of Davis [13] and Minkoff [14], among many others. In the following, we will only give a synopsis of the main achievements and approaches of the JH theory.

In the JH theory, the two-dimensional (2-D) diffusion equations are solved for the concentration variable assuming a flat liquid–solid interface. The force balance at the triple junction between the solidified phases and the liquid creates a curved solidification front. The Gibbs–Thomson effect associated with this curvature adds a contribution to the concentration undercooling called capillarity effect. Using the values of the solute concentration obtained from the solution of the diffusion equations, the total undercooling (except the kinetics undercooling term) at the interface on each phase was evaluated for curved interfaces and was set equal for both phases. At this point, a main assumption is introduced. In fact, at a given undercooling value, the lamellar structure could grow in a wide range of growth rates and interlamellar spacing. Zener [15] postulated that the growth rate is at the maximum possible. Using this assumption, growth at the maximum, the essential relationship between interlamellar spacing  $\lambda$ , and the solidification rate  $v$  is obtained:

$$\lambda^2 \cdot v = K_1. \quad (12.3)$$

$K_1$  is a constant, which depends on the eutectic system under study. This relationship also implies the following relationship between thermal undercooling  $\Delta T$  and lamellar interspacing:

$$\lambda \cdot \Delta T = K_2. \quad (12.4)$$

The constants  $K_1$  and  $K_2$  in Equations 12.3 and 12.4 are defined in Table 12.1 of Reference 16 for both lamellar and fibrous eutectic structures.

Equation 12.3 is the well-known JH law, which connects the interphase spacing with the solidification rate under coupled eutectic growth conditions. The important prediction of this law is that the “width” of the phases in a eutectic can be modified by simply changing the solidification rate. Hence, finer microstructures would be obtained at higher growth rates. However, this law has been obtained using the strong limiting condition imposed by the JH theory: The diffusion distance in the liquid is larger than the interphase spacing in the solid eutectic, which can only be valid at low growth rates. Moreover, at high growth rates, there will not be enough time for the solute to undergo lateral diffusion before being trapped at the solid surface. Trivedi et al. (TMK theory) [17] studied the eutectic growth at high solidification rates and established that coupled growth is unstable above a certain value of the solidification rate. In other words, the

relation  $\lambda^2 \cdot v = \text{constant}$  would only be valid for low eutectic Péclet number values, the eutectic Péclet number being defined by  $P_E = \lambda v / 2D$ , where  $D$  represents the interdiffusion coefficient.

In spite of these limitations, we must bear in mind that many experimental observations confirmed the JH law, not only in the case of strictly regular lamellar and fibrous eutectics but also in the case of several irregular eutectics (see fig. 2.5 in reference 1). In DSEC materials, typical interphase spacing values range from 0.2 to 10  $\mu\text{m}$ , corresponding to growth rates between 1 and 1500 mm/h. If DSEC systems follow the law depicted in Equation 12.3,  $K_1$  can be determined from the experimental  $\lambda^2 \cdot v$  plots where  $\lambda$  is obtained by an analysis of the microscope microstructure images. The  $K_1$  values have also been used to estimate some important physicochemical parameters, which control the solidification kinetics, such as the interfacial surface energy and the diffusion coefficient of the solute in the liquid. This was done, for example, by Bourban et al. [18], who compared the  $K_1$  value obtained from the plot of the measured interphase spacing versus the growth rate for the  $\text{Al}_2\text{O}_3/\text{ZrO}_2$  DSEC with the value calculated using the thermophysical parameters entering  $K_1$  obtained from the literature. They obtained an experimental  $K_1$  value more than 10 times larger than the calculated one, and the discrepancy was attributed to a subestimation of the diffusion coefficients. On the other hand, assuming that the rest of the constants contributing to  $C_1$  were accurate, they obtained quite a large diffusion coefficient of  $D \approx 5 \times 10^{-10} \text{ m}^2/\text{s}$ . Minford et al. [19] also used Equation 12.3 and parameters taken from the literature, including a value of  $D \approx 2 \cdot 10^{-9} \text{ m}^2/\text{s}$ , to find the surface energy in the  $\text{MgO}/\text{MgAl}_2\text{O}_4$  system from the  $v \cdot \lambda^2$  experiments. In this case, the calculated interfacial energy,  $8.5 \cdot 10^{-1} \text{ J/m}^2$ , was in good agreement with other independent estimations.

Table 12.2 collects experimental  $K_1$  values obtained for several DSEC systems. It is interesting to realize that in all the cases, the growth conditions were such that the eutectic Péclet number, which can be alternatively defined as  $P_E \approx K_1 / (2\lambda D)$ , was  $< 1$  for interspacing larger than 0.2  $\mu\text{m}$ . Accordingly, coupled eutectic growth conditions could always be attained even at the relatively faster growth rates. Consequently, fast solidification techniques could be, in principle, applied to produce nanometric-sized ordered microstructures. However, two effects limit the realization of nanoscale eutectic microstructures by fast solidification. On the one hand, a minimum interspacing,  $\lambda_0$ , for the very high growth rates has been observed, and the interspacing–growth rate curve follows a dependence,  $(\lambda - \lambda_0)^2 \cdot v = \text{constant}$ , rather than that given by Equation 12.3 [20]. On the other hand, as will be shown below, a new effect occurring at those high growth rates introduces a restriction to the production of very fine microstructures by merely increasing the solidification growth rate.

## 12.2.2 Eutectic Range

A characteristic of coupled eutectic growth is the ability of the system to self-adapt to local growth instabilities. Self-adaptation takes place by means of small changes in the eutectic microstructure [11]. However, in the case of ceramics, there are some material characteristics that impede or restrict this self-regulation mechanism and therefore the eutectic coupled growth. The first one is the strong tendency of ceramic compounds to

TABLE 12.2.  $K_1$  Values of Some DSEC Materials

Components	$K_1$ ( $\mu\text{m}^3/\text{s}$ )
$\text{Al}_2\text{O}_3/\text{YSZ}$	11.0
$\text{Al}_2\text{O}_3/\text{Y}_3\text{Al}_5\text{O}_{12}$	100.0
$\text{Al}_2\text{O}_3/\text{Er}_3\text{Al}_5\text{O}_{12}$	120.0
$\text{Al}_2\text{O}_3/\text{GdAlO}_3$	6.3
$\text{Al}_2\text{O}_3/\text{YAG}/\text{YSZ}$	70.0
$\text{Al}_2\text{O}_3/\text{Er}_3\text{Al}_5\text{O}_{12}/\text{ErSZ}$	53
$\text{CaSZ}/\text{CaZrO}_3$	400.0
$\text{MgSZ}/\text{MgO}$	50.0
$\text{MgAl}_2\text{O}_4/\text{MgO}$	150
$\text{YSZ}/\text{NiAl}_2\text{O}_4$	8.0
Ca or YSZ/NiO	32.5
Ca or YSZ/CoO	25.0
$\text{CeO}_2/\text{NiO}$	36.0
$\text{CeO}_2/\text{CoO}$	41.0
GDC/CoO	26.0
$\text{CaF}_2/\text{MgO}$	68.0
$\text{NaF}/\text{NaMgF}_3$	85.0
$\text{NaF}/\text{CaF}_2$	37.5
$\text{NaF}/\text{BaF}_2$	35.5
$\text{NaCl}/\text{LiF}$	21.3

grow along preferred directions because of the large melting entropies (see Table 12.1). Anisotropic growth makes changes in growth direction very difficult and impedes the soft adaptation of microstructure to the unavoidable front instabilities required for regular eutectic patterns. The second one occurs when the alloy composition deviates from the exact eutectic composition and the component in excess nucleates in the form of primary phase dendrites or cells (see Fig. 12.2). Both situations produce a departure from the plane-solidification-front conditions typical of eutectic coupled growth, which leads to irregular microstructures. The question now is how far can we deviate from ideal conditions without perturbing eutectic regular growth conditions?

If phases grow faceted, the tendency is always to form irregular eutectic microstructures with the exception of nonfaceted–faceted eutectics, where the faceted phase is the majority phase. In this case, the eutectic develops large macrofaceted cells whose size decreases with the solidification rate as  $D/v$ , and with a regular eutectic rod- or lamellar-like microstructure inside the colonies [21]. This is, for example, the case of the  $\text{Al}_2\text{O}_3$ /yttria-stabilized zirconia (YSZ) eutectic depicted in Figure 12.3. The morphology of this eutectic corresponds to a complex microstructure of macrofaceted cells with triangular symmetry and an intracell structure of regularly distributed YSZ rods. Macrofaceting is better developed if the liquid–solid interface is convex toward the liquid, which depends, for example, on the way heat is removed from melt.

For small departures of the exact eutectic composition or for high growth rates, dendrites or cells are formed. Occurrence of these macrodefects has been found to

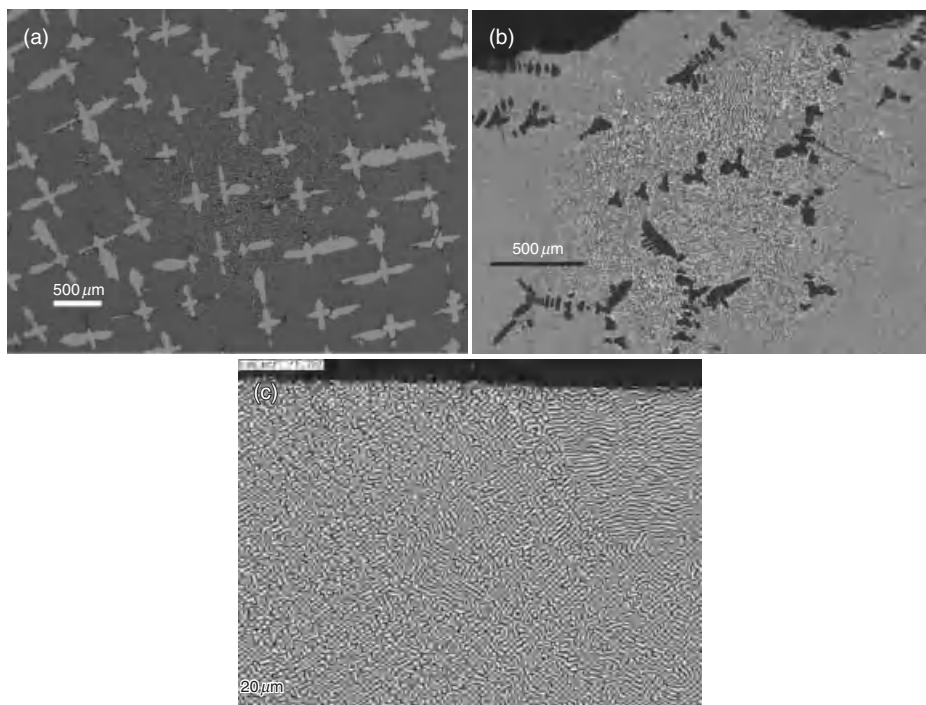


**Figure 12.2.** NaF/CaF<sub>2</sub> DESC. SEM micrographs of transverse sections perpendicular to growth direction) of an ingot grown by the Bridgman method at 10 mm/h with different compositions: (a) 50 mol % NaF, dendrites correspond to CaF<sub>2</sub> phase; (b) 52.5 mol % NaF showing NaF dendrites; (c) 51.5 mol %, which corresponds to the eutectic composition (reprinted with permission from Elsevier from Reference 22).

depend strongly on the growth rate, the solidification thermal gradient  $G_T$ , and the departure from eutectic composition  $\Delta c$ , which are the three control parameters of directional solidification. It has been found that for given  $G_T$  and  $\Delta c$  values as the growth rate increases from zero, the planar front is stable up to a certain critical growth rate; above this critical growth rate, shallow cells start to appear as a secondary phase. If  $v$  keeps increasing, one-phase dendrites appear. Dendrites become deep cells and eventually, a planar front is established again at higher  $v$  values. This behavior is illustrated in Figure 12.2 with several scanning electron microscopy (SEM) images corresponding to a NaF/CaF<sub>2</sub> composite with different compositions around the eutectic point [22]. Burden and Hunt suggested that dendrites instead of a coupled eutectic grow when the temperature at the dendrite tip is greater than the eutectic growth temperature [23]. According to these authors, if dendrites of the A-phase are produced, the undercooling at the A-dendrite tip is

$$\Delta T_D = T_l - T_D = \frac{G_T D}{v} + M_3 v^{1/2}. \quad (12.5)$$

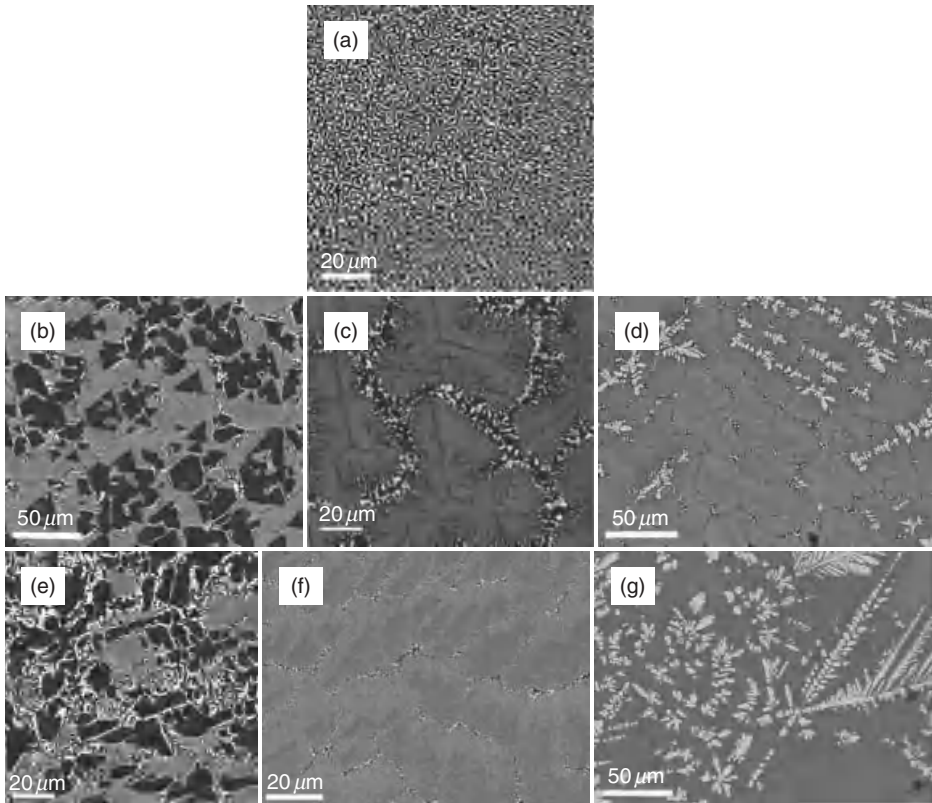


**Figure 12.3.**  $\text{Al}_2\text{O}_3/\text{ZrO}_2$  (3%  $\text{Y}_2\text{O}_3$ ) DESC. SEM micrographs of transverse sections (perpendicular to growth direction) of an ingot grown by laser float zone method at different compositions and growth rates: (a, c, f) 62%  $\text{Al}_2\text{O}_3$  that corresponds to the eutectic composition, grown at 10, 300 and 1000 mm/h showing interpenetrate, colonies and cells microstructure respectively, (b, e) 75 mol%  $\text{Al}_2\text{O}_3$  grown at 300 and 1000 mm/h respectively, showing  $\text{Al}_2\text{O}_3$  dendrites, (d, g) 50 mol%  $\text{Al}_2\text{O}_3$  grown at 300 and 1000 mm/h respectively, showing  $\text{ZrO}_2$  dendrites.

$T_l$  is the liquidus temperature,  $T_D$  is the dendrite tip temperature, and  $M_3$  is a constant. The undercooling for a coupled growth condition is obtained from Equations 12.3 and 12.4:

$$\Delta T_E = T_E - T_l = (K_1 K_2^{1/2}) v^{1/2}. \quad (12.6)$$

Consequently, dendrites grow if  $T_D > T_E$ , which may occur at intermediate growth rate values. Notice that the thermal gradient and the growth rate are entangled magnitudes. In fact, the thermal-gradient term dominates in the low growth rate regime where



Equations 12.5 and 12.6 can be combined to give the following constitutional undercooling:

$$m_i \Delta c = T_l - T_E = \frac{G_T D}{v} + (T_D - T_0). \quad (12.7)$$

$m_i$  is the liquidus slope of the phase in excess. Clearly, coupled eutectic growth occurs if the following inequality holds:

$$m_i \frac{\Delta c}{D} < \frac{G_T}{v}. \quad (12.8)$$

To establish the conditions of coupled growth, experiments at different growth rates and with small controlled deviations from the accurate eutectic composition can be performed. Observation of the sample microstructure for dendrites or cell formation gives the necessary information for the assessment of the coupled growth regime. As an example of the latter in Figure 12.3, we give SEM micrographs showing the microstructure of the  $\text{Al}_2\text{O}_3/\text{ZrO}_2$  eutectic obtained when grown at three different growth rate and composition conditions. The material was grown using the laser float zone (LFZ) crystal growth method and relatively high solidification thermal gradients of  $6 \cdot 10^5$  K/m. Dendrite formation is observed for concentration deviations of  $\Delta c > 1$  mol % from the true eutectic composition. These experimental observations can be put together to obtain a skew-symmetric eutectic coupled zone diagram projected over the  $\text{Al}_2\text{O}_3/\text{ZrO}_2$  phase diagram (Fig. 12.4). Notice that there is a limiting growth rate for coupled growth of about 90 mm/h in this case. At higher growth rates, the microstructure changes from coupled to cellular with coarser microstructure cell boundaries. The practical implications in terms of mechanical and functional applications of this coupled growth limit are enormous as many applications of eutectics strongly depend on microstructure homogeneity.

According to Equation 12.8, coupled eutectic growth implies either low growth rates or high growth gradients. For instance, thermal gradients as large as  $10^5$  K/m would be needed to obtain a planar solidification front at  $v > 20$  mm/h in eutectic oxides with typical values of  $m \approx 10$  K per percent,  $D \approx 10^{-10}$  m<sup>2</sup>/s, and  $\Delta c > 0.1\%$ . A direct consequence of Equation 12.8 is that for the finest eutectic microstructure, we need the highest growth rates with the largest solidification thermal gradients. Unfortunately, large thermal gradients imply that the sample is going to accumulate high thermal stresses so we reach a kind of trade-off situation between fine microstructure and large sample size. We will discuss this fundamental technological aspect in the next sections.

The balance between cooperative coupled eutectic growth and competitive dendrite/cell growth explains some of the experimental findings in ceramic eutectics; however, the strong tendency to develop facets introduces a degree of complexity in the theoretical analysis of ceramic eutectics, which has not yet been described by existing solidification theories. For example, the JH theory and most of the diffusion-based analysis consider the liquid–solid front as a mathematical interface of zero thickness, which is



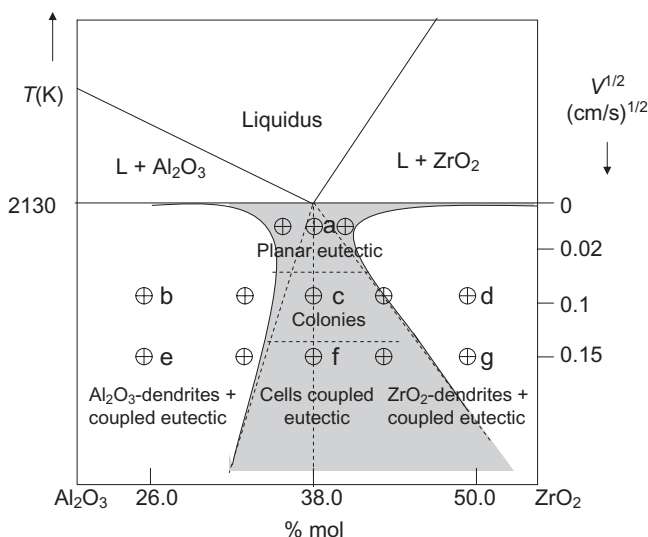


**Figure 12.4.** Outline of the skew-symmetric eutectic coupled growth zone projected over the phase diagram of the  $\text{Al}_2\text{O}_3/\text{ZrO}_2$  eutectic, near to the eutectic point. Experimental points correspond to SEM microstructure observations on several samples grown by the laser floating zone method with different growth rates and compositions (Fig. 12.3). Notice that tentative thermal undercooling values proportional to  $v^{1/2}$  (Eqs. 12.3 and 12.4) are also depicted in the diagram.

a very crude approximation. New theories based in phase field models (PFMs) allow for a diffuse solidification front to be considered. In this diffuse solidification front, typically of the order of only a few nanometers, the temperature and concentration fields continuously vary through the diffuse interface [24]. Still in its infancy, PFM is being applied to calculations of dendritic growth, and the most appealing advantage of PFMs related to eutectic growth is that they can deal with numerical computation of complex eutectic phenomena such as that of tilting of lamellae in hypereutectic alloys, the presence of oscillatory patterns, and nucleation at the interfaces [25].

## 12.3 FABRICATION METHODS

Many of the applications on which eutectics are focused require resistance to sliding/rolling wear, erosion, oxidation, and corrosion, as well as good chemical stability and long-term durability, high strength from cryogenic to elevated temperatures, and aging resistance in oxidizing environments. Moreover, it is imperative to develop reliable and economical manufacturing methods. On the other hand, as we have seen above, to obtain the desired fine and homogeneous microstructure, we need step solidification thermal gradients, which further introduce a limitation to the ceramic size.

In the 1970s, where the first eutectics based on refractory oxides were presented, well-established bulk crystal growth techniques like Czochralski or Bridgman growth were used to obtain ceramic eutectics [26, 27]. However, the new so-called shaped growth techniques offer remarkable advantages over these conventional methods, the most important of these being the capability for production of ready-to-use samples such as ribbons, tubes, or fibers, and the structural and chemical perfection obtained by these new methods. In fact, the best mechanical behavior is found in fibers grown that way that fulfill several requirements such as uniformity in the fiber diameter, structural perfection (free of cracks and pores) [28–30], and compositional homogeneity (absence of any phase segregation) [31, 32]. Because of the high melting point of eutectic ceramics and due to the contamination and corrosion problems derived from the use of dies and containers, other crucibleless growth techniques have been developed. Of great significance is the float zoning method because of the absence of any crucible, which permits the melt of high-temperature ceramics. Zirconia was one of the components of several eutectics grown using these techniques, which also involved aluminum, magnesium, calcium, and yttrium oxides. These DSECs were grown in the form of fibers of diameters ranging from a few millimeters to hundreds of microns in diameter. However, as can be concluded from previous studies, the growth aspects leading to structural and shape perfectness are still far from being completely understood.

In the next section, we will focus on some meniscus growth methods applied to eutectic growth. In Figure 12.5, we show some schemes of such growth techniques that can be classified into two categories: float zoning methods and pulling from shaper methods.

### 12.3.1 Melt Zone Technique

Crystal growth of refractory oxides by the floating zone method was first introduced by Poplawsky and Tomas [33]. This growth process differs considerably from traditional methods using crucibles. In directional solidification techniques, a well-defined distribution of the temperature in the melt volume and on the crystallization front is necessary. In 1970, Gasson and Cockayne were the first to use the laser heating method in crystal growth [34, 35]. Then, Haggerty et al. [36] developed a new method of producing fiber crystals that was further improved by Feigelson [37] and Fejer et al. [38] at Stanford University. They used an original optical system to focus the laser onto the fiber in an axially symmetric irradiance field (refluxicon). Since the melt is sustained by the liquid surface tension, this method is also called the laser floating zone (LFZ) method. The basics of the technique is the formation of a small melt liquid zone that moves at a controlled speed throughout the precursor ceramics generating a directionally solidified rod. When the fiber is pulled from the melt at a higher speed than the translation of the supply, a diameter reduction of the solidified rod is achieved because of the mass conservation law. The major advantages of the float zone techniques are the absence of contamination from crucible materials, the high melt temperatures achievable, and the possibility of easy control of the solidification atmosphere.

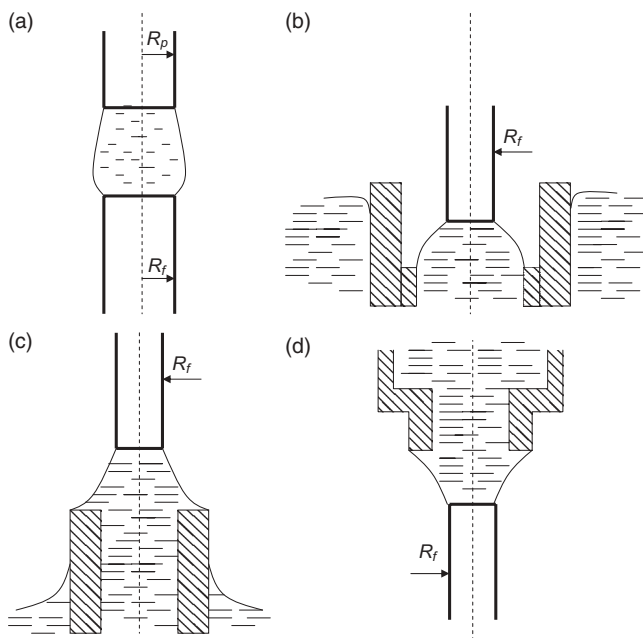


**Figure 12.5.** This diagram shows the types of “grown from meniscus” fiber growth assemblies: (a) float zoning; (b) Stepanov method, from nonwetting shaper; (c) edge defined, film fed grown, from wetting shaper; and (d) micropulling down.  $R_p$  and  $R_f$  are the precursor and fiber radii, respectively.

Other heating sources on zone melting techniques are radio frequency (RF) induction coupling [39], electron beam [40], strip heater [41–43], or thermal imaging (mirror furnace) [44] heating. In the first case, the materials must be electrical conductors. The electron beam floating zone melting (EBFZM) process has been successfully used in the purification and growth of highly pure crystals of refractory metals and alloys. The so-called immersed-heater process or modified floating zone technique uses a perforated and heated iridium or platinum strip immersed in the melt during the growth process. Thermal imaging and laser heating have the advantage of easy application in almost any kind of material and in different growth atmospheres, combining optimum energy use because of focusing properties and minimum energy losses. Ellipsoidal mirrors with the heat source in one focus and the rod in the other one have been proven very convenient for zone melting of refractory materials. In that case, the sample temperature can be controlled by the heating lamp voltage. The asymmetry of the heating, the hottest part being the side of the rod facing the heat source, is reduced by rotating the rod around the pulling axis or by using another ellipsoidal mirror with a common focus on the rod. Some authors have reported attractive experimental setups for float zoning having ellipsoidal mirrors with halogen or xenon arc lamps [45]. Interestingly, a small double-ellipsoid mirror furnace was used by Eyer et al. [46] for growing single

crystals in space. Among these techniques, the LFZ stands out as a very effective tool for exploring new DSEC materials because of the rapid growth rates allowed by the high axial temperature gradient near the growth interface and of the small amounts of material needed. The main advantage of this method of fabrication is found in inorganic compounds with high melting points or with difficult preparation and allows basic studies on phase diagrams, crystallographic relationships between phases, growth kinetics, or the simplest geometry for studies of heat and mass transport. One of the main restrictions of the technique is the geometry of the samples; they are cylinders with a limited diameter that depends on the mechanical and thermal properties of the materials and on the thermal gradients at the interface of solidification and heating power.

Figure 12.6 shows a basic LFZ growth system consisting of a CO<sub>2</sub> or neodymium doped yttrium aluminium garnet (Nd:YAG) laser as heating source, a growth chamber with an optical system for the laser beam focusing and two vertical axes for the ceramic cylinder and solidified rod displacement. Both axes must have independent rotation and translation movement devices. Typical laser power levels for the growth of eutectic oxides are between 100 and 200 W, depending on the rod diameter, and the laser has to be operated in a continuous wave mode or quasi-cw mode with high pulse repetition frequency (above 1 kHz) for optimum heating. The optical system inside the chamber is usually composed of a reflexicon that transforms the circular laser spot into a ring-shaped beam. To achieve homogeneous heating, it is necessary that the two mirrors are perfectly aligned. Then, the ring is deflected by a flat mirror at 45° and focused in the ceramic rod by a parabolic mirror obtaining a homogeneous laser ring heating (Fig. 12.7). The mirrors are usually made of copper with a golden coating to improve the reflectivity at the laser wavelength and to prevent the copper substratum from corrosion.

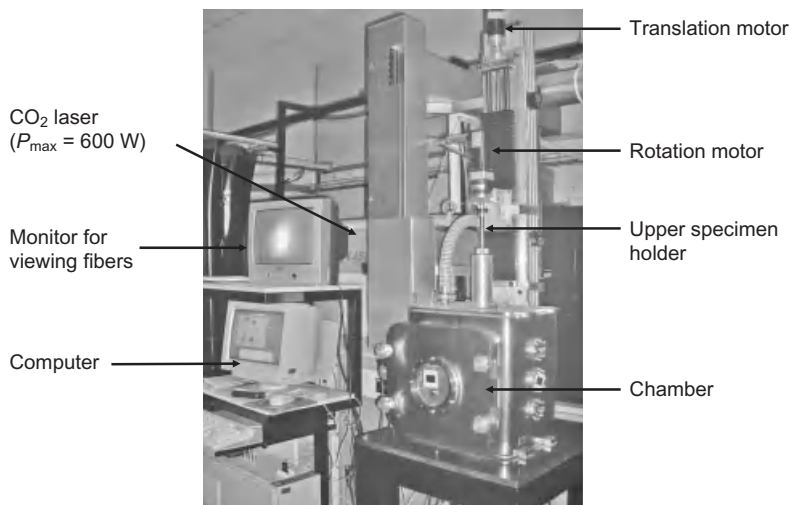


**Figure 12.6.** Laser floating zone system showing the chamber and the control panel with the image of the molten zone of a growing DSEC fiber in the monitor.

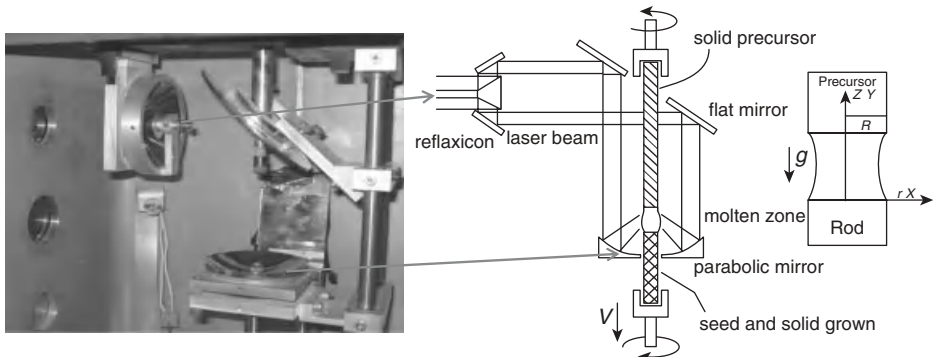


**Figure 12.7.** (a) View of the laser beam delivery system inside the growth chamber and (b) schematic illustration for the reflecting mirror arrangement in a laser floating zone growth equipment. The coordinate system and geometry of the molten zone is also given.

When a  $\text{CO}_2$  laser is used, correct optical alignment is obtained with the aid of a red diode or He–Ne laser beam coaxial with the high-power infrared beam. A sealed chamber is necessary when a controlled atmosphere or vacuum is required. In this case, ZnSe or quartz windows are used for  $\text{CO}_2$  and Nd:YAG lasers, respectively. An additional quartz window is used for growth process observation with a video camera.

The growth process starts by heating the lower end of the precursor. Once a drop is formed, a small seed placed in the other axis is brought into contact until a liquid bridge between the precursor and seed is established. During the growth, the cylinder precursor is pushed toward the liquid zone and the seed withdrawn from it. The apparatus permits the simultaneous opposite sense rotation during growth of both the eutectic rod and the feed material rod. When the fiber is grown upward from a sintered powder rod, some gas bubbles can be trapped within the grown crystal. The downward growth eliminates most of the bubbles, but at high growth rates, they can still persist inside the crystal. Because the axes are moved by step or continuous motors, vibrations can be generated due to the friction between these and the elements of the chamber, provoking small perturbations during growth that can be reflected in defects affecting the quality of the resulting samples. Other commonly found instabilities come from laser power fluctuations, nonuniformity in heat distribution, poor alignment of the rods, excessive zone length, and so on. The maximum length of the large fiber depends on the limitations of the movement systems.

### 12.3.2 Laser Surface Melting Technique

Laser surface melting is a recently developed technique to produce flat plates of directionally solidified eutectics [47, 48]. There are several ways to melt the ceramic surface. When a diode laser is used, the laser spot can be shaped as a line (typically of  $1 \times 10 \text{ mm}^2$ ) using cylindrical quartz lenses. The laser line scans over the precursor

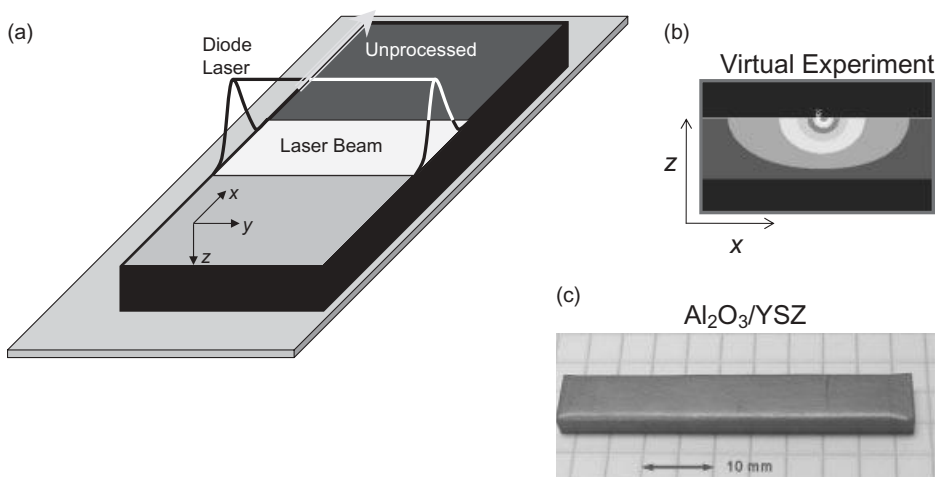


**Figure 12.8.** (a) Schematics of the laser surface directional solidification procedure, (b) example of temperature profiles obtained by numerical solution of Equation 12.9, and (c)  $\text{Al}_2\text{O}_3/\text{YSZ}$  eutectic ceramic after surface directional solidification treatment. The DSEC coating has a thickness of about 0.5 mm (courtesy of R. I. Merino and F. Ester).

surface. The surface of the material can also be covered by overlapping single  $\text{CO}_2$  laser beam tracks [18]. In this case, the laser spot can be transformed into a more or less linear/elliptic spot using a cylindrical lens. However, the intensity distribution of the beam is that of the emitted beam, a more or less Gaussian profile, that is, more intense at the spot center. In this case, a kaleidoscope can be used to homogenize the intensity distribution. A linear spot can also be created by moving the laser beam quickly in one direction. The length of the laser line is defined adjusting the twisting angle of two small mirrors driven by a galvanometer. In Figure 12.8, we give a diagram of the surface directionally solidifying process. When the laser beam hits the surface, the absorbed energy is conducted from the surface into the bulk of the ceramic by thermal conduction and convection in the liquid melt pool. One critical parameter in surface melting processing is the temperature distribution in the sample that can be calculated by solving the heat equation for the heating source traveling along the  $x$ -axis at a speed of  $v$ :

$$\frac{\partial}{\partial x} \left( k_x \frac{\partial T}{\partial x} \right) + \frac{\partial}{\partial y} \left( k_y \frac{\partial T}{\partial y} \right) + \frac{\partial}{\partial z} \left( k_z \frac{\partial T}{\partial z} \right) + Q = \rho H \left( \frac{\partial T}{\partial t} - v \frac{\partial T}{\partial x} \right). \quad (12.9)$$

$k_{i=x,y,z}$  is the thermal conductivity,  $Q$  stands for the heat income and heat losses,  $\rho$  is the material density, and  $H$  the sum of the specific heat and latent heat. By solving Equation 12.9 by numerical methods, temperature profiles such as those depicted in Figure 12.8b can be calculated. In these calculations, the critical issues to be addressed are the material properties that depend on  $T$ ; therefore, the integral form should be used, and also

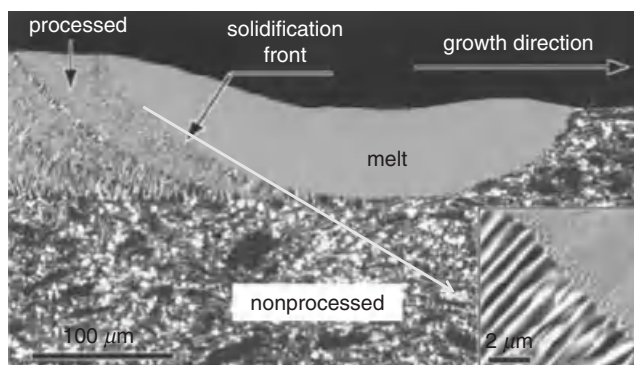


**Figure 12.9.** SEM longitudinal section (parallel to the growth direction) of a DSEC  $\text{Al}_2\text{O}_3/\text{ZrO}_2$  eutectic ceramic coating on a  $\text{Al}_2\text{O}_3$  ceramic support. The figure shows the coating zone at the end of the laser surface processing. Notice the lens-type shape of the quenched molten zone. The inset shows a detail of the interface between the quenched melt (upright with the finest microstructure) and the DSEC processed ceramics. The black phase corresponds to  $\text{Al}_2\text{O}_3$ .

on composition, porosity, and so on; the laser beam profile and the absorbance of the melt and the heat losses by convection and emission processes. The depth of the melt pool depends on several parameters such as material properties, laser power, and processing speed. Usual traveling speeds in surface processing are in the range 20–1500 mm/h, and the ceramic can be melted to depths from 50 to 1500  $\mu\text{m}$ .

Surface melt materials grown at high solidification rates present a very thin eutectic microstructure on the surface. However, the higher the scan speed, the smaller the depth attained. As shown in Figure 12.9, the melt–crystal interface is concave to the melt, so the local solidification direction changes with the vertical position of the volume element being solidified. As a consequence, the local growth rate is also dependent on the vertical position, and there is a continuous change of the interspacing,  $\lambda$ , along the sample cross section. Notice that surface laser treatment can be used for sealing the surface pores in porous ceramic materials as well as to produce a smoother finished surface with columnar grains parallel to the growth direction.

### 12.3.3 Melt Stability and Defects

Bubbles and large pores are the most frequent defects found in solidified eutectic ceramics. During growth, the presence of bubbles in the melt can even be clearly seen when the eutectic melt is transparent. These bubbles have been associated with the presence of evaporating impurities, of gas trapped at the pores of the precursor ceramic, of moisture absorbed during processing, or, with segregation during solidification of atmosphere components dissolved in the melt, specifically of oxygen incorporated into the oxide melt. In this case, the presence of bubbles in the solidified ceramic depends both on the ambient gas pressure and oxygen content and also on the growth rate and melt zone size. For example, it was not possible to obtain dense  $\text{Al}_2\text{O}_3/\text{YAG}$  and

$\text{Al}_2\text{O}_3/\text{YAG}/\text{YSZ}$  fibers at growth rates higher than 500 mm/h when grown in air. The gas released during melt freezing could not escape before being trapped at the solid phase. Decreasing the rod diameter also decreased the size and total volume of gas inclusions, but they were not completely eliminated from solidified rod. However, using nonoxidant atmospheres instead of air allowed the growth of rods free of voids at growth rates as high as 1200 mm/h [28].

Other matters of concern are the thermomechanical stability of the grown rods and the stability of the melt zone. If the liquid zone is not stable, both macroscopic defects related to composition inhomogeneity and lack of uniformity in the rod diameter appear. If the melt instability is severe, even the separation of the liquid zone into two drops may occur. The stability of the melt zone strongly depends on its shape and length to diameter ratio. Ester and Peña [49] studied the shape and stability of the eutectic  $\text{Al}_2\text{O}_3/\text{YSZ}$  melt. They obtained the stability range (maximum zone length) through the analysis of the floating zone profile and also some interesting parameters. First, the experimental profile was obtained from the experimental optical images of the stable melt, and second, it was fitted by the equation

$$x = \frac{z^3}{6C^2} + \frac{\xi z^2}{2C} + C_0 z + C_1 C. \quad (12.10)$$

as defined in Figure 12.7b;  $x$  is the distance to the rod axis  $z$ , and the origin  $z = 0$  is at the solid–melt interface.  $\xi$  and  $C_0$  are constants, which depend on the zone height  $h$  and diameter  $2R$ .  $C_1$  is an integration constant and  $C$  is, in this case, the capillary constant. Equation 12.10 is an approximate solution proposed by Reyes Ardila et al. [50] to the profile zone model of Saitou [51]. The constants in Equation 12.10 can be obtained by adjusting this equation to the measured zone profile [49]. The capillary constant is given by  $C = (2\gamma/\rho g)^{1/2}$ , where  $g$  is the gravity constant and  $\gamma$  is the melt surface tension that can be otherwise estimated from the experimental  $C$  values. In the case of the  $\text{Al}_2\text{O}_3/\text{YSZ}$  melt, Ester and Peña obtained a value of  $\gamma = 0.42$  N/m [49].

The stability condition for rods growing without a change in diameter is given by

$$R = h \frac{\left(1 - \frac{h^2}{4C^2}\right)}{6|n-1|}. \quad (12.11)$$

$h$  is the length of the liquid zone and  $n$  is a positive real number greater than 1 when the shape of the floating zone is convex to the exterior that can be obtained from the  $C_0$  and  $C$  parameters using the following expression given by Saitou [51]:

$$C_0 = \frac{h^2}{12C^2} + 6(n-1) \frac{R}{h}. \quad (12.12)$$

Ester and Peña obtained values of  $n = 1.07$  and  $h_{\max} = 9.2$  mm for a rod of  $\text{Al}_2\text{O}_3/\text{YSZ}$  eutectic of  $R = 1$  mm. Several years ago, Heywang [52] gave another expression of the maximum stable zone length,  $h_{\max} = 2.84(\gamma/\rho g)^{1/2}$ . Using the surface tension value given



above for the  $\text{Al}_2\text{O}_3/\text{YSZ}$  melt and Heywang expression, we obtain  $h_{\max} = 9.46$  mm, which agrees fairly well with that obtained from the Saitou model. The profile analysis given above is only valid for relatively large melt zones. Pfann and Hagelbarger [53] established that in a zero-gravity environment, the zone remains stable when the length does not exceed its circumference (Rayleigh limit),  $h_{\max} = 2\pi \times R$ . This simplified relationship between zone length and diameter is being applied to thin rods, where the small zone makes the weight of the melt not so important.

Another critical problem in zone growth is the appearance of cracks in the solidified rod. The motive of sample failure is the large thermal gradient along the growth direction, up to  $7 \cdot 10^5$  K/m. When the thermal stresses induced during the cooling exceed the breaking stress of the eutectic ceramics, the sample fails. To discuss this point, we refer to the Brice model [54] for the temperature distribution in a growing rod:

$$T(r, z) = T_m + (T_m - T_0) \frac{\left(1 - \frac{\zeta r^2}{2R}\right)}{1 - \frac{\zeta R}{2}} \exp\left[-\left(\frac{2\zeta}{R}\right)^{1/2} z\right]. \quad (12.13)$$

$\zeta$  is the cooling constant that can be considered here as a parameter obtained from fitting Equation 12.13 to the experimental temperature distribution profile;  $T_0$  is the ambient temperature; and  $0 < r < R$  is the radial position. The maximum strain occurs at the cylinder surface, where

$$\left(\frac{dT}{dr}\right)_{z=0, r=R} \approx \left(\frac{\zeta R}{2}\right)^{1/2} G_T. \quad (12.14)$$

Here, the approximation  $\zeta R \ll 1$  was used. The maximum axial gradient is given by

$$G_{T, \max} = \frac{dT}{dz} \Big|_{\max} = \frac{4\varepsilon_b}{\alpha(\zeta R^3)^{1/2}}. \quad (12.15)$$

$\varepsilon_b$  is the breaking strain and  $\alpha$  the thermal expansion coefficient. It is possible to grow eutectic ceramic rods free of cracks if the diameter does not exceed some critical value. Critical radius values have been established for typical LFZ thermal gradients around  $6 \cdot 10^5$  K/m and low growth rates in 3.4 mm for  $\text{Al}_2\text{O}_3/\text{YAG}$  and 1.2 mm for  $\text{Al}_2\text{O}_3/\text{ZrO}_2(\text{Y}_2\text{O}_3)$  [55].

### 12.3.4 Edge-Defined, Film-Fed Growth (EFG)

In 1959, Stepanov [56] produced shaped crystals by growing from melt using a molybdenum or tungsten shaper. The technique allows direct pulling of the crystals with a variety of cross-sectional shapes such as tubing, multibore tubing, or ribbons. The Stepanov technique generally uses a nonwetted shaper to make a melt column that controls the crystal profile [57]. By contrast, the EFG process, a particular case of the

Stepanov method, uses wettable shapers. A liquid pool, from which the crystal is withdrawn, is formed on the planar top surface of the shaper, which feeds from a liquid reservoir by capillary through the die. The crystal shape, or edge definition, is maintained by the geometry of the surface at the top of the die. Then, in the EFG method, it is the shape of the die and not the melt column that controls the shape of the crystal [57]. It is of interest to note that capillary effects play an important role in most crystal growth from melt techniques.

The pioneering work on this technique was done by Pollock [58], who grew, using the EFG technique, filamentary sapphire in the  $\langle 0001 \rangle$  growth direction from tungsten orifices. In this case, the high thermal conductivity of tungsten results in a very efficient heat removal at the growth interface and allows stable growth of filamentary sapphire at rates as high as 150 mm/min. With reference to eutectic ceramics, Finch et al. [59] studied the effect of die-top geometry (planar, convex, or concave) on solidification interface shape during the EFG of the  $\text{Mn}_2\text{SiO}_4/\text{MnO}$  eutectic. An aligned microstructure comprising less than 1- $\mu\text{m}$ -diameter MnO rods in a  $\text{Mn}_2\text{SiO}_4$  matrix was obtained at growth rates of  $<15$  mm/h. A cellular microstructure predominated in samples grown at 20 mm/h or above. Starostin et al. [60] described the microstructure and crystallographic textures of phases in crystals of  $\text{Al}_2\text{O}_3/\text{ZrO}_2(\text{Y}_2\text{O}_3)$  directionally solidified using the EFG technique. They grew rods of up to 6 mm in diameter at a growth rate of 40 mm/h from a molybdenum die heated by RF through a graphite susceptor in an argon atmosphere.

### 12.3.5 Micropulling-Down ( $\mu$ -PD) Technique

Much activity is recently found in ceramic eutectics grown by the so-called  $\mu$ -PD method. In principle, the  $\mu$ -PD technique is considered by some authors simply an upside-down version of the EFG technique. Nonetheless, it is a well-established technique for fiber growth, which makes use of a die placed at the bottom of the melt crucible from which the fiber is withdrawn (Fig. 12.10). Though a crucible is used, the small convection currents and meniscus at the bottom yields to a precise and stable control of the growth front and to a homogeneous microstructure throughout the entire sample cross section. The method also has some technological advantages over their competing methods such as the unnecessary preparation of source samples, simpler heating procedure, better control of the fiber diameter (within 5–10%), and the possibility of longer fiber fabrication. In 1992, the first development of single-crystalline fiber growth by the  $\mu$ -PD method was established at the Fukuda Laboratory in Japan. The method has been thoroughly described by Yoon and Fukuda [61]. The axial temperature gradients are as high as  $5 \cdot 10^5$  K/m, which permit high growth rates of eutectic ceramics. In addition, an afterheater can be easily placed to lower the temperature gradients to avoid sample cracking.

Several oxides and eutectic fibers from 10 to 1500  $\mu\text{m}$  in diameter have been grown using this procedure [62–66]. As in other growth-from-meniscus methods, establishing capillary stable growth conditions is also the critical issue here. Lan [67] has published a comprehensive analysis of the  $\mu$ -PD growth processes, taking into consideration some

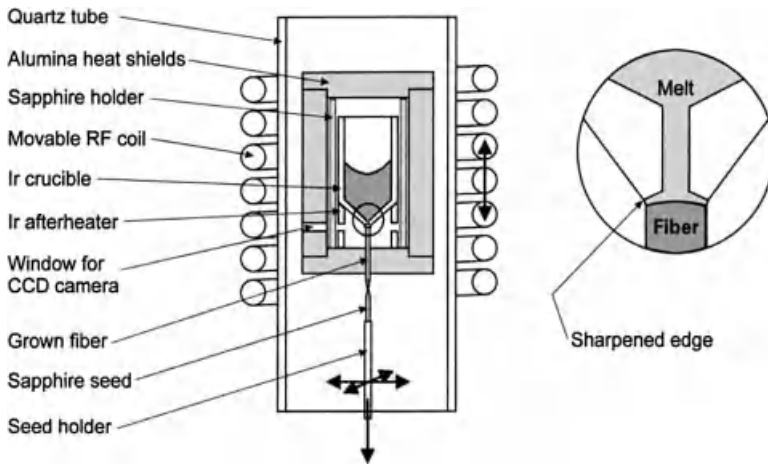


**Figure 12.10.** Schematic diagram of the micropulling-down ( $\mu$ -PD) apparatus (reprinted with permission from Elsevier from Reference 89).

important parameters such as the meniscus shape, the fiber size, the convection in the melt, the pulling rate, the die temperature, and the melt height.

## 12.4 CERAMIC EUTECTIC SYSTEMS

In this section, we describe some of the best-known ceramic eutectic systems whose components are either simple oxides, transition metal ion oxides, complex oxides and alkaline, or alkaline earth halides. Also of significance is the large diversity of microstructure morphologies found in ceramic eutectics. Geometrical motifs such as lamellar, fibrous, complex-faceted, and sometimes called Chinese script microstructures have been reported to occur in various DSECs (see Fig. 12.11).

This morphological diversity is in part due to the high melting entropy values of the crystalline phases, which otherwise make it difficult to create the necessary conditions for regular growth (see Table 12.1). In ceramic eutectics, phases often grow preferentially along well-defined crystallographic directions, which are not necessarily the directions of easy growth but which generate solid–solid interfaces with minimum interfacial energy (see Eq. 12.1). A complete picture of the microstructures including the solidification directions and the orientation relationships of many DSECs is now being completed. This is due in part to recent advances in the microstructure characterization methods. For example, the high-resolution electron microscopy (HREM) methods used by Mazerolles et al. [68] and others allow performing detailed studies of the orientation relationships and interface planes and also of the structure and defects at the interfaces. In addition, high-resolution X-ray tomography is a unique method to study entangled microstructures at the micron scale and has been recently applied to the study of the three-dimensional (3-D)-interpenetrated microstructures in  $\text{Al}_2\text{O}_3/\text{YAG}$

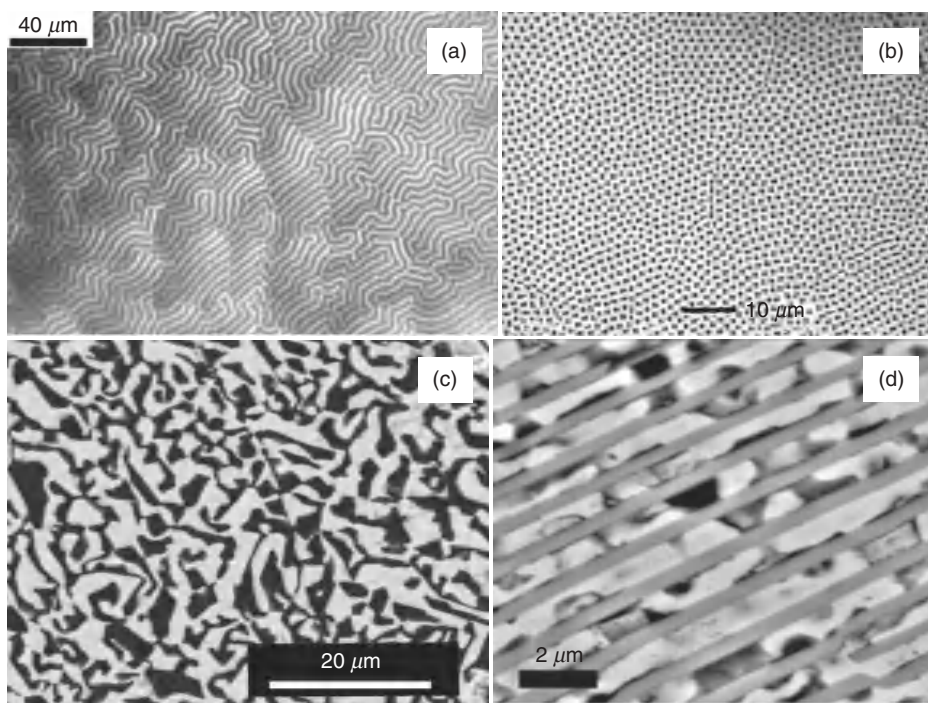


**Figure 12.11.** Micrographs showing the microstructure of some DSECs showing different geometry motifs: (a) transmission optical microscope image of the CaSZ(bright)/CaZrO<sub>3</sub> eutectic showing a meander-type microstructure, (b) SEM image of a fibrous MgO(rods)/MgSZ eutectic, (c) Chinese script microstructure of a Al<sub>2</sub>O<sub>3</sub>/YAG(bright) DSEC (printed with permission from Elsevier, EMSAT:02094), and (d) lamellar structure of a Co/YSZ cermet (porous phase is metallic Co).

[69] (Fig. 12.12a) and Al<sub>2</sub>O<sub>3</sub>/YAG/YSZ [70] (Fig. 12.12b). The orientation of crystalline phases and the texture of ceramic eutectics are better studied by electron backscatter diffraction (EBSD) techniques (Fig. 12.13).

Reference to earliest work on the microstructure and crystallography of ceramic eutectics can be found in the reviews of Minford et al. [19], Ashbrook [71], Stubican and Bradt [26], and Revcolevschi et al. [72]. In the last two decades, most efforts have been focused toward the study of alumina and zirconia-based ceramic eutectics because of their exceptional thermomechanical properties. Nearly every phase diagram of binary and ternary Al<sub>2</sub>O<sub>3</sub>-related eutectic ceramics have been studied by Lakiza [73, 74]. At present, the best characterized DSECs are the binary Al<sub>2</sub>O<sub>3</sub>/Y<sub>3</sub>Al<sub>5</sub>O<sub>12</sub> (YAG) and pseudobinary Al<sub>2</sub>O<sub>3</sub>/ZrO<sub>2</sub>(Y<sub>2</sub>O<sub>3</sub>) systems and their orientation relationships, and observed interface orientations can be found in Reference 1. More binary and pseudobinary Al<sub>2</sub>O<sub>3</sub>-related ceramic eutectics have also been grown, and their composition, component phases, eutectic temperature, and microstructure type are collected in Table 12.3.

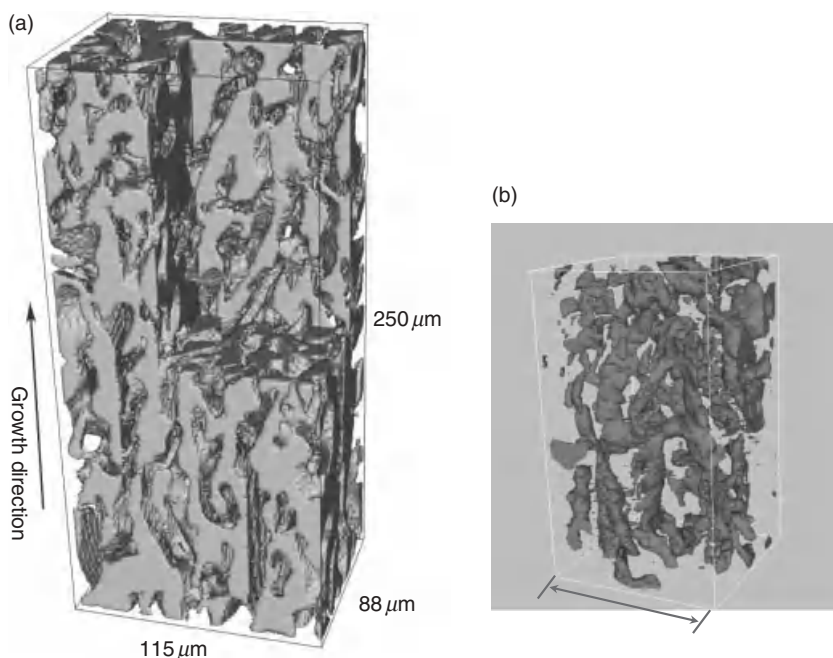


**Figure 12.12.** (a) 3-D image of the YAG phase in the unidirectionally solidified  $\text{Al}_2\text{O}_3/\text{YAG}$  eutectic structure, (b) 3-D image of the  $\text{ZrO}_2$  phase in the  $\text{Al}_2\text{O}_3\text{-YAG-ZrO}_2$  specimen unidirectionally solidified at the growth rate of 0.5 mm/h (printed with permission from Elsevier, courtesy of Prof. Y. Waku, from References 69 and 70).

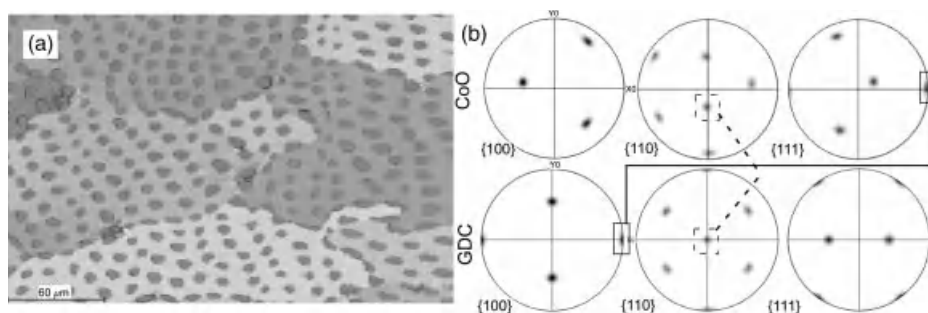


**Figure 12.13.** EBSD orientation map showing the different eutectic grains (a) and associated pole figures (b) of a fibrous region of a CoO/GDC DSEC grown at 10 mm/h. Dashed line in (b) links the growth directions, and the continuous line links interfacial planes (printed with permission from Elsevier from Reference 126).

TABLE 12.3. Composition, Components, Eutectic Temperature, and  $C_1$  Values of Some Ceramic Eutectics

Components	$T_E$ (K)	Composition (% wt)	% Vol	Microstructure	Reference
$\text{Al}_2\text{O}_3/\text{YSZ}$	2135	42 YSZ + 58 $\text{Al}_2\text{O}_3$	32.7 $\text{ZrO}_2$	I, F	[98, 127]
$\text{Al}_2\text{O}_3/\text{Y}_3\text{Al}_5\text{O}_{12}$	2100	33.5 $\text{Y}_2\text{O}_3$ + 66.5 $\text{Al}_2\text{O}_3$	45 $\text{Al}_2\text{O}_3$	I, CF	[89]
$\text{Al}_2\text{O}_3/\text{Er}_3\text{Al}_5\text{O}_{12}$	2075	47.5 $\text{Er}_2\text{O}_3$ + 52.5 $\text{Al}_2\text{O}_3$	42.5 $\text{Al}_2\text{O}_3$	I, CF	[89]
$\text{Al}_2\text{O}_3/\text{EuAlO}_3$	1985	53.5 $\text{Eu}_2\text{O}_3$ + 46.5 $\text{Al}_2\text{O}_3$	44 $\text{Al}_2\text{O}_3$	I, CF	[70]
$\text{Al}_2\text{O}_3/\text{GdAlO}_3$	2015	51.5 $\text{Gd}_2\text{O}_3$ + 48.5 $\text{Al}_2\text{O}_3$	48 $\text{Al}_2\text{O}_3$	I, CF	[128]
$\text{PrAlO}_3/\text{PrAl}_{11}\text{O}_{18}$	2075	45.8 $\text{Pr}_2\text{O}_3$ + 54.2 $\text{Al}_2\text{O}_3$	34 $\text{PrAlO}_3$	BL	[86]
$\text{PrAlO}_3/\text{Pr}_2\text{O}_3$	2095	90.65 $\text{Pr}_2\text{O}_3$ + 9.35 $\text{Al}_2\text{O}_3$	$\approx 50$ $\text{Pr}_2\text{O}_3$	F	[65]
$\text{SrTiO}_3/\text{TiO}_2$	1715	25.6 $\text{SrO}$ + 74.4 $\text{TiO}_2$	29.5 $\text{TiO}_2$	CF	[121]
$\text{Al}_2\text{O}_3/\text{YAG}/\text{YSZ}$	1990	54 $\text{Al}_2\text{O}_3$ + 27 $\text{Y}_2\text{O}_3$ + 19 $\text{ZrO}_2$	18 YSZ	I, CF	[83]
$\text{Al}_2\text{O}_3/\text{Er}_3\text{Al}_5\text{O}_{12}/\text{ErSZ}$	1990	45 $\text{Al}_2\text{O}_3$ + 39.7 $\text{Er}_2\text{O}_3$ + 15.3 $\text{ZrO}_2$	21 ErSZ	I, CF	[74]
$\text{Al}_2\text{O}_3/\text{SmAlO}_3/\text{SmSZ}$	1953	36 $\text{Al}_2\text{O}_3$ + 44.5 $\text{Sm}_2\text{O}_3$ + 19.5 $\text{ZrO}_2$	27.6 SmSZ	I, CF	[73]
$\text{Al}_2\text{O}_3/\text{GdAlO}_3/\text{GdSZ}$	1935	39.7 $\text{Al}_2\text{O}_3$ + 43.7 $\text{Gd}_2\text{O}_3$ + 16.6 $\text{ZrO}_2$	25.4 GdSZ	I, CF	[73]
$\text{CaSZ}/\text{CaZrO}_3$	2525	23.5 $\text{CaO}$ + 76.5 $\text{ZrO}_2$	41 CaSZ	L	[129]
$\text{MgSZ}/\text{MgO}$	2445	27 $\text{MgO}$ + 73 $\text{ZrO}_2$	28 MgO	F	[19]
$\text{MgAl}_2\text{O}_4/\text{MgO}$	2270	55 $\text{Al}_2\text{O}_3$ + 45 $\text{MgO}$	23.5 MgO	F	[81]
$\text{YSZ}/\text{NiAl}_2\text{O}_4$	2270	54 $\text{NiAl}_2\text{O}_4$ + 46 $\text{Zr}_{0.85}\text{Y}_{0.15}\text{O}_{1.92}$	39 YSZ	F	[5]
$\text{Ca or YSZ}/\text{NiO}$	2115	61 $\text{NiO}$ + 39 $\text{Zr}_{0.85}\text{Ca}_{0.15}\text{O}_{1.85}$	44 CaSZ	L	[130]
$\text{Ca or YSZ}/\text{CoO}$	2025	64 $\text{CoO}$ + 36 $\text{Zr}_{0.89}\text{Ca}_{0.11}\text{O}_{1.89}$	38.5 CaSZ	L	[75]
$\text{CeO}_2/\text{NiO}$	1925	50.3 $\text{NiO}$ + 49.7 $\text{CeO}_2$	48 $\text{CeO}_2$	L	
$\text{CeO}_2/\text{CoO}$	1925	66.5 $\text{CoO}$ + 33.5 $\text{CeO}_2$	31.5 $\text{CeO}_2$	L	[131]
$\text{CaF}_2/\text{MgO}$	1625	90 $\text{CaF}_2$ + 10 $\text{MgO}$	9 MgO	F	[85]
$\text{NaF}/\text{NaMgF}_3$	1095	70.7 $\text{NaF}$ + 29.3 $\text{MgF}_2$	47 NaMgF <sub>3</sub>	L	[22]
$\text{NaF}/\text{CaF}_2$	1115	51.5 $\text{NaF}$ + 49.5 $\text{CaF}_2$	43.15 $\text{CaF}_2$	L	[22]
$\text{NaF}/\text{BaF}_2$	1090	71.85 $\text{NaF}$ + 28.15 $\text{BaF}_2$	42.9 NaF	L	[22]
$\text{NaCl}/\text{LiF}$	955	29 $\text{LiF}$ + 71 $\text{NaCl}$	25 LiF	F	[20]

F, fibrous; L, lamellar; I, interpenetrated; BL, broken lamellae; CF, complex faceted.



(Ca or YSZ)/NiO or CoO and CaSZ/CaZrO<sub>3</sub> DSECs show a microstructure of relatively large, well-aligned eutectic grains with a lamellar microstructure. In the 3d-oxide compounds, Echigoya and Hayashi performed HREM interface studies [75] and verified that the phases are well bonded by low-energy interface planes: (111)NiO or CoO// (002)YSZ with periodic steps for the accommodation of the near coincidence planes. This interface is about the lowest energy one that has been studied up to now in DSE oxides [76]. However, at least two different growth directions have also been found in this case: [100] YSZ//[110] NiO and [110]YSZ//[110] NiO [77]. It is interesting to note that in many DSECs, an exact epitaxial relationship may not be established. This occurs, for example, in the CaSZ/CaZrO<sub>3</sub> lamellar eutectic where X-ray diffraction pole figures give the following orientation relationships: (100) CaSZ approx.//(011) pseudocubic CaZrO<sub>3</sub> and (010) CaSZ approx.//(100) pseudocubic CaZrO<sub>3</sub> [78], at the same time as diffraction experiments in the transmission electron microscopy (TEM) showed that there is a misorientation of up to 12° between adjacent lamellae [79]. This lamellar eutectic ceramic combines a perfect single-crystalline material, the CaZrO<sub>3</sub>, with a highly defective ionic conductor zirconia crystal and shows interesting functional properties such as anisotropic ionic conductivity [80] and light waveguide effects. A related eutectic oxide family but with no oxygen ion conducting phase was constituted by eutectics involving either MO (M = 3d ions) or RE<sub>2</sub>O<sub>3</sub> (RE = rare earth ions) oxides. The systems comprised lamellar NiO/CaO, NiO/Y<sub>2</sub>O<sub>3</sub> and NiO/Gd<sub>2</sub>O<sub>3</sub>, or fibrous NiO in NiAl<sub>2</sub>O<sub>4</sub> microstructure type. The compositions, melting points, and fabrication procedures of these eutectics can be found in the review of Revcolevschi et al. [72].

Ceramics with the spinel crystal structure are also of interest for structural applications. In the case of the magnesium spinel (MgAl<sub>2</sub>O<sub>4</sub>), two different eutectics have been grown, the MgO/MgAl<sub>2</sub>O<sub>4</sub> eutectic that contains MgO crystalline fibers embedded into the spinel matrix [81] and the MgAl<sub>2</sub>O<sub>4</sub>/Mg<sub>2</sub>SiO<sub>4</sub> eutectic of spinel fibers in the fosterite matrix [82]. In recent times, attention has switched toward oxide ternary compounds looking for a phase refinement and for proper combinations of phases in order to improve the ceramic properties [2, 83]. Perfectness in microstructure makes fibrous eutectics the easiest way of obtaining good quality, very narrow single-crystal fibers of ceramic compounds. In fact, LiF single crystals less than 1-μm diameter and of millimeter length range were obtained from a NaCl/LiF eutectic after removing the NaCl matrix [20]. Fibrous MgO single crystals are also found in the MgSZ/MgO [84], MgF<sub>2</sub>/MgO, and CaF<sub>2</sub>/MgO eutectics. In the latter, light is transmitted by the highest refractive index MgO micron-size single-crystalline fibers [85]. There are also some cases in which two different eutectic compositions can be found in the same compound, as is the case of the Pr<sub>2</sub>O<sub>3</sub>/Al<sub>2</sub>O<sub>3</sub> eutectic. The PrAlO<sub>3</sub>/Pr<sub>2</sub>O<sub>3</sub> [86] and the PrAlO<sub>3</sub>/PrAl<sub>11</sub>O<sub>18</sub> [65] DSEC show interesting luminescence properties, and the latter gives the first evidence of the existence of crystalline PrAl<sub>11</sub>O<sub>18</sub>.

The field of eutectic ceramics is still in its infancy and chances for new compositions are enormous, for example, using borides, carbides, and nitrides as eutectic components. For the sake of completeness, we want to mention the special case of the CaSiO<sub>3</sub>/Ca<sub>3</sub>(PO<sub>4</sub>)<sub>2</sub> eutectic. The degenerated lamellar structure of this eutectic promoted the biological transformation of a tricalcium phosphate phase into hydroxyapatite, resulting in a material of composition and microstructure similar to that of the

human bone [87]. Eutectic compositions can also promote glass formation, as in the above-mentioned case where a eutectic glass with excellent optical properties can be produced [88].

## 12.5 APPLICATIONS OF CERAMIC EUTECTICS

### 12.5.1 Mechanical Properties and Structural Applications

The working temperature for materials in gas turbine engines and other systems for energy generation are continually increasing to the point where new materials other than nickel and cobalt-based superalloys must be developed. Pure oxide ceramics present a number of interesting properties, but they show low tensile strength and creep resistance. On the other hand, hot-pressed ceramic components contain many grain boundaries that are not thermodynamically stable at high temperatures. DSEs based on  $\text{Al}_2\text{O}_3$  (i.e.,  $\text{Al}_2\text{O}_3/\text{Y}_2\text{O}_3$  or  $\text{Al}_2\text{O}_3/\text{ZrO}_2(\text{Y}_2\text{O}_3)$ ,  $\text{Al}_2\text{O}_3/\text{Gd}_2\text{O}_3$  systems) improve on the mechanical properties of most ceramics because of their nearly perfect component arrangements (fibrous, lamellar, or no ordered homogeneous interpenetrating phases). Since the DSEC microstructure can be tailored by simply modifying the processing conditions, ultrahigh strength and creep resistance up to temperatures close to melting point together with excellent chemical stability can be accomplished in these compounds.

**12.5.1.1 Mechanical Strength** Among the oxides, the directionally solidified materials of the  $\text{Al}_2\text{O}_3\text{-ZrO}_2\text{-Y}_2\text{O}_3$  system have been confirmed to be the best in terms of their mechanical properties. The sapphire-yttrium garnet eutectic ceramic ( $\text{Al}_2\text{O}_3/\text{YAG}$ ) shows exceptional mechanical resistance in air up to temperatures above 2000 K [89], but with relatively low toughness values  $\approx 2 \text{ MPa}\sqrt{\text{m}}$  [90]. The flexural strength of  $\text{Al}_2\text{O}_3/\text{YAG}$  eutectic was measured by Waku et al. [91] as a function of temperature and compared with that of a sintered composite of the same composition. The  $\text{Al}_2\text{O}_3/\text{YAG}$  eutectic maintained its room-temperature strength in the range of 350–400 MPa up to 1880°C, just below melting point. In contrast, the strength of the sintered composite dropped at about 800°C. A systematic study of the mechanical properties of several eutectics based on mixtures of  $\text{Al}_2\text{O}_3$  and rare earth oxides was reported by Yoshikawa [64].  $\text{Al}_2\text{O}_3/\text{garnet}$  eutectic fibers showed superior high-temperature-strength properties because of their uniform microstructure (no colony formation), the strongest one (tensile strength of 624 MPa at 1500°C) being the  $\text{Al}_2\text{O}_3/\text{Tm}_3\text{Al}_5\text{O}_{12}$  eutectic. Flexural strength values up to 1.5 GPa and toughness of  $7.8 \text{ MPa m}^{1/2}$  were measured in  $\text{Al}_2\text{O}_3\text{-ZrO}_2(\text{Y}_2\text{O}_3)$  eutectics at room temperature by Pastor et al. [92]. Echigoya et al. [93] revealed the high anisotropy in the propagation of the cracks in these materials using Vickers microindentation tests. Depending on the content of yttria in the zirconia phase, hardness values between 10 and 17 GPa and toughness values between 4 and 9  $\text{MPa m}^{1/2}$  have been found [94]. Similar data were reported by Borodin et al. [95]. Courtright et al. [96] obtained higher values of mechanical resistance, between 1.13 and 2.45 GPa, and verified that samples treated up to 1560°C for 24 h did not present

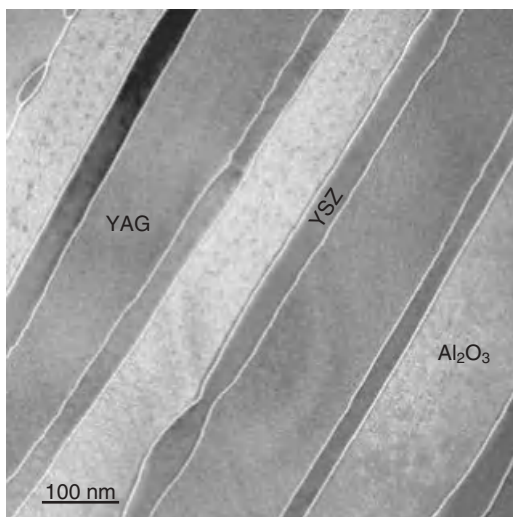


TABLE 12.4. Mechanical Properties of Some Eutectic Ceramics Compared with Those of Some Industrial Ceramics

Material	$\sigma_f$ (GPa) at 300 K	$\sigma_f$ (GPa) (at $T$ indicated)	$K_c$ (MPa·m <sup>1/2</sup> )
YSZ/Al <sub>2</sub> O <sub>3</sub>	1.55	0.9 (1600 K)	5.0–7.8
Al <sub>2</sub> O <sub>3</sub> /Y <sub>3</sub> Al <sub>5</sub> O <sub>12</sub>	1.9	1.7 (1700 K)	2.0
Al <sub>2</sub> O <sub>3</sub> /Y <sub>3</sub> Al <sub>5</sub> O <sub>12</sub> /YSZ	4.0	2.5 (1700 K)	3.3
Al <sub>2</sub> O <sub>3</sub> /Er <sub>3</sub> Al <sub>5</sub> O <sub>12</sub>	2.7	2.7 (1600 K)	1.9
YSZ (ceram.)	0.24		5.0
SiC (ceram.)	0.21–0.38		4.0
Al <sub>2</sub> O <sub>3</sub> (ceram.)	0.33		4.0

important losses of their mechanical properties. Hulse and Batt [97] observed plastic deformation at very high temperature in bending tests by three points and obtained flexural strength values of 524 MPa at 1575°C, among the highest published to date for oxides at these temperatures. In Table 12.4, the values of some physical properties of different eutectics are compared with those of some ceramic materials. Notice the outstanding mechanical resistance of some ceramic eutectics and moderate toughness values in most of them.

**12.5.1.2 Creep** Both Al<sub>2</sub>O<sub>3</sub>/ZrO<sub>2</sub>(Y<sub>2</sub>O<sub>3</sub>) and Al<sub>2</sub>O<sub>3</sub>/YAG eutectic oxides directionally solidified at low growth rates present phase interspacing values in the micrometer range. They have a remarkable creep resistance superior to that of each constituent phase independently because the strong interfaces prevent interfacial sliding. Sayir and Farmer [98] studied creep resistance of Al<sub>2</sub>O<sub>3</sub>/ZrO<sub>2</sub>(Y<sub>2</sub>O<sub>3</sub>) eutectic at 1400°C and 300 MPa, arriving at the conclusion that this eutectic is an order of magnitude more resistant than the single-crystalline cubic zirconia and is even superior than the off-axis sapphire. They also verified that the mechanical resistance of these eutectics produced by LFZ remains almost constant up to 1400°C, contrasting with sapphire single crystals that presented a sudden deterioration. Waku and Sakuma [99] observed that plastic deformation mechanism in Al<sub>2</sub>O<sub>3</sub>/YAG eutectics is controlled by dislocation motion, as was suggested by stress exponent values at high temperatures of  $n = 5$ – $6$ . Waku and Sakuma [99] and Yoshida et al. [100] detected the presence of dislocation structures in both Al<sub>2</sub>O<sub>3</sub> and YAG after plastic deformation. However, it is expected that in compounds with a finer microstructure, mass transport mechanisms (diffusion mechanisms) will also play an important role on creep. This idea was supported by the results of Matson and Hecht [101] on Al<sub>2</sub>O<sub>3</sub>/YAG monofilaments with small lamellar interspacing of 1  $\mu$ m. These authors observed that the YAG phase deforms by a diffusion mechanism, which explained the total absence of dislocations in this phase. Recently, Ramirez-Rico et al. [102] studied creep deformation in Al<sub>2</sub>O<sub>3</sub>/YAG eutectic rods grown by the LFZ method at different growth rates from 25 to 750 mm/h. Bulk diffusion was the main creep mechanism with stress exponents in the range of  $n \sim 1.9$ – $3.0$  for samples with the smaller interphase spacing, whereas for larger phase sizes, the role of dislocations becomes more important with exponential values as high as  $n \sim 6$ .



**Figure 12.14.** TEM image of a longitudinal cross section of the directionally solidified  $\text{Al}_2\text{O}_3/\text{YAG/YSZ}$  nanofibrillar eutectic. The sample is formed by  $\text{Al}_2\text{O}_3$ , YAG, and YSZ aligned whiskers (courtesy of A. Larrea).

The ternary compound  $\text{Al}_2\text{O}_3\text{-ZrO}_2\text{-YAG}$  when produced by LFZ at 1200 mm/h shows a superplastic behavior at 1700 K with strain rates as high as 1 mm/min. This material also exhibits an outstanding flexural strength of about 5 GPa at room temperature, the highest strength ever reported in a bulk material [2]. These exceptional properties are induced by the nonconventional microstructure formed by bundles of single-crystal c-oriented  $\text{Al}_2\text{O}_3$  and  $\text{Y}_3\text{Al}_5\text{O}_{12}$  whiskers of  $\sim 100\text{-nm}$  width and with smaller YSZ whiskers between them (Fig. 12.14). Superplasticity is particularly significant for forming and joining ceramic pieces with a near-net-shape form. These processing procedures can significantly reduce the manufacturing costs of ceramic components, especially because they require relatively moderated temperatures, and the final machining processes are reduced.

**12.5.1.3 Wear and Erosion** Wear takes place when the surface of a component is in contact with another part in relative movement. There are many factors that have an effect on the degree of wear; temperature, relative movement, and applied load. There have only been a few studies on the wear resistance of DSEC in bulk or coating form. Miyoshia et al. [103] subjected near-eutectic  $\text{Al}_2\text{O}_3/\text{Zr}_2\text{O}_3(\text{Y}_2\text{O}_3)$  rods grown by LFZ to reciprocating sliding friction experiments against  $\text{B}_4\text{C}$  plates and showed satisfactory wear resistance in the 296–1073 K temperature range. Similar high values of the specific wear resistances were reported by Ester et al. [104] in fully dense, homogeneous, and crack-free  $\text{Al}_2\text{O}_3/\text{Zr}_2\text{O}_3(\text{Y}_2\text{O}_3)$  eutectic oxide coatings obtained by laser melting of surfaces of sintered ceramic plates with a microstructure made up of colonies, elongated along the traveling direction. The Vickers hardness, friction coefficient,

and specific wear resistance, measured at room temperature, were dependent on the solidification rate, obtaining the optimum wear behavior (maximum hardness and minimum friction coefficient and wear rate) in samples processed at 500 mm/h. Specimens grown at a lower traveling speed presented a coarser microstructure, while those grown at a higher growth rate presented a higher concentration of defects (voids) in the intercolony regions. The wear rate of the optimum laser-melted specimens was almost an order of magnitude smaller than that of the conventionally sintered ceramic of the same composition. It can be concluded that, as in the case of other mechanical properties, the microstructure (colony diameter, intercolony thickness, and interlamellar spacing) plays a dominant role in controlling the wear and friction properties.

The surface of a component can lose material by erosion when surrounded by a moving fluid that contains solid particles. Erosion is usually measured as the mass or volume of target lost per mass or volume of erodent particles impacting the surface under study. The resistance to solid particle erosion has been recently studied by Goretta et al. [105] in directionally solidified  $\text{Al}_2\text{O}_3/\text{ZrO}_2$ . The samples were impacted with sharp SiC particles, and the individual damage sites were measured and compared with those produced in related target ceramics: polycrystalline  $\text{Al}_2\text{O}_3$ , sapphire, and polycrystalline and single-crystal tetragonally stabilized  $\text{ZrO}_2$ . The smallest damage zones occurred in the eutectics containing 3 and 9 mol% of  $\text{Y}_2\text{O}_3$  stabilized  $\text{ZrO}_2$  and the largest damage zones in pure  $\text{ZrO}_2$  specimens. It was concluded that the eutectics with zirconia in cubic or tetragonal phase were resistant to erosion because of the presence of large compressive residual stresses in the  $\text{Al}_2\text{O}_3$  phases. These residual stresses have been determined using piezo-spectroscopic techniques [1].

DSEC in the form of monofilament fibers [101], rods [106] and, more recently, plates [48] and even relatively large bulk pieces can be produced using different fabrication techniques. They are used as reinforcing fibers in composites, hard or thermal barrier coatings, or as bulk materials. In fact, the application in the gas turbine system of bulk  $\text{Al}_2\text{O}_3/\text{YAG}$  and  $\text{Al}_2\text{O}_3/\text{GAP}$  fabricated by the Bridgman method have been reported by Nakagawa et al. [107]. Nevertheless, the most important application of eutectic ceramics at the industrial scale is perhaps that in the abrasive industry. Production of eutectic ceramic grains using fusion technologies such as arc furnaces (Herault furnace) is being performed in the Saint-Gobain Ceramic Materials Division. This technique allows the production of huge amounts of dense ceramic material for their use in abrasives, refractories, plasma coatings, and recently, also in solid oxide fuel cells (SOFCs). In Figure 12.15a, we show some  $\text{Al}_2\text{O}_3/\text{ZrO}_2$  grains of about 0.5 mm in size produced in this way. The grains preserve the typical eutectic microstructure with colonies of this eutectic as shown in Figure 12.15b.

## 12.5.2 Functional Applications

DSECs are also attractive as functional materials. The interest derives in part from their multicomponent character, which permits the fabrication of materials with mixed properties such as ferromagnetic and insulator, conductor and insulator, or electric and magnetic as was the case of the  $\text{BaTiO}_3/\text{CoFe}_2\text{O}_4$  eutectic studied by Echigoya et al. [108]. Moreover, there are other possible functional applications emanating from the

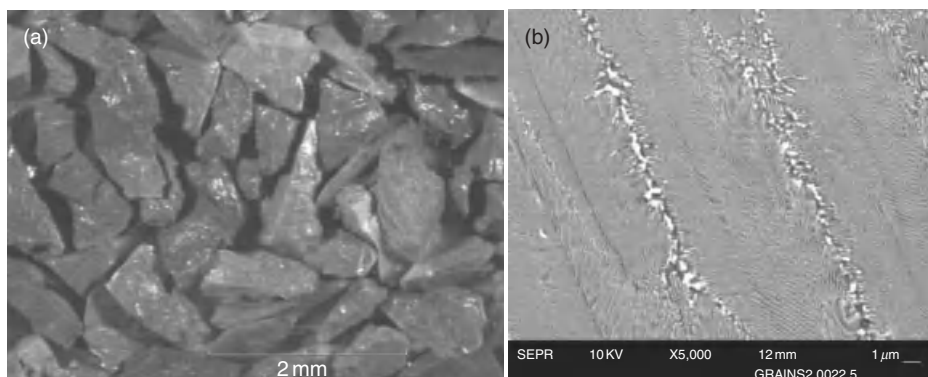


**Figure 12.15.** (a)  $\text{Al}_2\text{O}_3/\text{YSZ}$  eutectic grains fabricated by solidification of arc fusion melts. (b) SEM image of one grain showing the typical colony-type microstructure, (courtesy of S. Marlin from Saint-Gobain Laboratory at CREE, France).

unique ordered microstructure found in regular eutectics. Directional solidification induces phase alignment and hence anisotropic properties in the material. Actually, the structure of periodic and ordered arrays of alternating lamellae or fibers with sharp and clean interfaces conveys interesting functional properties to eutectics, such as the directional transport of light and electricity, among others [109, 110]. The application of DSEC as substrates for deposition of textured high  $T_c$  superconductors and manganites thin films has recently been reviewed by Llorca and Orera [1]. Other applications include anisotropic electroceramics and highly textured biomaterials. Here, we will only focus on some new developments.

**12.5.2.1 Textured Cermets** DSEC based on stabilized zirconia (SZ) and ceria are of great significance because of their practical repercussion. Being good oxygen ion conductors, the SZ and gadolinium-doped ceria (GDC) phases perform as conduits for oxygen ions moving in and out of the eutectic matrix. Oxidation and reduction of bulk ceramic eutectics is in this way feasible and opens the door to the production of a large variety of new oxide–metal composites. In this way, DSEC oxides can be used as precursor materials to obtain cermets, which may find applications in the fields of heterogeneous catalysis and SOFC technology. This method has been used to fabricate Ni or Co/SZ or GDC porous cermets (Fig. 12.16). In fact, reduction of the eutectic ceramic leads to channeled Ni(Co)–YSZ (GDC) porous cermets with alternating porous metal and ionic conductor lamellae, a configuration that offers good electrical conductivity, gas permeation, and a thermal expansion coefficient suitable for convenient thermomechanical integration with other components of the SOFC [111]. These cermets are unique in the sense that the catalyzer particles, of submicron size, are confined between the YSZ fine lamellae [112]. Good adhesion through low-energy interfaces between the metal and the ceramic scaffold induces great stability against metallic particle coarsening [77]. The effect is strongly dependent on the interface properties, and the microstructure, orientation relationships, growth habits, and interfaces in

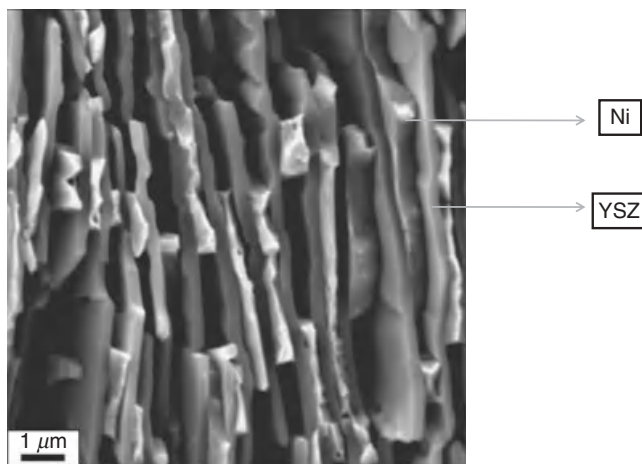


**Figure 12.16.** SEM image of a fractured section of a porous Ni/YSZ cermet produced by the reduction of a NiO/YSZ DSEC.

Ni/YSZ cermets have been recently reported [113]. Directional solidification has also been developed for texturing planar surfaces and cylindrical surfaces of Ni cermets [114, 115]. Additionally, using these cermets as a precursor material, porous YSZ with more than 50% volume porosity can be produced simply by acid leaching out the metal from the textured cermets (see Fig. 12.16). These porous ceramics can find applications in filters, gas burners, bioceramics, membranes, and so on.

**12.5.2.2 Photonic Materials and Metamaterials** Some efforts in the study of the optical properties of DSEC have been recently made. For example, the planar optical waveguide effect was demonstrated in  $\text{CaSZ}/\text{CaZrO}_3$  lamellar regular eutectics [116], and micrometer size MgO single crystals in  $\text{CaF}_2/\text{MgO}$  DSEC perform as a bundle of optical fibers with a density of 40,000 fibers/mm<sup>2</sup> [85]. The pertinent advantages of DSEC are mainly presumed from the very step refraction index profile characteristic of eutectic interfaces. There is reason to believe that cleanness and perfectness of interfaces will help in the transmission of light. Another positive aspect of DSEC as photonic materials is related to the self-assembled nature of eutectic structures where bunches of planar or fiber waveguides of micrometric or nanometric size are grown *in situ*. In most cases, a regular distribution of crystalline fibers may demonstrate 2-D photonic crystal effects, opal effects, and so on, in electromagnetic regions where the refractive index contrast is high enough (see Fig. 12.17). In particular, most DSEC can be easily doped with optically active ions such as 3d or 4f ions in just one or in several component phases. In the latter, we produce an optical material with the unusual characteristic of being at the same time a monolith but also with optical properties of a multiphase material where optical active ions are placed in a number of different crystal field environments. This effect has been reported to occur in  $\text{ZrO}_2/\text{CaO}$  eutectics activated with  $\text{Er}^{3+}$  ions [117]. This finding is in line with recently reported efficient green

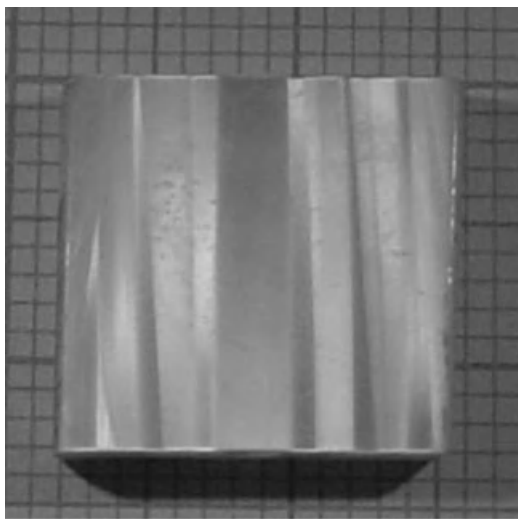


**Figure 12.17.** Optical image of a piece of LiF/NaCl DSEC grown by the Bridgman method showing opal effect under white light illumination.

and red upconversion emissions in erbium-doped  $\text{ZrO}_2/\text{CaO}$  DSEC. As a result of the diversity in crystal environments, either sharp or broad emission bands can simply be tuned by small changes in the excitation wavelength [118]. Actually, an effective lasing effect has been observed in this compound. Furthermore, the thermal emission of  $\text{Er}^{3+}$  ions in the alumina/erbium aluminum garnet DSEC has been considered as promising material for application in thermophotovoltaic (TPV) devices [119].

DSECs have been postulated as potential metamaterials. Metamaterials are defined as artificial materials, not found in nature, with a microstructure smaller than the wavelength of the electromagnetic field showing unconventional electromagnetic properties such as negative refraction index materials, cloaking effects, and giant dielectric constants. [120] Metamaterials are structured materials comprising metals and dielectrics, polymers, or magnetic oxides, which are currently fabricated by electron lithography, focused ion beam milling, and other nanotechnologies. It must also be borne in mind that there is a need for new low-cost fabrication technologies. The positive aspect here is that, as has already been said, eutectics are self-organized, highly textured materials where realization of microstructures with geometries suitable for metamaterials fabrication is possible. For example, the existence of split-ring resonator-like (SSR) cross-sectional features has been confirmed in the  $\text{SrO-TiO}_2$  DSEC [121]. Moreover, the SSR structure is the first demonstrated example of a negative refraction index metamaterial [122]. However, the point at issue is to obtain DSEC materials not only with the appropriate microstructure but also with the right optical properties: high dielectric or magnetic permeability. Generally, metals working at frequencies close to the plasmon resonance region are the best choice for these kinds of materials, but there are only very few metal/dielectric eutectics available for fabrication, which, in the case of

ceramic components, limits us to some few eutectics involving very refractive metals such as W, Ta, and Mo [123].

## 12.6 CONCLUSIONS AND FINAL REMARKS

The mechanical and functional properties of ceramics are mainly determined by the characteristics of their microstructure. The important point here is that in DSEC, the microstructure can be tailored by processing. In recent years, new processing techniques with very high solidification thermal gradients such as LFZ, EFG, and  $\mu$ -PD permit higher growth rates than old solidification techniques derived from Bridgman crystal growth methods. Consequently, DSECs with finer microstructures nearly touching the nanometer range are now available. Finer microstructure means not only better mechanical resistance, but it also opens the possibility for solidified ceramics to enter the nanoworld. New processing techniques have even opened the door to the fabrication of compositionally graded ceramics from melt as has been recently reported [124].

Additionally, a deeper understanding of the correlation between processing, microstructure, and properties has led to outstanding mechanical achievements, such as impressive mechanical resistance values and creep resistance as have been described in Section 12.5. The critical point still concerns the mediocre toughness values of DSEC. Another point of interest is the relatively low size of DSEC materials, a consequence of interconnection between thermal solidification gradient, growth rate, phase size and sample size, as we have described in Section 12.2. In general, fast solidification rates needed for finer microstructure means high thermal stresses and consequently small solidified bodies. Fabrication of large eutectic ceramic pieces with finer microstructures is one of the future challenges. Laser surface melting and EGF techniques seem to be in the best position for achieving this task, but we should also take into consideration that high-temperature pressure (HIP) sintering and spark plasma sintering (SPS) of ad hoc prepared eutectic grains could be a new procedure for the fabrication of large eutectic ceramics.

The required advances in processing techniques also have to be sustained for analogous efforts in eutectic growth modeling. We can now add to this conclusion a new one: In DSEC, not only the microstructure size but also the microstructure morphology and interface characteristics strongly depend on the growth procedure. New efforts in microstructure characterization including texture and crystallographic studies of DSEC are also needed.

Although still in its very early stages, the study of directional solidified ceramics for functional applications has to receive more support in the near future. The tendency to develop microdevices perfectly matches the possibility of fabrication of relatively small pieces of eutectic ceramics with a very regular and ordered microstructure. Being an *in situ* self-assembled method, directional solidification may compete with other nano- and microtechnologies in perfectness, cleanness, and low cost.

Fascinating structures revealed by directionally solidified ceramics invite us to imagine many different material combinations with synergetic properties, but they could only be fabricated if a eutectic point for this combination exists. Alternatively,



by removing one of the eutectic component phases, one can develop a highly porous “single-crystalline” material susceptible to being infiltrated with the desired phases, for example, with metals, to obtain the desired metal-dielectric regular ordered composite. On the other hand, some metal-dielectric composites were already obtained several years ago by Revcolevschi and Dhahlenne [125] by simply reducing one of the eutectic oxide phases.

## ACKNOWLEDGMENTS

The authors are indebted to their colleagues A. Larrea, R. I. Merino, and P. B. Oliete from the Instituto de Ciencia de Materiales de Aragón (CSIC-Universidad de Zaragoza) for helpful discussions. We also thank the Spanish Government under grants MAT2009-14324-C02-01 and MAT2009-13979-C03-03 for financial support. The European project ENSEMBLE NMP4-2008-213669 is also acknowledged for funding.

## REFERENCES

1. J. Llorca and V. M. Orera (2006) Directionally solidified eutectic ceramic oxides, *Prog. Mater. Sci.*, **51** 711–809.
2. P. B. Oliete, J. I. Peña, A. Larrea, V. M. Orera, J. Llorca, J. Y. Pastor, A. Martín, and J. Segurado (2007) Ultra-high-strength nanofibrillar  $\text{Al}_2\text{O}_3$ -YAG-YSZ eutectics, *Adv. Mater.*, **19** 2313–2318.
3. H. Su, J. Zhang, Cui, L. Lin, and H. Fu (2008) Rapid solidification behaviour of  $\text{Al}_2\text{O}_3/\text{Y}_3\text{Al}_5\text{O}_{12}$  binary eutectic in situ composites, *Mater. Sci. Eng. A*, **479** 380–388.
4. J. D. Hunt and K. A. Jackson (1966) Binary eutectic solidification, *Trans. Metal. Soc. AIME*, **236** 843–852.
5. A. Sayir, S. C. Farmer, P. O. Dickerson, and A. M. Yun (1993) High temperature mechanical properties of  $\text{Al}_2\text{O}_3/\text{ZrO}_2(\text{Y}_2\text{O}_3)$  fibers, *Mater. Res. Soc. Symp. Proc.*, **365** 21–27.
6. C. O. Hulse and J. A. Batt (1974) Final Tech. Rept. UARL-N910803-10, NTIS AD-781995/6GA.
7. Y. Waku, N. Nakagawa, T. Wakamoto, H. Ohtsubo, K. Shimizu, and Y. Kohtoku (1997) A ductile ceramic eutectic composite with high strength at 1873 K, *Nature*, **389** 49–52.
8. J. Y. Pastor, A. Martín, J. Llorca, P. B. Oliete, J. I. Peña, A. Larrea, and V. M. Orera (2009) Superplastic behavior of  $\text{Al}_2\text{O}_3$ - $\text{Y}_3\text{Al}_5\text{O}_{12}$ -YSZ eutectic ceramics at 1700 K, in *Proc. of the 3<sup>rd</sup> DSEC Workshop*, November, Sevilla, Spain.
9. F. S. Galasso (1967) Unidirectionally solidified eutectics for optical, electronic, and magnetic applications, *J. Met.*, **19** 17–21.
10. K. A. Jackson, Interface structure, in *Growth and Perfection of Crystals*, eds. R. H. Doremus, D. Turnbull, and B. W. Roberts, pp. 319–323, John Wiley and Sons, New York, 1958.
11. K. A. Jackson and J. D. Hunt (1966) Lamellar and rod eutectic growth, *Trans. Metal. Soc. AIME*, **236** 1128–1142.
12. W. Kurtz and D. J. Fisher, *Fundamentals of Solidification*, 4th revised edition, Trans. Tech Publications, Switzerland, 1998.



13. S. H. Davis "Theory of solidification" *Cambridge Monographs on Mechanics*, Chapter 8, Cambridge University Press, Cambridge, 2001.
14. I. Minkoff *Solidification and Cast Structure*, Chapter 4, John Wiley and Sons, Chichester, 1986.
15. C. Zener (1946) Kinetics decomposition of austenite, *Trans. Metal. Soc. AIME*, **167** 550–595.
16. L. L. Zheng, D. J. Larson, Jr., and H. J. Zhang (2000) Revised form of Jackson-Hunt theory: Application to directional solidification of MnBi/Bi eutectics, *J. Cryst. Growth*, **209** 110–121.
17. R. Trivedi, P. Magnin, and W. Kurz (1987) Effect of growth rate dependent partition coefficient on the dendritic growth in undercooled melts, *Acta Metal.*, **35** 971–980.
18. S. Bourban, N. Karapatis, H. Hofmann, and W. Kurz (1997) Solidification microstructure of laser remelted  $\text{Al}_2\text{O}_3\text{-ZrO}_2$  eutectic, *Acta Mater.*, **45** 5069–5075.
19. W. J. Minford, R. C. Bradt, and V. S. Stubican (1979) Crystallography and microstructure of directionally solidified eutectics, *J. Am. Ceram. Soc.*, **62** 154–157.
20. V. M. Orera and A. Larrea (2005) NaCl-asisted growth of micrometer-wide long single crystalline fluoride fibres, *Opt. Mater.*, **27** 1726–1729.
21. J. D. Hunt and D. T. J. Hurle (1968) The structure of faceted/nonfaceted eutectics, *Trans. Metal. Soc. AIME*, **242** 1043–1047.
22. A. Larrea and V. M. Orera (2007) Porous cristal structures obtained from directionally solidified eutectic precursors, *J. Cryst. Growth*, **300** 387–393.
23. M. H. Burden and J. D. Hunt (1974) Cellular and dendritic growth. I, *J. Cryst. Growth*, **22** 99–108.
24. S. G. Kim, W. T. Kim, T. Suzuki, and M. Ode (2004) Phase-field modelling of eutectic solidification, *J. Cryst. Growth*, **261** 135–158.
25. G. I. Tóth and L. Gránásy (2007) Phase field theory of interfaces and crystal nucleation in a eutectic system of fcc structure: I. Transitions in the one-phase liquid region, *J. Chem. Phys.*, **127** 074709–074711.
26. V. S. Stubican and R. C. Bradt (1981) Eutectic solidification in ceramic eutectics, *Ann. Rev. Mater. Sci.*, **11** 267–297.
27. D. Viechnicki and F. Schmid (1969) Eutectic solidification in the system  $\text{Al}_2\text{O}_3/\text{Y}_3\text{Al}_5\text{O}_{12}$ , *J. Mater. Sci.*, **4** 84–88.
28. P. B. Oliete and J. I. Peña (2007) Study of the gas inclusions in  $\text{Al}_2\text{O}_3/\text{Y}_3\text{Al}_5\text{O}_{12}$  and  $\text{Al}_2\text{O}_3/\text{Y}_3\text{Al}_5\text{O}_{12}/\text{ZrO}_2$  eutectic fibres grown by laser floating zone, *J. Cryst. Growth*, **304** 514–519.
29. J. I. Peña, M. Larsson, R. I. Merino, I. de Francisco, V. M. Orera, J. Llorca, J. Y. Pastor, A. Martín, and J. Segurado (2006) Processing, microstructure and mechanical properties of directionally-solidified  $\text{Al}_2\text{O}_3\text{-Y}_3\text{Al}_5\text{O}_{12}\text{-ZrO}_2$  ternary eutectics, *J. Eur. Ceram. Soc.*, **26** 3113–3121.
30. M. Saito (1986) Growth process of Gas Bubble in Ruby single crystals by floating zone method, *J. Cryst. Growth*, **74** 385–390.
31. H. J. Lim, R. C. DeMattei, R. S. Feigelson, and K. Rochford (2000) Striations in YIG fibers grown by the laser heated pedestal method, *J. Cryst. Growth*, **212** 191–203.
32. I. de Francisco, R. I. Merino, V. M. Orera, A. Larrea, and J. I. Peña (2005) Growth of  $\text{Al}_2\text{O}_3/\text{ZrO}_2(\text{Y}_2\text{O}_3)$  eutectic rods by the laser floating zone technique: Effect of the rotation, *J. Eur. Ceram. Soc.*, **25** 1341–1350.

33. R. P. Poplawsky and J. E. Tomas (1960) Floating zone crystals using an arc image furnace, *Rev. Sci. Instrum.*, **31** 1303–1309.
34. D. B. Gasson and B. Cockayne (1970) Oxide crystal growth using gas lasers, *J. Mater. Sci.*, **5** 100–104.
35. B. Cockayne, D. B. Gasson, and N. Forbes (1970) Further developments in oxide crystal growth using gas lasers, *J. Mater. Sci.*, **5** 837–838.
36. J. S. Haggerty, W. P. Menashi, and J. F. Wenckus (1976) Method for forming refractory fibres by laser energy, U.S. Patent n. 3,944,640.
37. R. S. Feigelson (1985) The laser-heated pedestal growth method: To powerful tool in the search for laser high performance crystals, *Springer Ser. Opt. Sci.*, **47** 129–142.
38. M. M. Fejer, J. L. Nightingale, G. A. Magel, and R. L. Byer (1984) Laser-heated miniature pedestal growth apparatus for single-crystal optical fibers, *Rev. Sci. Instrum.*, **55** 1791–1796.
39. M. Kimura, H. Arai, T. Mori, and H. Yamagishi (1993) Facet formation in silicon single crystal grown by VMFZ method, *J. Cryst. Growth*, **128** 282–287.
40. V. N. Semenov, B. B. Straumal, V. G. Glebovsky, and W. Gust (1995) Preparation of Fe-Si single crystal and bicrystal for diffusion experiments by the electron-beam floating zone technique, *J. Cryst. Growth*, **151** 180–186.
41. D. B. Gasson (1965) The preparation of calcium tungstate crystal by a modified floating zone recrystallization technique, *J. Sci. Instrum.*, **42** 114–115.
42. K. Muto and K. Awazu (1969) Growth of yttrium vanadate crystal by modified floating zone technique, *Jpn. J. Appl. Phys.*, **8** 1360–1361.
43. H. J. Koh, Y. Furukawa, P. Rudolph, and T. Fukuda (1995) Oxide mixed crystals grown by heater-immersed zone melting method with multi-capillary holes, *J. Cryst. Growth*, **149** 236–240.
44. T. Yamakawa, N. Ishizawa, K. Uematsu, N. Mizutani, and M. Kato (1986) Growth of yttria partially and fully stabilized zirconia crystals by xenon arc image floating zone method, *J. Cryst. Growth*, **75** 623–629.
45. J. G. Bednorz and H. Arend (1984) A 1kW mirror furnace for growth of refractory oxide single crystal by a floating zone technique, *J. Cryst. Growth*, **67** 660–662.
46. A. Eyer, R. Nitsche, and H. Zimmermann (1979) A double-ellipsoid mirror furnace for zone crystallization experiments in spacelab, *J. Cryst. Growth*, **47** 219–229.
47. A. Larrea, G. F. de la Fuente, R. I. Merino, and V. M. Orera (2002)  $\text{ZrO}_2\text{-Al}_2\text{O}_3$  eutectic plates produced by laser zone melting, *J. Eur. Ceram. Soc.*, **22** 191–198.
48. A. Larrea, V. M. Orera, R. I. Merino, and J. I. Peña (2005) Microstructure and mechanical properties of  $\text{Al}_2\text{O}_3\text{-YSZ}$  and  $\text{Al}_2\text{O}_3\text{-YAG}$  directionally solidified eutectic plates, *J. Eur. Ceram. Soc.*, **25** 1419–1429.
49. F. J. Ester and J. I. Peña (2007) Análisis de la zona fundida en el crecimiento del compuesto eutéctico  $\text{Al}_2\text{O}_3\text{-ZrO}_2$  ( $\text{Y}_2\text{O}_3$ ) por fusión zonal con láser, *Bol. Soc. Esp. Ceram. V.*, **46** 240–246.
50. D. Reyes Ardila, L. V. Cofré, L. B. Barbosa, and J. P. Andreeta (2004) Study of floating zone profiles in materials grown by the laser-heated pedestal growth technique under iso-static atmosphere, *Cryst. Res. Technol.*, **39** 855–858.
51. M. Saitou (1997) Shape and stability of a floating liquid zone between two solids, *J. Appl. Phys.*, **82** 6343.

52. W. Heywang (1956) Zur stabilität senkrechter smelzzonen, *Z. Naturforsch A*, **11** 238–243.
53. W. G. Pfann and D. W. Hagelbarger (1956) Electromagnetic suspension of a molten zone, *J. Appl. Phys.*, **27** 12–18.
54. J. C. Brice (1977) Cracking of Czochralski-grown crystals, *J. Cryst. Growth*, **42** 427–430.
55. F. J. Ester, D. Sola, and J. I. Peña (2008) Thermal stresses in the  $\text{Al}_2\text{O}_3\text{-ZrO}_2$  ( $\text{Y}_2\text{O}_3$ ) eutectic composite during the growth by the laser floating zone technique, *Bol. Soc. Esp. Ceram. V.*, **47** 352–357.
56. A. V. Stepanov (1959) New method of producing articles (sheets, tubes, rods, various sections, etc) directly from liquid metal.1., *Soviet Phys. Tech. Phys.*, **4** 339–348.
57. H. E. LaBelle, Jr. (1980) EFG, the invention and application to sapphire growth, *J. Cryst. Growth*, **50** 8–17.
58. J. T. A. Pollock (1972) Filamentary sapphire. Part1. Growth and microstructural characterisation, *J. Mater. Sci.*, **7** 787–792.
59. C. B. Finch, J. D. Holder, G. W. Clark, and H. L. Yakel (1977) Edge-defined, film-fed growth of  $\text{Mn}_2\text{SiO}_4\text{-MnO}$  eutectic composites. Effect of die-top geometry on solidification interface shape, *J. Cryst. Growth*, **37** 245–252.
60. M. Y. Starostin, B. A. Gnesin, and T. N. Yalovets (1997) Microstructure and crystallographic textures of the alumina-zirconia eutectics, *J. Cryst. Growth*, **171** 119–124.
61. D.-H. Yoon and T. Fukuda (1994) Characterization of  $\text{LiNbO}_3$  micro single crystals by the micro-pulling-down method, *J. Cryst. Growth*, **144** 201–206.
62. B. M. Epelbaum, K. Inaba, S. Uda, K. Shimamura, M. Imaeda, V. V. Kochurikhin, and T. Fukuda (1997) A double-die modification of micro-pulling-down for in situ clad/core doping of fiber crystal, *J. Cryst. Growth*, **179** 559–566.
63. Y. M. Yu, V. I. Chani, K. Shimamura, K. Inaba, and T. Fukuda (1997) Growth of vanadium garnet fiber crystals and variation of lattice parameter, *J. Cryst. Growth*, **177** 74–78.
64. A. Yoshikawa, K. Hasegawa, J. H. Lee, S. D. Durbin, B. M. Epelbaum, D. H. Yoon, T. Fukuda, and Y. Waku (2000) Phase identification of  $\text{Al}_2\text{O}_3/\text{RE}_3\text{Al}_5\text{O}_{12}$  and  $\text{Al}_2\text{O}_3/\text{REAlO}_3$  ( $\text{RE} = \text{Sm, Lu, Y}$ ) eutectics, *J. Cryst. Growth*, **218** 67–73.
65. K. Kolodziejek, S. Turczynski, R. Diduszko, L. Klimek, and D. A. Pawlak (2006)  $\text{Tb}_3\text{Sc}_2\text{Al}_3\text{O}_{12}\text{-TbScO}_3$  eutectic self-organized microstructure for metamaterials and photonic crystals application, *Opto-Electron. Rev.*, **14** 205–211.
66. D. A. Pawlak, K. Kolodziejek, K. Rozniatowski, R. Diduszko, M. Kaczkan, M. Malinowski, M. Piersa, J. Kisiulewski, and T. Lukasiewicz (2008)  $\text{PrAlO}_3\text{-PrAl}_{11}\text{O}_{18}$  eutectic: Its microstructure and spectroscopic properties, *Cryst. Growth Des.*, **8** 1243–1249.
67. C. W. Lan, Theoretical analysis of the micro-pulling down process, in *Fiber Crystal Growth Form Melt*, Chapter 3, eds. T. Fukuda, P. Rudolph, and S. Uda, pp. 89–100, Springer, Berlin, 2004.
68. L. Mazerolles, D. Michel, and M. J. Hytch (2005) Microstructures and interfaces in directionally solidified oxide-oxide eutectics, *J. Eur. Ceram. Soc.*, **25** 1389–1395.
69. H. Yasuda, I. Ohnka, Y. Mizutani, T. Morikawa, S. Takeshima, A. Sugiyama, Y. Waku, A. Tsuchiyama, T. Nakano, and K. Uesugi (2005) Three-dimensional observation of the entangled eutectic structure in the  $\text{Al}_2\text{O}_3\text{-YAG}$  system, *J. Eur. Ceram. Soc.*, **25** 1397–1403.
70. T. Nagira, H. Yasuda, S. Takeshima, T. Sakimura, Y. Waku, and K. Uesugi (2009) Chain structure in the unidirectionally solidified  $\text{Al}_2\text{O}_3\text{-YAG-YSZ}$  eutectic composite, *J. Cryst. Growth*, **311** 3765–3770.

71. R. L. Ashbrook (1977) Directionally solidified ceramic eutectics, *J. Am. Ceram. Soc.*, **60** 428–435.
72. A. Revcolevschi, G. Dhalenne, and D. Michel (1988) Interfaces in directionally solidified oxide-oxide eutectics, *Mater. Sci. Forum*, **29** 173–198.
73. S. M. Lakiza (2009) Directionally solidified eutectics in the  $\text{Al}_2\text{O}_3\text{-ZrO}_2\text{-Ln(Y)}_2\text{O}_3$  systems (Review), *Powder Metall. Met. Ceram.*, **48** 42–59. and references herein.
74. S. M. Lakiza and L. M. Lopato (2008) Phase diagram of the  $\text{Al}_2\text{O}_3\text{-ZrO}_2\text{-Er}_2\text{O}_3$  system, *J. Eur. Ceram. Soc.*, **28** 2389–2397.
75. J. Echigoya and S. Hayashi (1993) Directional solidification of  $\text{CoO-ZrO}_2$  eutectics, *J. Cryst. Growth*, **129** 699–705.
76. S. B. Sinnott and E. C. Dickey (2003) Ceramic/metal interface structures and their relationship to atomic- and meso-scale properties, *Mater. Sci. Eng. R*, **43** 1–59.
77. M. A. Laguna-Bercero, A. Larrea, R. I. Merino, J. I. Peña, and V. M. Orera (2005) Stability of channelled Ni-YSZ cermets produced from self-assembled NiO-YSZ directionally solidified eutectics, *J. Am. Ceram. Soc.*, **88** 3215–3217.
78. J. Santiso, V. Laukhin, M. Doudkowsky, G. García, A. Figueras, L. A. Angurel, R. I. Merino, J. I. Peña, M. L. Sanjuán, and V. M. Orera (2000) A new approach to obtain strip-structured biepitaxial  $\text{YBa}_2\text{Cu}_3\text{O}_{7-\delta}$  films by using Ca-stabilized zirconia- $\text{CaZrO}_3$  eutectic substrates, *Adv. Mater.*, **12** 116–119.
79. A. Larrea, V. M. Orera, J. I. Peña, and R. I. Merino (1999) Orientation relationship and interfaces in nonfaceted-nonfaceted  $\text{ZrO}_2$  (c)- $\text{CaZrO}_3$  lamellar eutectics, *J. Mater. Res.*, **14** 2588–2593.
80. R. I. Merino, J. I. Peña, V. M. Orera, and G. F. de la Fuente (1997) Conductivity anisotropy in directionally solidified  $\text{CaZrO}_3\text{-CaSZ}$  and  $\text{MgO-MgSZ}$  eutectics, *Solid State Ionics*, **100** 313–318.
81. F. L. Kennard, R. C. Bradt, and V. S. Stubican (1973) Eutectic solidification of  $\text{MgO-MgAl}_2\text{O}_4$ , *J. Am. Ceram. Soc.*, **56** 566–569.
82. S. Kawakami, T. Yamada, S. Sakakibara, and H. Tabata (1995) Preparation of spinel fibers by directional solidification of  $\text{MgAl}_2\text{O}_4\text{-Mg}_2\text{SiO}_4$  eutectic, *J. Cryst. Growth*, **154** 193–196.
83. J. H. Lee, A. Yoshikawa, T. Fukuda, and Y. Waku (2001) Growth and characterization of  $\text{Al}_2\text{O}_3/\text{Y}_3\text{Al}_5\text{O}_{12}/\text{ZrO}_2$  ternary eutectic fibers, *J. Cryst. Growth*, **231** 115–120.
84. J. D. Parsons and A. S. Yue (1981) Growth of fiber optic eutectics and their applications, *J. Cryst. Growth*, **55** 470–476.
85. A. Larrea, L. Contreras, R. I. Merino, J. Llorca, and V. M. Orera (2000) Microstructure and physical properties of  $\text{CaF}_2\text{-MgO}$  eutectics produced by the Bridgman method, *J. Mater. Res.*, **15** 1314–1319.
86. D. A. Pawlak, K. Kolodziejek, R. Diduszko, K. Rozniatowski, M. Kaczkan, M. Malinowski, J. Kisielowski, and T. Lukasiewicz (2007) The  $\text{PrAlO}_3\text{-Pr}_2\text{O}_3$  eutectic, its microstructure, instability, and luminescence properties, *Chem. Mat.*, **19** 2195–2202.
87. P. N. De Aza, F. Guitian, and S. De Aza (1997) Bioeutectic: A new ceramic material for human bone replacement, *Biomaterials*, **18** 1285–1291.
88. J. A. Pardo, J. I. Peña, R. I. Merino, R. Cases, A. Larrea, and V. M. Orera (2002) Spectroscopic properties of  $\text{Er}^{3+}$  and  $\text{Nd}^{3+}$  doped glasses with the  $0.8\text{CaSiO}_3\text{-}0.2\text{Ca}_3(\text{PO}_4)_2$  eutectic composition, *J. Non-Cryst. Solids*, **298** 23–31.

89. B. M. Epelbaum, K. Yoshikawa, K. Shimamura, T. Fukuda, K. Suzuki, and Y. Waku (1999) Microstructure of  $\text{Al}_2\text{O}_3/\text{YAG}$  eutectic fibers grown by the  $\mu$ -PD method, *J Cryst. Growth*, **198/199** 471–475.
90. J. M. Yang and X. Q. Zhu (1997) Thermo-mechanical stability of directionally solidified  $\text{Al}_2\text{O}_3\text{-ZrO}_2$  ( $\text{Y}_2\text{O}_3$ ) eutectic fibers, *Scr. Mater.*, **36** 961–966.
91. Y. Waku, N. Nakagawa, T. Wakamoto, H. Otsubo, K. Shimizu, and Y. Kohtoku (1998) High temperature strength and thermal stability of unidirectionally solidified  $\text{Al}_2\text{O}_3/\text{YAG}$  eutectic composite, *J. Mater. Sci.*, **33** 1217–1224.
92. J. Y. Pastor, P. Poza, J. Llorca, J. I. Peña, R. I. Merino, and V. M. Orera (2001) Mechanical properties of directionally solidified  $\text{Al}_2\text{O}_3\text{-ZrO}_2(\text{Y}_2\text{O}_3)$  eutectics, *Mater. Sci. Eng. A*, **308** 241–249.
93. J. Echigoya, Y. Takabayashi, and H. Suto (1986) Hardness and fracture toughness of directionally solidified  $\text{Al}_2\text{O}_3\text{-ZrO}_2(\text{Y}_2\text{O}_3)$  eutectics, *J. Mater. Sci. Lett.*, **5** 153–154.
94. J. Llorca, J. Y. Pastor, P. Poza, J. I. Peña, I. de Francisco, A. Larrea, and V. M. Orera (2004) Influence of the  $\text{Y}_2\text{O}_3$  content and temperature on the mechanical properties of melt-grown  $\text{Al}_2\text{O}_3\text{-ZrO}_2$  eutectics, *J. Am. Ceram. Soc.*, **87** 633–639.
95. V. A. Borodin, M. Yu. Starostin, and T. N. Yalovets (1990) Structure and related properties of shaped eutectic  $\text{Al}_2\text{O}_3\text{-ZrO}_2(\text{Y}_2\text{O}_3)$  composites, *J. Cryst. Growth*, **104**[1] 148–153.
96. E. L. Courtright, J. S. Haggerty, and J. Sigalovsky (1993) Controlling microstructures in  $\text{ZrO}_2(\text{Y}_2\text{O}_3)\text{-Al}_2\text{O}_3$  eutectic fibers, *Ceram. Eng. Sci. Proc.*, **14**[7–8] 671–681.
97. C. O. Hulse and J. A. Batt (1974) Effect of eutectic microstructures on the mechanical properties of ceramic oxides. (Final Technical Report N910803-10, United Aircraft Research Laboratories). Government Reports Announcements. (U.S.) **74**[19] 86.
98. A. Sayir and S. C. Farmer (2000) The effect of the microstructure on mechanical properties of directionally solidified  $\text{Al}_2\text{O}_3/\text{ZrO}_2(\text{Y}_2\text{O}_3)$  eutectic, *Acta Mater.*, **48** 4691–4697.
99. Y. Waku and T. Sakuma (2000) Dislocation mechanism of deformation and strength of  $\text{Al}_2\text{O}_3\text{-YAG}$  single crystal composites at high temperatures above  $1500^\circ\text{C}$ , *J. Eur. Ceram. Soc.*, **20** 1453–1458.
100. H. Yoshida, K. Shimura, S. Suginoara, Y. Ikuhara, T. Sakuma, N. Nakagawa, and Y. Waku (2000) High-temperature deformation in unidirectionally solidified eutectic  $\text{Al}_2\text{O}_3\text{-YAG}$  single crystal, *Key Eng. Mater.*, **171–174** 855–862.
101. L. E. Matson and N. Hecht (1999) Microstructural stability and mechanical properties of directionally solidified alumina/YAG eutectic monofilaments, *J. Eur. Ceram. Soc.*, **19** 2487–2508.
102. J. Ramirez-Rico, A. R. Pinto-Gómez, J. Martínez-Fernández, A. R., de Arellano-López, P. B. Oliete, J. I. Peña, and V. M. Orera (2006) High-temperature plastic behaviour of  $\text{Al}_2\text{O}_3\text{-Y}_3\text{Al}_5\text{O}_{12}$  directionally solidified eutectics, *Acta Mater.*, **54** 3107–3116.
103. K. Miyoshia, S. C. Farmer, and A. Sayir (2005) Wear properties of two-phase  $\text{Al}_2\text{O}_3/\text{ZrO}_2$  ( $\text{Y}_2\text{O}_3$ ) ceramics at temperatures from 296 to 1073 K, *Tribol. Int.*, **38** 974–986.
104. F. J. Ester, R. I. Merino, J. Y. Pastor, A. Martín, and J. Llorca (2008) Surface modification of  $\text{Al}_2\text{O}_3\text{-ZrO}_2$  ( $\text{Y}_2\text{O}_3$ ) eutectic oxides by laser melting: Processing and wear resistance, *J. Am. Ceram. Soc.*, **91** 3552–3559.
105. K. C. Goretta, J. I. Peña, V. M. Orera, N. Chenc, D. Singh, and J. L. Routbort (2010) Solid-particle erosion of directionally solidified  $\text{Al}_2\text{O}_3\text{-ZrO}_2$  ( $\text{Y}_2\text{O}_3$ ) eutectics, *Wear*, **268** 571–578.

106. S. C. Farmer, A. Sayir, and P. O. Dickerson *In situ Composites: Science and Technology*. TMS, Warrendale, 1993.
107. N. Nakagawa, H. Ohtsubo, A. Mitani, K. Shimizu, and Y. Waku (2005) High temperature strength and thermal stability for melt growth composite, *J. Eur. Ceram. Soc.*, **25** 1251–1257.
108. J. Echigoya, S. Hayashi, and Y. Obi (2000) Directional solidification and interface structure of  $\text{BaTiO}_3\text{-CoFe}_2\text{O}_4$  eutectic, *J. Mater. Sci.*, **35** 5587–5591.
109. R. I. Merino, J. I. Peña, A. Larrea, G. F. de la Fuente, and V. M. Orera (2003) Melt grown composite ceramics obtained by directional solidification: Structural and functional applications, *Recent Res. Dev. Mat. Sci.*, **4** 1–24.
110. V. M. Orera, R. I. Merino, J. A. Pardo, A. Larrea, J. I. Peña, C. González, P. Poza, J. Y. Pastor, and J. Llorca (2000) Microstructure and physical properties of some oxide eutectic composites processed by directional solidification, *Acta Mater.*, **48** 4683–4689.
111. M. A. Laguna-Bercero, A. Larrea, J. I. Peña, R. I. Merino, and V. M. Orera (2008) Crystallography and thermal stability of textured Co-YSZ cermets from eutectic precursors, *J. Eur. Ceram. Soc.*, **28** 2325–2329.
112. A. Larrea, M. A. Laguna-Bercero, J. I. Peña, R. I. Merino, and V. M. Orera (2009) Orientation relationships and interfaces in Ni- and Co-YSZ cermets prepared from directionally solidified eutectics, *Cent. Eur. J. Phys.*, **7**[2] 245–250.
113. M. A. Laguna-Bercero and A. Larrea (2007) YSZ-Induced crystallographic reorientation of Ni particles in Ni-YSZ cermets, *J. Am. Ceram. Soc.*, **90** 2954–2960.
114. R. I. Merino, J. I. Peña, M. A. Laguna-Bercero, A. Larrea, and V. M. Orera (2004) Directionally solidified calcia stabilised zirconia-nickel oxide plates in anode supported solid oxide fuel cells, *J. Eur. Ceram. Soc.*, **24** 1349–1353.
115. R. Campana, A. Larrea, J. I. Peña, and V. M. Orera (2009) Ni-YSZ cermet micro-tubes with textured surface, *J. Eur. Ceram. Soc.*, **29** 85–90.
116. V. M. Orera, J. I. Peña, R. I. Merino, J. A. Lázaro, J. A. Vallés, and M. A. Rebolledo (1997) Prospects of new planar optical waveguides based on eutectic microcomposites of insulating crystals: The  $\text{ZrO}_2\text{-CaZrO}_3$  erbium doped system, *Appl. Phys. Lett.*, **71** 2746–2748.
117. R. I. Merino, J. A. Pardo, J. I. Peña, G. F. de la Fuente, A. Larrea, and V. M. Orera (1997) Luminescence properties of  $\text{ZrO}_2\text{-CaO}$  eutectic crystals with ordered lamellar microstructure activated with Er ions, *Phys. Rev.*, **B 56** 10907–10915.
118. R. Balda, S. García-Revilla, J. Fernández, R. I. Merino, J. I. Peña, and V. M. Orera (2009) Near infrared to visible upconversion of  $\text{Er}^{3+}$  in  $\text{CaZrO}_3/\text{CaSZ}$  eutectic crystals with ordered lamellar microstructure, *J. Lumin.*, **129** 1422–1427.
119. N. Nakagawa, H. Ohtsubo, Y. Waku, and H. Yugami (2005) Thermal emission properties of  $\text{Al}_2\text{O}_3/\text{Er}_3\text{Al}_5\text{O}_{12}$  eutectic ceramics, *J. Eur. Ceram. Soc.*, **25** 1285–1291.
120. N. I. Zheludev (2010) The road ahead for metamaterials, *Science*, **328** 582–583.
121. D. A. Pawlak, S. Turczynski, M. Gajc, K. Kolodziejak, R. Didusko, K. Rozniatowski, J. Smalc, and I. Vendik (2010) How far are we from making metamaterials by self-organisation? The microstructure of highly anisotropic particles with SSR-like geometry, *Adv. Funct. Mater.*, **20** 1116–1124.
122. R. Shelby, D. R. Smith, and S. Schultz (2001) Experimental verification of a negative refraction index, *Science*, **292** 77–79.
123. J. Briggs and P. E. Hart (1976) Refractory oxide-metal eutectics, *J. Am. Ceram. Soc.*, **59** 11–12.

124. R. I. Merino, J. I. Peña, and V. M. Orera (2010) Compositionally graded YSZ/NiO composites by surface laser melting, *J. Eur. Ceram. Soc.*, **30** 147–152.
125. A. Revcolevschi and G. Dhallenne (1985) Crystallographically aligned metal-oxide composite made by reduction of a directionally solidified oxide-oxide eutectic, *Nature*, **316** 335–336.
126. L. Ortega-San-Martin, J. I. Peña, Á. Larrea, and V. M. Orera (2011) Directionally solidified CeO<sub>2</sub> (or GDC)/CoO eutectic ceramics as cermet precursors for SOFCs anodes. Microstructure cross-over, *J. Eur. Ceram. Soc.*, **31** 1269–1276.
127. J. H. Lee, A. Yoshikawa, S. D. Durbin, D. H. Yoo, T. Fukuda, and Y. Waku (2001) Microstructure of Al<sub>2</sub>O<sub>3</sub>/ZrO<sub>2</sub> eutectic fibers grown by the micro-pulling down method, *J. Cryst. Growth*, **222** 791–796.
128. E. R. M. Andreetta, M. R. B. Andreetta, and A. C. Hernandez (2002) Laser heated pedestal growth of Al<sub>2</sub>O<sub>3</sub>/GdAlO<sub>3</sub> eutectic fibers, *J. Cryst. Growth*, **234** 782–785.
129. J. I. Peña, R. I. Merino, G. F. de la Fuente, and V. M. Orera (1996) Aligned ZrO<sub>2</sub> (c)-CaZrO<sub>3</sub> eutectics grown by the laser floating zone method: Electrical and optical properties, *Adv. Mat.*, **8** 909–912.
130. G. Dhallenne and A. J. Revcolevschi (1984) Directional solidification in the NiO-ZrO<sub>2</sub> system, *J. Cryst. Growth*, **69** 616–618.
131. L. Ortega-San-Martín, J. I. Peña, V. Gil, and V. M. Orera (2010) Textured cermets of CoO(GDC) with Co for solid oxide fuel cells, *Int. J. Hydrogen Energy*, **18** 13842–13850.



# SOLID FREE-FORM FABRICATION OF 3-D CERAMIC STRUCTURES

JAMES E. SMAY AND JENNIFER A. LEWIS

## 13.1 INTRODUCTION

Solid free-form fabrication (SFF) refers to a set of computer-aided design and manufacturing (CAD/CAM) tools for building three-dimensional (3-D) objects through a layer-by-layer patterning of materials. In the last two decades, SFF has evolved to enable the assembly of complex structures with a rich pallet of materials for myriad applications. In contrast to subtractive techniques, such as machining, SFF deposits or selectively fuses the feedstock material in an additive manner [1]. SFF feedstock materials can range from hydrogels to alloy metals and advanced ceramics. The breadth of materials used and techniques developed has led to a number of nearly synonymous names for SFF, including rapid prototyping, 3-D printing (3DP), and direct writing. Each name has a slightly different meaning to a specialized group of practitioners. In this chapter, SFF is used as the common descriptor for additive manufacturing techniques and specific processes are defined as they arise. Here, the most popular SFF techniques used by the ceramics community are highlighted, along with the commonalities and differences between them.

The steps common to all SFF techniques are (1) *computer-aided design* (CAD), (2) *deposition*, and (3) postprocessing of the component, which may include further

---

*Ceramics and Composites Processing Methods*, First Edition. Edited by Narottam P. Bansal and Aldo R. Boccaccini.

© 2012 The American Ceramic Society. Published 2012 by John Wiley & Sons, Inc.



assembly [2], sintering, or machining. The design strategy is in part dictated by both the SFF tool as well as component geometry and performance requirements. Although there are several SFF techniques that enable patterning of ceramic materials, they can be broadly divided into two types: ones using pixel (or voxel)-based assembly, including 3DP [3–5], direct ink-jet printing [6–8], and laser-based printing [9–11], and others using filament-based assembly, including fused deposition modeling (FDM) [12–15], robocasting [16–22], and micropen writing [23]. Sheet assembly methods such as computer-aided manufacturing of laminated engineering materials (CAM-LEM) [24], which involved cutting and lamination of tape-cast layers, is another viable approach but will not be addressed in detail here. In the first section of this chapter, CAD will be described in the context of deposition processes that use either pixels (0-dimension), lines (1-dimension), or areas (2-dimensions) as the basic deposition unit. In the second section, processes that involve droplet- or filament-based direct writing of material will be described along with some of the critical process variables that affect the SFF techniques. The end result of the *deposition process* of ceramic SFF is a green body that must be sintered to obtain the desired ceramic component. Like other ceramic forming operations, the quality of printed structures depends on process variables such as particle size and uniformity within the green compact, binder content, rheology, drying behavior, and residual stress.

## 13.2 CAD

In all SFF methods, 3-D objects are formed by the sequential deposition of materials, typically in a layer-wise manner. The layers are of finite (and usually uniform) thickness and are parallel to a flat substrate. The fabrication process begins with defining the geometry to be deposited within each layer and preparing machine instructions for the motion controller of the SFF tool. For commercialized SFF methods, the user simply needs to master the particular software interface for the tool of choice. For customized SFF methods, one must create and/or translate a .stl (stereolithography) data file that describes the slicing and filling schemes required for a given 3-D component and then output machine instructions suitable for patterning it.

### 13.2.1 Stereolithography Files

The most common description of a 3-D object used in SFF is called a stereolithography file or .stl. The user may derive a .stl file by an export command from a solid modeling program (e.g., SolidWorks, AutoDesk Inventor, and Pro Engineer) or from medical imaging software. Whatever the source, the .stl file is an approximation of the solid model by a mesh of triangles covering the surface of the desired 3-D object. Each triangle has an outward pointing normal vector and three vertices. Figure 13.1 illustrates a simple 3-D object (a cup with stem) represented as a .stl file. In Figure 13.1b, the triangular mesh is highlighted. For this particular object, a query of the .stl indicates  $N = 1716$  facets in the mesh. The data structure of the .stl file consists of a simple listing of the spatial coordinates of vertices for each triangle along with the normal vector for

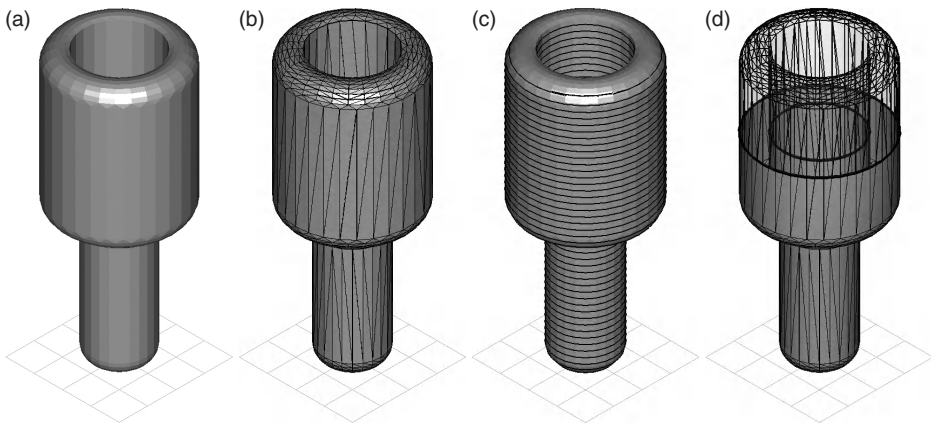


**Figure 13.1.** 3-D object represented as a .stl file. (a) Rendered representation with opaque surface skin, (b) rendered with highlighted surface mesh, (c) sliced .stl data showing perimeter lines, and (d) cutaway view showing the hollow interior of the .stl dataset.

```

Solid
:
  facet normal 0.0000000e+000 -4.5893296e-001 -8.8847090e-001
    outer loop
      vertex 2.7879299e+000 9.2413042e+000 1.7950979e+001
      vertex 1.5952655e+000 8.4439580e+000 1.8362842e+001
      vertex 1.4765428e+000 9.2413042e+000 1.7950979e+001
    endloop
  endfacet
  facet normal 0.0000000e+000 -1.4160305e-001 -9.8992352e-001
    outer loop
      vertex 2.7879299e+000 8.0170734e+000 1.8489814e+001
      vertex 2.7879299e+000 7.5760379e+000 1.8552901e+001
      vertex 1.7337974e+000 7.5760379e+000 1.8552901e+001
    endloop
  endfacet
  facet normal -1.4124857e-004 4.9353245e-001 -8.6972737e-001
    outer loop
      vertex 2.7879299e+000 6.1052390e+000 1.8278076e+001
      vertex 2.0947803e+000 5.6700298e+000 1.8031226e+001
      vertex 1.9970567e+000 6.1040825e+000 1.8277548e+001
    endloop
  endfacet
:
EndSolid

```

**Figure 13.2.** Excerpt from a .stl text file showing three facets.

each triangle pointing from the interior to the exterior of the object. An excerpt from a text-based .stl file is given in Figure 13.2, although .stl files are usually encoded into binary format for efficiency.

In this example, the facet label is followed by the key word *normal* and three floating point numbers that represent the *x*, *y*, and *z* coordinates of a normalized vector. The text between *outer loop* and *end loop* defines three vertices, each with three floating

point numbers representing spatial coordinates. In the .stl file, there is no information about node or edge sharing between the facets. The .stl mesh is simply a shell with no information about how to fill the interior of the object with material. For SFF, this shell must be sliced into parallel layers and tool paths designed for actual material deposition.

### 13.2.2 Slicing

The second operation in preparing .stl data for SFF is to intersect the 3-D object with a set of planes parallel to the deposition substrate and to extract a set of continuous polygons (perimeters) that separate the interior from the exterior of the object within each plane. In Figure 13.1, a set of perimeters is shown together with the .stl rendering and a cutaway at a single layer, respectively. In the cutaway view, it is apparent that the region between the two perimeter polygons is the interior of the object and the region outside these perimeters (including the hole in the middle) is the exterior of the object.

In Figure 13.3, another .stl object (a disk with six holes) is shown to have a uniform cross section. The slicing process yields a set of polygons in each layer, where the number of sides in each polygon corresponds to the number of facets intersected by

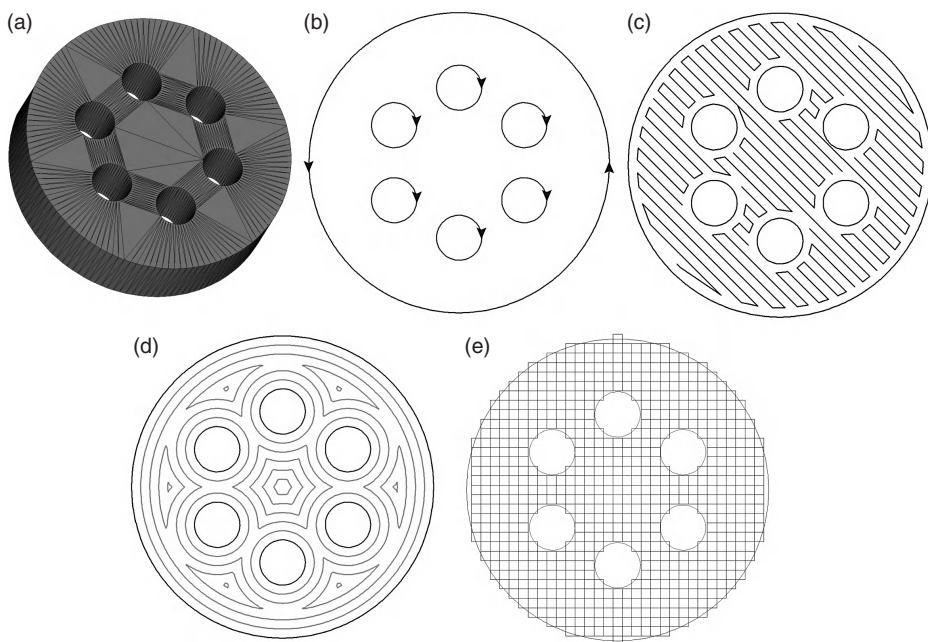


**Figure 13.3.** (a) Stereolithography (.stl) model of a disk with vias, (b) positive and negative loops from a representative slice, (c) raster fill tool path, (d) contour fill tool path, (e) pixel fill pattern [60].

the cutting plane. Since the facet data of the .stl houses the polygons in no particular order, the initial set of line segments defining each polygon is not necessarily linked in an orderly way. Thus, the second task of the slicing algorithm is to group and orient the line segments such that they form a set of continuous loops. The loops in Figure 13.3b are oriented counterclockwise if they enclose the interior of the .stl object or clockwise if they represent a hole. This orientation of loops is convenient for subsequent algorithms that must determine the method for filling the interior of the layer.

### 13.2.3 Filling (Tool-Path Generation)

The next step in the preparation of the dataset to be used in the deposition process depends on the way that material will be physically assembled to reproduce the layers on the SFF machine. For a process that can deposit an entire layer at once, for example, CAM-LEM [24], the closed loops shown in Figure 13.3b are sufficient to define a pattern to be traced by a cutting tool on a sheet of feedstock material prior to lamination (e.g., a laser cutting path on a green ceramic tape). For pixel- and filament-based processes, explicit instructions must be derived that command the deposition device to fill the interior of the slice.

For processes that use small droplets as the basic assembly unit, a pixel-based approach to filling the layer is appropriate. In Figure 13.3e, a rectangular grid is overlaid atop the perimeters defined for the layer. Each pixel in the grid is determined to be inside, on, or outside the perimeter. This grid is a simple bitmap with internal and edge pixels representing material deposition points and those outside the perimeters as blank pixels. For the pixel approach to be a successful strategy, the deposition tool must possess the capability to rapidly and repeatedly switch the state of material deposition from on to off or vice versa. For laser printing and ink-jet devices, the deposition tools can simply raster across the area and deposit material in the required pixels. The size of the pixels depends on the minimum spot (or drop) size of the deposition tool. For a coarse spot size, there may be some aliasing of curved edges.

Tool paths for filament-based printing devices are usually defined as raster patterns (Fig. 13.3c), contour patterns (Fig. 13.3d), or a combination of these styles. The key constraints of these patterns are the discrete width of the deposited filament and an acknowledgement that the deposition tool works best when the number of on-off sequences is minimized. The tool path is designed with a fixed spacing between the lines (sometimes called road width) while avoiding intersections of lines. In Figures 13.3c–d, the centerline for the filament deposition is shown as solid lines and the white space between is considered to be filled by adjacent filaments. For raster filling, as in Figure 13.3c, the parallel raster lines are connected in such a way as to minimize the number of times the deposition tool must execute the on-off-on sequence associated with the end point of one line and the start of a new line. The algorithm for generating the raster pattern consists of overlaying a set of parallel lines atop the slice perimeters, trimming away sections of those lines outside the perimeters, and connecting the remaining parallel segments into the raster pattern. The raster filling approach is subject to systematic errors attributed to filling layers that may contain curved perimeters with a finite set of straight, fixed width lines.

Contour filling, illustrated in Figure 13.3d, is the most complex tool-path calculation scheme. As can be seen in the figure, each set of contour lines is a fixed distance away from the perimeter lines defining the slice. The increment between contour line sets is the road width of the filament to be deposited. Many strategies for calculating offset contours have been devised, usually with accuracy and low computation time as the motivating factors. One straightforward approach to calculate the offset contours is to calculate a distance function from the perimeter lines on a series of grid points that are interior to the layer. Next, isodistance contour lines are calculated within this grid using an interpolation scheme (e.g., marching squares). The number and shape of the contour lines at each distance from the perimeter, as illustrated in Figure 13.3d, evolves as one moves from the exterior to the interior of the layer. Artifacts in the tool path are present with contour filling including potentially vacant regions at sharp corners in the pattern and loops that are internally too close as the distance function converges toward the interior of the layer.

### 13.2.4 Support Structure

After slicing and calculation of tool paths for each layer, the 3-D object is examined to identify whether support structures are needed. Figure 13.4 shows the four basic patterns encountered in SFF, with emphasis on a filament-based deposition tool. For space-filling solids, the deposited material must flow to form a continuous body without “knit lines” in or between layers. For high-aspect-ratio walls and spanning structures, the tool-path spacing within individual layers must exceed the deposited droplet or filament width. In the case of spanning structures, gaps in underlying layers must be bridged by overlying layers. The final case is cantilevered and floating elements, in which portions of layers are either completely unsupported (floating) or attached to underlying layers in a cantilevered fashion. For filling patterns that consist of solid layers, their stacking may lead to unsupported or cantilevered features in the overall structure. Hence, the calculation of a support structure is often required to complete the design process. A calculated support structure implies that the SFF process is capable of depositing a fugitive material that fulfills this function during the build process but may be easily removed in postprocessing. A mechanism for the removal of the support structure in the SFF of ceramics is often burnout along with any binder present in the deposited material.

### 13.2.5 Computer Numerical Control (CNC) Instructions

The result of the tool-path calculation is finally translated into machine instructions to control the positioning of the patterning device of the SFF machine. The CNC machining of materials is a well-established and documented manufacturing process. The commands used for SFF are a subset of these standards for motion control. Most often, the output commands for tool paths use G01 (linear interpolation) and G02 or G03 (clockwise and counterclockwise circular interpolation, respectively) for the tool commands within a layer. In addition to position, the velocity of the motion segments is equally important to the success of the SFF method. Subtractive machining rates are typically limited by the depth of cut, material properties, and cutting tool characteristics.

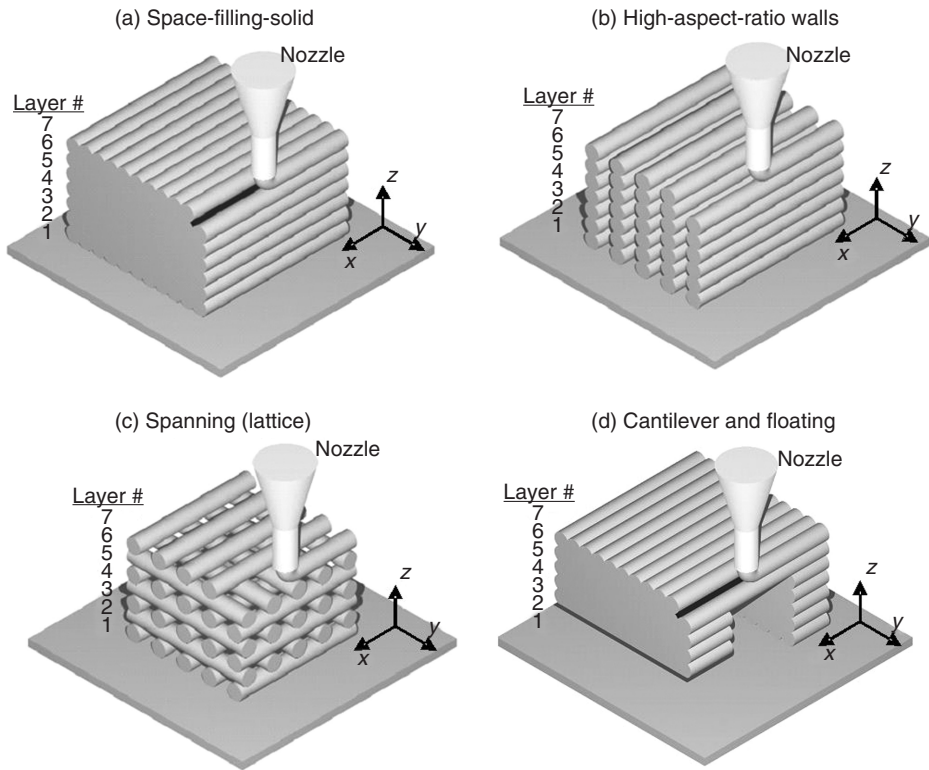


**Figure 13.4.** Four basic structural features encountered during solid free-form fabrication (a) space-filling solid layers, (b) high-aspect-ratio walls, (c) spanning elements, and (d) floating and cantilevered elements [61].

By contrast, SFF techniques (especially filament-based processes) usually deposit materials with a fixed volumetric flow rate. Hence, moving too quickly results in underfilling of the tool path, while moving too slowly results in overfilling. The CNC code for the SFF process must account for the deposition tool physics and calculate deposition speeds accordingly. The mechanical system of SFF machines is typically a set of three perpendicular linear actuators driven by servo or stepper motors. Straight and curved line segments within a layer can be accomplished by the coordinated motion of two axes. In addition to ensuring that the motion segments execute with fixed velocity, the CNC code must coordinate the on-off-on sequence of the deposition tool with the position in the calculated pattern. After defining a tool path, the deposition of material may begin.

### 13.3 COMPONENT DEPOSITION AND POSTPROCESSING

3-D ceramic components are typically produced by the droplet- or filament-based SFF techniques highlighted in Table 13.1. In Figure 13.5, the schematics of the SFF tools



TABLE 13.1. Droplet- and Filament-Based Solid Free-Form Fabrication Techniques [60]

Droplet-Based SFF	Ink Design	Minimum Printed Feature Size	References
3-D printing	Binder solution printed on powder bed	170- $\mu\text{m}$ lateral 45- $\mu\text{m}$ depth	[3]
Ink-jet printing	Colloidal fluid	20- $\mu\text{m}$ lateral 100-nm height	[7, 8, 25]
Hot-melt ink-jet printing	Concentrated colloid-filled wax (max solids ~40%)	70- $\mu\text{m}$ lateral <1- $\mu\text{m}$ height	[26–29]
Robocasting (in air)	Concentrated colloidal fluid	500- $\mu\text{m}$ diameter	[16–19, 46, 57]
Robocasting (in oil)	Concentrated colloidal gel	200- $\mu\text{m}$ diameter	[20, 21, 44]
	Concentrated nanoparticle gel	30- $\mu\text{m}$ diameter	[42]
Fused deposition	Particle-filled polymer melt (max solids ~50%)	100- $\mu\text{m}$ diameter	[12, 13, 15, 53, 63]
Micropen writing	Concentrated colloidal fluid	25- $\mu\text{m}$ diameter	[23]

used for four of these techniques are provided. Each SFF method has a unique set of requirements on the feedstock (or ink) design, as described below.

### 13.3.1 Droplet-Based SFF Techniques

Droplet-based approaches to fabricating 3-D ceramic structures typically rely on ink-jet printing of materials. Conventional inks for reprographic applications include dye- or pigment-based inks that are formulated using either a low-viscosity fluid that must be removed by absorption and evaporation or a wax-based system that is heated during droplet formation and then solidified upon impact cooling. These inks serve as models for the development of inks used in droplet-based deposition of ceramics.

**13.3.1.1 Ink Delivery** There are two types of ink delivery systems for droplet-based writing: (1) continuous [6, 7] and (2) drop-on-demand [8, 25–29] ink-jet printing. In either system, the ink is delivered as discrete droplets (see Fig. 13.5a,b) of fixed volume dispensed from a single or multinozzle array. The droplet size depends on the nature of the drop-generating nozzle and on the ink rheology. In continuous-jet printing, ink droplets must be electrically charged upon exiting the nozzle so that the droplet stream can be steered through deflecting electrodes before the ink reaches the substrate [7]. The deflected (or unprinted) droplets are recovered and recirculated through the ink reservoir. In drop-on-demand printing, ink droplets are produced only when required, either by exciting a piezoelectric actuator at a controlled frequency or by locally heating to create pressure pulses in a fluid chamber that cause the ejection of an ink droplet with each pressure cycle. A schematic illustration of a drop-on-demand nozzle is shown in Figure 13.5b. The continuous-jet method allows large areas to be patterned at rela-

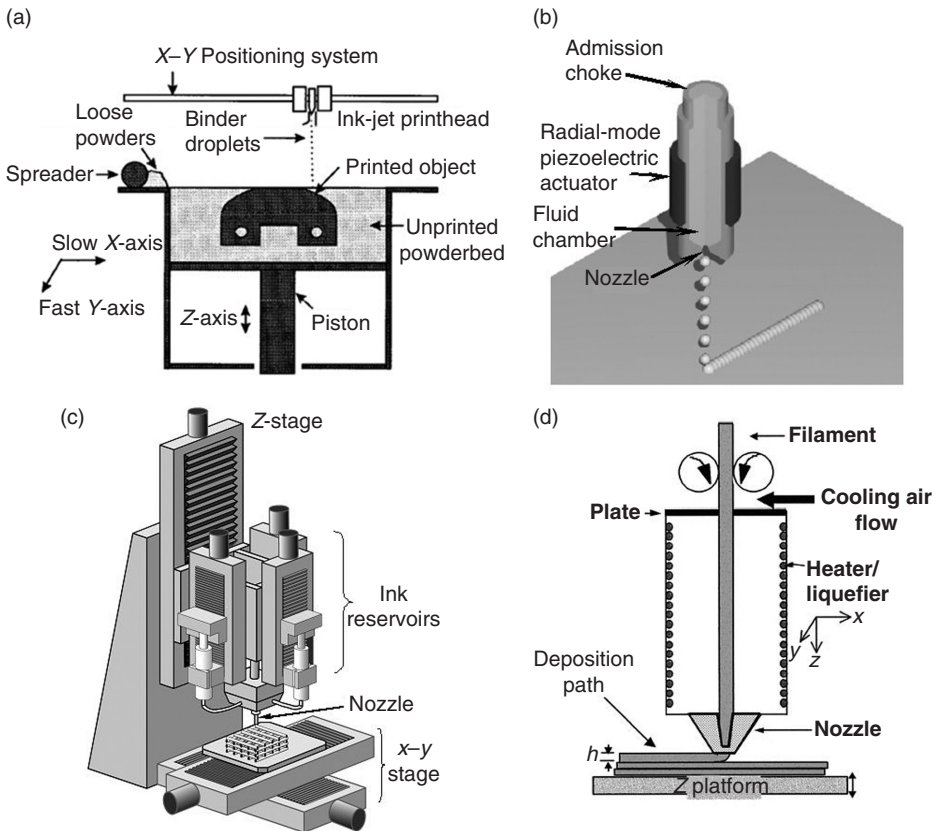


**Figure 13.5.** Schematic illustrations of both droplet- and filament-based direct ink writing techniques: (a) three-dimensional printing (3DP™) [20], (b) direct ink-jet printing (DIJP) [22], (c) robocasting [21], and (d) fused deposition of ceramics (FDC) [13]

tively high speeds, whereas the drop-on-demand method is better suited for depositing small and controlled quantities of material [3].

The fluid dynamics involved in drop formation and spreading plays an important role in the ink design. Reis et al. [26] and Seerden et al. [29] describe considerations for drop-on-demand printing, the salient features of which are summarized here. The behavior of fluid inks during the droplet formation process is dependent upon the Ohnesorge number ( $Z$ ) given by Equation 13.1:

$$Z = \frac{We^{1/2}}{Re} = \frac{\eta}{(\gamma \rho a)^{1/2}}, \quad (13.1)$$

where  $We$  is the Weber number ( $=\rho v^2 a / \gamma$ );  $Re$  is the Reynolds number ( $=\rho v a / \eta$ );  $v$  is the ink velocity;  $a$  is a characteristic length (i.e., nozzle diameter); and  $\eta$ ,  $\gamma$  and  $\rho$ ,



respectively, are the viscosity, surface tension, and density of the ink.  $Z$  expresses the relative importance of viscous, surface tension, and inertial forces on fluid flow. If  $Z$  is too high, then viscous forces dominate and a large pressure drop is required for droplet ejection. If  $Z$  is too low, then unwanted satellite droplets are produced. Successful drop formation (ejection) generally occurs for  $Z$  values of 0.1–1.

Drop spreading on impact influences the thickness of the deposited layer and the lateral resolution of materials produced by ink-jet printing. Drop spreading can be estimated by [29]

$$\frac{r_{\max}}{r} = \left( \frac{We^2 + 12}{3(1 - \cos \theta) + 4We^2/Re^{1/2}} \right)^{1/2}, \quad (13.2)$$

where  $r_{\max}$  is the maximum drop radius after impact,  $r$  is the initial drop radius, and  $\theta$  is the contact angle between the ink and the substrate. This expression represents an upper value for  $r_{\max}$  because drop spreading is evaluated for a dense substrate in the absence of solidification. In practice, droplet spreading is influenced by the porous nature of the underlying powder bed or printed structure as well as the time required for a given droplet to solidify after deposition.

A final concern for droplet-based SFF is the potential for the impinging droplets to splash on impact with the substrate (or underlying layers). Drop splashing occurs above a critical value of the parameter  $K$ :

$$K = WeRe^{1/4}. \quad (13.3)$$

For example, Seerden et al. [29] have reported  $K_{\text{crit}}$  values of 57.7 for water and methanol, and 102 and 137 for paraffin wax on cold (23°C) and hot (73°C) surfaces, respectively.

The speed with which a component can be assembled using droplet-based SFF is a function of the frequency of droplet generation, the dot pitch of the printer, and ink solidification kinetics. Assuming a fixed droplet diameter, the volumetric droplet delivery rate ( $Q$ ) for single-nozzle scales with its driving frequency ( $f$ ) is given by

$$Q = f \frac{4}{3} \pi r^3, \quad (13.4)$$

where  $r$  is the droplet radius. The linear write speed for a space-filling layer is given by

$$v = \frac{Q}{h\Delta y}, \quad (13.5)$$

where  $h$  is the layer thickness and  $\Delta y$  is the lateral droplet spacing (i.e., dot pitch). For example, a  $f = 5$  kHz jet of  $r = 35\text{-}\mu\text{m}$  droplets with layer and lateral spacings of  $h = 18\text{ }\mu\text{m}$  and  $\Delta y = 100\text{ }\mu\text{m}$ , respectively, result in  $Q = 0.9\text{ }\mu\text{L/s}$  and  $v = 0.5\text{ m/s}$ . This write speed does not account for delays that may be needed due to the solidification of previously deposited ink.

**13.3.1.2 Ink Rheology and Solidification** Three ink designs have been utilized to date in droplet-based approaches: (1) binder solutions [3–5], (2) colloidal fluids [6, 8, 30], and (3) colloid-filled waxes [26–29]. In each case, the inks must be formulated to achieve the desired drop formation and solidification behavior during assembly. In 3DP, ceramic structures are formed by spreading powder in a thin layer followed by selective deposition of binder-based droplets that locally fuse particles together upon drying (see Fig. 13.5a). Cima and coworkers [3] have shown that the infiltration behavior of these droplets into the powder bed depends strongly on polymer molecular weight, and that values less than 15,000 g/mol are required for this approach. Aqueous-based binder solutions are preferred over solvent-based formulations due to their improved jet stability. Binder concentration (or dose) has been shown to influence the size of the printed features created by 3DP (see Fig. 13.6).

Direct ink-jet printing of ceramics from colloidal inks was first demonstrated using inks that were solvent based [25, 28, 30], in which the droplets solidify by drying. More recently, wax-based [8, 26–29] inks, in which the droplets solidify by freezing the wax carrier, have been developed. For solvent-based systems, stable inks with a colloid volume fraction ( $\phi$ ) ranging from 0.025 [25] to 0.20 [28] have been successfully used. For these inks, particle agglomeration can lead to poor performance of the droplet-producing jet and eventual nozzle clogging. Steric dispersion of the ceramic particles followed by ultrasonication and sedimentation (or filtration) has been used to remove

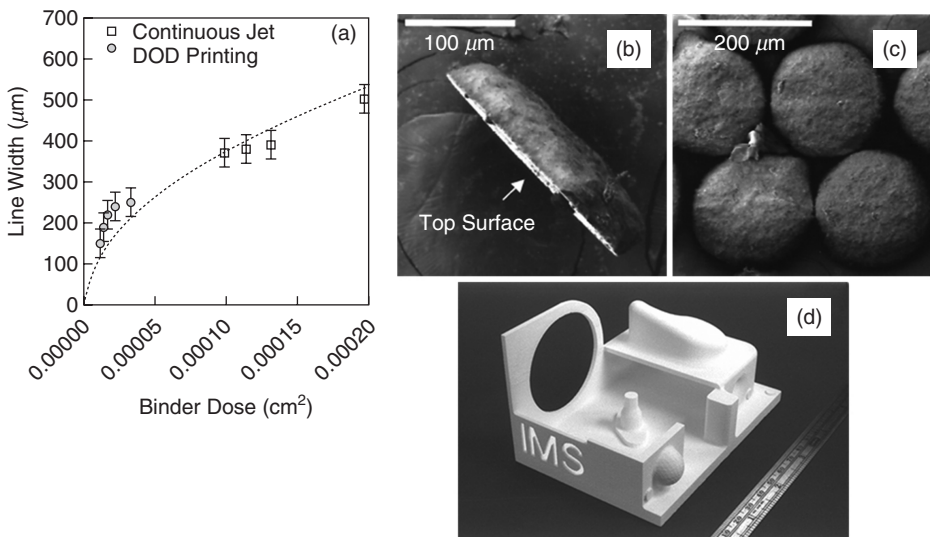


**Figure 13.6.** (a) Line width created by three-dimensional printing (3DP) of a 20 v/o polyacrylic acid (PAA) binder solution onto a 1-μm powder bed using a continuous jet or drop-on-demand (DOD) printhead. Corresponding (b) side view and (c) bottom view of a single-droplet primitive printed by the latter approach. (d) Optical image of component printed by 3DP ([a–c] from Reference 3).

problematic agglomerates [25]. Dilute inks ( $\phi = 0.025$ ) undergo significant droplet spreading and shrinkage upon drying, leading to printed layers with thin vertical and large lateral dimensions (i.e., approximately 0.4 and 200  $\mu\text{m}$ , respectively) [25]. To create structures of substantial thickness ( $>1 \mu\text{m}$ ), more concentrated colloidal fluids are necessary [8]. Dewetting of the substrate or underlying layers after droplet deposition can occur when the mobile fluid layer persists for appreciable times. To improve print quality, heated air can be flowed over the structure to enhance drying kinetics; however, the dwell time ( $\sim 20$  s) required leads to a significant bottleneck in the process [6, 8].

Wax-based inks [26–29] offer great promise for direct ink-jet printing of ceramics. These inks allow for rapid deposition, good lateral resolution, and high solids loading. In this case, the ink consists of a stable dispersion of ceramic particles in low melting temperature paraffin wax. Inks with high colloid volume fraction ( $\phi \sim 0.40$ ) have been successfully formulated, which exhibit a good fit to Krieger–Dougherty relation under suitable printing conditions (e.g., 110°C at shear rates of  $\sim 100$ – $200 \text{ s}^{-1}$ ) (see Fig. 13.7) [29]. These inks solidify upon deposition by initially cooling at a ring of contact with the underlying substrate, which mitigates further droplet spreading [29].

**13.3.1.3 Potential Shapes** To create 3-D ceramic components of predefined shape and dimensions, droplet-based SFF techniques rely on the pixel array approach illustrated in Figure 13.3e. In this scheme, each square in the overlaid mesh is filled by

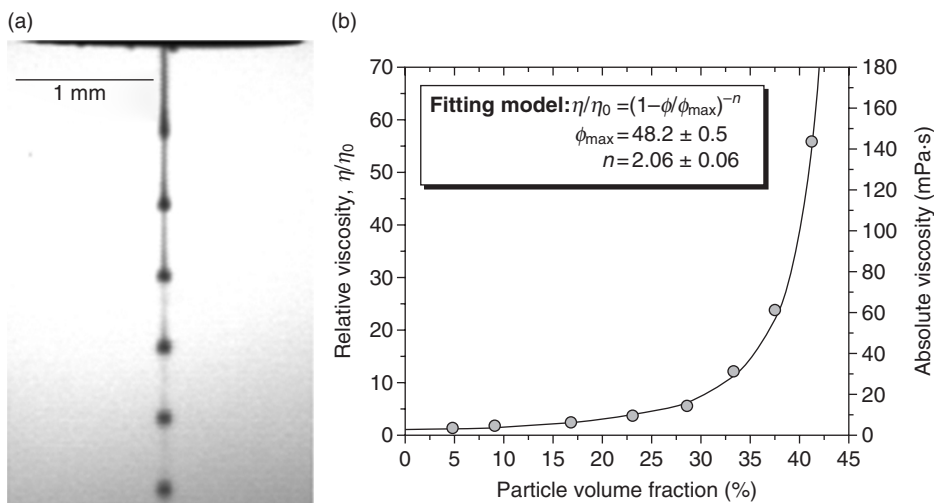


**Figure 13.7.** (a) Stroboscopic image of a concentrated lead zirconate titanate (PZT) suspension (40 vol % solids) being deposited by an ink-jet printhead with a nozzle diameter of 70  $\mu\text{m}$  at a pulse voltage of 70 V, a frequency of 10.5 kHz, a pulse width of 40  $\mu\text{s}$ , and a temperature of 110°C; and (b) suspension viscosity as a function of PZT volume fraction measured at a shear rate of  $\sim 100$ – $200 \text{ s}^{-1}$  and a temperature of 110°C. The continuous line in (b) is a fit of the data to the Krieger–Dougherty relation (from Reference 26).

a single droplet. The lateral and vertical resolution within the layer are determined by the droplet size, the extent of droplet spreading upon deposition on the substrate (or underlying layers), and the deformation of the droplet upon solidification. The printing rate is limited by the drying or solidification time required for the as-deposited droplets as well as the rate of droplet delivery by the nozzle.

3DP can be used to produce ceramic components with any of the four structural elements shown in Figure 13.3 since the unprinted regions of the powder bed provide support to the as-printed features (see, e.g., Fig. 13.6d). In sharp contrast, direct ink-jet printing is incapable of producing structures with spanning, cantilevered, or floating elements without the use of a fugitive support material. Fugitive formulations, such as unfilled wax or water-soluble inks, have been developed that can be removed during postprocessing [27].

Wang and Derby [27] recently printed solid, pyramidal  $\text{Pb}(\text{Zr}_{0.53}\text{Ti}_{0.47})\text{O}_3$  structures using a wax support as a buttress. Figure 13.8a–c shows the evolution from as-printed to sintered ( $\sim 99\%$  of theoretical) structures for this functional ceramic component [27]. This work builds on earlier efforts by Derby and coworkers [29], in which an alumina-filled ( $\phi = 0.30$ ) wax was printed at  $100^\circ\text{C}$  to form 3-D structures composed of high-aspect-ratio walls with a minimum lateral feature size of  $\sim 100\ \mu\text{m}$  (see Fig. 13.8d). In this example, the ink viscosity ranged from 7 to 15 mPa·s, the droplet velocity ranged from 5 to 10 m/s scaling linearly with the amplitude of the pressure pulse, and  $Z = 0.365$ . Alternatively, Evans and coworkers [8] demonstrated that similar structures (minimum wall thickness of  $\sim 200\ \mu\text{m}$ ) could be ink-jet printed under ambient conditions from colloidal fluids ( $\phi \sim 0.14$ ), as shown in Figure 13.8e.

**13.3.1.4 Post-Deposition Processing** The ceramic green bodies produced by droplet-based SFF can be sintered to high density (i.e.,  $>97\%$  of theoretical) [8, 27]. For binder solution (3DP) and solvent-based colloidal fluids, the as-dried green body contains sufficient polymeric binder ( $\sim 2\text{--}5\ \text{v/o}$ ) to facilitate post-deposition handling as well as their rapid removal during heat treatment. In the 3DP process, removal of the printed structure from the powder bed is a necessary step that may result in trapped powder in complex geometries.

For colloid-filled wax-derived structures, the organic content typically exceeds 50% by volume. While this results in high green strength, it also leads to two major problems that arise during binder removal. First, the overall time required to remove the organic phase can be rather lengthy. For example, the samples shown in Figure 13.4a–c required 62 h of debinding [27]. Second, these components can experience significant dimensional changes (or slumping) during the debinding process since both ink and fugitive support liquefy at modest temperatures. To combat dimensional changes, Wang and Derby [27] have packed their structures in carbon black powder to aid in initial wax removal and to provide additional structural support.

## 13.3.2 Filament-Based SFF Techniques

Filament-based approaches to fabricating 3-D ceramic structures include robocasting [16–19, 31], fused deposition of ceramics (FDC) [12–15], multiphase jet solidification

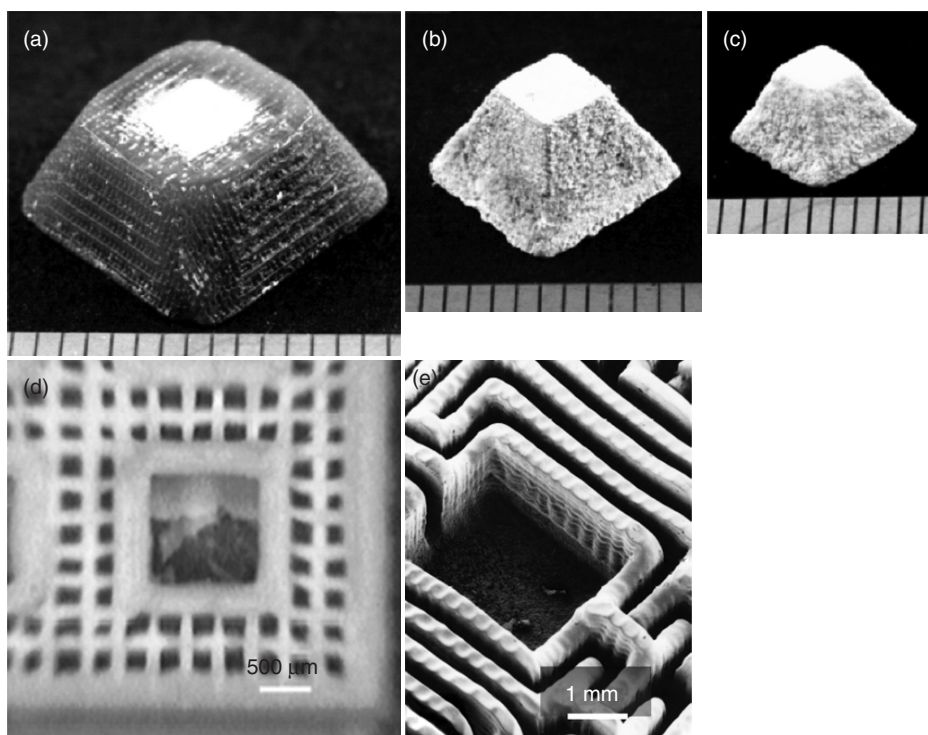


**Figure 13.8.** (a–c) Optical image sequence of a ceramic object produced by hot-melt printing of a lead zirconate titanate ink (40 vol % solids) at 110°C, showing (a) the as-printed object with external wax support, (b) the object after the external support is removed, and (c) the structure after sintering. (Note: Scale divisions are 1 mm.) (d) Optical image of a ceramic object produced by hot-melt printing of an alumina ink (30 vol %) at 100°C, in which the pore channels are connected in only one dimension. (e) Optical image of a ceramic object produced by direct ink-jet printing of a zirconia ink (14 vol % solids) (images [a–c] from Reference 26, [d] from Reference 29, and [e] from Reference 8).

(MJS) [32], extrusion free-form fabrication (EFF) [33–35], and micropen writing [23]. In each approach, ink is continuously extruded through a fine cylindrical nozzle (or orifice) to create a filamentary element. Robocasting, FDC, EFF, and MJS are well suited for the assembly of 3-D ceramic components, while micropen writing is better suited for producing multilayer electroceramic devices on planar and curvilinear substrates.

**13.3.2.1 Ink Delivery** There are two types of ink delivery systems for filament-based patterning: (1) constant displacement and (2) constant pressure extrusion. In either system, the ink is extruded as a continuous filament through a single or multi-nozzle array. The filament diameter is determined by the nozzle diameter, ink rheology,

and printing speed. During constant displacement printing, ink filaments are extruded at a uniform volumetric flow rate. For example, in robocasting, this is done by mechanically displacing the plunger on the ink reservoir at the pressure required to maintain the desired flow conditions (see Fig. 13.5c). In fused deposition, a colloid-filled polymer filament is extruded at a constant rate through a heated liquefier, where it melts to form a shear-thinning, particle-filled organic fluid. The flow rate is controlled by the rate at which the starting filament is fed into the heated liquifier chamber (see Fig. 13.5d). EFF and MJS feed the liquefier chamber with a powder blend of ceramic and binder [32, 36, 37]. In constant pressure writing, ink filaments are extruded by applying a uniform pressure to the reservoir. This approach is less common since slight variations in rheological properties induce fluctuations in the volumetric flow rate.

The ink flows through the deposition nozzle when a pressure gradient,  $\Delta P$ , is applied along the length and a radially varying shear stress ( $\tau_r$ ) develops:

$$\tau_r = \frac{r\Delta P}{2\ell}, \quad (13.6)$$

where  $r$  is the radial position within the nozzle (i.e.,  $r = 0$  at the center axis and  $r = R$  at the nozzle wall). Depending upon the velocity profile and the ink stability, plug or laminar flow may occur within the nozzle [20, 38]. For example, colloidal gel-based inks consisting of a percolating network of attractive particles are capable of transmitting stress above a critical volume fraction,  $\phi_{\text{gel}}$  [20]. When stressed beyond their yield point ( $\tau_y$ ), they exhibit shear-thinning flow behavior due to the attrition of particle-particle bonds within the gel, as described by [39]

$$\tau = \tau_y + K\dot{\gamma}^n, \quad (13.7)$$

where  $\tau$  is the shear stress,  $n$  is the shear-thinning exponent ( $<1$ ),  $K$  is the viscosity parameter, and  $\dot{\gamma}$  is the shear rate. Gel-based inks flow with a three-zone velocity profile within the cylindrical deposition nozzle that consists of an unyielded (gel) core moving at a constant velocity surrounded by a yielded (fluid) shell experiencing laminar flow and a thin slip layer devoid of colloidal particles at the nozzle wall [38, 40]. The ink exits the nozzle as a continuous, rodlike filament with a rigid (gel) core-fluid shell architecture, which simultaneously promotes their shape retention while allowing the rods to fuse together at their contact points. The rod architecture is dynamic in nature, such that the fluid shell transforms to the gelled state as particle bonds reform [41]. Inks without yield stress are extruded with a laminar flow pattern.

**13.3.2.2 Ink Rheology and Solidification** Two ink designs are used in filament-based SFF approaches: (1) Robocasting utilizes colloidal gels carried in a volatile solvent [20, 21, 31, 42], and (2) FDC utilizes colloid-filled thermoplastic polymers [12–15]. In each case, the inks must be formulated to achieve the desired rheological filament formation and solidification behavior during assembly. In its original conception, robocasting involved the filamentary extrusion of concentrated colloidal gels that were cast and dried in air [19]. More recently, concentrated colloidal [20] and



nanoparticle gels [42] have been extruded into a nonwetting oil bath that suppresses drying and allows finer features to be deposited without clogging the nozzle. Initial shape retention is achieved by the rapid dynamic recovery ( $\sim 1$  s) of the gel elasticity (i.e., yield stress and modulus) after extrusion [20, 43], followed by the removal of the oil and final drying. In FDC [12, 15], a colloid-filled polymer melt is extruded at elevated temperature and solidification occurs upon cooling. This process evolved from FDM, in which pure polymeric filaments are used as feedstock.

Cesarano et al. [19] pioneered the use of flocculated colloidal suspensions (or gels) as inks for robocasting of ceramics. Filament formation and initial shape retention were achieved by the yield strength and high viscosity of the ink coupled with drying. These inks were formulated close to the maximum solids loading (ca.  $\phi_{\max} \sim 0.6\text{--}0.64$ ) to minimize drying-induced shrinkage and cracking. Upon slight drying, the ink filaments experienced a rapid increase in viscosity and transition from a pseudoplastic to a dilatant behavior. Robocasting in air is well suited to deposition through nozzles with diameters exceeding  $500\text{ }\mu\text{m}$ . Rapid drying of finer filaments caused ink buildup on the deposition nozzle and led to clogging. Robocasting with *in situ* drying is well suited for assembling relatively large ceramic structures including those with spanning features. For successful printing, the ink deposition rate must be matched to allow for sufficient drying during the build sequence since drying kinetics are influenced by component geometry.

More recently, Smay et al. [20, 21, 44] have demonstrated that robocasting inks utilizing a higher initial yield stress, but with reduced solids loading, allow for direct writing of structures without commensurate drying. In fact, these inks may be cast in an oil bath to eliminate ink clogging in nozzles with features finer than  $100\text{ }\mu\text{m}$ . Depositing inks into a nonwetting oil reservoir suppresses drying and decouples the build process from the drying process.

In either case, these inks must have a controlled viscoelastic response; that is, the colloidal gels must flow through a deposition nozzle and then “set” immediately to facilitate shape retention of the deposited features even if they span gaps in the underlying layer(s). The colloidal gel must also have the capability to fuse to previously deposited material. These characteristics are achieved with careful control of colloidal forces to first generate a highly concentrated, stable dispersion followed by inducing a system change (e.g.,  $\Delta\text{pH}$ , ionic strength, or solvent quality) that promotes the fluid-to-gel transition illustrated schematically in Figure 13.9a. Specifically, the colloid volume fraction ( $\phi$ ) of the gel-based inks is held constant, while their elastic properties are tuned by tailoring the strength of the interparticle attractions according to the scaling relationship [45] given by

$$y = k \left( \frac{\phi}{\phi_{\text{gel}}} - 1 \right)^x, \quad (13.8)$$

where  $y$  is the elastic property of interest (shear yield stress  $[\tau_y]$  or elastic modulus  $[G']$ ),  $k$  is a constant,  $\phi_{\text{gel}}$  is the colloid volume fraction at the gel point, and  $x$  is the scaling exponent ( $\sim 2.5$ ). The equilibrium mechanical properties of a colloidal gel are governed by two parameters:  $\phi$ , which is proportional to the interparticle bond density,

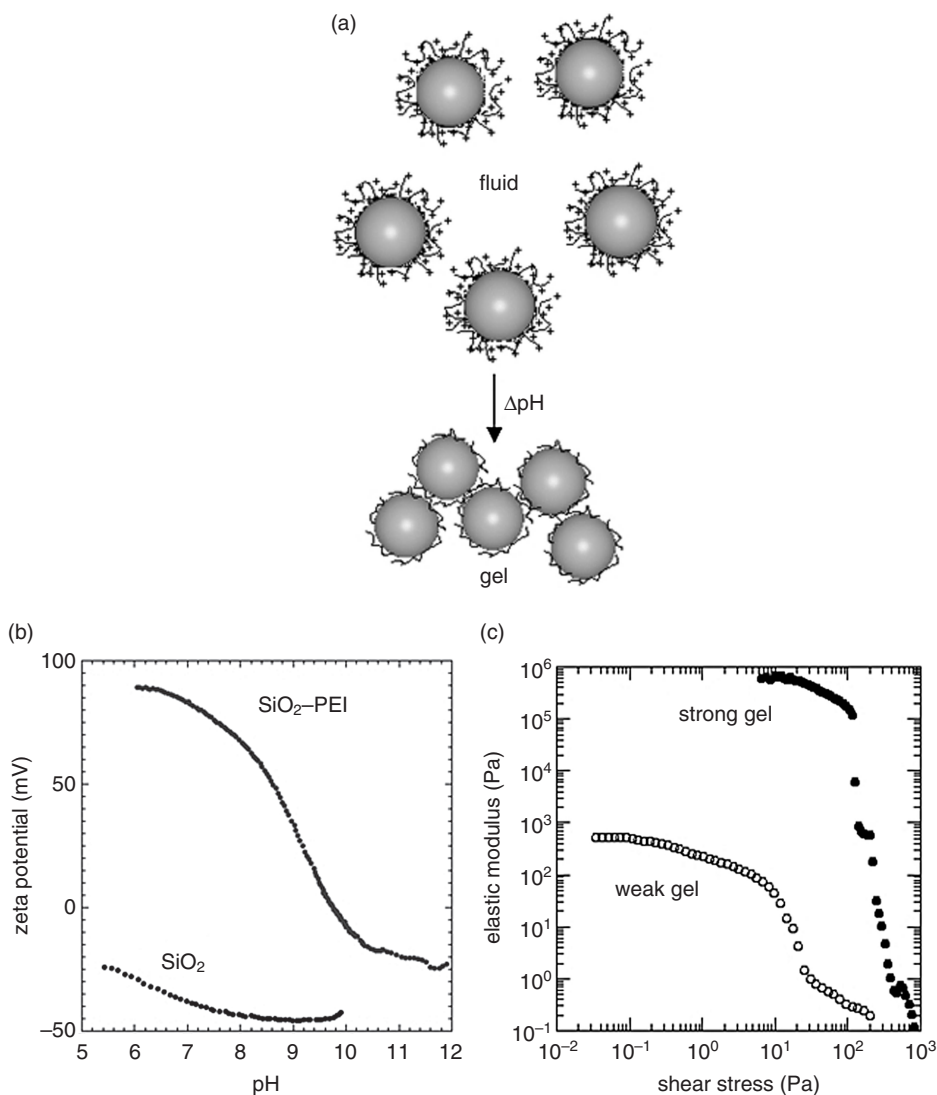


**Figure 13.9.** (a) Schematic illustration of the fluid-to-gel transition observed for colloidal inks, (b) plot of zeta potential versus pH for a dilute suspension of poly(ethylenimine) (PEI)-coated silica ( $SiO_2$ -PEI) and bare silica ( $SiO_2$ ) microspheres in water, (c) corresponding log-log plot of their shear elastic modulus versus shear stress for concentrated silica gels of varying strength: open symbols denote weak gel (pH 9.5) and filled symbols denote strong gel (pH 9.75) (Note: The point-of-zero charge for PEI-coated silica microspheres occurs at pH 9.75, which is significantly above the value [pH 2–3] observed for bare silica particles. The weak gel had insufficient strength to support its own weight during deposition, whereas the strong gel could be successfully patterned into 3-D periodic structures) (from Reference 21).



and  $\phi_{\text{gel}}$ , which scales inversely with bond strength. As the attractive forces between particles strengthen, colloidal gels (of constant  $\phi$ ) experience a significant increase in their elastic properties (see Fig. 13.9b,c). As described by Smay et al. [20], the magnitude of the yield stress and the time required for the deposited ink to fully return to its gelled state control the ability of the ink to build unsupported spanning structures.

This general approach of creating colloidal gel-based inks can be extended to any type of colloidal or nanoparticulate material provided their interparticle forces are controlled to produce the desired viscoelastic response. In addition to a simple pH change, the requisite ink rheology may be achieved through the addition of salt [42, 46] or oppositely charged polyelectrolyte species [43, 47], as recently demonstrated for nanoparticle and other colloidal inks, respectively. These strategies have been employed to produce colloidal inks from a broad array of ceramic materials, including silica [21], alumina [19, 47], lead zirconate titanate (PZT) [22, 44], barium titanate [42, 43], mullite [46], silicon nitride [48–50], and hydroxyapatite [51, 52].

Safari and coworkers [12, 15, 53] pioneered FDC, where the stiffness of the filamentary feedstock as well as the viscosity of the colloid-filled, molten polymeric ink that exits the heated liquefier must be well controlled. In the molten state, inks must possess both a low viscosity and a high solids loading (to minimize firing shrinkage). Akin to injection molding [53], a high degree of dispersion of the ceramic particles in the polymer is necessary to achieve these requirements. As a result of their high colloid volume fraction ( $\sim 0.5$ – $0.55$ ), molten FDC inks exhibit a strong shear-thinning behavior (see Fig. 13.10). Upon deposition, these filaments solidify first at their outer surface and then radially through their core—the exact opposite of the solidification profile observed for colloidal gel-based inks used in robocasting.

Numerous inks have been formulated for FDC including those based on structural, biomedical, and electrical ceramics [12–15]. The filled polymer filaments have the advantage of long shelf life after initial forming. Melt temperature and extrusion rate

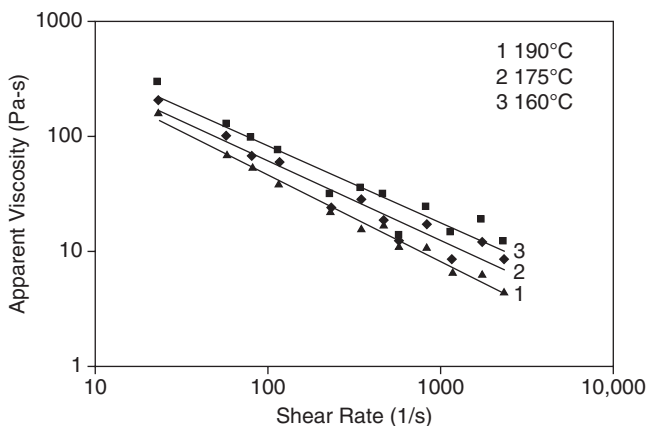


**Figure 13.10.** Apparent viscosity as a function of shear rate for a lead zirconate titanate ink formulated for FDC heated to varying temperatures [53].

(write speed) must be coordinated to match the specific cooling kinetics of a given ink. Fugitive support materials, for example, unfilled wax filament or water-soluble material developed for FDM, are readily available. A key disadvantage of the FDC approach is significant binder content in printed structures, which necessitates a lengthy binder removal procedure. It has recently been reported that the burnout cycle may take several days and can lead to structural defects such as slumping or blistering due to melting of the thermoplastic polymers [15].

**13.3.2.3 Potential Shapes** In filament-based SFF, the ink is deposited as a continuous filament. Hence, the interruption of ink flow during assembly is not desirable, so calculations of area filling patterns (tool paths) that minimize the number of start-stop events are useful. Two strategies are employed: (1) direction-parallel (or raster) filling and (2) contour-offset filling, as illustrated in Figure 13.2c,d, respectively. Optimized computational algorithms for each of these tool-path calculations have been described in the literature for milling processes [54]. In both cases, the spacing between adjacent lines is chosen by the user, most often set to be equivalent to the width of the extruded ink filament.

A coordinated three-axis motion is achieved by outputting the calculated tool path to a CNC controller. The CNC controller also controls the plunger motion of syringe pumps holding the ink, such that volumetric flow rate is tied to position in the tool path. The tool-path calculations yield either raster or contour offset fill patterns. In either case, filament-based printing faces at least three problems. First, when building solid objects, the ink delivery system must precisely deliver the proper volume of material to perfectly fill the space between adjacent tool-path lines. The tool-path lines represent the locus of points traced by the centerline of the deposition nozzle, but the extruded filament has a finite diameter (assuming the orifice is circular). The required volumetric flow rate required for filling space is given by

$$Q = h \cdot RW \cdot v, \quad (13.9)$$

where  $RW$  is the road width (distance between adjacent tool-path lines). For example, if  $RW$  is set equal to the deposition nozzle diameter ( $d$ ) and

$$Q = \frac{\pi d^2}{4} v,$$

the layer thickness must be

$$h = \frac{\pi d}{4}.$$

The selection of which variables to fix is a matter of user preference and ink behavior. Since the extrusion nozzle is nearly always circular in cross section, the filament must deform upon extrusion to fill the space traced by the nozzle.

The second challenge faced when using a raster or contour tool path is the inevitable need to stop the ink flow, to reposition the nozzle on a new tool path, to reinitiate

the flow, and to continue printing. For filament-based printing, it is desirable to minimize the number of start-stop events. Algorithms have been proposed to minimize either the number of start-stop events or the distance between the start and stop positions when changing tool-path lines [55]. Figure 13.2c is generated based on the latter algorithm. A corollary to the first and second challenges to layer filling is the potential for underfilling at locations with small radii of curvature along the tool path (e.g., at the hairpin turns in the raster pattern) or where curved paths must be approximated with straight segments, such as near the interior holes in the raster pattern. Intelligent algorithms are still under development for these calculations [55] that should enable local variations in flow rate during the writing process.

The third challenge of tool-path calculation involves consideration of the stacking of layers when spanning, cantilevered, or floating elements exist. Algorithms for calculating unsupported regions of the pattern are required along with a suitable fugitive ink. FDC utilizes a second deposition nozzle to print an unfilled wax or water-soluble support material. In the case of printing colloidal fluids or gels, a suitable support should print, solidify, and be chemically compatible with the colloidal ink. Recently, a concentrated ( $\phi \approx 0.48$ ) aqueous gel of carbon black nanoparticles was used as a support material to assemble structures containing both cantilevered elements composed of a spanning lattice [56]. Figure 13.11a–c illustrates green, bisque-fired, and sintered hydroxyapatite hollow cubes, respectively. In Figure 13.11b, the carbon black support has been removed without deformation of the ceramic structure.

High-aspect-ratio wall and spanning lattice structures assembled from the piezoelectric ceramic  $\text{Pb}(\text{Zr}_{0.53}\text{Ti}_{0.47})\text{O}_3$  illustrate the similar capabilities of robocasting and FDC (see Fig. 13.12). These structures serve as the ceramic skeletons for 2-2 and 3-3 PZT–polymer composites, which are known to display high piezoelectric coefficients and low acoustic impedance, making them attractive for modern sonar and ultrasound systems [15, 44]. In both techniques, high-aspect-ratio and lattice structures are created without the need for support structures. Spanning structures require a solidification time comparable to the time required to traverse the gap in underlying layers. For gel-based inks, the solidification time is of the order of 1 s such that structures with appreciable spanning features may be printed at high speed ( $\sim 1$  cm/s), whereas FDC requires longer

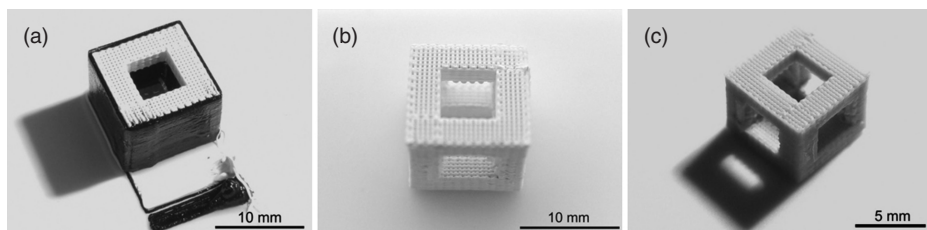


**Figure 13.11.** Open cubic structure assembled from by robocasting a concentrated hydroxyapatite ink and a carbon black ink as a fugitive support: (a) as-printed, (b) bisque-fired structure, and (c) sintered ceramic (from Reference 60).

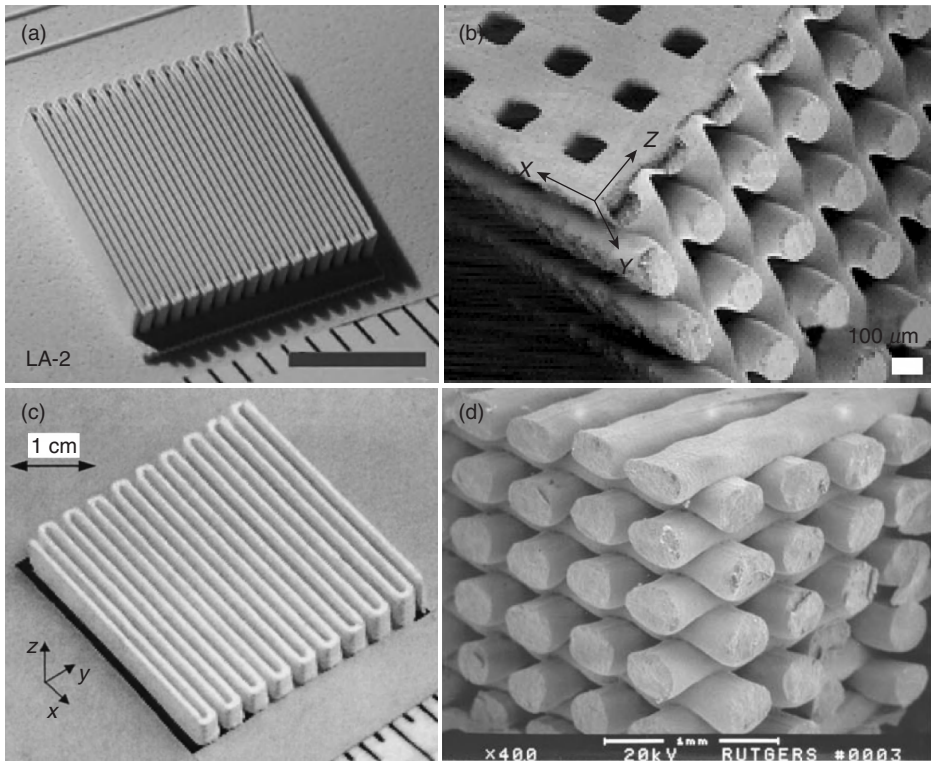


**Figure 13.12.** Piezoelectric ceramic structures formed by filament-based SFF of lead zirconate titanate inks: (a) high-aspect-ratio walls (green, scale bar = 5 mm) [62] and (b) spanning lattice structure (sintered) formed by robocasting [62]. (c) High aspect ratio [63] and (d) spanning lattice structures [12] (green) formed by FDC.

to solidify (especially as filament size increases), thereby reducing the printing speed or span distance.

**13.3.2.4 Post-Deposition Processing** Analogous to droplet-based SFF techniques, ceramic green bodies produced via filamentary SFF contain varying amounts of binder and can be sintered to high density (>97% of theoretical). Robocasting of concentrated gel-based inks yields ceramic green bodies with minimal binder (~2–3 v/o). While their green strength is lower than that of FDC, it may be improved by chemically cross-linking the polymeric species [57]. An important advantage of this route is that binder removal is rather straightforward, with typical debinding schedules of only a few hours required. In sharp contrast, FDC relies on a polymer-rich ink that must be carefully removed on subsequent heat treatment. The binder removal issues are similar to that for wax-based droplet SFF (and injection molding) in that debinding times of several days are often required and component slumping may occur.

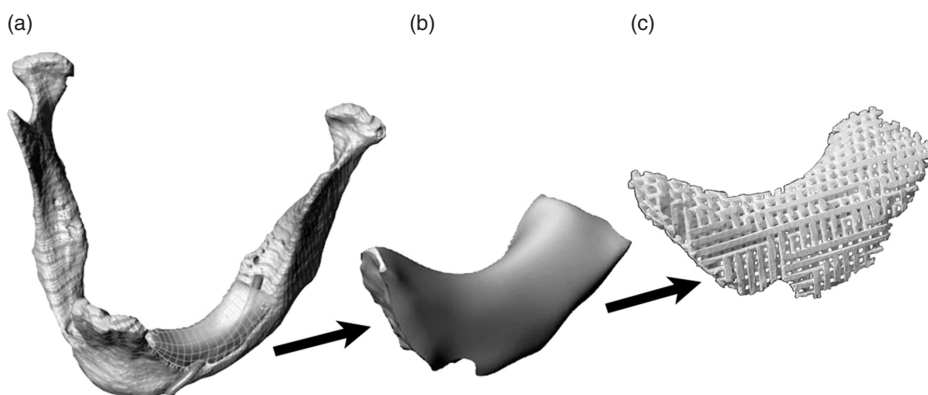


**Figure 13.13.** An image sequence representing the processing steps required to customize a hydroxyapatite (HA) scaffold that fits into a damaged site in a patient's mandible (jaw bone): (a) 3-D rendered image compiled from a computed tomography (CT) scan of the severely deteriorated mandible shown along with the desired anatomy of the mandible, (b) an isolated view of the solid 3-D model defining the desired implant shape, and (c) an optical image of a periodic HA structure that has been machined into a porous bone scaffold [58].

Despite the promise of near-net-shape fabrication, some applications require precise geometric tolerances that may not be achieved solely through SFF. In these cases, it is advantageous to subsequently machine either the green- or bisque-fired ceramic component via CNC milling. As one example, hydroxyapatite scaffolds of controlled filament size, spacing, and porosity have shown great promise for bone repair [58, 59]. Cesarano and coworkers [58] have shown that robocast scaffolds can be further machined into a customized implant that fits into an individual's unique defect following the methodology shown in Figure 13.13. The defective region is first mapped using computed tomography (CT), and these data are then used to manufacture a customized implant prior to surgery. This final shaping of the 3-D scaffold is required because the dimensional tolerance necessary for an implant is less than the diameter of the individual HA filaments.

## 13.4 CONCLUSIONS

In this chapter, SFF for assembling 3-D ceramic objects has been discussed. The direct write techniques described revolved around strategies for delivering ceramic particles to an evolving structure by droplet or filament deposition. Although the laser-based and laminated object manufacturing techniques were not discussed in detail, the underlying motif of layer-by-layer assembly of materials is the key hallmark. The ceramist wishing to utilize SFF to assemble a prototype structure must consider the preprocessing, deposition, and postprocessing aspects of SFF. The examples given here illustrate the diverse types of structures that may be assembled and some typical process parameters that impact the fidelity of the produced parts.

## REFERENCES

1. D. B. Chrisey (2000) The power of direct writing, *Science*, **289**[5481] 879–881.
2. B. Y. Ahn, et al. (2010) Printed origami structures, *Advanced Materials*, **22** 2251–2254.
3. J. Moon, et al. (2002) Ink-jet printing of binders for ceramic components, *Journal of the America Ceramic Society*, **85**[4] 755–762.
4. E. Sachs, et al. (1992) CAD-casting: Direct fabrication of ceramic shells and cores by three dimensional printing, *Manufacturing Review*, **5**[2] 117–126.
5. E. Sachs, et al. (1992) 3-Dimensional printing—Rapid tooling and prototypes directly from a Cad model, *Journal of Engineering for Industry-Transactions of the Asme*, **114**[4] 481–488.
6. J. H. Song, M. J. Edirisinghe, and J. R. G. Evans (1999) Formulation and multilayer jet printing of ceramic inks, *Journal of the American Ceramic Society*, **82**[12] 3374–3380.
7. W. D. Teng and M. J. Edirisinghe (1998) Development of ceramic inks for direct continuous jet printing, *Journal of the American Ceramic Society*, **81**[4] 1033–1036.
8. X. Zhao, J. R. G. Evans, and M. J. Edirisinghe (2002) Direct ink-jet printing of vertical walls, *Journal of the American Ceramic Society*, **85**[8] 2113–2115.
9. T. M. Chu, et al. (2001) Hydroxyapatite implants with designed internal architecture, *Journal of Materials Science: Materials in Medicine*, **12** 471–478.
10. M. L. Griffith and J. W. Halloran (1996) Freeform fabrication of ceramics via stereolithography, *Journal of the America Ceramic Society*, **79**[10] 2601–2608.
11. B. K. Balla, S. Bose, and A. Bandyopadhyay (2008) Processing of bulk alumina ceramics using laser engineered net shaping, *International Journal of Applied Ceramic Technology*, **5**[3] 234–242.
12. M. Agarwala, et al. (1996) FDC, rapid fabrication of structural components, *American Ceramic Society Bulletin*, **75**[11] 60–66.
13. M. Allahverdi, et al. (2001) Processing of Advanced electroceramic components by fused deposition technique, *Journal of the European Ceramic Society*, **21** 1485–1490.
14. S. Rangarajan, et al. (2000) Powder processing, rheology, and mechanical properties of feedstock for fused deposition of  $\text{Si}_3\text{N}_4$  ceramics, *Journal of the America Ceramic Society*, **83**[7] 1663–1669.
15. A. Safari and E. K. Akdogan (2006) Rapid prototyping of novel piezoelectric composites, *Ferroelectrics*, **331** 153–179.
16. J. Cesarano, III (1999) A review of robocasting technology, in *Symposium on Solid Freeform and Additive Fabrication*, Boston, MA, Materials Research Society, Pittsburg, MA.
17. J. Cesarano, III, T. A. Baer, and P. Calvert (1997) Recent developments in freeform fabrication of dense ceramics from slurry deposition, *8th Solid Freeform Fabrication (SFF) Symposium*. University of Texas; Austin, TX.
18. J. Cesarano, III, and P. Calvert Freeforming objects with low-binder slurry. USA. 2000.
19. J. Cesarano, III, R. Segalman, and P. Calvert (1998) Robocasting provides moldless fabrication from slurry deposition, *Ceramic Industry*, **148**[4] 94–102.
20. J. E. Smay, J. Cesarano, III, and J. A. Lewis (2002) Colloidal inks for directed assembly of 3-D periodic structures, *Langmuir*, **18**[14] 5429–5437.
21. J. E. Smay, et al. (2002) Directed colloidal assembly of 3D periodic structures, *Advanced Materials*, **14**[18] 1279–1283.



22. B. A. Tuttle, et al. (2001) Robocast  $\text{Pb}(\text{Zr}_{0.95}\text{Ti}_{0.05})\text{O}_3$  ceramic monoliths and composites, *Journal of the America Ceramic Society*, **84**[4] 872–874.
23. S. L. Morissette, et al. (2001) Direct-write fabrication of  $\text{Pb}(\text{Nb}, \text{Zr}, \text{Ti})\text{O}_3$  devices: Influence of paste rheology on print morphology and component properties, *Journal of the America Ceramic Society*, **84**[11] 2462–2468.
24. J. Cawley, et al. (1996) Computer-aided manufacturing of laminated engineering materials, *American Ceramic Society Bulletin*, **75**[5] 75–79.
25. A. R. Bhatti, et al. (2001) PZT pillars for 1–3 composites prepared by ink-jet printing, *Journal of Materials Science Letters*, **20** 1245–1248.
26. N. Reis, C. Ainsley, and B. Derby (2005) Viscosity and acoustic behavior of ceramic suspensions optimized for phase-change ink-jet printing, *Journal of the American Ceramic Society*, **88**[4] 802–808.
27. T. Wang and B. Derby (2005) Ink-jet printing and sintering of PZT, *Journal of the American Ceramic Society*, **88**[8] 2053–2058.
28. D. H. Lee and B. Derby (2004) Preparation of PZT suspensions for direct ink-jet printing, *Journal of the European Ceramic Society*, **24** 1069–1072.
29. K. A. M. Seerden, et al. (2001) Ink-jet printing of wax-based alumina suspensions, *Journal of the American Ceramic Society*, **84**[11] 2514–2520.
30. W. D. Teng, M. J. Edirisinghe, and J. R. G. Evans (1997) Optimization of dispersion and viscosity of a ceramic jet printing ink, *Journal of the America Ceramic Society*, **80**[2] 486–494.
31. J. N. Stuecker Freeform fabrication and near net shape processing of composites from mullite and kaolin ceramics, Materials Science and Engineering. New Mexico Institute of Mining and Technology: Socorro, NM. 1999.
32. M. Greul, F. Petzoldt, and M. Greulich (1997) Rapid prototyping of powder binder mixtures using the multiphase jet solidification (MJS) process, *Advances in Powder Metallurgy & Particulate Materials*, **3** 18/153–18/159.
33. T. Huang, et al. (2006) Freeze-form extrusion fabrication of ceramic parts, *Virtual and Physical Prototyping*, **1**[2] 93–100.
34. T. Huang, et al. (2008) Aqueous-based freeze-form extrusion fabrication of alumina components, *Rapid Prototyping Journal*, **15**[2] 88–95.
35. R. Vaidyanathan, et al. (2000) The Extrusion freeforming of functional ceramic prototypes, *Journal of the Minerals Metals & Materials Society*, **52**[12] 34–37.
36. M. Greul, T. Pintat, and M. Greulich (1996) Rapid prototyping of functional metallic and ceramic parts using the multiphase jet solidification (MJS) process, *Advances in Powder Metallurgy & Particulate Materials*, **2** 7/281–7/287.
37. R. Lenk (2000) Rapid prototyping of ceramic components, *Advanced Engineering Materials*, **2**[1–2] 40–47.
38. R. Buscall, J. I. McGowan, and A. J. Morton-Jones (1993) The rheology of concentrated dispersions of weakly attracting colloidal particles with and without wall slip, *Journal of Rheology*, **37**[4] 621–641.
39. W. H. Herschel and R. Bulkley (1926) Konsistenzmessungen von Gummi-Benzollosungen, *Kolloid Zeit*, **39** 291.
40. D. M. Kalyon, et al. (1993) Rheological behavior of a concentrated suspension: A solid rocket fuel simulant, *Journal of Rheology*, **37**[1] 35–53.

41. R. J. Hunter *Foundations of Colloid Science*, Vol. 1. Oxford University Press, New York, 1992.
42. Q. Li and J. A. Lewis (2003) Nanoparticle inks for directed assembly of three-dimensional periodic structures, *Advanced Materials*, **15**[19] 1639–1643.
43. S. Nadkarni and J. E. Smay (2006) Concentrated barium titanate colloidal gels prepared by bridging flocculation for use in solid freeform fabrication, *Journal of the American Ceramic Society*, **89**[1] 96–103.
44. J. E. Smay, et al. (2002) Piezoelectric properties of 3-X periodic Pb(ZrxTi1-x)O3-polymer composites, *Journal of Applied Physics*, **92**[10] 6119–6127.
45. G. M. Channell, K. T. Miller, and C. F. Zukoski (2000) Effects of microstructure on the compressive yield stress, *Aiche Journal*, **46**[1] 72–78.
46. J. N. Stuecker, J. Cesarano, III, and D. A. Hirschfeld (2003) Control of the viscous behavior of highly concentrated mullite suspensions for robocasting, *Journal of Materials Processing Technology*, **142**[2] 318–325.
47. R. B. Rao, et al. (2005) Microfabricated deposition nozzles for direct-write assembly of three-dimensional periodic structures, *Advanced Materials*, **17**[3] 289–293.
48. E. L. Corral, et al. (2002) Processing of carbon nanofiber reinforced silicon nitride matrix composites, in *Symposium on Rapid Prototyping of Materials*. TMS, Columbus, OH.
49. G. He, D. A. Hirschfeld, and J. Cesarano, III (2000) Processing and mechanical properties of Si<sub>3</sub>N<sub>4</sub> formed by robocasting aqueous slurries, in *24th International Conference & Exposition on Engineering Ceramics and Structures*. Cocoa Beach, FL.
50. G. He, et al. Processing of silicon nitride-tungsten prototypes. ceramics transactions, in *Functionally Graded Materials 2000*, Vol. 114, pp. 325–332, ed. K. Trumble, et al., American Ceramic Society, Westerville, OH, 2001.
51. J. G. Dellinger, J. A. C. Eurell, and R. D. Jamison (2006) Bone response to 3D periodic hydroxyapatite scaffolds with and without tailored microporosity to deliver morphogenetic protein 2, *Journal of Biomedical Materials Research. Part A*, **76A**[2] 366–376.
52. S. Michna, W. Wu, and J. A. Lewis (2005) Concentrated hydroxyapatite inks for direct-write assembly of 3-D periodic scaffolds, *Biomaterials*, **26**[28] 5632–5639.
53. T. F. McNulty, et al. (1999) Dispersion of lead zirconate titanate for fused deposition of ceramics, *Journal of the American Ceramic Society*, **82**[7] 1757–1760.
54. M. Held On the computational geometry of pocket machining, in *Lecture Notes in Computer Science*, eds. G. Goos and J. Hartmanis, Springer-Verlag, Berlin Heidelberg, 1991.
55. D. Qiu, et al. (2001) Intelligent toolpath for extrusion-based LM processes, *Rapid Prototyping Journal*, **7**[1] 18–23.
56. J. Xu and J. E. Smay (2006) Concentrated, aqueous carbon black colloidal gel ink for support structures in solid freeform fabrication, *Journal of the American Ceramic Society* (in preparation).
57. S. L. Morissette, et al. (2000) Solid freeform fabrication of aqueous alumina-poly(vinyl alcohol) gelcasting suspensions, *Journal of the American Ceramic Society*, **83**[10] 2409–2416.
58. J. Cesarano, III, et al. (2005) Customization of load-bearing hydroxyapatite lattice scaffolds, *International Journal of Applied Ceramic Technology*, **2**[3] 212–220.
59. J. G. Dellinger Development of model hydroxyapatite bone scaffolds with multiscale porosity for potential load bearing applications, Materials Science and Engineering. University of Illinois: Urbana-Champaign. 2005.



60. A. Lewis Jennifer, et al. (2006) Direct ink writing of three-dimensional ceramic structures, *Journal of the America Ceramic Society*, **89**[12] 3599–3609.
61. J. A. Lewis, et al. (2006) Direct ink writing of three-dimensional ceramic structures, *Journal of the America Ceramic Society*, **89**[12] 3599–3609.
62. J. E. Smay Directed colloidal assembly and characterization of PZT-polymer composites, Materials Science and Engineering. University of Illinois: Urbana-Champaign. 2002.
63. G. M. Lous, et al. (2000) Fabrication of piezoelectric ceramic/polymer composite transducers using fused deposition of ceramics, *Journal of the America Ceramic Society*, **83**[1] 124–128.

# MICROWAVE PROCESSING OF CERAMIC AND CERAMIC MATRIX COMPOSITES

CRISTINA LEONELLI AND PAOLO VERONESI

## 14.1 PRINCIPLES OF DIELECTRIC HEATING

The use of microwaves to materials processing was studied intensively in the 1970s and 1980s and has now been applied to a wide variety of materials [1]. Initially, success in microwave heating and sintering was confined mainly to oxide and some nonoxide ceramics.

Microwaves can interact directly with the material, thus avoiding heating other parts that are not directly involved in the process, like the air or the furnace's metallic walls. The main parameter used to quantify such microwave–matter interaction is the complex relative permittivity, which is a measure of how an electric field affects, and is affected by, a dielectric medium. Different mechanisms (electronic, atomic, orientation or dipolar, and ionic polarization) are involved, at different frequencies, in determining the permittivity. Thus, permittivity is not a constant, and it is a frequency-dependent quantity, influenced also by the dielectric material temperature and chemical composition. The complex relative permittivity can be expressed as

$$\epsilon^* = \epsilon' - j\epsilon'' = \epsilon_0(\epsilon_r' - j\epsilon_{\text{eff}}''), \quad (14.1)$$

*Ceramics and Composites Processing Methods*, First Edition. Edited by Narottam P. Bansal and Aldo R. Boccaccini.

© 2012 The American Ceramic Society. Published 2012 by John Wiley & Sons, Inc.

where

$$\begin{aligned} j &= (-1)^{1/2} \\ \epsilon_0 &= 8.86 \times 10^{-12} \text{ F/m, free space permittivity;} \\ \epsilon'_r &= \text{relative dielectric constant; and} \\ \epsilon''_{\text{eff}} &= \text{effective loss factor.} \end{aligned}$$

Alternatively, the loss tangent, defined as the ratio between the imaginary and real part of the complex permittivity, can be used. Equation 14.1 contains the term  $\epsilon''_{\text{eff}}$ , which takes into account all the dissipation phenomena, not only due to polarization but including also the contributions due to conduction losses. This plays an important role in ceramic and glass processing, which usually present an increase of conductivity (ionic conduction) as temperature increases. The loss factor allows to quantify the power density, which will be dissipated in a generic material exposed to microwaves, according to the simplified equation

$$P_d(x, y, z) = \omega \epsilon_0 \epsilon''_{\text{eff}} E_{\text{rms}}^2 + \omega \mu_0 \mu''_{\text{eff}} H_{\text{rms}}, \quad (14.2)$$

where

$$\begin{aligned} P_d &= \text{power density in the material (W/m}^3\text{), at the position (x, y, z);} \\ \omega &= 2\pi f \text{ (Hz), } f = \text{frequency of the incident microwaves;} \\ \epsilon''_{\text{eff}} &= \text{effective loss factor, including conductivity losses;} \\ \mu''_{\text{eff}} &= \text{imaginary part of the effective magnetic permeability;} \\ E_{\text{rms}} &= \text{local (x, y, z) electric field intensity (V/m); and} \\ H_{\text{rms}} &= \text{local (x, y, z) magnetic field intensity (A/m).} \end{aligned}$$

The second term of the sum in Equation 14.2 takes into account magnetic losses, but this term is usually negligible for most ceramics and glasses, unless they possess relevant magnetic properties, like ferrites. Equation 14.2, neglecting magnetic losses, states that the power density in a microwave-processed material depends on the frequency of the microwaves (which is usually fixed and determined by regulations—industrial, scientific, and medical [ISM] frequencies), the loss factor of the material, and the local value of the electric field. In other words, the nature of the material and the geometric characteristics of the microwave furnace (applicator) affect the power density value, and thus the heat generation, inside the material.

The power penetration depth, instead, allows to quantify how deep the power from the electromagnetic field will penetrate in the material until a given attenuation is achieved. The power penetration depth is used to denote the depth at which the power density has decreased to 1/e of its value at the surface. Materials with higher loss factor present higher microwave energy absorption; thus, the power density will decrease (exponentially) faster from the surface to the core region. For dielectrics, an equation describing the power penetration depth in a semi-infinite slab is

$$D_p = \frac{\lambda_0}{2\pi} \sqrt{\frac{1}{2\mu\epsilon_0\epsilon'}} \left[ \sqrt{1 + \left( \frac{\epsilon''_{\text{eff}}}{\epsilon'} \right)^2} - 1 \right]^{-1/2}, \quad (14.3a)$$

which, in case of  $\epsilon'' \ll \epsilon'$ , becomes the largely used

$$D_p = \frac{\lambda_0 \sqrt{\epsilon'_r}}{2\pi \epsilon''_r}, \quad (14.3b)$$

where  $\lambda_0$  is the wavelength of the incident microwaves.

The power penetration depth is a very important parameter allowing to estimate the temperature distribution in a semi-infinite slab, or at least to have an indication of the more suitable workload dimensions. However, Equation 14.3 does not state that there is no heating at depths exceeding  $D_p$ , but only that slightly more than 63% of the incident power is dissipated within the penetration depth, the balance being dissipated in the material lying below  $D_p$ .

Equations 14.1–14.3 allow to understand which are the peculiarities of microwave processing of dielectric materials as well as mixed conductive/dielectric compounds as in the composites. These peculiarities are listed below and are more extensively discussed in Reference 2.

### 14.1.1 Selective Heating

According to Equation 14.2, in case a multiphase material, or simply two materials having different  $\epsilon''$ , is exposed to the same E-field, the power density will result higher for the material with the highest loss factor (see Table 14.2 for numerical values). This means that it is possible to convey energy selectively to one of the phases, which is an important feature in case of composite materials, but also at the basis of the claimed better energy efficiency of microwave sintering furnaces with respect to the conventional ones. The different heating rate when exposed to microwaves allowed, without measuring dielectric properties, to classify minerals according to their capability to absorb microwaves, as shown in Table 14.1. However, this approach is prone to errors since it neglects the thermal properties of the material under testing and the different efficiency of the microwave applicator used when performing the measurements with different loads.

Considering the components of a generic sintering furnace, walls are nondissipative (conductors), the lining, if properly selected, has a very low  $\epsilon''$  (alumina fiber, at room temperature, has a loss factor lower than  $10^{-4}$ ), and the air inside the furnace can

TABLE 14.1. Heating Behavior of Some Minerals When Heated in a Microwave Oven at 2.45 GHz Starting from Room Temperature [91]

Heating Behavior	Material
Hyperactive (several hundreds °C/s)	UO <sub>2</sub> , MoS <sub>2</sub> , C (carbon), Fe <sub>3</sub> O <sub>4</sub> , FeS <sub>2</sub> , CuCl, MnO <sub>2</sub>
Active (few hundred °C/min)	Ni <sub>2</sub> O <sub>3</sub> , Co <sub>2</sub> O <sub>3</sub> , CuO, Fe <sub>2</sub> O <sub>3</sub> , FeS, CuS
Difficult to heat (few tens °C/min)	Al <sub>2</sub> O <sub>3</sub> , PbO, MgO, ZnO, MoO <sub>3</sub>
Inactive (maximum temperature of 50–80°C in some minutes)	CaO, CaCO <sub>3</sub> , quartz, amorphous SiO <sub>2</sub> , borosilicate glass

be considered lossless, meaning that only the workload is likely to present values of  $\epsilon''$  high enough to generate a relevant power density. Figure 14.1 shows the simulated electric field, power density, and temperature distribution in a cross section of a cylindrical workload composed of a SiC compact ( $\epsilon^* = 30-j.11$ ) surrounded by fused silica lining ( $\epsilon^* = 3.78-j.0.001$ ), placed in a single-mode microwave furnace.

It is interesting to point out the difference between the power density (or resistive heating; Fig. 14.1b) and the temperature distribution (Fig. 14.1c): The former only indicates where the heat is generated, while the latter takes into account also heat transfer. This is the reason why part of the lining is heated by conduction from the inner SiC compact.

### 14.1.2 Volumetric Heating

According to Equation 14.3, microwaves can penetrate deep in the material, depending on its properties. This allows to heat the workload also inside, and not only relying on heat transfer from the surface to the core. For this reason, the heating can be considered volumetric since it can involve large parts of—or the whole—workload. Considering a low-loss ceramic, like fused silica, the power penetration depth at 2.45 GHz is more than 40 m, while in SiC, it is less than 0.01 m but still higher than what is achievable, for instance, by infrared (IR) heating (much shorter wavelength compared to microwaves).

Figure 14.1b, besides confirming the low power penetration depth in SiC, shows also that the power density is maximum at the workload surface, and then it is progressively attenuated toward the core. As a matter of fact, microwave heating is volumetric, but, especially for large enough samples, it is not generally true that the heat is generated from the inside of the workload: Heat is generated starting from its surface and also in parts of the volume.

### 14.1.3 Inversion of Temperature Profile

As a consequence of selective and volumetric heating, sometimes, the workload can undergo temperature profile inversion. In other words, while in conventional heating usually the outer surface of the sample is hotter and temperature progressively decreases toward the inside, in microwave heating, temperature can result higher in the inner parts of the load, while the surface remains colder. This is due to the fact that the air is not heated by microwaves (selectivity), while the load is, and volumetrically. Thus, the surface of the workload is exposed to “cold” air, which lowers its temperature, while the inside is “protected” by the outer layers of the material itself. Figure 14.2a shows the simulated microwave heating of the same SiC compact of Figure 14.1, but with the fused silica lining removed and in the presence of a strong convective flux of cold air, in order to evidence the temperature profile inversion. Figure 14.2b shows the same arrangement, but using conventional heating by hot air flux.

### 14.1.4 Rapid Heating

As a consequence of the possibility of achieving volumetric heating, and possibly having high power densities in the material, microwave heating can be more rapid than

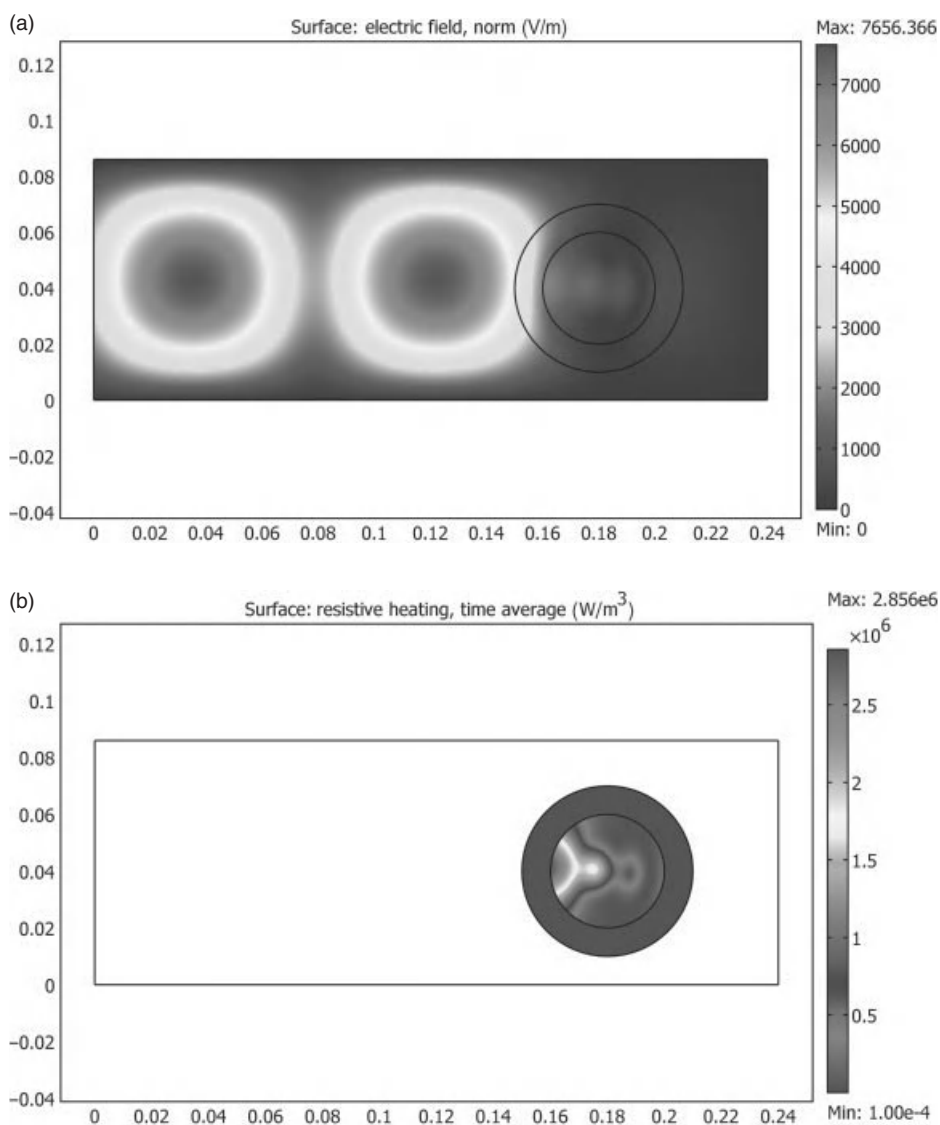


**Figure 14.1.** Microwave heating selectivity: (a) electric field time averaged strength (V/m); (b) power density ( $\text{W/m}^3$ ) distribution; (c) temperature (K) distribution in the SiC compact and in the surrounding fused silica glass, after 300 s of microwave heating. Dimensions on the x- and y-axes are in meters.

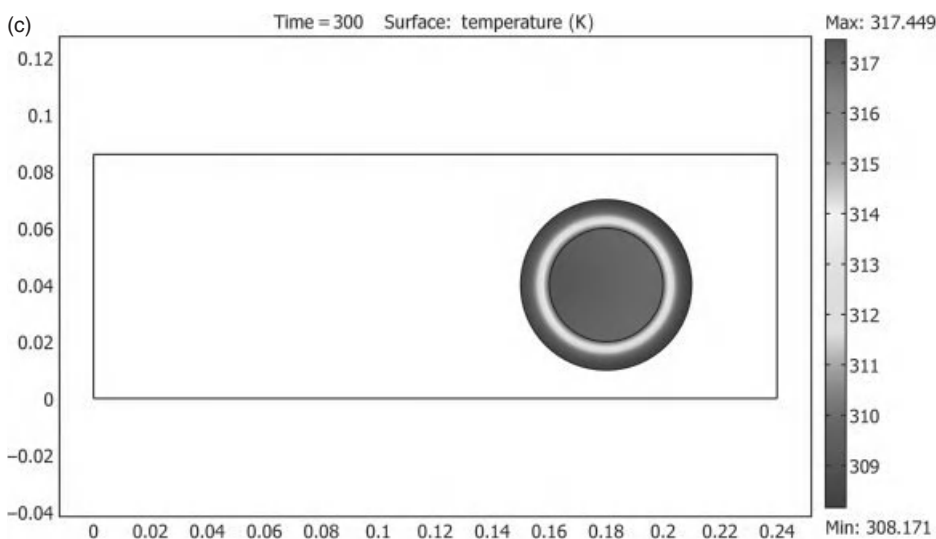
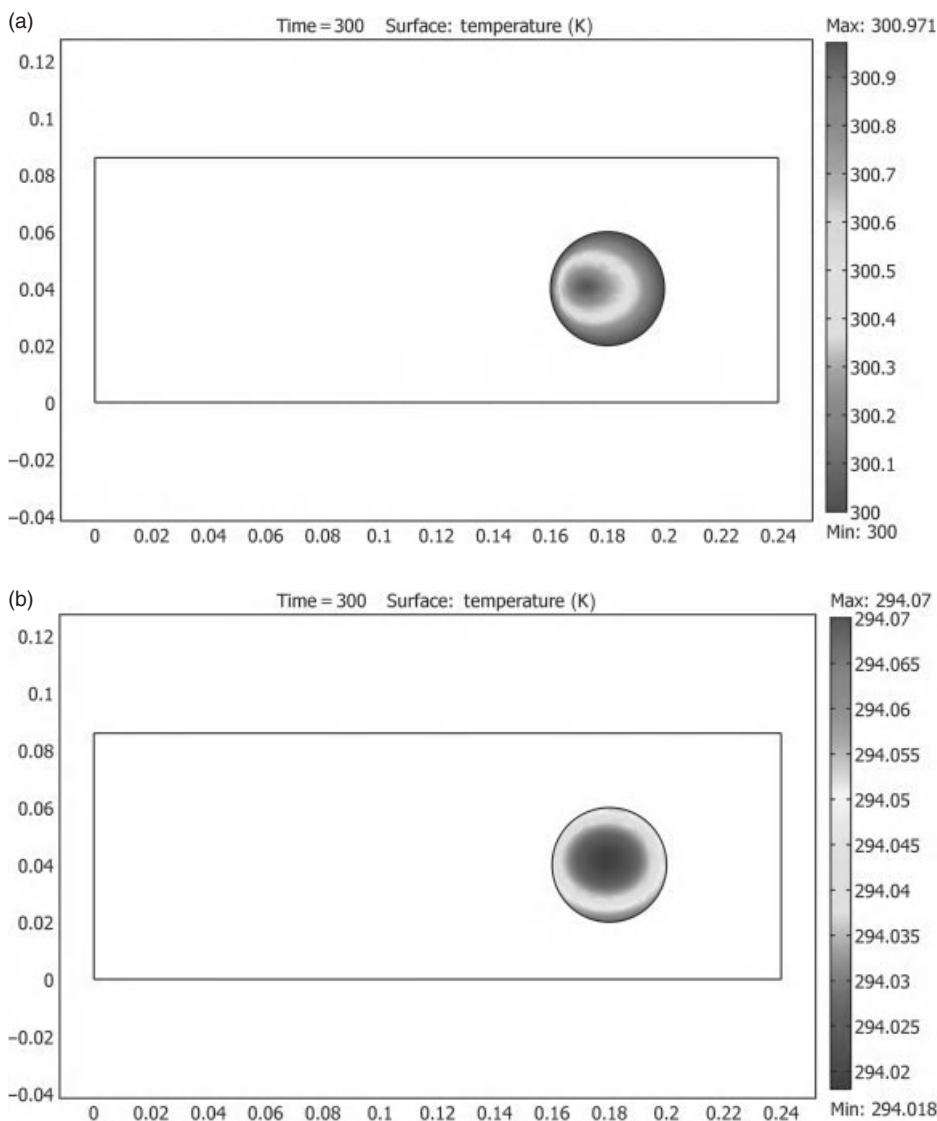


Figure 14.1. (Continued)

conventional heating. In particular, in the case of materials having low thermal conductivity, like many ceramic materials, microwave heating can help in minimizing the temperature gradients, thus preventing distortion and cracking of the workload during firing. However, it should be pointed out that for such kind of materials, it is mandatory to achieve a rather homogeneous heating, and this is not always the case when applying microwaves: The power density distribution in Fig. 14.1a is unacceptable for workloads that have a poor thermal conductivity, unlike SiC, since this would lead to an extremely high temperature gradient inside the cylindrical sample. Other limits to the rapid heating are due to the dielectric strength of the material: In case electric field strength surpasses this limit, breakdown phenomena, like arcing, occur, with damage to the microwave-processed part. A too fast heating rate, moreover, is likely to lead to thermal runaway, as described in the next paragraph.

### 14.1.5 Thermal Runaway

If the loss factor of the material to be microwave processed is an increasing function of temperature,  $\epsilon''(T)$ , and if the heat transfer phenomena are not rapid enough to homogenize temperature distribution, thermal runaway can occur. Thermal runaway is the rapid and uncontrollable overheating of parts of the material under processing. Considering a low thermal conductivity material, initially subject to a gradient of temperature (for instance, due to an uneven distribution of the electric field strength, like in Fig 14.1a, or being colder in the regions where heat is dissipated, and hotter in the remaining zones), it will present a higher power density in the hotter regions (higher  $\epsilon''$ ). These zones will further raise their temperature with respect to the colder ones (lower  $\epsilon''$ ), and consequently, their local value of  $\epsilon''$  will increase further, leading to an



**Figure 14.2.** Temperature distribution of a SiC sample after 300 s in case of (a) microwave heating and (b) conventional heating by hot air.

even higher power density, and hence heat generation, strengthening the phenomenon, with critical effects. Strong variations of loss factor as a function of temperature are typical of most ceramics and glasses. For example, mullite has a loss factor of less than 0.1 at room temperature, while at 800°C it becomes almost 0.5 and reaches 1.5 at 1200°C [3]. Glasses present a strong increase of  $\epsilon''$  as temperature approaches the glass



transition temperature due to the species' higher mobility, and above this temperature, glasses become strong microwave absorbers.

## 14.2 MICROWAVE APPLICATORS

A microwave device, whether it is a simple domestic oven or a large-scale industrial plant, is made of a series of basic components, able to generate, transmit, and have the material interact with the electromagnetic field. Many different components and combinations of components exist, and they can operate in quite different manners. The choice of one kind of device, or the adoption of particular solutions, can determine the success of a promising microwave application. The direct transfer of laboratory experiences on a larger scale is not easy, and it presents many difficulties. It is thus suggested to conduct the development and the preindustrialization on prototypes having dimensions of at least 25% of the final dimensions of the future industrial plant [4]. The availability, cost, lifetime, maintenance, and compliance to national rules are only some of the aspects that can help in evaluating and choosing the proper microwave-assisted furnace. Finally, it is quite unlikely that a commercial furnace will be available to perform the heat treatment of interest: Even the more versatile one will require a certain degree of customization, to optimize yields and to be compatible with the production line it will be inserted in.

The main components of a high-power microwave device are

*Generators.* Magnetrons are more widely used with respect to klystrons. The maximum declared efficiency of magnetrons can be high, being approximately 90% for magnetron operating at 900 MHz and more than 70% for the 2450 MHz [2]. The remaining percentage of the energy is dissipated into the generator as heat, and it is necessary to provide adequate cooling to the anode, using forced convection of air or, for high-power magnetron ( $>2$  kW), water. As far as the lifetime of a magnetron is concerned, it strictly depends on the operating conditions, but it can be stated that it usually ranges from 8000 to 12000 h at 915 MHz and between 4000 and 6000 h at 2450 MHz, even if, for well-designed and protected systems, it can easily reach 20,000 h [5]. Finally, in the case of pulsed operation of the magnetron (on-off), shortening of the lifetime is reported, up to 30–50%.

*Transmission Lines.* Coaxial cables and waveguides, which, due to the confinement of the electromagnetic field, do not possess high losses, are preferred to antennas for high microwave power applications. A waveguide is essentially composed of an empty metallic tube, having a rectangular or circular (elliptical) section. An electromagnetic field is generated at one end of the waveguide, and the conductive inner walls “force” the electromagnetic energy to be confined in the tube and to propagate along the transmission line, with no dissipation in the external space.

*Applicator/Cavity.* The term “applicator” identifies, in the microwave technology, the device where the material (load) is inserted to be exposed to microwaves.

A complete treatment of the applicators is impossible due to the large variety of shapes and dimensions, but it is possible to identify two main categories, among the “closed applicators” (open or radiant applicators present interesting characteristics, but they are usually difficult to shield to reduce microwave emission in industrial environments): single-mode and multimode applicators [6]. Microwave applicators are designed to optimize the energy transfer from the transmission line, connected to the source, to the load. The shape of the applicator depends on the nature and on the dimensions of the load, the operating frequency, the microwave power, as well as on the process the material will be subjected to. The design of an applicator is subordinated to a certain number of restraints, such as the impedance matching between load and generator, the type of material under treatment, the ability to uniformly expose the load to microwaves, and the safety of the operators placed in the applicator surroundings [2].

*Mode Stirrers.* Usually installed in multimode applicators, the mode stirrer consists of metallic reflectors, having dimensions greater than half wavelength, which are moving inside the applicator, causing multiple reflections and avoiding the formation of field nodes and antinodes. The effectiveness of this device is still debated, and it is a recommended practice to install many mode stirrers, rotating around an orthogonal axis (linearly independent directions) with no reciprocal relationships on the angular speed.

Figure 14.3 shows a badly designed mode stirrer installed on a small multimode applicator, loaded with a block of clay, and the electric field distribution in a section of the load, deriving from a series of  $15^\circ$  rotations of the stirrer [7]: The mode stirrer is not effective in improving the heating homogeneity since there are, in all cases, two regions of higher electric field intensity, which will certainly lead to thermal runaway problems.

*Load Rotating or Translating Devices.* Usually installed in multimode cavities, rotating dishes or conveyor belts can help improve the homogeneity of heating. Their action is to move the load with respect to the regions of higher or lower electric field intensity, and meanwhile to act as a mode stirrer, perturbing the field itself.

*Auxiliary Absorbers and Additives.* Auxiliary absorbers (like SiC and ferrites) or additives are used, in general, to change the material’s properties, improving its capabilities of coupling with microwaves. However, they could also improve heating homogeneity acting like “dispersed” heat sources, providing heat by conduction and irradiation, or locally “subtracting” energy to the electric field, and thus to the power density. Additives are usually dispersed in the load and are not recoverable, meaning they dissolve or they become embedded in the final product; auxiliary absorbers are generally placed around the load and can be recovered. Not being a necessary part of the final product, additives and auxiliary absorber can be considered detrimental to the energy efficiency of the process since they increase the heat capacity and the volume of the load. Moreover, they tend to subtract energy from the main process, but in some cases,

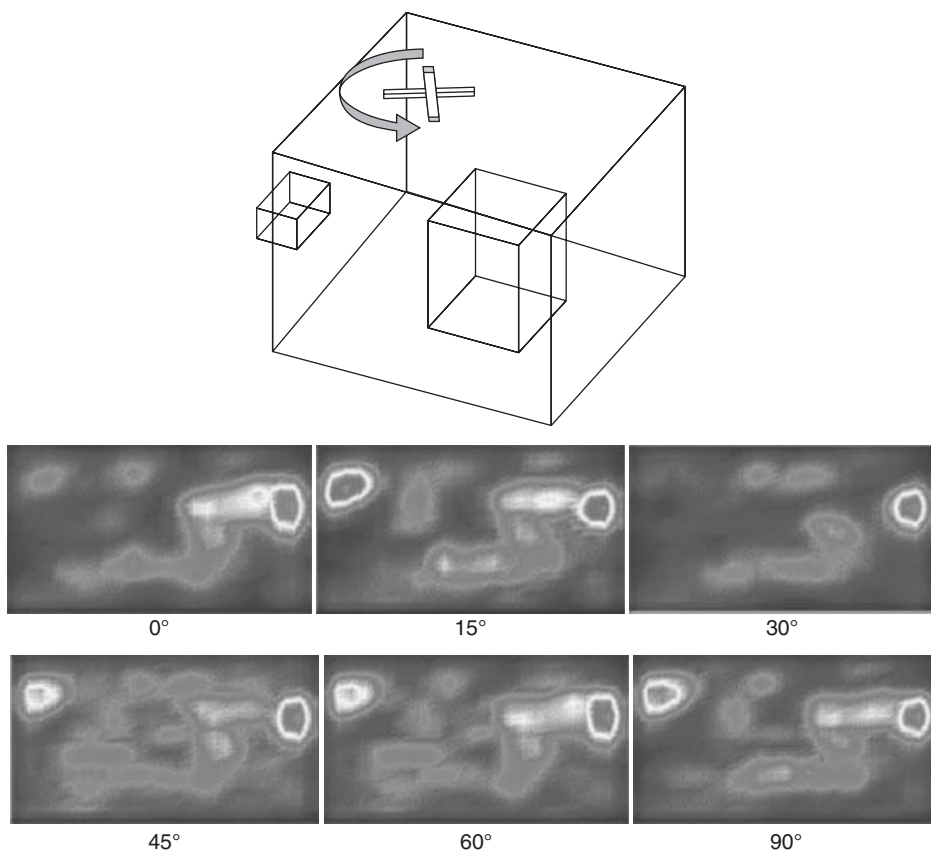


**Figure 14.3.** Mode stirrer and E-field intensity variations as a function of the stirrer angular position.

they are absolutely necessary. For example, low-loss materials, which require preheating to start coupling with microwaves, could benefit from the presence of auxiliary absorbers or additives.

**Power Measurement and Control.** Two of the most widely used devices to measure power levels are the diode placed on a circulator and the directional coupler. The signals provided by the directional coupler can be directly used and elaborated to control the process, for instance, varying the generator power output or the power absorbed by the load. The latter is particularly important since dielectric property variations or impedance matching fluctuations can be compensated in real time: To foresee how the load characteristics will vary with time and temperature is almost impossible, so a predictive system could not be so effective as a real-time control on the dissipated power (power converted in heat in the material).

As far as techniques for power modulation are concerned, there are substantially two ways of regulating the power emitted toward the load: *constant*

*power time slicing* (The generator, in this case, emits only *on average* the required power, but it presents peaks of maximum power emitted, which could damage or overheat the load. It is the easiest control system, very cheap, but also not so precise and *continuous power variation* (the power is varied continuously and can allow better and more reproducible heat treatments).

*Temperature Measurements.* Conventional furnaces are usually controlled in terms of temperature rather than power. However, controlling the temperature in a microwave furnace is feasible, but it can present some unexpected difficulties.

The first issue is, in case of “point” temperature control, is the choice of a meaningful area of the material, representative of the whole, to be subjected to measurements. As mentioned earlier, in microwave heating, it is not so unusual to have temperature profile inversion (inner parts hotter than the surface); thus, measuring surface temperature can have no practical meaning since there always will be parts of the material having a higher temperature. This phenomenon limits the use of noncontact temperature measurements, which would be preferable due to the presence of high electromagnetic fields. Contact temperature techniques seem to be more appropriate since the measuring tip can be inserted into the material.

Coming back to noncontact measurement systems, radiometers (microwave frequency, different from the furnace operating one) or pyrometers can be successfully applied, provided there is no interference with the field in the applicator, but the accuracy of the measurement can be quite low. Radiometers are still under development, and quite expensive, while pyrometers start to have low costs and reliability. However, for an optical pyrometer to work properly, it is necessary to know the emissivity of the material to be measured and how emissivity changes as temperature changes. A precalibration on the emissivity is usually required since reference data are usually affected by large approximations. Moreover, in many furnaces, it is necessary to have a straight line of sight from the pyrometer, external to the furnace, and the load, placed internally. This requires the use of special windows, transparent to the main pyrometer wavelength, and it must be assured that no fumes or droplets tend to stick to the window; otherwise, the measured temperature would not be the materials' one. It has been estimated [4] that using optical devices to measure a 1500°C temperature, a 15–20% error on the emissivity leads to more than 200°C deviations from the real temperature. Moreover, as mentioned earlier, the temperature is only referred to the surface, which is not necessarily the hottest or more meaningful part of the material.

The many difficulties existing in noncontact temperature measurements would make the experimenter move toward contact probes, like thermocouples. However, this approach is prone to even higher errors if not properly applied. In particular, thermocouples are metallic, and their introduction in the microwave applicator tends to perturb the fields. Moreover, if not properly installed, they could also act like antennas, bringing microwaves out of the confined space of the applicator and leading to unacceptable leakage levels.

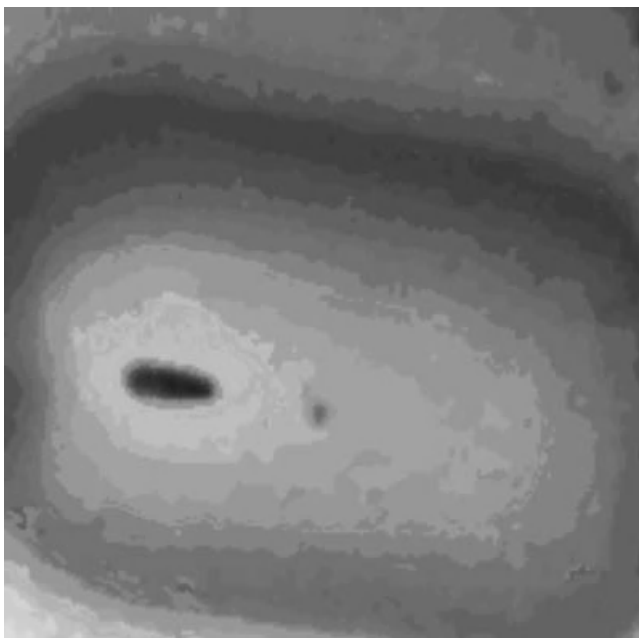


**Figure 14.4.** Enhanced contrast photograph showing the overheating of a ceramic sample in proximity of the tip of a shielded thermocouple used during sintering.

The way thermocouples perturb the electric field, in particular concentrating the field around their tips, can be responsible for unexpected heating behavior, like a very rapid heating of a low lossy material. This is due to the field concentration and usually due to the presence of arcing between the thermocouple and the load. Figure 14.4 shows the result of the microwave heating of a ceramic material in a multimode applicator (5 min at 1000-W variable power) using a K-type thermocouple to measure temperature. The localized overheating near the region where the thermocouple tip is lying is evident.

The main disadvantage of contact probes is that it is very difficult, in the industrial practice, to maintain the contact with a moving load and that all the information is always referred to a single point.

It is possible to combine the contact measurements to nonperturbing optical probes, for instance, using optical fibers or, for high temperatures, sapphire fibers. In this case, however, the probes tend to be fragile, and particular care must be taken in assuring their cleanliness.

### 14.3 MICROWAVE PROCESSING OF CERAMICS AND COMPOSITES

The conversion of microwave energy into heat within a bulk material has been explained in detail in the previous paragraph, and it appears clear how it depends on the dielectric

and magnetic properties of the material itself as well as from its dimension and the local strength of the electromagnetic field. Remembering the fact that the localization of the specimen to be treated within the electromagnetic field has a great, if not fundamental, importance, and that the choice of the appropriate cavity and the microwave feeding system is also a strategic choice, this chapter will be focused on the final products of the application of dielectric heating. In particular, an updated (from 2005 until 2010 included) list of current and possible applications of dielectric heating to ceramics and composites (with ceramic matrices) will be provided, starting from low-temperature treatments up to melting.

### 14.3.1 Ceramic Powder Syntheses

Dielectric heating in the case of the production of ceramic powders dates back in the 1980s with the first work of Baghurt [8]; since then, many other heat treatments have been tested using microwaves as heating source (combustion synthesis for powder preparation is discussed in the next paragraph):

- microwave plasma [9];
- sol-gel-derived precursors [10]; and
- hydrothermal and solvothermal [11].

The ceramic powders produced by such routes are pure single-phase oxides [12], mixed or doped oxides, ferrites [13], titanates [14], perovskites [15], carbonates [16], carbides [17], nitrides [18], up to more complex structures as phosphates [19], hydroxyapatites [20], zeolites [21], hydrotalcites [22], and carbon nanotubes [23].

The achievable primary particle dimension lies in the micro- or in the nanosize range, with the peculiarity to present a very homogeneous particle size distribution (Fig. 14.5) [10, 11, 16, 24].

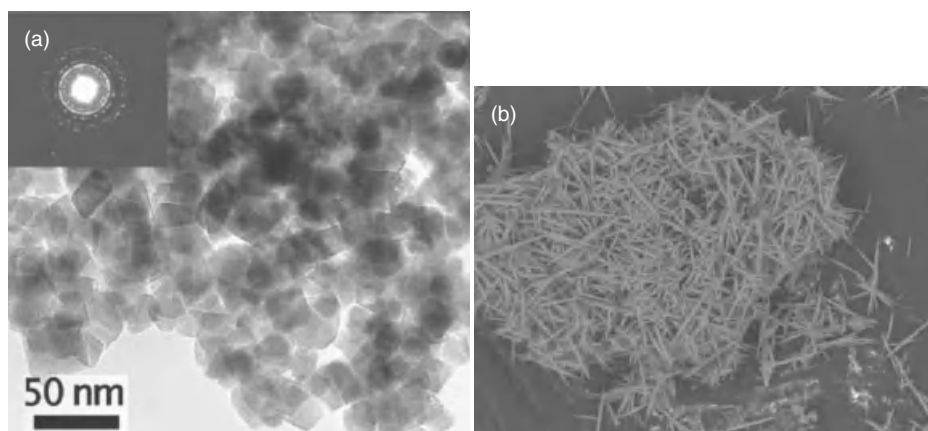


**Figure 14.5.** Homogeneous diameter distribution of (a) primary (left: magnetite, after Reference 11) and (b) secondary particles (aragonite after Reference 16).

This aspect is distinctive of microwave irradiated environments, and it can be related to the homogeneity of the temperature distribution within the reaction vessel volume in the early stages of formation, as recently demonstrated by numerical modeling by Leonelli and Veronesi [25] and as experimentally measured by Horikoshi et al. [26]

Similarly, but using a purely experimental approach [14], it has been proven that stirring under microwave-assisted hydrothermal conditions (in the temperature range of 150–240°C) leads to enhanced crystallization and to smaller and more uniform crystals, compared to those crystallized without stirring.

During the last 5 years, peculiar synthetic approaches have been pursued under a microwave irradiated environment. As an example, tungsten carbide powders can be obtained by microwave heating using as precursor tungsten dissolved in hydrogen peroxide and carbon black powder, with high yield and in 20 min [27]. Carbon powder is consumed over the course of the synthesis; it functions as both reducing agent and carburizing agent. Carbon powder is also a microwave susceptor (see Table 14.1) that is responsible for heating the reagents under microwave irradiation. Hence, careful control of the precursor carbon content was found to be important.

Functionalization of the powders [23] as well as their coating [28] or intercalation [29] is also possible in microwave irradiated reactors and, very often, good results are attained with one-pot routes. Very recently, the increasing request for specific nanoparticles for nanostructured ceramics and composites has promoted a new direction for microwave heating: nanosized composite powder preparation. As an example, the preparation of  $\text{ZrO}_2\text{-Al}_2\text{O}_3$  composites with dimensions of 20–40 nm has been reported (Fig. 14.6) [30]. Even after calcinations, the grain size has not grown and the two oxides are not separated into different crystalline habitus.

Experimentally good results are obtained when reactants are microwave absorbers themselves; in these cases, a lossless microwave reactor is required to avoid energy dissipation within the reaction vessel itself. In Table 14.2, the dielectric properties of different vessel materials and solvents are reported.

When a continuous-flow process is performed, the thermal equilibrium is reached when also the reactor reaches the synthesis temperature; hence, it is important that this temperature lies well below the maximum operating temperature of the vessel material and that no thermal runaway phenomena occur.

### 14.3.2 Drying

Microwave-assisted drying of ceramics and composites has already reached an efficient industrialization [2]. The efficiency relies in the fact that water or the most common solvents (Table 14.2) have a much higher loss factor (or loss tangent) with respect to ceramic powders and/or binders. As far as the thickness of the piece to be dried allows microwaves to penetrate its interior, the process will proceed rapidly and energy will be saved at two more conditions: Water vapor has to be removed from microwave cavity to avoid condensation on the cold walls and, second, the ceramic body has to be porous enough to allow the rapid removal of gaseous compounds. For these reasons, most of the industrial drying processes are “combined” or “hybrid,” that is, doubly assisted by



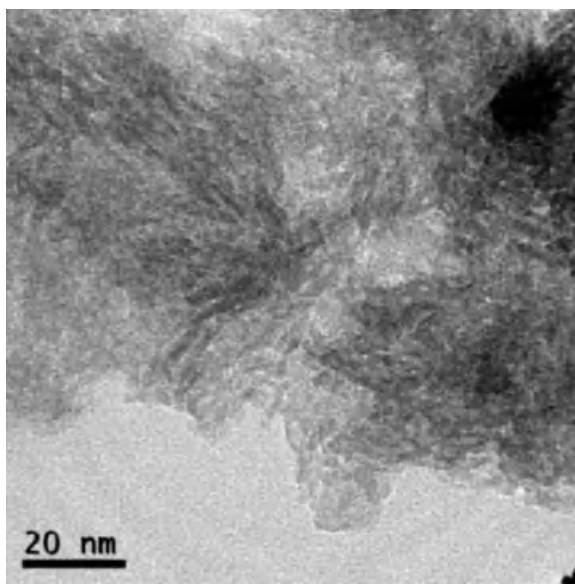


**Figure 14.6.** Transmission electron microscopy (TEM) micrographs of  $\text{ZrO}_2\text{-Al}_2\text{O}_3$  nanoparticles obtained by microwave hydrothermal synthesis ( $200^\circ\text{C}/2\text{ h}$ ) after thermal treatment in air at  $500^\circ\text{C}/5\text{ min}$ .

microwave and hot air or IR heating. Studies are still being performed for application to large ceramic bodies obtained by slip casting [31] as sanitaryware, sewage tubes, and so on.

It has to be noticed that if the ceramic material is a poor microwave absorber, the drying process can be self-limiting since as water is removed, the temperature rise in the ceramic body is progressively decreased. This situation renders the process particularly easy to control and localized superheating is rarely encountered.

### 14.3.3 Binder Removal

Ceramic materials containing organic compounds, as a result of a manufacturing process (e.g., ceramic injection molding [CIM]) or coming from an unwanted contamination, can be efficiently heat treated using microwave's rapid, volumetric, and selective heating. One of the first debinding attempts dates back to 1995 [32]. It was already clear that treating ceramic structures in a conventional oven is a lengthy procedure in which a large oven must be slowly heated to the required temperature, with multiple isothermal steps, and then carefully cooled to prevent cracking of the ceramic material. Microwave selective and volumetric heating is used to reduce temperature gradients in the material to be processed, provided a satisfactorily homogeneous power density is generated in the load, according to Equation 14.2. So far, electromagnetic field modeling of microwave-matter interactions inside the microwave applicator can help choose the best experimental conditions, leading to fast cycles (reduction of six to eight times)



TABLE 14.2. Dielectric Constant and Loss Tangent for the Most Common Solvents (2.45 GHz) and Reaction Vessels' Materials (1–10 GHz) Determined at 25°C

	Dielectric Constant ( $\epsilon'$ )	Loss Tangent ( $\tan \delta$ )
<b>Solvent</b>		
Hexane	1.9	
Carbon tetrachloride	2.2	
Benzene	2.3	
Chloroform	4.8	
Acetic acid	6.1	0.091
Ethyl acetate	6.2	0.174
THF	7.6	0.059
Methylene chloride	9.1	0.047
Acetone	20.6	0.042
Ethanol	24.6	0.054
Methanol	32.7	0.941
Acetonitrile	36	0.659
Dimethylformamide	36.7	0.062
DMSO	47	0.161
Formic acid	58	0.722
Water	80.4	0.123
<b>Material<sup>a</sup></b>		
Magnesium carbonate	1.2	0.01–0.05
Teflon <sup>®</sup>	2.1	0.0001–0.0002
Natural rubber (uncured)	2.1	0.002–0.005
Polypropylene	2.2	0.0003–0.0004
Polyethylene	2.3	0.0001–0.0002
Butyl rubber (uncured)	2.3	0.0009–0.001
CTFE fluoropolymer	2.3	0.002–0.005
Styrene/butadiene rubber (25/75)	2.4	0.0009–0.001
Polystyrene	2.5	0.0002–0.0003
Neoprene <sup>®</sup>	2.5	0.01–0.05
Fused quartz	3	0.0001–0.0002
Fused silica	3	0.0002–0.0003
Mylar <sup>®</sup>	3	0.002–0.005
Nylon <sup>®</sup> , epoxy, silicone rubber	3	0.01–0.05
Zinc oxide	3	0.1–1.0
Boron nitride	4	0.0003–0.0004
Borosilicate glass	4	0.001–0.002
Pyrex <sup>®</sup> glass	4	0.005–0.01
Mica	5	0.0003–0.0004
Beryllium oxide	6	0.0004–0.0005
Steatite	6	0.001–0.002
Wollastonite	6	0.002–0.005
Soda lime glass	6	0.01–0.05
Molybdenum sulfide	6	0.1–1.0
Sapphire	9	0.0003–0.0004
Magnesium oxide	9	0.0004–0.0005

TABLE 14.2. (Continued)

	Dielectric Constant ( $\epsilon'$ )	Loss Tangent ( $\tan \delta$ )
Aluminum oxide	9	0.0006–0.0007
Magnesium titanate	10	0.002–0.005
Zirconia	20	0.05–0.1
Titanium dioxide (rutile)	50	0.002–0.005
Strontium titanate	>100	0.002–0.005
Barium titanate	>100	0.1–1.0

<sup>a</sup> Properties of common materials from *Tables of Dielectric Materials*, Vols. IV, V, and VI, and Technical Reports AFML-TR-72-39 and 74-250, Laboratory for Insulation Research, Massachusetts Institute of Technology.

THF, tetrahydrofuran; DMSO, dimethylsulfoxide; CTFE, polychlorotrifluoroethylene.

and maximization of energy transfer from the microwave source to the load [33]. The debinding process of  $\text{Al}_2\text{O}_3$ ,  $\text{ZrO}_2$ , and  $\text{TiO}_2$  components added with organic compounds can be a self-limiting process as drying since at the burnout temperatures (often lower than  $600^\circ\text{C}$ ), the organic part absorbs microwaves, but the ceramic one still presents a low loss factor.

#### 14.3.4 Calcination, Solid-State Reactions, and Combustion Synthesis

For the calcination and combustion synthesis, typically a microwave transparent crucible is employed. The crucible is usually made of a light insulating material, alumina fibers mostly, which is transparent to microwaves allowing the waves to pass through, unimpeded, to the sample. Alternatively, crucible designs are also speckled with silicon carbide granules or have geometry to accept SiC bars and/or rings, which act as a susceptor, helping to rapidly increase the heat inside nonabsorbing specimens. As described in Section 14.2, the idea of using a susceptor material, also indicated as hybrid heating, is to make temperature even and to fasten ramp-up times for the sample and at the same time not to waste energy to heat the entire furnace.

There are many examples where microwave fast calcination, and hence super-rapid gas evolution, leads to powders that do not need any grinding and can be easily obtained in the nanometric range. As an example, the recent preparation of single-phase lead zirconate from lead zirconyl oxalate precursors, calcined for only 1 h at  $600^\circ\text{C}$  under microwave irradiation [34], is reported. The obtained particles of  $\text{PbZrO}_3$  are spherical in shape and the particle size varies between 20 and 22 nm. The same precursor, when heated in a resistance-heated furnace at  $850^\circ\text{C}$  for 3 h, did not give a pure product.

#### 14.3.5 Sintering and Crystallization

The last half of the 1980s saw a great deal of interest in the area of microwave sintering of ceramics, and starting from 2005, there has been an increasing number of

commercially available laboratory microwave furnaces dedicated to this high-temperature process.

The first pioneering experiments in this field were performed by Tinga and Voss as early as 1968 [35], followed by Sutton in 1988 [36], Katz and Blake in 1991 [37], and many others [38] who usually processed single green parts in multimode cavities.

Sintering of multiple samples is now a commercially satisfied request. As an example, in dental zirconia sintering, the advantages claimed for microwave sintering over traditional sintering are the following:

- Reduce sintering time by 80%
- Save up to 90% on electricity
- Create up to 20% stronger structures

It is now possible for a small dental laboratory to have an easy-to-run hybrid heated oven, where a refractory casket with a silicon carbide layer can treat up to 50 units at a time with a short standard 90-min sintering cycle controlled by an optical IR pyrometer, up to 1600°C [39].

Other examples of sintered zirconia samples in commercially available hybrid furnaces are already widespread in literature [40]. These furnaces avoid the inversion of the temperature profile within the sample, providing a very homogeneous sintering process as evidenced by ex post scanning electron microscopy (SEM) observations.

Recently [41], it was found that integrated passive devices (IPDs) with varistor/capacitor formulations could be microwave sintered at 1025–1050°C to fully dense device components within 3 h of the total cycle time, which is less than 1/10th of the time required by conventional methods. Microwave sintering resulted in products with a finer grain structure and without delamination or significant interdiffusion between the ceramic/electrode and varistor/capacitor interfaces. The microwave method also completely eliminated the need for a separate binder burnout step. The electrical properties of the microwave-sintered samples were found to be better or to match those obtained by conventional, industrial processing.

Again in the field of applied electronic devices, the application of localized selective heating [42] allowed the formation of conductive thick films screen printed on dielectric substrates starting from pastes made of silver powder and a glass frit mixture (Fig. 14.7). A single-mode microwave (2.45 GHz) applicator was used to reduce the processing time and to improve the energy efficiency compared to conventional heating. After 5 min of microwave treatment, the shrinkage of the microwave-fired Ag conductive thick films was similar to films processed conventionally at 580°C for 30 min but with superior optical properties. The results suggested that the drastic reduction of the substrate temperature and the rapid processing time were significant advantages because both helped to minimize the Ag diffusion into the glass, thus reducing the unwanted yellowing phenomena.

More examples and comments on the sintering of composites are reported in Section 14.4.3.

Even though more than one frequency has been used for the study of the sintering process, the less expensive still appear to be the 0.915 and 2.45 GHz. For the 28 GHz [43] and 30 GHz [44], please see the quoted references.

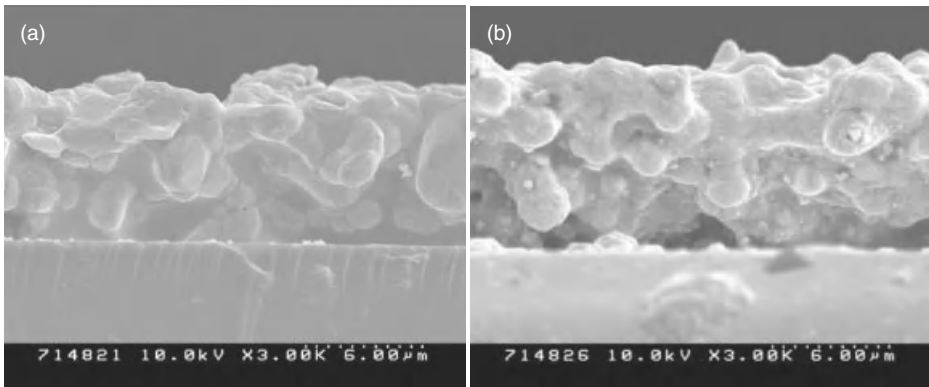


**Figure 14.7.** SEM images of the section of electrodes fired in (a) conventional (left, 30 min) and (b) microwave (right, 5 min, 540 W) heating. Courtesy of Seongjin Hwang and Hyungsun Kim.

### 14.3.6 Melting

An extensive review on glass melting has been recently published [45]. Starting from the first attempts in 1994 [46], exploiting the peculiarity of thermal runaway has easily taken a glass batch to melt for different applications, such as shaping, coating, sealing, electronic circuits or screen multilayer fabrication, nuclear waste encapsulation, and toxic waste immobilization [47]. One of the applications that was more diffused was the glass batch melting and/or glass scraps melting via microwave in small dedicated furnaces for artistic crystal glass in the Czech Republic [48].

The presence of carbonates or hydrates is often sufficient to allow the batch powder to start heating under microwave radiation at room temperature; otherwise, hybrid heating is required due to low-loss tangent values of most of the silicate and allumino-silicate glassy systems.

In case of nuclear waste or toxic wastes (mainly fly ashes), the presence of lossy compounds or carbonaceous particles is sufficient to start melting without the need for an additional susceptor [47].

### 14.3.7 Joining

Since 1999, different techniques have been investigated with dielectric heating, with transient liquid-phase bonding and joining with refractory glass compositions being the two most exploited [49]. Heating with microwave radiation has been used to join buried ceramic interfaces, for example, SiC to SiC, exploiting selective heating and localized plasma. Microwave hybrid and local heating was used to join silicon nitride [50]. Glass was placed at the joint between two silicon nitride pipes, and a silicon carbide susceptor was placed around the joint. The susceptor was locally heated by absorbing the microwave radiation. On heating to 1500°C, the glass melted and filled the space between

the pipes, thereby joining the two pipes. The average strength of the specimen cut out from the joined pipe was 446 MPa.

More complex joining can be realized by pure microwave heating igniting a self-propagating high-temperature synthesis (SHS) reaction at the interface of SiCf/SiC composites starting from loose or pressed powders of reactants [51].

Diffusion bonding assisted by microwaves has been used for zirconia, 85–94% alumina, and reaction-bonded SiC [52].

## **14.4 ADVANTAGES/DISADVANTAGES OF MICROWAVE PROCESSING OF CERAMICS AND COMPOSITES**

The application of microwave energy to ceramics and composite heating offers exciting new possibilities for new microstructures. In addition to improving material properties, microwave processing may reduce processing time, reduce the required factory floor space for kilns, and decrease energy requirements.

### **14.4.1 Moisture Leveling and Self-Regulation in Drying Processes or in Solvent/Binder Removal**

According to Equation 14.2, power density distribution is affected by the dielectric properties of the load. When the load is made of a high-loss component (like water, or some binders) and a low-loss one (like most of the ceramic powders), for a given E-field strength, power generation in the load is proportional to the content of the high-loss component. These results are particularly useful when processing nonhomogeneous loads, like natural materials, having, for instance, an uneven moisture content [53]. This spatial lack of water or binder content can occur not only in natural products but also as a consequence of not properly controlled industrial processes. The possibility of generating more heat exactly where the component to be removed is more abundant offers the unique chance of leveling its content in the workload volume. Moreover, if the remaining components are not lossy, or if their loss factor decreases as temperature increases, the microwave drying or debinding can be self-regulating; that is, no heat is generated after the removal of the lossy component [54]. Of course, moisture leveling requires also a proper distribution of the electromagnetic field; that is, according to Equation 14.1, each region to be leveled must be subjected to the same E-field strength to enhance loss factor differences [55].

### **14.4.2 Enhanced Sintering and Nanostructured Materials**

Microwave processing has gained worldwide acceptance as a novel method for sintering a wide range of materials. Its claimed advantages are in terms of enhanced diffusion processes, reduced energy consumption and processing cost, very rapid heating rates and significantly reduced processing times, decreased sintering temperatures, improved physical and mechanical properties, simplicity, unique properties, new

materials and products, and lower environmental hazards with respect to conventional processes [56]. These phenomena are probably the result of a driving force for ionic mass transport. This “ponderomotive (= mass-moving)” force derives from the application of intense, high-frequency electric fields near physical interfaces like free surfaces and grain boundaries [57].

As a matter of fact, experiments measuring short pulse and long pulse dynamics of microwave irradiated halide salt ceramics showed that the microwave fields do not enhance the ionic mobility, but rather are responsible for an additional driving force for ionic diffusion [58]. This means that the densification rate can be somehow controlled due to the presence of the microwave field, but recently, it has been proven that the sintering rate becomes less significant as the sintering time increases [59]. Considering also that subsequent studies [60, 61] have revealed considerable intensification of the electric field in the neck regions between particles undergoing microwave sintering, and that the mass transport in the course of sintering occurs predominantly within the neck region, this result suggests the importance of the role of ponderomotive forces in microwave sintering, especially of thermal sensitive materials.

Moreover, the volumetric heating offered by microwaves allows to inhibit surface diffusion at the initial stage of densification (and hence enhancing sintering) [62] by increasing the rate of heating at the onset of densification, in the so-called rate-controlled processing [63]. In this approach, the heating rate is varied in a way that at the intermediate and final stages of sintering, it occurs with high rates, to avoid grain growth, resulting in ceramic materials with finer microstructures. Compared to conventional heating, where the thermal inertia of furnace and workload make rate-controlled sintering difficult to achieve, the microwave rapid, and volumetric heating results in a suitable technique, leading to the possibility of manufacturing nanostructured ceramic materials and their composites.

#### 14.4.3 Preferential Heating of Matrix or Reinforcement

Composite materials can benefit from the selectivity of microwave heating, being generally composed of two or more phases. Depending on the more lossy phase, microwave energy can be preferentially conveyed to the matrix or to the reinforcement. In this latter case, conditions can arise to achieve overheating also of the matrix near the reinforcement, with the creation of peculiar microstructures [64], foaming [65], or enhanced adhesion at the matrix/reinforcement interface [66].

In case the reinforcement is conductive, like metal particles in a low-loss host material, the composite may absorb microwaves due to the induction of eddy currents in the particles [67], but also due to the electric field intensification in the space between the particles [68]. If the reinforcement presents also magnetic properties, further possibilities of controlling the temperature distribution in the composite arises when the workload is processed in preferential electric or magnetic field regions of the applicator [69]. Last, but not least, a promising application of microwave processing is the development of functionally gradient materials, where also the permittivity, and hence microwave absorption, changes with a spatial coordinate due to a different composition or simply to a different porosity [70].

#### 14.4.4 Direct Deposition of Microwave Energy

Microwave heating relies on the conversion of energy from the electromagnetic field into heat, within the workload. Thus, during microwave heating, it is energy, and not heat, that is transferred. This plays an important role in a highly exothermic reaction, like combustion synthesis, where in conventional heating, after ignition, the heat flux is reversed; that is, the heat is no longer conveyed to the workload, but, due to its higher temperature, it is transferred from the workload to the surrounding environment. Using the energy transfer of microwave heating, it is possible to continue to heat the workload despite the existence of an adverse temperature gradient, allowing, for instance, to control the cooling rate of combustion synthesis reactions [71]. Again, the peculiar temperature profile and cooling rates achievable by microwave heating can lead to completely different microstructures than conventionally heated samples, with improved mechanical properties [72] and formation of nonequilibrium phases [73].

#### 14.4.5 Microwave Plasma

Microwave excited plasmas present some advantages over DC and low-frequency plasmas, useful for material processing and/or deposition [74]: a higher degree of ionization and disassociation that commonly gives 10 times higher yield of active species; the possibility to sustain a microwave plasma over a very wide pressure range, from  $10^{-5}$  Torr to several atmospheres; the electron-to-gas temperature ratio is very high, so the carrier gas and the substrate remain moderately cool despite the presence of high electron energy; and the absence of internal electrodes (potential sources of contamination).

In microwave plasma processing, the workload is the plasma itself, and the material under processing can be exposed also to microwaves [75] or to the microwave-generated plasma alone [76].

#### 14.4.6 Uneven Power Density Distribution

Besides depending on permittivity, microwave heating is strongly affected by the electromagnetic field distribution, according to Equation 14.2. Many industrial processes require heating homogeneity, and this can be difficult to achieve by applying pure microwave heating. Thus, when load movement or the use of mode stirrers or multi-frequency microwave generators is not feasible, a certain lack of power density homogeneity is expected. However, this is not always detrimental, like in joining operations, where it is preferable to selectively heat only the parts to be joined. This can be accomplished both by using high-loss brazing materials [77] or by focusing the electric field strength in the joining region [78]. Another case in which an uneven power density could be required is in surface processing. However, in this case, it is important that the power penetration depth remains small, and according to Equation 14.3, this happens preferably at high frequency, making microwave surface processing feasible in the 24- to 83-GHz range using quasi-optically focused wave beams [43].

### 14.4.7 Green Technology

Microwave heating can be considered a “green technology” since it can significantly reduce energy consumption (for instance, in high-temperature processing of ceramics, where heat losses by conduction and irradiation grow dramatically with temperature) and can speed up processes especially when the process involves endothermic reactions between thermal sensitive reactants [79, 80]. In the use of ceramics (pelletized zeolites) for heterogeneous catalyses in organic industrial syntheses, the coupling of microwaves with the new technology of microreactors has proved an important energy transfer increase with a consequent increase of green index [80].

### 14.4.8 Nonthermal Effects

The existence of the so-called microwave nonthermal effect is still a debated subject despite the increasing number of evidences addressing the deviations of microwave processes from conventional ones that occur given the same temperature distribution in the workload [81]. However, it should be pointed out that it is practically impossible to achieve by conventional heating exactly the same temperature distribution occurring during microwave heating, and that temperature measurement in a microwave field is subject to errors (surface temperature measured by optical pyrometers, local temperature measured by optical fibers) or can be perturbative (thermocouples) [82]. As a matter of fact, some claimed microwave effects can be ascribed to poor temperature monitoring [83], but still a large number of evidences exist, especially in organic chemistry, and are currently exploited [84]. Moreover, the realization of complex experimental setups, aimed at stressing possible microwave-specific effects allowed to gather a deeper understanding of the phenomenon. For example, the aforementioned ponderomotive force belongs to such “nonthermal effects,” as well as the fact that the electromagnetic field is concentrated in the region between particles, with possible breakdown phenomena taking place at the microscale during microwave processing. The different sintering behavior in the predominant electric or magnetic field, though originating a different temperature distribution in the load, could be practically considered a nonthermal effect. Some authors claimed also that it is possible to “decrystallize” materials by short pulses in the predominant magnetic field [85], or even that electrochemistry deposition processes are influenced by the presence of microwave and its field strength [86].

The importance of nonthermal effects is due to the fact that, if properly exploited, they could originate unique ways of processing materials, or controlling their microstructure, in a similar way with other well-established field-assisted sintering techniques (FASTs), like SPS, where the effect of the external electric field can be manifested through the electron wind effect (electromigration) [87], or by an increase in point defect [88], or by a decrease in the activation of migration of the defects [89].

Considering also that the economic feasibility of microwave processes compared to conventional ones has often to rely on the uniqueness of the achievable products, the existence of such specific nonthermal effects could represent the key factor to determine the success of a potential microwave application.



## 14.5 CONCLUDING REMARKS: SCALE-UP AND INDUSTRIAL PERSPECTIVES

The knowledge of the microwave–material interactions on a laboratory scale usually finds many difficulties in being transferred to the industrial practice, mainly due to the nonlinear behavior of the systems involved. The use of electromagnetic simulation software helps the designer in the scale-up of the process, but usually the lack of a proper knowledge on the variation of the material properties (mainly dielectric) as a function of temperature limits the depth of analysis. A consolidated praxis involves the development of the industrial applicator starting from simple experimental tests, aimed at determining the effective efficiency of the process, and the correlated costs. The costs involved in the development of the whole process are almost impossible for a general case since it depends on the specific requisites.

It is mandatory, before even thinking of an applicator, to perform a process analysis, answering simple questions involving the kind of process, the material properties, and the existing constraints, as summarized in Table 14.3 (adapted from Reference 4).

Once the process analysis is performed, it is necessary to assess the feasibility and cost analysis, which will provide the necessary information regarding whether it is technically and economically advantageous to use microwaves or to opt for other electroheating methods (laser, radio frequency [RF], resistance, plasma, etc.) or more conventional ones (hot air, burners, etc.).

TABLE 14.3. Process Analysis

---

What is the composition of the load? Is it composed of more than one material?
Is it toxic before/during/after the treatment? Does it emit noxious gases?
Is it flammable/corrosive/explosive?
Is it not compatible with other materials (corrosion, contamination)?
What shape is it (liquid, powder, particles, blocks, etc.)?
What is the input flux (mass)? Continuous or batch?
What processing time is expected or requested??
Which is the input and output load density??
Specific heat? Thermal conductivity?
What is the load input temperature?
Which is the moisture content (input and output)?
Are output temperature and moisture important?
Dielectric properties as a function of temperature?
Is loading and unloading dependent on existing devices?
How is the mass flux measured in continuous systems?
How is the conveyor speed measured in continuous systems?
How is the stationary state for the process defined?
How is temperature measured during the process? And moisture?
How is the dissipated power measured?
Are there auxiliary plants? Are their performances to be monitored?
Are there restrictions to be respected (electrical plant, interference, ISM frequency, pressure levels, toxic emissions, fire hazards, etc.)?

---

In particular, the use of hybrid heating systems, that is, systems involving the simultaneous or subsequent application of microwave heating and conventional heating, like hot air or IR, presents many advantages in terms of energy efficiency (usually hot air is produced with higher efficiency compared to microwave generation), temperature homogeneity (superimposition of two temperature profiles of microwave and conventional heating), and process control.

Another option for industrial processing could be the use of dual or multifrequency devices, but the main problems remain avoiding the cross coupling between the generators and the high cost of the less standard microwave generators operating at frequencies different from 915 or 2450 MHz.

It is almost impossible to guess which will be the most promising areas of high-temperature microwave applications since too many factors, not only technical, are involved, first of all the relatively high cost of industrial microwave generators.

Ceramic manufacturing and ceramic composite preparation have been considered for a long time as the best nonfood field of application for microwave heating [90]. As a matter of fact, their generally low thermal conductivity and/or multiphase constitution makes selective and volumetric heating particularly attractive. However, in order to compete with the best available conventional heating technologies, proper process control and temperature homogeneity are mandatory. For this reason, microwave methods of high-temperature processing of ceramic materials have relevant industrial application potential, only partially exploited. The most promising applications still remain those that utilize the specificity of microwave processing and that result in novel materials/microstructures or unique material properties.

## REFERENCES

1. D. E. Clark and W. H. Sutton (1996) Microwave processing of materials, *Annual Review of Materials Science*, **26**[1] 299–331.
2. A. C. Metaxas and R. J. Meredith, *Industrial Microwave Heating*. Peter Peregrinus, London, 1993.
3. C. C. Goodson *Simulation of microwave heating of mullite rods*. Master's thesis, Virginia Polytechnic Institute and State University, 1997.
4. R. J. Meredith, *Engineer's Handbook of Industrial Microwave Heating*. IEEE, London, 1999.
5. National Materials Advisory Board, *Commission on Engineering and Technical Systems, "Microwave Processing of Materials,"* National Academy Press, Washington, DC, 1994.
6. T. V. Chow Ting Chan and H. C. Reader, *Understanding Microwave Heating Cavities*. Artech House, Boston, 2000.
7. P. Veronesi, M. Franchini, and C. Leonelli (2001) Application of microwave heating to ceramics III-applicators, *Ceramica Informazione*, **403** 77–83. (in Italian).
8. D. R. Baghurt and D. M. P. Mingos (1988) Application of microwave heating techniques for the synthesis of solid state inorganic compounds, *Journal of the Chemical Society. Chemical Communications*, 1988, 829–830.
9. D. Vollath and D. V. Szabó (2006) The microwave plasma process—A versatile process to synthesise nanoparticulate materials, *Journal of Nanoparticle Research*, **8**[3–4] 417–428.

10. E. Mily, A. González, J. J. Iruin, L. Irusta, and M. J. Fernández-Berridi (2010) Silica nanoparticles obtained by microwave assisted sol-gel process: Multivariate analysis of the size and conversion dependence, *Journal of Sol-Gel Science and Technology*, **53**[3] 667–672.
11. C. Leonelli and W. Lojkovski (2008) Main development directions in the application of microwave irradiation to the synthesis of nanopowders, *Chemistry Today*, **26**[1 Suppl. Comp.] 26–29.
12. S. Baldassari, S. Komarneni, E. Mariani, and C. Villa (2005) Rapid microwave–hydrothermal synthesis of anatase form of titanium dioxide, *Journal of the American Ceramic Society*, **88**[11] 3238–3240.
13. D. A. Vieira, V. C. S. Diniz, H. L. Lira, R. H. G. A. Kiminami, D. Cornejo, and A. C. F. M. Costa (2010) Ni-Zn nanoferrites synthesized by microwave energy: Influence of exposure time and power, *Materials Science Forum*, **660–661** 910–915.
14. S. Komarneni and H. Katsuki (2010) Microwave-hydrothermal synthesis of barium titanate under stirring condition, *Ceramics International*, **36**[3] 1165–1169.
15. R. Kahia, C. Menu, J.-M. Giraudon, and J.-F. Lamonier (2010) Investigation of the microwave heating techniques for the synthesis of  $\text{LaMnO}_{3+\delta}$ : Influence of the starting materials, *Studies in Surface Science and Catalysis*, **175**[C] 533–536.
16. A. Rizzuti and C. Leonelli (2008) Crystallization of aragonite particles from solution under microwave irradiation, *Powder Technology*, **186**[3] 255–262.
17. P. K. Shen, S. Yin, Z. Li, and C. Chen (2010) Preparation and performance of nanosized tungsten carbides for electrocatalysis, *Electrochimica Acta*, **55**[27] 7969–7974.
18. T. N. Tieg, O. Kiggans, and K. L. Plötz, Application of microwave heating for fabrication of silicon nitride ceramics, in *Proceedings of the 17th Annual Conference on Composites and Advanced Ceramic Materials*, Part 2 of 2, [9/10], ed. J. B. Wachtman, Jr., pp. 744–752, Wiley, New York, 2008. Ceramic Engineering and Science Proceedings 14.
19. S. Komarneni, Q. H. Li, and R. Roy (1994) Microwave-hydrothermal processing for synthesis of layered and network phosphates, *Journal of Materials Chemistry*, **4**[12] 1903–1906.
20. S. Bose, S. Dasgupta, S. Tarafder, and A. Bandyopadhyay (2010) Microwave-processed nanocrystalline hydroxyapatite: Simultaneous enhancement of mechanical and biological properties, *Acta Biomaterialia*, **6**[9] 3782–3790.
21. Y. Li and W. Yang (2008) Microwave synthesis of zeolite membranes: A review, *Journal of Membrane Science*, **316**[1–2] 3–17.
22. P. Benito, M. Herrero, C. Barriga, F. M. Labajos, and V. Rives (2008) Microwave-assisted homogeneous precipitation of hydrotalcites by urea hydrolysis, *Inorganic Chemistry*, **47**[12] 5453–5463.
23. Z. Iqbal and S. Mitra (2005) Microwave-induced rapid chemical functionalization of single-walled carbon nanotubes, *Carbon*, **43**[5] 1015–1020.
24. A. B. Corradi, F. Bondioli, A. M. Ferrari, B. Focher, and C. Leonelli (2006) Synthesis of silica nanoparticles in a continuous-flow microwave reactor, *Powder Technology*, **167**[1] 45–48.
25. C. Leonelli, A. Rizzuti, R. Rosa, A. Corradi, and P. Veronesi (2010) Numerical simulation of a microwave reactor used in synthesis of nanoparticles, in *Proceedings of 2010 IMPI 44th Annual Microwave Power Symposium*, July 14–16, Denver, Colorado, USA.
26. S. Horikoshi, H. Abe, K. Torigoe, M. Abe, and N. Serpone (2010) Access to small size distributions of nanoparticles by microwave-assisted synthesis. Formation of Ag nanopar-

- ticles in aqueous carboxymethylcellulose solutions in batch and continuous-flow reactors, *Nanoscale*, **2** 1441–1447.
27. K. Essaki, E. J. Rees, and G. T. Burstein (2010) Synthesis of nanoparticulate tungsten carbide under microwave irradiation, *Journal of the American Ceramic Society*, **93**[3] 692–695.
  28. M. Becuwe, F. Cazier, P. Woisel, D. Landy, and F. Delattre (2010) Rapid synthesis of a versatile organic/inorganic hybrid material based on pyrogenic silica, *Journal of Colloid and Interface Science*, **350**[1] 83–89.
  29. M. Mehdipourghazi, A. Moheb, and H. Kazemian (2010) Incorporation of boron into nano-size MFI zeolite structure using a novel microwave-assisted two-stage varying temperatures hydrothermal synthesis, *Microporous and Mesoporous Materials*, **136**[1–3] 18–24.
  30. F. Prete, A. Rizzuti, L. Esposito, A. Tucci, and C. Leonelli (2011) Highly homogeneous  $\text{Al}_2\text{O}_3$ - $\text{ZrO}_2$  nanopowder via microwave assisted hydro- and solvo-thermal synthesis, *Journal of the American Ceramic Society*, **94**[10] 3587–3590.
  31. T. Shirai, M. Yasuoka, Y. Hotta, and K. Watari (2006) Rapid microwave drying for slip cast bodies, *Journal of the Ceramic Society of Japan*, **114** 217–219.
  32. Z. Xie, Y. Huang, J. Wu, and L. Zheng (1995) Microwave debinding of a ceramic injection moulded body, *Journal of Materials Science Letters*, **14**[11] 794–795.
  33. P. Veronesi, C. Leonelli, G. Poli, L. Denti, and A. Gatto (2010) Microwave rapid debinding and sintering of MIM/CIM parts, *Advances in Sintering Science and Technology—Ceramic Transactions*, **209** 259–270.
  34. Y. S. Malghe (2009) Nanosized  $\text{PbZrO}_3$  powder from oxalate precursor: Microwave-aided synthesis and thermal characterization, *Journal of the American Ceramic Society*, **92**[9] 2155–2158.
  35. W. R. Tinga and W. A. G. Voss, *Microwave Power Engineering*. Academic Press, New York, 1968.
  36. W. H. Sutton, Microwave firing of high-alumina ceramics, in *Microwave Processing of Materials, MRS Symp. Proc.*, Vol. 124, eds. W. H. Sutton, M. H. Brooks, and I. J. Chabinsky, pp. 287–295, Materials Research Society, Pittsburgh, PA, 1988.
  37. J. D. Katz and R. D. Blake (1991) Microwave sintering of multiple alumina and composite components, *American Ceramic Society Bulletin*, **70**[8] 1304–1307.
  38. (a) D. E. Clark, D. C. Folz, C. E. Folgar, M. M. Mahmoud, *Microwave Solutions for Ceramic Engineers*. The American Ceramic Society, Westerville, OH, 2005; (b) *Microwave Processing of Materials, National Materials Advisory Board Publication NMAB-473*. National Academy Press, Washington, DC, 1994; (c) A. C. Metaxas and J. C. P. Binner, Microwave processing of ceramics, in *Advanced Ceramic Processing and Technology*, Vol. 1, ed. J. G. P. Binner, pp. 285–362, Noyes Publications, Park Ridge, NJ, 1990.
  39. <http://www.sinteringovens.com/> (accessed December 26, 2010).
  40. <http://www.ceralink.com/>
  41. B. Vaidhyanathan, K. Annapoorani, J. G. P. Binner, and R. Raghavendra (2010) Microwave sintering of multilayer integrated passive devices, *Journal of the American Ceramic Society*, **93**[8] 2274–2280.
  42. S. Hwang, P. Veronesi, C. Leonelli, and H.-S. Kim (2010) Forming silver conductive thick films by microwave heating, *Journal of the American Ceramic Society*, **93**[10] 3201–3205.
  43. Y. Bykov, A. Ereemeev, M. Glyavin, V. Kholoptsev, A. Luchinin, I. Plotnikov, G. Denisov, A. Bogdashev, G. Kalynova, V. Semenov, and N. Zharova (2004) 24-84-GHz gyrotron

- systems for technological microwave applications, *IEEE Transactions on Plasma Science*, **32**[1] 67–72.
44. G. Link, L. Feher, M. Thumm, H.-J. Ritzhaupt-Kleissl, R. Bohme, and A. Weisenburger (1999) Sintering of advanced ceramics using a 30-GHz, 10-kW, CW industrial gyrotron, *IEEE Transactions on Plasma Science*, **27**[2] 547–554.
  45. O. V. Kharissova, B. I. Kharisov, and J. J. R. Valdés (2010) Review: The use of microwave irradiation in the processing of glasses and their composites, *Industrial and Engineering Chemistry Research*, **49**[4] 1457–1466.
  46. B. Vaidhyanathan, M. Ganguli, and K. J. Rao (1994) A novel method of preparation of inorganic glasses by microwave irradiation, *Journal of Solid State Chemistry*, **113**[2] 448–450.
  47. L. Barbieri, I. Lancellotti, F. Andreola, A. Corradi, C. Leonelli, and M. La Robina (2009) Processing fly ash from coal burning power station in a variable radiofrequency field, *Ceramic Transactions*, **207** 21–28.
  48. M. Hajek (2001) Process for melting glass materials and glass furnace for making the same, patent CZ289193.
  49. R. E. Loehman (1999) Recent progress in ceramic joining, *Key Engineering Materials*, **161-163** 657–662.
  50. N. Kondo, H. Hyuga, H. Kita, and K. Hirao (2010) Joining of silicon nitride by microwave local heating, *Journal of the Ceramic Society of Japan*, **118**[1382] 959–962.
  51. R. Rosa, P. Veronesi, A. Corradi, C. Leonelli, M. Salvo, V. Casalegno, and M. Ferraris (2009) SiCf/SiC composites joining by microwave assisted SHS, in *33rd International Conference and Exposition on Advanced Ceramics and Composites*, January 18–23, Daytona Beach, Florida, <http://www.ceramics.org/daytona2009>
  52. J. G. P. Binner, P. A. Davis, T. E. Cross, and J. A. Fernie, Microwave joining of engineering ceramics, in *Microwave Solutions for Ceramic Engineers*, eds. D. E. Clark, D. C. Folz, C. E. Folgar, and M. M. Mahmoud, pp. 287–297, The American Ceramic Society, Westerville, OH, 2005.
  53. G. Bond, R. B. Moyes, and D. A. Whan (1993) Recent applications of microwave heating in catalysis, *Catalysis Today*, **17**[3] 427–437.
  54. I.-N. Lin, W.-C. Lee, K.-S. Liu, H.-F. Cheng, and M.-W. Wu (2001) On the microwave sintering technology for improving the properties of semiconducting electronic ceramics, *Journal of the European Ceramic Society*, **21**[10–11] 2085–2088.
  55. J. Monzó-Cabrera, A. Díaz-Morcillo, J. M. Catalá-Civera, and E. De Los Reyes (2001) Effect of dielectric properties on moisture levelling in microwave-assisted drying of laminar materials, *Microwave and Optical Technology Letters*, **30**[3] 165–168.
  56. M. Oghbaei and O. Mirzaee (2010) Microwave versus conventional sintering: A review of fundamentals, advantages and applications, *Journal of Alloys and Compounds*, **494**[1–2] 175–189.
  57. J. H. Booske, R. F. Cooper, S. A. Freeman, and K. R. Binger (1998) Enhancement of ionic diffusion by microwave-field-induced ponderomotive forces at physical interfaces, *Materials Research Society Symposium Proceedings*, **527** 525–532.
  58. J. H. Booske, R. F. Cooper, and S. A. Freeman (1997) Microwave enhanced reaction kinetics in ceramics, *Materials Research Innovations*, **1** 77–84.
  59. A. G. Whittaker (2005) Diffusion in microwave-heated ceramics, *Chemistry of Materials*, **17** 3426–3432.

60. A. Birnboim, J. P. Calame, and Y. Carmel (1999) Microfocusing and polarization effects in spherical neck ceramic microstructures during microwave processing, *Journal of Applied Physics*, **85** 478–482.
61. P. Veronesi, C. Leonelli, and G. Poli, Microwave enhancement of the early stages of sintering of metallic powder compacts and metal-containing composites, in *Microwaves in the Engineering and Applied Science*, ed. E. Caponetti, pp. 125–138, ENEA, Rome, Italy, 2007, free on line: [http://www.enea.it/produzione\\_scientifica/edizioni\\_anno/2007.html](http://www.enea.it/produzione_scientifica/edizioni_anno/2007.html).
62. W. D. Kingery, H. K. Bowen, and D. R. Uhlmann, *Introduction to Ceramics*. Wiley, New York, 1976.
63. H. Palmour III, M. L. Huckabee, and T. M. Hare, Microstructural development during optimized rate controlled sintering, in *Ceramic Microstructures*, Vol. 176, eds. R. M. Fulrath and J. A. Pask, pp. 308–319, Westview Press, Boulder, CO, 1977.
64. E. J. Minay, P. Veronesi, C. Leonelli, and A. R. Boccaccini (2004) Control of pore size by metallic fibres in glass matrix composite foams produced by microwave heating, *Journal of the European Ceramic Society*, **24** 3203–3208.
65. P. Veronesi, C. Leonelli, G. C. Pellacani, and A. R. Boccaccini (2003) Unique microstructure of glass-metal composites obtained by microwave assisted heat-treatments, *Journal of Thermal Analysis and Calorimetry*, **72** 1141–1149.
66. L. Barbieri, M. C. D'Arrigo, C. Leonelli, C. Siligardi, G. C. Pellacani, C. C. Sorrel, M. Hoffman, and S. Moricca (2000) Effect of silicon carbide whisker reinforcement on the CaO-ZrO<sub>2</sub>-SiO<sub>2</sub> glass-ceramic system, *British Ceramic Transaction*, **99**[6] 274–277.
67. M. Gupta and E. Wong Wai Leong, *Microwave and Metals*. Wiley-Interscience, Singapore, 2007.
68. E. J. Minay, A. R. Boccaccini, P. Veronesi, V. Cannillo, and C. Leonelli (2004) Processing of novel glass matrix composites by microwave heating, *Journal of Materials Processing Technology*, **155–156** 1749–1755.
69. E. J. Minay, A. R. Boccaccini, P. Veronesi, V. Cannillo, and C. Leonelli (2005) Sintering of metal fibre reinforced glass matrix composites using microwave radiation, *Advances in Applied Ceramics*, **104**[2] 49–54.
70. R. Rosa, P. Veronesi, C. Leonelli, and A. B. Corradi (2009) Microwave-assisted combustion synthesis and compaction of intermetallic-based functionally graded materials: Numerical simulation and experimental results, *International Journal of Self-Propagating High-Temperature Synthesis*, **18**[3] 163–172.
71. P. Veronesi, C. Leonelli, G. Poli, and A. Casagrande (2007) Enhanced reactive NiAl coatings by microwave assisted SHS, *COMPEL-The International Journal for Computation and Mathematics in Electrical and Electronic Engineering*, **27** 491–499.
72. G. P. Cammarota, A. Casagrande, G. Poli, and P. Veronesi (2009) Ni-Al-Ti coatings obtained by microwave assisted SHS: Effect of annealing on microstructural and mechanical properties, *Surface and Coatings Technology*, **203**[10–11] 1429–1437.
73. (a) S. C. Kashyap (2009) Microwave processing—A new dimension in synthesis of materials, in *Applied Electromagnetics Conference (AEMC)*, pp. 1–4, 14–16 Dec. 2009; (b) G. P. Cammarota, A. Casagrande, G. Poli, and P. Veronesi (2009) Ni-Al-Ti coatings obtained by microwave assisted SHS: Effect of annealing on microstructural and mechanical properties, *Surface and Coatings Technology*, **203**[10–11] 1429–1437.
74. (a) T.-R. Ji and J. E. Gerling (1988) A versatile microwave plasma applicator, *Materials Research Society Symposium Proceedings*, **124** 353–365; (b) C. Leonelli, G. Poli,



- P. Veronesi, and M. Garuti (2007) Design and optimisation of a new microwave plasma source by numerical simulation, *Plasma Devices and Operations*, **15**[1] 13–26.
75. R. Peelamedu, D. Kumar, and S. Kumar (2006) Microwave atmospheric pressure plasma for surface treatment and reactive coating on steel surfaces, surface and coatings technology, in *Proceedings of the 33rd International Conference on Metallurgical Coatings and Thin Films—ICMCTF 2006, The 33rd International Conference on Metallurgical Coatings and Thin Films*, 20 December, 201[7] 4008–4013.
  76. S. R. Wylie, A. I. Al-Shamma'a, J. Lucas, and R. A. Stuart (2004) An atmospheric microwave plasma jet for ceramic material processing, *Journal of Materials Processing Technology*, **153–154** 288–293.
  77. (a) W. Pan and J. Gong (2008) Microwave joining of 95Al<sub>2</sub>O<sub>3</sub> using interlayer containing SiC, *Key Engineering Materials*, **368–372** 1612–1613; (b) R. Rosa, P. Veronesi, C. Leonelli, A. Bonamartini Corradi, M. Ferraris, V. Casalegno, M. Salvo, and S. Han (2010) Microwave activated combustion synthesis and compaction in separate E and H fields: Numerical simulation and experimental results, *Advances in Science and Technology*, **63** 197–202.
  78. A. Ahmed and E. Siores (2001) Microwave joining of 48% alumina-32% zirconia-20% silica ceramics, *Journal of Materials Processing Technology*, **118**[1–3] 88–94.
  79. R. Cecilia, U. Kunz, and T. Turek (2007) Possibilities of process intensification using microwaves applied to catalytic microreactors, *Chemical Engineering and Processing*, **46** 870–881.
  80. A. I. Stankiewicz and J. A. Moulijn (2000) Process intensification: Transforming chemical engineering, *Chemical Engineering Progress*, **96** 1–22.
  81. Y. V. Bykov, K. I. Rybakov, and V. E. Semenov (2001) High-temperature microwave processing of materials, *Journal of Physics D: Applied Physics*, **34** R55–R75.
  82. P. Both and N. Lequeux (1997) Do microwaves increase the sinterability of ceramics? *Solid State Ionics*, **101–103** 1229–1233.
  83. M. A. Herrero, J. M. Kremsner, and C. O. Kappe (2008) Nonthermal microwave effects revisited: On the importance of internal temperature monitoring and agitation in microwave chemistry, *The Journal of Organic Chemistry*, **73** 36–47.
  84. (a) A. Loupy, (ed.), *Microwaves in Organic Synthesis*. Wiley-WCH, Weinheim, 2002; (b) B. L. Hayes, *Microwave Synthesis: Chemistry at the Speed of Light*. CEM Publishing, Matthews, NC, 2002.
  85. R. Roy, Y. Fang, J. Cheng, and D. Agrawal (2005) Decrystallizing solid crystalline titania, without melting, using microwave magnetic fields, *Journal of the American Ceramic Society*, **88**[6] 1640–1642.
  86. U. K. Sur, F. Marken, R. G. Compton, and B. A. Coles (2004) Microwave effects on the electrochemical deposition of copper, *New Journal of Chemistry*, **28** 1544–1549.
  87. E. Olevsky and L. Froyen (2006) Constitutive modeling of spark-plasma sintering of conductive materials, *Scripta Materialia*, **55**[12] 1175–1178.
  88. Z. A. Munir, U. Anselmi-Tamburini, and M. Ohyanagi (2006) The effect of electric field and pressure on the synthesis and consolidation of materials: A review of the spark plasma sintering method, *Journal of Materials Science*, **41** 763–777.
  89. J. E. Garay, S. C. Glade, U. Anselmi-Tamburini, P. Asoka-Kumar, and Z. A. Munir (2004) Electric current enhanced defect mobility in Ni<sub>3</sub>Ti intermetallics, *Applied Physics Letters*, **85** 573.

90. D. E. Clark, Microwave processing: Present status and future promise, in *Proceedings of the 17th Annual Conference on Composites and Advanced Ceramic Materials: Ceramic Engineering and Science Proceedings*, ed. J. B. Wachtman, pp. 3–21, John Wiley & Sons, Hoboken, NJ, 2008.
91. J. A. Tyburchy and D. K. Fisler, Electric properties of minerals and melts, in *Mineral Physics and Crystallography, A Handbook of Physical Constants*, pp. 185–209, Am. Geophys. Union, Washington, DC, 1995.



# ELECTROPHORETIC DEPOSITION

MARIA CANNIO, SAŠA NOVAK, LAXMIDHAR BESRA,  
AND ALDO R. BOCCACCINI

## 15.1 INTRODUCTION

Electrophoretic deposition (EPD) is a well-established ceramic processing technique [1–3] that is usually carried out in a two-electrode cell, as schematically shown in Figure 15.1. The basic mechanism of EPD involves two steps. In the first step, an electric field is applied between two electrodes and charged particles suspended in a suitable solvent move toward the oppositely charged electrode (electrophoresis). In the second step, the particles accumulate on the deposition electrode surface forming a homogeneous film (deposition). EPD requires a stable colloidal suspension, and it is applicable in principle to any particulate solid, including metals, polymers, ceramics, and glasses. In the case of ceramic materials, after EPD, a heat treatment step (sintering) is needed to densify the deposit [1–5].

Until the early 1990s, EPD was mainly used for the processing of traditional ceramics [5]. In the last 20 years, the applications of EPD have been expanded to produce a broad range of advanced materials, including ceramics, metals, polymers, and composites [2–4, 6]. EPD is a useful tool also in the field of nanomaterials processing, and complex material combinations can be fabricated by EPD, which enables the ordered

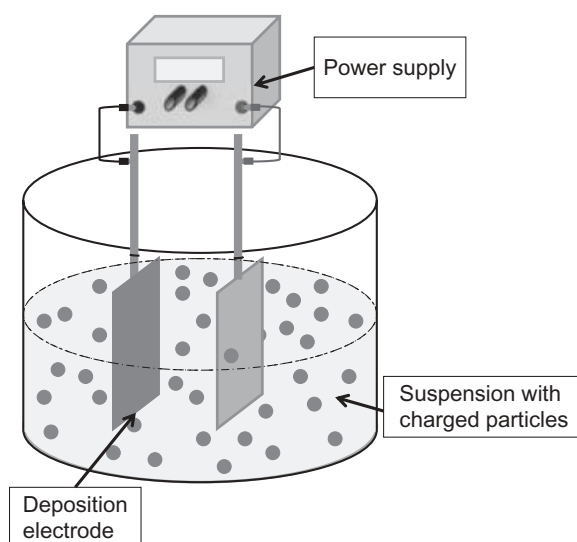


**Figure 15.1.** Basic EPD cell with parallel electrodes showing charged particles in suspension migrating toward the deposition electrode (figure courtesy of S. Keim, Erlangen).

assembly of nanoparticles and other nanostructures (e.g., carbon nanotubes [CNT]) in a variety of macroscopic dimensions and shapes [6, 7].

EPD offers several advantages, including its high versatility for application with different materials and combinations of materials, its cost-effectiveness, the requirement of relatively simple equipment, and the ability of EPD to be scaled up to large product volumes and sizes [2–4]. The success of EPD for advanced materials processing and the increasing opportunities being explored for applications in a wide range of materials are reflected by the increasing number of scientific publications in the field.

This chapter presents a summary of relevant previous work on the EPD of ceramics, describing the application of the technique in the processing of traditional and advanced ceramics considering also coatings and ceramic composites. The chapter includes also a section dedicated to briefly revise the fundamentals of EPD and the mechanisms proposed to explain the phenomena involved in EPD.

## 15.2 MECHANISMS AND FUNDAMENTALS OF EPD

Although EPD has been used successfully for many applications over the years, the exact mechanisms by which the deposit forms are still not entirely clear. As mentioned above, it is now recognized that EPD is a two-step process [1, 8]: (1) First, the particles in the suspension must migrate to the deposition electrode and (2) the particles must be destabilized at the electrode to form the deposit on the electrode surface.

The mechanism of particle stabilization and electrophoretic migration is now well established as discussed in the literature (for an overview, see Reference 2). The migra-

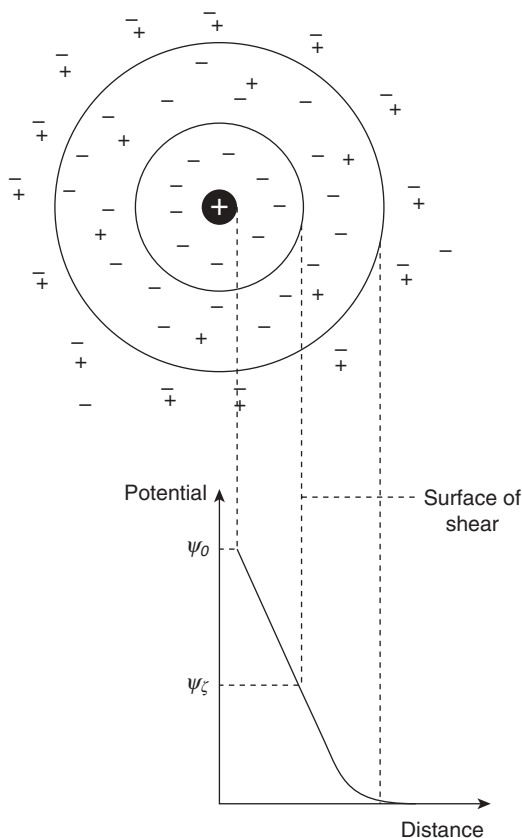


**Figure 15.2.** Schematic of the electrical double layer surrounding a charged particle [4] (reprinted with written permission from the publisher).

tion step is controlled by the bulk properties of the particle dispersion (suspension conductivity, viscosity, particle concentration, size distribution, and surface charge density) and the actual field strength in the suspension.

A charged particle in a suspension is surrounded by ions with an opposite charge in a concentration higher than the bulk concentration of these ions, forming the so-called electrical double layer (EDL) (Fig. 15.2). When an electric field is applied, these ions and the particles should move in the opposite direction. However, the ions are also attracted by the particle, and as a result, a fraction of the ions surrounding the particle will move along with the particle [4].

A general consensus pertaining to particle destabilization near the electrode (the deposition step) has not yet been reached. In this context, it must be noted that there is no single mechanism of EPD [9]. Just as there are several mechanisms for creating a stable colloidal suspension, there are several mechanisms by which particles can be destabilized to form an adherent deposit at the electrode surface. Particles can be

brought to an electrode by electrophoresis, but if there is no difference between the properties of the suspension in the bulk and at the electrode surface, particles will remain stable and no deposition will occur. By recognizing the electrochemical changes that occur at the electrode, there can be several ways to change the nature of a suspension so that particles that repel in the bulk can be made to deposit at the electrode. Thus, the deposition step proceeds by a complex superposition of electrochemical and aggregation phenomena.

Fukada et al. [10] have presented an excellent account of the mechanisms proposed to explain deposit formation by EPD, and Van Tassel and Randall [9] have given an overview describing how particles come into contact with each other to form a rigid particulate structure. They summarized the mechanisms on the basis of densification, direct electrostatic force, electrosedimentation, ion depletion enhanced electrostatic interaction, salting out, charge reduction/neutralization, squeezing out, bridging flocculation and desorption of neutral/charge polymer, and polyelectrolyte neutralization. According to Zhitomirsky [11], the EPD mechanisms can be divided into three categories: (1) charge neutralization or electrocoagulation, (2) zeta-potential (ZP) lowering, and (3) particle accumulation. Several other reviews on the mechanisms and kinetics of EPD and the application thereof to ceramics have been published [1, 2, 6, 12].

Each charged particle in suspension has an associated EDL (Fig. 15.2); thus, it is possible that the first layer of deposited particles will repel and prevent deposition of the incoming particles. The main question that remains to be answered pertains to the mechanism by which the repulsion between the deposited particle and the incoming particle is overcome for particle coagulation at the electrode during EPD. Several of the mechanisms proposed to explain the deposition phenomenon are presented below. These mechanisms are not exclusive and two or more mechanisms could occur simultaneously.

### 15.2.1 Flocculation by Particle Accumulation

The first attempts to explain the phenomenon of EPD were made by Hamaker [13] and Hamaker and Verwey [14]. It was identified that a particulate suspension, when allowed to stand undisturbed, produces a strongly adhering sediment. Hamaker and Verwey [14] suggested that the formation of a deposit by electrophoresis is akin to the formation of a sediment due to gravitation and that the primary function of the applied electric field in EPD is to move the particles toward the electrode to accumulate. The pressure exerted by the incoming particles enables particles next to the deposit to overcome the interparticle repulsion. However, this mechanism is feasible when deposition does not occur at the electrodes but on porous membranes such as a dialysis membrane [15].

### 15.2.2 Particle Charge Neutralization Mechanism

Grillon et al. [16] have suggested that when an electric field is applied to a particle suspension, the charges on the particle would neutralize upon contact with the oppositely charged deposition electrode and then become static. The mechanism is valid for single particles and monolayer deposits during the initial stages of deposition. It holds

good for deposition of powders that develop a charge on salt addition to the suspension and for deposition from very dilute suspensions. The mechanism is invalid, however, under the following conditions: (1) EPD for longer times (thick deposits); (2) when particle–electrode processes are prevented, for example, a semipermeable membrane induces deposition between the electrodes; and (3) when reactions occur at the electrode, which alters the pH thereabout.

### 15.2.3 Electrochemical Particle Coagulation Mechanism

Koelmans [17] suggested that the interparticle repulsion decreases near the electrode due to an increase in electrolyte concentration near it leading to aggregation and consolidation of particles. The expected increase in ionic strength next to an electrode was calculated and it was found that the ionic strength was of the same order as required to flocculate a suspension. The increase in electrolyte concentration near the deposition electrode lowers the ZP and induces flocculation of particles, which collapse to form a deposit. Since a finite time is required for the electrolyte concentration to build up near the electrode, it is expected that deposition would not occur before a certain time has passed. Koelmans [17] found, for example, that  $\text{MgCO}_3$  particles suspended in methanol deposited on the electrode as soon as the potential was applied, and that they remained there only after a certain critical time after voltage was cut off. The magnitude of the critical time was found to be inversely proportional to the applied voltage to the second power. Hence, the critical time can be very short, which explains why it is frequently not observed. This mechanism is plausible when the electrode reactions generate  $\text{OH}^-$  ions, for example, suspensions containing water. It is invalid when there is no increase of electrolyte concentration near the electrode.

### 15.2.4 EDL Distortion and Thinning Mechanism

A widely accepted mechanism of EPD is based on an EDL distortion and thinning process, proposed by Sarkar and Nicholson [1]. They considered the movement of positively charged oxide particles toward the cathode in an EPD cell as shown in Figure 15.3. When the particle lyosphere system moves (the lyosphere is formed by the counter ions from liquid around the charged particle, also called diffuse double layer), fluid dynamics and the applied electric field will distort the double-layer envelope in a way such that it becomes thinner ahead and wider behind the particle. The cations in the liquid also move to the cathode along with the positively charged particle. The counter ions in the extended “tail” will tend to react with these accompanying cations in high concentration around them. As a result of this reaction, the double layer around the tail will thin so that the next incoming particle (which has a thin leading double layer) can approach close enough for London–van der Waals (LVDW) attractive force to dominate and induce coagulation and deposition. The distortion of the double layer leading to coagulation is plausible considering the high concentration of particles near the electrode (or high collision efficiency). Second, this mechanism works for incoming particles with thin double-layer heads, coagulating with particles already in the deposit.

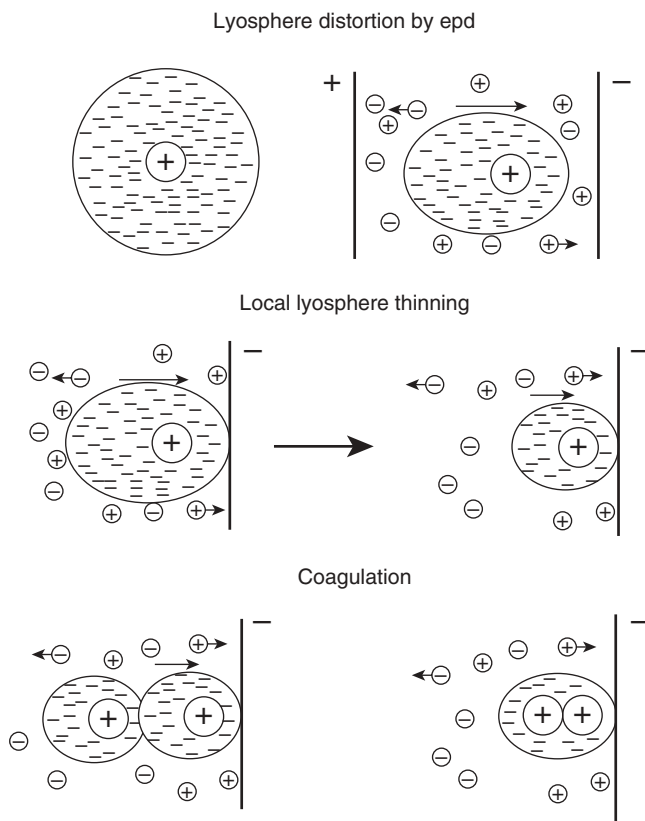


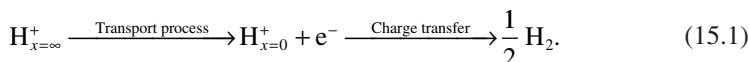
**Figure 15.3.** Electrical double-layer distortion and thinning mechanism for EPD [1] (reprinted with written permission from the publisher).

### 15.2.5 pH Localization Mechanism

Although the EDL distortion and thinning process proposed by Sarkar and Nicholson [1] remains the most accepted mechanism of particle coagulation during EPD, no experimental data confirming the mechanism have been presented. Following this, De and Nicholson [18] noted that as the cations carry the majority of current to the cathode, their concentration in the vicinity of the cathode must decrease because of discharge. The co-ions (ions of same charge as the particle surface in double layer) concentration should be a function of position and time in the EPD cell. This situation is different from the Sarkar and Nicholson [1] mechanism, and thus the real coagulation process must include a decrease of the co-ion concentration as a function of position and time in the EPD cell.

De and Nicholson [18] developed a model and showed by theoretical calculation using the fundamental characteristics of powder, solvent, and current densities that the  $H^+$  ion concentration near the cathode will deplete by discharge at the electrode, thereby

modifying the local pH in the vicinity of the electrode. The application of DC voltage in the EPD cell sets up a drift of ions in a preferred direction, for example,  $H^+$  ions toward the cathode. These ions will be discharged at the cathode. In the absence of this drift, the electrode would soon run out of ions for necessary charge transfer reactions. To maintain the charge transfer process at virtual equilibrium, the  $H^+$  ions must be supplied by the bulk solution ( $x = \infty$ ) to the cathode ( $x = 0$ ). The charge transfer process involves two steps and can be described by the following reaction:



If the charge transfer process is at virtual equilibrium, the process will be controlled by the rate of diffusion of  $H^+$  from the bulk to the interface. If the charge transfer process at the electrode consumes  $H^+$ , its concentration at the solution/electrode interface will drop below the bulk value.

Using the model of De and Nicholson [18], it is possible to predict the co-ion concentration gradient as a function of location within the suspension and deposition time, as well as its role in particle coagulation during EPD. But again, no experimental data have been presented to support this approach, understandably because of the difficulty in measuring ion concentration (or pH) reliably and reproducibly at locations very close to the electrode surface. Recently, pulse voltage/currents have been employed to obtain smooth and bubble-free deposits of significantly improved quality from aqueous suspensions [19]. The mechanism of deposition during pulse EPD is different from that of EPD using continuous electric field. Besra et al. [19] experimentally verified the pH localization mechanism of aqueous EPD by continuous as well as pulsed DC. The use of pulsed DC for EPD has been shown to control the extent of bubble incorporation and consequently to control the quality of deposits formed by EPD (Fig. 15.4). The application of continuous DC incorporates the maximum amount of bubbles in the deposit during aqueous EPD. The bubble incorporation decreases with the decreasing size of pulsed DC. The bubbles can be completely eliminated at a suitable

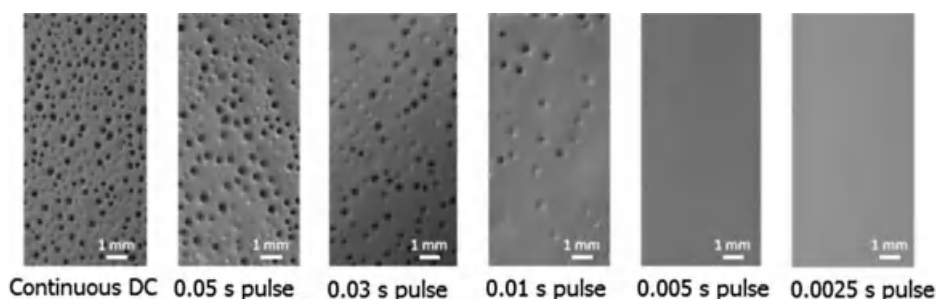


**Figure 15.4.** Surface morphology of deposits obtained by pulsed DC EPD in a constant current mode (suspension: 5 vol %; pH 4.5; applied current: 0.004 A; pulse duty cycle: 50%) [19] (reprinted with written permission from the publisher).

pulse width. Since the charge transfer process at the electrode consumes  $H^+$ , its concentration at the solution/electrode interface drops below the bulk value. Also, evolution of hydrogen as gas bubble at the cathode decreases the total concentration of hydrogen at the solution/cathode interface. In this context, the local pH near the cathode is expected to increase. Similarly, the evolution of  $O_2$  at the anode/solution interface will decrease the concentration of  $OH^-$  there. Thus, a decrease in pH is expected at the anode/solution interface.

The measured value of local pH at cathode/solution and anode/solution interfaces during constant voltage electrolysis of water of bulk pH 4.5, both on the application of continuous as well as pulse DC voltage of 20 V, is shown in Figure 15.5 [19]. The experimental data clearly show a substantial increase in local pH at the cathode/solution interface (Fig. 15.5a) and a marked decrease in the local pH at the anode/solution interface (Fig. 15.5b). The rise in pH reached as high as 10.7 on the application of 20 V continuous DC.

The rise in pH was very rapid and reached the plateau value of pH 10.7 in 30 s. A further increase in electrolysis time did not increase the pH any further. The rise in pH was gradual on the application of pulse voltage. It was observed that the plateau value of pH decreased with decreasing pulse size. Also, longer electrolysis time was needed to attain the plateau pH with decreasing pulse size. The rise in pH for a pulse size of 0.001 s for a 20 V applied potential was negligible. The local pH at the anode/electrolyte interface dropped from bulk pH to as low as pH 2.9 within 30 s of electrolysis on the application of a continuous voltage of 20 V. A further increase in electrolysis time did not decrease the pH any more. The decrease in pH was less on the application of pulse voltage. It was seen that the lower the pulse size, the less was the decrease in the anode/solution interface. A similar increase in pH at the cathode/solution interface and a decrease in pH at the anode/interface were observed for constant current electrolysis.

The change in local pH near the electrode/solution interface has a significant influence on the coagulation of particles during EPD. As an example, Besra et al. [19] showed for alumina suspensions that a shift in pH at the cathode from its initial bulk value of 4.5 to the alkaline region on application of the electric field will increase the pH toward the isoelectric point ( $pH_{iep}$ ). As soon as the local pH near the cathode/solution interface reaches the  $pH_{iep}$  of the suspension, the particles will spontaneously coagulate because of strong van der Waals attraction, resulting in the formation of a deposit on the cathode. Since the attainment of a plateau pH at the cathode/solution interface is fastest for continuous DC, one can expect to reach the  $pH_{iep}$  earlier and closer for continuous DC than for pulsed DC. Moreover, the application of a larger pulse will tend to reach the  $pH_{iep}$  earlier and closer than smaller pulses. Therefore, maximum deposition occurs for continuous DC and decreases progressively with a decrease in pulse size (Fig. 15.6) [20].

## 15.2.6 Mechanism of EPD on Porous Nonconducting Substrates

Conventionally, one of the prerequisites for EPD is that the substrate be electrically conductive. However, the possibility of forming deposits on nonconducting substrates by EPD is attractive for applications in a wider spectrum of materials and components.



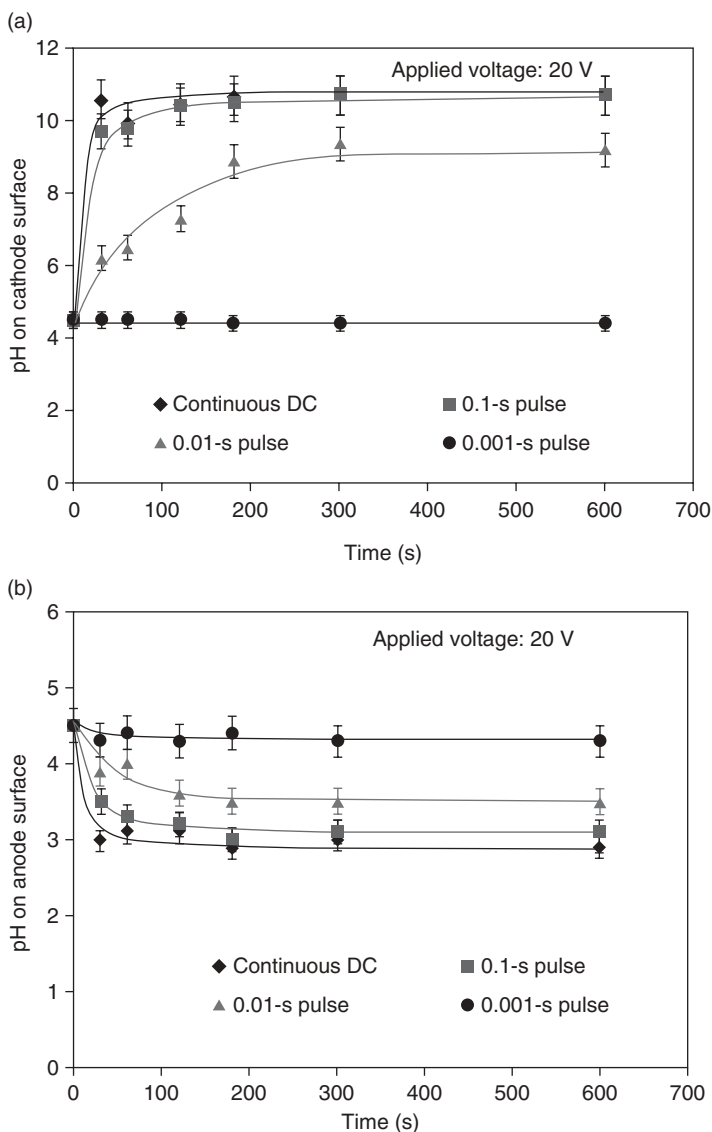


**Figure 15.5.** pH localization during constant voltage electrolysis of water at the (a) cathode/solution interface and (b) anode/solution interface (initial bulk pH = 4.5; conductivity =  $110 \mu\text{S}/\text{cm}$ ; applied voltage = 20 V) [19]. Reprinted with written permission from the publisher.

Several approaches have been adopted for EPD on nonconducting surfaces. These approaches included heat treatments in reducing atmospheres [21] or sputtering of a conducting coating [22] to make the substrate electrically conductive before EPD. A thin layer of conductive graphite coating [23] or a carbon sheet [24] were used on the back side of nonconducting NiO-yttria-stabilized zirconia (YSZ) porous substrates.

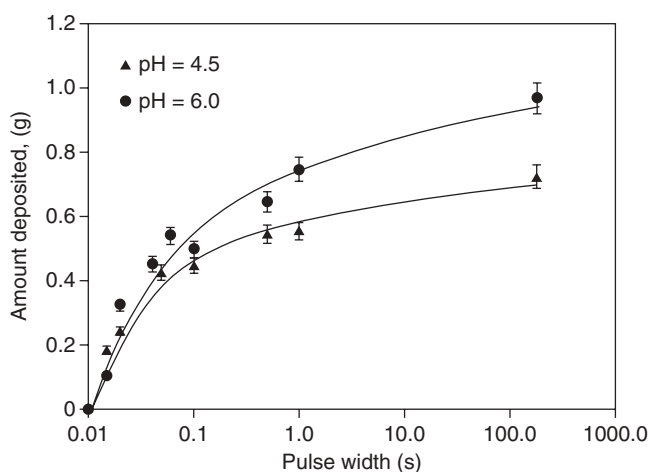


**Figure 15.6.** Deposit yield as a function of pulse width on a stainless steel substrate (suspension: 5 vol %; applied potential: 20 V; interelectrode distance: 20 mm; deposition area:  $20 \times 20$  mm). A pulse width of 180 s is equivalent to continuous DC voltage application for 3 min [20] (reprinted with written permission from the publisher).

Deposition of YSZ occurred on the front face in contact with the suspension. In this case, the deposition is made possible because of the porosity of the substrate. The importance of substrate porosity for EPD on nonconducting substrates was demonstrated by Besra et al. [24, 25]. It was demonstrated that the use of adequately porous substrates facilitates the availability of an electric field at the surface of the substrate. The porous substrates, when saturated with the solvent, help in establishing a “conductive path” between the electrical contact and the particles in suspension (Fig. 15.7). A similar mechanism has been proposed by Stoll et al. [26] to explain the deposition of alumina particles onto alumina fibers.

Deposition has been found to increase with increasing substrate porosity up to a certain value. Moreover, with increasing applied potential, the extent of deposition was seen to increase. For a given applied potential, there exists a threshold porosity value above which deposition by EPD was possible (Fig. 15.8). No deposition was possible on substrates with porosity below the threshold value. The threshold porosity is lower for higher applied potentials compared to lower applied potentials.

## 15.3 APPLICATIONS OF EPD

### 15.3.1 EPD in Traditional Ceramic Technology

EPD initially found commercial interest and industrial applications for the deposition of uniform coatings made of clay-based materials, vitreous enamel, or alumina on electrically conductive surfaces from aqueous suspensions. The use of EPD for the

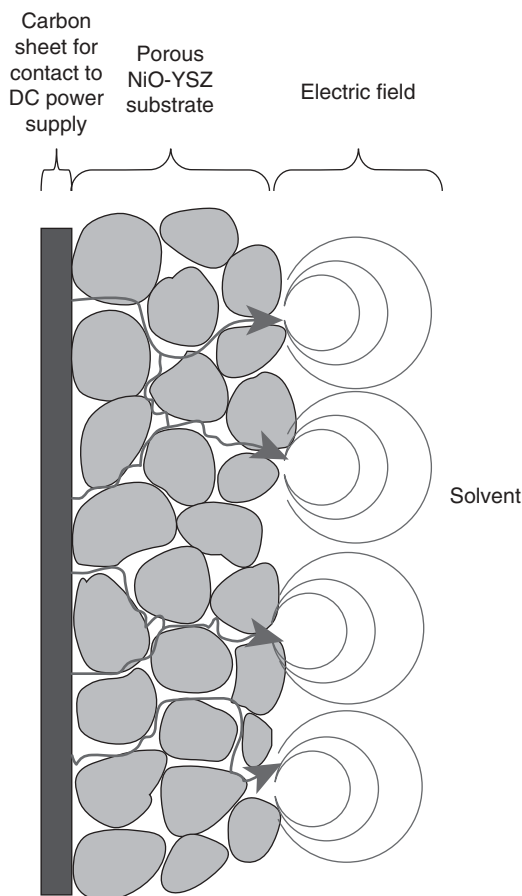


**Figure 15.7.** Conceptual representation of possible EPD mechanism on nonconducting substrates with a conductive backing of carbon sheet [24] (reprinted with written permission from the publisher).

production of clay-based bodies, for example, sanitaryware, tiles, and tableware, on an industrial scale has been investigated because of the expected order of magnitude improvement in formation rates achieved compared to slip casting. In fact, the production of clay-based materials by EPD can take a few minutes, whereas casting forming or slip casting requires more than 1 h. Several investigations have been carried out to describe the effect of the suspension's composition and the EPD process parameters such as pH, voltage, amount of stabilizer used, and deposition time on the yield, deposition rate, and the properties of the deposits formed to determine the conditions for effective and reproducible fabrication deposits, and hence to promote industrialization of the process [5]. The importance of a high ZP and an appropriate conductivity of suspensions for successful EPD has been emphasized [2, 3]. It is well-known that all these parameters affect the structure and the packing density of ceramic green parts and

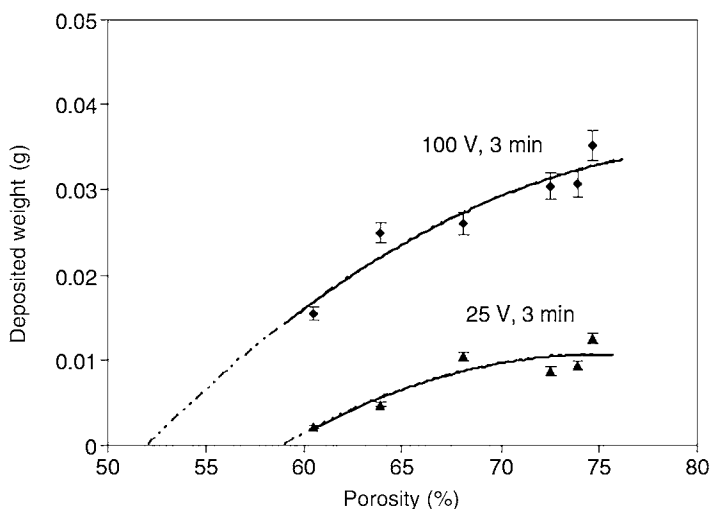


**Figure 15.8.** Influence of substrate porosity on the electrophoretic deposition of YSZ on a nonconducting NiO-YSZ substrate, from its suspension in acetylacetone [24] (reprinted with written permission from the publisher).

the final quality of the deposits. For example, the particle packing density in green bodies determines the sintering shrinkage, the density of the sintered components (or coatings), and the number and size of defects. In addition, aqueous EPD is preferred for commercial applications because it is advantageous from the viewpoints of ecology, safety, and cost. However, three problems of EPD from aqueous suspensions must be solved for this method to be used successfully as discussed by Ryan et al. [27] and Mihailescu et al. [28]:

- Water is decomposed into hydrogen and oxygen when a DC is passed through an aqueous medium.
- Galvanic attack on the metallic electrodes leads to contamination of the slip and the deposit followed by the deterioration of the deposit.
- The uneven water content in the casting is due to possible heating up of the deposit during the forming process.

Nevertheless, there have been reports of the fabrication of a bubble-free deposit from aqueous suspensions [5]. First, the use of a cement/graphite mixture solved the problem of oxygen bubble formation and enabled the production of complex-shaped molds at acceptable costs. However, the as-deposited layer was seen to be porous and nonuniform. Table 15.1 summarizes reports on the EPD of clay on different anode materials obtained by different investigators using different approaches to avoid the electrolysis of water and oxygen evolution, which accompanies electrolysis. The information in Table 15.1 indicates that uniform deposits exhibiting easy removal from the electrode (anode) could be obtained on zinc, copper, and black iron sheets. The main

TABLE 15.1. EPD of Clay from Aqueous Solutions on Different Anode Materials (Adapted from Reference 5)

Anode	Quality of Casting	Ease of Removal from the Anode
Zinc	Uniform	Easy
Aluminum	Cracked, porous, nonuniform	Easy
Copper	Uniform	Very easy
Black iron sheet	Cracked, uniform	Easy
Stainless steel	Very porous, nonuniform	Very difficult
Cement/graphite	Porous, nonuniform	Very easy
Polyester/graphite	Soft, porous, nonuniform	Easy

problem in these cases was the deposit contamination by the galvanic attack on the substrate. Another method of overcoming the formation of gas bubbles is the placement of an ion-permeable membrane filter in front of the anode, where the deposition of the dispersed particles takes place. Hence, oxygen evolution at the anode occurs without causing porosity within the coatings [29, 30]. Recently, Uchikoshi et al. [31] investigated the EPD characteristics of positively charged particles onto various cathodic substrates using aqueous alumina suspensions with various concentrations of hydroquinone (HQ) as an effective additive for bubble-free EPD at basic pH. In this case, the hydrogen gas produced at the cathode surface was readily absorbed into this metal. The oxygen produced electrolytically by the EPD process at basic pH would be consumed by the chemical oxidation of HQ to quinone (Q) so that a bubble-free deposit can be produced on the substrate. Significantly, they found that the green density and sintered properties of the deposits were the same as those produced by the slip casting process.

Heating of the deposited material (in particular clay) during EPD can lead to an uneven water content, which can cause uneven deformation and shrinkage of the deposit during the drying and firing processes. The problem could be solved by the lamination of two sheets leading to a balance of the gradient in moisture content [5]. The effect of uneven water content should be negligible in thick ( $>10\text{ }\mu\text{m}$ ) deposits. In particular, the electrochemical effects of deflocculating agents, organic materials, and the electrode nature have been investigated in the production of deposits with uniform thickness.

EPD has also been employed to produce vitreous (or porcelain) enamel coatings on metals. To achieve good adhesion between the metal substrate (e.g., steel) and the enamel, a pretreatment of the surface is essential including cleaning, picking in sulfuric acid, and coating of the surface with nickel deposits similar to that used for conventional enameling processes. After the deposition of a layer of glass particles, inorganic coatings can be obtained by fusing the powder deposited on the metal surface at temperatures above  $425^{\circ}\text{C}$  [5, 32]. It was found that EPD coatings presented superior smoothness and uniformity compared to those obtained by conventional dipping or spraying processes. In the early 1970s, these coatings found several applications (especially in Europe) in the industrial production of domestic whiteware [33].

On the other hand, nonaqueous EPD has been explored for the production of a range of ceramic coatings. Nonaqueous suspensions (namely, based on methanol, ethanol, isopropanol, *n*-propanol, acetone, acetylacetone, or mixtures of ethanol and acetylacetone) prevent electrolysis of water and oxygen evolution, which accompanies electrolysis and offer the possibility of depositing powders that react with water, such as nitrides, carbides, and superconducting ceramic powders. Joule heating is greatly reduced compared to aqueous slurries because of the lower electrical conductivities involved. Furthermore, ceramic powders could also develop large electrostatic potentials when dispersed in organic solvents, and the resulting repulsion between particles tends to stabilize dispersions from flocculation and to reduce sediment volumes. Finally, nonaqueous solutions offer the possibility of using EPD to deposit otherwise readily oxidizable metals. The disadvantages of organic liquids can be toxicity, safety aspects related to flammability, costs, and the relatively low dielectric constants, which lead to the requirement of high deposition voltages. Several criteria must be satisfied when selecting solvents for EPD suspensions. The ionic concentration in the liquid must remain low, which is a condition favoring low dielectric constant solvents. The ceramic powder should be stable in the solvent (no reaction with the solvent, no agglomeration) and the solvent should be able to generate charges on the surface of the powder (high ZP). In addition, there should be minimum charge carriers (ionic species) in the solvent since the current should be carried mostly by the suspended particles. Moreover, the solvent should have low surface tension and evaporation rate to prevent cracking during drying. Suitable organic additives can be added to achieve effective suspension stabilization and a sufficiently high electrophoretic mobility of the particles, which are the basic requirements for a successful EPD. Therefore, a proper selection of suitable solvent and optimization of the operating parameters are necessary for obtaining homogeneous deposits of the desired thickness by EPD. Several authors have conducted EPD in a variety of nonaqueous suspensions of submicron powders and various dispersants [2–6]. Within the range of nonaqueous media, alcohols are similar to water regarding the mechanisms by which the particles can acquire a surface charge. Relatively high electrophoretic mobilities can be achieved in alcoholic suspensions. In the early 1970s, the production of ceramic bodies from ethanol/shellac suspensions was demonstrated to form large ogives for use as rocket nose cones [5]. During the 1970s, a number of papers and patents were published describing a method of production of Na- $\beta$ -alumina tubes, used as an electrolyte in sodium sulfur batteries, by EPD from nonaqueous suspensions (nitromethane/chloroform mixture) [5, 34, 35]. Recent articles give several examples of applications of nonaqueous suspension systems for a number of ceramic materials [2–4]. A recent novel development is the use of ketone-based suspensions with amine additions for the EPD of  $\text{Al}_2\text{O}_3$  and  $\text{ZrO}_2$  [36]. It was shown that the electric field strength for methylethylketone (MEK) with *n*-butylamine-based suspensions is constant, and no potential drop at the electrodes is observed. This is in contrast with ethanol with acid-based suspensions where the deposit acts as an extra-resistive layer. Therefore, a MEK-based suspension with *n*-butylamine represents an interesting system for the EPD of thick deposits. Despite a good deposition yield, the suspension stability is rather low, which can generate rough surfaces for thick deposits (>5 mm). These suspensions therefore need vigorous stirring, which is not always applicable, as for

example, for the EPD of complex-shaped components, and the addition of dispersants is essential to improve the suspension stability. Some further investigations have revealed that nitrocellulose is an ideal additive to disperse metal oxide powders in MEK suspensions with *n*-butylamine. Deposits with a high green density, smooth surface, and a high deposition yield can be obtained when adding 10–15 vol % *n*-butylamine and 1 wt % nitrocellulose.

### 15.3.2 EPD in Coatings and Film Processing

The first reports on the use of EPD to prepare advanced ceramic coatings were published in the late 1980s [5, 37]. Hydrated alumina prepared by sol–gel was deposited by EPD on aluminum alloy substrates. The coatings were thicker, denser, and more adherent than those produced by conventional dip-coating techniques [38]. More recently, EPD has been confirmed as a suitable method to develop advanced ceramic coatings on a variety of substrates to improve wear and oxidation resistance, to impart bioactive character for biomedical implants, and to produce functional coatings for electronic, magnetic, and related applications, as reviewed in the literature [2–4, 6, 7]. Novel metal–ceramic composite coatings have been also produced combining EPD with electroplating or galvanic deposition of metals [39–44]. It is clear that the most difficult task to be solved when producing ceramic coatings on metal substrates is related to the limited temperature capability of the metals, which cannot resist the high temperatures required for sintering the ceramic layer. The development of densification techniques requiring lower temperatures has been highlighted by Wang et al. [45], who demonstrated the application of reaction bonding as an alternative to conventional sintering. EPD has also been used to join ceramic components. For example, mixtures of SiC or Si<sub>3</sub>N<sub>4</sub> and reactive carbon were deposited onto SiC or Si<sub>3</sub>N<sub>4</sub> parts to provide intermediate layers for reaction bonding with molten silicon [46]. The fabrication of composite ceramic coatings by the EPD of diphasic suspensions has also been a subject of investigations in the recent years. For example, smooth, uniform, dense diamond/borosilicate-glass composite coatings have been deposited onto stainless steel [47]. It was shown that it is possible to control the coating microstructure and composition by tailoring the initial EPD suspension. Usually, the concentration ratio of the two materials in the coatings can be controlled by varying the diphasic suspension concentration.

EPD has also found successful applications in the production of bioactive coatings for biomedical implants and devices. A recent review has discussed the EPD of biomaterials, focusing on the deposition of bioactive glasses and hydroxyapatite on medical alloys for orthopedic applications [48]. Examples include EPD of Bioglass® layers on stainless steel, of hydroxyapatite and related calcium phosphate films on TiAl<sub>4</sub>V alloys and FeCr alloys [49, 50] and the deposition of zirconia layers on dental crowns and bridges [51]. Some other significant recent developments of advanced ceramic functional coatings by EPD have been discussed elsewhere [6]. The developments include fabrication of BaTiO<sub>3</sub> thick films for sensor and actuator applications [52], ZnO films for gas sensors [53], composite TiO<sub>2</sub>–MnO<sub>2</sub> films [54], LiCoO<sub>2</sub> electrodes for rechargeable

lithium batteries [55],  $V_2O_5$  microparticles for cathodes for Li-secondary batteries [55], MgO thick films [56],  $BaNd_2Ti_5O_{14}$  thick films for microwave devices [57], zeolites for supported membranes for gas separations [58], PZT coatings for embedded components or for optical switches [59, 60], and Pb-Zr-Ti-Nb-Si-O ferroelectric thick films [61]. EPD has been also developed to fabricate high-temperature superconducting films with controlled thickness on substrates of various shapes and dimensions [62].

EPD has been progressively considered for the fabrication of cathode- and anode-supported solid oxide fuel cells (SOFCs) of both planar and tubular geometry [2, 63–66]. The relative advantages of EPD in the production of SOFC components include (1) the ability to deposit coatings on substrates of any shape; (2) the possibility of controlling deposition conditions, thus being able to prepare porous coatings as electrode and dense coatings as electrolyte; (3) the capability to obtain laminate structures of electrodes and electrolyte; and (4) the production of Ni-YSZ cermets (anodes) by electrophoretic codeposition. Zhitomirsky and Petric [67] have underlined relevant issues related to the selection of adequate solvents and additives, in particular concerning the chemical compatibility of the components of the binder–dispersant–solvent system, the solubility of the binder, the viscosity, and the electrical resistivity of the suspensions.

### 15.3.3 Laminated, Functionally Graded, and Composite Materials

Ceramic matrix composites (CMCs) combine the properties of the ceramic matrix and the reinforcing phase, which is discontinuously or continuously distributed in the matrix. For the reinforcement, particulates such as whiskers, platelets, and short or long fibers are introduced. Long “continuous” fibers woven into ceramic fabric infiltrated with a ceramic matrix form a special class of CMC that may fulfill also especially demanding requirements given by specific high-performance applications [68]. The specially tailored microstructure of CMC contributes to significantly reduced susceptibility to catastrophic failure that is especially important in large engineering structures.

In particular, in the case of complex-structured ceramic composites, that is, layered, functionally graded, and continuous fiber-reinforced CMC, fabrication is usually complex and/or cost intensive, which is a limiting factor for the wide industrial production of components. In this context, the principles of colloidal processing and the rapidly increasing level of knowledge about EPD-based manufacturing strategies are opening new possibilities for the production of various types of CMC with tailored structures and properties at a moderate price [69, 70].

EPD has been successfully employed to fabricate particulate ceramic composites, laminates, and functionally graded materials (FGMs) as well as fiber-reinforced ceramic composites, as reviewed elsewhere [3, 4, 70]. Particulate composites with a homogeneous or controllably gradient microstructure are relatively easily formed by EPD from stable and homogeneous colloidal aqueous or nonaqueous suspensions. By careful control of the process, homogeneous distribution can be attained also in the case of two(or more)-phase systems in which the components exhibit opposite surface charges in a certain range of pH values. For example, by controlling the  $\zeta$ -potential, Hadraba



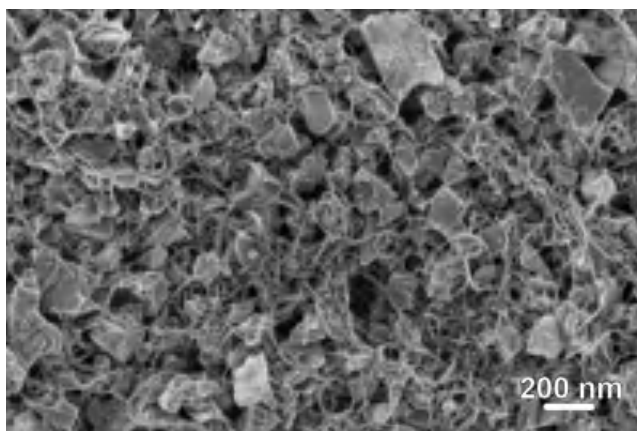


**Figure 15.9.** Field emission (FE) SEM image of the fracture surface of a SiC-CNT composite prepared by EPD in ethanol suspension of the particle mixture.

et al. [71] successfully deposited particulate composites from a mixture of  $\text{Al}_2\text{O}_3$  and  $\text{ZrO}_2$  powders in isopropanol suspension stabilized with monochloroacetic acid. By selecting the conditions where the electrophoretic mobility of  $\text{Al}_2\text{O}_3$  and  $\text{ZrO}_2$  particles are similar, ceramic composites with a controlled microstructure were prepared, such as a particulate, layered, or functionally gradient composite with continuous gradient concentration transition. Similarly, Jean and coauthors [72] showed that during deposition  $\text{Al}_2\text{O}_3$  particles and SiC whiskers migrate and deposit at approximately the same rate, resulting in a nearly unchanged composition of the composite green parts. Homogeneous distribution of the phases can be achieved even in the case when the constituents significantly differ in particle aspect ratio, providing that the surface charges of both phases was approximately equalized. Figure 15.9 illustrates a green part with homogeneously distributed silicon carbide particles and CNTs, deposited on a graphite electrode from aqueous suspensions at conditions where the  $\zeta$ -potential of both SiC and CNT were highly negatively charged.

Progresses in FGM fabrication by EPD have been reported by Put et al. [73], showing the manufacture of graded WC-Co composites using a suspension of WC powder in acetone with variable Co powder content. Other significant developments in this field include anodic codeposition of  $\text{Al}_2\text{O}_3$  and  $\text{CeO}_2$ -stabilized zirconia powders to produce cylindrical and tubular-shaped  $\text{Al}_2\text{O}_3$ /zirconia FGM components [74] and the production of functionally graded  $\text{Si}_3\text{N}_4$ - $\text{TiC}_{0.5}\text{N}_{0.5}$  composites using  $\text{Si}_3\text{N}_4$  as a matrix and  $\text{TiC}_{0.5}\text{N}_{0.5}$  as the hard phase [75]. Other studies on the EPD production of nickel-alumina [9, 76], alumina-zirconia [77–79],  $\text{Al}_2\text{O}_3$ - $\text{ZrO}_2$ -Ti(C,N) [80], and hydroxyapatite-bioactive glass [81] FGM coatings have been discussed in the literature.

Laminated materials can be produced via EPD by moving the deposition electrode to a second suspension for the deposition of a layer of different composition when the desired thickness of the first layer is reached. By changing back and forth, a layered

material is readily obtained. The system zirconia/alumina has been widely investigated in this regard. For example, Ferrari and coworkers [82] prepared  $\text{Al}_2\text{O}_3/\text{Y-TZP}$  layered composites with 10 layers by EPD from aqueous suspensions. Dense bubble-free laminated ceramics were also deposited from aqueous suspensions by Fischer et al. [83] and Uchikoshi et al. [31]. The deposition was performed using various metal electrodes. You et al. [84] reported the fabrication of  $\text{SiC-TiC}$  laminated structures by EPD from acetone-based suspensions.

EPD has been also employed in the fabrication of continuous fiber-reinforced CMC with a variety of ceramic matrices and fibers [70, 85–89]. EPD allows adequate infiltration of ceramic particles into the interfiber spaces of 2-D and 3-D fiber preforms, which is difficult to be achieved by other processing routes. The fibers used can be either nonconductive (e.g., alumina or mullite) or conductive (e.g.,  $\text{SiC}$ , carbon). The fiber weave is typically placed in front of the deposition electrode so that ceramic deposit develops on the electrode and grows through the fiber mat.

In the reported works, the use of 2-D fiber reinforcements strongly prevails [70]. For example, Bao and Nicholson [90] fabricated alumina–alumina CMC by means of EPD from a suspension of submicron-sized  $\text{Al}_2\text{O}_3$  particles (100–300 nm) and with Nextel®-type (alumina) fibers. The same type of composite was fabricated by Stoll et al. [26]. They used 25 wt % of  $\alpha$ -alumina powder ( $d = 100\text{--}300$  nm) dispersed in ethanol and 4-hydroxybenzoic acid as a dispersant agent that rendered alumina particles positively charged in ethanol. Thick CMC components ( $>10\text{-mm}$  thickness) were fabricated, opening the possibility of greater industrial application of these materials. The EPD of alumina–mullite composites has been reported by Kaya and Butler [91]. They used mullite fibers coated with a crack-deflecting layer of  $\text{NdPO}_4$ .

Based on experimental evidence, Stoll et al. [26] and Bao and Nicholson [90] have suggested that in electrophoretic infiltration, particles and fibers must possess equal surface charge. Due to the applied external electric field, each charged particle is attracted by the oppositely charged electrode behind the fiber mat, and due to the repulsion force taking place between the particles and the fibers, adhesion of the particles to the fibers is prevented. It has been hypothesized [26] that under the effect of the repulsive forces due to the surrounding fibers, the particles follow the path with the fewest possible obstacles. Therefore, when the particles reach the electrode or the surface of previously deposited particles, they have no further possibility to move and, consequently, the electrophoretic ceramic deposit grows. Conversely, if the fiber and particles exhibit an opposite surface charge, coagulation can occur on the fibers encountered by the traveling particles. In this case, a deposit on the outer fiber layer will block the movement of the particles toward the interior of the fiber mat, resulting in poor impregnation and low-quality microstructure.

Illston et al. [92] patented originally a suitable EPD-based method to fabricate silica matrix composites reinforced with  $\text{SiC}$ -fiber mats coated with carbon. Several mats were stacked after EPD in a suitably shaped graphite dye. A similar procedure to produce a 3-D  $\text{SiC/SiC}$  composite was used by Kaya et al. [93]. In their work, 20 wt % of  $\text{SiC}$  powder ( $d_{50} = 200$  nm) was dispersed in distilled water at pH 9 with the addition of boehmite and  $\text{Y}_2\text{Si}_2\text{O}_7$  as sintering aids. The conductive carbon-coated  $\text{SiC}$ -fibers were used directly as the deposition electrode. A 3-D composite was prepared by com-

pacting six or eight EPD-infiltrated layers together using pressure filtration. 2-D carbon-coated SiC-fiber mats (Nicalon,  $5 \times 5 \text{ cm}^2$ ) were also used to reinforce the mullite matrix, which was prepared by aqueous suspensions of fumed silica (28 wt %) and alumina (72 wt %) particles at pH 3.1. The fiber mat was employed as the deposition electrode (cathode), while the counter electrode was stainless steel foil [94].

Based on a systematic study of the electrokinetic properties of SiC-fibers and powders as well as the deposition and infiltration processes, Novak and coworkers [95] presented a method to control the infiltration of 2-D and 3-D SiC-fiber mats with SiC particles in aqueous suspension. Tyrano SA and Nicalon fiber mats were used for the infiltration of a submicron  $\beta$ -SiC powder. Due to the strict requirements for the target material proposed to be used in the first wall blanket of future fusion reactors, a graphite electrode was used as the only acceptable to avoid any contamination with metals. The graphite electrode also prevented bubble formation due to gas evolution during water electrolysis.

The applicability of EPD in forming SiC-reinforced SiC ceramics by the infiltration of 3-D woven fiber mat (3 mm thick) has been first shown by Novak et al. [96]. It was confirmed that for the effective impregnation of fiber mats by EPD, the suspended particles and the fibers must have the same polarity and hence, that surface charge modification of the fibers and particles to be infiltrated into the fiber preform is an essential step for the preparation of these CMCs. Moreover, results revealed that the position of the conductive SiC-fibers is crucial for successful infiltration. Full infiltration through the thickness of the 3-mm-thick 3-D weave was achieved only in the case when fibers were not attached directly on the anode, as illustrated in Figure 15.10. At carefully selected conditions, the SiC particles ( $d_{50} \sim 0.5 \mu\text{m}$ ) entered even the very thin gaps between the SiC-fibers, as shown in Figure 15.11.

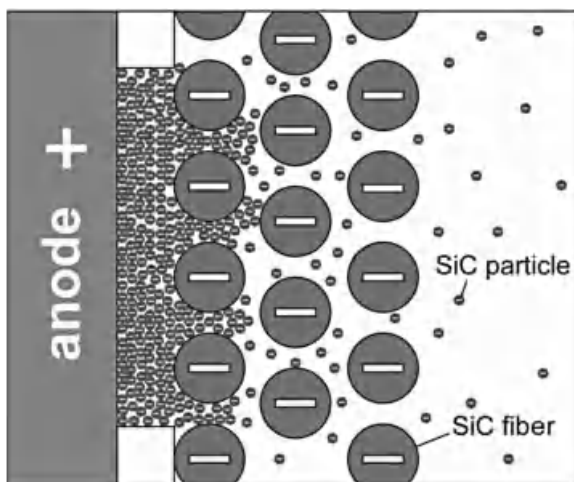


**Figure 15.10.** Schematic presentation of the electrophoretic infiltration of the fiber mat to produce SiC-SiC composites.

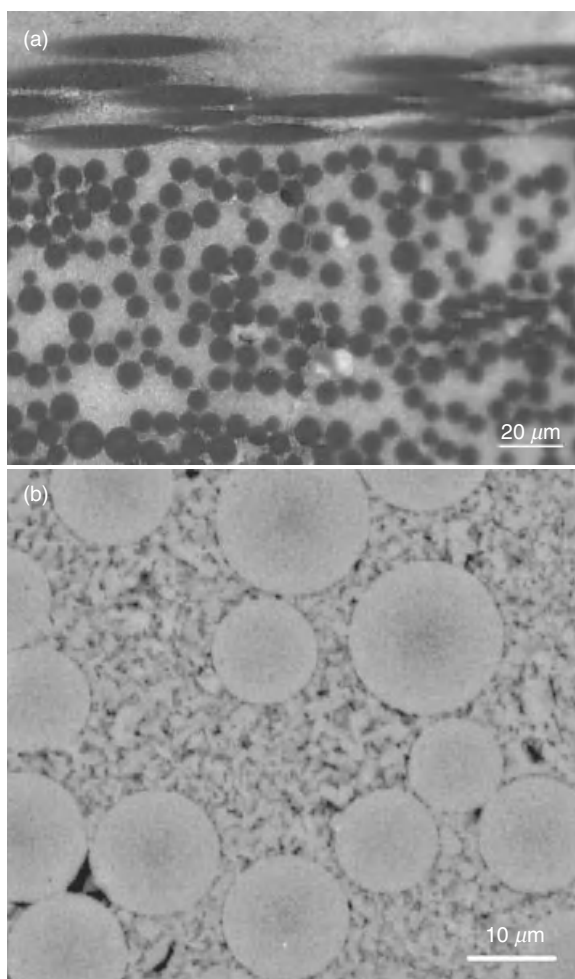


**Figure 15.11.** Optical (a) and SEM (b) micrographs of the polished cross section of a  $\text{SiC}_f/\text{SiC}$  composite prepared by electrophoretic infiltration of 3-D  $\text{SiC}$ -fiber fabric (Tyrano SA) with  $\text{SiC}$  powder and further densified by the aid of polymer precursor AHCP.

Conversely, when conductive fibers ( $\text{SiC}$ , C) were attached to the electrode, similar effects appeared as observed in the case of oppositely charged particles and fibers. Since in this case the fiber mat acted as the electrode, the oppositely charged particles were attracted by and deposited onto the fiber mat instead of infiltrating it. As presented in Figure 15.12, the deposit is formed on the external side of the fiber mat, and thus it hinders the movement of particles into the interior of the structure, which remains nonimpregnated.

A composite with an even more complex structure has been recently prepared by König et al. [97] incorporating CNTs. For a  $\text{CNT-SiC}_f/\text{SiC}$  composite, 2-D woven  $\text{SiC}$ -

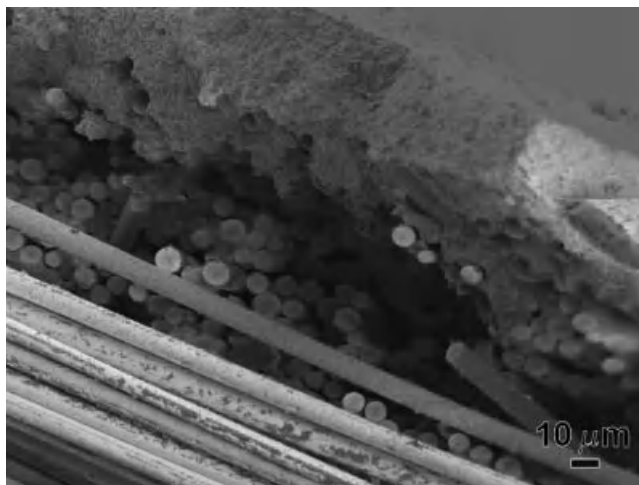


**Figure 15.12.** Fracture surface of a SiC-fiber mat electrophoretically infiltrated with SiC particles when the mat was in contact with the electrode. Only the outer (ca. 10  $\mu\text{m}$  thick) layer is impregnated with the powder.

fibers were first electrophoretically coated by CNT, and then the coated fabric was infiltrated with SiC powder in aqueous suspension by EPD. In both cases, well-dispersed alkaline suspensions with  $\zeta$ -potential approximately  $-50$  mV were used. It was pointed out that in order to ensure the effectiveness of the infiltration, these two stages have to be performed at different conditions. While in the coating step, the SiC-fiber mat was attached as the anode and was deposited with a layer of CNT at an applied voltage of 2.8 V; in the infiltration stage, the fiber mat was separated from the electrode and the infiltration was performed at 30 V/cm from a suspension with high solids loading (60 wt %).

A literature survey indicates that a variety of solvents have been successfully used in EPD for the fabrication of CMC [70]. Ethanol appears to be quite frequently used. Its main drawback is the hygroscopicity, which makes it difficult to control the content of water, which may destabilize the suspension [98]. Due to a high dielectric constant, water results in relatively high  $\zeta$ -potential values and it is therefore, in addition to its more environment friendly nature, the preferred media in EPD, as mentioned in Section 15.3, provided that bubble formation due to electrolysis is prevented. The selection of the liquid media is one of the basic decisions that determine most of the further parameters in EPD; namely, the solvent must dissolve the surfactant, but not the suspended powders; it must provide appropriate conductivity to the suspension and must wet effectively the powder particles as well as the fibers. In contrast to the oxides, nonoxide particles and fibers are typically more hydrophobic, and therefore the addition of appropriate wetting agents is also important for the successful infiltration of fiber mats [95, 96].

In general, the key parameters affecting the efficiency of the electrophoretic infiltration of fiber mats can be summarized and classified into three main groups:

1. *Parameters Related to the Properties of the Suspensions:* solvent properties,  $\zeta$ -potential and conductivity, solid content in the suspension
2. *Parameters Related to the Inherent Properties of the Fibers:* electrical conductivity, preform architecture, surface charge of the fibers at working pH
3. *Parameters Related to the Process:* applied voltage, time, EPD cell configuration, vacuum degassing.

In summary, there are a number of requirements for the successful infiltration of fiber fabrics for CMC fabrication, such as the use of suitable solvents and surfactants to provide sufficient electrical net charge at the particle's surface to penetrate and efficiently fill the voids within the fabric, as well as optimal solids loading. The resulting deposit (matrix) within the fiber mats must exhibit high particle packing density, which is also related to the absence of bubbles and attaining the highest possible homogeneity.

### 15.3.4 EPD of Nanoparticles

EPD of ceramic nanoparticles (size < 100 nm) is used to produce a variety of materials, including monolithic ceramics, ceramic coatings and films, FGMs, as well as ceramic laminates and CMCs of high microstructural homogeneity. Previous work on the EPD of nanoparticles has been reviewed comprehensively [6].

Tabellion and Clasen [99] reported on the fabrication of large components, free-standing objects, hollow bodies, and objects of complex 3-D shapes by EPD of silica nanoparticles in aqueous suspensions. Nanostructured BaTiO<sub>3</sub> and Eu-doped BaTiO<sub>3</sub> thin films have been produced by the EPD of nanoparticles from acetylacetone suspensions [100], aqueous suspensions [101], and ethanol suspensions [102]. The production of nanostructured zirconia coatings by EPD has been reported both from aqueous suspensions to produce dental crowns [103] and from ethanol suspensions to produce thermal barrier coatings [104]. Moreover, a wide range of nanostructured functional layers have been developed by the EPD of nanoparticles, including nanocrystalline europium oxide (Eu<sub>2</sub>O<sub>3</sub>) thin films [105]. The deposition of nanostructured titania films by EPD is well-known [106–108]. EPD TiO<sub>2</sub> coatings are useful for a range of applications, including batteries, displays, photocatalysis, and solar energy conversion systems. A few examples include Ti(III)-doped nanocrystalline TiO<sub>2</sub> films on optically transparent electrodes [109], nanosized titania films on stainless steel for photoelectrocatalytic applications [110], and TiO<sub>2</sub>-Ag composite coatings for antibacterial orthopedic applications [111]. Numerous other types of ceramic nanoparticles have been deposited by EPD, such as hydroxyapatite [112], lead zirconate titanate (PZT) [113], silicon carbide [114], ceria [115], gamma ferric oxide [116], titania nanotubes [117], and YSZ [118].



### 15.3.5 EPD of CNT

There is continuous interest in CNTs, both single-walled CNTs (SWCNTs) and multi-walled CNTs (MWCNTs), for a broad range of applications [119]. EPD is an attractive method to manipulate CNT in order to form ordered, oriented nanotubes arrays [120].

CNT suspensions for EPD are prepared using different solvents such as distilled water, acetone/ethanol mixtures, and pure organic solvents such as ethanol, isopropyl alcohol, n-pentanol, ethyl alcohol, tetrahydrofuran, dimethylformamide, and deionized water with pyrrole. Stable suspensions of CNT for EPD should contain CNT with high  $\zeta$ -potential and should exhibit low ionic conductivity. Due to the intrinsically uncharged surface of the CNT, effective methods to disperse them in a liquid medium involve performing an acid treatment to provide active sites (functionalization), adding surfactants, and application of ultrasonication [120]. In early experiments, Du and Pan [121] deposited MWCNT thin films by EPD to produce supercapacitors with high specific power density and a very small equivalent series resistance. These thin films could be applied as coating layers over ordinary current collectors to considerably enhance the electrode performance. Previous research on the EPD of CNT, both MWCNT and SWCNT, has been reviewed elsewhere [120], indicating the variety of suspension systems investigated to develop suitable CNT suspensions for EPD.

Applications of CNT EPD coatings include field emission devices [122], photochemical solar cells [123], electrochemical capacitors [124], and biomedical coatings [48, 125, 126]. In addition to developing CNT-based coatings on planar substrates, EPD can be conveniently applied to deposit CNTs onto complex-shaped components, including microwires, porous substrates, and fibrous bodies or textiles [120, 127]. There have been also recent developments on the fabrication by EPD of CNT reinforced hydroxyapatite and bioactive glass coatings for biomedical applications [128, 129]. The fabrication of more complex patterns of CNT deposits can be realized by using masks or by designing combinations of conductive and nonconductive surfaces. In this context, the application of EPD for the development of CMC was briefly discussed in Section 15.3.3 (see Fig. 15.9). Moreover, composites consisting of ceramic nanoparticles and MWCNT have been produced recently by sequential EPD and by electrophoretic codeposition, as reviewed elsewhere [7].

## 15.4 FUTURE DEVELOPMENTS

Besides the established application of EPD in the areas discussed above, ranging from traditional ceramics to functional and structural coatings, ceramic composites, CNTs, and EPD of nanoparticles, there is increasing interest in the application of EPD-based techniques for the fabrication of ceramic nanoarchitectures, including nanorods, nanowires, nanotubes, and nanosheets for advanced functional applications. In this context, for example, zinc oxide nanorods and nanotubes have been synthesized and electrophoretically deposited for sensor applications [130]. Kim et al. [131] converted commercial titania nanoparticles to nanotubes using a hydrothermal method and then

deposited a titanate nanotube film on a Si substrate by EPD. The development of composite electrodes by EPD, for example, based on porous nanosheet-stacked  $\text{NiCo}_2\text{O}_4/\text{Ni}$  composites, has been investigated by the calcination method. These electrode films are crystalline and are composed of regular hexagonal  $\text{NiCo}_2\text{O}_4$  nanosheets with an average diameter of 200 nm. Ruthenic acid nanosheets have been deposited by EPD on gold, indium–tin oxide-coated glass and indium–tin oxide-coated poly(ethylene terephthalate) electrodes [132]. As mentioned above, EPD has great potential for manipulation of CNT and for their assembly into ordered layers including thin films and coatings. Manipulation of CNT by EPD is likely to be further explored in the near future for the fabrication of functional ceramic composites [7]. For example, EPD may represent a powerful tool to produce CNT-based devices, considering that few alternative techniques exist to deposit and align CNT.

Another sector likely to see increased research efforts in EPD developments is the biomedical materials field. Here, EPD has the significant advantage, compared with other fabrication routes, of operating at low temperatures, and it can be scaled up using inexpensive equipment. EPD has the potential to be a commercial viable technology for the large-scale production of biomedical coatings [48]. Further specific areas in which EPD is expected to expand, particularly in the field of bionanotechnology, include the fabrication of nanostructured and hybrid composite biomaterials, functionally graded bioactive and biomimetic coatings, biosensors, and porous materials (e.g., porous bioceramic scaffolds) for regenerative medicine.

Despite the mentioned advantages, further theoretical and modeling work is required to increase our understanding of the mechanisms involved in EPD, especially when combinations of (nano)particles in suspension are considered. The optimization of EPD parameters is usually carried out by time-consuming trial-and-error approaches, which reflects the lack of available quantitative relationships linking EPD parameters, that is, deposition time, voltage, suspension concentration, deposition kinetics, and final deposit properties.

## 15.5 CONCLUSIONS

EPD presents several advantages for the processing of ceramic materials from particulate suspensions, including its high versatility, cost-effectiveness, ability to control nano- and microstructure, as well as its suitability for microscopic and macroscopic dimensions. This chapter has reviewed the mechanisms and fundamentals of EPD, as well as presented a broad overview of EPD application areas in traditional ceramics, coatings, ceramic composites, as well as the use of EPD for the manipulation of nanoparticles, nanotubes, and other nanostructures. Specific areas where EPD is expected to expand were discussed; these include the fabrication of nanostructured composite materials, films, and coatings for functional and biomedical applications. The versatility of the EPD process can be exploited for the fabrication of novel materials where the emerging in-depth understanding of the process itself and the ability to tailor the properties of suspensions will enable an expanding area of applications leading to complex materials with enhanced properties. In this context, the fabrication



of particulate composites with a homogeneous, layered, or functionally graded microstructure, as well as the production of even more complex fiber-reinforced composites, including CNT-based structures, is slowly approaching the point of sufficient maturity to enter industrial production.

It has been also widely accepted in the EPD community that increased research efforts in the field of analytical and numerical modeling of the mechanisms of EPD are necessary [133]. A goal is to increasingly avoid the empirical and time-consuming trial-and-error approaches that dominate the experimental work and technological developments in the area. The availability of quantitative relationships between EPD processing parameters, EPD kinetics, and characteristics of deposits will allow a better design of EPD systems for given applications.

## ACKNOWLEDGMENTS

One of the authors (S. Novak) acknowledges financial support from the Slovenian Research Agency. The authors acknowledge also the contributions of Mrs. K. König and Mr. A. Iveković.

## REFERENCES

1. P. Sarkar and P. S. Nicholson (1996) Electrophoretic deposition (EPD): Mechanism, kinetics and application to ceramics, *Journal of the American Ceramic Society*, **79** 1987–2002.
2. L. Besra and M. Liu (2007) A review on fundamentals and applications of electrophoretic deposition (EPD), *Progress in Materials Science*, **52** 1–61.
3. A. R. Boccaccini and I. Zhitomirsky (2002) Application of electrophoretic and electrolytic deposition techniques in ceramics processing, *Current Opinion in Solid State and Materials Science*, **6** 251–260.
4. O. O. Van Der Biest and L. J. Vandeperre (1999) Electrophoretic deposition of materials, *Annual Review of Material Science*, **29** 327–352.
5. M. S. J. Gani (1994) Electrophoretic deposition. A Review, *Industrial Ceramics*, **14** 163–174.
6. I. Corni, M. P. Ryan, and A. R. Boccaccini (2008) Electrophoretic deposition: From traditional ceramics to nanotechnology, *Journal of the European Ceramic Society*, **28** 1353–1367.
7. A. R. Boccaccini, J. Cho, T. Subhani, C. Kaya, and F. Kaya (2010) Electrophoretic deposition of carbon nanotube–ceramic nanocomposites, *Journal of the European Ceramic Society*, **30** 1115–1129.
8. F. Bouyer and A. Foissy (1999) Electrophoretic deposition of silicon carbide, *Journal of the American Ceramic Society*, **82**[8] 2001–2010.
9. J. Van Tassel and C. A. Randall (2006) Mechanism of Electrophoretic deposition, *Key Engineering Materials*, **314** 167–174.

10. Y. Fukada, N. Nagarajan, W. Mekky, Y. Bao, H. S. Kim, and P. S. Nicholson (2004) Electrophoretic deposition—Mechanisms, myths and materials, *Journal of Materials Science*, **39** 787–801.
11. I. Zhitomirsky (2002) Cathodic electrophoretic deposition of ceramic and organoceramic materials—Fundamenta aspects, *Advances in Colloids and Interface Science*, **97** 279–317.
12. B. Ferrari and R. Moreno (2010) EPD Kinetics: A review, *Journal of the European Ceramic Society*, **30** 1069–1078.
13. H. C. Hamaker (1940) Formation of deposition by electrophoresis, *Transactions of the Faraday Society*, **36** 279–283.
14. H. C. Hamaker and E. J. W. Verwey (1940) The Role of the Forces between the Particles in Electrodeposition and other Phenomena, *Transactions of the Faraday Society*, **36** 180–185.
15. N. Heavens, Electrophoretic deposition as a processing route for ceramics, in *Advanced Ceramic Processing and Technology*, Chapter 7, Vol. 1, ed. G. P. Binner, pp. 255–283, Noyes Publications, Park Ridge, NJ, 1990.
16. F. Grillon, D. Fayeulle, and M. Jeandin (1992) Quantitative image analysis of electrophoretic coatings, *Journal of Materials Science Letters*, **11** 272–275.
17. H. Koelmans (1995) Suspensions in nonaqueous media, *Philips Research Reports*, **10** 161–193.
18. D. De and P. S. Nicholson (1999) Role of ionic depletion in deposition during electrophoretic deposition, *Journal of the American Ceramic Society*, **81**[11] 3031–3036.
19. L. Besra, T. Uchikoshi, T. S. Suzuki, and Y. Sakka (2010) Experimental verification of pH localization mechanism of particle consolidation at the electrode/solution interface and its application to pulsed DC Electrophoretic deposition (EPD), *Journal of the European Ceramic Society*, **30** 1187–1193.
20. L. Besra, T. Uchikoshi, T. S. Suzuki, and Y. Sakka (2008) Bubble-free aqueous electrophoretic deposition (EPD) by pulse potential application, *Journal of the American Ceramic Society*, **91**[10] 3154–3159.
21. J. Will, M. K. M. Hruschka, L. Gubler, and L. J. Gauckler (2002) Electrophoretic deposition of zirconia on porous anodic substrate, *Journal of the American Ceramic Society*, **84**[2] 328–332.
22. J. Van Tassel and C. A. Randall (2004) Potential for integration of electrophoretic deposition into electronic device manufacture; demonstrations using silver/palladium, *Journal of Materials Science*, **39** 867–879.
23. M. Matsuda, T. Hosomi, K. Murata, T. Fukui, and M. Miyake (2005) Direct EPD of YSZ electrolyte film onto porous NiO-YSZ composite substrate for reduced—temperature operating anode-supported SOFC, *Electrochemical and Solid State letters*, **8**[1] A8–A11.
24. L. Besra, C. Compson, and M. Liu (2007) Electrophoretic deposition on non conducting substrates: The case of YSZ film on NiO-YSZ composite substrates for Solid oxide fuel cell application, *Journal of Power Sources*, **173**[1] 130–136.
25. L. Besra, C. Compson, and M. Liu (2006) Electrophoretic deposition of YSZ particles on non-conducting NiO-YSZ substrates for Solid oxide fuel cell (SOFC) application, *Journal of the American Ceramic Society*, **89**[10] 3003–3009.
26. E. Stoll, P. Mahr, H.-G. Krüger, H. Kern, B. J. C. Thomas, and A. R. Boccaccini (2006) Fabrication technologies for oxide–oxide ceramic matrix composites based on electrophoretic deposition, *Journal of the European Ceramic Society*, **26** 1567–1576.

27. W. Ryan, E. Massoud, and C. T. S. B. Perera (1979) Electrophoretic deposition could speed up ceramic casting, *Interceram*, **2** 117–119.
28. M. Mihailescu, M. Emami, V. Vancea, and M. Marcu (1991) Electrophoretic behavior of ceramic sanitaryware slips, *Interceram*, **40** 165.
29. J. Tabellion and R. Clasen (2008) Electrophoretic deposition from aqueous suspensions for near-shap manufacturing of advanced ceramics and glasses—applications, *Journal of the American Ceramic Society*, **91**[10] 3154–3159.
30. J. Tabellion (2006) Manufacturing of ceramics and glasses by aqueous electrophoretic deposition, *Interceram*, **55** 338–342.
31. T. Uchikoshi, et al. (2001) Dense, bubble-free ceramic deposits from aqueous suspensions by electrophoretic deposition, *Journal of Materials Research*, **16**[2] 321–324.
32. H. Q. Nguyen, W. Fuerbeth, and M. Schuetze (2002) Nano-enamel: A new way to produce glass-like protective coatings for metals, *Materials and Corrosion*, **53** 772–782.
33. Th. Engelhardt, P. Rijkenen, L. Hellkuhl, F. Kaup, and H. Warnke (1990) Physical and chemical processes in electrophoretic enameling I, *Mitt. Ver. Dtsch. Emailfachleute*, **38**[4] 37–48.
34. J. H. Kennedy and A. A. Foissy (1975) Fabrication of beta-alumina tubes by electrophoretic deposition from suspensions in dichloromethane, *Journal of The Electrochemical Society*, **122** 482–486.
35. R. W. Powers (1975) The electrophoretic forming of beta-alumina ceramics, *Journal of The Electrochemical Society*, **122** 490–500.
36. G. Anné, K. Vanmeensel, B. Neirinck, O. Van Der Biest, and J. Vleugels (2006) Ketone-amine based suspensions for electrophoretic deposition of  $\text{Al}_2\text{O}_3$  and  $\text{ZrO}_2$ , *Journal of the European Ceramic Society*, **26** 3531–3537.
37. M. Hein, G. Mueller, H. Piel, L. Ponto, M. Becks, U. Klein, and M. Peiniger (1989) Electrophoretic deposition of textured YBA2CU3O7-x films on silver substrates, *Journal of Applied Physics*, **66** 5940–5943.
38. D. E. Clark, W. J. Dalzell, and D. C. Folz (1988) Electrophoretic alumina sol-gel coatings on metallic substrates, *Ceramic Engineering and Science Proceedings*, **9** 1111–1118.
39. Z. Wang, J. Shemilt, and P. Xiao (2000) Novel fabrication technique for the production of ceramic/ceramic and metal/ceramic composite coatings, *Scripta Materialia*, **42** 653–659.
40. N. K. Shrestha, K. Sakurada, M. Masuko, and T. Saji (2001) Composite coatings of nickel and ceramic particles prepared in two steps, *Surface Coatings*, **140** 175–181.
41. W. E. Windes, J. Zimmerman, and I. E. Reimanis (2002) Electrophoretic deposition applied to thick metal-ceramic coatings, *Surface & Coatings Technology*, **157** 267–273.
42. H. G. Kruger, A. Knotte, U. Schindler, H. Kern, and A. R. Boccaccini (2004) Composite ceramic-metal coatings by means of combined electrophoretic deposition and galvanic methods, *Journal of Materials Science*, **39** 839–844.
43. E. A. Olevsky, X. Wang, J. Ma, A. Maximenko, and M. B. Stern (2007) Sequential deposition and electroforming of metal-ceramic composites for thermal management applications, *Surface Engineering*, **23** 12–17.
44. A. Knotte, H. G. Krueger, S. Selve, T. Kups, H. Kern, and L. Spiess (2007) Metal-ceramic composite layers on stainless steel through the combination of electrophoretic deposition and galvanic processes, *Journal of Materials Science*, **42** 4545–4551.
45. Z. Wang, J. Shemilt, and P. Xiao (2002) Fabrication of ceramic composite coatings using electrophoretic deposition, reaction bonding and low temperature sintering, *Journal of the European Ceramic Society*, **22** 183–189.

46. P. A. Lessing, A. W. Erickson, and D. C. Kuerth (2000) Electrophoretic deposition (EPD) applied to reaction joining of silicon carbide and silicon nitride ceramics, *Journal of Materials Science*, **35** 2913–2925.
47. Y. H. Wang, Q. Z. Chen, J. Cho, and A. R. Boccaccini (2007) Electrophoretic co-deposition of diamond/borosilicate glass composite coatings, *Surface and coatings Technology*, **201** 7645–7651.
48. A. R. Boccaccini, S. Keim, R. Ma, Y. Li, and I. Zhitomirsky (2010) Electrophoretic deposition of biomaterials, *Journal of the Royal Society Interface*, **7** S581–S613.
49. J. Ma, et al. (2003) Colloidal characterization and electrophoretic deposition of hydroxyapatite on titanium substrate, *Journal of Materials Science-Materials in Medicine*, **14** 797–801.
50. G. Garcia-Ruiz, G. Vargas, J. Mendez, and A. Uribe (2006) Water versus acetone electrophoretic deposition of hydroxyapatite on 316L stainless steel. Electrophoretic Deposition: Fundamentals and Applications II, *Key Engineering Materials*, **314** 237–242.
51. T. Moritz, W. Eiselt, and K. Moritz (2006) Electrophoretic deposition applied to ceramic dental crowns and bridges, *Journal of Materials Science*, **41** 8123–8129.
52. J. Zhang and B. I. Lee (2000) Electrophoretic deposition and characterisation of micrometer-scale BaTiO<sub>3</sub> based X7R dielectric thick films, *Journal of the American Ceramic Society*, **83** 2417–2422.
53. F. Hossein-Babaei and F. Taghibakhsh (2000) Electrophoretically deposited zinc oxide thick film gas sensor, *Electronics Letters*, **36** 1815–1816.
54. K. Wu, Y. Wang, and I. Zhitomirsky (2010) Electrophoretic deposition of TiO<sub>2</sub> and composite TiO<sub>2</sub>-MnO<sub>2</sub> films using benzoic acid and phenolic molecules as charging additives, *Journal of Colloid and Interface Science*, **352** 371–378.
55. A. Matsuda, Y. Higashi, K. Tadanaga, T. Minami, and M. Tatsumisago (2006) Electrophoretic deposition of sol-gel derived V<sub>2</sub>O<sub>5</sub> microparticles and its application for cathodes for Li-secondary batteries. Electrophoretic Deposition: Fundamentals and Applications II, *Key Engineering Materials*, **314** 107–111.
56. B. Ferrari, R. Moreno, P. Sarkar, and P. S. Nicholson (2000) Electrophoretic deposition of MgO from organic suspensions, *Journal of the European Ceramic Society*, **20** 99–106.
57. Z. Fu, A. Y. Wu, P. M. Vilarinho, A. I. Kingon, and R. Wordenweber (2007) Low dielectric loss BaNd<sub>2</sub>Ti<sub>5</sub>O<sub>14</sub> thick films prepared by an electrophoretic deposition technique, *Applied Physics Letters*, **90** ARTN 052912.
58. W. S. Sweet, J. B. Talbot, and R. Higgins (2006) Electrophoretic deposition of zeolite 5A for use in supported gas separation membranes, Electrophoretic Deposition: Fundamentals and Applications II, *Key Engineering Materials*, **314** 39–44.
59. A. Y. Wu, P. M. Vilarinho, and A. I. Kingon (2006) Electrophoretic deposition of lead zirconate titanate films on metal foils for embedded components, *Journal of the American Ceramic Society*, **89** 575–581.
60. A. Nourmohammadi, M. A. Bahrevar, and M. Hietschold (2008) Sol-gel electrophoretic deposition of PZT nanotubes, *Materials Letters*, **62** 3349–3351.
61. Y. Idemoto, S. Yoshida, K. Ui, and N. Koura (2006) Preparation of Pb-Zr-Ti-Nb-Si-O ferroelectric thick film by electrophoretic deposition, *Electrochemistry*, **74** 883–889.
62. L. Dusoulier, et al. (2006) Preparation of YBa<sub>2</sub>Cu<sub>3</sub>O<sub>7-x</sub> superconducting thick films by the electrophoretic deposition method, *Journal of Materials Science*, **41** 8109–8114.

63. M. J. Santillán, A. Caneiro, N. Quaranta, and A. R. Boccaccini (2009) Electrophoretic deposition of  $\text{La}_{0.6}\text{Sr}_{0.4}\text{Co}_{0.8}\text{Fe}_{0.2}\text{O}_{3-\delta}$  cathodes on  $\text{Ce}_{0.9}\text{Gd}_{0.1}\text{O}_{1.95}$  substrates for intermediate temperature solid oxide fuel cell (IT-SOFC), *Journal of the European Ceramic Society*, **29** 1125–1132.
64. I. Zhitomirsky and A. Petric (2000) Electrophoretic deposition of ceramic materials for fuel cell application, *Journal of the European Ceramic Society*, **20** 2055–2061.
65. C. Szepanski, J. Grosse-Brauckmann, and C. Argiris (2009) Electrophoretic deposition as preparation method for intermediate temperature SOFC half cells, *Key Engineering Materials*, **412** 209–214.
66. Z. G. Xu, G. Rajaram, J. Sankar, and D. Pai (2006) Electrophoretic deposition of YSZ electrolyte coatings for solid oxide fuel cells, *Surface and Coatings Technology*, **201** 4484–4488.
67. I. Zhitomirsky and A. Petric (2001) The electrodeposition of ceramic and organoceramic films for fuel cells, *JOM: The member journal of The Minerals, Metals & Materials Society*, **53** 48–50.
68. W. Krenkel (ed.), *Ceramic Matrix Composites: Fiber Reinforced Ceramics and Their Applications*. Wiley-VCH, Weinheim, 2008.
69. L. Vandeperre, et al. (1998) SiC-graphite laminates shaped by EPD, *American Ceramic Society Bulletin*, **77**[1] 53–58.
70. A. R. Boccaccini, C. Kaya, and K. K. Chawla (2001) Use of electrophoretic deposition in the processing of fibre reinforced ceramic and glass matrix composites. A Review, *Composites Part A*, **32** 997–1006.
71. H. Hadraba, K. Maca, and J. Cihlar (2004) Electrophoretic deposition of alumina and zirconia—II. Two-component systems, *Ceramics International*, **30**[6] 853–863.
72. J. H. Jean (1995) Electrophoretic deposition of  $\text{Al}_2\text{O}_3$ -SiC COMPOSITE, *Materials Chemistry and Physics*, **40**[4] 285–290.
73. S. Put, J. Vleugels, and O. Van Der Biest (2001) Functionally graded WC-Co materials produced by electrophoretic deposition, *Scripta Materialia*, **45**[10] 1139–1145.
74. C. Zhao, et al. (2000) Cylindrical  $\text{Al}_2\text{O}_3$ /TZP functionally graded materials by EPD, *British Ceramic Transactions*, **99**[6] 284–287.
75. K. Vanmeensel, et al. (2004) Homogeneous and functionally graded  $\text{Si}_3\text{N}_4$ -TiCN composites shaped by electrophoretic deposition, *Silicates Industriels*, **69**[7–8] 233–239.
76. N. Nagarajan and P. S. Nicholson (2004) Nickel-alumina functionally graded materials by electrophoretic deposition, *Journal of the American Ceramic Society*, **87**[11] 2053–2057.
77. M. Popa, et al. (2006) Thermal residual stress gradients in an alumina-zirconia composite obtained by electrophoretic deposition, *Journal of the European Ceramic Society*, **26**[4–5] 553–558.
78. G. Anné, K. Vanmeensel, J. Vleugels, and O. Van der Biest (2006) Electrophoretic deposition as a novel near net shaping technique for functionally graded biomaterials, *Key Engineering Materials*, **314** 213–218.
79. P. Hvizdos, et al. (2007) Mechanical properties and thermal shock behaviour of an alumina/zirconia functionally graded material prepared by electrophoretic deposition, *Journal of the European Ceramic Society*, **27**[2–3] 1365–1371.
80. K. Vanmeensel, G. Anné, D. Jiang, J. Vleugels, and O. Van der Biest (2005) Processing of a graded ceramic cutting tool in the  $\text{Al}_2\text{O}_3$ - $\text{ZrO}_2$ -Ti(C,N) system by electrophoretic deposition, *Materials Science Forum*, **492–493** 705–710.

81. L. Yao, et al. (2005) Advancement in preparation of hydroxyapatite/bioglass graded coatings by electrophoretic deposition, *Surface Review and Letters*, **12**[5–6] 773–779.
82. B. Ferrari, A. J. Sanchez-Herencia, and R. Moreno (1998) Aqueous electrophoretic deposition of  $\text{Al}_2\text{O}_3/\text{ZrO}_2$  layered ceramics, *Materials Letters*, **35**[5–6] 370–374.
83. R. Fischer, et al. (1995) Preparation of ceramic micro-laminate by electrophoresis in aqueous system, *Journal of Materials Science Letters*, **14**[1] 25–27.
84. C. You, D. L. Jiang, and S. H. Tan (2004) SiC/TiC laminated structure shaped by electrophoretic deposition, *Ceramics International*, **30**[5] 813–815.
85. C. Kaya, et al. (2001) Fabrication and characterisation of Ni-coated carbon fibre-reinforced alumina ceramic matrix composites using electrophoretic deposition, *Acta Materialia*, **49**[7] 1189–1197.
86. S. Novak, K. König, A. Iveković, and A. R. Boccaccini (2009) Infiltration of 3-D fabric for the production of SiC/SiC composites by means of EPD, *Key Engineering Materials*, **412** 237–242.
87. P. A. Trusty, A. R. Boccaccini, E. G. Butler, and C. B. Ponton (1995) Novel techniques for manufacturing woven fiber reinforced ceramic matrix composites-I: Preform fabrication, *Materials and Manufacturing Processes*, **10** 1215–1226.
88. C. Kaya, A. R. Boccaccini, and P. A. Trusty (1999) Processing and characterisation of 2-D woven metal fibre-reinforced multilayer silica matrix composites using electrophoretic deposition and pressure filtration, *Journal of the European Ceramic Society*, **19** 2859–2666.
89. S. Kooner, W. S. Westby, C. M. A. Watson, and P. M. Farries (2000) Processing of Nextel™ 720/mullite composition. composite using electrophoretic deposition, *Journal of the European Ceramic Society*, **20** 631–638.
90. Y. H. Bao and P. S. Nicholson (2007) Constant current electrophoretic infiltration deposition of fiber-reinforced ceramic composites, *Journal of the American Ceramic Society*, **90**[4] 1063–1070.
91. C. Kaya and E. G. Butler (2009) Unidirectional all-oxide mini-composites with crack-deflecting NdPO4 interface, *Journal of the European Ceramic Society*, **29**[3] 363–367.
92. T. J. Illston, D. P. A. Doleman, E. Butler, C. B. Ponton, M. J. Gilbert, and R. Piramoon (1993) Method of manufacturing a composite material, in patent WO 93/10056.
93. C. Kaya, K. K. Chawla, and A. R. Boccaccini Processing of oxide and non-oxide light-weight ceramic composites suitable for very high temperature applications using electrophoretic deposition, in *Electrophoretic Deposition: Fundamentals and Applications*, eds. A. R. Boccaccini, O. van der Biest, and J. B. Talbot, pp. 263–270, The Electrochemical Society, Pennington, NJ, 2002.
94. A. R. Boccaccini, et al. (1997) Electrophoretic deposition infiltration of 2-D woven SiC fibre mats with mixed sols of mullite composition, *Journal of the European Ceramic Society*, **17**[13] 1545–1550.
95. S. Novak, K. Rade, K. König, and A. R. Boccaccini (2008) Electrophoretic deposition in the production of SiC/SiC composites for fusion reactor applications, *Journal of the European Ceramic Society*, **28** 2801–2807.
96. S. Novak, K. Koenig, A. Ivekovic, and A. R. Boccaccini (2009) Infiltration of a 3-D fabric for the production of SiC/SiC composites by means of electrophoretic deposition, *Key Engineering Materials*, **412** 237–242.



97. K. König, et al. (2010) Fabrication of CNT-SiC/SiC composites by electrophoretic deposition, *Journal of the European Ceramic Society*, **30**[5] 1131–1137.
98. S. Novak and K. König (2009) Fabrication of alumina parts by electrophoretic deposition from ethanol and aqueous suspensions, *Ceramics International*, **35**[7] 2823–2829.
99. J. Tabellion and R. Clasen (2004) Electrophoretic deposition from aqueous suspensions for near-shape manufacturing of advanced ceramics and glasses—Applications, *Journal of Materials Science*, **39** 803–811.
100. Y. J. Wu, J. Li, H. Tanaka, and M. Kuwabara (2005) Preparation of nano-structured BaTiO<sub>3</sub> thin film by electrophoretic deposition and its characterization, *Journal of the European Ceramic Society*, **25** 2041–2044.
101. J. Zhao, X. Wang, and L. Li (2006) Electrophoretic deposition of BaTiO<sub>3</sub> films from aqueous suspensions, *Materials Chemistry and Physics*, **99** 350–353.
102. A. Dogan, G. Gunkaya, E. Suvaci, and M. Niederberger (2006) Electrophoretic deposition of nano-sized BaTiO<sub>3</sub>, *Journal of Materials Science*, **41** 8196–8201.
103. C. Oetzel and R. Clasen (2006) Preparation of zirconia dental crowns via electrophoretic deposition, *Journal of Materials Science*, **41** 8130–8137.
104. O. O. Van Der Biest, E. Joos, J. Vleugels, and B. Baufeld (2006) Electrophoretic deposition of zirconia layers for thermal barrier coatings, *Journal of Materials Science*, **41** 8086–8092.
105. S. V. Mahajan, D. W. Kavich, M. L. Redigolo, and J. H. Dickerson (2006) Structural properties of electrophoretically deposited europium oxide nanocrystalline thin films, *Journal of Materials Science*, **41** 8160–8165.
106. A. Ofir, T. Dittrich, S. Tirosh, L. Grinis, and A. Zaban (2006) Influence of sintering temperature, pressing, and conformal coatings on electron diffusion in electrophoretically deposited porous TiO<sub>2</sub>, *Journal of Applied Physics*, **100** Art. No. 074317.
107. A. Salant, M. Shalom, I. Hod, A. Faust, and A. Zaban (2010) Banin, Quantum dot sensitized solar cells with improved efficiency prepared using electrophoretic deposition, *ACS Nano*, **4** 5962–5968.
108. G. J. Wang and S. W. Chou (2010) Electrophoretic deposition of uniformly distributed TiO<sub>2</sub> nanoparticles using an anodic aluminum oxide template for efficient photolysis, *Nanotechnology*, **21** 115206.
109. J. Manríquez and L. A. Godínez (2007) Tuning the structural, electrical and optical properties of Ti(III)-doped nanocrystalline TiO<sub>2</sub> films by electrophoretic deposition time, *Thin Solid Films*, **515** 3402–3413.
110. E. Valatka and Z. Kulesius (2007) TiO<sub>2</sub>-mediated photoelectrochemical decoloration of methylene blue in the presence of peroxodisulfate, *Journal of Applied Electrochemistry*, **37** 415–420.
111. M. J. Santillan, N. E. Quaranta, and A. R. Boccaccini (2010) Titania and titania-silver nanocomposite coatings grown by electrophoretic deposition from aqueous suspensions, *Surface and Coatings Technology*, **205** 2562–2571.
112. X. W. Meng, T.-Y. Kwon, Y. Z. Yang, J. L. Ong, and K.-H. Kim (2006) Effects of applied voltages on hydroxyapatite coating of titanium by electrophoretic deposition, *Journal of Biomedical Materials Research Part B-Applied Biomaterials*, **78B** 373–377.
113. S. Doudgaw, T. Uchikoshi, Y. Noguchi, C. Eamchotchawalit, and Y. Sakka (2005) Electrophoretic deposition of lead zirconate titanate (PZT) powder from ethanol suspension

- prepared with phosphate ester, *Science and Technology of Advanced Materials*, **6** 927–932.
114. S. Wildhack and F. Aldinger (2006) Electrophoretic deposition of nanocrystalline SiC ceramics. Electrophoretic deposition: Fundamentals and applications II, *Key Engineering Materials*, **314** 33–38.
  115. T. Oshita, Y. Sawaki, and A. Kishimoto (2006) Grinding performance of pellet prepared using nanosize ceria particles, *Journal of Alloys and Compounds*, **408** 1118–1122.
  116. T. M. Bhave, C. Balasubramanian, H. Nagar, S. Kulkarni, R. Pasricha, P. P. Bakare, S. K. Date, and S. V. Bhoraskar (2005) Oriented growth of nanocrystalline gamma ferric oxide in electrophoretically deposited films, *Hyperfine Interactions*, **160** 199–209.
  117. N. Wang, H. Lin, J. B. Li, X. Z. Yang, and B. Chi (2006) Electrophoretic deposition and optical property of titania nanotubes films, *Thin Solid Films*, **496** 649–652.
  118. Y. H. Lee, C. W. Kuo, C. J. Shih, I. M. Hung, K. Z. Fung, S. B. Wen, and M. C. Wang (2007) Characterization on the electrophoretic deposition of the 8 mol% yttria-stabilized zirconia nanocrystallites prepared by a sol–gel process, *Materials Science and Engineering A*, **445** 347–354.
  119. R. H. Baughman, A. A. Zakhidov, and W. A. de Heer (2002) Carbon nanotubes—The route towards applications, *Science*, **297** 787–792.
  120. A. R. Boccaccini, J. Cho, J. A. Roether, B. J. C. Thomas, E. J. Minay, and M. S. P. Shaffer (2006) Electrophoretic deposition of carbon nanotubes, *Carbon*, **44** 3149–3160.
  121. C. S. Du and N. Pan (2006) High power density supercapacitor electrodes of carbon nanotube films by electrophoretic deposition, *Nanotechnology*, **17** 5314–5318.
  122. S. M. Jung, J. Hahn, H. Y. Jung, and J. S. Suh (2006) Clean carbon nanotube field emitters aligned horizontally, *Nano Letters*, **6** 1569–1573.
  123. S. Pimanpong, W. Maiaugree, W. Jarerborn, S. Maensiri, and V. Amornkitbamrung (2009) Influences of magnesium particles incorporated on electrophoretically multiwall carbon nanotube film on dye-sensitized solar cell performance, *Synthetic Metals*, **159** 1996–2000.
  124. T. Bordjiba and D. Belanger (2010) Development of new nanocomposite based on nanosized-manganese oxide and carbon nanotubes for high performance electrochemical capacitors, *Electrochimica Acta*, **55** 3428–3433.
  125. A. R. Boccaccini, F. Chicatun, J. Cho, O. Bretcanu, Q. Chen, J. A. Roether, and S. Novak (2007) Carbon nanotube coatings on bioglass-based tissue engineering scaffolds, *Advanced Functional Materials*, **17** 2815–2822.
  126. S. Minnikanti, P. Skeath, and N. Peixoto (2009) Electrochemical characterisation of multi-walled carbon nanotube coated electrodes for biological applications, *Carbon*, **47** 884–893.
  127. A. J. Rodriguez, M. E. Guzman, C.-S. Lim, and B. Minaie (2010) Synthesis of multiscale reinforcement fabric by electrophoretic deposition of amine-functionalized carbon nanofibers onto carbon fiber layers, *Carbon*, **48** 3256–3259.
  128. I. Singh, C. Kaya, M. S. P. Shaffer, B. C. Thomas, and A. R. Boccaccini (2006) Bioactive ceramic coatings containing carbon nanotubes on metallic substrates by electrophoretic deposition, *Journal of Materials Science*, **41** 8144–8151.
  129. M. C. Schausten, D. Meng, R. Telle, and A. R. Boccaccini (2010) Electrophoretic deposition of carbon nanotubes and bioactive glass particles for bioactive composite coatings, *Ceramics International*, **36** 307–312.



130. C. S. Rout, S. H. Krishna, S. R. C. Vivekchand, A. Govindaraj, and C. N. R. Rao (2006) Hydrogen and ethanol sensors based on ZnO nanorods, nanowires and nanotubes, *Chemical Physics Letters*, **418** 586–590.
131. G. S. Kim, S. G. Ansari, H. K. Seo, Y. S. Kim, and H. S. Shin (2007) Effect of annealing temperature on structural and bonded states of titanate nanotube films, *Journal of Applied Physics*, **101** Art. No. 024314.
132. W. Sugimoto, K. Yokoshima, K. Ohuchi, Y. Murakami, and Y. Takasu (2006) Fabrication of thin-film, flexible, and transparent electrodes composed of ruthenic acid nanosheets by electrophoretic deposition and application to electrochemical capacitors, *Journal of the Electrochemical Society*, **153** A255–A260.
133. J. Cordelair and P. Greil (2004) Discrete element modelling of solid formation during electrophoretic deposition, *Journal of Materials Science*, **39** 1017–1021.

# PROCESSING OF CERAMICS BY PLASMA SPRAYING

ROBERT VABEN

## 16.1 INTRODUCTION AND BACKGROUND

The plasma-spraying process has been described by numerous authors [1, 2]; therefore, only a brief summary of the main features will be given.

Within the plasma-spraying process, powderous materials with a melting temperature are heated and accelerated in a hot plasma plume and then deposited on a substrate. As the production rate of the process can be rather high (up to about 0.5 kg/min), in addition to a coating process, also bulk ceramic parts can be obtained after substrate removal. Due to the manufacturing process, the plasma-sprayed ceramic shows some specific microstructural properties that implement also specific properties as excellent thermal shock resistance.

In the literature, a number of studies can be found in which the plasma-spraying process is used as forming process. Net shaping of mainly metallic structures is demonstrated in Reference 3, while examples of the manufacture of composite structures as metal–ceramic and ceramic–ceramic matrix composites are found in References 4–7. Plasma spraying can also be used to produce the metallic matrix of a ceramic fiber-reinforced metal matrix composite [8, 9]. In particular, a number of articles focus on

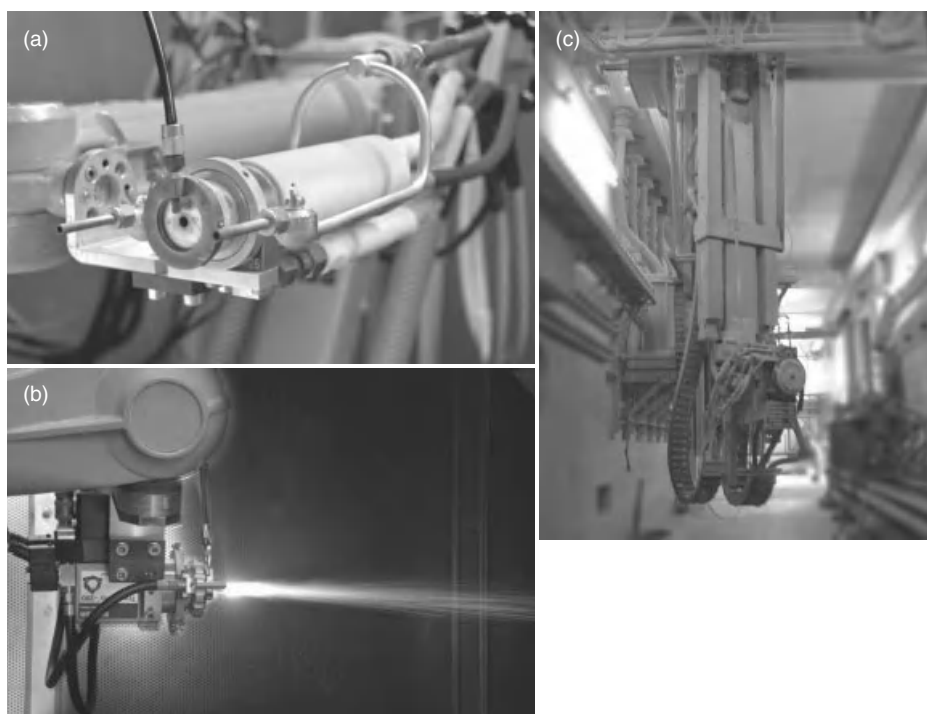


**Figure 16.1.** Different atmospheric plasma-spraying (APS) guns: (a) F4, (b) TriplexPro, and (c) LWK guns.

the manufacture of bulk ceramics by plasma spraying [10–16], which will be the major topic of this chapter. Other authors also show the possibility to produce composite structures as alumina titania [17] by spray forming. Hongwei et al. [18] showed that the manufacture of ceramic composites based on titanium diboride and titanium carbide is possible by reactive thermal spraying.

In the plasma-spraying process, a hot plume is generated by the heating of process gases as argon, hydrogen, nitrogen, or helium by DC arc ignited between a central cathode and a cylindrical anode. A typical setup of such a single-cathode gun is shown in Figure 16.1a. Several modern plasma-spraying guns make use of three cathodes as the Triplex guns by Sulzer Metco (see Fig. 16.1b). These guns have the advantage of rather stable arcs with no so-called restrikes [19], giving more stable and efficient spraying conditions. The plasma gun powers are often in the range above 50 kW but can also go up to about 200 kW (Fig. 16.1c) [20]. The energy transfer to the plasma gases results in plasma temperatures within the plasma gun above 10,000 K. It also leads to high gas velocities of up to about 1000 m/s at the torch exit [21]. The plasma-spraying process can be performed in different environments as in a vacuum chamber at typical inert gas pressures of about 50 mbar (vacuum plasma spraying [VPS]) or under atmospheric conditions (atmospheric plasma spraying [APS]). For the deposition of plasma ceramic in most cases, the more cost-efficient APS is used.

The powders are introduced into the plume by applying a feeding gas. Commercial available feeding systems imply that the powders should have good flowability. This typically corresponds to a size of the powders above about  $10\text{ }\mu\text{m}$ . The upper limit is set by the fact that the powders should be heated rather homogeneously close to the melting point. Therefore, particle sizes are, in most cases, below  $100\text{ }\mu\text{m}$ ; the typical size range is between  $30$  and  $80\text{ }\mu\text{m}$ . As for the production of plasma ceramics, in most cases, APS is used; the processed ceramics are mainly oxides; nonoxides tend to oxidize during spraying. It was stated in Reference 22 that the reduction of the particle sizes leads to a more than reciprocal increase of strength. This indicates that not only the smaller defect size associated with the smaller particle size but also other parameters, as the observed higher density combined with a modification of the pore size distribution or improved interparticle bonding, play an important role.

In the plasma plume, the particles are accelerated mainly by viscous drag forces and are heated predominately by convective heat transfer. At typical spray distances of about  $80\text{--}150\text{ mm}$ , the particles reach velocities in the range of several hundred meters per second, and the mean temperature is often well above the melting temperature. So, for zirconia particles, temperatures of more than  $3000\text{ K}$  have been reported [23, 24]. These hot and fast particles are then deposited on a substrate. Due to their high kinetic energy, the particles will deform during impact and form pancake-like structures. A typical image of such so-called splats is shown in Figure 16.2a. Depending on the deposition conditions and especially at low substrate temperatures, the splats can also show splashing (Fig. 16.2b) [25]. Within the splats, often intralamellar cracks are formed. These cracks are a result of the cooling down of the splats from the melting down to the substrate temperature. The contraction leads to tensile stress levels, which promotes the formation of the cracks. In addition to the intralamellar cracks, relaxation of the tensile stress in the splats often also leads to cracking between the splats, so-called intersplat cracks. A good intersplat bonding, as observed for high substrate temperatures, will reduce this type of cracking [26]; however, as will be outlined below, segmentation cracks might be introduced.

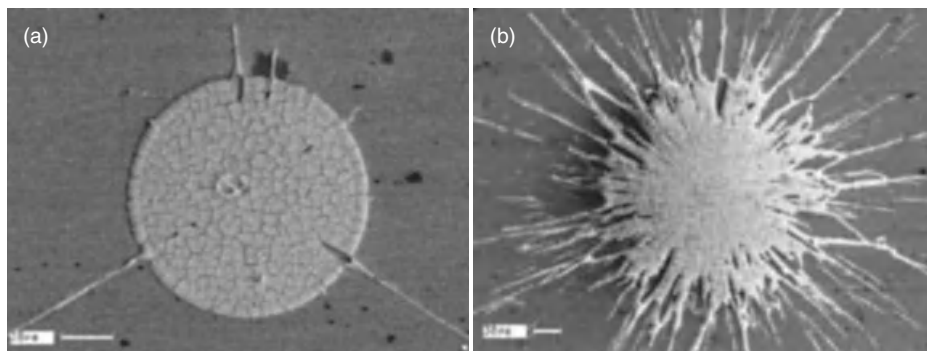


**Figure 16.2.** Scanning electron microscopy (SEM) images of YSZ splats (a) without and (b) with a fingering structure [24].

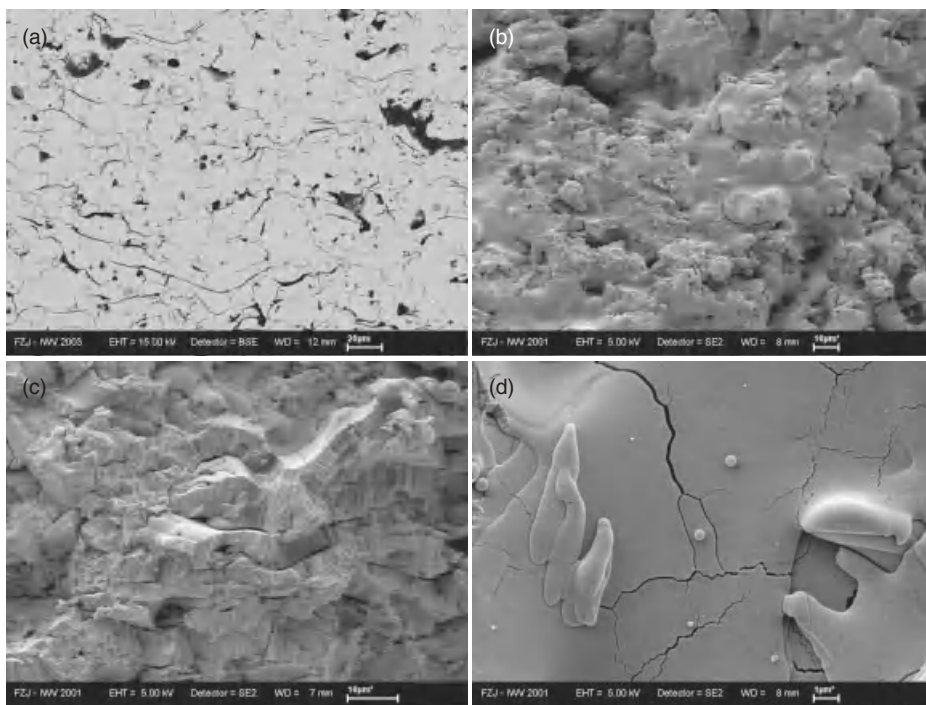


**Figure 16.3.** SEM images: (a) a metallographical section, a surface view with (b) low and (c) high magnification, and (d) a fracture surface of a plasma-sprayed YSZ coating.

In addition to the crack-like pores, also globular pores are generated in the plasma-sprayed coatings as during the deformation cooling and solidification process it is typically not possible to close all underlying volumes. Figure 16.3a shows a polished section with pores and cracks visible. Figure 16.3b shows a view on the top of the coating revealing the rough surface structure with the original particle morphology still visible. In a higher resolution, the intrasplat cracks can be detected (Fig. 16.3c). In Figure 16.3d, a fracture surface of a plasma-sprayed yttria-stabilized zirconia (YSZ) coating also reveals clearly intersplat cracks as well as pores.

The typical lamellar microstructure of a plasma-sprayed coating leads to highly anisotropic material properties. This will be discussed below.

Pore size distributions can be measured with mercury porosimetry as the far largest part of the porosity is accessible from the surface (“open porosity”). The deviation between theoretical bulk densities and those determined by Hg porosimetry indicates close porosities below 1%. Two plasma-sprayed coatings, a rather porous one with about 18% porosity and a denser one with about 12%, are shown in Figure 16.4. The range between 10% and 20% porosity is typically found in plasma-sprayed ceramics.

The globular pores with sizes above 1  $\mu\text{m}$  contribute to about one-fourth of the total porosity. The fine pores below 1  $\mu\text{m}$  can be identified as microcracks. The crack

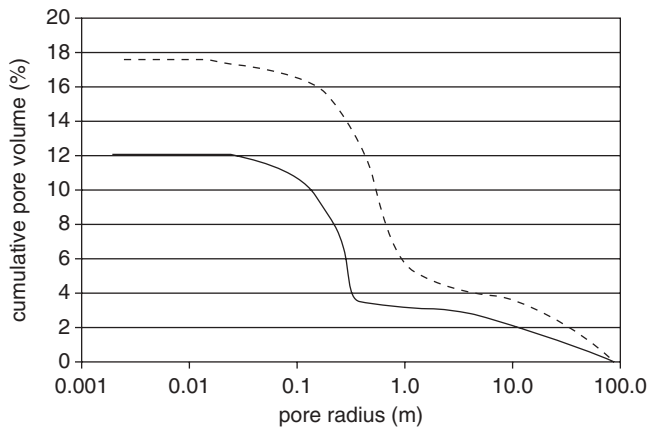


**Figure 16.4.** Pore size distribution of two plasma-sprayed YSZ coatings measured by Hg porosimetry.

opening typically lies in the range between about 100 and 1000 nm. In so-called microcracked coatings, which are the most frequently used ceramic coatings especially for thermomechanically loaded parts, the porosity related to microcracks is the dominant one.

In contrast to these coatings, special spray conditions, typically rather hot ones with elevated substrate temperatures above 500°C, allow the deposition of rather dense ceramic coatings. With this technology, even gas tight, thin ceramic layers with a limited number of microcracks can be produced [27, 28]. When the thickness of the coatings exceed about 100  $\mu\text{m}$ , the coatings tend to form segmentation cracks. This type of coating structure is not suitable for the production of thick freestanding structures as the segmentation cracks can lead to the fracture of the whole part. The microcracked coatings are more suitable as they give a highly strain-tolerant structure with no through-thickness cracks.

As the microstructure and hence the properties of plasma ceramic is considerably different from those of sintered ceramics, it is necessary to describe the properties in some more detail.

The microcracked and porous structure of the plasma ceramic leads to a reduction of the absolute value of several properties, for example, density, thermal conductivity, strength, and Young's modulus. Other properties as thermal expansion coefficients (TECs) and specific heat remain rather unchanged, while especially the thermal shock resistance can even be increased considerably due to the strain-tolerant microstructure, part sliding of the sprayed lamellae might reduce stress levels [29]. In addition, the highly porous microstructure has a positive effect on thermal shock resistance. This can be understood by the work of Hasselman [30], who explained the good thermal shock resistance of highly porous, low-strength materials. In this type of material, only a gradual decrease of strength is observed by increasing the thermal shock temperature difference.

TABLE 16.1. Some Average Properties of Plasma Ceramics

	Alumina	Mullite	Zirconia	Spinel
Composition	$\text{Al}_2\text{O}_3$	$3\text{Al}_2\text{O}_3 \cdot 2\text{SiO}_2$	4–5 mol % $\text{Y}_2\text{O}_3$ stabilized $\text{ZrO}_2$	$\text{MgAl}_2\text{O}_4$
Strength (MPa) <sup>a</sup>	35 <sup>a</sup>	29 <sup>a</sup>	40 <sup>b</sup>	27 <sup>a</sup>
Young's modulus (GPa)	13–17 <sup>a</sup>	16 <sup>a</sup>	11 [37]	16 <sup>a</sup>
Thermal conductivity at 1000°C (W/m/K)	~5 [38] 0.63 <sup>d</sup>	~0.2 [39] 1 <sup>d</sup>	0.8 [33] 0.2 <sup>c,d</sup>	0.8 <sup>d</sup>
Thermal shock $\Delta T$ (K) [13]	1150	>1200	>1200 <sup>c</sup>	1000
Fracture toughness ( $\text{MPa m}^{1/2}$ ) <sup>a</sup>	1.7 [10]	–	2.5 [40]	–

<sup>a</sup> From ring tests [13], measured parallel to the spray direction [10].

<sup>b</sup> Bending test [41].

<sup>c</sup> For MgO-stabilized  $\text{ZrO}_2$ .

<sup>d</sup> At 1200°C [14].

For a number of oxide ceramics, data have been published; for several oxide ceramics, a summary of these data is given in Table 16.1. These data can only give an indication of the material properties as the absolute values largely depend on the microstructure and especially on the porosity of the material.

As many sintered ceramics, also plasma ceramics made of oxides often show an excellent corrosion resistance against liquid metals, corrosive gases, acids, or bases [14]. In addition, many liquid metals as zinc, tin, aluminum, or steel do hardly penetrate into the pores of the plasma ceramic. Together with their excellent thermal shock resistance, these properties lead to many applications as discussed later.

Another property that differs from typical isotropic sintered ceramics is the anisotropy in the properties. The large number of microcracks perpendicular to the spraying direction leads, for example, to about a factor of 3 lower-strength and toughness values in this direction compared with the perpendicular one. Also, sintering does not change this relation considerably [14].

For the important engineering ceramic alumina, it has to be mentioned that plasma spraying leads to a considerable amount of undesirable  $\gamma$ -alumina with worse properties compared to the  $\alpha$ -alumina. Therefore, alumina parts are annealed after spraying at above 1100°C in air to retain the  $\alpha$ -alumina [22]. This is accompanied by a shrinkage of about 1–2%.

Also, other oxide ceramics as mullite, zircon, or cordierite show phase changes that can at least partly be recovered after heat treatment between 1200 and 1400°C [22]. The sometimes observed different phase content of the powder and the heat-treated coatings might be related to the loss of constituents during spraying. For complex oxides like perovskites, this has been intensively studied [31].

In particular, for alumina containing ceramics in the as-sprayed condition, a large amount of amorphous phase is observed, which crystallizes during heat treatment, leading to shrinkage and often microcracks in the ceramic.

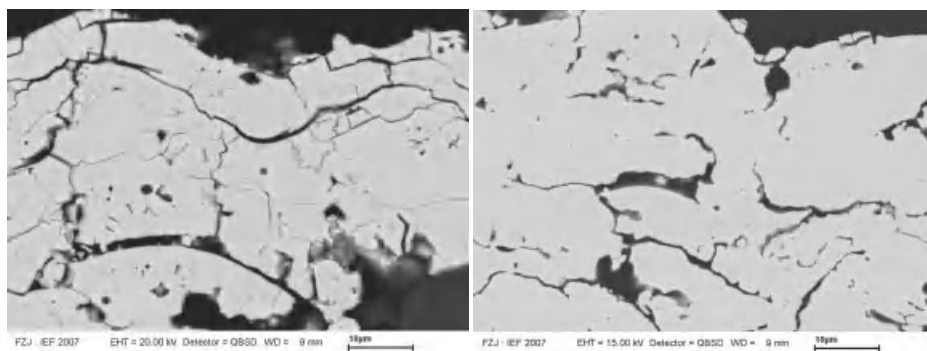


**Figure 16.5.** Plasma-sprayed coating in the as-sprayed condition (left) and after 100 h at 1400°C (right).

The high amount of porosity having free surfaces in conventional plasma-sprayed ceramics leads to the fact that the microstructure tends to change during thermal treatment. As it is well-known from sintering of ceramics, the surface area of the pores will be reduced by different mechanisms as surface or grain boundary diffusion. Typically, at temperatures of about one-third of the melting temperature, sintering sets in for plasma-sprayed oxide ceramics. Depending on the specific mechanism, one might observe predominantly a coarsening of the pores with little densification or a distinct shrinkage of the pores with a porosity decrease. In Reference 32, a model is described, which takes into account the different diffusion paths and also an approximate geometry of a plasma-sprayed coating to predict the changes of the pore morphology and the densification during heat treatment in a semiquantitative way. Figure 16.5 shows an example of a plasma-sprayed coating in the as-sprayed condition and after 100 h at 1400°C. It is clearly visible that only a few microcracks remained, while the very fine cracks disappeared completely.

The sintering of the plasma-sprayed coating does not only change the microstructure but also the properties of the coatings. This was shown in numerous papers especially for YSZ-based thermal barrier coatings (TBCs). Sintering is generally accepted as one of the most critical degradation mechanisms of TBCs as it increases Young's modulus (and by that, the stress level in the coating [29]), reduces strain tolerance (splats can no longer slide along their interfaces), and increases thermal conductivity (and hence reduces the thermal insulation [33]). On the other hand, sintering can also improve the properties as stated for strength or fracture toughness. Lutz [13] reported a more than twofold increase in strength and a 3- to more than 10-fold increase in Young's modulus for several oxide ceramics after sintering at 1550°C for 4 h. Damani and Lutz [10] found about a threefold increase in fracture toughness for the same conditions in alumina. The larger increase in Young's modulus might be related to the fact that it is sensitive to the sintering of the microcracks, which sets in earlier than the sintering of the globular, rather large pores. As the defect size remains rather unchanged, hence, strength correlates with the toughness increase, an assumption that fits very well for the alumina data.



## 16.2 DETAILED DESCRIPTION OF THE TECHNIQUE

In the following, the manufacture of plasma ceramics is outlined in more detail. A description of several aspects of the manufacture of plasma ceramics is also given in Reference 22.

A basic requirement for the production of plasma ceramics is the selection of adequate substrates, which can be removed easily after spraying. For simple cylindrical symmetries, for example, nondestructive ways to remove the substrates can be used. This method makes use of the mismatch of the TECs of the substrate and the coating. If the substrate has a higher TEC, as frequently found for oxides deposited on steel substrates, the cooling from deposition temperature to room temperature will lead to tensile stresses on the substrate/coating interface, which can induce delamination and freestanding plasma-sprayed parts. For cylindrical components, the removal from the substrate is facilitated by slightly conical substrates. The deposition temperature for the manufacture of microcracked coatings is rather low (about 100–200°C), which is obtained by intense cooling of the deposited ceramics, for example, by compressed air cooling nozzles. Therefore, the temperature gap from deposition to room temperature is rather low, and it might be necessary to use additional liquid nitrogen cooling of the substrate as pointed out by Schultze [22]. Of course, also the use of substrates with rather high TECs, for example, Al with a TEC of  $23 \times 10^{-6}/\text{K}$  is advantageous. As the absolute width of the gap will be reduced with decreasing diameter, it becomes difficult to remove the substrate for diameters below about 20 mm.

An additional fact is the surface preparation of the substrate. In the plasma-spraying process, the bonding process to the substrate is a mechanical interlocking of the splats with the surface. Hence, a certain roughness is necessary for a coating deposition. This is often achieved by sandblasting, giving  $R_a$  values above  $5 \mu\text{m}$ . For the deposition of plasma ceramics, the roughness should be lower in the range of some micrometers to obtain only a slight bonding of the coating.

For more complex-shaped parts, materials might be used, which can be removed easily after the deposition. Graphite is such a material that can be burned in air furnace at about 800°C. However, due to the low TEC, this substrate can induce tensile stresses in ceramics with considerably higher TECs (e.g., YSZ), which then can lead to cracking of the coating. Other strategies to remove substrate materials can include breaking, melting, or dissolving [6].

For the deposition of the plasma ceramic, the substrate is fixed in the substrate holder of the plasma-spraying facility (Fig. 16.6, left). The main components of a plasma-spraying unit are the spray booth with the gun mounted on a robotic handling system, the substrate holder (at least with one rotational axis) and the exhaust system, plus the control unit, the powder feeding systems, and media, cooling, and power supply systems. In Figure 16.6 (right), a plasma torch in operation is seen with a particle diagnostic system in the background. These systems allow the determination of particle velocities and temperatures to control the deposition process and to improve the reproducibility of the coatings.

For larger cylindrical parts, it may be suitable to have a horizontal rotational axis for the substrate holder. The plasma gun can be placed on linear positioning systems. With such a setup, large sputter targets are produced, for example.



**Figure 16.6.** Atmospheric plasma-spraying unit (left) and plasma torch with particle diagnostic system (right).

For the deposition on a flat substrate, the spray gun moves in the course of a meander with a meander width of several millimeters. This corresponds to the size of the footprint of the sprayed spot. If the meander spacing chosen is too large, the overlapping of the individual spray paths will result in an inhomogeneous coating thickness. Typical gun speeds are several hundred millimeters per second up to some meters per second. For the manufacture of cylindrical parts, the substrate will rotate around its cylindrical axis and the gun will move linearly along the cylindrical axis. The rotational speed and the gun speed have to be adjusted in such a way that during a single rotation, the gun moves a distance in the order of the footprint of the spray gun (several millimeters).

Typical deposition rates for coatings of oxides ceramics are in the order of 50–100 g/min for plasma torches with a power of about 50–80 kW. However, to achieve a higher productivity for the plasma ceramics, high power torches as the LWK burner [34] stabilized by water and operated at 175 kW can be used with feeding rates of more than 500 g/min and deposition efficiencies of 50% and above. The feeding rate cannot be increased arbitrarily as the heating of the powders extracts heat from the plasma and cools it down. The heating of the particles will be reduced and with that, also the efficiency of the process, as more and more particles are not fully molten and will not stick on the surface. The deposition efficiency is also reduced for smaller substrate diameters leading to the fact that parts with diameters of below about 30 mm can hardly be made economically with that process.

Assuming a gun speed of 500 mm/s and a meander width of 5 mm with a feeding rate of 50 g/min with 50% efficiency gives a deposited layer thickness per path for a typical oxide ceramic (density 3.5 g/cm<sup>3</sup>) of nearly 50  $\mu\text{m}$ .

In the introduction, it has already been mentioned that typical particle size distributions are between 10 and 100  $\mu\text{m}$ . However, also the morphology of the particle can influence the microstructure. The mainly used types of powders are spray-dried, agglomerated and sintered, and fused and crushed powders. Examples of these types of powders are given in Figure 16.7. As stated in Reference 35, spray-dried powders typically give a higher amount of porosity in the coating. The used powders for the preparation of the suspension for the spray-drying process are typically in the

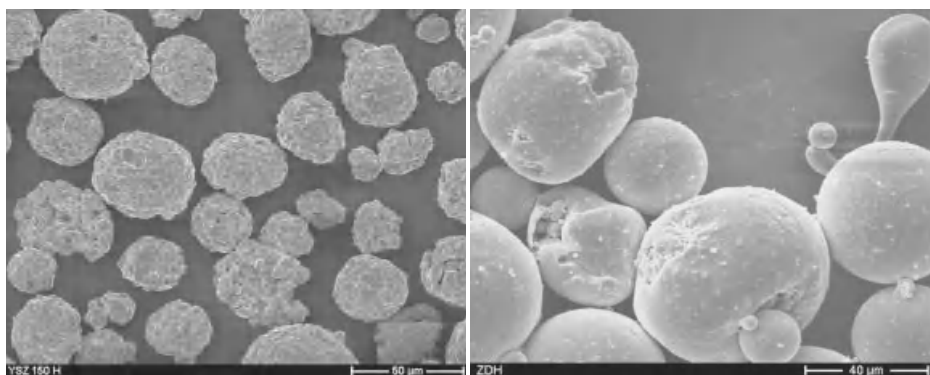


Figure 16.7. SEM micrographs of agglomerated and sintered (left) and hollow spherical powders (right).

TABLE 16.2. Process Parameters Used for Plasma Spraying of Mullite and Zirconia

Parameter	Mullite	Zirconia (5YSZ)
Power (kW)	49	50
Gun type	TriplexPro	TriplexPro
Process gas + flow rate (slpm)	Ar + He 50 + 4	Ar + He 50 + 4
Stand-off distance (mm)	150	150
Feeding rate (g/min)	20%	25%
Feeding gas (slpm)	3	2.2
Gun speed (mm/s)	5	5
Rotational speed (rpm)	140	120
Number of paths	40	40
Efficiency (%)		
Sample thickness (mm)	7.5	
Porosity (%)		
Substrate	Graphite	Graphite/stainless steel

submicrometer range. It is also possible to mix conventional powders with nanophase powders to obtain sufficient flowability of the nanophase powders [16]. Also, spray-dried powders made from suspensions of nanophase powders were used for plasma spraying. By only partly melting the powders in the plasma-spraying process, a part of the nanophase structure can be retained in the plasma-sprayed ceramic [36].

As an example, Table 16.2 shows the process parameters used for the deposition of a mullite and zirconia ceramics.

Figure 16.8 shows photos of samples produced by the given spraying conditions on graphite and on stainless steel substrates. As discussed above, the low TEC of the graphite substrates leads to tensile stress levels in the coating. For YSZ, the mismatch to the graphite is larger than for the mullite, leading to a massive cracking of the YSZ

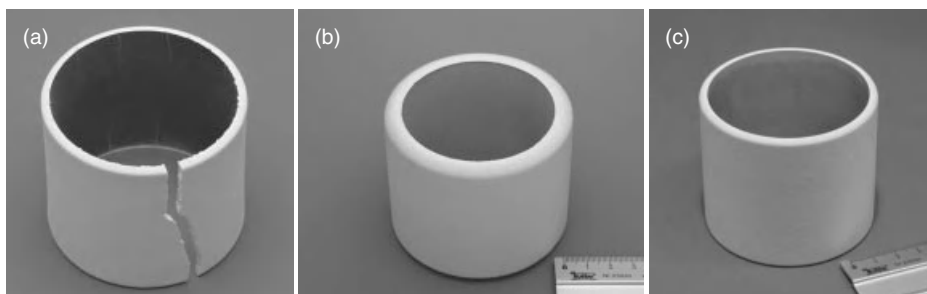


**Figure 16.8.** YSZ (a) and mullite (b) ceramics after removal from graphite substrates and YSZ from a stainless steel substrate (c).

ceramic. This can be avoided if stainless steel substrates are used. Figure 16.8c shows such a freestanding YSZ ceramic after removal.

### 16.3 APPLICATIONS IN PROCESSING/FABRICATION OF CERAMICS AND COMPOSITES

In the previous chapters specific properties of plasma ceramics as excellent thermal shock resistance and inertness against corrosive environments have been mentioned. These properties lead to a number of specific applications at elevated temperatures. In addition, the plasma spray ceramics can be produced as large-scale products with sizes in the several meter range. Large ceramic components made by conventional sintering technologies will be very costly as shaping methods and high-temperature furnaces for this size range are needed.

Also, parts that need a combination of metal and ceramic can be efficiently produced by thermal spray methods, as this process typically leads to a well-bonded ceramic metal interface.

So the combinations of advantages and properties of plasma spray ceramics lead to a number of components that can be hardly or at least not so cost-efficiently manufactured by other technologies. A number of such applications will be given in the following. A large rotating furnace tube made out of alumina is shown in Figure 16.9a. It is used for the calcination of different materials at very high temperatures above 1200°C. The large thermoshock resistance of the plasma-sprayed ceramic makes the application of such large, freestanding components as parts of furnaces possible. In Figure 16.9b, a component of mullite used in the annealing of Si is shown at a temperature of 1250°C. The holes were made by laser drilling.

In addition to the freestanding ceramics, plasma-sprayed ceramics are also often used as thick coatings for different applications, for example, as rolls in a liquid metal bath (e.g., for coating of metal sheets with Zn) or as large sputter targets. An example of the last category is shown in Figure 16.10. Such large targets are also used in PVD coaters, for example, for the coating of float glass.

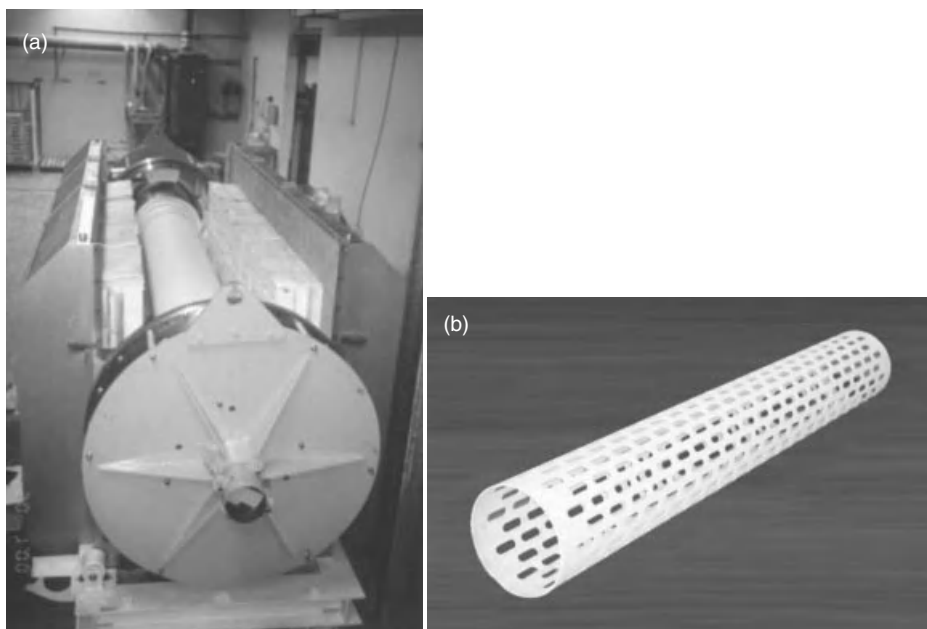


**Figure 16.9.** (a) Rotating furnace tube made of plasma-sprayed alumina with a diameter of 450 mm for calcination of different materials at temperatures above 1200°C. (b) Liner tube (outer diameter, wall 3 mm thick, 1800-mm length) made of mullite as mechanical and electrical barrier for annealing of silicon, application temperature 1250°C, laser treated (both courtesy LWK-PlasmaCeramic GmbH, Wiehl, Germany).



**Figure 16.10.** Zinc oxide cylindrical targets on steel substrates for large-area PVD coaters, up to 4-m length (courtesy GfE Fremat GmbH, Freiberg, Germany).

## 16.4 GENERAL DISCUSSION

As discussed above, plasma-sprayed ceramics can be produced in large dimensions with diameters above 1 m and a length of more than 5 m. Even thin wall thicknesses (<10 mm) are possible for these large lengths. Also, the dimensional accuracy is excellent as determined by the used substrates. These unique properties can be hardly obtained with conventional processing methods. Another specific advantage of the plasma-sprayed ceramics is its specific microstructure, giving a high strain tolerance and excellent thermal shock resistance.

Due to the manufacturing process, only ceramics with a melting point can be processed. Complex oxides, for example, many perovskites, are rather difficult to produce in a stoichiometric way due to a large difference in the evaporation pressure of the constituents. Also, nonoxides are difficult to process by APS due to severe oxidation during spraying.

According to these properties, a rather large number of different industrial applications have been found for plasma-sprayed ceramics, typically simple oxide and silicate ceramics, often for operation in rather harsh environments; some of them are mentioned above.

## 16.5 CONCLUDING REMARKS AND FUTURE DIRECTIONS

APS is a powerful tool for the processing of simple oxides and silicate ceramics. Large (dimensions in the meter range), strain-tolerant, and thermoshock-resistant parts can be produced in a highly efficient way, which is hardly possible with conventional techniques. Parts of many kilogram weights can be produced within an hour.

The technology also offers a high potential for the manufacture of ceramic matrix composites or multilayer structures especially for metal–ceramic multilayers. In addition, the manufacture of ultra-high-temperature ceramics might be efficient by this technique. For nonoxide ceramics, VPS might be a suitable process.

## ACKNOWLEDGMENTS

The author would like to thank Dr. Tiberius Vilics (LWK-PlasmaCeramic) and Dr. Michael Oechsle (Fremat) for the supply of information and pictures. I would also like to thank Karl-Heinz Rauwald (IEF-1, Forschungszentrum Jülich GmbH) for the manufacture of several plasma-sprayed samples and the other members of the plasma-spraying group for the fruitful discussions and their support.

## REFERENCES

1. R. B. Heimann, *Plasma Spray Coating*. Wiley-VCH Verlag GmbH & KGaA, Weinheim, 2008.
2. P. Fauchais, A. Vardelle, and B. Dussoubs, Quo vadis thermal spraying? *Thermal Spray 2001: New Surfaces for a New Millennium*, eds. C. C. Berndt, K. A. Khor, and E. F. Lugscheider, pp. 1–32, ASM International, Materials Park, OH, 2001.

3. L. E. Weiss, F. B. Prinz, D. A. Adams, and D. P. Siewiorek (1992) Thermal spray shape deposition, *Journal of Thermal Spray Technology*, **1**[3] 231–237.
4. P. Georgieva, V. Viswanathan, S. J. Hong, K. Rea, S. C. Kuiry, and S. Seal, *Plasma Manufacturing of Near-Net-Shape Large Scale Nanocomposite Structures—A Potential Bulk Nanofabrication Tolls, NSTI-Nanotech 2005*, Vol. 2. May 8-12, Anaheim, CA, 2005.
5. M. Boncoeur and G. Schnedecker (1994) Fabrication of yttria/niobium laminar composites by plasma spraying, *Journal of the European Ceramic Society*, **14** 29–35.
6. Z. Y. Zhao, L. Wang, J. C. Fang, and W. J. Xu Near net forming of metal-ceramic parts by plasma spraying, *Key Engineering Materials*, **280–283** (2005) 1815–1818.
7. M. V. Gopalakrishnan, K. Metzgar, D. Rosetta, and R. Krishnamurthy (2003) Structural characterisation and strength evaluation of spray formed ceramic composite near-net shapes, *Journal of Materials Processing Technology*, **135** 228–234.
8. Y. Waku and T. Nagasawa (1994) Future trends and recent developments of fabrication technology for advanced metal matrix composites, *Materials And Manufacturing Processes*, **9**[5] 937–963.
9. R. Gadow and K. V. Niessen (2008) Thermally sprayed prepregs for advanced metal matrix composites, Chapter 34, in *Advances in Ceramic Coatings and Ceramic-Metal Systems: Ceramic Engineering and Science Proceedings*, 26 (3), 298–307.
10. R. J. Damani and E. H. Lutz (1997) Microstructure, strength and fracture characteristics of a free-standing plasma-sprayed alumina, *Journal of the European Ceramic Society*, **17** 1351–1359.
11. E. H. Lutz (1997) Plasma ceramics—Properties and applications, cfi/Ber. DKG 74 No. 3 140-150.
12. E. H. Lutz (1995) The Effect of Specimen Size on the Thermal Shock Resistance of Plasma-Sprayed Ceramics, cfi/Ber. DKG 72 No. 7, 387-389.
13. E. H. Lutz (1994) Microstructure and properties of plasma ceramics, *Journal of the American Ceramic Society*, **77**[5] 1274–1280.
14. E. H. Lutz, “Plasmakeramik”, Kapitel 3.4.9.1, in *Technische Keramische Werkstoffe*, ed. J. Kriegesmann, Deutscher Wirtschaftsdienst, Köln, Germany, 1998.
15. K.-S. Shi, Z.-Y. Qian, and M.-S. Zhuang (1998) Microstructure and properties of sprayed ceramic coating, *Journal of the American Ceramic Society*, **71**[11] 924–929.
16. A. Agarwal, T. McKechnie, and S. Seal (2003) Net shape nanostructured aluminum oxide structures fabricated by plasma spray forming, *Journal of Thermal Spray Technology*, **12**[3] 350–359.
17. M. V. Gopalakrishnan, R. Krishnamurthy, and C. V. Gokurlarathnam (2007) Rolling contact fatigues studies on spray formed ceramics composite rolling elements, *Journal of Materials Processing Technology*, **185** 233–237.
18. L. Hongwei, Z. Long, W. Jianjiang, and D. Xinkang (2008) Feasibility analysis of self-reactive spray forming TiC-TiB<sub>2</sub>-based composite ceramic preforms, *Key Engineering Materials*, **368–372** 1126–1129.
19. E. Moreau, C. Chazelas, G. Mariaux, and A. Vardelle (2006) Modeling the restrike mode operation of a DC plasma spray torch, *Journal of Thermal Spray Technology*, **15**[4] 524–530.
20. T. Vilics, personal communication.



21. A. Vardelle, P. Fauchais, B. Dussoubs, and N. J. Themelis (1998) Heat generation and particle injection in a thermal plasma torch, *Plasma Chemistry and Plasma Processing*, **18**[4] 551–574.
22. W. Schultze, “Plasmaspritzen” Kapitel 3.4.9.0, in *Technische Keramische Werkstoffe*, ed. J. Kriesemann, Deutscher Wirtschaftsdienst, Köln, Germany, 1989.
23. O. P. Solonenko, M. A. Anatol’ Yevich, K. E. Vladimirovich, B. M. Petrovna, K. Ogawa, T. Shoji, and M. Tanno (2003) Theoretical and experimental study of thermal barrier coatings, *Materials Transactions*, **44**[11] 2311–2321.
24. S. Solonenko, A. A. Mikhachenko, and E. V. Kartaev Splat formation under YSZ hollow droplet impact onto substrate, *Proc. Of the International Thermal Spray Conference, Basel*, 2005, Ed. E. Lugscheider, DVS, Germany.
25. P. Fauchais, M. Fukumoto, A. Vardelle, and M. Vardelle (2004) Knowledge concerning splat formation: An invited review, *Journal of Thermal Spray Technology*, **13**[3] 337–360.
26. H. Guo, R. Vaßen, and D. Stöver (2004) Atmospheric plasma sprayed thick thermal barrier coatings with high segmentation crack density, *Surface and Coatings Technology*, **186**[3] 353–363.
27. R. Vassen, D. Hathiramani, and D. Stöver (2006) Verfahren zur Herstellung dünner, dichter Keramischichten, Deutsches Patent 102004 044597.
28. R. Vaßen, D. Hathiramani, J. Mertens, V. Haanappels, and I. C. Vincke (2007) Manufacturing of high performance solid oxide fuel cells (SOFCs) with atmospheric plasma spraying (APS), *Surface and Coatings Technology*, **202**[3] 499–508.
29. M. Ahrens, S. Lampenscherr, R. Vaßen, and D. Stöver (2004) Sintering and creep processes in plasma-sprayed thermal barrier coatings, *Journal of Thermal Spray Technology*, **13**[3] 432–442.
30. D. P. H. Hasselman (1969) Unified theory of fracture initiation and propagation in brittle ceramics, *Journal of the American Ceramic Society*, **52**[11] 600–604.
31. M. O. Jarligo, D. E. Mack, G. Mauer, R. Vaßen, and D. Stöver (2010) Atmospheric plasma spraying of high melting temperature complex perovskites for TBC application, *Journal of Thermal Spray Technology*, **19**[1–2] 303–310.
32. A. Cipitria, I. O. Golosnoy, T. W. Clyne, and A. Sintering (2009) Model for plasma-sprayed zirconia TBCs, Part I: Free-standing coatings, *Acta Materialia*, **57** 980.
33. H. J. Rätzer-Scheibe and U. Schulz (2007) The effects of heat treatment and gas atmosphere on the thermal conductivity of APS and EB-PVD PYSZ thermal barrier coatings, *Surface & Coatings Technology*, **201** 7880–7888.
34. V. Veseley (1963) Wasserstabilisierter Plasmabrenner und seine Anwendung beim Plasmaspritzen, *Schweißtechnik* **19**, **9** 393–395. Heft.
35. R. W. Trice, B. Ercan, K. J. Bowman, H. Wang, and W. Porter (2006) Effect of initial powder morphology on thermal and mechanical properties of stand-alone plasma-sprayed 7wt.%  $Y_2O_3$ - $ZrO_2$  coatings, *Materials Science & Engineering A*, **435–436** 212–220.
36. R. S. Lima and B. R. Marple (2007) Thermal spray coatings engineered from nanostructured ceramic agglomerated powders for structural, thermal barrier and biomedical applications: A review, *Journal of Thermal Spray Technology*, **16**[1] 40–63.
37. T. Wakui, J. Malzbender, and R. W. Steinbrech (2006) Strain dependent stiffness of plasma sprayed thermal barrier coatings, *Surface and Coatings Technology*, **200** 4995–5002.
38. S. Costil, C. Verdy, R. Bolot, and C. Coddet (2007) On the role of spraying process on microstructural, mechanical, and thermal response of alumina coatings, *Journal of Thermal Spray Technology*, **16**[5–6] 839–843.



39. S. Seifert, E. Litovsky, J. I. Kleimann, and R. B. Heimann (2006) Thermal resistance and apparent thermal conductivity of thin plasma-sprayed mullite coatings, *Surface & Coatings Technology*, **200** 3404–3410.
40. J. Chevalier, L. Gremillard, A. V. Virkar, and D. R. Clarke (2009) The tetragonal-monoclinic transformation in zirconia: Lessons learned and future trends, *Journal of the American Ceramic Society*, **92**[9] 1901–1920.
41. K. A. Khor, Y. W. Gu, and Z. I. Dong (2001) Mechanical behaviour of plasma sprayed functionally graded YSZ/NiCoCrAlY composite coatings, *Surface and Coatings Technology*, **139** 200–206.

# INDEX

Note: Page numbers in **bold** represent tables; those in *italics*, figures.

- abbreviations, table of, **127–128**
- ab initio calculations, 321
- ACC. *See* amorphous covalent ceramics
- acrylamide premix solution, during gelation, 210
- acrylamide system, polymerization in, 201, 202
- acrylic-based systems, use of alcohols in, 225
- acrylics, for ceramic processing, 205, 206
- aerogels
  - formation of, 186
  - microstructures of, 188
  - in sol-gel process, 185–186, 186, **187**
  - structure of, 186
  - supercritically dried, **187**
- aerospace industry, CVI-processed CMCs in, 336, 339, 342, 343, 344
- agar
  - gelatin hysteresis of, 205, 205
  - used for gelcasting, 203, 204
- agarose
  - gelatin hysteresis of, 205, 205
  - used for gelcasting, 203, 204
- AlliedSignal Composites, 381
- $\alpha$ -Al<sub>2</sub>O<sub>3</sub> coating, for cutting tools, 306–307, 306–307
- alumina suspensions, zeta potentials of, 159, 159
- aluminides, in electromagnetic CS, 401–402
- aluminum, in eutectic growth, 428
- aluminum oxide (Al<sub>2</sub>O<sub>3</sub>), fabrication of, 408
- ambigels
  - microstructures of, 188
  - supercritically dried, **187**
  - synthesis of, 186–187, **187**, 187
- amorphous covalent ceramics (ACC), 238
- anisotropy, in viscous sintering, 102, 103
- Arrhenius law, 91
- atmospheric plasma-spraying (APS), 552, 553, 563. *See also* plasma-spraying process
- atmospheric plasma-spraying (APS) guns, 552, 552
- atmospheric plasma-spraying (APS) unit, 558, 559
- autoclave methods, in green body formation, 359–360
- barium-alumo-borosilicate glass/alumina composites (BABS/A), 110–113, 111, 112
- beneficiation processes, 149
- binder removal, in microwave processing, 499, 501
- binders, in ceramic processing, **152**, 153
- Bingham rheological model, **164**
- bioactive glass, CNT reinforced, 539
- biocatalysis studies, 192–193

- biofuel cells
  - enzymatic, 190–191
  - enzymatic glucose-oxygen, 191, 191–192, 193, 193
- Bioglass®, EPD of, 531
- biomaterials, EPD of, 531
- biomolecules, and sol-gel encapsulation, 195
- biosensors, bioactive glasses for, 187–188
- blowing agents, in direct foaming techniques, 248
- boiling film technique, 328, 332–333
- borides
  - in electromagnetic CS, 404
  - as eutectic component, 441
  - thermodynamic calculations for, 395
- boron nitride (BN), in RMI, 358
- borosilicate glasses, crystallizing, 106
- brake disks
  - aircraft, 378
  - nonoxide CMCs in, 377–378, 379, 380, 380
  - tribological properties of, 378
- brakes
  - C/C composites in, 342
  - CVI-processed CMCs in, 336, 342, 343
- Brembo Carbon Ceramic Brakes Systems, 343
- Brice model, 435
- Bridgman method, 424, 448
- brittleness, of ceramic materials, 148
- bulk ceramics, gelcasting of, 214, 215, 216, 217
- bulk transport, 48
- calcination, in microwave processing, 501
- calcium, in eutectic growth, 428
- CAM-LEM, 460, 463
- Carbenix® brake, 343
- carbide formation
  - and thermal expansion, 362
  - volume change in, 361–362
- carbides
  - in electromagnetic CS, 404
  - as eutectic component, 441
  - thermodynamic calculations for, 395
- carbon formation, chemistry of, 325, 325–326
- carbon nanotubes (CNTs), EPD of, 539
- carrageenan
  - gelatin hysteresis of, 205, 205
  - used for gelcasting, 203, 204
- Carreau rheological model, 164
- Casson rheological model, 164, 164
- C/C-SiC composites
  - for advanced friction systems, 378, 379
  - in brake disk manufacture, 377–378, 379, 380
- ceramic composites
  - EPD in fabrication of, 533, 533–537
  - EPD in fiber-reinforced, 532, 534
- ceramic eutectic systems, 437–438, 438, 439, 440, 441–442
  - alumina-based, 438
  - applications of
    - creep, 443–444, 444
    - mechanical strength, 442–443, 443
    - wear and erosion, 444–445, 446
  - crystallography of, 438
  - experimental findings in, 426–427
  - functional applications, 445–446
    - metamaterials, 447–449, 448
    - photonic materials, 447–449, 448
    - textured cermets, 446–447, 447
  - preparation techniques for, 418–419
  - properties of, 440
  - zirconia-based, 438
- ceramic fibers, cost analysis for, 381, 382
- ceramic materials, characteristics of, 147–148
- ceramic matrix, ideal, 351
- ceramic matrix composites (CMCs). *See also* melt-infiltrated composites
  - complex-structured, 532
  - CVI-processed
    - advantages and disadvantages, 339, 339
    - applications of, 335–337, 344
    - properties of, 335
  - and CVI technology, 313–314
  - fiber-reinforced, 344
  - high-performance nonoxide, 351
  - infiltration processes for, 353–354, 354
  - as inverse composites, 356–357
  - and manufacturing costs, 345
  - processes for, 351–352
    - comparison of RMI and CVI, 354–355, 355, 356
    - liquid-state routes, 353–354, 354

- solid-state routes, 352
- vapor-phase routes, 352–353
- processing costs for, 382
- reinforcement for, 532, 534
- ceramic matrix composites (CMCs),
  - nonoxide
  - applications for
    - brake disks, 377–378, **379**, 380, 380
    - engines and gas turbines, 375–377, 377
    - hypersonic vehicles, 381
    - space vehicles, 381
- ceramic powder synthesis, 497, 497–498, 499, **500–501**
- ceramic processing
  - additives for, 151–153, **152**
  - of glass powders, 78–79
  - steps in, 149–151, 150
- ceramics
  - alumina containing, 556
  - direct ink-jet printing of, 469–470
  - microwave heating, 509 (*see also* microwave processing)
    - advantages/disadvantages of, 504–507
    - components of, 496–504, 497, 499, **500–501**, 503
  - properties of, 449
  - with spinel crystal structure, 441
- Ceramic Stationary Gas Turbine (CSGT) Program, of DOE, 376
- ceramic suspensions, rheology of
  - flow behavior, 162–166, 163, **164**, **165**, 165
  - viscoelasticity, 166–168, 167, 168
- ceramization
  - of PDCs, 238–239
  - process, 244
  - during pyrolysis, 240
- Cerasep<sup>®</sup>, 344
- cermets, textured, 446–447, 447
- cetyl trimethylammonium bromide (CTAB), 195
- C<sub>f</sub>/C composites
  - applications in brake field, 342
- CVI, 336–337
- chemical vapor deposition (CVD), 271
  - advantages of, 272
  - cold wall-type chamber, 276, 276
  - conventional, 273
  - CVI process derived from, 317
  - deposition rate of, 272, 274–275
  - deposition steps of, 272–273, 274
  - film formation in, 272–273, 274
  - grain growth in, 289, 290
  - of oxide structural ceramics and composites, 297
  - process, steps in, 317
  - process parameters for, 272, 273
  - SiC and related composites, 286–292, 287–291, 293–296
  - SiC–TiC composites
    - surface microstructure of, 292, 295
    - with Vicker's indentation, 292, 295
  - Si<sub>3</sub>N<sub>4</sub>-based composites, 275–278, 276–279, 281, 281
  - Si<sub>3</sub>N<sub>4</sub>-AlN, 286
  - Si<sub>3</sub>N<sub>4</sub>-BN, 285, 285–286, 286
  - Si<sub>3</sub>N<sub>4</sub>-C, 278, 280–282
  - Si<sub>3</sub>N<sub>4</sub>-TiN, 281, 282, 283, 283–285, 284
  - techniques, 246
  - thermal, 273
  - Ti<sub>3</sub>SiC<sub>2</sub>
    - unit of cell structure of, 292, 296
    - with Vicker's indentation, 292, 296
  - types of chambers, 275, 275
- chemical vapor deposition (CVD) SiC
  - coating, for use in space vehicles, 289
- chemical vapor deposition (CVD) SiC film, 286–287
  - deposition rate of, 288, 289
  - effects of CVD conditions on morphology of, 287
  - typical surface morphology of, 288
- chemical vapor infiltration (CVI)
  - advantages of, 313
  - commonly used chemical reactions in, **316**
  - compared with RMI, 354–355, 355, **356**
  - continuous fiber-reinforced composites, **356**
  - cost analysis of component fabrication with, 381–382
  - history of, 314, 314–315
  - on large production scale, 352
  - low deposition temperatures associated with, 352
  - principal scope of, 315
  - thermal-gradient, 345
  - vapor-phase routes, 352–353

- chemical vapor infiltration (CVI) apparatus,
  - technical equipment for, 333, 333–335
- chemical vapor infiltration (CVI) composites,
  - 315–319, 316–318
  - chemistry of carbon formation, 325, 325–326
  - chemistry of silicon carbide formation, 319–325
  - CVI modeling, 326–327
- chemical vapor infiltration (CVI) methods
  - categories, 327–328, 328
  - F-CVI, 329–330
  - isothermal/isobaric CVI, 329
  - microwave-heated CVI, 330–332, 332
  - pulsed-flow CVI, 330
  - rapid CVI methods, 332–333
  - thermal-gradient CVI, 329, 330
- chemical vapor infiltration (CVI) process
  - advantages and limitations of, 337, 339–341
  - chemical and physical phenomena in, 319
  - costs associated with, **341**, 341–342
  - heating sources for, 334
  - on industrial scale, 344
  - with infiltration of ceramic matrices in porous preforms, 337, **338**
  - materials produced by, 334
  - volatile gases as by-product of, 335
- chemical vapor infiltration (CVI) processing
  - materials, industrial applications of, 342–344
- Chinese script microstructures, 437, 438
- classical nucleation theory (CNT), 79
- closed porosity model, in viscous sintering, 7
- CMT. *See* critical micelle temperature
- coagulants, in ceramic processing, **152**
- coagulation
  - consolidation by, 171
  - flocculation, 169, 169
- coarsening, process of, 6
- coatings
  - brake disk, 380
  - CNT EPD, 539
  - EPD, 173–175, 175, 529, 531–532
    - biomedical, 540
    - nonaqueous, 530
  - immersion or dipping, 175–177, 176
  - microcracked, 555
  - PDC, 243–244, 245
  - plasma-sprayed, 557, 557
  - PZT, 532
  - SiC-filled PDC, 244
  - SiCN-based, 244, 245
  - thick, plasma-sprayed ceramics as, 561
- Coble creep shrinkage rate, 50
- coefficient of friction (COF), in C/C composites, 377, 378
- coefficient of thermal expansion (CTE)
  - in RMI process, 360–362, **362**
  - in viscous-phase silicate processing, 119
- cofiring, 123–124
- coherent anti-Stokes Raman spectroscopy (CARS), on CVD of SiC, 324
- colloidal methods
  - advantages of, 175–177
  - shaping
    - consolidation by coagulation and gelation methods, 171–172, 172
    - deposition/evaporation methods, 172–177, 173, 175, 176
    - filtration techniques, 169–171, 170
    - suspension forming techniques, 169, **169**, 177
- colloidal science
  - attractive potential, 153–154
  - colloidal dispersions in, 153
  - Derjaguin-Landau and Verwey-Overbeek theory, 157–159, 158, 159
  - polymeric stabilization, 159–162, 160–162
  - repulsive electrostatic potential, 154–156, 155, 157
  - suspensions in, 153
- colloidal suspensions, steric stabilization of, 160
- combustion synthesis (CS)
  - electromagnetic field, 396–399, 397, 398
  - gravity-assisted, **405**, 405–408, **406**, 408
  - kinetic considerations, 395–396
  - in microwave processing, 501
  - technique, 391
  - thermodynamic considerations, 392–395, **394**, **395**
- combustion synthesis (CS) research, sample geometrics used in, 402, 403

- composites. *See also specific composites*  
 microwave processing  
   advantages/disadvantages of, 504–507  
   components of, 496–504, 497, 499, **500–501**, 503  
   preparation for, 509  
   plain weave pattern, 359  
 computer-aided design and manufacturing  
   (CAD/CAM) tools, 459  
 computer-aided design (CAD)  
   CNC instructions, 464–465  
   filling (tool-path generation), 462, 463–464  
   slicing in, 462, 462–463  
   stereolithography files in, 460–462, 461  
   support structure, 464, 465  
 computer numerical control, in CAD, 464–465  
 constant rate period (CRP), in gel-casting process, 211  
 constrained sintering, 36  
 continuous sintering theory, 100  
 continuum models, 21, 22  
 copper powder, sintering map for, 10, 11  
 cordierite, 556, **556**  
 $\mu$ -cordierite, 92  
   surface crystallization of, 82  
   surface nucleation density of, 86  
 $\mu$ -cordierite crystals, 80, 85  
 cordierite glass powders  
   milling of, 104, 105, **106**  
   preparation of, 86  
 cortisol  
   optical sensing of, 189, 189  
   sol-gel immunoassay of, 189, 189, 190, 191  
   studies with, 194–195  
 counterions, monolayer of, 155–156  
 creep-recovery test, 166, 167  
 creep resistance, 443–444, 444, 449  
 critical micelle temperature (CMT), 205, 206  
 Cross rheological model, 164, **164**  
 crystalline BN, 382  
 crystallization  
   with concurrent surface, 104, 104–107, 105, **106**, 107, 108  
   of glass powders, 88–92, 89–92  
   kinetic understanding of, 78  
   in microwave processing, 501–502  
   quasi-homogeneous bulk, 90  
   simultaneous sintering and, 107, 109–110  
 crystal nucleating effect, 114  
 crystal nucleation, from glass powder  
   surfaces, 86, 86–87, 87  
 crystal powders, sintering of, 76, 76–78  
 CTE. *See* coefficient of thermal expansion  
 CVD. *See* chemical vapor deposition  
 CVI. *See* chemical vapor infiltration  
 Darcy's law, 363, 364, 366  
 Debye length, 156  
 defect reduction, 6  
 deflocculants, in ceramic processing, 152, **152**  
 deformation  
   in constrained sintering, 19–22, 22  
   methods, 148  
   during pressure-assisted sintering, 49  
 deformation behavior (electroplasticity), influence of electric current on, 62–64, 63  
 densification  
   in constrained sintering, 19–22, 22  
   during hot pressing, 50  
   in liquid-phase sintering, 77–78  
   by plastic deformation, 59  
   process, 6  
   for Scherer model, 8  
 densification behavior  
   influence of electric current on, 64–67  
   influence of high electric fields on, 68  
 dental applications, SGC for, 126–127, 127  
 dental crowns and bridges, EPD of, 531  
 depletion mechanisms, in polymeric  
   stabilization, 159–160, 160  
 deposition/evaporation methods  
   coatings, 173–177, 175, 176  
   substrates, 172–173, 173  
 deposition-evaporation technique, 169, **169**  
 Derjaguin-Landau and Verwey-Overbeek (DLVO) theory, 157–159, 158, 159  
 dielectric heating, principles of, 485–487  
   inversion of temperature profile, 488, 491  
   rapid heating, 488, 490  
   selective heating, **487**, 487–488  
   thermal runaway, 490–492  
   volumetric heating, 488, 489–490

- dielectric properties, of common solvents, **500–501**
- differential thermal analysis (DTA), 239
- diffusion processes, during sintering, 47
- dilatometry, optical, 102
- diopside crystals, 80, 82
- diopside glass spheres, sintering, 106, 107
- directed metal oxidation (DIMOX) process, 353
- direct electron transfer (DET), 193, 194
- directionally solidified eutectic ceramic (DSEC), 449
  - $\text{Al}_2\text{O}_3/\text{ZrO}_2$ , 423, 425
  - fabrication techniques, 445
  - $K_1$  values for, 422, **423**
  - LFZ method for, 430, 430
  - $\text{LiF}/\text{NaCl}$ , 448
  - materials, 418–419
  - microstructures of, 437–438, 438, 449
  - nondimensional melting entropy values of, 419, **420**
  - as potential metamaterials, 448
  - $\text{NaF}/\text{CaF}_2$ , 423, 424
- directionally solidified eutectic (DSE) oxides, 419
- directional solidification, 417, 449
  - background
    - eutectic growth in, 419–422, **420, 423**
    - eutectic range, 422–427, 424, 425, 427
  - ceramic eutectic systems, 437–438, 438, 439, **440**, 441–442
  - fabrication methods, 427–428, 429
    - edge-defined, film-fed growth, 435–436
    - laser surface melting technique, 431–433, 432, 433
    - melt stability and defects, 433–435
    - melt zone technique, 428–431, 430, 431
    - micropulling-down technique, 436–437, 437
  - research in, 418
- direct writing, 459
- discrete element simulations (DES), 25, 26
- dispersing substances, 151
- dissolution phenomena, effects on sintering and crystallization, 113, 113–114
- droplet-based SFF techniques
  - ink delivery, 466–468, 467
  - ink rheology and solidification in, 469, 469–470, 470
  - post-deposition processing, 471
  - potential shapes, 470–471
- drying, in microwave processing, 498–499, **500–501**, 504
- dry pressing, 151
- DSEC. *See* directionally solidified eutectic ceramic
- DTA. *See* differential thermal analysis
- DTA curves
  - experimental, 92
  - for surface crystallization of glass powders, 90–92, 91
  - topokinetic model for calculation of, 90, 91
- Dullien model, 364
- dust particles, nonoxide, 85
- edge-defined, film-fed growth (EFG)
  - process, 435–436
  - techniques, 449
- Einstein model, 165
- Einstein-Nernst equation, 23
- elastic energy, in mechanical damage to surface nucleation sites, 84
- electrical breakdown, 64
- electrical double layer (EDL)
  - defined, 155
  - distortion and thinning process, 521, 522
  - in EPD, 519, 519, 520, 522
- electrical insulation, in PECS, 55–58, 56–58
- electrical insulators, 67
- electrical resistance values, 53, 54
- electric current-assisted sintering (ECAS), 43
- electrochemical particle coagulation, in EPD, 521
- electrodes, composite, developed by EPD, 540
- electromagnetic dissipation, 32
- electromagnetic field combustion synthesis, 396–403, 397, 398, **400**
- electromagnetic field distribution, in microwave processing, 506
- electromagnetic simulation software, 508
- electromigration
  - defined, 65
  - occurrence of, 65–66
- electron backscatter diffraction (EBSD), 224, 224

- electron beam floating zone melting (EBFZM) process, 429
- electron wind, 62
- electrophoretic deposition (EPD), 169, 173, 174
  - advantages of, 175, 518, 532, 540
  - applications of, 532
  - coatings, 531–532
  - film processing, 531–532
  - infiltration of fiber mats in, 534, 535–537, 538
  - in SiC-reinforced SiC ceramics, 535–536, 535–537
  - traditional ceramic technology, 526–530, 527, 528, **529**
- from aqueous suspensions, 528–529, **529**
- of CNTs, 539
- expanded applications of, 517
- external electric field, 174
- kinetics, 174, 175
- mechanisms of, 518
  - categories of, 520
  - EDL distortion and thinning, 521, 522
  - electrochemical particle coagulation, 521
  - flocculation by particle accumulation, 520
  - particle charge neutralization, 520–521
  - particle stabilization, 518–520, 519
  - pH localization, 522–524, 523, 525, 526
  - on porous nonconducting substrates, 524–526
- of nanoparticles, 538
- process of, 517, 518, 540
- electrophoretic infiltration, 534, 535–537
- electroplastic effect, 62
- electrosteric mechanisms, in polymeric stabilization, 159–160, 160
- Ellis rheological model, **164**
- Enabling Propulsion Materials (EPM) program, 376, 377
- engineering materials, classification of, 147
- engines, nonoxide CMCs in, 375–377
- environmental barrier coatings (EBCs), 376
- EPD. *See* electrophoretic deposition
- eutectic ceramics, defined, 417
- eutectic composites
  - solidification of, 417
  - temperature-composition phase diagram of, 418
- eutectic coupled growth zone, skew-symmetric, 426, 427
- eutectic growth modeling, 449
- extended volume, in crystallization of glass powders, 88
- extrusion, 151
- FAST. *See* field-assisted sintering
- F-CVI, 329–330
  - advantages of, 340
  - disadvantages of, 340
  - on large production scale, 353
- Fe-Al, FACS used in, 402
- Fecralloys, EPD of, 531
- FGMs. *See* functionally graded materials
- fiber curing, 243
- fiber growth assemblies, “grown from meniscus,” 428, 429
- fiber-matrix interface, in RMI, 357
- fiber-matrix interphases, in CVI composites, 314
- fiber-reinforced composite market, 382
- fiber reinforcements, 2-D, 534
- fibers, used in CMCs, 357, **357**
- fiber strength loss, in melt-infiltrated composites, 382
- field-activated combustion synthesis (FACS), 396–397, 404
- field-assisted sintering (FAST), 29–34, 31–34, 35, 43
  - advantages of, 30
  - compared with HP, 31
  - experimental setup for, 31
  - microwave-assisted sintering, 32–34, 33, 34
  - SPS, 30–32, 31, 32
- filament-based SFF techniques, 471–472
  - ink delivery, 472–473
  - ink rheology and solidification, 473–477, 475, 476
  - post-deposition processing, 479–480, 480
  - potential shapes, 477–479, 478, 479, 480
- fillers, in ceramization
  - active, 240–242, 241
  - passive, 240, 240–241
- film-fed growth, edge-defined, 435–436
- filtration techniques, 169–171, 170
- flame hydrolysis, 95
- flash effect, 66



- flash sintering, 66
- flocculation-coagulation mechanism, 169, **169**, 171
- flow behavior, in rheology of ceramic suspensions, 162–166, *163*, **164**, **165**, *165*
- fluid-to-gel transition, for colloidal inks, *475*
- fluoroapatite SGC, leucite-free, *127*
- foaming techniques
  - direct foaming techniques, 247–248
  - infiltration of porous preforms, 249
  - for porous materials, 217, 218, 220, *221*
  - sacrificial fillers, 249
- foams, porous SiOC, 247, 248
- forming methods, 149–150
- FOTON (satellite experiment), 381
- freeze casting, 171, *172*
- freeze gelcasting, 216–217, *219*
- friction systems
  - C/C-SiC composites for advanced, 378, **379**
  - LSI process of, 382
- FTIR emission spectroscopy, 324
- functionally graded materials (FGMs)
  - design of, 170, *170*
  - EPD in fabrication of, 532–533, *533*
- fused deposition modeling (FDM), 460
- gadolinium-doped ceria (GDC) phases, 446
- gasless combustion, 391
- gas turbines
  - CVI-processed CMCs in, 336
  - nonoxide CMCs in, 375–377, *377*
- Gauss normal distribution, influence of electric current on, 62, *63*
- gelation, chemical, 171
- gelation technique, 169, **169**
- gelcasting, 199
  - alternate drying methods, 225–226
  - compound with sol-gel processing, 200
  - original method, 200
  - processing flowchart for, *207*
  - texturing with electric fields, 226
  - toxicity/environmental concerns, 225
- gelcasting process
  - binder burnout, 213–214
  - and casting atmosphere, 209–211, *210*
  - casting suspension, 207–208
  - drying, 211–213, **212**, *213*
- gelcasting systems
  - applications, 214, **215**
    - bulk ceramics, 214, **215**, *216*, *217*
    - laminates, 222–225, *223–225*
    - porous materials, 217–222, 220, *221*, *222*
    - textured materials, 214–217, *218–220*
  - cross-linking of polymer solutions, 201, *203*, *204*
  - cross-linking of polysaccharides and polymers, 201, 203, *204*, 205–206, *206*
  - of low toxicity, 201
  - optimal, 226
  - polymerization of monomers, 200–201, *202*
- gel formers, in ceramic processing, **152**
- General Electric (GE), 353
- German Aerospace Agency (DLR), 371, 381
- Gibbs-Thomson effect, 421
- glass. *See also* sol-gel process
  - sintering of, 76, 76–78
  - sol-gel, 183
- glass-bonded ceramics (GBC)
  - for LTCC, 123–126, *124*, **125**, *125*
  - viscous silicate phases, 75
- glass ceramics (GC),
  - fabrication process of, 119, *120*
  - viscous silicate phases, 75
- glasses
  - fiber-reinforced, 119, *120*
  - synthesis of organic-inorganic, 183
- glass formation, and eutectic compositions, 442
- glass matrix composites (GMCs), 75
  - for architectural applications, 121, *121*
  - continuous fiber-reinforced, 117–118, *118*
  - dispersion-reinforced, 117
  - effect of inclusion-induced stress on sintering of, 114
  - for LTCC, 123–126, *124*, *125*, **125**, 126
  - processing of reinforced, 118–119, *119*, *120*
  - for structural applications, 117–119, *118–120*
  - viscous sintering, 77, 77
  - from wastes, 122–123, *123*

- glass powders
  - ceramic processing of, 78–79
  - cordierite, shrinkage of sol-gel-derived, 94, 94
  - crystallization of
    - DTA curves for, 90–92, 91
    - formal kinetic approach, 88–92, 89–92
    - topokinetic approach, 89–92, 89–92
  - mixed alkaline earth silicate, 96
- GMCs. *See* glass matrix composites
- Grahame equation, 156
- grain boundary mobility, 64
- grain growth
  - discontinuous, 46
  - ideal, 45, 46
  - influence of electric field on, 61–62
  - retardation of, 66
  - during sintering, 45–46, 46
- grain size, and densification, 49
- graphitization, effect on fabricated C/C-SiC brake disks with, 378, 380, 380
- gravitational field combustion synthesis, materials processed by, **406**
- gravity-assisted combustion synthesis, 405, **405, 406**
  - high-gravity-assisted CS, 407–408, 408
  - microgravity CS, 405–407
- green bodies
  - in cross-linking and pyrolysis of alumina-filled polysilsesquioxane, 240
  - particle packing density in, 528
- green body formation, in RMI, 359–360
- green fibers, polycarbosilane-based, 242
- green machining, in gelcasting, **212**, 212–213, 213
- green technology, as microwave heating, 507
- growth dimensionality
  - in crystallization of glass powders, 88
  - topokinetic approach to, 89, 89–90, 90
- Hamaker constants, 154
- heat engines, CVI-processed CMCs in, 336
- heat exchangers, CVI-processed CMCs in, 336
- Herring equation, 23
- Herschel-Bulkey rheological model, 164, **164**
- Heywang expression, 435
- high-gravity-assisted CS technology, 407–408, 408
- high-pressure membrane reactors, 245–246
- high-resolution electron microscopy (HREM)
  - methods, 437, 441
- high-resolution X-ray tomography, 437–438
- High-Speed Civil Transport (HSCT) program, 376, 377
- high-temperature pressure (HIP) sintering, 449
- Hi-Nicalon SiC/epoxy, tensile data for, 374–375, **375**
- HiPerComp (GE) composites, 371, **372**
- HiPerComp process, 369–370
- HITCO, 343
- Hookean fluid, 167, 168
- Hooke's law, 162–163
- hot embossing, basis of, 253, 253
- hot forging, 28
- hot isostatic pressing, 28
- hot-melt printing, of lead zirconate titanate ink, 472
- hot pressing (HP), 27, 28
  - in pressure-assisted sintering, 50
  - for production of CMCs, 352
- HREM. *See* high-resolution electron microscopy
- hybrid heating systems, in microwave processing, 509
- hydraulic radius, 363–364
- hydrogen purification, PDC membranes in, 247, 248
- hydroquinone (HQ), for bubble-free EPD, 529
- hydrostatic pressure, effect on sintering of, 115
- hydrous oxide surfaces, 154–155
- hydroxyapatite (HA), 441
  - for bone implants, 219, 221
  - CNT reinforced, 539
  - EPD of, 531
  - scaffold, for damaged mandible, 480, 480
- hypersonic vehicles, melt-infiltrated CMCs in, 381
- hyroxymethylacrylamine (HMAM), 201
- immunoassays, with sol-gel silica, 189, 189, 190, 191
- induction field-activated combustion synthesis (IFACS), 403

- infiltration processes, for CMCs, 353–354, **354**
- ink delivery systems, for droplet-based writing, 466–468, 467
- ink-jet printing, direct, 466–470
- ink writing techniques, 466, 467
- inner Helmholtz plane (IHP), 156
- integrated passive devices (IPDs), 502
- intermetallics, CS techniques for, 402–403
- intersplat bonding, 553
- “intrinsic viscosity,” 165
- ionic conductors, 66
- ion irradiation, 258
- IPDs. *See* integrated passive devices
- irradiation, ion, 258
- isothermal-CVI (I-CVI) process, 314, 314–315
- advantages of, 339–340, 345
- costs associated with, **341**, 341–342
- 2-D model of, 327
- drawbacks of, 326, 345
- industrial applications of, 345
- in large production scale, 352–353
- steps in, 318, 318
- isothermal/isobaric CVI (I-CVI), 329
- isothermal process, 317
- JH law, 421, 422
- JH theory, 421, 426
- joining, 148
- in microwave processing, 503–504
- for RMI materials, 383
- kinetics transformation, 88
- KJMAE theory, 88
- Krieger-Dougherty equation, modified, 208
- Krieger-Dougherty model, 165
- laminates
- EPD fabrication of, 532, 533–534
- gelcasting of, 222–225, 223–225
- Langmuir-Hinselwood model, modified, 324
- large rigid inclusion, use of term, 114
- laser chemical vapor deposition (LCVD), 297
- deposition rate and laser density in, 298, 299, 300
- high-speed deposition by, 297–300, 298, 299
- pyrolytic, 297, 299
- schematics of, 297, 298
- structural oxide coating by
- $\alpha$ -Al<sub>2</sub>O<sub>3</sub> coating for cutting tools, 306–307, 306–307
- YSZ coating for gas turbine blades, 300–301, 302, 303, 304, 305
- time dependence of substrate temperature in, 301, 302
- laser floating zone (LFZ) crystal growth
- method, 426, 428, 430, 430, 431
- laser pyrolysis, 257
- laser sintering, 199
- laser surface melting
- in directional solidification, 431–433, 432, 433
- for large eutectic ceramic pieces, 449
- LCVD. *See* laser chemical vapor deposition
- lead zirconate titanate (PZT) ink, shear rate for, 476, 476
- lead zirconate titanate (PZT) suspension, 470, 470
- leucite SGCs, 126
- LFZ. *See* laser floating zone
- LIGA, 252–253
- liquid desiccant drying, 226
- liquid metal infiltration, 353. *See also* melt infiltration
- liquid phase sintering (LPS), 15–19, 77
- advantage of, 18
- and grain shape accommodation, 19
- microstructure, 16
- secondary rearrangement for
- polycrystalline particles during, 19
- stages of, 17, 17, 18, 18
- wetting behavior in, 16
- liquids, in ceramic processing, 152
- liquid silicon infiltration (LSI) composites (DLR), 371, **372**
- liquid silicon infiltration (LSI) process, 370–371, 371, **372**, 382
- lithium disilicate framework, 127
- lithography
- deep X-ray, 256, 256
- soft, 254, 255, 256
- lithography microstructuring methods, 251–252, 252
- load rotating or translating devices, in microwave technology, 493

- local heating zones, during PECS, 60
- local viscous flow, in mechanical damage to surface nucleation sites, 84
- London-van der Waals dispersion forces, in colloidal science, 153–154
- London-van der Waals (LVDW) attractive force, in EPD, 521
- low-temperature, of RMI materials, 383
- low-temperature cofired ceramics (LTCC) technology, 97, 123–124, 124, 125
  - advantages of, 124–125
  - commercial use of, 125
  - examples for, **125**
- LPS. *See* liquid phase sintering
- lubricants, in ceramic processing, **152**
- Mackenzie-Shuttleworth (MS) model, 6, 7
- magnesium, in eutectic growth, 428
- magnetrons, 492
- manufacturing processes, classification of, 148
- mass transport, during sintering process, 46–51, **48, 51**
  - pressure-assisted sintering, 49–51, **51**
  - pressureless sintering, 46–49, **48**
- materials. *See* engineering materials
- matrix, and microwave processing, 505
- matrix cracking, in RMI process, 361
- matrix microcracks, in RMI, 358
- matter transport
  - paths for, 9, **10, 10**
  - in solid-state sintering, 22
- mechanical milling, 6
- mechanical resistance values, 442–443, **443, 449**
- Meggitt Aircraft Braking Systems, 343
- melt, solidification from, 417
- melt-infiltrated (MI) composites
  - cost analysis of component fabrication with, 381–382
  - microstructure and properties of, 367–375, 369, 371, **372, 373, 373, 374, 375**
  - processing and property issues, 382–383
  - room temperature properties of, 371, **372**
  - silicon carbide and silicide matrices, 371–375, 373, **373–375**
  - SiC
    - LSI process, 370–371, 371, **372**
    - reaction bonding and REFEL process, 367–368, 369
    - SILCOMP and HiPerComp, 368–370
  - melt infiltration (MI) process modeling, 353.
    - See also* reactive melt infiltration
    - background, 362–363
    - infiltration, 362–365, 364
    - infiltration and reaction, 365–367
  - melting, in microwave processing, 503
  - melt materials, properties of, 361, **361**
  - melt zone
    - cracks in solidified rod, 435
    - in directional solidification, 428–431, 430, 431
    - stability of, 434–435
- membranes
  - amorphous ceramic, 246
  - amorphous silicon nitride-based ceramic, 246
  - microporous amorphous silica-based, 246
- MEMs. *See* microelectromechanical systems
- MEMS/nano electromechanical systems (NEMS), 257
- metal matrix composites (MMCs), 247
- metals
  - characteristics of, 147
  - vitreous enamel coatings on, 529
- metamaterials, defined, 448
- methoxypoly(ethylene glycol) monomethacrylate (MPEGMA), 201
- methylethylketone (MEK), electric field strength for, 530
- methyltrichlorosilane (MTS)
  - homogeneous deposition of, 321
  - pyrolysis of, 324
  - in silicon carbide formation, 319–321
  - unimolecular deposition of, 322
- microcasting, 253
- microcontact printing ( $\mu$ CP), 254
- microcracks, in plasma-spraying process, 554–555, 556
- microelectromechanical systems (MEMs), 250
  - derived from polymer precursors, 251
  - microfabrication of PDC-based components for, 249–257, 252–256
  - pyrolysis of, 251

- microgravity CS, 405–407
  - materials processed by, **405**
  - mechanical properties affected by, 406
- micromolding, 253, 253–254
- micromolding in capillaries (MIMIC), 254, 255, 256
- micropulling-down ( $\mu$ -PD) technique, 436–437, 437
- microscopy, heating, 102
- microstructural texture, via gelcasting, 215
- microstructure-based models
  - advanced structural evolution models, 25–26, 26, 27
  - mass transport and viscosity in, 22–25
- microtransfer molding ( $\mu$ TM), 254, 255
- microwave-activated combustion synthesis (MACS), 396, 397
  - advantages of, 398
  - features of, 398–399
- microwave applicators, 492–496, 494, 496
- microwave-assisted processes (MW-CVI)
  - advantages and disadvantages of, 341
  - for SiC<sub>f</sub>/SiC composites, 345
- microwave-assisted sintering, 32–34, 33, 34
- microwave device, components of, 492–495
- microwave energy, direct deposition of, 506
- microwave-heated CVI (MW-CVI), 330–332, 332
- microwave heating, nonfood field of
  - application for, 509
- microwave-material interactions, 508
- microwave processing, 496–497
  - advantages of, 504
  - binder removal in, 499, 501
  - calcination, 501
  - ceramic powder synthesis, 497, 497–498, 499, **500–501**
  - combustion synthesis, 501
  - crystallization, 501–502
  - direct deposition of microwave energy, 506
  - drying, 498–499, **500–501**
  - electromagnetic field distribution in, 506
  - enhanced sintering, 504–505
  - as green technology, 507
  - joining, 503–504
  - melting, 503
  - microwave plasma, 506
  - moisture leveling and self-regulation in, 504
  - nanostructured materials, 504–505
  - nonthermal effects, 507
  - preferential heating of matrix or reinforcement in, 505
  - process analysis, 508, **508**
  - sintering, 501–502, 503
  - solid-state reactions, 501
  - uneven power density distribution, 506
- microwave pyrolysis, 257–258
- microwaves
  - in materials processing, 485
  - in processing advanced materials, 397
- microwave technology
  - applicator in, 492–493
  - auxiliary absorbers and additives in, 493–494
- milling, 149. *See also* beneficiation processes
  - effect on sintering of, 104, 105
  - materials, 87, 87
- milling efficiency, and finely ground glass powder, 87, 87
- milling time, of cordierite glass powders, 86
- MMCs. *See* metal matrix composites
- mode stirrers, in microwave technology, 493, 494
- mold designs, for laminate gelcastings, 222, 223
- molding, 149
- molybdenum silicide (MoSi<sub>2</sub>), in
  - electromagnetic field CS, 399–401
- monofunctional monomers of methacryamide (MAM), 201
- mullite, 556
  - plasma spraying of, **560**, 561
  - properties of, **556**
- multiples of random distribution (MRD),
  - texture strength in, 215
- multiscale models for sintering, 25–26, 27
- multiwalled carbon nanotubes (MWCNTs), 192, 195
- MW-CVI. *See* microwave-heated CVI
- Nabarro-Herring creep, 50
- nanoarchitectures, ceramic, EPD-based
  - fabrication of, 539
- nanomaterials processing, EPD in, 517–518
- nanoparticles

- ceramic, 538
- EPD of, 538
- nanostereolithography, 252
- nanostructured materials, in microwave processing, 504–505
- Napper's model, of steric stabilization, 161
- National Material Advisory Board (NMAB), 382
- near-net-shape process, and CVI, 337
- near-net-shaping techniques, mechanisms of, 171
- neck formation, in pressureless sintering, 47
- neck-forming ability factor, in experimental shrinkage data, 97
- NEMS. *See* MEMS/nano electromechanical systems
- Neopariés™, applications of, 121, 121
- Nernst-Noyes-Whitney equation, 366
- net-shape techniques, 199
- Newtonian liquid, 167, 168
- Newton rheological model, **164**
- Nextel®-type (alumina) fibers, 534
- Next Generation Launch Technology (NGLT), 377
- NiO-yttria-stabilized zirconia (YSZ), in EPD, 525–526, 528. *See also* yttria-stabilized zirconia
- nitride, as eutectic component, 441
- nitride powders, in electromagnetic CS, 404
- nonthermal effects, in microwave processing, 507
- nuclear reactors, CVI-processed CMCs in, 336
- nucleation agents, glass-ceramic processing, 76
- nucleation density, low surface, 80, 81
- n*-vinyl pyrrolidone (NVP), 201
- Oak Ridge National Laboratory, 200
- optical applications, development of sol-gel-based materials for, 194
- organic solvents, in ceramic processing, 152
- organotitanate coupling agent, cross-linked with PVA, 201, 203
- oscillatory shear, 167
- Ostwald-de Waele rheological model, **164**
- Ostwald ripening process, 18
- outer Helmholtz plane (OHP), 156
- oxide ceramics, 556
- oxide particles, 85
- oxides, CVD of, 297
- particle packing density, in green bodies, 528
- particle size distribution (PSD)
  - bimodal PSD and aggregates, 94, 100, 101
  - broad, 97–98, 98
  - during milling, 87
  - narrow, 97–98, 98
- PDCs. *See* polymer-derived ceramics
- PECS. *See* pulsed electric current sintering
- PEG. *See* polyethylene glycol
- percolation threshold, of rigid inclusions, 113
- phase field models (PFMs), for diffuse solidification, 427
- pH localization mechanism, in EPD, 522–524, 523, 525, 526
- photo-CVD, 297
- photonic crystals, three-cylinder structures for, 256, 256–257
- pilot plant, MW-CVI, 331
- plain weave pattern, for composites, 359
- plasma, microwave, 506
- plasma-assisted sintering (PAS), 43
- plasma ceramics, properties of, **556**, 563. *See also* plasma spraying
- plasma CVD, 297
- plasma formation, 65
- plasma pressure compaction (P<sup>2</sup>C), 43
- plasma-sprayed ceramics, unique properties of, 563
- plasma-spraying process, 177, 551
  - applications, 561, 562
  - atmospheric, 553
  - different environments for, 552
  - as forming process, 551
  - manufacture of bulk ceramics by, 552
  - pore morphology in, 557, 557
  - technique, 558–561, 559, **560**, 560, 561
  - particle size distributions, 559, 560
  - process parameters, **560**
  - surface preparation of substrate, 558
  - typical deposition rates for, 559
- plastic flow, 49
- plastic-forming technique, 150–151
- plasticizers, in ceramic processing, **152**, 153
- Poiseuille capillary flow equation, 365

- polycarbosilanes, 236
  - cross-linking of, 237–238, 242
  - pyrolysis of, 238–239
  - synthetic route from dichlorosilanes to, 237
- poly(dimethylsiloxane) (PDMS), for microfabrication, 256
- polyethylene glycol (PEG), 192, 195, 201
- polymer-derived ceramics (PDCs)
  - coatings, 243–244, 245
  - foams, 247–249, 248
  - main advantage of, 258
  - membranes, 245–247, 247, 248
  - microcomponents manufacturing, 251
  - microstructure-property relations of, 258
  - nonconventional processing techniques for, 257–258
  - nonoxide, 242
  - PDC fibers, 242–243
  - preceramic polymers for preparation of, 236
  - processing of, 236
    - ceramization, 238–239
    - cross-linking, 237–238
    - synthesis, 236–237, 237
  - properties of, 235, 258
- polymer-derived ceramics (PDCs) monoliths, 239–242, 240, 241
- polymers, 147
  - characteristics of, 148
  - conformation of, 160–161, 161
  - stabilization of, 159–162, 160–162
  - thermoplastic, 151
- polysaccharides
  - gelation hysteresis of, 205, 205
  - used for gelcasting, 203, 204
- polysilanes, synthetic route from dichlorosilanes to, 237
- polysilazanes, 236
  - cross-linking of, 238
  - microcasting of, 253–254, 254
  - pyrolysis of, 239
  - synthetic route from dichlorosilanes to, 237
- polysiloxanes, 236
  - cross-linking of, 238
  - synthetic route from dichlorosilanes to, 237
- polysilylcarbodiimide derivatives, 239
- poly(silylcarbodiimides), synthetic route from dichlorosilanes to, 237
- poly(vinyl alcohol) (PVA), in cross-linking of polymer solutions, 201
- porosity
  - of RMI materials, 383
  - in sintering process, 4
  - volume fraction of, 222, 222
- porous gelcast ceramics, 220
- porous materials, gelcasting of, 217–222, 220, 221, 222
- powder compaction, events during, 45
- powder preparation techniques, 6
- powder processing techniques, 148, 149
- powders, ceramic
  - patterning of, 250
  - pressing of, 250
- powder surfaces, crystal nucleation from, 86, 86–87, 87
- power law creep, 50
- power measurement and control, in microwave technology, 494–495
- power series rheological model, **164**
- preceramic polymers, polymer-to-ceramic transformation of, 240, 241
- preferential current paths, 60
- pressure casting, 171, 177
- PSD. *See* particle size distribution
- pulsed electric current sintering (PECS), 43
  - macroscopic effects
    - temperature distributions, 51–58, 52, 54–58
    - temperature gradients, 67
  - microscopic effects, 59, 68
    - athermal or intrinsic current effects, 61–67, 63, 67
    - pressure influence, 58–59
    - thermal or extrinsic current effects, 60–61
  - process, 43–44, 44
  - thermal and electrical insulation in, 55–58, 56–58
  - tool geometry in, 54–55, 55
  - tool materials in, 51–54, 54
- pulsed-flow CVI (P-CVI), 330, 340
- PVA. *See* poly(vinyl alcohol)
- PVA-Ti system, 201, 204

- pyrocarbon deposition
  - kinetics of, 326
  - reaction scheme for, 325, 325–326
- pyrolysis
  - laser, 257
  - microwave, 257–258
  - of preceramic polymers, 239–240
- pyrolytic carbon (PyC), in RMI, 358
- pyrometers, 495
- radiometers, 495
- rapid CVI methods, 332–333, 340
- rapid infiltration techniques, 345
- rapid prototyping, 459
- raster patterns, 462, 463
- reaction dimensionality, in crystallization of
  - glass powders, 88
- reactive ion etching (RIE) technologies, 253
- reactive melt infiltration (RMI), 353
  - compared with CVI, 354–355, 355, **356**
  - continuous fiber-reinforced composites, **356**
  - cost analysis of component fabrication with, 381–382
  - fast processing times of, 383
  - general process
    - criteria for fiber and interphase selection, 356–358, **357**
    - green body formation, 359–360
    - infiltration and reaction, 360–362, **361**, **362**
    - preform, 358–359, 359, 360
    - steps in, 356
    - processing and property issues, 382–383
- REFEL process, 367–368
- reinforcement, and microwave processing, 505
- replica molding (REM), 254, 255
- replication technique, for porous materials, 217
- representative volume elements, for sintering studies, 25
- resin transfer molding (RTM), in green body formation, 359–360
- rheology
  - defined, 162
  - flow behavior in, 162–166, 163, **164**, **165**, 165
  - time-dependent behavior, 164–165, 165
  - viscoelasticity, 166–168, 167, 168
- Riedel model, 26
- Rietveld refinement, 60
- RMI. *See* reactive melt infiltration
- rotor, gelcast  $\text{Si}_3\text{N}_4$  radial-vane turbine, 214, 216
- RTM. *See* resin transfer molding
- sacrificial fillers, 249
- sacrificial templating, of porous materials, 213, 217, 220
- Saitou model, 435
- SAMIM. *See* solvent-assisted micromolding
- Scherer cell model, 7, 8, 9, 26, 100
- Scherer's self-consistent model, 115
- self-propagating high-temperature synthesis (SHS), 391
- SEP. *See* Société Européenne de Propulsion
- Sepcarb®, 343–344
- Sepcarbinox materials, 344
- Sepcarb materials, 344
- SFF. *See* solid free-form fabrication
- SGC. *See* sintered glass-ceramics
- shaping, 148, 149
  - by coagulation and gelation methods, 171–172, 172
  - defined, 169
  - filtration techniques, 169–171, 170
  - suspension forming techniques, 169, **169**
- Sharp Edge Flight Experiment (SHEFEX), 381
- SiBCN-based ceramic membrane, 246–247, 247
- SiBCN fibers, 243
- SiC-CNT composite, fracture surface of, 533
- SiC/SiC composites
  - CVI, 336
  - microwave-assisted processes for, 345
- SiC/MoSi<sub>2</sub>-SiC, tensile data for, 374–375, **375**
- SiCN-based ceramic membrane, 246
- SiCN ceramic fibers, 243
- SiC-SiC composites
  - CVI-made, 355, 355
  - mechanical properties of, 370
  - slurry and melt-infiltrated, 355, 355
  - tensile data for, 374–375, **375**
- Si-C system, peritectic temperature of, 289



- SiC-TiC eutectic composite, microstructure of, 290, 291
- SiC-ZrB<sub>2</sub> eutectic composite, microstructure of, 290, 291
- silanol groups, in sol-gel process, 184–185
- SILCOMP process, 353, 368–369
- kinetics of, 365
  - parabolic reaction rate and, 366
- silica, sol-gel derived, 195
- silica matrix composites, reinforced with SiC-fiber mats, 534, 535–537
- silica suspensions, zeta potentials of, 159, 159
- silicate glasses
- crystallization of, 79
  - internal and surface nucleation in, 82
- silicides, thermodynamic calculations for, 393, 394
- silicon carbide (SiC)
- properties of, 271–272
  - reaction bonding and REFEL process, 367–368, 369
  - SILCOMP and HiPerComp, 368
- silicon carbide (SiC) and silicide matrices
- in melt-infiltration process, 371–372
  - microporous carbon preforms infiltration with, 374
  - MoSi<sub>2</sub>-containing composite, 372, 373, 374
  - room temperature flexure properties of, 372, 373, 374
  - tensile strength of, 374–375, 375
- silicon carbide (SiC) fibers
- electrokinetic properties of, 535
  - properties of, 357
  - synthesis of, 242
- silicon carbide (SiC) formation, chemistry of, 319–325
- silicon carbide (SiC) matrix, industrial applications for, 343–344
- silicon nitride (Si<sub>3</sub>N<sub>4</sub>)
- CVD of, 275–277, 276–278
  - properties of, 271–272
- silicon nitride (Si<sub>3</sub>N<sub>4</sub>) films
- effects of CVD conditions on structure of CVD, 276, 277
  - surface morphology of CVD, 276, 278
- silicon oxycarbide (SiOC)-based materials, preceramic precursors for, 236
- Si-C kinetics, 366
- Si-doped BN, 382
- sintered ceramics, 556
- sintered glass-ceramics (SGC), 75, 122, 123
- for architectural applications, 121, 121
  - for dental applications, 126–127, 127
  - for LTCC, 123–126, 124, 125, 125
  - processing routes for, 76, 76
  - from wastes, 122–123, 123
- sintered glasses (SGs), 75
- sintering
- applications for, 36
  - and continuum theory of, 98–100
  - defined, 3, 46
  - deformation in, 19–22, 22
  - densification in, 19–22, 22
  - field-assisted, 29–34, 31–34
  - grain growth during, 45–46, 46
  - with large rigid inclusions, 114–117, 116
  - liquid-stage, 15–19, 16–19, 77
  - microstructure-based models, 22–27, 26, 27
  - in microwave processing, 501–502, 503, 504–505
  - plasma-assisted, 43
  - pressureless, 47
  - simultaneous, 107, 109–110
  - with small rigid inclusions
    - dissolution phenomena, 113, 113–114, 115
    - steric effects, 110–113, 111, 112  - solid-state, 9–15, 10, 10
  - stages of, 4, 5
  - stress-assisted, 27–29, 28, 29
  - of surface crystallization glass-ceramic, 121, 122
  - thermodynamic driving force for, 4–6
  - viscous, 6–9, 7, 8, 76, 92–93
    - anisotropic sintering and particle arrangement, 98–103, 101, 103
    - bimodal PSD and aggregates, 94, 100, 101
    - nonisotropic particle arrangement, 102–104, 104
    - particle shape, 95–97, 96
    - particle size, 93–94
    - PSD, 97, 98
    - submicron particles, 94–95, 95
- sintering behavior, flash, 66
- sintering map, for copper powder, 10, 11

- sintering powder compact, electrical conductivity of, 54–55
- sintering practice, 34–36
  - goal of, 3
  - processing defects in, 36
- sintering process
  - effective vs. applied pressure in, 58–59
  - mass transport during, 46–51, **48**, **51**
- sintering theory, 3, 34
- site saturation phenomenon, 79
- skeletal microstructures, 94, 95
- slip casting, 151, 199
  - classification of, 169, **169**
  - limitations of, 170–171
  - mechanism of, 169–170, 170
- slurries
  - processing, 177
  - properties of, 244
- slurry technique, 119
- Snecma Propulsion Solide, 343, 344
- Société Européenne de Propulsion (SEP), 315
- sodium sulfur batteries, Na- $\beta$ -alumina tubes for, 530
- SOFC. *See* solid oxide fuel cells
- sol-gel matrices, immobilization of
  - biomolecules in, 195
- sol-gel process, 183–184, 200
  - advantages of, 190, 194
  - aerogels in, 185–186, 186
  - applications, 187–194, 188, 189, 191, 193
  - biocatalysis studies in, 192–193
  - biomolecular studies, 195
  - drying in, 185
  - method/technique/approach, 184–187, 186, **187**, 187, 188
- sol-gel-slurry method, 119, 120
- solid free-form fabrication (SFF), 459
  - for assembling 3-D ceramic objects, 480
  - basic structural features during, 464, 465
  - CAD, 460–465, 461, 462
  - component deposition and postprocessing, 465–466, **466**, 467
  - droplet-based techniques, 466–471, 469, 470, 472
  - filament-based techniques, **466**, 467, 471–480
  - steps in, 459–460
  - wax-based droplet, 479
- solidification of composite materials, 417.
  - See also* directional solidification
- solid oxide fuel cells (SOFCs)
  - applications, 66
  - EPD in fabrication of, 532
  - SG and SGC for seals and solders for, 119–121
- solid-state reactions, in microwave processing, 501
- solid-state routes, for production of CMCs, 352
- solid-state sintering, 9–15, **10**, 10
  - final-stage models for, 14–15
  - initial-stage models, 9–12, 11, **12**
  - intermediate-stage models, 12–14, 13
  - pore-boundary interaction in, 15
- solvent-assisted micromolding (SAMIM), 254, 255
- solvent/binder removal, in microwave processes, 504
- solvents
  - dielectric properties of, **500–501**
  - for EPD fabrication of CMC, 537
  - for EPD suspensions, 530
  - organic, 152
- space vehicles, melt-infiltrated CMCs in, 381
- spark plasma sintering (SPS), 30–32, 31, 32, 43, 449
- splats, in plasma-spraying process, 553, 553
- split-ring resonator-like (SSR) cross-sectional features, 448
- spraying gun, 177. *See also* plasma spraying process
- SPS. *See* spark plasma sintering
- stabilizing moieties, 160
- stereolithography
  - of disk with vias, 462
  - two-photon, 252
- stereolithography files, 460–462, 461
- steric mechanisms, in polymeric stabilization, 159–160, 160
- steric stabilization
  - Napper's model of, 161
  - potential energy curve for, 162, 162
- Stern model, of double layer, 156, 157
- strength, of ceramic materials, 148
- stress, and densification, 49
- stress-assisted sintering, 27–29, 28, 29
- substrates, properties of, 244

- supercritical drying, 226
- surface diffusion, in pressureless sintering, 47
- surface nucleation
  - data analysis, 80
  - kinetics, 79–82, 80–82
  - sites, 82
    - mechanical damage, 83, 83–84
    - solid foreign particles, 84–85, 85
- surface nucleation density, influence of glass
  - particle size on, 86, 86
- surface treatment, 148
- suspension forming techniques, classification of, 169, **169**
- suspensions, in colloidal science, 153
- suspensions forming, slip casting for, 151
- symbols, table of, **127–128**
- tape casting
  - device, 173, 173
  - main market of, 173
- temperature distributions in PECS
  - influence of die design on, 51–58, 54–58
  - temperature measurement in, 51–53, 52
- temperature gradient (TG)-CVI, on large
  - production scale, 353
- temperature measurements, in microwave
  - technology, 495
- temperature profile, for PECS, 44
- textured materials, gelcasting of, 214–217, 218–220
- TGA. *See* thermogravimetry analysis
- thermal barrier coatings (TBCs), YSZ-based, 557
- thermal expansion coefficients (TECs), 555
- thermal-gradient CVI, 329, 330
- thermal instabilities (runaways), 331
- thermal insulation, in PECS, 55–58, 56–58
- thermodynamics, of combustion synthesis, 392–396, **394, 395**
- thermogravimetry analysis (TGA), 239
- thermophotovoltaic (TPV) devices, 448
- thermoshock resistance, of plasma-sprayed
  - ceramic, 561
- thick film coatings, 309
- thin film process, CVD as, 307
- thixotropy, 164
- 3-D printing (3DP), 459, 471
- throat and chamber model, of flow through
  - random porous structures, 365
- TiAl<sub>4</sub>V alloys, EPD of, 531
- TiN compact, in PECS tool setups, 57, 57
- titanium silicide (Ti<sub>5</sub>Si<sub>3</sub>), in electromagnetic
  - CS, 401
- TMK theory, 421–422
- tool paths, 462, 463–464
- topokinetic model, for calculation of DTA
  - curves, 90, 91
- toughness, of ceramic materials, 148
- trichlorosilane, in SiC formation, 323
- tungsten carbide powders, 498
- tungsten silicide (WSi<sub>2</sub>), in electromagnetic
  - CS, 401
- Ultra Efficient Engine Technology Program (UEET), 377
- vacuum plasma spraying (VPS), 563
- van der Waals force, in colloidal science, 153–154
- viscoelastic fluid, 167, 168
- viscoelasticity, of ceramic suspensions, 166–168, 167, 168
- viscosity
  - effective shear, 109, 111
  - in gelcasting systems, 208, 209
  - measured effective, 116
- viscous flow, 49
- viscous pastes, 150, 151
- viscous-phase silicate processing, 75
  - in glass forming and crystallization, 76
  - sintering and melting in, 78
  - sintering of glass and crystal powders, 76, 76–78, 77
- viscous sintering, 6–9, 7, 8, 76, 92–93
  - anisotropic sintering and particle
    - arrangement, 98–103, 101, 103
  - bimodal PSD and aggregates, 94, 100, 101
  - and continuum theory of sintering, 98–100
  - kinetics of, 6–7, 78
  - models for, 8–9
  - nonisotropic particle arrangement, 102–104, 104

- particle shape, 95–97, 96
- particle size, 93–94
- PSD, 97, 98
- retardation of
  - simultaneous sintering and crystallization, 107, 109–110
  - sintering with concurrent surface crystallization, 104, 104–107, 105, 106, 107, 108
- stages of, 6
- submicron particles, 94–95, 95
- voltammetry, cyclic, 193–194, 194
- volumetric heating
  - in microwave processing, 509
  - offered by microwaves, 505
- wall thickness, in I-CVI processes, 315
- Washburn equation, 364
- wastes, SGC and GMC from, 122–123, 123
- water
  - in ceramic processing, 152
  - dielectric properties of, **500**
- wax-based inks, 470
- Weibull modulus, 148
- “wet” gel, 184
- wet powder spraying, 177
- wet processing, 151
- wetting behavior
  - bad, 116–117
  - of rigid inclusions, 112, 112
- whiteware, domestic, industrial production of, 529
- xerogels
  - microstructures of, 188
  - supercritically dried, **187**
- YAG. *See* yttrium aluminum garnet
- Yajima process, 242
- Young-Laplace equation, 47
- Young’s modulus, 555, 557
- yttria-stabilized zirconia (YSZ)
  - plasma-sprayed coating, 554, 554–555, 555
  - plasma-spraying of, 560–561, 561
- yttria-stabilized zirconia (YSZ) coating
  - columnar grain boundary in, 303, 305
  - cross-sectional microstructure of, 303, 304
  - for gas turbine blades, 300–301, 302, 303, 304, 305
- yttria-stabilized zirconia (YSZ) eutectic, 423
- yttria-stabilized zirconia (YSZ) film, 297
- yttria-stabilized zirconia (YSZ) splats, 553, 553
- yttrium aluminum garnet (YAG), 438, 439, 442, 443, 444
- yttrium oxides, in eutectic growth, 428
- zero point of charge (ZPC), 155
- zeta potential, 156
- zircon, 556, **556**
- zirconia
  - in eutectic growth, 428
  - plasma spraying of, **560**
- zirconia, nanograined, “flash” sintering
  - behavior of, 66